CHALMERS

Gothenburg 2010

A Workshop on Numerical Ship Hydrodynamics

Proceedings, Volume II

Editors
LARS LARSSON
FREDERICK STERN
MICHEL VISONNEAU

Sponsor

Department of Shipping and Marine Technology
Hydrodynamics
CHALMERS UNIVERSITY OF TECHNOLOGY
Gothenburg, Sweden, 2010
Report No. R-10:122
ISSN No. 1652-9189

Gothenburg 2010

A Workshop on Numerical Ship Hydrodynamics

Proceedings, Volume II

Editors

LARS LARSSON

FREDERICK STERN

MICHEL VISONNEAU

Preface

The Gothenburg 2010 Workshop on Numerical Ship Hydrodynamics was held in Gothenburg on 8-10 December, 2010. It was the sixth in a series of workshops held alternatively in Gothenburg and Tokyo since 1980. The purpose has been to assess the performance of contemporary CFD codes used in hydrodynamics. In the present workshop three hulls of different types were used and 18 test cases using these hulls were specified by the organizers. 33 groups carried out computations for one or more cases and reported the results to the organizers who compiled the results. The present Volume II of the Proceedings contains a description of the hulls and test cases, the complete set of computed results and the papers on the computations submitted by each group. Volume I, published after the workshop, contains an introduction to the series of workshops, reviews of the submitted results written by the organizers and a summary of discussions at the workshop. There is also CD with the two Volumes and a table containing detailed information about each of the participating methods. The printed Volumes are in black and white, so for color pictures in the papers, see the CD.

Gothenburg in December 2010

Lars Larsson
For The Organizing Committee

Contents (VOLUME II)

PART 1: Hulls and Test Cases

Hulls

KRISO TANKER (KVLCC2) 1
MOERI Container Ship (KCS) 2
US Navy Combatant (DTMB 5415) 3

Test Cases

List of Test Cases and Requested Computations 4

KVLCC2 Case 1.1a 5
KVLCC2 Case 1.1b 7
KVLCC2 Case 1.2a 8
KVLCC2 Case 1.2b 9
KVLCC2 Case 1.4a 10
KVLCC2 Case 1.4b 12
KVLCC2 Case 1.4c 14

KCS Case 2.1 17
KCS Case 2.2a 18
KCS Case 2.2b 19
KCS Case 2.3a 20
KCS Case 2.3b 22
KCS Case 2.4 24

DTMB 5415 Case 3.1a 26
DTMB 5415 Case 3.1b 27
DTMB 5415 Case 3.2 28
DTMB 5415 Case 3.5 29
DTMB 5415 Case 3.6 31

PART 2: Computed Results

KVLCC2

Case 1.1a 33
Case 1.1b 79
Case 1.2a 91
Case 1.2b 93
Case 1.4a 107
Case 1.4b 121
Case 1.4c 127

KCS

Case 2.1 137
Case 2.2a 187
Case 2.2b 189
Case 2.3a 217
Case 2.3b 243
Case 2.4 247

DTMB 5415

Case 3.1a 271
Case 3.1b 315
Case 3.2 345
Case 3.5 357
Case 3.6 391

PART 3: Papers

CDadapco Sven Enger, Milovan Perić,Robinson Perić:
Simulation of Flow around KCS-Hull.....413

CEHINAV Jorge Izquierdo, Leo M. González:
URANS Computations of a DTMB 5415 419

Chalmers Lu Zou, Lars Larsson:
CFD Prediction of the Local Flow around the KVLCC2 Tanker in Fixed Condition 425

CSSRC Zhirong Zhang, Chengsheng Wu, Shaofeng Huang, Feng Zhao, Zhenping Weng:
Numerical Simulation of Free Surface Flow of KCS and the Interaction between Propeller and Hull
.....431

CSSRC Chengsheng Wu, Lei Yang, Zhirong Zhang, Feng Zhao, Kai Yan:
CFD Simulation of Ship Model Free to Sinkage and Trim Advancing in Calm Water.....437

CTO Tomasz Bugalski, Paweł Hoffmann:
Numerical Simulation of the Interaction between Ship Hull and Rotating Propeller 443

ECN-CNRS G.B. Deng, A. Leroyer, E. Guilmineau, P. Queutey, M. Visonneau and J. Wackers:
Verification and Validation for Unsteady Computation 449

ECN-HOE L. Gentaz, A. Drouet, P.-E. Guillerm, R. Luquet, C. Monroy, O. Payen, G. Reliquet,
B. Alessandrini, P. Ferrant, E. Jacquin:
Numerical Simulation of Ship Seakeeping by the SWENSE Functional Decomposition Method.....455

FLOWTECH Michał Orych, Lars Larsson, Björn Regnström:
Viscous Free Surface Calculations for the KCS Hull 463

FOI C. Fureby, N. Alin, M. Liefvendahl:
Large Eddy Simulation of the Flow Past the DTMB 5415 Surface Combatant Hull.....469

FORCE Claus D. Simonsen, Fredrick Stern:
CFD Simulation of KCS Sailing in Regular Head Waves 475

GL-UDE B. el Moctar, J. Kaufmann, J. Ley, J. Oberhagemann, V. Shigunov, T. Zorn:
Prediction of Ship Resistance and Ship Motions Using RANSE.....481

HSVA Marco Schneider:
RANS Simulation of the Flow around the KVLCC2 Tanker Using the FreSCo+ Code 493

IHI-WISDAM-UTokyo Hiromichi Akimoto, Takuya Omori, Hiroyuki Saito, Rahaman Md. Masiur:
Numerical Simulation of KCS Container Carrier in Head Wave Condition.....497

IIHR Tao Xing, Pablo Carrica, Frederick Stern:
Large-Scale RANS and DDES Computations of KVLCC2 at Drift Angle 0 Degree.....501

IIHR Hamid Sadat-Hosseini, Pablo M. Carrica, Ho Kim, Toda Yasuyuki, Frederick Stern:
URANS Simulation and Validation of Added Resistance and Motions of the KVLCC2 Crude Carrier
with Fixed and Free Surge Conditions 507

IIHR Alejandro M. Castro, Pablo M. Carrica, Frederick Stern:
Full Scale Self-Propulsion Computations with Discretized Propeller on KRISO Container Ship KCS 513

IIHR Pablo M. Carrica, Huiping Fu, Frederick Stern:
Self-Propulsion Free to Sink and Trim and Pitch and Heave in Head Waves of a KCS Model 519

IIHR Shanti Bhushan, Thad Michael, Jianming Yang, Pablo Carrica, and Frederick Stern:
Fixed Sinkage and Trim Bare Hull 5415 Simulations Using CFDSHIP-IOWA.....525

IIHR-SJTU Huiping Fu, Thad Michael, Pablo M. Carrica:
A Method to Perform Self-Propulsion Computations with a Simplified Body-Force Propeller Model 531

IST L. Eça, M. Hoekstra, H.C. Raven:
Calculation of the Flow around the KVLCC2 Tanker: Case 1.1a.....537

Kyushu University Changhong Hu, Masashi Kashiwagi:
CIP Based Cartesian Grid Method for Prediction of Nonlinear Ship Motions 543

MARIC H. Yu, X M. Feng, Q. Wu, J B. Wang and R Q. Cai:
Prediction of Ship Resistance and Wake Using Multi-Block Structural Grid.....547

MARIC Q. Wu, X M Feng, H. Yu, J B. Wang and R Q. Cai:
Prediction of Ship Resistance and Propulsion Performance Using Multi-Block Structural Grid 551

MARIC X M. Feng, H M. Chen, Q. Wu, H. Yu, J B. Wang and R Q. Cai:
Prediction of 5415 Resistance and Wave Pattern Using Multi-Block Structural Grid.....557

MARIN Bram Starke, Auke van der Ploeg, Hoyte Raven:
Viscous Free Surface Flow Computations for Self-Propulsion Conditions Using PARNASSOS 563

MOERI Jin Kim, IL-Ryong Park, Kwang-Soo Kim and Suak-Ho Van:
Feasibility Study on Numerical Towing Tank Application to Predictions of Resistance and Self-Propulsion Performances for a Ship.....569

NavyFOAM Sung-Eun Kim, Bong J. Rhee, Hua Shan, Joseph Gorski, Eric G. Paterson, Kevin Maki:
A Scalable Multiphase RANSE Capability Based on Object-Oriented Programming and Its Applications to Ship Hydrodynamics.....575

NMRI Takanori Hino, Kunihide Ohashi, Hiroshi Kobayashi:
Flow Simulations Using Navier-Stokes Solver SURF 581

NSWC-PC Mark Hyman:
Computation of Sinkage and Trim of a Bare-Hull 5415 at Three Froude Numbers 587

NTNU Bingjie Guo, Sverre Steen:
Computional Study on Ship Resistance and Flow Field of KVLCC2 591

SNUTT Ju Hyun Lee and Shin Hyung Rhee:
Flexible CFD Meshing Strategy for Prediction of Ship Resistance and Propulsion Performance.....601

Southampton&QinetiQ J B Banks, A B Phillips, P W Bull, S R Turnock:
RANS Simulations of the Multiphase Flow around the KCS Hull Form 607

SSPA Keunjae Kim, Da-qing Li:
Estimation of Numerical Uncertainty of SHIPFLOW in Self-Propulsion Simulation of KCS.....613

SSRC W. Jin, Q. Gao, D. Vassalos:
The Prediction of KCS Resistance and Self-Propulsion by RANSE 621

SSRC Q. Gao, W. Jin, D. Vassalos:
Computation of Wave Diffraction by RANS Approach 627

SSRC Q. Gao, W. Jin, D. Vassalos:
Simulation of Roll Decay by RANS Approach.....633

SVA Lars Ole Lübke:
Investigation of the KCS at Froude Number Fr = 0.26 639

TUHH M. Manzke, T. Rung:
Resistance Prediction and Sea Keeping Analysis with Fresco+.....645

TUHH&ANSYS M.Greve, M. Abdel-Maksoud, S. Eder, J. De Causmaecker:
Unsteady Viscous Flow Calculation around the KCS-Model With and Without Propeller under Consideration of the Free Surface 651

UoGe Stefano Brizzolara & Diego Villa:
Multiphase URANS Simulations of Surface Combatant Using Star-CCM+ 657

VTT J. Martio, A. Sanchez Caja, T. Sipilä´, I. Saisto, T. Siikonen:
Simulation of Free Surface Flow Using Code FINFLO for KVLCC2 and KCS Cases.....663

PART 1: Hulls and Test Cases

Hulls

The same hulls as in the 2005 workshop will be used, namely:

1) The Korean VLCC designed at MOERI: KVLCC2

2) The Korean container ship designed at MOERI: KCS

3) The US combatant model: DTMB 5415

KRISO VLCC
KVLCC2

Description:

KVLCC2 is the second variant of the MOERI tanker with more U-shaped stern frame-lines (Van et al, 1998a, b, Kim et al 2001). It differs from the KVLCC2M, used in the CFD Workshop Tokyo in 2005 (Hino, 2005), mainly at the stern contour near the propeller shaft. The difference is explained in Hino (2005). Since turbulence data are required the original hull (KVLCC2) is used in the present Workshop. Turbulence data were obtained at Postech, see Lee et al (2003).

Hull data are as follows:

Main particulars		Full scale
Length between perpendiculars	L_{PP} (m)	320.0
Length of waterline	L_{WL} (m)	325.5
Maximum beam of waterline	B_{WL} (m)	58.0
Depth	D (m)	30.0
Draft	T (m)	20.8
Displacement	&Delta (m^3)	312622
Wetted area w/o rudder	S_W (m^2)	27194
Wetted surface area of rudder	S_R (m^2)	273.3
Block coefficient (CB)	&Delta /($L_{PP}B_{WL}$ T)	0.8098
Midship section coefficient (CM)		0.9980
LCB (%L_{PP}), fwd+		3.48
Vertical Center of Gravity (from keel)	KG (m)	18.6
Metacentric height	GM (m)	5.71
Moment of Inertia	K_{xx}/B	0.40
Moment of Inertia	K_{yy}/L_{PP}, K_{zz}/L_{PP}	0.25

Service speed	
U (knots)	15.5
Fr	0.142

MOERI Container Ship (KCS)

Description:

The KCS was conceived to provide data for both explication of flow physics and CFD validation for a modern container ship with a bulbous bow (i.e., ca. 1997). The Korea Research Institute for Ships and Ocean Engineering (now MOERI) performed towing tank experiments to obtain resistance, mean flow data and free surface waves (Van et al, 1998a,b, Kim et al, 2001). Self propulsion tests were carried out at the Ship Research Institute (now NMRI) in Tokyo and are reported in the Proceedings of the CFD Workshop Tokyo in 2005 (Hino, 2005). Data for pitch, heave, and added resistance are also already available from Force/Dmi measurements reported in Simonsen et al. (2008).

No full scale ship exists.

Hull data are as follows:

Main particulars		Full scale
Length between perpendiculars	L_{PP} (m)	230.0
Length of waterline	L_{WL} (m)	232.5
Maximum beam of waterline	B_{WL} (m)	32.2
Depth	D (m)	19.0
Draft	T (m)	10.8
Displacement	&Delta (m^3)	52030
Wetted area w/o rudder	S_W (m^2)	9424
Wetted surface area of rudder	S_R (m^2)	115.0
Block coefficient (CB)	&Delta /($L_{PP}B_{WL}$ T)	0.6505
Midship section coefficient (CM)		0.9849
LCB (%L_{PP}), fwd+		-1.48
Vertical Center of Gravity (from keel)	KG (m)	7.28
Metacentric height	GM (m)	0.60
Moment of Inertia	K_{xx}/B	0.40
Moment of Inertia	K_{yy}/L_{PP}, K_{zz}/L_{PP}	0.25
Propeller center, long. location (from FP)	x/L_{PP}	0.9825
Propeller center, vert. location (below WL)	$-z/L_{PP}$	0.02913

Service speed	
U (knots)	24.0
Fr	0.26

US Navy Combatant, DTMB 5415

Description:

Model 5415 was conceived as a preliminary design for a Navy surface combatant ca. 1980. The hull geometry includes both a sonar dome and transom stern. Propulsion is provided through twin open-water propellers driven by shafts supported by struts.

No full-scale ship exists.

The model tests data for the 5415 includes:

1. Local flow measurements (Mean velocity and cross flow vectors). Olivieri et al (2001).
2. PIV-measured nominal wake in regular head waves (Mean velocity, turbulent kinetic energy, and Reynolds stresses). Longo et al (2007).
3. Resistance, sinkage, trim, and wave profiles. Olivieri et al (2001).
4. Wave diffraction (Waves, 1st harmonic amplitude of mean velocities, turbulent kinetic energy, and Reynolds stresses).Longo et al (2007), Hino et al (2005).
5. Roll decay (Motion, free surface, mean velocities). Irvine et al (2004).

Hull data and conditions are as follows:

Main particulars		Full scale
Length between perpendiculars	L_{PP} (m)	142.0
Length of waterline	L_{WL} (m)	142.18
Maximum beam of waterline	B_{WL} (m)	19.06
Draft	T (m)	6.15
Displacement	&Delta (m^3)	8424.4
Wetted area w/o rudder	S_W (m^2)	2972.6
Wetted surface area of rudder	S_R (m^2)	30.8
Block coefficient (CB)	&Delta /($L_{PP}B_{WL}$ T)	0.507
Midship section coefficient (CM)		0.821
LCB (%L_{PP}), fwd+		-0.683
Vertical Center of Gravity (from keel)	KG (m)	7.5473
Metacentric height	GM (m)	1.95
Moment of Inertia	K_{xx}/B	0.37
Moment of Inertia	K_{yy}/L_{PP}, K_{zz}/L_{PP}	0.25

Service speed	
U (knots)	18.0, 30.0
Fr	0.248, 0.413

Test Case Description

List of Test Cases and Requested Computations:

Case Number	Hull	Attitude	Measured quantity
1.1a	KVLCC2	FX_0	Mean velocity, Reynolds stresses (Postech WT)
1.1b		FX_0	Wave pattern (MOERI)
1.2a		FX_0	Resistance (MOERI)
1.2b		$FR_{z\theta}$	Resistance, sinkage and trim (MOERI)
1.4a		$FR_{z\theta}$	Pitch, heave, added resistance (INSEAN)
1.4b		$FR_{z\theta}$	Pitch, heave, added resistance (NTNU)
1.4c		$FR_{xz\theta}$	Surge, Pitch, heave, added resistance (Osaka Univ)
2.1	KCS	FX_0	Wave pattern, mean velocities (MOERI)
2.2a		FX_0	Resistance (MOERI)
2.2b		$FR_{z\theta}$	Resistance, sinkage and trim (MOERI)
2.3a		FX_0	Self propulsion at ship point (thrust, torque, force balance or RPM, mean velocity), local flow (NMRI)
2.3b		$FR_{z\theta}$	Self propulsion at model point (thrust, torque, force balance or RPM), sinkage and trim (FORCE)
2.4		$FR_{z\theta}$	Pitch, heave, added resistance (FORCE)
3.1a	DTMB 5415	$FX_{\sigma\tau}$	Mean velocity, resistance, wave pattern (INSEAN)
3.1b		$FX_{\sigma\tau}$	Mean velocity, resistance, wave pattern, Reynolds stresses (IIHR)
3.2		$FR_{z\theta}$	Resistance, sinkage and trim (INSEAN)
3.5		$FX_{\sigma\tau}$	Wave diffraction, Mean velocity (IIHR)
3.6		FR_{φ}	Roll decay (IIHR)

Hull Attitude Definitions:

The notation for the hull attitude is as follows:

- FX_0 = fixed at zero Sinkage and Trim
- $FX_{\sigma\tau}$ = fixed at dynamic Sinkage and Trim
- $FR_{z\theta}$ = free to heave and pitch
- $FR_{xz\theta}$ = free to surge, heave and pitch
- FR_{φ} = free to roll

KVLCC2 Case 1.1a

Conditions:

- Without rudder
- Calm water conditions
- FX_0
- $Re = 4.6\times10^6$, double model

References:

Van, S.H., Kim, W.J., Yim, D.H., Kim, G.T., Lee, C.J., and Eom, J.Y., (1998a), "Flow Measurement around a 300K VLCC Model," Proceedings of the Annual Spring Meeting, SNAK, Ulsan, pp. 185-188

Lee, S.-J., Kim, H.-R., Kim, W.-J., and Van, S.-H., (2003), "Wind tunnel tests on flow characteristics of the KRISO 3,600 TEU containership and 300K VLCC double-deck ship models", J. Ship Res., Vol. 47, No 1, pp. 24-38

Table/Figure #	Items
1.1a-1	Cross flow vectors, streamlines and axial velocity contours at x/L_{PP}=0.85
1.1a-2	Cross flow vectors, streamlines and axial velocity contours at x/L_{PP}=0.9825
1.1a-3	Cross flow vectors, streamlines and axial velocity contours at x/L_{PP}=1.1
1.1a-4	Total wake fraction (w_T) on the propeller plane (x/L_{PP}=0.9825) [propeller radius R=0.0425m, shaft centerline at z/L_{PP}= -0.04688]
1.1a-5	Velocity on the propeller plane (x/L_{PP}=0.9825) at z/L_{PP} = -0.05075
1.1a-6	Turbulent Kinetic energy (k) contours at x/L_{PP}=0.9825
1.1a-7	$\overline{uu}$ contours at x/L_{PP}=0.9825
1.1a-8	$\overline{vv}$ contours at x/L_{PP}=0.9825
1.1a-9	$\overline{ww}$ contours at x/L_{PP}=0.9825
1.1a-10	$\overline{uv}$ contours at x/L_{PP}=0.9825
1.1a-11	$\overline{uw}$ contours at x/L_{PP}=0.9825
1.1a-12	Hull surface pressure contours (port side view)
1.1a-13	Hull surface pressure contours (back view)
1.1a-14	Hull surface pressure contours (bottom view)
1.1a-15	Limiting streamlines (port side view)

Remarks:

- Total wake fraction $w_T = 1 - \frac{u}{U}$, where u is the total local velocity, U is the undisturbed velocity (ship speed).
- ϕ is the circumferential angle, counterclockwise from 0° (top position) to 360°; propeller radius R=0.0425m, shaft centerline O is at z/L_{PP}= -0.04688. The coordinate system is shown as following figure:

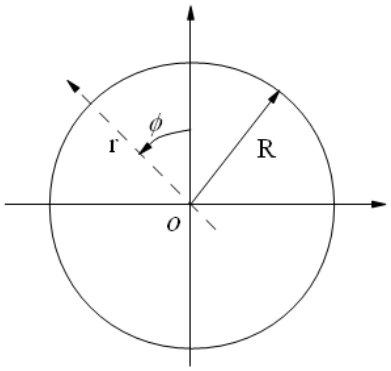

KVLCC2 Case 1.1b

Conditions:

- Without rudder
- Calm water conditions
- FX_0
- Re = 4.6×106, Fr = 0.142

References:

Kim, W.J., Van, S.H. and Kim, D.H., (2001), "Measurement of flows around modern commercial ship models,", Exp. in Fluids, Vol. 31, pp 567-578

Van, S.H., Kim, W.J., Yim, G.T., Kim, D.H., and Lee, C.J., (1998b), "Experimental Investigation of the Flow Characteristics Around Practical Hull Forms," Proceedings 3rd Osaka Colloquium on Advanced CFD Applications to Ship Flow and Hull Form Design, Osaka, Japan

Table/Figure #	Item
1.1b-1	Wave elevation contours
1.1b-2	Longitudinal wave cut at y/L_{PP} = -0.0964
1.1b-3	Longitudinal wave cut at y/L_{PP} = -0.1581
1.1b-4	Longitudinal wave cut at y/L_{PP} = -0.2993
1.1b-5	Grid density distribution along the waterline, and in transverse and vertical directions at mid-ship

KVLCC2 Case 1.2a

Conditions:

- With rudder
- Calm water conditions
- FX_0
- $Re = 4.6\times10^6$, $Fr = 0.142$

References:

Not yet available.

Table/Figure #	Item
1.2a-1	Computed C_T, C_F and C_{PV} of different grid densities
1.2a-2	V&V results for C_T, C_F and C_{PV}

Computation Instructions:

1. Resistance coefficients are based on wetted surface area (S/L^2) = 0.2682 with rudder for static orientation in calm water.
2. Comparison Error, $E\%D = (D-S)/D\times100$, where D is the EFD value, and S is the simulation value.
3. Relative change in solution: $\varepsilon_{12}\%S_1 = |(S_1-S_2)/S_1|\times100$, "1" refers to the finest grid.
4. Iterative uncertainty U_I is based on fine grid solution.
5. $p_{G,th}$ is the theoretical order of accuracy = order of convection scheme.
6. U_G is the grid uncertainty. $U_{SN} = \sqrt{U_I^2 + U_G^2}$ is the simulation numerical uncertainty.
7. U_D is the data uncertainty.
8. $U_V = \sqrt{U_D^2 + U_{SN}^2}$ is the validation uncertainty.

KVLCC2 Case 1.2b

Conditions:

- With rudder
- Calm water conditions
- $FR_{z\theta}$
- Six speeds:

No.	1	2	3	4	5	6
Froude number (*Fr*)	0.1010	0.1194	0.1377	0.1423	0.1469	0.1515
Reynolds number (*Re*)	3.5×10^6	4.1×10^6	4.8×10^6	4.9×10^6	5.1×10^6	5.2×10^6

References:

Not yet available.

Table/Figure #	Items
1.2b-1	V&V of resistances, sinkage (σ) and trim (τ)
1.2b-2	Coefficients of total resistance (C_T) versus *Fr* (results and uncertainties)
1.2b-3	Sinkage (σ) versus *Fr* (results and uncertainties)
1.2b-4	Trim (τ) versus *Fr* (results and uncertainties)

Note: a positive (+) sinkage value is defined upwards and a positive (+) trim value is defined bow up.

Computation Instructions:

1. Resistance coefficients are based on wetted surface area (S/L^2) = 0.2682 with rudder for static orientation in calm water.
2. Comparison Error, $E\%D = (D-S)/D\times100$, where D is the EFD value, and S is the simulation value.
3. Relative change in solution: $\varepsilon_{12}\%S_1 = |(S_1-S_2)/S_1|\times100$, "1" refers to the finest grid.
4. Iterative uncertainty U_I is based on fine grid solution.
5. $p_{G,th}$ is the theoretical order of accuracy = order of convection scheme.
6. U_G is the grid uncertainty. $U_{SN} = \sqrt{U_I^2 + U_G^2}$ is the simulation numerical uncertainty.
7. U_D is the data uncertainty.
8. $U_V = \sqrt{U_D^2 + U_{SN}^2}$ is the validation uncertainty.

KVLCC2 Case 1.4a

Conditions:

- Without rudder
- Towing condition in head waves
- $FR_{z\theta}$
- $Re = 2.55\times10^6$, $Fr = 0.142$
- Wave height= 60mm
- Three wave lengths:

No.	1	2	3
λ/L_{PP}	0.6	1.1	1.6

References:

Not yet available.

Instructions for Simulation: Simulation should be performed for THREE periods of the incoming wave.

Table/Figure #	Items
1.4a-1	Comparison of 0th and 1st harmonic amplitudes and 1st harmonic phase of the total resistance coefficient (C_T), heave motion (z) and pitch angle (θ)
1.4a-C1	Time histories of total resistance coefficient (C_T), heave motion (z) and pitch angle (θ) (λ/L_{PP}=0.6)
1.4a-C2	Time histories of total resistance coefficient (C_T), heave motion (z) and pitch angle (θ) (λ/L_{PP}=1.1)
1.4a-C3	Time histories of total resistance coefficient (C_T), heave motion (z) and pitch angle (θ) (λ/L_{PP}=1.6)

Note: a positive (+) heave value is defined upwards and a positive (+) pitch value is defined bow up.

Remarks:

- Coordinate system for comparisons is fixed to x=0.0 (FP) on the undisturbed water plane.
- The center of the pitching moment is same as the center of gravity.
- All CFD predicted force coefficients should be reported using the wetted surface area at rest (S_0/L^2). Force coefficients are defined as follows:

$$C_T(t) = \frac{F_x(t)}{\frac{1}{2}\rho U^2 S_0}$$

where F_x is the total resistance.

- Symbols:

A - Incident wave amplitude

A_k - Wave steepness, $A_k = \frac{2\pi A}{\lambda}$

f_ω - Frequency of the incident wave, $\sqrt{\frac{g}{2\pi\lambda}}$

f_e - Encounter frequency, $f_\omega + \frac{U}{\lambda}$

T_e - Encounter period, $\frac{1}{f_e}$

t - Time, at t=0 a crest of the incident wave is coincident with the FP of the ship

U - Ship speed

u, v, w - Velocity components in x, y, z directions, respectively

λ - Incident wave length

$\zeta_T(x, y, t)$ - Free surface elevation, $\frac{z(x, y, t)}{L_{PP}}$

- Instructions:

As a time reference, incident wave height at FP of the ship is defined as

$$\zeta_I(t) = \frac{A}{L_{PP}} \cos\left(2\pi f_e t + \gamma_I\right)$$

where γ_I is the initial phase and is equal to be zero from the present definition of t=0 above. Fourier Series for time history X ($X = C_T$, z, θ and ζ_T) are determined as follows:

$$X_F(t) = \frac{X_0}{2} + \sum_{n=1}^{N} X_n \cos\left(2\pi n f_e t + \Delta\gamma_n\right)$$

$$\Delta\gamma_n = \gamma_n - \gamma_I$$

$$a_n = \frac{2}{T}\int_0^T X(t)\cos\left(2\pi n f_e t\right)dt \quad (n = 0,1,2,\ldots)$$

$$b_n = \frac{2}{T}\int_0^T X(t)\sin\left(2\pi n f_e t\right)dt \quad (n = 1,2,\ldots)$$

$$X_n = \sqrt{a_n{}^2 + b_n{}^2}$$

$$\gamma_n = \tan^{-1}\left(-\frac{b_n}{a_n}\right)$$

X_n is n-th harmonic amplitude and γ_n is the corresponding phase.

KVLCC2 Case 1.4b

Conditions:

- Without rudder
- Towing condition in head waves
- $FR_{z\theta}$
- Five combined test conditions:

Condition No.	C1	C2	C3	C4	C5
Speed (m/s)	0.0	1.047	1.047	1.047	1.336
Froude number (Fr)	0.0	0.142	0.142	0.142	0.182
Reynolds number (Re)	0.0	5.4×10^6	5.4×10^6	5.4×10^6	6.9×10^6
λ/L_{PP}	0.9171	0.6364	0.6364	0.9171	0.6364
H_s (mm)	150	30	150	150	150

References:

Not yet available.

Instructions for Simulation: Simulation should be performed for THREE periods of the incoming wave.

Table/Figure #	Items
1.4b-1-1	Harmonic amplitudes and phases of the total resistance (R_T), heave motion (z), pitch angle (θ) (λ/L_{PP} = 0.9171, measured Hs = 122.66 mm, nominal Hs = 150 mm, Fr = 0.0)
1.4b-1-2	Harmonic amplitudes and phases of the total resistance (R_T), heave motion (z), pitch angle (θ) (λ/L_{PP} = 0.6364, measured Hs = 27 mm, nominal Hs = 30 mm, Fr = 0.142)
1.4b-1-3	Harmonic amplitudes and phases of the total resistance (R_T), heave motion (z), pitch angle (θ) (λ/L_{PP} = 0.6364, measured Hs = 140 mm, nominal Hs = 150 mm, Fr = 0.142)
1.4b-1-4	Harmonic amplitudes and phases of the total resistance (R_T), heave motion (z), pitch angle (θ) (λ/L_{PP} = 0.9171, measured Hs = 138 mm, nominal Hs = 150 mm, Fr = 0.142)
1.4b-1-5	Harmonic amplitudes and phases of the total resistance (R_T), heave motion (z), pitch angle (θ) (λ/L_{PP} = 0.6364, measured Hs = 140 mm, nominal Hs = 150 mm, Fr = 0.182)

Note: a positive (+) heave value is defined upwards and a positive (+) pitch value is defined bow up.

Remarks:

- Coordinate system for comparisons is fixed to x=0.0 (FP) on the undisturbed water plane.
- The center of the pitching moment is same as the center of gravity.

- Symbols:

A - Incident wave amplitude

A_k - Wave steepness, $A_k = \dfrac{2\pi A}{\lambda}$

f_ω - Frequency of the incident wave, $\sqrt{\dfrac{g}{2\pi\lambda}}$

f_e - Encounter frequency, $f_\omega + \dfrac{U}{\lambda}$

T_e - Encounter period, $\dfrac{1}{f_e}$

t - Time, at t=0 a crest of the incident wave is coincident with the FP of the ship

U - Ship speed

u, v, w - Velocity components in x, y, z directions, respectively

λ - Incident wave length

$\zeta_T(x, y, t)$ - Free surface elevation, $\dfrac{z(x, y, t)}{L_{PP}}$

- Instructions:

As a time reference, incident wave height at FP of the ship is defined as

$$\zeta_I(t) = \frac{A}{L_{PP}} \cos\left(2\pi f_e t + \gamma_I\right)$$

where γ_I is the initial phase and is equal to be zero from the present definition of t=0 above. Fourier Series for time history X ($X = R_T, z, \theta$ and ζ_T) are determined as follows:

$$X_F(t) = \frac{X_0}{2} + \sum_{n=1}^{N} X_n \cos\left(2\pi n f_e t + \Delta\gamma_n\right)$$

$$\Delta\gamma_n = \gamma_n - \gamma_I$$

$$a_n = \frac{2}{T}\int_0^T X(t)\cos\left(2\pi n f_e t\right)dt \quad (n = 0, 1, 2, \ldots)$$

$$b_n = \frac{2}{T}\int_0^T X(t)\sin\left(2\pi n f_e t\right)dt \quad (n = 1, 2, \ldots)$$

$$X_n = \sqrt{a_n{}^2 + b_n{}^2}$$

$$\gamma_n = \tan^{-1}\left(-\frac{b_n}{a_n}\right)$$

X_n is n-th harmonic amplitude and γ_n is the corresponding phase.

KVLCC2 Case 1.4c

Conditions:

- Without rudder
- Towing condition in head waves
- $FR_{xz\theta}$
- $Re = 2.55\times10^6$, $Fr = 0.142$
- Nominal Wave height= 60mm
- Three wave lengths and one calm water conditions

References:

Not yet available.

Test Setup:

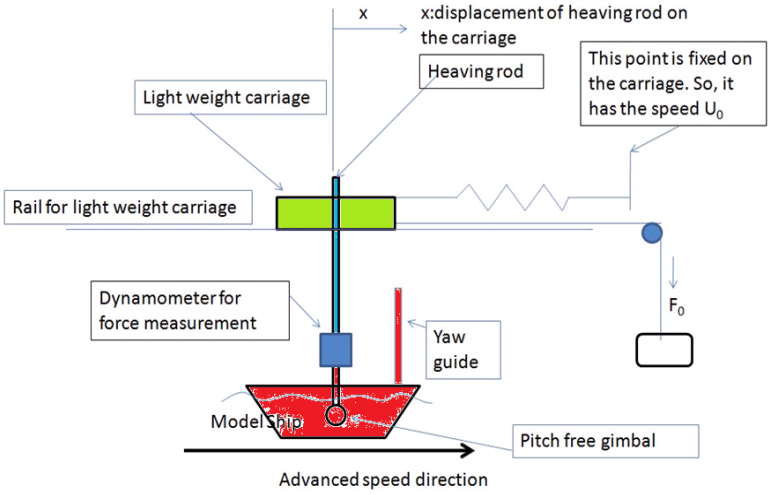

a. Spring Stiffness K and F_0:

No.	1	2	3	4
λ/L_{PP}	0.6	1.1	1.6	Calm Water
Measured mean wave height (mm)	57.676	58.484	57.817	0.011
Nominal wave height (mm)	60	60	60	0
F_0 (N)	4	6	10	6
K (N/m)	98	98	98	98

b. Mass:

Part	Mass (Kg)	Description
Red	m_1=306.2	Mass of hull and pitch free gimbals and a part of heaving rod under the dynamometer(including dynamometer moving part)
Blue	m_2=6.4	Mass of dynamometer (0.9Kg) and the rest of heaving rod (5.5Kg)
Green	m_3=2.5	Mass of light weight carriage on the rails including all movable parts

Note: $I_{yy} = (0.25L)^2(m_1+m_2)$. This value is adjusted by putting the m_2 at CG.

Instructions for Simulation:

Solve the following equations of motion along with flow code:

$$(m_1 + m_2 + m_3)\ddot{x} = -kx - F_0 + F_{x_Hydrodynamic\ Force}$$

$$(m_1 + m_2)\ddot{z} = F_{z_Hydrodynamic\ Force}$$

$$I_{yy}\ddot{\theta} = M_{y_Hydrodynamic\ Force} \quad (around\ \ Center\ \ of\ \ Gravity)$$

The comparison should be based on the following table:

Heave	*Pitch*	*Surge*	*Free Surface Elevation*	*Resistance Force*
+ upward	+ bow up	+ downstream	Measured at x=-5.304m ahead of original CG	$F_{x_resistance\,direction} = X = -F_{x_hydrodynamic\ force} + m_1\ddot{x}$ $(X \text{ is positive in downstream direction})$

* Simulation should be performed for one long period due to spring system (around 22, 12, 10 encounter period of the incoming wave for $\lambda/L = 0.6,\ 1.1$ and 1.6, respectively).

Table/Figure #	Items
1.4c-1-1	Harmonic amplitudes and phases of the *X* force (F_X), heave motion (*z*), pitch angle (θ), surge motion (*x*) (λ/L_{PP} = 0.6, measured *Hs* = 57.676 mm, nominal *Hs* = 60 mm, *Fr* = 0.142)
1.4c-1-2	Harmonic amplitudes and phases of the *X* force (F_X), heave motion (*z*), pitch angle (θ), surge motion (*x*) (λ/L_{PP} = 1.1, measured *Hs* = 58.484 mm, nominal *Hs* = 60 mm, *Fr* = 0.142)
1.4c-1-3	Harmonic amplitudes and phases of the *X* force (F_X), heave motion (*z*), pitch angle (θ), surge motion (*x*) (λ/L_{PP} = 1.6, measured *Hs* = 57.817 mm, nominal *Hs* = 60 mm, *Fr* = 0.142)
1.4c-1-4	Harmonic amplitudes and phases of the *X* force (F_X), heave motion (*z*), pitch angle (θ), surge motion (*x*) (Clam water, measured *Hs* = 0.011 mm, nominal *Hs* = 0 mm, *Fr* = 0.142)
1.4c-2-C1	Time histories of *X* force (F_X) in model scale, surge motion (*x*), heave motion (*z*) and pitch angle (θ) (λ/L_{PP}=0.6)
1.4c-2-C2	Time histories of *X* force (F_X) in model scale, surge motion (*x*), heave motion (*z*) and pitch angle (θ) (λ/L_{PP}=1.1)
1.4c-2-C3	Time histories of *X* force (F_X) in model scale, surge motion (*x*), heave motion (*z*) and pitch angle (θ) (λ/L_{PP}=1.6)
1.4c-2-C4	Time histories of *X* force (F_X) in model scale, surge motion (*x*), heave motion (*z*) and pitch angle (θ) (Calm water)

Data files show
t(sec) ζ(cm) F_X(N) *z*(cm) pitch(cm) *x*(cm) ζ(tank fixed) ζ(servo) *V*(m/s)

Remarks:

- Coordinate system for comparisons is fixed to x=0.0 (original CG on the carriage).
  x: positive downstream, y:starboard direction, z:upward
- Symbols:

  a - Incident wave amplitude

  f_ω - Frequency of the incident wave, $\sqrt{\frac{g}{2\pi\lambda}}$

  f_e - Encounter frequency, $f_\omega + \frac{U}{\lambda}$

  T_e - Encounter period, $\frac{1}{f_e}$

  t - Time, at t=0 a crest of the incident wave is coincident with the CG of the ship

  U - Carriage speed

  λ - Incident wave length

  $\zeta(t)$ - Free surface elevation,

- Instructions:

  As a time reference, incident wave height at mean x of CG is defined as

  $$\zeta_m(t) = \frac{a}{L_{PP}} \cos\left(2\pi f_e t + \gamma_I\right)$$

  $$\zeta_m(t) = \zeta_{at\,x=-5.304}(t - t_0)$$

  $$t_0 = \frac{5.304 + x_0}{c + V} \quad c = \sqrt{\frac{g\lambda}{2\pi}} \quad x_0 : mean\ surge$$

  where γ_I is the initial phase and is equal to be zero from the present definition of t=0 above. Fourier Series for time history $X\left(X = X, x, z, \theta \text{ and } \zeta\right)$ are determined as follows:

  $$X_F(t) = \frac{X_0}{2} + \sum_{n=1}^{N} X_n \cos\left(2\pi n f_e t + \Delta\gamma_n\right)$$

  $$\Delta\gamma_n = \gamma_n - \gamma_I$$

  $$a_n = \frac{2}{T}\int_0^T X(t)\cos\left(2\pi n f_e t\right)dt \quad (n = 0,1,2,\ldots)$$

  $$b_n = \frac{2}{T}\int_0^T X(t)\sin\left(2\pi n f_e t\right)dt \quad (n = 1,2,\ldots)$$

  $$X_n = \sqrt{a_n{}^2 + b_n{}^2}$$

  $$\gamma_n = \tan^{-1}\left(-\frac{b_n}{a_n}\right)$$

  X_n is n-th harmonic amplitude and γ_n is the corresponding phase.

KCS Case 2.1

Conditions:

- Without rudder
- Calm water conditions
- FX_0
- $Re = 1.4\times10^7$, $Fr = 0.26$

Reference:

Van, S.H., Kim, W.J., Yim, G.T., Kim, D.H., and Lee, C.J., (1998b), "Experimental Investigation of the Flow Characteristics Around Practical Hull Forms," Proceedings 3rd Osaka Colloquium on Advanced CFD Applications to Ship Flow and Hull Form Design, Osaka, Japan

Kim, W.J., Van, D.H. and Kim, D.H., (2001), "Measurement of flows around modern commercial ship models", Exp. in Fluids, Vol. 31, pp 567-578

Table/Figure #	Items
2.1-1	Wave elevation contours (global wave field)
2.1-2	Wave elevation contours (bow wave field)
2.1-3	Wave elevation contours (stern wave field)
2.1-4	Wave profile on the hull
2.1-5	Longitudinal wave cut at y/L_{PP} = -0.0741
2.1-6	Longitudinal wave cut at y/L_{PP} = -0.1509
2.1-7	Longitudinal wave cut at y/L_{PP} = -0.4224
2.1-8	Grid density distribution along the waterline, and in transverse and vertical directions at mid-ship
2.1-9	Cross flow vectors and streamlines, axial velocity contours at x/L_{PP} = 0.9825
2.1-10	Velocity on the propeller plane (x/L_{PP} = 0.9825) at z/L_{PP} = -0.0302

KCS Case 2.2a

Conditions:

- With rudder
- Calm water conditions
- FX_0
- $Re = 1.4\times10^7$, $Fr = 0.26$

References:

Van, S.H., Kim, W.J., Yim, G.T., Kim, D.H., and Lee, C.J., (1998b), "Experimental Investigation of the Flow Characteristics Around Practical Hull Forms," Proceedings 3rd Osaka Colloquium on Advanced CFD Applications to Ship Flow and Hull Form Design, Osaka, Japan

Kim, W.J., Van, D.H. and Kim, D.H., (2001), "Measurement of flows around modern commercial ship models", Exp. in Fluids, Vol. 31, pp 567-578

Table/Figure #	Item
2.2a-1	Computed C_T, C_F and C_{PV} of different grid densities
2.2a-2	V&V results for C_T, C_F and C_{PV}

Computation Instructions:

1. Resistance coefficients are based on wetted surface area (S/L^2) =0.1803 with rudder for static orientation in calm water.
2. Comparison Error, $E\%D = (D-S)/D\times100$, where D is the EFD value, and S is the simulation value.
3. Relative change in solution: $\varepsilon_{12}\%S_1 = |(S_1-S_2)/S_1|\times100$, "1" refers to the finest grid.
4. Iterative uncertainty U_I is based on fine grid solution.
5. $p_{G,th}$ is the theoretical order of accuracy = order of convection scheme.
6. U_G is the grid uncertainty. $U_{SN} = \sqrt{U_I^2 + U_G^2}$ is the simulation numerical uncertainty.
7. U_D is the data uncertainty.
8. $U_V = \sqrt{U_D^2 + U_{SN}^2}$ is the validation uncertainty.

KCS Case 2.2b

Conditions:

- With rudder
- Calm water conditions
- $FR_{z\theta}$
- Five speeds:

No.	1	2	3	4	5	6
Froude number (*Fr*)	0.1083	0.1516	0.1949	0.2274	0.2599	0.2816
Reynolds number (*Re*)	5.2×10^6	7.3×10^6	9.4×10^6	1.1×10^7	1.3×10^7	1.4×10^7

References:

Not yet available.

Table/Figure #	Items
2.2b-1	V&V of resistances, sinkage (σ) and trim (τ)
2.2b-2	Coefficients of total resistance (C_T) versus *Fr* (results and uncertainties)
2.2b-3	Sinkage (σ) versus *Fr* (results and uncertainties)
2.2b-4	Trim (τ) versus *Fr* (results and uncertainties)

Note: a positive (+) sinkage value is defined upwards and a positive (+) trim value is defined bow up.

Computation Instructions:

1. Resistance coefficients are based on wetted surface area (S/L^2) =0.1803 with rudder for static orientation in calm water.
2. Comparison Error, $E\%D = (D-S)/D\times100$, where D is the EFD value, and S is the simulation value.
3. Relative change in solution: $\varepsilon_{12}\%S_1 = |(S_1-S_2)/S_1|\times100$, "1" refers to the finest grid.
4. Iterative uncertainty U_I is based on fine grid solution.
5. $p_{G,th}$ is the theoretical order of accuracy = order of convection scheme.
6. U_G is the grid uncertainty. $U_{SN} = \sqrt{U_I^2 + U_G^2}$ is the simulation numerical uncertainty.
7. U_D is the data uncertainty.
8. $U_V = \sqrt{U_D^2 + U_{SN}^2}$ is the validation uncertainty.

KCS Case 2.3a

Conditions:

- Self propelled at ship point in calm water
- Fixed (even keel)
- With propeller, without rudder
- FX_0
- $Re = 1.4\times10^7$, $Fr = 0.26$

References:

Hino, T., (2005 ed.), "Proceedings of CFD Workshop Tokyo 2005", NMRI report 2005

Requested computations:

The self propulsion computation is to be carried out at the *ship point* following the experimental procedure. Thus, the rate of revolutions of the propeller n is to be adjusted to obtain force equilibrium in the longitudinal direction considering the applied towing force (Skin Friction Correction, SFC), i.e.
$T = R_{T(SP)}$-SFC

where T is the computed thrust, $R_{T(SP)}$ is the total resistance at self propulsion and SFC = 30.3 N (from the tests) Report rate of revolutions n, thrust and torque coefficients K_T, K_Q and resistance components $CT_{(SP)}$, $CP_{(SP)}$, $CF_{(SP)}$.

In case this procedure cannot be carried out, set n to the measured value 9.5 rps and report towing force ($R_{T(SP)}$-T), K_T, K_Q, $CT_{(SP)}$, $CP_{(SP)}$, $CF_{(SP)}$.

Table/Figure #	Items
2.3a-1	V&V of Requested values: n, K_T, K_Q, $CT_{(SP)}$, $CP_{(SP)}$, $CF_{(SP)}$ or (for given n) ($R_{T(SP)}$-T), K_T, K_Q, $CT_{(SP)}$, $CP_{(SP)}$, $CF_{(SP)}$
2.3a-2	Axial velocity contours and cross flow vectors downstream of propeller plane (x/L_{PP} = 0.9911)
2.3a-3	Velocity downstream of propeller plane (x/L_{PP} = 0.9911) at z/L_{PP} = -0.03
2.3a-4	Hull surface pressure contours (port side view)

Computation Instructions:

1. Resistance coefficients are based on wetted surface area (S/L^2) =0.1781 without rudder for static orientation in calm water.
2. Comparison Error, $E\%D = (D-S)/D\times100$, where D is the EFD value, and S is the simulation value.
3. Relative change in solution: $\varepsilon_{12}\%S_1 = |(S_1-S_2)/S_1|\times100$, "1" refers to the finest grid.
4. Iterative uncertainty U_I is based on fine grid solution.

5. $p_{G,th}$ is the theoretical order of accuracy = order of convection scheme.

6. U_G is the grid uncertainty. $U_{SN} = \sqrt{U_I^2 + U_G^2}$ is the simulation numerical uncertainty.

7. U_D is the data uncertainty.

8. $U_V = \sqrt{U_D^2 + U_{SN}^2}$ is the validation uncertainty.

All quantities are non-dimensionalized by density of water (ρ), ship speed (U), and length between perpendiculars (L_{PP}):

$$Fr = \frac{U}{\sqrt{g \cdot L_{PP}}}, \; Re = \frac{U \cdot L_{PP}}{\nu}$$

- where g is the gravitational acceleration and ν is the kinematic viscosity.
- All CFD predicted force coefficients should be reported using the provided wetted surface area at rest (S_0). Force coefficients are defined as follows:

$$C_T = \frac{R_T}{\frac{1}{2}\rho U^2 S_0}, \; C_F = \frac{R_F}{\frac{1}{2}\rho U^2 S_0}, \; C_P = \frac{R_P}{\frac{1}{2}\rho U^2 S_0}$$

Symbols:

D	Diameter of propeller [m]
d_h	Diameter of a propeller hub, D × (Hub ratio) [m]
K_T	Thrust coefficient, $\frac{T}{\rho n^2 D^4}$
K_Q	Torque coefficient, $\frac{Q}{\rho n^2 D^5}$
n	Propeller rate of revolution [rps]
Q	Propeller torque [Nm]
$R_{T(SP)}$	Total resistance in self-propelled condition [N]
SFC	Skin friction correction [N]
T	Propeller thrust [N]
U	Ship speed [m/s]

KCS Case 2.3b

Conditions:

- Self propelled at model point in calm water
- With rudder
- $FR_{z\theta}$
- $Re = 6.52\times10^6$, $Fr = 0.26$

References:

Not yet available

Requested computations:

The self propulsion computation is to be carried out at the *model point* following the experimental procedure. Thus, the rate of revolutions of the propeller n is to be adjusted to obtain force equilibrium in the longitudinal direction: $T = R_{T(SP)}$

Report rate of revolutions n, thrust and torque coefficients K_T, K_Q and resistance components $CT_{(SP)}$, $CP_{(SP)}$, $CF_{(SP)}$.

In case this procedure cannot be carried out, set n to the measured value 14.15 rps and report towing force ($R_{T(SP)}$-T), K_T, K_Q, $CT_{(SP)}$, $CP_{(SP)}$, $CF_{(SP)}$.

Table/Figure #	Item
2.3b-1	V&V of Requested values: n, K_T, K_Q, $CT_{(SP)}$, $CP_{(SP)}$, $CF_{(SP)}$, sinkage (σ) and trim (τ) or (for given n) ($R_{T(SP)}$-T), K_T, K_Q, $CT_{(SP)}$, $CP_{(SP)}$, $CF_{(SP)}$, sinkage (σ) and trim (τ)

Note: a positive (+) sinkage value is defined upwards and a positive (+) trim value is defined bow up.

Computation Instructions:

1. Resistance coefficients are based on wetted surface area (S/L^2) =0.1803 with rudder for static orientation in calm water.
2. Comparison Error, $E\%D = (D-S)/D\times100$, where D is the EFD value, and S is the simulation value.
3. Relative change in solution: $\varepsilon_{12}\%S_1 = |(S_1-S_2)/S_1|\times100$, "1" refers to the finest grid.
4. Iterative uncertainty U_I is based on fine grid solution.
5. $p_{G,th}$ is the theoretical order of accuracy = order of convection scheme.
6. U_G is the grid uncertainty. $U_{SN} = \sqrt{U_I^2 + U_G^2}$ is the simulation numerical uncertainty.
7. U_D is the data uncertainty.
8. $U_V = \sqrt{U_D^2 + U_{SN}^2}$ is the validation uncertainty.

All quantities are non-dimensionalized by density of water (ρ), ship speed (U), and length between perpendiculars (L_{PP}):

$$Fr = \frac{U}{\sqrt{g \cdot L_{PP}}}, \; Re = \frac{U \cdot L_{PP}}{\nu}$$

- where g is the gravitational acceleration and ν is the kinematic viscosity.
- All CFD predicted force coefficients should be reported using the provided wetted surface area at rest (S_0). Force coefficients are defined as follows:

$$C_T = \frac{R_T}{\frac{1}{2}\rho U^2 S_0}, \; C_F = \frac{R_F}{\frac{1}{2}\rho U^2 S_0}, \; C_P = \frac{R_P}{\frac{1}{2}\rho U^2 S_0}$$

Symbols:

D	Diameter of propeller [m]
d_h	Diameter of a propeller hub, D × (Hub ratio) [m]
K_T	Thrust coefficient, $\frac{T}{\rho n^2 D^4}$
K_Q	Torque coefficient, $\frac{Q}{\rho n^2 D^5}$
n	Propeller rate of revolution [rps]
Q	Propeller torque [Nm]
$R_{T(SP)}$	Total resistance in self-propelled condition [N]
SFC	Skin friction correction [N]
T	Propeller thrust [N]
U	Ship speed [m/s]

KCS Case 2.4

Conditions:

- With rudder
- Towing condition in head waves
- $FR_{z\theta}$
- Four combined test conditions:

Condition No.	C1	C2	C3	C4
Speed (m/s)	1.701	1.701	1.701	2.151
Froude number (Fr)	0.26	0.26	0.26	0.33
Reynolds number (Re)	6.52×10^6	6.52×10^6	6.52×10^6	8.27×10^6
wave length λ/L_{PP}	0.50	1.15	2.00	1.33
wave height H_s (mm)	36	84	146	97

Note: The wave heights given are the nominal ones. The achieved wave heights might differ slightly. New tests will be carried out shortly and the achieved heights will be presented thereafter. The heave and pitch motions are given at mid-ship position ($L_{PP}/2$) and the wave crest is at mid-ship at t=0.

References:

Not yet available.

Table/Figure #	Items
2.4-1-1	Harmonic amplitudes and phases of the total resistance coefficient (C_T), heave motion (z), pitch angle (θ) and wave amplitude (ζ) (λ/L_{PP} = 0.5, Hs = 36 mm, Fr = 0.26)
2.4-1-1	Harmonic amplitudes and phases of the total resistance coefficient (C_T), heave motion (z), pitch angle (θ) and wave amplitude (ζ) (λ/L_{PP} = 1.15, Hs = 84mm, Fr = 0.26)
2.4-1-1	Harmonic amplitudes and phases of the total resistance coefficient (C_T), heave motion (z), pitch angle (θ) and wave amplitude (ζ) (λ/L_{PP} = 2.00, Hs = 146 mm, Fr = 0.26)
2.4-1-1	Harmonic amplitudes and phases of the total resistance coefficient (C_T), heave motion (z), pitch angle (θ) and wave amplitude (ζ) (λ/L_{PP} = 1.33, Hs = 97mm, Fr = 0. 33)
2.4-2-C1	Time histories of total resistance coefficient (C_T), heave motion (z) and pitch angle (θ) (test condition 1)
2.4-2-C2	Time histories of total resistance coefficient (C_T), heave motion (z) and pitch angle (θ) (test condition 2)
2.4-2-C3	Time histories of total resistance coefficient (C_T), heave motion (z) and pitch angle (θ) (test condition 3)
2.4-2-C4	Time histories of total resistance coefficient (C_T), heave motion (z) and pitch angle (θ) (test condition 4)

Note: A positive (+) heave value is defined upwards and a positive (+) pitch value is defined bow up.

Remarks:

- Coordinate system for comparisons is fixed to x=0.0 (FP) on the undisturbed water plane.
- The center of the pitching moment is same as the center of gravity.
- All CFD predicted force coefficients should be reported using the wetted surface area at rest (S_0/L^2). Force coefficients are defined as follows:

$$C_T(t) = \frac{F_x(t)}{\frac{1}{2}\rho U^2 S_0}$$, where F_x is the total resistance.

- Symbols:

A - Incident wave amplitude

A_k - Wave steepness, $A_k = \frac{2\pi A}{\lambda}$

f_ω - Frequency of the incident wave, $\sqrt{\frac{g}{2\pi\lambda}}$

f_e - Encounter frequency, $f_\omega + \frac{U}{\lambda}$

T_e - Encounter period, $\frac{1}{f_e}$

t - Time, at t=0 a crest of the incident wave is coincident at mid-ship

U - Ship speed

u, v, w - Velocity components in x, y, z directions, respectively

λ - Incident wave length

$\zeta_T(x, y, t)$ - Free surface elevation, $\frac{z(x, y, t)}{L_{PP}}$

- Instructions:

As a time reference, incident wave height at FP of the ship is defined as

$$\zeta_I(t) = \frac{A}{L_{PP}} \cos\left(2\pi f_e t + \gamma_I\right)$$

where γ_I is the initial phase and is equal to be zero from the present definition of t=0 above. Fourier Series for time history X ($X = C_T$, z, θ and ζ_T) are determined as follows:

$$X_F(t) = \frac{X_0}{2} + \sum_{n=1}^{N} X_n \cos\left(2\pi n f_e t + \Delta\gamma_n\right)$$

$$\Delta\gamma_n = \gamma_n - \gamma_I$$

$$a_n = \frac{2}{T}\int_0^T X(t)\cos\left(2\pi n f_e t\right)dt \quad (n = 0, 1, 2, \ldots)$$

$$b_n = \frac{2}{T}\int_0^T X(t)\sin\left(2\pi n f_e t\right)dt \quad (n = 1, 2, \ldots)$$

$$X_n = \sqrt{a_n^2 + b_n^2}$$

$$\gamma_n = \tan^{-1}\left(-\frac{b_n}{a_n}\right)$$

X_n is n-th harmonic amplitude and γ_n is the corresponding phase.

DTMB 5415 Case 3.1a

Conditions:

- Bare hull
- Calm water conditions
- $FX_{\sigma\tau}$; $\sigma = -1.82\times10^{-3}$, $\tau = -0.108°$
- $Re = 1.19\times10^{7}$, $Fr = 0.28$

References:

Olivieri, A., Pistani. F., Avanaini, A., Stern, F., and Penna, R. (2001), "Towing Tank Experiments of Resistance, Sinkage and Trim, Boundary Layer, Wake, and Free Surface Flow Around a Naval Combatant INSEAN 2340 Model," Iowa Institute of Hydraulic Research, The University of Iowa, IIHR Report No. 421, 56 pp

Table/Figure #	Items
3.1a-T	Resistance, V&V
3.1a-1	Wave elevation contour
3.1a-1w	Longitudinal wave cut at $y/L_{PP} = 0.0082, 0.172, 0.301$ Grid density distribution along the waterline, and in transverse and vertical directions at mid-ship
3.1a-2	Cross flow vectors and streamlines, U contours at $x/L_{PP} = 0.1$
3.1a-3	Cross flow vectors and streamlines, U contours at $x/L_{PP} = 0.2$
3.1a-4	Cross flow vectors and streamlines, U contours at $x/L_{PP} = 0.6$
3.1a-5	Cross flow vectors and streamlines, U contours at $x/L_{PP} = 0.8$
3.1a-6	Cross flow vectors and streamlines, U contours at $x/L_{PP} = 0.935$
3.1a-7	Cross flow vectors and streamlines, U contours at at $x/L_{PP} = 1.1$

DTMB 5415 Case 3.1b

Conditions:

- Bare hull
- Calm water conditions
- $FX_{\sigma\tau}$; σ= -1.92x10^{-3}, τ = -0.136°
- Re = 5.13×10^{6}, Fr = 0.28

Reference:

Longo, J., Shao, J., Irvine, M., and Stern, F. (2007), "Phase-Averaged PIV for the Nominal Wake of a Surface Ship in Regular Head Waves," ASME J. Fluids Eng, Vol. 129, pp. 524-540

Table/Figure #	Items
3.1b-T	Resistance, V&V
3.1b-1	Wave elevation contour
3.1b-1w	Longitudinal Wave cut at y/L_{PP} = 0.082, 0.0172, 0.0302 Grid density distribution along the waterline, and in transverse and vertical directions at mid-ship
3.1b-2	Streamwise velocity contour at x/L_{PP} = 0.935
3.1b-3	TKE contour at x/L_{PP} = 0.935
3.1b-4	$\overline{uu}$ contours at x/L_{PP}=0.935
3.1b-5	$\overline{vv}$ contours at x/L_{PP}=0.935
3.1b-6	$\overline{ww}$ contours at x/L_{PP}=0.935
3.1b-7	$\overline{uv}$ contours at x/L_{PP}=0.935
3.1b-8	$\overline{uw}$ contours at x/L_{PP}=0.935

DTMB 5415 Case 3.2

Conditions:

- Bare hull
- Calm water conditions
- FR_{z0}

References:

Olivieri, A., Pistani. F., Avanaini, A., Stern, F., and Penna, R. (2001), "Towing Tank Experiments of Resistance, Sinkage and Trim, Boundary Layer, Wake, and Free Surface Flow Around a Naval Combatant INSEAN 2340 Model," Iowa Institute of Hydraulic Research, The University of Iowa, IIHR Report No. 421, 56 pp

Table/Figure #	Item
3.2-T123	Resistance, V&V

Computation Instructions:

1. Resistance coefficients are based on wetted surface area (S/L^2) = 0.1476 for static orientation in calm water.
2. ITTC-57: $C_F=0.075/(\log_{10}Re-2)^2$
3. $C_R=C_T - C_F$
4. Comparison Error, $E\%D=(D-S)/D\times100$, where D is the EFD value, and S is the simulation value. E%ITTC is computed based on ITTC value.
5. Relative change in solution: $\varepsilon_{12}\%S_1 = |(S_1-S_2)/S_1|\times100$.
6. Iterative uncertainty U_I is based on fine grid solution. The value is evaluated using change in solution in two consecutive time steps for converged solution.
7. $p_{G,th}$ is the theoretical order of accuracy = order of convection scheme.
8. U_G is the grid uncertainty. $U_{SN}=\sqrt{U_I^2+U_G^2}$ is the simulation numerical uncertainty.
9. U_D is the data uncertainty.
10. $U_V=\sqrt{U_D^2+U_{SN}^2}$ is the validation uncertainty.

DTMB 5415 Case 3.5

Conditions:

- Bare hull
- Towing condition in head waves
- $FX_{\sigma\tau}$; σ = -1.92x10^{-3}, τ = -0.136°
- Incident wave length $\lambda = 1.5L_{PP}$ and wave steepness: $A_k = 0.025$
- Re= 4.86×10^6, Fr=0.28
- Wetted surface area at rest (S/L^2) = 0.1476

Reference:

Longo, J., Shao, J., Irvine, M., and Stern, F. (2007), "Phase-Averaged PIV for the Nominal Wake of a Surface Ship in Regular Head Waves," ASME J. Fluids Eng, Vol. 129, pp. 524-540

Instructions for Simulation: Simulation should be performed for THREE periods of the incoming wave.

Table/Figure #	Items
3.5-T	Comparison of 0th and 1st harmonic amplitudes and 1st harmonic phase of the resistance and moment coefficients.
3.5-1	Time histories of C_T, C_H, and C_M
3.5-2	Wave-elevation ζ_T contours: t/T_e = 0, 1/4, 1/2, 3/4
3.5-3	Wave-elevation ζ_T contours: 0th amplitude
3.5-4	Wave-elevation ζ_T contours:1st amplitude
3.5-5	Wave-elevation ζ_T contours: 1st phase
3.5-6	U contours at x/L_{PP} = 0.935, and t/T_e = 0, 1/4, 1/2, 3/4
3.5-7	V contours at x/L_{PP} = 0.935, and t/T_e = 0, 1/4, 1/2, 3/4
3.5-8	W contours at x/L_{PP} = 0.935, and t/T_e = 0, 1/4, 1/2, 3/4
3.5-9	U contours of 0th and 1st amplitudes and 1st phase at x/L_{PP}=0.935
3.5-10	V contours of 0th and 1st amplitudes and 1st phase at x/L_{PP}=0.935
3.5-11	W contours of 0th and 1st amplitudes and 1st phase at x/L_{PP}=0.935

Nomenclature

- zt_0; 0th harmonic amplitude of total free surface elevation
- zt_1; 1st harmonic amplitude of total free surface elevation
- gt_1; 1st harmonic phase of total free surface elevation
- U_0, V_0, W_0; 0th harmonic amplitude of U, V, W, respectively.
- U_1, V_1, W_1; 1st harmonic amplitude of U, V, W, respectively.
- GU_1, GV_1, GW_1; 1st harmonic phase of U, V, W, respectively

Remarks:

- Coordinate system for comparisons is fixed to x=0.0 (FP) on the undisturbed waterplane.
- All CFD predicted force coefficients should be reported using the wetted surface area at rest (S_0/L^2). Force coefficients are defined as follows:

$$C_T(t)=\frac{F_x(t)}{\frac{1}{2}\rho U^2 S_0},\ C_H(t)=\frac{F_z(t)}{\frac{1}{2}\rho U^2 S_0},\ C_M(t)=\frac{M_y(t)}{\frac{1}{2}\rho U^2 S_0 L_{PP}},$$

where F_x, F_z, M_y are the total resistance, the heave force, and the pitching moment. The center of the pitching moment is ($x/L_{PP}=0.5,\ z/L_{PP}=0.031583$).

- Symbols:

A - Incident wave amplitude

A_k - Wave steepness, $A_k=\frac{2\pi A}{\lambda}$

f_ω - Frequency of the incident wave, $\sqrt{\frac{g}{2\pi\lambda}}$

f_e - Encounter frequency, $f_\omega+\frac{U}{\lambda}$

T_e - Encounter period, $\frac{1}{f_e}$

t - Time, at t=0 a crest of the incident wave is coincident with the FP of the ship

U - Ship speed

u,v,w - Velocity components in x,y,z directions, respectively

λ - Incident wave length

$\zeta_T(x,y,t)$ - Free surface elevation, $\frac{z(x,y,t)}{L_{PP}}$

- Instructions:

As a time reference, incident wave height at FP of the ship is defined as

$$\zeta_I(t)=\frac{A}{L_{PP}}\cos\left(2\pi f_e t+\gamma_I\right)$$

where γ_I is the initial phase and is equal to be zero from the present definition of t=0 above. Fourier Series for time history $X\left(X=C_T, C_H, C_M \text{ and } \zeta_T\right)$ are determined as follows:

$$X_F(t)=\frac{X_0}{2}+\sum_{n=1}^{N}X_n\cos\left(2\pi n f_e t+\Delta\gamma_n\right)$$

$$\Delta\gamma_n=\gamma_n-\gamma_I$$

$$a_n=\frac{2}{T}\int_0^T X(t)\cos\left(2\pi n f_e t\right)dt \quad (n=0,1,2,\ldots)$$

$$b_n=\frac{2}{T}\int_0^T X(t)\sin\left(2\pi n f_e t\right)dt \quad (n=1,2,\ldots)$$

$$X_n=\sqrt{a_n^2+b_n^2}$$

$$\gamma_n=\tan^{-1}\left(-\frac{b_n}{a_n}\right)$$

X_n is n-th harmonic amplitude and γ_n is the corresponding phase.

DTMB 5415 Case 3.6

Conditions:

- Bare hull with bilge keels
- Towing condition in calm water
- FR_φ ; $\sigma = 2.93\times10^{-4}$, $\tau = -3.47\times10^{-2}$ °
- $Re = 2.56\times10^{6}$, Fr=0.138, initial roll angle φ= 10°
- Wetted surface area at rest (S/L^2) = 0.1476

Reference:

Irvine, M., Longo, J., Stern, F. (2004), "Towing Tank Tests for Surface Combatant for Free Roll Decay and Coupled Pitch and Heave Motions," Proc. 25th ONR Symposium on Naval Hydrodynamics, St Johns, Canada.

Instructions for Simulation: Simulation should be performed for SIX periods of the roll.

Table/Figure #	Items
3.6-T	E_{RSS} for force and moment coefficients and roll angle time history
3.6-1	Time history of C_{TX}
3.6-2	Time history of roll angle
3.6-3	Mean wave-elevation ζ contours
3.6-4	Wave-elevation ζ_T contours during second cycle of roll decay: t/T_e = 0, 1/4, 1/2, 3/4
3.6-5	Contours of U velocity at x x/L_{PP}=0.675 during second cycle of roll decay: t/T_e = 0, 1/4, 1/2, 3/4
3.6-6	Contours of V velocity at x/L_{PP}=0.675 during second cycle of roll decay: t/T_e = 0, 1/4, 1/2, 3/4
3.6-7	Contours of W velocity at x/L_{PP}=0.675 during second cycle of roll decay: t/T_e = 0, 1/4, 1/2, 3/4

- CFD predicted force coefficients should be reported using the wetted surface area at rest (S/L^2).
- $C_{TX} = \dfrac{F_X}{\frac{1}{2}\rho U^2 S}$, where F_X is the total resistance.

PART 2: Computed Results

KVLCC2

Test Case 1.1a

Figure 1.1a-1 Cross flow vectors, streamlines and axial velocity contours at x/L_{PP} = 0.85
Figure 1.1a-2 Cross flow vectors, streamlines and axial velocity contours at x/L_{PP} = 0.9825
Figure 1.1a-3 Cross flow vectors, streamlines and axial velocity contours at x/L_{PP} = 1.1
Figure 1.1a-4 Total wake fraction (w_T) on the propeller plane
Figure 1.1a-5 Velocity on the propeller plane at z/L_{PP} = -0.05075
Figure 1.1a-6 Turbulent Kinetic energy (k) contours at x/L_{PP} = 0.9825
Figure 1.1a-7 $\overline{uu}$ contours on the propeller plane (x/L_{PP} = 0.9825)
Figure 1.1a-8 $\overline{vv}$ contours on the propeller plane (x/L_{PP} = 0.9825)
Figure 1.1a-9 $\overline{ww}$ contours on the propeller plane (x/L_{PP} = 0.9825)
Figure 1.1a-10 $\overline{uv}$ contours on the propeller plane (x/L_{PP} = 0.9825)
Figure 1.1a-11 $\overline{uw}$ contours at propeller plane (x/L_{PP} = 0.9825)
Figure 1.1a-12 Hull surface pressure contours (port side view)
Figure 1.1a-13 Hull surface pressure contours (back view)
Figure 1.1a-14 Hull surface pressure contours (bottom view)
Figure 1.1a-15 Limiting streamlines (port side view)

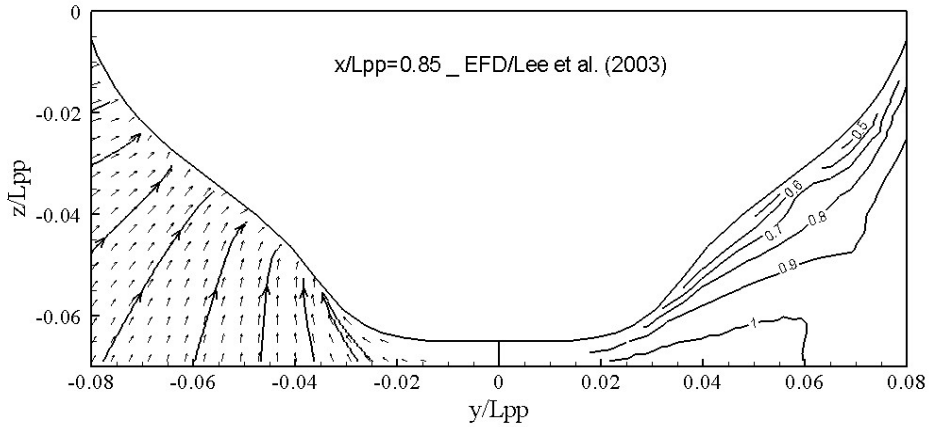

Experiment (Postech, Lee et al. 2003)

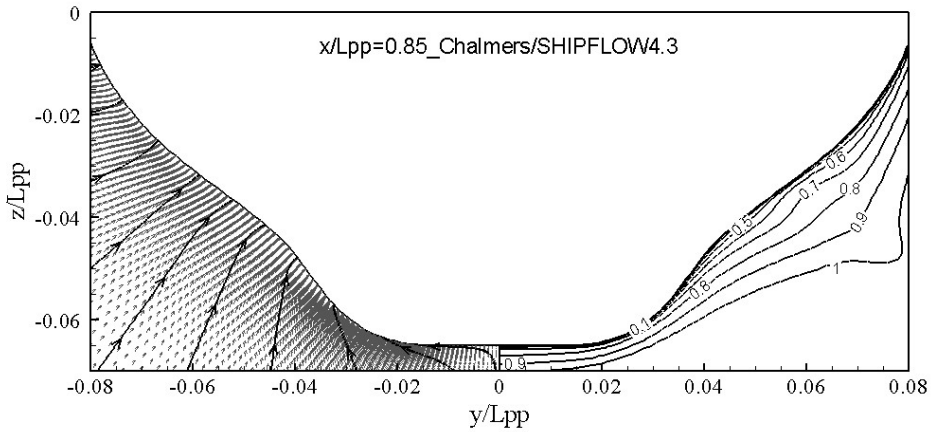

Chalmers-SHIPFLOW4.3

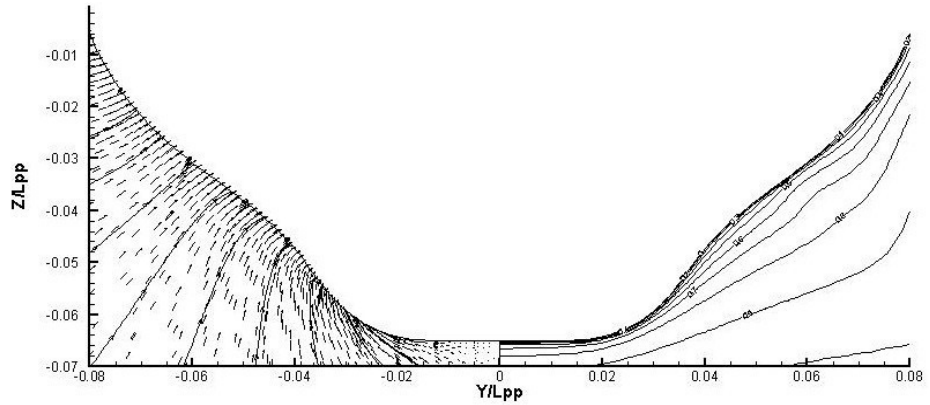

ECN/BEC/HO-Icare

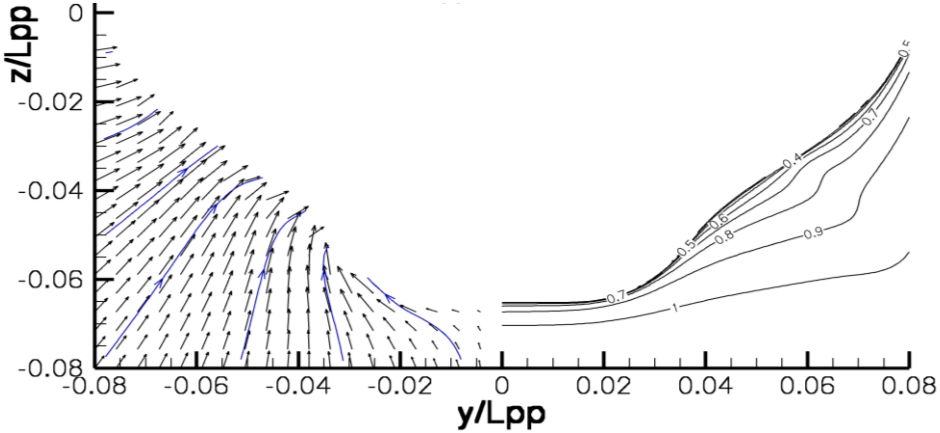

HSVA-FreSCo+

Fig. 1.1a-1 Cross flow vectors and streamlines (left panel), U contours (right panel) at x/L_{PP} = 0.85 [ΔU = 0.1]

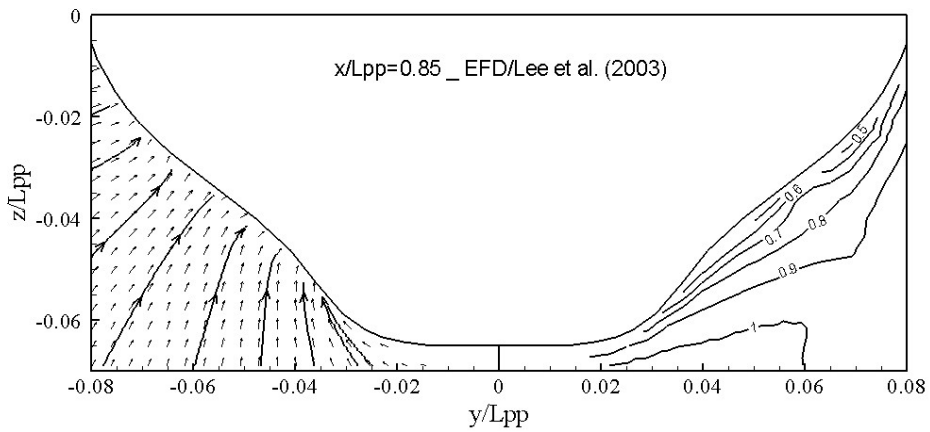

Experiment (Postech, Lee et al. 2003)

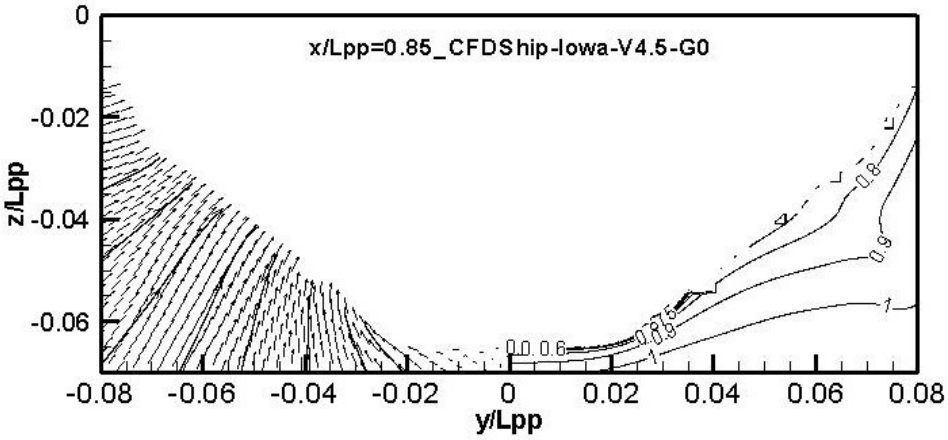

IIHR-CFDShip-Iowa-V4.5 (ARS)

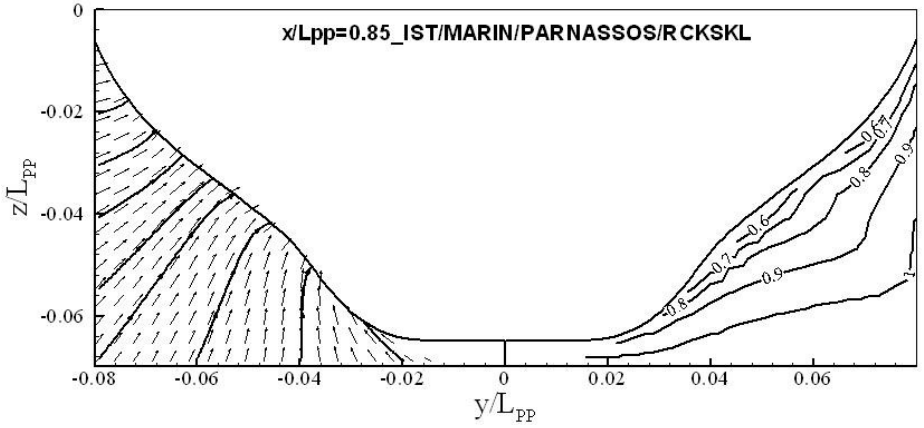

IST/MARIN-PARNASSOS (RCKSKL)

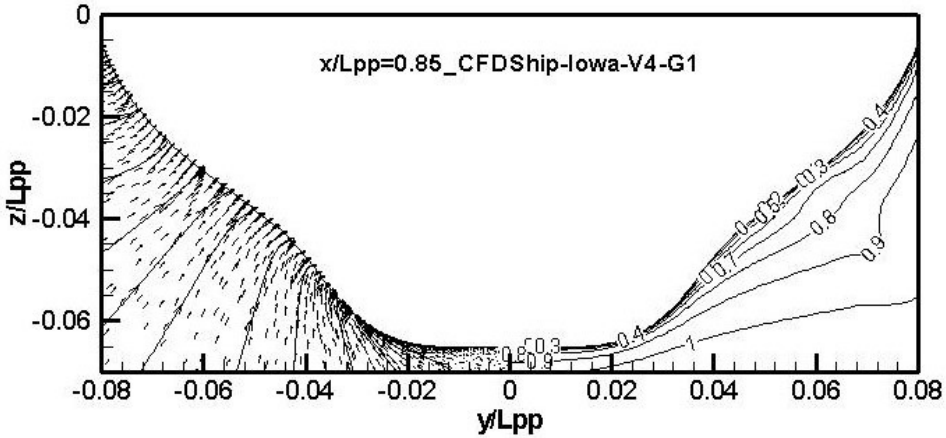

IIHR-CFDShip-Iowa-V4 (ARS-DES)

Fig. 1.1a-1 Cross flow vectors and streamlines (left panel), U contours (right panel) at $x/L_{PP} = 0.85$ [$\Delta U = 0.1$]

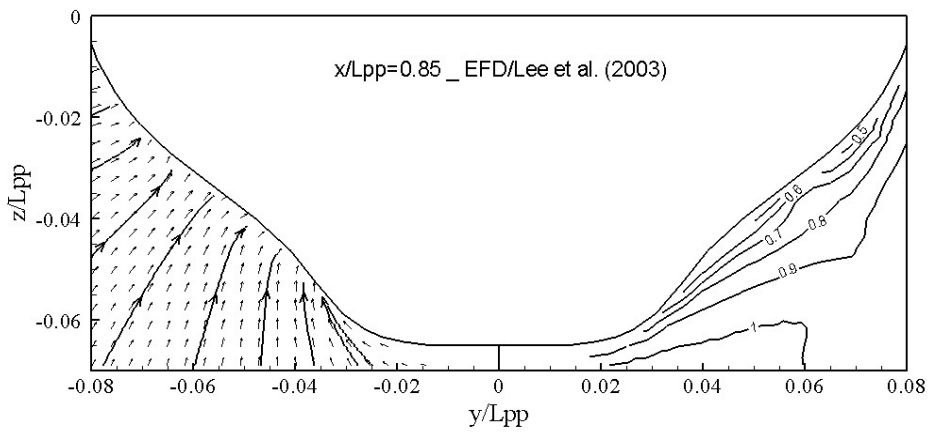

Experiment (Postech, Lee et al. 2003)

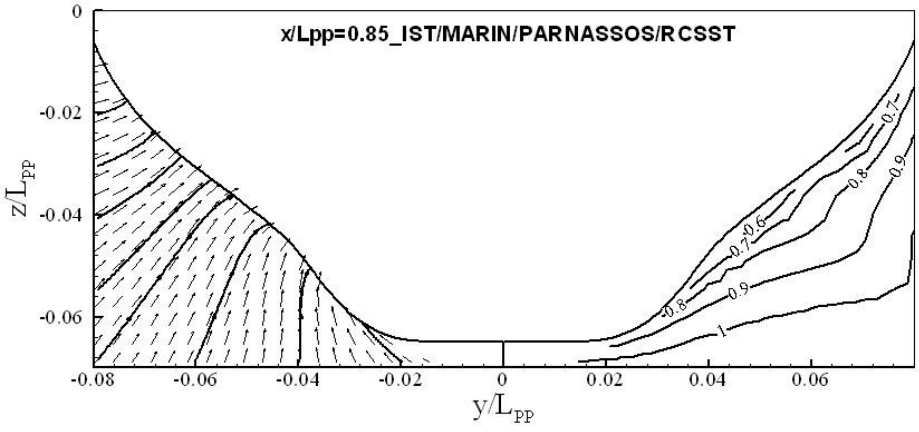

IST/MARIN-PARNASSOS (RCSST)

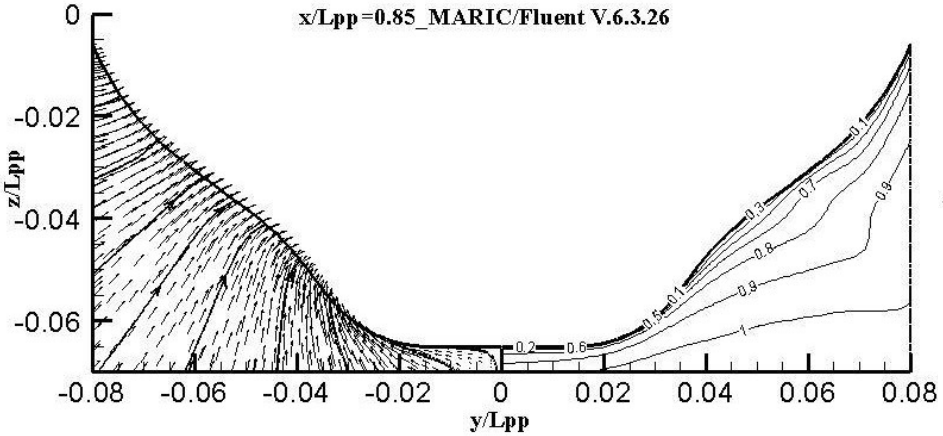

MARIC-Fluent6.3.26

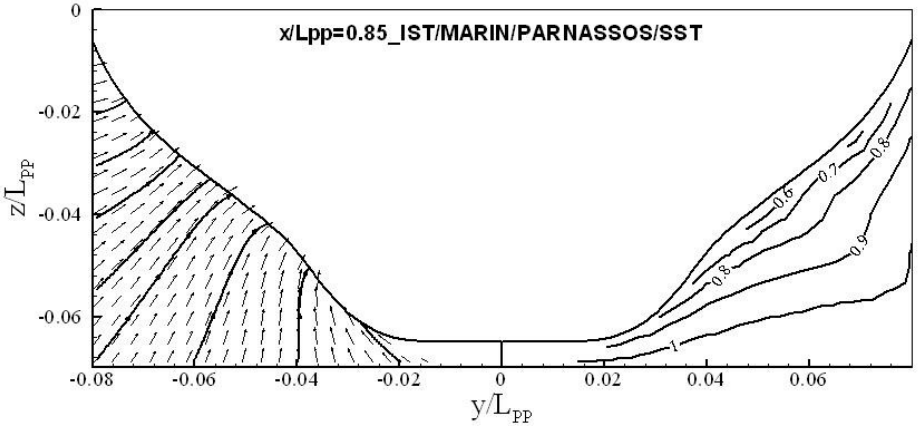

IST/MARIN-PARNASSOS (SST)

Fig. 1.1a-1 Cross flow vectors and streamlines (left panel), U contours (right panel) at $x/L_{PP} = 0.85$ [$\Delta U = 0.1$]

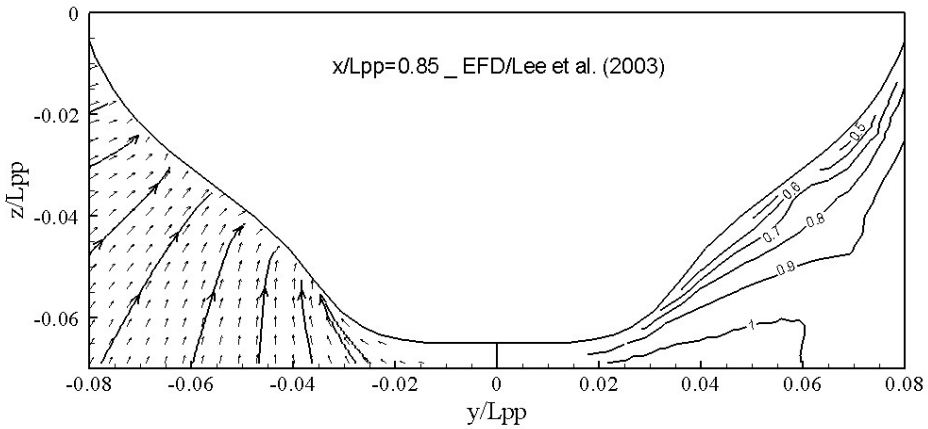

Experiment (Postech, Lee et al. 2003)

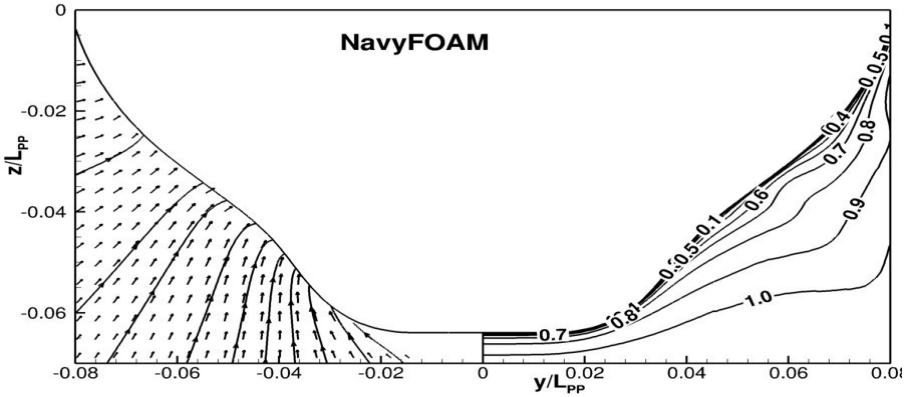

NavyFOAM-NavyFOAM

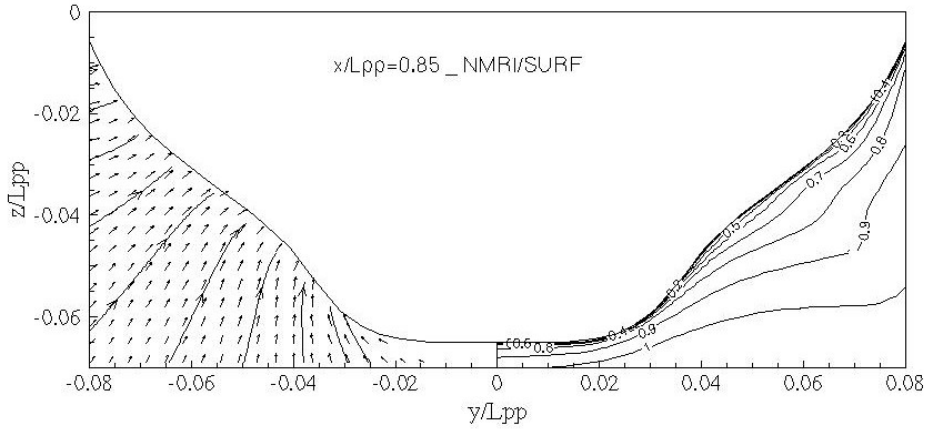

NMRI-SURF

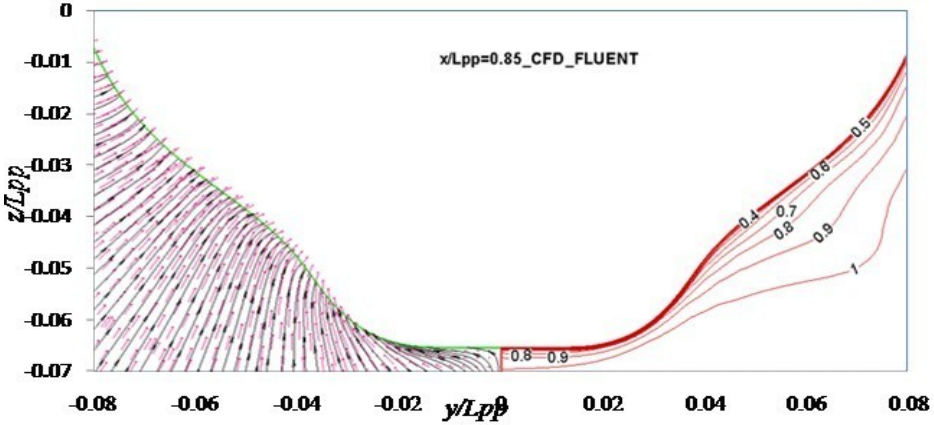

NTNU-FLUENT

Fig. 1.1a-1 Cross flow vectors and streamlines (left panel), U contours (right panel) at $x/L_{PP} = 0.85$ [$\Delta U = 0.1$]

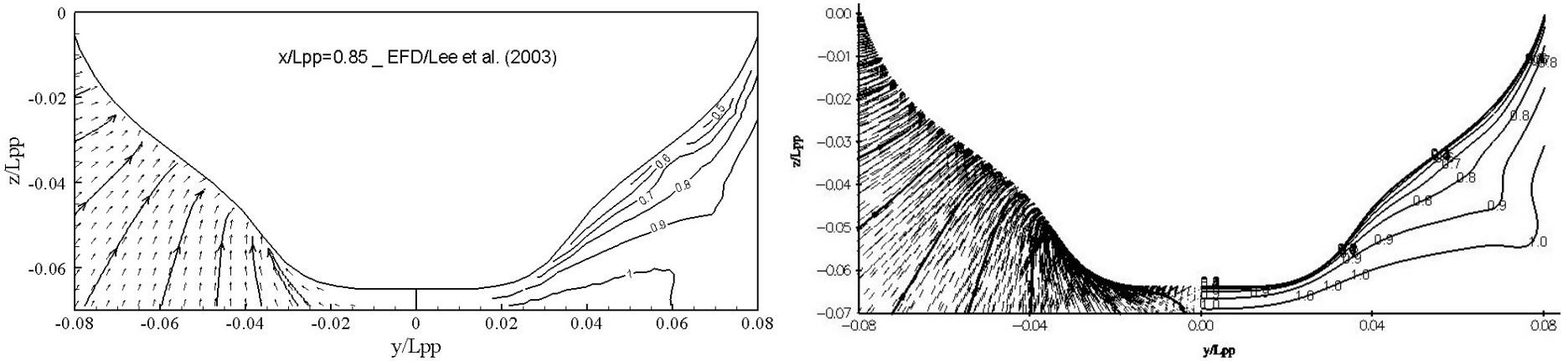

Experiment (Postech, Lee et al. 2003)

VTT-FINFLO

Fig. 1.1a-1 Cross flow vectors and streamlines (left panel), U contours (right panel) at $x/L_{PP} = 0.85$ [$\Delta U = 0.1$]

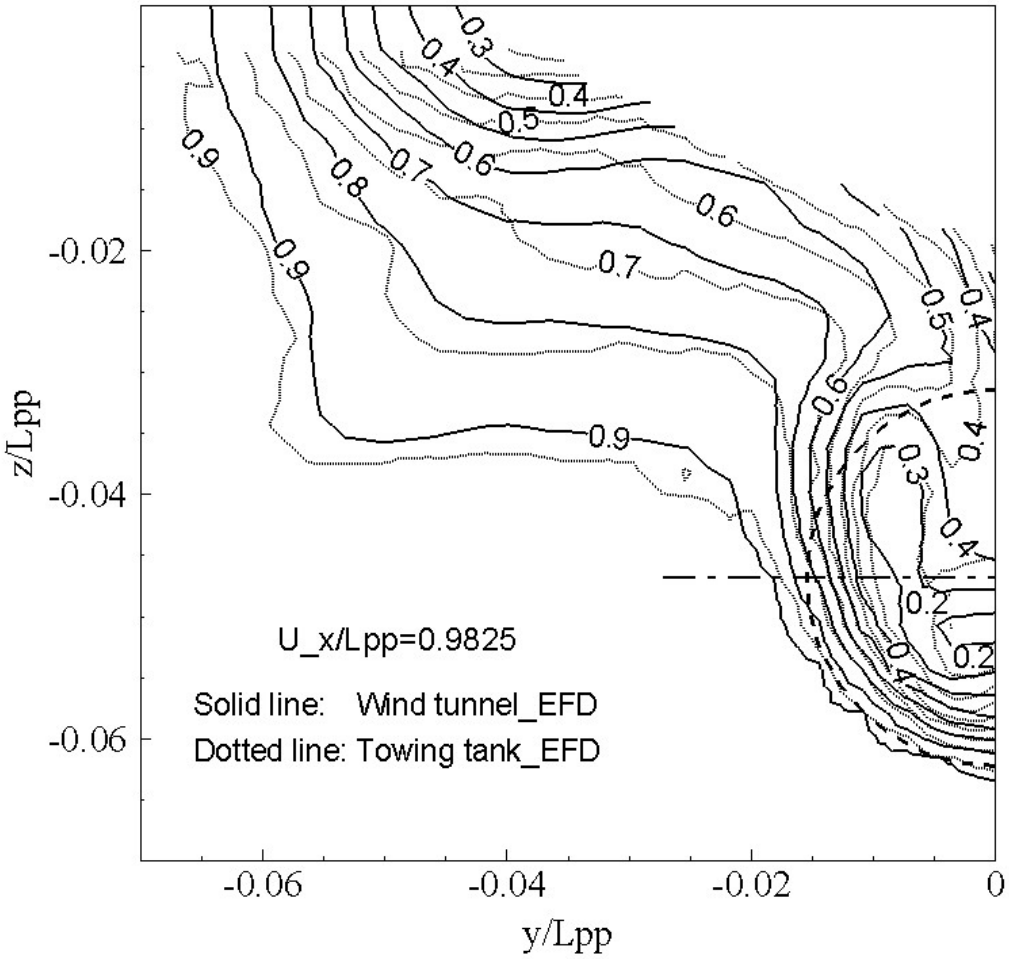

Experiments: Wind tunnel test (Postech) versus Towing tank test (KRISO)

Fig. 1.1a-2 U contours on the propeller plane (x/L_{PP} = 0.9825) [ΔU = 0.1]

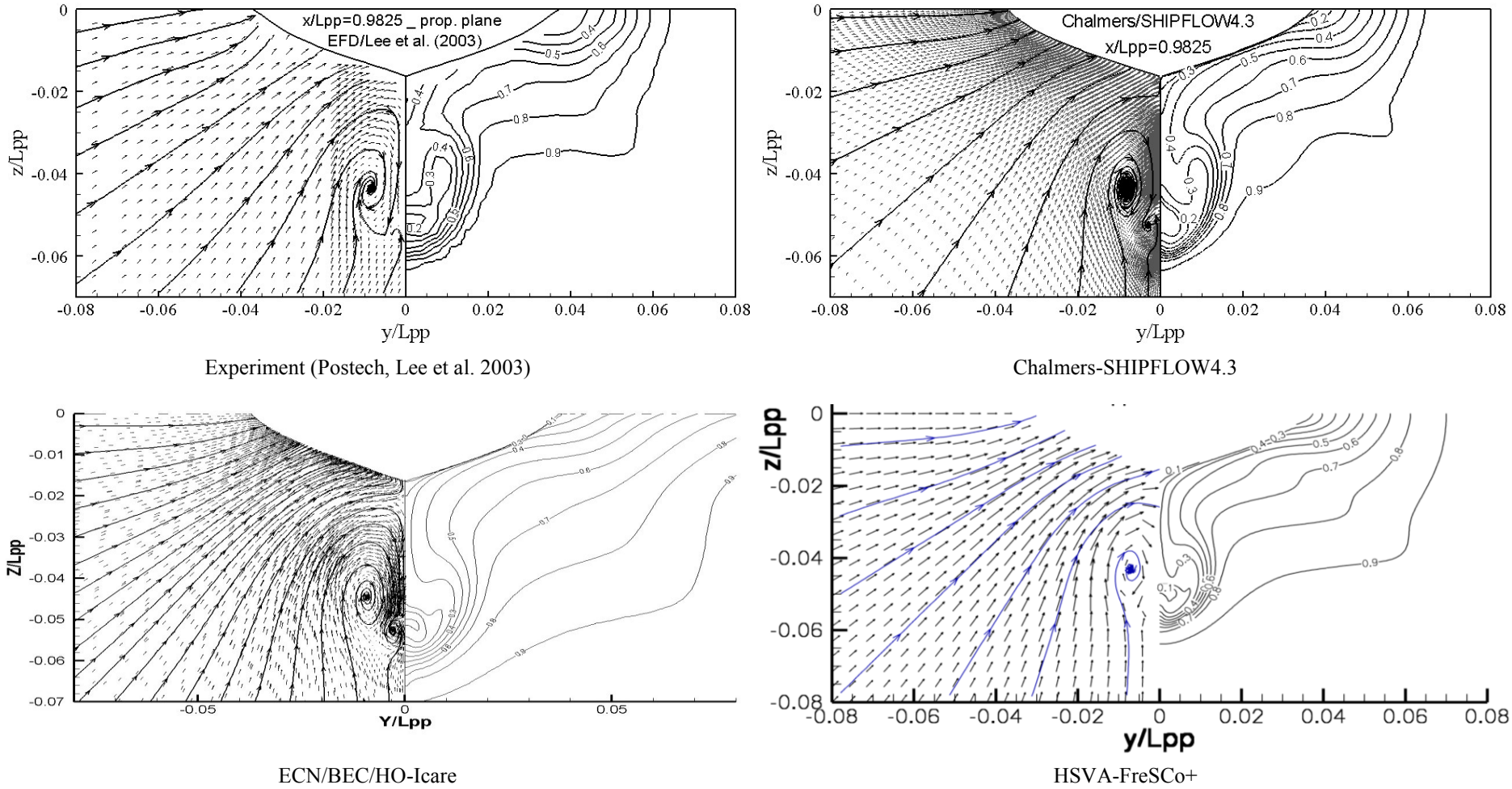

Experiment (Postech, Lee et al. 2003)

Chalmers-SHIPFLOW4.3

ECN/BEC/HO-Icare

HSVA-FreSCo+

Fig. 1.1a-2 Cross flow vectors and streamlines (left panel), U contours (right panel) on the propeller plane (x/L_{PP} = 0.9825) [ΔU = 0.1]

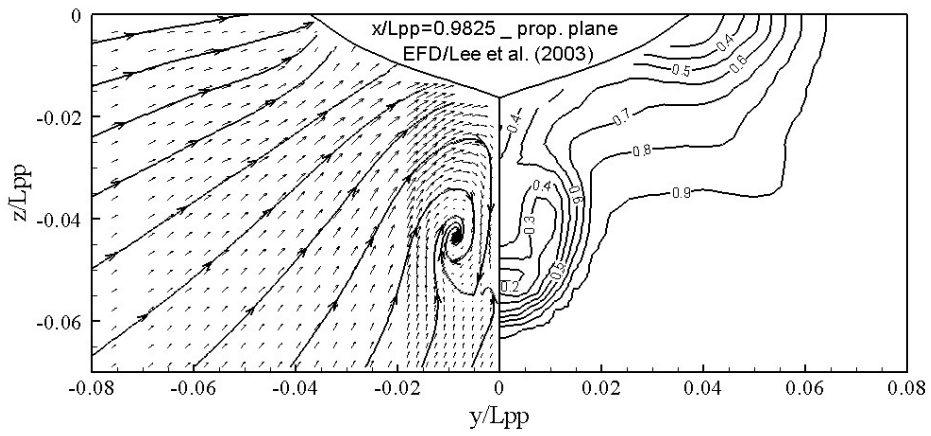

Experiment (Postech, Lee et al. 2003)

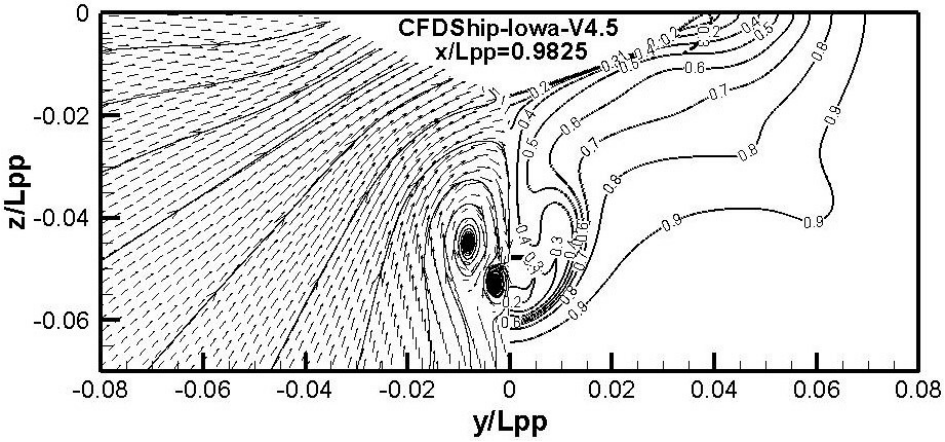

IIHR-CFDShip-Iowa-V4.5 (ARS)

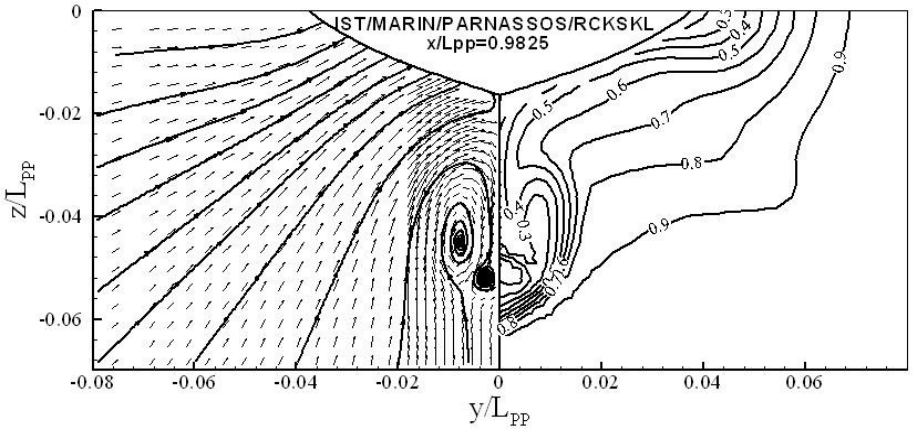

IST/MARIN-PARNASSOS (RCKSKL)

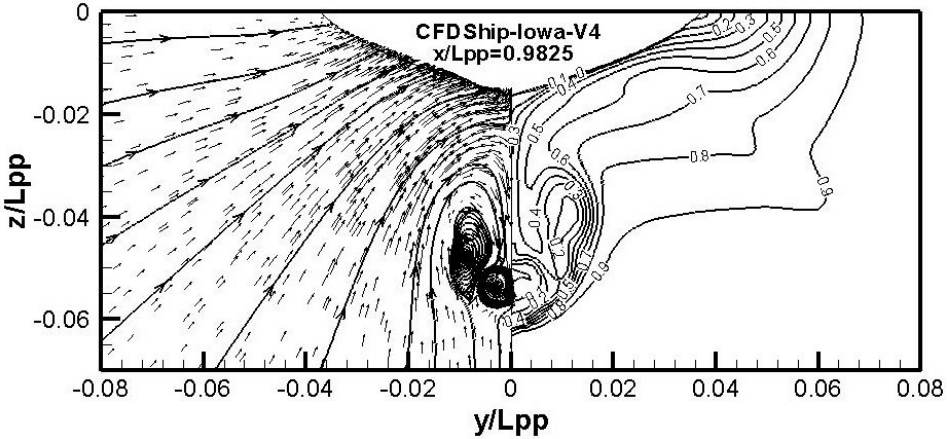

IIHR-CFDShip-Iowa-V4 (ARS-DES)

Fig. 1.1a-2 Cross flow vectors and streamlines (left panel), U contours (right panel)
on the propeller plane (x/L_{PP} = 0.9825) [ΔU = 0.1]

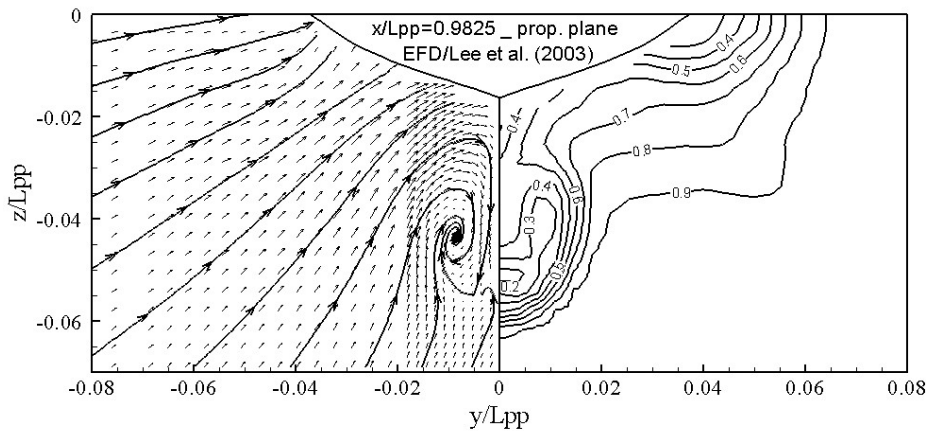

Experiment (Postech, Lee et al. 2003)

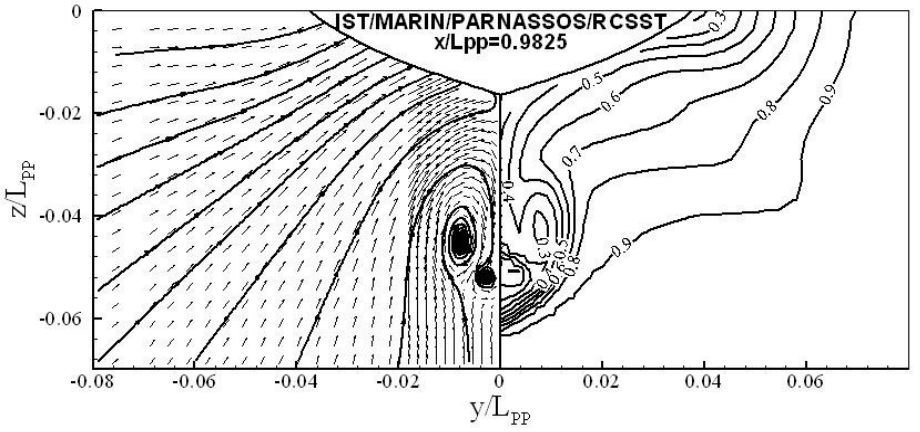

IST/MARIN-PARNASSOS (RCSST)

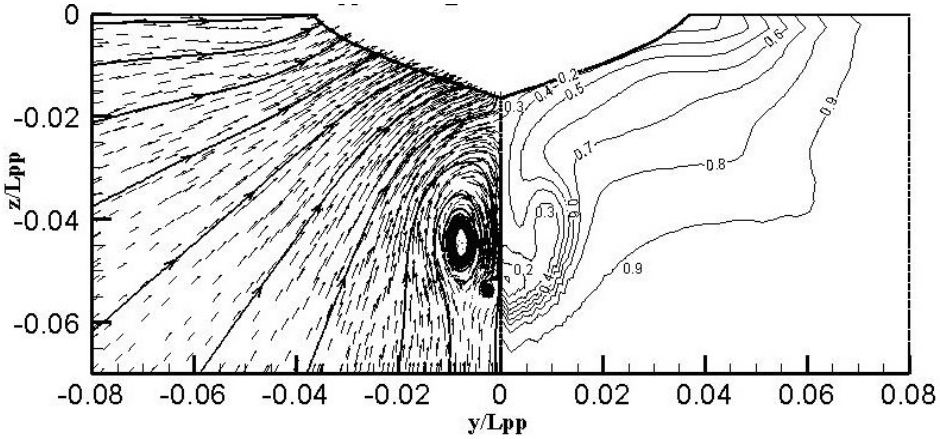

MARIC-Fluent6.3.26

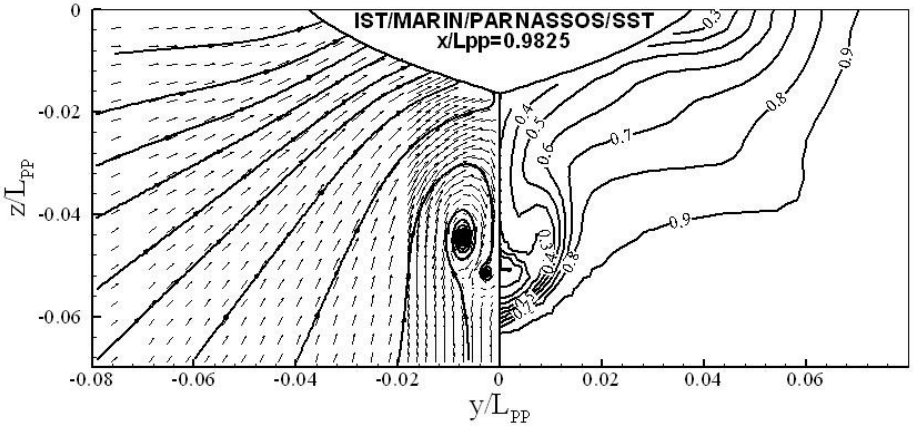

IST/MARIN-PARNASSOS (SST)

Fig. 1.1a-2 Cross flow vectors and streamlines (left panel), U contours (right panel)
on the propeller plane (x/L_{PP} = 0.9825) [ΔU = 0.1]

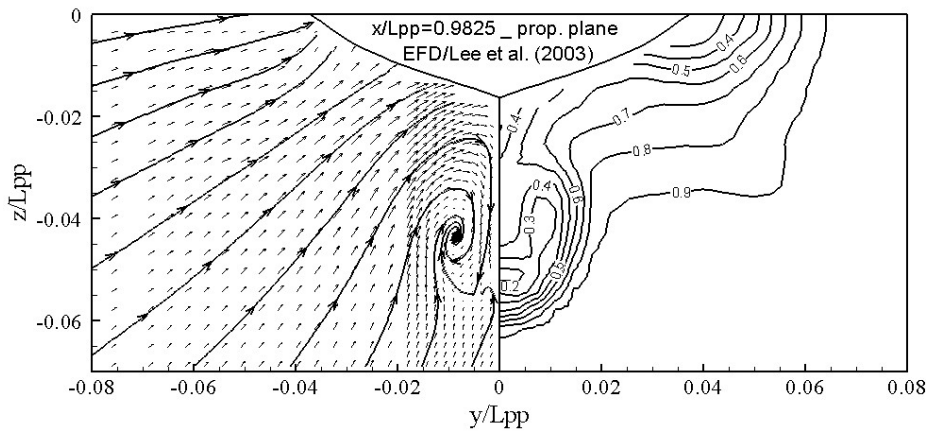

Experiment (Postech, Lee et al. 2003)

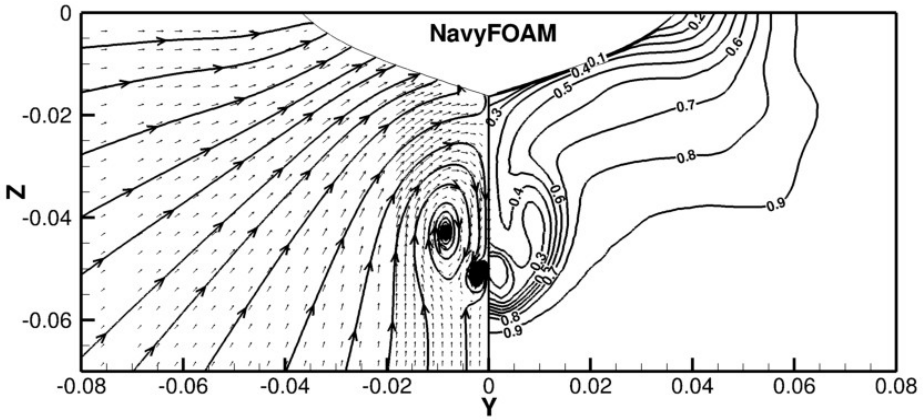

NavyFOAM-NavyFOAM

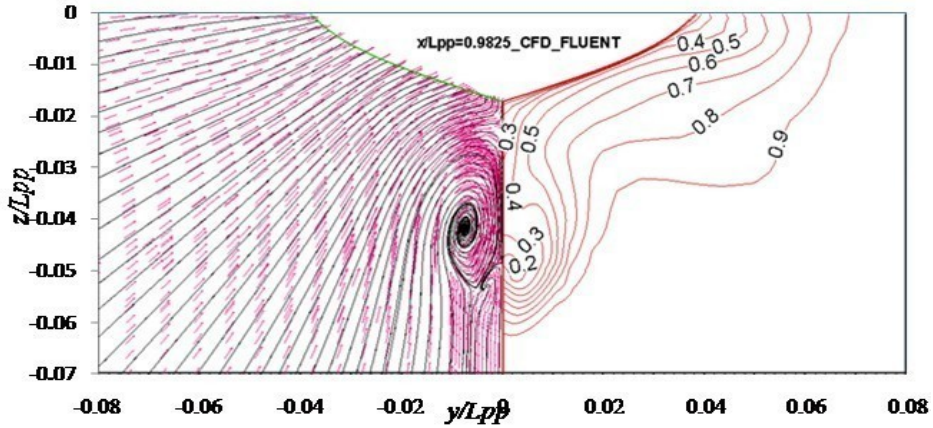

NTNU-FLUENT (coarse grid)

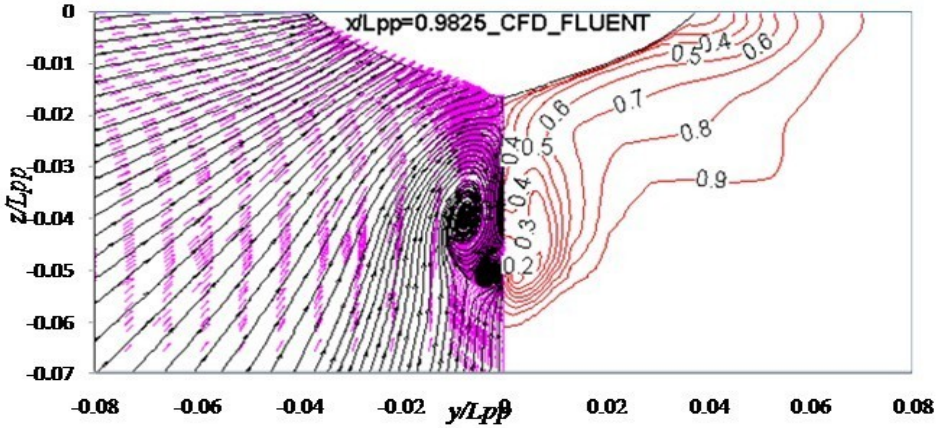

NTNU-FLUENT (fine grid)

Fig. 1.1a-2 Cross flow vectors and streamlines (left panel), U contours (right panel) on the propeller plane (x/L_{PP} = 0.9825) [ΔU = 0.1]

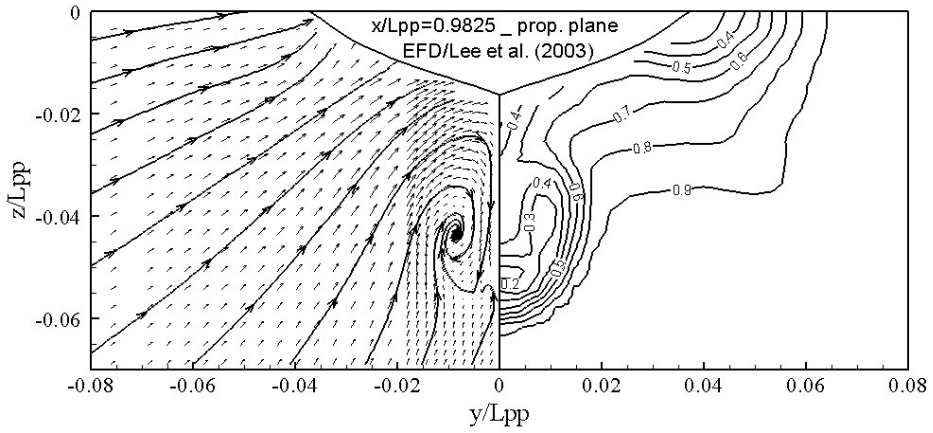

Experiment (Postech, Lee et al. 2003)

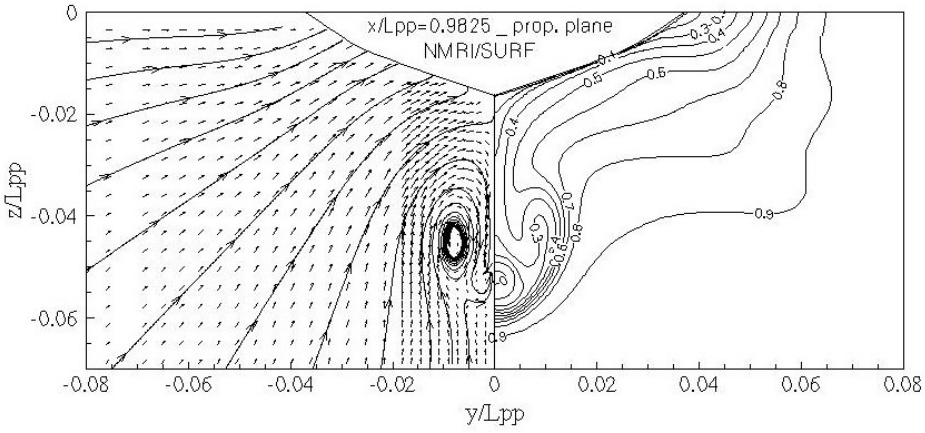

NMRI-SURF

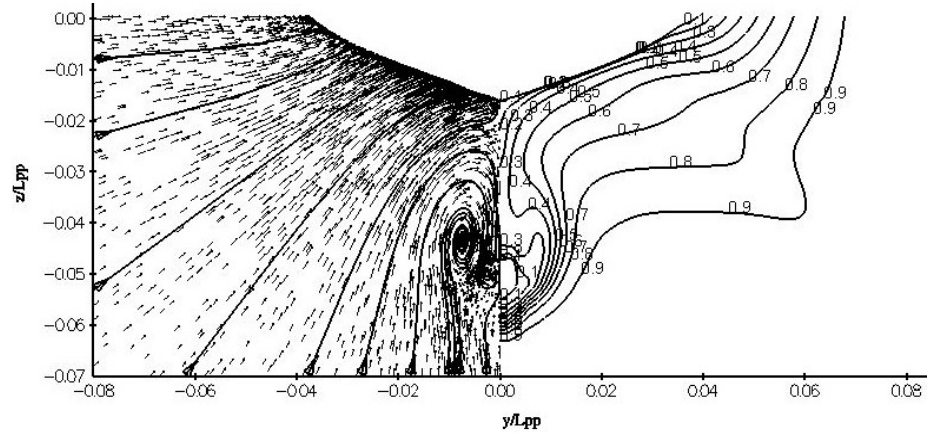

VTT-FINFLO

Fig. 1.1a-2 Cross flow vectors and streamlines (left panel), U contours (right panel) on the propeller plane (x/L_{PP} = 0.9825) [ΔU = 0.1]

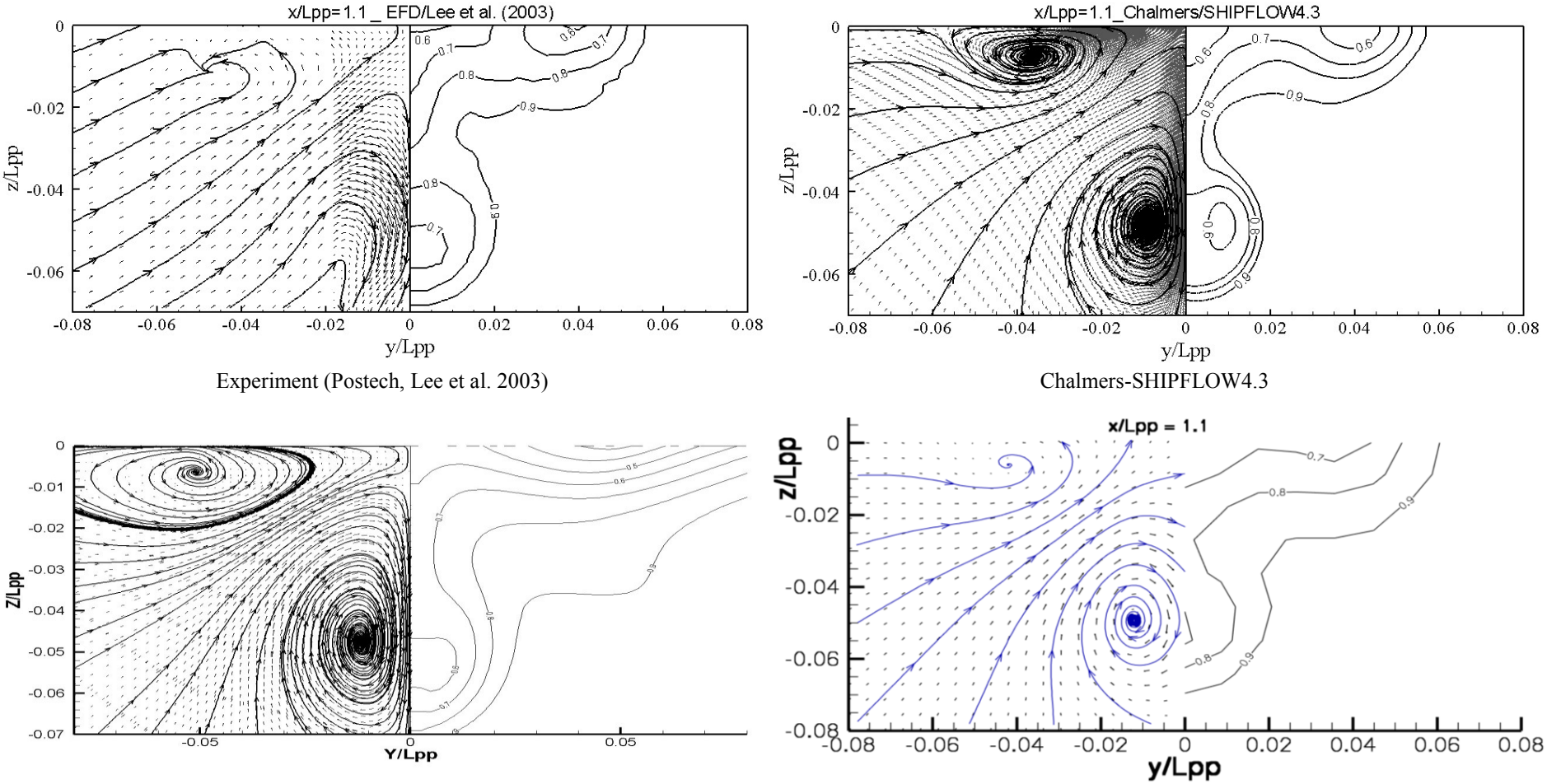

Fig. 1.1a-3 Cross flow vectors and streamlines (left panel), U contours (right panel) at x/L_{PP} = 1.1 [ΔU = 0.1]

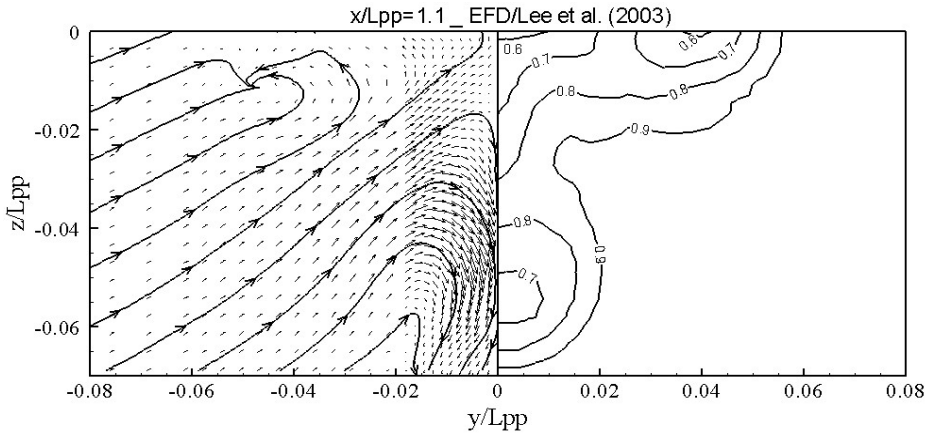

Experiment (Postech, Lee et al. 2003)

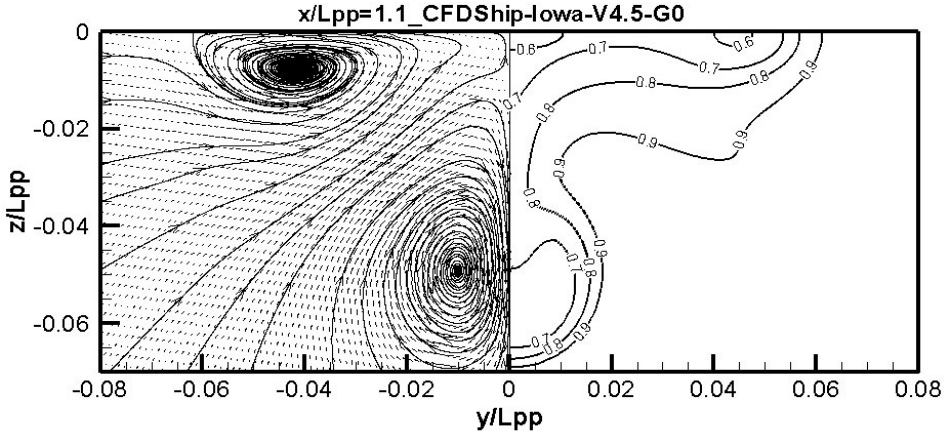

IIHR-CFDShip-Iowa-V4.5 (ARS)

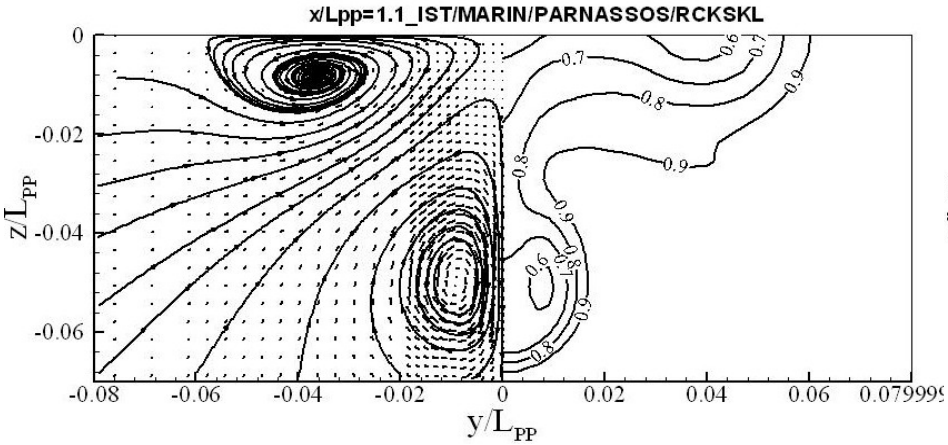

IST/MARIN-PARNASSOS (RCKSKL)

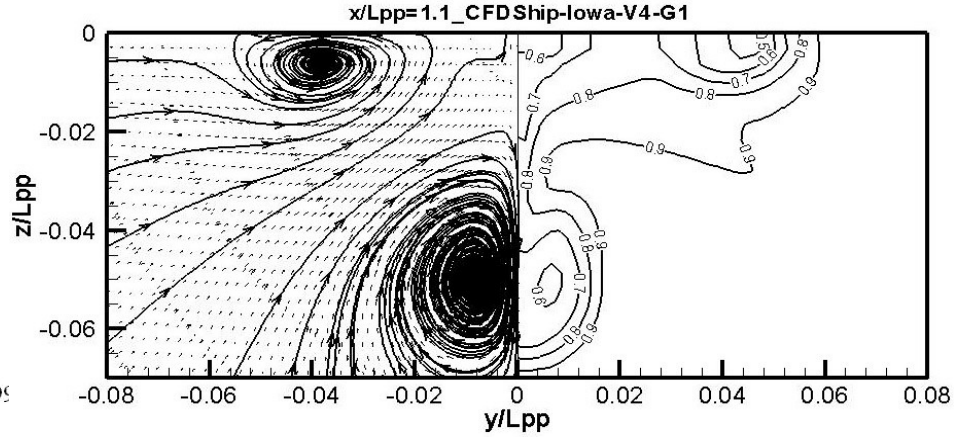

IIHR-CFDShip-Iowa-V4 (ARS-DES)

Fig. 1.1a-3 Cross flow vectors and streamlines (left panel), U contours (right panel) at x/L_{PP} = 1.1 [ΔU = 0.1]

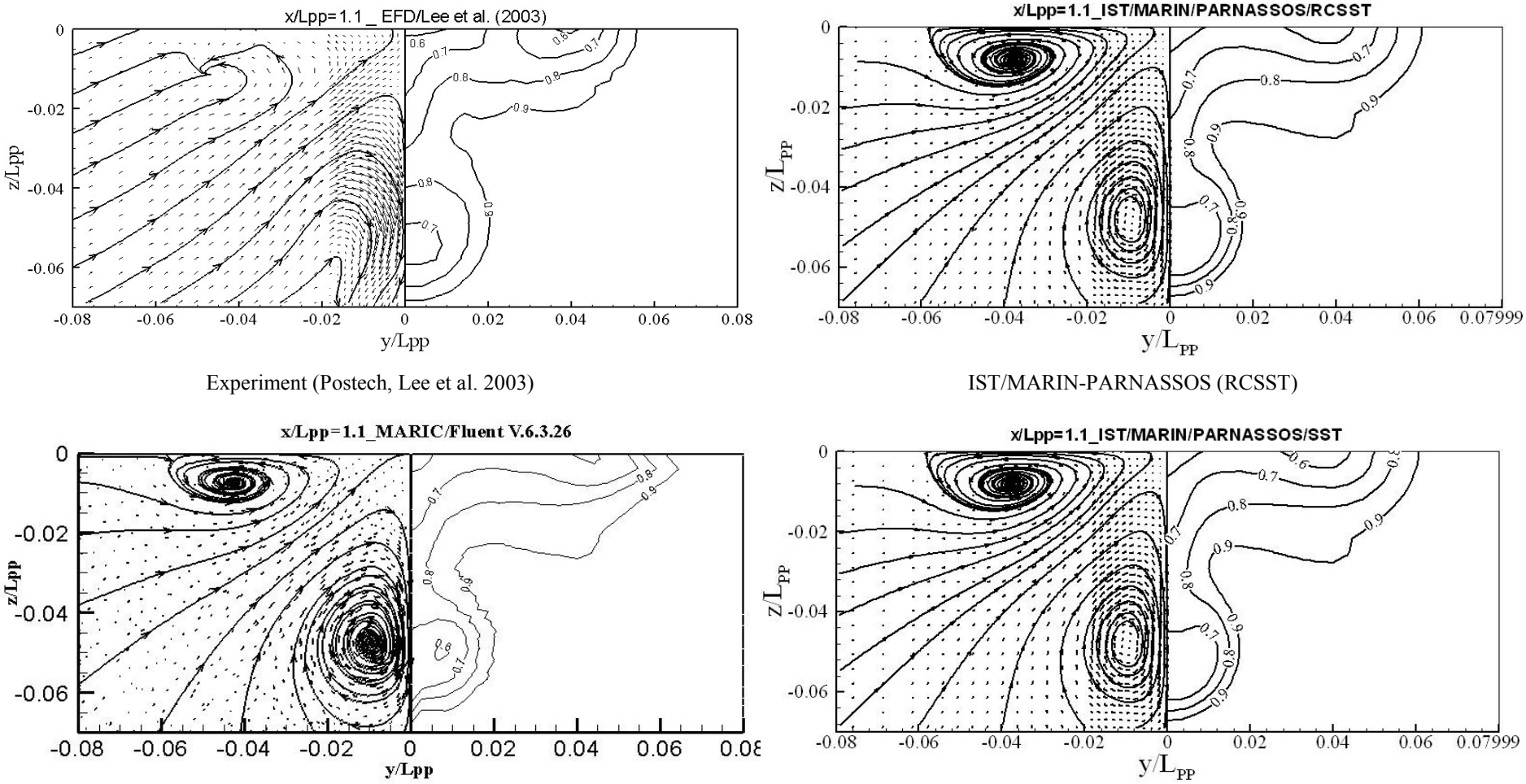

Experiment (Postech, Lee et al. 2003)

IST/MARIN-PARNASSOS (RCSST)

MARIC-Fluent6.3.26

IST/MARIN-PARNASSOS (SST)

Fig. 1.1a-3 Cross flow vectors and streamlines (left panel), U contours (right panel) at x/L_{PP} = 1.1 [ΔU = 0.1]

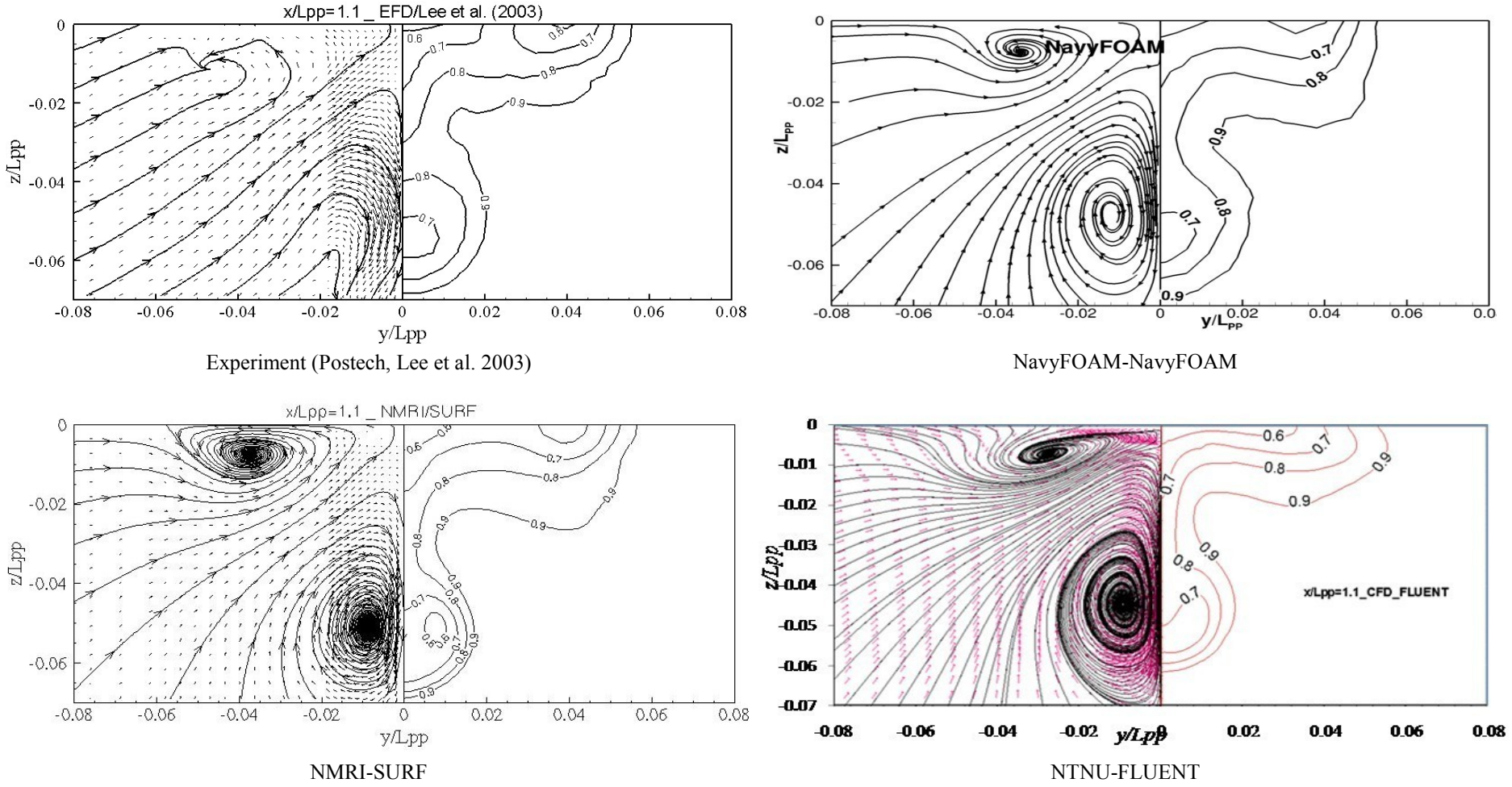

Experiment (Postech, Lee et al. 2003)

NavyFOAM-NavyFOAM

NMRI-SURF

NTNU-FLUENT

Fig. 1.1a-3 Cross flow vectors and streamlines (left panel), U contours (right panel) at x/L_{PP} = 1.1 [ΔU = 0.1]

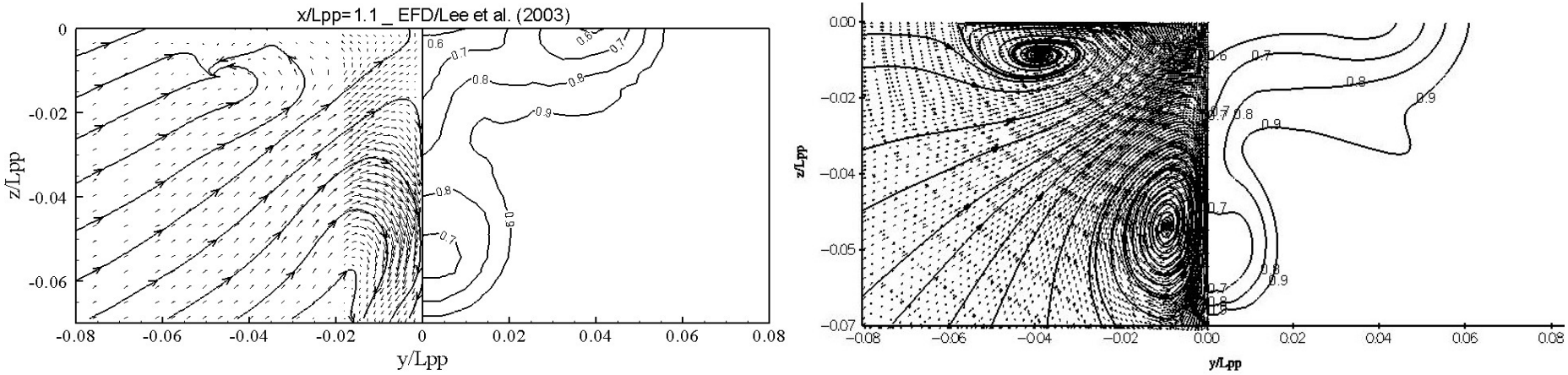

Experiment (Postech, Lee et al. 2003)

VTT-FINFLO

Fig. 1.1a-3 Cross flow vectors and streamlines (left panel), U contours (right panel) at $x/L_{PP} = 1.1$ [$\Delta U = 0.1$]

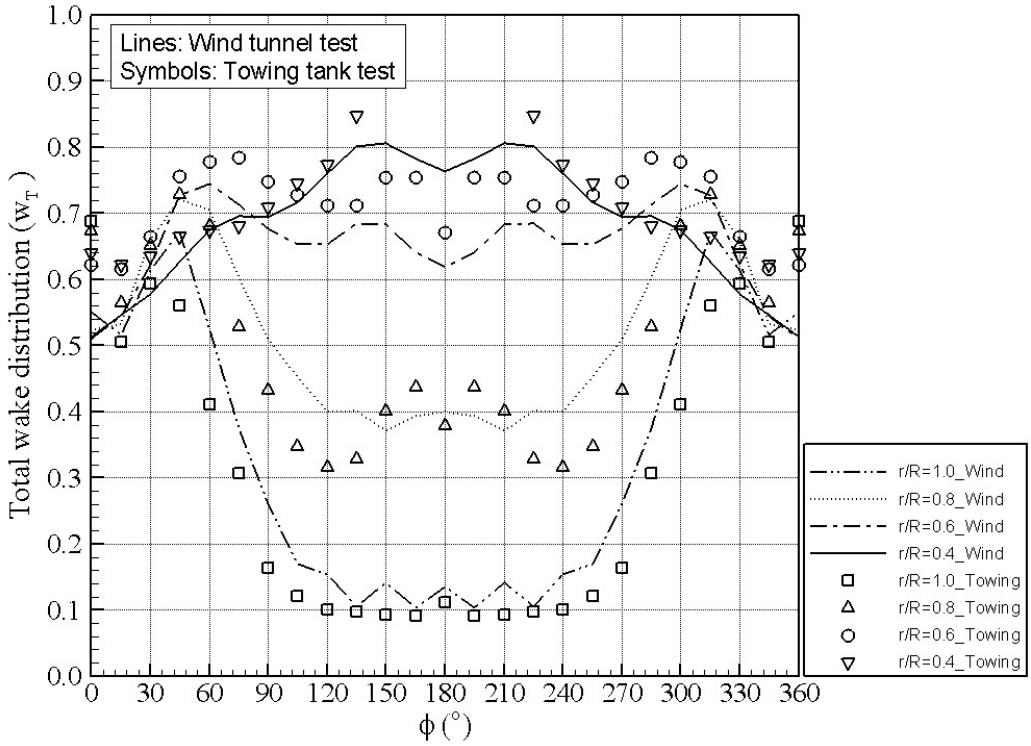

Experiments: Wind tunnel test (Postech) versus Towing tank test (KRISO)

Fig. 1.1a-4 Total wake fraction (w_T) on the propeller plane (at x/L_{PP} = 0.9825)

[Ppropeller radius R = 0.0425m, shaft centerline at z/L_{PP} = -0.04688]

(r/R=1.0: dot-dot-dash line (Wind tunnel test); open squares (Towing tank test)
r/R=0.8: dotted line (Wind tunnel test); open up-triangles (Towing tank test)
r/R=0.6: dot-dash line (Wind tunnel test); open circles (Towing tank test)
r/R=0.4: solid line (Wind tunnel test); open down-triangles (Towing tank test))

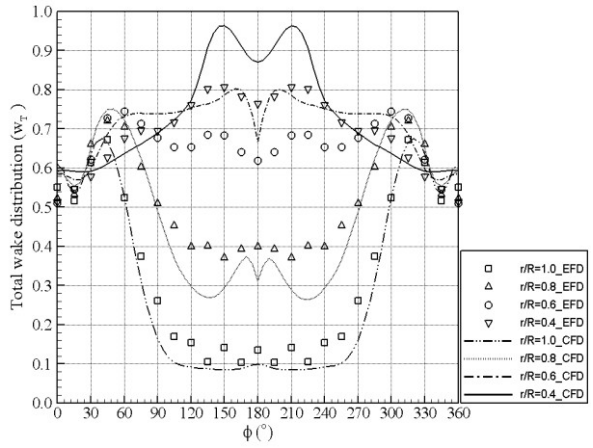

Chalmers-SHIPFLOW4.3

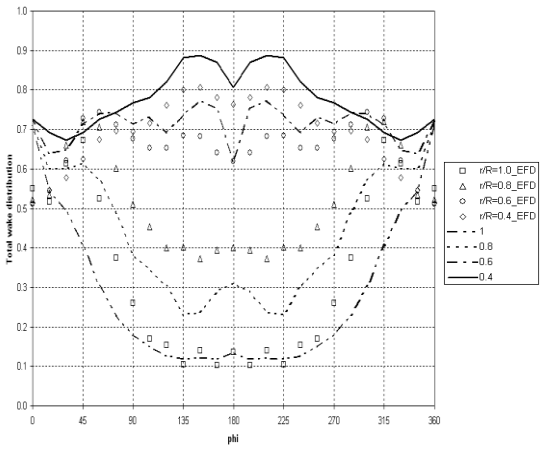

HSVA-FreSCo+

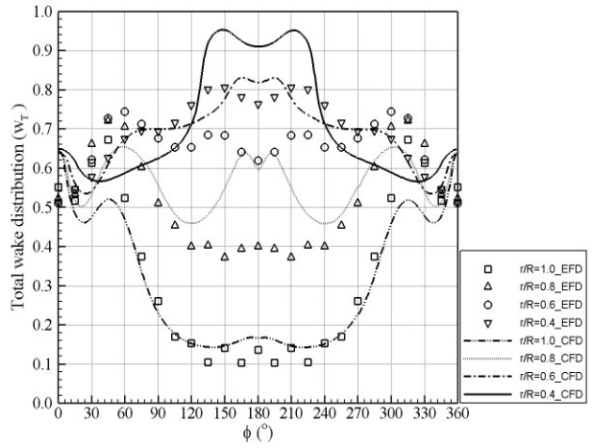

IIHR-CFDShip-Iowa-V4.5 (ARS)

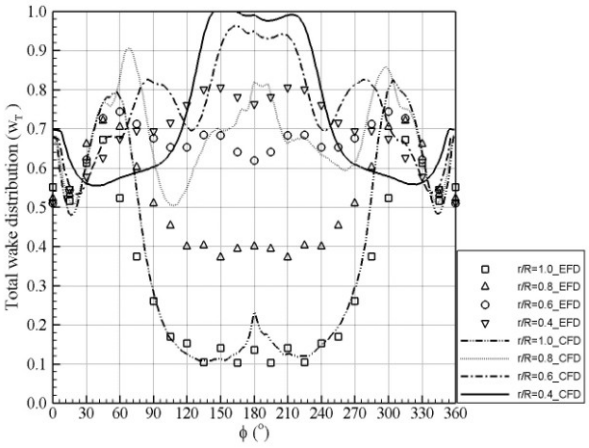

IIHR-CFDShip-Iowa-V4 (ARS-DES)

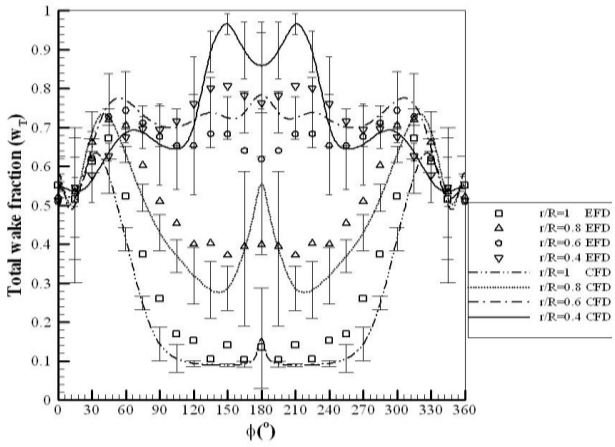

IST/MARIN-PARNASSOS (RCKSKL)

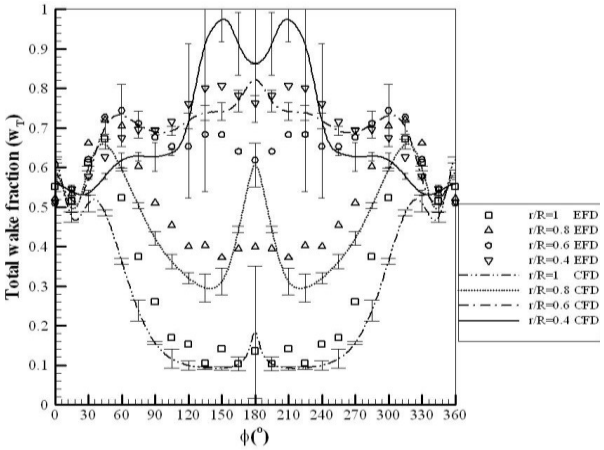

IST/MARIN-PARNASSOS (RCSST)

Fig. 1.1a-4 Total wake fraction (w_T) on the propeller plane (at x/L_{PP} = 0.9825)

[Ppropeller radius R = 0.0425m, shaft centerline at z/L_{PP} = -0.04688]

(r/R=1.0: CFD dot-dot-dash line; EFD open squares
r/R=0.8: CFD dotted line; EFD open up-triangles
r/R=0.6: CFD dot-dash line; EFD open circles
r/R=0.4: CFD solid line; EFD open down-triangles)

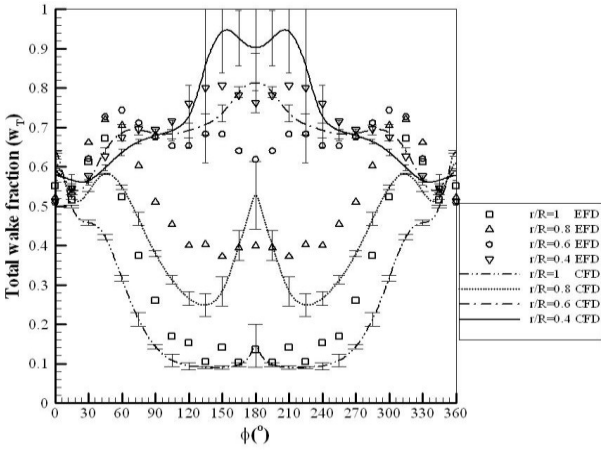

IST/MARIN-PARNASSOS (SST)

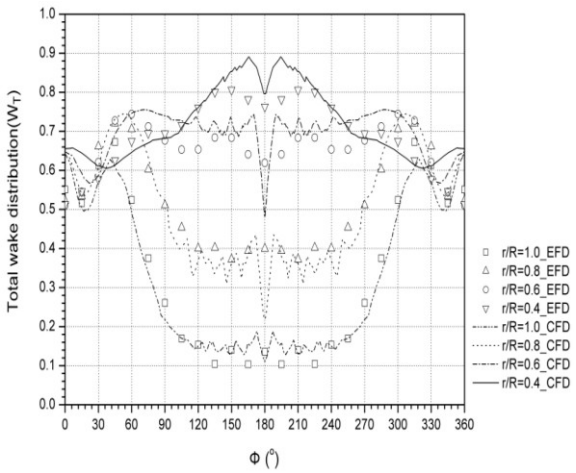

MARIC-Fluent6.3.26

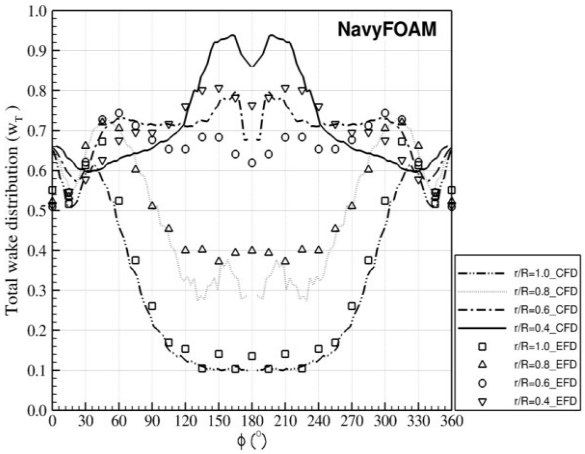

NavyFOAM-NavyFOAM

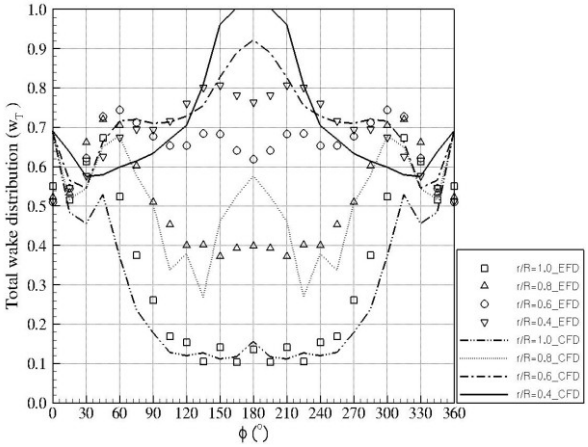

NMRI-SURF

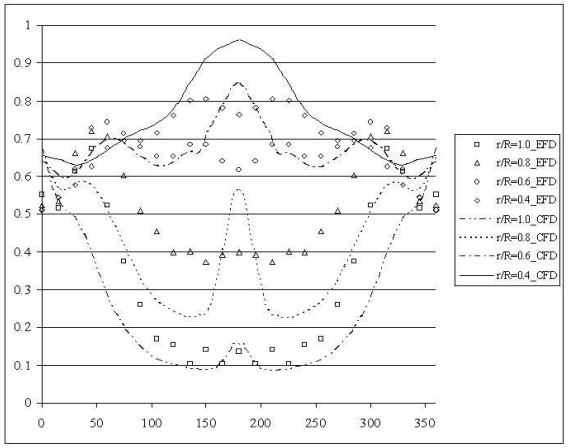

VTT-FINFLO

Fig. 1.1a-4 Total wake fraction (w_T) on the propeller plane (at x/L_{PP} = 0.9825)

[Ppropeller radius R = 0.0425m, shaft centerline at z/L_{PP} = -0.04688]

(r/R=1.0: CFD dot-dot-dash line; EFD open squares
r/R=0.8: CFD dotted line; EFD open up-triangles
r/R=0.6: CFD dot-dash line; EFD open circles
r/R=0.4: CFD solid line; EFD open down-triangles)

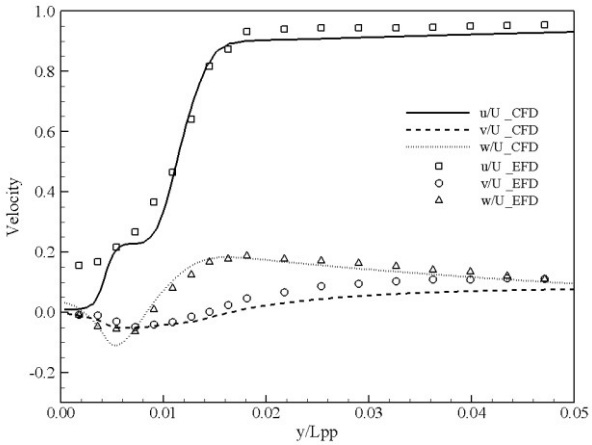

Chalmers-SHIPFLOW4.3

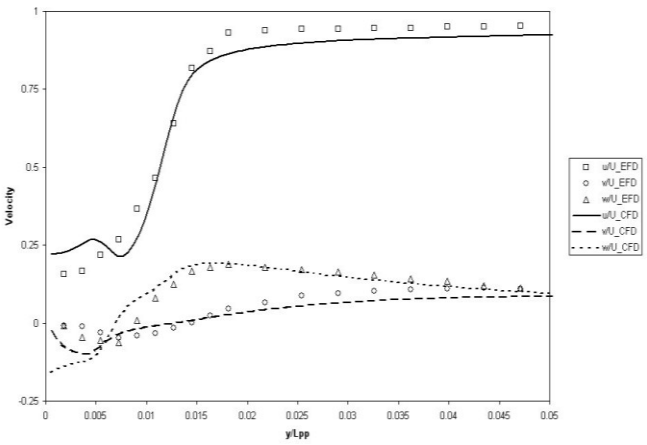

HSVA-FreSCo+

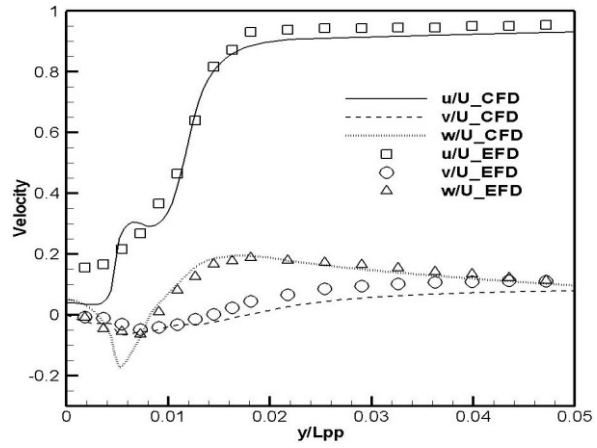

IIHR-CFDShip-Iowa-V4.5 (ARS)

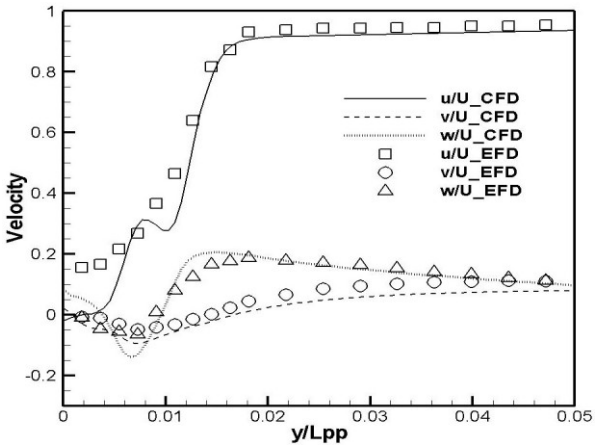

IIHR-CFDShip-Iowa-V4 (ARS-DES)

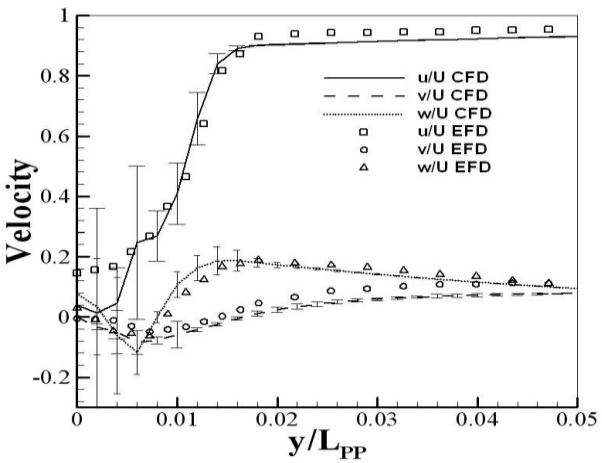

IST/MARIN-PARNASSOS (RCKSKL)

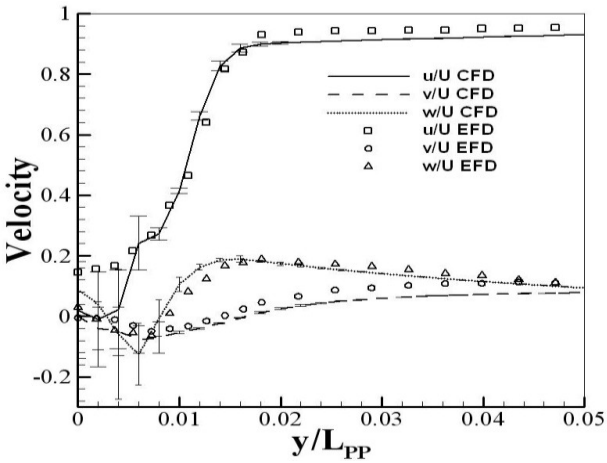

IST/MARIN-PARNASSOS (RCSST)

Fig. 1.1a-5 Velocity on the propeller plane (x/L_{PP} = 0.9825) at z/L_{PP} = -0.05075

u/*U*: CFD solid line; EFD open squares
v/*U*: CFD dashed line; EFD open circles
w/*U*: CFD dotted line; EFD open triangles

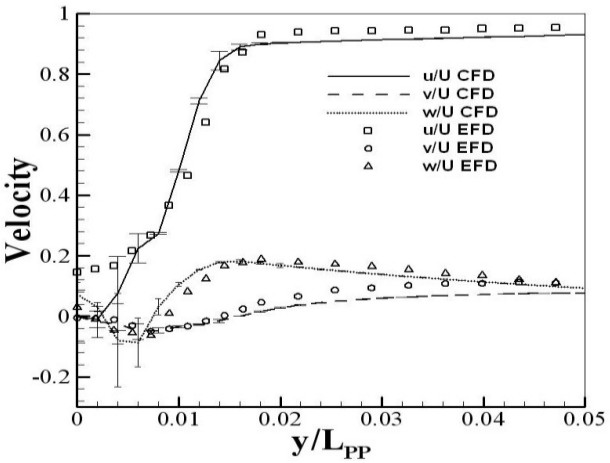

IST/MARIN-PARNASSOS (SST)

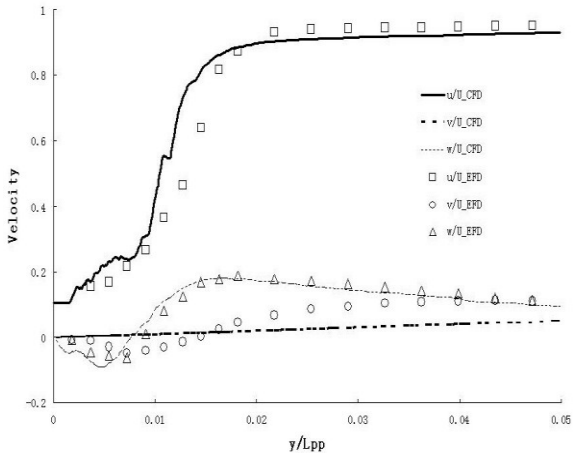

MARIC-Fluent6.3.26

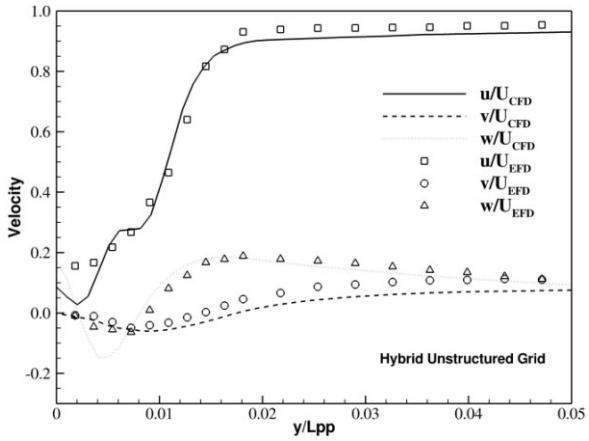

NavyFOAM-NavyFOAM

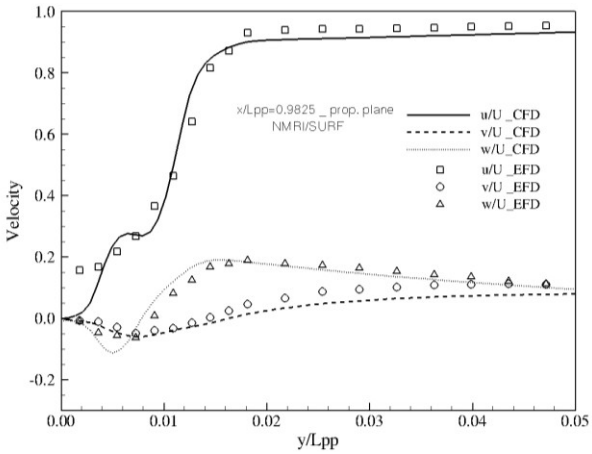

NMRI-SURF

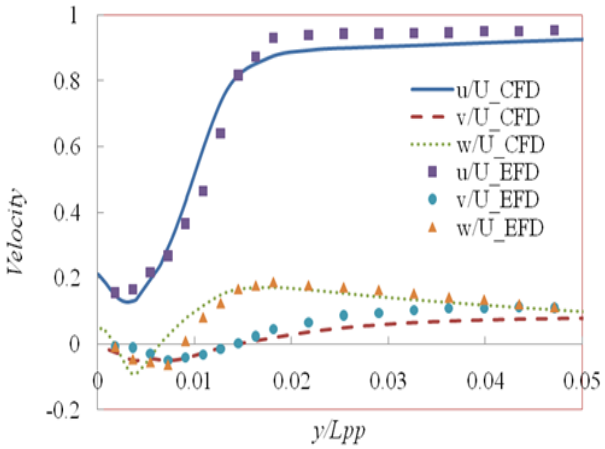

NTNU-FLUENT

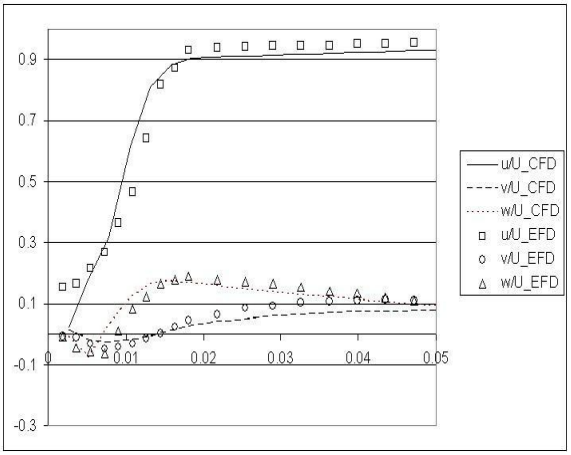

VTT-FINFLO

Fig. 1.1a-5 Velocity on the propeller plane (x/L_{PP} = 0.9825) at z/L_{PP} = -0.05075

u/U: CFD solid line; EFD open squares
v/U: CFD dashed line; EFD open circles
w/U: CFD dotted line; EFD open triangles

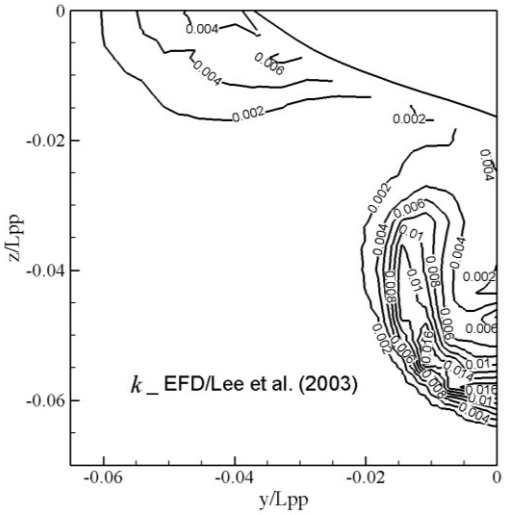

Experiment (Postech, Lee et al. 2003)

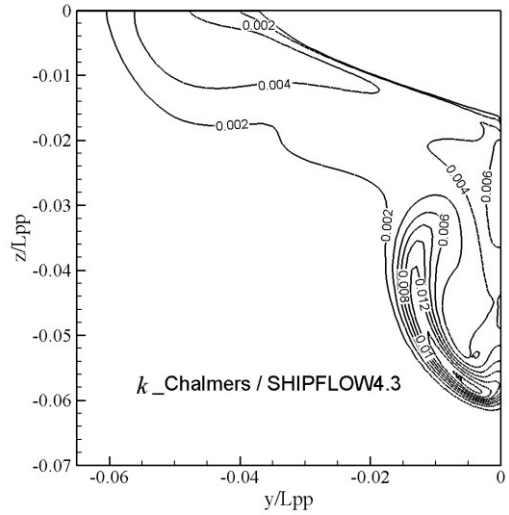

Chalmers-SHIPFLOW4.3

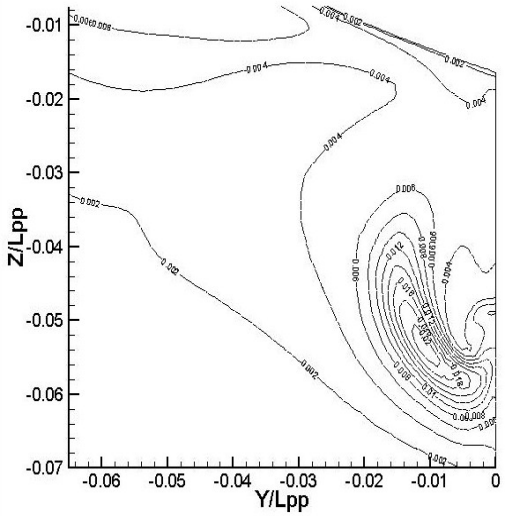

ECN/BEC/HO-Icare

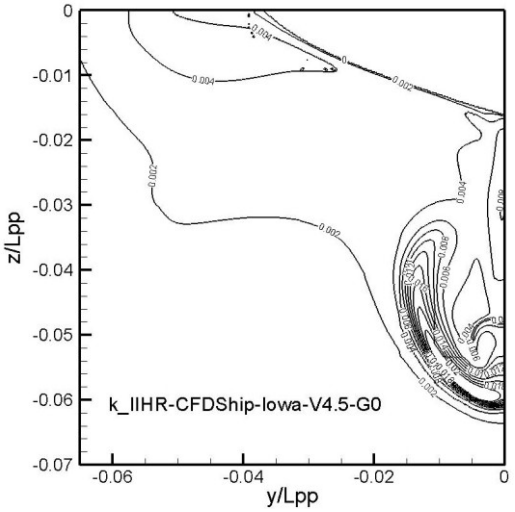

IIHR-CFDShip-Iowa-V4.5 (ARS)

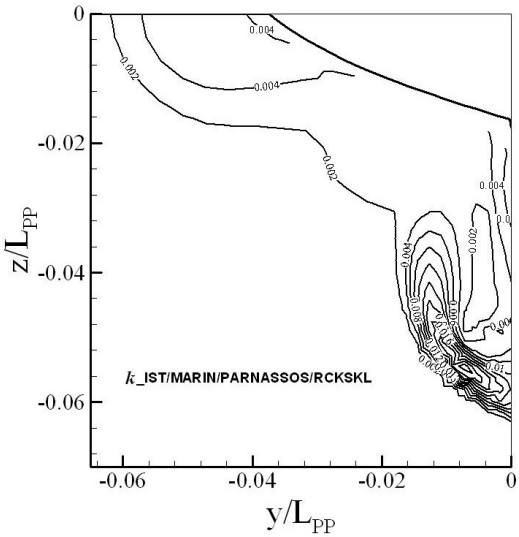

IST/MARIN-PARNASSOS (RCKSKL)

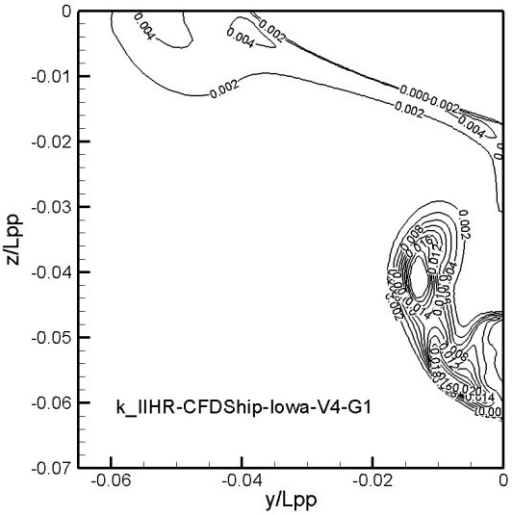

IIHR-CFDShip-Iowa-V4 (ARS-DES)

Fig. 1.1a-6 Turbulent Kinetic energy (k) contours at $x/L_{PP} = 0.9825$ [$\Delta k = 2\times10^{-3}$]

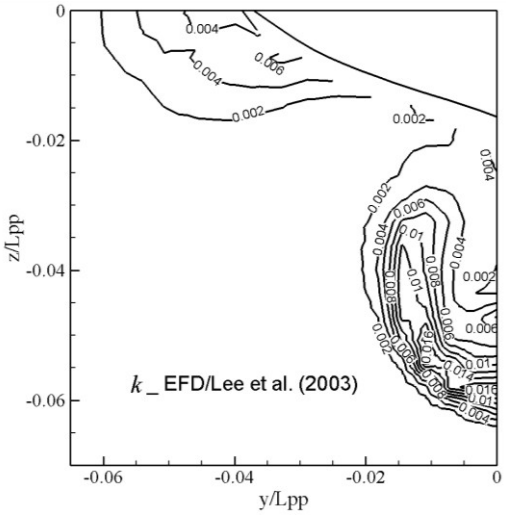

Experiment (Postech, Lee et al. 2003)

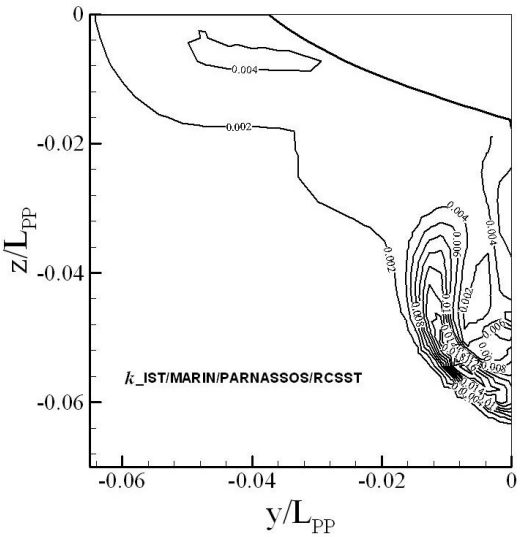

IST/MARIN-PARNASSOS (RCSST)

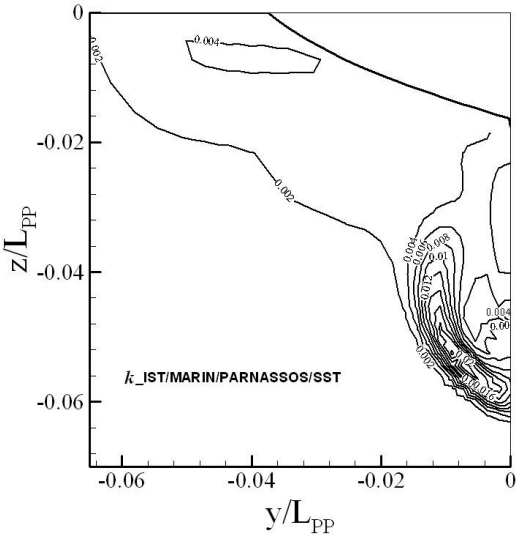

IST/MARIN-PARNASSOS (SST)

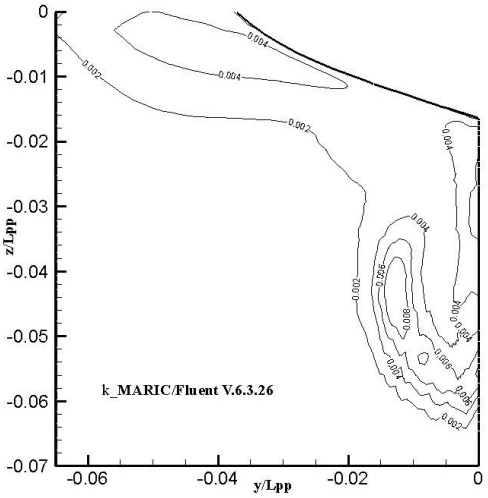

MARIC-Fluent6.3.26

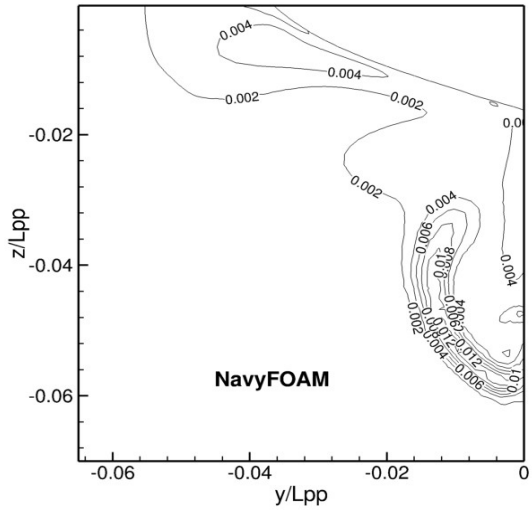

NavyFOAM-NavyFOAM

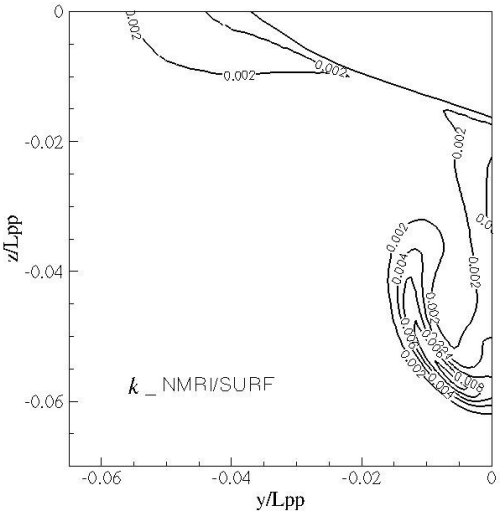

NMRI-SURF

Fig. 1.1a-6 Turbulent Kinetic energy (k) contours at $x/L_{PP} = 0.9825$ [$\Delta k = 2\times10^{-3}$]

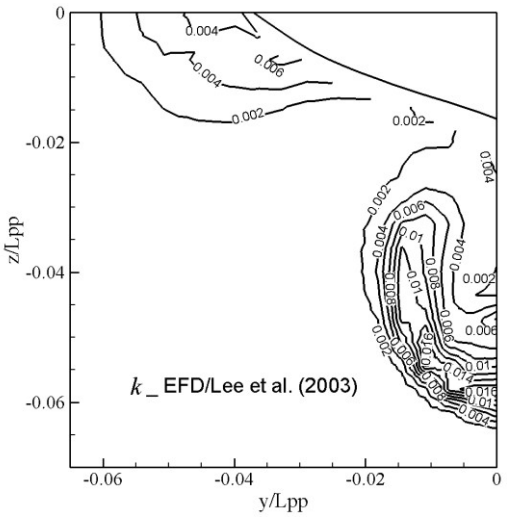

Experiment (Postech, Lee et al. 2003)

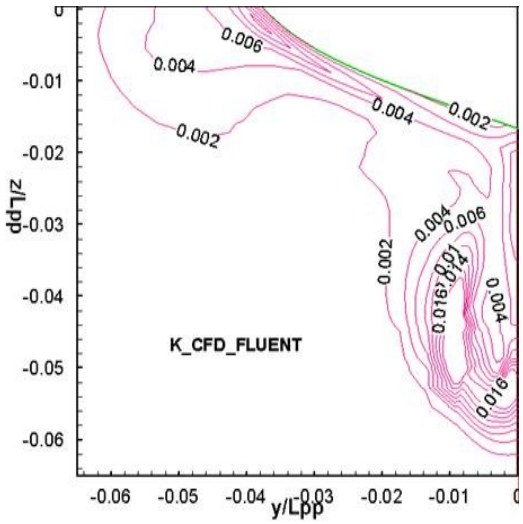

NTNU-FLUENT

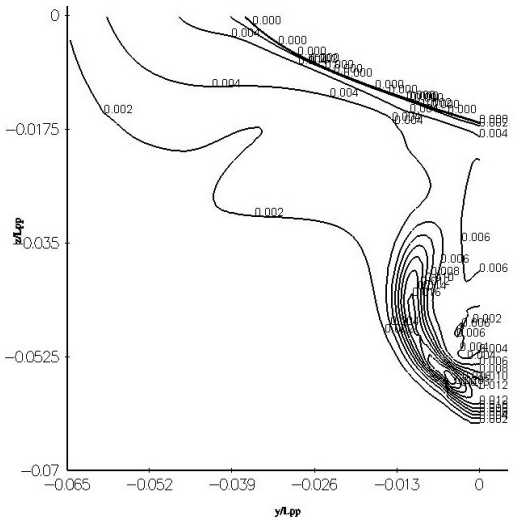

VTT-FINFLO

Fig. 1.1a-6 Turbulent Kinetic energy (k) contours at $x/L_{PP} = 0.9825$ [$\Delta k = 2\times10^{-3}$]

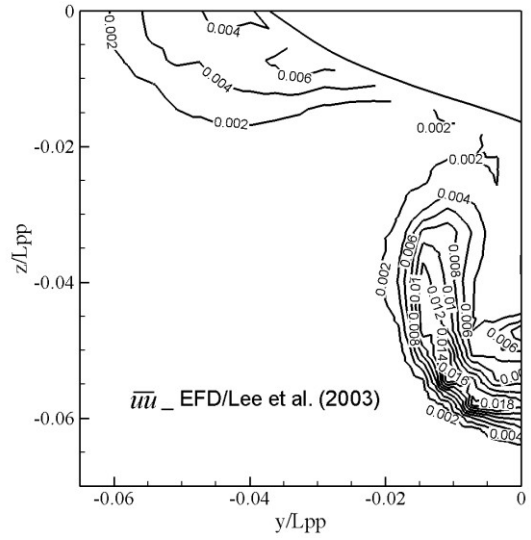

Experiment (Postech, Lee et al. 2003)

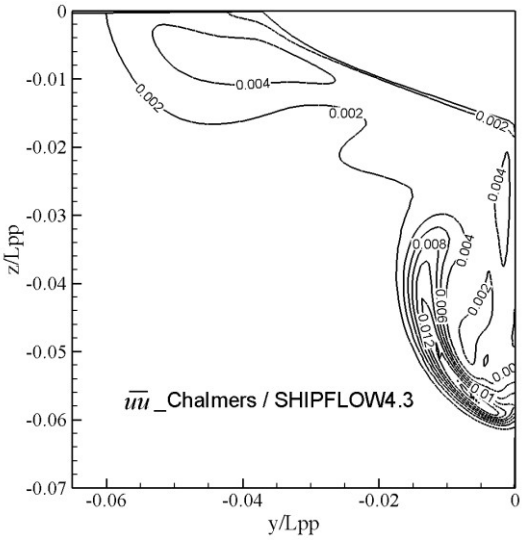

Chalmers-SHIPFLOW4.3

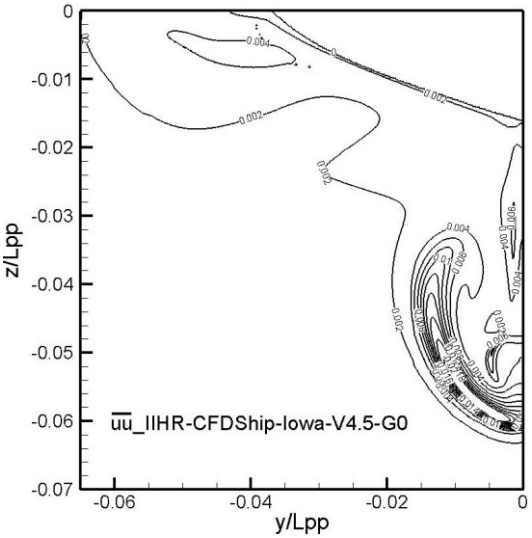

IIHR-CFDShip-Iowa-V4.5 (ARS)

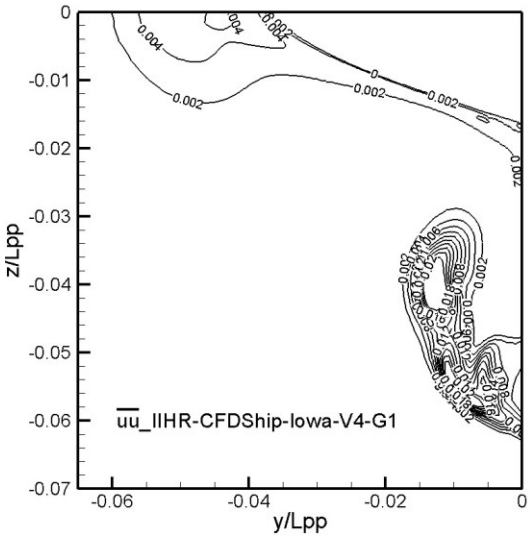

IIHR-CFDShip-Iowa-V4 (ARS-DES)

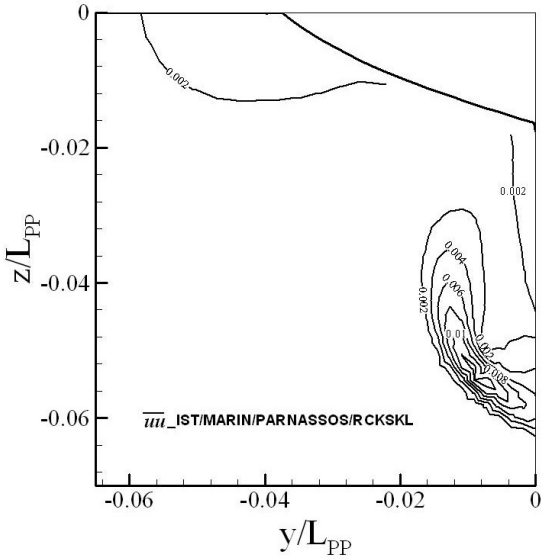

IST/MARIN-PARNASSOS (RCKSKL)

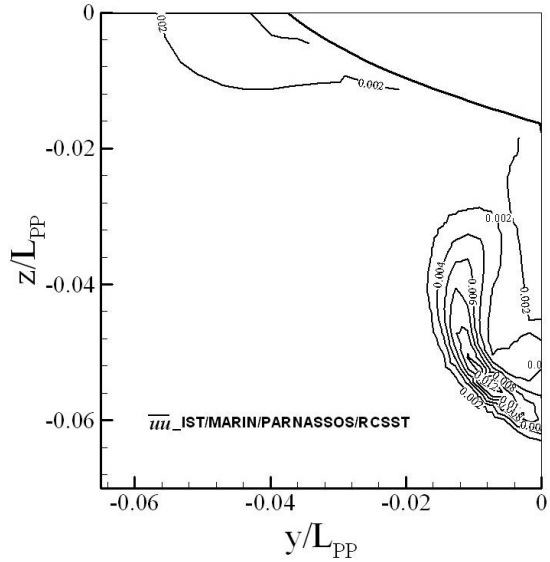

IST/MARIN-PARNASSOS (RCSST)

Fig. 1.1a-7 $\overline{uu}$ contours on the propeller plane (x/L_{PP} = 0.9825) [$\Delta\overline{uu} = 2\times10^{-3}$]

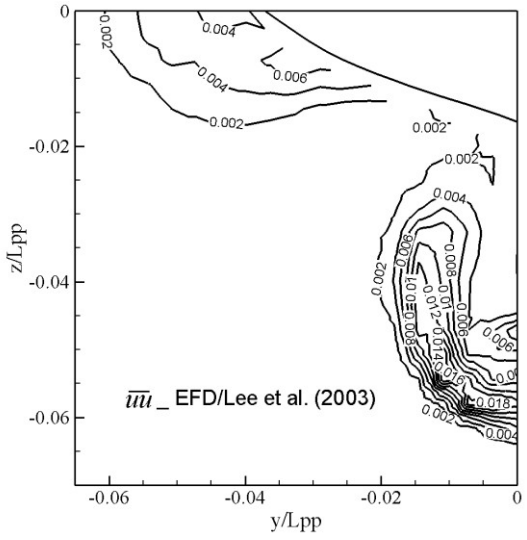

Experiment (Postech, Lee et al. 2003)

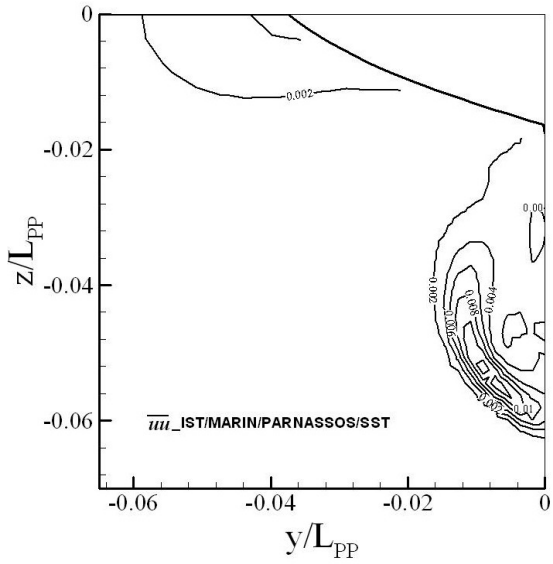

IST/MARIN-PARNASSOS (SST)

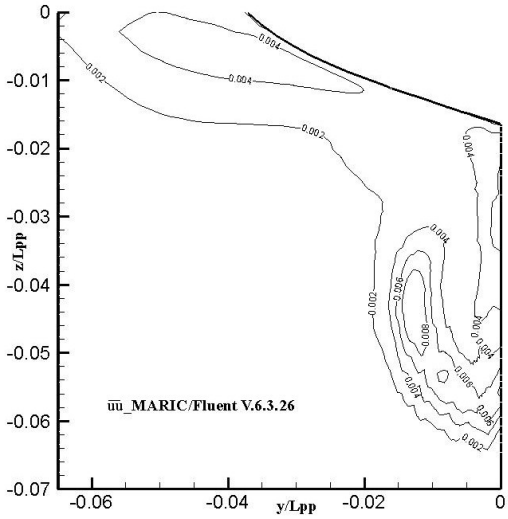

MARIC-Fluent6.3.26

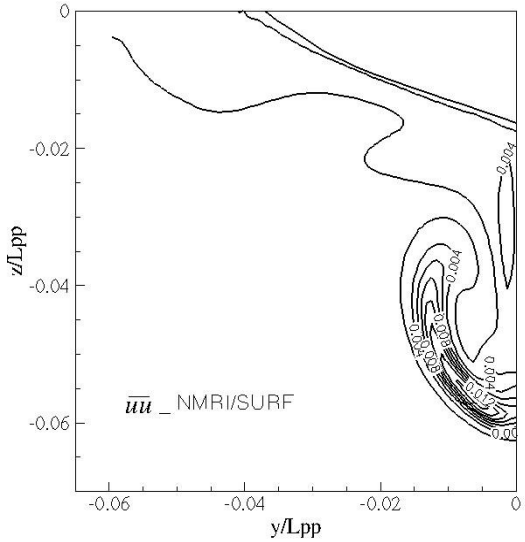

NMRI-SURF

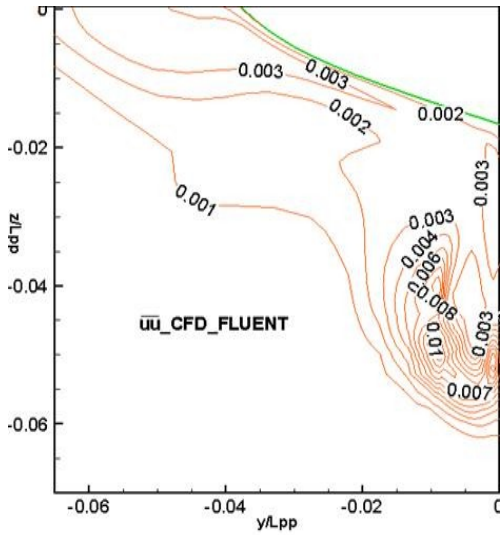

NTNU-FLUENT

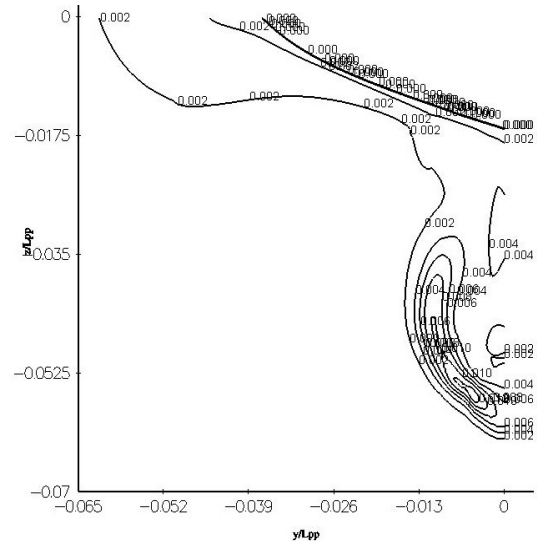

VTT-FINFLO

Fig. 1.1a-7 $\overline{uu}$ contours on the propeller plane (x/L_{PP} = 0.9825) [$\Delta\overline{uu} = 2\times10^{-3}$]

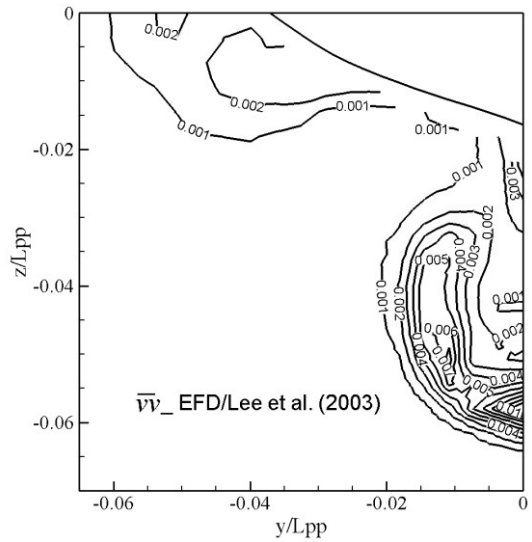

Experiment (Postech, Lee et al. 2003)

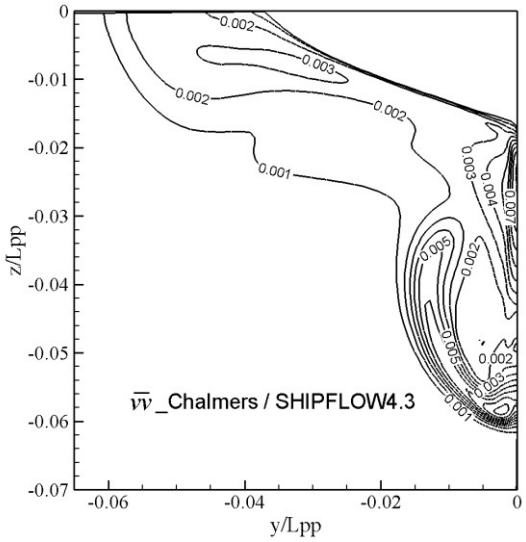

Chalmers-SHIPFLOW4.3

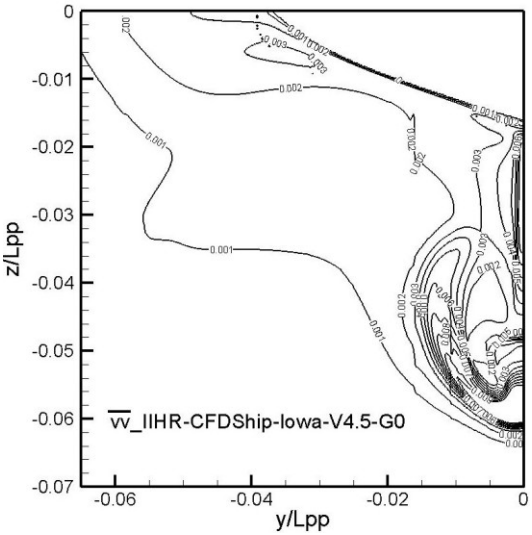

IIHR-CFDShip-Iowa-V4.5 (ARS)

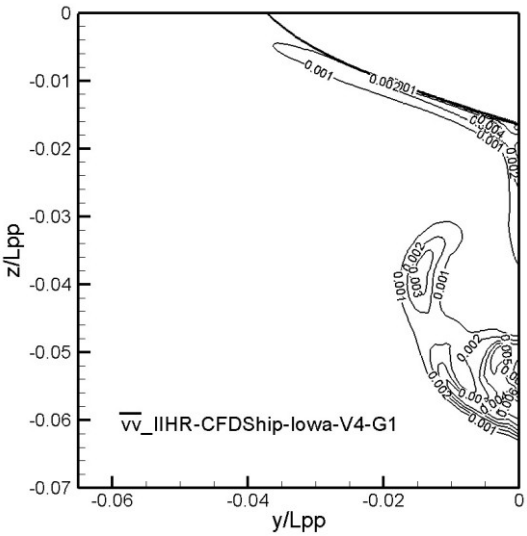

IIHR-CFDShip-Iowa-V4 (ARS-DES)

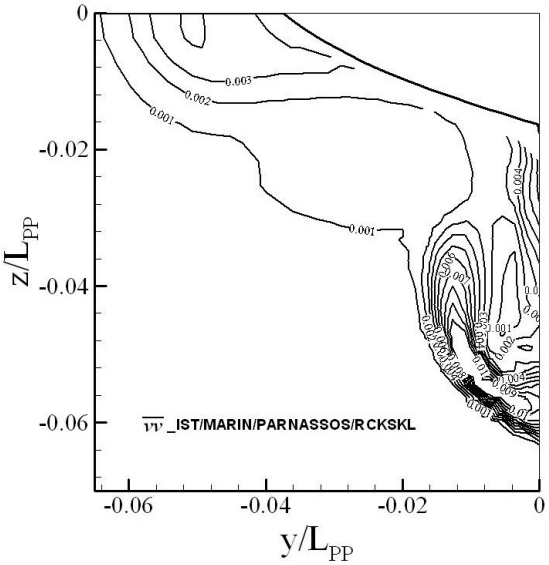

IST/MARIN-PARNASSOS (RCKSKL)

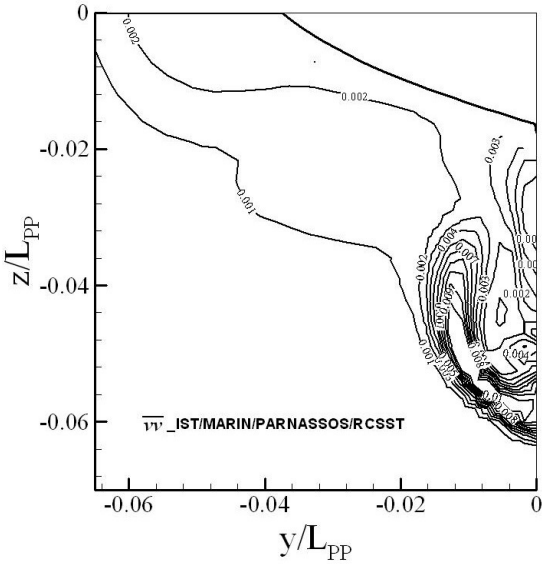

IST/MARIN-PARNASSOS (RCSST)

Fig. 1.1a-8 $\overline{vv}$ contours on the propeller plane (x/L_{PP} = 0.9825) [$\Delta\overline{vv} = 1\times10^{-3}$]

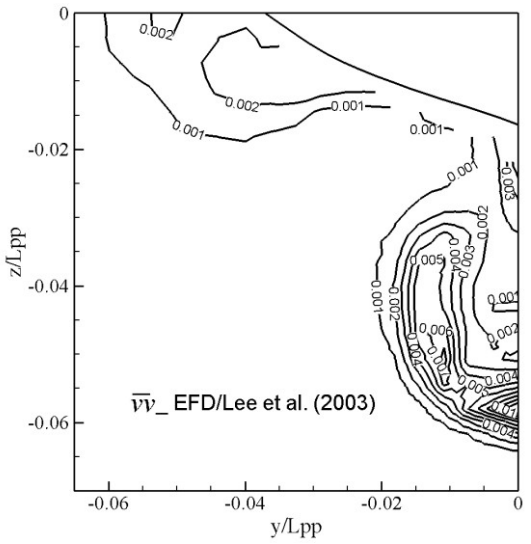

Experiment (Postech, Lee et al. 2003)

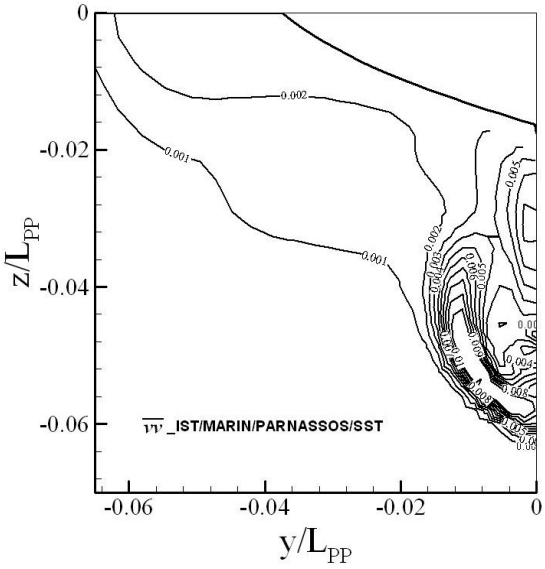

IST/MARIN-PARNASSOS (SST)

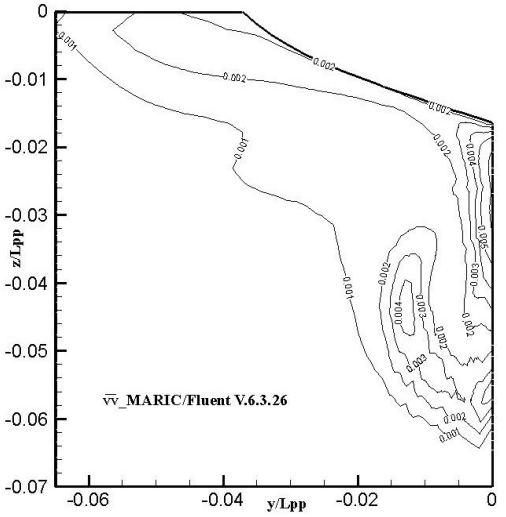

MARIC-Fluent6.3.26

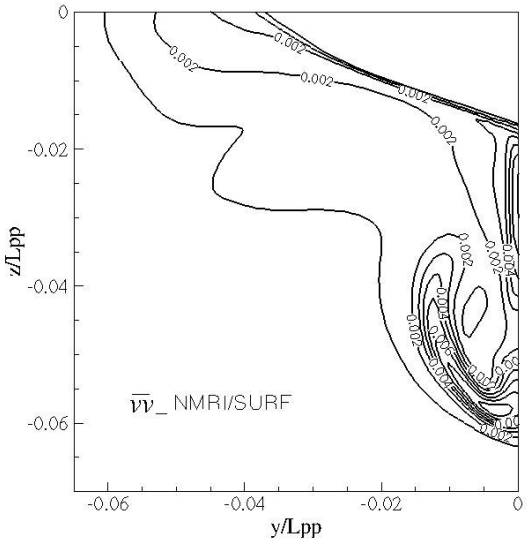

NMRI-SURF

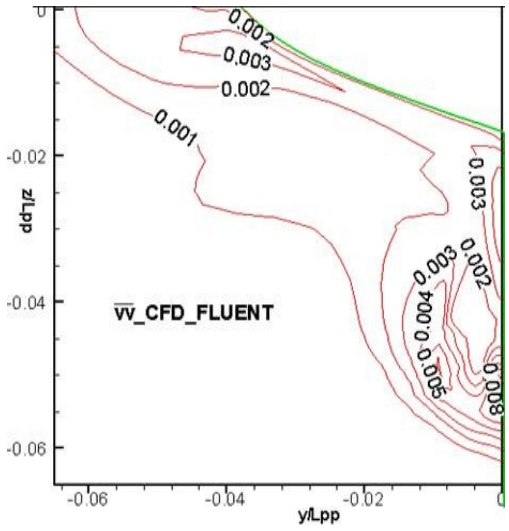

NTNU-FLUENT

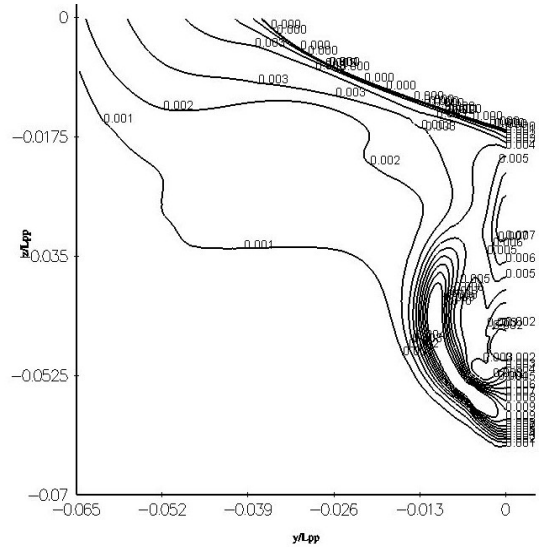

VTT-FINFLO

Fig. 1.1a-8 $\overline{vv}$ contours on the propeller plane (x/L_{PP} = 0.9825) [$\Delta\overline{vv} = 1\times10^{-3}$]

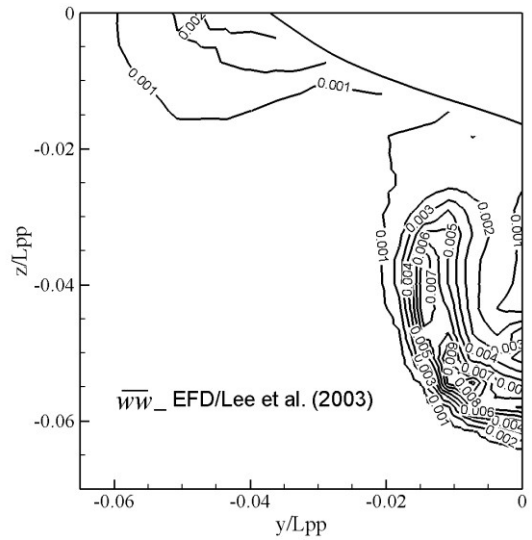

Experiment (Postech, Lee et al. 2003)

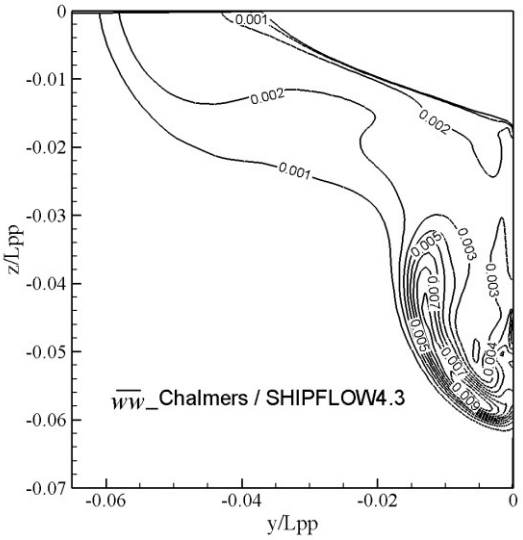

Chalmers-SHIPFLOW4.3

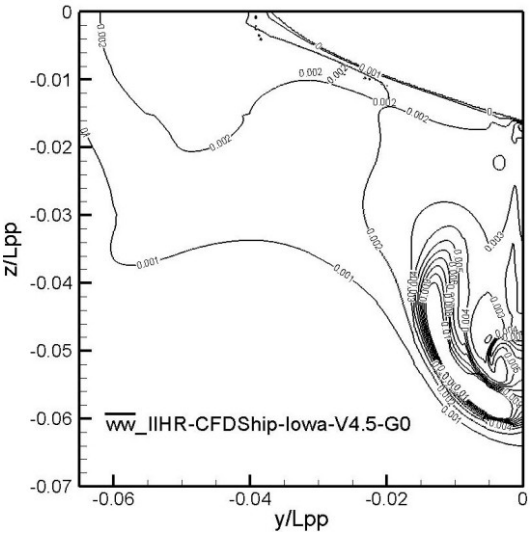

IIHR-CFDShip-Iowa-V4.5 (ARS)

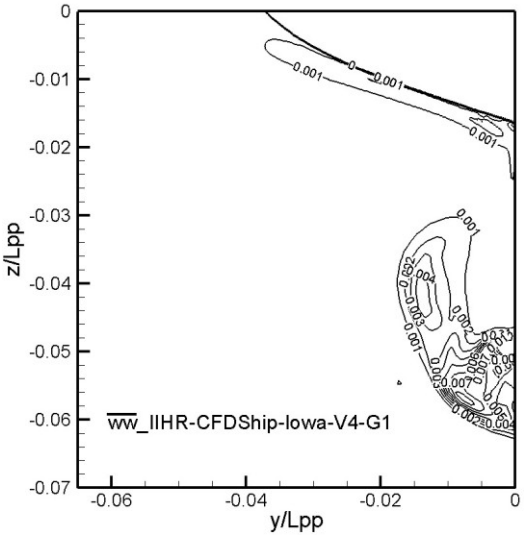

IIHR-CFDShip-Iowa-V4 (ARS-DES)

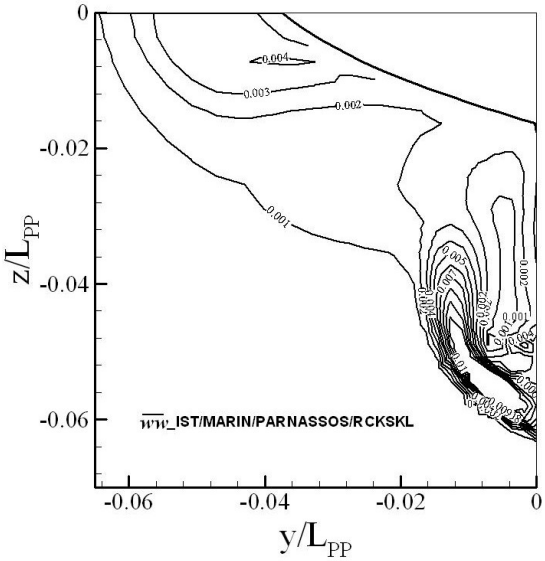

IST/MARIN-PARNASSOS (RCKSKL)

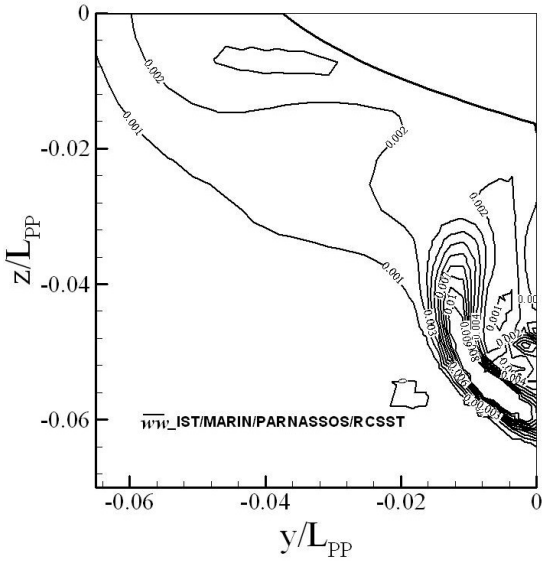

IST/MARIN-PARNASSOS (RCSST)

Fig. 1.1a-9 $\overline{ww}$ contours on the propeller plane (x/L_{PP} = 0.9825) [$\Delta\overline{ww} = 1\times10^{-3}$]

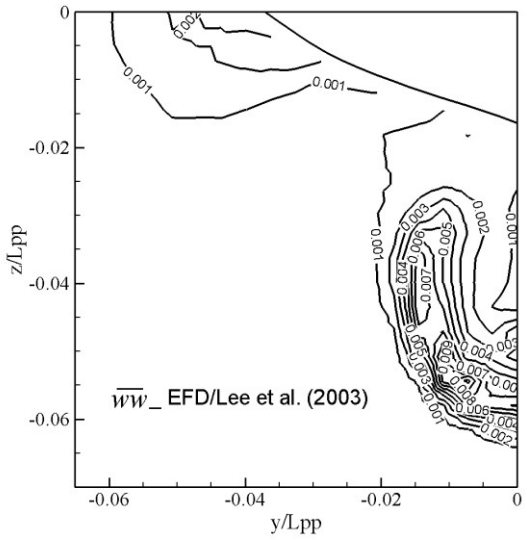

Experiment (Postech, Lee et al. 2003)

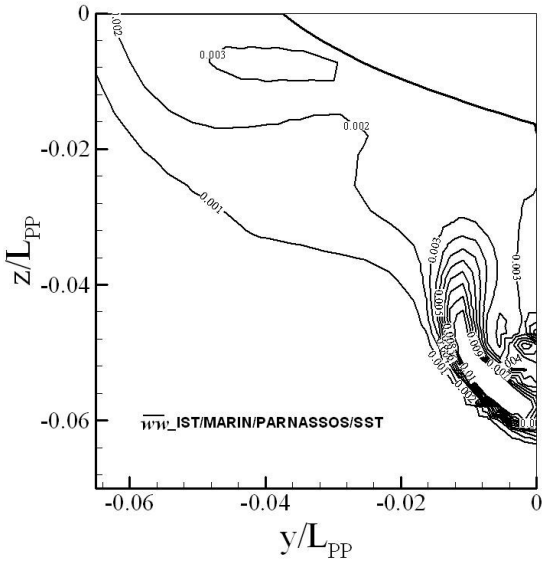

IST/MARIN-PARNASSOS (SST)

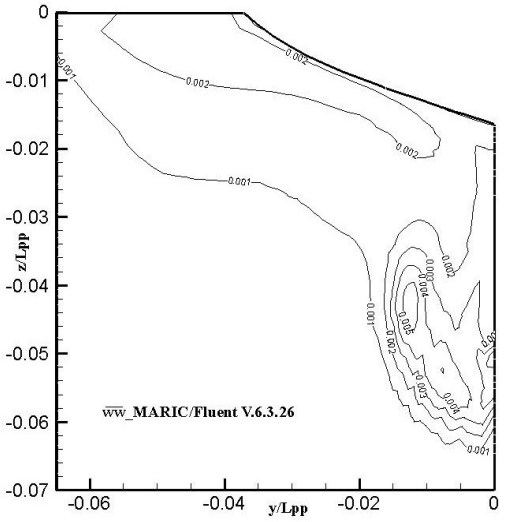

MARIC-Fluent6.3.26

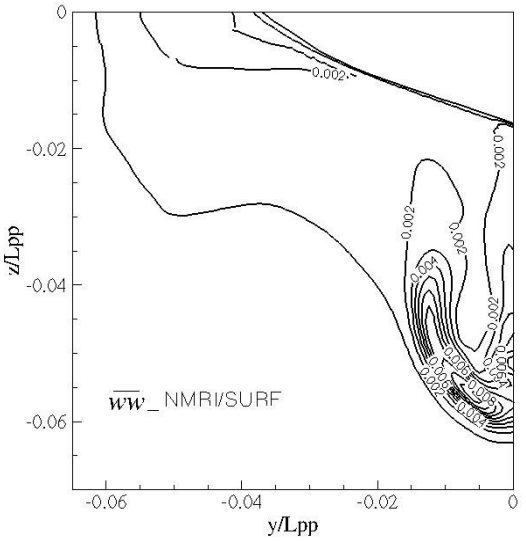

NMRI-SURF

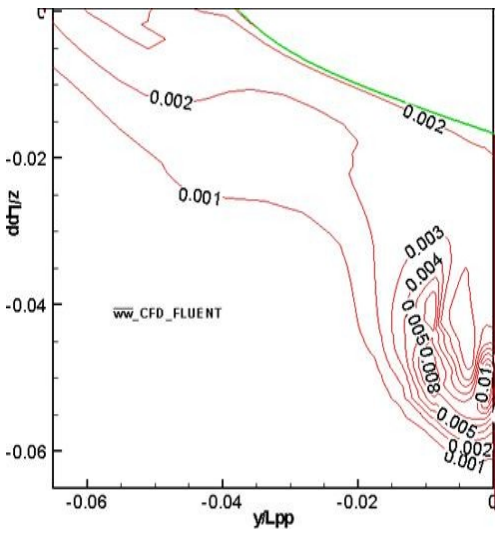

NTNU-FLUENT

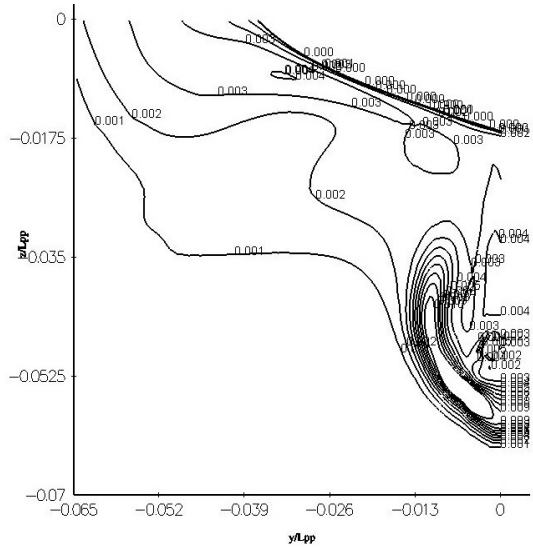

VTT-FINFLO

Fig. 1.1a-9 $\overline{ww}$ contours on the propeller plane (x/L_{PP} = 0.9825) [$\Delta\overline{ww}$ = 1×10^{-3}]

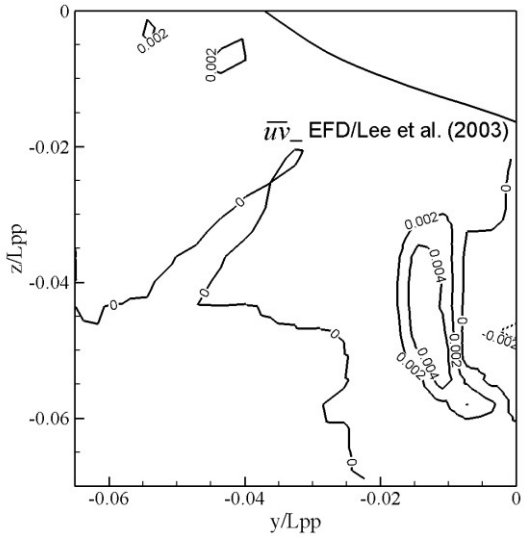

Experiment (Postech, Lee et al. 2003)

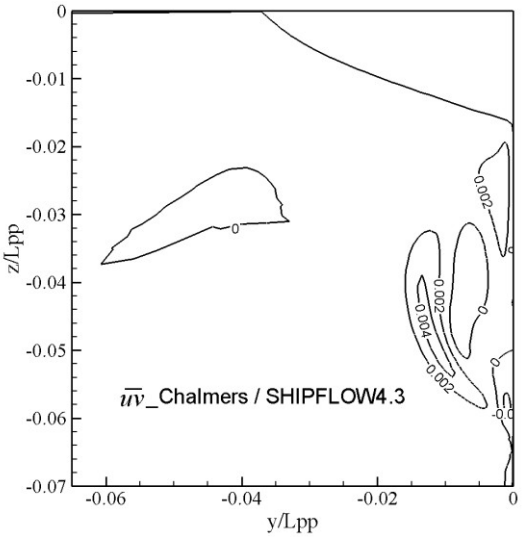

Chalmers-SHIPFLOW4.3

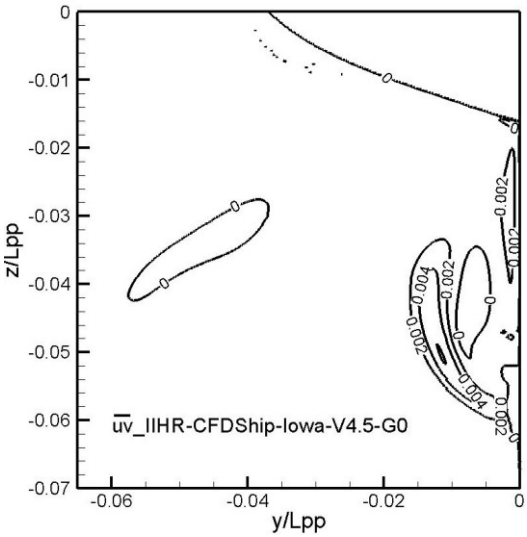

IIHR-CFDShip-Iowa-V4.5 (ARS)

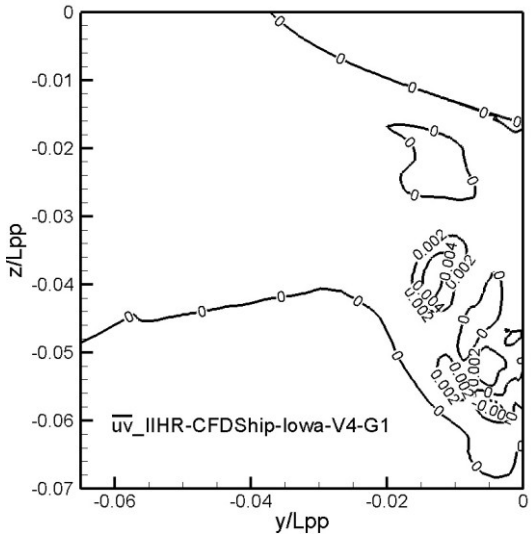

IIHR-CFDShip-Iowa-V4 (ARS-DES)

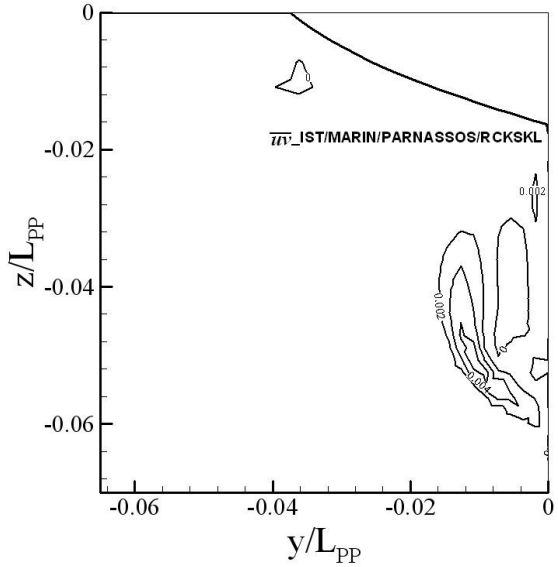

IST/MARIN-PARNASSOS (RCKSKL)

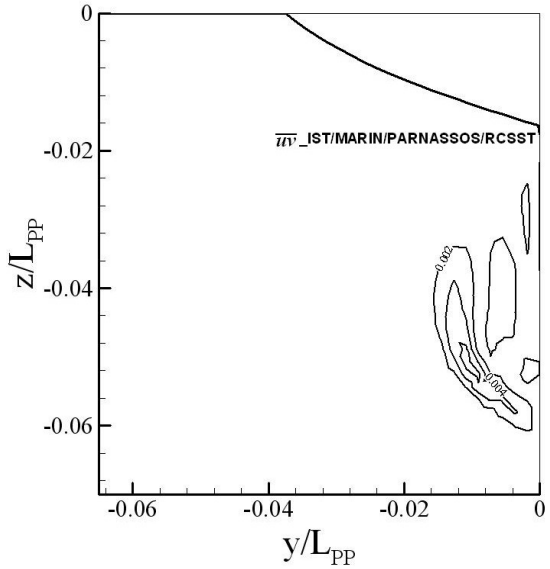

IST/MARIN-PARNASSOS (RCSST)

Fig. 1.1a-10 $\overline{uv}$ contours on the propeller plane (x/L_{PP} = 0.9825) [$\Delta\overline{uv} = 2\times10^{-3}$]
(Solid lines: positive (+) values; Dashed lines: negative (-) values)

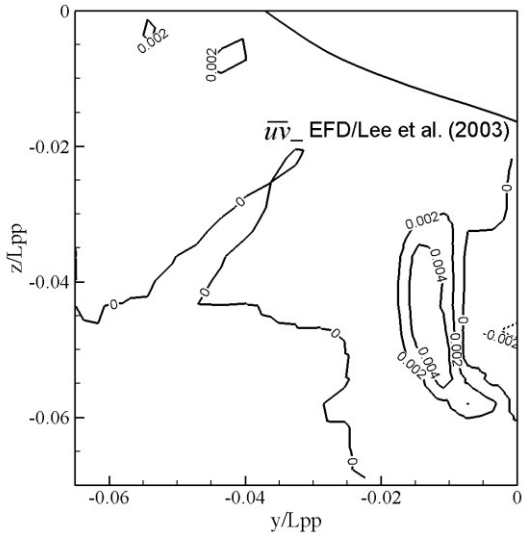

Experiment (Postech, Lee et al. 2003)

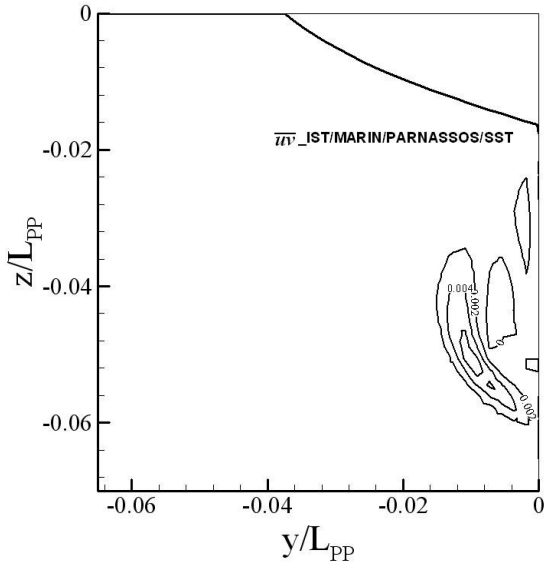

IST/MARIN-PARNASSOS (SST)

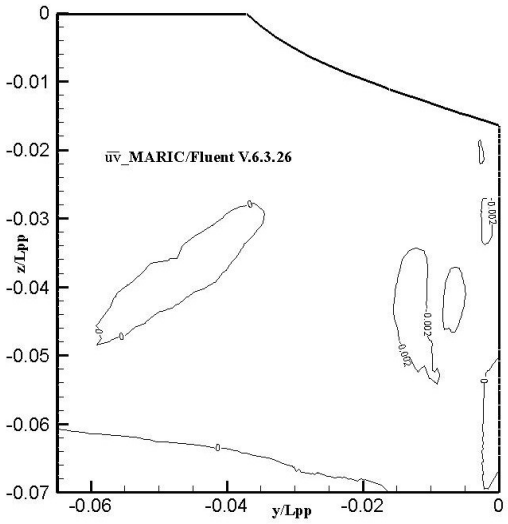

MARIC-Fluent6.3.26

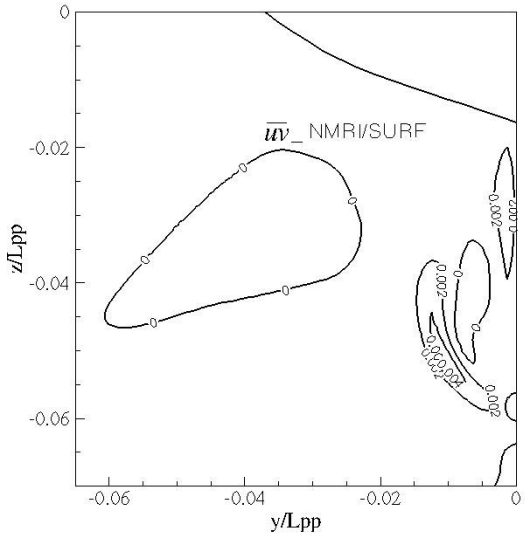

NMRI-SURF

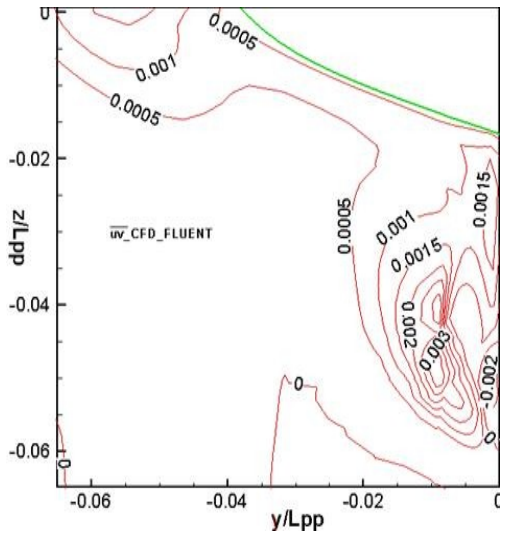

NTNU-FLUENT

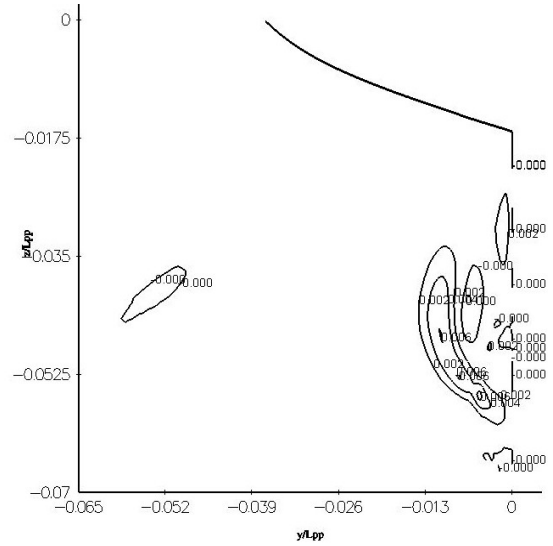

VTT-FINFLO

Fig. 1.1a-10 $\overline{uv}$ contours on the propeller plane (x/L_{PP} = 0.9825) [$\Delta\overline{uv} = 2\times10^{-3}$]
(Solid lines: positive (+) values; Dashed lines: negative (-) values)

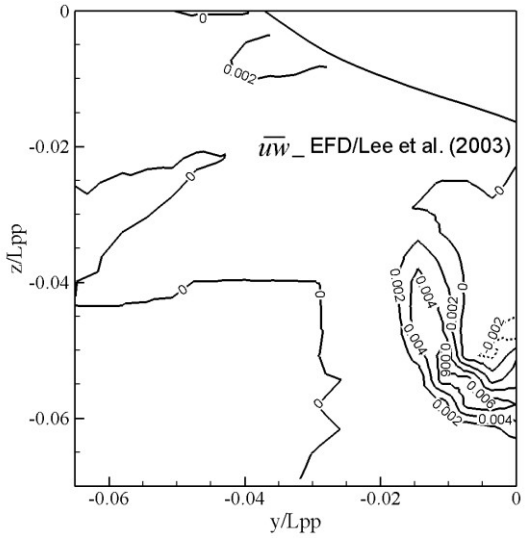

Experiment (Postech, Lee et al. 2003)

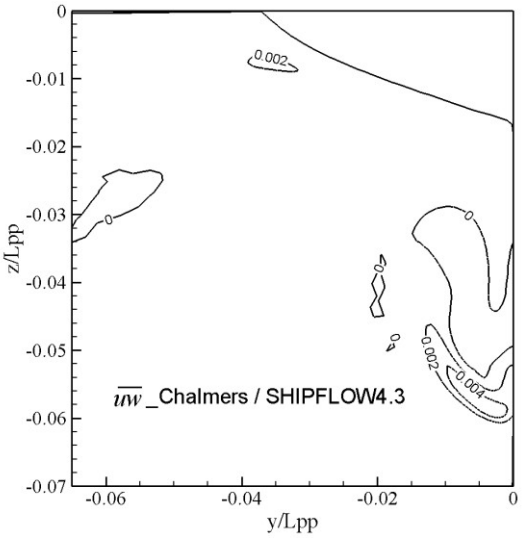

Chalmers-SHIPFLOW4.3

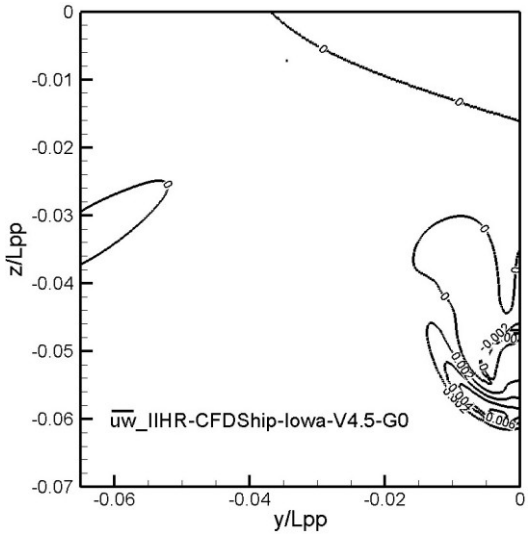

IIHR-CFDShip-Iowa-V4.5 (ARS)

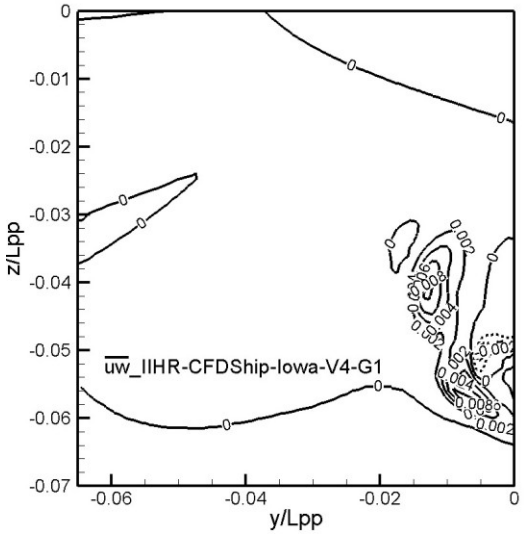

IIHR-CFDShip-Iowa-V4 (ARS-DES)

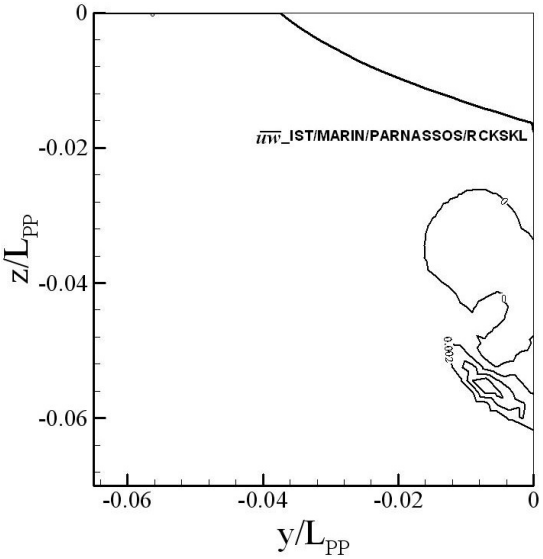

IST/MARIN-PARNASSOS (RCKSKL)

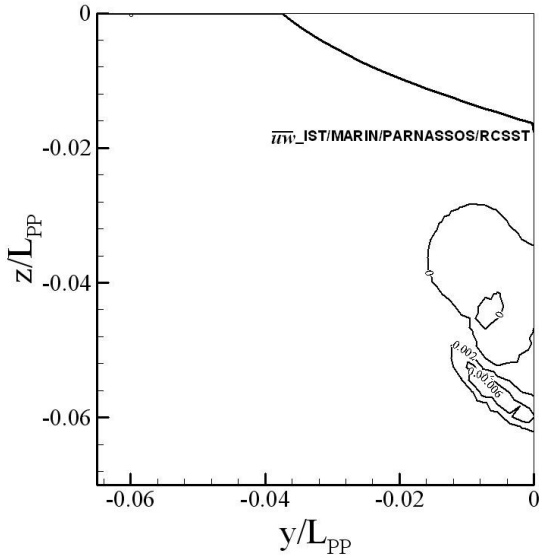

IST-MARIN-PARNASSOS (RCSST)

Fig. 1.1a-11 $\overline{uw}$ contours at propeller plane (x/L_{PP} = 0.9825) [$\Delta\overline{uw} = 2\times10^{-3}$]
(Solid lines: positive (+) values; Dashed lines: negative (-) values)

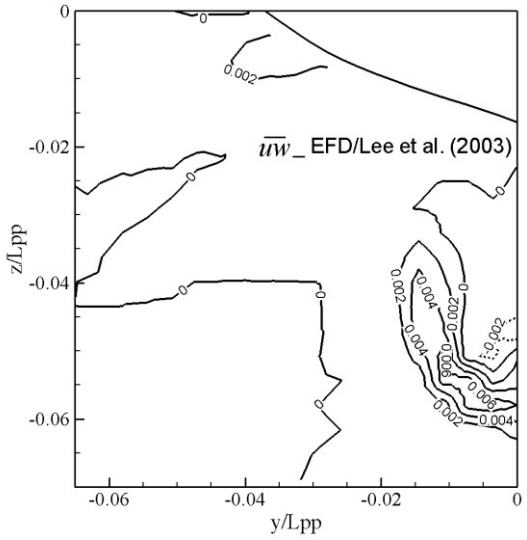

Experiment (Postech, Lee et al. 2003)

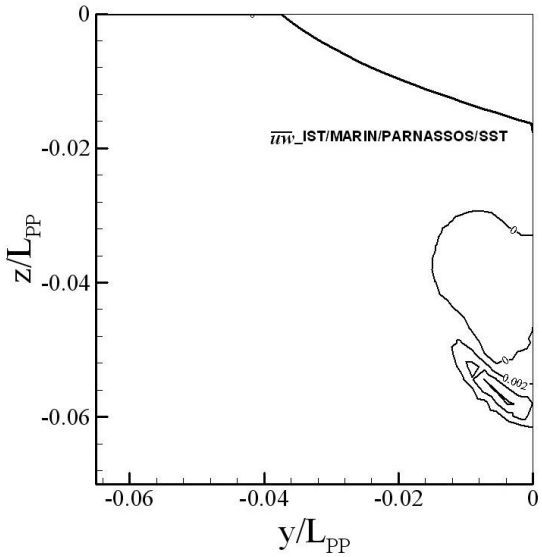

IST-MARIN-PARNASSOS (SST)

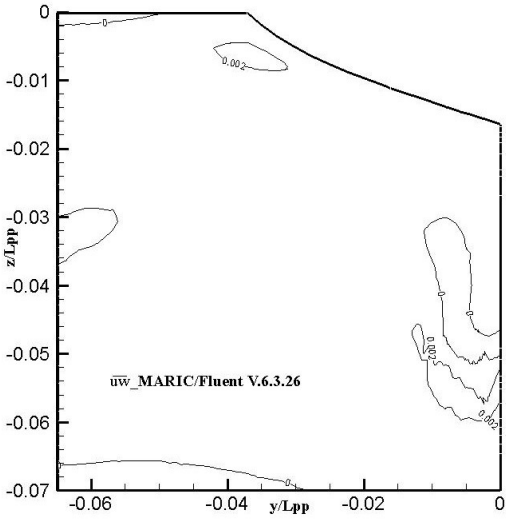

MARIC-Fluent6.3.26

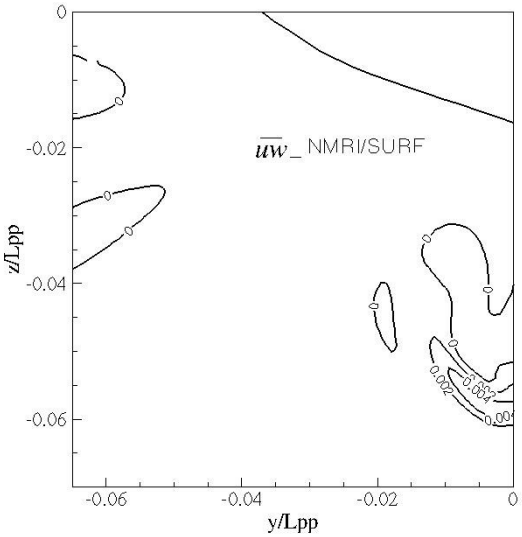

NMRI-SURF

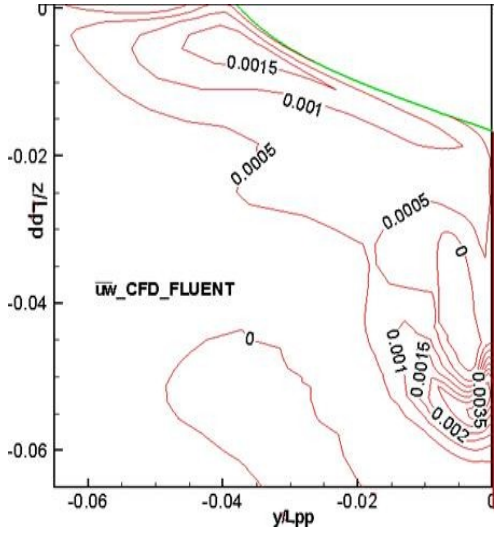

NTNU-FLUENT

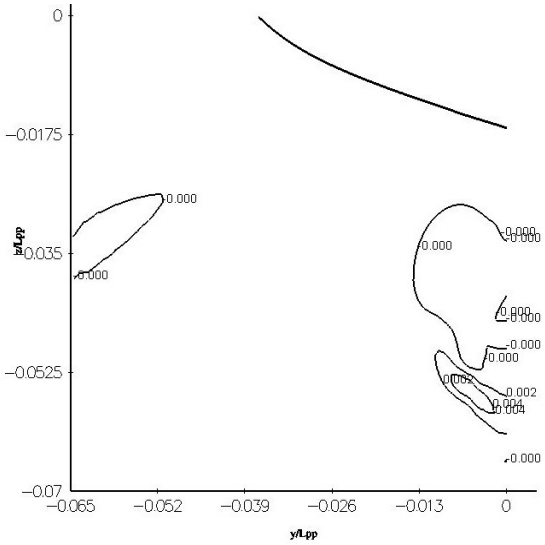

VTT-FINFLO

Fig. 1.1a-11 $\overline{uw}$ contours at propeller plane (x/L_{PP} = 0.9825) [$\Delta\overline{uw} = 2\times10^{-3}$]
(Solid lines: positive (+) values; Dashed lines: negative (-) values)

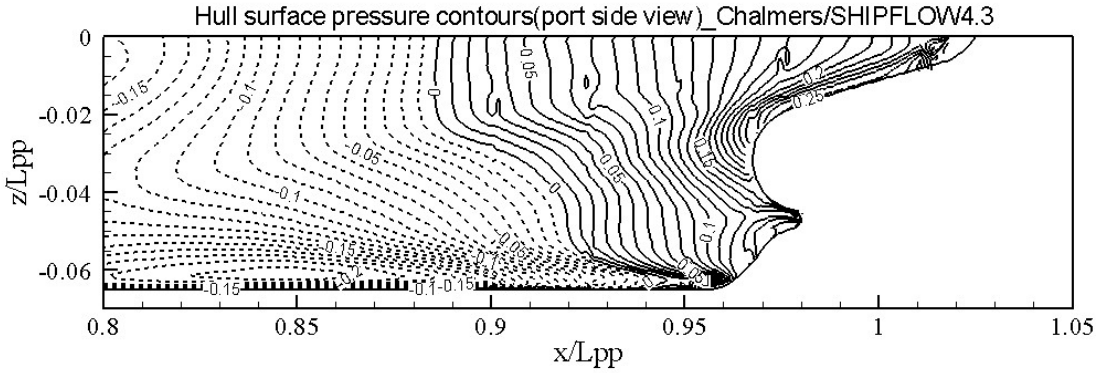

Chalmers-SHIPFLOW4.3

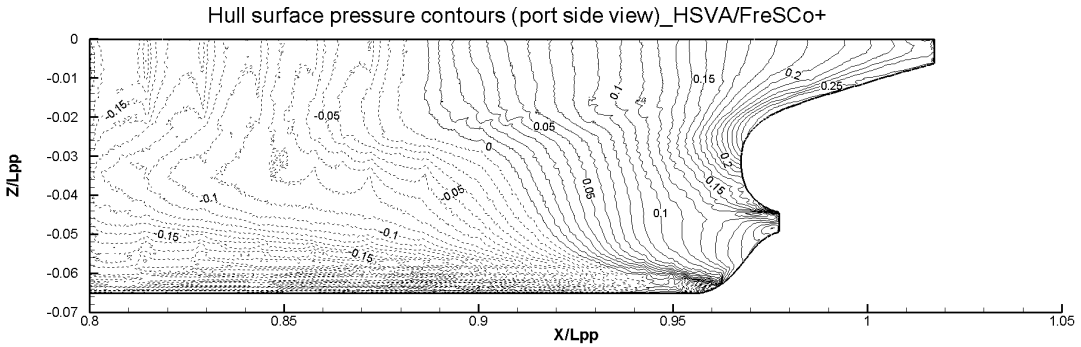

HSVA-FreSCo+

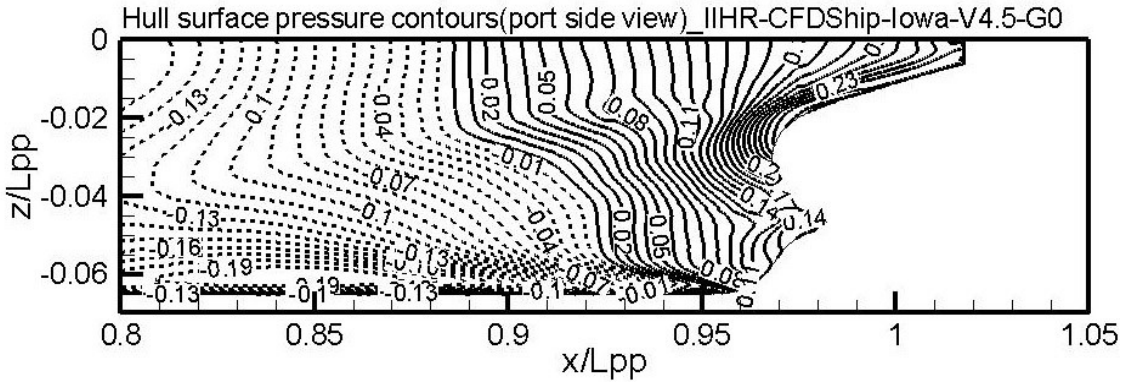

IIHR-CFDShip-Iowa-V4.5 (ARS)

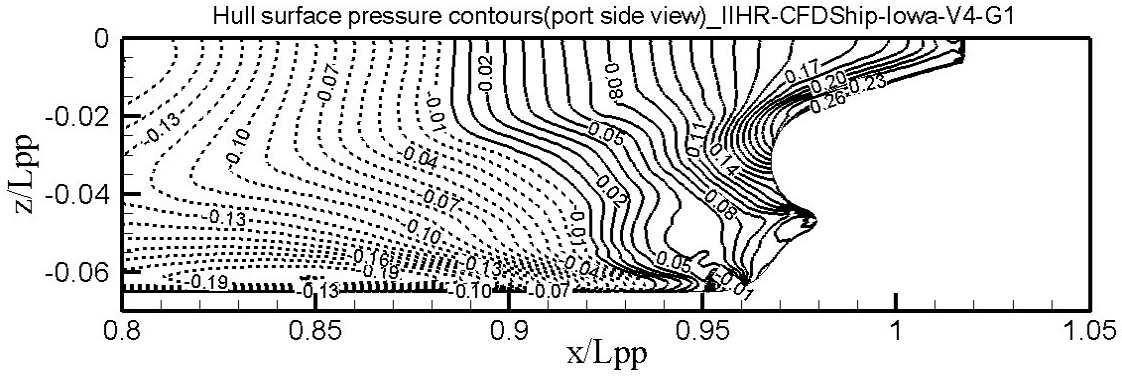

IIHR-CFDShip-Iowa-V4 (ARS-DES)

Fig. 1.1a-12 Hull surface pressure contours (port side view) [$\Delta Cp = 0.01$]
(Solid lines: positive (+) values; Dashed lines: negative (-) values)

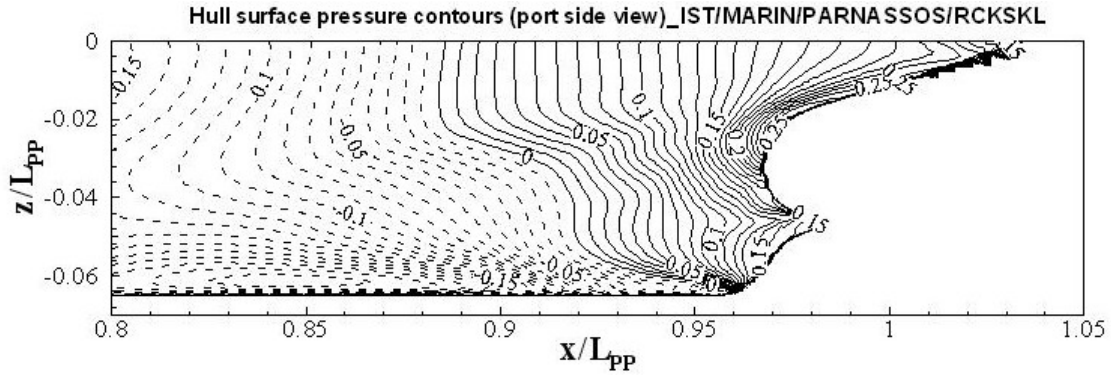

IST/MARIN-PARNASSOS (RCKSKL)

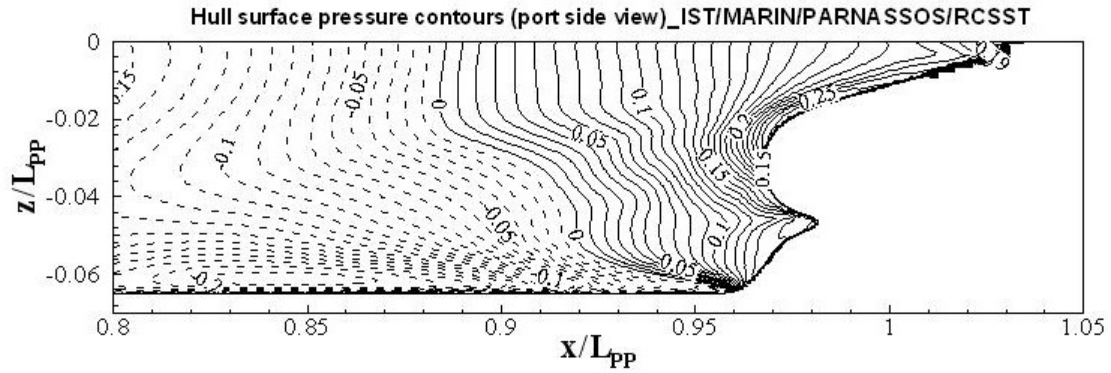

IST/MARIN-PARNASSOS (RCSST)

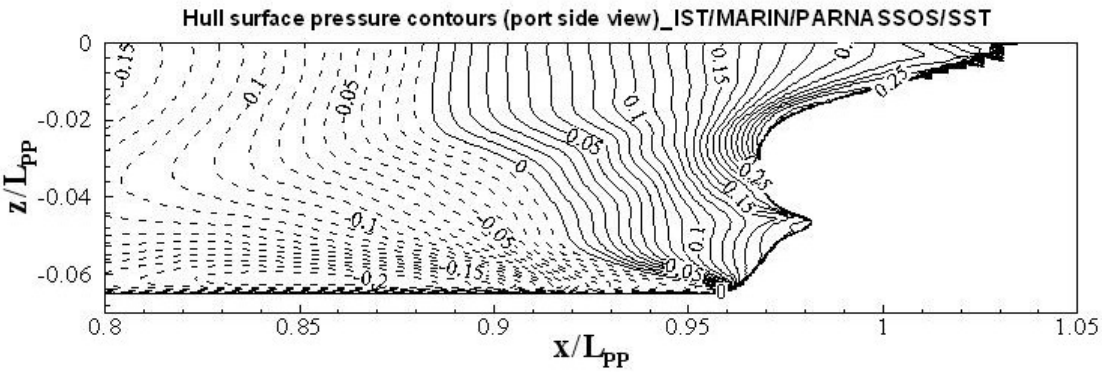

IST/MARIN-PARNASSOS (SST)

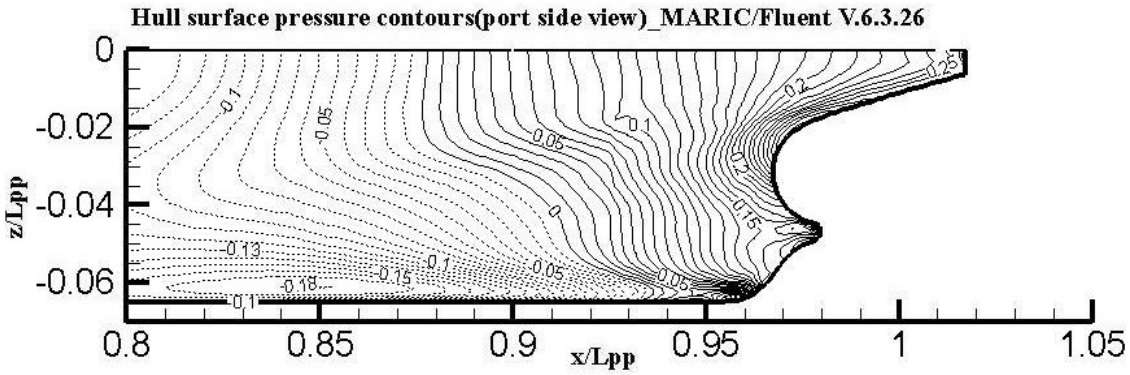

MARIC-Fluent6.3.26

Fig. 1.1a-12 Hull surface pressure contours (port side view) [$\Delta Cp = 0.01$]
(Solid lines: positive (+) values; Dashed lines: negative (-) values)

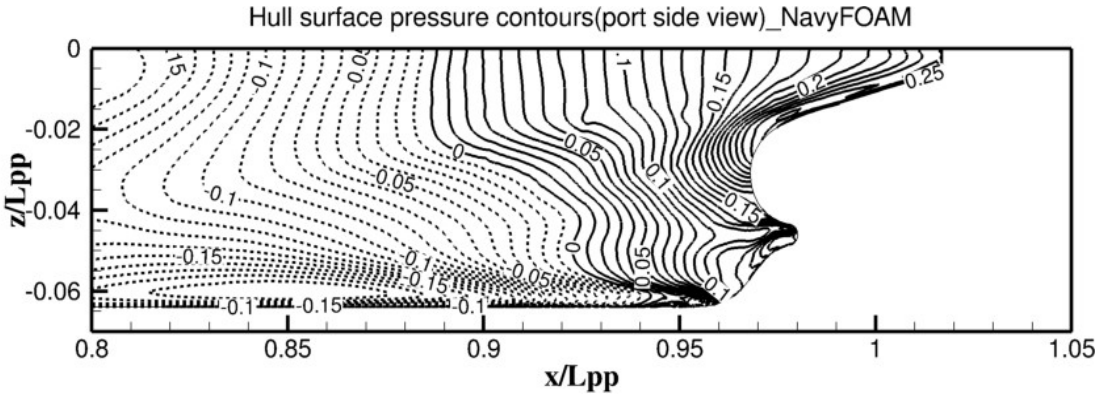

NavyFOAM-NavyFOAM

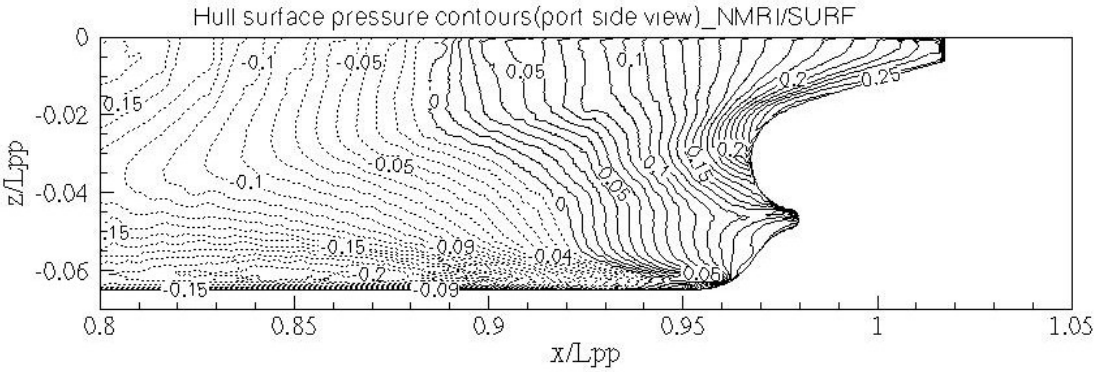

NMRI-SURF

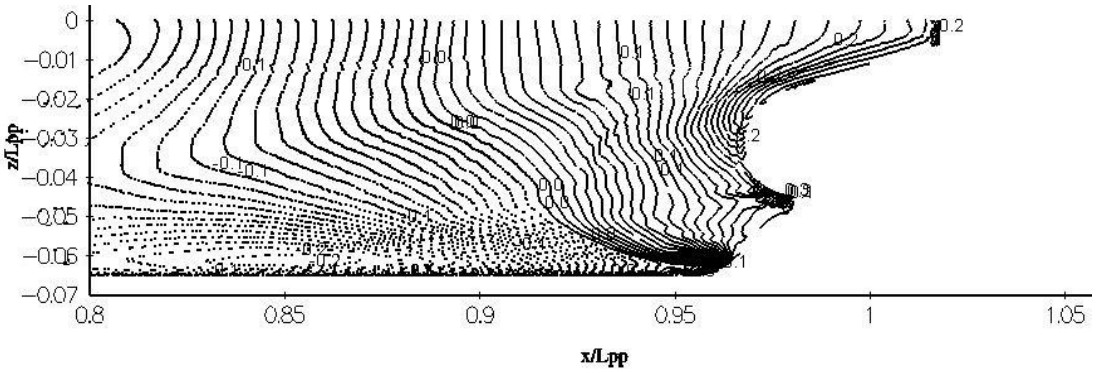

VTT-FINFLO

Fig. 1.1a-12 Hull surface pressure contours (port side view) [$\Delta Cp = 0.01$]
(Solid lines: positive (+) values; Dashed lines: negative (-) values)

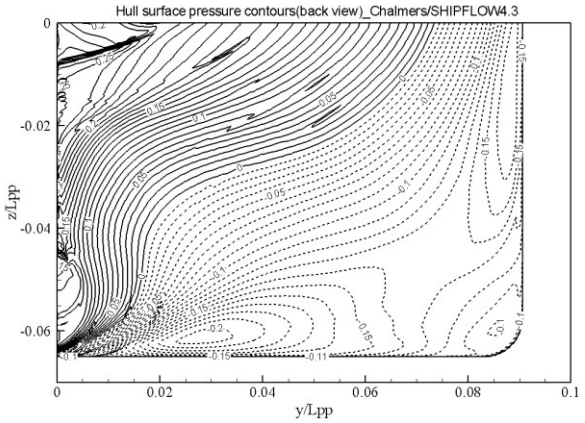

Chalmers-SHIPFLOW4.3

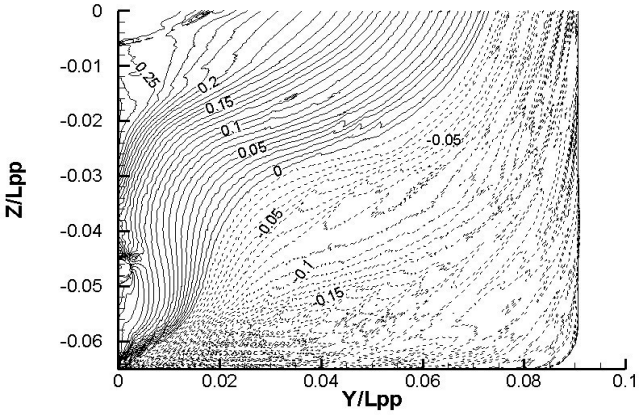

HSVA-FreSCo+

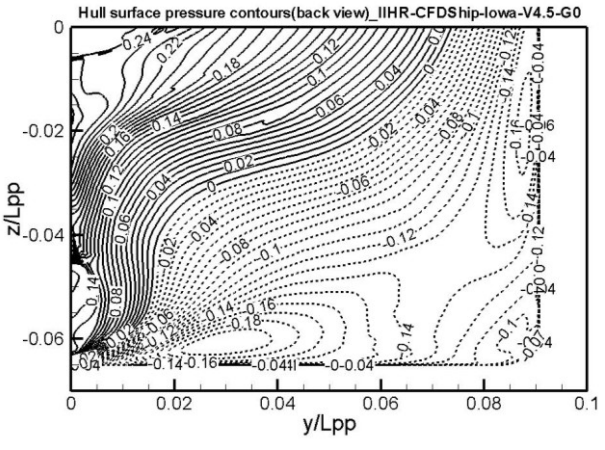

IIHR-CFDShip-Iowa-V4.5 (ARS)

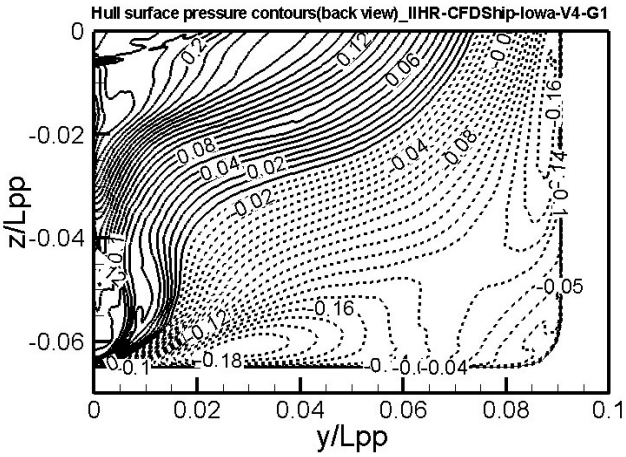

IIHR-CFDShip-Iowa-V4 (ARS-DES)

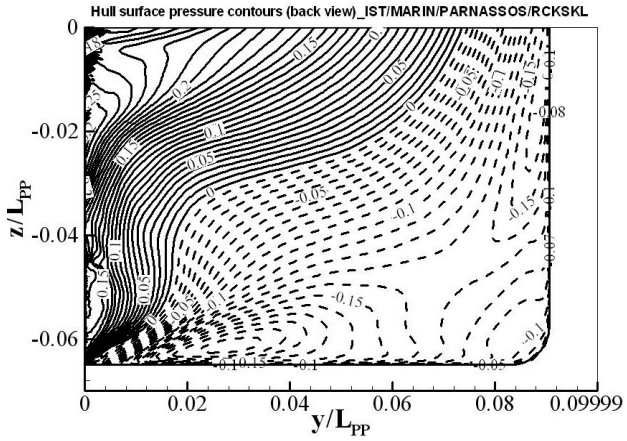

IST/MARIN-PARNASSOS (RCKSKL)

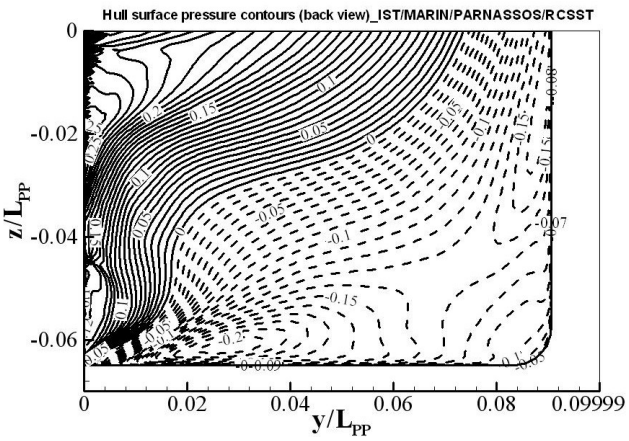

IST/MARIN-PARNASSOS (RCSST)

Fig. 1.1a-13 Hull surface pressure contours (back view) [$\Delta Cp = 0.01$]
(Solid lines: positive (+) values; Dashed lines: negative (-) values)

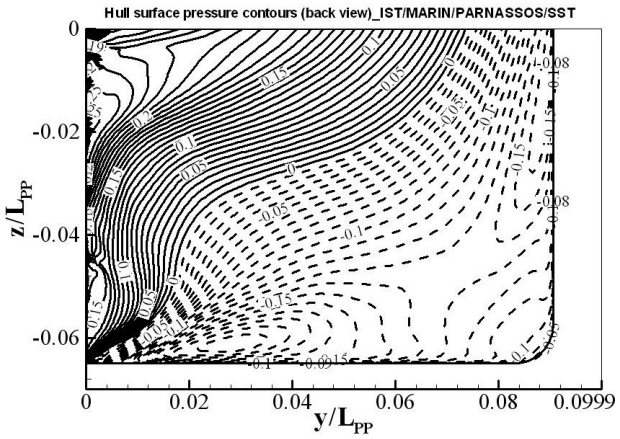

IST/MARIN-PARNASSOS (SST)

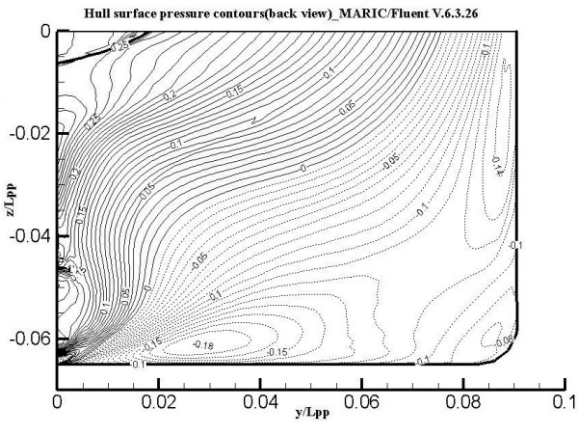

MARIC-Fluent6.3.26

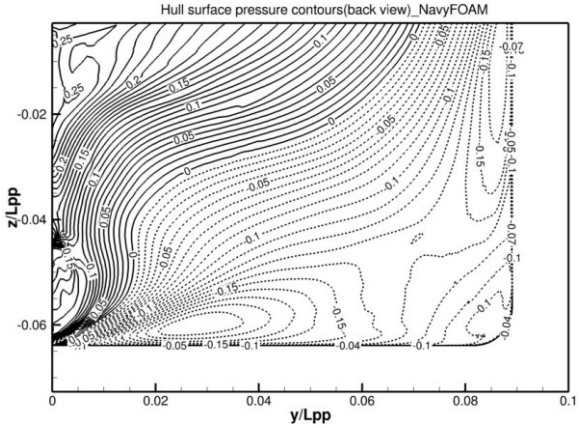

NavyFOAM-NavyFOAM

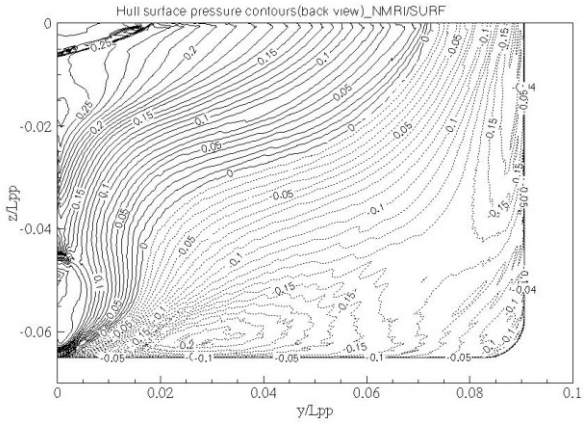

NMRI-SURF

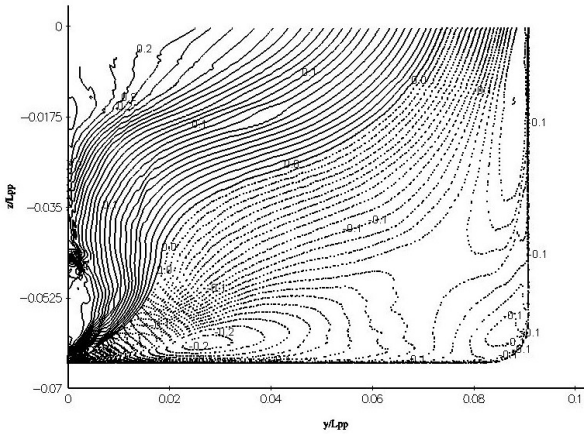

VTT-FINFLO

Fig. 1.1a-13 Hull surface pressure contours (back view) [$\Delta Cp = 0.01$]
(Solid lines: positive (+) values; Dashed lines: negative (-) values)

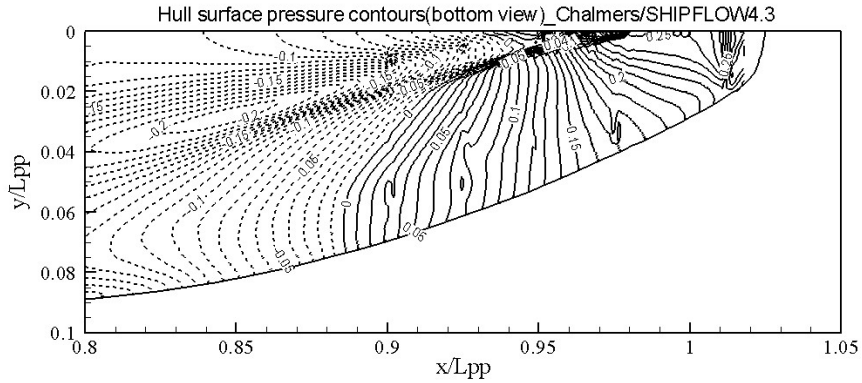

Chalmers-SHIPFLOW4.3

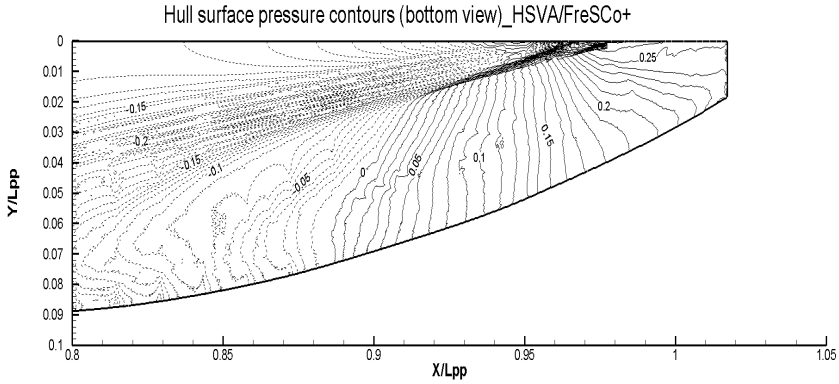

HSVA-FreSCo+

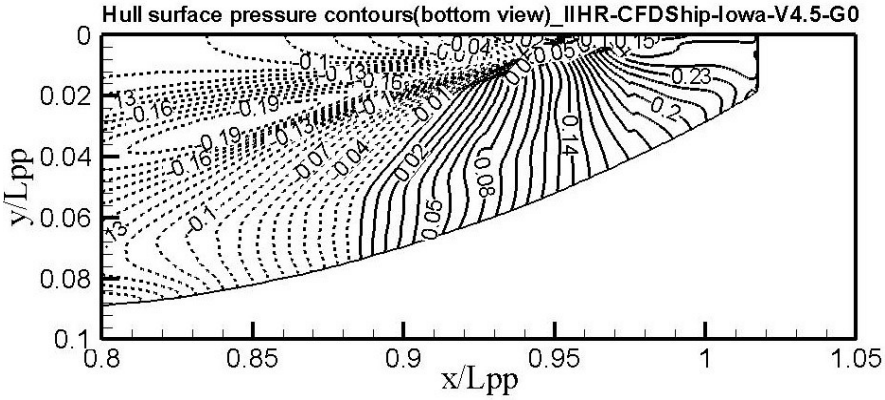

IIHR-CFDShip-Iowa-V4.5 (ARS)

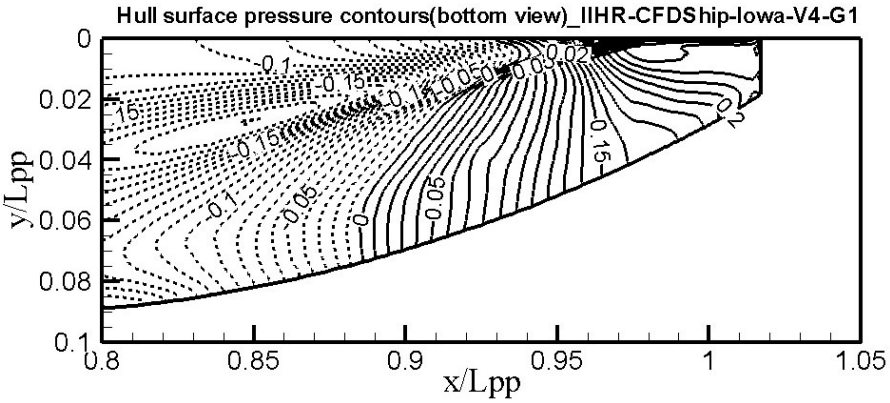

IIHR-CFDShip-Iowa-V4 (ARS-DES)

Fig. 1.1a-14 Hull surface pressure contours (bottom view) [$\Delta Cp = 0.01$]
(Solid lines: positive (+) values; Dashed lines: negative (-) values)

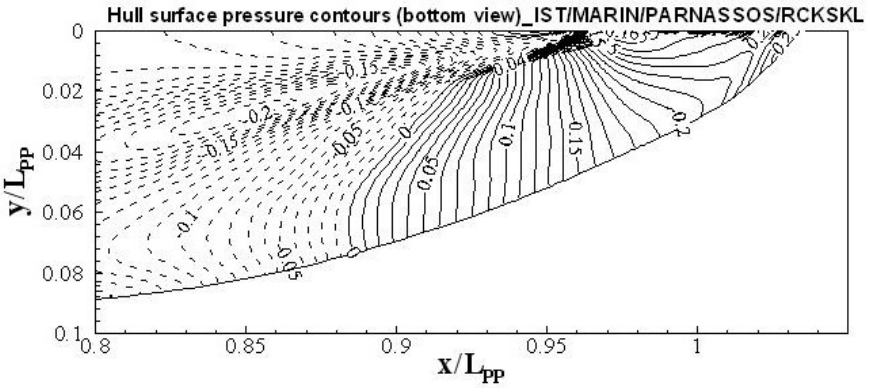

IST/MARIN-PARNASSOS (RCKSKL)

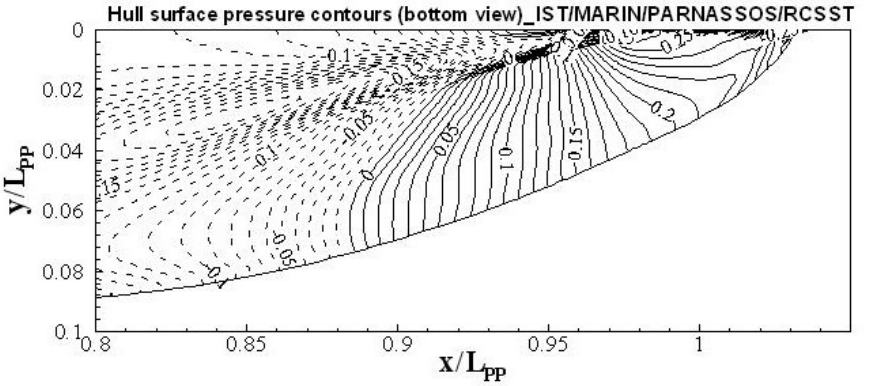

IST/MARIN-PARNASSOS (RCSST)

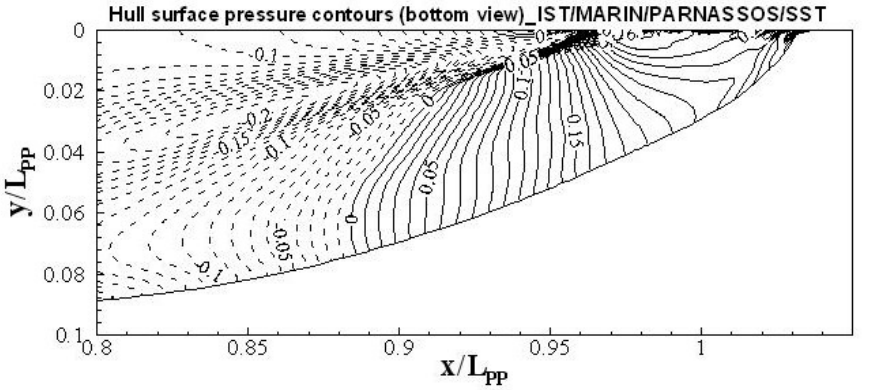

IST/MARIN-PARNASSOS (SST)

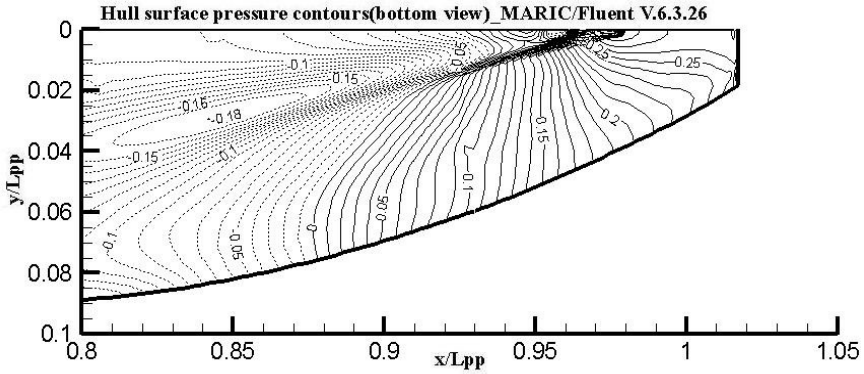

MARIC-Fluent6.3.26

Fig. 1.1a-14 Hull surface pressure contours (bottom view) [$\Delta Cp = 0.01$]
(Solid lines: positive (+) values; Dashed lines: negative (-) values)

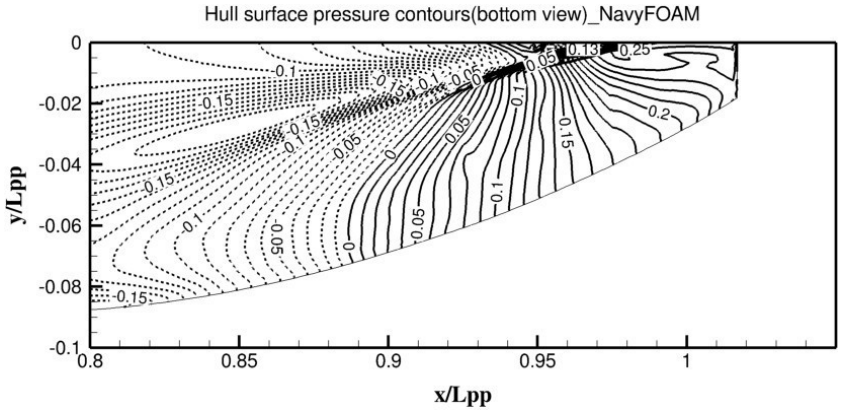

NavyFOAM-NavyFOAM

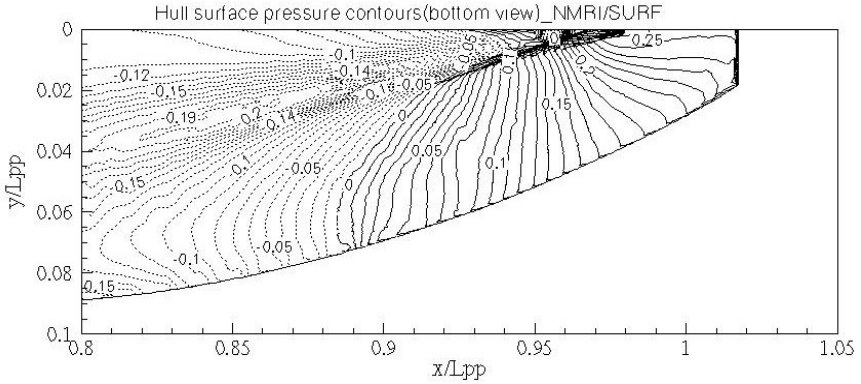

NMRI-SURF

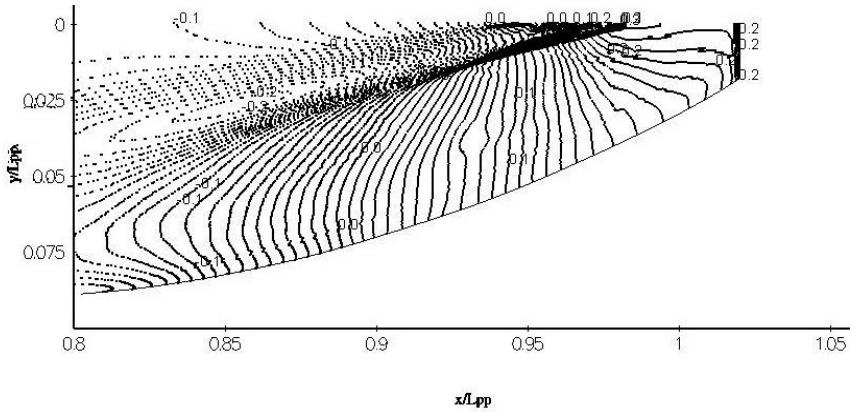

VTT-FINFLO

Fig. 1.1a-14 Hull surface pressure contours (bottom view) [$\Delta Cp = 0.01$]
(Solid lines: positive (+) values; Dashed lines: negative (-) values)

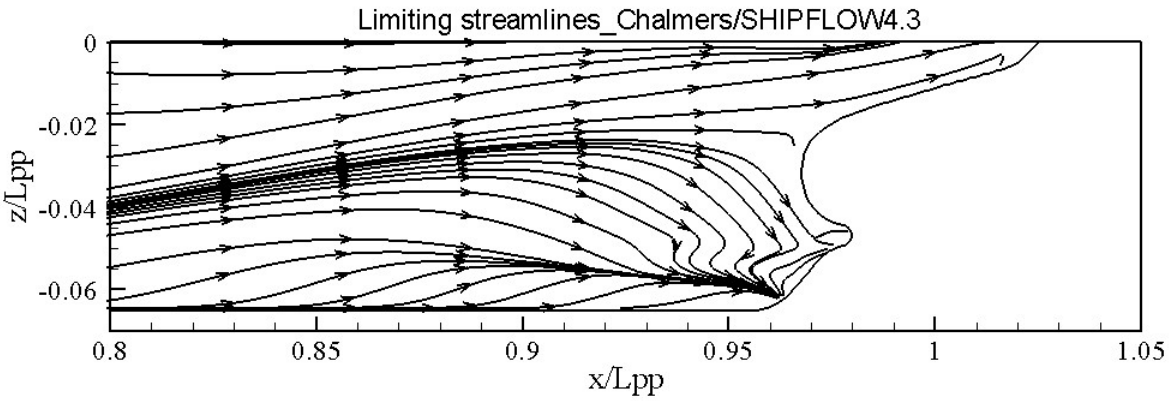

Chalmers-SHIPFLOW4.3

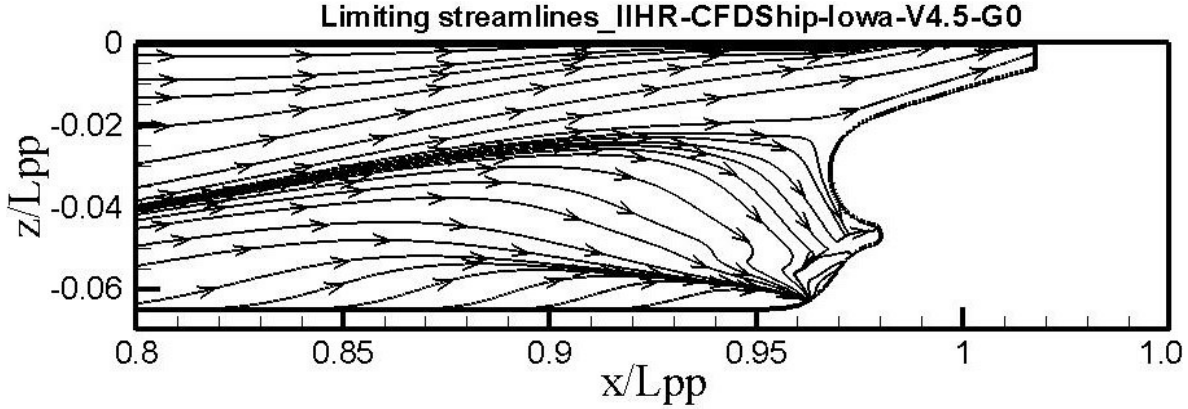

IIHR-CFDShip-Iowa-V4.5 (ARS)

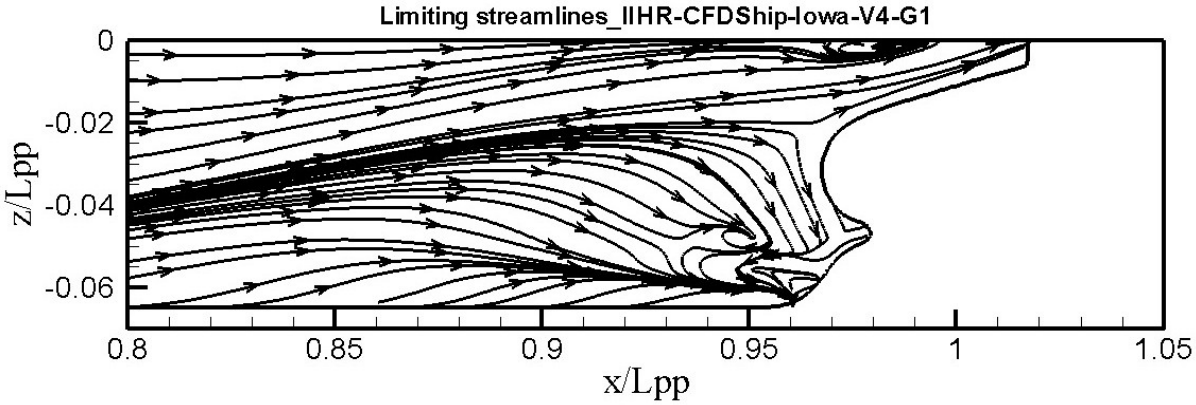

IIHR-CFDShip-Iowa-V4 (ARS-DES)

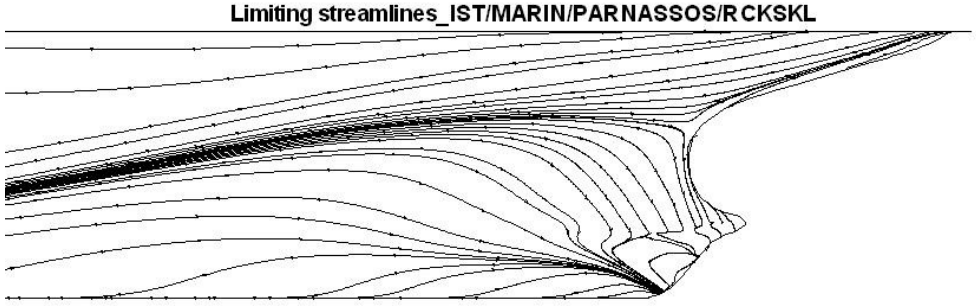

IST/MARIN-PARNASSOS (RCKSKL)

Fig. 1.1a-15 Limiting streamlines (port side view)

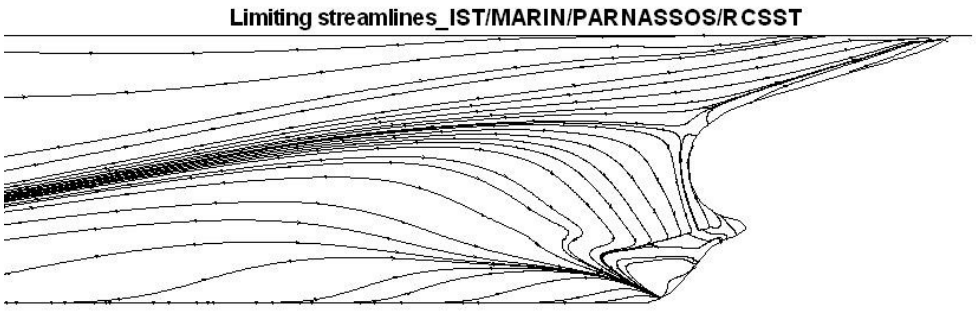

IST/MARIN-PARNASSOS (RCSST)

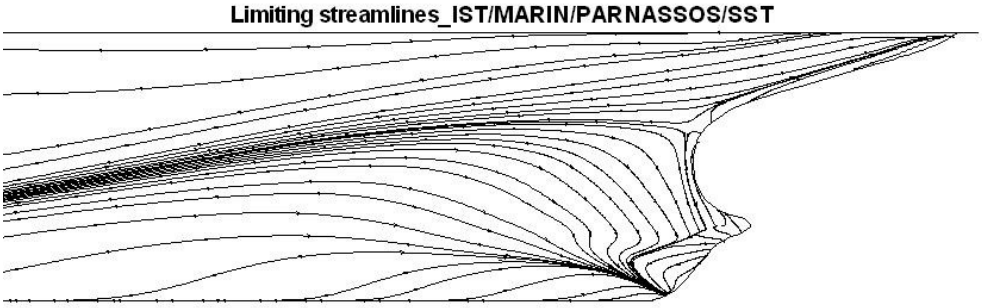

IST/MARIN-PARNASSOS (SST)

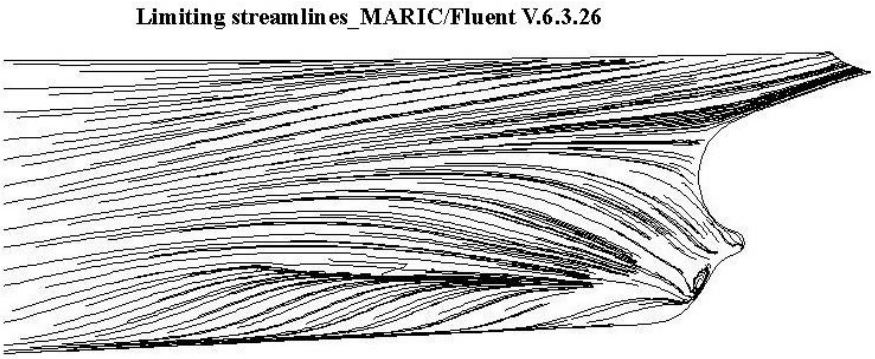

MARIC-Fluent6.3.26

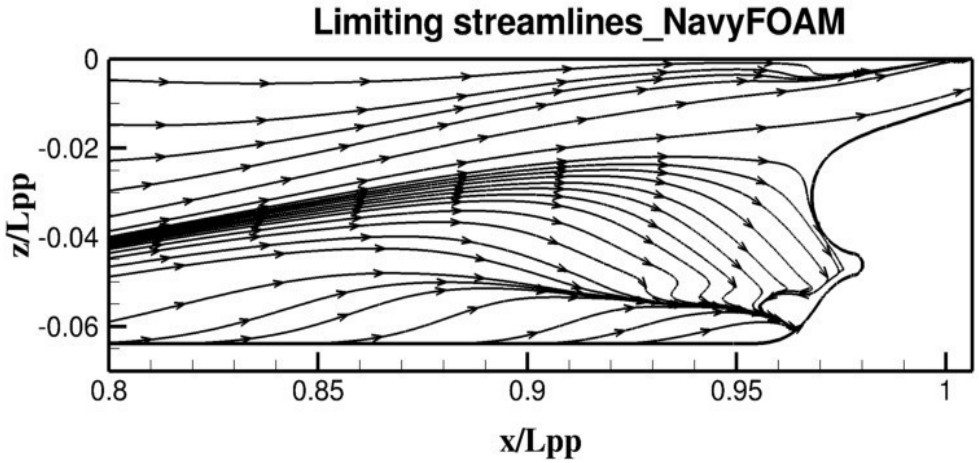

NavyFOAM-NavyFOAM

Fig. 1.1a-15 Limiting streamlines (port side view)

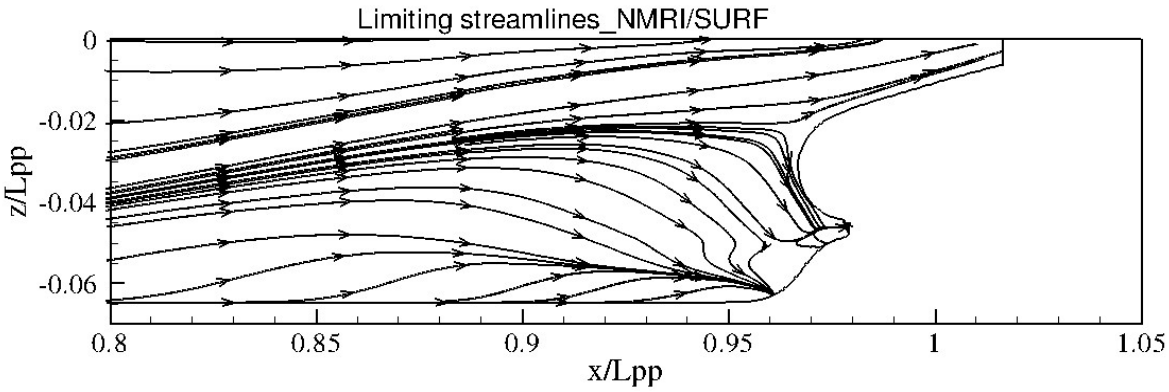

NMRI-SURF

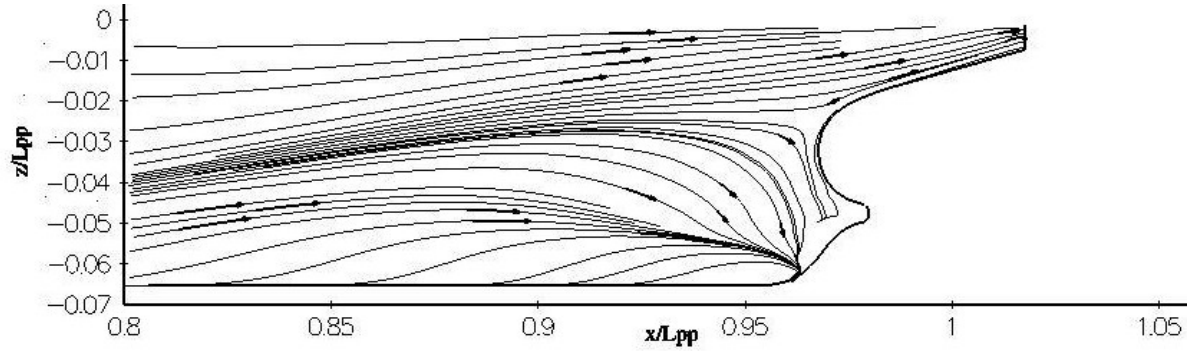

VTT-FINFLO

Fig. 1.1a-15 Limiting streamlines (port side view)

Test Case 1.1b

Figure 1.1b-1 Wave elevation contours
Figure 1.1b-2 Longitudinal wave cut at y/L_{PP} = -0.0964
Figure 1.1b-3 Longitudinal wave cut at y/L_{PP} = -0.1581
Figure 1.1b-4 Longitudinal wave cut at y/L_{PP} = -0.2993
Figure 1.1b-5 Grid density distribution along the waterline, and in transverse and vertical directions at mid-ship

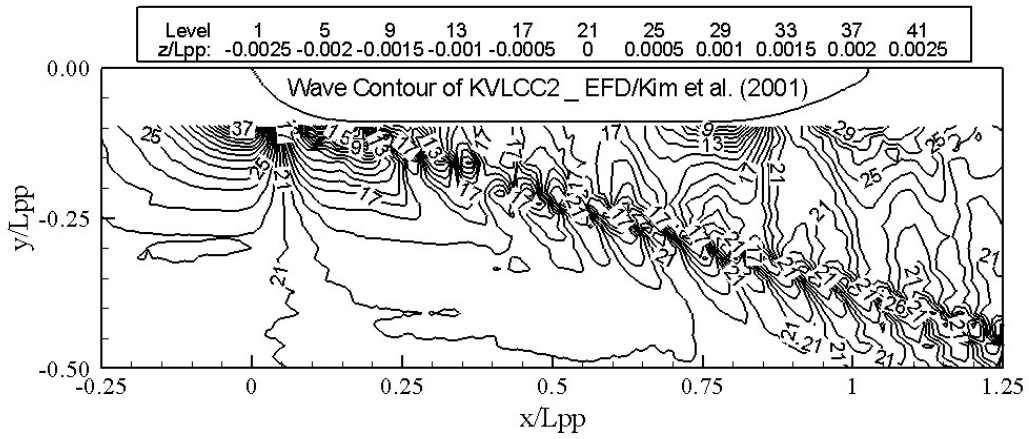

Experiment (MOERI, Kim et al. 2001)

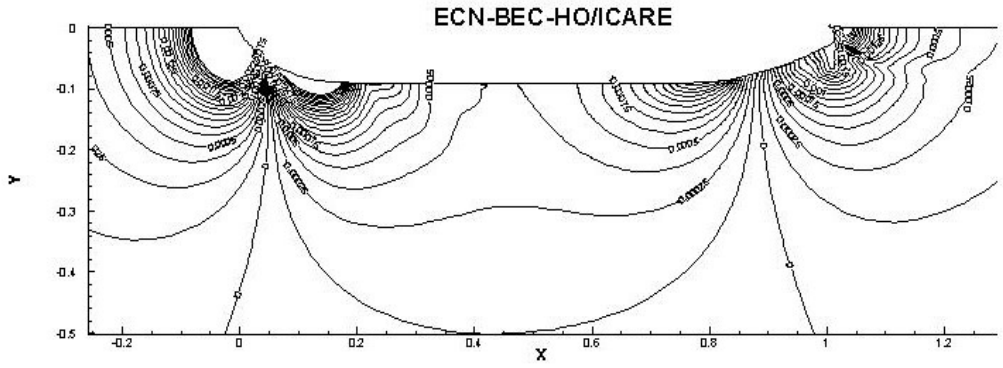

ECN/BEC/HO-Icare

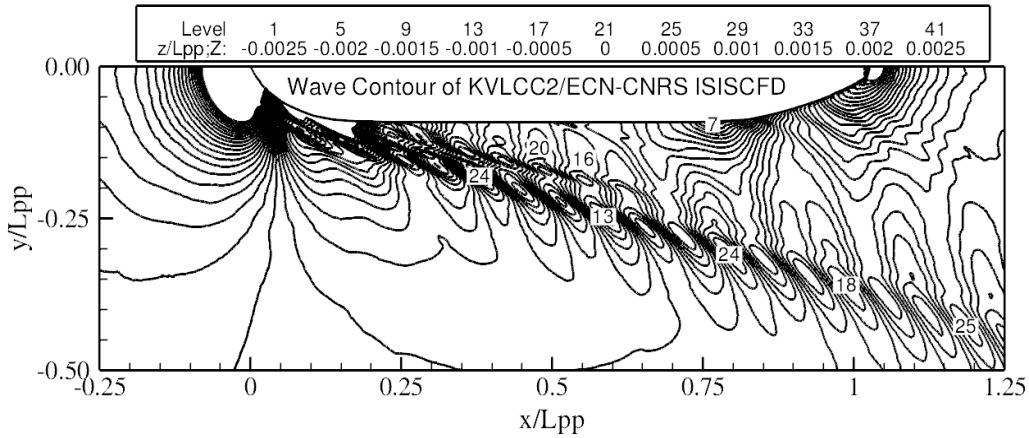

ECN/CNRS-ISISCFD

Fig. 1.1b-1 Wave elevation contours [$\Delta z/L_{PP} = 0.000125$]

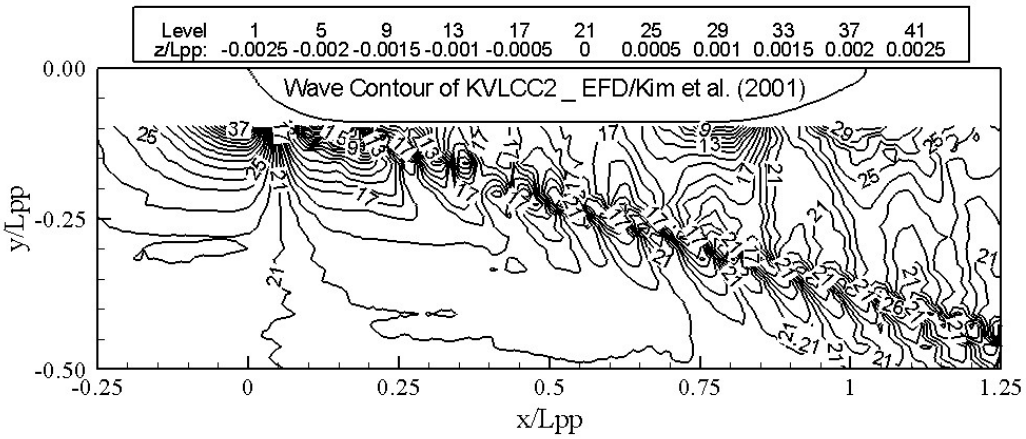

Experiment (MOERI, Kim et al. 2001)

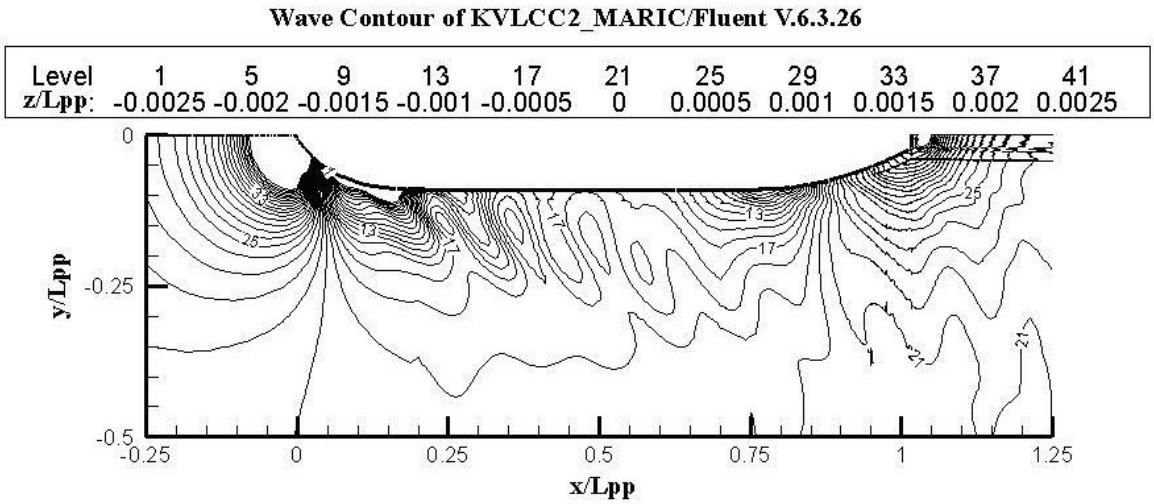

MARIC-Fluent V.6.3.26

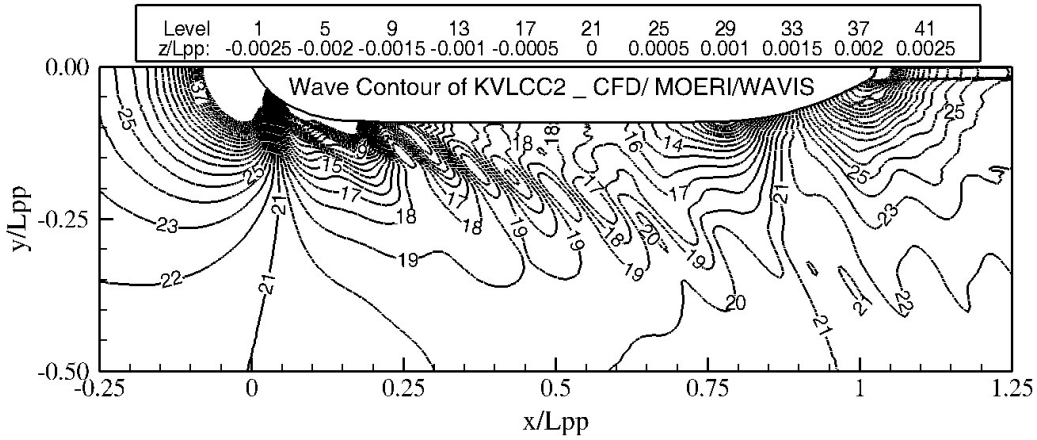

MOERI-WAVIS

Fig. 1.1b-1 Wave elevation contours [$\Delta z/L_{PP} = 0.000125$]

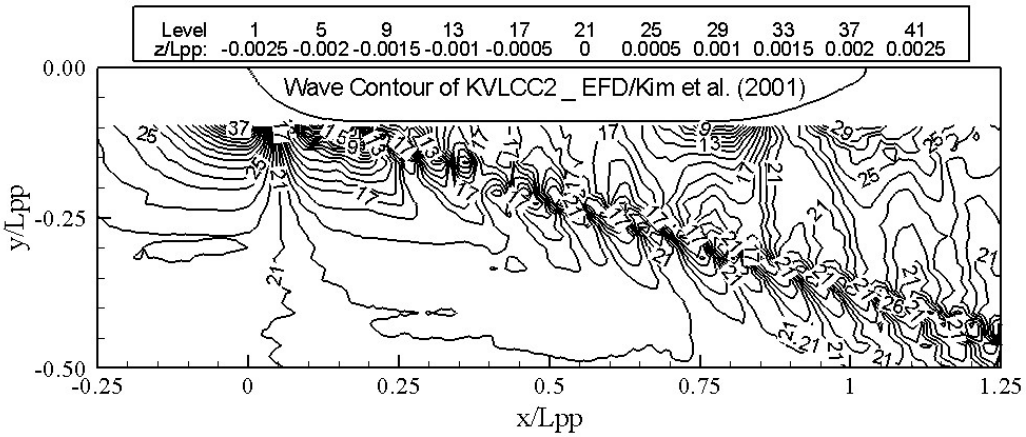

Experiment (MOERI, Kim et al. 2001)

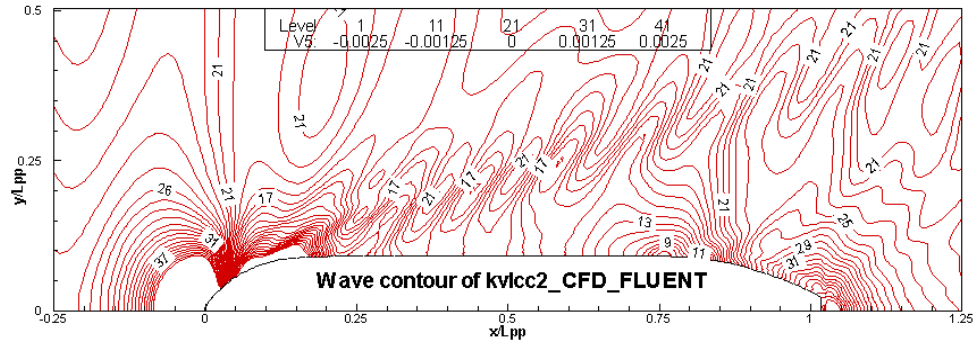

NTNU-FLUENT

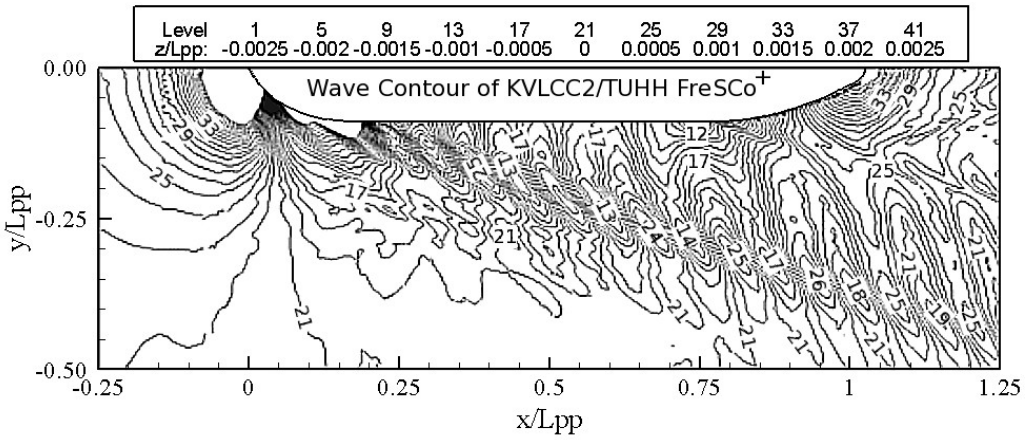

TUHH-FreSCo+

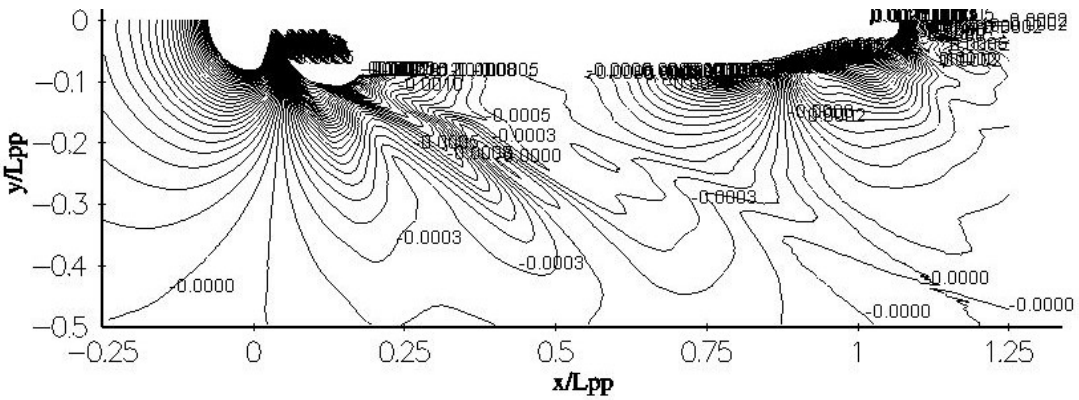

VTT-FINFLO

Fig. 1.1b-1 Wave elevation contours [$\Delta z/L_{PP} = 0.000125$]

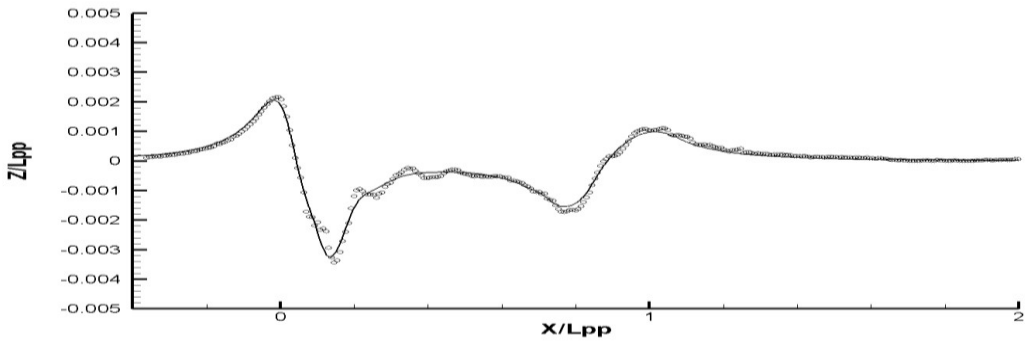

ECN/BEC/HO-Icare

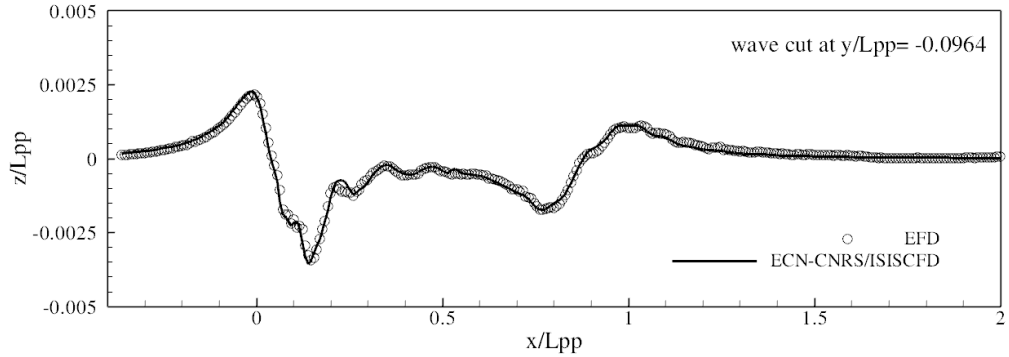

ECN/CNRS-ISISCFD

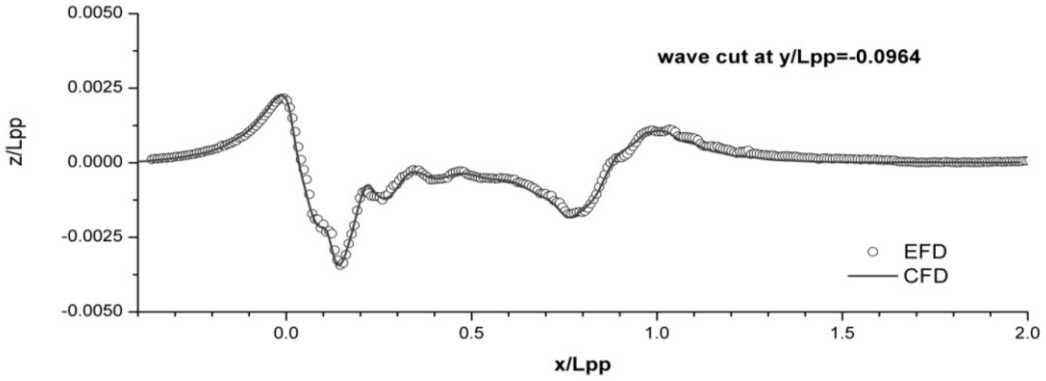

MARIC-Fluent V.6.3.26

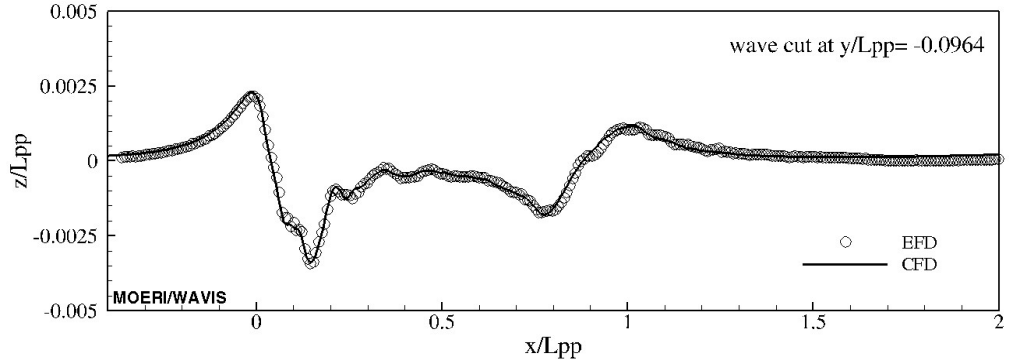

MOERI-WAVIS

Fig. 1.1b-2 Longitudinal wave cut at y/L_{PP} = -0.0964 (CFD: solid line; EFD: open circles)

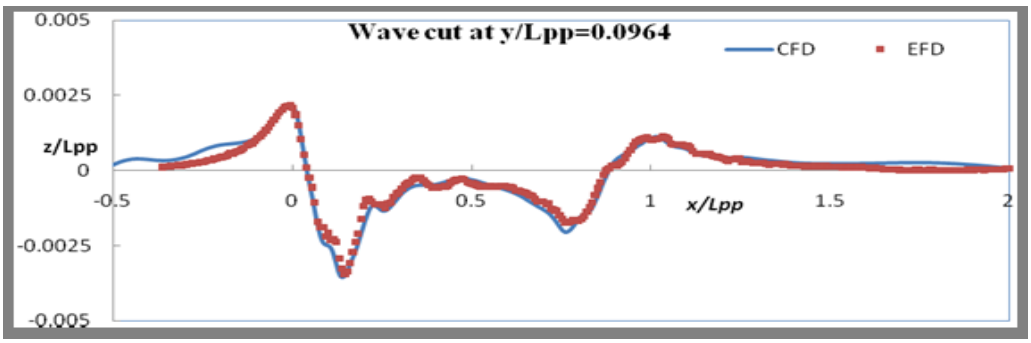

NTNU-FLUENT

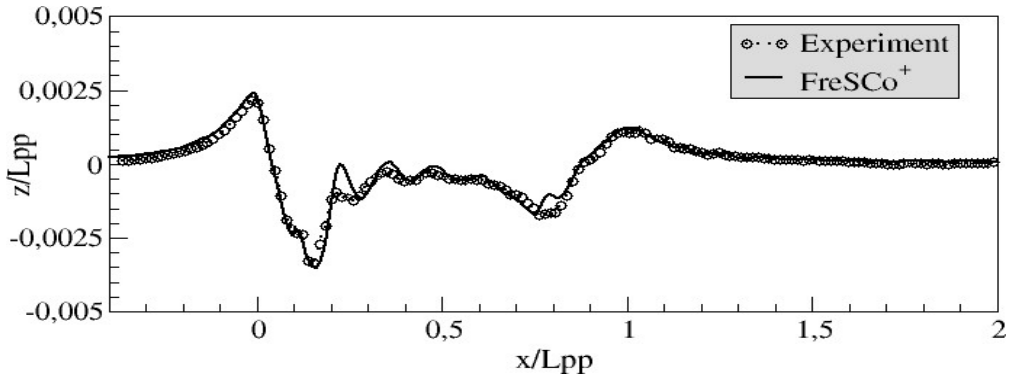

TUHH-FreSCo+

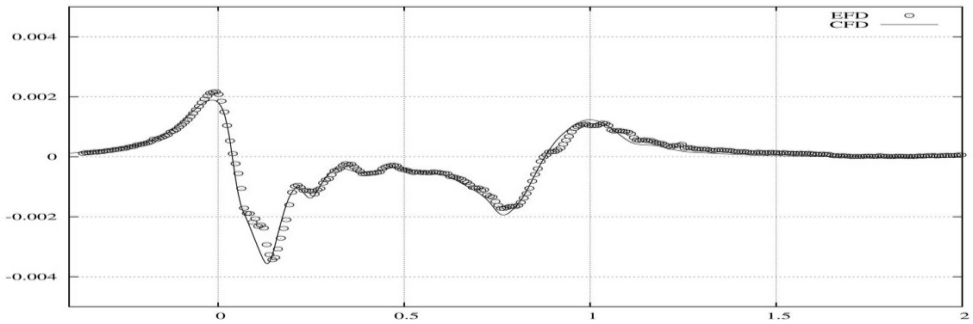

VTT-FINFLO

Fig. 1.1b-2 Longitudinal wave cut at y/L_{PP} = -0.0964 (CFD: solid line; EFD: open circles)

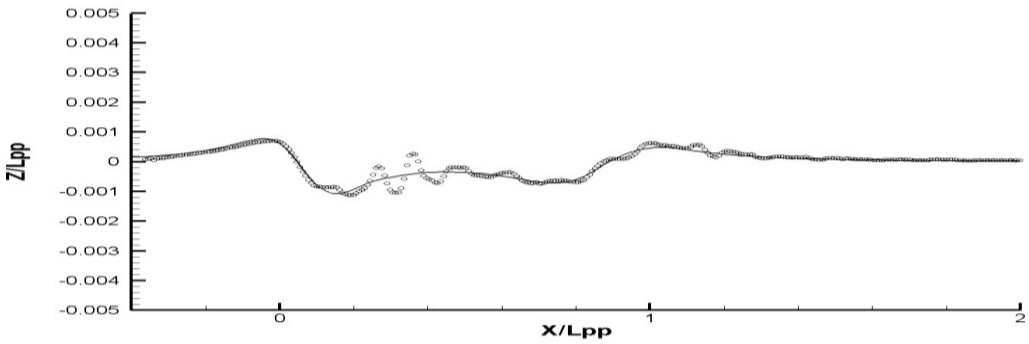

ECN/BEC/HO-Icare

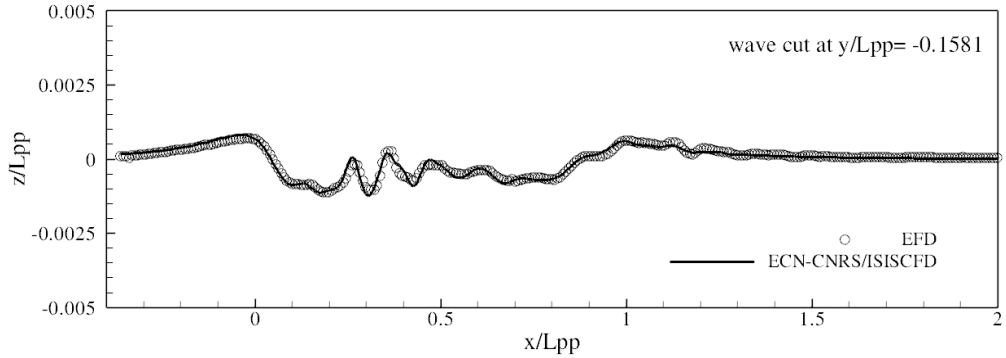

ECN/CNRS-ISISCFD

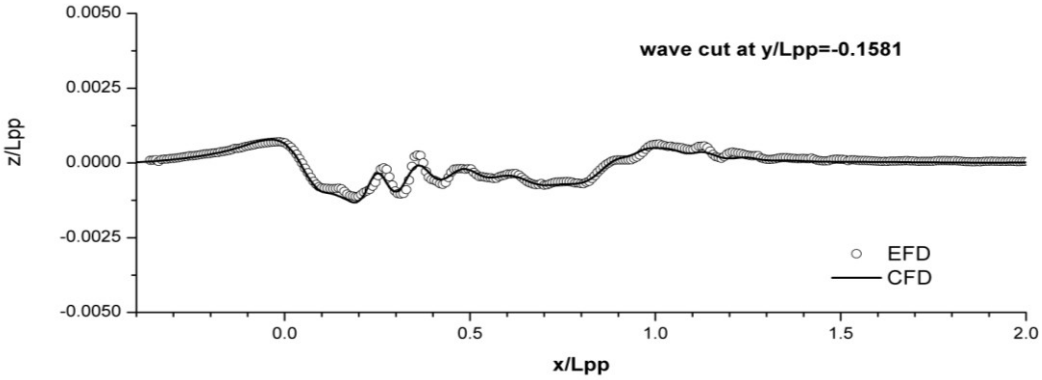

MARIC-Fluent V.6.3.26

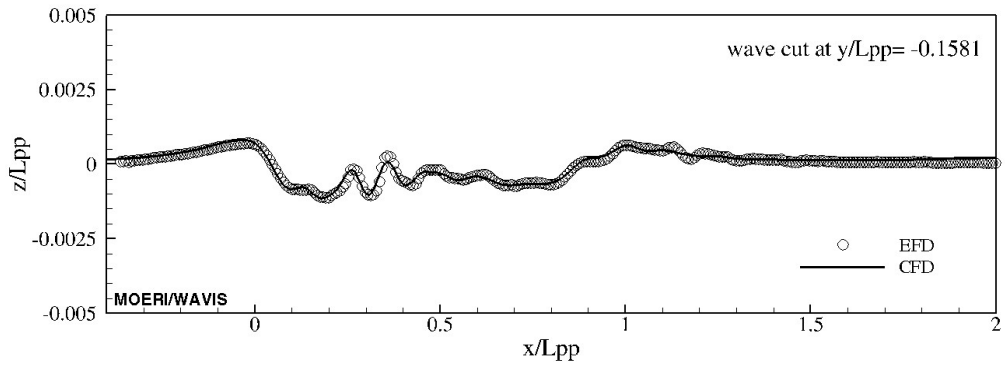

MOERI-WAVIS

Fig. 1.1b-3 Longitudinal wave cut at y/L_{PP} = -0.1581 (CFD: solid line; EFD: open circles)

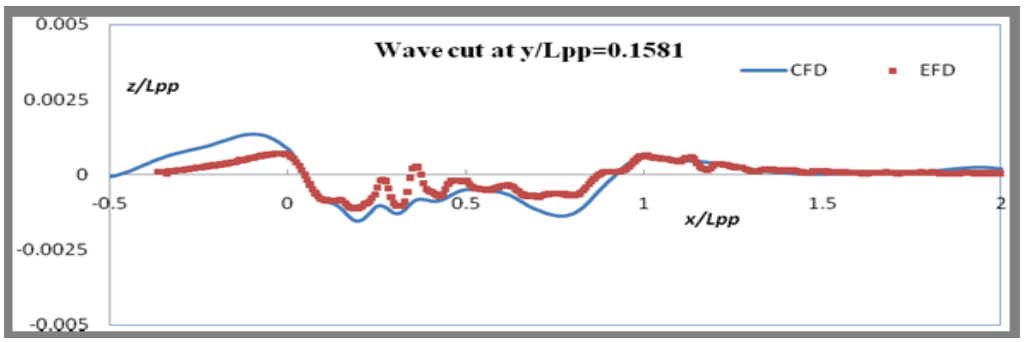

NTNU-FLUENT

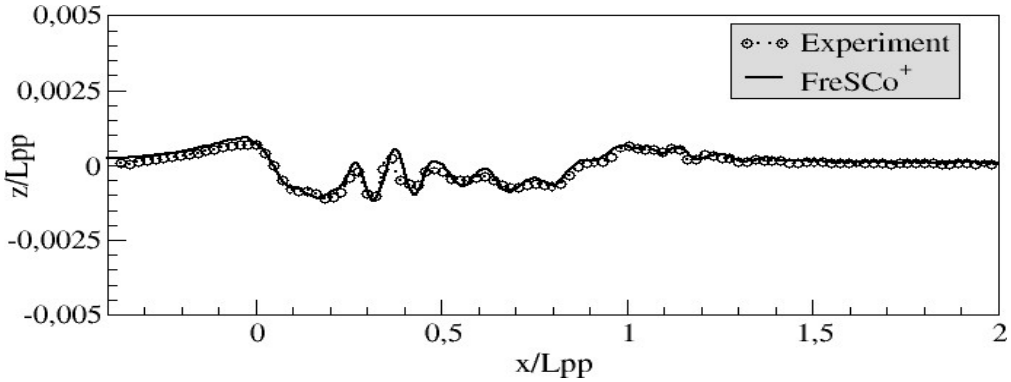

TUHH-FreSCo+

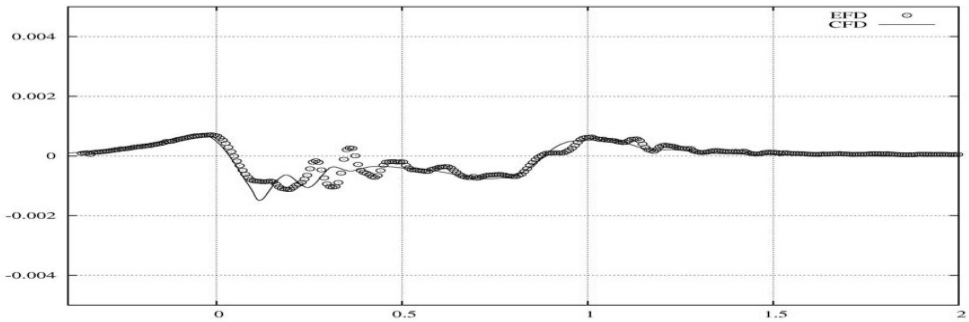

VTT-FINFLO

Fig. 1.1b-3 Longitudinal wave cut at y/L_{PP} = -0.1581 (CFD: solid line; EFD: open circles)

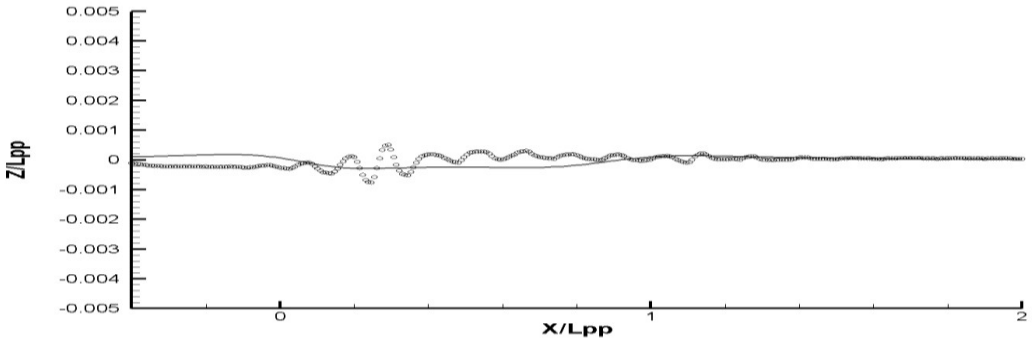

ECN/BEC/HO-Icare

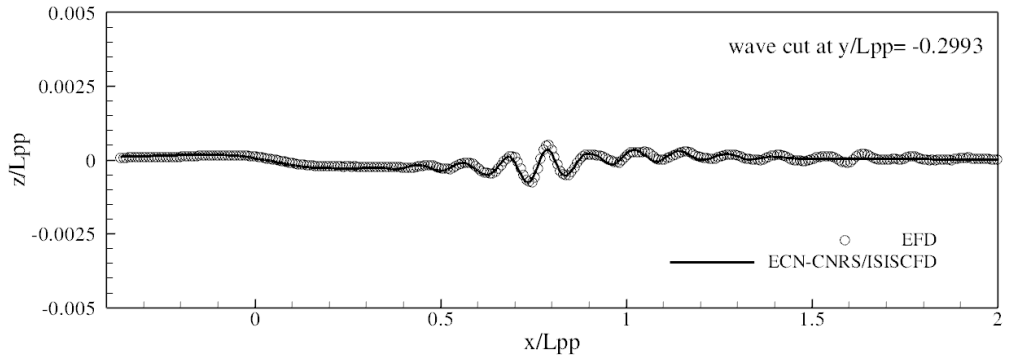

ECN/CNRS-ISISCFD

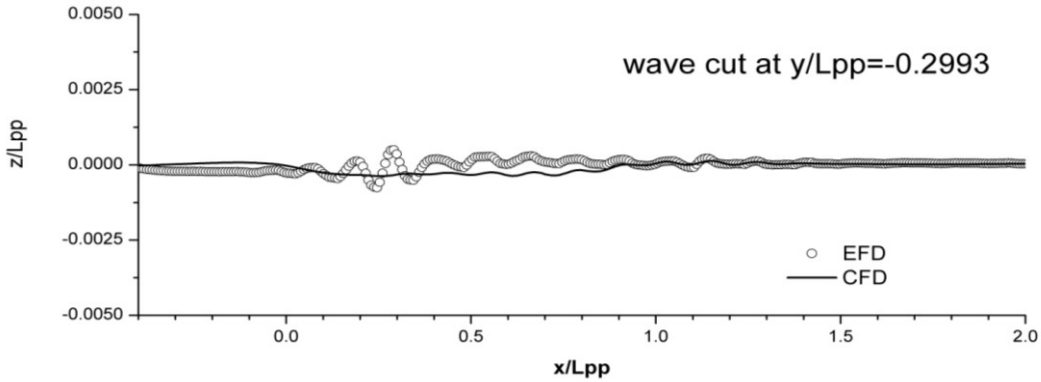

MARIC-Fluent V.6.3.26

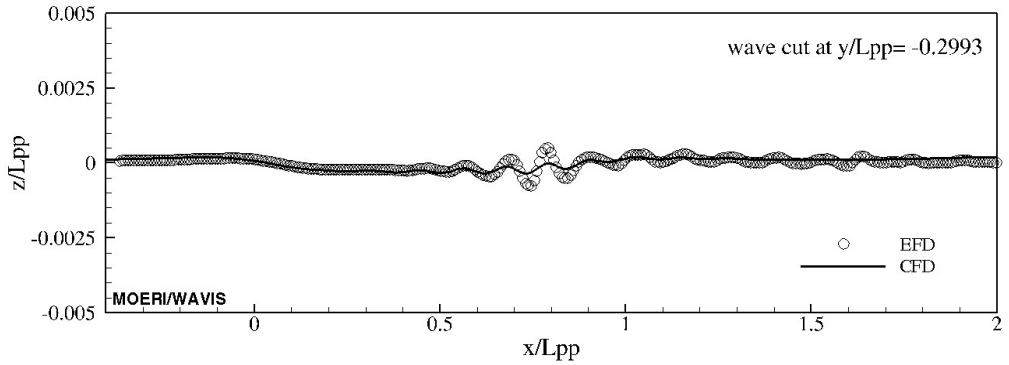

MOERI-WAVIS

Fig. 1.1b-4 Longitudinal wave cut at y/L_{PP} = -0.2993 (CFD: solid line; EFD: open circles)

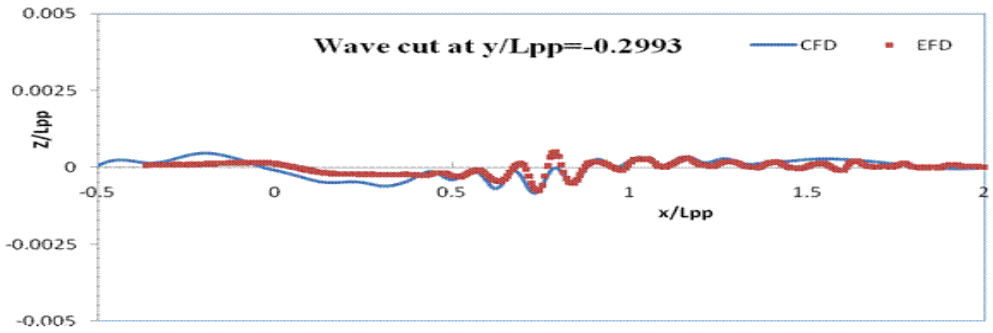

NTNU-FLUENT

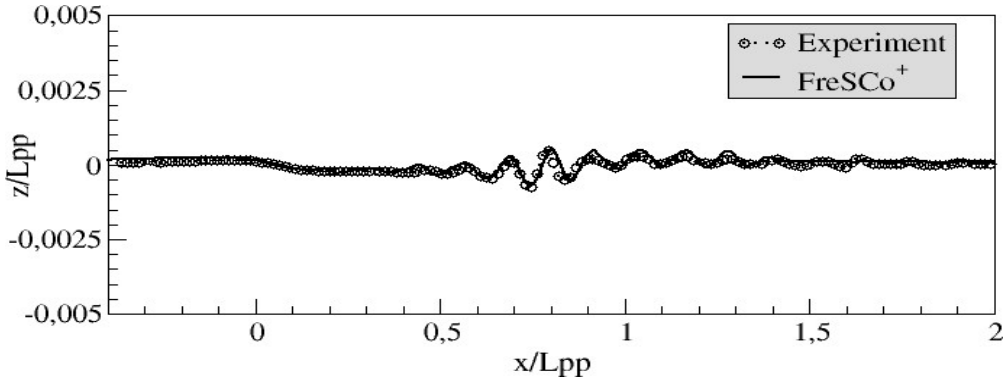

TUHH-FreSCo+

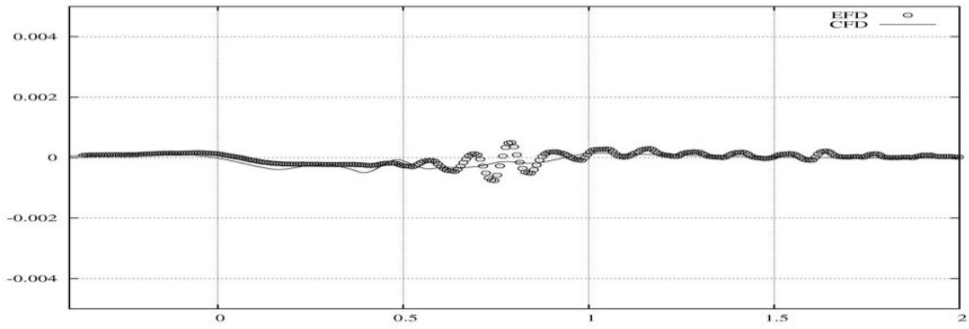

VTT-FINFLO

Fig. 1.1b-4 Longitudinal wave cut at y/L_{PP} = -0.2993 (CFD: solid line; EFD: open circles)

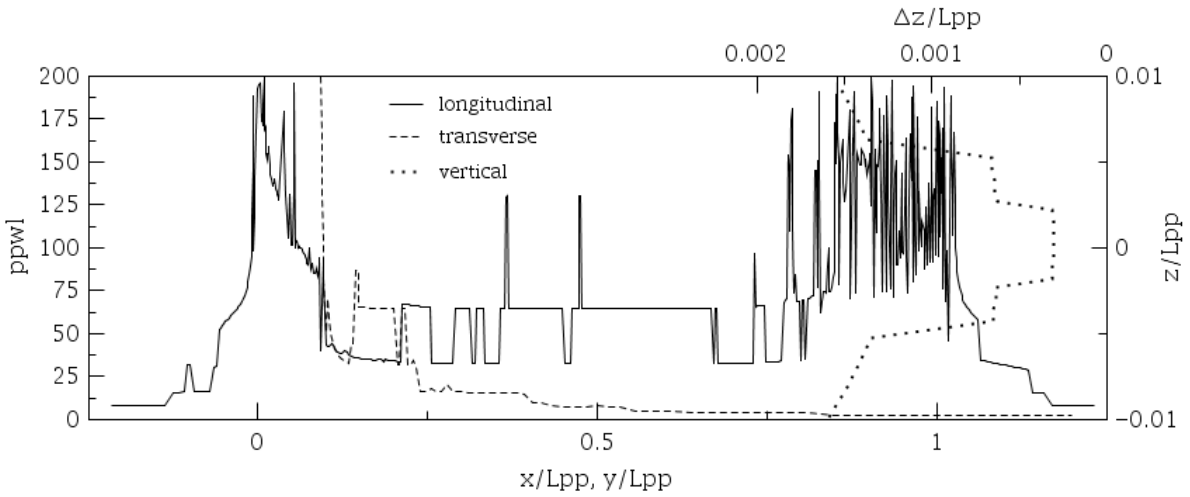

ECN/CNRS-ISISCFD

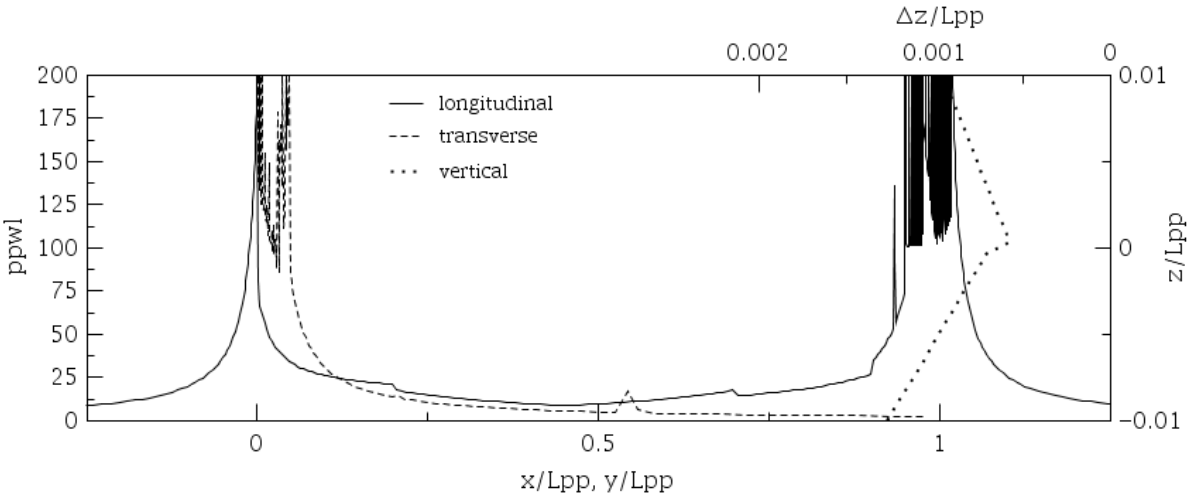

MARIC-Fluent V.6.3.26

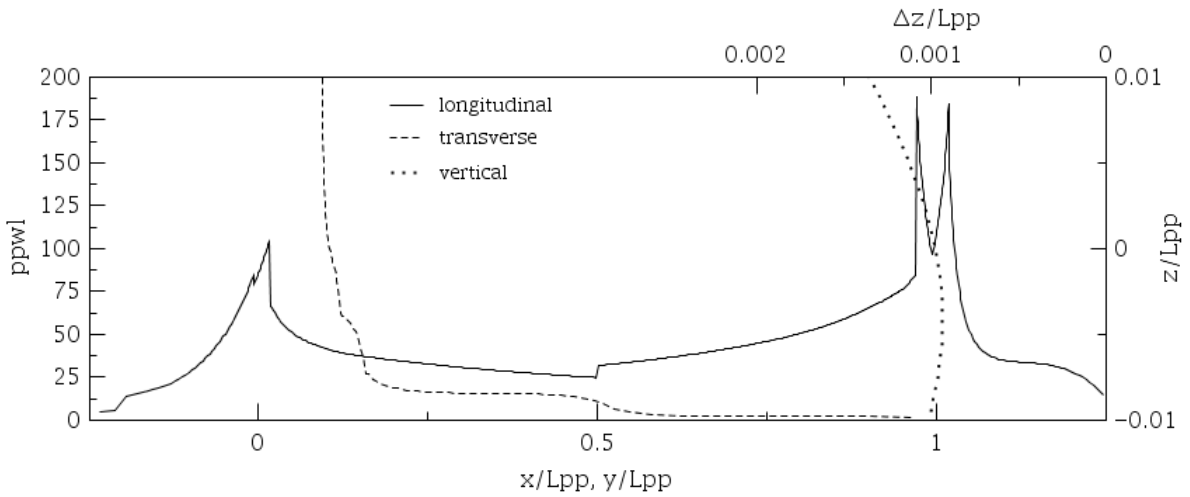

MOERI-WAVIS

Fig. 1.1b-5 Grid density distribution along the waterline (solid), and in transverse (dashed) and vertical (dotted) directions at mid-ship

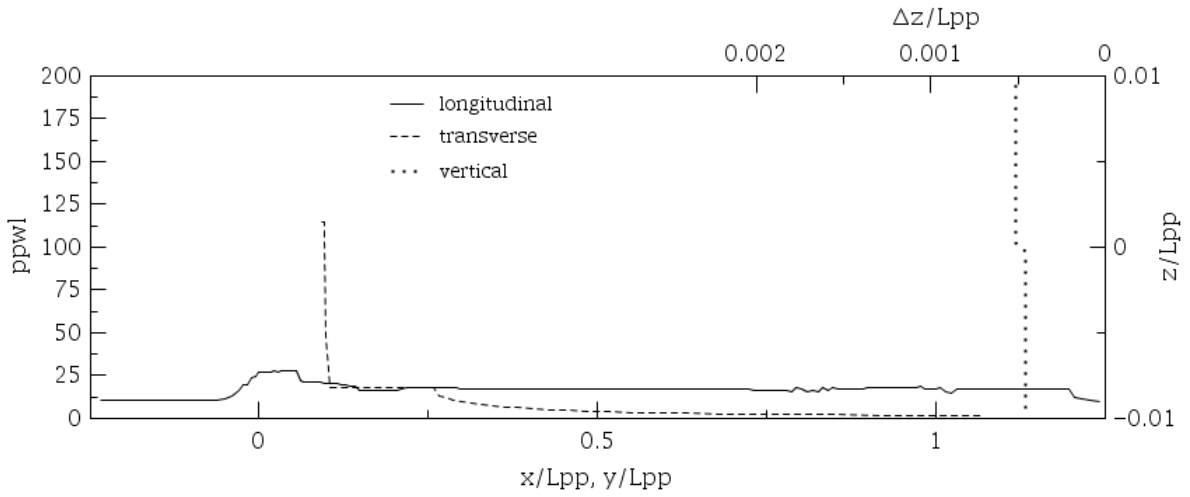

NTNU-FLUENT

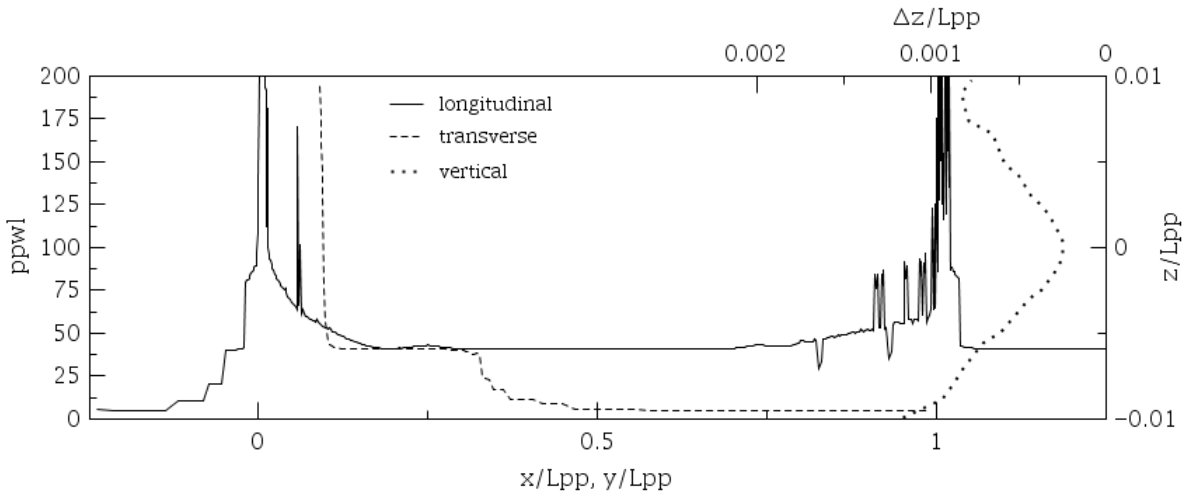

TUHH-FreSCo+

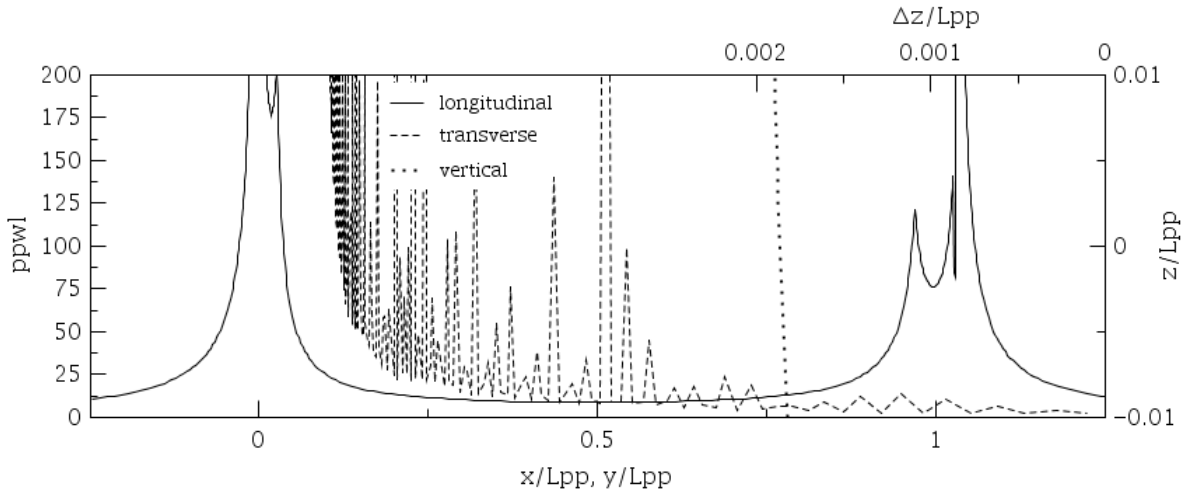

VTT-FINFLO

Fig. 1.1b-5 Grid density distribution along the waterline (solid), and in transverse (dashed) and vertical (dotted) directions at mid-ship

Test Case 1.2a

Table 1.2a-0 Computations information and V&V method
Table 1.2a-1 Computed C_T, C_F and C_{PV} of different grid densities
Table 1.2a-2 V&V results for C_T, C_F and C_{PV}

Table 1.2a-0: Computations information and V&V method

Organization (Code)	**V&V method (including the determination of U_I)**
HSVA (FreSCo+)	The V&V is based on ITTC Quality Manual. U_I was estimated with curve fitting.
MARIC (FLUENT6.3)	The V&V is based on ITTC - Quality Manual 7.5-03-01 -01, CFD General "Uncertainty Analysis in CFD Verification and Validation Methodology and Procedures" Richardson Extrapolation is used to compute the error for the fine grid $\delta^*_{RE_G} = \frac{\varepsilon_{21}}{r_G^{P_G}-1}$, $P_G = \frac{\ln(\varepsilon_{32}/\varepsilon_{21})}{\ln r_G}$, $C_G = \frac{r_G^{P_G}-1}{r_G^{P_{Gest}}-1}$, $U_G = \left\|C_G\delta^*_{RE_G}\right| + \left|(1-C_G)\delta^*_{RE_G}\right|$, $U_{SN} = \sqrt{U_G^2+U_I^2}$, $U_V = \sqrt{U_{SN}^2+U_D^2}$
MOERI (WAVIS)	-
NTNU (FLUENT)	Since O-grid is introduced to precise hull geometry, the mesh is usually refined around the hull and free surface locally, which means the mesh in the cases is not refined at a uniform grid refine rate. The resistance from CFD is the ship resistance without rudder. $\delta_{RE,G1} = \frac{\varepsilon_{21}}{r_{G21}^{P_G}-1}$, $P_G = \frac{\ln(\varepsilon_{32}/\varepsilon_{21})}{\ln r_{G21}} - \frac{1}{\ln r_{G21}}[\ln(r_{G32}^{P_G}-1) - \ln(r_{G21}^{P_G}-1)]$, $U_G = F_S\left\|\delta_{RE,G1}\right|$, $U_I = \left\|\frac{1}{2}(S_U - S_L)\right|$, $U_{SN} = \sqrt{U_I^2+U_G^2}$, $U_V = \sqrt{U_D^2+U_{SN}^2}$
VTT (FINFLO)	The computations were carried with three grids applying the refinement ratio sqrt(2) Furthermore, the 2nd and 3rd level grids were utilized also in the V&V analysis, that is, altogether nine meshes were computed. As the grid refinement ratio varied, the Richardson extrapolation was conducted as follows: The curve $S_i = \alpha h_i^p - S_0$ was fitted to the computed resistance coefficients. S_0 represents the estimated exact resistance coefficient (grid#0), whereas S_i is the resistance coefficient computed with the i th grid and h_i is (no_of_elements)^(-1/3). Finally p is the estimated order of accuracy. Once the fitting was completed, the U_G is evaluated using the root mean square error of the fitting (U_S) and the approximated uncertainty Uc=0.25×$\|\delta_{RE}\|$ so that $U_G = \sqrt{U_C^2+U_S^2}$ Finally, $U_{SN} = \sqrt{U_G^2+U_I^2}$ where U_I is the iterative uncertainty The term δ_{RE} is calculated as follows: δ_{RE} =S_1-S_0 U_I is determined by estimating the remaining oscillations in the C_T at the finest level grid#1 Remark, that U_I and U_G are given relative to S_0, not to S_1 as in the original sheet

Table 1.2a-1: Computed C_T, C_F and C_{PV} of different grid densities

Organization (Code)	r_G		C_T ($\times 10^{-3}$)					C_F ($\times 10^{-3}$)					C_{PV} ($\times 10^{-3}$)				
			Grid #5	Grid #4	Grid #3	Grid #2	Grid #1	Grid #5	Grid #4	Grid #3	Grid #2	Grid #1	Grid #5	Grid #4	Grid #3	Grid #2	Grid #1
EFD (MOERI)	-	D	4.110					-					-				
HSVA (FreSCo+)	2	S	4.539	4.226	4.215	4.198	4.140	3.252	3.495	3.538	3.515	3.447	1.287	0.731	0.678	0.682	0.692
		$E\%D$	-10.44	-2.83	-2.57	-2.13	-0.72										
MARIC (FLUENT6.3)	1.414	S	-	-	4.475	4.314	4.251	-	-	-	-	-	-	-	-	-	-
		$E\%D$	-	-	-8.88	-4.96	-3.43										
MOERI (WAVIS)	1.414	S	-	-	4.279	4.180	4.129	-	-	3.344	3.301	3.223	-	-	0.935	0.879	0.906
		$E\%D$	-	-	4.11	1.71	0.46										
NTNU (FLUENT)	-	S	-	-	4.772	4.316	4.162	-	-	-	-	-	-	-	-	-	-
		$E\%D$	-	-	16.11	5.01	1.27										
VTT (FINFLO) [9 grids]	0.39 ~ 0.79	S (grid5~grid1)	4.416	4.464	4.398	4.191	4.216	4.206*	-	-	-	-	-	-	-	-	-
		$E\%D$	-7.45	-8.61	-7.01	-1.97	-2.58	-2.33									
		S (grid9~grid6)		6.241	5.225	5.009	4.889	-	-	-	-	-	-	-	-	-	-
		$E\%D$		-51.85	-27.14	-21.87	-18.96										

* extrapolated C_T value, grid0

$E\%D = (D\text{-}S)/D \times 100$

Table 1.2a-2: V&V results for C_T, C_F and C_{PV}

Organization (Code)	r_G	C_T						C_F						C_{PV}					
		ε_{12} %S_1	$\frac{U_I}{\varepsilon_{12}}$	$\frac{P_G}{P_{G,th}}$	U_G %S_1	U_D %D	U_V%	ε_{12} %S_1	$\frac{U_I}{\varepsilon_{12}}$	$\frac{P_G}{P_{G,th}}$	U_G %S_1	U_D %D	U_V%	ε_{12} %S_1	$\frac{U_I}{\varepsilon_{12}}$	$\frac{P_G}{P_{G,th}}$	U_G %S_1	U_D %D	U_V%
HSVA (FreSCo+)	2	-1.40	-0.010	0.847	0.16		1.01	-1.98	-0.008	0.804	0.31			1.47	0.055	0.596	0.66		
MARIC (FLUENT6.3)	1.414	1.48	0.125	1.354	2.01		2.32	-	-	-	-			-	-	-	-		
MOERI (WAVIS)	1.414	1.24	-	0.947	0.10	1.0	1.00	-	-	0.872	0.50			-	-	1.050	0.20		
NTNU (FLUENT)	-	3.70	0.114	3.295	0.56		1.23	-	-	-	-			-	-	-	-		
VTT (FINFLO)	0.39~0.79	-	1.40	0.951	4.83		5.14	-	-	-	-			-	-	-	-		

$\varepsilon_{12}\%S_1 = |(S_1\text{-}S_2)/S_1|\times 100$; $U_{SN} = \sqrt{U_I^2 + U_G^2}$; $U_V = \sqrt{U_D^2 + U_{SN}^2}$

Test Case 1.2b

Table 1.2b-0 Computations information and V&V method
Table 1.2b-1-1 Computed C_T, C_F, C_{PV} of different grid densities at Fr = 0.1010
Table 1.2b-1-2 V&V results for C_T, C_F and C_{PV} at Fr = 0.1010
Table 1.2b-1-3 Computed Sinkage (σ) and Trim (τ) of different grid densities at Fr = 0.1010
Table 1.2b-1-4 V&V results for Sinkage (σ) and Trim (τ) at Fr = 0.1010
Table 1.2b-1-5 Computed C_T, C_F, C_{PV} of different grid densities at Fr = 0.1194
Table 1.2b-1-6 V&V results for C_T, C_F and C_{PV} at Fr = 0.1194
Table 1.2b-1-7 Computed Sinkage (σ) and Trim (τ) of different grid densities at Fr = 0.1194
Table 1.2b-1-8 V&V results for Sinkage (σ) and Trim (τ) at Fr = 0.1194
Table 1.2b-1-9 Computed C_T, C_F, C_{PV} of different grid densities at Fr = 0.1377
Table 1.2b-1-10 V&V results for C_T, C_F and C_{PV} at Fr = 0.1377
Table 1.2b-1-11 Computed Sinkage (σ) and Trim (τ) of different grid densities at Fr = 0.1377
Table 1.2b-1-12 V&V results for Sinkage (σ) and Trim (τ) at Fr = 0.1377
Table 1.2b-1-13 Computed C_T, C_F, C_{PV} of different grid densities at Fr = 0.1423
Table 1.2b-1-14 V&V results for C_T, C_F and C_{PV} at Fr = 0.1423
Table 1.2b-1-15 Computed Sinkage (σ) and Trim (τ) of different grid densities at Fr = 0.1423
Table 1.2b-1-16 V&V results for Sinkage (σ) and Trim (τ) at Fr = 0.1423
Table 1.2b-1-17 Computed C_T, C_F, C_{PV} of different grid densities at Fr = 0.1469
Table 1.2b-1-18 V&V results for C_T, C_F and C_{PV} at Fr = 0.1469
Table 1.2b-1-19 Computed Sinkage (σ) and Trim (τ) of different grid densities at Fr = 0.1469
Table 1.2b-1-20 V&V results for Sinkage (σ) and Trim (τ) at Fr = 0.1469
Table 1.2b-1-21 Computed C_T, C_F, C_{PV} of different grid densities at Fr = 0.1515
Table 1.2b-1-22 V&V results for C_T, C_F and C_{PV} at Fr = 0.1515
Table 1.2b-1-23 Computed Sinkage (σ) and Trim (τ) of different grid densities at Fr = 0.1515
Table 1.2b-1-24 V&V results for Sinkage (σ) and Trim (τ) at Fr = 0.1515

Figure 1.2b-2 Total resistance Coefficients (C_T) versus Fr
Figure 1.2b-3 Sinkage (σ) versus Fr
Figure 1.2b-4 Trim (τ) versus Fr

Table 1.2b-0: Computations information and V&V method

Organization (Code)	**V&V method (including the determination of U_I)**
MOERI (WAVIS)	-

Table 1.2b-1-1: Computed C_T, C_F, C_{PV} of different grid densities at $Fr = 0.1010$

Organization (Code)	r_G		C_T ($\times 10^{-3}$)					C_F ($\times 10^{-3}$)					C_{PV} ($\times 10^{-3}$)				
			Grid #5	Grid #4	Grid #3	Grid #2	Grid #1	Grid #5	Grid #4	Grid #3	Grid #2	Grid #1	Grid #5	Grid #4	Grid #3	Grid #2	Grid #1
EFD (MOERI)	-	D	4.237					-					-				
MOERI (WAVIS)	1.414	S	-	-	4.172	4.244	4.252	-	-	3.530	3.495	3.385	-	-	0.6416	0.7486	0.8663
		$E\%D$	-	-	1.53	-0.16	-0.34										

$E\%D = (D\text{-}S)/D \times 100$

Table 1.2b-1-2: V&V results for C_T, C_F and C_{PV} at $Fr = 0.1010$

Organization (Code)	r_G	C_T						C_F						C_{PV}					
		ε_{12} $\%S_1$	$\frac{U_I}{\varepsilon_{12}}$	$\frac{P_G}{P_{G,th}}$	U_G $\%S_1$	U_D $\%D$	$U_V\%$	ε_{12} $\%S_1$	$\frac{U_I}{\varepsilon_{12}}$	$\frac{P_G}{P_{G,th}}$	U_G $\%S_1$	U_D $\%D$	$U_V\%$	ε_{12} $\%S_1$	$\frac{U_I}{\varepsilon_{12}}$	$\frac{P_G}{P_{G,th}}$	U_G $\%S_1$	U_D $\%D$	$U_V\%$
MOERI (WAVIS)	1.414	0.18	-	3.252	0.16	1.0	1.01	3.25	-	1.651	1.73			13.58	-	0.137	122.75		

$\varepsilon_{12}\%S_1 = |(S_1\text{-}S_2)/S_1| \times 100$; $U_{SN} = \sqrt{U_I^2 + U_G^2}$; $U_V = \sqrt{U_D^2 + U_{SN}^2}$

Table 1.2b-1-3: Computed Sinkage (σ) and Trim (τ) of different grid densities at Fr = 0.1010

Organization (Code)	r_G		Sinkage $\sigma\times10^2$ (m)					Trim τ°				
			Grid #5	Grid #4	Grid #3	Grid #2	Grid #1	Grid #5	Grid #4	Grid #3	Grid #2	Grid #1
EFD (MOERI)	-	D	-0.147					-0.075				
MOERI (WAVIS)	1.414	S	-	-	-0.2588	-0.3007	-0.2794	-	-	-0.0681	-0.0638	-0.0622
		$E\%D$	-	-	-76.03	-104.55	-90.10	-	-	9.20	14.93	17.07

$E\%D = (D\text{-}S)/D\times100$

Table 1.2b-1-4: V&V results for Sinkage (σ) and Trim (τ) at Fr = 0.1010

Organization (Code)	r_G	Sinkage σ						Trim τ°					
		ε_{12} $\%S_1$	$\frac{U_I}{\varepsilon_{12}}$	$\frac{P_G}{P_{G,th}}$	U_G $\%S_1$	U_D $\%D$	$U_V\%$	ε_{12} $\%S_1$	$\frac{U_I}{\varepsilon_{12}}$	$\frac{P_G}{P_{G,th}}$	U_G $\%S_1$	U_D $\%D$	$U_V\%$
MOERI (WAVIS)	1.414	7.60	-	0.981	0.20	8.64	8.64	2.57	-	1.426	1.05	10.13	10.18

$\varepsilon_{12}\%S_1 = |(S_1\text{-}S_2)/S_1|\times100$; $U_{SN} = \sqrt{U_I^2 + U_G^2}$; $U_V = \sqrt{U_D^2 + U_{SN}^2}$

Table 1.2b-1-5: Computed C_T, C_F, C_{PV} of different grid densities at Fr = 0.1194

Organization (Code)	r_G		C_T ($\times 10^{-3}$)					C_F ($\times 10^{-3}$)					C_{PV} ($\times 10^{-3}$)				
			Grid #5	Grid #4	Grid #3	Grid #2	Grid #1	Grid #5	Grid #4	Grid #3	Grid #2	Grid #1	Grid #5	Grid #4	Grid #3	Grid #2	Grid #1
EFD (MOERI)	-	D	4.146					-					-				
MOERI (WAVIS)	1.414	S	-	-	4.211	4.199	4.199	-	-	3.405	3.360	3.299	-	-	0.8061	0.8396	0.9004
		$E\%D$	-	-	-1.56	-1.29	-1.29										

$E\%D = (D\text{-}S)/D \times 100$

Table 1.2b-1-6: V&V results for C_T, C_F and C_{PV} at Fr = 0.1194

Organization (Code)	r_G	C_T						C_F						C_{PV}					
		ε_{12} $\%S_1$	$\frac{U_I}{\varepsilon_{12}}$	$\frac{P_G}{P_{G,th}}$	U_G $\%S_1$	U_D $\%D$	$U_V\%$	ε_{12} $\%S_1$	$\frac{U_I}{\varepsilon_{12}}$	$\frac{P_G}{P_{G,th}}$	U_G $\%S_1$	U_D $\%D$	$U_V\%$	ε_{12} $\%S_1$	$\frac{U_I}{\varepsilon_{12}}$	$\frac{P_G}{P_{G,th}}$	U_G $\%S_1$	U_D $\%D$	$U_V\%$
MOERI (WAVIS)	1.414	0.003	-	6.332	0.00	1.0	1.00	1.85	-	0.443	3.29			6.75	-	0.858	1.55		

$\varepsilon_{12}\%S_1 = |(S_1\text{-}S_2)/S_1| \times 100$; $U_{SN} = \sqrt{U_I^2 + U_G^2}$; $U_V = \sqrt{U_D^2 + U_{SN}^2}$

Table 1.2b-1-7: Computed Sinkage (σ) and Trim (τ) of different grid densities at Fr = 0.1194

Organization (Code)	r_G		Sinkage $\sigma\times10^2$ (m)					Trim τ°				
			Grid #5	Grid #4	Grid #3	Grid #2	Grid #1	Grid #5	Grid #4	Grid #3	Grid #2	Grid #1
EFD (MOERI)	-	D	-0.281					-0.100				
MOERI (WAVIS)	1.414	S	-	-	-0.3280	-0.3594	-0.3542	-	-	-0.0904	-0.0886	-0.0873
		$E\%D$	-	-	-16.73	-27.92	-26.05	-	-	9.65	11.40	12.70

$E\%D = (D\text{-}S)/D\times100$

Table 1.2b-1-8: V&V results for Sinkage (σ) and Trim (τ) at Fr = 0.1194

Organization (Code)	r_G	Sinkage σ						Trim τ°					
		ε_{12} $\%S_1$	$\frac{U_I}{\varepsilon_{12}}$	$\frac{P_G}{P_{G,th}}$	U_G $\%S_1$	U_D $\%D$	$U_V\%$	ε_{12} $\%S_1$	$\frac{U_I}{\varepsilon_{12}}$	$\frac{P_G}{P_{G,th}}$	U_G $\%S_1$	U_D $\%D$	$U_V\%$
MOERI (WAVIS)	1.414	1.48	-	2.585	1.18	7.56	7.65	1.49	-	0.429	2.81	8.83	9.27

$\varepsilon_{12}\%S_1 = |(S_1\text{-}S_2)/S_1|\times100$; $U_{SN} = \sqrt{U_I^2 + U_G^2}$; $U_V = \sqrt{U_D^2 + U_{SN}^2}$

Table 1.2b-1-9: Computed C_T, C_F, C_{PV} of different grid densities at Fr = 0.1377

Organization (Code)	r_G		C_T ($\times 10^{-3}$)					C_F ($\times 10^{-3}$)					C_{PV} ($\times 10^{-3}$)				
			Grid #5	Grid #4	Grid #3	Grid #2	Grid #1	Grid #5	Grid #4	Grid #3	Grid #2	Grid #1	Grid #5	Grid #4	Grid #3	Grid #2	Grid #1
EFD (MOERI)	-	D	4.071					-					-				
MOERI (WAVIS)	1.414	S	-	-	4.238	4.184	4.164	-	-	3.326	3.280	3.231	-	-	0.9126	0.9042	0.9330
		$E\%D$	-	-	-4.10	-2.78	-2.30										

$E\%D = (D\text{-}S)/D \times 100$

Table 1.2b-1-10: V&V results for C_T, C_F and C_{PV} at Fr = 0.1377

Organization (Code)	r_G	C_T						C_F						C_{PV}					
		ε_{12} $\%S_1$	$\frac{U_I}{\varepsilon_{12}}$	$\frac{P_G}{P_{G,th}}$	U_G $\%S_1$	U_D $\%D$	$U_V\%$	ε_{12} $\%S_1$	$\frac{U_I}{\varepsilon_{12}}$	$\frac{P_G}{P_{G,th}}$	U_G $\%S_1$	U_D $\%D$	$U_V\%$	ε_{12} $\%S_1$	$\frac{U_I}{\varepsilon_{12}}$	$\frac{P_G}{P_{G,th}}$	U_G $\%S_1$	U_D $\%D$	$U_V\%$
MOERI (WAVIS)	1.414	0.48	-	1.435	0.20	1.0	1.02	1.51	-	0.105	18.50			3.09	-	1.779	1.82		

$\varepsilon_{12}\%S_1 = |(S_1\text{-}S_2)/S_1| \times 100$; $U_{SN} = \sqrt{U_I^2 + U_G^2}$; $U_V = \sqrt{U_D^2 + U_{SN}^2}$

Table 1.2b-1-11: Computed Sinkage (σ) and Trim (τ) of different grid densities at Fr = 0.1377

Organization (Code)	r_G		Sinkage $\sigma\times10^2$ (m)					Trim τ°				
			Grid #5	Grid #4	Grid #3	Grid #2	Grid #1	Grid #5	Grid #4	Grid #3	Grid #2	Grid #1
EFD (MOERI)	-	D	-0.409					-0.124				
MOERI (WAVIS)	1.414	S	-	-	-0.4877	-0.4902	-0.4946	-	-	-0.1208	-0.1194	-0.1181
		$E\%D$	-	-	-19.25	-19.85	-20.93	-	-	2.58	3.71	4.76

$E\%D = (D\text{-}S)/D\times100$

Table 1.2b-1-12: V&V results for Sinkage (σ) and Trim (τ) at Fr = 0.1377

Organization (Code)	r_G	Sinkage σ						Trim τ°					
		ε_{12} $\%S_1$	$\frac{U_I}{\varepsilon_{12}}$	$\frac{P_G}{P_{G,th}}$	U_G $\%S_1$	U_D $\%D$	$U_V\%$	ε_{12} $\%S_1$	$\frac{U_I}{\varepsilon_{12}}$	$\frac{P_G}{P_{G,th}}$	U_G $\%S_1$	U_D $\%D$	$U_V\%$
MOERI (WAVIS)	1.414	0.89	-	0.830	0.25	6.57	6.57	1.10	-	0.107	13.21	7.64	15.26

$\varepsilon_{12}\%S_1 = |(S_1\text{-}S_2)/S_1|\times100$; $U_{SN} = \sqrt{U_I^2 + U_G^2}$; $U_V = \sqrt{U_D^2 + U_{SN}^2}$

Table 1.2b-1-13: Computed C_T, C_F, C_{PV} of different grid densities at $Fr = 0.1423$

Organization (Code)	r_G		C_T ($\times 10^{-3}$)					C_F ($\times 10^{-3}$)					C_{PV} ($\times 10^{-3}$)				
			Grid #5	Grid #4	Grid #3	Grid #2	Grid #1	Grid #5	Grid #4	Grid #3	Grid #2	Grid #1	Grid #5	Grid #4	Grid #3	Grid #2	Grid #1
EFD (MOERI)	-	D	4.056					-					-				
MOERI (WAVIS)	1.414	S	-	-	4.245	4.181	4.175	-	-	3.305	3.257	3.245	-	-	0.9393	0.9240	0.9292
		$E\%D$	-	-	-4.65	-3.08	-2.93										

$E\%D = (D\text{-}S)/D \times 100$

Table 1.2b-1-14: V&V results for C_T, C_F and C_{PV} at $Fr = 0.1423$

Organization (Code)	r_G	C_T						C_F						C_{PV}					
		ε_{12} $\%S_1$	$\frac{U_I}{\varepsilon_{12}}$	$\frac{P_G}{P_{G,th}}$	U_G $\%S_1$	U_D $\%D$	$U_V\%$	ε_{12} $\%S_1$	$\frac{U_I}{\varepsilon_{12}}$	$\frac{P_G}{P_{G,th}}$	U_G $\%S_1$	U_D $\%D$	$U_V\%$	ε_{12} $\%S_1$	$\frac{U_I}{\varepsilon_{12}}$	$\frac{P_G}{P_{G,th}}$	U_G $\%S_1$	U_D $\%D$	$U_V\%$
MOERI (WAVIS)	1.414	0.15	-	3.298	0.14	1.0	1.01	0.36	-	2.048	0.24			0.56	-	1.549	0.27		

$\varepsilon_{12}\%S_1 = |(S_1\text{-}S_2)/S_1| \times 100$; $U_{SN} = \sqrt{U_I^2 + U_G^2}$; $U_V = \sqrt{U_D^2 + U_{SN}^2}$

Table 1.2b-1-15: Computed Sinkage (σ) and Trim (τ) of different grid densities at Fr = 0.1423

Organization (Code)	r_G		Sinkage $\sigma\times10^2$ (m)					Trim τ°				
			Grid #5	Grid #4	Grid #3	Grid #2	Grid #1	Grid #5	Grid #4	Grid #3	Grid #2	Grid #1
EFD (MOERI)	-	D	-0.437					-0.132				
MOERI (WAVIS)	1.414	S	-	-	-0.5068	-0.4921	-0.5166	-	-	-0.1296	-0.1272	-0.1277
		$E\%D$	-	-	-15.96	-12.62	-18.22	-	-	1.82	3.64	3.23

$E\%D = (D\text{-}S)/D\times100$

Table 1.2b-1-16: V&V results for Sinkage (σ) and Trim (τ) at Fr = 0.1423

Organization (Code)	r_G	Sinkage σ						Trim τ°					
		ε_{12} $\%S_1$	$\frac{U_I}{\varepsilon_{12}}$	$\frac{P_G}{P_{G,th}}$	U_G $\%S_1$	U_D $\%D$	$U_V\%$	ε_{12} $\%S_1$	$\frac{U_I}{\varepsilon_{12}}$	$\frac{P_G}{P_{G,th}}$	U_G $\%S_1$	U_D $\%D$	$U_V\%$
MOERI (WAVIS)	1.414	4.74	-	0.744	2.28	6.33	6.73	0.42	-	2.149	0.30	7.36	7.37

$\varepsilon_{12}\%S_1 = |(S_1\text{-}S_2)/S_1|\times100$; $U_{SN} = \sqrt{U_I^2 + U_G^2}$; $U_V = \sqrt{U_D^2 + U_{SN}^2}$

Table 1.2b-1-17: Computed C_T, C_F, C_{PV} of different grid densities at $Fr = 0.1469$

Organization (Code)	r_G		C_T ($\times 10^{-3}$)					C_F ($\times 10^{-3}$)					C_{PV} ($\times 10^{-3}$)				
			Grid #5	Grid #4	Grid #3	Grid #2	Grid #1	Grid #5	Grid #4	Grid #3	Grid #2	Grid #1	Grid #5	Grid #4	Grid #3	Grid #2	Grid #1
EFD (MOERI)	-	D	4.046					-					-				
MOERI (WAVIS)	1.414	S	-	-	4.233	4.182	4.157	-	-	3.276	3.255	3.218	-	-	0.9569	0.9272	0.9388
		$E\%D$	-	-	-4.63	-3.37	-2.75										

$E\%D = (D\text{-}S)/D \times 100$

Table 1.2b-1-18: V&V results for C_T, C_F and C_{PV} at $Fr = 0.1469$

Organization (Code)	r_G	C_T						C_F						C_{PV}					
		ε_{12} $\%S_1$	$\frac{U_I}{\varepsilon_{12}}$	$\frac{P_G}{P_{G,th}}$	U_G $\%S_1$	U_D $\%D$	$U_V\%$	ε_{12} $\%S_1$	$\frac{U_I}{\varepsilon_{12}}$	$\frac{P_G}{P_{G,th}}$	U_G $\%S_1$	U_D $\%D$	$U_V\%$	ε_{12} $\%S_1$	$\frac{U_I}{\varepsilon_{12}}$	$\frac{P_G}{P_{G,th}}$	U_G $\%S_1$	U_D $\%D$	$U_V\%$
MOERI (WAVIS)	1.414	0.61	-	1.015	0.01	1.0	1.00	1.14	-	0.795	0.41			1.23	-	1.359	0.44		

$\varepsilon_{12}\%S_1 = |(S_1\text{-}S_2)/S_1| \times 100$; $U_{SN} = \sqrt{U_I^2 + U_G^2}$; $U_V = \sqrt{U_D^2 + U_{SN}^2}$

Table 1.2b-1-19: Computed Sinkage (σ) and Trim (τ) of different grid densities at Fr = 0.1469

Organization (Code)	r_G		Sinkage $\sigma\times10^2$ (m)					Trim τ°				
			Grid #5	Grid #4	Grid #3	Grid #2	Grid #1	Grid #5	Grid #4	Grid #3	Grid #2	Grid #1
EFD (MOERI)	-	D	-0.472					-0.138				
MOERI (WAVIS)	1.414	S	-	-	-0.5214	-0.5636	-0.5821	-	-	-0.1375	-0.1371	-0.1369
		$E\%D$	-	-	-10.46	-19.40	-23.32	-	-	0.36	0.65	0.80

$E\%D = (D\text{-}S)/D\times100$

Table 1.2b-1-20: V&V results for Sinkage (σ) and Trim (τ) at Fr = 0.1469

Organization (Code)	r_G	Sinkage σ						Trim τ°					
		ε_{12} $\%S_1$	$\frac{U_I}{\varepsilon_{12}}$	$\frac{P_G}{P_{G,th}}$	U_G $\%S_1$	U_D $\%D$	$U_V\%$	ε_{12} $\%S_1$	$\frac{U_I}{\varepsilon_{12}}$	$\frac{P_G}{P_{G,th}}$	U_G $\%S_1$	U_D $\%D$	$U_V\%$
MOERI (WAVIS)	1.414	3.18	-	1.191	0.70	6.10	6.14	0.15	-	1.000	0.00	7.08	7.08

$\varepsilon_{12}\%S_1 = |(S_1\text{-}S_2)/S_1|\times100$; $U_{SN} = \sqrt{U_I^2 + U_G^2}$; $U_V = \sqrt{U_D^2 + U_{SN}^2}$

Table 1.2b-1-21: Computed C_T, C_F, C_{PV} of different grid densities at $Fr = 0.1515$

Organization (Code)	r_G		C_T ($\times 10^{-3}$)					C_F ($\times 10^{-3}$)					C_{PV} ($\times 10^{-3}$)				
			Grid #5	Grid #4	Grid #3	Grid #2	Grid #1	Grid #5	Grid #4	Grid #3	Grid #2	Grid #1	Grid #5	Grid #4	Grid #3	Grid #2	Grid #1
EFD (MOERI)	-	D	4.037					-					-				
MOERI (WAVIS)	1.414	S	-	-	4.240	4.181	4.148	-	-	3.252	3.234	3.200	-	-	0.9888	0.9476	0.9481
		$E\%D$	-	-	-5.04	-3.57	-2.75										

$E\%D = (D\text{-}S)/D \times 100$

Table 1.2b-1-22: V&V results for C_T, C_F and C_{PV} at $Fr = 0.1515$

Organization (Code)	r_G	C_T						C_F						C_{PV}					
		ε_{12} $\%S_1$	$\frac{U_I}{\varepsilon_{12}}$	$\frac{P_G}{P_{G,th}}$	U_G $\%S_1$	U_D $\%D$	$U_V\%$	ε_{12} $\%S_1$	$\frac{U_I}{\varepsilon_{12}}$	$\frac{P_G}{P_{G,th}}$	U_G $\%S_1$	U_D $\%D$	$U_V\%$	ε_{12} $\%S_1$	$\frac{U_I}{\varepsilon_{12}}$	$\frac{P_G}{P_{G,th}}$	U_G $\%S_1$	U_D $\%D$	$U_V\%$
MOERI (WAVIS)	1.414	0.80	-	0.835	0.22	1.0	1.02	1.05	-	0.905	0.15			0.06	-	6.227	0.06		

$\varepsilon_{12}\%S_1 = |(S_1\text{-}S_2)/S_1| \times 100$; $U_{SN} = \sqrt{U_I^2 + U_G^2}$; $U_V = \sqrt{U_D^2 + U_{SN}^2}$

Table 1.2b-1-23: Computed Sinkage (σ) and Trim (τ) of different grid densities at Fr = 0.1515

Organization (Code)	r_G		Sinkage $\sigma\times10^2$ (m)					Trim τ°				
			Grid #5	Grid #4	Grid #3	Grid #2	Grid #1	Grid #5	Grid #4	Grid #3	Grid #2	Grid #1
EFD (MOERI)	-	D	-0.499					-0.154				
MOERI (WAVIS)	1.414	S	-	-	-0.5186	-0.5341	-0.6052	-	-	-0.1452	-0.1447	-0.1449
		$E\%D$	-	-	-3.93	-7.03	-21.29	-	-	5.71	6.04	5.91

$E\%D = (D\text{-}S)/D\times100$

Table 1.2b-1-24: V&V results for Sinkage (σ) and Trim (τ) at Fr = 0.1515

Organization (Code)	r_G	Sinkage σ						Trim τ°					
		ε_{12} $\%S_1$	$\frac{U_I}{\varepsilon_{12}}$	$\frac{P_G}{P_{G,th}}$	U_G $\%S_1$	U_D $\%D$	$U_V\%$	ε_{12} $\%S_1$	$\frac{U_I}{\varepsilon_{12}}$	$\frac{P_G}{P_{G,th}}$	U_G $\%S_1$	U_D $\%D$	$U_V\%$
MOERI (WAVIS)	1.414	11.76	-	2.204	8.50	5.87	10.33	0.14	-	1.322	0.05	6.81	6.81

$\varepsilon_{12}\%S_1 = |(S_1\text{-}S_2)/S_1|\times100$; $U_{SN} = \sqrt{U_I^2 + U_G^2}$; $U_V = \sqrt{U_D^2 + U_{SN}^2}$

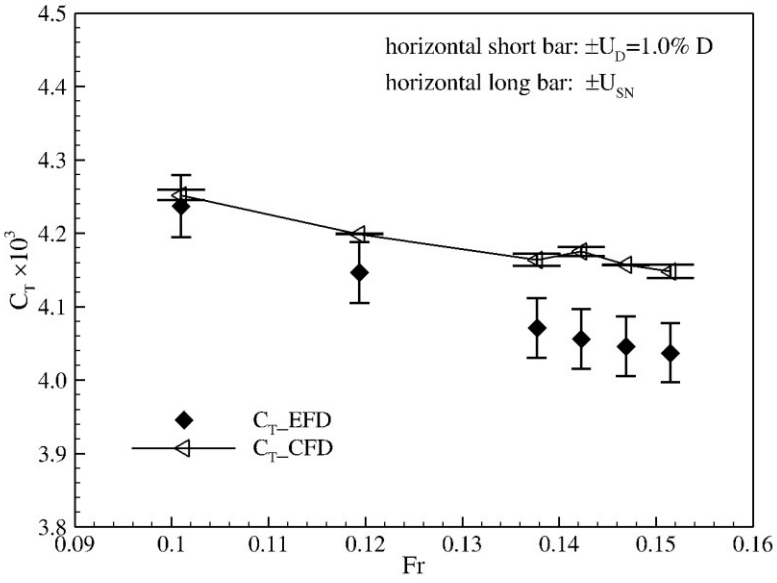

MOERI-WAVIS

Fig. 1.2b-2 Total resistance Coefficients (C_T) versus Fr

(CFD: solid line with open left-triangles; EFD: solid diamonds
$\pm U_D$: horizontal short bars; $\pm U_{SN}$: horizontal long bars)

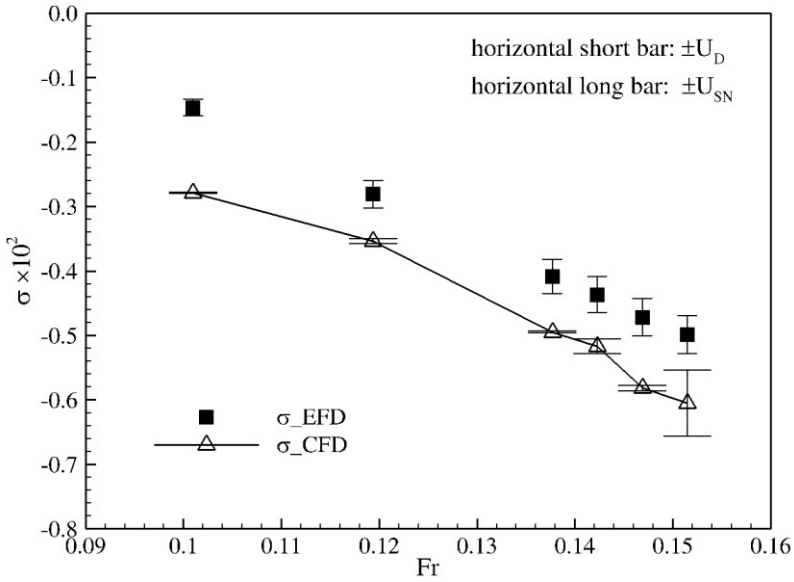

MOERI-WAVIS

Fig. 1.2b-3 Sinkage (σ) versus Fr

(CFD solid line with open up-triangles; EFD: solid squares
$\pm U_D$: horizontal short bars; $\pm U_{SN}$: horizontal long bars)

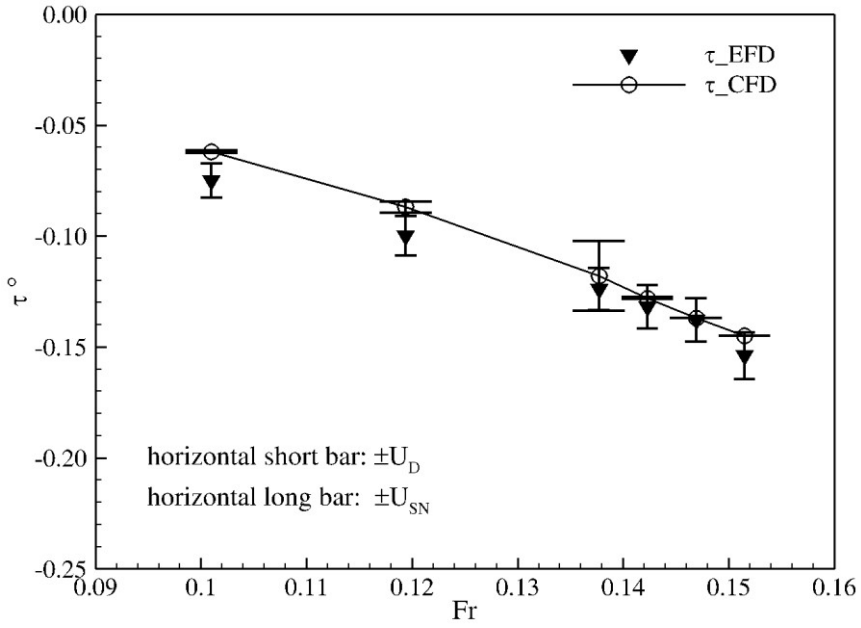

MOERI-WAVIS

Fig. 1.2b-4 Trim (τ) versus Fr

(CFD: solid line with open circles; EFD: solid down-triangles
$\pm U_D$: horizontal short bars; $\pm U_{SN}$: horizontal long bars)

Test Case 1.4a

Table 1.4a-1-1 Harmonic amplitudes and phases of the total resistance coefficient (C_T), heave motion (z), pitch angle (θ)
(λ/L_{PP} = 0.6, Re = 2.55×10^6, Fr = 0.142, wave height Hs = 60mm)

Table 1.4a-1-2 Harmonic amplitudes and phases of the total resistance coefficient (C_T), heave motion (z), pitch angle (θ)
(λ/L_{PP} = 1.1, Re = 2.55×10^6, Fr = 0.142, wave height Hs = 60mm)

Table 1.4a-1-3 Harmonic amplitudes and phases of the total resistance coefficient (C_T), heave motion (z), pitch angle (θ)
(λ/L_{PP}= 1.6, Re = 2.55×10^6, Fr = 0.142, wave height Hs = 60mm)

Table 1.4a-1-4 Harmonic amplitudes and phases of the total resistance coefficient (C_T), heave motion (z), pitch angle (θ)
(Calm water, Re= 2.55×10^6, Fr = 0.142, wave height Hs = 60mm)

Figure 1.4a-C1-1 Time histories of total resistance coefficient (C_T) at λ/L_{PP}= 0.6
Figure 1.4a-C1-2 Time histories of heave motion (z) at λ/L_{PP}=0.6
Figure 1.4a-C1-3 Time histories of pitch angle (θ) at λ/L_{PP}= 0.6
Figure 1.4a-C2-1 Time histories of total resistance coefficient (C_T) at λ/L_{PP}= 1.1
Figure 1.4a-C2-2 Time histories of heave motion (z) at λ/L_{PP}= 1.1
Figure 1.4a-C2-3 Time histories of pitch angle (θ) at λ/L_{PP}= 1.1
Figure 1.4a-C3-1 Time histories of total resistance coefficient (C_T) at λ/L_{PP}= 1.6
Figure 1.4a-C3-2 Time histories of heave motion (z) at λ/L_{PP}= 1.6
Figure 1.4a-C3-3 Time histories of pitch angle (θ) at λ/L_{PP}= 1.6

Table 1.4a-1-1: harmonic amplitudes and phases of the total resistance coefficient (C_T), heave motion (z), pitch angle (θ)
(λ/L_{PP} = 0.6, Re = 2.55×10^6, Fr = 0.142, wave height Hs = 60mm)

Organization (Code)		$C_T \times 10^3$			z			θ		
		0th Amplitude	1st Amplitude	1st Phase°	0th Amplitude (mm)	1st Amplitude (mm)	1st Phase°	0th Amplitude°	1st Amplitude°	1st Phase°
EFD (INSEAN)	*D*	-	-	-	-	-	-	-	-	-
ECN/CNRS (ISISCFD)	*S*	7.758	43.410		-3.360	1.850		-0.120	0.144	
	E%D	-	-	-	-	-	-	-	-	-
ECN (ICARE)	*S*	7.550	45.200	15.000	-3.350	2.080	108.000	-0.117	0.152	-159.000
	E%D	-	-	-	-	-	-	-	-	-
GL&UDE (Comet)	*S*	-	-	-	-3.521	1.281	102.130	-0.242	0.091	-172.780
	E%D	-	-	-	-	-	-	-	-	-
GL&UDE (OpenFOAM)	*S*	-	-	-	-2.386	1.633	103.590	-0.109	0.109	-167.690
	E%D	-	-	-	-	-	-	-	-	-
UIOWA (CFDShipIowa)	*S*	7.796	40.204	-110.161	-3.324	1.584	4.957	-0.116	0.118	94.885
	E%D	-	-	-	-	-	-	-	-	-

$E\%D = (D\text{-}S)/D \times 100$

Table 1.4a-1-2: harmonic amplitudes and phases of the total resistance coefficient (C_T), heave motion (z), pitch angle (θ)
(λ/L_{PP}= 1.1, Re = 2.55×10^6, Fr = 0.142, wave height Hs = 60mm)

Organization (Code)		$C_T \times 10^3$			z			θ		
		0th Amplitude	1st Amplitude	1st Phase°	0th Amplitude (mm)	1st Amplitude (mm)	1st Phase°	0th Amplitude°	1st Amplitude°	1st Phase°
EFD (INSEAN)	*D*	12.480	43.179	118.973	-3.567	19.833	-93.871	-0.183	1.710	-5.650
ECN/ CNRS (ISISCFD)	*S*	12.520	22.280	-	-3.040	20.770	-	-0.138	1.820	-
	E%D	-0.32	48.40	-	14.78	-4.73	-	24.63	-6.45	-
ECN (ICARE)	*S*	11.950	26.500	35.000	-3.280	24.540	159.000	-0.159	1.900	-136.000
	E%D	4.25	38.63	70.58	191.94	-23.74	269.38	13.16	-11.13	-2307.27
GL&UDE (Comet)	*S*	-	-	-	-3.291	17.699	151.610	-0.244	1.418	-142.670
	E%D	-	-	-	7.75	10.76	261.51	-33.27	17.06	-2425.34
GL&UDE (OpenFOAM)	*S*	-	-	-	-1.054	21.620	156.410	-0.121	1.812	-135.470
	E%D	-	-	-	70.45	-9.01	266.62	33.91	-5.98	-2297.89
UIOWA (CFDShipIowa)	*S*	13.109	27.353	-94.867	-3.309	19.663	-55.872	-0.142	1.601	5.817
	E%D	-5.04	36.65	179.74	7.24	0.85	40.48	22.43	6.33	202.97

$E\%D = (D-S)/D \times 100$

Table 1.4a-1-3: harmonic amplitudes and phases of the total resistance coefficient (C_T), heave motion (z), pitch angle (θ) (λ/L_{PP}= 1.6, Re = 2.55×10^6, Fr = 0.142, wave height Hs = 60mm)

Organization (Code)		C_T×10^3			z			θ		
		0th Amplitude	1st Amplitude	1st Phase°	0th Amplitude (mm)	1st Amplitude (mm)	1st Phase°	0th Amplitude°	1st Amplitude°	1st Phase°
EFD (INSEAN)	*D*	8.256	79.433	58.279	-3.593	26.905	-22.978	-0.155	2.554	39.246
ECN/ CNRS (ISISCFD)	*S*	6.950	59.900	-	-2.890	28.310	-	-0.127	2.220	-
	E%D	15.82	24.59	-	19.56	-5.22	-	18.03	13.08	-
ECN (ICARE)	*S*	6.200	55.600	-29.000	-3.000	29.410	-96.000	-0.129	2.270	-41.000
	E%D	24.90	30.00	149.76	16.50	-9.31	-317.79	17.06	11.12	204.47
GL&UDE (Comet)	*S*	-	-	-	-3.225	27.040	-103.000	-0.242	2.001	-50.330
	E%D	-	-	-	10.23	-0.50	-348.25	-56.20	21.65	228.24
GL&UDE (OpenFOAM)	*S*	-	-	-	-1.574	27.749	-101.300	-0.112	2.239	-46.810
	E%D	-	-	-	56.19	-3.14	-340.85	27.71	12.33	219.27
UIOWA (CFDShipIowa)	*S*	9.362	52.389	76.124	-3.046	25.548	-4.691	-0.124	2.043	48.885
	E%D	-13.40	34.05	-30.62	15.23	5.04	79.58	19.85	19.99	-24.56

$E\%D = (D\text{-}S)/D\times100$

Table 1.4a-1-4: harmonic amplitudes and phases of the total resistance coefficient (C_T), heave motion (z), pitch angle (θ) (Calm water, $Re = 2.55\times10^6$, $Fr = 0.142$, wave height $Hs = 60$mm)

Organization (Code)		$C_T\times10^3$	z	θ
		0th Amplitude	0th Amplitude (mm)	0th Amplitude°
EFD (INSEAN)	*D*	5.141	-2.590	-0.142
ECN/ CNRS (ISISCFD)	*S*	4.630	-3.210	-0.130
	E%D	9.93	-23.94	8.45
ECN (ICARE)	*S*	-	-	-
	E%D	-	-	-
GL&UDE (Comet)	*S*	-	-	-
	E%D	-	-	-
GL&UDE (OpenFOAM)	*S*	-	-	-
	E%D	-	-	-
UIOWA (CFDShipIowa)	*S*	5.491	-3.246	-0.124
	E%D	-6.82	-25.33	12.82

$E\%D = (D\text{-}S)/D\times100$

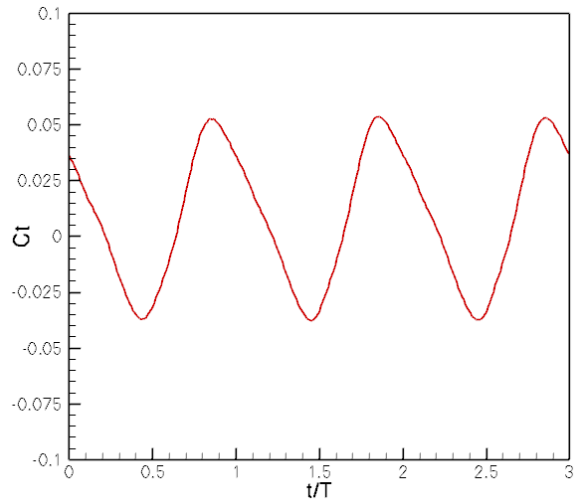

ECN/CRNS-ISISCFD

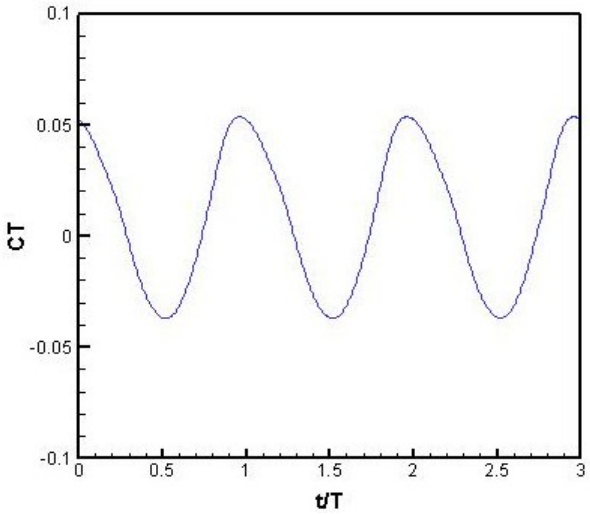

ECN-Icare

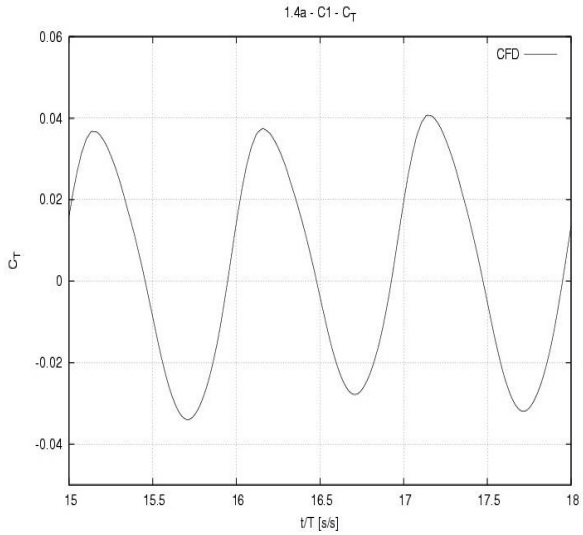

GL&UDE-Comet

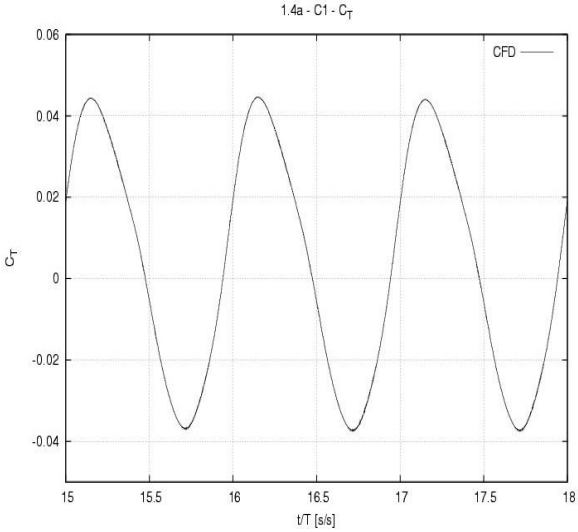

GL&UDE-OpenFOAM

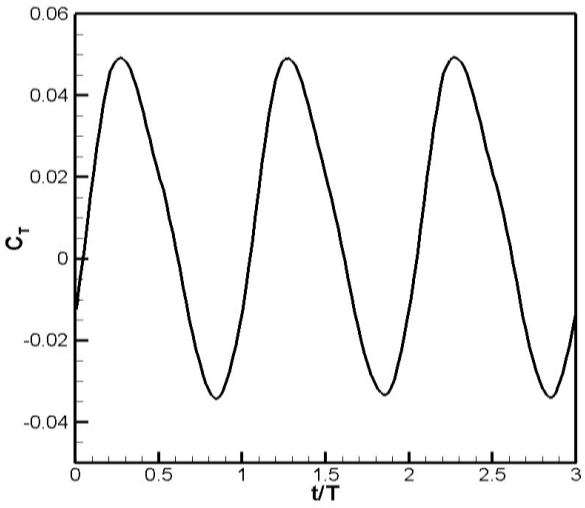

UIOWA-CFDShipIowa

Fig. 1.4a-C1-1 Time histories of total resistance coefficient (C_T) at λ/L_{PP}= 0.6

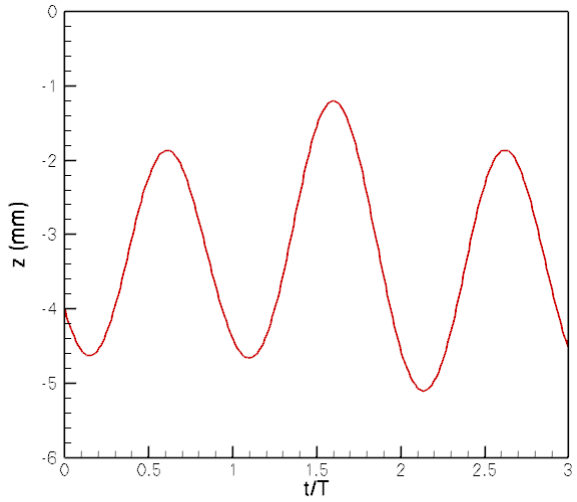

ECN/CRNS-ISISCFD

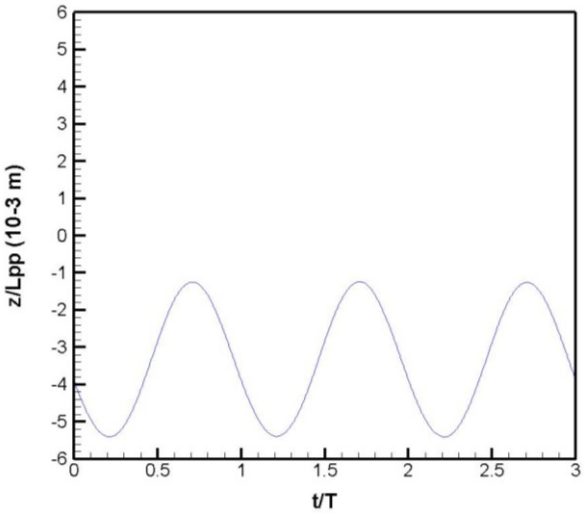

ECN-Icare

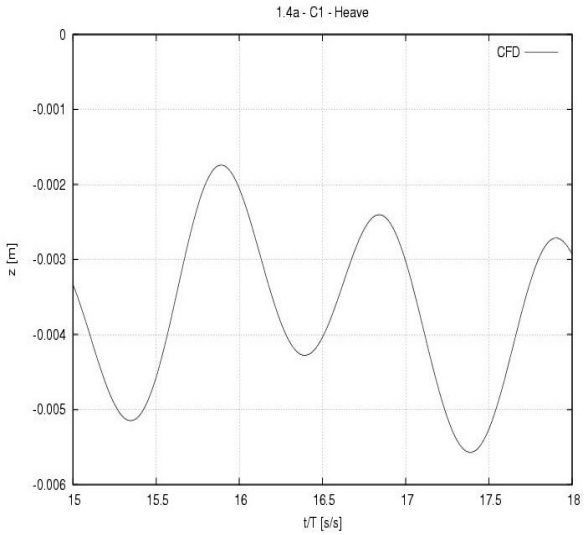

GL&UDE-Comet

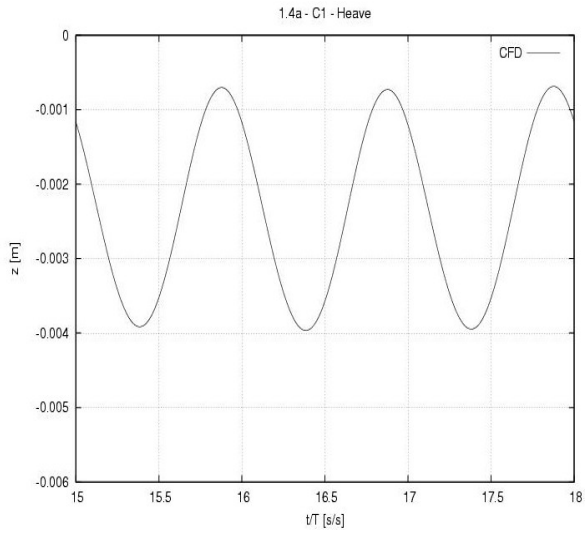

GL&UDE-OpenFOAM

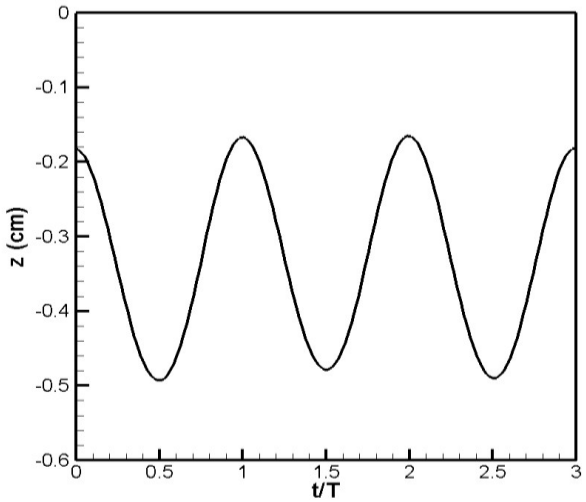

UIOWA-CFDShipIowa

Fig. 1.4a-C1-2 Time histories of heave motion (z) at λ/L_{PP}=0.6

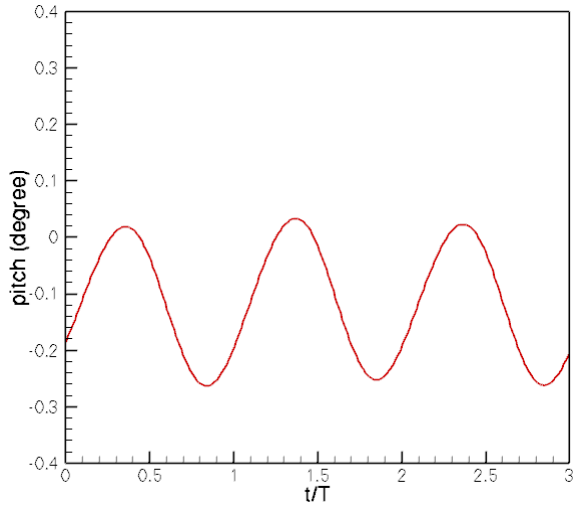

ECN/CRNS-ISISCFD

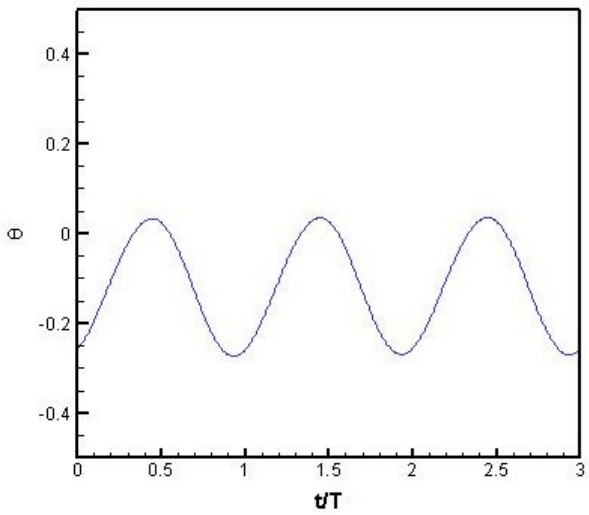

ECN-Icare

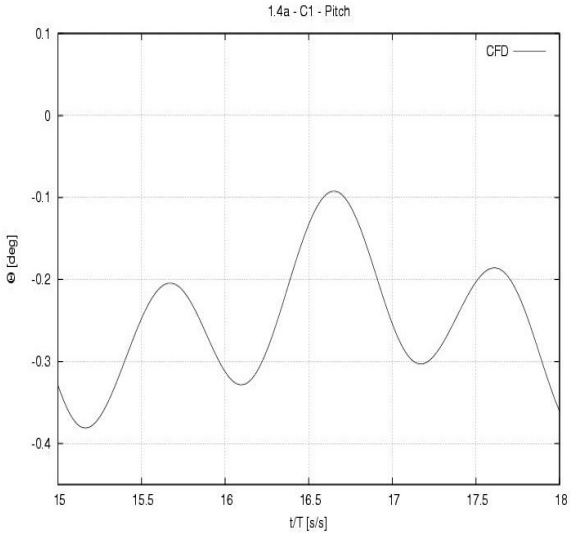

GL&UDE-Comet

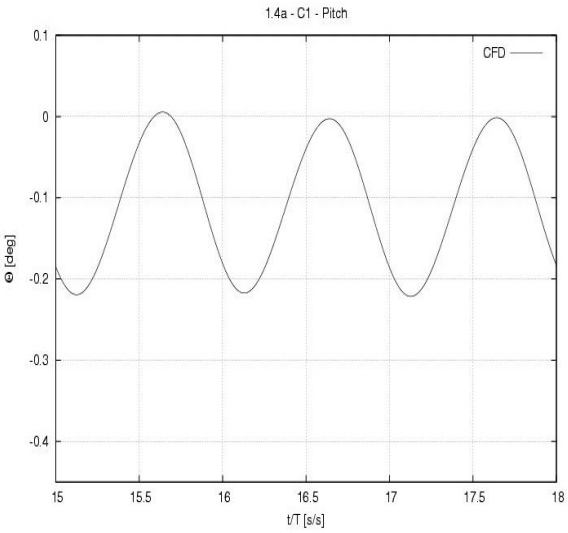

GL&UDE-OpenFOAM

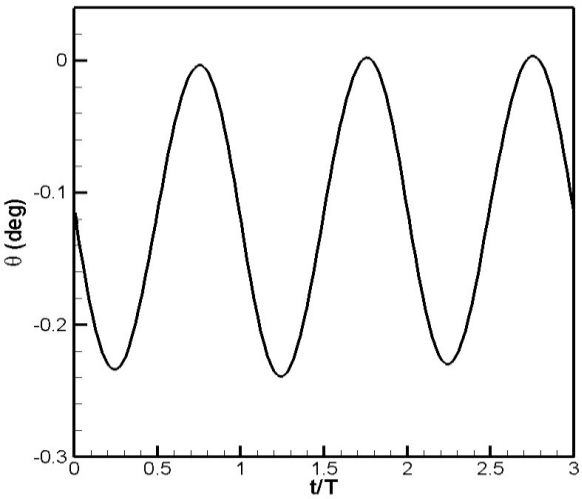

UIOWA-CFDShipIowa

Fig. 1.4a-C1-3 Time histories of pitch angle (θ) at λ/L_{PP}= 0.6

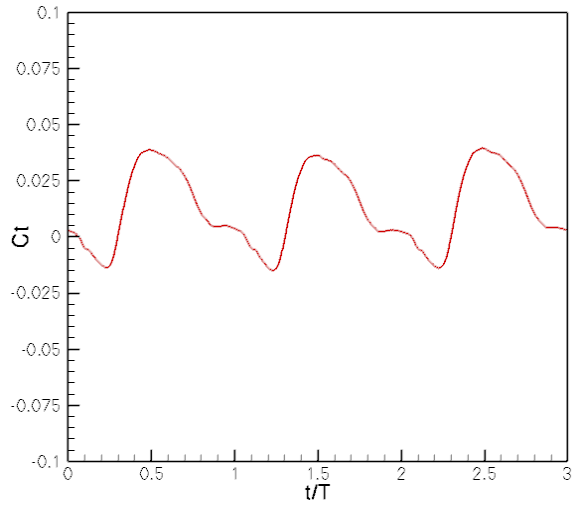

ECN/CRNS-ISISCFD

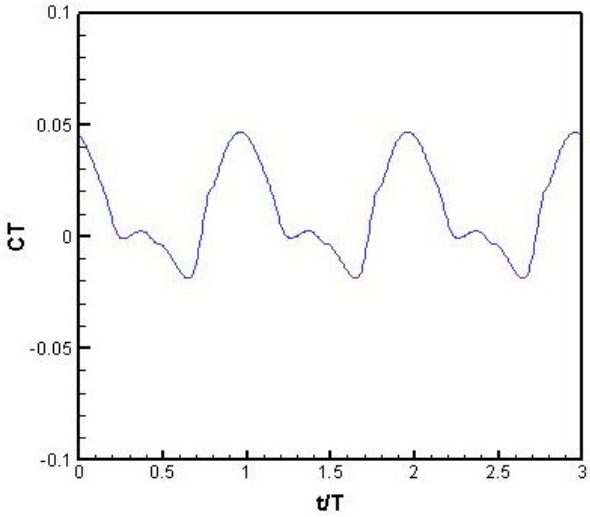

ECN-Icare

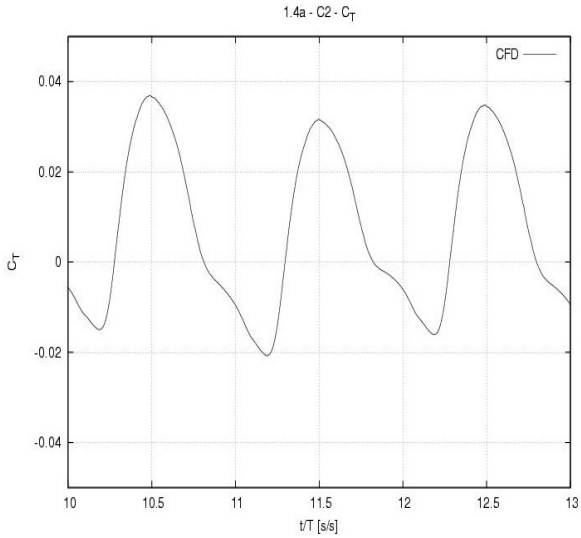

GL&UDE-Comet

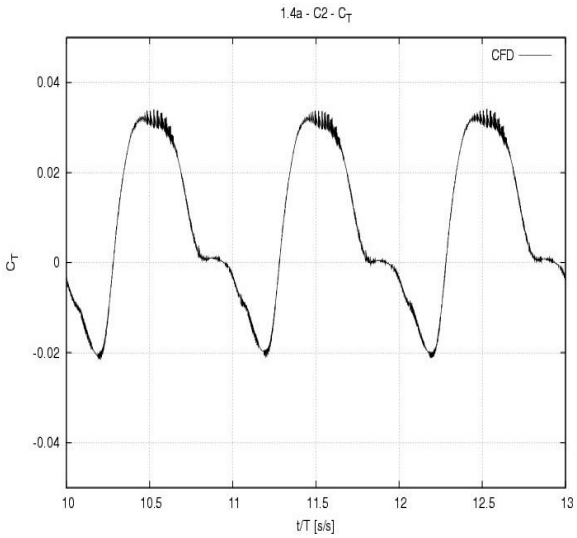

GL&UDE-OpenFOAM

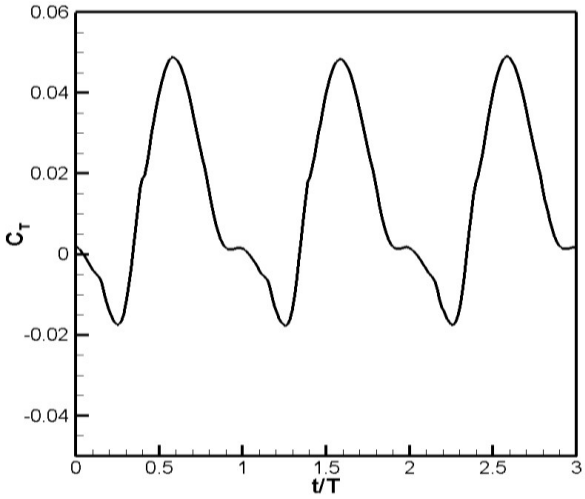

UIOWA-CFDShipIowa

Fig. 1.4a-C2-1 Time histories of total resistance coefficient (C_T) at λ/L_{PP}= 1.1

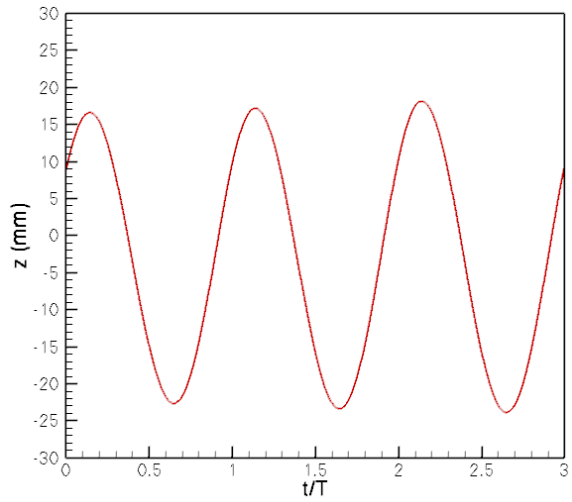

ECN/CRNS-ISISCFD

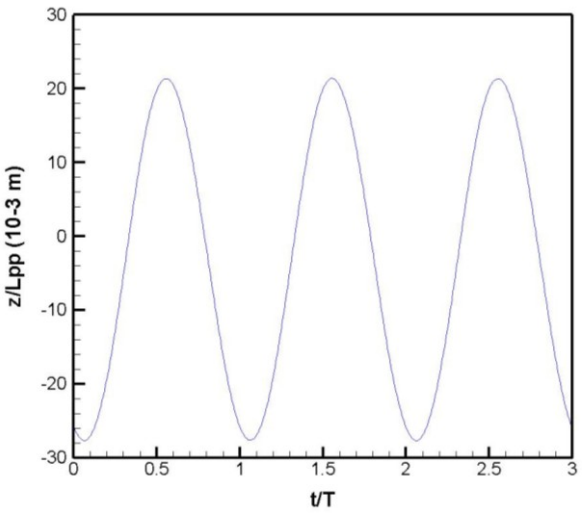

ECN-Icare

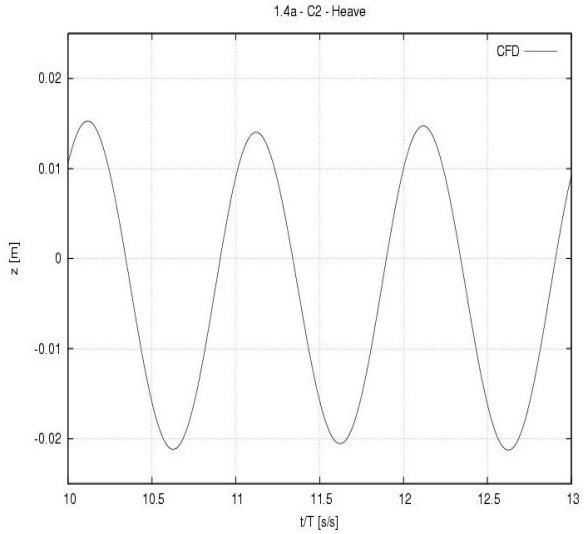

GL&UDE-Comet

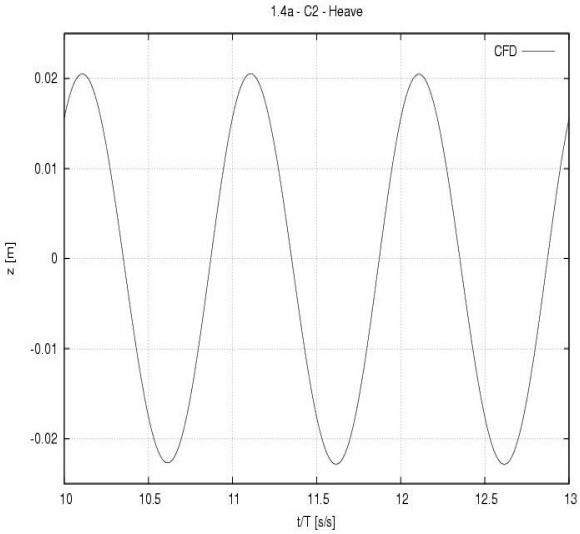

GL&UDE-OpenFOAM

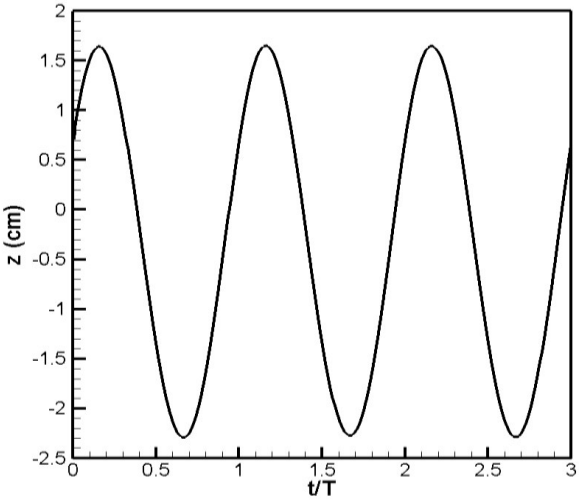

UIOWA-CFDShipIowa

Fig. 1.4a-C2-2 Time histories of heave motion (z) at λ/L_{PP}= 1.1

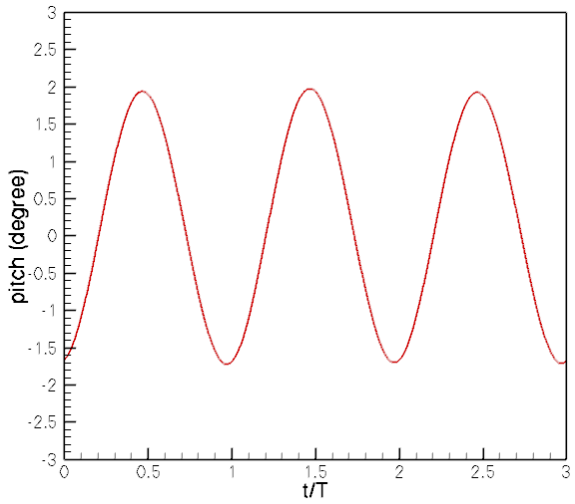

ECN/CRNS-ISISCFD

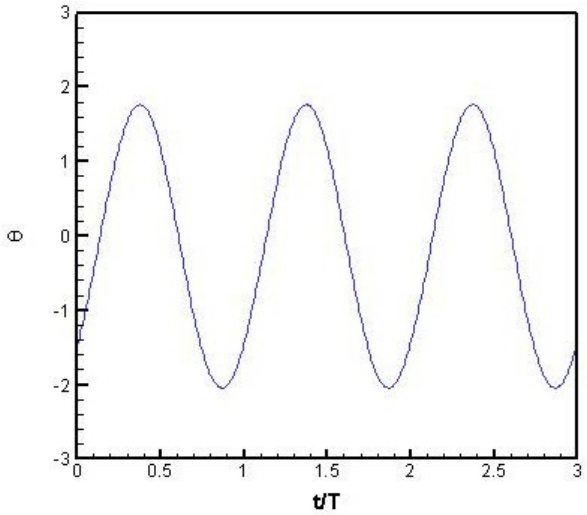

ECN-Icare

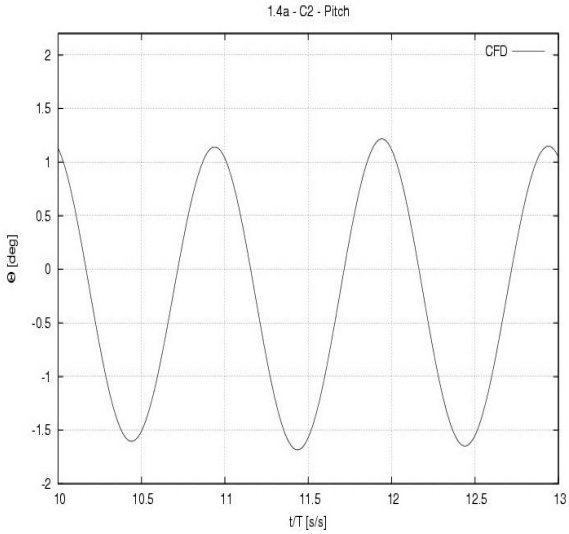

GL&UDE-Comet

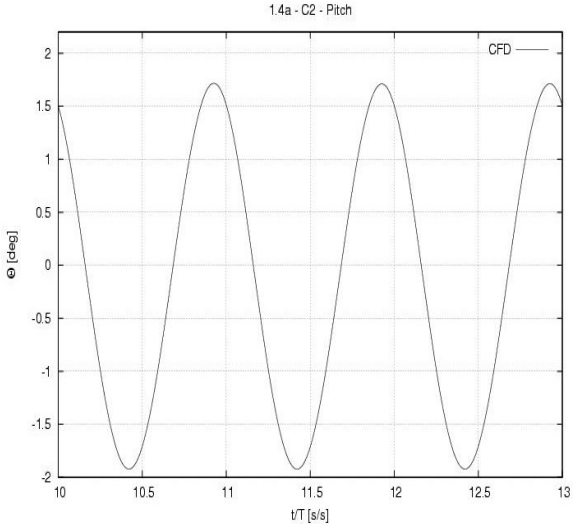

GL&UDE-OpenFOAM

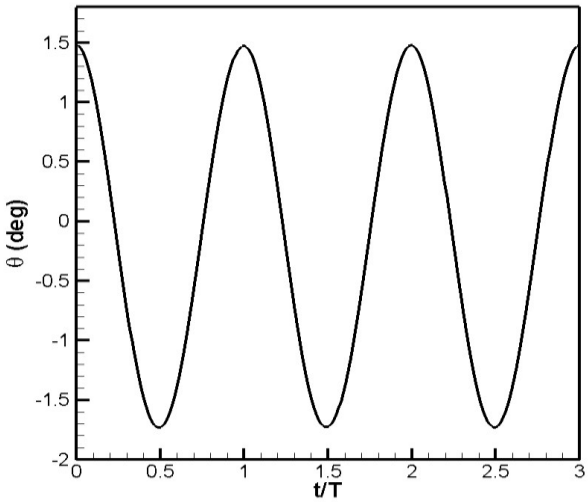

UIOWA-CFDShipIowa

Fig. 1.4a-C2-3 Time histories of pitch angle (θ) at λ/L_{PP}= 1.1

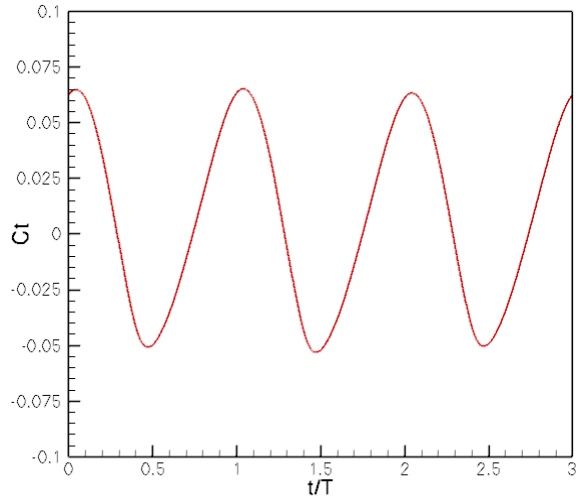

ECN/CRNS-ISISCFD

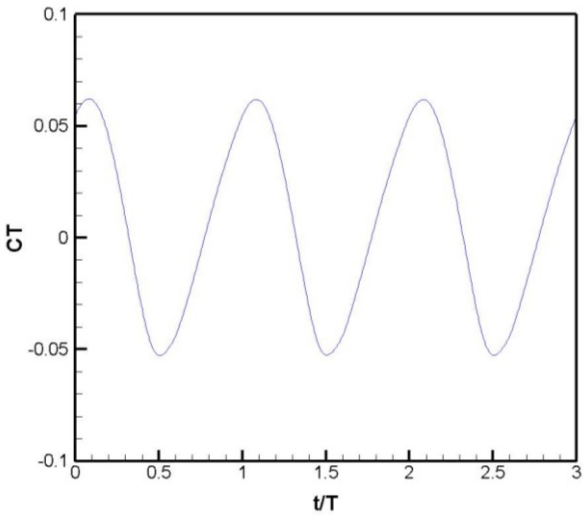

ECN-Icare

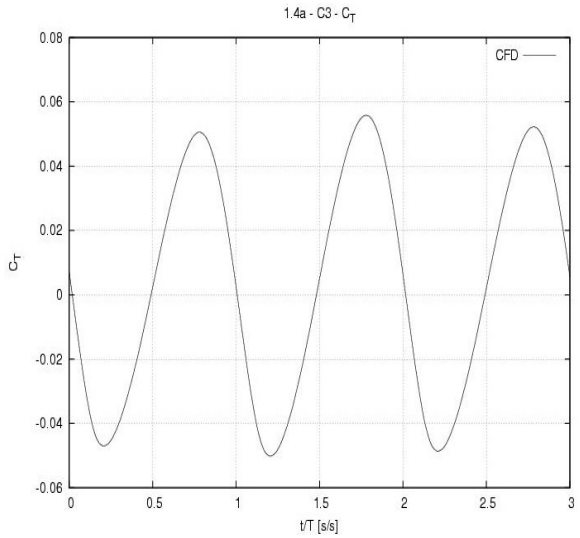

GL&UDE-Comet

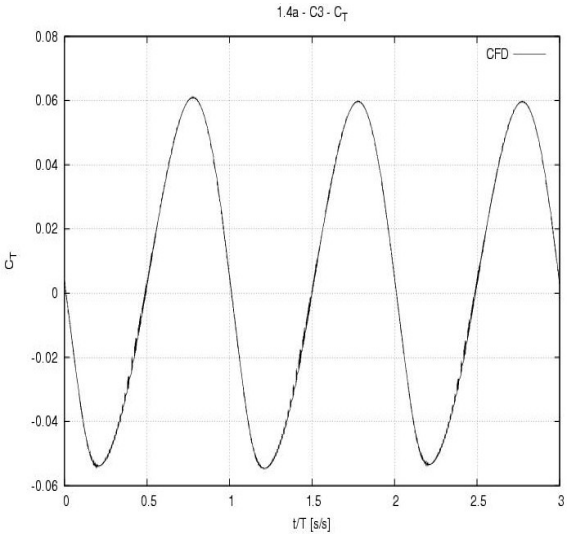

GL&UDE-OpenFOAM

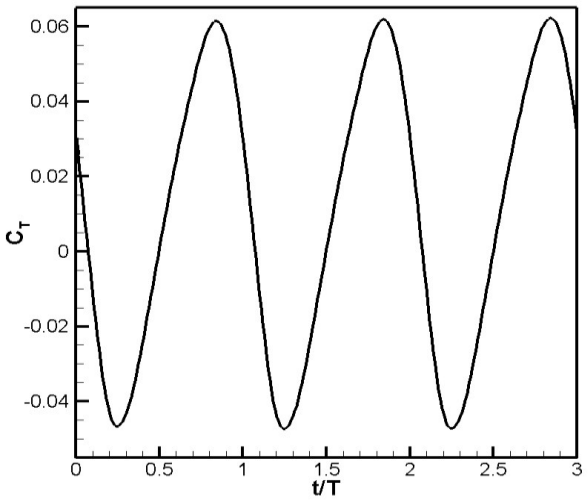

UIOWA-CFDShipIowa

Fig. 1.4a-C3-1 Time histories of total resistance coefficient (C_T) at λ/L_{PP}= 1.6

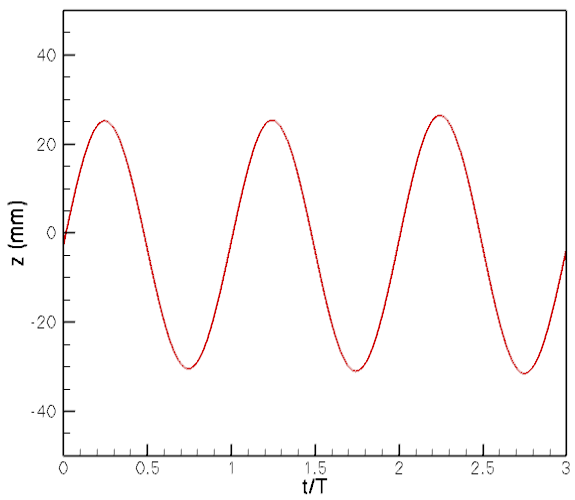

ECN/CRNS-ISISCFD

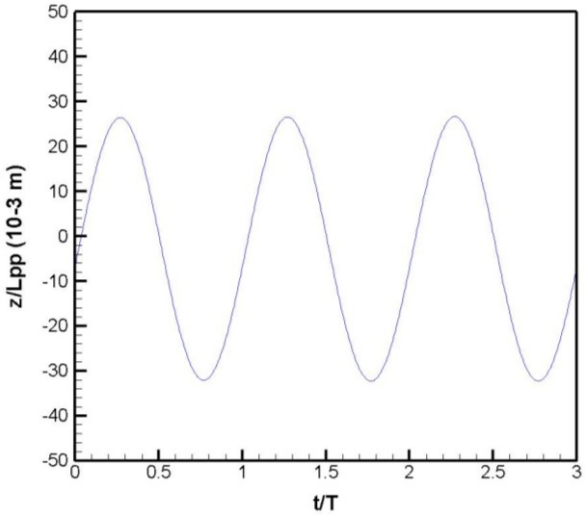

ECN-Icare

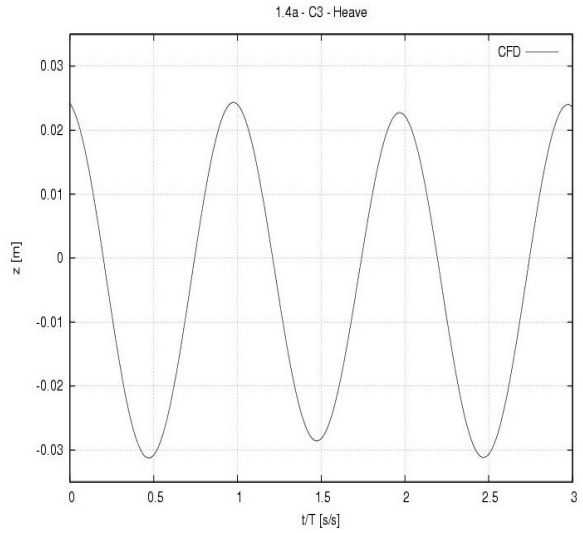

GL&UDE-Comet

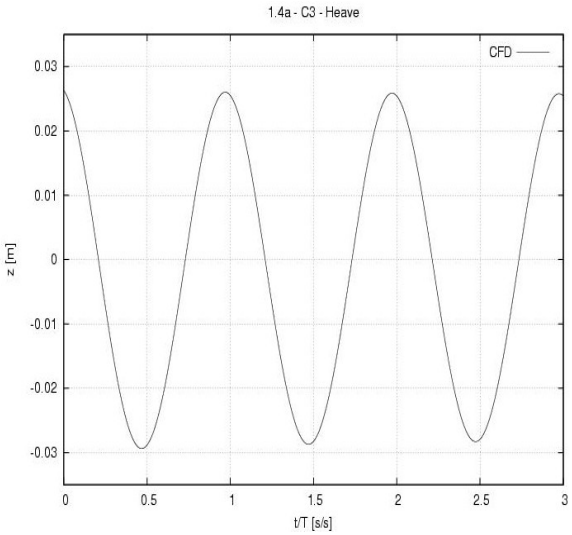

GL&UDE-OpenFOAM

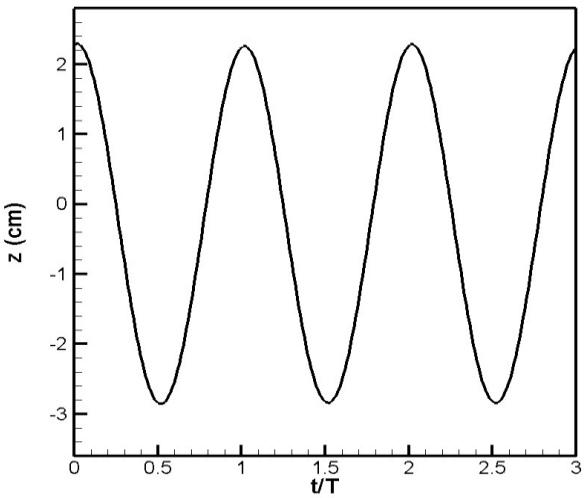

UIOWA-CFDShipIowa

Fig. 1.4a-C3-2 Time histories of heave motion (z) at λ/L_{PP}= 1.6

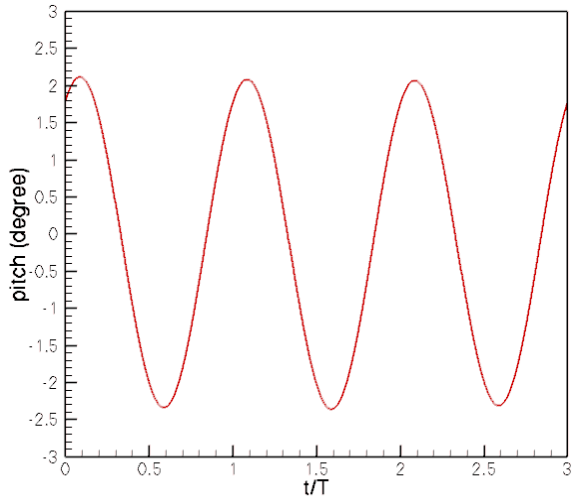

ECN/CRNS-ISISCFD

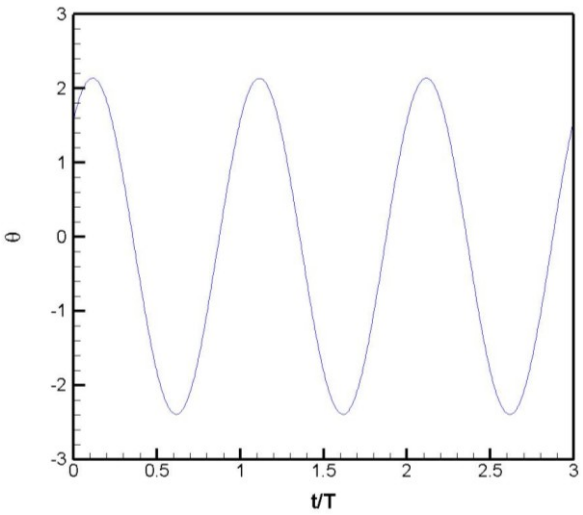

ECN-Icare

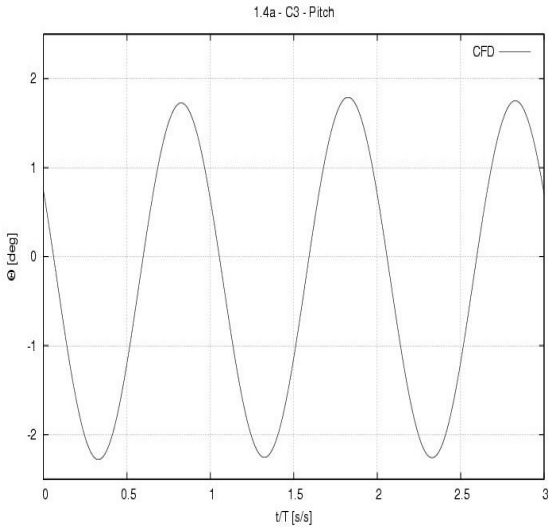

GL&UDE-Comet

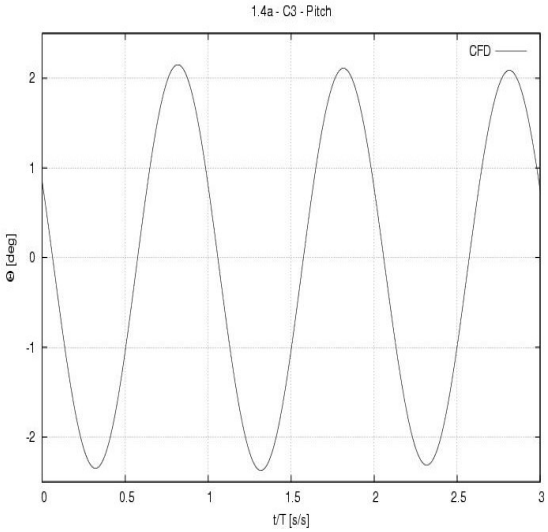

GL&UDE-OpenFOAM

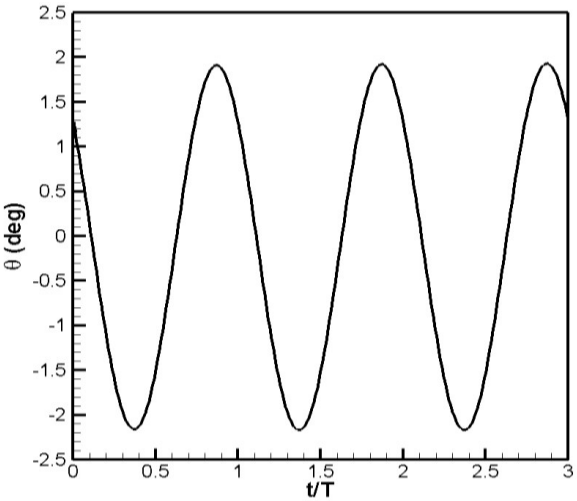

UIOWA-CFDShipIowa

Fig. 1.4a-C3-3 Time histories of pitch angle (θ) at λ/L_{PP}= 1.6

Test Case 1.4b

Table 1.4b-1-1 Harmonic amplitudes and phases of the total resistance (R_T), heave motion (z), pitch angle (θ) (λ/L_{PP} = 0.9171, measured Hs = 122.66 mm, nominal Hs = 150 mm, Fr = 0.0)

Table 1.4b-1-2 Harmonic amplitudes and phases of the total resistance (R_T), heave motion (z), pitch angle (θ) (λ/L_{PP} = 0.6364, measured Hs = 27 mm, nominal Hs = 30 mm, Fr = 0.142)

Table 1.4b-1-3 Harmonic amplitudes and phases of the total resistance (R_T), heave motion (z), pitch angle (θ) (λ/L_{PP} = 0.6364, measured Hs = 140 mm, nominal Hs = 150 mm, Fr = 0.142)

Table 1.4b-1-4 Harmonic amplitudes and phases of the total resistance (R_T), heave motion (z), pitch angle (θ) (λ/L_{PP} = 0.9171, measured Hs = 138 mm, nominal Hs = 150 mm, Fr = 0.142)

Table 1.4b-1-5 Harmonic amplitudes and phases of the total resistance (R_T), heave motion (z), pitch angle (θ) (λ/L_{PP} = 0.6364, measured Hs = 140 mm, nominal Hs = 150 mm, Fr = 0.182)

Table 1.4b-1-6 Total Resistance (R_T) , sinkage (z) and trim (θ) in calm water, Fr = 0.142

Table 1.4b-1-7 Total Resistance (R_T) , sinkage (z) and trim (θ) in calm water, Fr = 0.182

Table 1.4b-1-1: harmonic amplitudes and phases of the total resistance (R_T), heave motion (z), pitch angle (θ)
(λ/L_{PP} = 0.9171, measured Hs = 122.66 mm, nominal Hs = 150 mm, Fr = 0.0)

Organization (Code)		R_T			z			θ		
		0th Amplitude (N)	1st Amplitude (N)	1st Phase°	0th Amplitude (mm)	1st Amplitude (mm)	1st Phase°	0th Amplitude°	1st Amplitude°	1st Phase°
EFD (NTNU)	*D*	18.461	442.342	-	- 0.153	19.814	39.493	- 0.023	1.638	53.978
ECN/ CNRS (ISISCFD)	*S*	4.520	82.500	-	0.460	15.900	-	-0.024	1.530	-
	E%D	75.52	81.35	-	400.07	19.75	-	-4.35	6.59	-
ECN (ICARE)	*S*	5.875	70.500	-116.000	-0.060	22.700	-97.000	-0.017	1.560	-103.000
	E%D	68.18	84.06	-	60.86	-14.57	345.61	28.26	4.76	290.82
GL&UDE (Comet)	*S*	-	-	-	0.223	18.439	-125.520	-0.091	1.541	-124.270
	E%D	-	-	-	245.47	6.94	417.83	-295.65	5.92	330.22
GL&UDE (OpenFOAM)	*S*	-	-	-	-2.315	15.491	-119.220	-0.004	1.414	-116.570
	E%D	-	-	-	-1410.11	21.82	401.88	82.61	13.68	315.96
Kyushu University (RIAM-CMEN)	*S*	3.443	92.125	-72.089	-1.312	22.593	-122.221	-0.028	1.547	-118.387
	E%D	81.35	79.17	-	-755.84	-14.03	409.48	-20.87	5.56	319.32

$E\%D = (D-S)/D \times 100$

Table 1.4b-1-2: harmonic amplitudes and phases of the total resistance (R_T), heave motion (z), pitch angle (θ)
(λ/L_{PP} = 0.6364, measured Hs = 27 mm, nominal Hs = 30 mm, Fr = 0.142)

Organization (Code)		R_T			z			θ		
		0th Amplitude (N)	1st Amplitude (N)	1st Phase°	0th Amplitude (mm)	1st Amplitude (mm)	1st Phase°	0th Amplitude°	1st Amplitude°	1st Phase°
EFD (NTNU)	*D*	21.216	58.459	-	-6.148	1.176	5.418	-0.125	0.032	107.010
ECN/ CNRS (ISISCFD)	*S*	20.080	55.390	-	-5.320	1.550	-	-0.128	0.027	-
	E%D	5.354	5.250	-	13.468	-31.803	-	-2.236	15.625	-
ECN (ICARE)	*S*	23.000	53.500	2.900	-5.750	1.050	126.700	-0.125	0.026	-132.100
	E%D	-8.41	8.48	-	6.47	10.71	-2238.50	0.16	18.75	223.45
GL&UDE (Comet)	*S*	-	-	-	-5.805	0.779	114.670	-0.193	0.024	-151.970
	E%D	-	-	-	5.58	33.76	-2016.46	-54.15	25.00	242.01
GL&UDE (OpenFOAM)	*S*	-	-	-	-2.793	0.887	114.820	-0.112	0.021	-150.280
	E%D	-	-	-	54.57	24.57	-2019.23	10.54	34.38	240.44
Kyushu University (RIAM-CMEN)	*S*	32.199	58.470	-27.680	-13.694	1.131	107.316	-0.208	0.032	-134.005
	E%D	-51.77	-0.02	-	-122.74	3.83	-1880.73	-66.13	0.00	225.23

$E\%D = (D-S)/D \times 100$

Table 1.4b-1-3: harmonic amplitudes and phases of the total resistance (R_T), heave motion (z), pitch angle (θ)
(λ/L_{PP} = 0.6364, measured Hs = 140 mm, nominal Hs = 150 mm, Fr = 0.142)

Organization (Code)		R_T			z			θ		
		0th Amplitude (N)	1st Amplitude (N)	1st Phase°	0th Amplitude (mm)	1st Amplitude (mm)	1st Phase°	0th Amplitude°	1st Amplitude°	1st Phase°
EFD (NTNU)	*D*	40.347	269.354	-	-6.409	5.549	9.141	-0.123	0.147	106.435
ECN/ CNRS (ISISCFD)	*S*	41.880	252.800	-	-5.910	5.490	-	-0.119	0.155	-
	E%D	-3.800	6.146	-	7.786	1.063	-	3.409	-5.442	-
ECN (ICARE)	*S*	45.000	255.000	22.000	-6.000	5.400	119.000	-0.120	0.160	-139.000
	E%D	-11.53	5.33	-	6.38	2.69	-1201.83	2.60	-8.84	230.60
GL&UDE (Comet)	*S*	-	-	-	-6.294	4.743	117.760	-0.181	0.124	-149.670
	E%D	-	-	-	1.79	14.53	-1188.26	-46.92	15.65	240.62
GL&UDE (OpenFOAM)	*S*	-	-	-	-4.986	4.464	122.010	-0.109	0.099	-158.050
	E%D	-	-	-	22.20	19.55	-1234.76	11.53	32.65	248.49
Kyushu University (RIAM-CMEN)	*S*	50.171	279.172	-18.470	-8.488	4.980	116.320	-0.194	0.208	-153.359
	E%D	-24.35	-3.65	-	-32.44	10.25	-1172.51	-57.47	-41.50	244.09

$E\%D = (D-S)/D \times 100$

Table 1.4b-1-4: harmonic amplitudes and phases of the total resistance (R_T), heave motion (z), pitch angle (θ)
(λ/L_{PP} = 0.9171, measured Hs = 138 mm, nominal Hs = 150 mm, Fr = 0.142)

Organization (Code)		R_T			z			θ		
		0th Amplitude (N)	1st Amplitude (N)	1st Phase°	0th Amplitude (mm)	1st Amplitude (mm)	1st Phase°	0th Amplitude°	1st Amplitude°	1st Phase°
EFD (NTNU)	*D*	59.359	603.078	-	-6.516	12.631	-175.672	-0.137	1.357	-126.001
ECN/ CNRS (ISISCFD)	*S*	63.960	210.000	-	-5.910	13.230	-	-0.138	1.467	-
	E%D	-7.751	65.179	-	9.300	-4.742	-	-0.511	-8.106	-
ECN (ICARE)	*S*	65.500	230.500	17.000	-6.100	14.350	110.000	-0.145	1.504	174.000
	E%D	-10.35	61.78	-	6.38	-13.61	162.62	-5.92	-10.83	238.09
GL&UDE (Comet)	*S*	-	-	-	-6.100	12.482	98.390	-0.191	1.323	160.430
	E%D	-	-	-	6.38	1.18	156.01	-39.52	2.51	227.32
GL&UDE (OpenFOAM)	*S*	-	-	-	-3.427	13.079	105.410	-0.118	1.358	163.690
	E%D	-	-	-	47.41	-3.55	160.00	13.81	-0.07	229.91
Kyushu University (RIAM-CMEN)	*S*	59.694	206.351	1.827	-8.499	9.929	96.390	-0.186	1.324	156.074
	E%D	-0.56	65.78	-	-30.43	21.39	154.87	-35.87	2.43	223.87

$E\%D = (D-S)/D \times 100$

Table 1.4b-1-5: harmonic amplitudes and phases of the total resistance (R_T), heave motion (z), pitch angle (θ)
(λ/L_{PP} = 0.6364, measured Hs = 140 mm, nominal Hs = 150 mm, Fr = 0.182)

Organization (Code)		R_T			z			θ		
		0th Amplitude (N)	1st Amplitude (N)	1st Phase°	0th Amplitude (mm)	1st Amplitude (mm)	1st Phase°	0th Amplitude°	1st Amplitude°	1st Phase°
EFD (NTNU)	*D*	53.764	247.183	-	-11.162	4.571	154.947	-0.216	0.123	-109.503
ECN/CNRS (ISISCFD)	*S*	53.230	258.270	-	-9.830	4.500	-	-0.205	0.120	-
	E%D	0.994	-4.485	-	11.933	1.553	-	5.005	2.123	-
ECN (ICARE)	*S*	65.000	268.000	13.000	-9.850	4.800	122.000	-0.210	0.120	-143.000
	E%D	-20.90	-8.42	-	11.75	-5.01	21.26	2.69	2.12	-30.59
GL&UDE (Comet)	*S*	-	-	-	-10.252	3.995	113.760	-0.269	0.106	-151.620
	E%D	-	-	-	8.15	12.60	26.58	-24.65	13.54	-38.46
GL&UDE (OpenFOAM)	*S*	-	-	-	-10.061	3.704	119.710	-0.196	0.083	-162.670
	E%D	-	-	-	9.86	18.97	22.74	9.18	32.30	-48.55
Kyushu University (RIAM-CMEN)	*S*	80.446	289.287	-25.722	-15.943	3.676	115.482	-0.346	0.123	151.518
	E%D	-49.63	-17.03	-	-42.83	19.58	25.47	-60.33	-0.32	238.37

$E\%D = (D-S)/D \times 100$

Table 1.4b-1-6: Total Resistance (R_T) , sinkage (z) and trim (θ) in calm water, Fr = 0.142

		R_T (N)	z (mm)	θ (°)
EFD (NTNU)	*D*	20.149	-6.419	-0.126

Table 1.4b-1-7: Total Resistance (R_T) , sinkage (z) and trim (θ) in calm water, Fr = 0.182

		R_T (N)	z (mm)	θ (°)
EFD (NTNU)	*D*	33.292	-11.059	-0.223

Test Case 1.4c

Table 1.4c-1-1 Harmonic amplitudes and phases of the X force (F_X), heave motion (z), pitch angle (θ), surge motion (x) (λ/L_{PP} = 0.6, measured Hs = 57.676 mm, nominal Hs = 60 mm, Fr = 0.142)

Table 1.4c-1-2 Harmonic amplitudes and phases of the X force (F_X), heave motion (z), pitch angle (θ), surge motion (x) (λ/L_{PP} = 1.1, measured Hs = 58.484 mm, nominal Hs = 60 mm, Fr = 0.142)

Table 1.4c-1-3 Harmonic amplitudes and phases of the X force (F_X), heave motion (z), pitch angle (θ), surge motion (x) (λ/L_{PP} = 1.6, measured Hs = 57.817 mm, nominal Hs = 60 mm, Fr = 0.142)

Table 1.4c-1-4 Harmonic amplitudes and phases of the X force (F_X), heave motion (z), pitch angle (θ), surge motion (x) (Clam water, measured Hs = 0.011 mm, nominal Hs = 0 mm, Fr = 0.142)

Figure 1.4c-2-C1-1 Time histories of X force (F_X) at λ/L_{PP} = 0.6
Figure 1.4c-2-C1-2 Time histories of surge motion (x) at λ/L_{PP} = 0.6
Figure 1.4c-2-C1-3 Time histories of heave motion (z) at λ/L_{PP} = 0.6
Figure 1.4c-2-C1-4 Time histories of pitch angle (θ) at λ/L_{PP} = 0.6
Figure 1.4c-2-C2-1 Time histories of X force (F_X) at λ/L_{PP} = 1.1
Figure 1.4c-2-C2-2 Time histories of surge motion (x) at λ/L_{PP} = 1.1
Figure 1.4c-2-C2-3 Time histories of heave motion (z) at λ/L_{PP} = 1.1
Figure 1.4c-2-C2-4 Time histories of pitch angle (θ) at λ/L_{PP} = 1.1
Figure 1.4c-2-C3-1 Time histories of X force (F_X) at λ/L_{PP} = 1.6
Figure 1.4c-2-C3-2 Time histories of surge motion (x) at λ/L_{PP} = 1.6
Figure 1.4c-2-C3-3 Time histories of heave motion (z) at λ/L_{PP} = 1.6
Figure 1.4c-2-C3-4 Time histories of pitch angle (θ) at λ/L_{PP} = 1.6
Figure 1.4c-2-C4-1 Time histories of X force (F_X) in clam water
Figure 1.4c-2-C4-2 Time histories of surge motion (x) in clam water
Figure 1.4c-2-C4-3 Time histories of heave motion (z) in clam water
Figure 1.4c-2-C4-4 Time histories of pitch angle (θ) in clam water

Table 1.4c-1-1: harmonic amplitudes and phases of the X force (F_X), heave motion (z), pitch angle (θ), surge motion (x)
(λ/L_{PP} = 0.6, measured Hs = 57.676 mm, nominal Hs = 60 mm, Fr = 0.142)

Organization (Code)		F_X			z			θ			x		
		0th Amplitude (N)	1st Amplitude (N)	1st Phase°	0th Amplitude (cm)	1st Amplitude (cm)	1st Phase°	0th Amplitude°	1st Amplitude°	1st Phase°	0th Amplitude° (cm)	1st Amplitude° (cm)	1st Phase°
EFD (Osaka Univ.)	*D*	6.852	1.089	-155.389	-0.315	0.181	32.501	-0.124	0.099	132.396	2.839	0.167	95.480
GL&UDE (Comet)	*S*	-	-	-	-0.352	0.132	105.490	-0.241	0.085	-165.580	-	-	-
	E%D	-	-	-	-11.73	27.43	-224.57	-94.35	14.06	225.06	-	-	-
UIOWA (CFDSHIP-IOWA)	*S*	6.344	0.498	-133.052	-0.331	0.162	-27.816	-0.115	0.111	64.504	2.842	0.167	37.250
	E%D	7.40	54.29	14.37	-5.28	10.76	185.58	7.18	-12.55	51.28	-0.11	-0.11	60.99

Table 1.4c-1-2: harmonic amplitudes and phases of the X force (F_X), heave motion (z), pitch angle (θ), surge motion (x)
(λ/L_{PP} = 1.1, measured Hs = 58.484 mm, nominal Hs = 60 mm, Fr = 0.142)

Organization (Code)		F_X			z			θ			x		
		0th Amplitude (N)	1st Amplitude (N)	1st Phase°	0th Amplitude (cm)	1st Amplitude (cm)	1st Phase°	0th Amplitude°	1st Amplitude°	1st Phase°	0th Amplitude° (cm)	1st Amplitude° (cm)	1st Phase°
EFD (Osaka Univ.)	*D*	10.390	0.786	60.400	-0.320	1.986	-55.344	-0.134	1.523	10.902	7.078	0.218	-39.774
GL&UDE (Comet)	*S*	-	-	-	-0.330	1.762	152.180	-0.243	1.396	-142.010	-	-	-
	E%D	-	-	-	-3.06	11.30	374.97	-81.34	8.34	1402.59	-	-	-
UIOWA (CFDSHIP-IOWA)	*S*	10.743	0.563	67.026	-0.329	1.952	-60.646	-0.138	1.565	0.757	7.052	0.237	-41.746
	E%D	-3.40	28.33	-10.97	-2.63	1.71	-9.58	-2.92	-2.76	93.06	0.38	-8.77	-4.96

$E\%D = (D\text{-}S)/D \times 100$

Table 1.4c-1-3: harmonic amplitudes and phases of the X force (F_X), heave motion (z), pitch angle (θ), surge motion (x)
(λ/L_{PP} = 1.6, measured Hs = 57.817 mm, nominal Hs = 60 mm, Fr = 0.142)

Organization (Code)		F_X			z			θ			x		
		0th Amplitude (N)	1st Amplitude (N)	1st Phase°	0th Amplitude (cm)	1st Amplitude (cm)	1st Phase°	0th Amplitude°	1st Amplitude°	1st Phase°	0th Amplitude° (cm)	1st Amplitude° (cm)	1st Phase°
EFD (Osaka Univ.)	*D*	5.989	1.828	6.266	-0.351	2.633	0.807	-0.145	1.799	61.903	1.665	0.728	-84.504
GL&UDE (Comet)	*S*	-	-	-	-3.188	2.675	-103.260	-0.243	1.958	-48.490	-	-	-
	E%D	-	-	-	-809.29	-1.60	12901.10	-67.59	-8.85	178.33	-	-	-
UIOWA (CFDSHIP-IOWA)	*S*	8.373	0.737	46.999	-0.302	2.529	-9.311	-0.122	1.986	46.248	1.701	0.724	-104.051
	E%D	-39.80	59.66	-650.07	13.91	3.95	1254.28	15.84	-10.40	25.29	-2.22	0.52	-23.13

Table 1.4c-1-4: harmonic amplitudes and phases of the X force (F_X), heave motion (z), pitch angle (θ), surge motion (x)
(Clam water, measured Hs = 0.011 mm, nominal Hs = 0 mm, Fr = 0.142)

Organization (Code)		F_X	z	θ	x
		0th Amplitude (N)	0th Amplitude (cm)	0th Amplitude°	0th Amplitude° (cm)
EFD (Osaka Univ.)	*D*	4.384	-0.318	-0.129	1.243
GL&UDE (Comet)	*S*	-	-	-	-
	E%D	-	-	-	-
UIOWA (CFDSHIP-IOWA)	*S*	4.727	-0.325	-0.124	1.299
	E%D	-7.81	-2.13	4.04	-4.55

$E\%D = (D\text{-}S)/D \times 100$

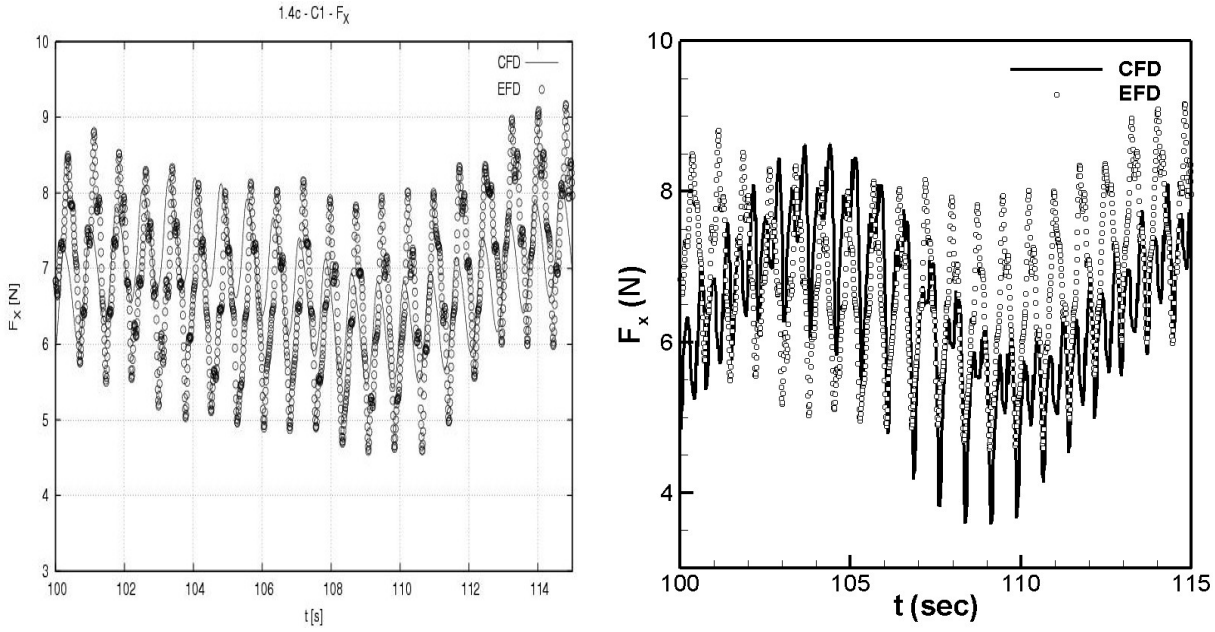

GL&UDE-Comet UIOWA-CFDSHIPIOWA

Fig. 1.4c-2-C1-1 Time histories of X force (F_X) at λ/L_{PP}= 0.6

(CFD: solid line; EFD: open circles)

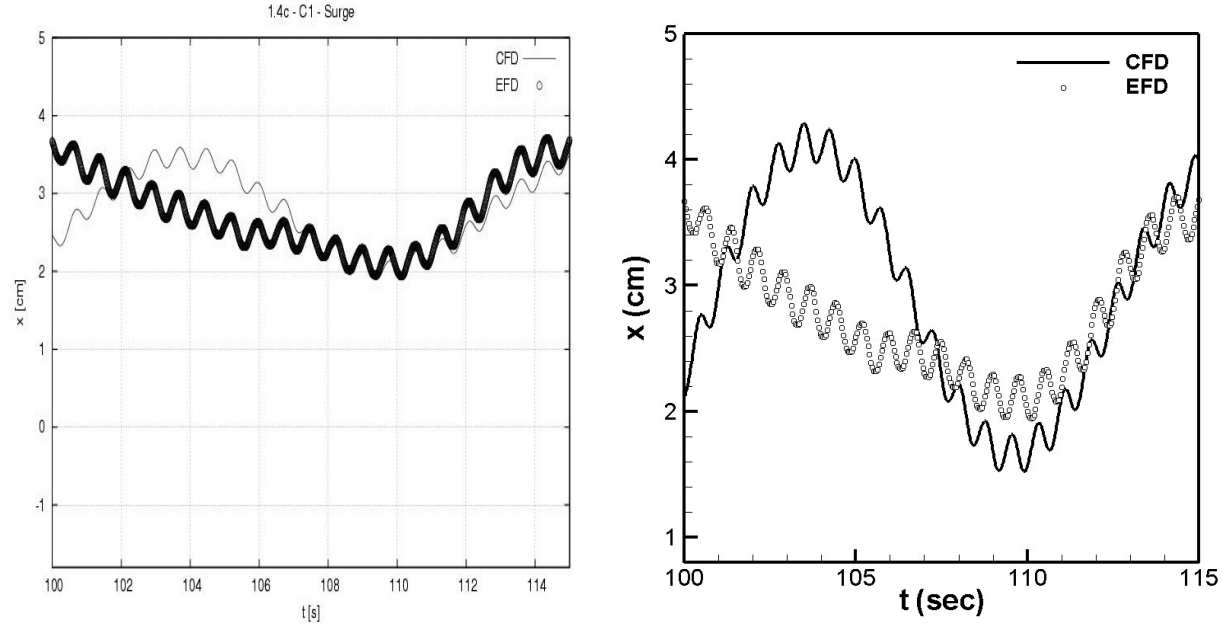

GL&UDE-Comet UIOWA-CFDSHIPIOWA

Fig. 1.4c-2-C1-2 Time histories of surge motion (x) at λ/L_{PP}= 0.6

(CFD: solid line; EFD: open circles)

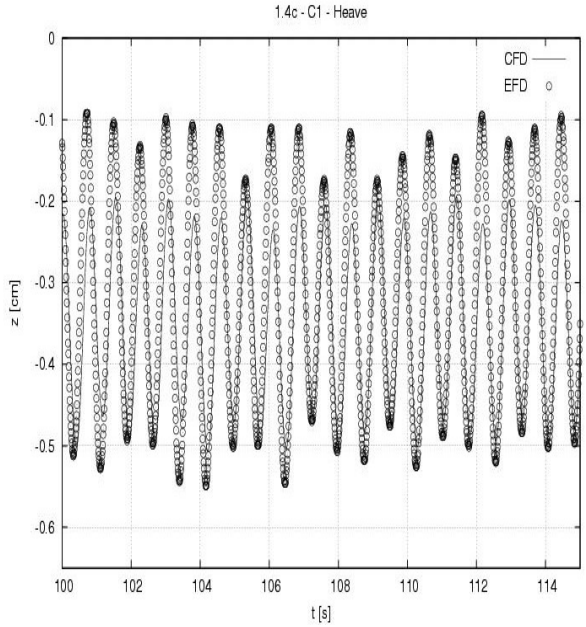

GL&UDE-Comet

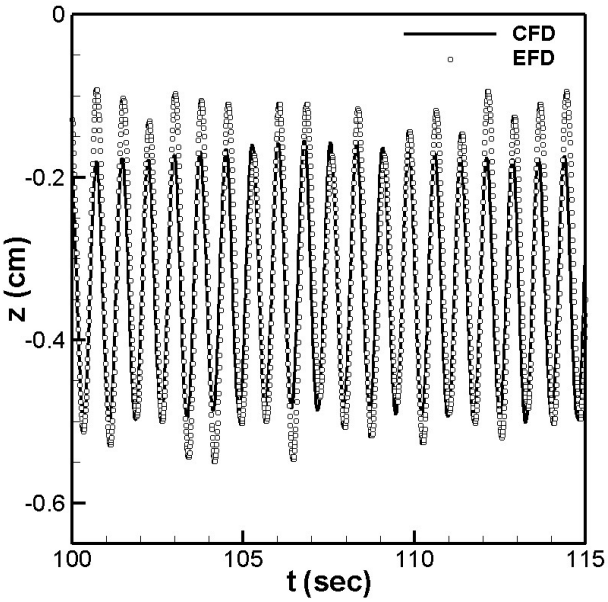

UIOWA-CFDSHIPIOWA

Fig. 1.4c-2-C1-3 Time histories of heave motion (z) at λ/L_{PP} = 0.6

(CFD: solid line; EFD: open circles)

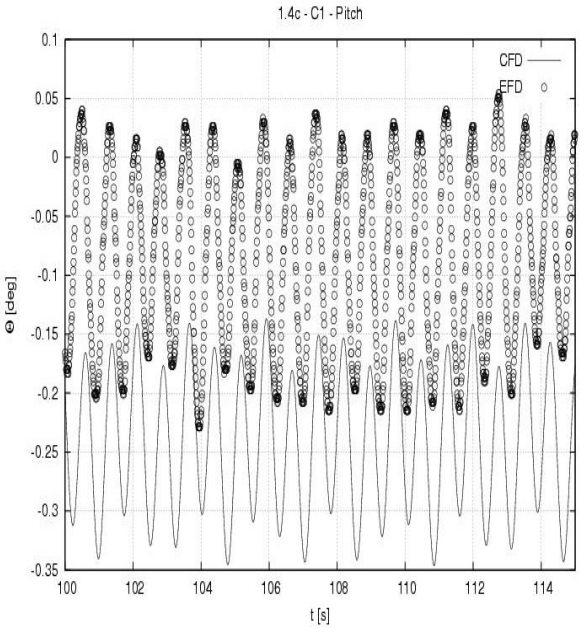

GL&UDE-Comet

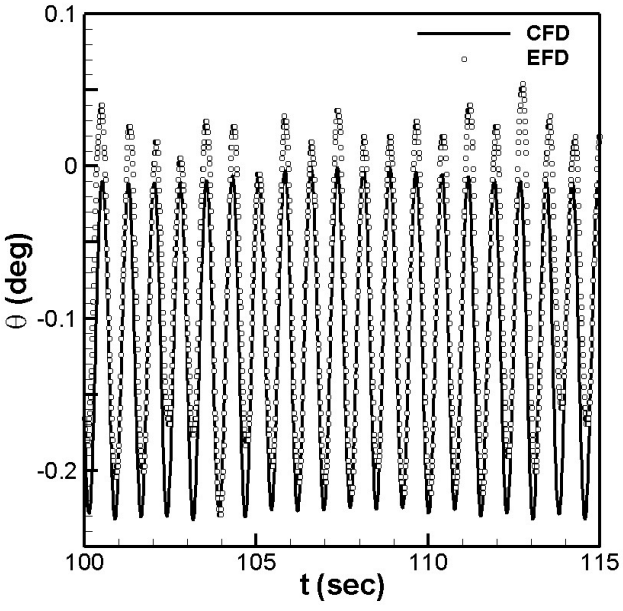

UIOWA-CFDSHIPIOWA

Fig. 1.4c-2-C1-4 Time histories of pitch angle (θ) at λ/L_{PP} = 0.6

(CFD: solid line; EFD: open circles)

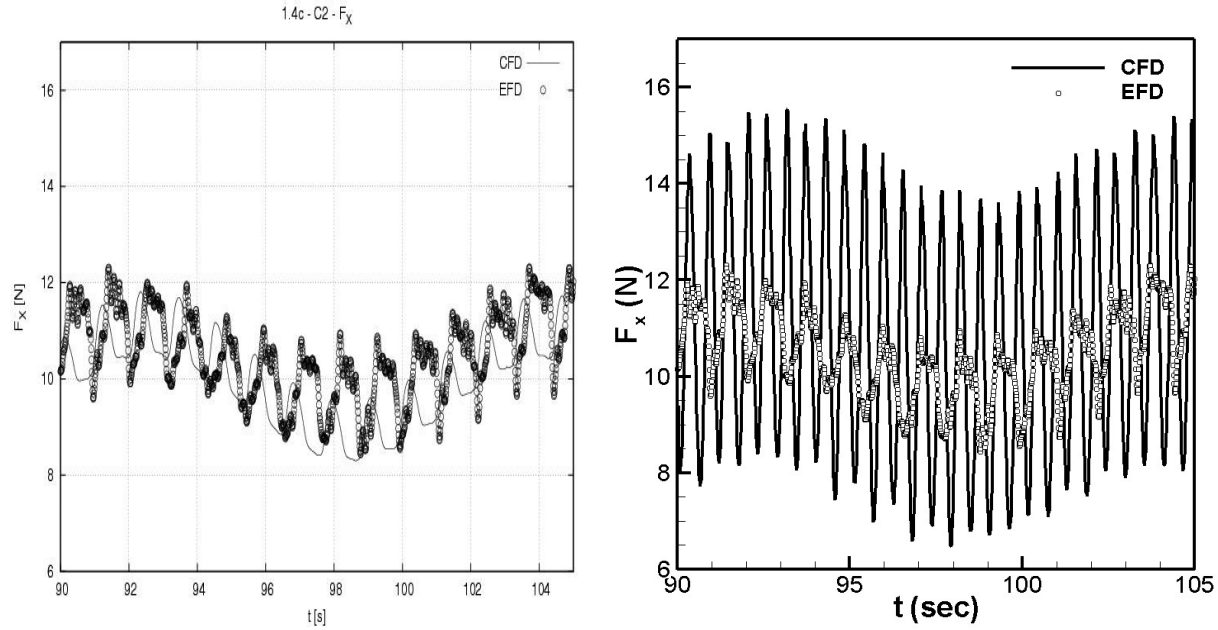

GL&UDE-Comet UIOWA-CFDSHIPIOWA

Fig. 1.4c-2-C2-1 Time histories of X force (F_X) at λ/L_{PP} = 1.1

(CFD: solid line; EFD: open circles)

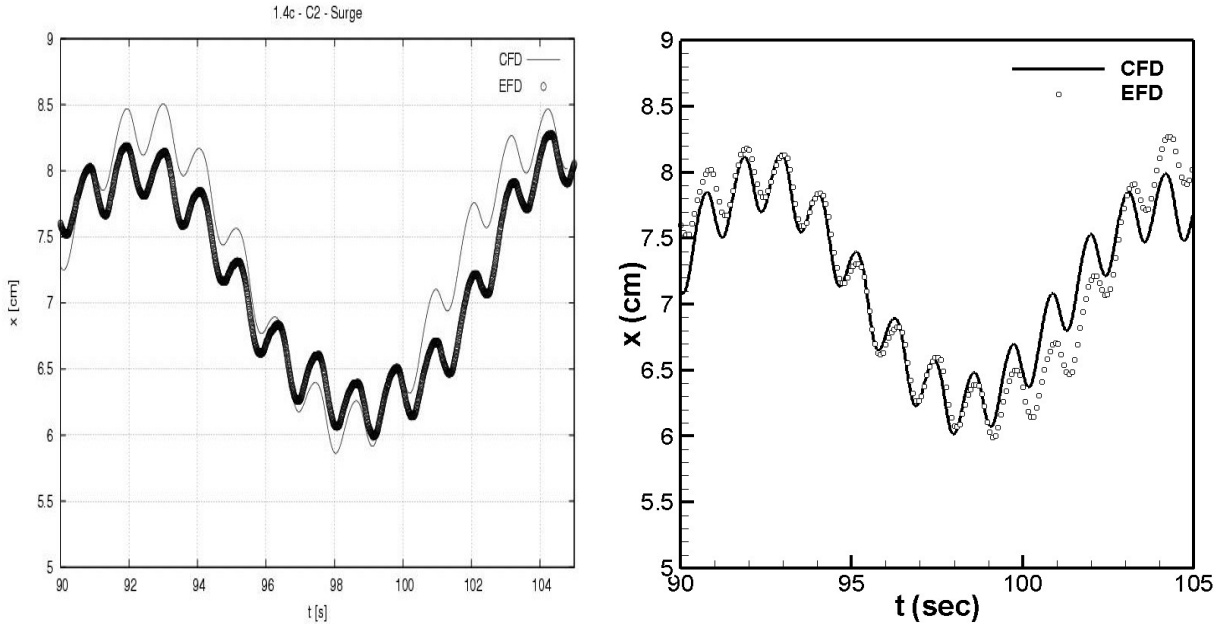

GL&UDE-Comet UIOWA-CFDSHIPIOWA

Fig. 1.4c-2-C2-2 Time histories of surge motion (x) at λ/L_{PP} = 1.1

(CFD: solid line; EFD: open circles)

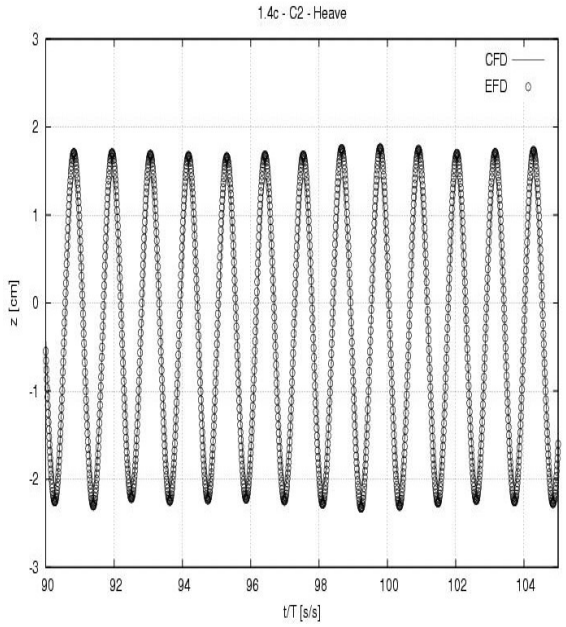

GL&UDE-Comet

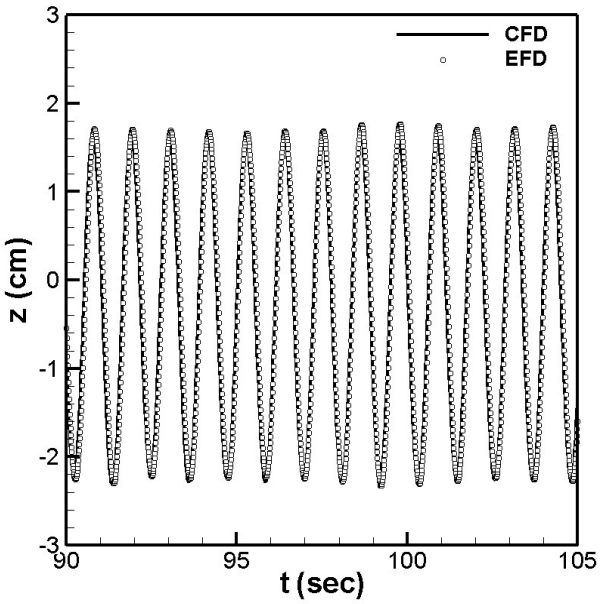

UIOWA-CFDSHIPIOWA

Fig. 1.4c-2-C2-3 Time histories of heave motion (z) at λ/L_{PP} = 1.1

(CFD: solid line; EFD: open circles)

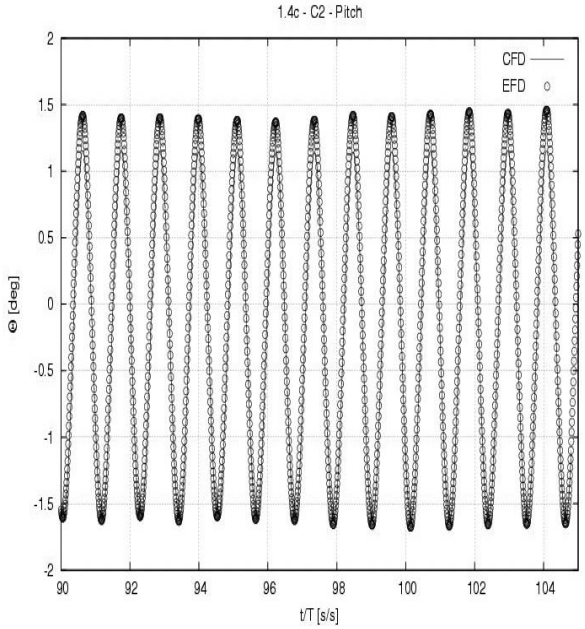

GL&UDE-Comet

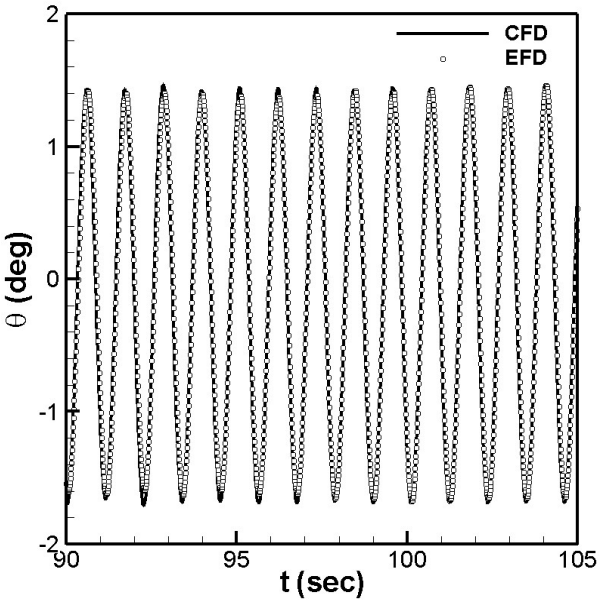

UIOWA-CFDSHIPIOWA

Fig. 1.4c-2-C2-4 Time histories of pitch angle (θ) at λ/L_{PP} = 1.1

(CFD: solid line; EFD: open circles)

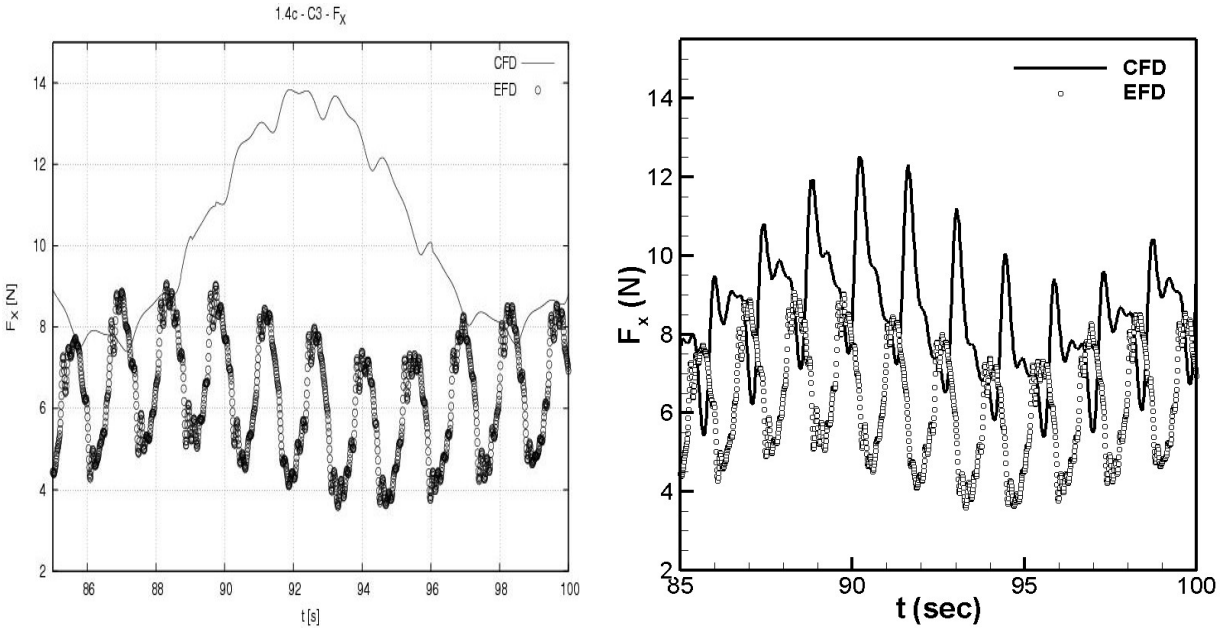

GL&UDE-Comet UIOWA-CFDSHIPIOWA

Fig. 1.4c-2-C3-1 Time histories of X force (F_X) at λ/L_{PP} = 1.6

(CFD: solid line; EFD: open circles)

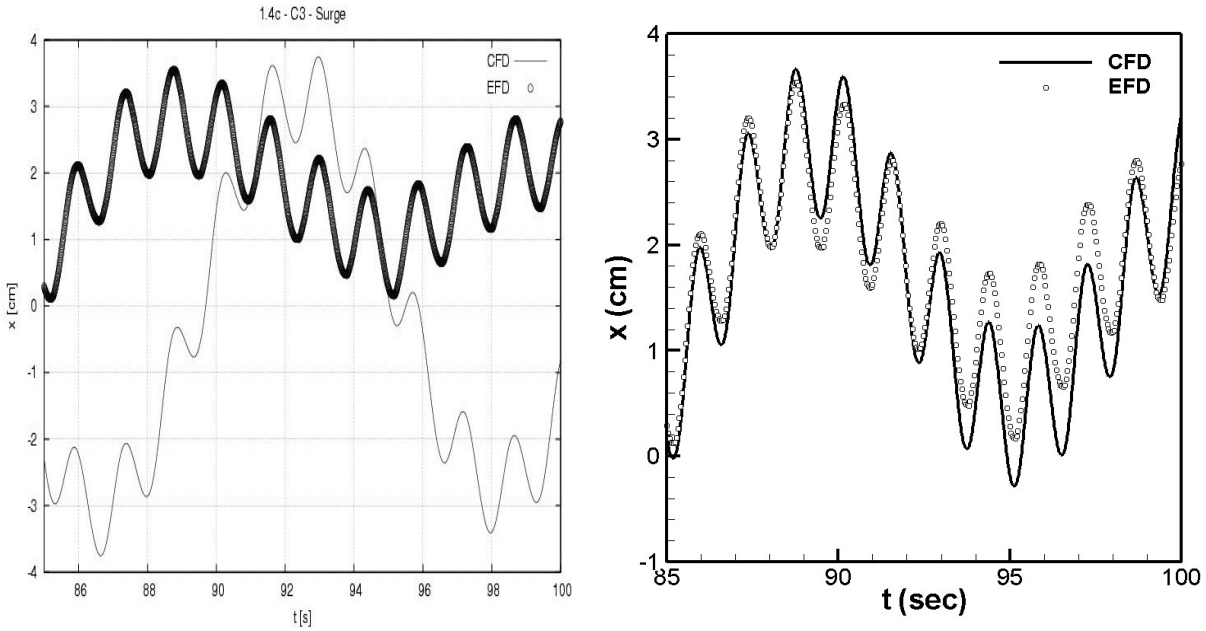

GL&UDE-Comet UIOWA-CFDSHIPIOWA

Fig. 1.4c-2-C3-2 Time histories of surge motion (x) at λ/L_{PP} = 1.6

(CFD: solid line; EFD: open circles)

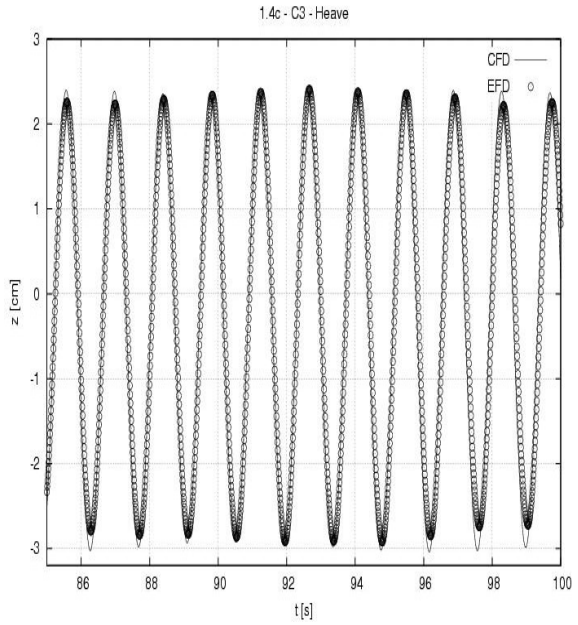

GL&UDE-Comet

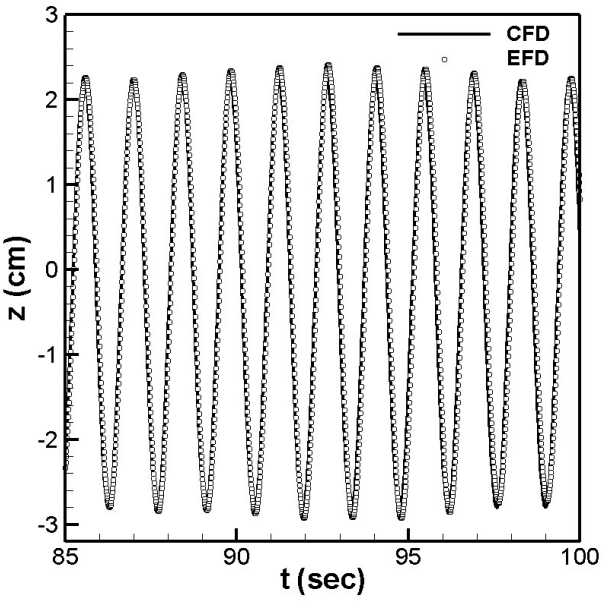

UIOWA-CFDSHIPIOWA

Fig. 1.4c-2-C3-3 Time histories of heave motion (z) at λ/L_{PP} = 1.6

(CFD: solid line; EFD: open circles)

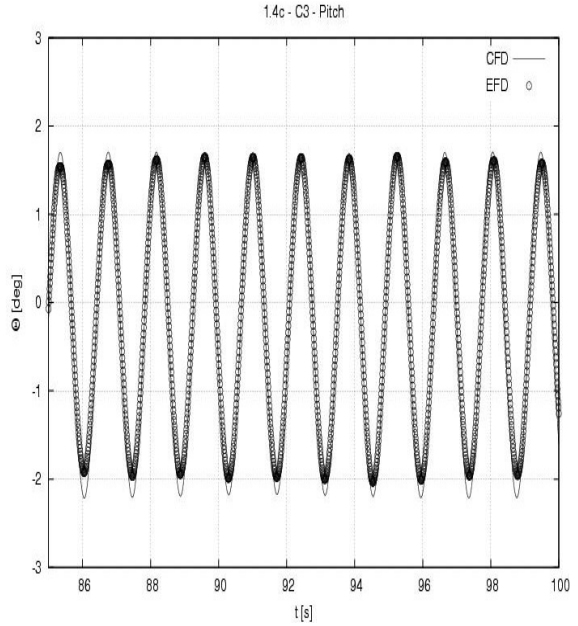

GL&UDE-Comet

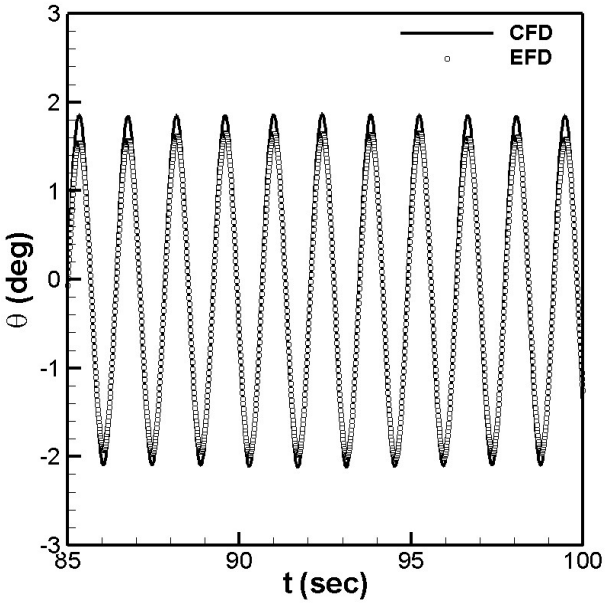

UIOWA-CFDSHIPIOWA

Fig. 1.4c-2-C3-4 Time histories of pitch angle (θ) at λ/L_{PP} = 1.6

(CFD: solid line; EFD: open circles)

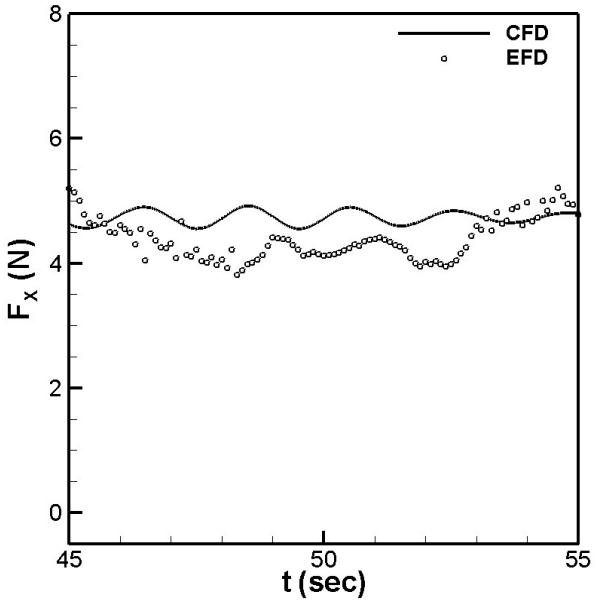

UIOWA-CFDSHIPIOWA

Fig. 1.4c-2-C4-1 Time histories of X force (F_X) in clam water

(CFD: solid line; EFD: open circles)

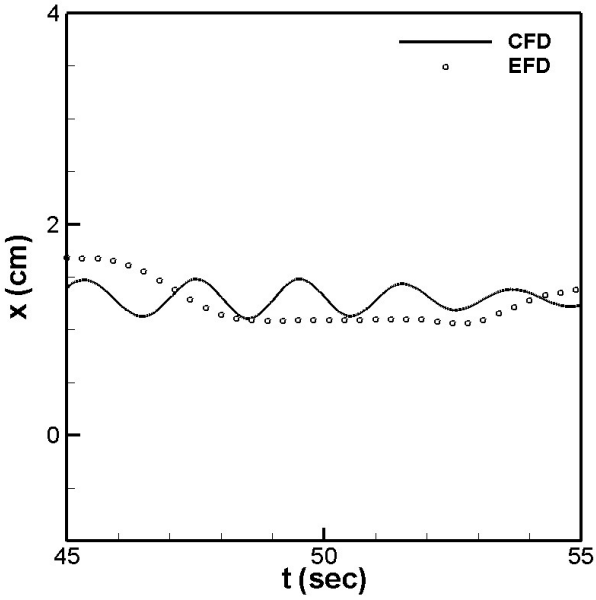

UIOWA-CFDSHIPIOWA

Fig. 1.4c-2-C4-2 Time histories of surge motion (x) in calm water

(CFD: solid line; EFD: open circles)

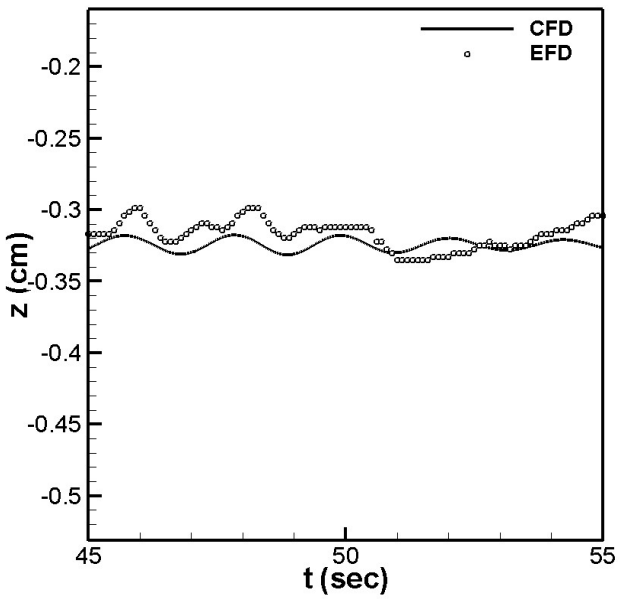

Fig. 1.4c-2-C4-3 Time histories of heave motion (z) in calm water
(CFD: solid line; EFD: open circles)

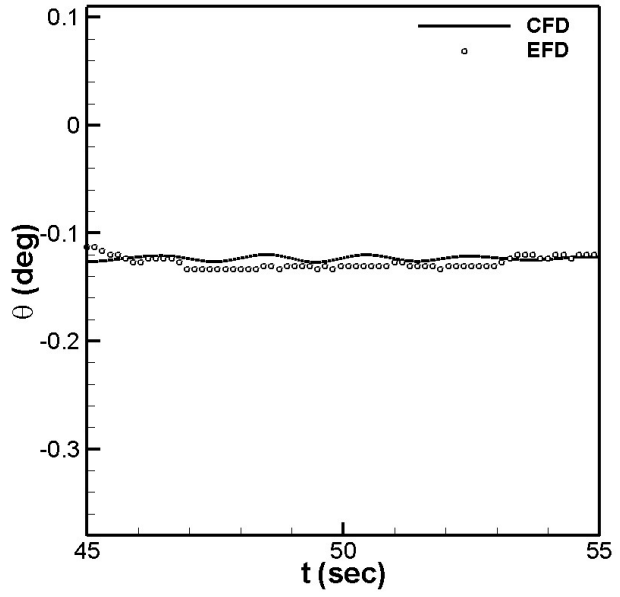

Fig. 1.4c-2-C4-4 Time histories of pitch angle (θ) in calm water
(CFD: solid line; EFD: open circles)

KCS

Test Case 2.1

Figure 2.1-1 Wave elevation contours (global wave field)
Figure 2.1-2 Wave elevation contours (bow wave field)
Figure 2.1-3 Wave elevation contours (stern wave field)
Figure 2.1-4 Wave profile on the hull
Figure 2.1-5 Longitudinal wave cut at y/L_{PP} = -0.0741
Figure 2.1-6 Longitudinal wave cut at y/L_{PP} = -0.1509
Figure 2.1-7 Longitudinal wave cut at y/L_{PP} = -0.4224
Figure 2.1-8 Grid density distribution along the waterline, and in transverse and vertical directions at mid-ship
Figure 2.1-9 Cross flow vectors and streamline, axial velocity contours at propeller plane (x/L_{PP} = 0.9825)
Figure 2.1-10 Velocity on the propeller plane (x/L_{PP} = 0.9825) at z/L_{PP} = -0.0302

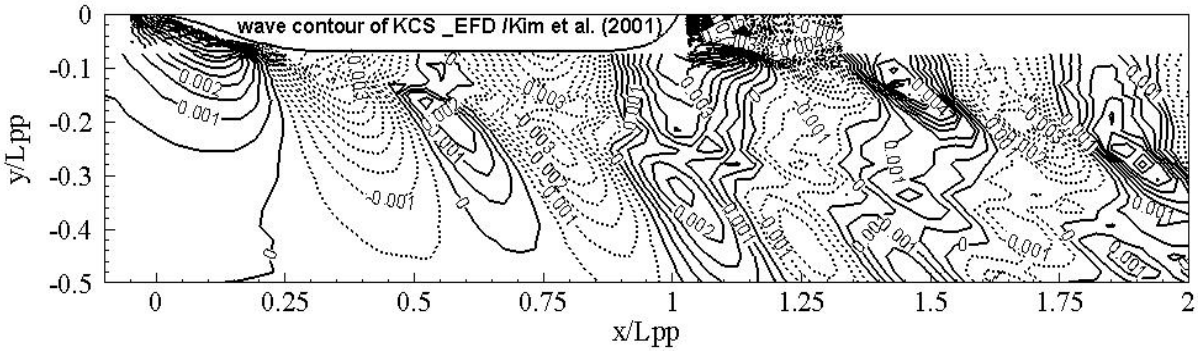

Experiment (MOERI, Kim et al. 2001)

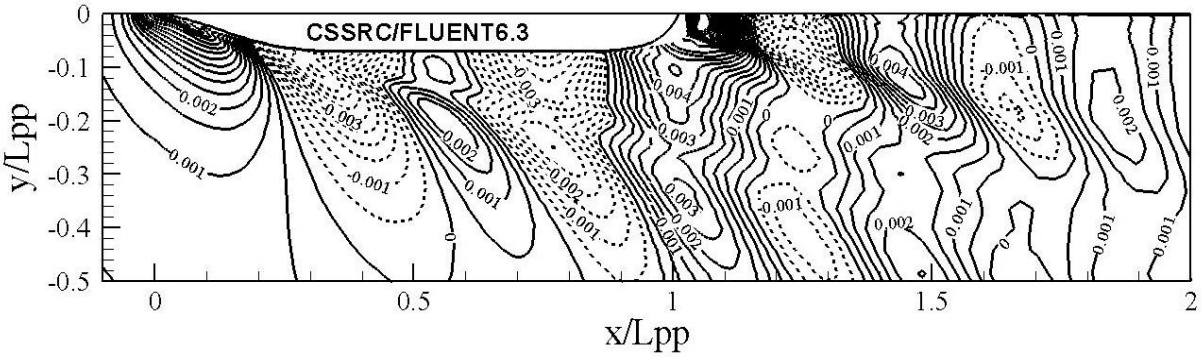

CSSRC-Fluent6.3

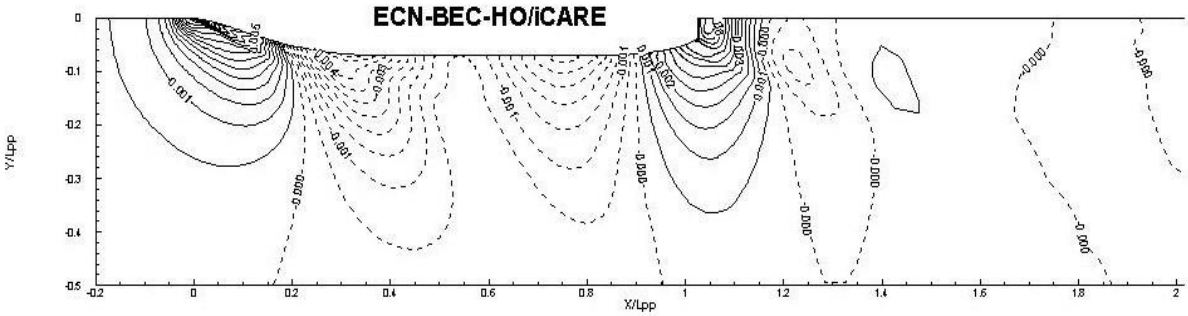

ECN/BEC/HO-Icare

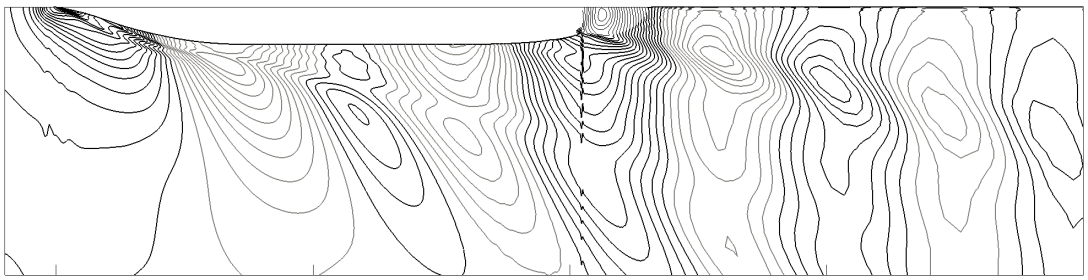

FLOWTECH-SHIPFLOW-VOF-4.3

Fig. 2.1-1 Wave elevation contours (global wave field) [$\Delta z = 0.0005$]
(Solid lines: positive (+) values; Dashed lines: negative (-) values)

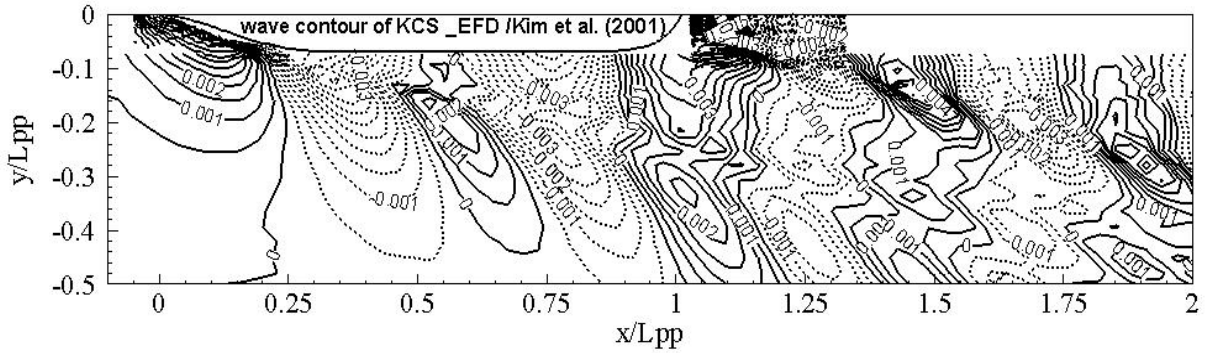

Experiment (MOERI, Kim et al. 2001)

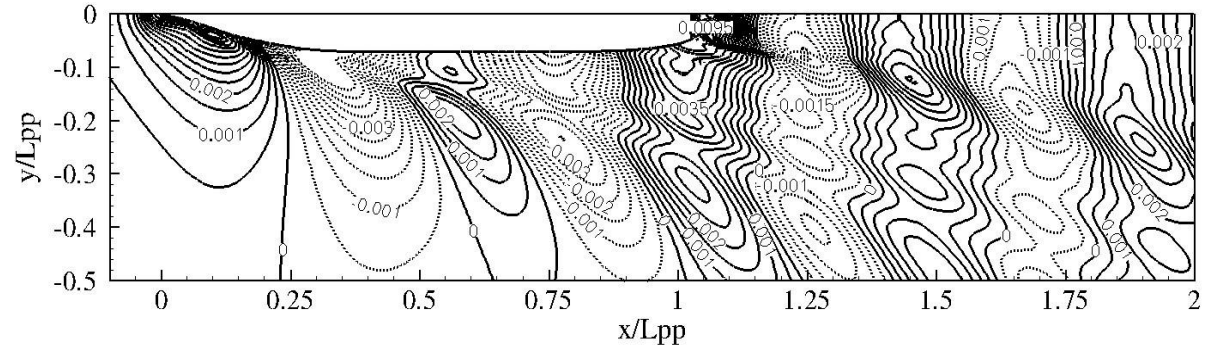

IIHR-CFDShipIowaV4.0 (DES)

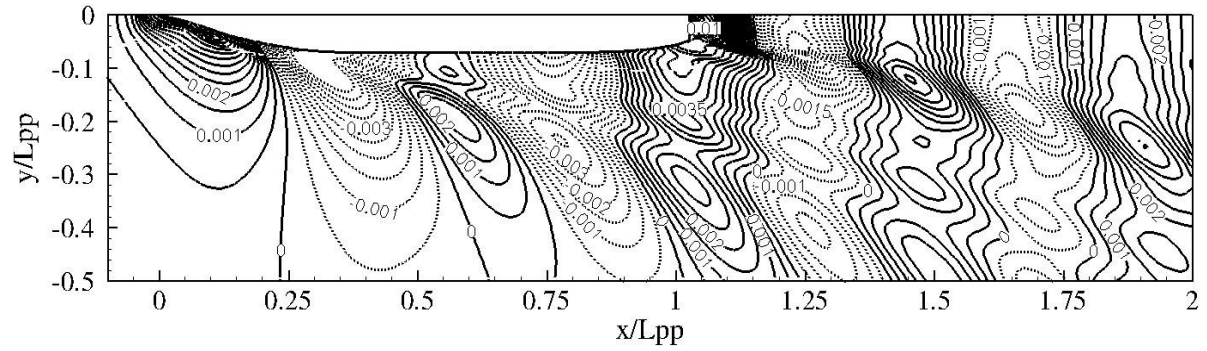

IIHR-CFDShipIowaV4.0 (RANS)

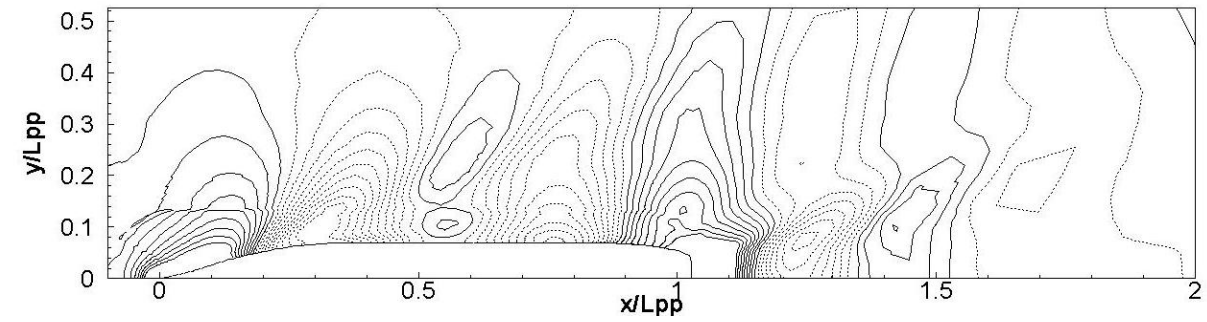

IIHR/SJTU-FLUENT12.0.16

Fig. 2.1-1 Wave elevation contours (global wave field) [$\Delta z = 0.0005$]
(Solid lines: positive (+) values; Dashed lines: negative (-) values)

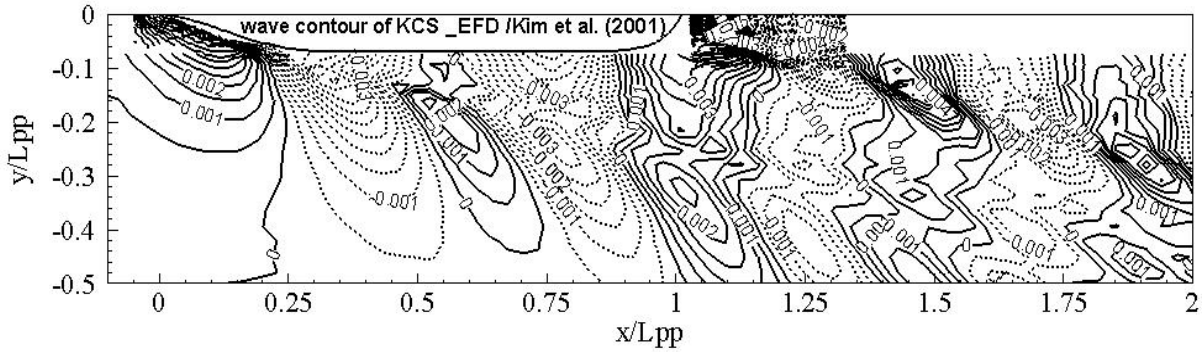

Experiment (MOERI, Kim et al. 2001)

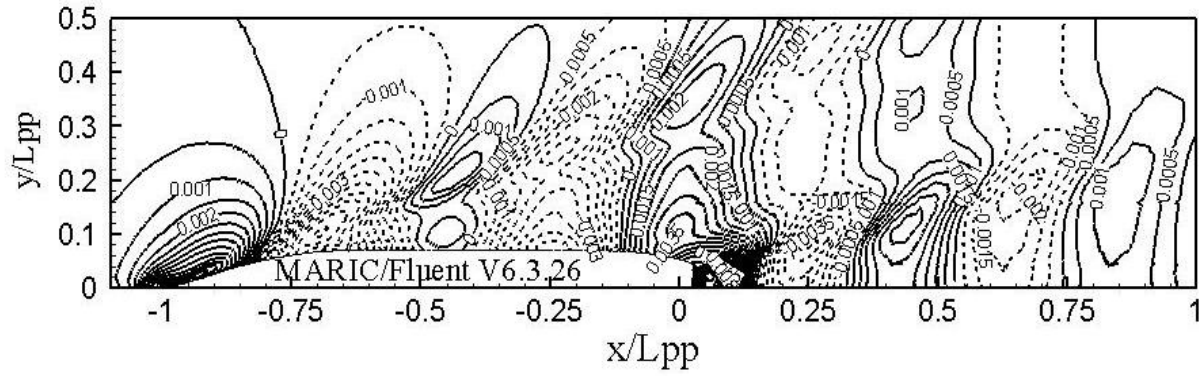

MARIC-FLUENT6.3

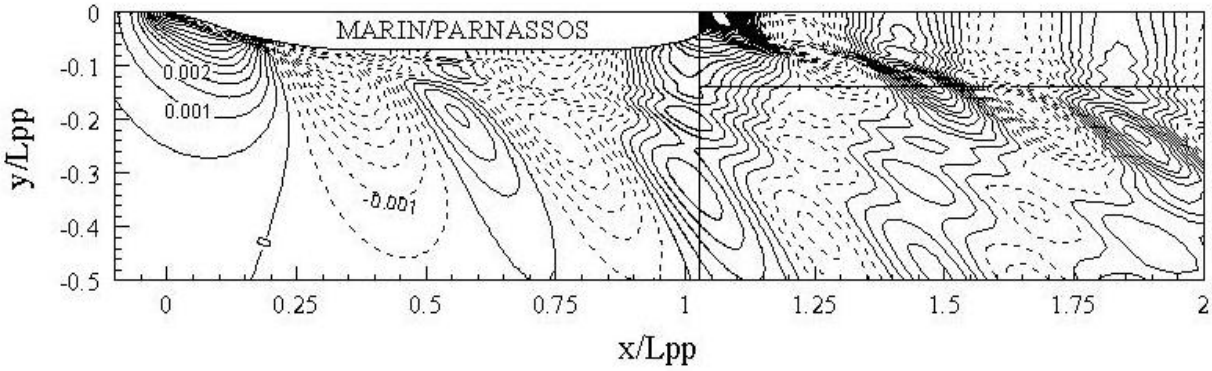

MARIN-PARNASSOS

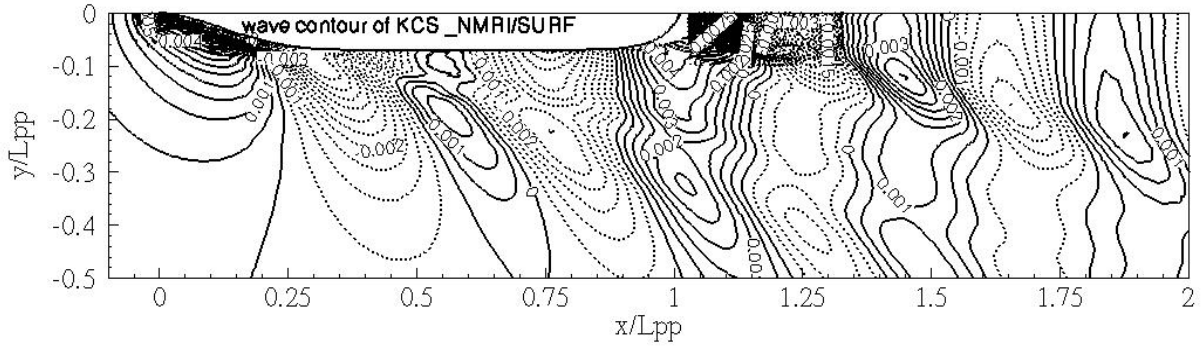

NMRI-SURF

Fig. 2.1-1 Wave elevation contours (global wave field) [$\Delta z = 0.0005$]
(Solid lines: positive (+) values; Dashed lines: negative (-) values)

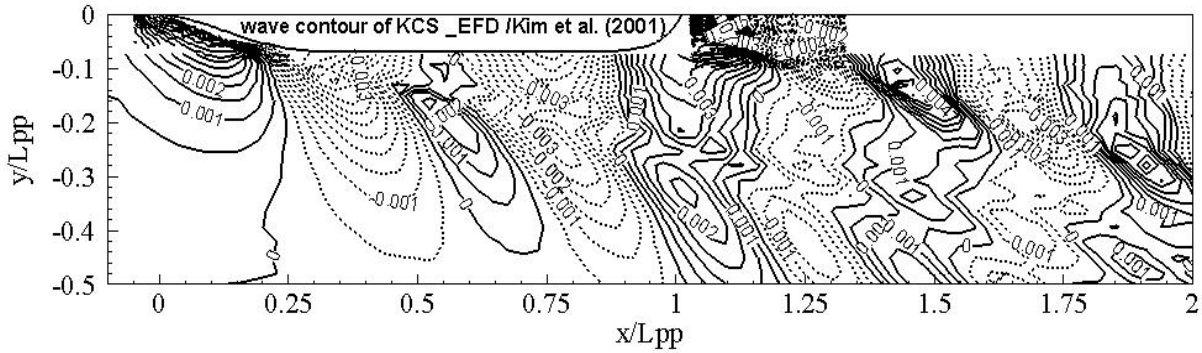

Experiment (MOERI, Kim et al. 2001)

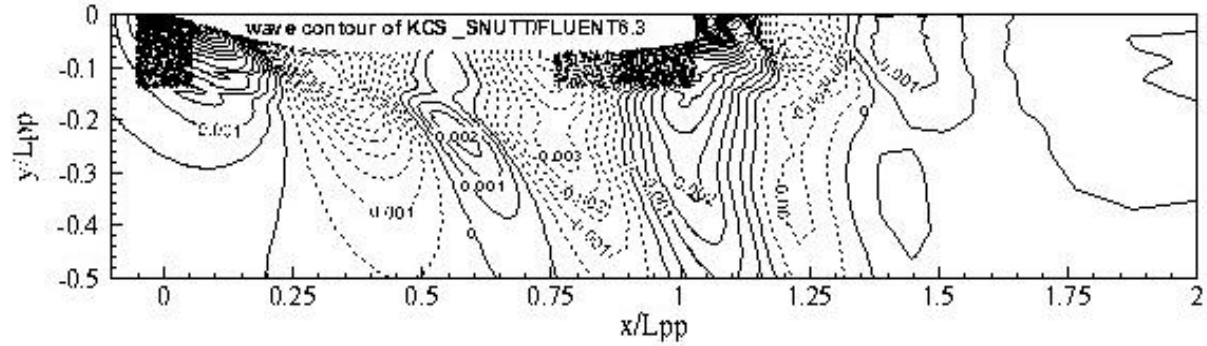

SNUTT-FLUENT6.3

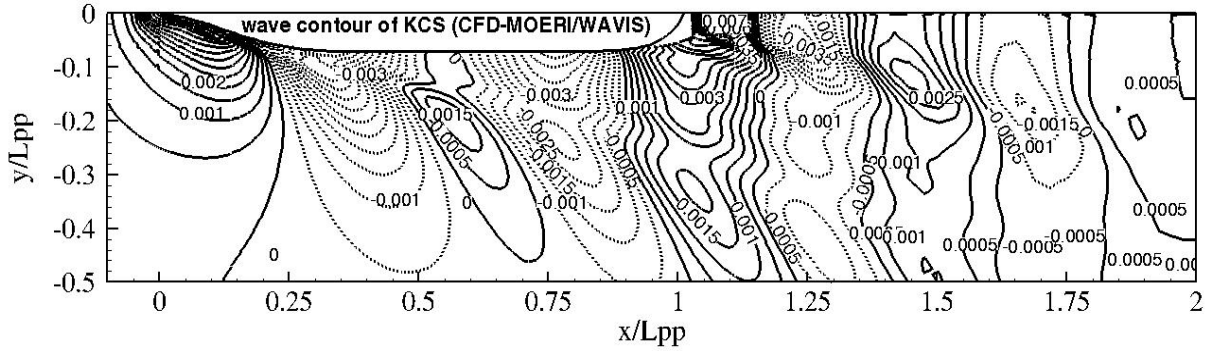

MOERI-WAVIS

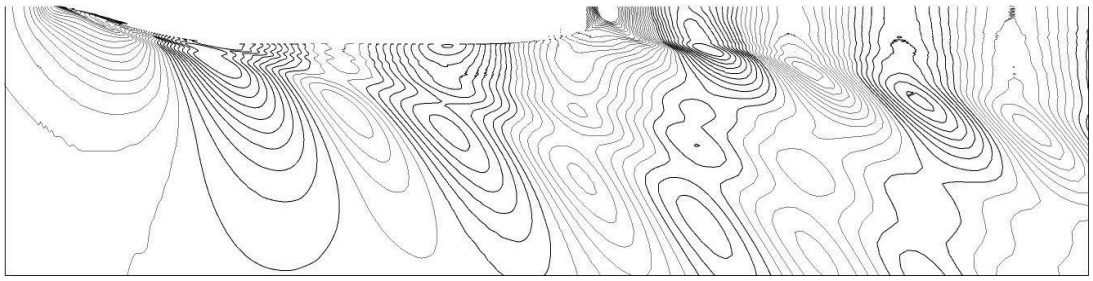

Southampton-CFX (BSL)

Fig. 2.1-1 Wave elevation contours (global wave field) [$\Delta z = 0.0005$]
(Solid lines: positive (+) values; Dashed lines: negative (-) values)

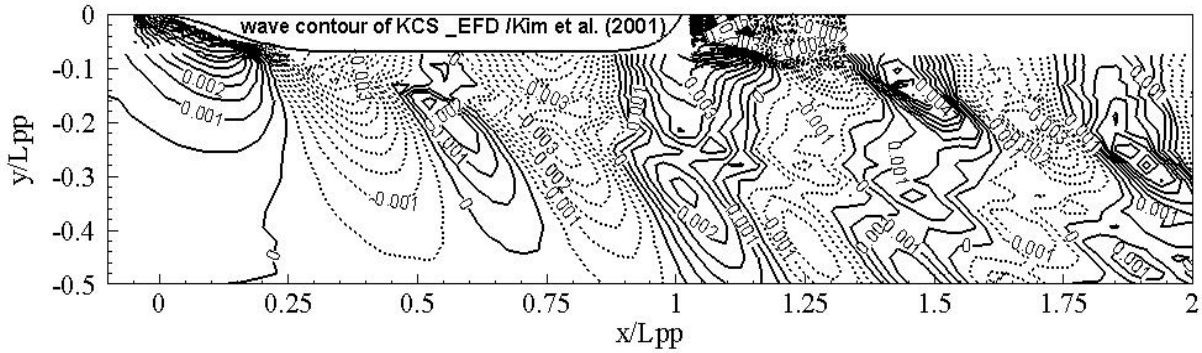

Experiment (MOERI, Kim et al. 2001)

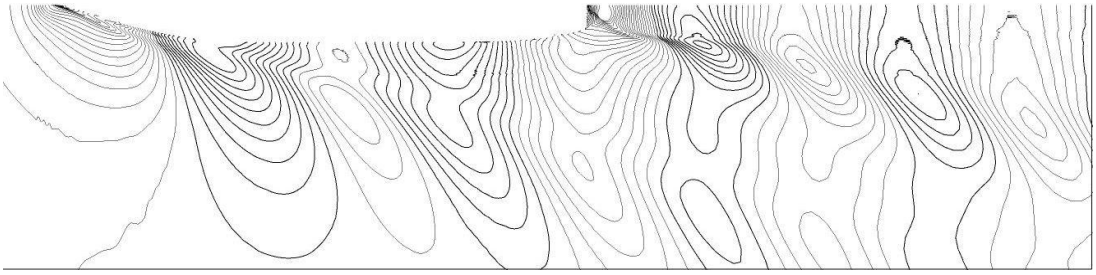

Southampton-CFX (SST)

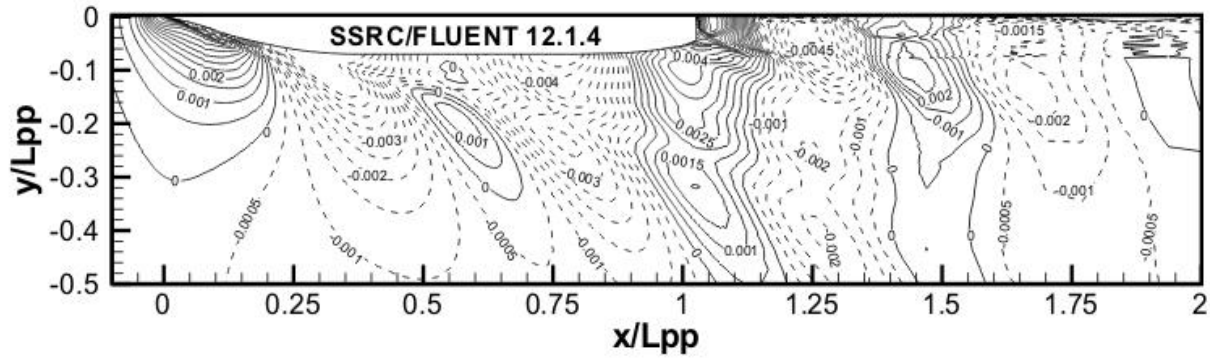

SSRC-FLUENT12.1

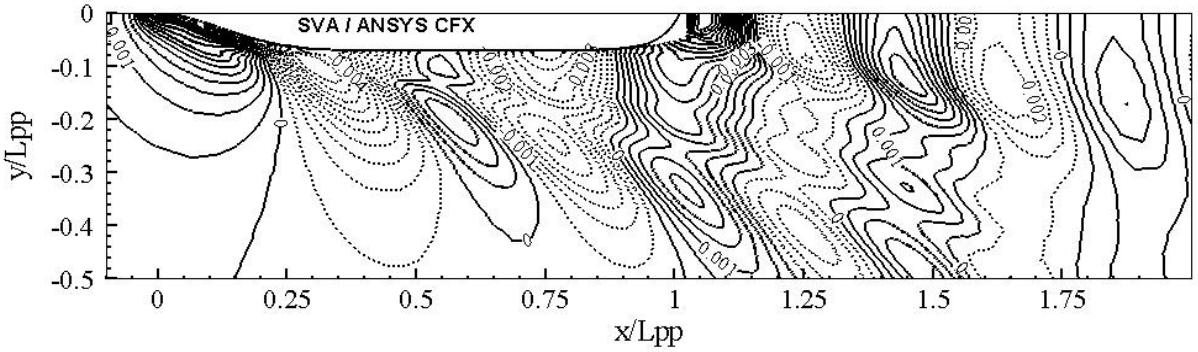

SVA-CFX12

Fig. 2.1-1 Wave elevation contours (global wave field) [$\Delta z = 0.0005$]
(Solid lines: positive (+) values; Dashed lines: negative (-) values)

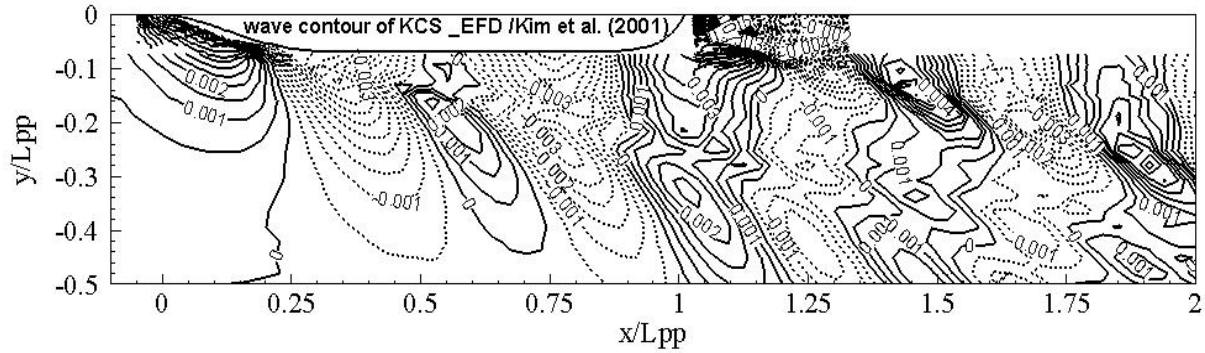

Experiment (MOERI, Kim et al. 2001)

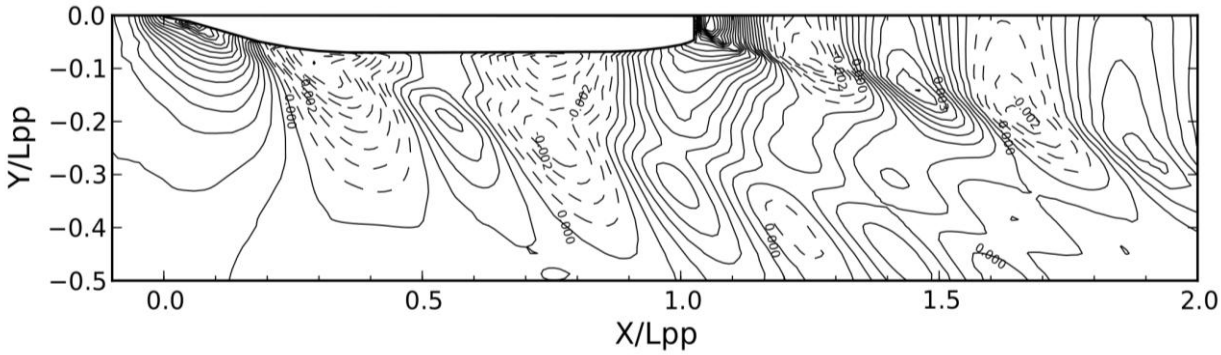

TUHH&ANSYS-CFX12.1

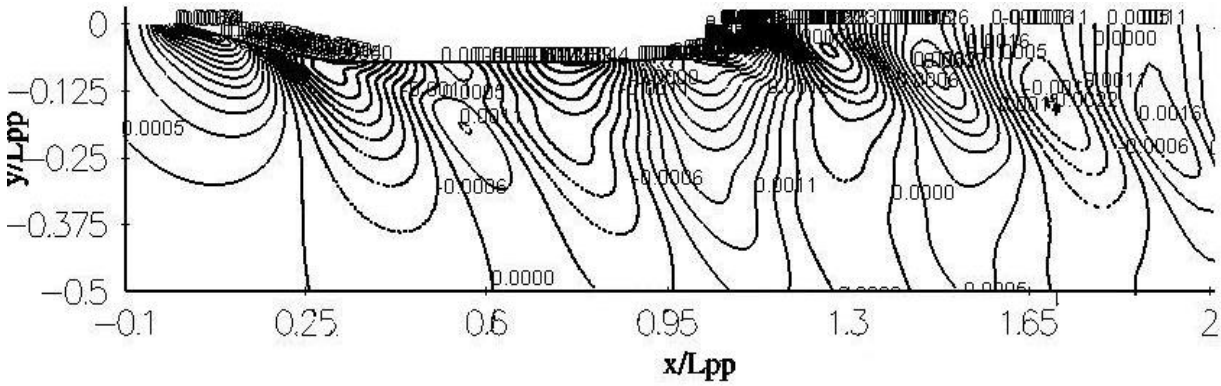

VTT-FINFLO

Fig. 2.1-1 Wave elevation contours (global wave field) [Δz = 0.0005]
(Solid lines: positive (+) values; Dashed lines: negative (-) values)

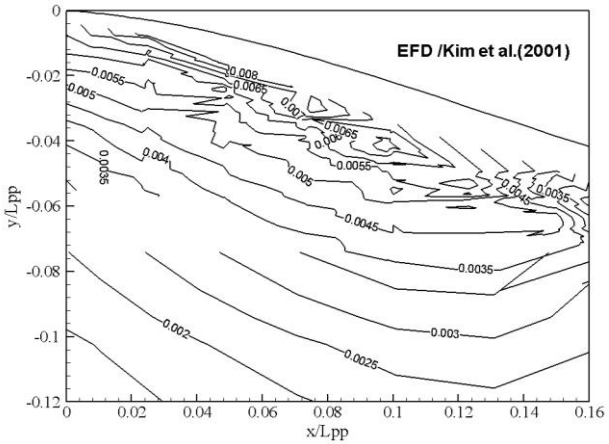

Experiment (MOERI, Kim et al. 2001)

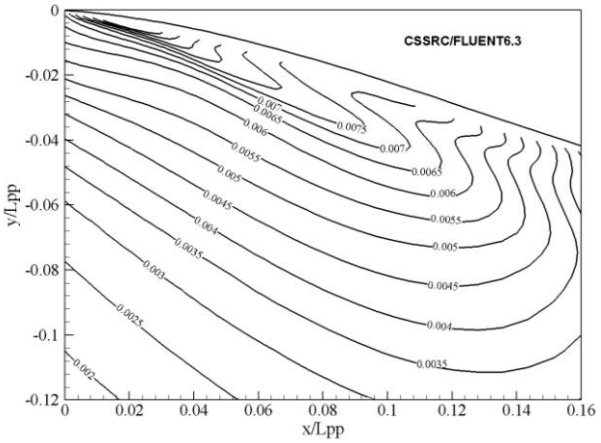

CSSRC-Fluent6.3

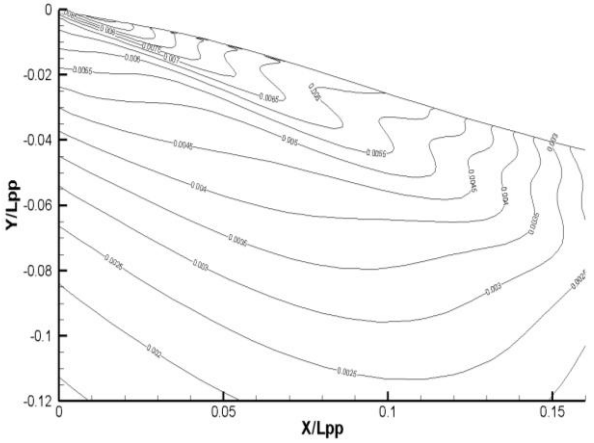

ECN/BEC/HO-Icare

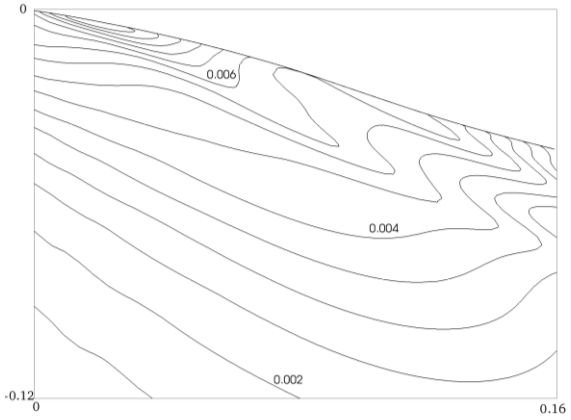

FLOWTECH-SHIPFLOW-VOF-4.3

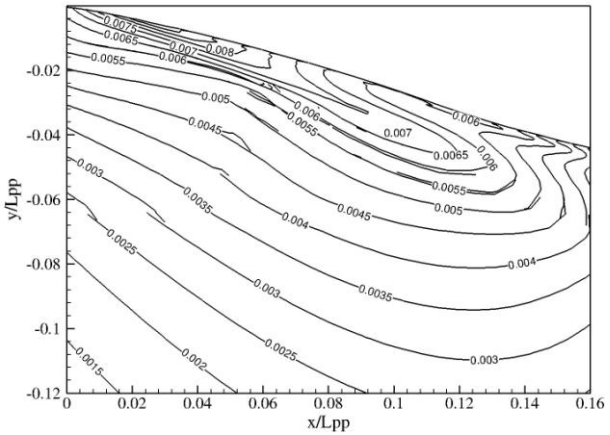

IIHR-CFDShipIowaV4.0 (DES)

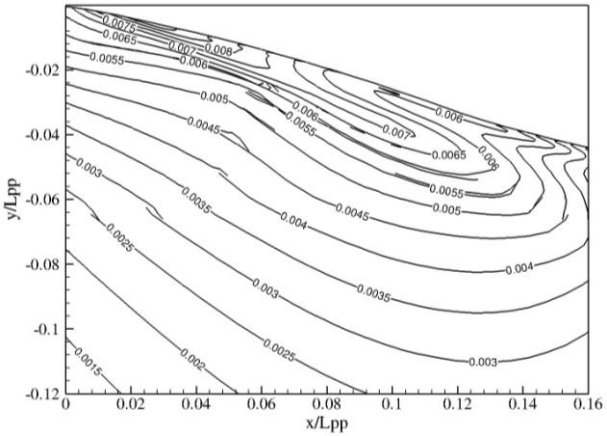

IIHR-CFDShipIowaV4.0 (RANS)

Fig. 2.1-2 Wave elevation contours (bow wave field) [$\Delta z = 0.0005$]
(Solid lines: positive (+) values; Dashed lines: negative (-) values)

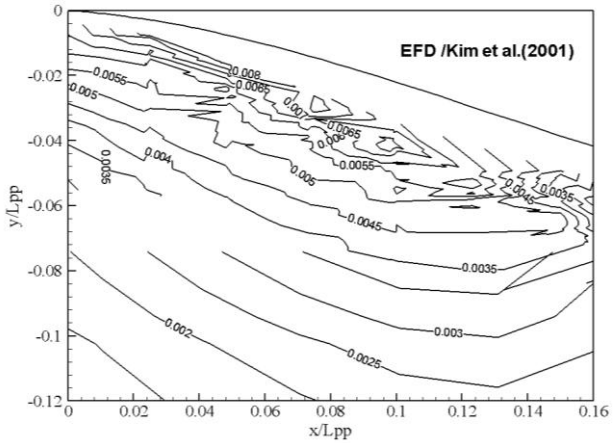

Experiment (MOERI, Kim et al. 2001)

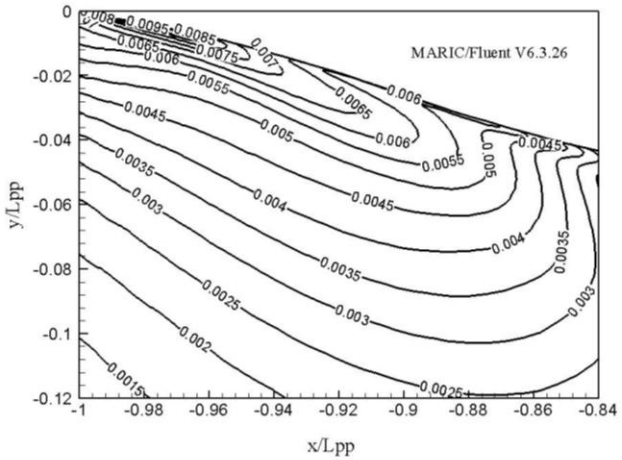

MARIC-FLUENT6.3

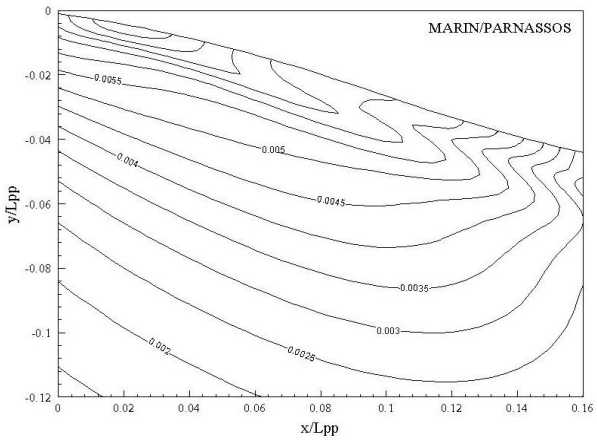

MARIN-PARNASSOS

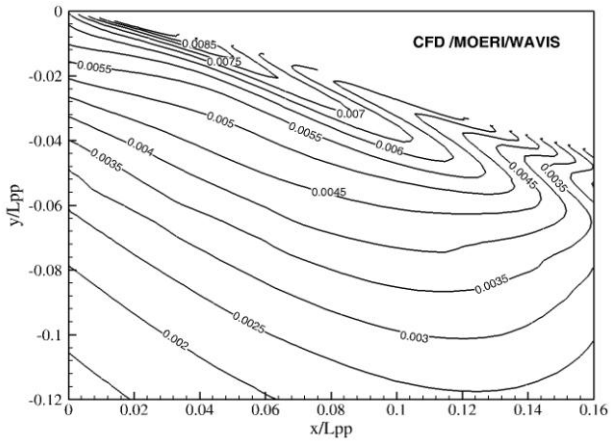

MOERI-WAVIS

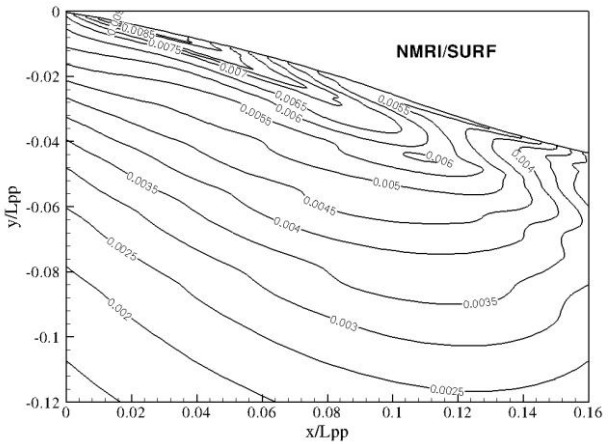

NMRI-SURF

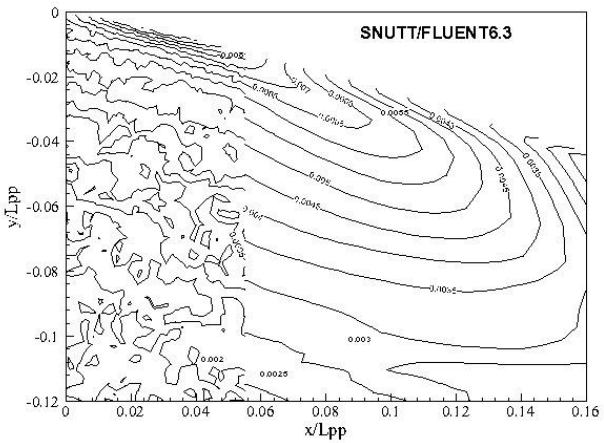

SNUTT-FLUENT6.3

Fig. 2.1-2 Wave elevation contours (bow wave field) [$\Delta z = 0.0005$]
(Solid lines: positive (+) values; Dashed lines: negative (-) values)

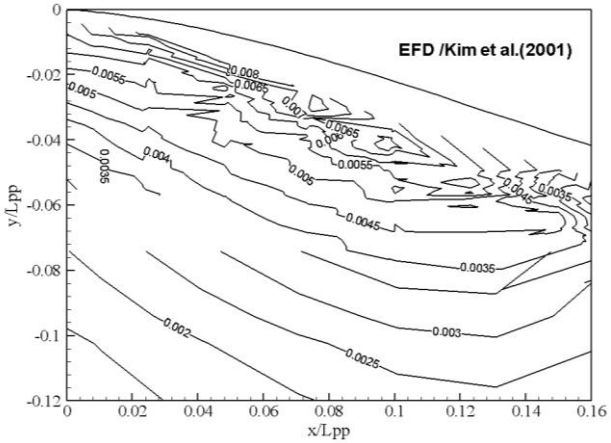

Experiment (MOERI, Kim et al. 2001)

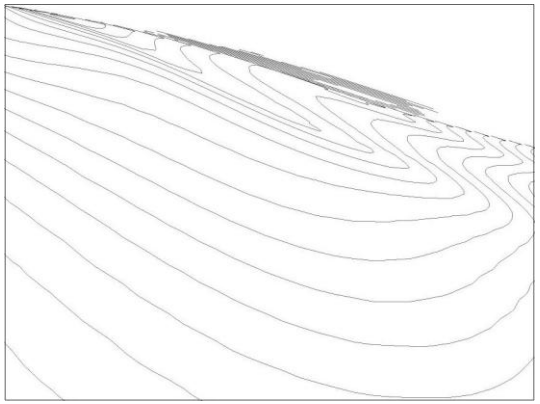

Southampton-CFX (BSL)

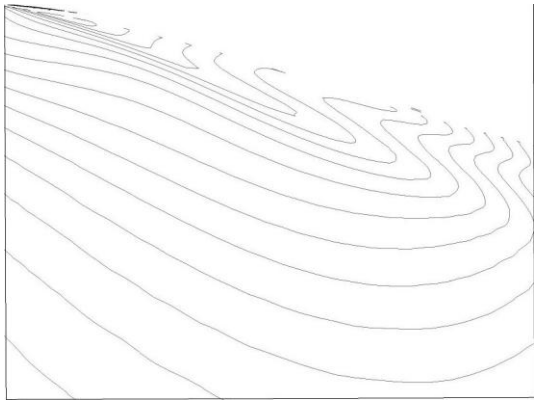

Southampton-CFX (SST)

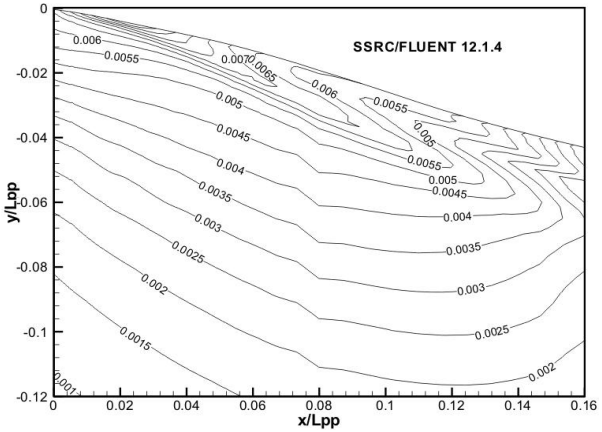

SSRC-FLUENT12.1

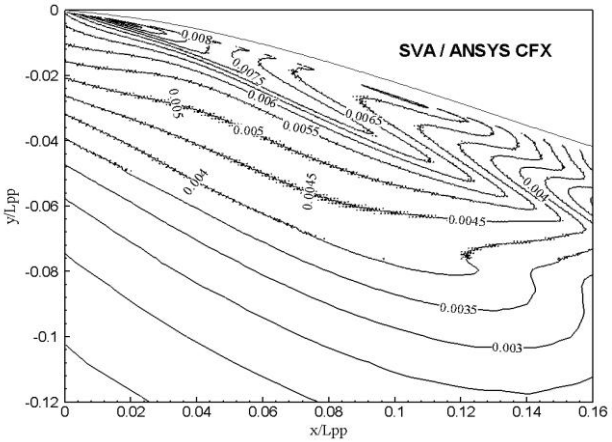

SVA-CFX12

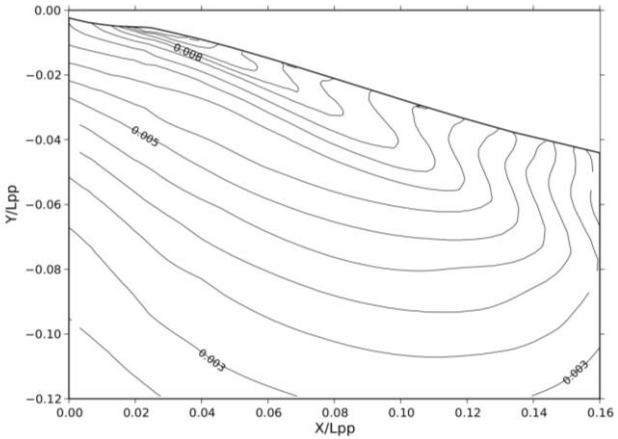

TUHH&ANSYS-CFX12.1

Fig. 2.1-2 Wave elevation contours (bow wave field) [$\Delta z = 0.0005$]
(Solid lines: positive (+) values; Dashed lines: negative (-) values)

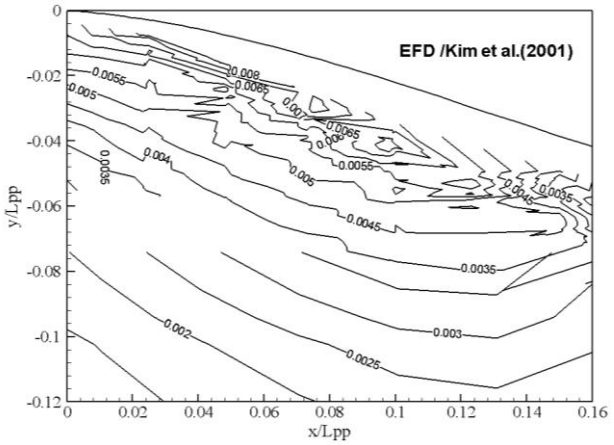

Experiment (MOERI, Kim et al. 2001)

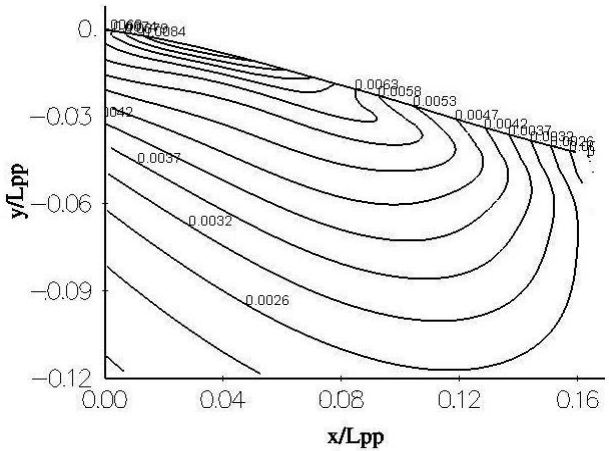

VTT-FINFLO

Fig. 2.1-2 Wave elevation contours (bow wave field) [$\Delta z = 0.0005$]
(Solid lines: positive (+) values; Dashed lines: negative (-) values)

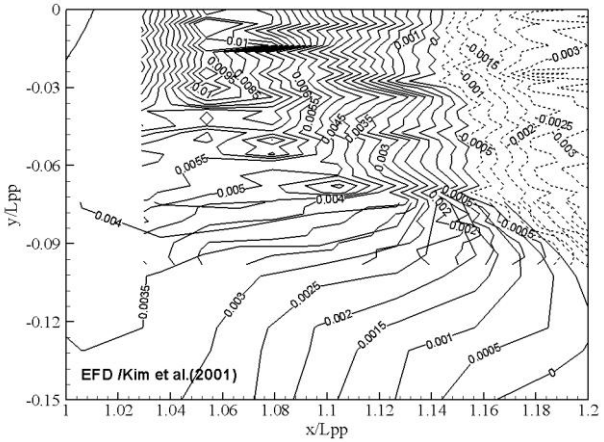

Experiment (MOERI, Kim et al. 2001)

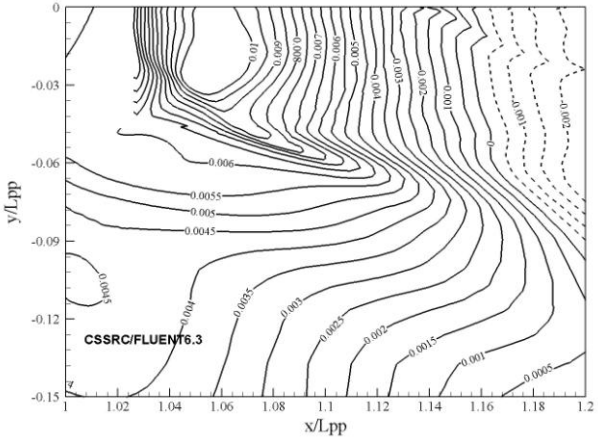

CSSRC-Fluent6.3

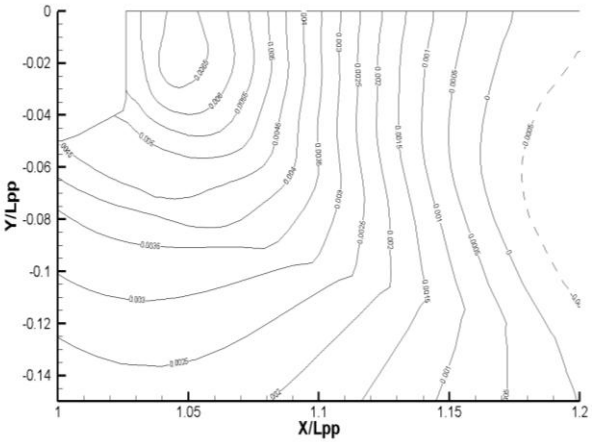

ECN/BEC/HO-Icare

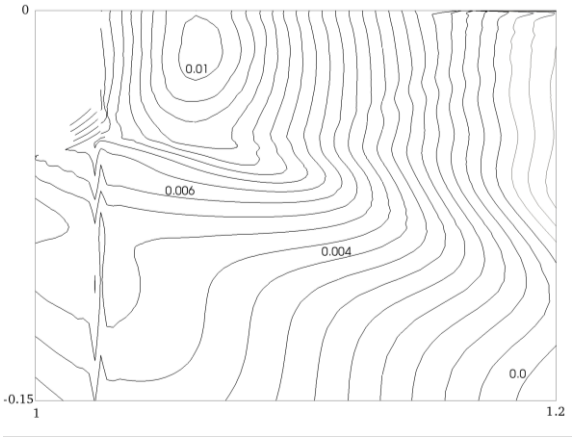

FLOWTECH-SHIPFLOW-VOF-4.3

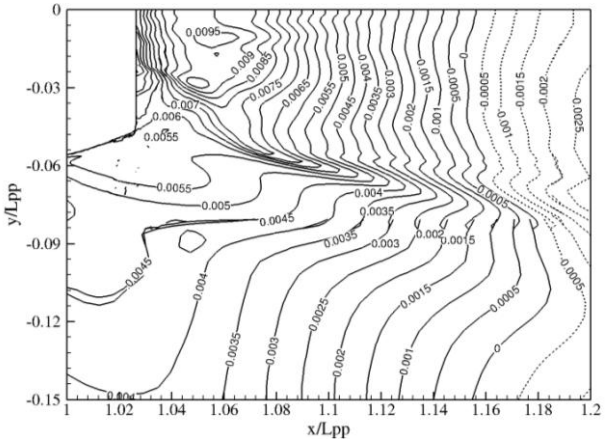

IIHR-CFDShipIowaV4.0 (DES)

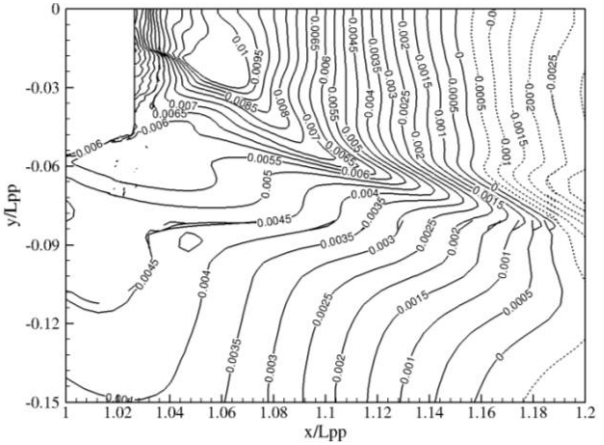

IIHR-CFDShipIowaV4.0 (RANS)

Fig. 2.1-3 Wave elevation contours (stern wave field) [$\Delta z = 0.0005$]
(Solid lines: positive (+) values; Dashed lines: negative (-) values)

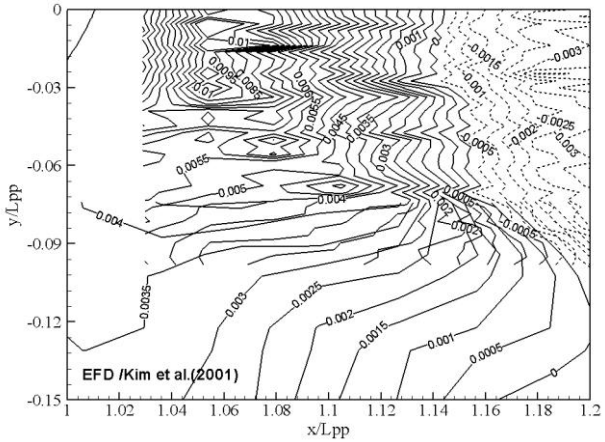

Experiment (MOERI, Kim et al. 2001)

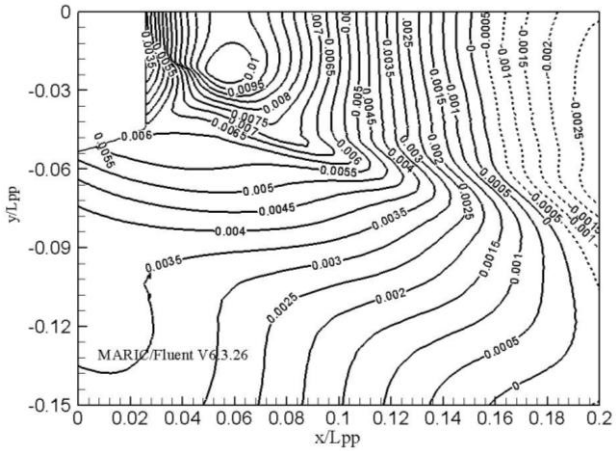

MARIC-FLUENT6.3

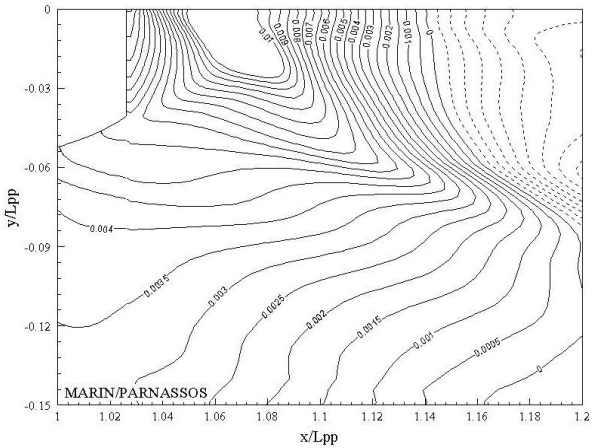

MARIN-PARNASSOS

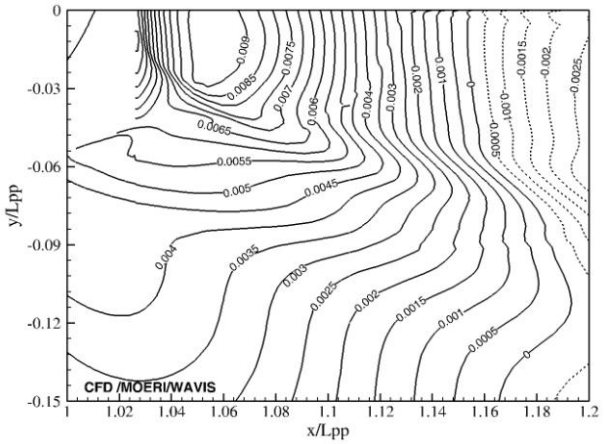

MOERI-WAVIS

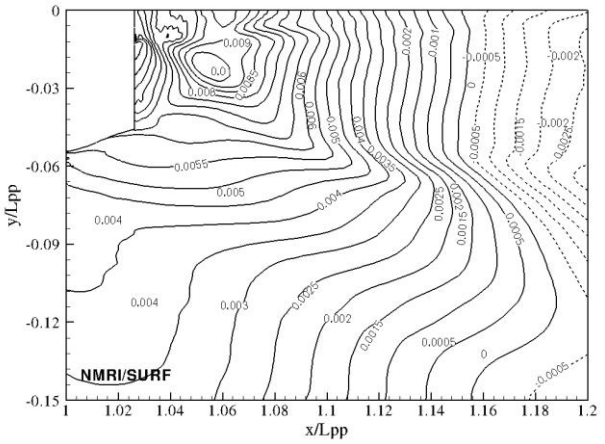

NMRI-SURF

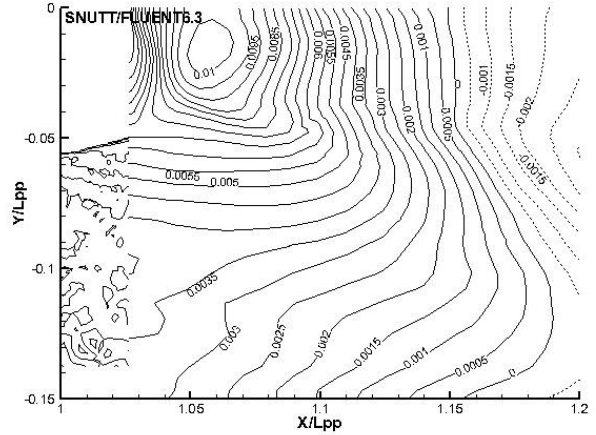

SNUTT-FLUENT6.3

Fig. 2.1-3 Wave elevation contours (stern wave field) [$\Delta z = 0.0005$]
(Solid lines: positive (+) values; Dashed lines: negative (-) values)

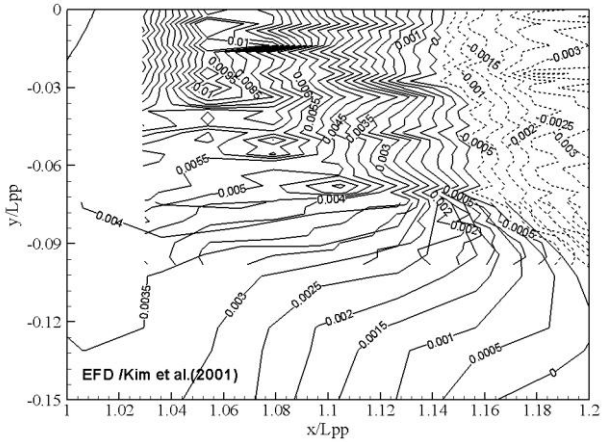

Experiment (MOERI, Kim et al. 2001)

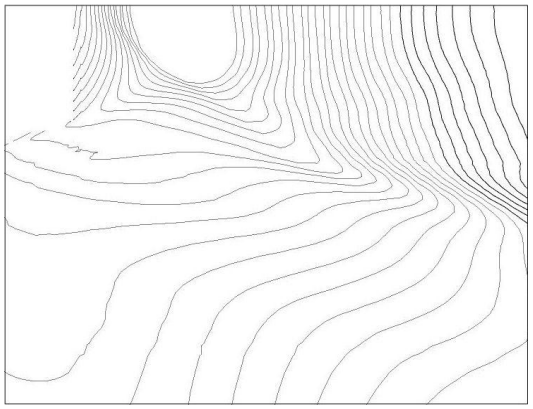

Southampton-CFX (BSL)

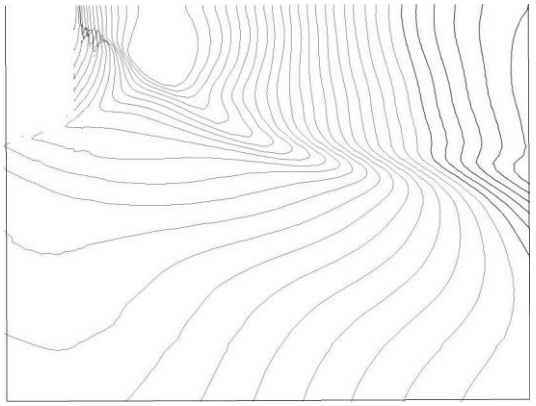

Southampton-CFX (SST)

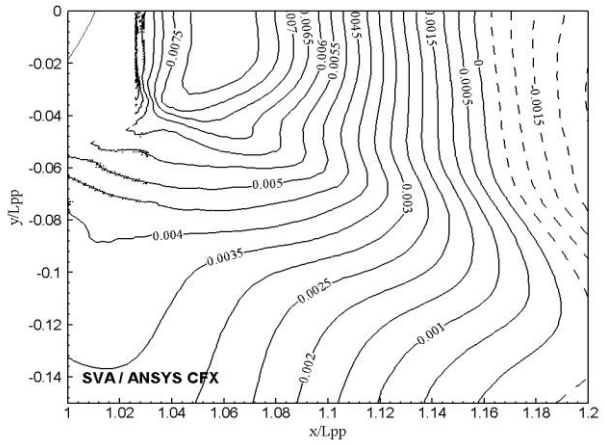

SVA-CFX12

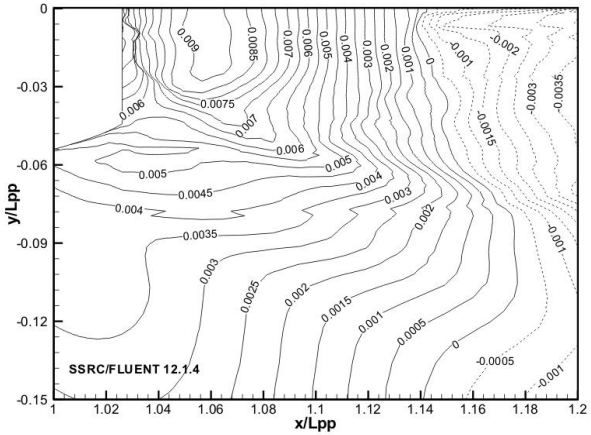

SSRC-FLUENT12.1

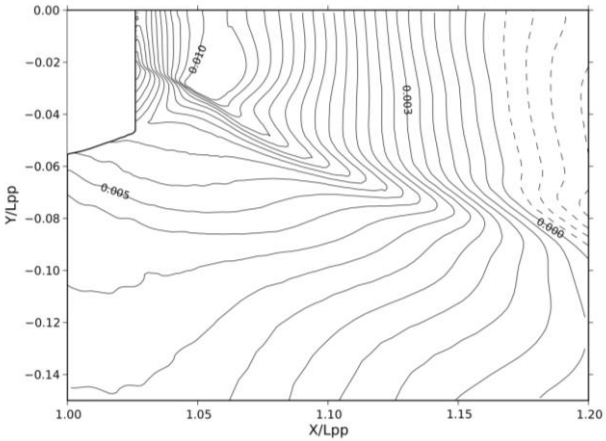

TUHH&ANSYS-CFX12.1

Fig. 2.1-3 Wave elevation contours (stern wave field) [$\Delta z = 0.0005$]
(Solid lines: positive (+) values; Dashed lines: negative (-) values)

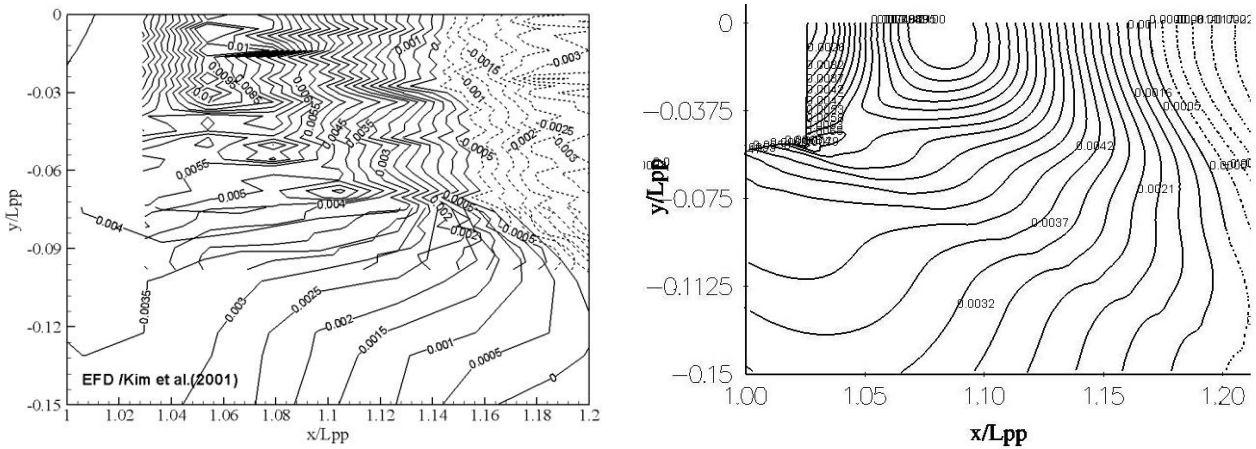

Experiment (MOERI, Kim et al. 2001) VTT-FINFLO

Fig. 2.1-3 Wave elevation contours (stern wave field) [$\Delta z = 0.0005$]
(Solid lines: positive (+) values; Dashed lines: negative (-) values)

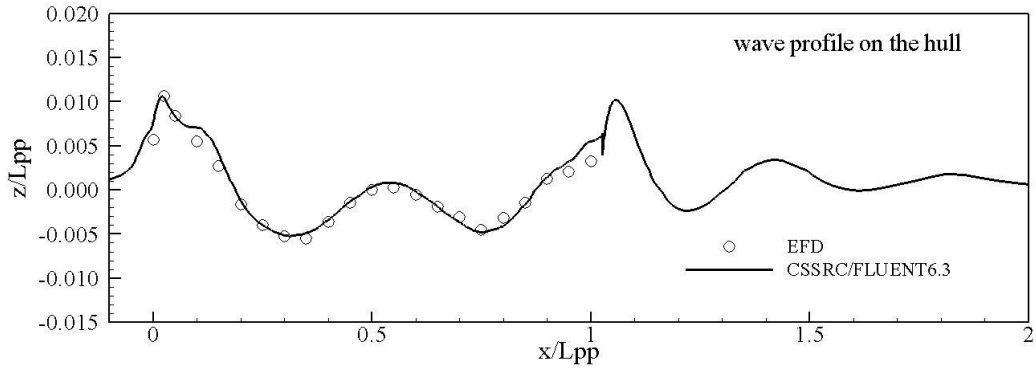

CSSRC-Fluent6.3

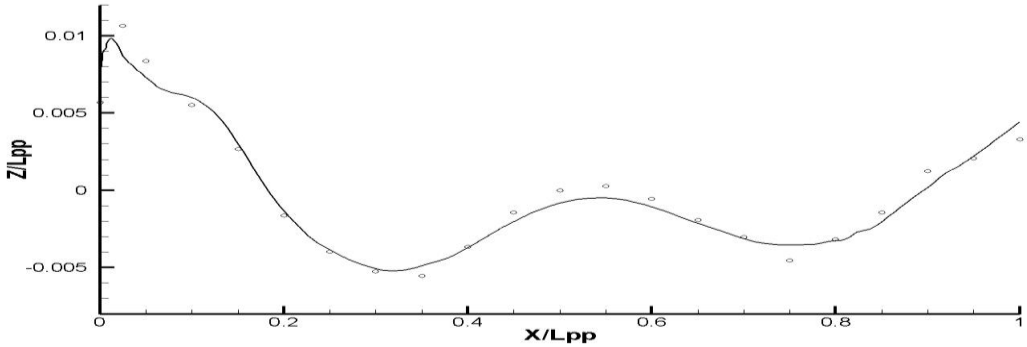

ECN/BEC/HO-Icare

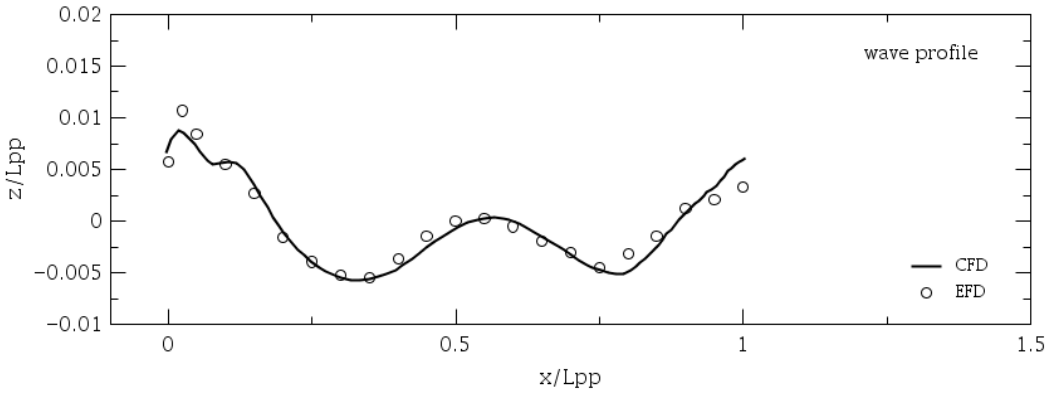

FLOWTECH-SHIPFLOW-VOF-4.3

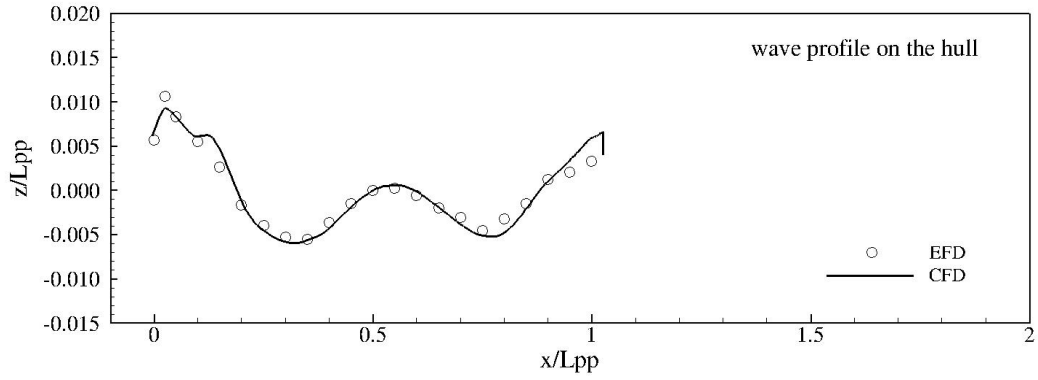

IIHR-CFDShipIowaV4.0 (DES)

Fig. 2.1-4 Wave profile on the hull (CFD: solid line; EFD: open circles)

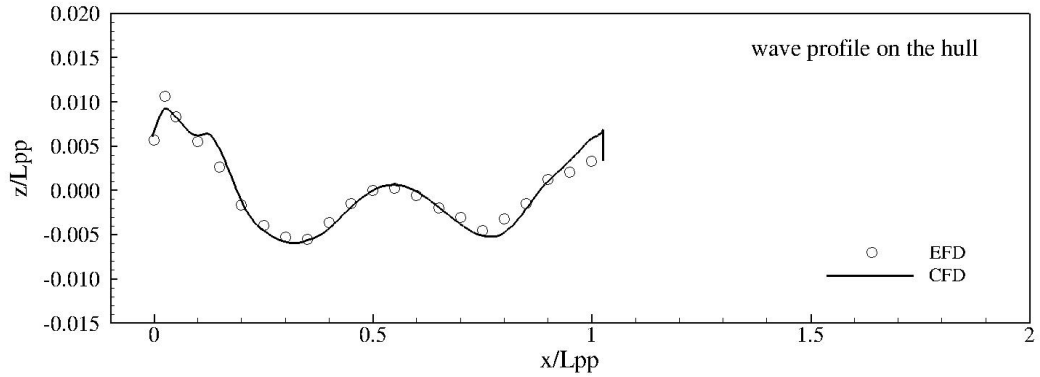

IIHR-CFDShipIowaV4.0 (RANS)

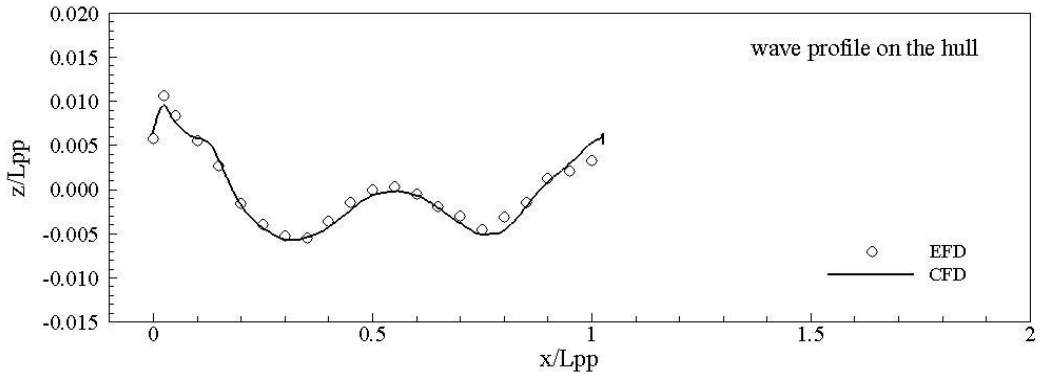

IIHR/SJTU-FLUENT12.0.16

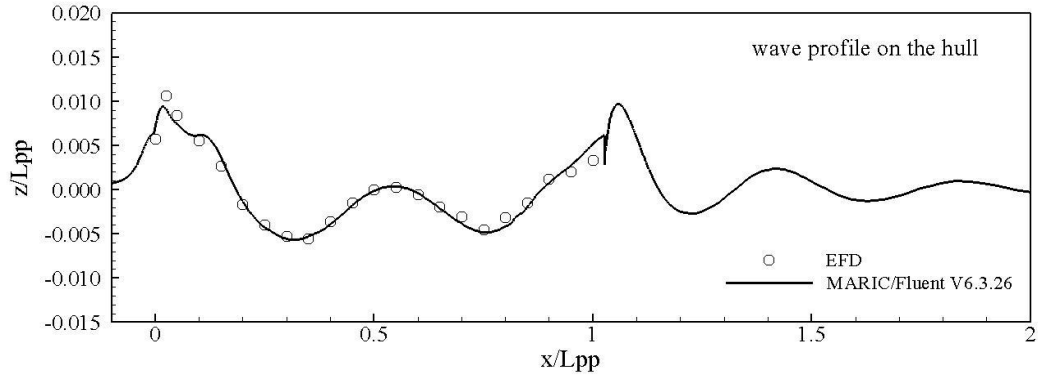

MARIC-FLUENT6.3

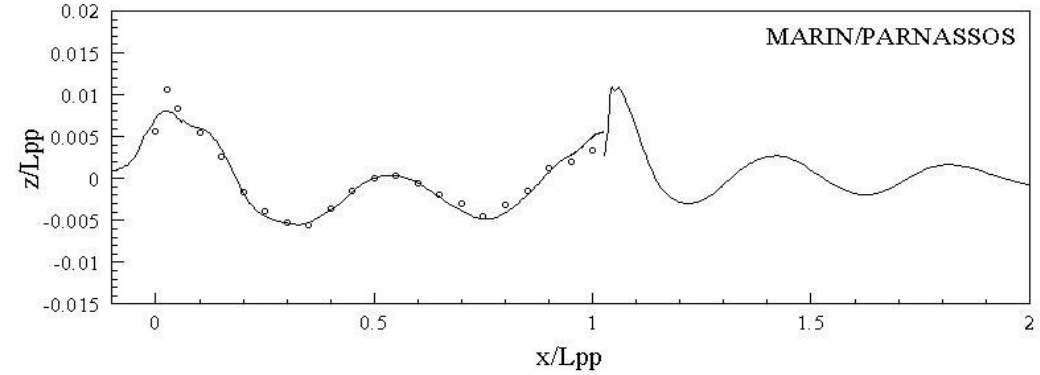

MARIN-PARNASSOS

Fig. 2.1-4 Wave profile on the hull (CFD: solid line; EFD: open circles)

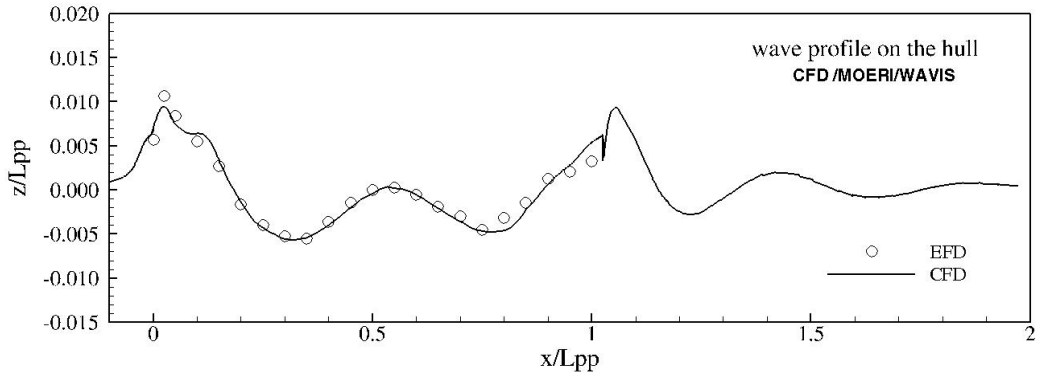

MOERI-WAVIS

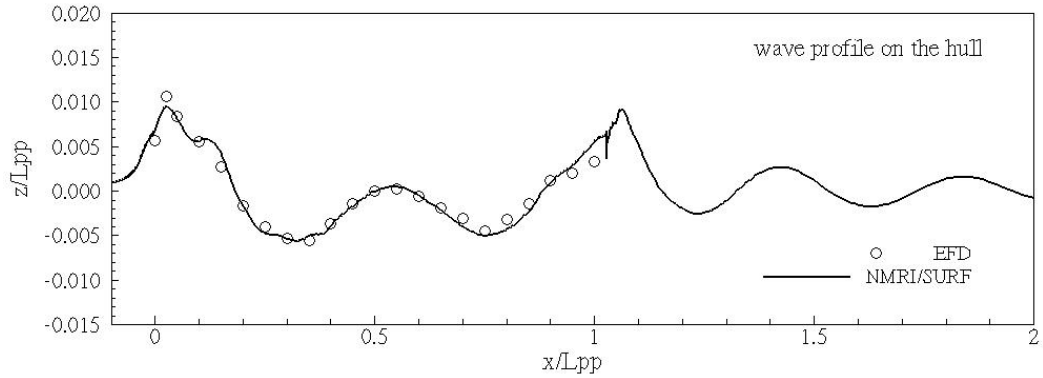

NMRI-SURF

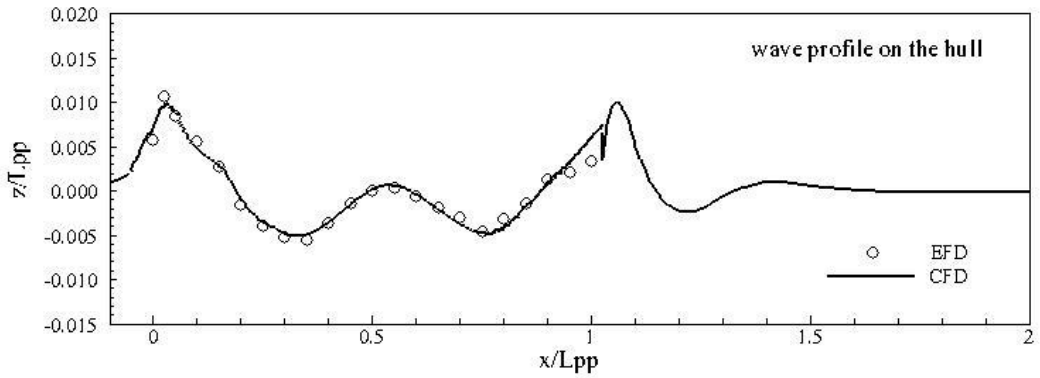

SNUTT-FLUENT6.3

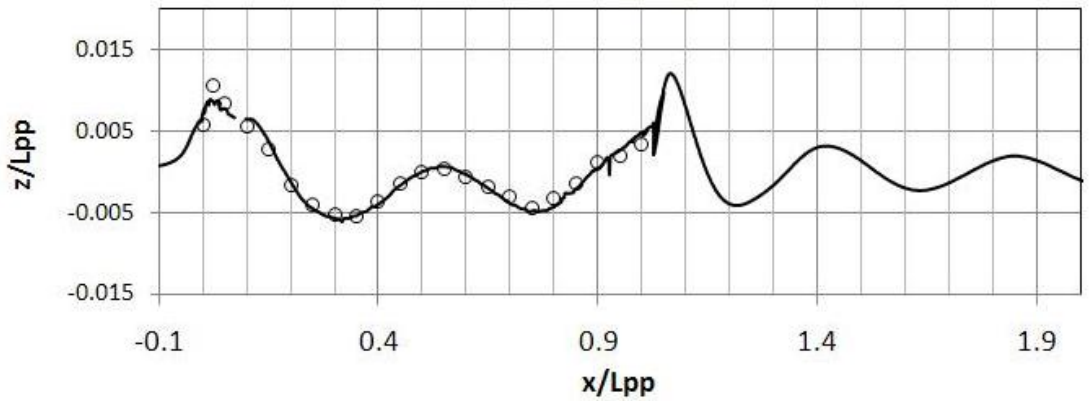

Southampton-CFX (BSL)

Fig. 2.1-4 Wave profile on the hull (CFD: solid line; EFD: open circles)

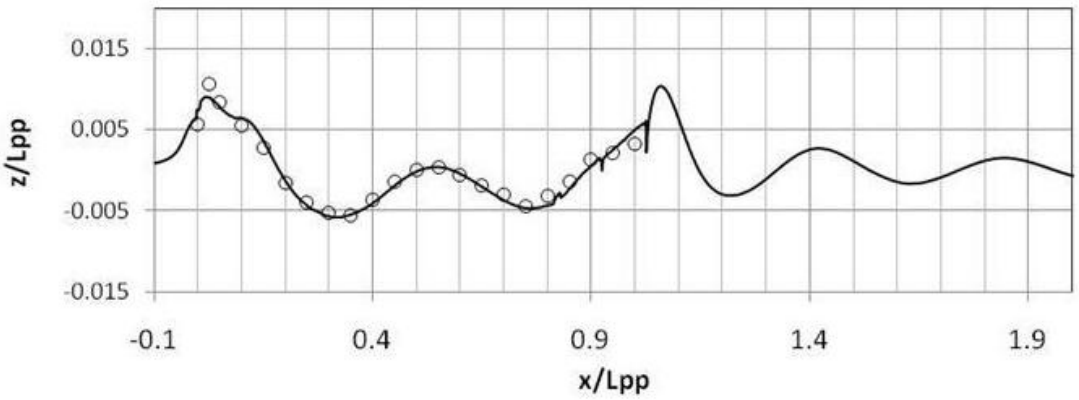

Southampton-CFX (SST)

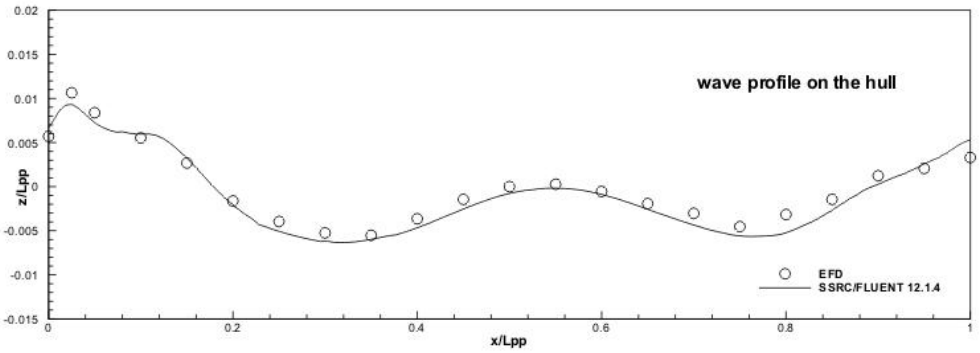

SSRC-FLUENT12.1

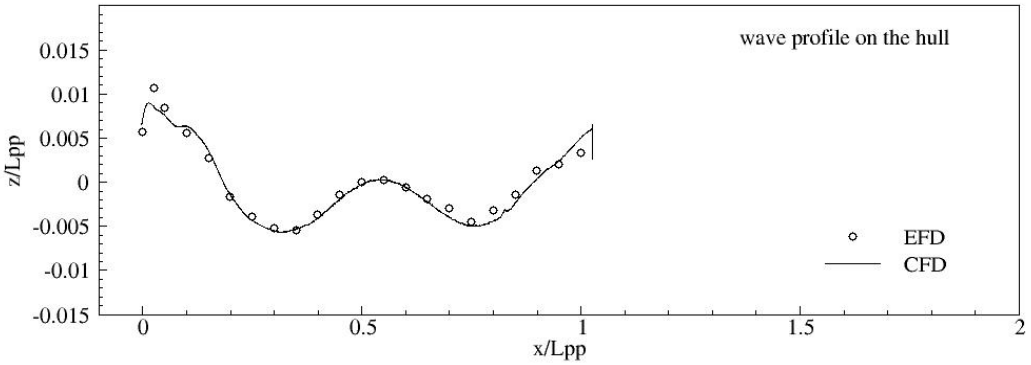

SVA-CFX12

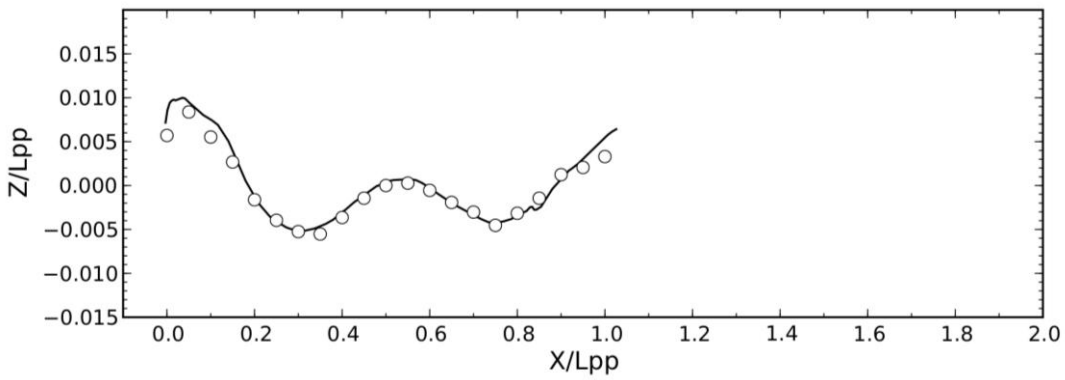

TUHH&ANSYS-CFX12.1

Fig. 2.1-4 Wave profile on the hull (CFD: solid line; EFD: open circles)

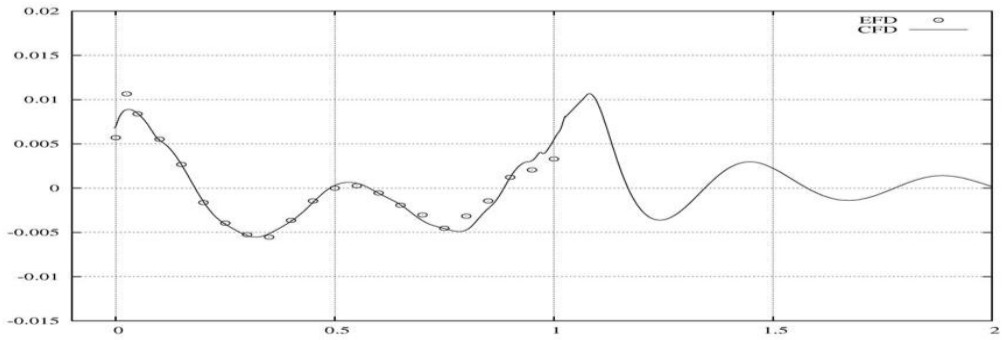

VTT-FINFLO

Fig. 2.1-4 Wave profile on the hull (CFD: solid line; EFD: open circles)

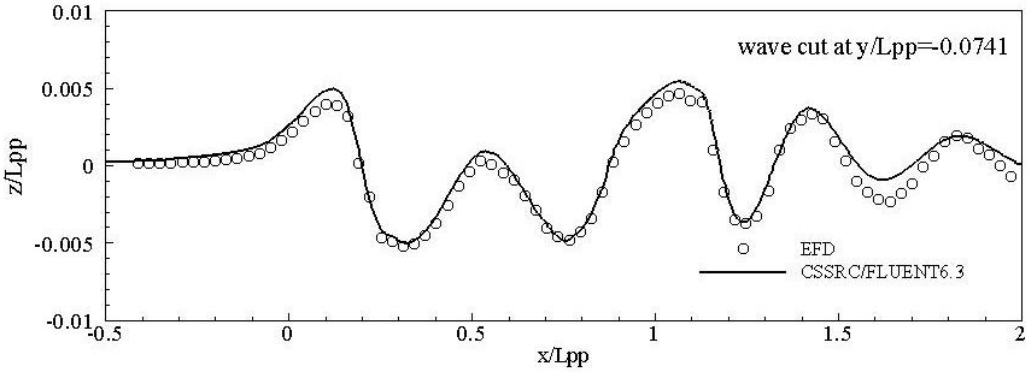

CSSRC-Fluent6.3

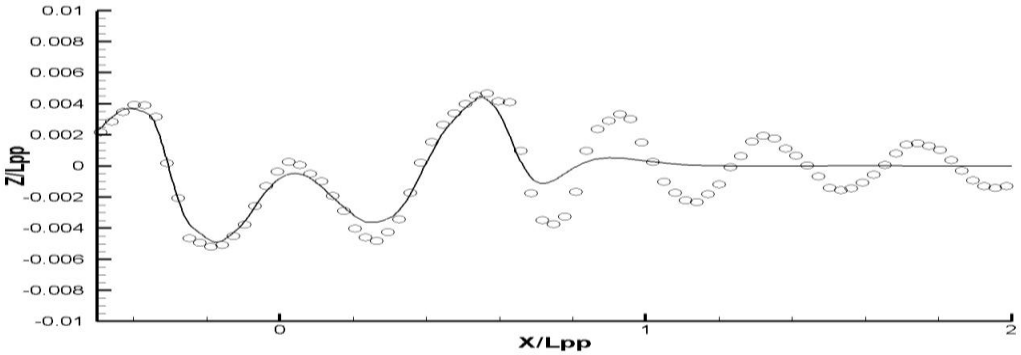

ECN/BEC/HO-Icare

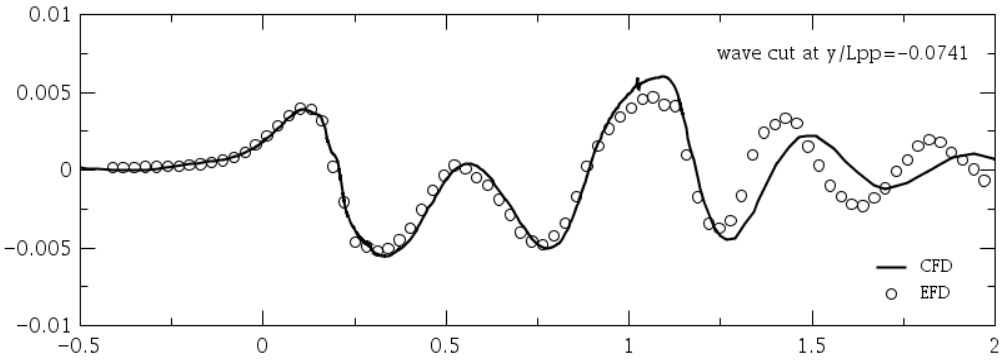

FLOWTECH-SHIPFLOW-VOF-4.3

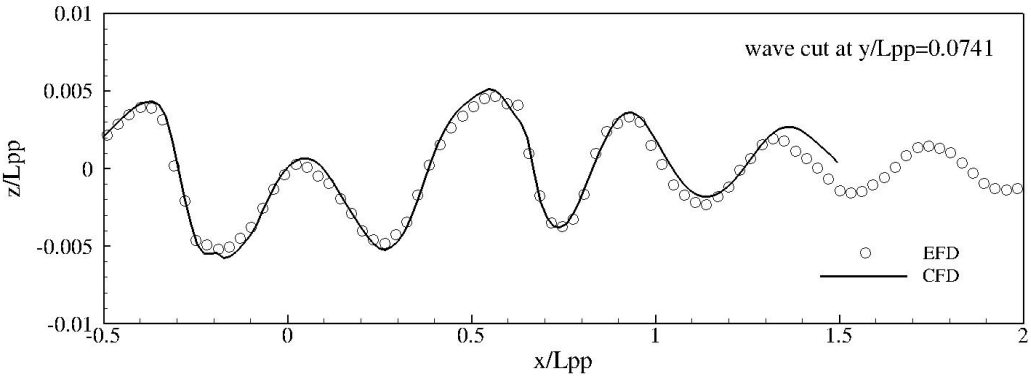

IIHR-CFDShipIowaV4.0 (DES)

Fig. 2.1-5 Longitudinal wave cut at y/L_{PP} = -0.0741 (CFD: solid line; EFD: open circles)

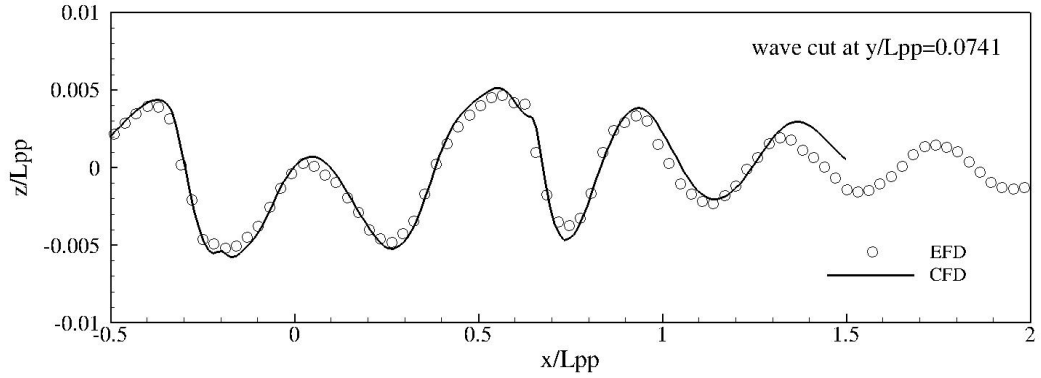

IIHR-CFDShipIowaV4.0 (RANS)

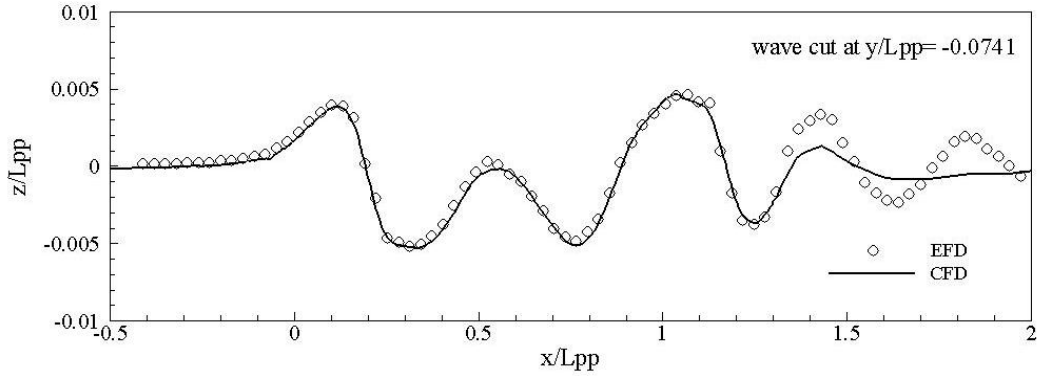

IIHR/SJTU-FLUENT12.0.16

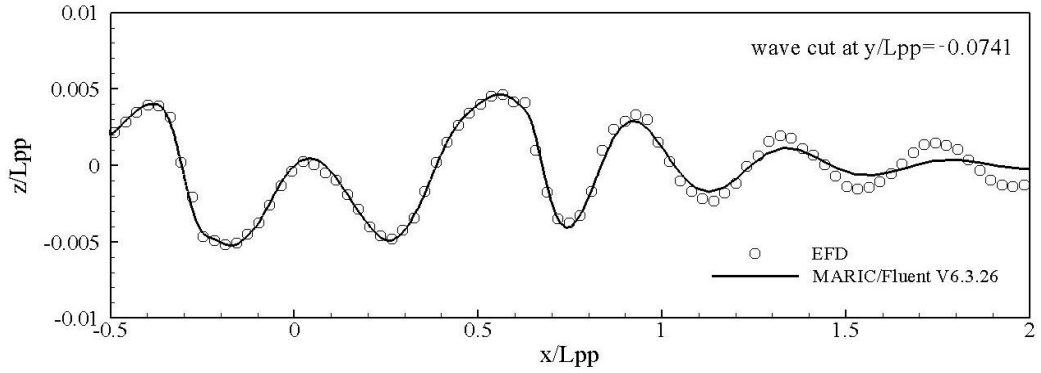

MARIC-FLUENT6.3

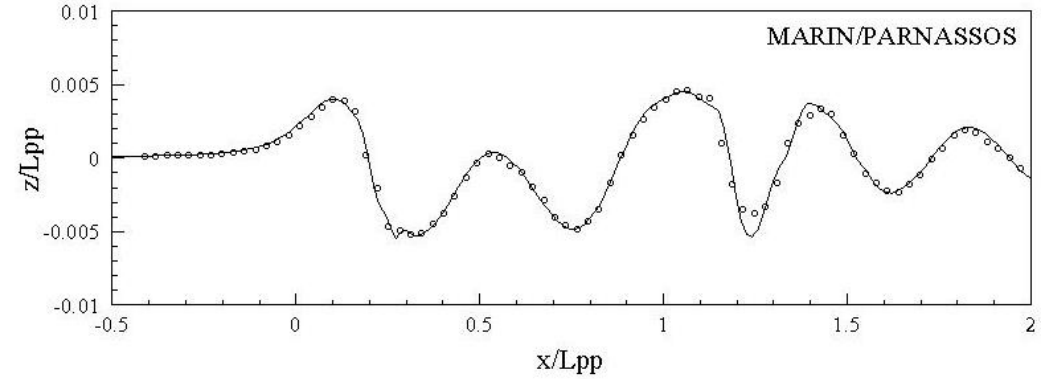

MARIN-PARNASSOS

Fig. 2.1-5 Longitudinal wave cut at y/L_{PP} = -0.0741 (CFD: solid line; EFD: open circles)

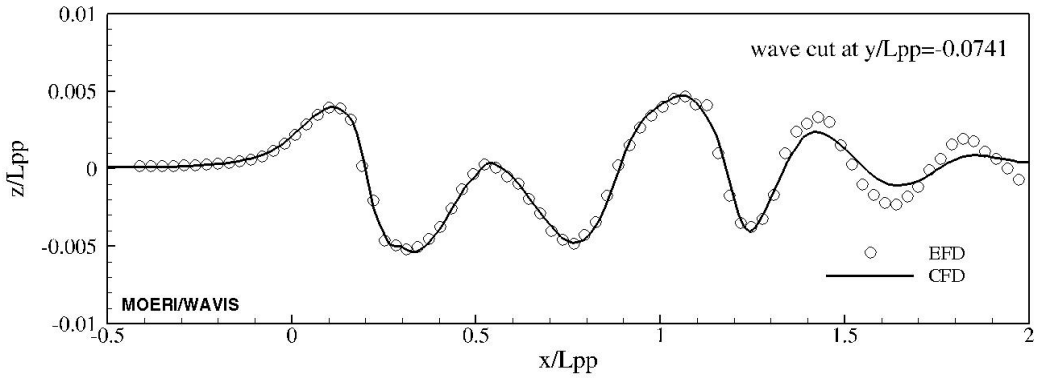

MOERI-WAVIS

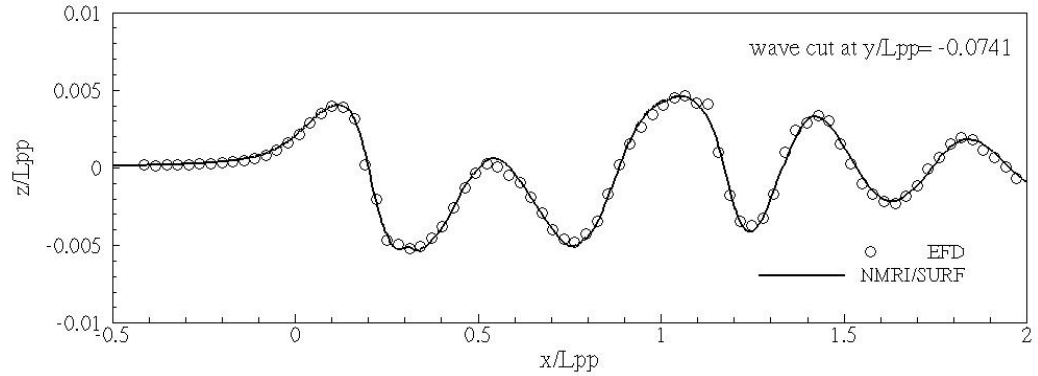

NMRI-SURF

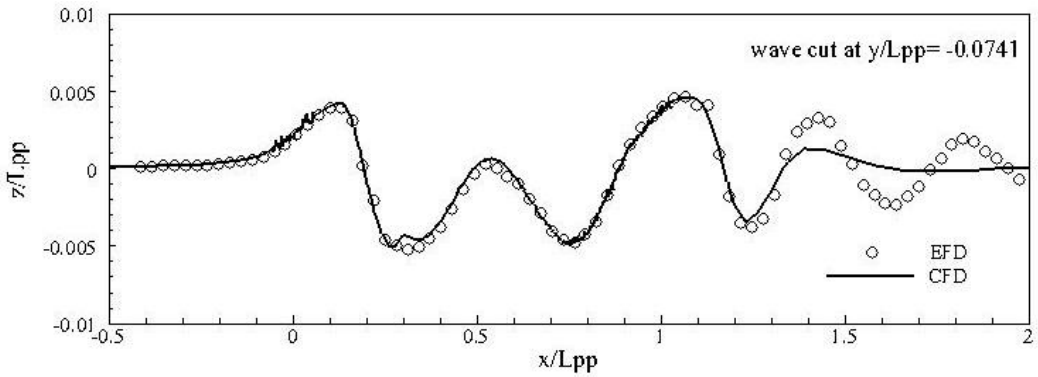

SNUTT-FLUENT6.3

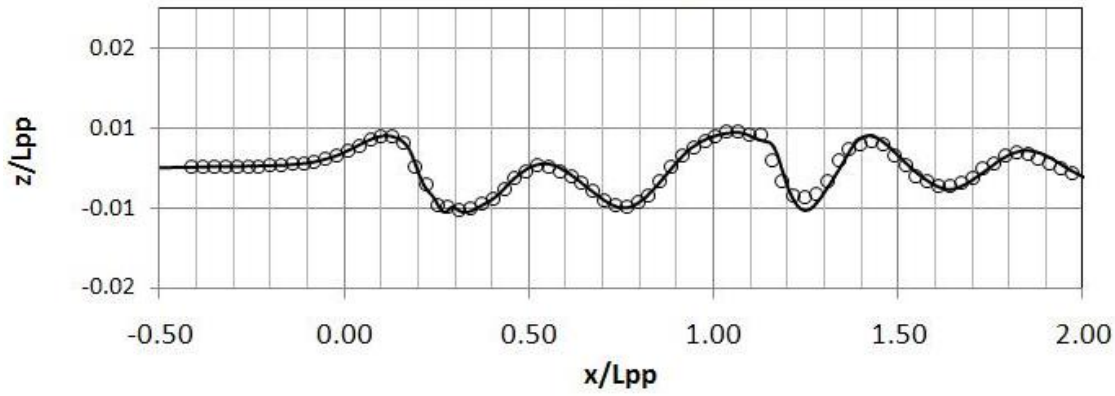

Southampton-CFX (BSL)

Fig. 2.1-5 Longitudinal wave cut at y/L_{PP} = -0.0741 (CFD: solid line; EFD: open circles)

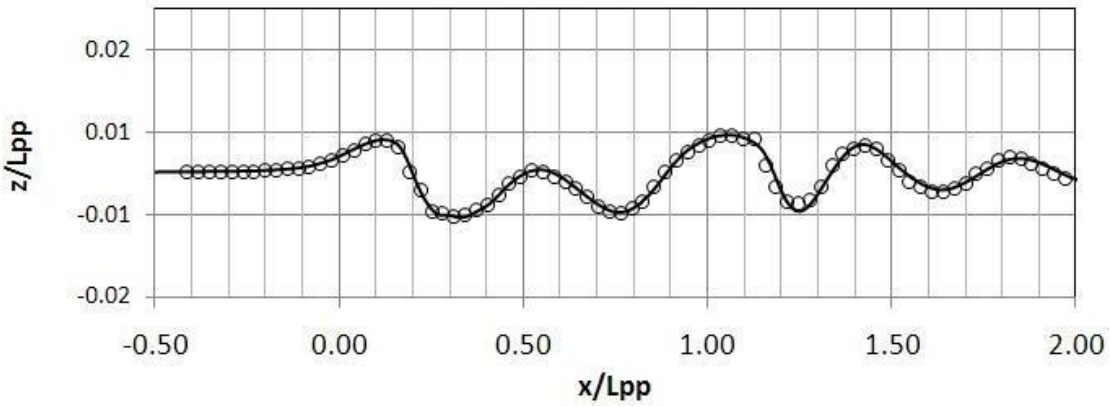

Southampton-CFX (SST)

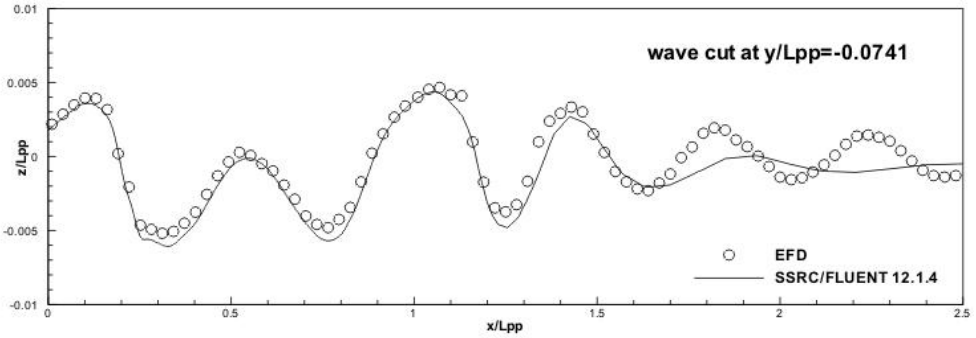

SSRC-FLUENT12.1.4

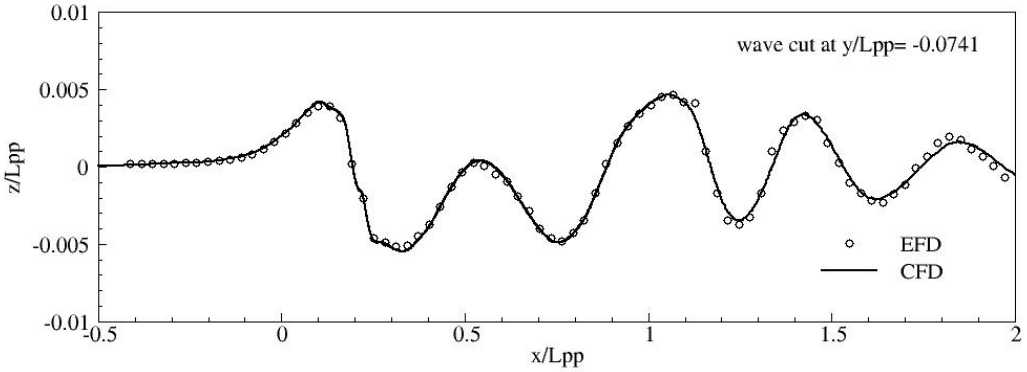

SVA-CFX12

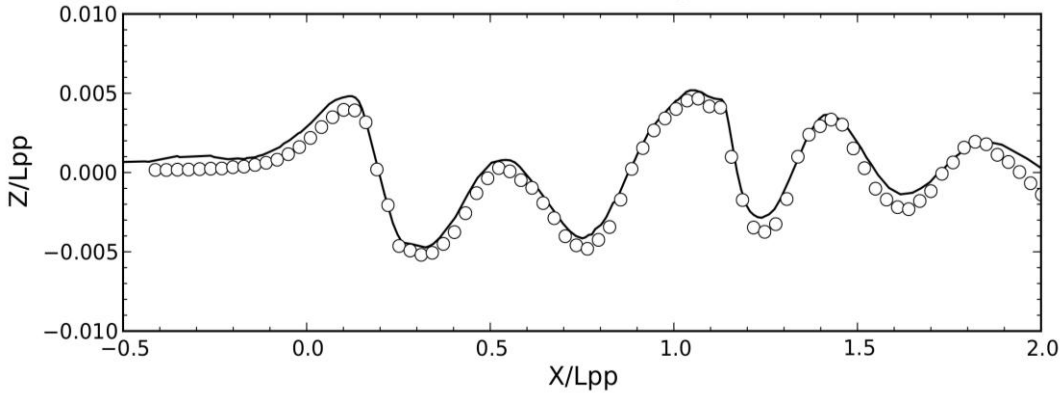

TUHH&ANSYS-CFX12.1

Fig. 2.1-5 Longitudinal wave cut at y/L_{PP} = -0.0741 (CFD: solid line; EFD: open circles)

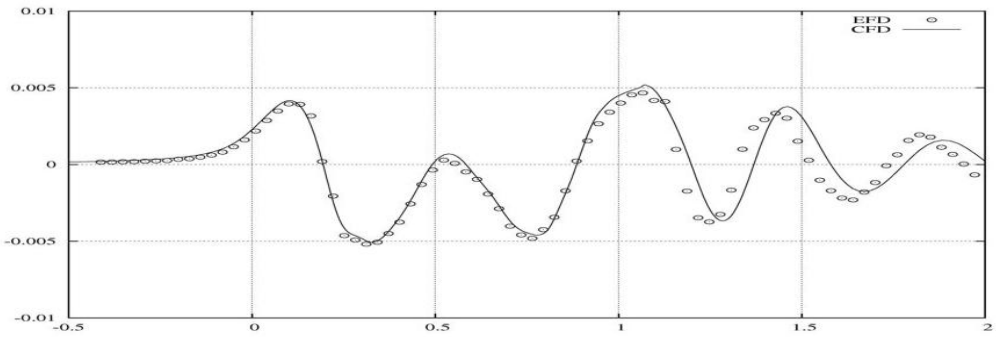

VTT-FINFLO

Fig. 2.1-5 Longitudinal wave cut at y/L_{pp} = -0.0741 (CFD: solid line; EFD: open circles)

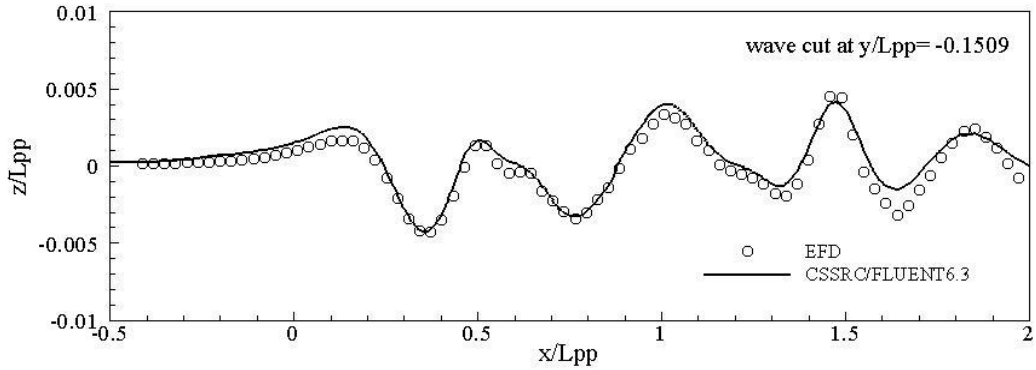

CSSRC-Fluent6.3

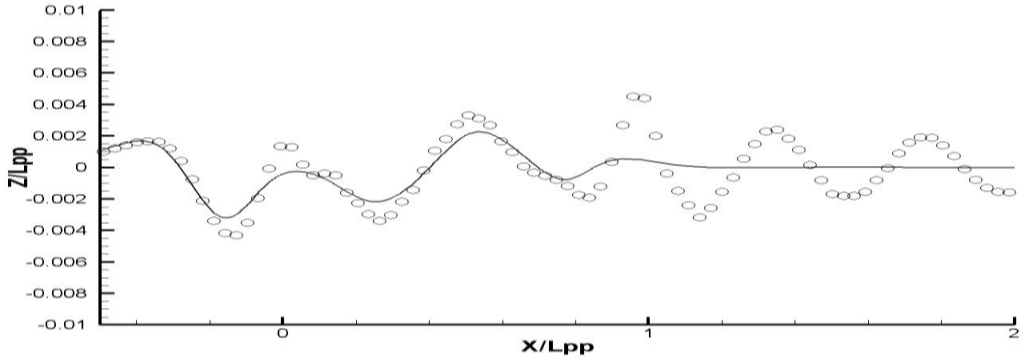

ECN/BEC/HO-Icare

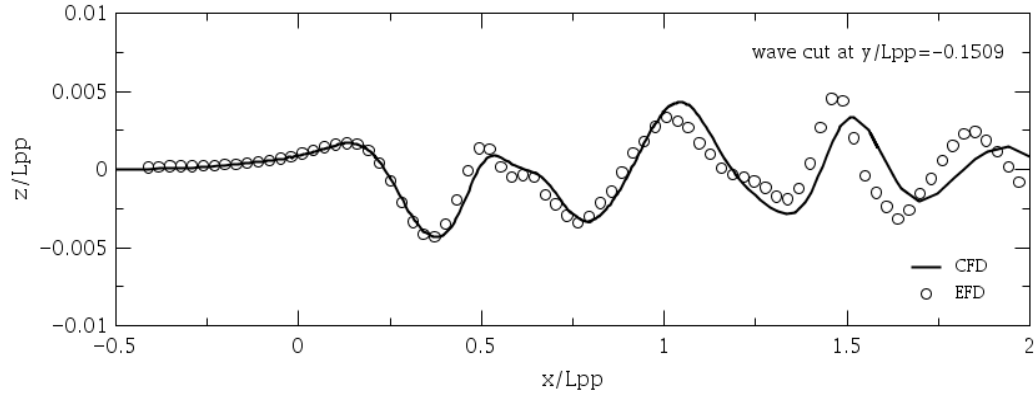

FLOWTECH-SHIPFLOW-VOF-4.3

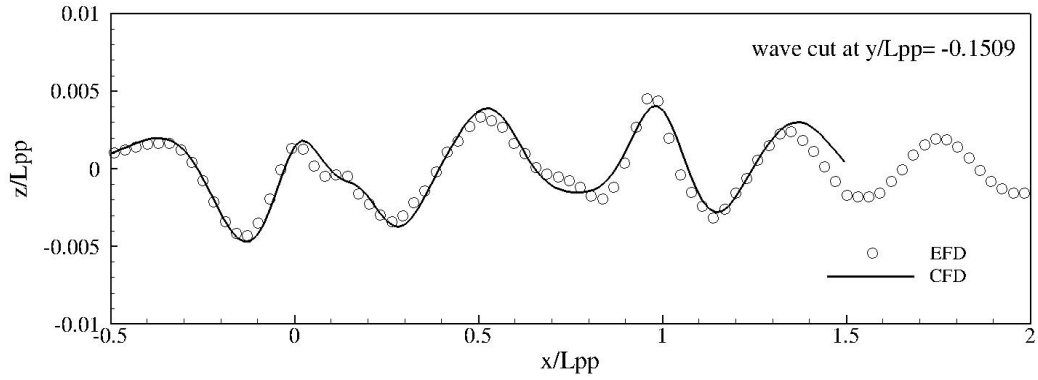

IIHR-CFDShipIowaV4.0 (DES)

Fig. 2.1-6 Longitudinal wave cut at y/L_{pp} = -0.1509 (CFD: solid line; EFD: open circles)

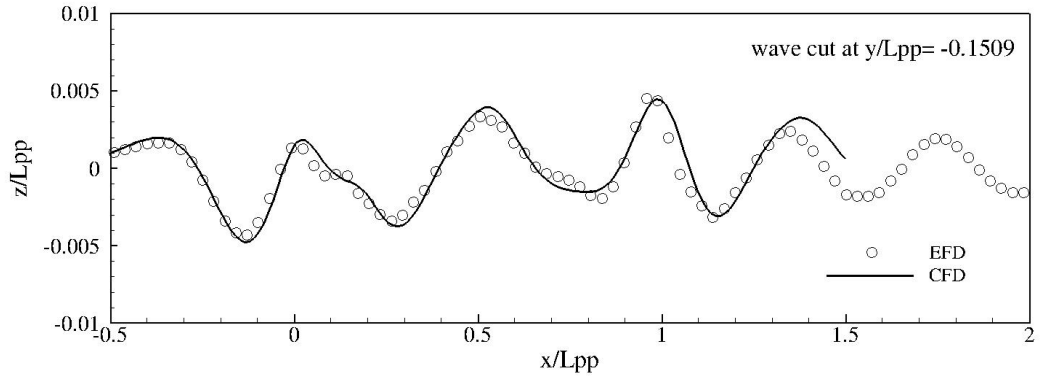

IIHR-CFDShipIowaV4.0 (RANS)

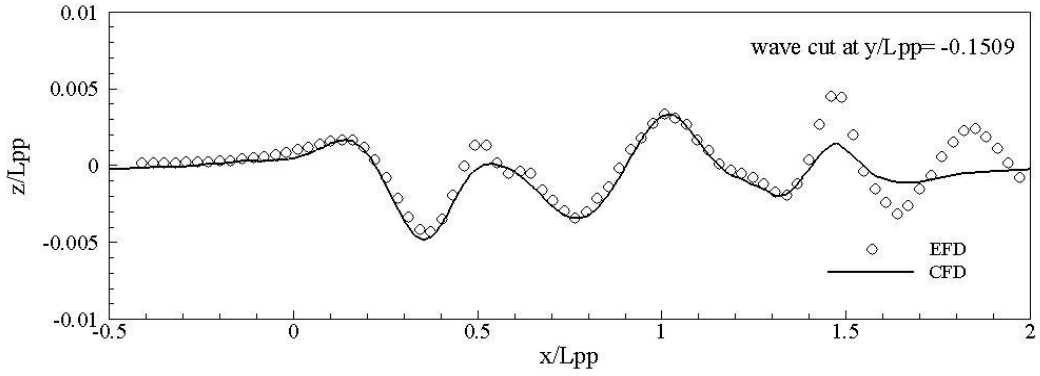

IIHR/SJTU-FLUENT12.0.16

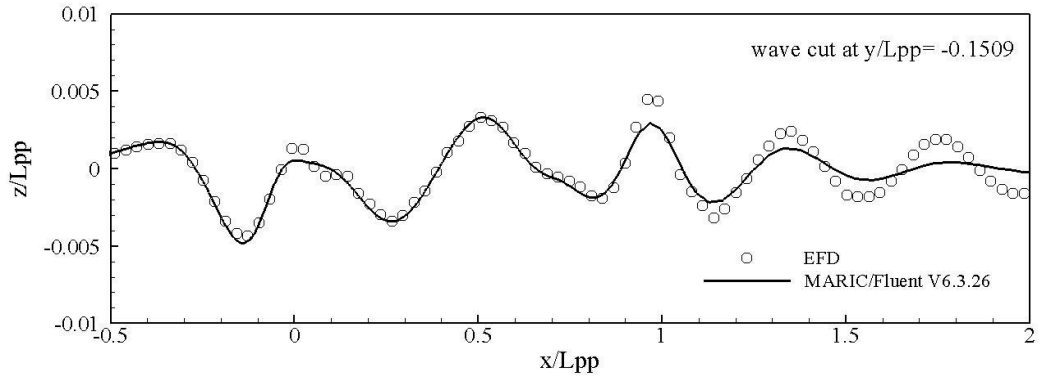

MARIC-FLUENT6.3

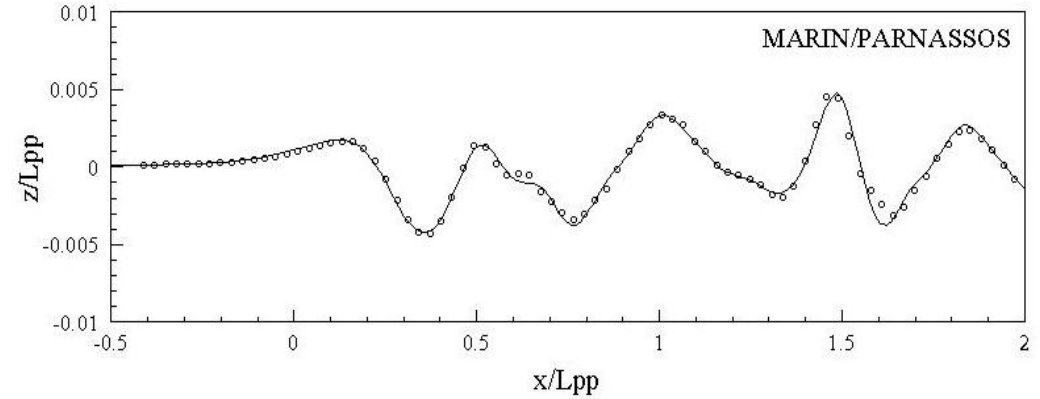

MARIN-PARNASSOS

Fig. 2.1-6 Longitudinal wave cut at y/L_{PP} = -0.1509 (CFD: solid line; EFD: open circles)

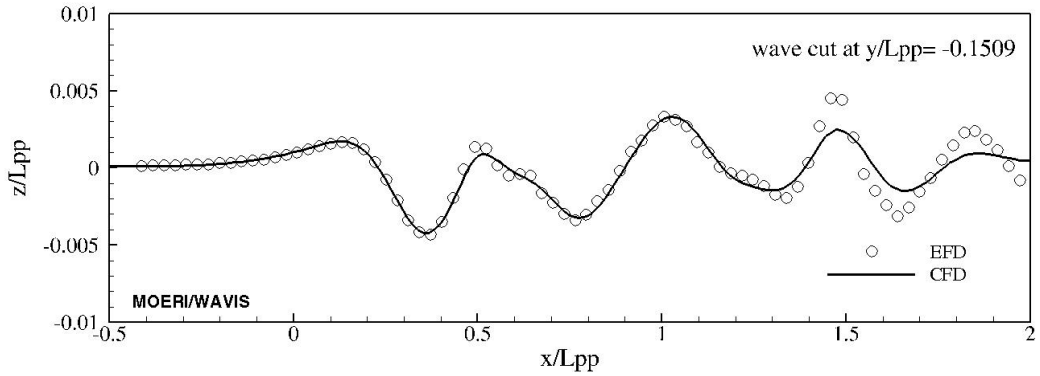

MOERI-WAVIS

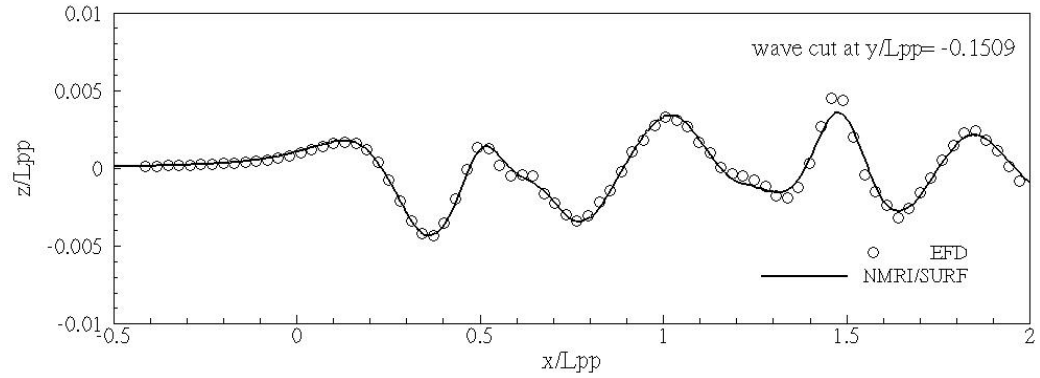

NMRI-SURF

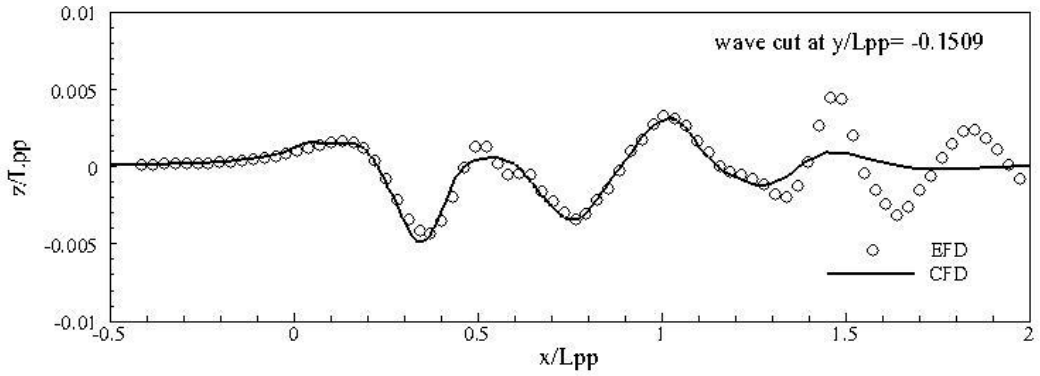

SNUTT-FLUENT6.3

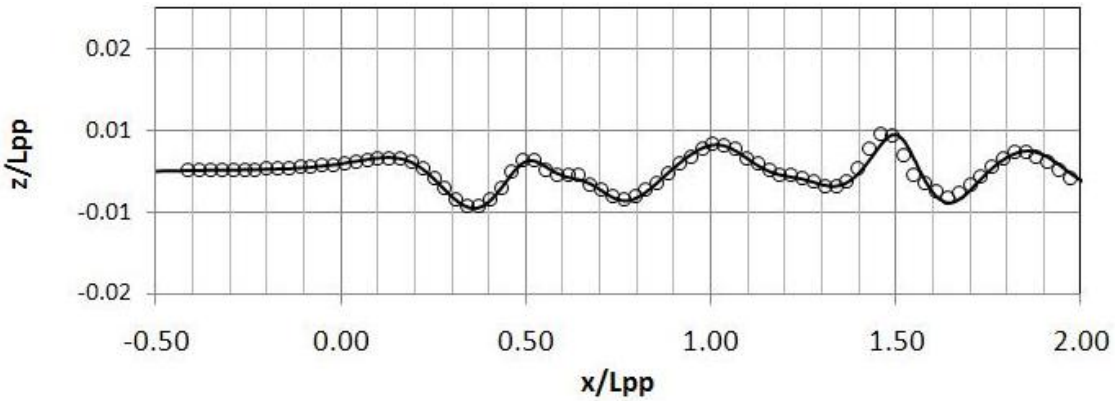

Southampton-CFX (BSL)

Fig. 2.1-6 Longitudinal wave cut at y/L_{PP} = -0.1509 (CFD: solid line; EFD: open circles)

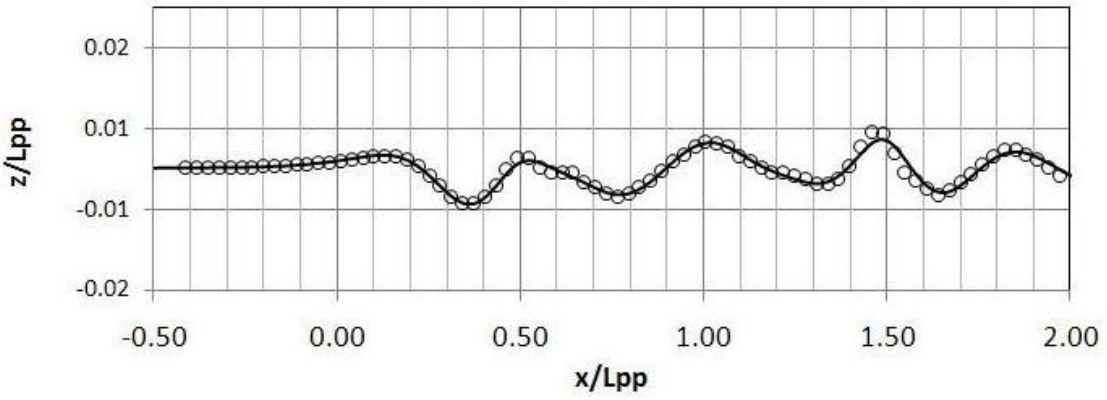

Southampton-CFX (SST)

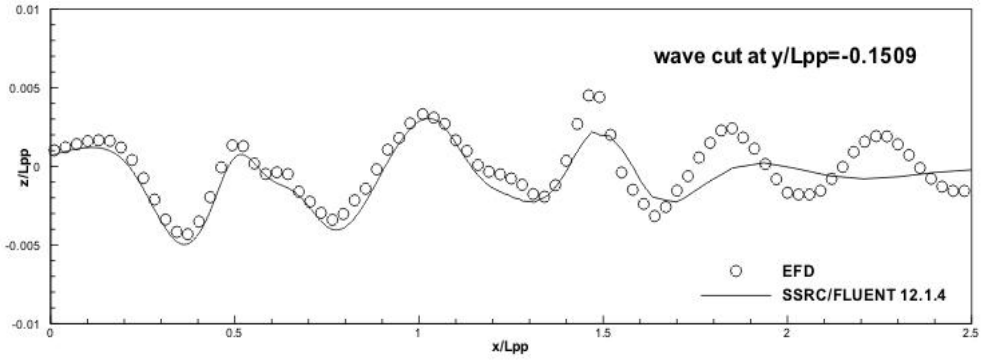

SSRC-FLUENT12.1

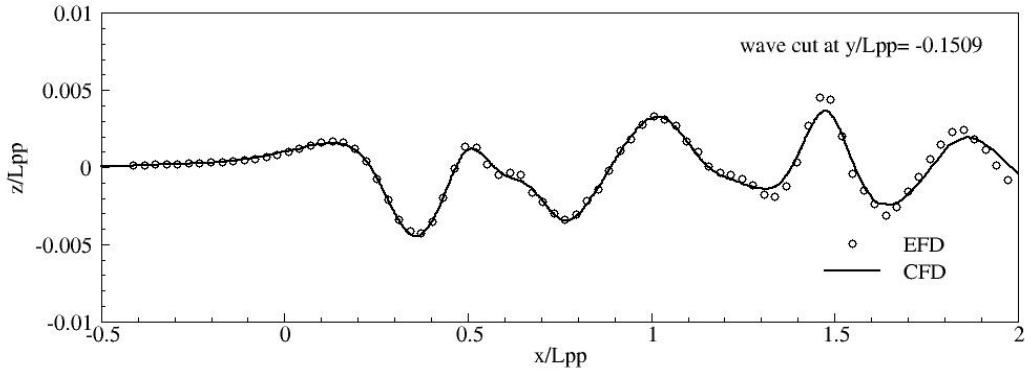

SVA-CFX12

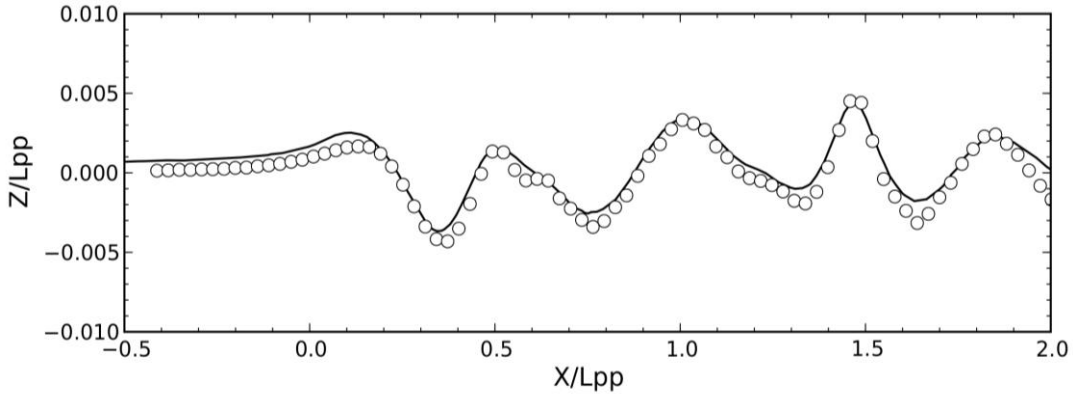

TUHH&ANSYS-CFX12.1

Fig. 2.1-6 Longitudinal wave cut at y/L_{PP} = -0.1509 (CFD: solid line; EFD: open circles)

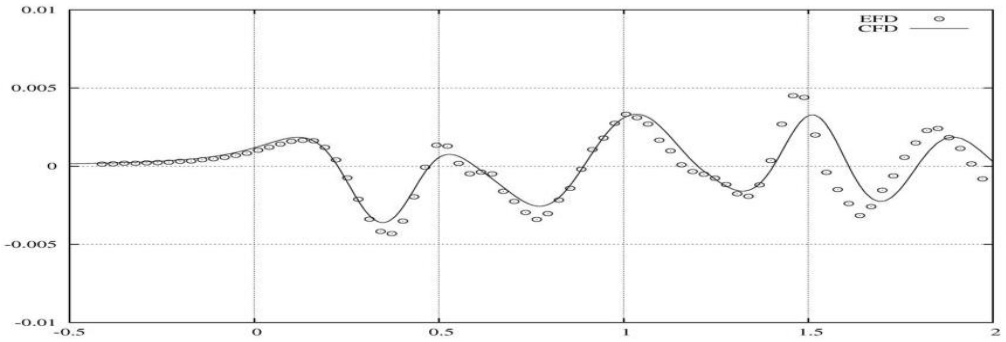

VTT-FINFLO

Fig. 2.1-6 Longitudinal wave cut at y/L_{PP} = -0.1509 (CFD: solid line; EFD: open circles)

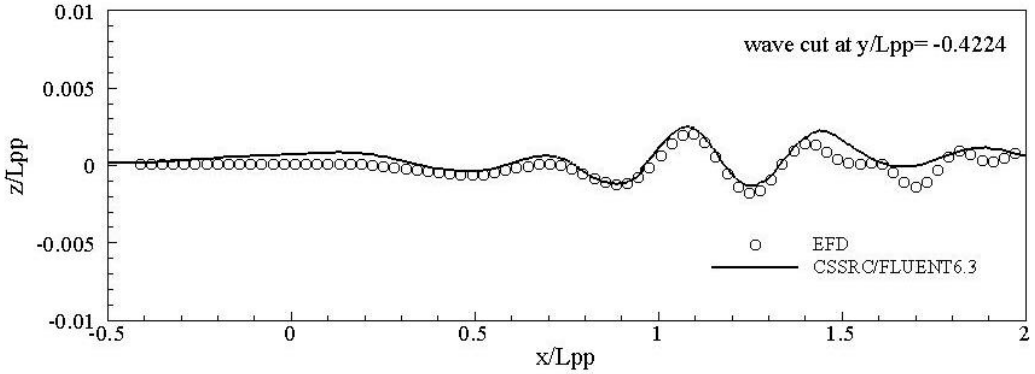

CSSRC-Fluent6.3

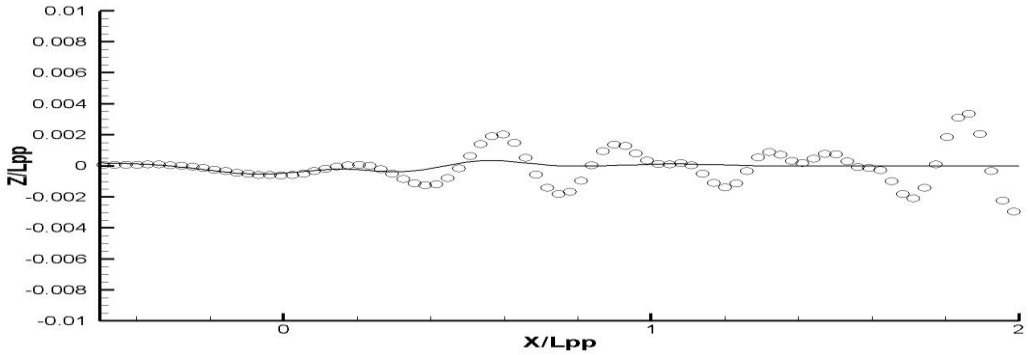

ECN/BEC/HO-Icare

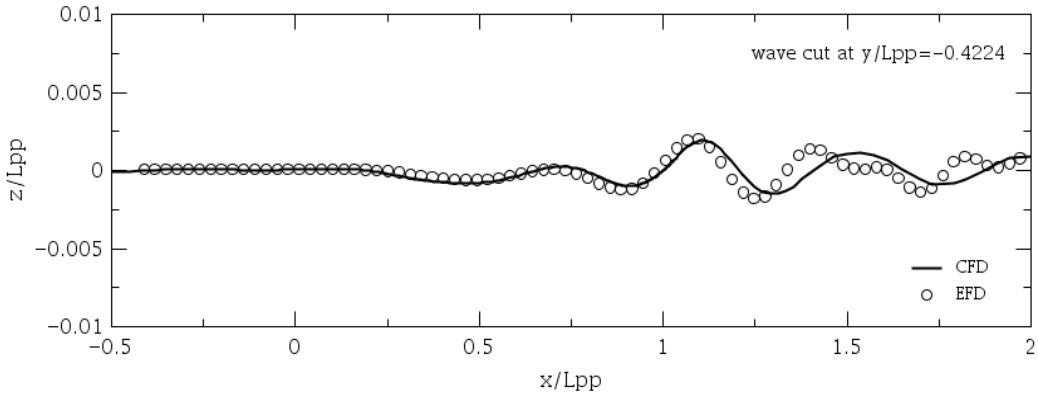

FLOWTECH-SHIPFLOW-VOF-4.3

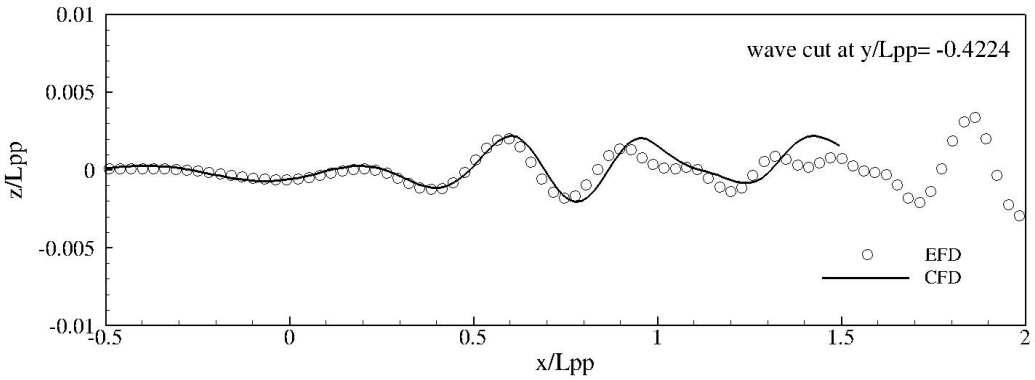

IIHR-CFDShipIowaV4.0 (DES)

Fig. 2.1-7 Longitudinal wave cut at y/L_{pp} = -0.4224 (CFD: solid line; EFD: open circles)

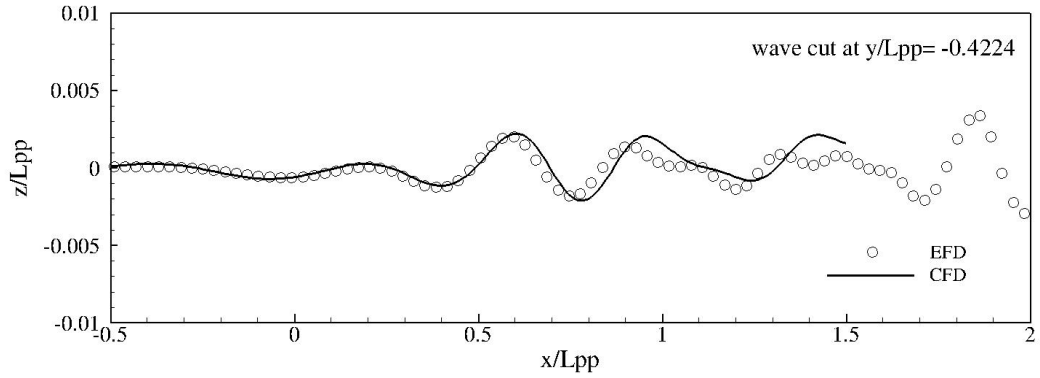

IIHR-CFDShipIowaV4.0 (RANS)

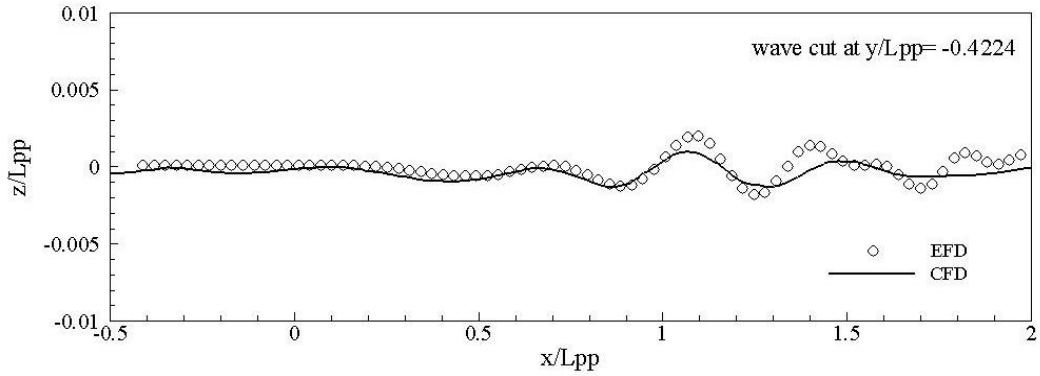

IIHR/SJTU-FLUENT12.0.16

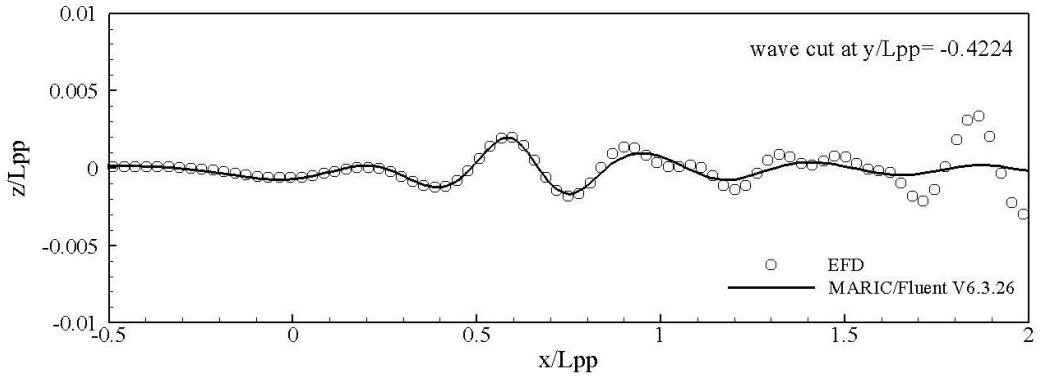

MARIC-FLUENT6.3

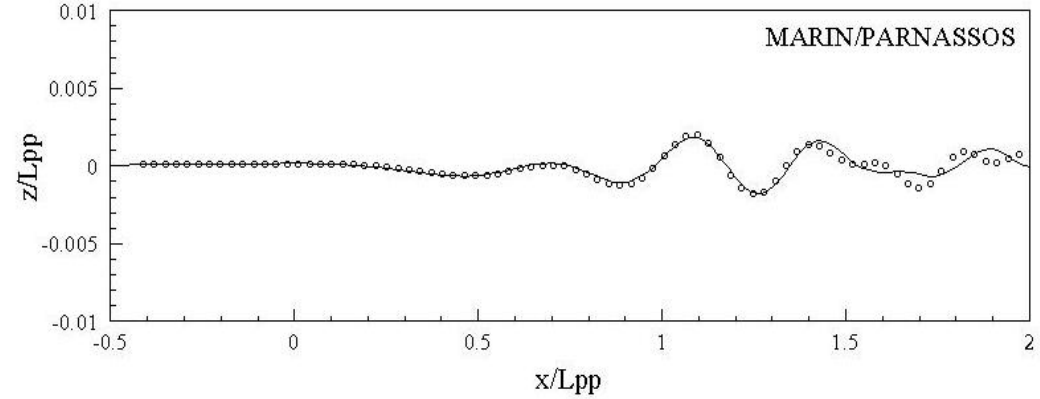

MARIN-PARNASSOS

Fig. 2.1-7 Longitudinal wave cut at y/L_{PP} = -0.4224 (CFD: solid line; EFD: open circles)

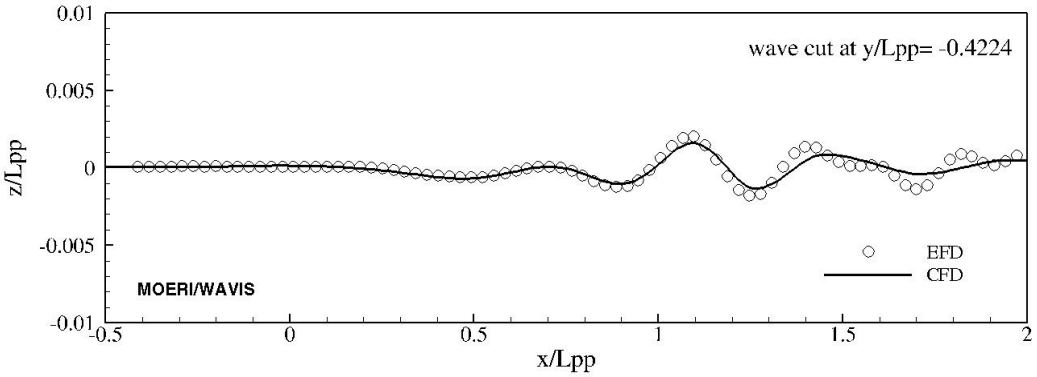

MOERI-WAVIS

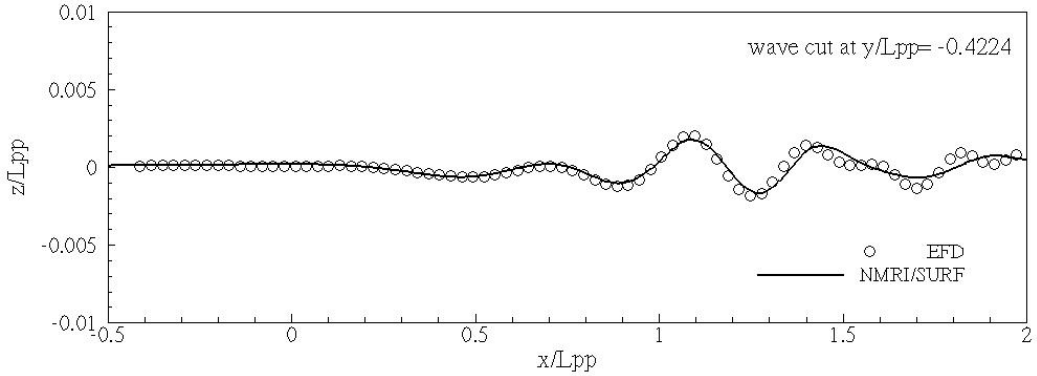

NMRI-SURF

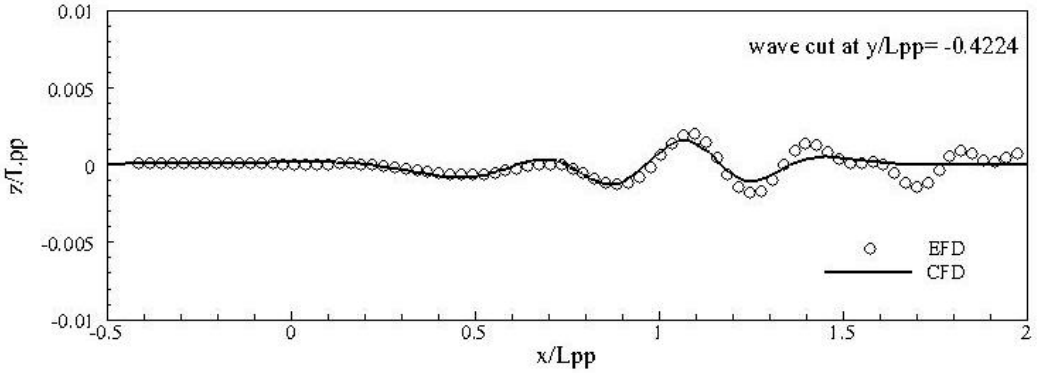

SNUTT-FLUENT6.3

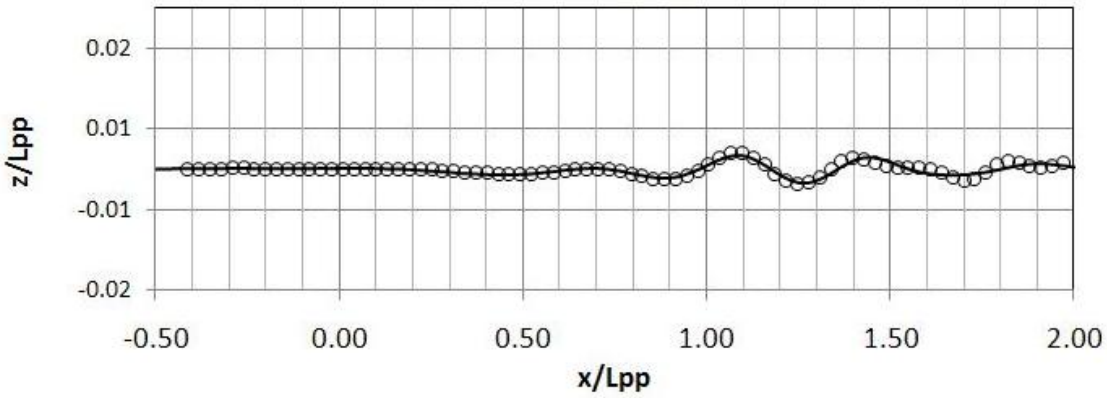

Southampton-CFX (BSL)

Fig. 2.1-7 Longitudinal wave cut at y/L_{PP} = -0.4224 (CFD: solid line; EFD: open circles)

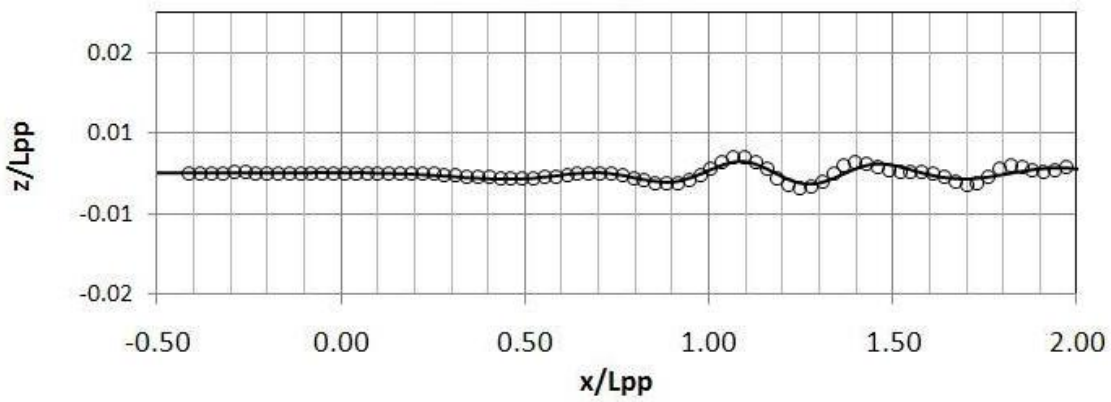

Southampton-CFX (SST)

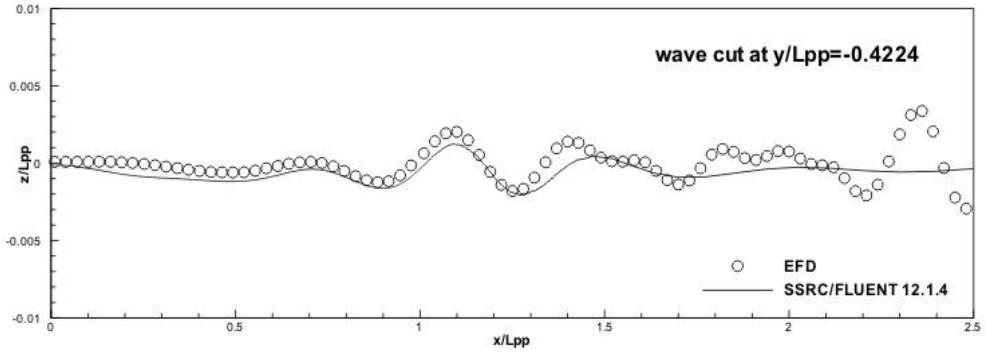

SSRC-FLUENT12.1

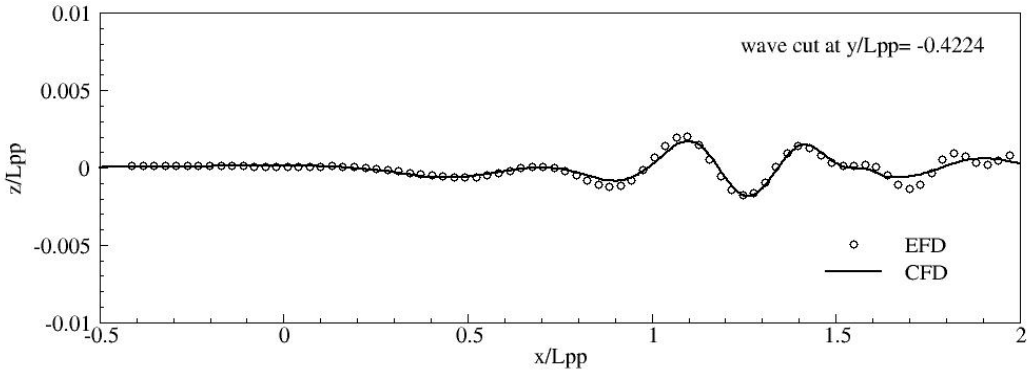

SVA-CFX12

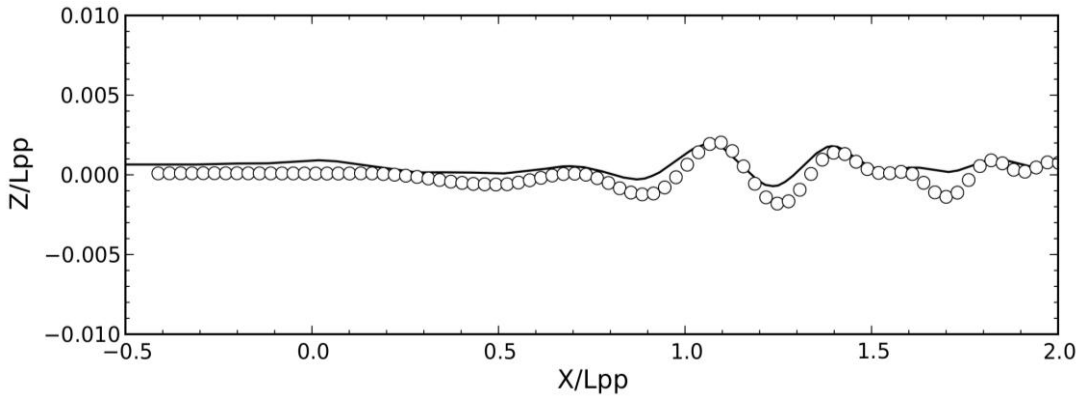

TUHH&ANSYS-CFX12.1

Fig. 2.1-7 Longitudinal wave cut at y/L_{PP} = -0.4224 (CFD: solid line; EFD: open circles)

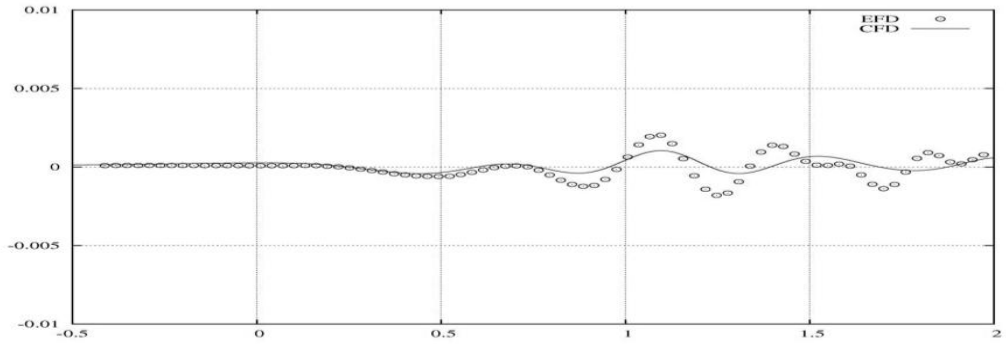

VTT-FINFLO

Fig. 2.1-7 Longitudinal wave cut at y/L_{PP} = -0.4224 (CFD: solid line; EFD: open circles)

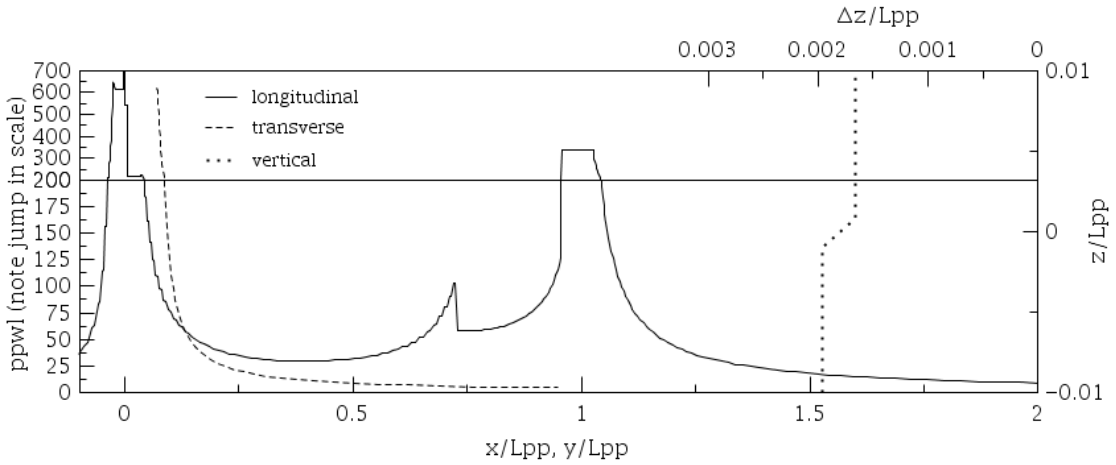

CSSRC-Fluent6.3

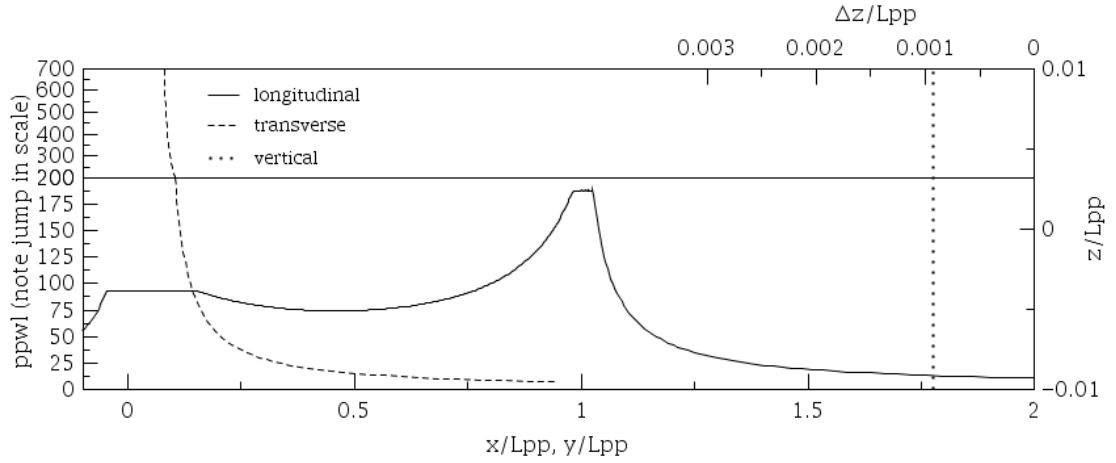

FLOWTECH-SHIPFLOW-VOF-4.3

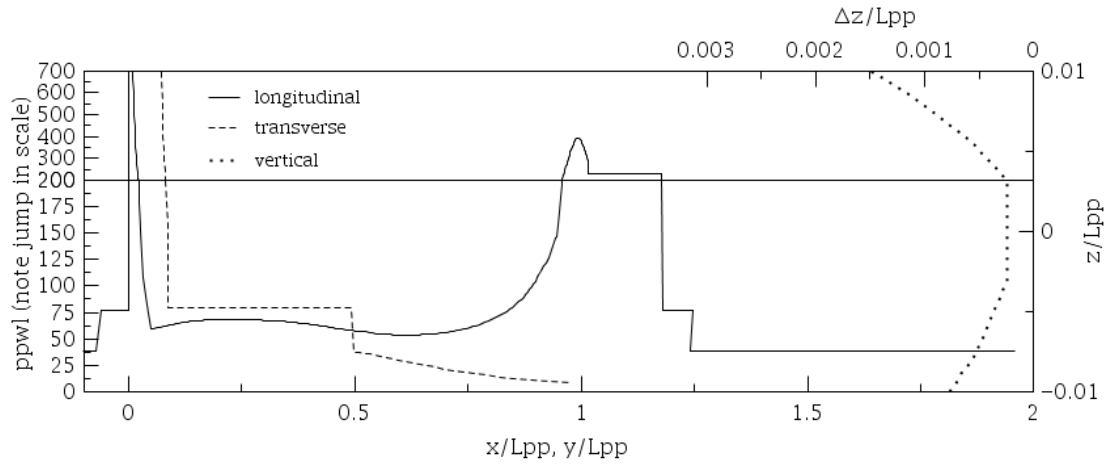

IIHR-CFDShipIowaV4.0 (DES)

Fig. 2.1-8 Grid density distribution along the waterline (solid), and in transverse (dashed) and vertical (dotted) directions at mid-ship

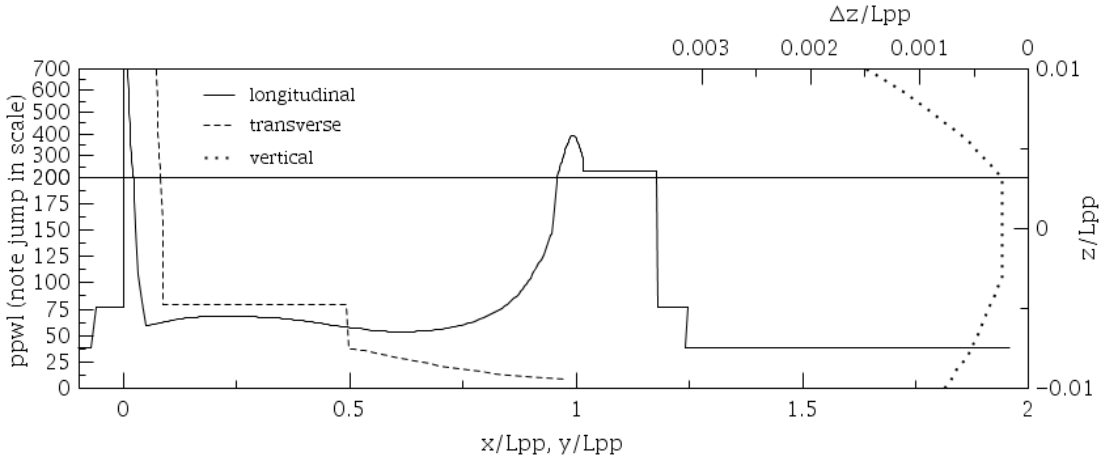

IIHR-CFDShipIowaV4.0 (RANS)

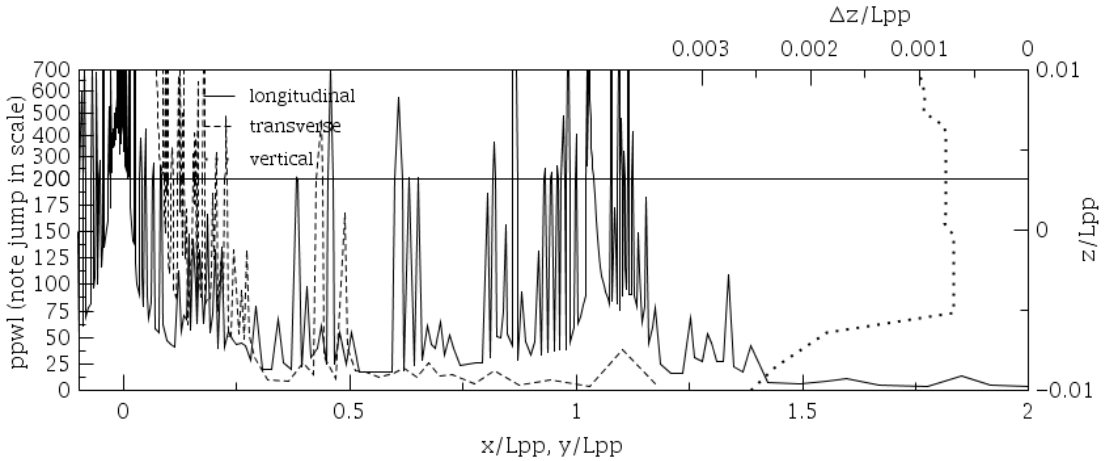

IIHR/SJTU-FLUENT12.0.16

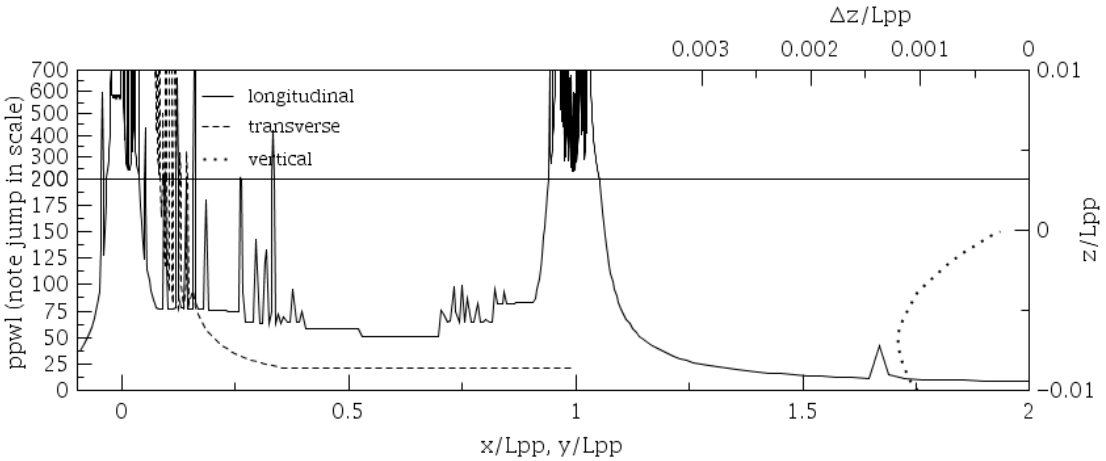

MARIC-FLUENT6.3

Fig. 2.1-8 Grid density distribution along the waterline (solid), and in transverse (dashed) and vertical (dotted) directions at mid-ship

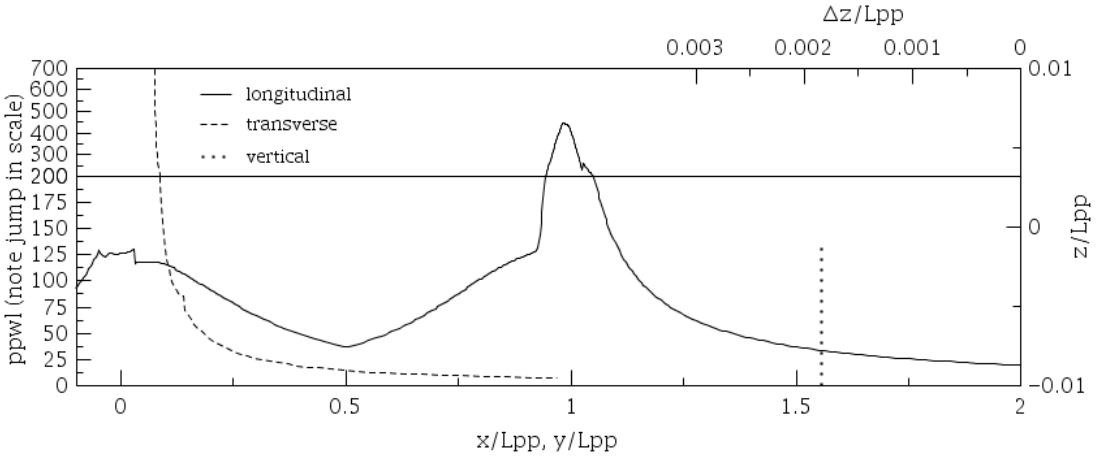

MARIN-PARNASSOS

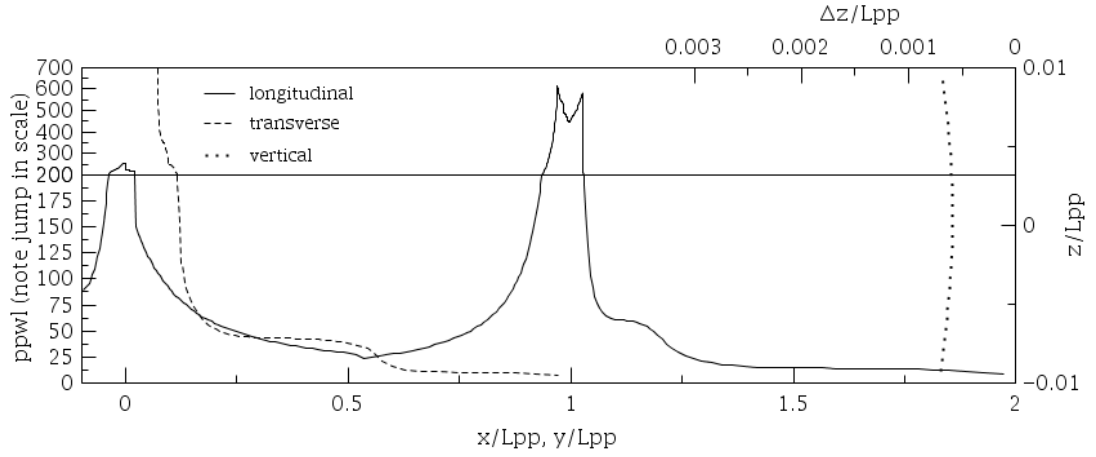

MOERI-WAVIS

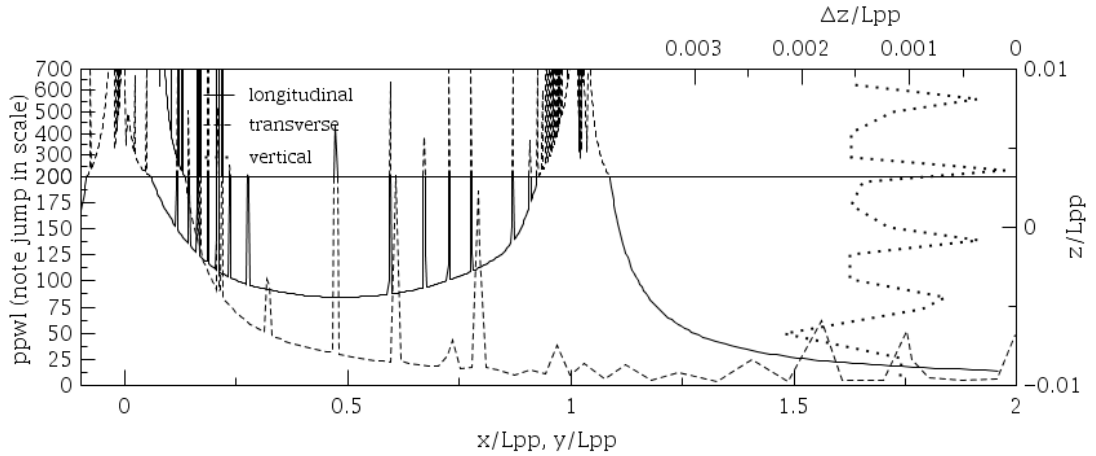

NMRI-SURF

Fig. 2.1-8 Grid density distribution along the waterline (solid), and in transverse (dashed) and vertical (dotted) directions at mid-ship

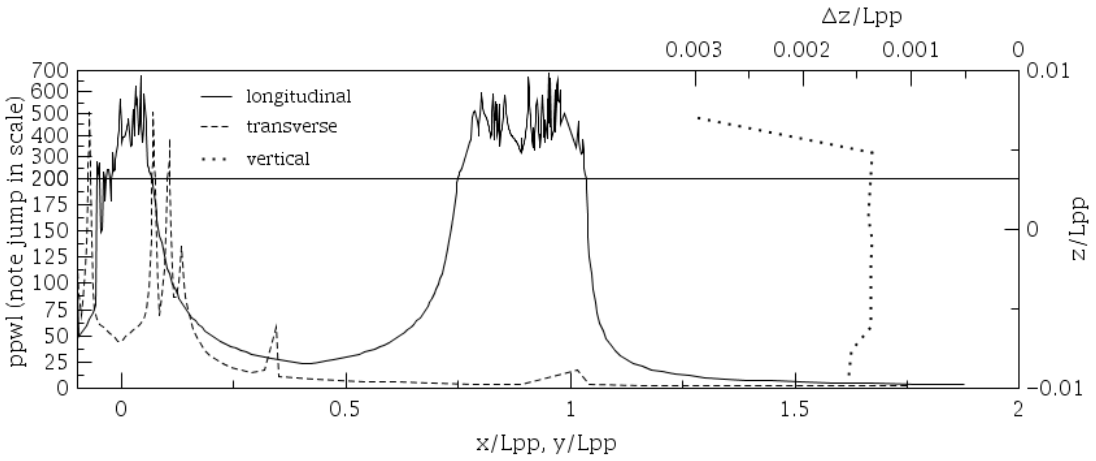

SNUTT-FLUENT6.3

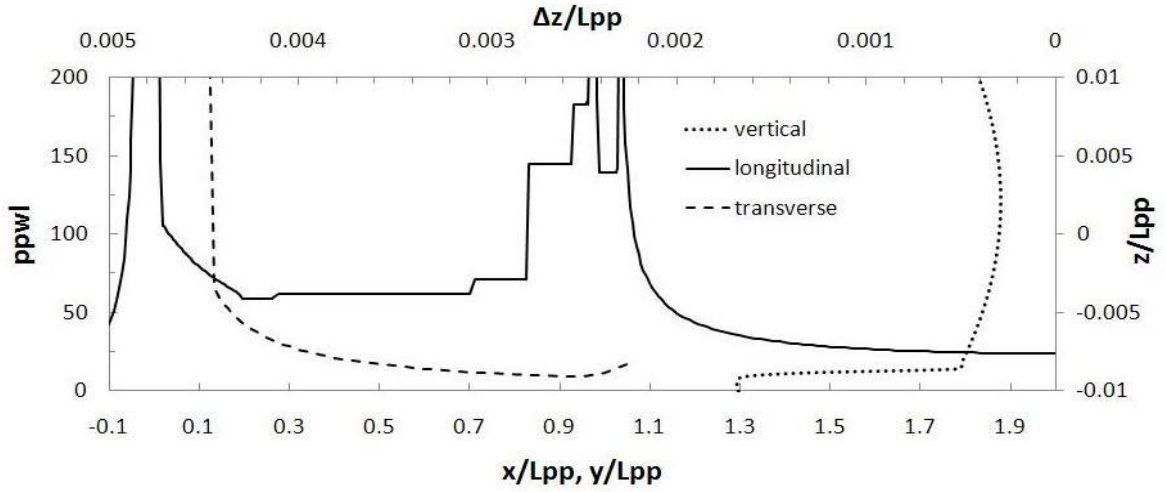

Southampton-CFX (BSL)

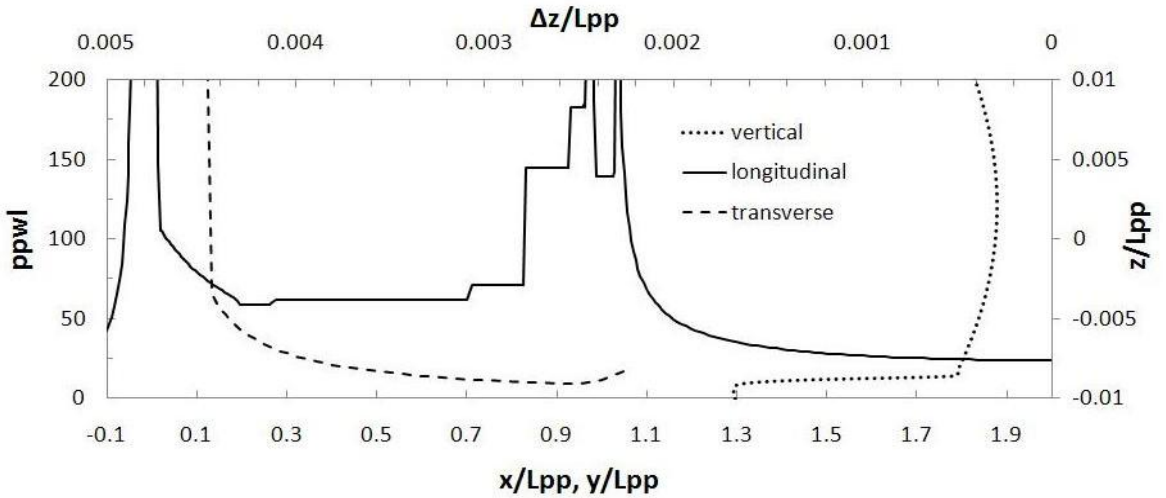

Southampton-CFX (SST)

Fig. 2.1-8 Grid density distribution along the waterline (solid), and in transverse (dashed) and vertical (dotted) directions at mid-ship

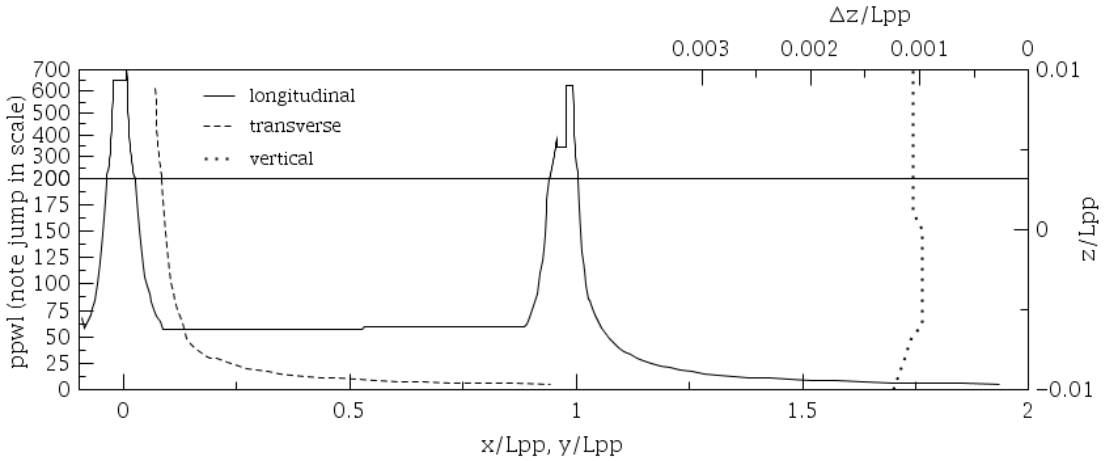

SSRC-FLUENT12.1

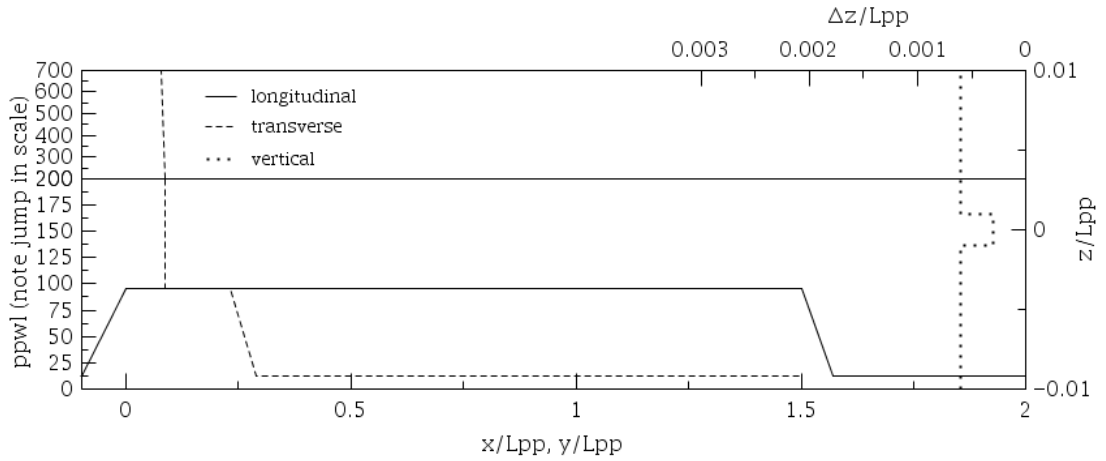

SVA-CFX12

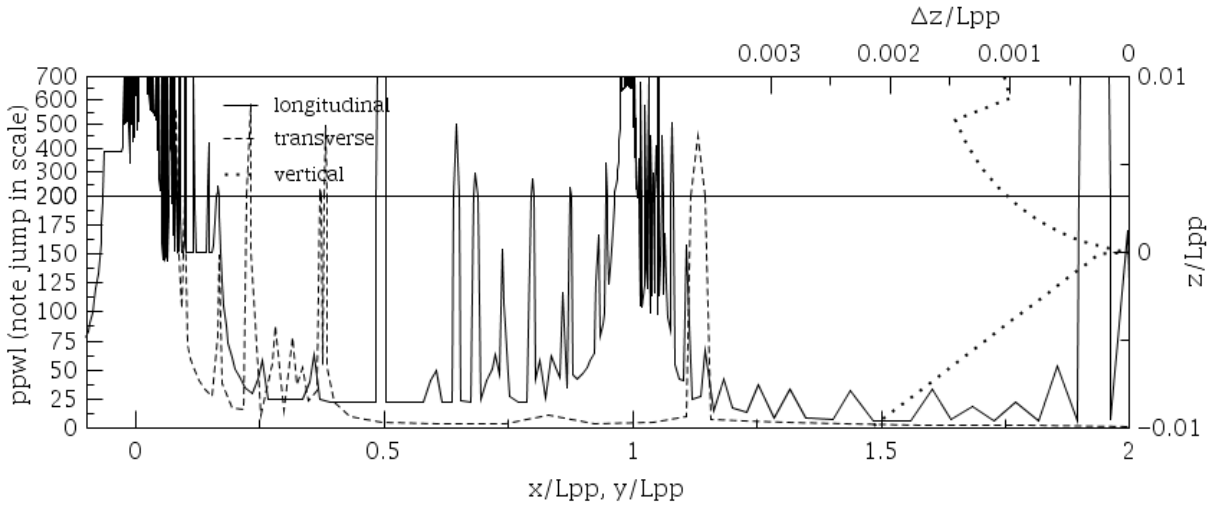

TUHH&ANSYS-CFX12.1

Fig. 2.1-8 Grid density distribution along the waterline (solid), and in transverse (dashed) and vertical (dotted) directions at mid-ship

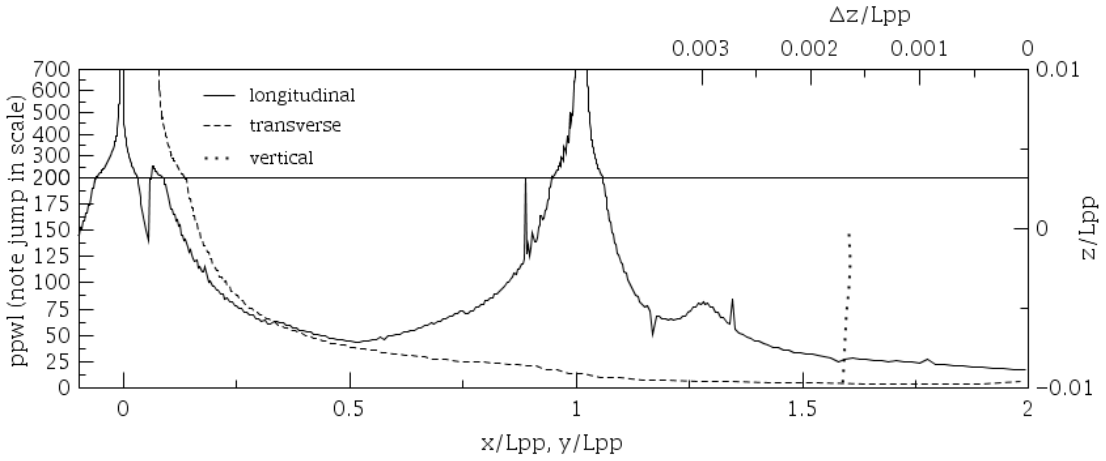

VTT-FINFLO

Fig. 2.1-8 Grid density distribution along the waterline (solid), and in transverse (dashed) and vertical (dotted) directions at mid-ship

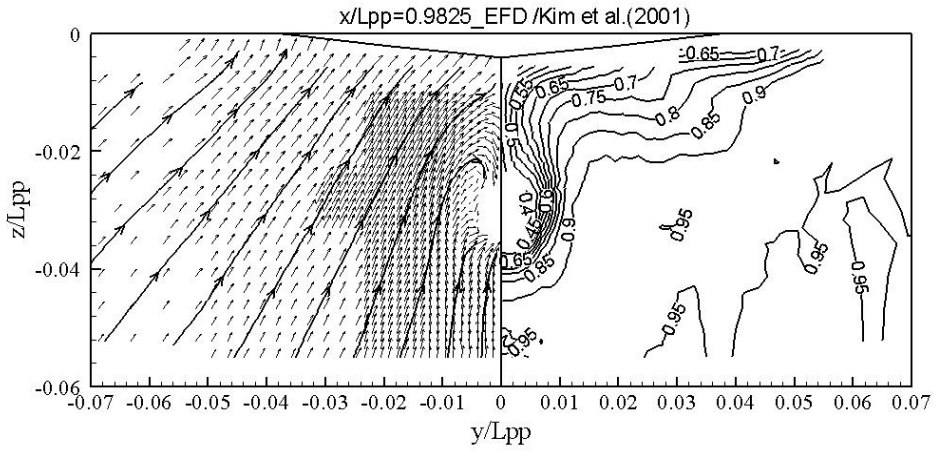

Experiment (MOERI, Kim et al. 2001)

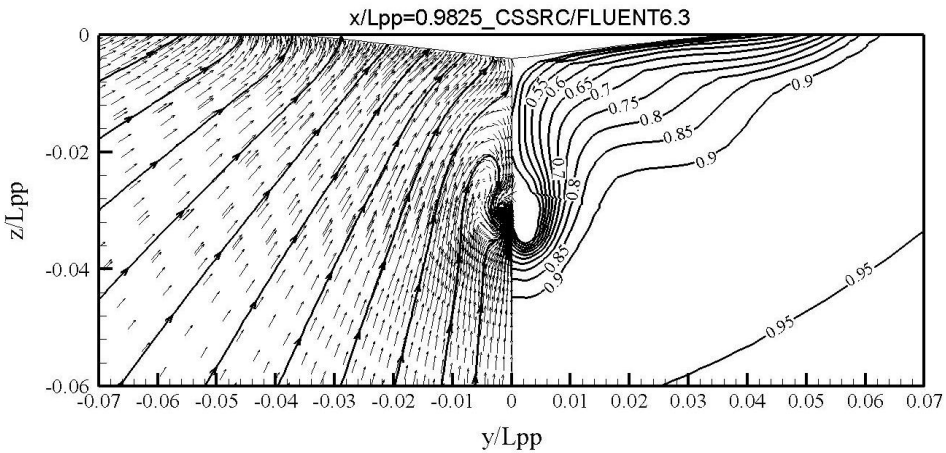

CSSRC-Fluent6.3

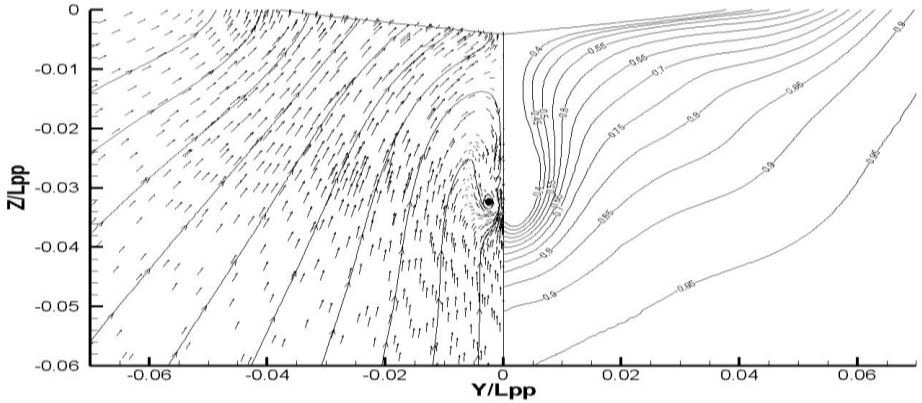

ECN/BEC/HO-Icare

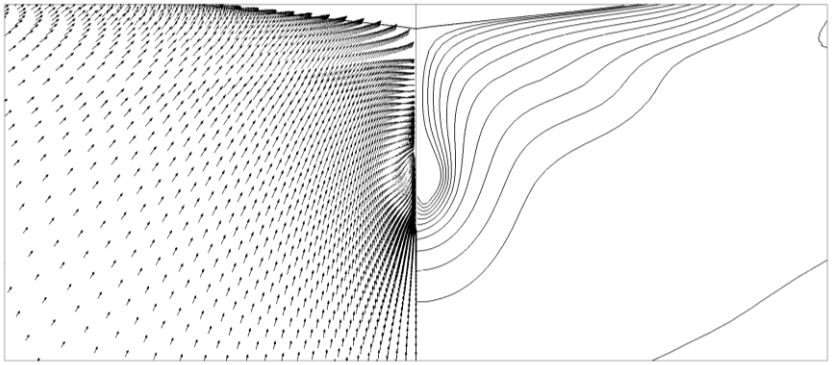

FLOWTECH-SHIPFLOW-VOF-4.3

Fig. 2.1-9 Cross flow vectors and streamlines (left panel), axial velocity contours (right panel) at propeller plane (x/L_{PP} = 0.9825) [ΔU = 0.05]

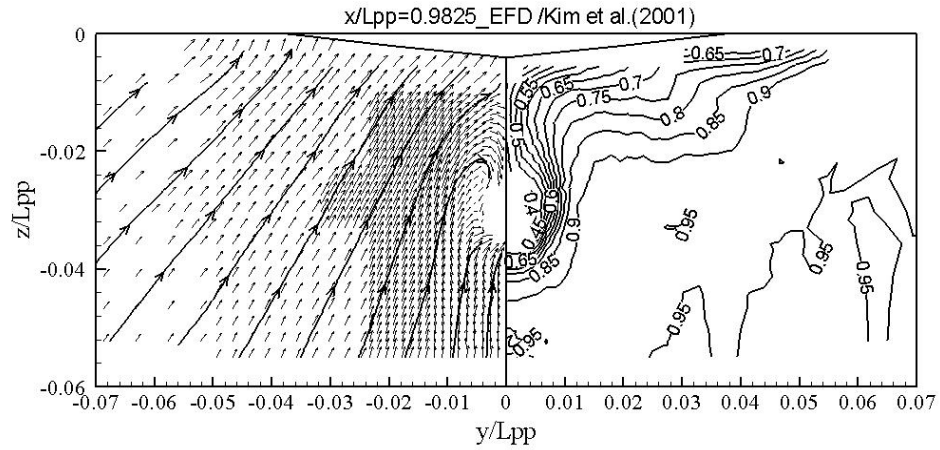

Experiment (MOERI, Kim et al. 2001)

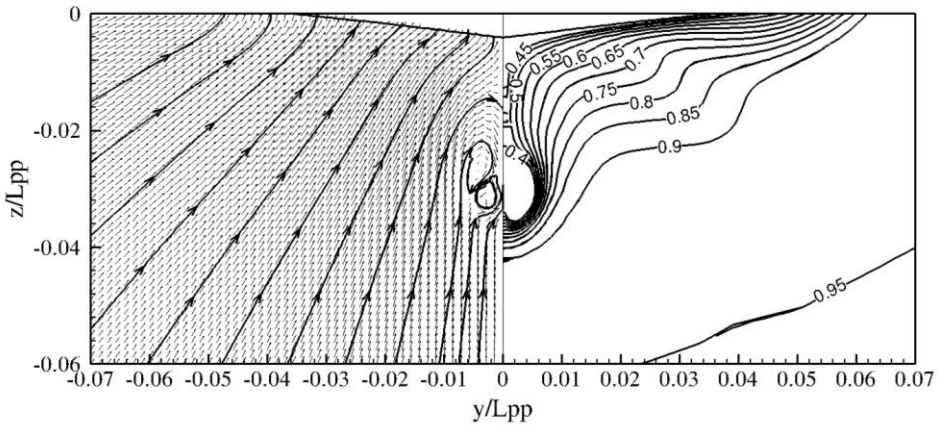

IIHR-CFDShipIowaV4.0 (DES)

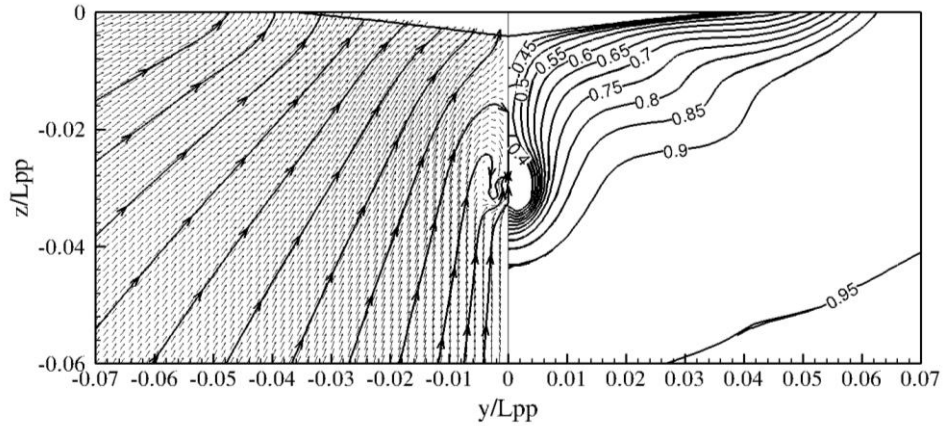

IIHR-CFDShipIowaV4.0 (RANS)

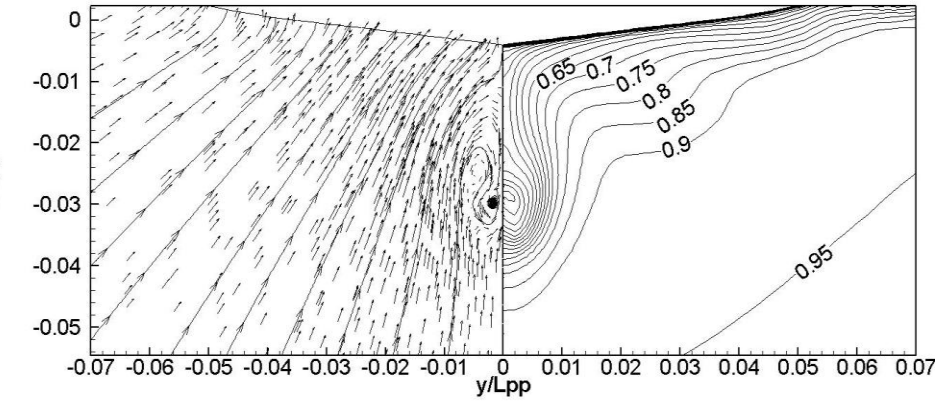

IIHR/SJTU-FLUENT12.0.16

Fig. 2.1-9 Cross flow vectors and streamlines (left panel), axial velocity contours (right panel) at propeller plane (x/L_{pp} = 0.9825) [ΔU = 0.05]

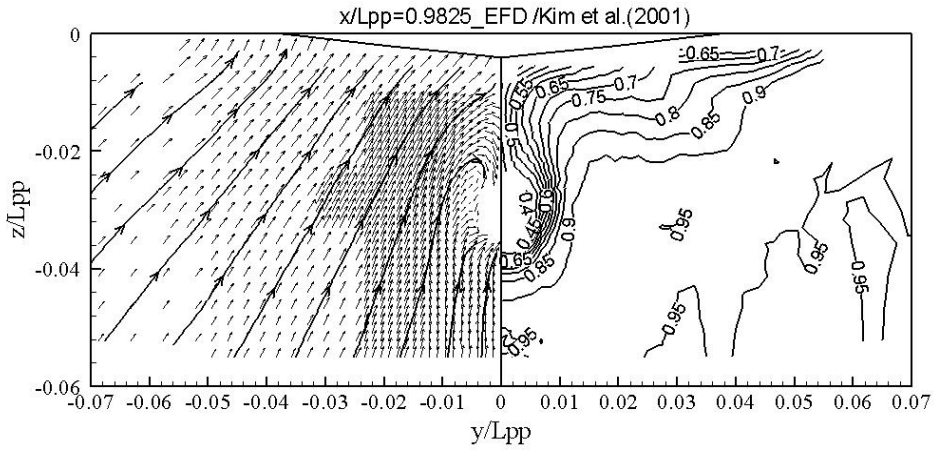

Experiment (MOERI, Kim et al. 2001)

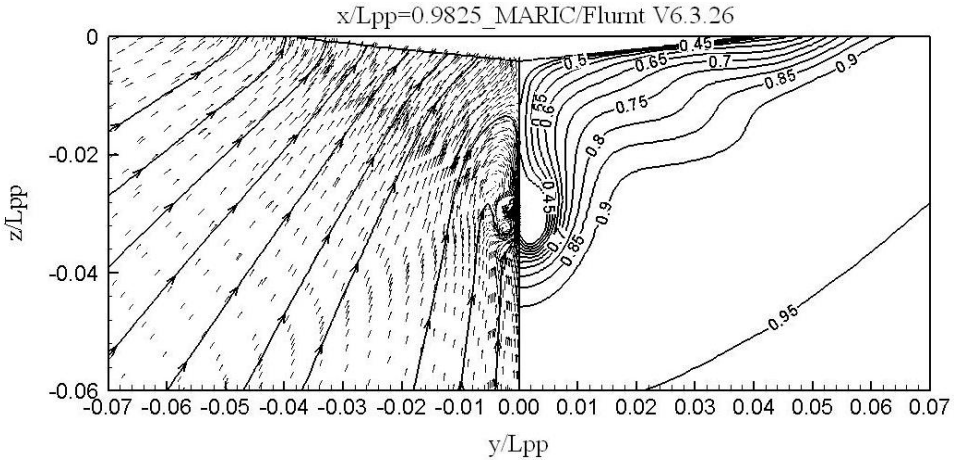

MARIC-FLUENT6.3

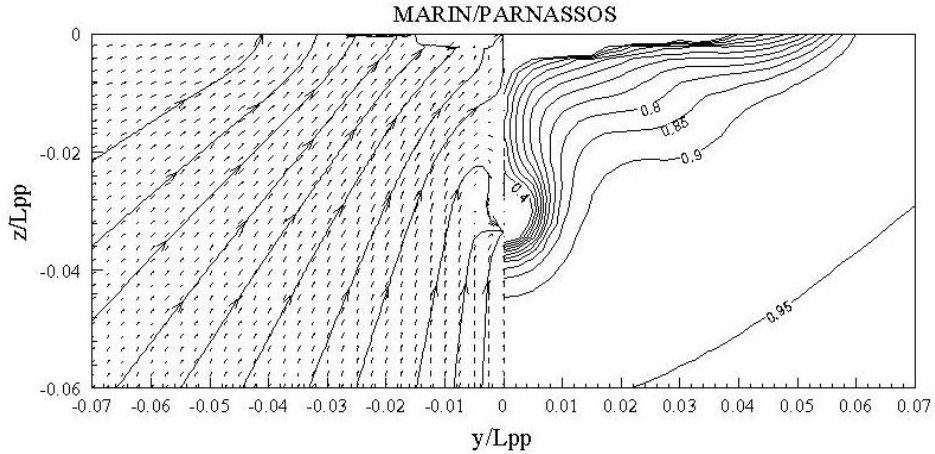

MARIN-PARNASSOS

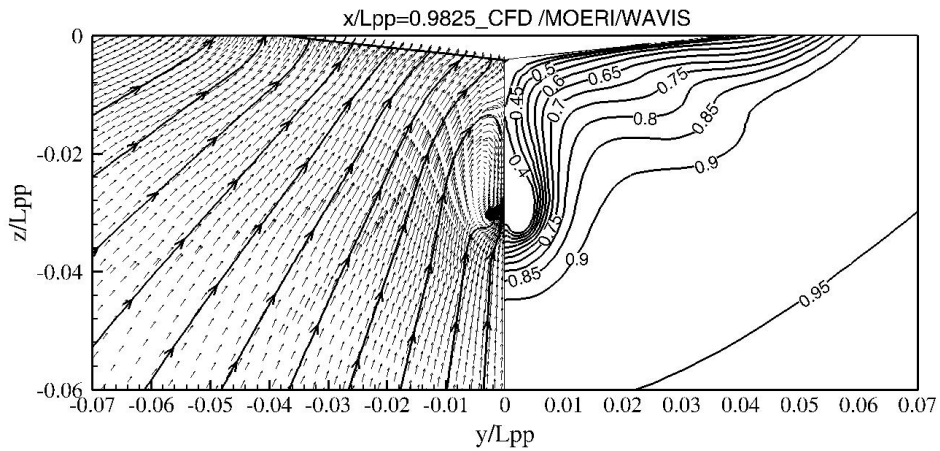

MOERI-WAVIS

Fig. 2.1-9 Cross flow vectors and streamlines (left panel), axial velocity contours (right panel) at propeller plane (x/L_{PP} = 0.9825) [ΔU = 0.05]

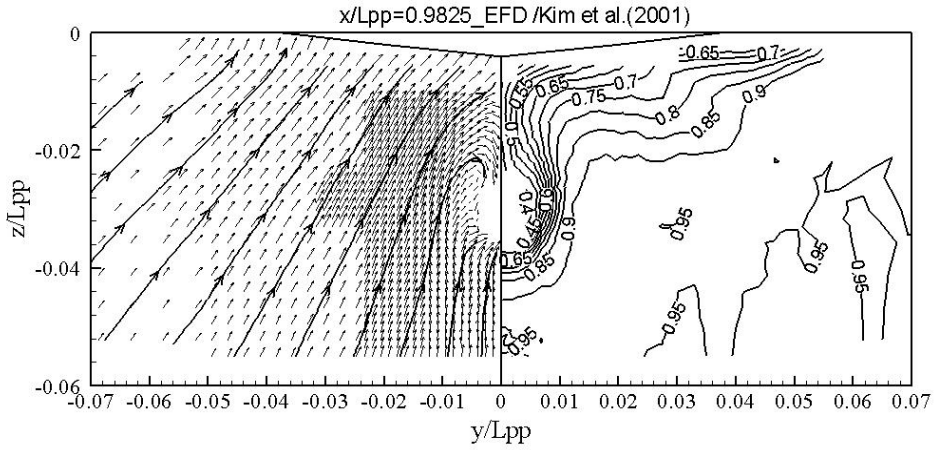

Experiment (MOERI, Kim et al. 2001)

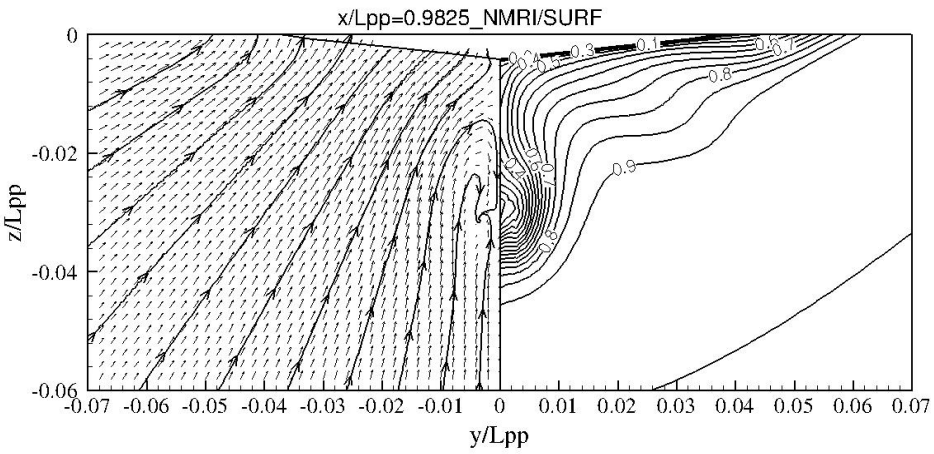

NMRI-SURF

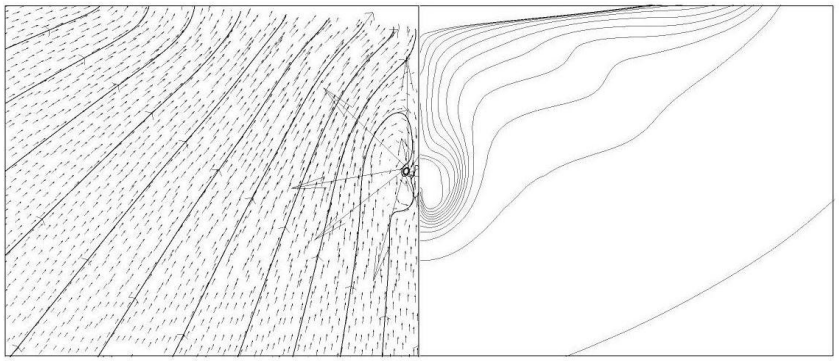

Southampton-CFX (BSL)

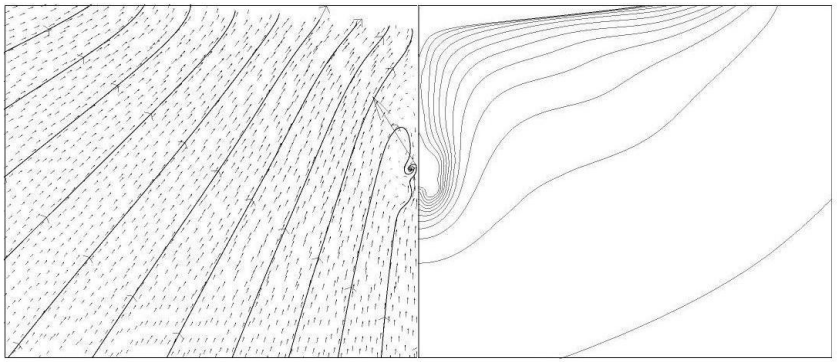

Southampton-CFX (SST)

Fig. 2.1-9 Cross flow vectors and streamlines (left panel), axial velocity contours (right panel) at propeller plane (x/L_{pp} = 0.9825) [ΔU = 0.05]

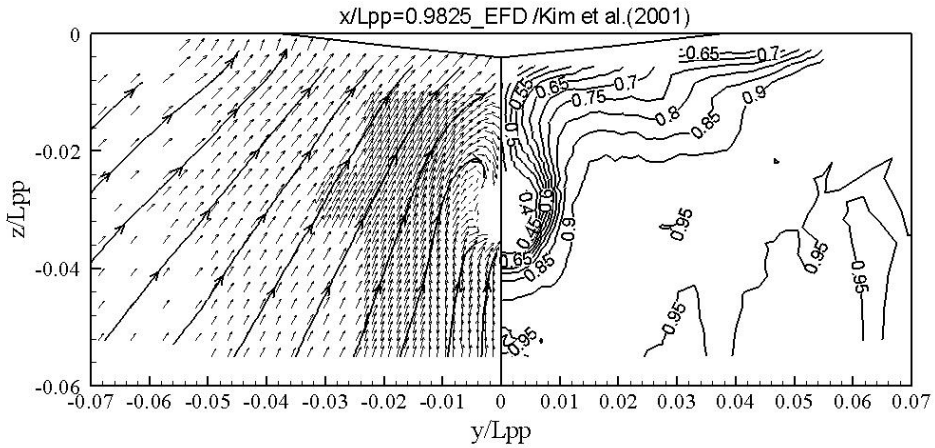

Experiment (MOERI, Kim et al. 2001)

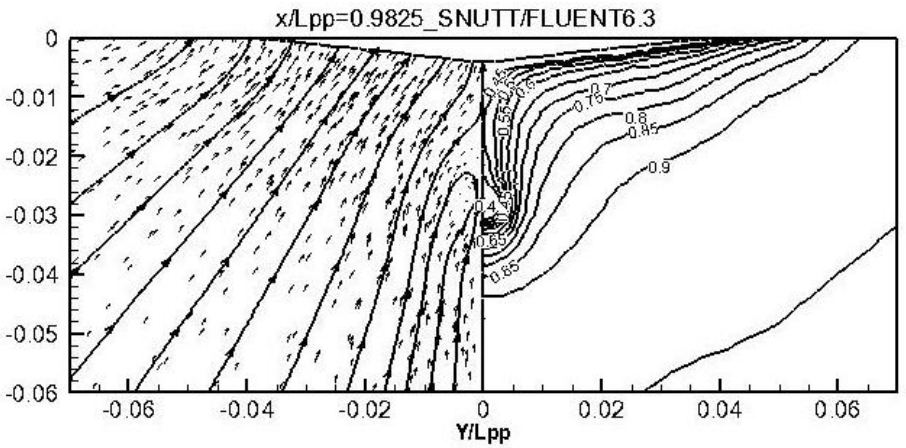

SNUTT-FLUENT6.3

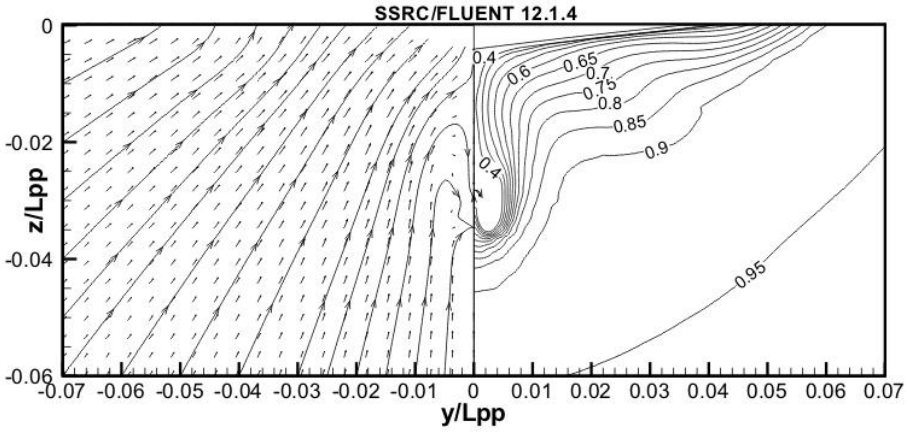

SSRC-FLUENT12.1

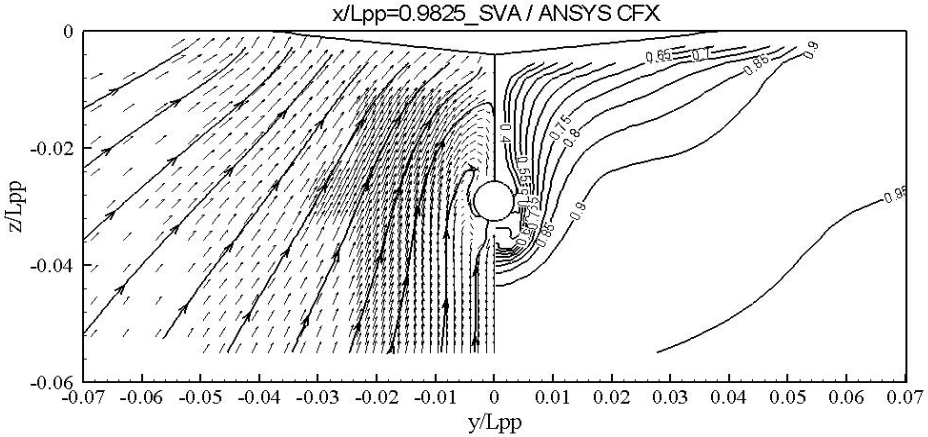

SVA-CFX12

Fig. 2.1-9 Cross flow vectors and streamlines (left panel), axial velocity contours (right panel) at propeller plane (x/L_{PP} = 0.9825) [ΔU = 0.05]

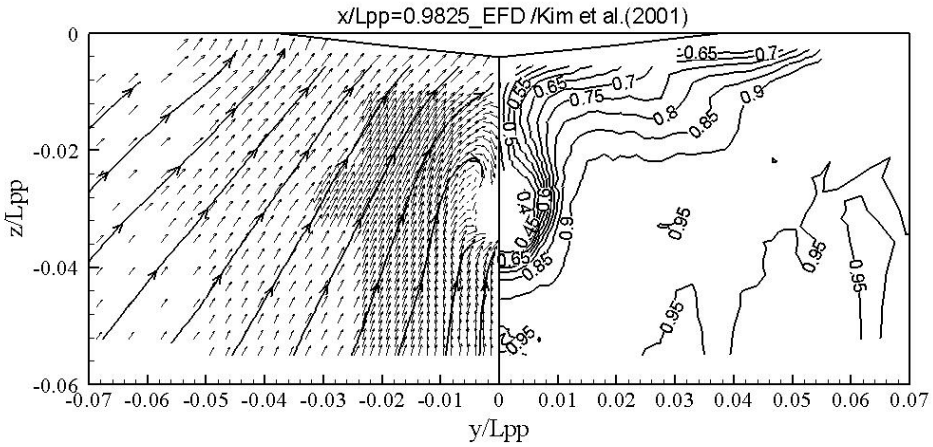

Experiment (MOERI, Kim et al. 2001)

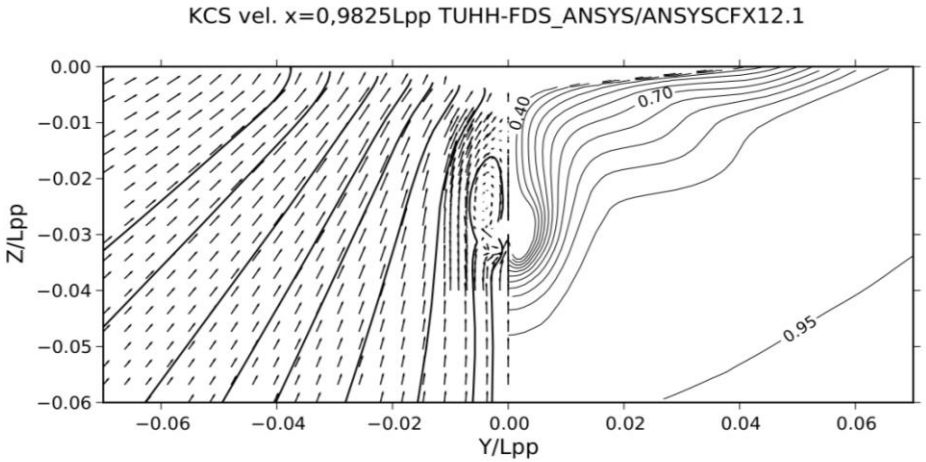

TUHH&ANSYS-CFX12.1

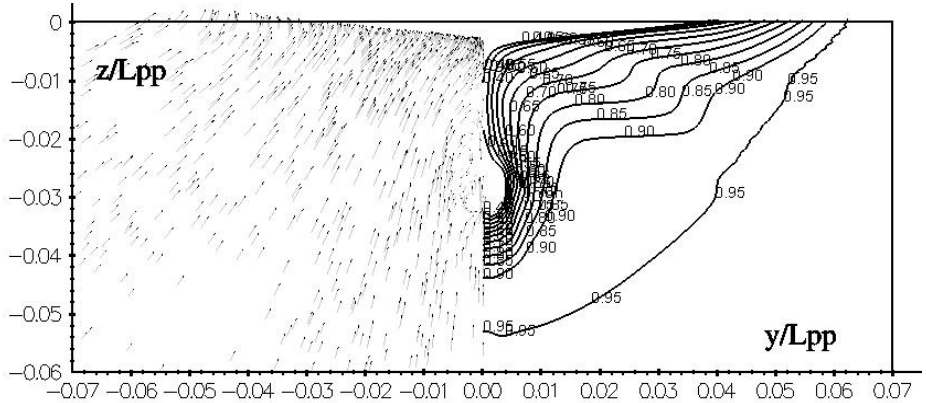

VTT-FINFLO

Fig. 2.1-9 Cross flow vectors and streamlines (left panel), axial velocity contours (right panel) at propeller plane (x/L_{pp} = 0.9825) [ΔU = 0.05]

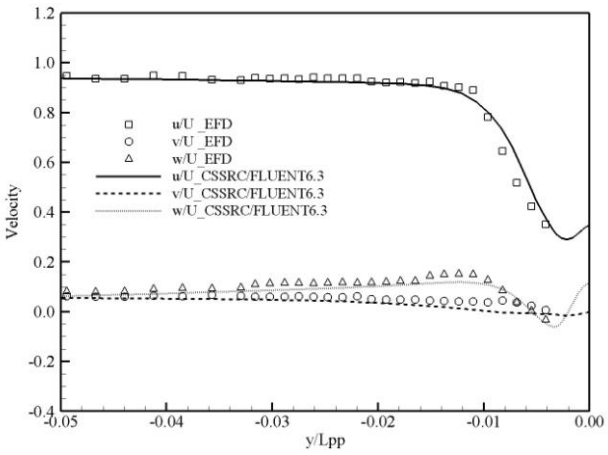

CSSRC-Fluent6.3

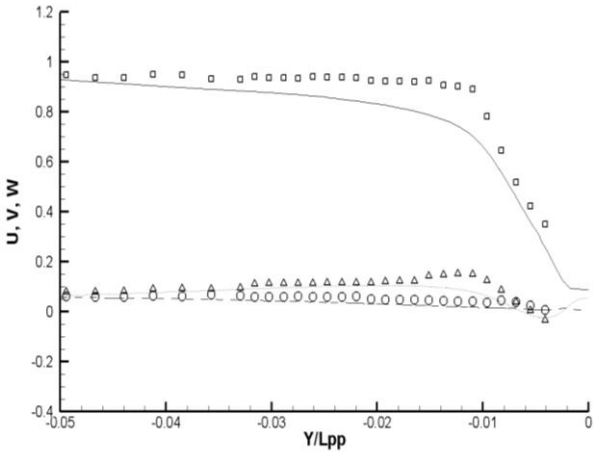

ECN/BEC/HO-Icare

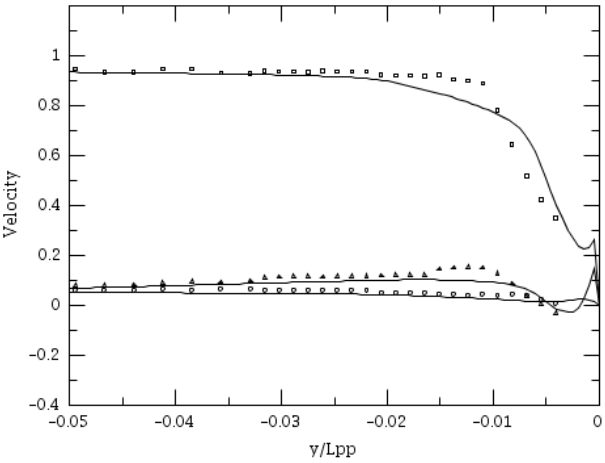

FLOWTECH-SHIPFLOW-VOF-4.3

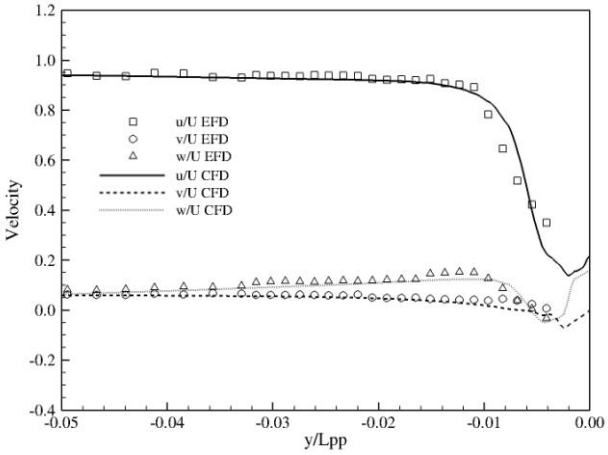

IIHR-CFDShipIowaV4.0 (DES)

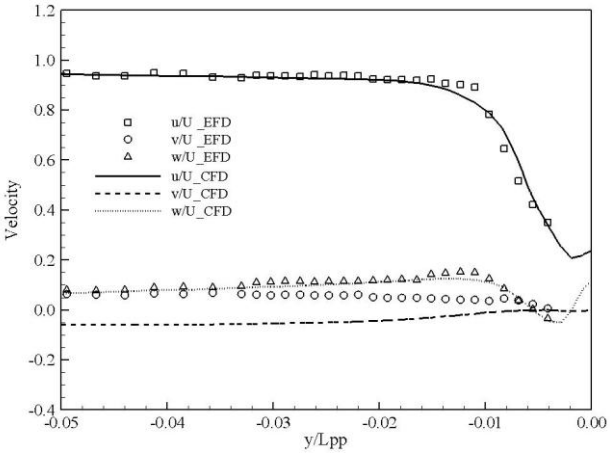

IIHR/SJTU-FLUENT12.0.16

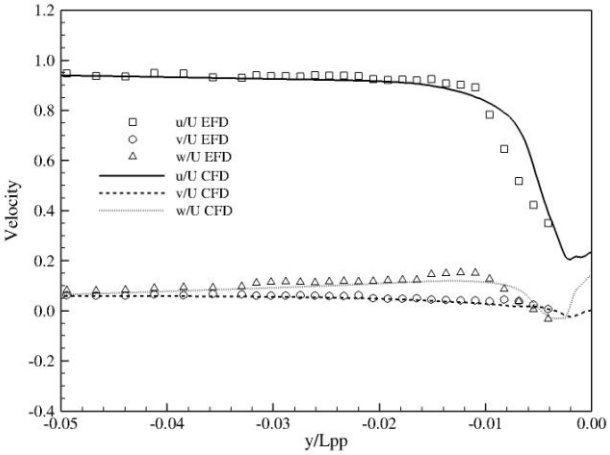

IIHR-CFDShipIowaV4.0 (RANS)

Fig. 2.1-10 Velocity on the propeller plane (x/L_{PP} = 0.9825) at z/L_{PP} = -0.0302

(u/U: CFD solid line; EFD open squares
v/U: CFD dashed line; EFD open circles
w/U: CFD dotted line; EFD open)

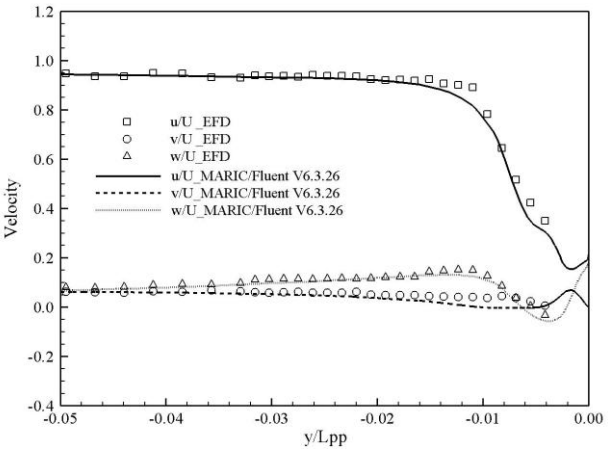

MARIC-FLUENT6.3

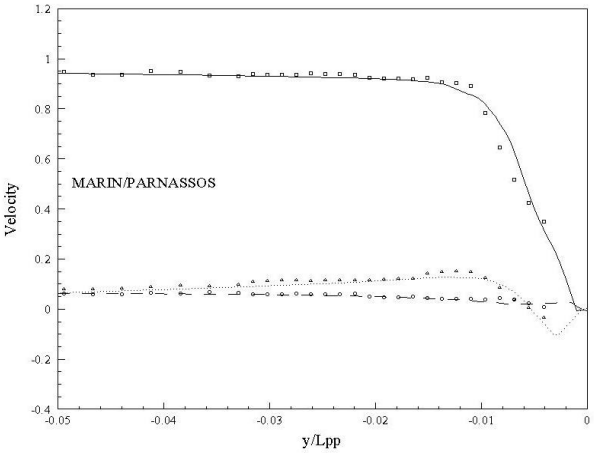

MARIN-PARNASSOS

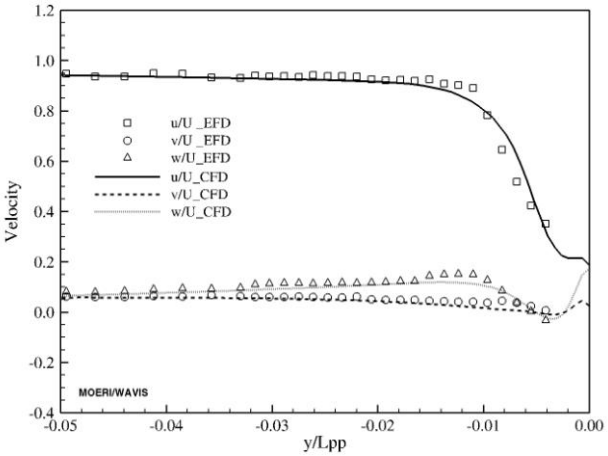

MOERI-WAVIS

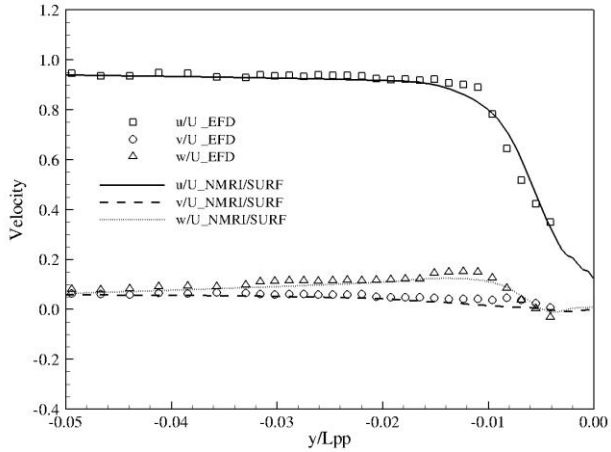

NMRI-SURF

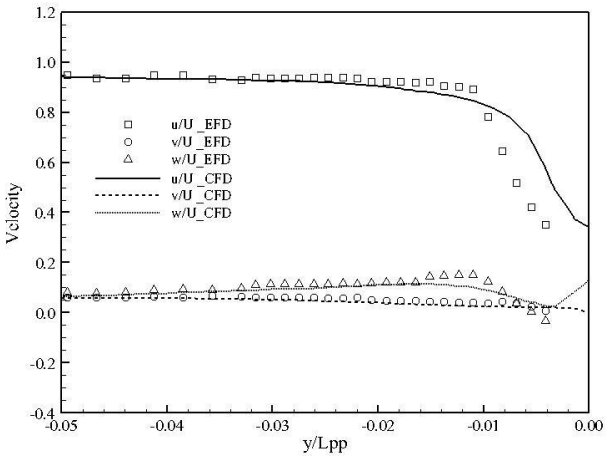

SNUTT-FLUENT6.3

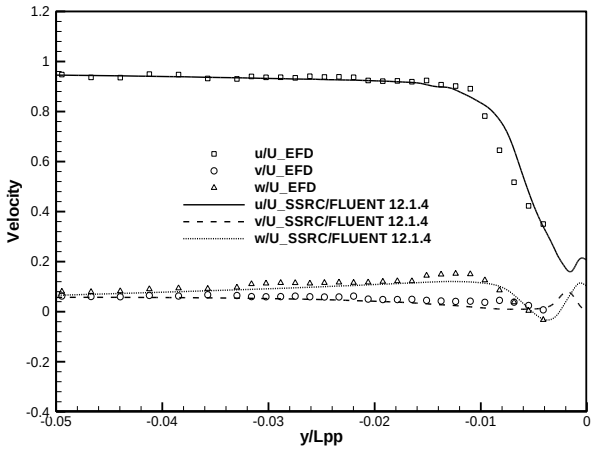

SSRC-FLUENT12.1

Fig. 2.1-10 Velocity on the propeller plane (x/L_{PP} = 0.9825) at z/L_{PP} = -0.0302

(u/U: CFD solid line; EFD open squares
v/U: CFD dashed line; EFD open circles
w/U: CFD dotted line; EFD open)

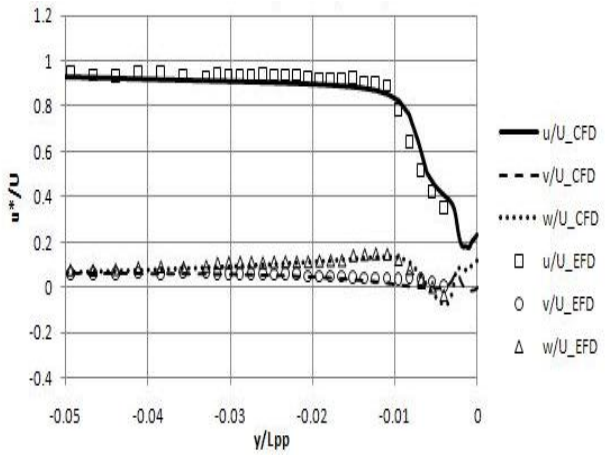

Southampton-CFX (BSL)

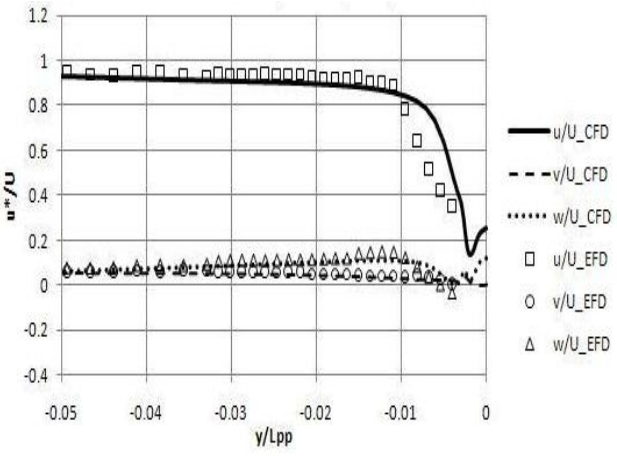

Southampton-CFX (SST)

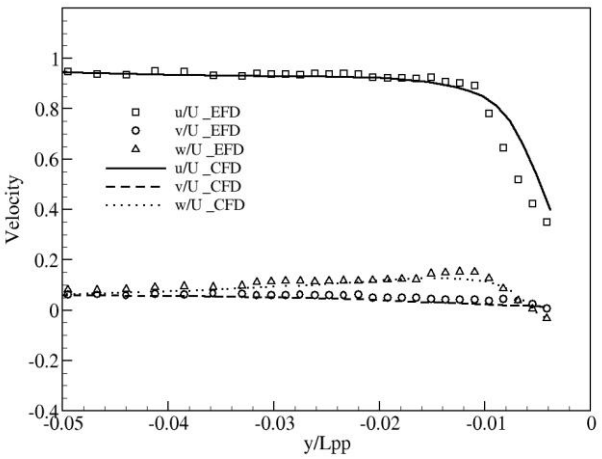

SVA-CFX12

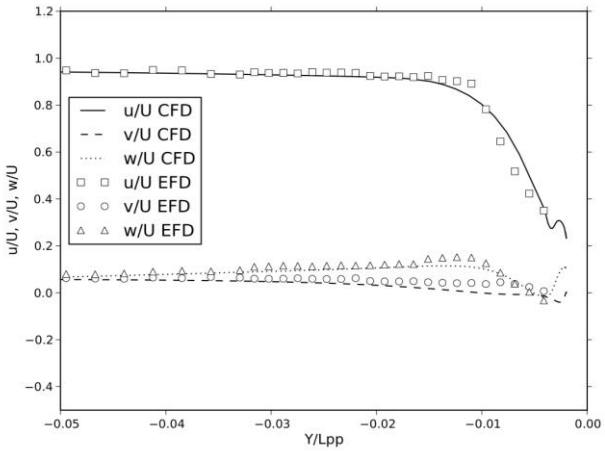

TUHH&ANSYS-CFX12.1

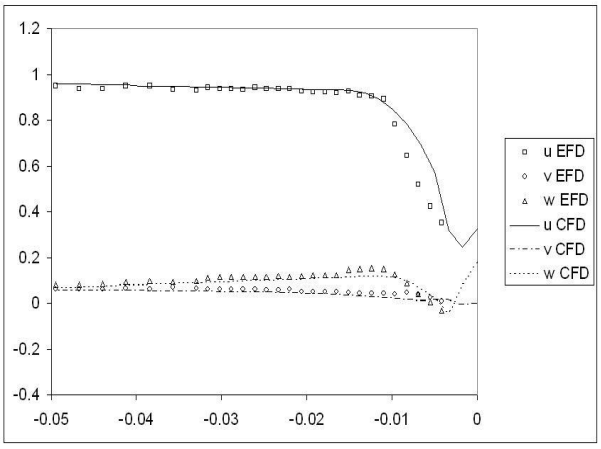

VTT-FINFLO

Fig. 2.1-10 Velocity on the propeller plane (x/L_{PP} = 0.9825) at z/L_{PP} = -0.0302

(*u*/*U*: CFD solid line; EFD open squares
v/*U*: CFD dashed line; EFD open circles
w/*U*: CFD dotted line; EFD open)

Test Case 2.2a

Table 2-2a-0 Computations information and V&V method
Table 2-2a-1 Computed C_T, C_F and C_{PV} of different grid densities
Table 2-2a-2 V&V results for C_T, C_F and C_{PV}

Table 2-2a-0: Computations information and V&V method

Organization (Code)	**V&V method (including the determination of U_I)**
CDadapco (STARCCM+)	The coarse, medium and fine mesh had 544138, 1220966 and 2997355 control volumes, respectively. The mesh base sizes were 0.1125, 0.075 and 0.05 m, respectively (refinement ratio 1.5). The prism layer along walls was on average 20 mm thick, contained 6 cell layers and the near-wall cell was 0.9 mm thick. The k-epsilon turbulence model with wall functions was used. The pressure drag reduces monotonically with grid refinement, but friction drag first increases and then decreases, so Richardson extrapolation cannot be used.
CSSRC (FLUENT6.3)	The V&V is based on ITTC - Quality Manual 7.5-03-01-01, CFD General "Uncertainty Analysis in CFD Verification and Validation Methodology and Procedures" RG=ε21/ε32=0.12, Richardson Extrapolation can be used to compute the error for the fine grid $\delta^*_{RE_G} = \frac{\varepsilon_{21}}{r_G^{P_G} - 1}$, $P_G = \frac{\ln(\varepsilon_{32}/\varepsilon_{21})}{\ln r_G}$, $C_G = \frac{r_G^{P_G} - 1}{r_G^{P_{Gest}} - 1}$, $U_G = \left\|C_G \delta^*_{RE_G}\right\| + \left\|(1 - C_G)\delta^*_{RE_G}\right\|$, $U_{SN} = \sqrt{U_G^2 + U_I^2}$, $U_V = \sqrt{U_{SN}^2 + U_D^2}$
GL&UDE (Comet)	-
GL&UDE (OpenFOAM)	-
MARIC (FLUENT6.3)	The V&V is based on ITTC - Quality Manual 7.5-03-01- 01, "Verification and Validation of CFD Simulations" U_I is determined due to oscillatory iterative convergence with S_Upper and S_Lower - for the finest grid U_I=0.3*10^{-4} U_G is based on half the solution range of the upper and lower bounds of solution oscillation U_G =0.5*(S_U-S_L)
MOERI (WAVIS)	-
SVA (CFX12)	The rudder is not included in the calculations No systematic grid refinement, tetra/prism mesher grid refinment factor approximately 3 between GRID2 and GRID3 and factor 1.8 between GRID1 and GRID2 U_I uncertainty on basis of S_Upper and S_Lower for C_F : U_I =0.0, for C_{PV} : U_I =0.0005 and for C_T : U_I =0.0005
TUHH&ANSYS (ANSYS-FX12.1)	U_I is determined due to oszillatory iterative convergence with S_Upper and S_Lower $U_I = \left\|\frac{1}{2}\left(S_{Lower} - S_{Upper}\right)\right\|$ For the determination of U_G the values for C_K and $\delta_{RE,\,k1}$ have to be calculated

Table 2-2a-1: Computed C_T, C_F and C_{PV} of different grid densities

Organization (Code)	r_G		C_T ($\times 10^{-3}$)					C_F ($\times 10^{-3}$)					C_{PV} ($\times 10^{-3}$)				
			Grid #5	Grid #4	Grid #3	Grid #2	Grid #1	Grid #5	Grid #4	Grid #3	Grid #2	Grid #1	Grid #5	Grid #4	Grid #3	Grid #2	Grid #1
EFD (MOERI)		*D*	3.557					-					-				
CDadapco (STARCCM+)	1.5	*S*	-	-	3.568	3.574	3.561	-	-	2.873	2.911	2.909	-	-	0.695	0.663	0.652
		E%D	-	-	-0.31	-0.48	-0.11										
CSSRC (FLUENT6.3)	$\sqrt{2}$	*S*	-	-	3.756	3.639	3.625	-	-	-	-	-	-	-	-	-	-
		E%D	-	-	-5.59	-2.31	-1.91										
GL&UDE (Comet)	-	*S*	-	-	-	3.706	3.618	-	-	-	2.872	2.879	-	-	-	0.834	0.739
		E%D	-	-	-	-4.19	-1.71										
GL&UDE (OpenFOAM)	-	*S*	-	-	-	4.000	3.544	-	-	-	2.842	2.856	-	-	-	1.158	0.688
		E%D	-	-	-	-12.45	0.37										
MARIC (FLUENT6.3)	1.414	*S*	-	3.935	3.645	3.660	3.650	-	2.812	2.750	2.830	2.890	-	1.123	0.895	0.830	0.760
		E%D	-	-10.63	-2.47	-2.90	-2.62										
MOERI (WAVIS)	$\sqrt{2}$	*S*	-	-	3.696	3.581	3.564	-	-	2.770	2.809	2.808	-	-	0.926	0.772	0.756
		E%D	-	-	-3.91	-0.67	-0.20										
SVA (CFX12)	-	*S*	-	-	3.990	3.770	3.650	-	-	2.553	2.555	2.585	-	-	1.437	1.215	1.065
		E%D	-	-	-12.17	-5.99	-2.61										
TUHH&ANSYS (CFX12.1)	1.5	*S*	-	-	3.410	3.590	3.602	-	-	2.995	2.989	2.972	-	-	0.416	0.601	0.630
		E%D	-	-	4.13	-0.92	-1.26										

$E\%D = (D\text{-}S)/D \times 100$

Table 2-2a-2: V&V results for C_T, C_F and C_{PV}

Organization (Code)	r_G	C_T						C_F						C_{PV}					
		ε_{12} %S_1	$\frac{U_I}{\varepsilon_{12}}$	$\frac{P_G}{P_{G,th}}$	U_G %S_1	U_D %D	U_V%	ε_{12} %S_1	$\frac{U_I}{\varepsilon_{12}}$	$\frac{P_G}{P_{G,th}}$	U_G %S_1	U_D %D	U_V%	ε_{12} %S_1	$\frac{U_I}{\varepsilon_{12}}$	$\frac{P_G}{P_{G,th}}$	U_G %S_1	U_D %D	U_V%
CDadapco (STARCCM+)	1.5	0.37	-	-	-	1.0	-	0.07	-	-	-			1.69	-	-	-		
CSSRC (FLUENT6.3)	$\sqrt{2}$	-0.39	24.640	3.060	0.76		9.80	-	-	-	-			-	-	-	-		
GL&UDE (Comet)	-	2.43	-	-	-		-	-0.24	-	-	-			12.86	-	-	-		
GL&UDE (OpenFOAM)	-	12.87	-	-	-		-	0.49	-	-	-			68.31	-	-	-		
MARIC (FLUENT6.3)	1.414	0.27	-0.030	-	3.97		9.42	-	-	-	-			-	-	-	-		
MOERI (WAVIS)	$\sqrt{2}$	0.48	0.000	2.758	0.87		1.33	0.04	0.000	5.285	0.07			2.12	0.000	3.267	3.99		
SVA (CFX12)	-	-3.29	-1.52E-04	-	-		-	1.16	0	-	-			-14.08	-3.55E-05	-	-		
TUHH&ANSYS (CFX12.1)	1.5	0.34	0.001	3.323	0.02		1.00	0.58	0.000	-1.326	4.19			4.64	0.000	2.333	0.82		

$\varepsilon_{12}\%S_1 = |(S_1\text{-}S_2)/S_1|\times 100$; $U_{SN} = \sqrt{U_I^2 + U_G^2}$; $U_V = \sqrt{U_D^2 + U_{SN}^2}$

Test Case 2.2b

Table 2.2b-0 Computations information and V&V method
Table 2.2b-1-1 Computed C_T, C_F, C_{PV} of different grid densities at Fr = 0.1083
Table 2.2b-1-2 V&V results for C_T, C_F and C_{PV} at Fr = 0.1083
Table 2.2b-1-3 Computed Sinkage (σ) and Trim (τ) of different grid densities at Fr = 0.1083
Table 2.2b-1-4 V&V results for Sinkage (σ) and Trim (τ) at Fr = 0.1083
Table 2.2b-1-5 Computed C_T, C_F, C_{PV} of different grid densities at Fr = 0.1516
Table 2.2b-1-6 V&V results for C_T, C_F and C_{PV} at Fr = 0.1516
Table 2.2b-1-7 Computed Sinkage (σ) and Trim (τ) of different grid densities at Fr = 0.1516
Table 2.2b-1-8 V&V results for Sinkage (σ) and Trim (τ) at Fr = 0.1516
Table 2.2b-1-9 Computed C_T, C_F, C_{PV} of different grid densities at Fr = 0.1949
Table 2.2b-1-10 V&V results for C_T, C_F and C_{PV} at Fr = 0.1949
Table 2.2b-1-11 Computed Sinkage (σ) and Trim (τ) of different grid densities at Fr = 0.1949
Table 2.2b-1-12 V&V results for Sinkage (σ) and Trim (τ) at Fr = 0.1949
Table 2.2b-1-13 Computed C_T, C_F, C_{PV} of different grid densities at Fr = 0.2274
Table 2.2b-1-14 V&V results for C_T, C_F and C_{PV} at Fr = 0.2274
Table 2.2b-1-15 Computed Sinkage (σ) and Trim (τ) of different grid densities at Fr = 0.2274
Table 2.2b-1-16 V&V results for Sinkage (σ) and Trim (τ) at Fr = 0.2274
Table 2.2b-1-17 Computed C_T, C_F, C_{PV} of different grid densities at Fr = 0.2599
Table 2.2b-1-18 V&V results for C_T, C_F and C_{PV} at Fr = 0.2599
Table 2.2b-1-19 Computed Sinkage (σ) and Trim (τ) of different grid densities at Fr = 0.2599
Table 2.2b-1-20 V&V results for Sinkage (σ) and Trim (τ) at Fr = 0.2599
Table 2.2b-1-21 Computed C_T, C_F, C_{PV} of different grid densities at Fr = 0.2816
Table 2.2b-1-22 V&V results for C_T, C_F and C_{PV} at Fr = 0.2816
Table 2.2b-1-23 Computed Sinkage (σ) and Trim (τ) of different grid densities at Fr = 0.2816
Table 2.2b-1-24 V&V results for Sinkage (σ) and Trim (τ) at Fr = 0.2816

Figure 2.2b-2 Total resistance Coefficients (C_T) versus Fr
Figure 2.2b-3 Sinkage (σ) versus Fr
Figure 2.2b-4 Trim (τ) versus Fr

Table 2.2b-0: Computations information and V&V method

Organization (Code)	**V&V method (including the determination of U_I)**
CDadapco (STAR-CCM+)	The results obtained on different grids do not show monotonous convergence towards grid-independent results, so no reliable estimation of discretization errors by Richardson extrapolation is possible.
CSSRC (FLUENT6.3)	-
GL&UDE (Comet)	-
GL&UDE (OpenFOAM)	-
MOERI (WAVIS)	-
Southampton/QinetiQ (CFX12)	-

Table 2.2b-1-1: Computed C_T, C_F, C_{PV} of different grid densities at Fr = 0.1083

Organization (Code)	r_G		C_T ($\times 10^{-3}$)					C_F ($\times 10^{-3}$)					C_{PV} ($\times 10^{-3}$)				
			Grid #5	Grid #4	Grid #3	Grid #2	Grid #1	Grid #5	Grid #4	Grid #3	Grid #2	Grid #1	Grid #5	Grid #4	Grid #3	Grid #2	Grid #1
EFD (MOERI)	-	*D*	3.796					-					-				
CDadapco (STAR-CCM+)	-	*S*	-	-	-	-	-	-	-	-	-	-	-	-	-	-	-
		E%D	-	-	-	-	-										
CSSRC (FLUENT6.3)	-	*S*	-	-	-	-	3.777	-	-	-	-	3.303	-	-	-	-	0.474
		E%D	-	-	-	-	0.51										
GL&UDE (Comet)	-	*S*	-	-	-	3.836	3.691	--	-	-	3.293	3.297	-	-	-	0.543	0.394
		E%D	-	-	-	-1.05	2.77										
GL&UDE (OpenFOAM)	-	*S*	-	-	-	-	-	-	-	-	-	-	-	-	-	-	-
		E%D	-	-	-	-	-										
MOERI (WAVIS)	1.414	*S*	-	-	3.529	3.666	3.684	-	-	3.134	3.231	3.213	-	-	0.396	0.435	0.471
		E%D	-	-	7.03	3.42	2.94										
Southampton/QinetiQ (CFX12)	1.2	*S*	grid3 → grid1	-	3.860	3.824	3.786	-	-	-	-	-	-	-	-	-	-
		E%D		-	-1.70	-0.73	0.25										
		S	grid6 → grid4	-	4.039	3.978	3.908	-	-	-	-	-	-	-	-	-	-
		E%D		-	-6.41	-4.79	-2.95										

$E\%D = (D\text{-}S)/D \times 100$

Table 2.2b-1-2: V&V results for C_T, C_F and C_{PV} at $Fr = 0.1083$

Organization (Code)	r_G	C_T						C_F						C_{PV}					
		ε_{12} %S_1	$\frac{U_I}{\varepsilon_{12}}$	$\frac{P_G}{P_{G,th}}$	U_G %S_1	U_D %D	U_V%	ε_{12} %S_1	$\frac{U_I}{\varepsilon_{12}}$	$\frac{P_G}{P_{G,th}}$	U_G %S_1	U_D %D	U_V%	ε_{12} %S_1	$\frac{U_I}{\varepsilon_{12}}$	$\frac{P_G}{P_{G,th}}$	U_G %S_1	U_D %D	U_V%
CDadapco (STAR-CCM+)	-	-	-	-	-	1.0	-	-	-	-	-			-	-	-	-		
CSSRC (FLUENT6.3)	-	-	-	-	-		-	-	-	-	-			-	-	-	-		
GL&UDE (Comet)	-	-3.93	-	-	-		-	0.12	-	-	-			-37.82	-	-	-		
GL&UDE (OpenFOAM)	-	-	-	-	-		-	-	-	-	-			-	-	-	-		
MOERI (WAVIS)	1.414	0.50	0.000	2.902	0.92		1.36	0.55	0.000	2.462	0.97			7.58	0.000	0.157	65.98		
Southampton/QinetiQ (CFX12)	1.2	0.99	0.004	0.486	7.23		7.30	-	-	-	-			-	-	-	-		

$\varepsilon_{12}\%S_1 = |(S_1\text{-}S_2)/S_1| \times 100$; $U_{SN} = \sqrt{U_I^2 + U_G^2}$; $U_V = \sqrt{U_D^2 + U_{SN}^2}$

Table 2.2b-1-3: Computed Sinkage (σ) and Trim (τ) of different grid densities at Fr = 0.1083

Organization (Code)	r_G		Sinkage $\sigma\times10^2$ (m)					Trim τ °				
			Grid #5	Grid #4	Grid #3	Grid #2	Grid #1	Grid #5	Grid #4	Grid #3	Grid #2	Grid #1
EFD (MOERI)	-	*D*	-0.090					-0.017				
CDadapco (STAR-CCM+)	-	*S*	-	-	-	-	-	-	-	-	-	-
		E%D	-	-	-	-	-	-	-	-	-	-
CSSRC (FLUENT6.3)	-	*S*	-	-	-	-	-0.1500	-	-	-	-	-0.0230
		E%D	-	-	-	-	-66.67	-	-	-	-	-35.29
GL&UDE (Comet)	-	*S*	-	-	-	-0.1450	-0.1450	-	-	-	-0.0330	-0.0340
		E%D	-	-	-	-61.11	-61.11	-	-	-	-94.12	-100.00
GL&UDE (OpenFOAM)	-	*S*	-	-	-	-	-	-	-	-	-	-
		E%D	-	-	-	-	-	-	-	-	-	-
MOERI (WAVIS)	1.414	*S*	-	-	-0.2089	-0.1004	-0.1456	-	-	-0.0250	-0.0156	-0.0204
		E%D	-	-	-132.11	-11.61	-61.75	-	-	-46.82	8.33	-20.00
Southampton/QinetiQ (CFX12)	1.2	*S*	grid3 → grid1	-	-0.1598	-0.1616	-0.1609	-	-	-0.0319	-0.0318	-0.0316
		E%D		-	-77.58	-79.53	-78.82	-	-	-87.43	-87.25	-85.98
		S	grid6 → grid4	-	-0.1663	-0.1646	-0.1606	-	-	-0.0331	-0.0326	-0.0321
		E%D		-	-84.78	-82.86	-78.40	-	-	-94.49	-91.79	-88.88

$E\%D = (D\text{-}S)/D\times100$

Table 2.2b-1-4: V&V results for Sinkage (σ) and Trim (τ) at Fr = 0.1083

Organization (Code)	r_G	Sinkage σ						Trim τ °					
		ε_{12} $\%S_1$	$\frac{U_I}{\varepsilon_{12}}$	$\frac{P_G}{P_{G,th}}$	U_G $\%S_1$	U_D $\%D$	$U_V\%$	ε_{12} $\%S_1$	$\frac{U_I}{\varepsilon_{12}}$	$\frac{P_G}{P_{G,th}}$	U_G $\%S_1$	U_D $\%D$	$U_V\%$
CDadapco (STAR-CCM+)	-	-	-	-	-	8.20	-	-	-	-	-	9.60	-
CSSRC (FLUENT6.3)	-	-	-	-	-		-	-	-	-	-		-
GL&UDE (Comet)	-	0.00	-	-	-		-	2.94	-	-	-		-
GL&UDE (OpenFOAM)	-	-	-	-	-		-	-	-	-	-		-
MOERI (WAVIS)	1.414	31.00	0.000	1.265	39.91		40.74	23.61	0.000	0.961	24.93		26.72
Southampton/QinetiQ (CFX12)	1.2	0.39	0.001	p<0	-		-	0.68	0.033	1.115	3.33		10.16

$\varepsilon_{12}\%S_1 = |(S_1\text{-}S_2)/S_1|\times 100$; $U_{SN} = \sqrt{U_I^2 + U_G^2}$; $U_V = \sqrt{U_D^2 + U_{SN}^2}$

Table 2.2b-1-5: Computed C_T, C_F, C_{PV} of different grid densities at Fr = 0.1516

Organization (Code)	r_G		C_T ($\times 10^{-3}$)					C_F ($\times 10^{-3}$)					C_{PV} ($\times 10^{-3}$)				
			Grid #5	Grid #4	Grid #3	Grid #2	Grid #1	Grid #5	Grid #4	Grid #3	Grid #2	Grid #1	Grid #5	Grid #4	Grid #3	Grid #2	Grid #1
EFD (MOERI)	-	*D*	3.641					-					-				
CDadapco (STAR-CCM+)	-	*S*	-	-	-	-	-	-	-	-	-	-	-	-	-	-	-
		E%D	-	-	-	-	-										
CSSRC (FLUENT6.3)	-	*S*	-	-	-	-	3.646	-	-	-	-	3.118	-	-	-	-	0.528
		E%D	-	-	-	-	-0.13										
GL&UDE (Comet)	-	*S*	-	-	-	-	-	-	-	-	-	-	-	-	-	-	-
		E%D	-	-	-	-	-										
GL&UDE (OpenFOAM)	-	*S*	-	-	-	-	-	-	-	-	-	-	-	-	-	-	-
		E%D	-	-	-	-	-										
MOERI (WAVIS)	1.414	*S*	-	-	3.481	3.585	3.607	-	-	3.025	3.096	3.103	-	-	0.456	0.489	0.504
		E%D	-	-	4.40	1.55	0.94										
Southampton/QinetiQ (CFX12)	1.2	*S*	grid3 → grid1	-	3.762	3.719	3.684	-	-	-	-	-	-	-	-	-	-
		E%D		-	-3.32	-2.16	-1.19										
		S	grid6 → grid4	-	3.964	3.880	3.813	-	-	-	-	-	-	-	-	-	-
		E%D		-	-8.88	-6.57	-4.71										

E%D = (*D*-*S*)/*D*×100

Table 2.2b-1-6: V&V results for C_T, C_F and C_{PV} at $Fr = 0.1516$

Organization (Code)	r_G	C_T						C_F						C_{PV}					
		ε_{12} %S_1	$\frac{U_I}{\varepsilon_{12}}$	$\frac{P_G}{P_{G,th}}$	U_G %S_1	U_D %D	U_V%	ε_{12} %S_1	$\frac{U_I}{\varepsilon_{12}}$	$\frac{P_G}{P_{G,th}}$	U_G %S_1	U_D %D	U_V%	ε_{12} %S_1	$\frac{U_I}{\varepsilon_{12}}$	$\frac{P_G}{P_{G,th}}$	U_G %S_1	U_D %D	U_V%
CDadapco (STAR-CCM+)	-	-	-	-	-	1.0	-	-	-	-	-			-	-	-	-		
CSSRC (FLUENT6.3)	-	-	-	-	-		-	-	-	-	-			-	-	-	-		
GL&UDE (Comet)	-	-	-	-	-		-	-	-	-	-			-	-	-	-		
GL&UDE (OpenFOAM)	-	-	-	-	-		-	-	-	-	-			-	-	-	-		
MOERI (WAVIS)	1.414	0.61	0.000	2.235	1.06		1.46	0.22	0.000	3.378	0.42			3.05	0.000	1.113	3.48		
Southampton/QinetiQ (CFX12)	1.2	0.96	0.008	0.624	5.65		5.73	-	-	-	-			-	-	-	-		

$\varepsilon_{12}\%S_1 = |(S_1\text{-}S_2)/S_1| \times 100$; $U_{SN} = \sqrt{U_I^2 + U_G^2}$; $U_V = \sqrt{U_D^2 + U_{SN}^2}$

Table 2.2b-1-7: Computed Sinkage (σ) and Trim (τ) of different grid densities at Fr = 0.1516

Organization (Code)	r_G		Sinkage $\sigma\times10^2$ (m)					Trim τ °				
			Grid #5	Grid #4	Grid #3	Grid #2	Grid #1	Grid #5	Grid #4	Grid #3	Grid #2	Grid #1
EFD (MOERI)	-	*D*	-0.275					-0.053				
CDadapco (STAR-CCM+)	-	*S*	-	-	-	-	-	-	-	-	-	-
		E%D	-	-	-	-	-	-	-	-	-	-
CSSRC (FLUENT6.3)	-	*S*	-	-	-	-	-0.3800	-	-	-	-	-0.0520
		E%D	-	-	-	-	-38.18	-	-	-	-	1.88
GL&UDE (Comet)	-	*S*	-	-	-	-	-	-	-	-	-	-
		E%D	-	-	-	-	-	-	-	-	-	-
GL&UDE (OpenFOAM)	-	*S*	-	-	-	-	-	-	-	-	-	-
		E%D	-	-	-	-	-	-	-	-	-	-
MOERI (WAVIS)	1.414	*S*	-	-	-0.3654	-0.3370	-0.4433	-	-	-0.0598	-0.0420	-0.0504
		E%D	-	-	-32.87	-22.55	-61.19	-	-	-12.84	20.71	4.98
Southampton/QinetiQ (CFX12)	1.2	*S*	grid3 → grid1	-	-0.3640	-0.3652	-0.3653	-	-	-0.0553	-0.0554	-0.0555
		E%D		-	-32.35	-32.80	-32.84	-	-	-4.38	-4.62	-4.74
		S	grid6 → grid4	-	-0.3714	-0.3701	-0.3686	-	-	-0.0548	-0.0552	-0.0555
		E%D		-	-35.05	-34.57	-34.05	-	-	-3.38	-4.08	-4.74

$E\%D = (D\text{-}S)/D\times100$

Table 2.2b-1-8: V&V results for Sinkage (σ) and Trim (τ) at Fr = 0.1516

Organization (Code)	r_G	Sinkage σ						Trim τ °					
		ε_{12} $\%S_1$	$\frac{U_I}{\varepsilon_{12}}$	$\frac{P_G}{P_{G,th}}$	U_G $\%S_1$	U_D $\%D$	$U_V\%$	ε_{12} $\%S_1$	$\frac{U_I}{\varepsilon_{12}}$	$\frac{P_G}{P_{G,th}}$	U_G $\%S_1$	U_D $\%D$	$U_V\%$
CDadapco (STAR-CCM+)	-	-	-	-	-	5.87	-	-	-	-	-	6.80	-
CSSRC (FLUENT6.3)	-	-	-	-	-		-	-	-	-	-		-
GL&UDE (Comet)	-	-	-	-	-		-	-	-	-	-		-
GL&UDE (OpenFOAM)	-	-	-	-	-		-	-	-	-	-		-
MOERI (WAVIS)	1.414	23.97	0.000	1.904	39.21		39.65	16.55	0.000	1.093	18.50		19.71
Southampton/QinetiQ (CFX12)	1.2	0.03	0.011	0.894	-		6.03	0.11	0.079	p<0	-		-

$\varepsilon_{12}\%S_1 = |(S_1\text{-}S_2)/S_1|\times 100$; $U_{SN} = \sqrt{U_I^2 + U_G^2}$; $U_V = \sqrt{U_D^2 + U_{SN}^2}$

Table 2.2b-1-9: Computed C_T, C_F, C_{PV} of different grid densities at Fr = 0.1949

Organization (Code)	r_G		C_T ($\times 10^{-3}$)					C_F ($\times 10^{-3}$)					C_{PV} ($\times 10^{-3}$)				
			Grid #5	Grid #4	Grid #3	Grid #2	Grid #1	Grid #5	Grid #4	Grid #3	Grid #2	Grid #1	Grid #5	Grid #4	Grid #3	Grid #2	Grid #1
EFD (MOERI)	-	*D*	3.475					-					-				
CDadapco (STAR-CCM+)	-	*S*	-	-	3.490	-	-	-	-	3.035	-	-	-	-	0.455	-	-
		E%D	-	-	-0.43	-	-										
CSSRC (FLUENT6.3)	-	*S*	-	-	-	-	3.506	-	-	-	-	3.010	-	-	-	-	0.496
		E%D	-	-	-	-	-0.90										
GL&UDE (Comet)	-	*S*	-	-	-	-	-	-	-	-	-	-	-	-	-	-	-
		E%D	-	-	-	-	-										
GL&UDE (OpenFOAM)	-	*S*	-	-	-	-	-	-	-	-	-	-	-	-	-	-	-
		E%D	-	-	-	-											
MOERI (WAVIS)	1.414	*S*	-	-	3.417	3.405	3.442	-	-	2.933	2.977	3.000	-	-	0.484	0.428	0.442
		E%D	-	-	1.67	2.01	0.96										
Southampton/QinetiQ (CFX12)	1.2	*S*	grid3 → grid1	-	3.656	3.614	3.583	-	-	-	-	-	-	-	-	-	-
		E%D		-	-5.21	-3.99	-3.11										
		S	grid6 → grid4	-	3.875	3.781	3.711	-	-	-	-	-	-	-	-	-	-
		E%D		-	-11.51	-8.82	-6.78										

$E\%D = (D\text{-}S)/D \times 100$

Table 2.2b-1-10: V&V results for C_T, C_F and C_{PV} at Fr = 0.1949

Organization (Code)	r_G	C_T						C_F						C_{PV}					
		ε_{12} %S_1	$\frac{U_I}{\varepsilon_{12}}$	$\frac{P_G}{P_{G,th}}$	U_G %S_1	U_D %D	U_V%	ε_{12} %S_1	$\frac{U_I}{\varepsilon_{12}}$	$\frac{P_G}{P_{G,th}}$	U_G %S_1	U_D %D	U_V%	ε_{12} %S_1	$\frac{U_I}{\varepsilon_{12}}$	$\frac{P_G}{P_{G,th}}$	U_G %S_1	U_D %D	U_V%
CDadapco (STAR-CCM+)	-	-	-	-	-	1.0	-	-	-	-	-			-	-	-	-		
CSSRC (FLUENT6.3)	-	-	-	-	-		-	-	-	-	-			-	-	-	-		
GL&UDE (Comet)	-	-	-	-	-		-	-	-	-	-			-	-	-	-		
GL&UDE (OpenFOAM)	-	-	-	-	-		-	-	-	-	-			-	-	-	-		
MOERI (WAVIS)	1.414	1.06	0.000	1.654	1.63		1.91	0.75	0.000	0.987	0.76			3.17	0.000	2.000	5.28		
Southampton/QinetiQ (CFX12)	1.2	0.86	0.006	0.741	4.69		4.79	-	-	-	-			-	-	-	-		

$\varepsilon_{12}\%S_1 = |(S_1-S_2)/S_1|\times 100$; $U_{SN} = \sqrt{U_I^2 + U_G^2}$; $U_V = \sqrt{U_D^2 + U_{SN}^2}$

Table 2.2b-1-11: Computed Sinkage (σ) and Trim (τ) of different grid densities at Fr = 0.1949

Organization (Code)	r_G		Sinkage $\sigma\times10^2$ (m)					Trim τ °				
			Grid #5	Grid #4	Grid #3	Grid #2	Grid #1	Grid #5	Grid #4	Grid #3	Grid #2	Grid #1
EFD (MOERI)	-	*D*	-0.599					-0.097				
CDadapco (STAR-CCM+)	-	*S*	-	-	-0.6450	-	-	-	-	-0.0960	-	-
		E%D	-	-	-7.68	-	-	-	-	1.03	-	-
CSSRC (FLUENT6.3)	-	*S*	-	-	-	-	-0.6600	-	-	-	-	-0.1000
		E%D	-	-	-	-	-10.18	-	-	-	-	-3.09
GL&UDE (Comet)	-	*S*	-	-	-	-	-	-	-	-	-	-
		E%D	-	-	-	-	-	-	-	-	-	-
GL&UDE (OpenFOAM)	-	*S*	-	-	-	-	-	-	-	-	-	-
		E%D	-	-	-	-	-	-	-	-	-	-
MOERI (WAVIS)	1.414	*S*	-	-	-0.6674	-0.6762	-0.7344	-	-	-0.0938	-0.0967	-0.0911
		E%D	-	-	-11.43	-12.89	-22.61	-	-	3.35	0.32	6.12
Southampton/QinetiQ (CFX12)	1.2	*S*	grid3 → grid1	-	-0.6636	-0.6660	-0.6653	-	-	-0.0936	-0.0944	-0.0947
		E%D		-	-10.78	-11.19	-11.07	-	-	3.49	2.68	2.38
		S	grid6 → grid4	-	-0.6681	-0.6674	-0.6655	-	-	-0.0897	-0.0912	-0.0928
		E%D		-	-11.54	-11.41	-11.10	-	-	7.52	5.98	4.35

$E\%D = (D\text{-}S)/D\times100$

Table 2.2b-1-12: V&V results for Sinkage (σ) and Trim (τ) at Fr = 0.1949

Organization (Code)	r_G	Sinkage σ						Trim τ °					
		ε_{12} $\%S_1$	$\frac{U_I}{\varepsilon_{12}}$	$\frac{P_G}{P_{G,th}}$	U_G $\%S_1$	U_D $\%D$	$U_V\%$	ε_{12} $\%S_1$	$\frac{U_I}{\varepsilon_{12}}$	$\frac{P_G}{P_{G,th}}$	U_G $\%S_1$	U_D $\%D$	$U_V\%$
CDadapco (STAR-CCM+)	-	-	-	-	-	3.90	-	-	-	-	-	4.57	-
CSSRC (FLUENT6.3)	-	-	-	-	-		-	-	-	-	-		-
GL&UDE (Comet)	-	-	-	-	-		-	-	-	-	-		-
GL&UDE (OpenFOAM)	-	-	-	-	-		-	-	-	-	-		-
MOERI (WAVIS)	1.414	7.93	0.000	2.737	14.46		14.98	6.18	0.000	0.937	6.76		8.16
Southampton/QinetiQ (CFX12)	1.2	0.11	0.002	p<0	-		-	0.31	0.048	0.859	2.64		5.28

$\varepsilon_{12}\%S_1 = |(S_1\text{-}S_2)/S_1|\times 100$; $U_{SN} = \sqrt{U_I^2 + U_G^2}$; $U_V = \sqrt{U_D^2 + U_{SN}^2}$

Table 2.2b-1-13: Computed C_T, C_F, C_{PV} of different grid densities at Fr = 0.2274

Organization (Code)	r_G		C_T ($\times 10^{-3}$)					C_F ($\times 10^{-3}$)					C_{PV} ($\times 10^{-3}$)				
			Grid #5	Grid #4	Grid #3	Grid #2	Grid #1	Grid #5	Grid #4	Grid #3	Grid #2	Grid #1	Grid #5	Grid #4	Grid #3	Grid #2	Grid #1
EFD (MOERI)	-	*D*	3.467					-					-				
CDadapco (STAR-CCM+)	-	*S*	-	-	3.505	-	-	-	-	2.985	-	-	-	-	0.520	-	-
		E%D	-	-	-1.10	-	-										
CSSRC (FLUENT6.3)	-	*S*	-	-	-	-	3.481	-	-	-	-	2.941	-	-	-	-	0.540
		E%D	-	-	-	-	-0.41										
GL&UDE (Comet)	-	*S*	-	-	-	3.577	3.493	-	-	-	2.979	2.99	-	-	-	0.598	0.503
		E%D	-	-	-	-3.17	-0.75										
GL&UDE (OpenFOAM)	-	*S*	-	-	-	3.583	3.505	-	-	-	2.876	2.995	-	-	-	-	-
		E%D	-	-	-	-3.35	-1.10										
MOERI (WAVIS)	1.414	*S*	-	-	3.499	3.464	3.439	-	-	2.901	2.947	2.949	-	-	0.598	0.517	0.490
		E%D	-	-	-0.92	0.10	0.81										
Southampton/QinetiQ (CFX12)	1.2	*S*	grid3 → grid1	-	3.664	3.621	3.591	-	-	-	-	-	-	-	-	-	-
		E%D		-	-5.68	-4.43	-3.57										
		S	grid6 → grid4	-	3.895	3.793	3.724	-	-	-	-	-	-	-	-	-	-
		E%D		-	-12.35	-9.41	-7.41										

$E\%D = (D\text{-}S)/D \times 100$

Table 2.2b-1-14: V&V results for C_T, C_F and C_{PV} at Fr = 0.2274

Organization (Code)	r_G	C_T						C_F						C_{PV}					
		ε_{12} %S_1	$\frac{U_I}{\varepsilon_{12}}$	$\frac{P_G}{P_{G,th}}$	U_G %S_1	U_D %D	U_V%	ε_{12} %S_1	$\frac{U_I}{\varepsilon_{12}}$	$\frac{P_G}{P_{G,th}}$	U_G %S_1	U_D %D	U_V%	ε_{12} %S_1	$\frac{U_I}{\varepsilon_{12}}$	$\frac{P_G}{P_{G,th}}$	U_G %S_1	U_D %D	U_V%
CDadapco (STAR-CCM+)	-	-	-	-	-	1.0	-	-	-	-	-			-	-	-	-		
CSSRC (FLUENT6.3)	-	-	-	-	-		-	-	-	-	-			-	-	-	-		
GL&UDE (Comet)	-	-2.40	-	-	-		-	0.37	-	-	-			-18.89	-	-	-		
GL&UDE (OpenFOAM)	-	2.23	-	-	-		-	3.97	-	-	-			-	-	-	-		
MOERI (WAVIS)	1.414	0.72	0.000	0.507	1.71		1.98	0.08	0.000	4.189	0.16			5.56	0.000	1.569	8.29		
Southampton/QinetiQ (CFX12)	1.2	0.83	0.033	0.772	4.63		4.74	-	-	-	-			-	-	-	-		

$\varepsilon_{12}\%S_1 = |(S_1\text{-}S_2)/S_1|\times 100$; $U_{SN} = \sqrt{U_I^2 + U_G^2}$; $U_V = \sqrt{U_D^2 + U_{SN}^2}$

Table 2.2b-1-15: Computed Sinkage (σ) and Trim (τ) of different grid densities at Fr = 0.2274

Organization (Code)	r_G		Sinkage $\sigma\times10^2$ (m)					Trim τ °				
			Grid #5	Grid #4	Grid #3	Grid #2	Grid #1	Grid #5	Grid #4	Grid #3	Grid #2	Grid #1
EFD (MOERI)	-	*D*	-0.944					-0.127				
CDadapco (STAR-CCM+)	-	*S*	-	-	-0.9515	-	-	-	-	-0.1312	-	-
		E%D	-	-	-0.79	-	-	-	-	-3.31	-	-
CSSRC (FLUENT6.3)	-	*S*	-	-	-	-	-1.0000	-	-	-	-	-0.1350
		E%D	-	-	-	-	-5.93	-	-	-	-	-6.30
GL&UDE (Comet)	-	*S*	-	-	-	-0.9470	-0.9450	-	-	-	-0.1301	-0.1318
		E%D	-	-	-	-0.32	-0.11	-	-	-	-2.44	-3.78
GL&UDE (OpenFOAM)	-	*S*	-	-	-	-0.9860	-	-	-	-	-0.1210	-
		E%D	-	-	-	-4.45	-	-	-	-	4.72	-
MOERI (WAVIS)	1.414	*S*	-	-	-1.0132	-1.0532	-1.0496	-	-	-0.1301	-0.1352	-0.1381
		E%D	-	-	-7.33	-11.57	-11.18	-	-	-2.41	-6.48	-8.76
Southampton/QinetiQ (CFX12)	1.2	*S*	grid3 → grid1	-	-0.9662	-0.9679	-0.9682	-	-	-0.1279	-0.1291	-0.1295
		E%D		-	-2.35	-2.53	-2.57	-	-	-0.67	-1.62	-1.98
		S	grid6 → grid4	-	-0.9666	-0.9644	-0.9655	-	-	-0.1210	-0.1235	-0.1260
		E%D		-	-2.39	-2.16	-2.27	-	-	4.71	2.72	0.81

$E\%D = (D\text{-}S)/D\times100$

Table 2.2b-1-16: V&V results for Sinkage (σ) and Trim (τ) at Fr=0.2274

Organization (Code)	r_G	Sinkage σ						Trim τ °					
		ε_{12} %S_1	$\frac{U_I}{\varepsilon_{12}}$	$\frac{P_G}{P_{G,th}}$	U_G %S_1	U_D %D	U_V%	ε_{12} %S_1	$\frac{U_I}{\varepsilon_{12}}$	$\frac{P_G}{P_{G,th}}$	U_G %S_1	U_D %D	U_V%
CDadapco (STAR-CCM+)	-	-	-	-	-	2.78	-	-	-	-	-	3.26	-
CSSRC (FLUENT6.3)	-	-	-	-	-		-	-	-	-	-		-
GL&UDE (Comet)	-	-0.21	-	-	-		-	1.29	-	-	-		-
GL&UDE (OpenFOAM)	-	-	-	-	-		-	-	-	-	-		-
MOERI (WAVIS)	1.414	0.35	0.000	3.459	0.66		2.86	2.10	0.000	0.837	2.66		4.21
Southampton/QinetiQ (CFX12)	1.2	0.04	0.006	0.015	8.11		8.57	0.35	0.068	0.803	3.68		4.92

$\varepsilon_{12}\%S_1 = |(S_1\text{-}S_2)/S_1|\times 100$; $U_{SN} = \sqrt{U_I^2 + U_G^2}$; $U_V = \sqrt{U_D^2 + U_{SN}^2}$

Table 2.2b-1-17: Computed C_T, C_F, C_{PV} of different grid densities at Fr = 0.2599

Organization (Code)	r_G		C_T ($\times 10^{-3}$)					C_F ($\times 10^{-3}$)					C_{PV} ($\times 10^{-3}$)				
			Grid #5	Grid #4	Grid #3	Grid #2	Grid #1	Grid #5	Grid #4	Grid #3	Grid #2	Grid #1	Grid #5	Grid #4	Grid #3	Grid #2	Grid #1
EFD (MOERI)	-	*D*	3.711					-					-				
CDadapco (STAR-CCM+)	1.5	*S*	-	-	3.689	3.662	3.672	-	-	2.943	2.976	2.971	-	-	0.746	0.686	0.701
		E%D	-	-	0.59	1.32	1.05										
CSSRC (FLUENT6.3)	-	*S*	-	-	-	-	3.72	-	-	-	-	2.886	-	-	-	-	0.834
		E%D	-	-	-	-	-0.24										
GL&UDE (Comet)	-	*S*	-	-	-	-	-	-	-	-	-	-	-	-	-	-	-
		E%D	-	-	-	-	-										
GL&UDE (OpenFOAM)	-	*S*	-	-	-	-	-	-	-	-	-	-	-	-	-	-	-
		E%D	-	-	-	-	-										
MOERI (WAVIS)	1.414	*S*	-	-	3.780	3.738	3.707	-	-	2.848	2.894	2.911	-	-	0.931	0.845	0.795
		E%D	-	-	-1.85	-0.73	0.12										
Southampton/QinetiQ (CFX12)	1.2	*S*	grid3 → grid1	-	3.860	3.814	3.782	-	-	-	-	-	-	-	-	-	-
		E%D		-	-4.01	-2.76	-1.92										
		S	grid6 → grid4	-	4.093	3.995	3.921	-	-	-	-	-	-	-	-	-	-
		E%D		-	-10.30	-7.66	-5.65										

$E\%D = (D\text{-}S)/D \times 100$

Table 2.2b-1-18: V&V results for C_T, C_F and C_{PV} at Fr = 0.2599

Organization (Code)	r_G	C_T						C_F						C_{PV}					
		ε_{12} $\%S_1$	$\frac{U_I}{\varepsilon_{12}}$	$\frac{P_G}{P_{G,th}}$	U_G $\%S_1$	U_D $\%D$	$U_V\%$	ε_{12} $\%S_1$	$\frac{U_I}{\varepsilon_{12}}$	$\frac{P_G}{P_{G,th}}$	U_G $\%S_1$	U_D $\%D$	$U_V\%$	ε_{12} $\%S_1$	$\frac{U_I}{\varepsilon_{12}}$	$\frac{P_G}{P_{G,th}}$	U_G $\%S_1$	U_D $\%D$	$U_V\%$
CDadapco (STAR-CCM+)	1.5	0.27	-	-	-	1.0	-	-0.17	-	-	-			2.14	-	-	-		
CSSRC (FLUENT6.3)	-	-	-	-	-		-	-	-	-	-			-	-	-	-		
GL&UDE (Comet)	-	-	-	-	-		-	-	-	-	-			-	-	-	-		
GL&UDE (OpenFOAM)	-	-	-	-	-		-	-	-	-	-			-	-	-	-		
MOERI (WAVIS)	1.414	0.85	0.000	0.394	2.70		2.88	0.61	0.000	1.349	0.82			6.20	0.000	0.811	8.22		
Southampton/QinetiQ (CFX12)	1.2	0.82	0.011	0.714	5.08		7.18	-	-	-	-			-	-	-	-		

$\varepsilon_{12}\%S_1 = |(S_1-S_2)/S_1|\times 100$; $U_{SN} = \sqrt{U_I^2 + U_G^2}$; $U_V = \sqrt{U_D^2 + U_{SN}^2}$

Table 2.2b-1-19: Computed Sinkage (σ) and Trim (τ) of different grid densities at Fr = 0.2599

Organization (Code)	r_G		Sinkage $\sigma\times10^2$ (m)					Trim τ °				
			Grid #5	Grid #4	Grid #3	Grid #2	Grid #1	Grid #5	Grid #4	Grid #3	Grid #2	Grid #1
EFD (MOERI)	-	*D*	-1.394					-0.169				
CDadapco (STAR-CCM+)	1.5	*S*	-	-	-1.3200	-1.3020	-1.2960	-	-	-0.1770	-0.1740	-0.1702
		E%D	-	-	5.31	6.60	7.03	-	-	-4.73	-2.96	-0.71
CSSRC (FLUENT6.3)	-	*S*	-	-	-	-	-1.4300	-	-	-	-	-0.1800
		E%D	-	-	-	-	-2.58	-	-	-	-	-6.51
GL&UDE (Comet)	-	*S*	-	-	-	-	-	-	-	-	-	-
		E%D	-	-	-	-	-	-	-	-	-	-
GL&UDE (OpenFOAM)	-	*S*	-	-	-	-	-	-	-	-	-	-
		E%D	-	-	-	-	-	-	-	-	-	-
MOERI (WAVIS)	1.414	*S*	-	-	-1.3080	-1.3771	-1.4281	-	-	-0.1661	-0.1767	-0.1768
		E%D	-	-	6.17	1.21	-2.44	-	-	1.73	-4.53	-4.64
Southampton/QinetiQ (CFX12)	1.2	*S*	grid3 → grid1	-	-1.3381	-1.3402	-1.3396	-	-	-0.1667	-0.1691	-0.1699
		E%D		-	4.01	3.86	3.90	-	-	1.38	-0.07	-0.55
		S	grid6 → grid4	-	-1.3312	-1.3346	-1.3360	-	-	-0.1558	-0.1592	-0.1635
		E%D		-	4.51	4.26	4.16	-	-	7.80	5.78	3.27

$E\%D = (D\text{-}S)/D\times100$

Table 2.2b-1-20: V&V results for Sinkage (σ) and Trim (τ) at Fr = 0.2599

Organization (Code)	r_G	Sinkage σ						Trim τ °					
		ε_{12} $\%S_1$	$\frac{U_I}{\varepsilon_{12}}$	$\frac{P_G}{P_{G,th}}$	U_G $\%S_1$	U_D $\%D$	$U_V\%$	ε_{12} $\%S_1$	$\frac{U_I}{\varepsilon_{12}}$	$\frac{P_G}{P_{G,th}}$	U_G $\%S_1$	U_D $\%D$	$U_V\%$
CDadapco (STAR-CCM+)	1.5	-0.46	-	-	-	1.85	-	-2.23	-	-	-	2.27	-
CSSRC (FLUENT6.3)	-	-	-	-	-		-	-	-	-	-		-
GL&UDE (Comet)	-	-	-	-	-		-	-	-	-	-		-
GL&UDE (OpenFOAM)	-	-	-	-	-		-	-	-	-	-		-
MOERI (WAVIS)	1.414	3.57	0.000	0.441	9.99		10.16	0.10	0.000	5.871	0.20		2.28
Southampton/QinetiQ (CFX12)	1.2	0.04	0.004	0.909	-		-	0.48	0.044	0.624	6.99		9.89

$\varepsilon_{12}\%S_1 = |(S_1\text{-}S_2)/S_1|\times 100$; $U_{SN} = \sqrt{U_I^2 + U_G^2}$; $U_V = \sqrt{U_D^2 + U_{SN}^2}$

Table 2.2b-1-21: Computed C_T, C_F, C_{PV} of different grid densities at Fr = 0.2816

Organization (Code)	r_G		C_T ($\times 10^{-3}$)					C_F ($\times 10^{-3}$)					C_{PV} ($\times 10^{-3}$)				
			Grid #5	Grid #4	Grid #3	Grid #2	Grid #1	Grid #5	Grid #4	Grid #3	Grid #2	Grid #1	Grid #5	Grid #4	Grid #3	Grid #2	Grid #1
EFD (MOERI)	-	*D*	4.501					-					-				
CDadapco (STAR-CCM+)	-	*S*	-	-	4.576	4.542	-	-	-	2.940	2.971	-	-	-	1.636	1.571	-
		E%*D*	-	-	-1.67	-0.91	-										
CSSRC (FLUENT6.3)	-	*S*	-	-	-	-	4.532	-	-	-	-	2.850	-	-	-	-	1.682
		E%*D*	-	-	-	-	-0.70										
GL&UDE (Comet)	-	*S*	-	-	-	4.574	4.517	-	-	-	2.925	2.945	-	-	-	1.649	1.572
		E%*D*	-	-	-	-1.62	-0.36										
GL&UDE (OpenFOAM)	-	*S*	-	-	-	3.900	4.450	-	-	-	2.860	2.920	-	-	-	1.040	1.530
		E%*D*	-	-	-	13.35	1.13										
MOERI (WAVIS)	1.414	*S*	-	-	4.549	4.491	4.519	-	-	2.852	2.891	2.915	-	-	1.697	1.600	1.605
		E%*D*	-	-	-1.06	0.23	-0.41										
Southampton/QinetiQ (CFX12)	1.2	*S*	grid3 → grid1	-	4.604	4.579	4.560	-	-	-	-	-	-	-	-	-	-
		E%*D*		-	-2.28	-1.74	-1.30										
		S	grid6 → grid4	-	4.746	4.683	4.644	-	-	-	-	-	-	-	-	-	-
		E%*D*		-	-5.44	-4.05	-3.18										

E%*D* = (*D*-*S*)/*D*×100

Table 2.2b-1-22: V&V results for C_T, C_F and C_{PV} at Fr = 0.2816

Organization (Code)	r_G	C_T						C_F						C_{PV}					
		ε_{12} %S_1	$\frac{U_I}{\varepsilon_{12}}$	$\frac{P_G}{P_{G,th}}$	U_G %S_1	U_D %D	U_V%	ε_{12} %S_1	$\frac{U_I}{\varepsilon_{12}}$	$\frac{P_G}{P_{G,th}}$	U_G %S_1	U_D %D	U_V%	ε_{12} %S_1	$\frac{U_I}{\varepsilon_{12}}$	$\frac{P_G}{P_{G,th}}$	U_G %S_1	U_D %D	U_V%
CDadapco (STAR-CCM+)	-	-	-	-	-	1.0	-	-	-	-	-			-	-	-	-		
CSSRC (FLUENT6.3)	-	-	-	-	-		-	-	-	-	-			-	-	-	-		
GL&UDE (Comet)	-	-1.26	-	-	-		-	0.68	-	-	-			-4.90	-	-	-		
GL&UDE (OpenFOAM)	-	12.36	-	-	-		-	2.05	-	-	-			32.03	-	-	-		
MOERI (WAVIS)	1.414	0.64	0.000	1.022	0.65		1.20	0.82	0.000	0.714	1.28			0.30	0.000	4.344	0.58		
Southampton/QinetiQ (CFX12)	1.2	0.43	0.003	0.798	2.15		3.03	-	-	-	-			-	-	-	-		

$\varepsilon_{12}\%S_1 = |(S_1\text{-}S_2)/S_1|\times 100$; $U_{SN} = \sqrt{U_I^2 + U_G^2}$; $U_V = \sqrt{U_D^2 + U_{SN}^2}$

Table 2.2b-1-23: Computed Sinkage (σ) and Trim (τ) of different grid densities at Fr = 0.2816

Organization (Code)	r_G		Sinkage $\sigma\times10^2$ (m)					Trim τ °				
			Grid #5	Grid #4	Grid #3	Grid #2	Grid #1	Grid #5	Grid #4	Grid #3	Grid #2	Grid #1
EFD (MOERI)	-	*D*	-1.702					-0.159				
CDadapco (STAR-CCM+)	-	*S*	-	-	-1.6600	-1.6400	-	-	-	-0.1470	-0.1440	-
		E%D	-	-	2.47	3.64	-	-	-	7.55	9.43	-
CSSRC (FLUENT6.3)	-	*S*	-	-	-	-	-1.8300	-	-	-	-	-0.1600
		E%D	-	-	-	-	-7.52	-	-	-	-	-0.63
GL&UDE (Comet)	-	*S*	-	-	-	-1.6550	-1.6560	-	-	-	-0.1490	-0.1500
		E%D	-	-	-	2.76	2.70	-	-	-	6.29	5.66
GL&UDE (OpenFOAM)	-	*S*	-	-	-	-1.6300	-1.7800	-	-	-	-0.2010	-0.1610
		E%D	-	-	-	4.23	-4.58	-	-	-	-26.42	-1.26
MOERI (WAVIS)	1.414	*S*	-	-	-1.6581	-1.7316	-1.8575	-	-	-0.1471	-0.1530	-0.1556
		E%D	-	-	2.58	-1.74	-9.14	-	-	7.47	3.76	2.16
Southampton/QinetiQ (CFX12)	1.2	*S*	grid3 → grid1	-	-1.6636	-1.6678	-1.6671	-	-	-0.1475	-0.1488	-0.1495
		E%D		-	2.25	2.01	2.05	-	-	7.26	6.42	6.00
		S	grid6 → grid4	-	-1.6527	-1.6576	-1.6613	-	-	-0.1434	-0.1438	-0.1459
		E%D		-	2.89	2.61	2.39	-	-	9.79	9.54	8.27

$E\%D = (D\text{-}S)/D\times100$

Table 2.2b-1-24: V&V results for Sinkage (σ) and Trim (τ) at Fr = 0.2816

Organization (Code)	r_G	Sinkage σ						Trim τ °					
		ε_{12} $\%S_1$	$\frac{U_I}{\varepsilon_{12}}$	$\frac{P_G}{P_{G,th}}$	U_G $\%S_1$	U_D $\%D$	$U_V\%$	ε_{12} $\%S_1$	$\frac{U_I}{\varepsilon_{12}}$	$\frac{P_G}{P_{G,th}}$	U_G $\%S_1$	U_D $\%D$	$U_V\%$
CDadapco (STAR-CCM+)	-	-	-	-	-	1.36	-	-	-	-	-	1.78	-
CSSRC (FLUENT6.3)	-	-	-	-	-		-	-	-	-	-		-
GL&UDE (Comet)	-	0.06	-	-	-		-	0.67	-	-	-		-
GL&UDE (OpenFOAM)	-	8.43	-	-	-		-	24.84	-	-	-		-
MOERI (WAVIS)	1.414	6.78	0.000	0.776	9.51		9.61	1.64	0.000	1.205	2.03		2.70
Southampton/QinetiQ (CFX12)	1.2	0.04	0.002	0.804	-		-	0.45	0.033	0.291	8.12		11.49

$\varepsilon_{12}\%S_1 = |(S_1\text{-}S_2)/S_1|\times 100$; $U_{SN} = \sqrt{U_I^2 + U_G^2}$; $U_V = \sqrt{U_D^2 + U_{SN}^2}$

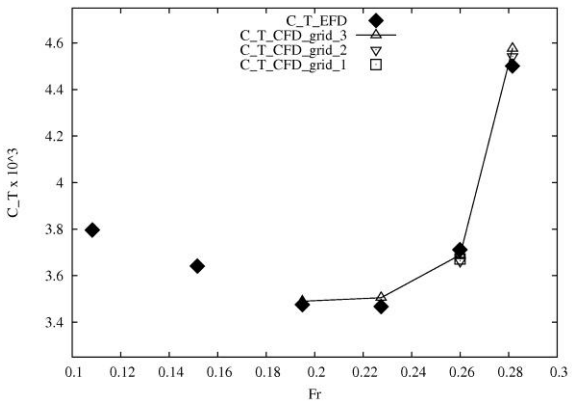

CDadapco-STAR-CCM+

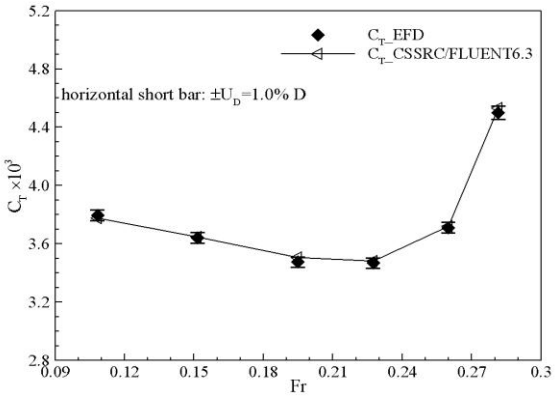

CSSRC-FLUENT6.3

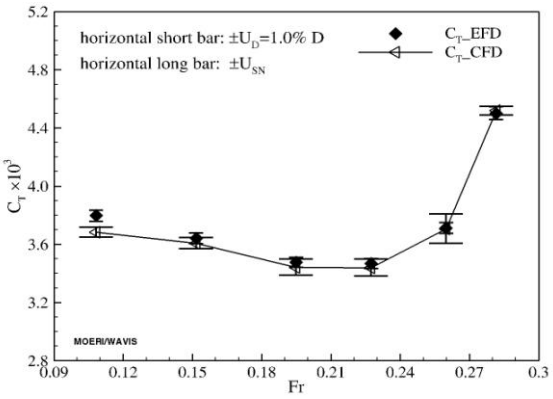

MOERI-WAVIS

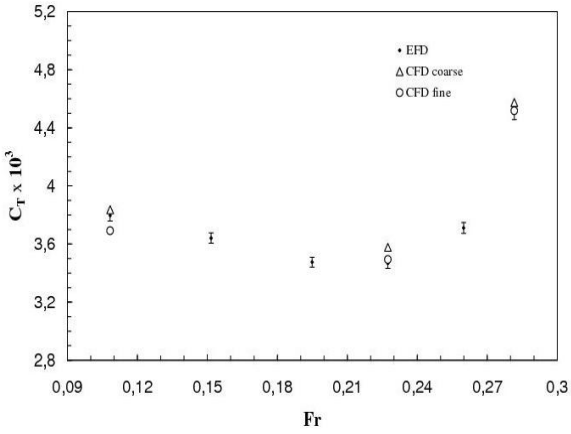

GL&UDE-Comet

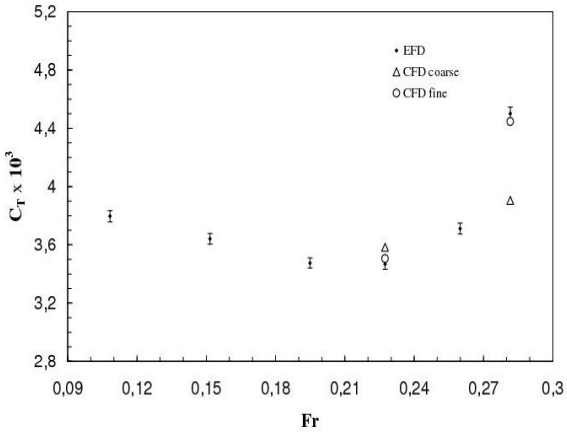

GL&UDE-OpenFOAM1.6libSixDoFv1.1.0

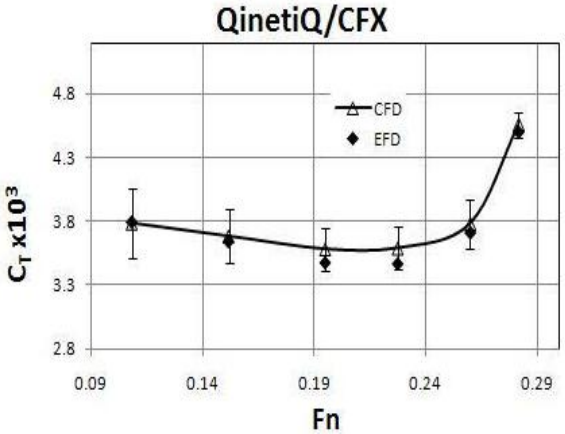

Soton&QinetiQ-CFX12

Fig. 2.2b-2 Total resistance Coefficients (C_T) versus *Fr*

CFD: solid line with open left-triangles; EFD: solid diamonds
$\pm U_D$: horizontal short bars; $\pm U_{SN}$: horizontal long bars

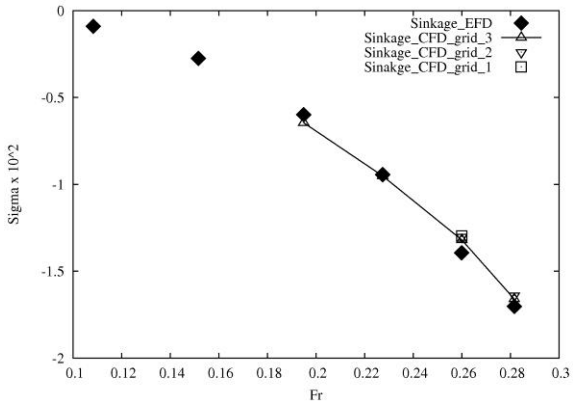

CDadapco-STAR-CCM+

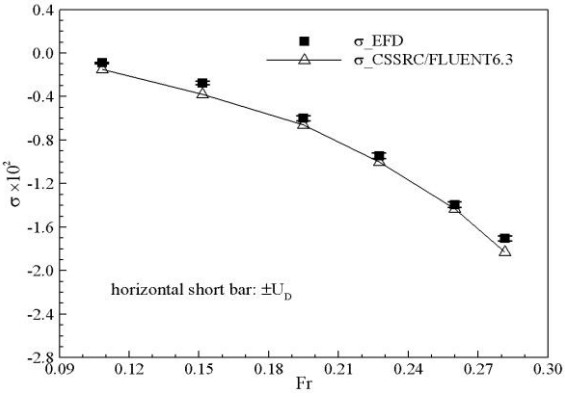

CSSRC-FLUENT6.3

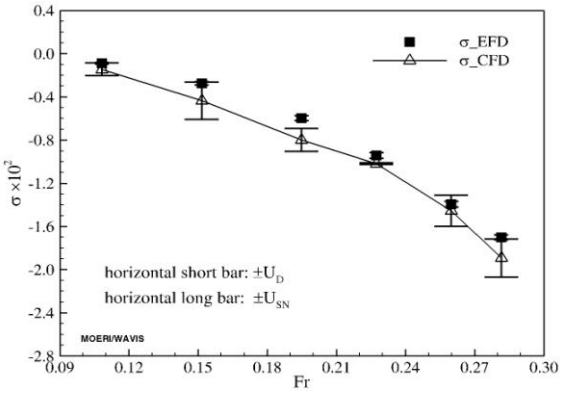

MOERI-WAVIS

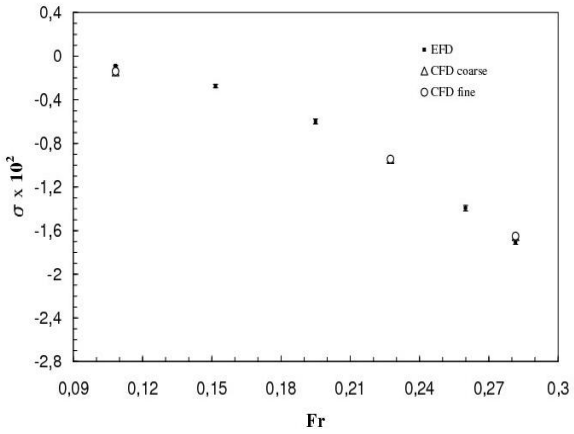

GL&UDE-Comet

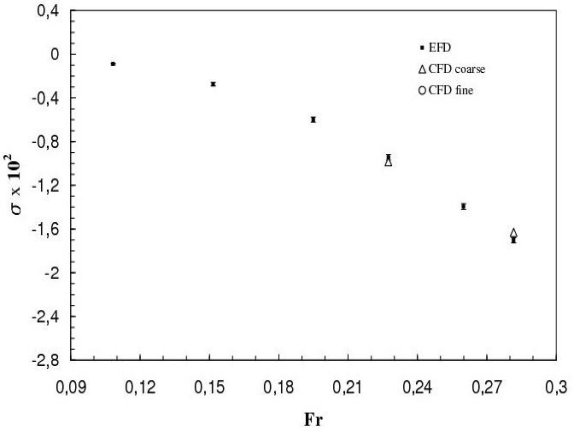

GL&UDE-OpenFOAM1.6libSixDoFv1.1.0

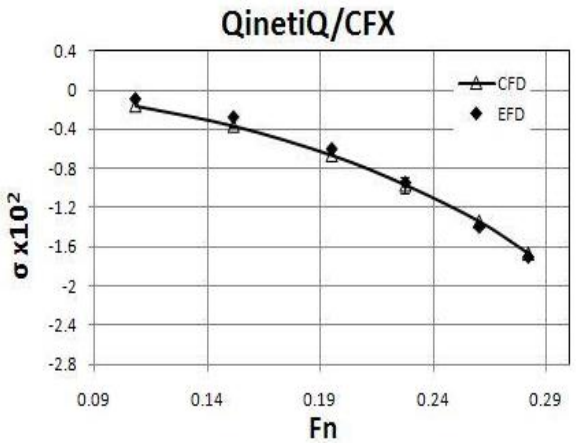

Soton&QinetiQ-CFX12

Fig. 2.2b-3 Sinkage (σ) versus *Fr*

CFD solid line with open up-triangles; EFD: solid squares
$\pm U_D$: horizontal short bars; $\pm U_{SN}$: horizontal long bars

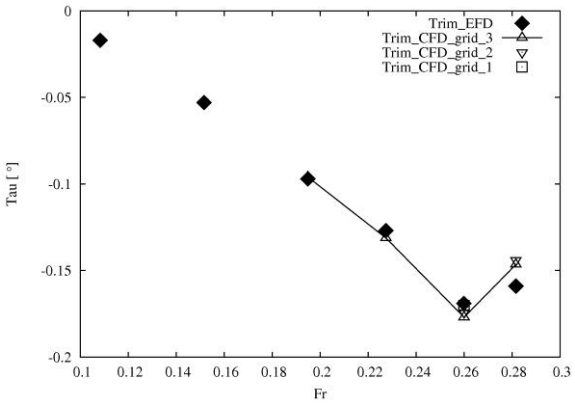

CDadapco-STAR-CCM+

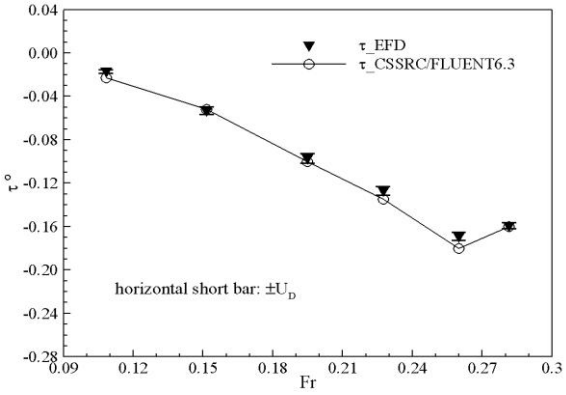

CSSRC-FLUENT6.3

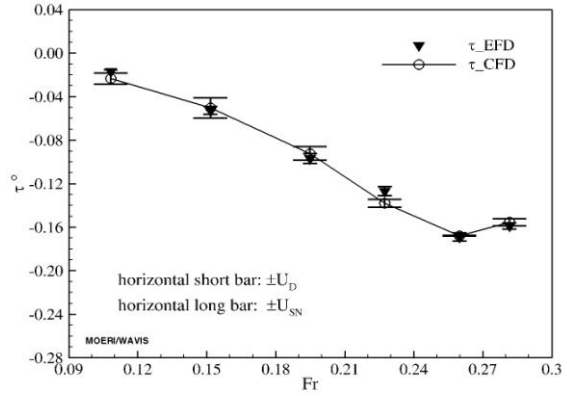

MOERI-WAVIS

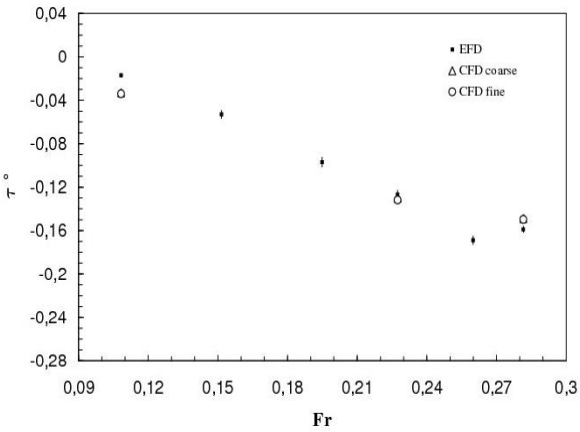

GL&UDE-Comet

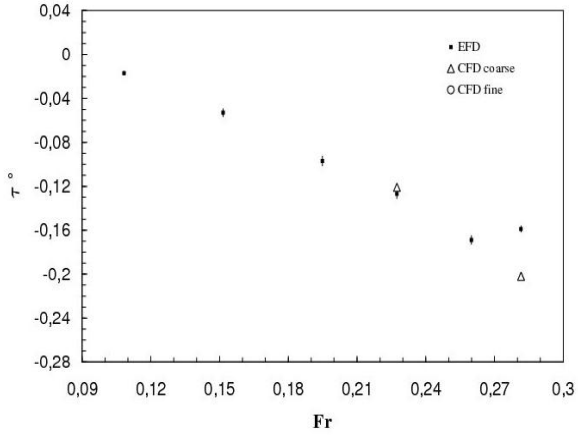

GL&UDE-OpenFOAM1.6libSixDoFv1.1.0

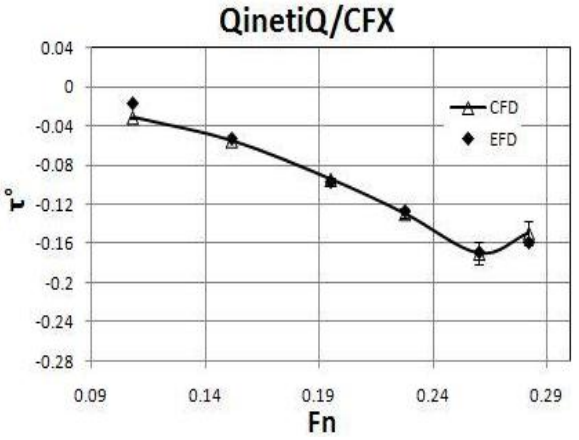

Soton&QinetiQ-CFX12

Fig. 2.2b-4 Trim (τ) versus Fr

CFD: solid line with open circles; EFD: solid down-triangles
$\pm U_D$: horizontal short bars; $\pm U_{SN}$: horizontal long bars

Test Case 2.3a

Table 2.3a-0 Computations information and V&V method
Table 2.3a-1-1 Computed C_T, C_F and C_{PV} of different grid densities
Table 2.3a-1-2 V&V results for C_T, C_F and C_{PV}
Table 2.3a-1-3 Computed K_T, K_Q of different grid densities
Table 2.3a-1-4 V&V results for K_T, K_Q
Table 2.3a-1-5 Computed n, [RT(SP)-T] of different grid densities
Table 2.3a-1-6 V&V results for n, [RT(SP)-T]

Figure 2.3a-2-1 Axial velocity contours downstream of propeller plane (at x/L_{PP} = 0.9911)
Figure 2.3a-2-2 Axial velocity vectors downstream of propeller plane (at x/L_{PP} = 0.9911)
Figure 2.3a-3 Velocity downstream of the propeller plane (at x/L_{PP} = 0.9911, z/L_{PP} = -0.03)
Figure 2.3a-4 Hull surface pressure contours (port side view)

Table 2.3a-0: Computations information and V&V method

Organization (Code)	**V&V method (including the determination of U_I)**
CSSRC (FLUENT6.3)	without V&V
CTO (STAR_CCM+)	without V&V
IIHR (CFDShipIowaV4.0)	without V&V
IIHR/SJTU (FLUENT12.0.16)	without V&V
MARIC (FLUENT6.3)	without V&V
MARIN (PARNASSOS-ROCAL)	-
MOERI (WAVIS)	Stern et al. 2001
NMRI (SURF)	Following the ITTC recommended procedure 7.5-03. U_I is computed using the maximum and minimum values of last 1000 steps
SNUTT (FLUENT6.3)	-
Southampton/QinetiQ (CFX12)	Lisbon Workshop on Uncertainty Analysis
SSPA (SHIPFLOWv4.3)	Eca and Hoekstra proposal
SSRC (FLUENT12.1)	-
TUHH-FDS&ANSYS (CFX12.1)	-

Table 2.3a-1-1 (1): Computed C_T, C_F and C_{PV} of different grid densities

Organization (Code)	r_G		C_T ($\times 10^{-3}$)					C_F ($\times 10^{-3}$)					C_{PV} ($\times 10^{-3}$)				
			Grid #5	Grid #4	Grid #3	Grid #2	Grid #1	Grid #5	Grid #4	Grid #3	Grid #2	Grid #1	Grid #5	Grid #4	Grid #3	Grid #2	Grid #1
EFD (NMRI)	-	*D*	3.966					-					-				
CSSRC (FLUENT6.3)	-	*S*	-	-	-	-	4.050	-	-	-	-	2.880	-	-	-	-	1.160
		E%D	-	-	-	-	-2.12										
CTO (STAR_CCM+)	-	*S*	-	-	3.804	-	-	-	-	-	-	-	-	-	-	-	-
		E%D	-	-	4.08	-	-										
IIHR (CFDShipIowaV4.0)	-	*S*	-	-	-	-	4.011	-	-	-	-	2.847	-	-	-	-	1.172
		E%D	-	-	-	-	-1.13										
IIHR/SJTU (FLUENT12.0.16)	-	*S*	-	-	-	-	3.863	-	-	-	-	-	-	-	-	-	-
		E%D	-	-	-	-	2.60										
MARIC (FLUENT6.3) [without hub cap]	-	*S*	-	-	-	-	3.906	-	-	-	-	2.471	-	-	-	-	1.435
		E%D	-	-	-	-	1.51										
MARIC (FLUENT6.3) [with hub cap]	-	*S*	-	-	-	-	4.315	-	-	-	-	-	-	-	-	-	-
		E%D	-	-	-	-	-8.80										
MARIN (PARNASSOS-PROCAL)	2	*S*	-	-	4.070	3.970	3.950	-	-	2.950	2.940	2.940	-	-	1.110	1.020	1.020
		E%D	-	-	-2.60	-0.10	0.40										

$E\%D = (D\text{-}S)/D \times 100$

Table 2.3a-1-1 (2): Computed C_T, C_F and C_{PV} of different grid densities

Organization (Code)	r_G		C_T ($\times 10^{-3}$)					C_F ($\times 10^{-3}$)					C_{PV} ($\times 10^{-3}$)				
			Grid #5	Grid #4	Grid #3	Grid #2	Grid #1	Grid #5	Grid #4	Grid #3	Grid #2	Grid #1	Grid #5	Grid #4	Grid #3	Grid #2	Grid #1
EFD (NMRI)	-	*D*	3.966					-					-				
MOERI (WAVIS)	1.414	*S*	-	-	4.184	4.007	3.965	-	-	2.831	2.834	2.830	-	-	1.353	1.173	1.135
		E%D	-	-	-5.50	-1.03	0.03										
NMRI (SURF)	1.414	*S*	-	-	4.031	3.852	3.825	-	-	1.334	1.117	1.062	-	-	2.698	2.735	2.762
		E%D	-	-	-1.64	2.87	3.56										
SNUTT (FLUENT6.3)	-	*S*	-	-	-	-	3.927	-	-	-	-	2.670	-	-	-	-	0.880
		E%D	-	-	-	-	0.98										
Southampton/QinetiQ (CFX)	$\sqrt{2}$	*S*	-	4.345	4.322	4.287	-	-	2.903	2.959	2.988	-	-	1.441	1.362	1.300	-
		E%D	-	-9.55	-8.97	-8.11	-										
SSPA (SHIPFLOWv4.3)	1.3195	*S*	-	4.061	4.022	4.002	3.994	-	2.633	2.709	2.740	2.755	-	0.825	0.711	0.660	0.637
		E%D	-	-2.39	-1.41	-0.90	-0.71										
SSRC (FLUENT12.1) [9.5 rps]	-	*S*	-	-	-	-	3.985	-	-	-	-	2.835	-	-	-	-	1.150
		E%D	-	-	-	-	-0.48										
SSRC (FLUENT12.1) [self-propulsion]	-	*S*	-	-	-	-	4.121	-	-	-	-	2.839	-	-	-	-	1.282
		E%D	-	-	-	-	-3.91										
TUHH-FDS&ANSYS (CFX12.1)	-	*S*	-	-	-	3.985	-	-	-	-	2.856	-	-	-	-	1.139	-
		E%D	-	-	-	-0.48	-										

$E\%D = (D\text{-}S)/D \times 100$

Table 2.3a-1-2 (1): V&V results for C_T, C_F and C_{PV}

Organization (Code)	r_G	C_T						C_F						C_{PV}					
		ε_{12} %S_1	$\frac{U_I}{\varepsilon_{12}}$	$\frac{P_G}{P_{G,th}}$	U_G %S_1	U_D %D	U_V%	ε_{12} %S_1	$\frac{U_I}{\varepsilon_{12}}$	$\frac{P_G}{P_{G,th}}$	U_G %S_1	U_D %D	U_V%	ε_{12} %S_1	$\frac{U_I}{\varepsilon_{12}}$	$\frac{P_G}{P_{G,th}}$	U_G %S_1	U_D %D	U_V%
CSSRC (FLUENT6.3)	-	-	-	-	-			-	-	-	-			-	-	-	-		
CTO (STAR_CCM+)	-	-	-	-	-			-	-	-	-			-	-	-	-		
IIHR (CFDShipIowaV4.0)	-	-	-	-	-			-	-	-	-			-	-	-	-		
IIHR/SJTU (FLUENT12.0.16)	-	-	-	-	-			-	-	-	-			-	-	-	-		
MARIC (FLUENT6.3) [without hub cap]	-	-	-	-	-			-	-	-	-			-	-	-	-		
MARIC (FLUENT6.3) [with hub cap]	-	-	-	-	-			-	-	-	-			-	-	-	-		
MARIN (PARNASSOS-PROCAL)	2	-	-	-	-			-	-	-	-			-	-	-	-		

$E_{12}\%S_1 = |(S_1-S_2)/S_1|\times 100$; $U_{SN} = \sqrt{U_I^2 + U_G^2}$; $U_V = \sqrt{U_D^2 + U_{SN}^2}$

Table 2.3a-1-2 (2): V&V results for C_T, C_F and C_{PV}

Organization (Code)	r_G	C_T						C_F						C_{PV}					
		ε_{12} %S_1	$\frac{U_I}{\varepsilon_{12}}$	$\frac{P_G}{P_{G,th}}$	U_G %S_1	U_D %D	U_V%	ε_{12} %S_1	$\frac{U_I}{\varepsilon_{12}}$	$\frac{P_G}{P_{G,th}}$	U_G %S_1	U_D %D	U_V%	ε_{12} %S_1	$\frac{U_I}{\varepsilon_{12}}$	$\frac{P_G}{P_{G,th}}$	U_G %S_1	U_D %D	U_V%
MOERI (WAVIS)	1.414	1.05	0.000	2.088	1.78			0.16	0.000	0.400	0.51			3.35	0.000	2.245	5.80		
NMRI (SURF)	1.414	0.71	0.245	2.730	0.13			5.18	0.122	1.980	1.76			0.98	0.102	0.450	2.64		
SNUTT (FLUENT6.3)	-	-	-	-	-			-	-	-	-			-	-	-	-		
Southampton/QinetiQ (CFX)	$\sqrt{2}$	-	-	-	-			-	-	-	-			-	-	-	-		
SSPA (SHIPFLOWv4.3)	1.3195	0.19	0.006	1.295	1.195			0.54	0.001	1.466	3.266			3.52	0.009	1.404	21.467		
SSRC (FLUENT12.1)	-	-	-	-	-			-	-	-	-			-	-	-	-		
TUHH-FDS&ANSYS (CFX12.1)	-	-	-	-	-			-	-	-	-			-	-	-	-		

$E_{12}\%S_1 = |(S_1\text{-}S_2)/S_1|\times 100$; $U_{SN} = \sqrt{U_I^2 + U_G^2}$; $U_V = \sqrt{U_D^2 + U_{SN}^2}$

Table 2.3a-1-3 (1): Computed K_T, K_Q of different grid densities

Organization (Code)	r_G		K_T					K_Q				
			Grid #5	Grid #4	Grid #3	Grid #2	Grid #1	Grid #5	Grid #4	Grid #3	Grid #2	Grid #1
EFD (NMRI)	-	*D*	0.170					0.0288				
CSSRC (FLUENT6.3)	-	*S*	-	-	-	-	0.1699	-	-	-	-	0.0292
		E%D	-	-	-	-	0.06	-	-	-	-	-1.39
CTO (STAR_CCM+)	-	*S*	-	-	0.1502	-	-	-	-	0.0283	-	-
		E%D	-	-	11.65	-	-	-	-	1.77	-	-
IIHR (CFDShipIowaV4.0)	-	*S*	-	-	-	-	0.1689	-	-	-	-	0.0296
		E%D	-	-	-	-	0.65	-	-	-	-	-2.81
IIHR/SJTU (FLUENT12.0.16)	-	*S*	-	-	-	-	0.1660	-	-	-	-	0.0285
		E%D	-	-	-	-	2.40	-	-	-	-	1.00
MARIC (FLUENT6.3) [without hub cap]	-	*S*	-	-	-	-	0.1630	-	-	-	-	0.0299
		E%D	-	-	-	-	4.12	-	-	-	-	-2.88
MARIC (FLUENT6.3) [with hub cap]	-	*S*	-	-	-	-	0.1660	-	-	-	-	0.0306
		E%D	-	-	-	-	2.35	-	-	-	-	-6.25
MARIN (PARNASSOS-PROCAL)	2	*S*	-	-	0.1750	0.1760	0.1780	-	-	0.0305	0.0306	0.0309
		E%D	-	-	-2.90	-3.50	-4.70	-	-	-5.90	-6.30	-7.30

$E\%D = (D\text{-}S)/D \times 100$

Table 2.3a-1-3 (2): Computed K_T, K_Q of different grid densities

Organization (Code)	r_G		K_T					K_Q				
			Grid #5	Grid #4	Grid #3	Grid #2	Grid #1	Grid #5	Grid #4	Grid #3	Grid #2	Grid #1
EFD (NMRI)	-	*D*	0.170					0.0288				
MOERI (WAVIS)	1.414	*S*	-	-	0.1736	0.1660	0.1670	-	-	0.0296	0.0276	0.0286
		E%D	-	-	-2.12	2.37	1.76	-	-	-2.74	4.03	0.66
NMRI (SURF)	1.414	*S*	-	-	0.1981	0.1843	0.1811	-	-	0.0356	0.0336	0.0335
		E%D	-	-	-16.53	-8.41	-6.53	-	-	-23.61	-16.67	-16.32
SNUTT (FLUENT6.3)	-	*S*	-	-	-	-	0.1733	-	-	-	-	0.0311
		E%D	-	-	-	-	-1.94	-	-	-	-	-7.99
Southampton/QinetiQ (CFX)	$\sqrt{2}$	*S*	-	0.1996	0.1988	0.2022	-	-	0.0335	0.0333	0.0340	-
		E%D	-	-17.42	-16.94	-18.92	-	-	-16.32	-15.63	-17.99	-
SSPA (SHIPFLOWv4.3)	1.3195	*S*	-	0.1849	0.1837	0.1797	0.1791	-	0.0314	0.0312	0.0307	0.0306
		E%D	-	-8.74	-8.08	-5.72	-5.34	-	-8.89	-8.44	-6.64	-6.26
SSRC (FLUENT12.1) [9.5 rps]	-	*S*	-	-	-	-	0.1643	-	-	-	-	0.0289
		E%D	-	-	-	-	3.35	-	-	-	-	-0.35
SSRC (FLUENT12.1) [self-propulsion]	-	*S*	-	-	-	-	0.1727	-	-	-	-	0.0299
		E%D	-	-	-	-	-1.59	-	-	-	-	-3.82
TUHH-FDS&ANSYS (CFX12.1)	-	*S*	-	-	-	0.1590	-	-	-	-	0.0289	-
		E%D	-	-	-	6.47	-	-	-	-	-0.42	-

$E\%D = (D\text{-}S)/D \times 100$

Table 2.3a-1-4 (1): V&V results for K_T, K_Q

Organization (Code)	r_G	K_T						K_Q					
		ε_{12} $\%S_1$	$\frac{U_I}{\varepsilon_{12}}$	$\frac{P_G}{P_{G,th}}$	U_G $\%S_1$	U_D $\%D$	$U_V\%$	ε_{12} $\%S_1$	$\frac{U_I}{\varepsilon_{12}}$	$\frac{P_G}{P_{G,th}}$	U_G $\%S_1$	U_D $\%D$	$U_V\%$
CSSRC (FLUENT6.3)	-	-	-	-	-			-	-	-	-		
CTO (STAR_CCM+)	-	-	-	-	-			-	-	-	-		
IIHR (CFDShipIowaV4.0)	-	-	-	-	-			-	-	-	-		
IIHR/SJTU (FLUENT12.0.16)	-	-	-	-	-			-	-	-	-		
MARIC (FLUENT6.3) [without hub cap]	-	-	-	-	-			-	-	-	-		
MARIC (FLUENT6.3) [with hub cap]	-	-	-	-	-			-	-	-	-		
MARIN (PARNASSOS-PROCAL)	2	-	-	-	-			-	-	-	-		

$E_{12}\%S_1 = |(S_1-S_2)/S_1|\times 100$; $U_{SN} = \sqrt{U_I^2 + U_G^2}$; $U_V = \sqrt{U_D^2 + U_{SN}^2}$

Table 2.3a-1-4 (2): V&V results for K_T, K_Q

Organization (Code)	r_G	K_T						K_Q					
		ε_{12} %S_1	$\frac{U_I}{\varepsilon_{12}}$	$\frac{P_G}{P_{G,th}}$	U_G %S_1	U_D %D	U_V%	ε_{12} %S_1	$\frac{U_I}{\varepsilon_{12}}$	$\frac{P_G}{P_{G,th}}$	U_G %S_1	U_D %D	U_V%
MOERI (WAVIS)	1.414	0.61	0.000	2.899	1.13			3.40	0.000	1.006	3.43		
NMRI (SURF)	1.414	1.77	0.078	2.110	0.53			0.30	0.350	4.330	0.02		
SNUTT (FLUENT6.3)	-	-	-	-	-			-	-	-	-		
Southampton/QinetiQ (CFX)	$\sqrt{2}$	-	-	-	-			-	-	-	-		
SSPA (SHIPFLOWv4.3)	1.3175	0.37	0.003	0.131	15.024			0.35	0.000	0.040	12.436		
SSRC (FLUENT12.1)	-	-	-	-	-			-	-	-	-		
TUHH-FDS&ANSYS (CFX12.1)	-	-	-	-	-			-	-	-	-		

$E_{12}\%S_1 = |(S_1\text{-}S_2)/S_1| \times 100$; $U_{SN} = \sqrt{U_I^2 + U_G^2}$; $U_V = \sqrt{U_D^2 + U_{SN}^2}$

Table 2.3a-1-5 (1): Computed n, [$RT(SP)$-T] of different grid densities

Organization (Code)	r_G		n (rps) (for given SFC)					[$RT(SP)$-T] (N) (for given n)				
			Grid #5	Grid #4	Grid #3	Grid #2	Grid #1	Grid #5	Grid #4	Grid #3	Grid #2	Grid #1
EFD (NMRI)	-	D	9.500					30.250				
CSSRC (FLUENT6.3)	-	S	-	-	-	-	-	-	-	-	-	32.680
		$E\%D$	-	-	-	-	-	-	-	-	-	-8.03
CTO* (STAR_CCM+)	-	S	-	-	9.80	-	-	-	-	30.20	-	-
		$E\%D$	-	-	-3.16	-	-	-	-	0.17	-	-
IIHR (CFDShipIowaV4.0)	-	S	-	-	-	-	9.621	-	-	-	-	-
		$E\%D$	-	-	-	-	-1.27	-	-	-	-	-
IIHR/SJTU (FLUENT12.0.16)	-	S	-	-	-	-	9.429	-	-	-	-	-
		$E\%D$	-	-	-	-	0.70	-	-	-	-	-
MARIC (FLUENT6.3) [without hub cap]	-	S	-	-	-	-	-	-	-	-	-	31.496
		$E\%D$	-	-	-	-	-	-	-	-	-	-4.12
MARIC (FLUENT6.3) [with hub cap]	-	S	-	-	-	-	-	-	-	-	-	39.500
		$E\%D$	-	-	-	-	-	-	-	-	-	-30.57
MARIN (PARNASSOS-PROCAL)	2	S	-	-	9.520	9.390	9.250	-	-	-	-	-
		$E\%D$	-	-	-0.20	1.20	2.60	-	-	-	-	-

$E\%D = (D\text{-}S)/D \times 100$

Table 2.3a-1-5 (2): Computed n, [$RT(SP)$-T] of different grid densities

Organization (Code)	r_G		n (rps) (for given SFC)					[$RT(SP)$-T] (N) (for given n)				
			Grid #5	Grid #4	Grid #3	Grid #2	Grid #1	Grid #5	Grid #4	Grid #3	Grid #2	Grid #1
EFD (NMRI)	-	D	9.500					30.250				
MOERI (WAVIS)	1.414	S	-	-	9.781	9.686	9.606	-	-	-	-	-
		$E\%D$	-	-	-2.95	-1.96	-1.11	-	-	-	-	-
NMRI (SURF)	1.414	S	-	-	8.910	8.930	8.960	-	-	-	-	-
		$E\%D$	-	-	6.21	6.00	5.68	-	-	-	-	-
SNUTT (FLUENT6.3)	-	S	-	-	-	-	9.592	-	-	-	-	31.288
		$E\%D$	-	-	-	-	-0.97	-	-	-	-	-3.43
Southampton/QinetiQ (CFX)	$\sqrt{2}$	S	-	9.463	9.464	9.358	-	-	31.320	30.590	30.980	-
		$E\%D$	-	0.39	0.38	1.49	-	-	-3.54	-1.12	-2.41	-
SSPA (SHIPFLOWv4.3)	1.3175	S	-	9.242	9.204	9.271	9.278	-	-	-	-	-
		$E\%D$	-	2.72	3.12	2.41	2.34	-	-	-	-	-
SSRC (FLUENT12.1) [9.5 rps]	-	S	-	-	-	-	-	-	-	-	-	32.940
		$E\%D$	-	-	-	-	-	-	-	-	-	-8.89
SSRC (FLUENT12.1) [self-propulsion]	-	S	-	-	-	-	9.7	-	-	-	-	-
		$E\%D$	-	-	-	-	-2.11	-	-	-	-	-
TUHH-FDS&ANSYS (CFX12.1)	-	S	-	-	-	-	-	-	-	-	34.600	-
		$E\%D$	-	-	-	-	-	-	-	-	-14.38	-

$E\%D = (D\text{-}S)/D \times 100$

Table 2.3a-1-6 (1): V&V results for n, [$RT(SP)$-T]

Organization (Code)	r_G	n (rps) (for given SFC)						[$RT(SP)$-T] (N) (for given n)					
		ε_{12} %S_1	$\frac{U_I}{\varepsilon_{12}}$	$\frac{P_G}{P_{G,th}}$	U_G %S_1	U_D %D	U_V%	ε_{12} %S_1	$\frac{U_I}{\varepsilon_{12}}$	$\frac{P_G}{P_{G,th}}$	U_G %S_1	U_D %D	U_V%
CSSRC (FLUENT6.3)	-	-	-	-	-			-	-	-	-		
CTO (STAR_CCM+)	-	-	-	-	-			-	-	-	-		
IIHR (CFDShipIowaV4.0)	-	-	-	-	-			-	-	-	-		
IIHR/SJTU (FLUENT12.0.16)	-	-	-	-	-			-	-	-	-		
MARIC (FLUENT6.3) [without hub cap]	-	-	-	-	-			-	-	-	-		
MARIC (FLUENT6.3) [with hub cap]	-	-	-	-	-			-	-	-	-		
MARIN (PARNASSOS-PROCAL)	2	-	-	-	-			-	-	-	-		

$E_{12}\%S_1 = |(S_1\text{-}S_2)/S_1|\times 100$; $U_{SN} = \sqrt{U_I^2 + U_G^2}$; $U_V = \sqrt{U_D^2 + U_{SN}^2}$

Table 2.3a-1-6 (2): V&V results for n, [$RT(SP)$-T]

Organization (Code)	r_G	n (rps) (for given SFC)						[$RT(SP)$-T] (N) (for given n)					
		ε_{12} $\%S_1$	$\frac{U_I}{\varepsilon_{12}}$	$\frac{P_G}{P_{G,th}}$	U_G $\%S_1$	U_D $\%D$	$U_V\%$	ε_{12} $\%S_1$	$\frac{U_I}{\varepsilon_{12}}$	$\frac{P_G}{P_{G,th}}$	U_G $\%S_1$	U_D $\%D$	$U_V\%$
MOERI (WAVIS)	1.414	0.83	0.000	0.239	4.63			-	-	-	-		
NMRI (SURF)	1.414	0.33	0.200	-	-			-	-	-	-		
SNUTT (FLUENT6.3)	-	-	-	-	-			-	-	-	-		
Southampton/QinetiQ (CFX)	$\sqrt{2}$	-	-	-	-			-	-	-	-		
SSPA (SHIPFLOWv4.3)	1.3175	0.08	0.002	0.024	0.155			-	-	-	-		
SSRC (FLUENT12.1)	-	-	-	-	-			-	-	-	-		
TUHH-FDS&ANSYS (CFX12.1)	-	-	-	-	-			-	-	-	-		

$E_{12}\%S_1 = |(S_1\text{-}S_2)/S_1|\times 100$; $U_{SN} = \sqrt{U_I^2 + U_G^2}$; $U_V = \sqrt{U_D^2 + U_{SN}^2}$

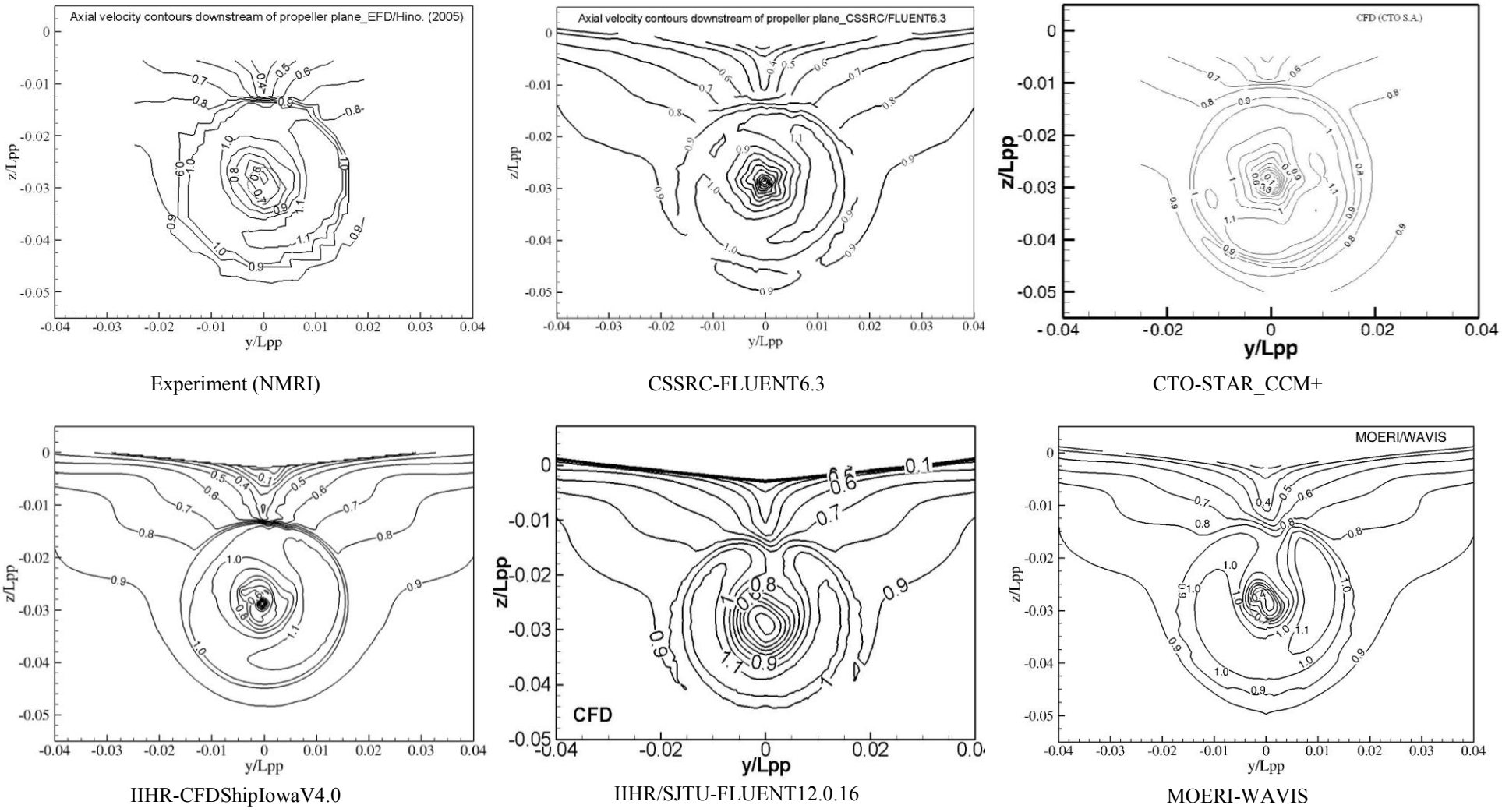

Experiment (NMRI) | CSSRC-FLUENT6.3 | CTO-STAR_CCM+

IIHR-CFDShipIowaV4.0 | IIHR/SJTU-FLUENT12.0.16 | MOERI-WAVIS

Fig. 2.3a-2-1 Axial velocity contours downstream of propeller plane (at $x/L_{PP} = 0.9911$) [$\Delta U = 0.1$]

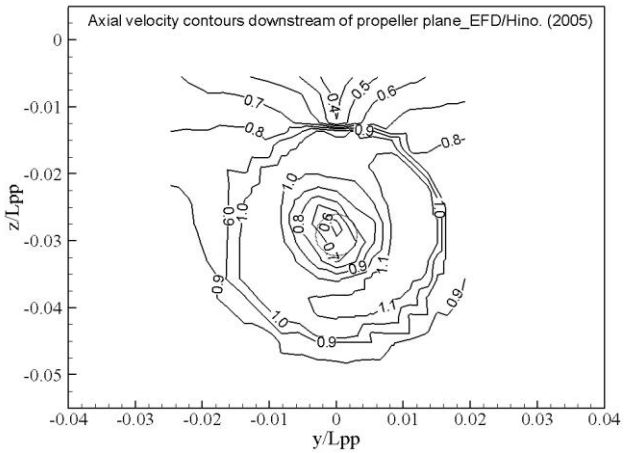

Experiment (NMRI)

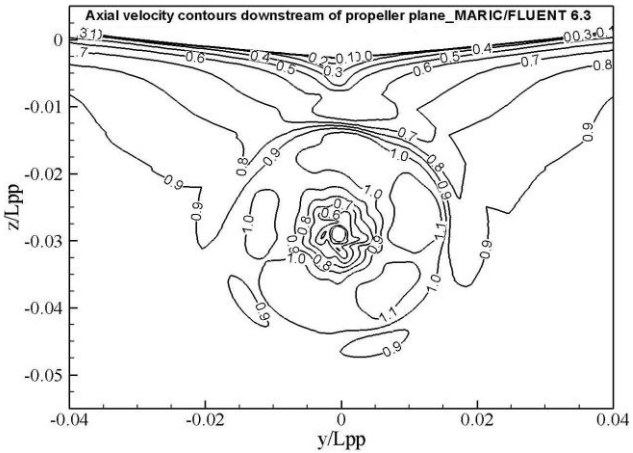

MARIC-FLUENT6.3 (without hub cap)

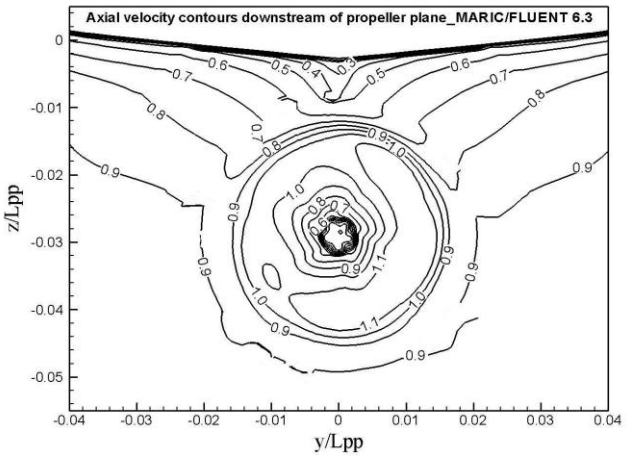

MARIC-FLUENT6.3 (with hub cap)

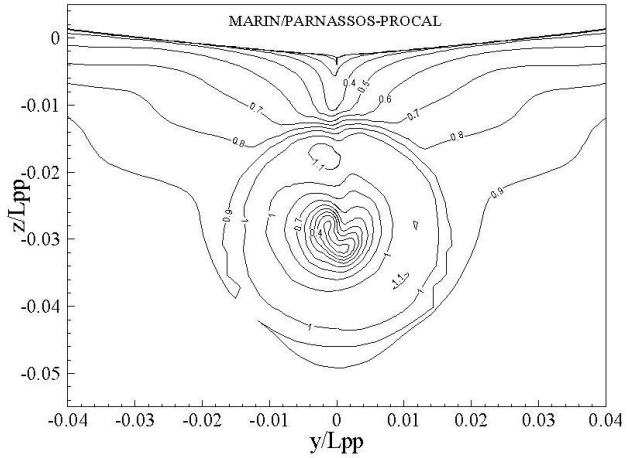

MARIN-PARNASSOS-PROCAL

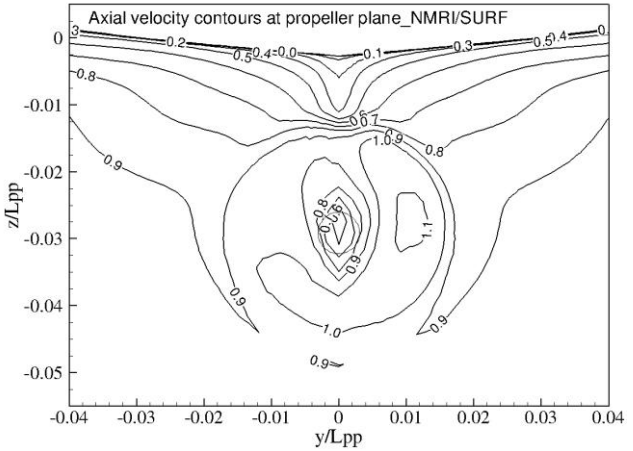

NMRI-SURF

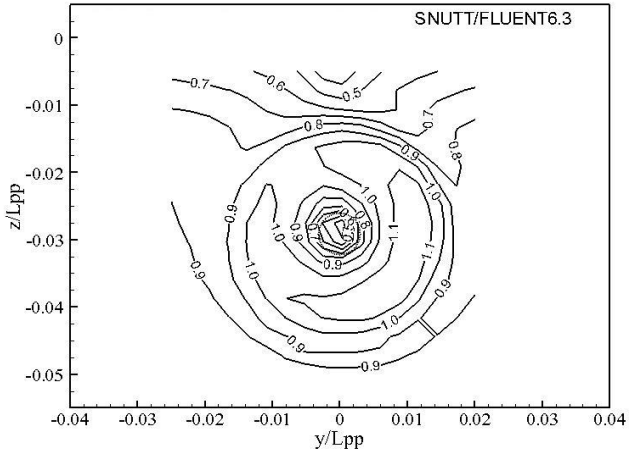

SNUTT-FLUENT6.3

Fig. 2.3a-2-1 Axial velocity contours downstream of propeller plane (at $x/L_{PP} = 0.9911$) [$\Delta U = 0.1$]

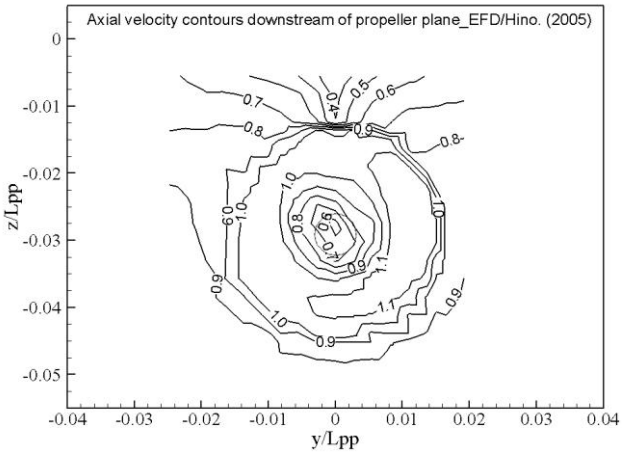

Experiment (NMRI)

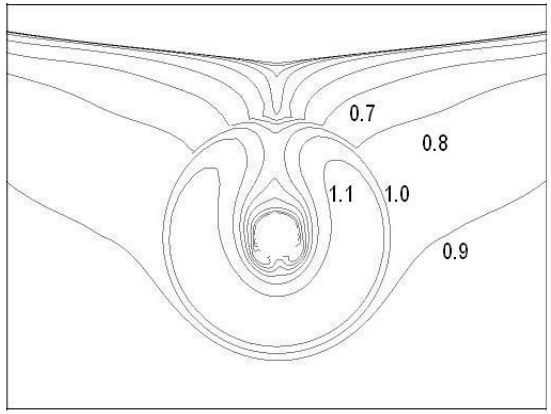

Southampton-CFX

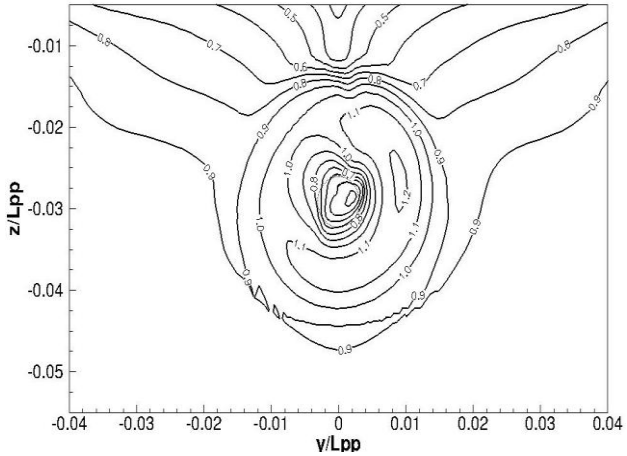

SSPA-SHIPFLOWv4.3

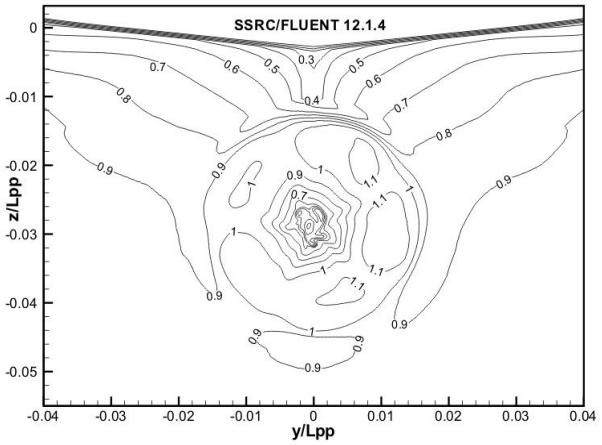

SSRC-FLUENT12.1

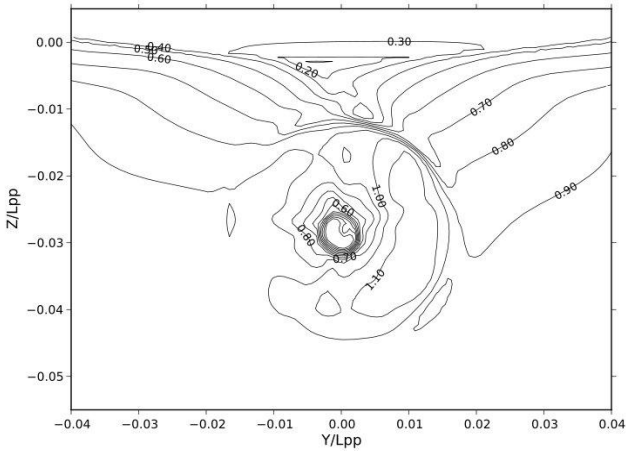

TUHH-FDS&ANSYS-CFX12.1

Fig. 2.3a-2-1 Axial velocity contours downstream of propeller plane (at $x/L_{PP} = 0.9911$) [$\Delta U = 0.1$]

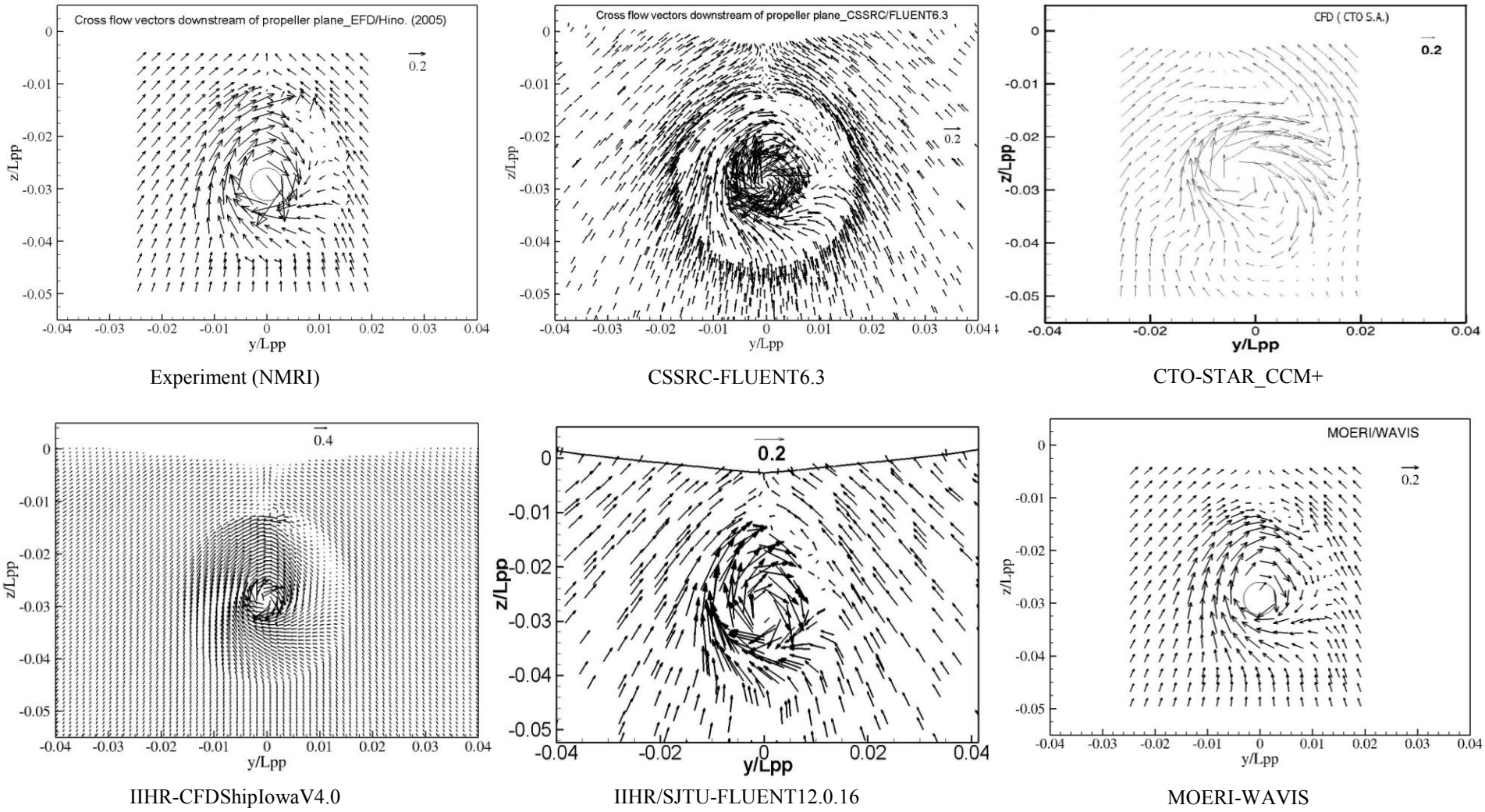

Experiment (NMRI) CSSRC-FLUENT6.3 CTO-STAR_CCM+

IIHR-CFDShipIowaV4.0 IIHR/SJTU-FLUENT12.0.16 MOERI-WAVIS

Fig. 2.3a-2-2 Axial velocity vectors downstream of propeller plane (at x/L_{PP} = 0.9911)

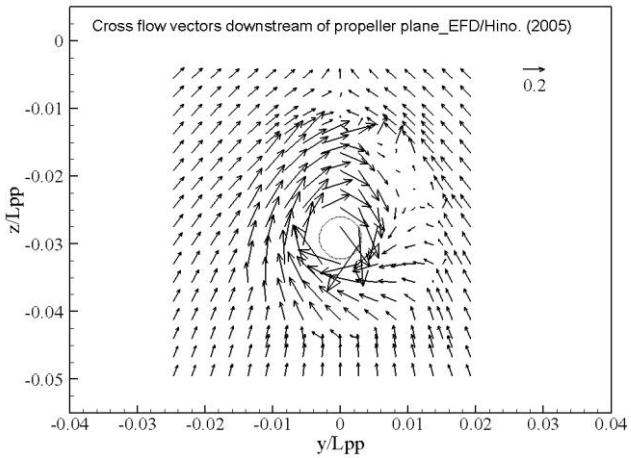

Experiment (NMRI)

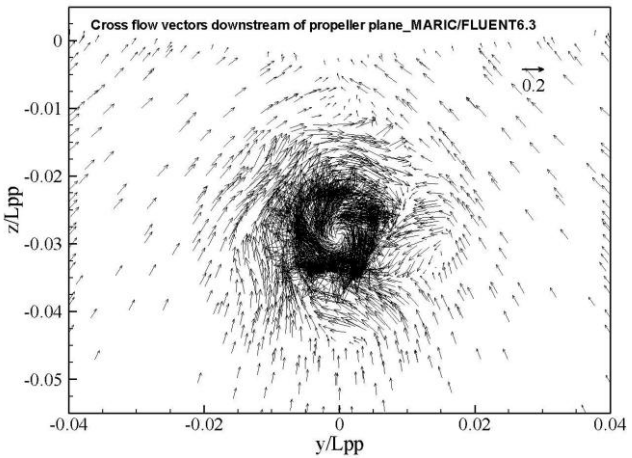

MARIC-FLUENT6.3 (without hub cap)

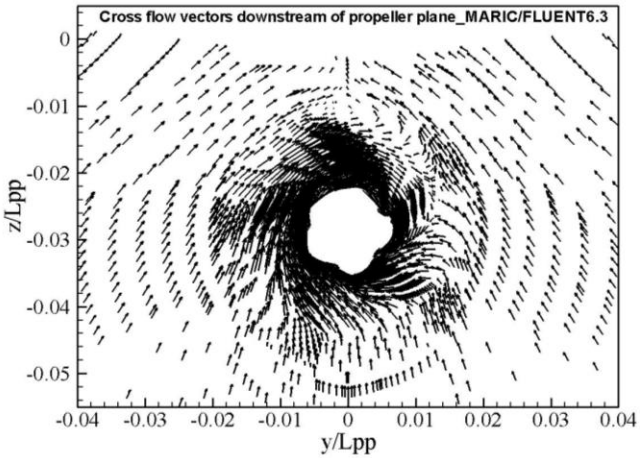

MARIC-FLUENT6.3 (with hub cap)

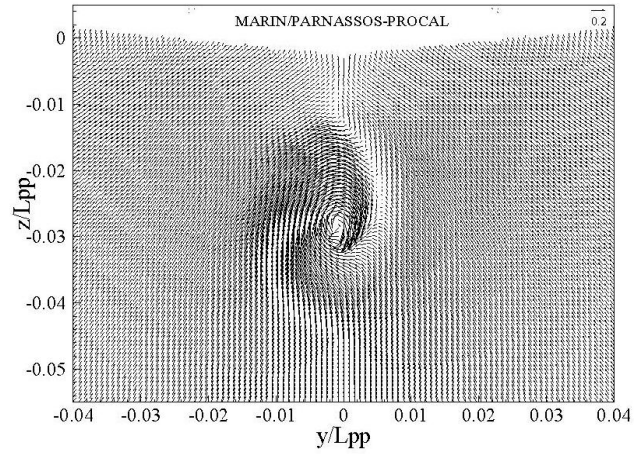

MARIN-PARNASSOS-PROCAL

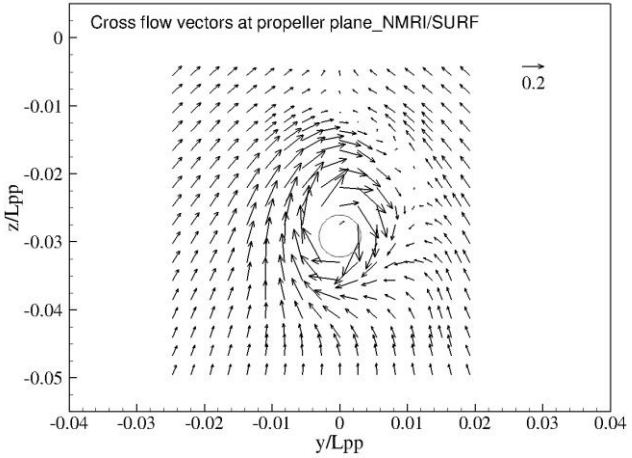

NMRI-SURF

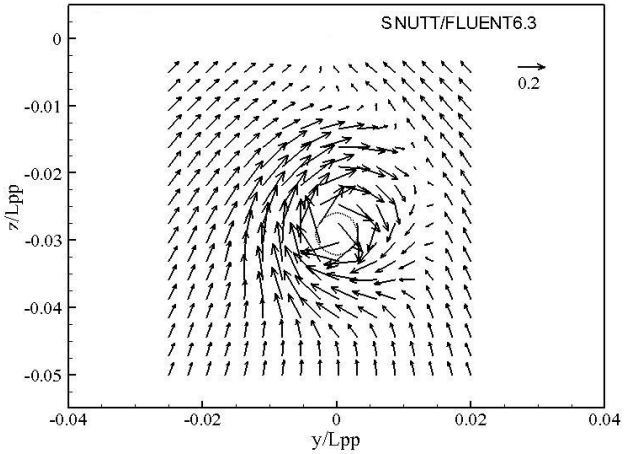

SNUTT-FLUENT6.3

Fig. 2.3a-2-2 Axial velocity vectors downstream of propeller plane (at $x/L_{PP} = 0.9911$)

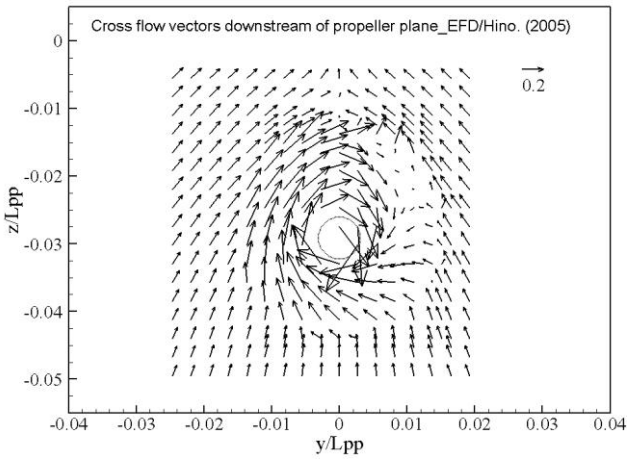

Experiment (NMRI)

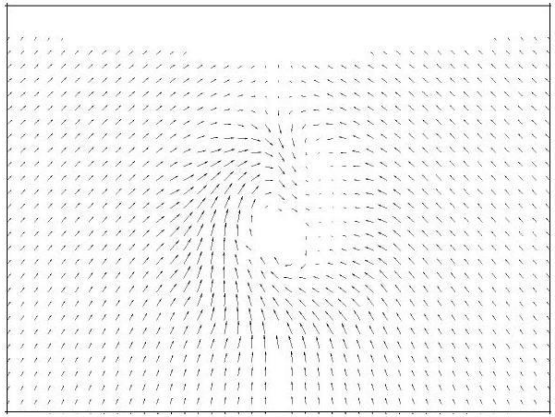

Southampton-CFX

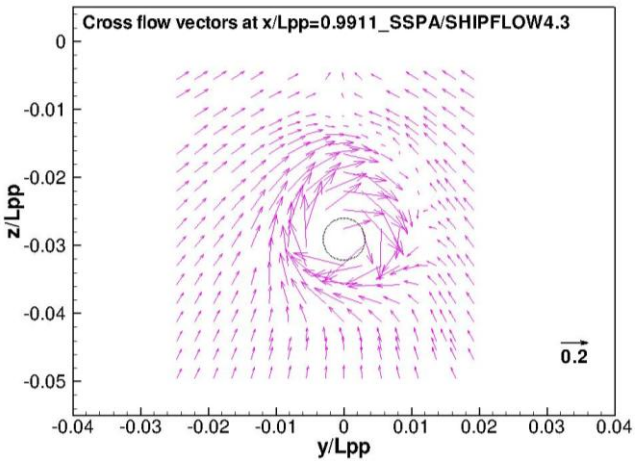

SSPA-SHIPFLOWv4.3

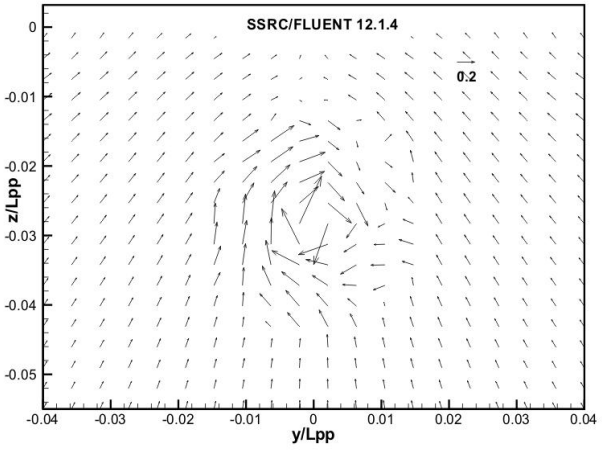

SSRC-FLUENT12.1

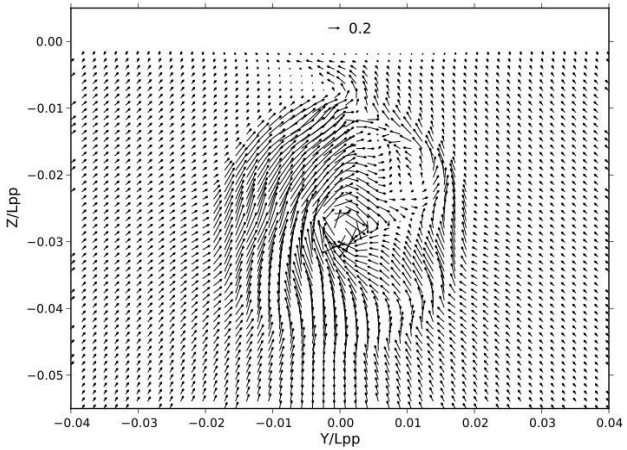

TUHH-FDS&ANSYS-CFX12.1

Fig. 2.3a-2-2 Axial velocity vectors downstream of propeller plane (at $x/L_{PP} = 0.9911$)

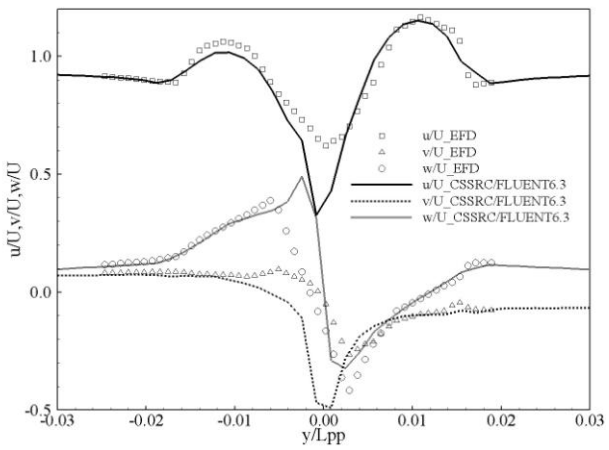

CSSRC-FLUENT6.3

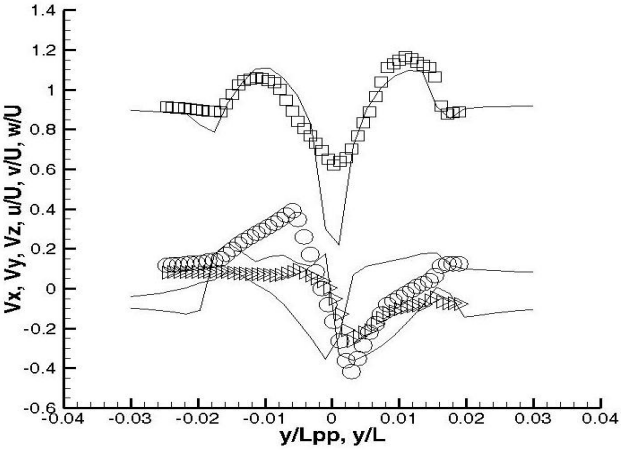

CTO-STAR_CCM+

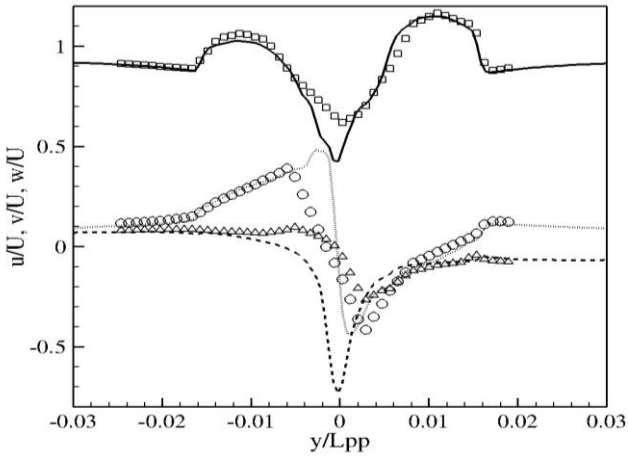

IIHR-CFDShipIowaV4.0

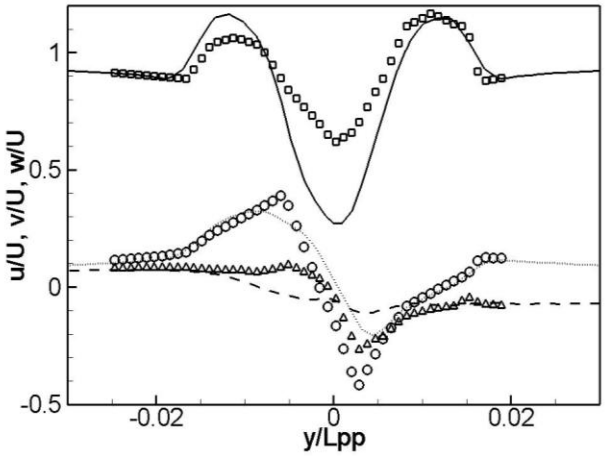

IIHR/SJTU-FLUENT12.0.16

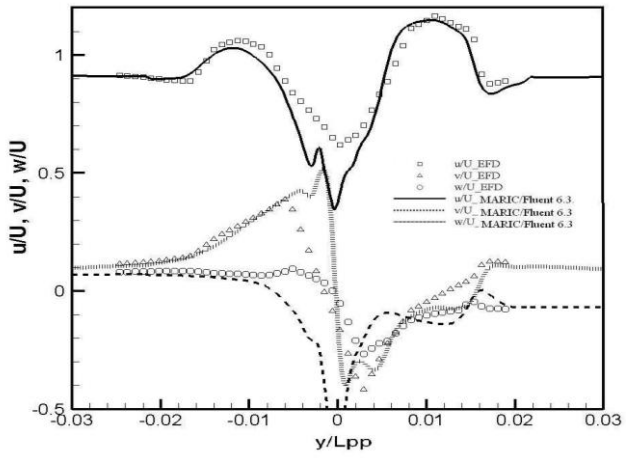

MARIC-FLUENT6.3 (without hub cap)

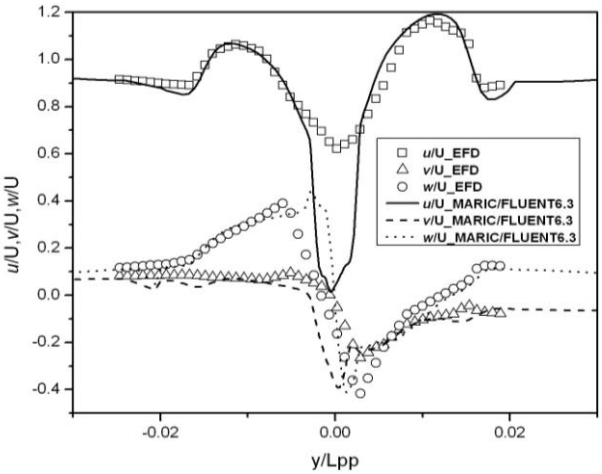

MARIC-FLUENT6.3 (with hub cap)

Fig. 2.3a-3 Velocity downstream of the propeller plane (at x/L_{PP} = 0.9911, z/L_{PP} = -0.03)

u/U: CFD solid line; EFD open squares
v/U: CFD dashed line; EFD open triangles
w/U: CFD dotted line; EFD open circles

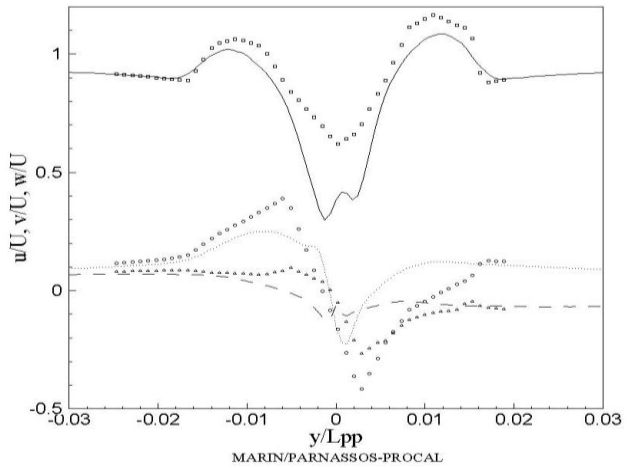

MARIN-PARNASSOS-PROCAL

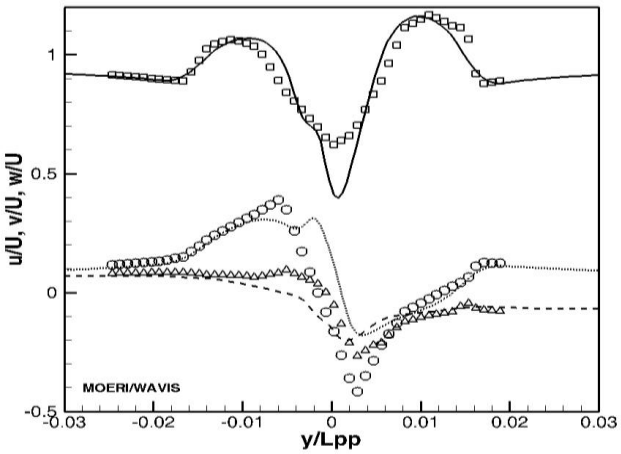

MOERI-WAVIS

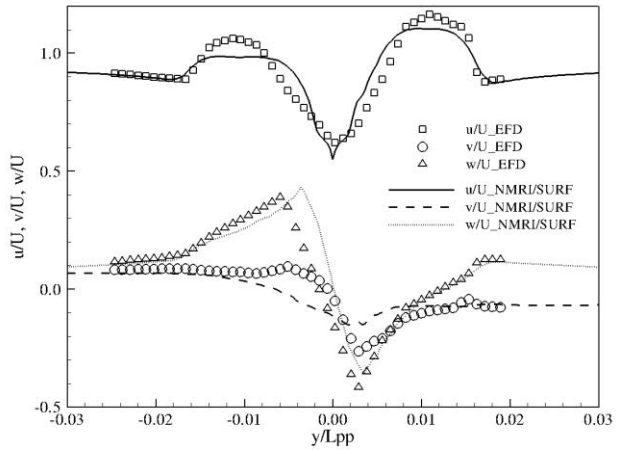

NMRI-SURF

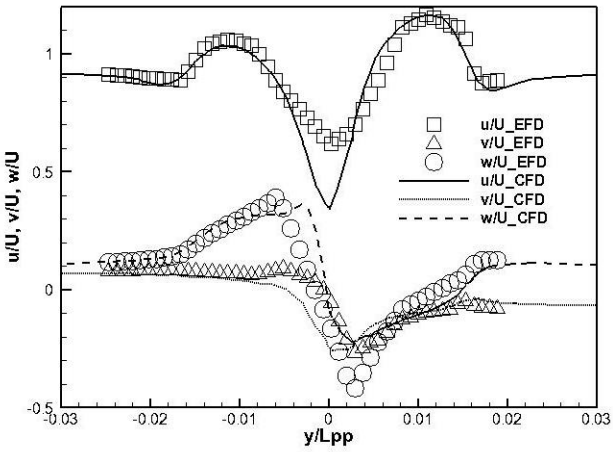

SNUTT-FLUENT6.3

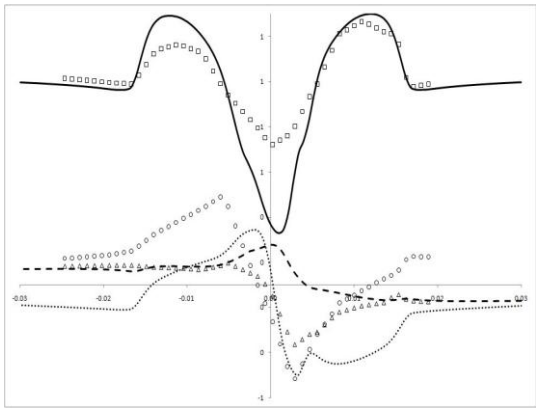

Southampton-CFX

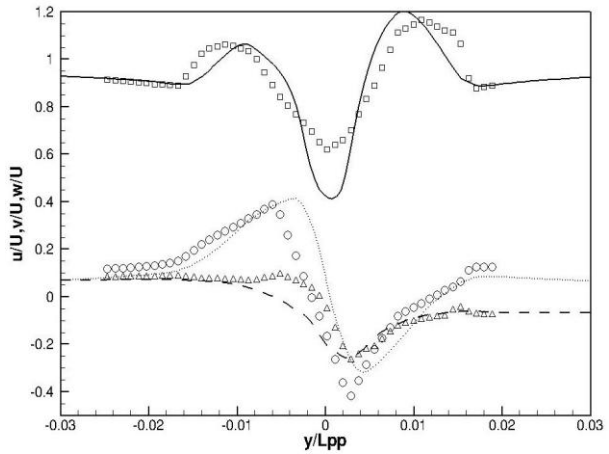

SSPA-SHIPFLOWv4.3

Fig. 2.3a-3 Velocity downstream of the propeller plane (at $x/L_{PP} = 0.9911$, $z/L_{PP} = -0.03$)

u/U: CFD solid line; EFD open squares
v/U: CFD dashed line; EFD open triangles
w/U: CFD dotted line; EFD open circles

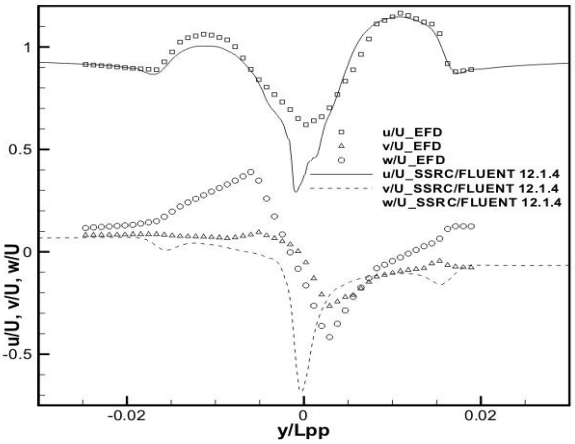

SSRC-FLUENT12.1

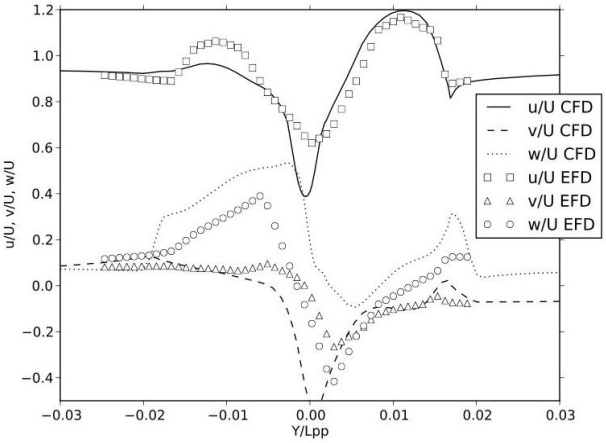

TUHH-FDS&ANSYS-CFX12.1

Fig. 2.3a-3 Velocity downstream of the propeller plane (at x/L_{PP} = 0.9911, z/L_{PP} = -0.03)

u/U: CFD solid line; EFD open squares
v/U: CFD dashed line; EFD open triangles
w/U: CFD dotted line; EFD open circles

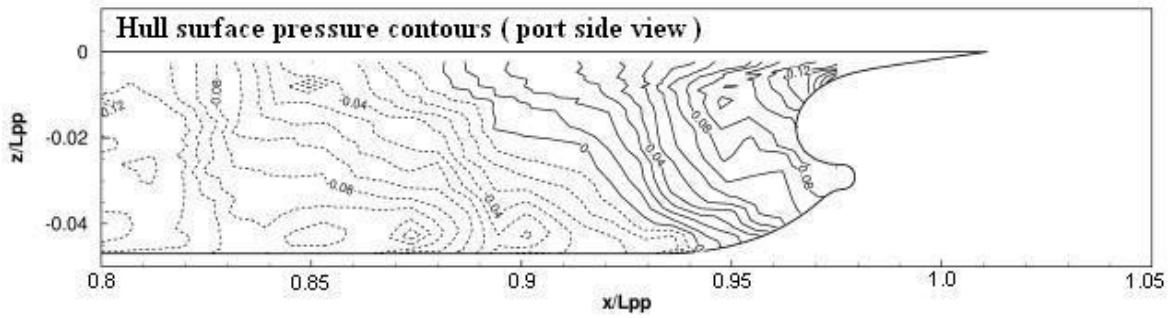

Experiment (Hino 2005)

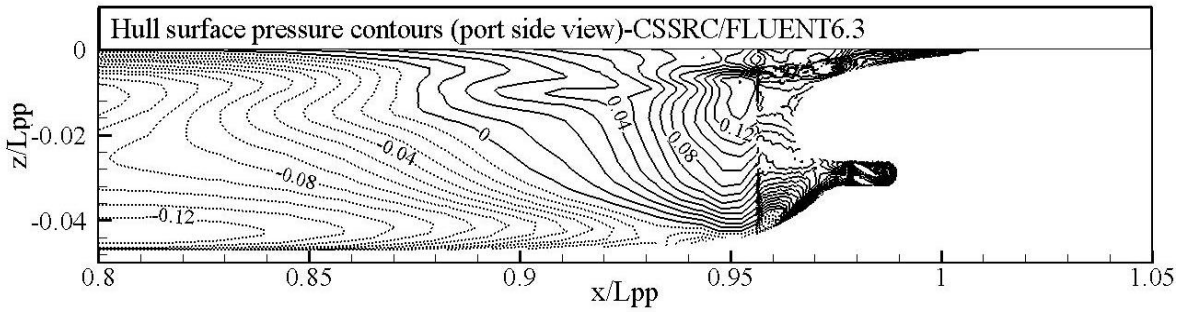

CSSRC-FLUENT6.3

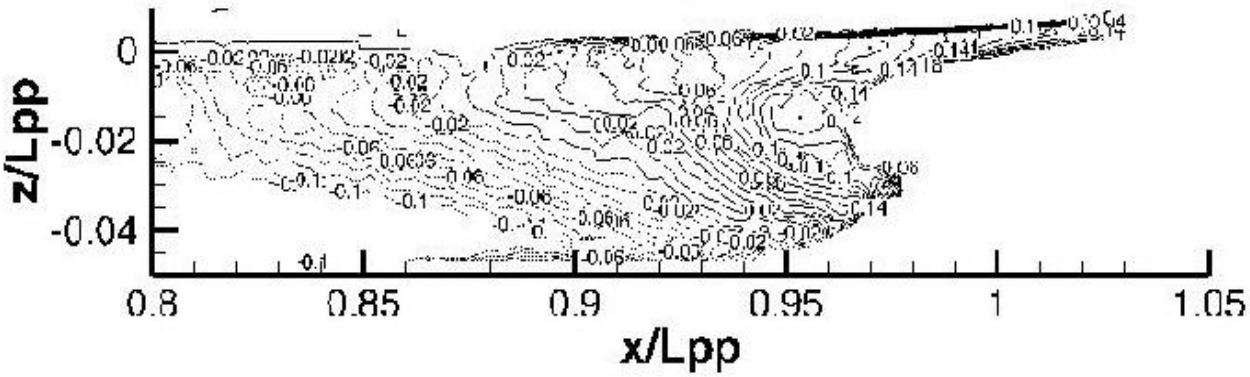

CTO-STAR_CCM+

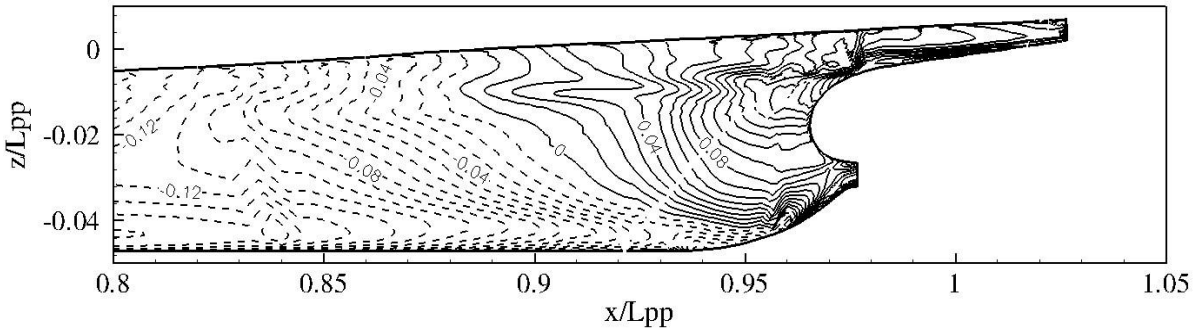

IIHR-CFDShipIowaV4.0

Fig. 2.3a-4 Hull surface pressure contours (port side view) [$\Delta Cp = 0.01$]
(Solid lines: positive (+) values; Dashed lines: negative (-) values)

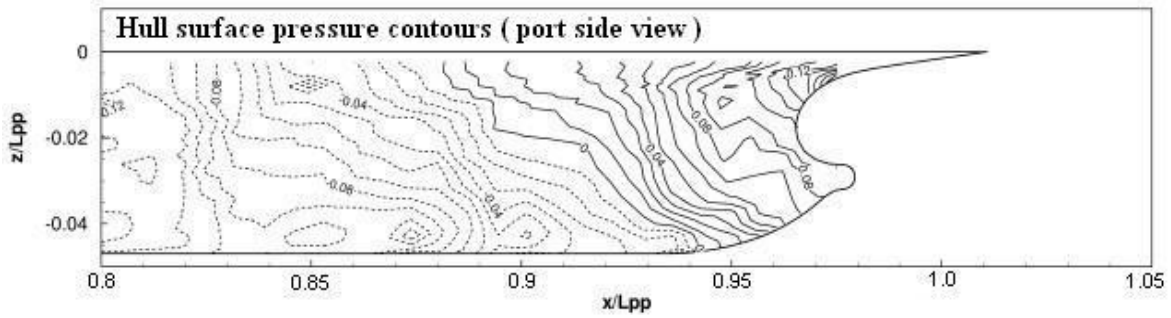

Experiment (Hino 2005)

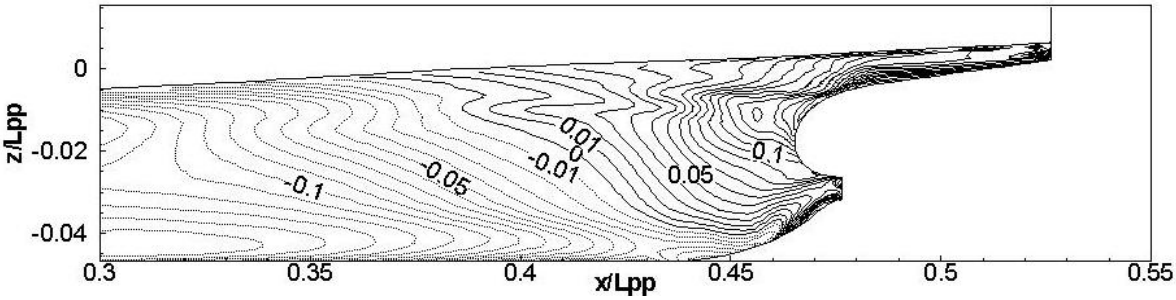

IIHR/SJTU-FLUENT12.0.16

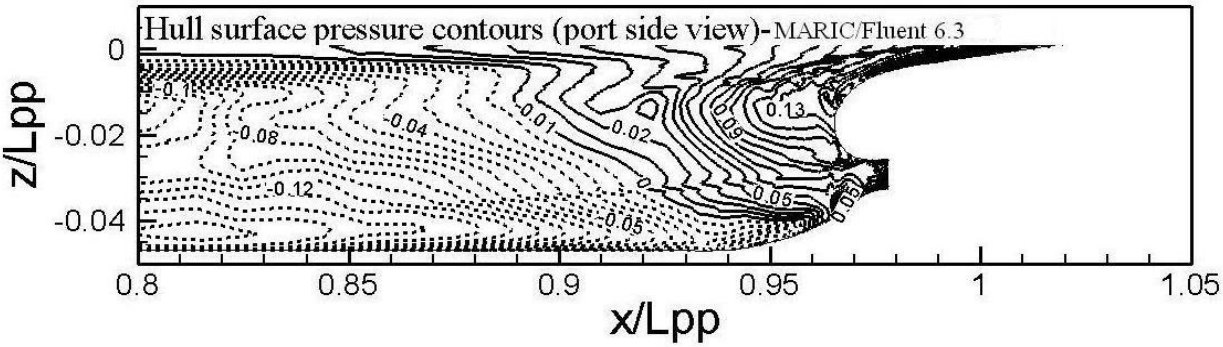

MARIC-FLUENT6.3 (without hub cap)

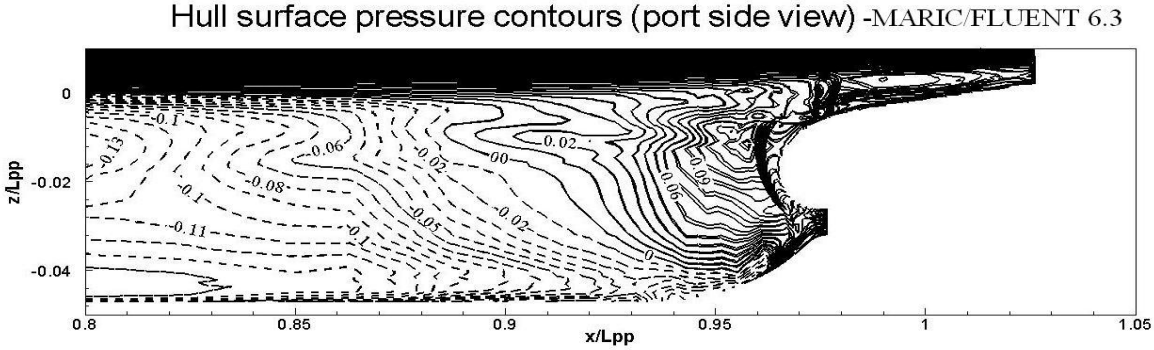

MARIC-FLUENT6.3 (with hub cap)

Fig. 2.3a-4 Hull surface pressure contours (port side view) [$\Delta Cp = 0.01$]
(Solid lines: positive (+) values; Dashed lines: negative (-) values)

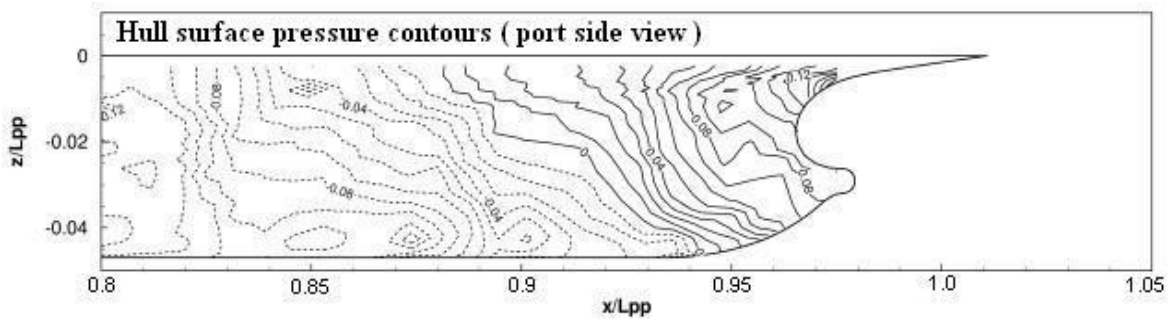

Experiment (Hino 2005)

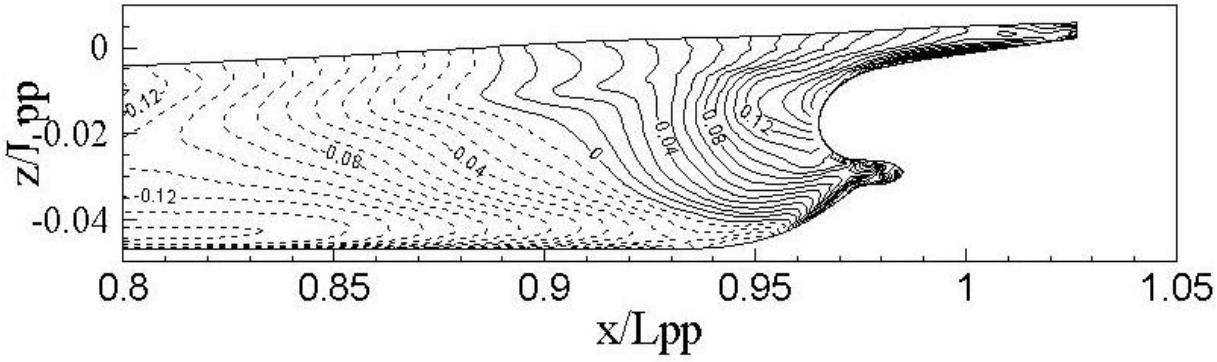

MARIN-PARNASSOS-PROCAL

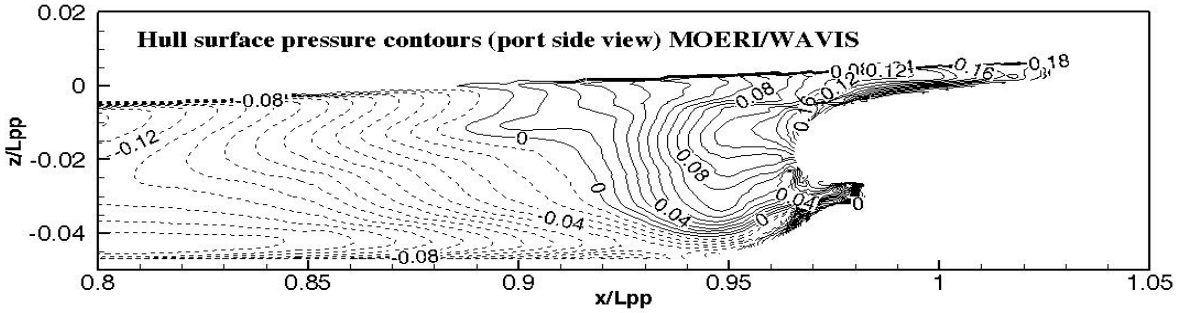

MOERI-WAVIS

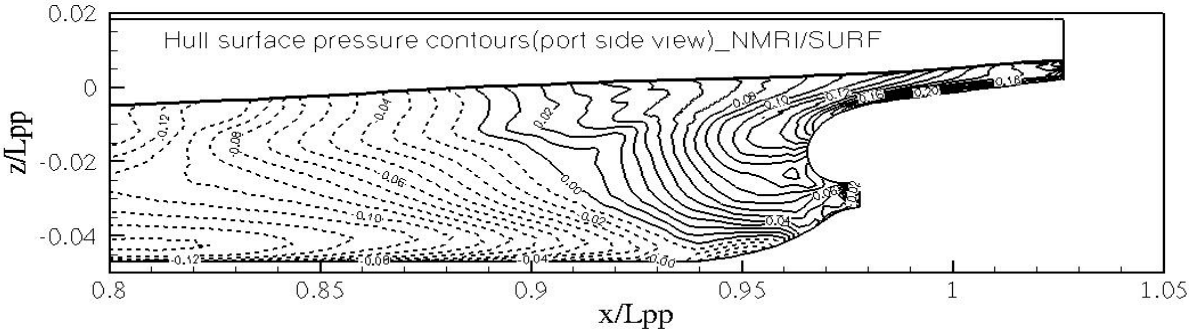

NMRI-SURF

Fig. 2.3a-4 Hull surface pressure contours (port side view) [$\Delta Cp = 0.01$]
(Solid lines: positive (+) values; Dashed lines: negative (-) values)

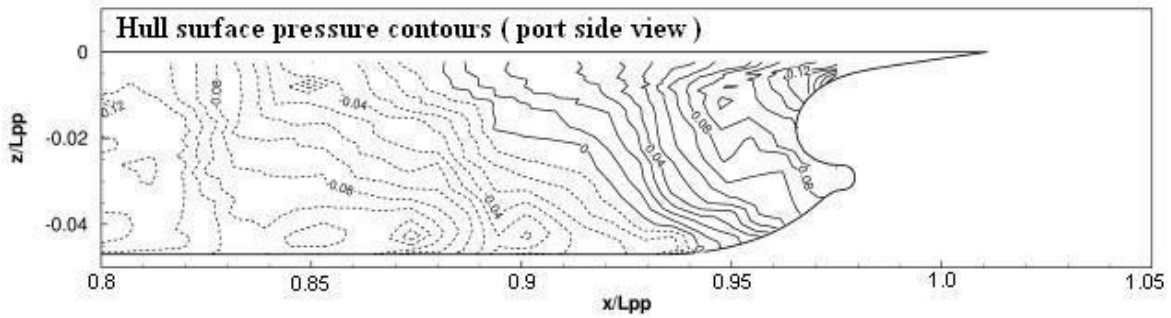

Experiment (Hino 2005)

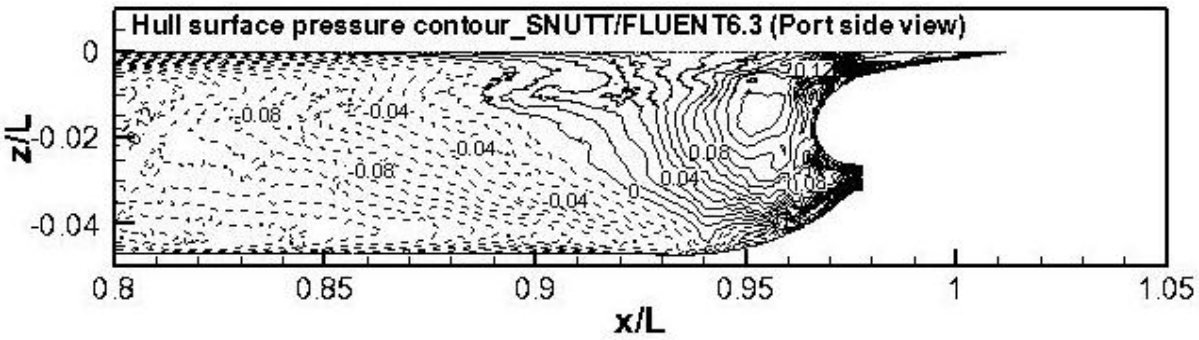

SNUTT-FLUENT6.3

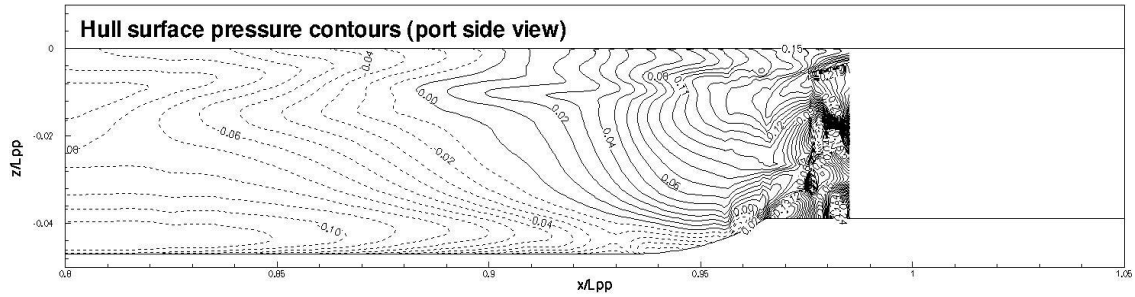

SSPA-SHIPFLOWv4.3

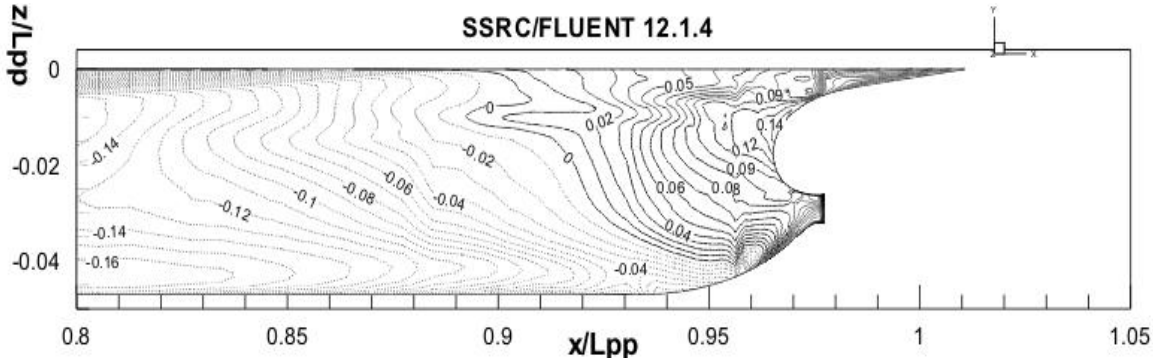

SSRC-FLUENT12.1.4

Fig. 2.3a-4 Hull surface pressure contours (port side view) [$\Delta Cp = 0.01$]
(Solid lines: positive (+) values; Dashed lines: negative (-) values)

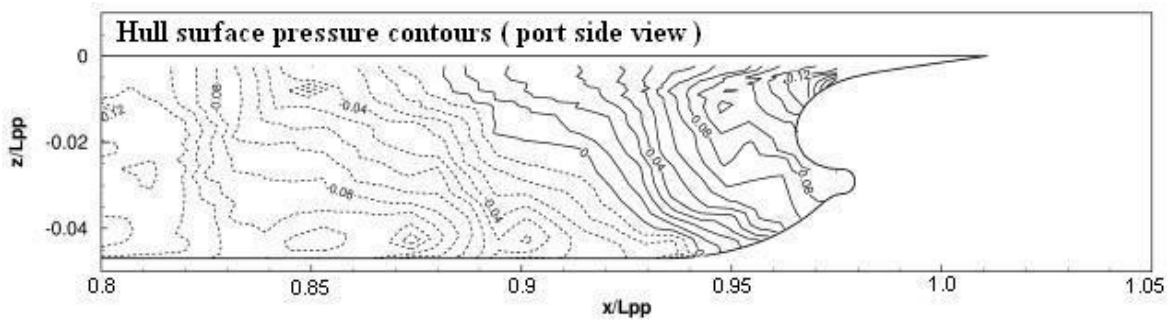

Experiment (Hino 2005)

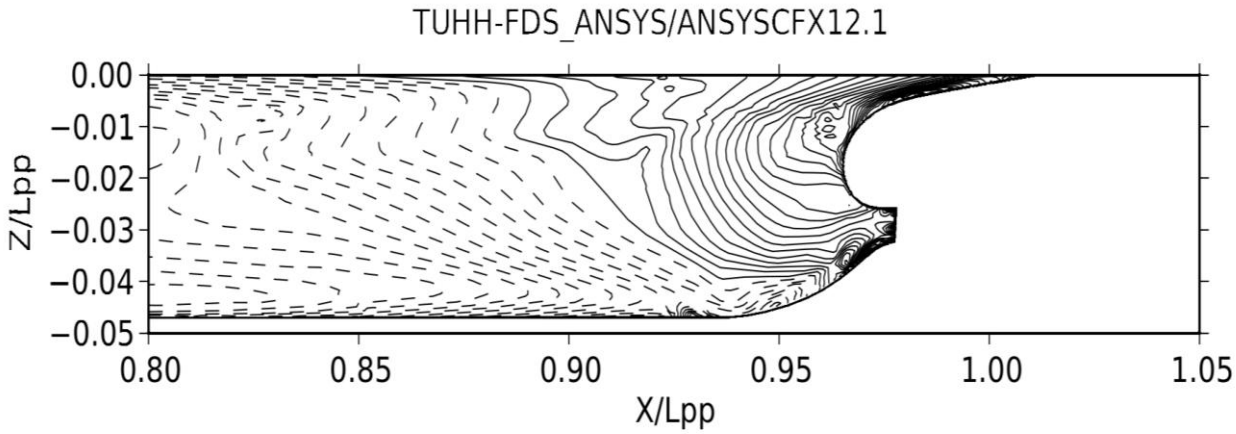

TUHH-FDS&ANSYS-CFX12.1

Fig. 2.3a-4 Hull surface pressure contours (port side view) [$\Delta Cp = 0.01$]
(Solid lines: positive (+) values; Dashed lines: negative (-) values)

Test Case 2.3b

Table 2.3b-0 Computations information and V&V method
Table 2.3b-1-1 Computed C_T, C_F and C_{PV} of different grid densities
Table 2.3b-1-2 V&V results for C_T, C_F and C_{PV}
Table 2.3b-1-3 Computed Sinkage (σ) and Trim (τ) of different grid densities
Table 2.3b-1-4 V&V results for Sinkage (σ) and Trim (τ)
Table 2.3b-1-5 Computed K_T, K_Q of different grid densities
Table 2.3b-1-6 V&V results for K_T, K_Q
Table 2.3b-1-7 Computed n, [RT(SP)-T] of different grid densities
Table 2.3b-1-8 V&V results for n, [RT(SP)-T]

Table 2.3b-0: Computations information and V&V method

Organization (Code)	**V&V method (including the determination of U_I)**
IIHR (CFDShipIowaV4.0)	-
MOERI (WAVIS)	Stern et al. 2001
SSPA (SHIPFLOWv4.3)	Eca and Hoekstra proposal

Table 2.3b-1-1: Computed C_T, C_F and C_{PV} of different grid densities

Organization (Code)	r_G		C_T ($\times 10^{-3}$)					C_F ($\times 10^{-3}$)					C_{PV} ($\times 10^{-3}$)				
			Grid #5	Grid #4	Grid #3	Grid #2	Grid #1	Grid #5	Grid #4	Grid #3	Grid #2	Grid #1	Grid #5	Grid #4	Grid #3	Grid #2	Grid #1
EFD (FORCE)	-	D	5.222					-					-				
IIHR (CFDShipIowaV4.0)	-	S	-	-	-	-	5.010	-	-	-	-	-	-	-	-	-	-
		$E\%D$	-	-	-	-	4.10										
MOERI (WAVIS)	1.414	S	-	-	5.157	4.911	4.862	-	-	3.226	3.273	3.283	-	-	1.932	1.638	1.579
		$E\%D$	-	-	1.24	5.97	6.89										
SSPA (SHIPFLOWv4.3)	1.3195	S	-	4.723	4.715	4.668	4.663	-	2.983	3.060	3.088	3.101	-	0.970	0.884	0.811	0.792
		$E\%D$	-	9.56	9.71	10.61	10.70										

$E\%D = (D\text{-}S)/D \times 100$

Table 2.3b-1-2: V&V results for C_T, C_F and C_{PV}

Organization (Code)	r_G	C_T						C_F						C_{PV}					
		$\varepsilon_{12}\%S_1$	$\frac{U_I}{\varepsilon_{12}}$	$\frac{P_G}{P_{G,th}}$	$U_G\%S_1$	$U_D\%D$	$U_V\%$	$\varepsilon_{12}\%S_1$	$\frac{U_I}{\varepsilon_{12}}$	$\frac{P_G}{P_{G,th}}$	$U_G\%S_1$	$U_D\%D$	$U_V\%$	$\varepsilon_{12}\%S_1$	$\frac{U_I}{\varepsilon_{12}}$	$\frac{P_G}{P_{G,th}}$	$U_G\%S_1$	$U_D\%D$	$U_V\%$
IIHR (CFDShipIowaV4.0)	-	-	-	-	-			-	-	-	-			-	-	-	-		
MOERI (WAVIS)	1.414	1.00	0.000	2.347	1.75			0.33	0.000	2.122	0.56			3.76	0.000	2.309	6.56		
SSPA (SHIPFLOWv4.3)	1.3195	0.11	0.325	0.088	1.61			0.42	0.001	1.714	4.76			2.40	0.014	0.939	10.07		

$\varepsilon_{12}\%S_1 = |(S_1\text{-}S_2)/S_1| \times 100$; $U_{SN} = \sqrt{U_I^2 + U_G^2}$; $U_V = \sqrt{U_D^2 + U_{SN}^2}$

Table 2.3b-1-3: Computed Sinkage (σ) and Trim (τ) of different grid densities

Organization (Code)	r_G		Sinkage $\sigma\times10^2$ (m)					Trim τ °				
			Grid #5	Grid #4	Grid #3	Grid #2	Grid #1	Grid #5	Grid #4	Grid #3	Grid #2	Grid #1
EFD (FORCE)	-	D	-0.833					-0.143				
IIHR (CFDShipIowaV4.0)	-	S	-	-	-	-	-1.183	-	-	-	-	-0.172
		$E\%D$	-	-	-	-	-42.00	-	-	-	-	-20.30
MOERI (WAVIS)	1.414	S	-	-	-0.922	-0.851	-0.887	-	-	-0.124	-0.123	-0.133
		$E\%D$	-	-	-10.73	-2.18	-6.53	-	-	13.29	14.06	6.88
SSPA (SHIPFLOWv4.3)	1.3195	S	-	-	-	-	-	-	-	-	-	-
		$E\%D$	-	-	-	-	-	-	-	-	-	-

$E\%D = (D\text{-}S)/D\times100$

Table 2.2b-1-4: V&V results for Sinkage (σ) and Trim (τ)

Organization (Code)	r_G	Sinkage σ						Trim τ °					
		ε_{12} $\%S_1$	$\frac{U_I}{\varepsilon_{12}}$	$\frac{P_G}{P_{G,th}}$	U_G $\%S_1$	U_D $\%D$	$U_V\%$	ε_{12} $\%S_1$	$\frac{U_I}{\varepsilon_{12}}$	$\frac{P_G}{P_{G,th}}$	U_G $\%S_1$	U_D $\%D$	$U_V\%$
IIHR (CFDShipIowaV4.0)	-	-	-	-	-			-	-	-	-		
MOERI (WAVIS)	1.414	4.08	0.000	0.974	4.24			7.71	0.000	3.222	14.49		
SSPA (SHIPFLOWv4.3)	-	-	-	-	-			-	-	-	-		

$\varepsilon_{12}\%S_1 = |(S_1\text{-}S_2)/S_1|\times100$; $U_{SN} = \sqrt{U_I^2 + U_G^2}$; $U_V = \sqrt{U_D^2 + U_{SN}^2}$

Table 2.3b-1-5: Computed K_T, K_Q of different grid densities

Organization (Code)	r_G		K_T					K_Q				
			Grid #5	Grid #4	Grid #3	Grid #2	Grid #1	Grid #5	Grid #4	Grid #3	Grid #2	Grid #1
EFD (FORCE)	-	D	0.253					0.0408				
IIHR (CFDShipIowaV4.0)	-	S	-	-	-	-	0.2360	-	-	-	-	0.0387
		$E\%D$	-	-	-	-	6.70	-	-	-	-	5.10
MOERI (WAVIS)	1.414	S	-	-	0.2259	0.2207	0.2223	-	-	0.0368	0.0354	0.0357
		$E\%D$	-	-	10.71	12.77	12.13	-	-	9.78	13.14	12.55
SSPA (SHIPFLOWv4.3)	1.3195	S		0.2676	0.2652	0.2560	0.2535		0.0415	0.0412	0.0401	0.0398
		$E\%D$		-5.75	-4.82	-1.18	-0.18		-1.61	-1.00	1.73	2.45

$E\%D = (D\text{-}S)/D \times 100$

Table 2.3b-1-6: V&V results for K_T, K_Q

Organization (Code)	r_G	K_T						K_Q					
		ε_{12} $\%S_1$	$\frac{U_I}{\varepsilon_{12}}$	$\frac{P_G}{P_{G,th}}$	U_G $\%S_1$	U_D $\%D$	$U_V\%$	ε_{12} $\%S_1$	$\frac{U_I}{\varepsilon_{12}}$	$\frac{P_G}{P_{G,th}}$	U_G $\%S_1$	U_D $\%D$	$U_V\%$
IIHR (CFDShipIowaV4.0)	-	-	-	-	-			-	-	-	-		
MOERI (WAVIS)	1.414	0.72	0.000	1.700	1.12			0.67	0.000	2.513	1.20		
SSPA (SHIPFLOWv4.3)	1.3195	1.00	0.001	0.002	6.95			0.74	0.000	0.001	5.20		

$\varepsilon_{12}\%S_1 = |(S_1\text{-}S_2)/S_1| \times 100$; $U_{SN} = \sqrt{U_I^2 + U_G^2}$; $U_V = \sqrt{U_D^2 + U_{SN}^2}$

Table 2.3b-1-7: Computed n, [$RT(SP)$-T] of different grid densities

Organization (Code)	r_G		n (rps) (for given SFC)					[$RT(SP)$-T] (N) (for given n)				
			Grid #5	Grid #4	Grid #3	Grid #2	Grid #1	Grid #5	Grid #4	Grid #3	Grid #2	Grid #1
EFD (FORCE)	-	D	14.15					0.4				
IIHR (CFDShipIowaV4.0)	-	S	-	-	-	-	14.440	-	-	-	-	-
		$E\%D$	-	-	-	-	-2.00	-	-	-	-	-
MOERI (WAVIS)	1.414	S	-	-	15.020	14.814	14.697	-	-	-	-	-
		$E\%D$	-	-	-6.15	-4.69	-3.87	-	-	-	-	-
SSPA (SHIPFLOWv4.3)	1.3195	S	-	13.172	13.218	13.387	13.445	-	-	-	-	-
		$E\%D$	-	6.91	6.59	5.39	4.98	-	-	-	-	-

$E\%D = (D\text{-}S)/D\times 100$

Table 2.3b-1-8: V&V results for n, [$RT(SP)$-T]

Organization (Code)	r_G	n (rps) (for given SFC)						[$RT(SP)$-T] (N) (for given n)					
		$\varepsilon_{12}\%S_1$	$\frac{U_I}{\varepsilon_{12}}$	$\frac{P_G}{P_{G,th}}$	$U_G\%S_1$	$U_D\%D$	$U_V\%$	$\varepsilon_{12}\%S_1$	$\frac{U_I}{\varepsilon_{12}}$	$\frac{P_G}{P_{G,th}}$	$U_G\%S_1$	$U_D\%D$	$U_V\%$
IIHR (CFDShipIowaV4.0)	-	-	-	-	-			-	-	-	-		
MOERI (WAVIS)	1.414	0.80	0.000	0.808	1.06			-	-	-	-		
SSPA (SHIPFLOWv4.3)	1.3195	0.43	0.071	0.002	2.54			-	-	-	-		

$\varepsilon_{12}\%S_1 = |(S_1\text{-}S_2)/S_1|\times 100$; $U_{SN} = \sqrt{U_I^2 + U_G^2}$; $U_V = \sqrt{U_D^2 + U_{SN}^2}$

Test Case 2.4

Table 2.4-1-1 Harmonic amplitudes and phases of the total resistance coefficient (C_T), heave motion (z), pitch angle (θ) and wave amplitude (ζ) (λ/L_{PP} = 0.5, Hs = 36 mm, Fr = 0.26)

Table 2.4-1-2 Harmonic amplitudes and phases of the total resistance coefficient (C_T), heave motion (z), pitch angle (θ) and wave amplitude (ζ) (λ/L_{PP} = 1.15, Hs = 84mm, Fr = 0.26)

Table 2.4-1-3 Harmonic amplitudes and phases of the total resistance coefficient (C_T), heave motion (z), pitch angle (θ) and wave amplitude (ζ) (λ/L_{PP} = 2.00, Hs = 146 mm, Fr = 0.26)

Table 2.4-1-4 Harmonic amplitudes and phases of the total resistance coefficient (C_T), heave motion (z), pitch angle (θ) and wave amplitude (ζ) (λ/L_{PP} = 1.33, Hs = 97mm, Fr = 0. 33)

Figure 2.4-2-C1-1 Time histories of total resistance coefficient (C_T) (λ/L_{PP} = 0.5, Hs = 36mm, Fr = 0.26)

Figure 2.4-2-C1-2 Time histories of heave motion (z) (λ/L_{PP} = 0.5, Hs =36mm, Fr =0.26)

Figure 2.4-2-C1-3 Time histories of pitch angle (θ) (λ/L_{PP} = 0.5, Hs =36mm, Fr =0.26)

Figure 2.4-2-C2-1 Time histories of total resistance coefficient (C_T) (λ/L_{PP} = 1.15, Hs = 84mm, Fr = 0.26)

Figure 2.4-2-C2-2 Time histories of heave motion (z) (λ/L_{PP} = 1.15, Hs=84mm, Fr = 0.26)

Figure 2.4-2-C2-3 Time histories of pitch angle (θ) (λ/L_{PP} = 1.15, Hs=84mm, Fr = 0.26)

Figure 2.4-2-C3-1 Time histories of total resistance coefficient (C_T) (λ/L_{PP} = 2.00, Hs = 146mm, Fr = 0.26)

Figure 2.4-2-C3-2 Time histories of heave motion (z) (λ/L_{PP} = 2.00, Hs = 146mm, Fr = 0.26)

Figure 2.4-2-C3-3 Time histories of pitch angle (θ) (λ/L_{PP} = 2.00, Hs = 146mm, Fr = 0.26)

Figure 2.4-2-C4-1 Time histories of total resistance coefficient (C_T) (λ/L_{PP} = 1.33, Hs = 97mm, Fr = 0.33)

Figure 2.4-2-C4-2 Time histories of heave motion (z) (λ/L_{PP} = 1.33, Hs = 97mm, Fr = 0.33)

Figure 2.4-2-C4-3 Time histories of pitch angle (θ) (λ/L_{PP} = 1.33, Hs = 97mm, Fr = 0.33)

Table 2.4-1-1: harmonic amplitudes and phases of the total resistance coefficient (C_T), heave motion (z), pitch angle (θ) and wave amplitude (ζ)
(λ/L_{PP} = 0.5, Hs = 36 mm, Fr = 0.26)

Organization (Code)		C_T							z			θ			ζ
		0^{th} Amplitude ($\times 10^3$)	1^{st} Amplitude ($\times 10^3$)	2^{nd} Amplitude ($\times 10^3$)	3^{rd} Amplitude ($\times 10^3$)	1^{st} Phase °	2^{nd} Phase °	3^{rd} Phase °	0^{th} Amplitude (mm)	1^{st} Amplitude (mm)	1^{st} Phase °	0^{th} Amplitude °	1^{st} Amplitude °	1^{st} Phase °	1^{st} Amplitude (mm)
EFD (FORCE)	*D*	-	-	-	-	-	-	-	-	-	-	-	-	-	-
IHI (WISDAM-UTokyo)	*S*	2.143	0.013	0.013	1.926	-14.490	-39.633	-151.773	-75.497	0.040	2.405	-0.117	0.002	-9.679	-
	E%D	-	-	-	-	-	-	-	-	-	-	-	-	-	-

$E\%D = (D\text{-}S)/D \times 100$

Table 2.4-1-2: harmonic amplitudes and phases of the total resistance coefficient (C_T), heave motion (z), pitch angle (θ) and wave amplitude (ζ) (λ/L_{PP} = 1.15, Hs = 84mm, Fr = 0.26)

Organization (Code)		C_T							z			θ			ζ
		0^{th} Amplitude ($\times 10^3$)	1^{st} Amplitude ($\times 10^3$)	2^{nd} Amplitude ($\times 10^3$)	3^{rd} Amplitude ($\times 10^3$)	1^{st} Phase °	2^{nd} Phase °	3^{rd} Phase °	0^{th} Amplitude (mm)	1^{st} Amplitude (mm)	1^{st} Phase °	0^{th} Amplitude °	1^{st} Amplitude °	1^{st} Phase °	1^{st} Amplitude (mm)
EFD (FORCE)	*D*	7.159	20.425	4.726	1.556	81.870	-144.917	-160.443	-5.436	39.544	-20.566	0.064	2.095	8.485	41.275
FORCE (CFDship-Iowa V4)	*S*	6.760	3.610	1.925	1.426	77.893	-266.273	-10.541	-5.714	43.541	-11.352	-0.028	2.389	22.979	42.000
	E%D	5.57	82.33	59.27	8.35	4.86	-83.74	93.43	-5.11	-10.11	44.80	143.44	-14.03	-170.82	-1.76
GL&UDE (Comet)	*S*	-	-	-	-	-	-	-	-6.496	37.808	-21.130	0.019	2.122	12.890	-
	E%D	-	-	-	-	-	-	-	-19.50	4.39	-2.74	70.31	-1.29	-51.92	-
GL&UDE (OpenFOAM)	*S*	-	-	-	-	-	-	-	-5.869	38.819	-19.770	0.023	2.165	14.050	-
	E%D	-	-	-	-	-	-	-	-7.97	1.83	3.87	64.06	-3.34	-65.59	-
IHI (WISDAM-UTokyo)	*S*	5.627	0.292	0.260	0.296	87.247	-84.102	-43.418	-6.244	33.615	-29.639	0.045	2.108	19.616	-
	E%D	21.40	98.57	94.50	80.98	-6.57	41.97	72.94	-14.86	14.99	-44.12	29.69	-0.62	-131.18	-
IIHR (CFDShip-Iowa V4)	*S*	6.971	6.032	1.417	0.543	67.111	55.505	1.533	-6.372	33.964	-7.548	-0.077	2.209	29.956	-
	E%D	2.63	70.47	70.02	65.10	18.03	138.30	100.96	-17.22	14.11	63.30	220.31	-5.44	-253.05	-
TUHH (FreSCo+)	*S*	8.628	3.153	1.970	1.590	117.850	-73.650	-12.030	-6.001	37.932	-22.290	0.002	1.984	22.340	-
	E%D	-20.53	84.56	58.32	-2.19	-43.95	49.18	92.50	-10.39	4.08	-8.36	96.25	5.30	-163.29	-

$E\%D = (D-S)/D \times 100$

Table 2.4-1-3: harmonic amplitudes and phases of the total resistance coefficient (C_T), heave motion (z), pitch angle (θ) and wave amplitude (ζ) (λ/L_{PP} = 2.00, Hs = 146 mm, Fr = 0.26)

Organization (Code)		C_T							z			θ			ζ
		0^{th} Amplitude ($\times 10^3$)	1^{st} Amplitude ($\times 10^3$)	2^{nd} Amplitude ($\times 10^3$)	3^{rd} Amplitude ($\times 10^3$)	1^{st} Phase °	2^{nd} Phase °	3^{rd} Phase °	0^{th} Amplitude (mm)	1^{st} Amplitude (mm)	1^{st} Phase °	0^{th} Amplitude °	1^{st} Amplitude °	1^{st} Phase °	1^{st} Amplitude (mm)
EFD (FORCE)	*D*	6.033	32.067	29.587	6.956	70.811	-17.631	-99.706	-6.573	67.328	-3.095	0.062	3.156	50.273	71.777
FORCE (CFDship-Iowa V4)	*S*	-	-	-	-	-	-	-	-	-	-	-	-	-	-
	E%D	-	-	-	-	-	-	-	-	-	-	-	-	-	-
GL&UDE (Comet)	*S*	-	-	-	-	-	-	-	-6.540	65.020	-1.140	-0.037	3.129	63.800	-
	E%D	-	-	-	-	-	-	-	0.50	3.43	63.17	159.68	0.86	-26.91	-
GL&UDE (OpenFOAM)	*S*	-	-	-	-	-	-	-	-7.074	65.088	0.760	0.080	3.141	65.090	-
	E%D	-	-	-	-	-	-	-	-7.62	3.33	124.56	-29.03	0.48	-29.47	-
IHI (WISDAM-UTokyo)	*S*	4.168	24.134	0.611	0.237	84.306	-36.668	-31.580	-7.228	91.644	-8.534	0.035	3.117	71.591	-
	E%D	30.91	24.74	97.93	96.59	-19.06	-107.97	68.33	-9.97	-36.12	-175.74	43.55	1.24	-42.40	-
IIHR (CFDShip-Iowa V4)	*S*	5.599	25.214	0.731	0.146	82.296	81.979	44.569	-6.490	62.426	2.000	-0.210	2.987	70.000	-
	E%D	7.19	21.37	97.53	97.90	-16.22	564.97	144.70	1.26	7.28	164.62	438.71	5.35	-39.24	-
TUHH (FreSCo+)	*S*	7.841	26.062	0.550	0.230	72.760	10.440	22.600	-6.348	69.978	-2.030	0.025	3.556	60.539	-
	E%D	-29.97	18.73	98.14	96.69	-2.75	159.21	122.67	3.42	-3.94	34.52	59.38	-12.68	-20.42	-

$E\%D = (D\text{-}S)/D \times 100$

Table 2.4-1-4: harmonic amplitudes and phases of the total resistance coefficient (C_T), heave motion (z), pitch angle (θ) and wave amplitude (ζ) (λ/L_{PP} = 1.33, Hs = 97mm, Fr = 0. 33)

Organization (Code)		C_T							z			θ			ζ
		0^{th} Amplitude ($\times10^3$)	1^{st} Amplitude ($\times10^3$)	2^{nd} Amplitude ($\times10^3$)	3^{rd} Amplitude ($\times10^3$)	1^{st} Phase °	2^{nd} Phase °	3^{rd} Phase °	0^{th} Amplitude (mm)	1^{st} Amplitude (mm)	1^{st} Phase °	0^{th} Amplitude °	1^{st} Amplitude °	1^{st} Phase °	1^{st} Amplitude (mm)
EFD (FORCE)	*D*	8.716	35.394	2.841	1.839	-260.205	-74.121	-100.403	-12.274	61.811	-18.283	-0.067	2.523	46.097	45.572
FORCE (CFDship-Iowa V4)	*S*	-	-	-	-	-	-	-	-	-	-	-	-	-	-
	E%D	-	-	-	-	-	-	-	-	-	-	-	-	-	-
GL&UDE (Comet)	*S*	-	-	-	-	-	-	-	-11.905	55.334	-26.050	0.141	2.548	16.440	-
	E%D	-	-	-	-	-	-	-	3.01	10.48	-42.48	310.45	-0.99	64.34	-
GL&UDE (OpenFOAM)	*S*	-	-	-	-	-	-	-	-11.278	55.999	-24.620	0.117	2.573	17.660	-
	E%D	-	-	-	-	-	-	-	8.11	9.40	-34.66	274.63	-1.98	61.69	-
IHI (WISDAM-UTokyo)	*S*	4.070	14.050	0.212	0.310	-77.319	61.360	-29.704	-6.600	56.316	-17.182	0.021	2.372	33.115	-
	E%D	53.30	60.30	92.54	83.14	70.29	182.78	70.42	46.23	8.89	6.02	131.34	5.98	28.16	-
IIHR (CFDShip-Iowa V4)	*S*	8.189	5.085	0.973	0.343	86.411	67.219	85.746	-11.800	50.960	-14.000	0.040	2.592	21.000	-
	E%D	6.05	85.63	65.75	81.35	133.21	190.69	185.40	3.86	17.56	23.43	159.70	-2.73	54.44	-
TUHH (FreSCo+)	*S*	10.533	5.041	2.441	0.970	-224.005	-50.837	-4.401	-15.210	61.230	-20.870	-0.202	2.458	33.800	-
	E%D	-20.85	85.76	14.08	47.25	13.91	31.41	95.62	-23.92	0.94	-14.17	-200.75	2.57	26.68	-

$E\%D = (D\text{-}S)/D\times100$

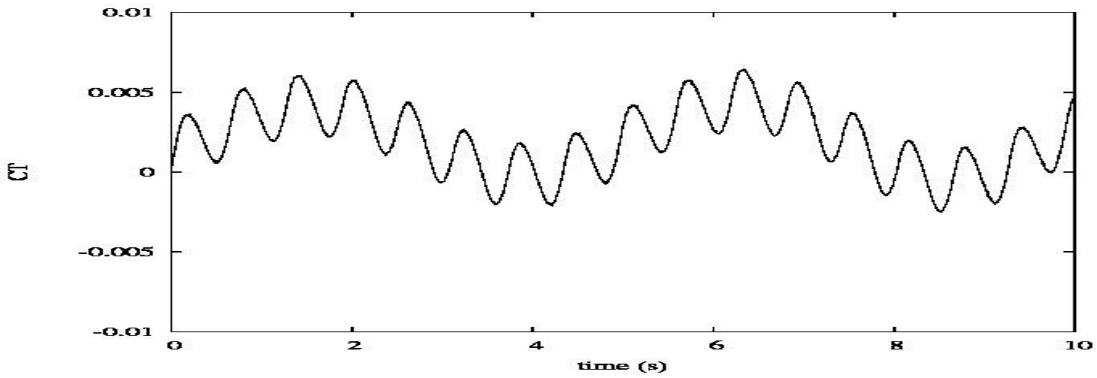

IHI-WISDAM-UTokyo

Fig. 2.4-2-C1-1 Time histories of total resistance coefficient (C_T)
(λ/L_{PP} = 0.5, Hs = 36mm, Fr = 0.26)

[CFD: solid line; EFD: open circles]

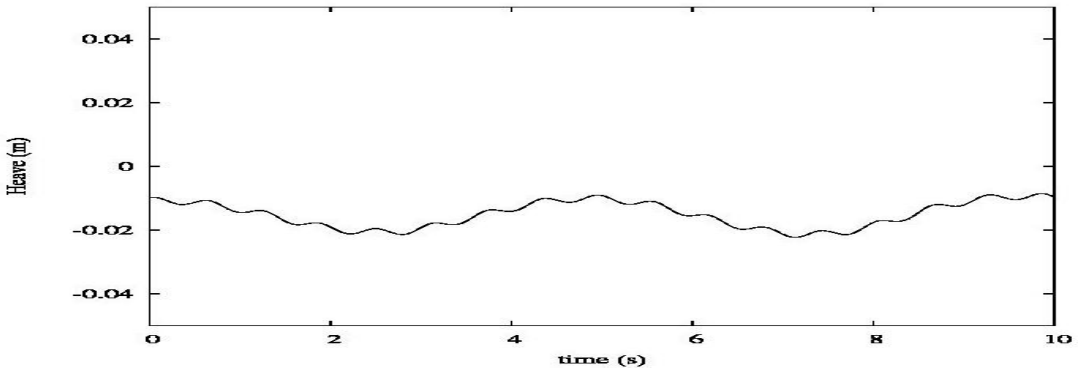

IHI-WISDAM-UTokyo

Fig. 2.4-2-C1-2 Time histories of heave motion (z)
(λ/L_{PP} = 0.5, Hs = 36mm, Fr = 0.26)

[CFD: solid line; EFD: open circles]

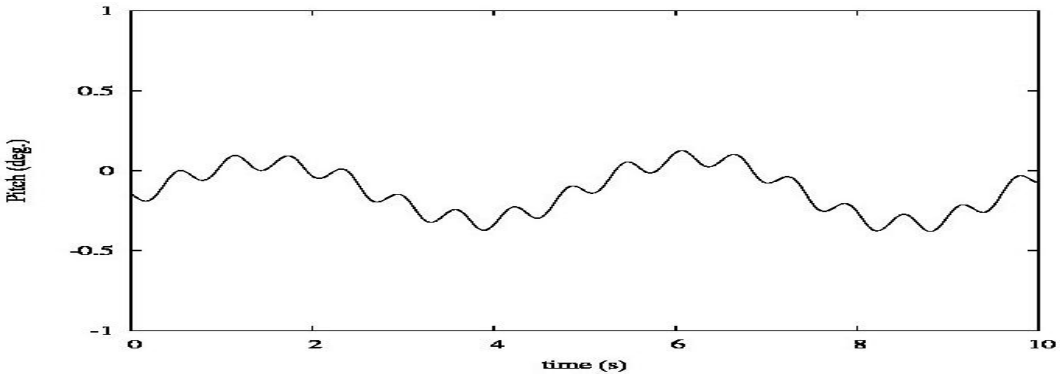

IHI-WISDAM-UTokyo

Fig. 2.4-2-C1-3 Time histories of pitch angle (θ)
(λ/L_{PP} = 0.5, Hs = 36mm, Fr = 0.26)

[CFD: solid line; EFD: open circles]

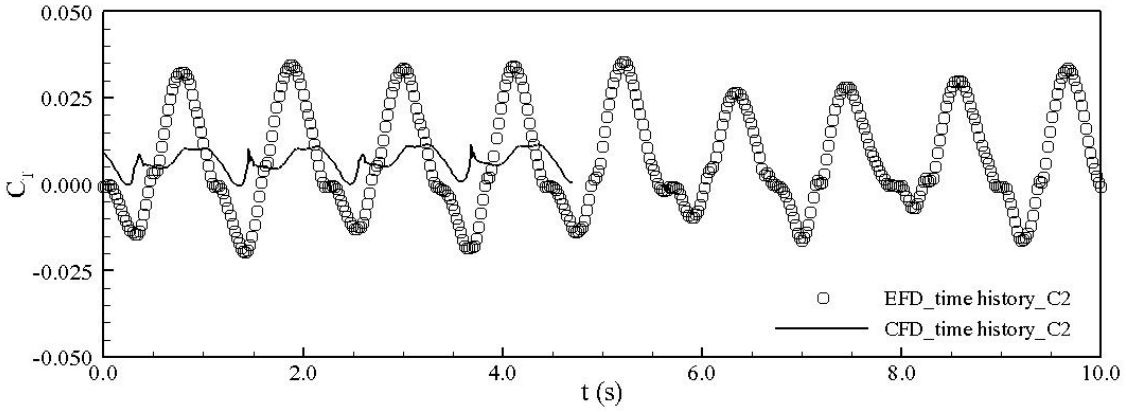

FORCE-CFDship-Iowa V4

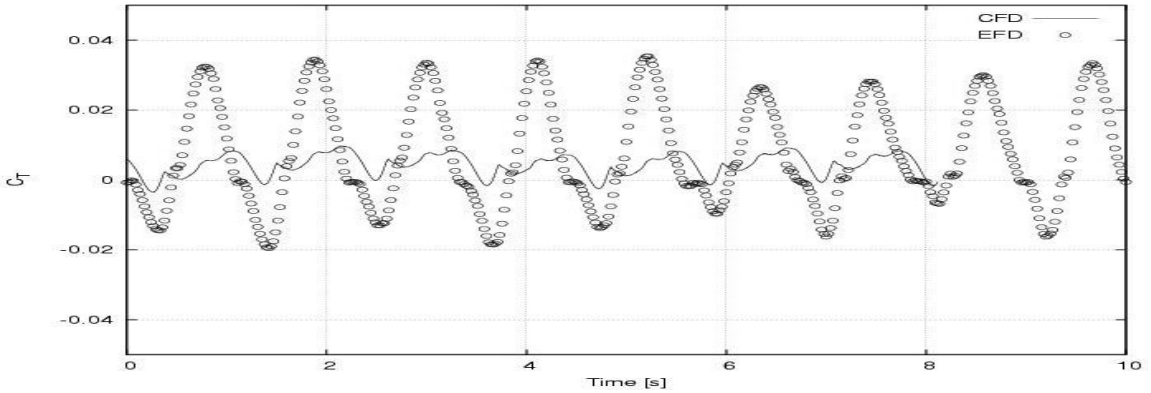

GL&UDE-Comet

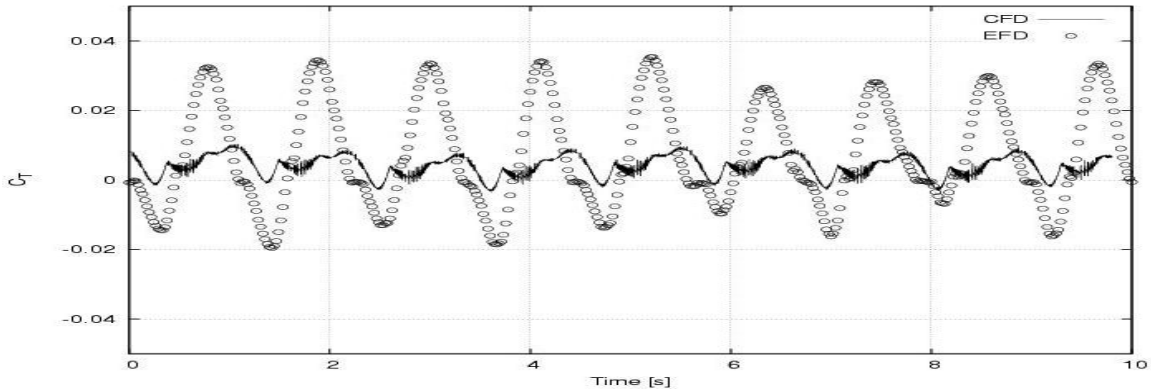

GL&UDE-OpenFOAM1.6libSixDoFv1.1.0

Fig. 2.4-2-C2-1 Time histories of total resistance coefficient (C_T)
(λ/L_{PP} = 1.15, Hs = 84mm, Fr = 0.26)

[CFD: solid line; EFD: open circles]

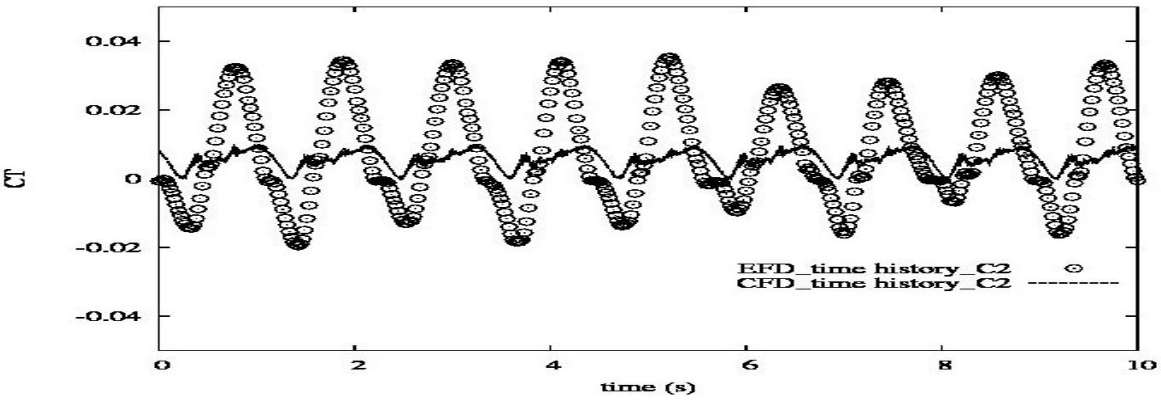

IHI-WISDAM-UTokyo

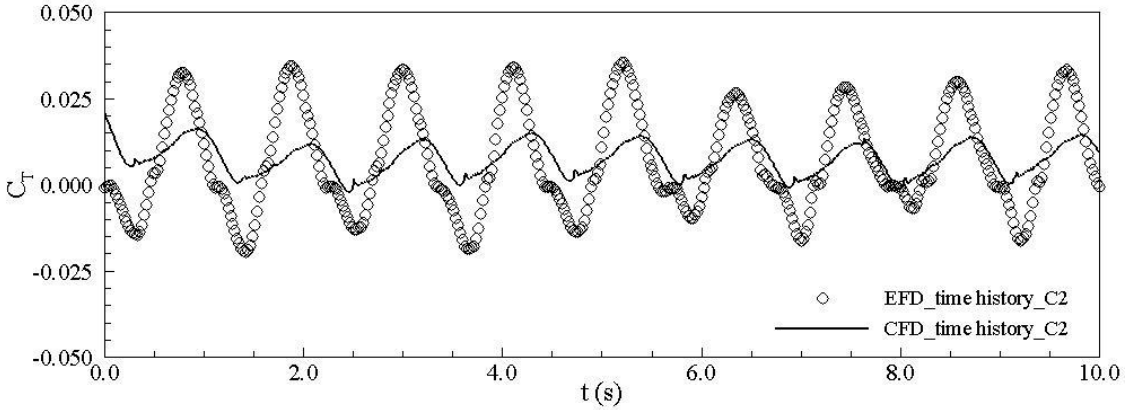

IIHR-CFDShip-Iowa V4

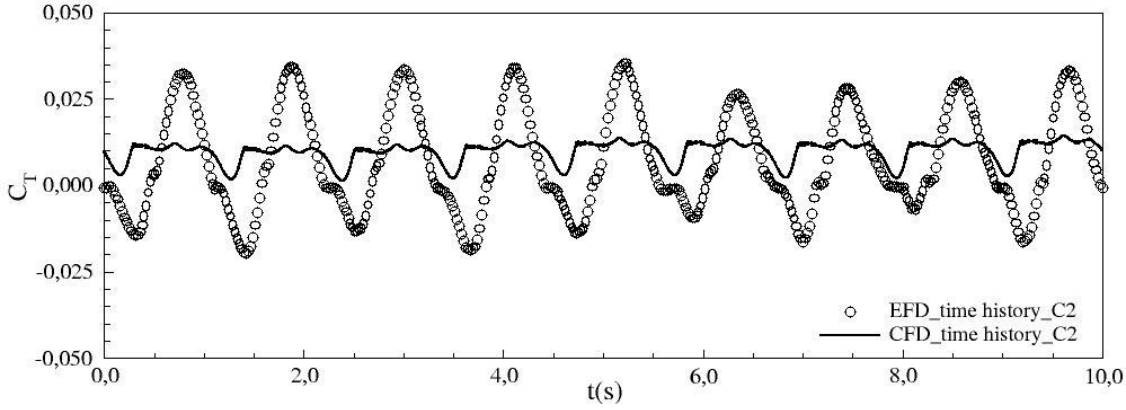

TUHH-FreSCo+

Fig. 2.4-2-C2-1 Time histories of total resistance coefficient (C_T)
(λ/L_{PP} = 1.15, Hs = 84mm, Fr = 0.26)

[CFD: solid line; EFD: open circles]

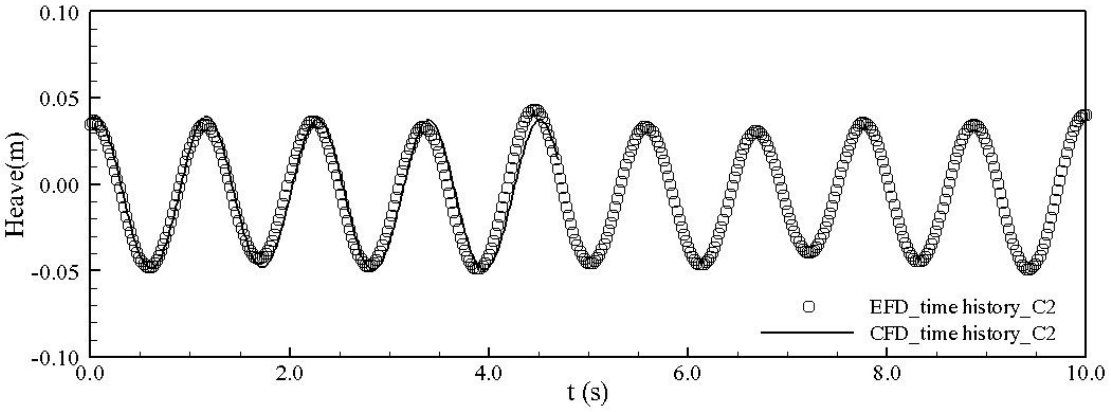

FORCE-CFDship-Iowa V4

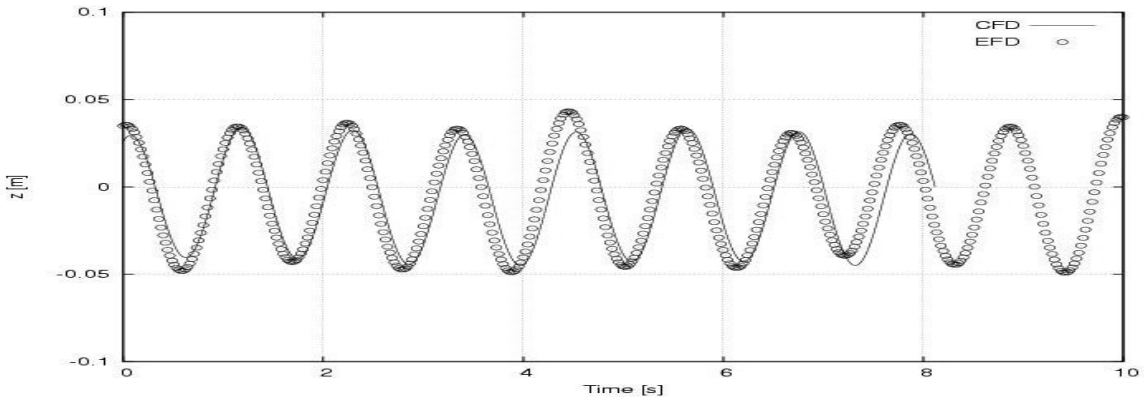

GL&UDE-Comet

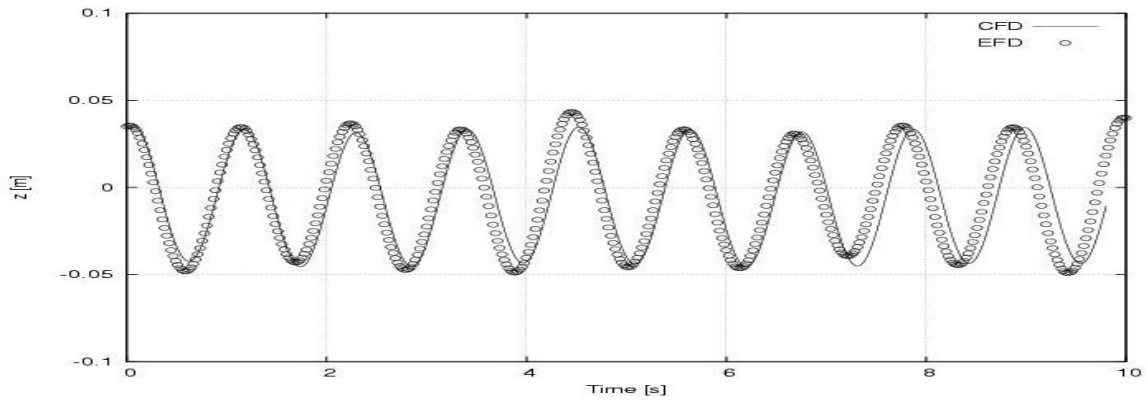

GL&UDE-OpenFOAM1.6libSixDoFv1.1.0

Fig. 2.4-2-C2-2 Time histories of heave motion (z)
(λ/L_{PP} = 1.15, Hs = 84mm, Fr = 0.26)

[CFD: solid line; EFD: open circles]

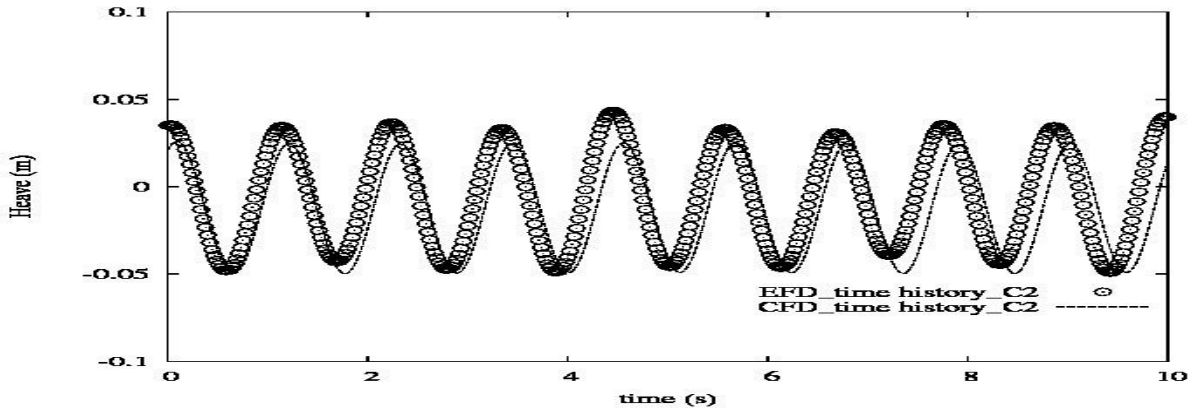

IHI-WISDAM-UTokyo

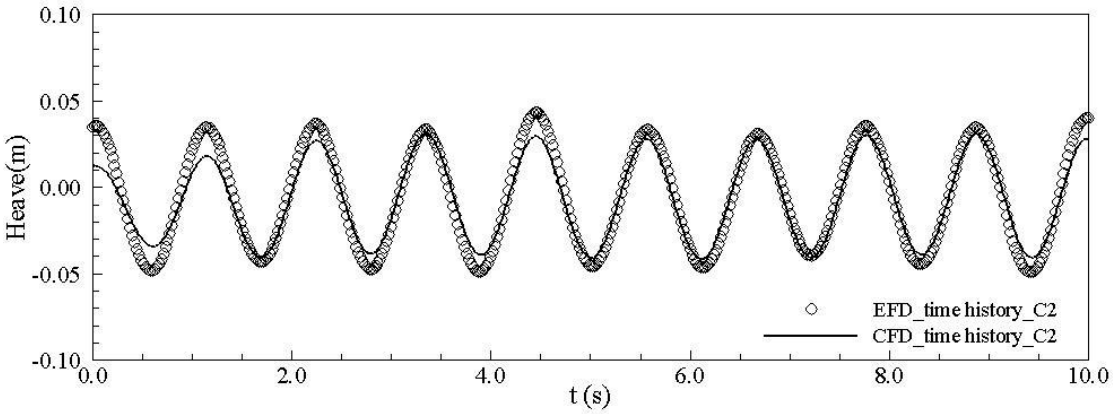

IIHR-CFDShip-Iowa V4

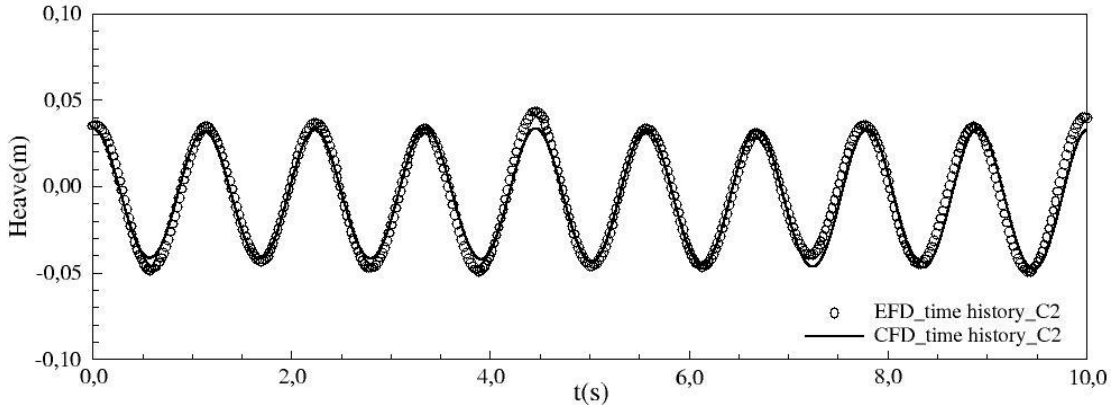

TUHH-FreSCo+

Fig. 2.4-2-C2-2 Time histories of heave motion (z)
(λ/L_{pp} = 1.15, Hs = 84mm, Fr = 0.26)

[CFD: solid line; EFD: open circles]

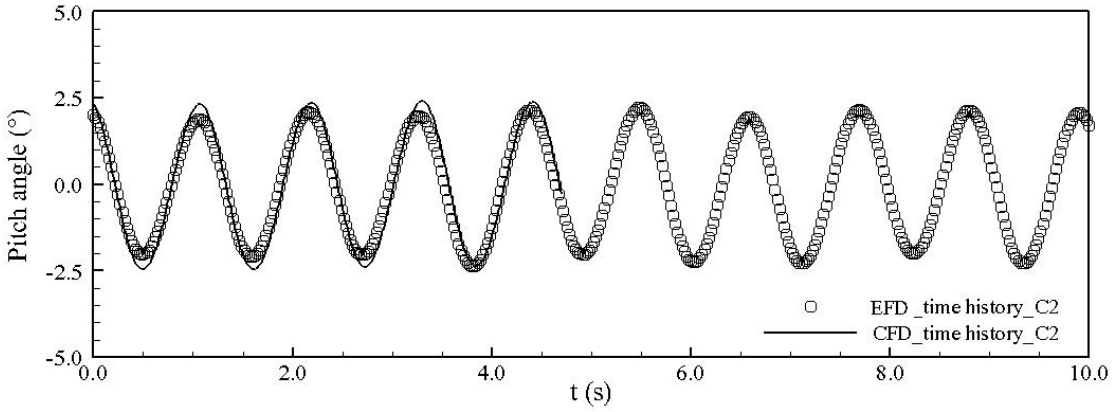

FORCE-CFDship-Iowa V4

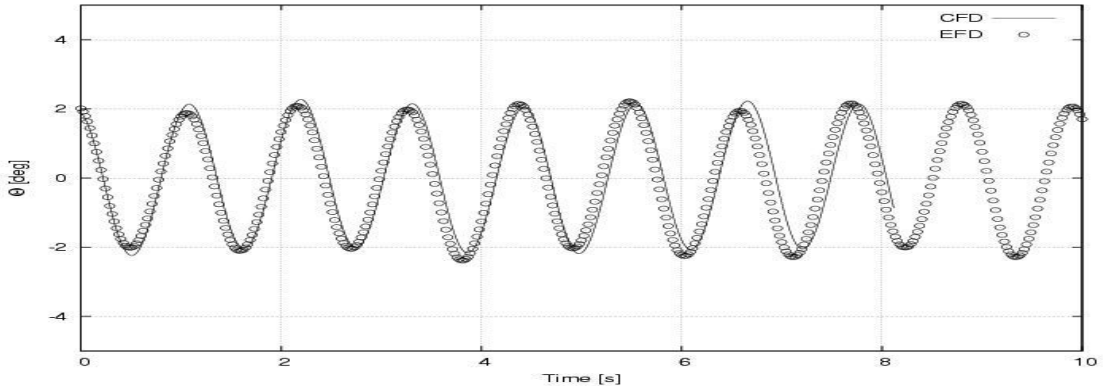

GL&UDE-Comet

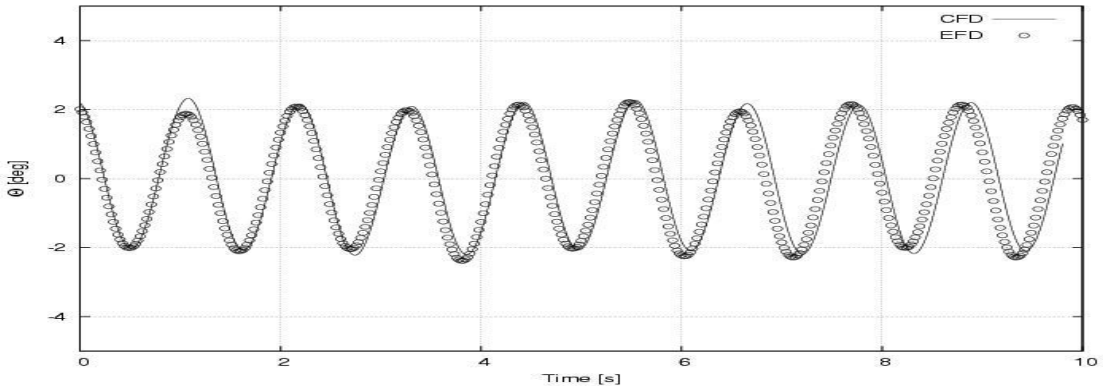

GL&UDE-OpenFOAM1.6libSixDoFv1.1.0

Fig. 2.4-2-C2-3 Time histories of pitch angle (θ)
(λ/L_{PP} = 1.15, Hs = 84mm, Fr = 0.26)

[CFD: solid line; EFD: open circles]

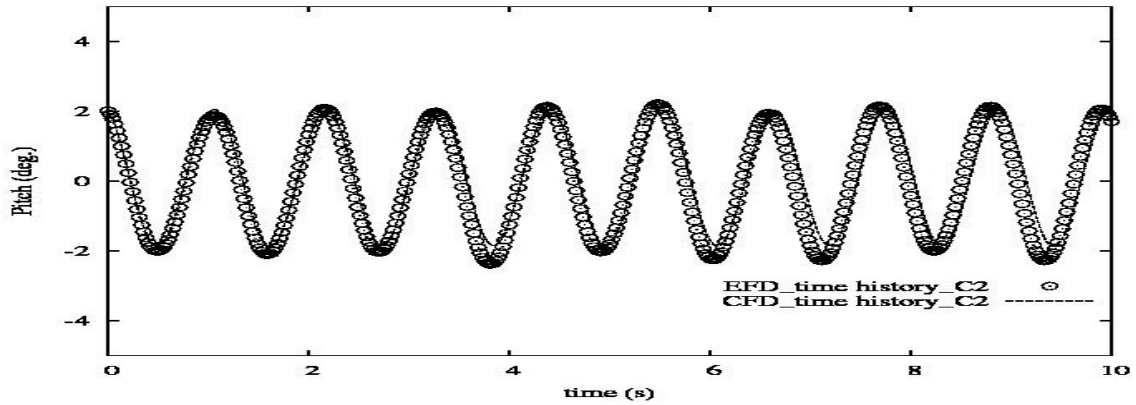

IHI-WISDAM-UTokyo

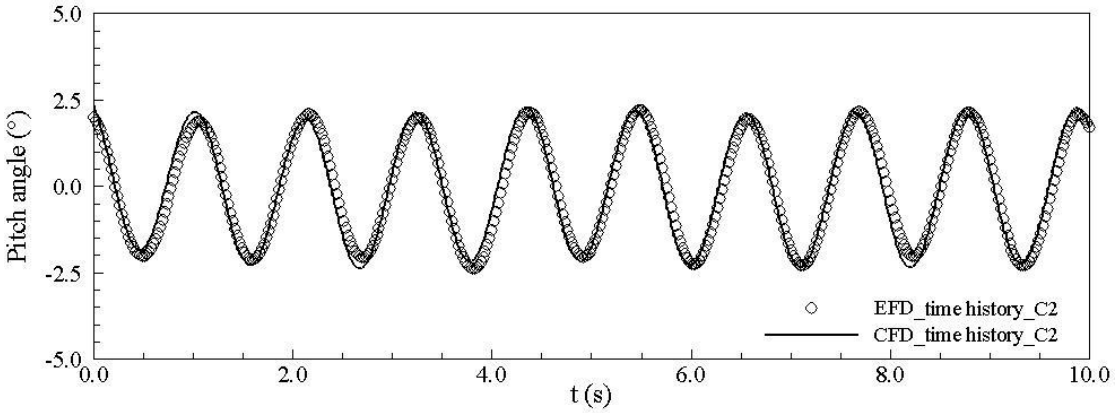

IIHR-CFDShip-Iowa V4

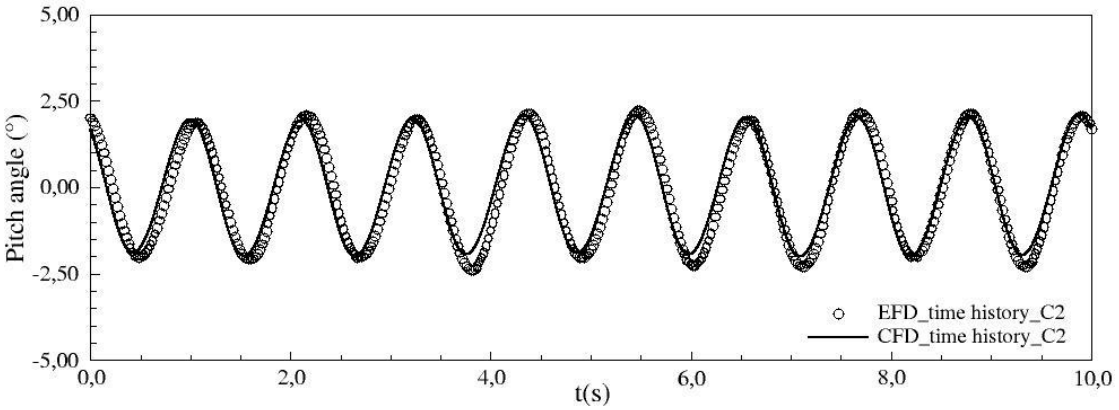

TUHH-FreSCo+

Fig. 2.4-2-C2-3 Time histories of pitch angle (θ)
(λ/L_{pp} = 1.15, Hs = 84mm, Fr = 0.26)

[CFD: solid line; EFD: open circles]

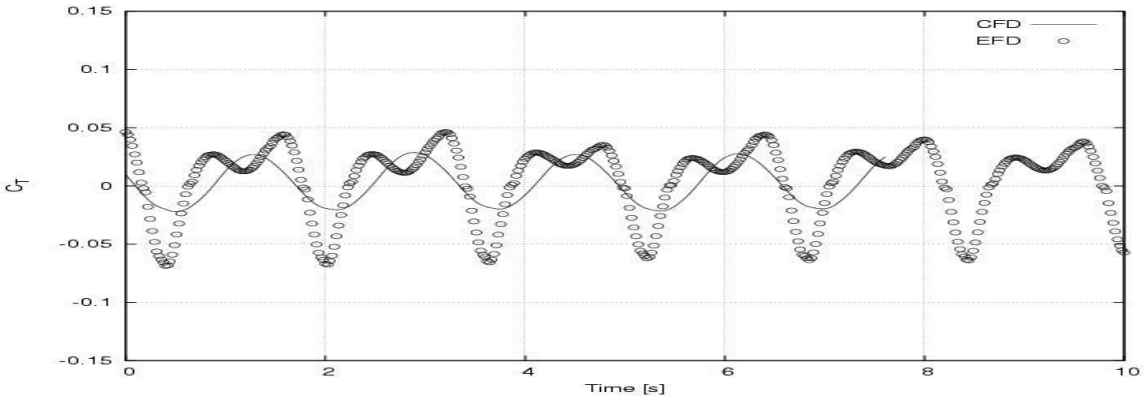

GL&UDE-Comet

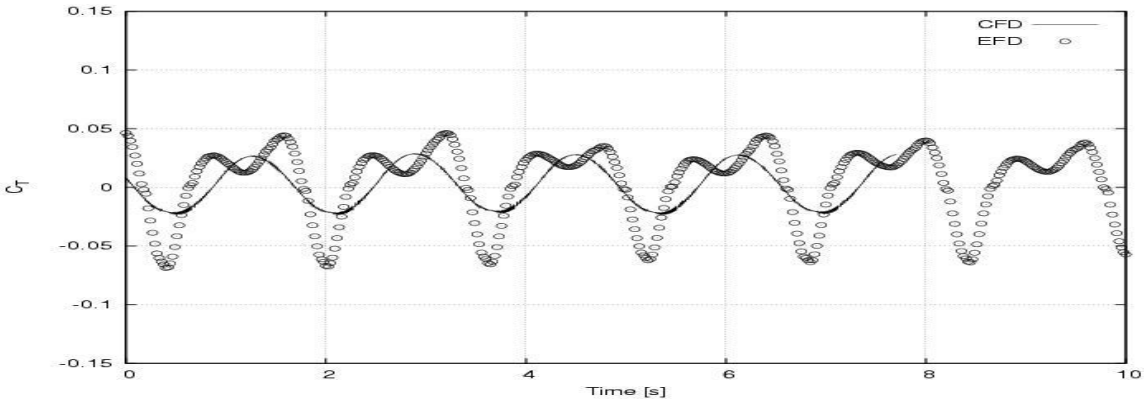

GL&UDE-OpenFOAM1.6libSixDoFv1.1.0

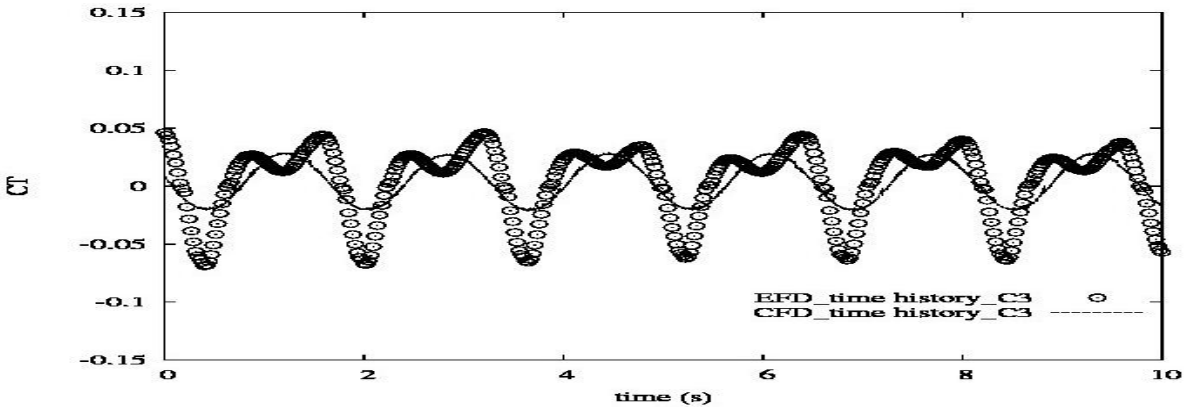

IHI-WISDAM-UTokyo

Fig. 2.4-2-C3-1 Time histories of total resistance coefficient (C_T)
(λ/L_{PP} = 2.00, Hs = 146mm, Fr = 0.26)

[CFD: solid line; EFD: open circles]

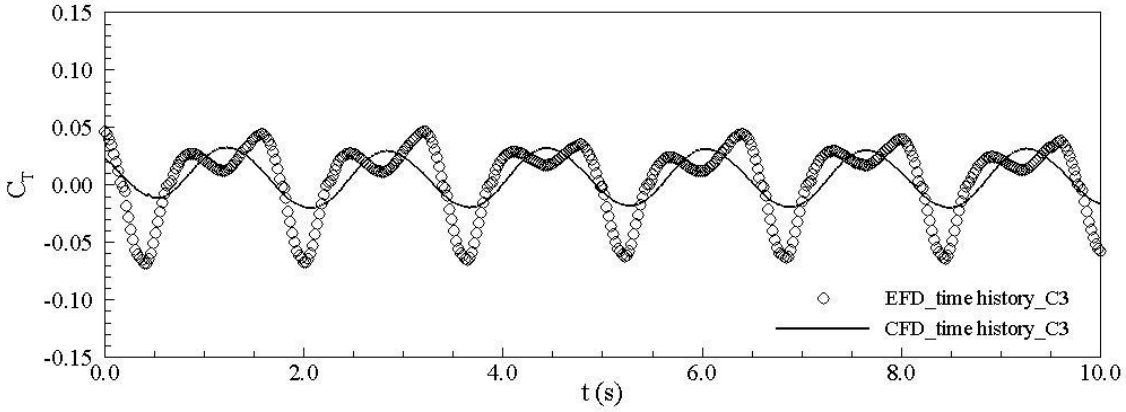

IIHR-CFDShip-Iowa V4

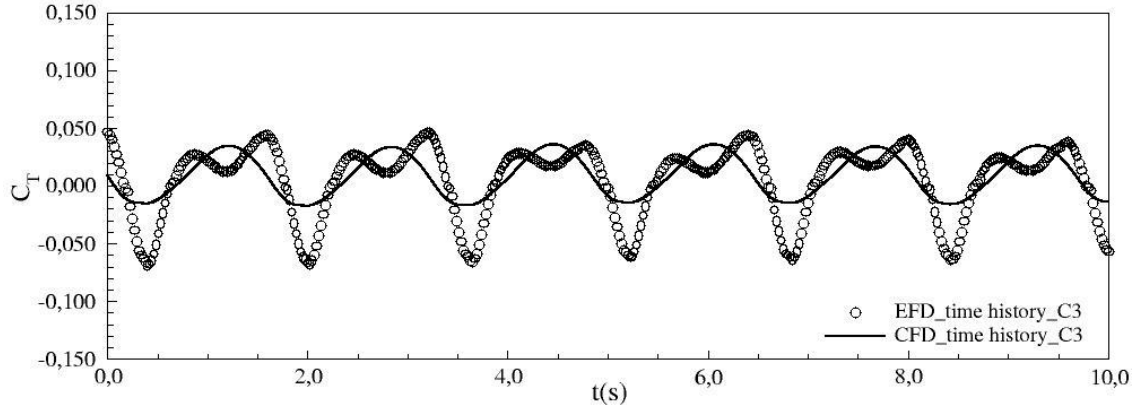

TUHH-FreSCo+

Fig. 2.4-2-C3-1 Time histories of total resistance coefficient (C_T)
(λ/L_{PP} = 2.00, Hs = 146mm, Fr = 0.26)

[CFD: solid line; EFD: open circles]

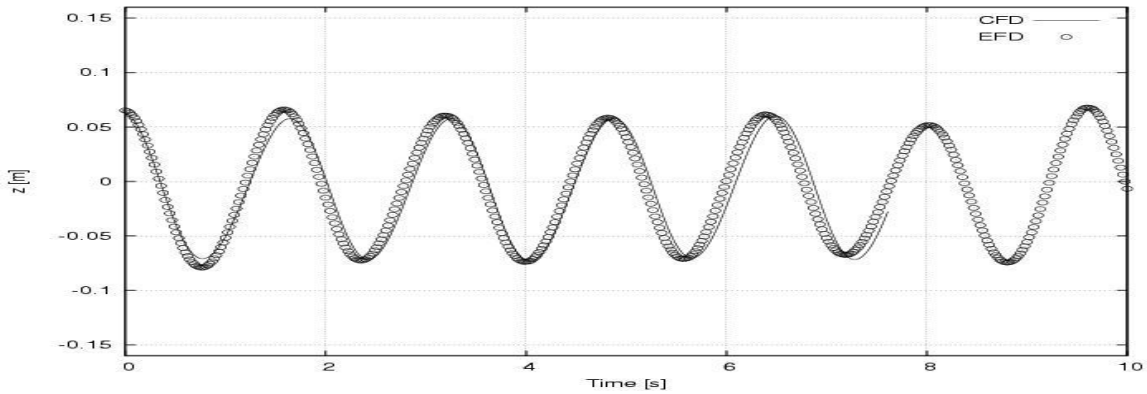

GL&UDE-Comet

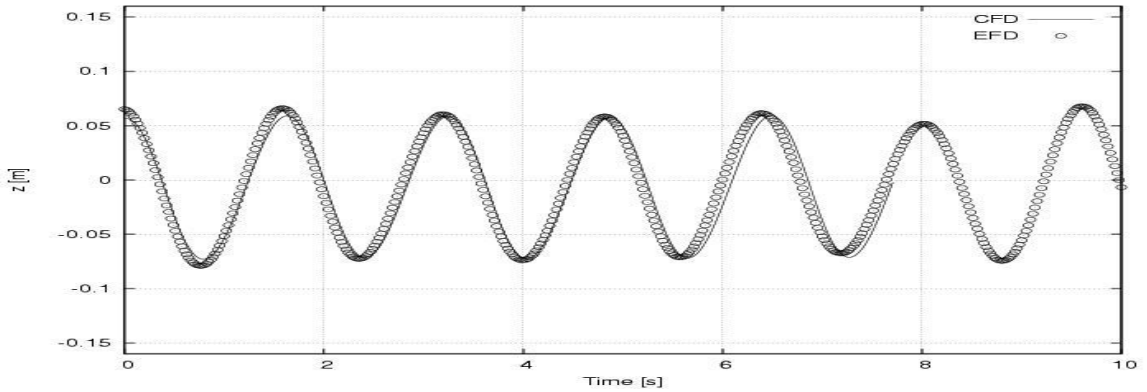

GL&UDE-OpenFOAM1.6libSixDoFv1.1.0

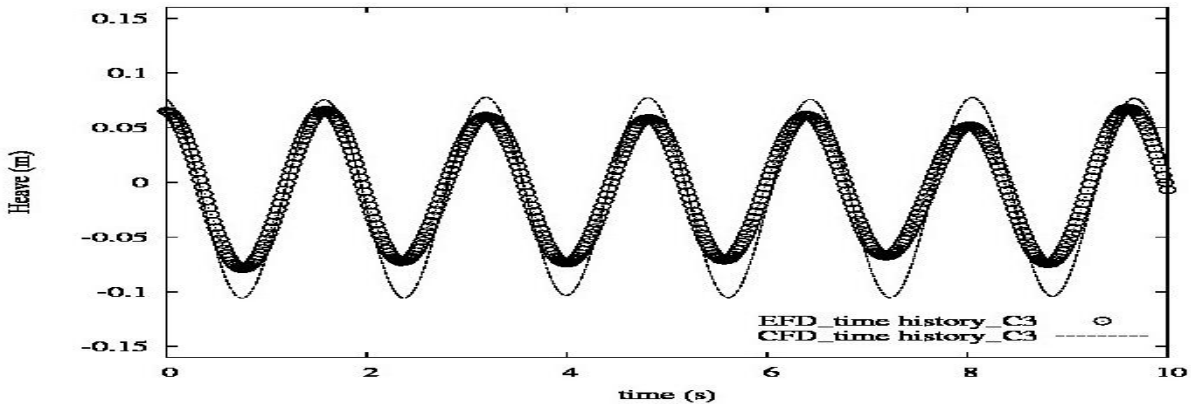

IHI-WISDAM-UTokyo

Fig. 2.4-2-C3-2 Time histories of heave motion (z)
(λ/L_{pp} = 2.00, Hs = 146mm, Fr = 0.26)

[CFD: solid line; EFD: open circles]

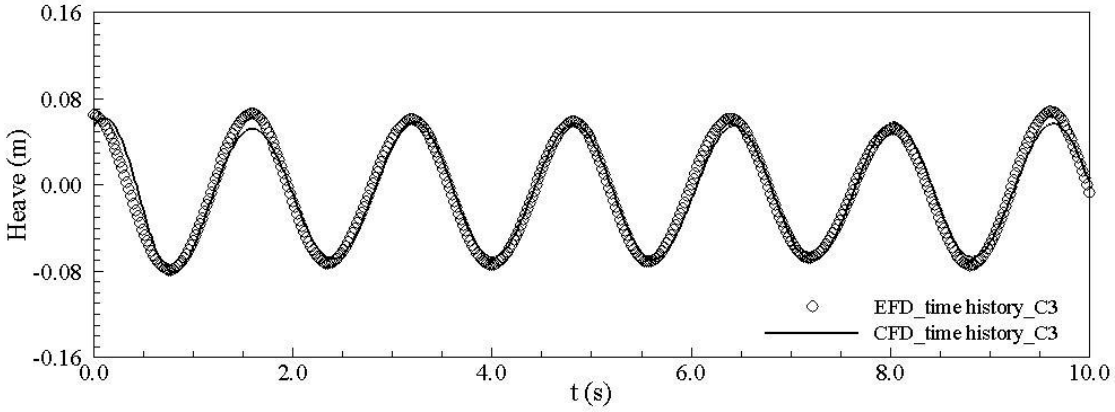

IIHR-CFDShip-Iowa V4

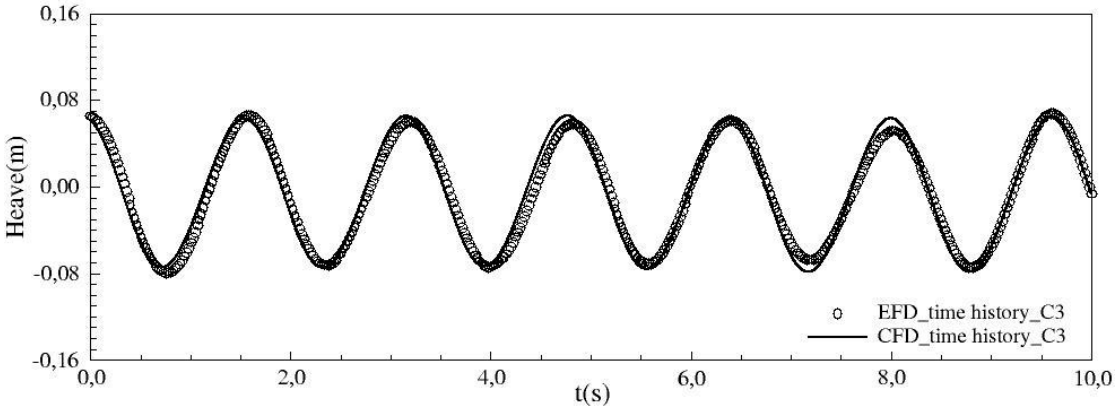

TUHH-FreSCo+

Fig. 2.4-2-C3-2 Time histories of heave motion (z)
($\lambda/L_{PP} = 2.00$, $Hs = 146$mm, $Fr = 0.26$)

[CFD: solid line; EFD: open circles]

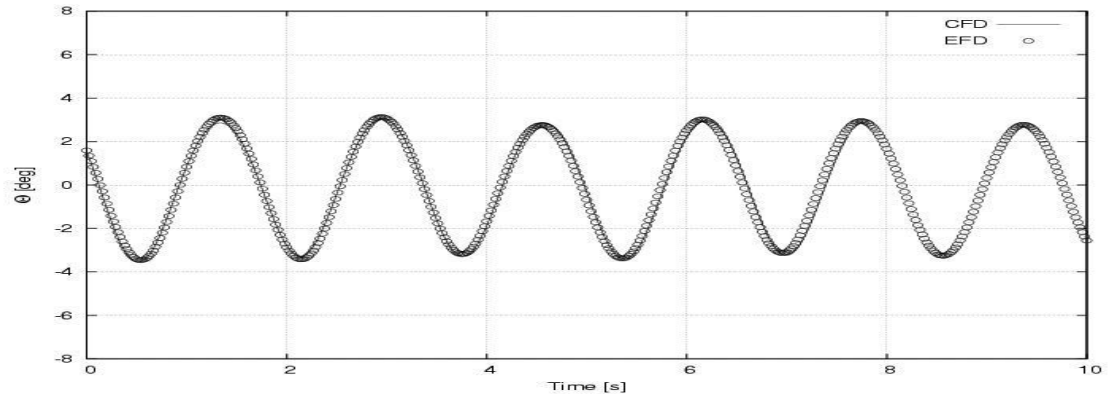

GL&UDE-Comet

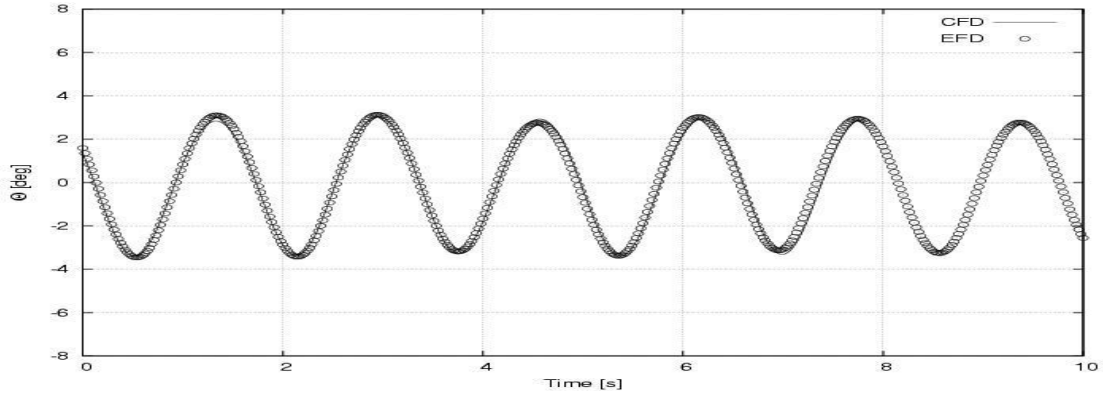

GL&UDE-OpenFOAM1.6libSixDoFv1.1.0

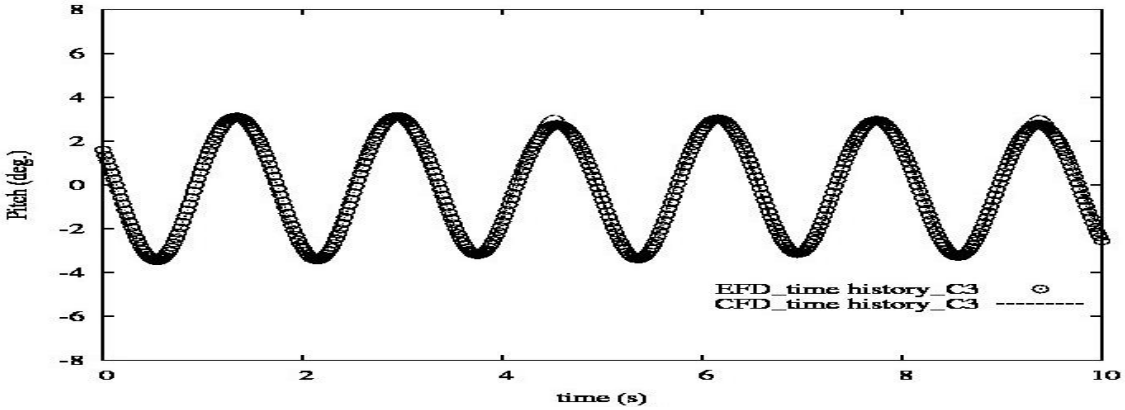

IHI-WISDAM-UTokyo

Fig. 2.4-2-C3-3 Time histories of pitch angle (θ)
(λ/L_{PP} = 2.00, Hs = 146mm, Fr = 0.26)

[CFD: solid line; EFD: open circles]

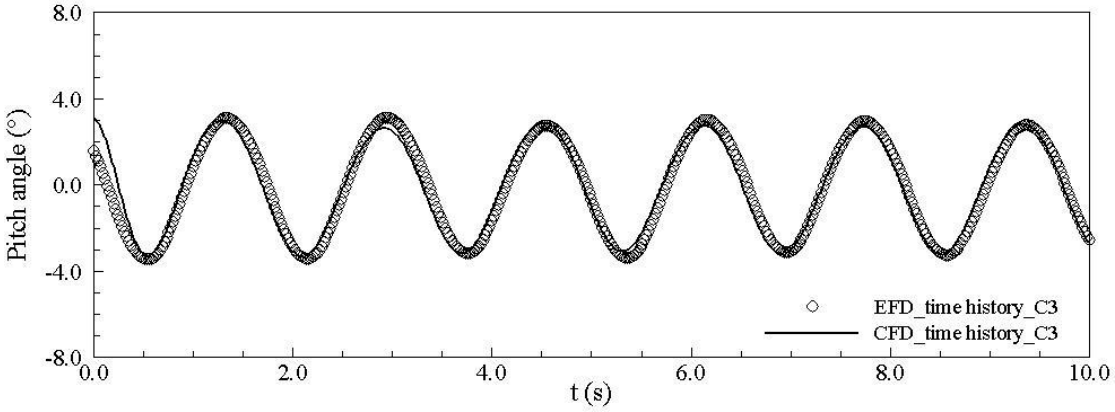

IIHR-CFDShip-Iowa V4

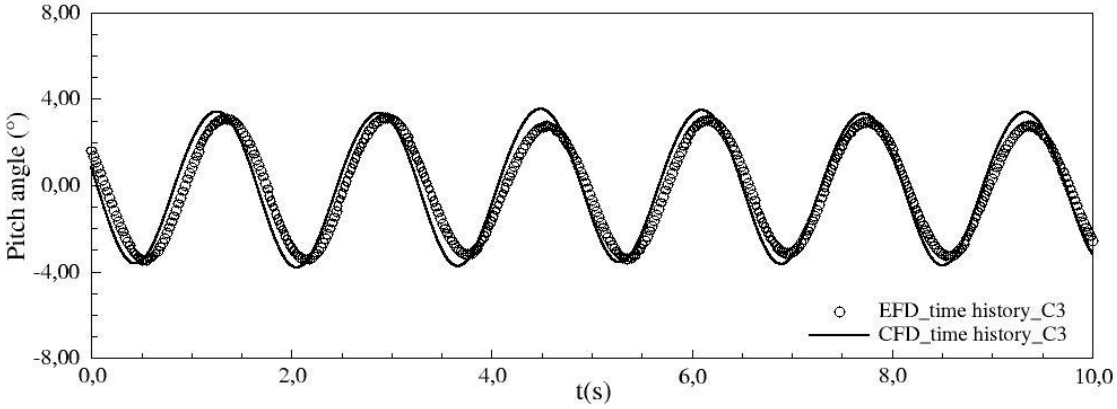

TUHH-FreSCo+

Fig. 2.4-2-C3-3 Time histories of pitch angle (θ)
(λ/L_{PP} = 2.00, Hs = 146mm, Fr = 0.26)

[CFD: solid line; EFD: open circles]

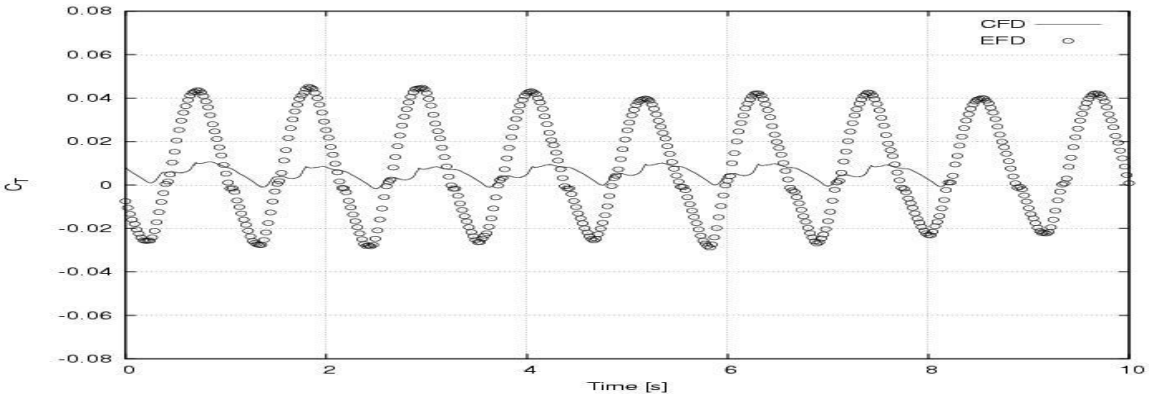

GL&UDE-Comet

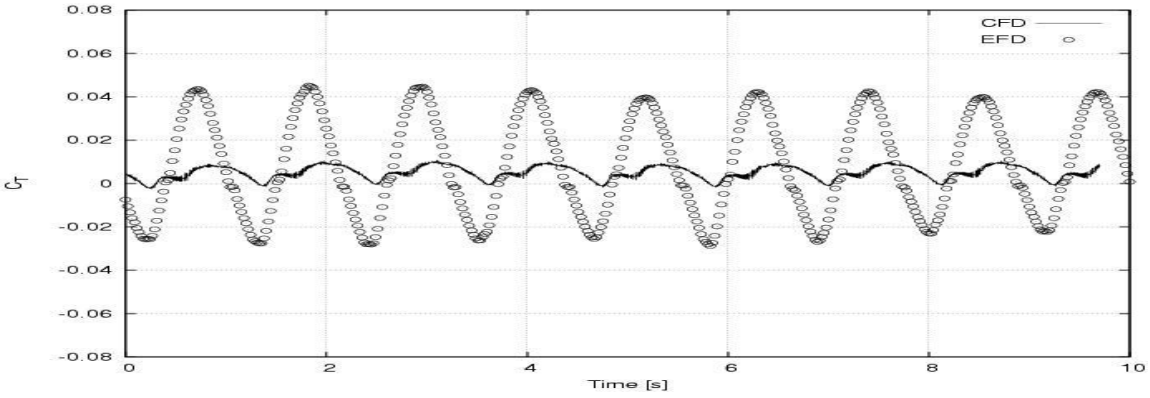

GL&UDE-OpenFOAM1.6libSixDoFv1.1.0

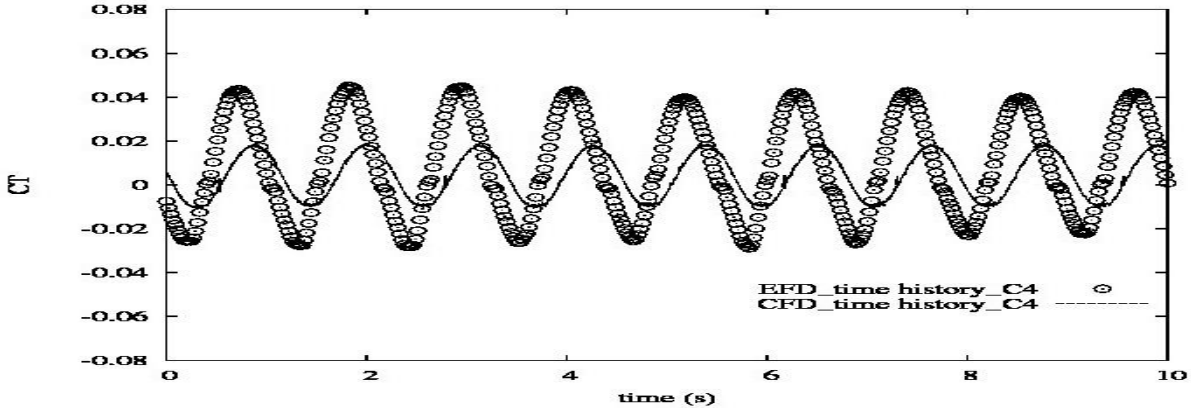

IHI-WISDAM-UTokyo

Fig. 2.4-2-C4-1 Time histories of total resistance coefficient (C_T)
(λ/L_{pp} = 1.33, Hs = 97mm, Fr = 0.33)

[CFD: solid line; EFD: open circles]

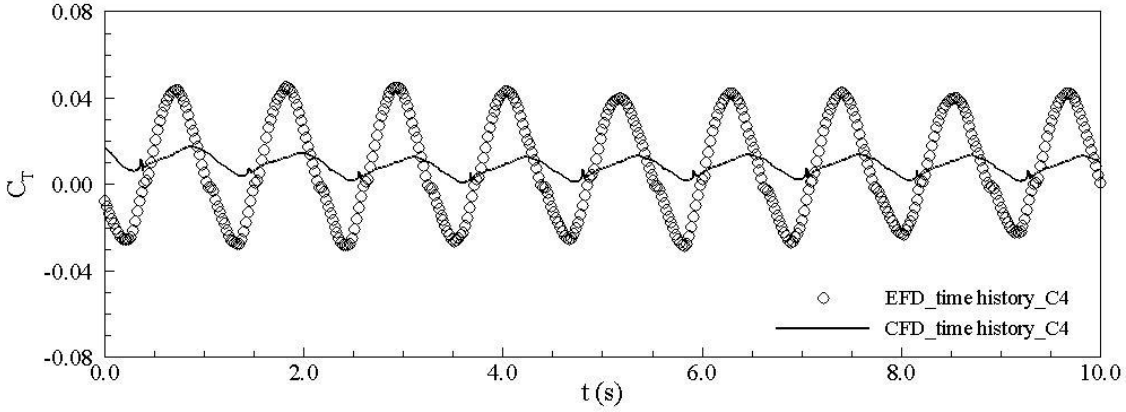

IIHR-CFDShip-Iowa V4

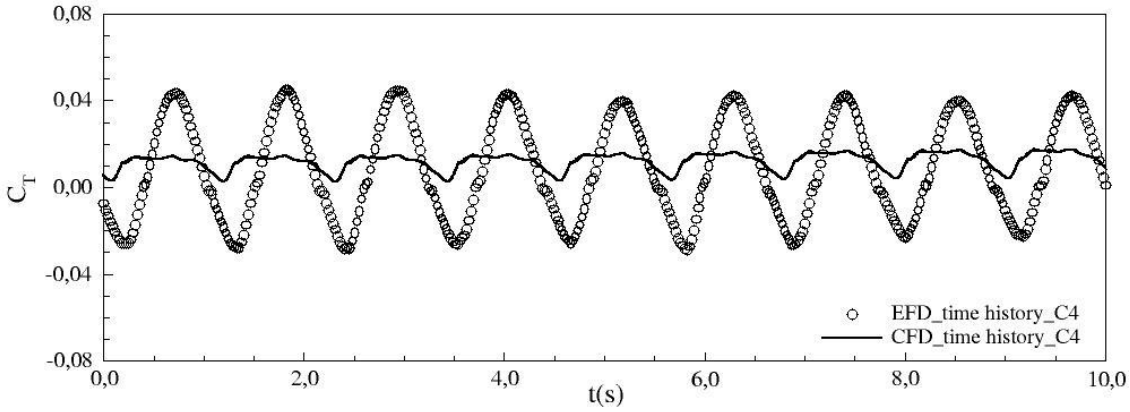

TUHH-FreSCo+

Fig. 2.4-2-C4-1 Time histories of total resistance coefficient (C_T)
(λ/L_{PP} = 1.33, Hs = 97mm, Fr = 0.33)

[CFD: solid line; EFD: open circles]

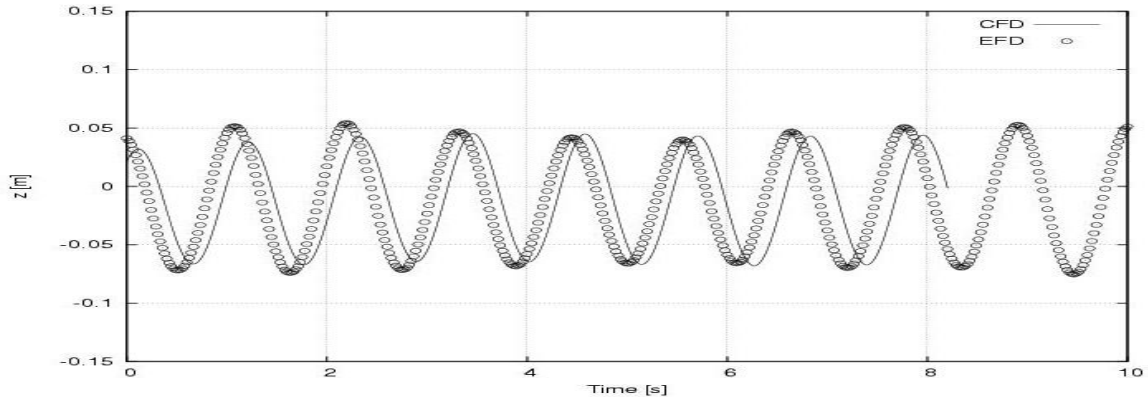

GL&UDE-Comet

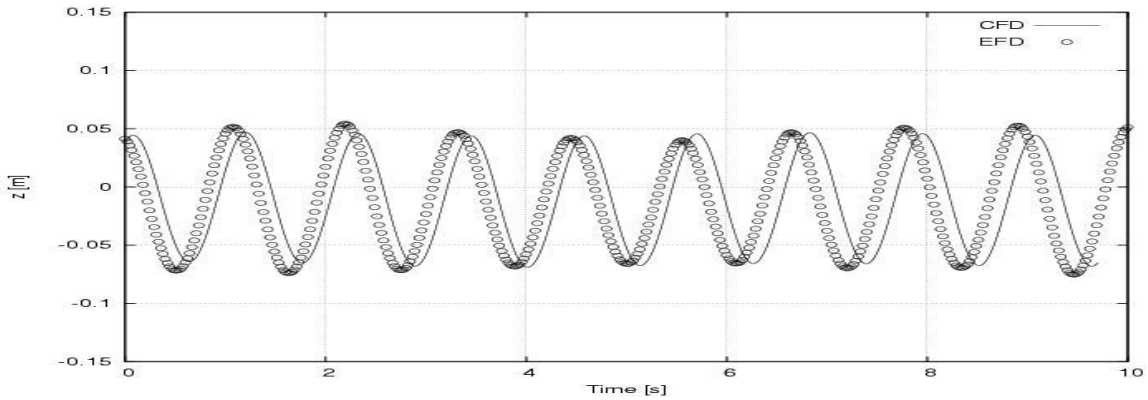

GL&UDE-OpenFOAM1.6libSixDoFv1.1.0

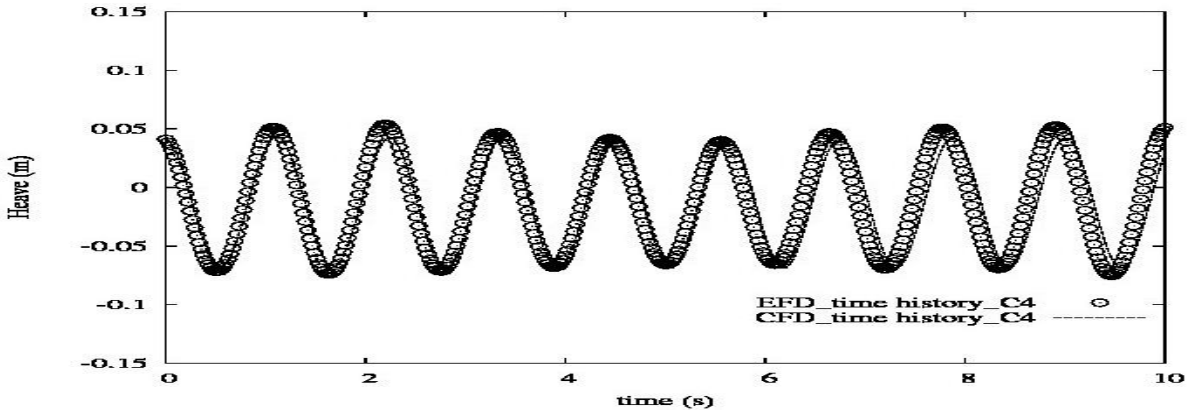

IHI-WISDAM-UTokyo

Fig. 2.4-2-C4-2 Time histories of heave motion (z)
(λ/L_{pp} = 1.33, Hs = 97mm, Fr = 0.33)

[CFD: solid line; EFD: open circles]

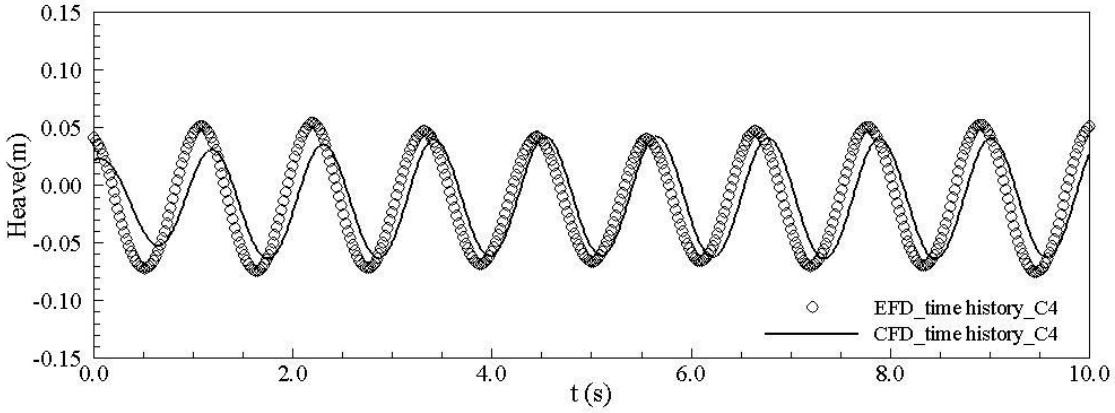

IIHR-CFDShip-Iowa V4

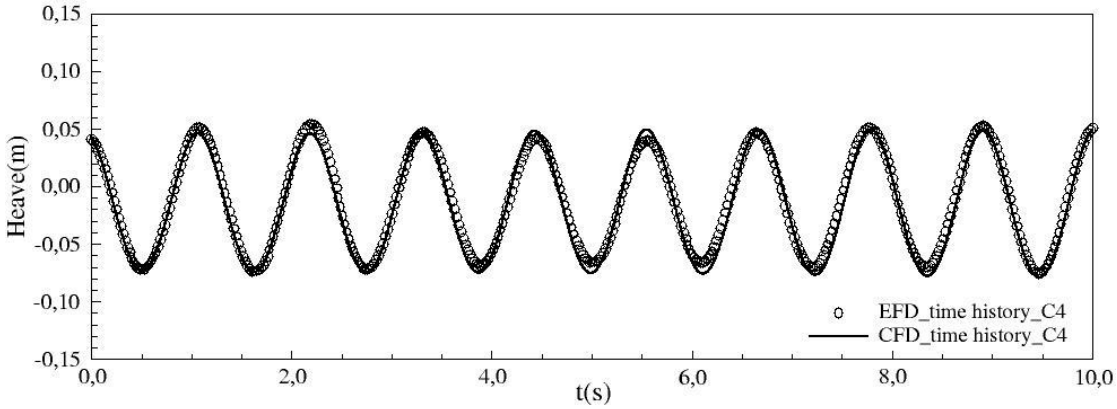

TUHH-FreSCo+

Fig. 2.4-2-C4-2 Time histories of heave motion (z)
(λ/L_{pp} = 1.33, *Hs* = 97mm, *Fr* = 0.33)

[CFD: solid line; EFD: open circles]

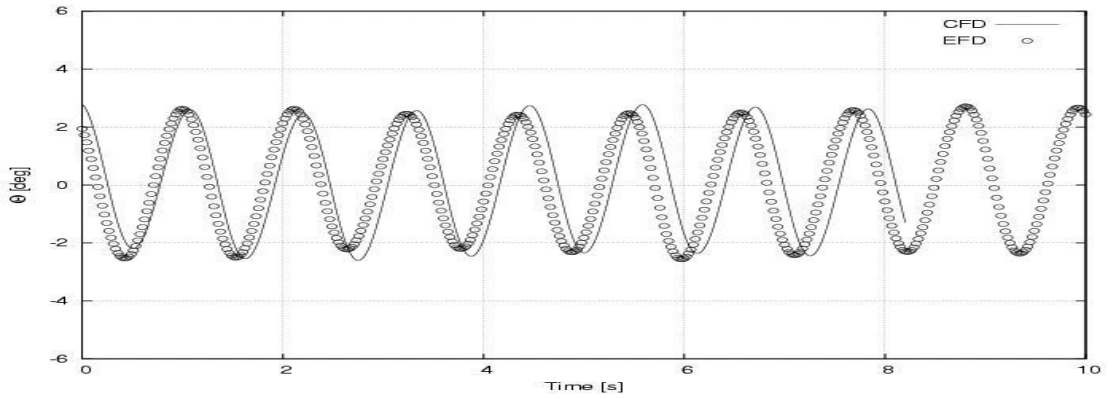

GL&UDE-Comet

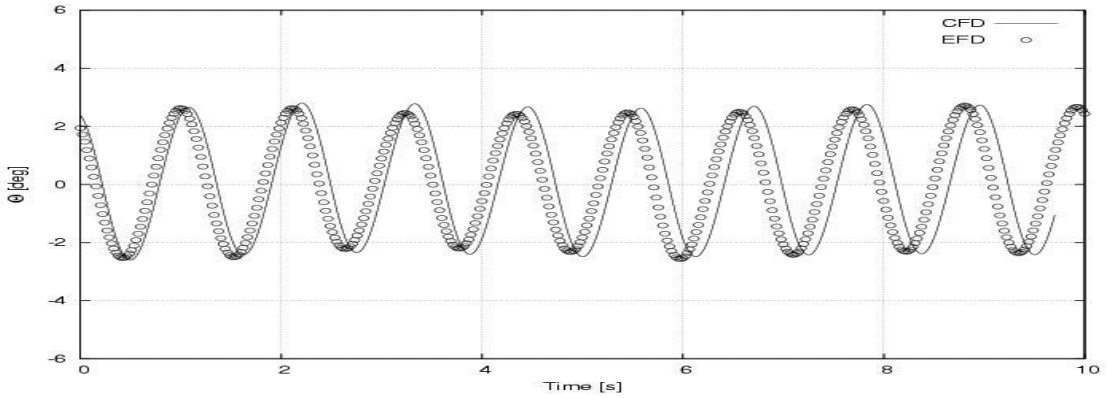

GL&UDE-OpenFOAM1.6libSixDoFv1.1.0

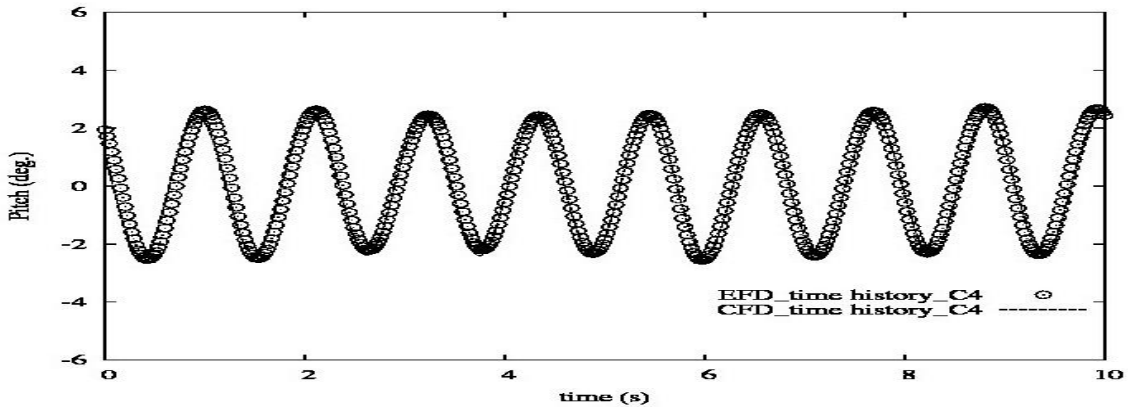

IHI-WISDAM-UTokyo

Fig. 2.4-2-C4-3 Time histories of pitch angle (θ)
(λ/L_{pp} = 1.33, Hs = 97mm, Fr = 0.33)

[CFD: solid line; EFD: open circles]

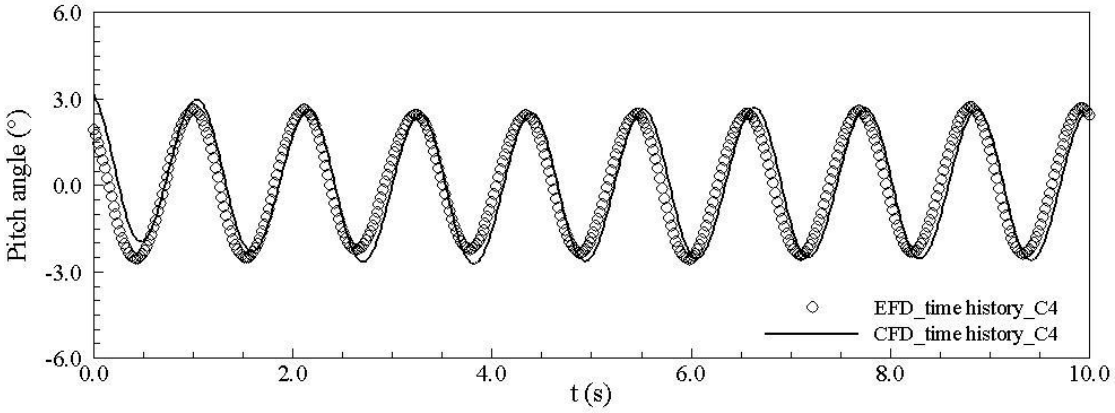

IIHR-CFDShip-Iowa V4

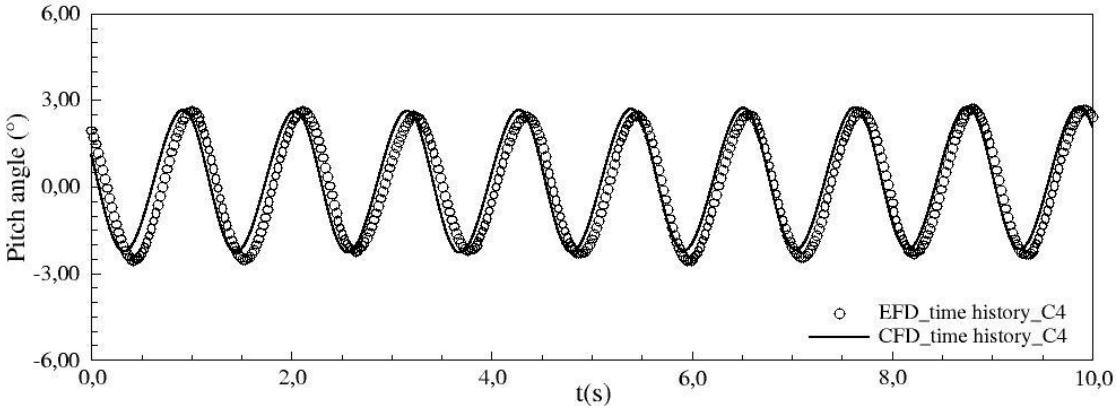

TUHH-FreSCo+

Fig. 2.4-2-C4-3 Time histories of pitch angle (θ)
(λ/L_{pp} = 1.33, Hs = 97mm, Fr = 0.33)

[CFD: solid line; EFD: open circles]

DTMB 5415

Test Case 3.1a

Table 3.1a-T-0 Computations information and V&V method
Table 3.1a-T-1 Computed C_T, C_F and C_R of different grid densities
Table 3.1a-T-2 V&V results for C_T, C_F and C_R

Figure 3.1a-1 Wave elevation contours
Figure 3.1a-1w-1 Longitudinal wave cut at $y/L_{PP} = 0.082$
Figure 3.1a-1w-2 Longitudinal wave cut at $y/L_{PP} = 0.172$
Figure 3.1a-1w-3 Longitudinal wave cut at $y/L_{PP} = 0.301$
Figure 3.1a-1w-4 Grid density distribution along the waterline, and in transverse and vertical directions at mid-ship
Figure 3.1a-2 Cross flow vectors and streamlines, U contours at $x/L_{PP} = 0.1$
Figure 3.1a-3 Cross flow vectors and streamlines, U contours at $x/L_{PP} = 0.2$
Figure 3.1a-4 Cross flow vectors and streamlines, U contours at $x/L_{PP} = 0.6$
Figure 3.1a-5 Cross flow vectors and streamlines, U contours at $x/L_{PP} = 0.8$
Figure 3.1a-6 Cross flow vectors and streamlines, U contours at $x/L_{PP} = 0.935$
Figure 3.1a-7 Cross flow vectors and streamlines, U contours at $x/L_{PP} = 1.1$

Table 3.1a-T-0: Computations information and V&V method

Organization (Code)	**V&V method (including the determination of U_I)**
CEHINAV (STAR-CCM+)	-
CSSRC (FLUENT6.3)	-
IIHR [CFDShip-IowaV4] (DES&URANS) [CFDShip-IowaV6]	V&V not performed
MARIC (FLUENT6.3)	The V&V is based on ITTC - Quality Manual 7.5-03-01- 01, CFD General "Uncertainty Analysis in CFD Verification and Validation Methodology and Procedures" Richardson Extrapolation is used to compute the error for the fine grid $\delta^*_{RE_G} = \frac{\varepsilon_{21}}{r_G^{P_G} - 1}, P_G = \frac{\ln(\varepsilon_{32}/\varepsilon_{21})}{\ln r_G},$ $C_G = \frac{r_G^{P_G} - 1}{r_G^{P_{Gest}} - 1}, U_G = \left\|C_G \delta^*_{RE_G}\right\| + \left\|(1 - C_G)\delta^*_{RE_G}\right\|,$ $U_{SN} = \sqrt{U_G^2 + U_I^2}\ ,\ U_V = \sqrt{U_{SN}^2 + U_D^2}$
MARIN (PARNASSOS)	-
UoGe (STAR-CCM+)	-

Table 3.1a-T-1: Computed C_T, C_F and C_R of different grid densities

Organization (Code)	r_G		C_T ($\times 10^{-3}$)					C_F ($\times 10^{-3}$)					C_R ($\times 10^{-3}$)				
			Grid #5	Grid #4	Grid #3	Grid #2	Grid #1	Grid #5	Grid #4	Grid #3	Grid #2	Grid #1	Grid #5	Grid #4	Grid #3	Grid #2	Grid #1
EFD (INSEAN)	-	*D*	4.23					2.91 (ITTC-57) *					1.32				
CEHINAV (STAR-CCM+)	1.67	*S*	-	-	4.207	4.059	4.036	-	-	2.967	2.930	2.933	-	-	1.240	1.130	1.103
		E%D	-	-	0.55	4.04	4.59	-	-	-1.97	-0.67	-0.78	-	-	6.09	14.42	16.43
CSSRC (FLUENT6.3)		*S*	-	-	-	-	4.238	-	-	-	-	2.908	-	-	-	-	1.33
		E%D	-	-	-	-	-0.19	-	-	-	-	0.07	-	-	-	-	-0.76
MARIC (FLUENT6.3)	1.414	*S*	-	-	4.603	4.357	4.237	-	-	3.074	3.004	3.004	-	-	1.529	1.353	1.233
		E%D	-	-	-8.82	-3.00	-0.17	-	-	-5.64	-3.23	-3.23	-	-	-15.83	-2.50	6.59
MARIN (PARNASSOS)	2	*S*	-	4.300	4.300	4.250	4.230	-	-	-	-	-	-	1.390	1.390	1.340	1.320
		E%D	-	-1.70	-1.70	-0.50	0.00	-	-	-	-	-	-	-5.30	-5.30	-1.50	0.00
UoGe (STAR-CCM+)	1.5	*S*	-	-	3.972	3.876	3.879	-	-	2.725	2.772	2.817	-	-	1.247	1.104	1.062
		E%D	-	-	6.10	8.36	8.29	-	-	6.34	4.74	3.21	-	-	5.56	16.33	19.51

* $C_F = 0.075 / (\log_{10} Re - 2)^2$ (ITTC 1957 Model-Ship Correlation Line)

$E\%D = (D\text{-}S)/D \times 100$

Table 3.1a-T-2: V&V results for C_T, C_F and C_R

Organization (Code)	r_G	C_T						C_F						C_R					
		ε_{12} $\%S_1$	$\frac{U_I}{\varepsilon_{12}}$	$\frac{P_G}{P_{G,th}}$	U_G $\%S_1$	U_D $\%D$	$U_V\%$	ε_{12} $\%S_1$	$\frac{U_I}{\varepsilon_{12}}$	$\frac{P_G}{P_{G,th}}$	U_G $\%S_1$	U_D $\%D$	$U_V\%$	ε_{12} $\%S_1$	$\frac{U_I}{\varepsilon_{12}}$	$\frac{P_G}{P_{G,th}}$	U_G $\%S_1$	U_D $\%D$	$U_V\%$
CEHINAV (STAR-CCM+)	1.67	3.51	0.002	6.404	3.51		3.57	1.27	0.002	0.658	1.27			8.87	0.001	1.369	8.87		
CSSRC (FLUENT6.3)	-	-	-	-	-		-	-	-	-	-			-	-	-	-		
MARIC (FLUENT6.3)	1.414	2.83	0.208	1.036	2.97	0.64	3.10	-	-	-	-			-	-	-	-		
MARIN (PARNASSOS)	2	1.40	0.006%	-	1.40		1.54	-	-	-	-			-	-	-	-		
UoGe (STAR-CCM+)	1.5	0.07	0.0215	-	-		-	1.59	2.460E-05	-	-			3.96	1.497E-03	-	-		

$\varepsilon_{12}\%S_1 = |(S_1\text{-}S_2)/S_1| \times 100$; $U_{SN} = \sqrt{U_I^2 + U_G^2}$; $U_V = \sqrt{U_D^2 + U_{SN}^2}$

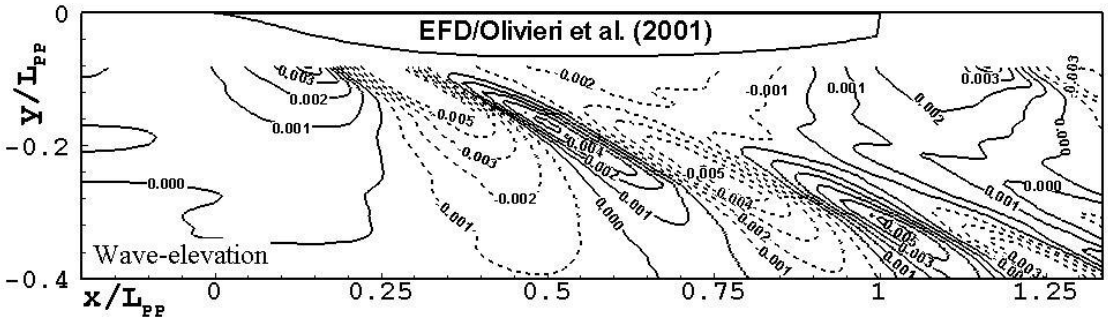

Experiment (INSEAN, Olivieri et al. 2001)

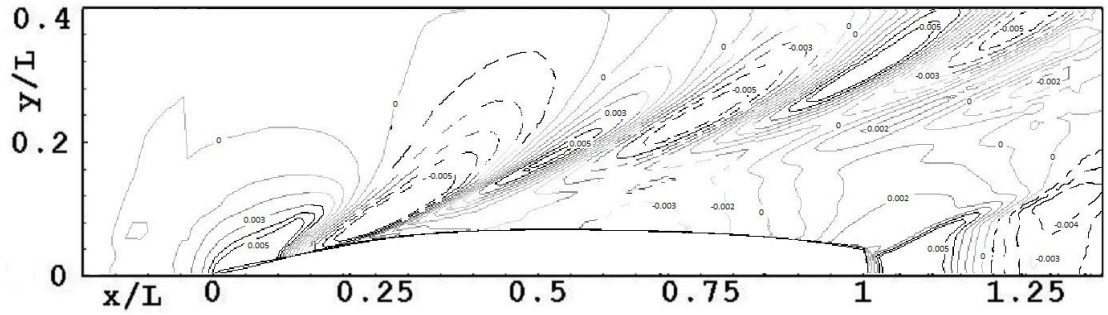

CEHINAV-STAR-CCM+

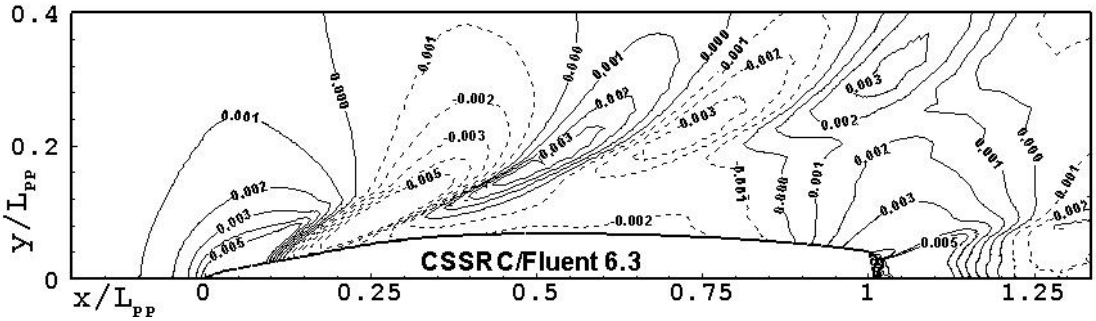

CSSRC-FLUENT6.3

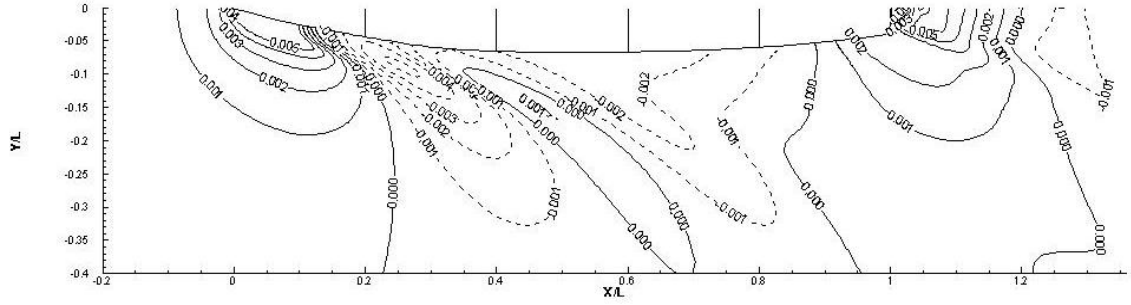

ECN/BEC/HO-Icare

Fig. 3.1a-1 Wave elevation contours [$\Delta z/L_{PP} = 0.001$]

(Solid lines: positive (+) values; Dashed lines: negative (-) values)

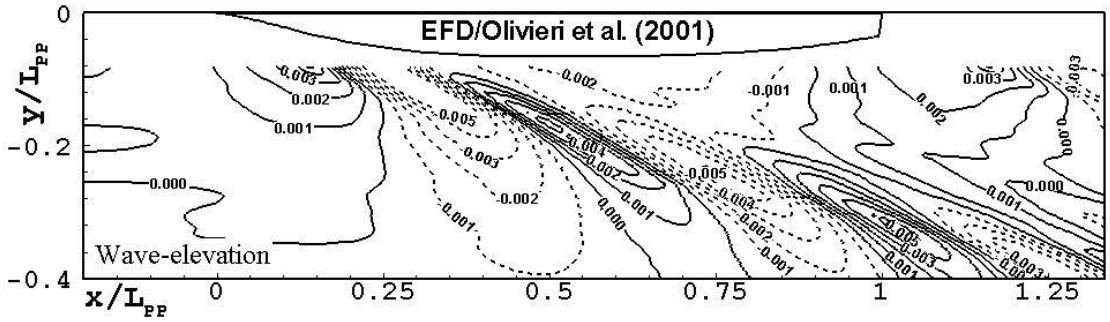

Experiment (INSEAN, Olivieri et al. 2001)

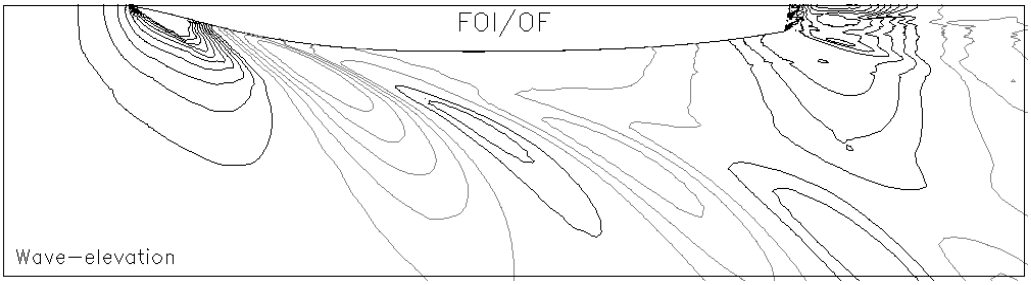

FOI-OF

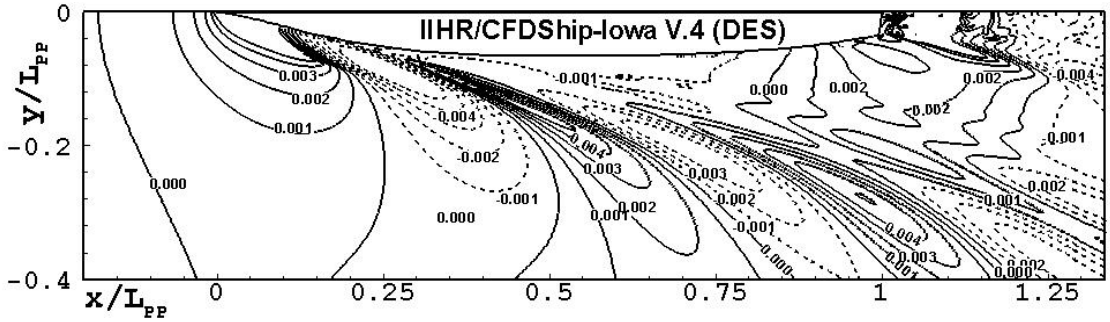

IIHR-CFDShip-IowaV4 (DES)

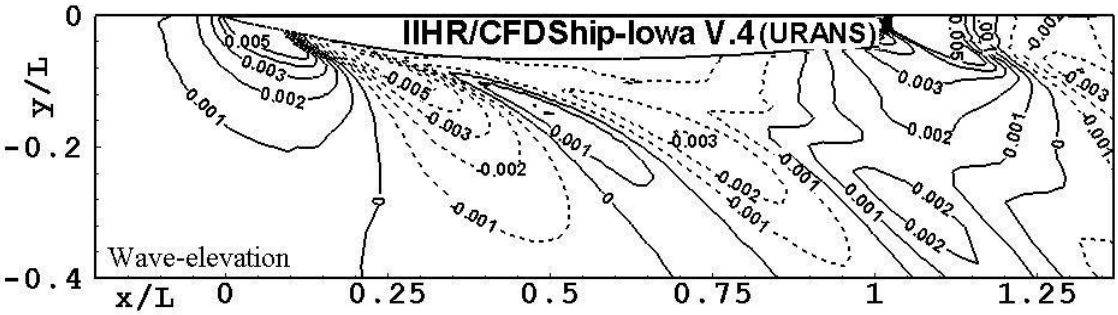

IIHR-CFDShip-IowaV4 (URANS)

Fig. 3.1a-1 Wave elevation contours [$\Delta z/L_{PP} = 0.001$]

(Solid lines: positive (+) values; Dashed lines: negative (-) values)

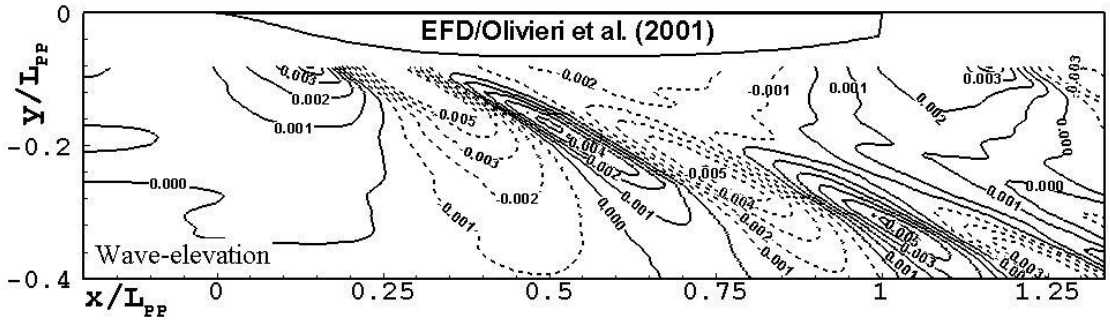

Experiment (INSEAN, Olivieri et al. 2001)

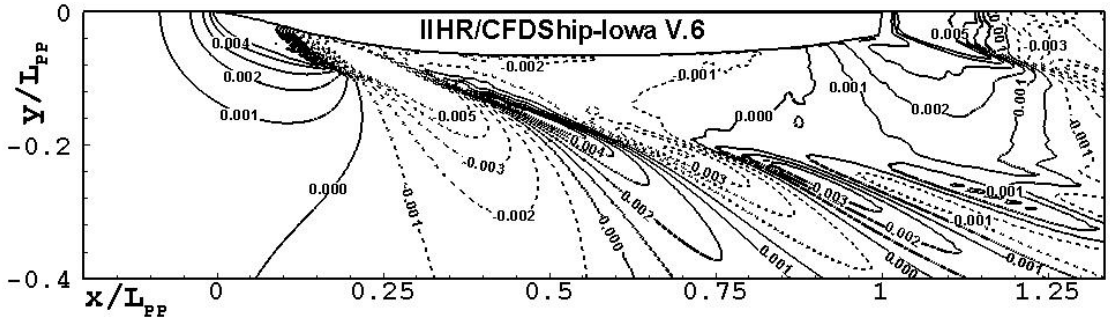

IIHR-CFDShip-IowaV6

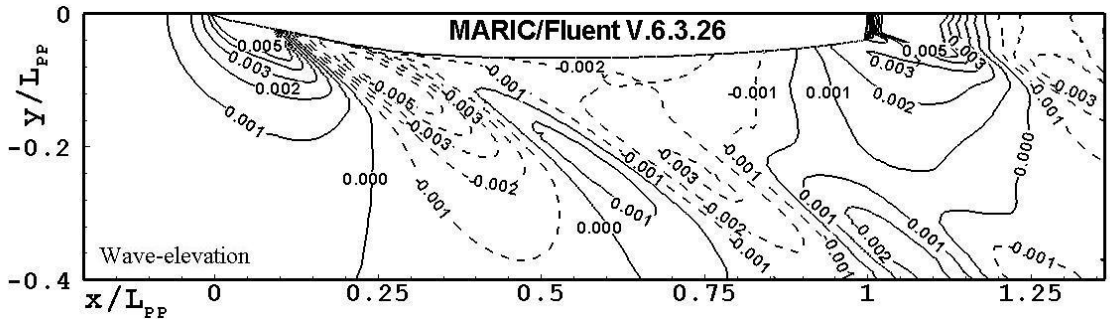

MARIC-FLUENT6.3.26

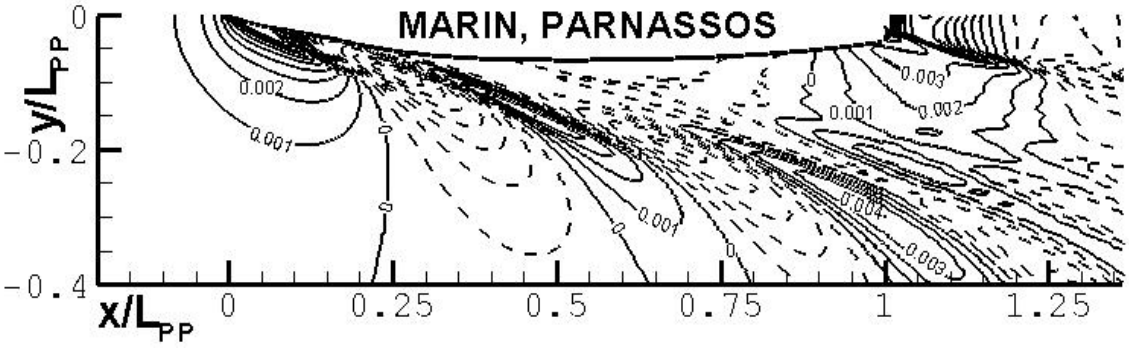

MARIN-PARNASSOS

Fig. 3.1a-1 Wave elevation contours [$\Delta z/L_{PP} = 0.001$]

(Solid lines: positive (+) values; Dashed lines: negative (-) values)

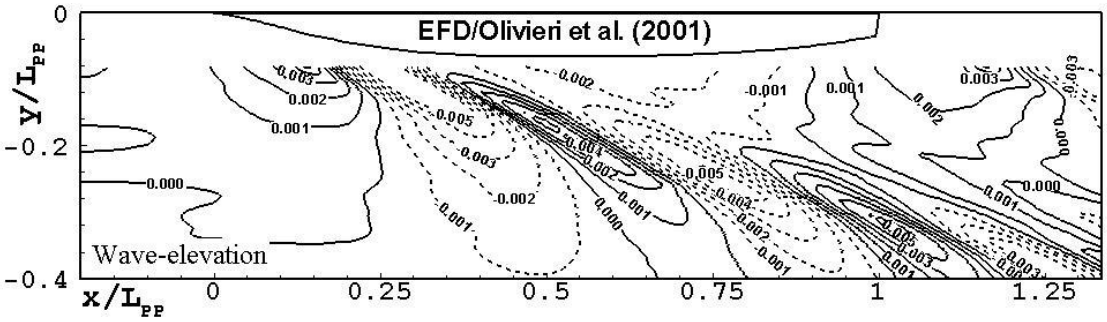

Experiment (INSEAN, Olivieri et al. 2001)

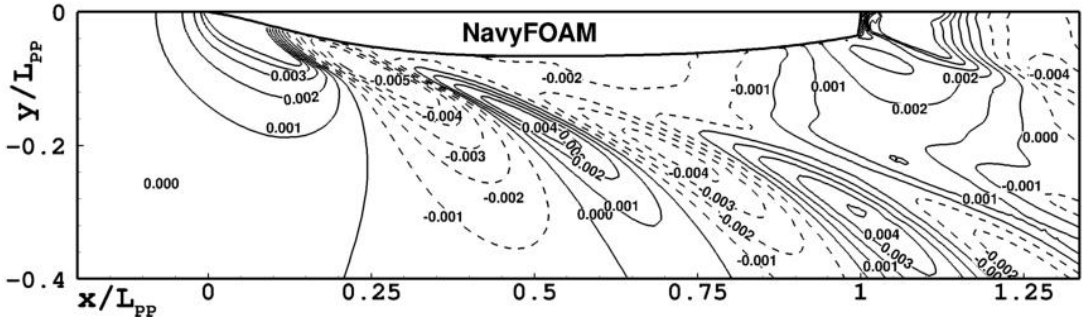

NavyFOAM-NavyFOAM

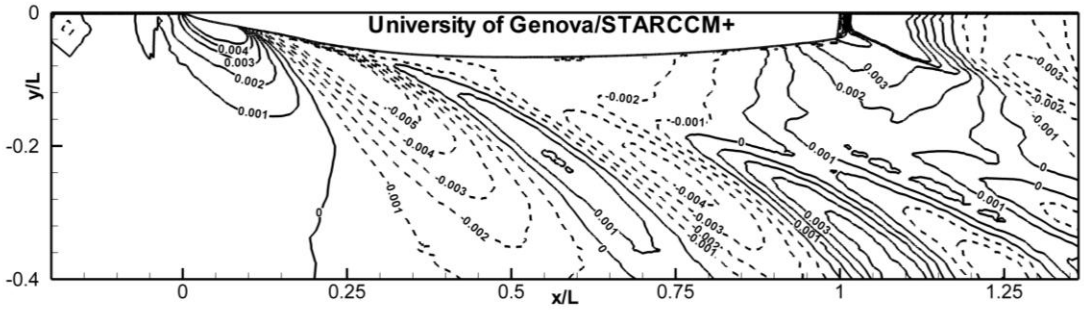

UoGe-STAR-CCM+

Fig. 3.1a-1 Wave elevation contours [$\Delta z/L_{PP} = 0.001$]

(Solid lines: positive (+) values; Dashed lines: negative (-) values)

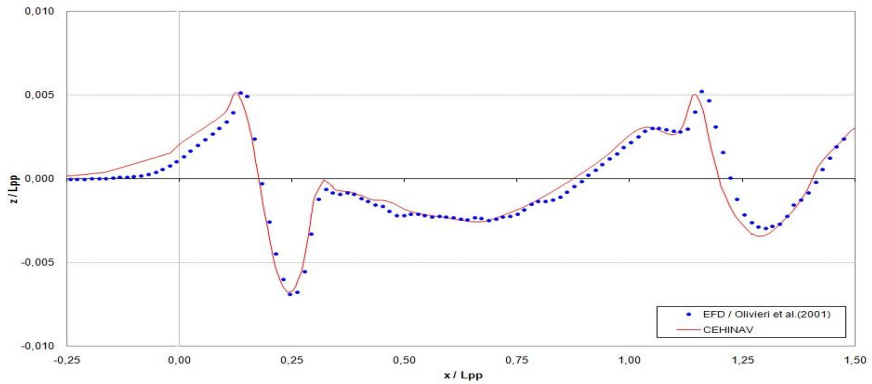

CEHINAV-STAR-CCM+

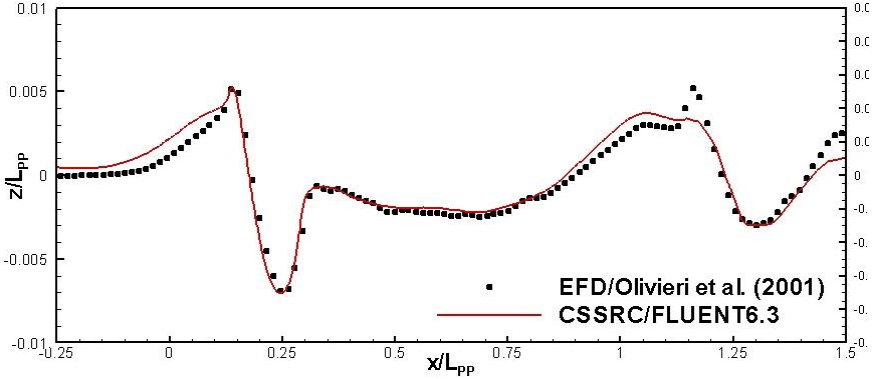

CSSRC-FLUENT6.3

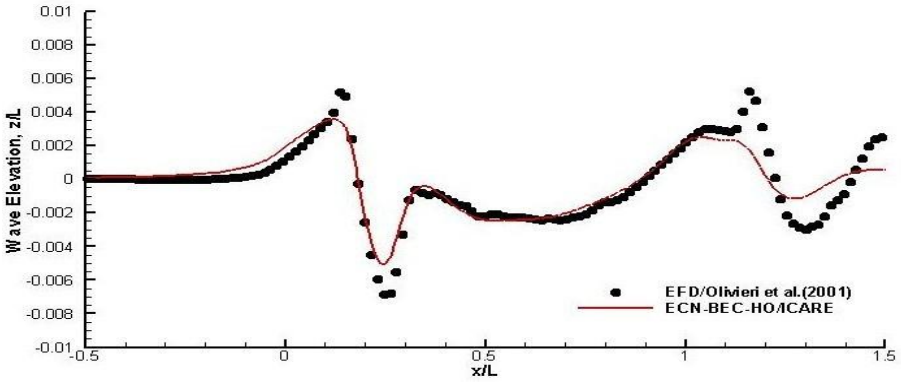

ECN/BEC/HO-Icare

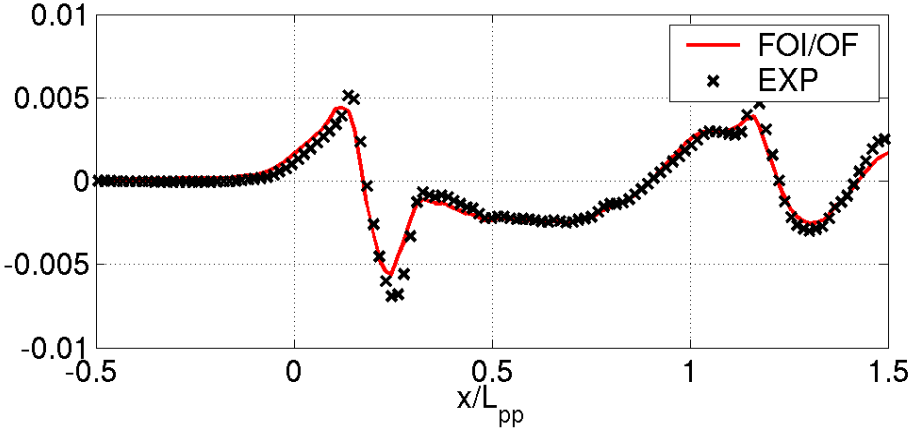

FOI-OF

Fig. 3.1a-1w-1 Longitudinal wave cut at $y/L_{PP} = 0.082$ (CFD: solid line; EFD: circles)

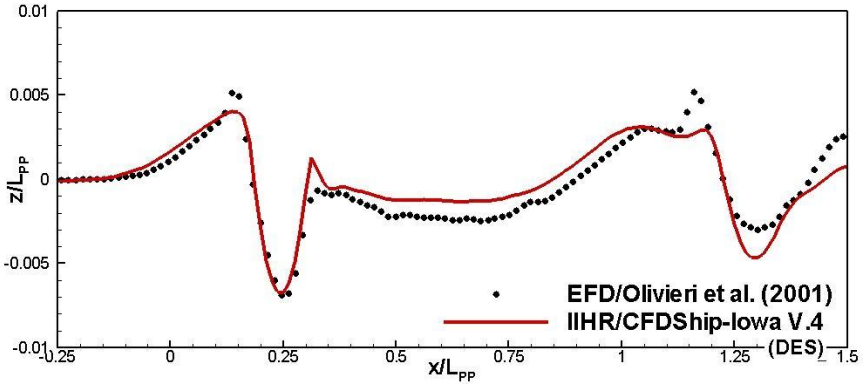

IIHR-CFDShip-IowaV4 (DES)

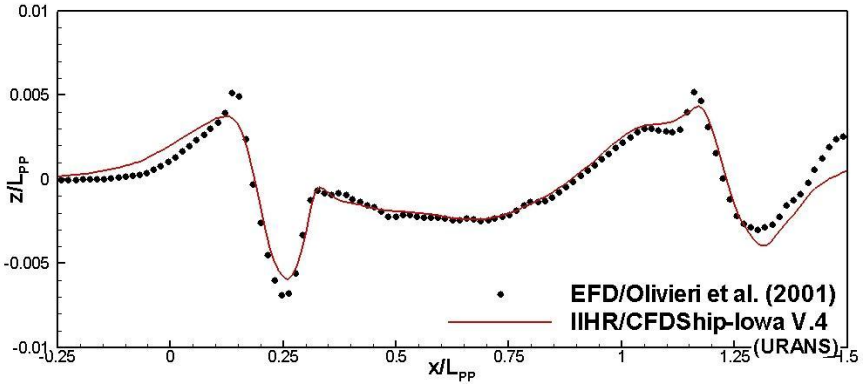

IIHR-CFDShip-IowaV4 (URANS)

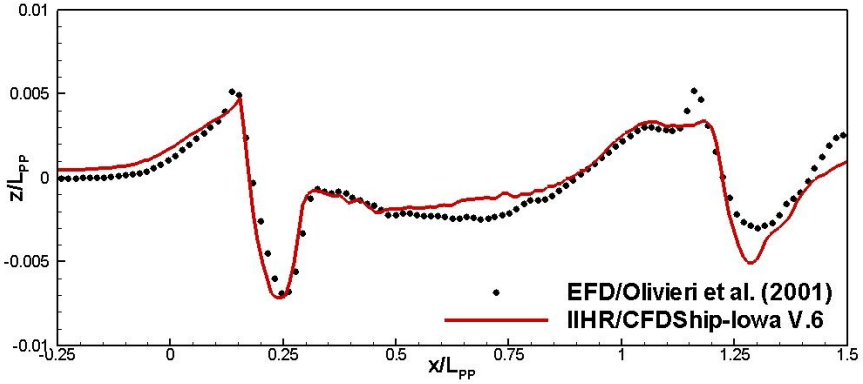

IIHR-CFDShip-IowaV6

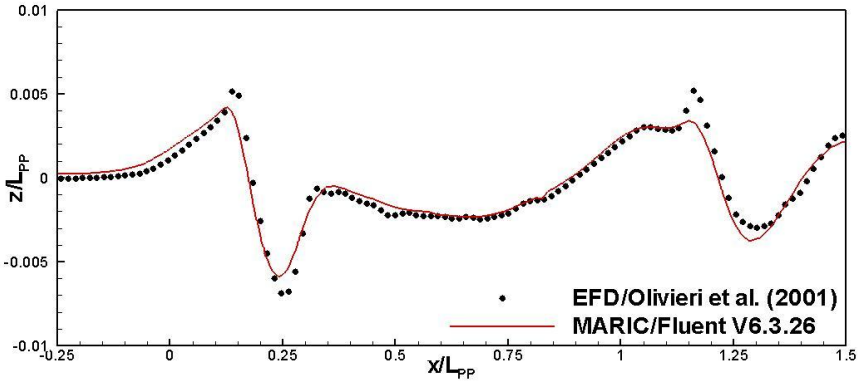

MARIC-FLUENT6.3.26

Fig. 3.1a-1w-1 Longitudinal wave cut at $y/L_{PP} = 0.082$ (CFD: solid line; EFD: circles)

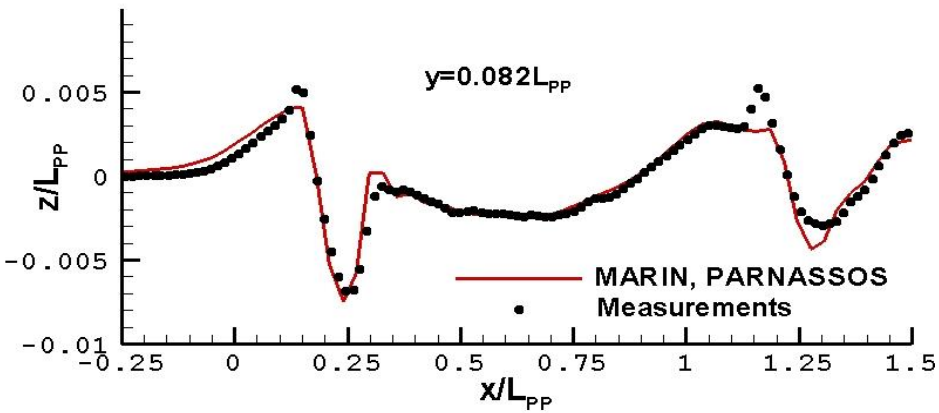

MARIN-PARNASSOS

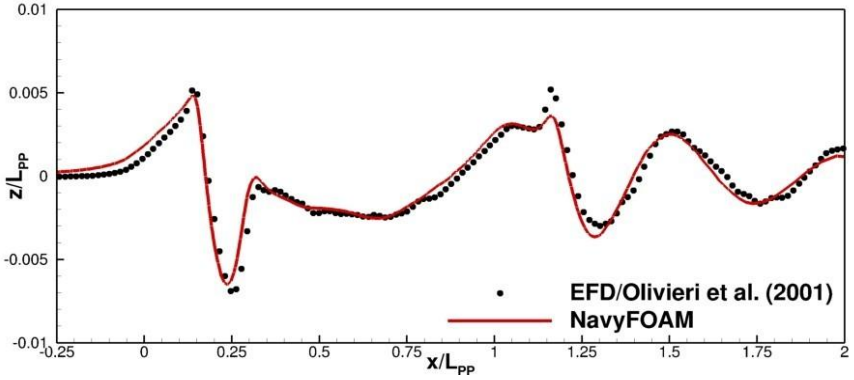

NavyFOAM-NavyFOAM

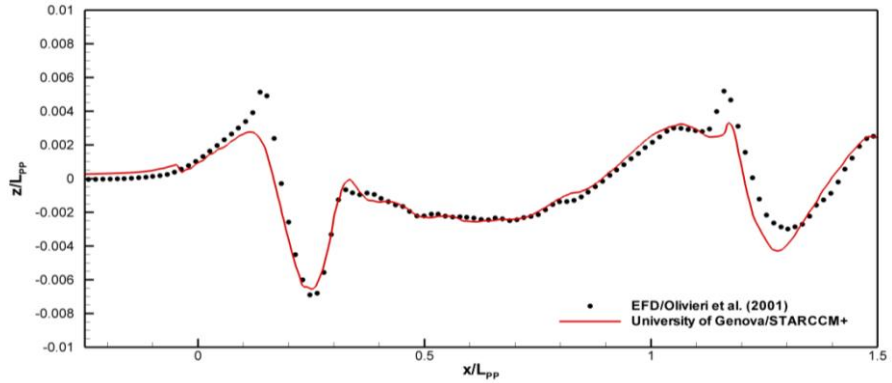

UoGe-STAR-CCM+

Fig. 3.1a-1w-1 Longitudinal wave cut at $y/L_{PP} = 0.082$ (CFD: solid line; EFD: circles)

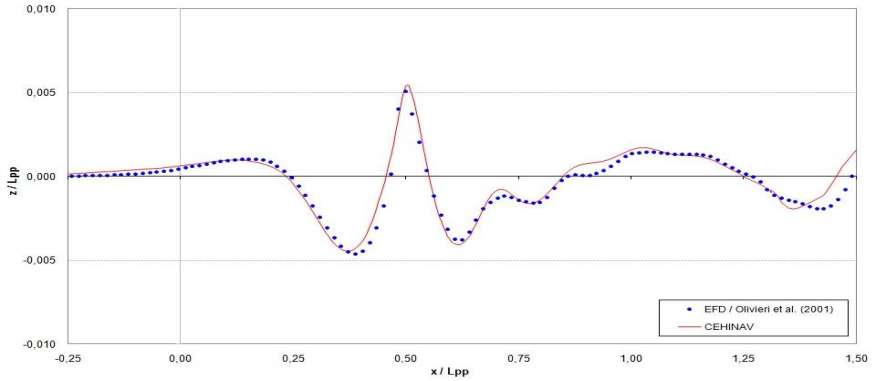

CEHINAV-STAR-CCM+

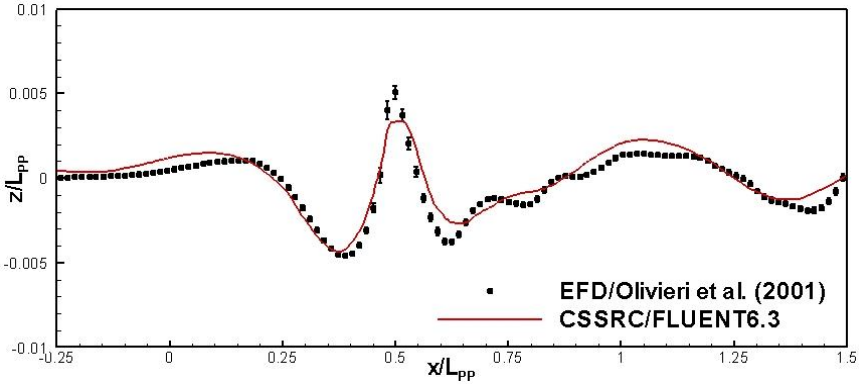

CSSRC-FLUENT6.3

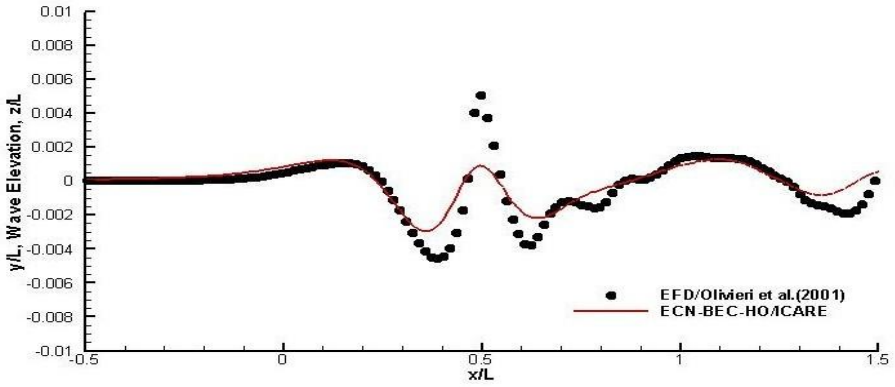

ECN/BEC/HO-Icare

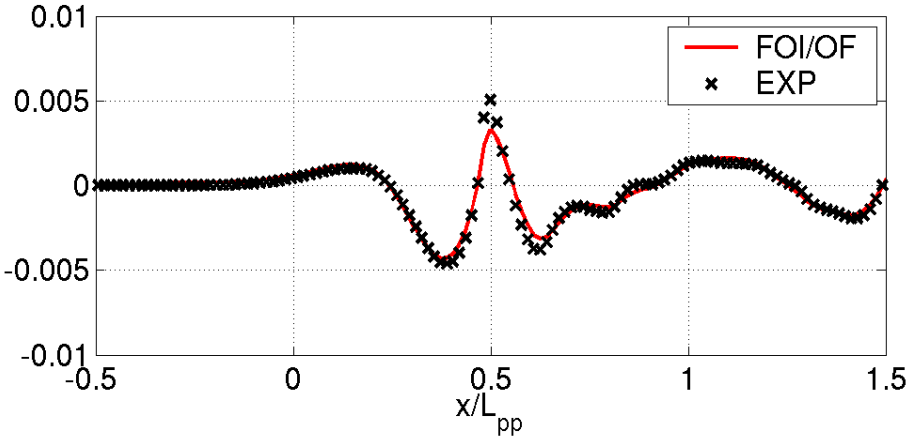

FOI-OF

Fig. 3.1a-1w-2 Longitudinal wave cut at $y/L_{PP} = 0.172$ (CFD: solid line; EFD: circles)

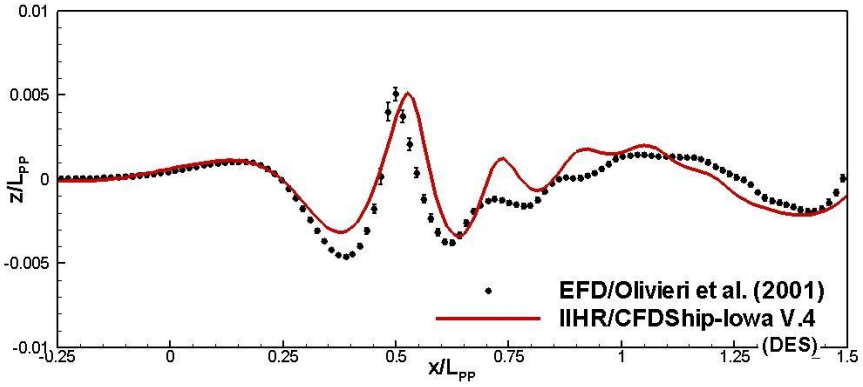

IIHR-CFDShip-IowaV4 (DES)

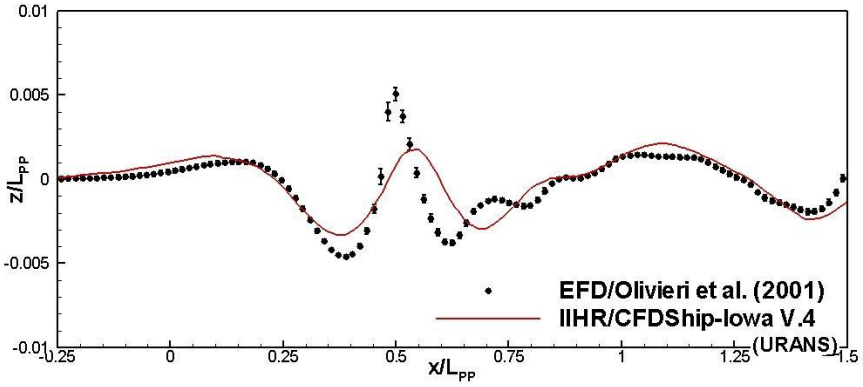

IIHR-CFDShip-IowaV4 (URANS)

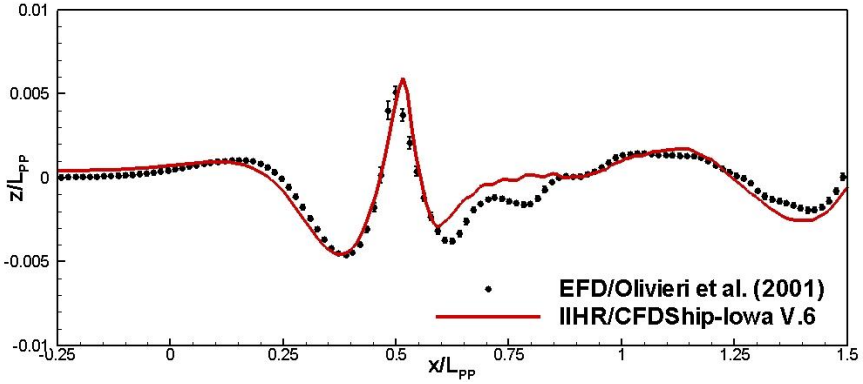

IIHR-CFDShip-IowaV6

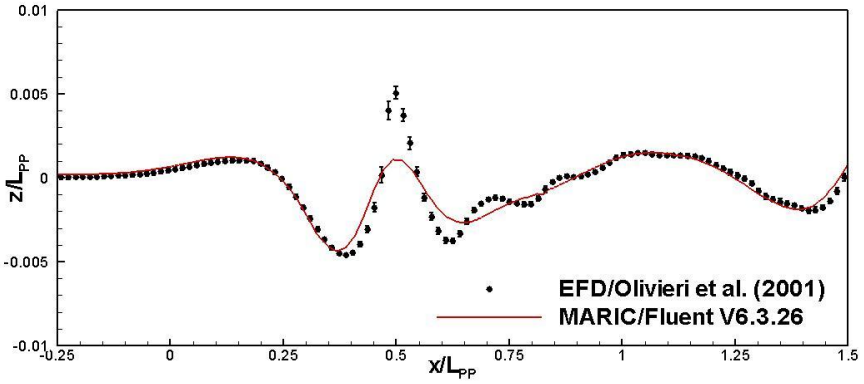

MARIC-FLUENT6.3.26

Fig. 3.1a-1w-2 Longitudinal wave cut at $y/L_{PP} = 0.172$ (CFD: solid line; EFD: circles)

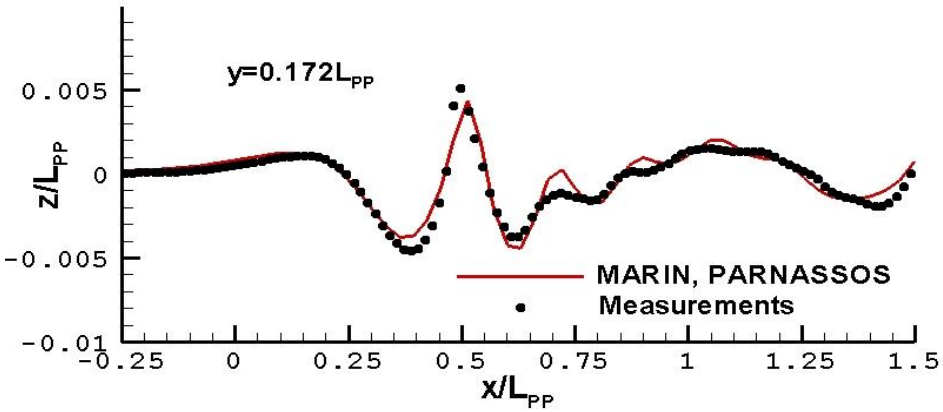

MARIN-PARNASSOS

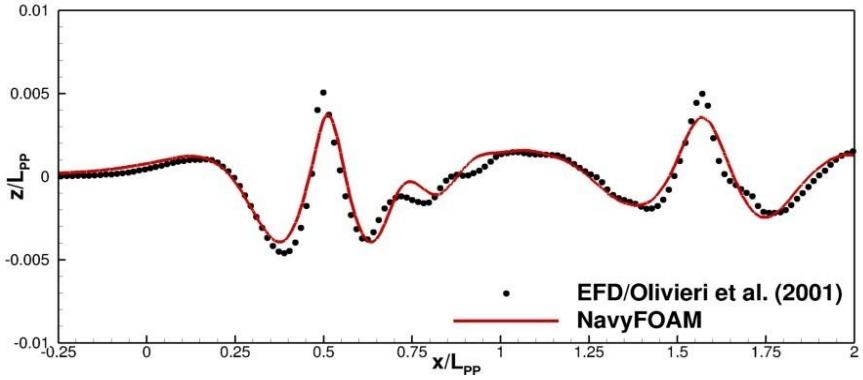

NavyFOAM-NavyFOAM

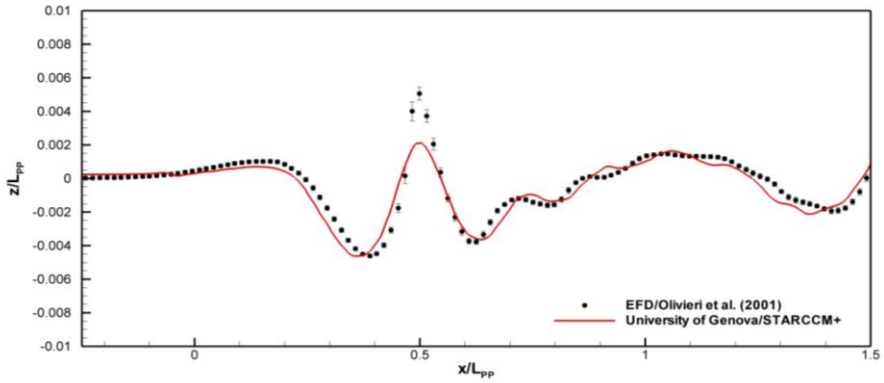

UoGe-STAR-CCM+

Fig. 3.1a-1w-2 Longitudinal wave cut at $y/L_{PP} = 0.172$ (CFD: solid line; EFD: circles)

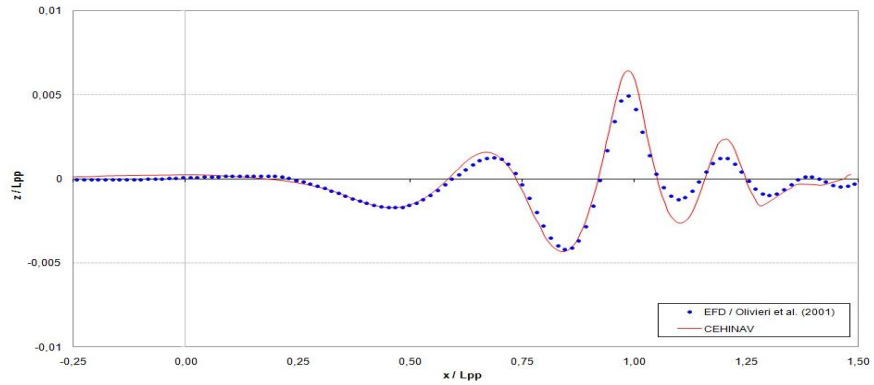

CEHINAV-STAR-CCM+

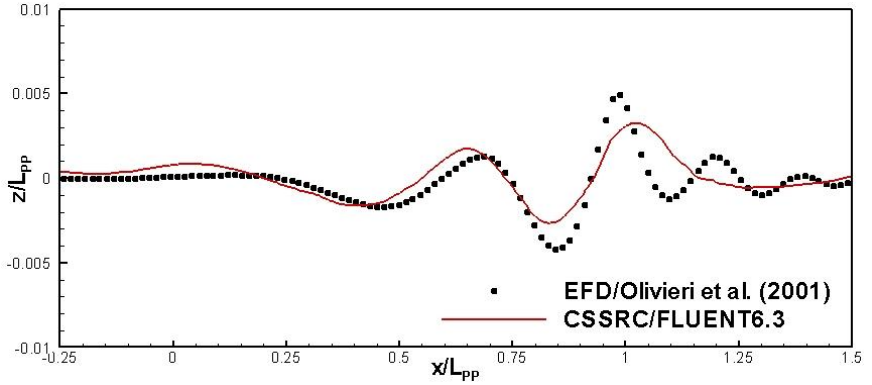

CSSRC-FLUENT6.3

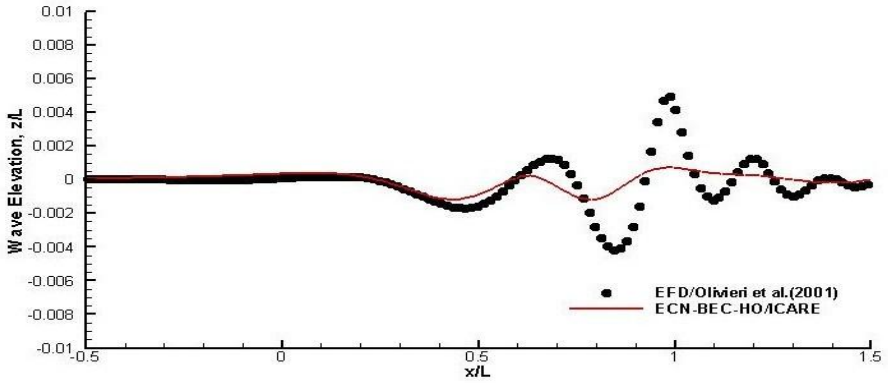

ECN/BEC/HO-Icare

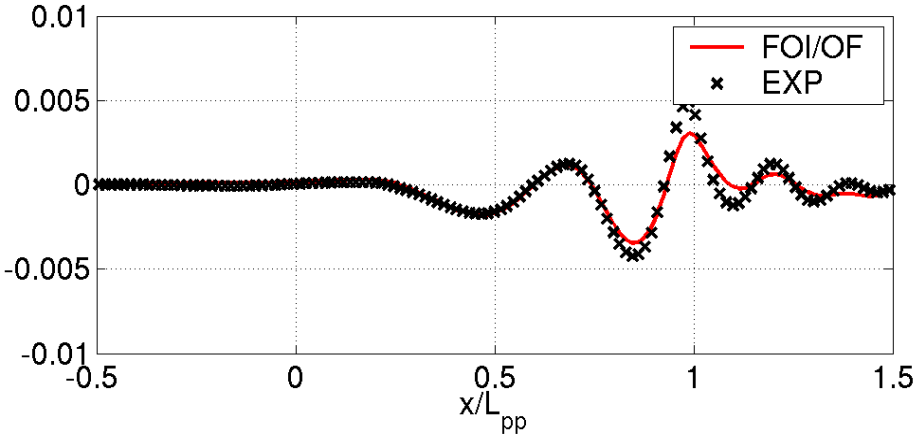

FOI-OF

Fig. 3.1a-1w-3 Longitudinal wave cut at $y/L_{pp} = 0.301$ (CFD: solid line; EFD: circles)

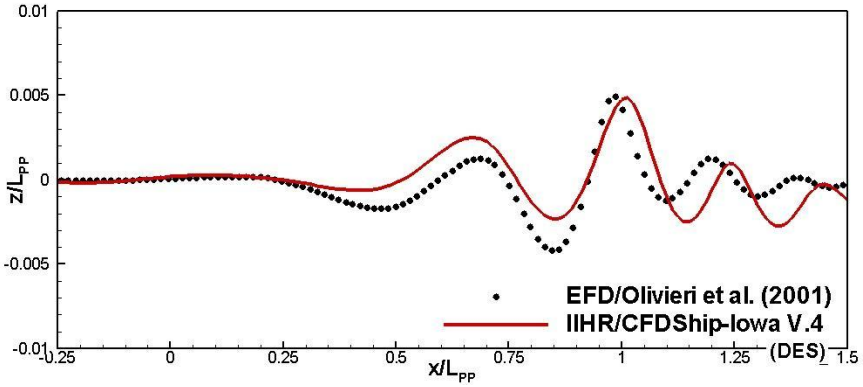

IIHR-CFDShip-IowaV4 (DES)

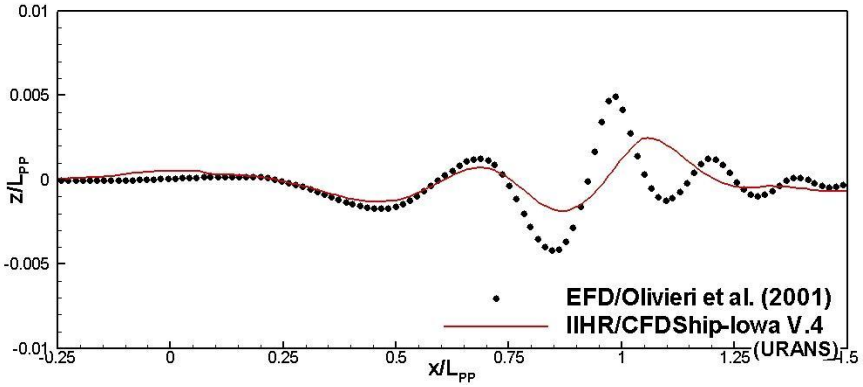

IIHR-CFDShip-IowaV4 (URANS)

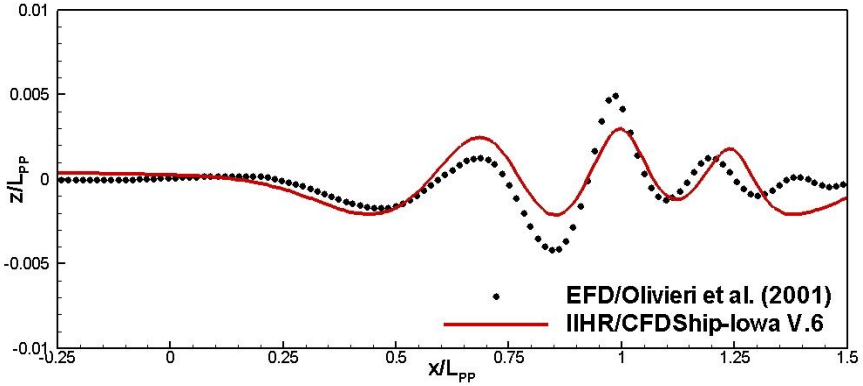

IIHR-CFDShip-IowaV6

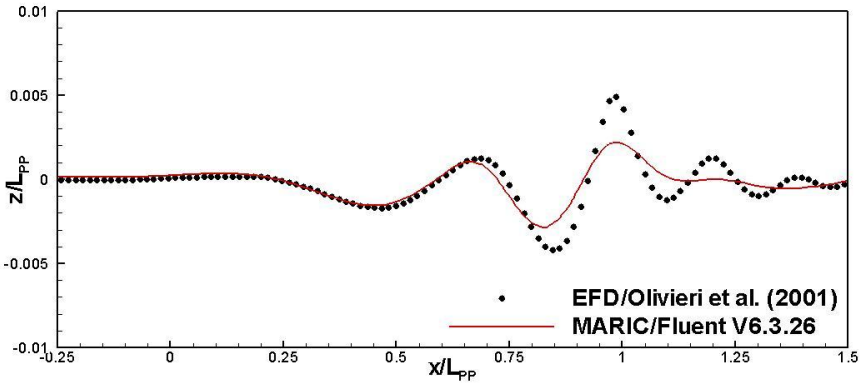

MARIC-FLUENT6.3.26

Fig. 3.1a-1w-3 Longitudinal wave cut at $y/L_{PP} = 0.301$ (CFD: solid line; EFD: circles)

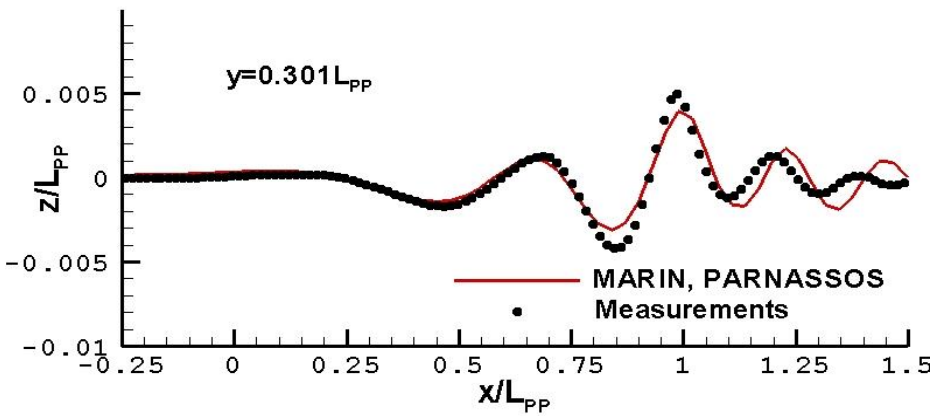

MARIN-PARNASSOS

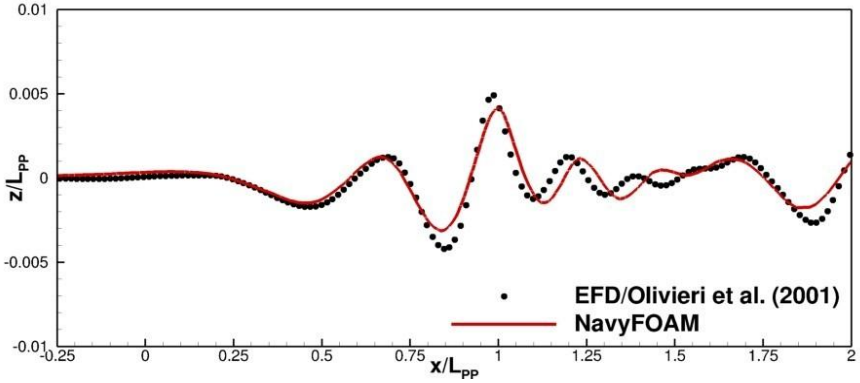

NavyFOAM-NavyFOAM

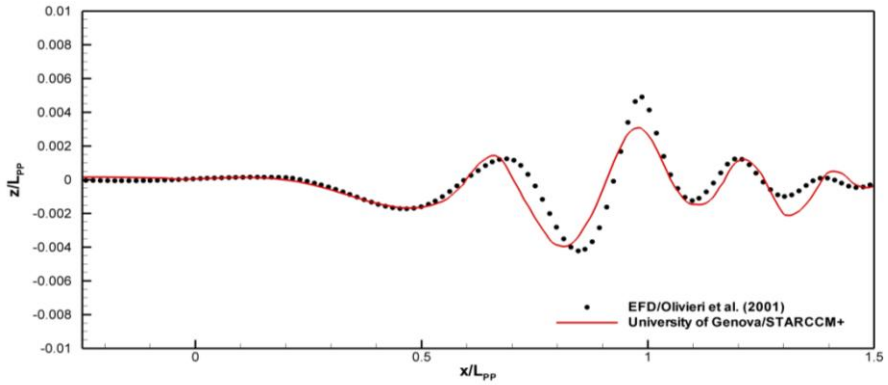

UoGe-STAR-CCM+

Fig. 3.1a-1w-3 Longitudinal wave cut at $y/L_{PP} = 0.301$ (CFD: solid line; EFD: circles)

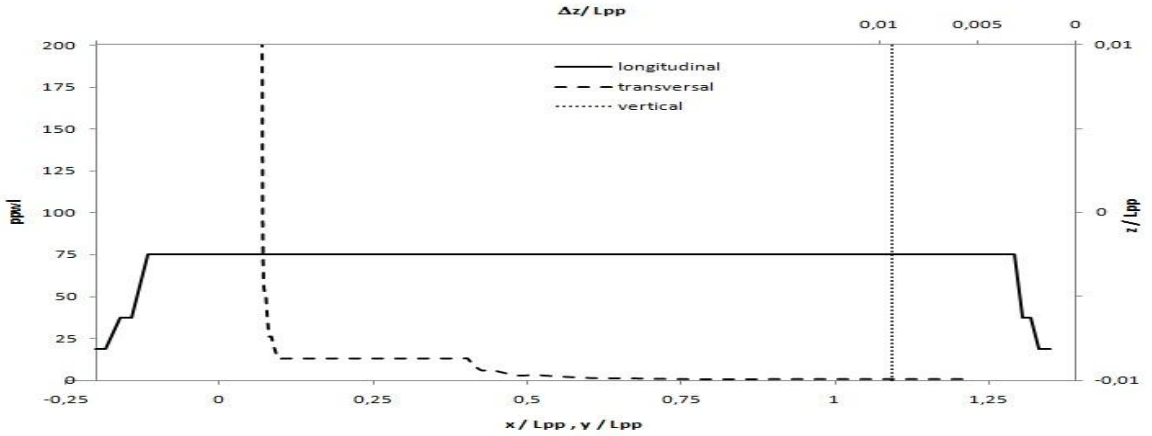

CEHINAV-STAR-CCM+

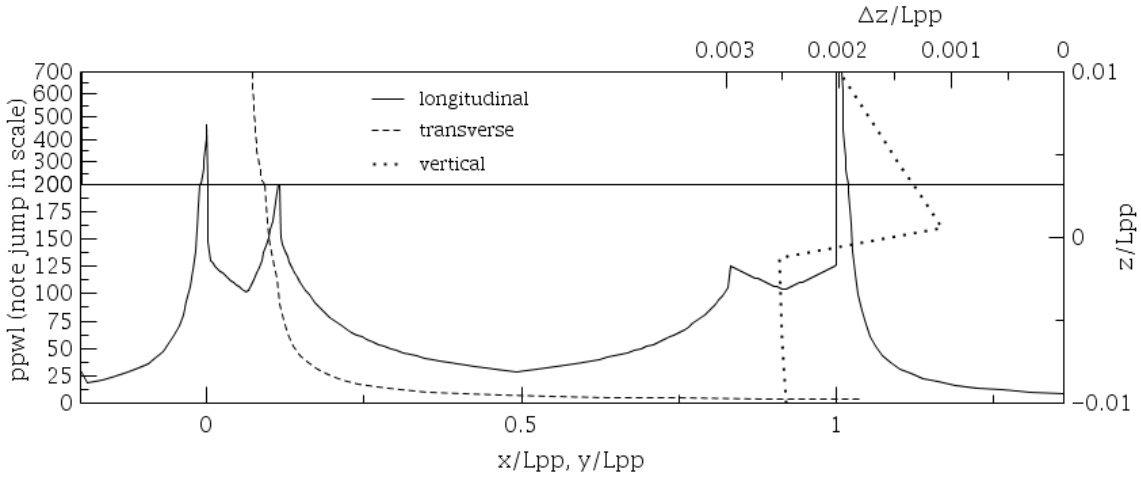

CSSRC-FLUENT6.3

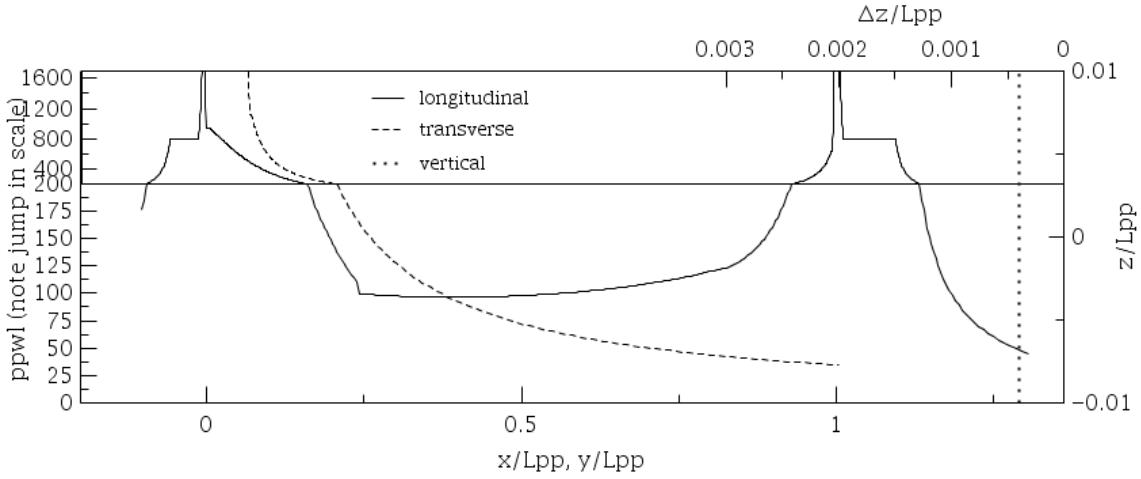

IIHR-CFDShip-IowaV4 (DES)

Fig. 3.1a-1w-4 Grid density distribution along the waterline (solid), and in transverse (dashed) and vertical (dotted) directions at mid-ship

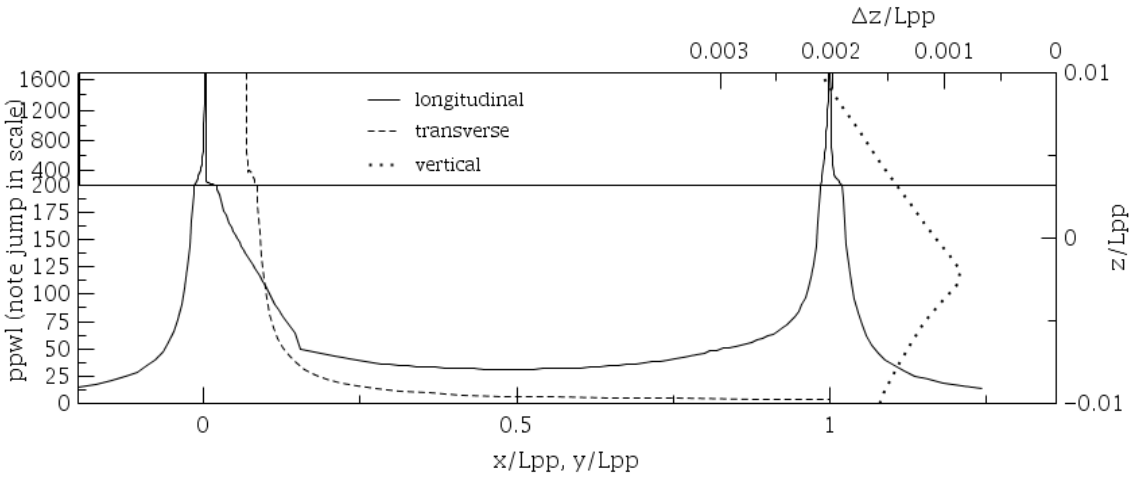

IIHR-CFDShip-IowaV4 (URANS)

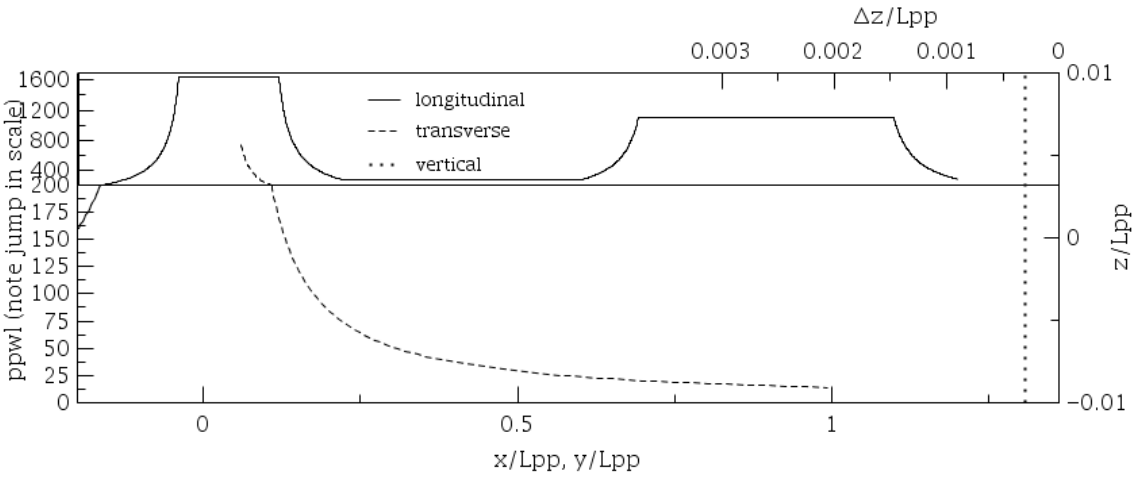

IIHR-CFDShip-IowaV6

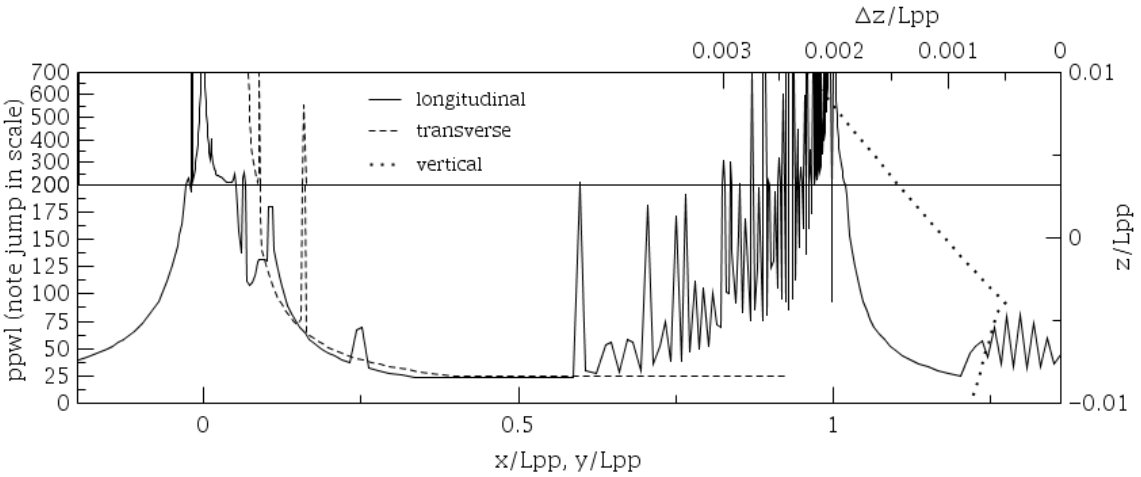

MARIC-FLUENT6.3.26

Fig. 3.1a-1w-4 Grid density distribution along the waterline (solid), and in transverse (dashed) and vertical (dotted) directions at mid-ship

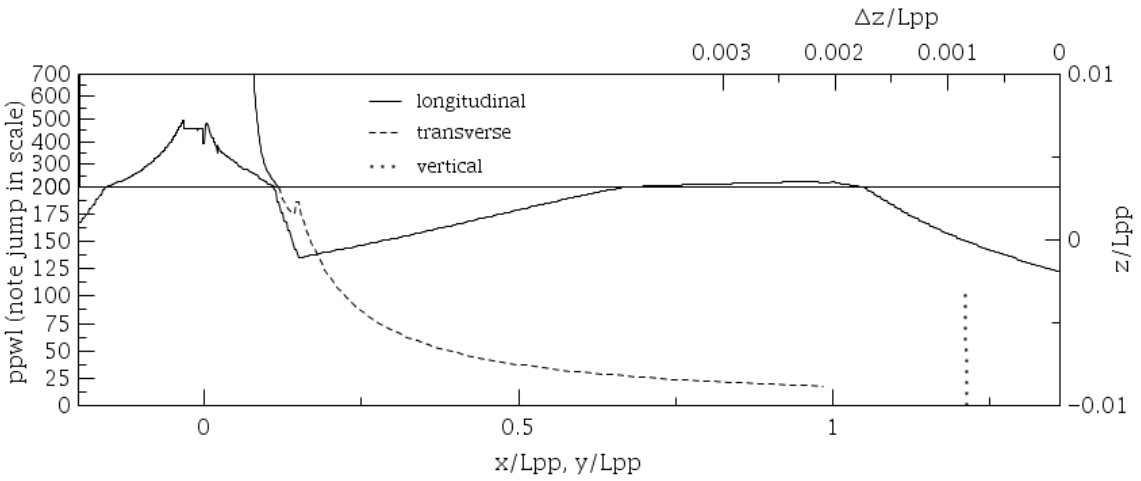

MARIN-PARNASSOS

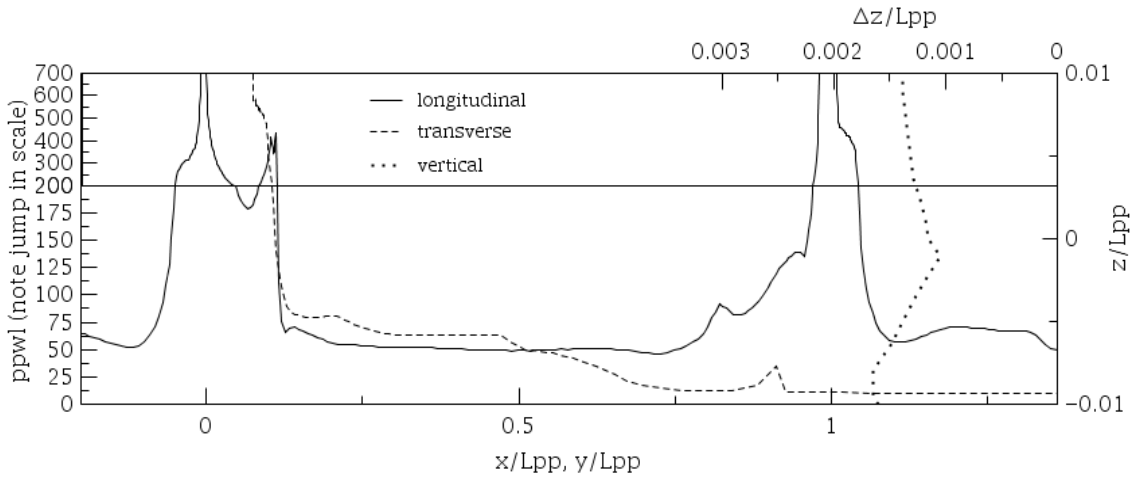

NavyFOAM-NavyFOAM

Fig. 3.1a-1w-4 Grid density distribution along the waterline (solid), and in transverse (dashed) and vertical (dotted) directions at mid-ship

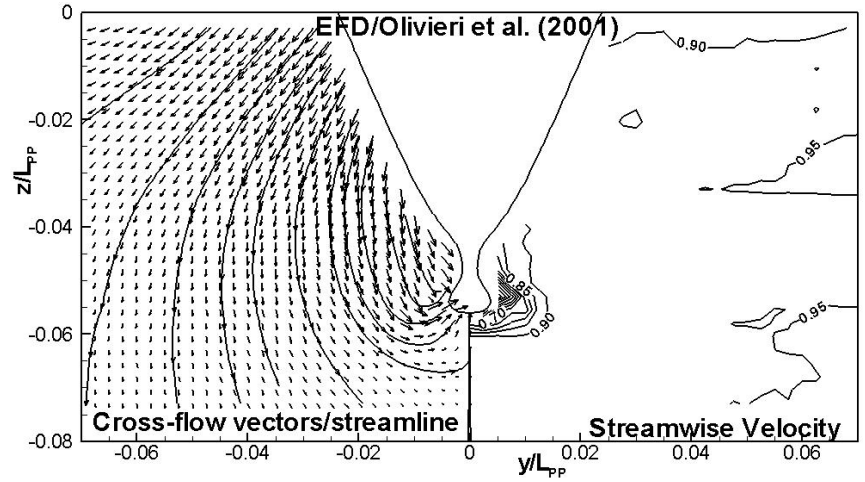

Experiment (INSEAN, Olivieri et al. 2001)

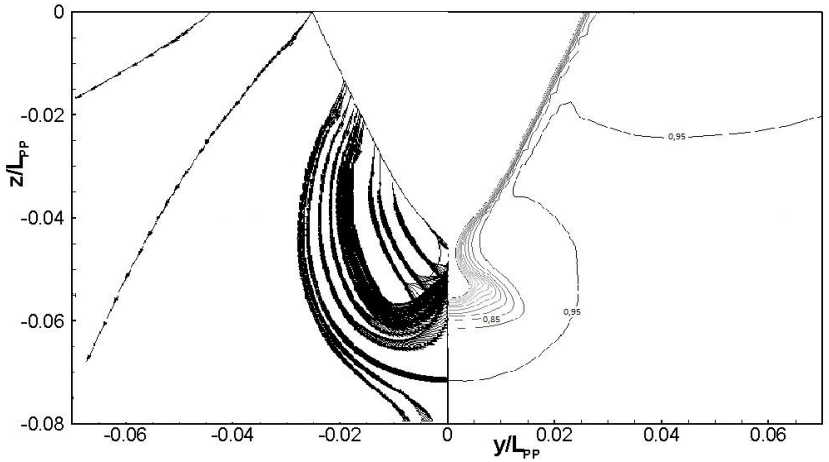

CEHINAV-STAR-CCM+

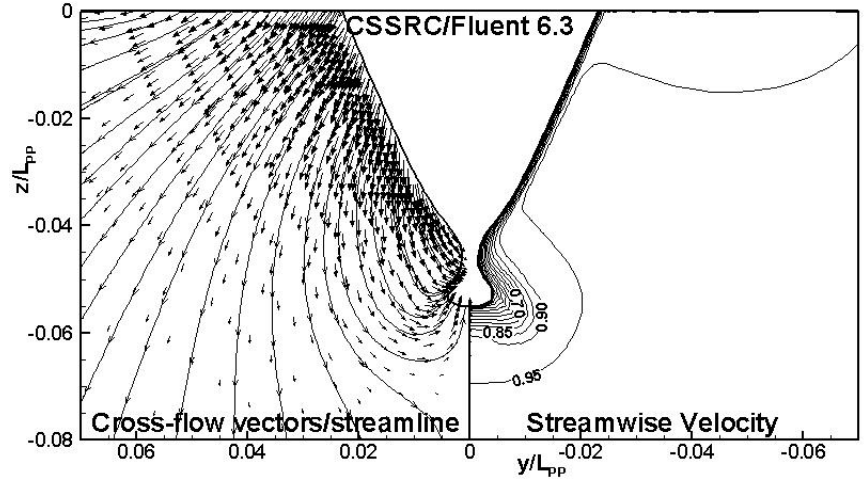

CSSRC-FLUENT6.3

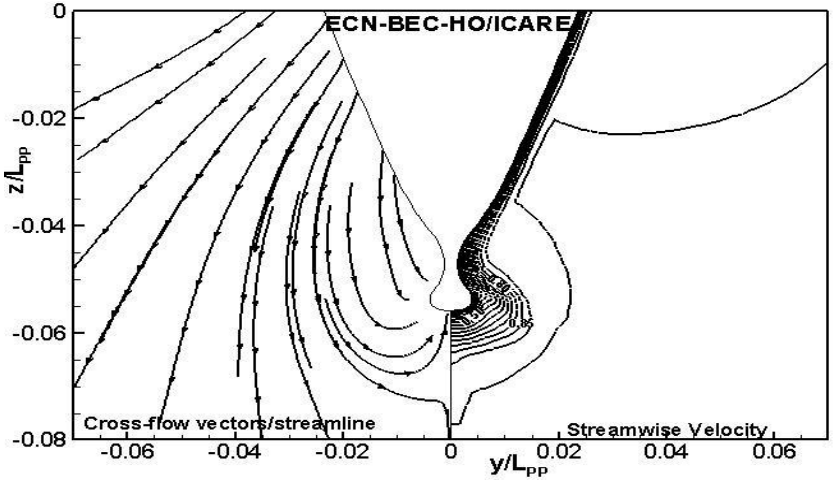

ECN/BEC/HO-Icare

Fig. 3.1a-2 Cross flow vectors and streamlines (left panel), U contours (right panel) at $x/L_{PP} = 0.1$ [$\Delta U = 0.05$]

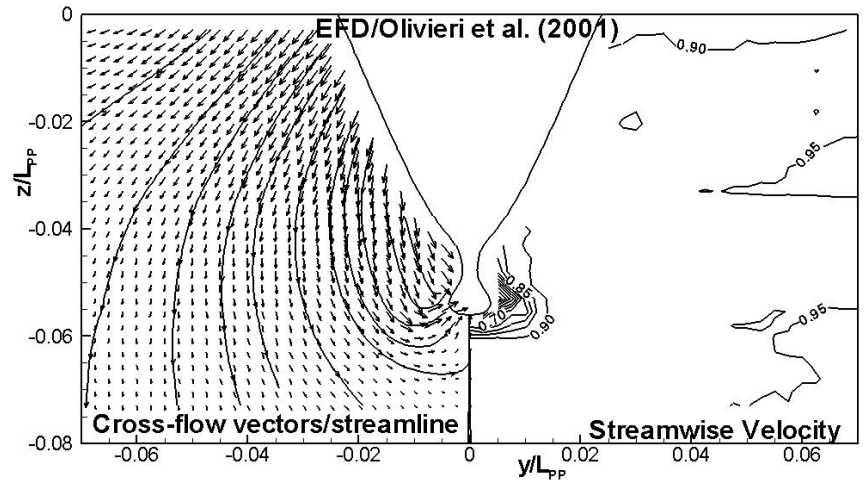

Experiment (INSEAN, Olivieri et al. 2001)

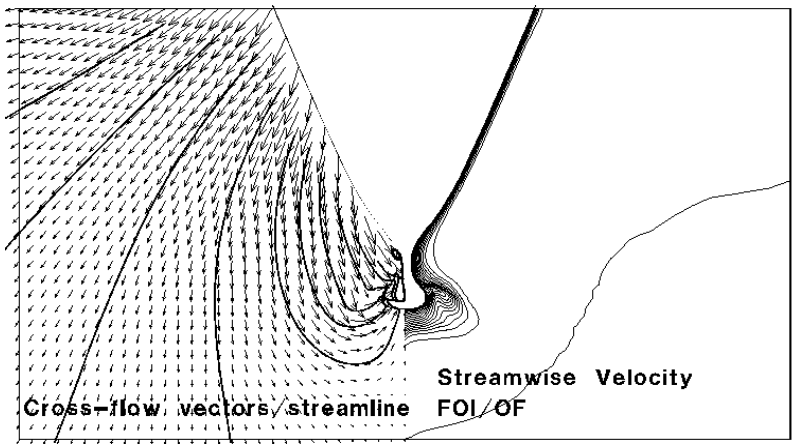

FOI-OF

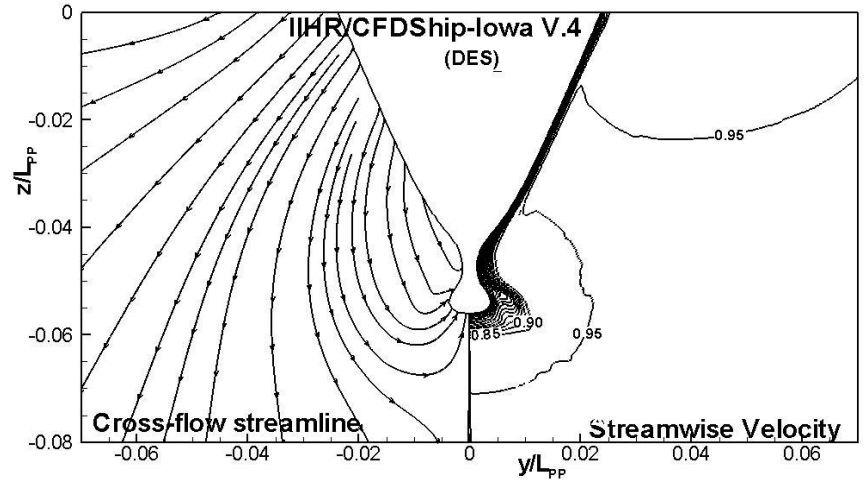

IIHR-CFDShip-IowaV4 (DES)

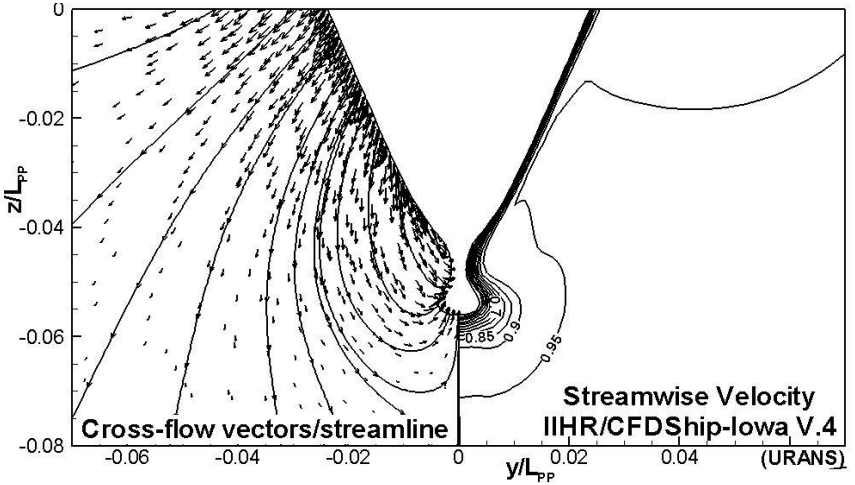

IIHR-CFDShip-IowaV4 (URANS)

Fig. 3.1a-2 Cross flow vectors and streamlines (left panel), U contours (right panel) at $x/L_{PP} = 0.1$ [$\Delta U = 0.05$]

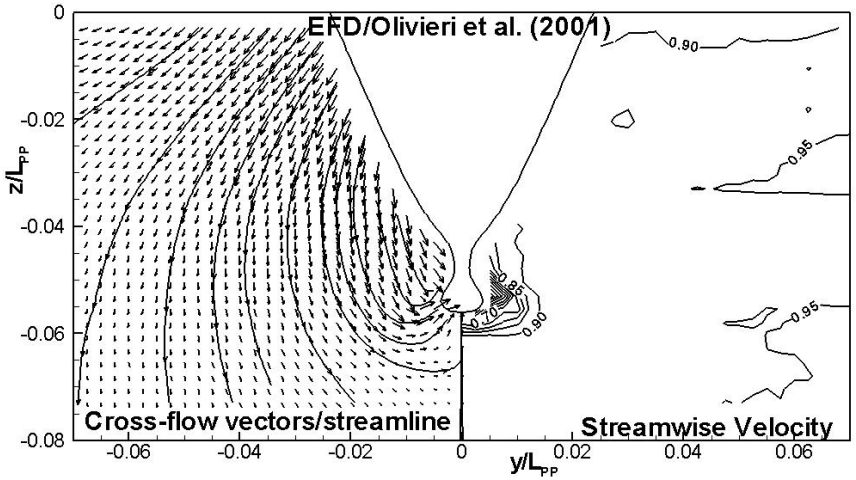

Experiment (INSEAN, Olivieri et al. 2001)

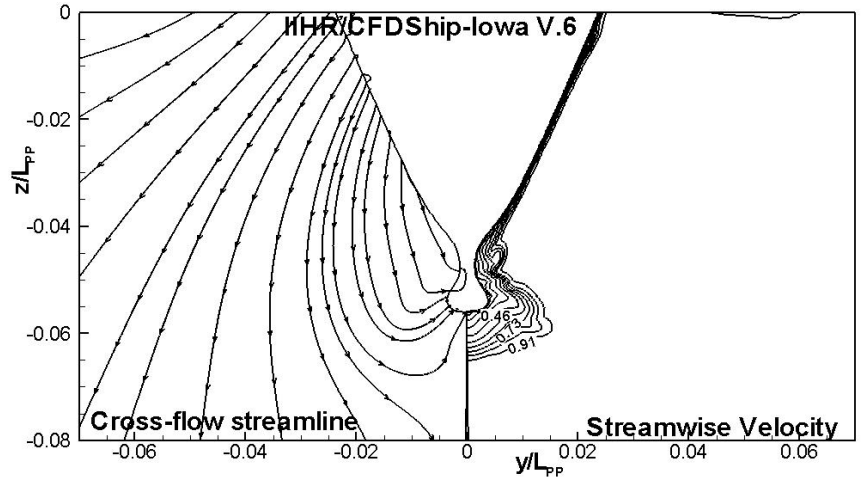

IIHR-CFDShip-IowaV6

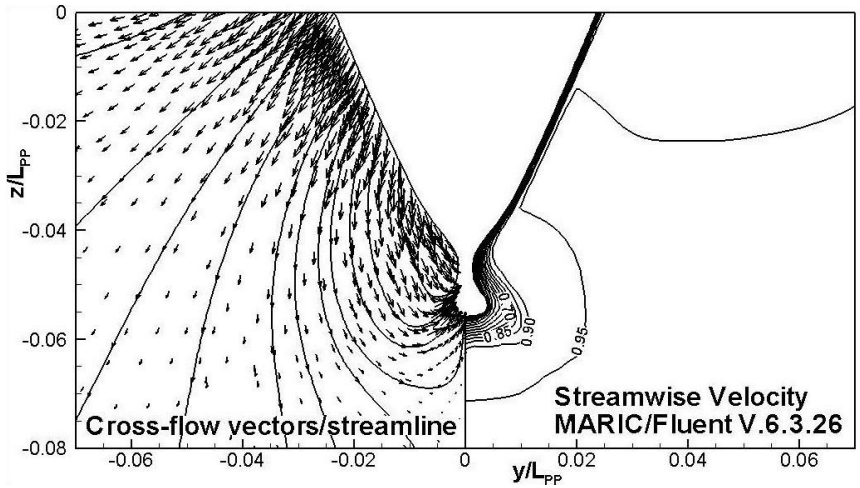

MARIC-FLUENT6.3.26

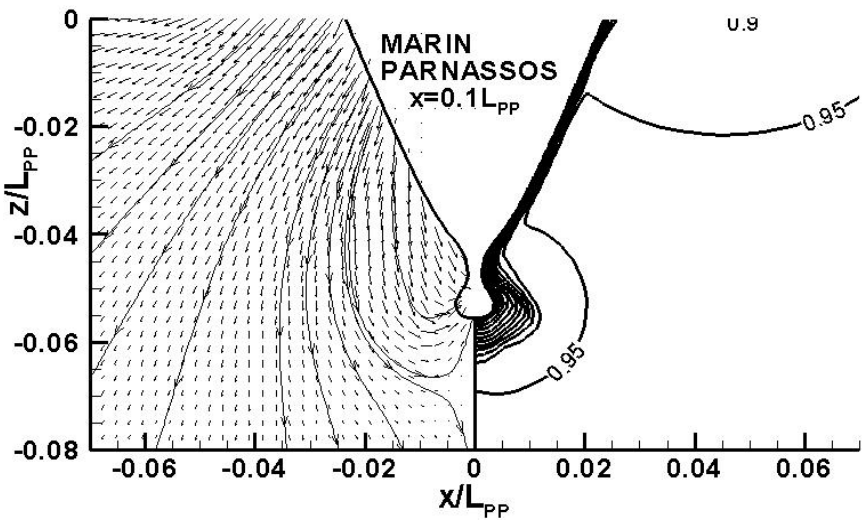

MARIN-PARNASSOS

Fig. 3.1a-2 Cross flow vectors and streamlines (left panel), U contours (right panel) at $x/L_{PP} = 0.1$ [$\Delta U = 0.05$]

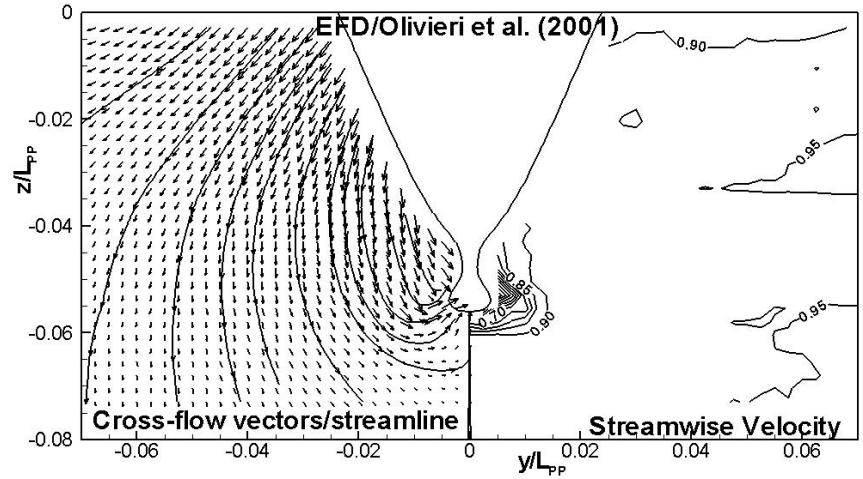

Experiment (INSEAN, Olivieri et al. 2001)

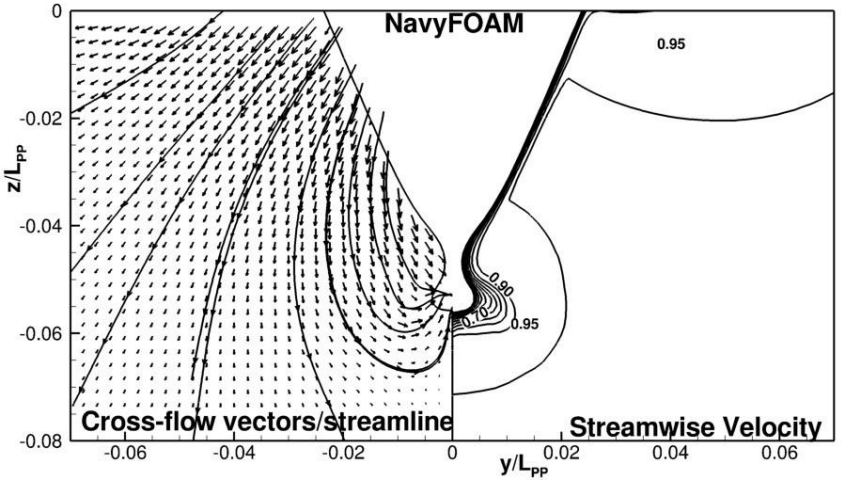

NavyFOAM-NavyFOAM

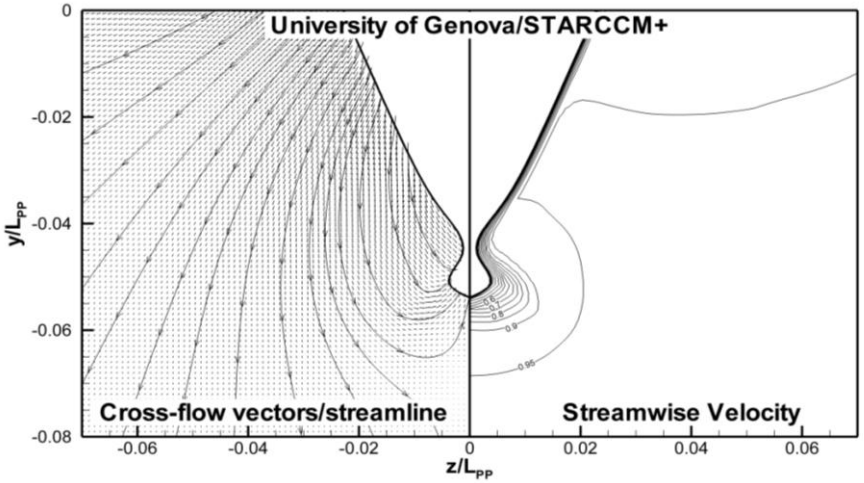

UoGe-STAR-CCM+

Fig. 3.1a-2 Cross flow vectors and streamlines (left panel), U contours (right panel) at $x/L_{PP} = 0.1$ [$\Delta U = 0.05$]

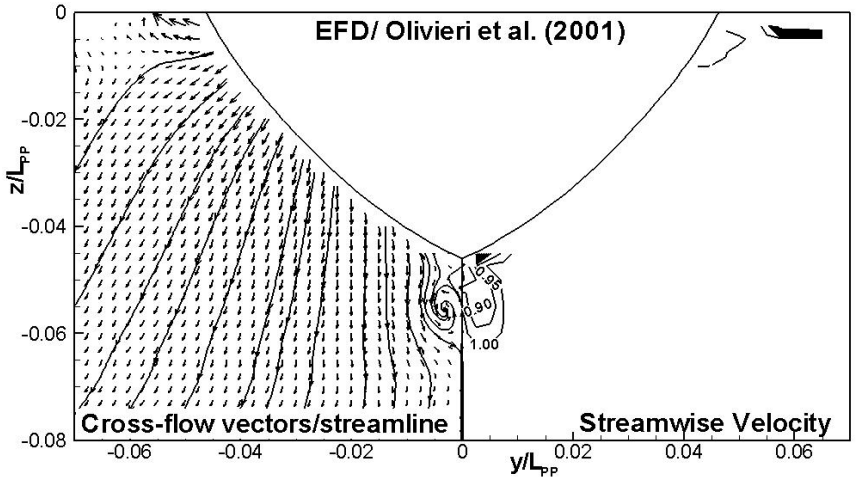

Experiment (INSEAN, Olivieri et al. 2001)

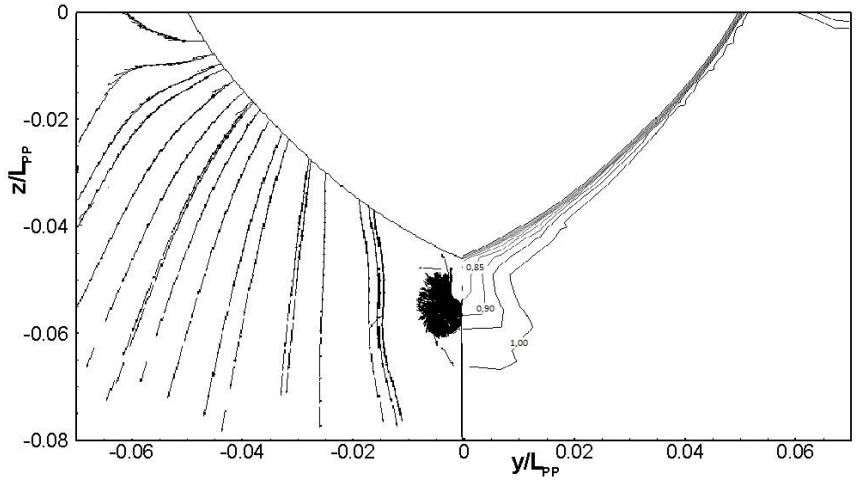

CEHINAV-STAR-CCM+

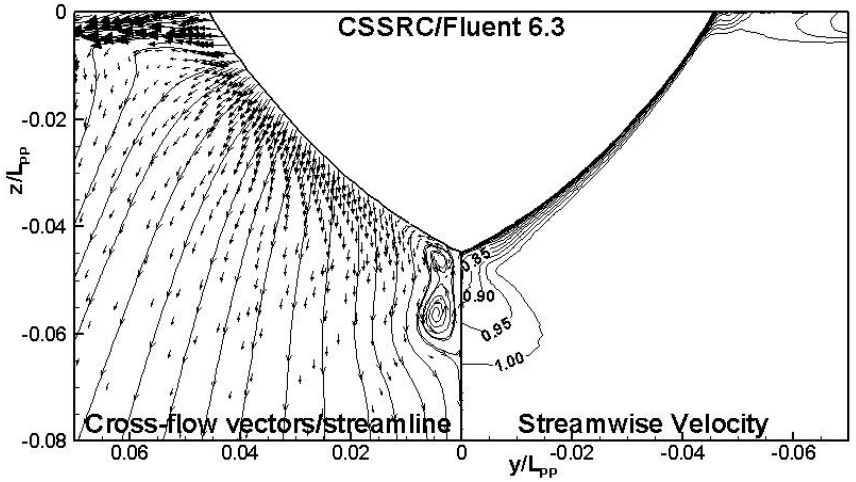

CSSRC-FLUENT6.3

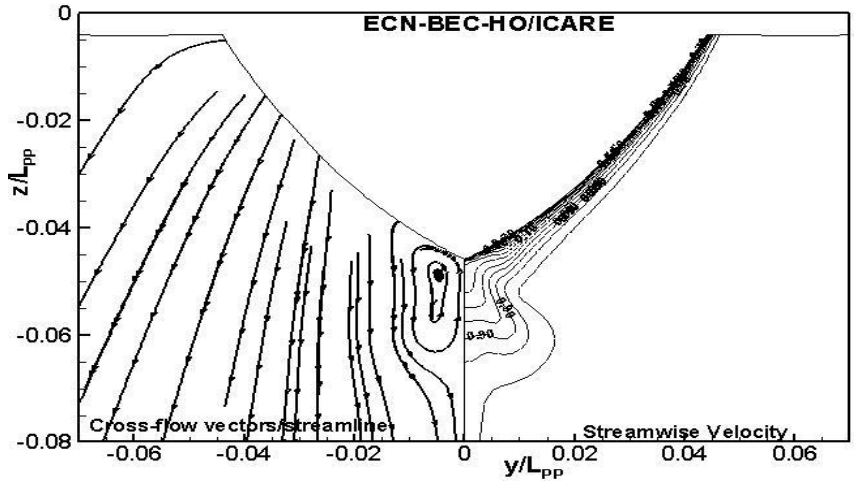

ECN/BEC/HO-Icare

Fig. 3.1a-3 Cross flow vectors and streamlines (left panel), U contours (right panel) at $x/L_{PP} = 0.2$ [$\Delta U = 0.05$]

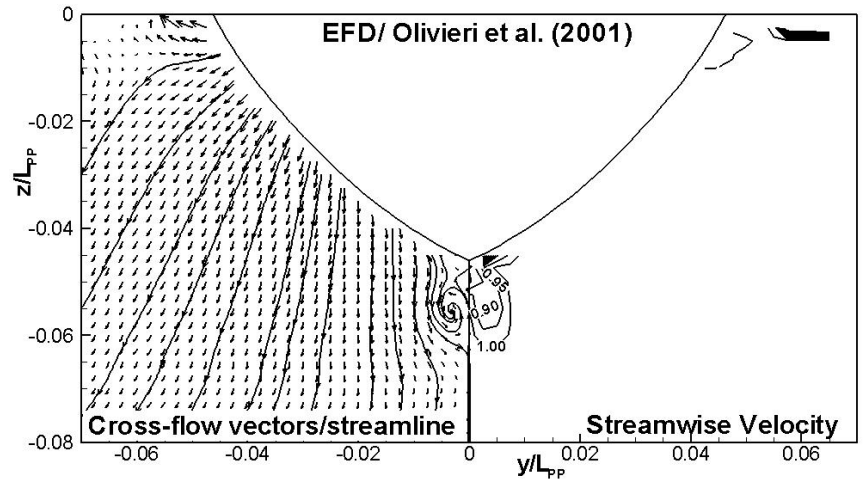

Experiment (INSEAN, Olivieri et al. 2001)

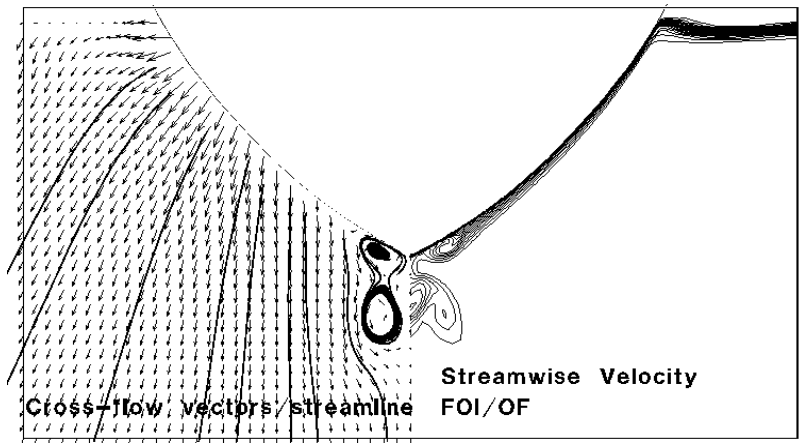

FOI-OF

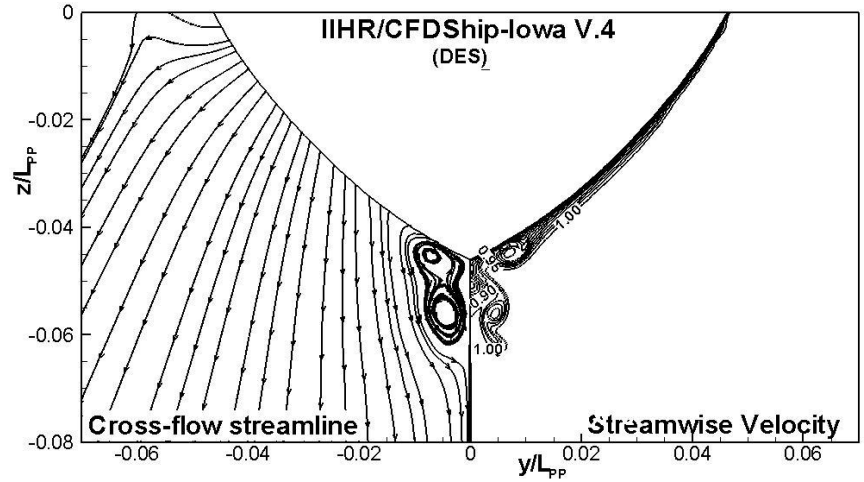

IIHR-CFDShip-IowaV4 (DES)

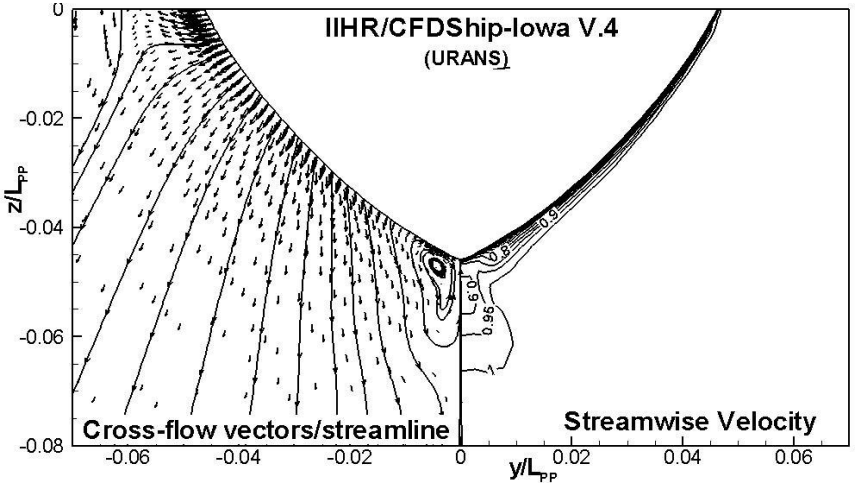

IIHR-CFDShip-IowaV4 (URANS)

Fig. 3.1a-3 Cross flow vectors and streamlines (left panel), U contours (right panel) at $x/L_{PP} = 0.2$ [$\Delta U = 0.05$]

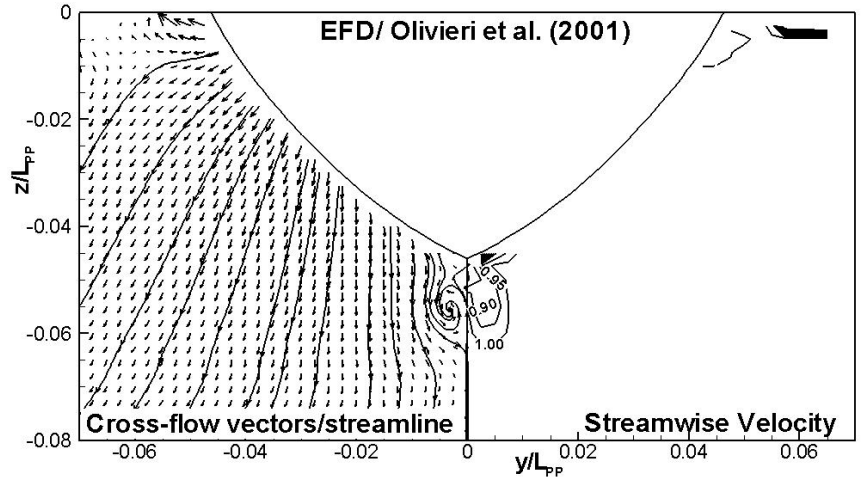

Experiment (INSEAN, Olivieri et al. 2001)

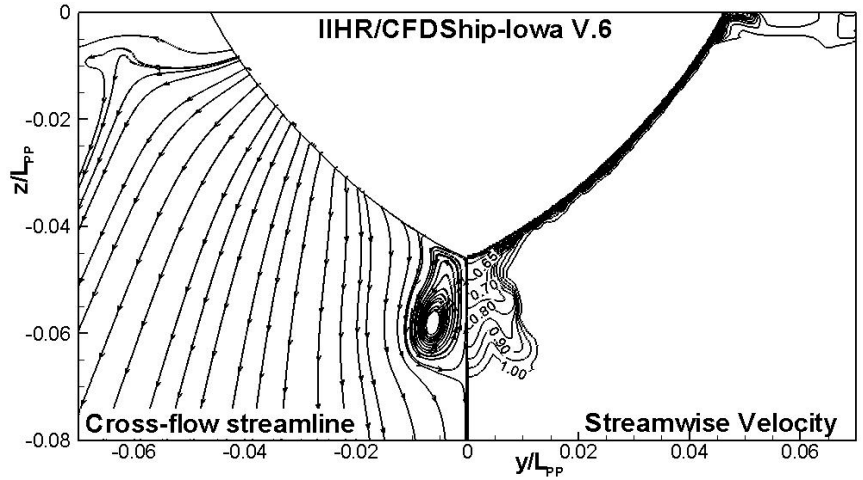

IIHR-CFDShip-IowaV6

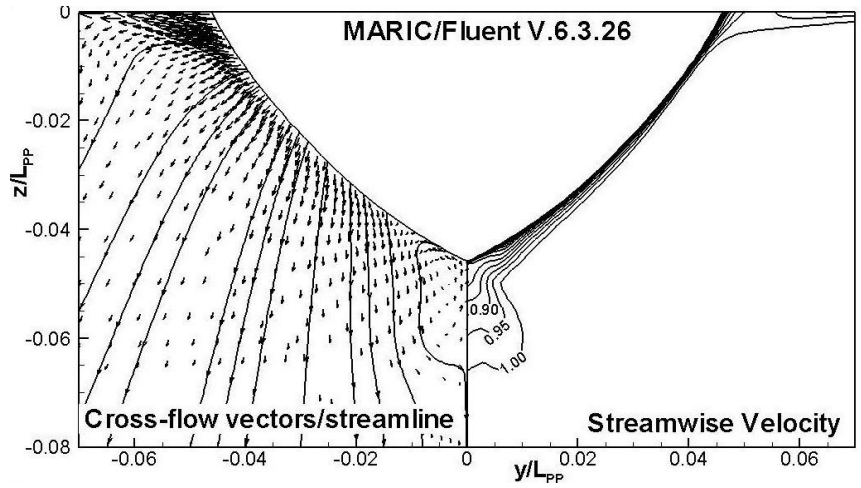

MARIC-FLUENT6.3.26

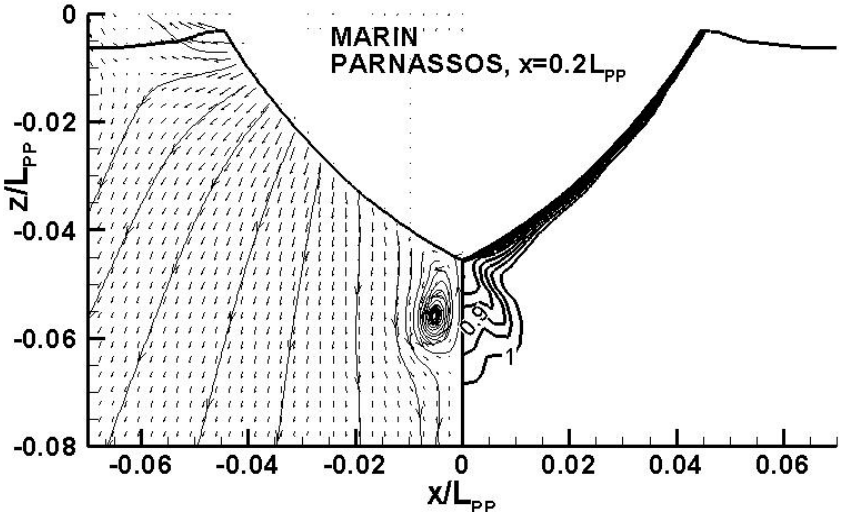

MARIN-PARNASSOS

Fig. 3.1a-3 Cross flow vectors and streamlines (left panel), *U* contours (right panel) at $x/L_{PP} = 0.2$ [$\Delta U = 0.05$]

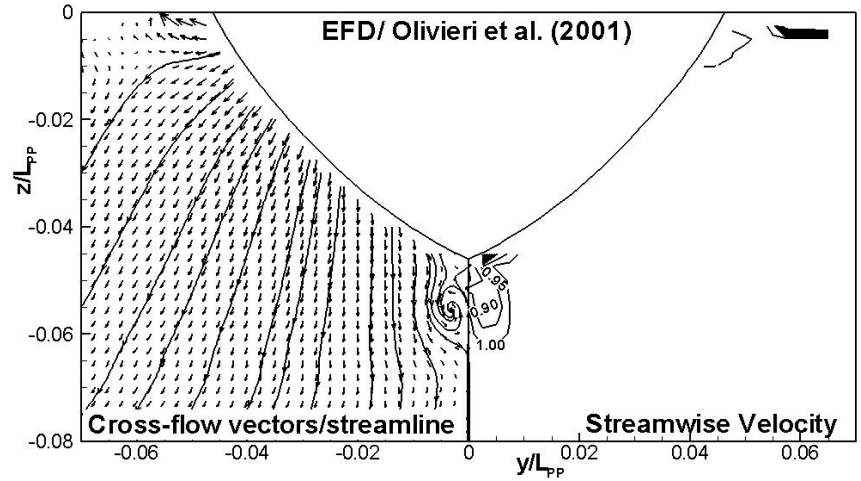

Experiment (INSEAN, Olivieri et al. 2001)

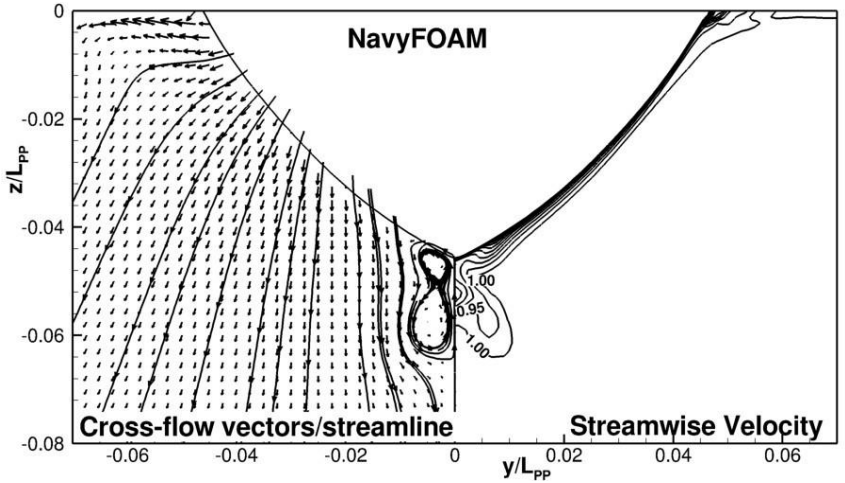

NavyFOAM-NavyFOAM

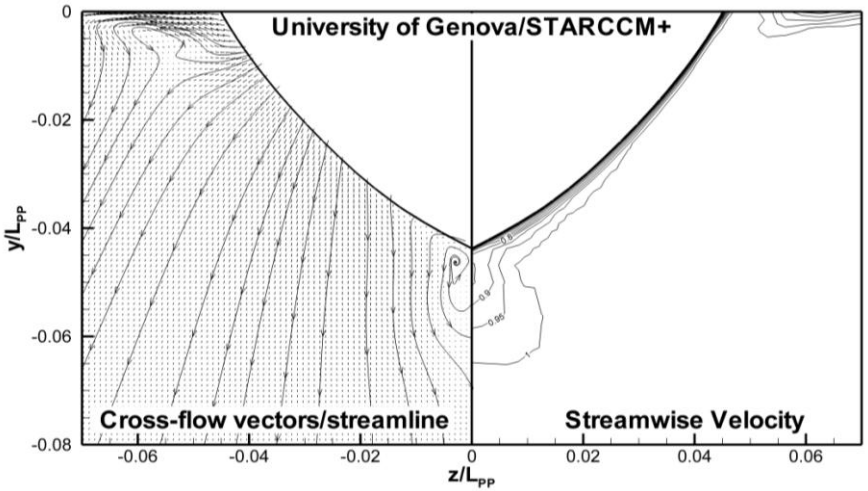

UoGe-STAR-CCM+

Fig. 3.1a-3 Cross flow vectors and streamlines (left panel), U contours (right panel) at $x/L_{PP} = 0.2$ [$\Delta U = 0.05$]

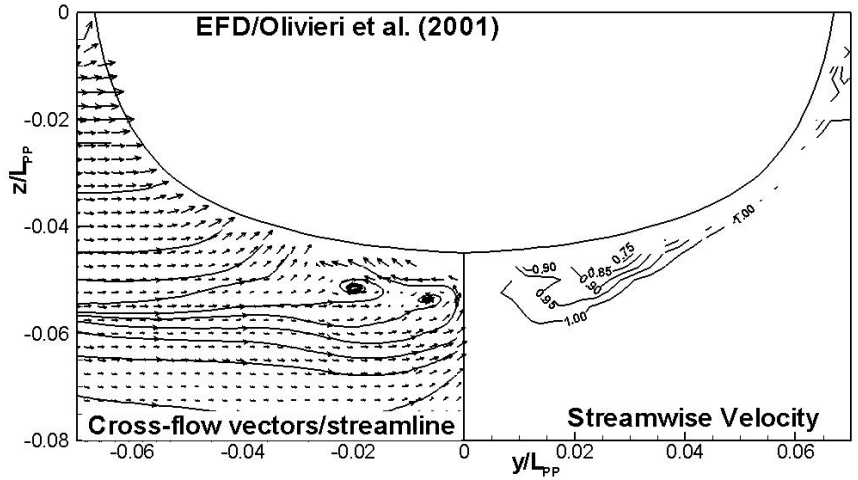

Experiment (INSEAN, Olivieri et al. 2001)

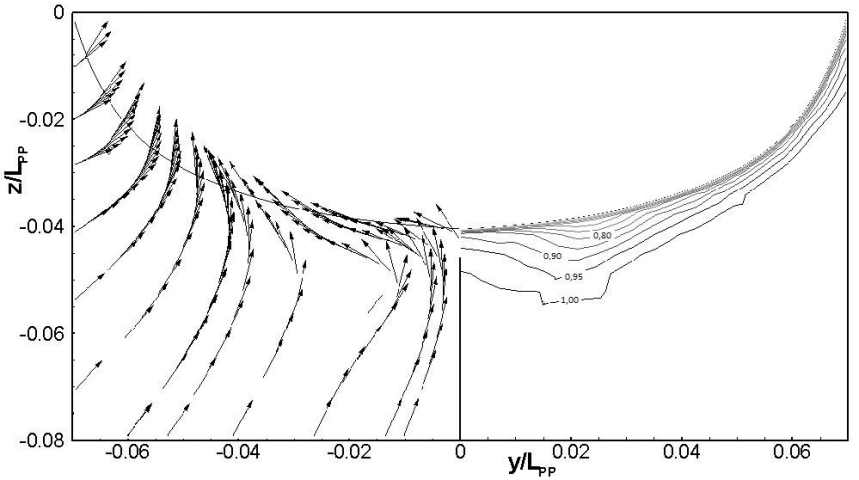

CEHINAV-STAR-CCM+

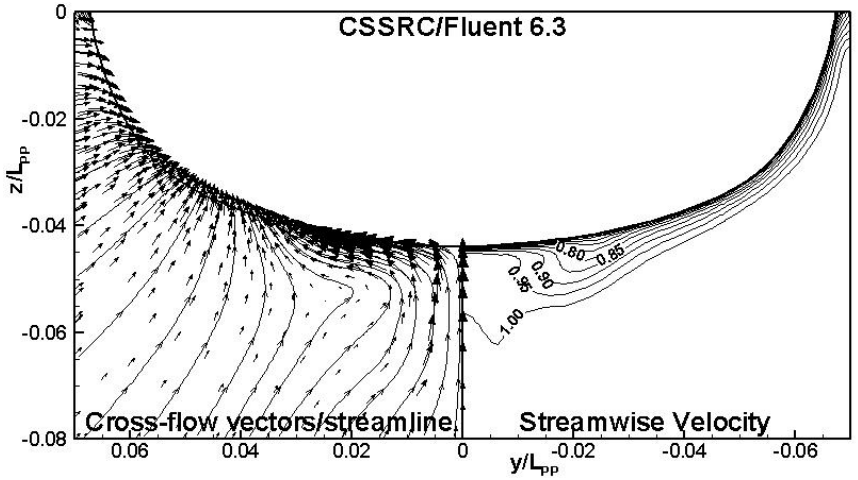

CSSRC-FLUENT6.3

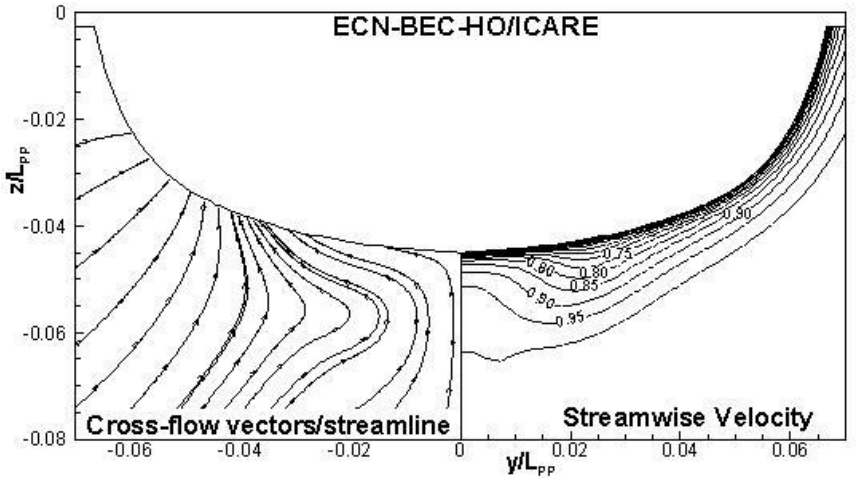

ECN/BEC/HO-Icare

Fig. 3.1a-4 Cross flow vectors and streamlines (left panel), U contours (right panel) at $x/L_{PP} = 0.6$ [$\Delta U = 0.05$]

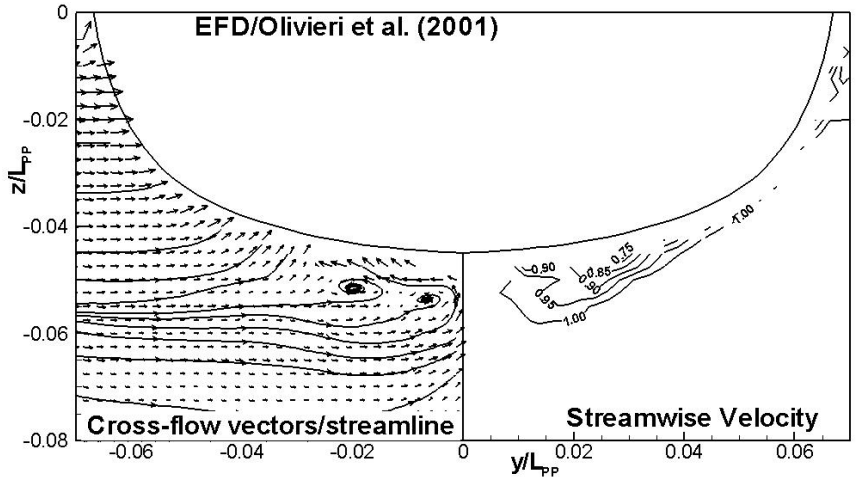

Experiment (INSEAN, Olivieri et al. 2001)

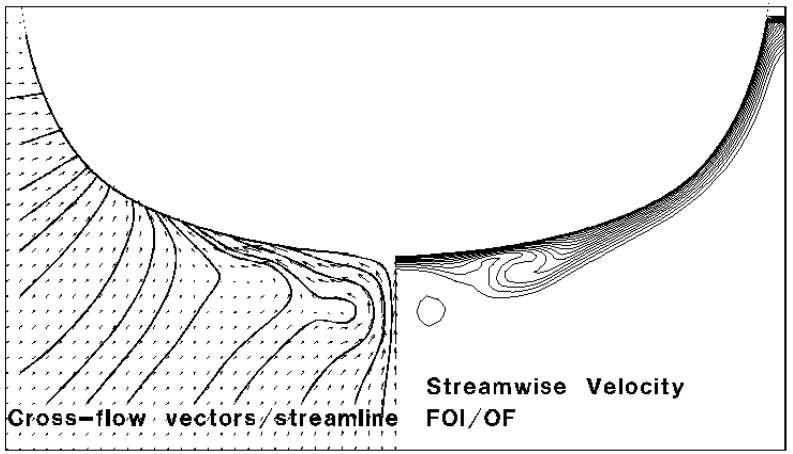

FOI-OF

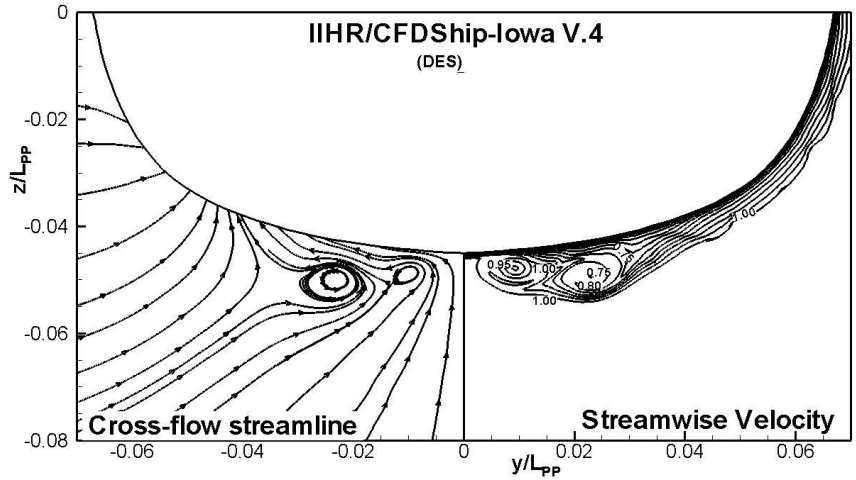

IIHR-CFDShip-IowaV4 (DES)

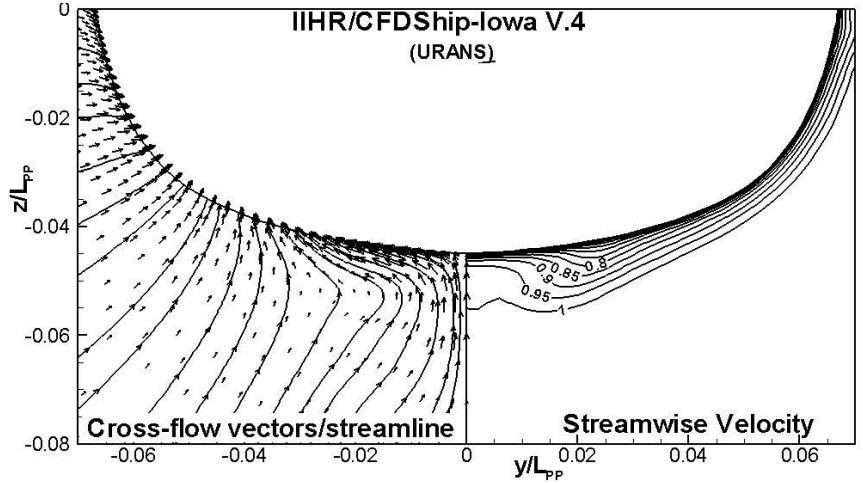

IIHR-CFDShip-IowaV4 (URANS)

Fig. 3.1a-4 Cross flow vectors and streamlines (left panel), U contours (right panel) at $x/L_{PP} = 0.6$ [$\Delta U = 0.05$]

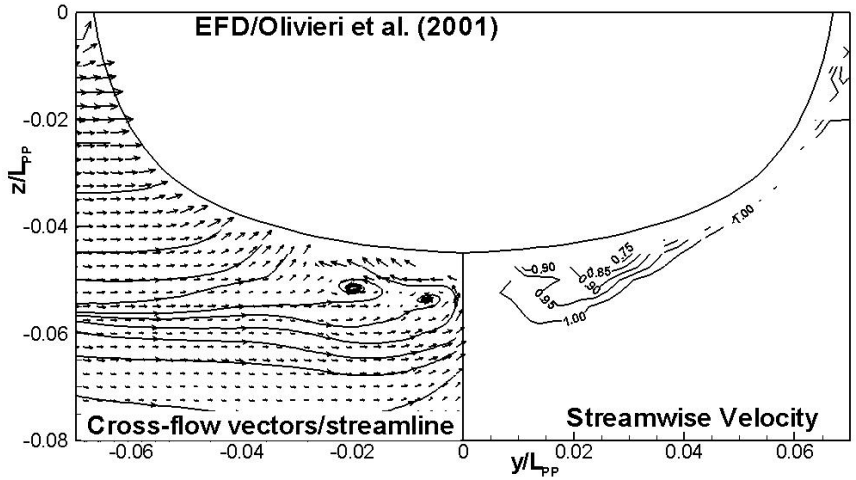

Experiment (INSEAN, Olivieri et al. 2001)

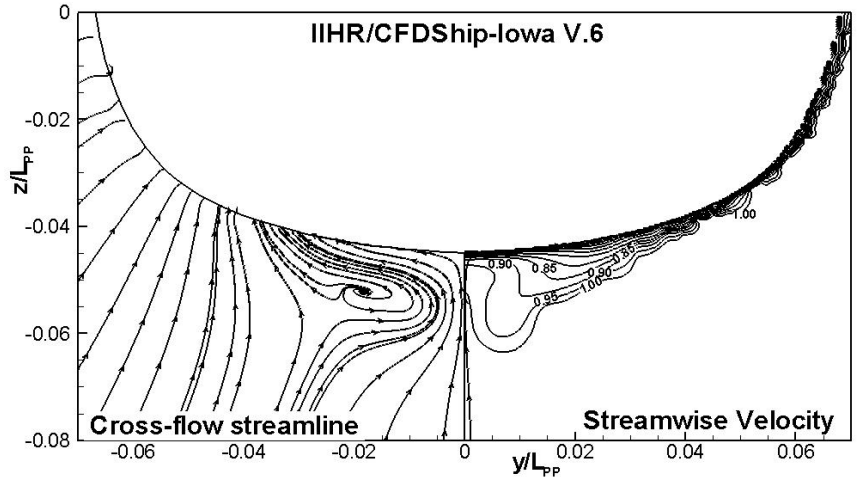

IIHR-CFDShip-IowaV6

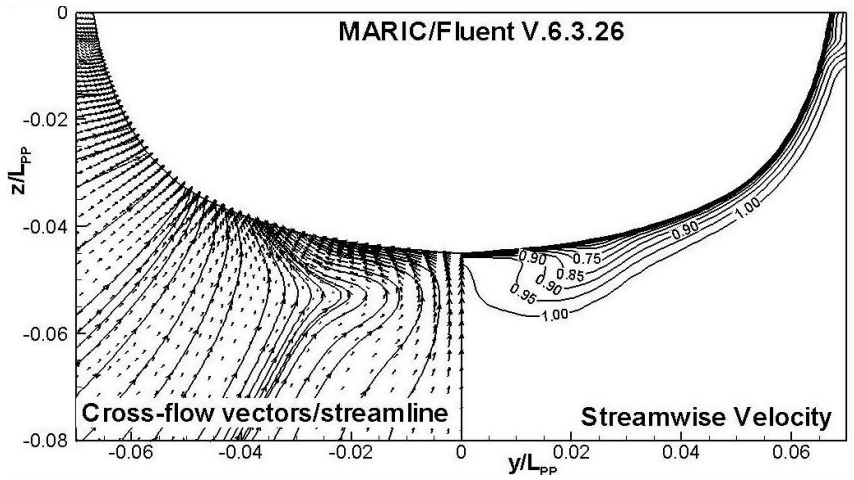

MARIC-FLUENT6.3.26

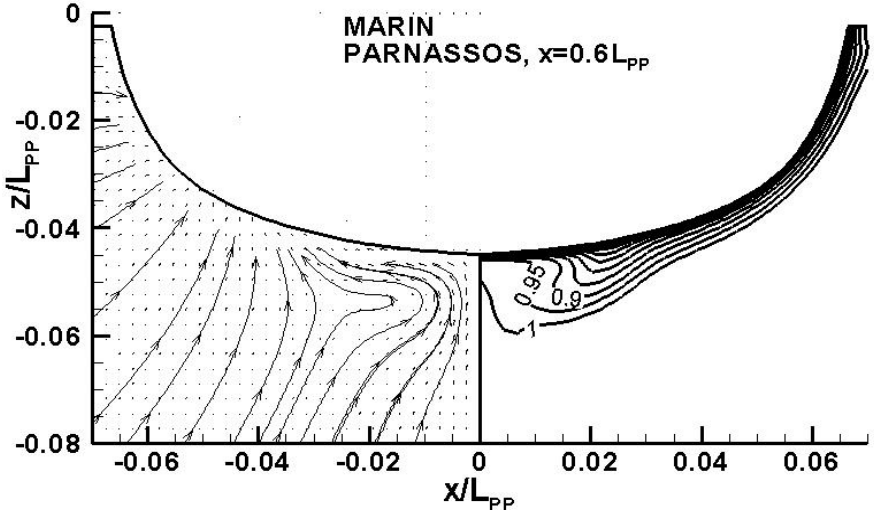

MARIN-PARNASSOS

Fig. 3.1a-4 Cross flow vectors and streamlines (left panel), U contours (right panel) at $x/L_{PP} = 0.6$ [$\Delta U = 0.05$]

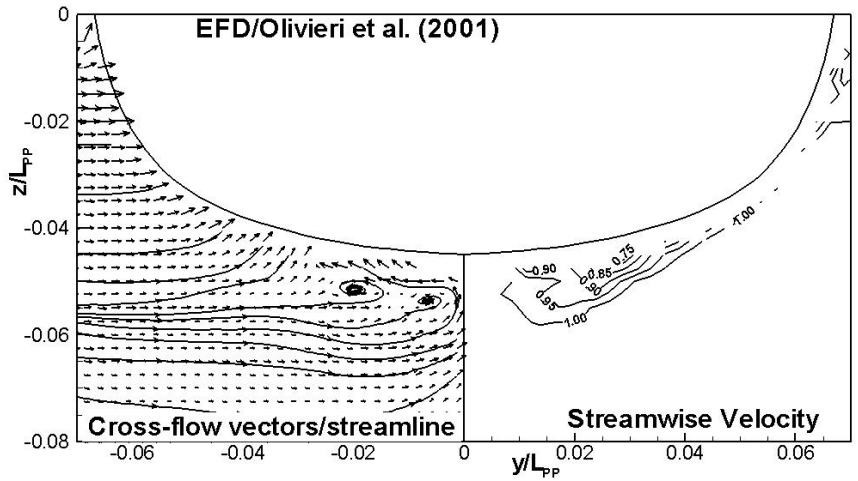

Experiment (INSEAN, Olivieri et al. 2001)

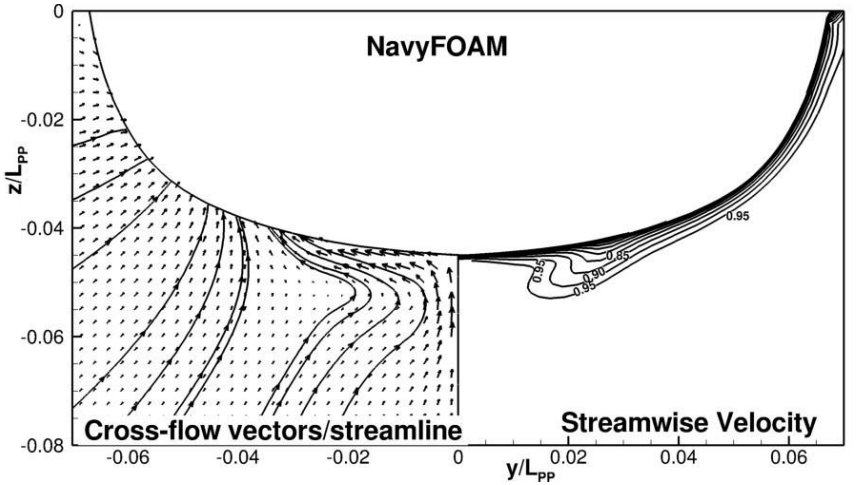

NavyFOAM-NavyFOAM

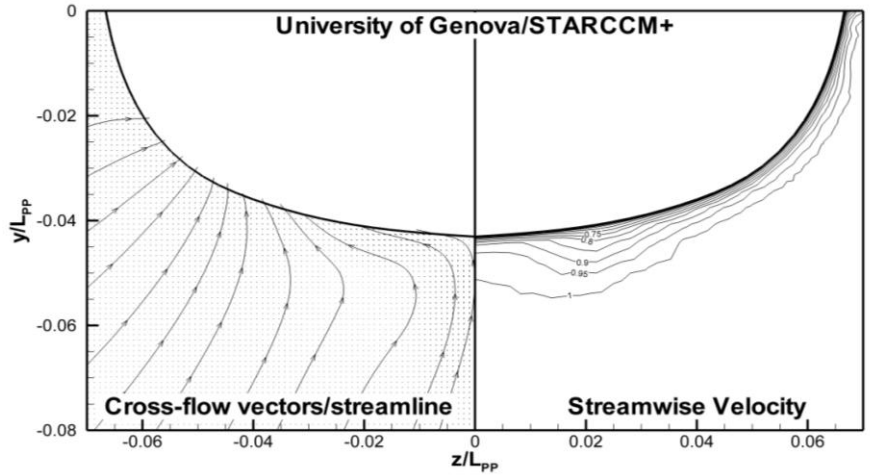

UoGe-STAR-CCM+

Fig. 3.1a-4 Cross flow vectors and streamlines (left panel), U contours (right panel) at $x/L_{PP} = 0.6$ [$\Delta U = 0.05$]

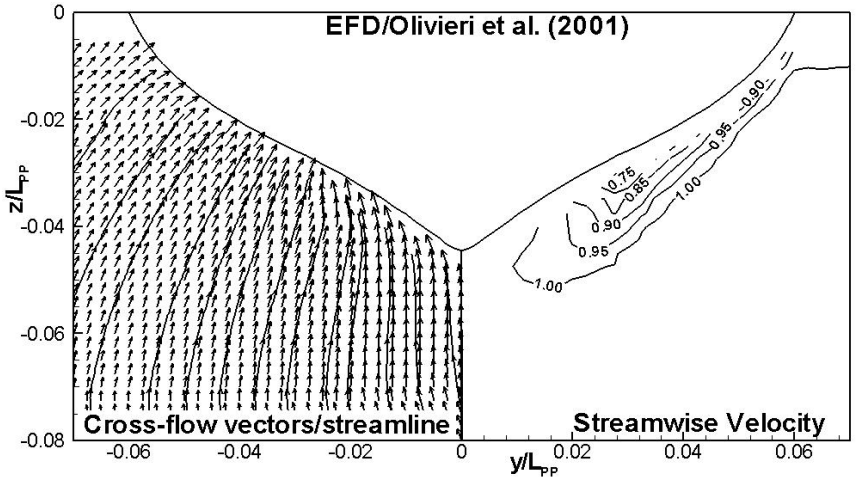

Experiment (INSEAN, Olivieri et al. 2001)

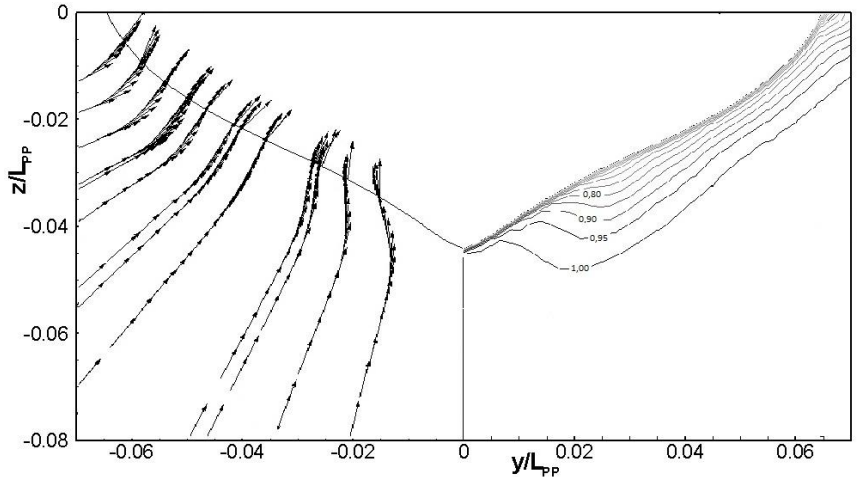

CEHINAV-STAR-CCM+

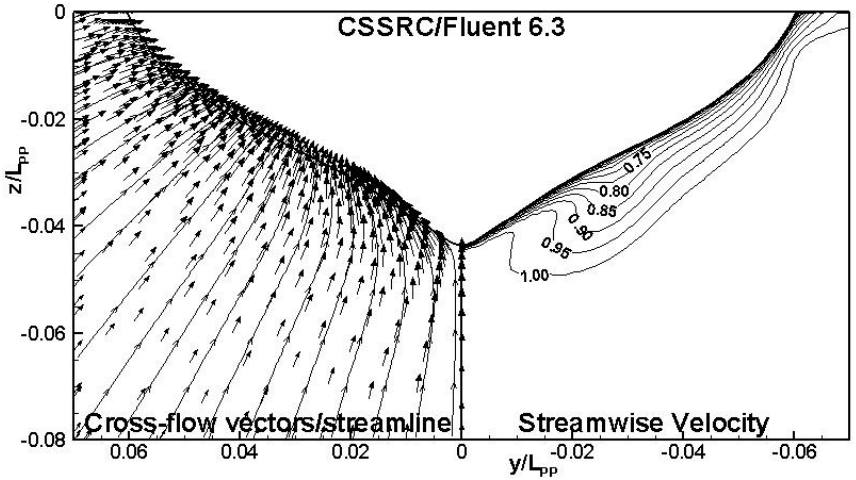

CSSRC-FLUENT6.3

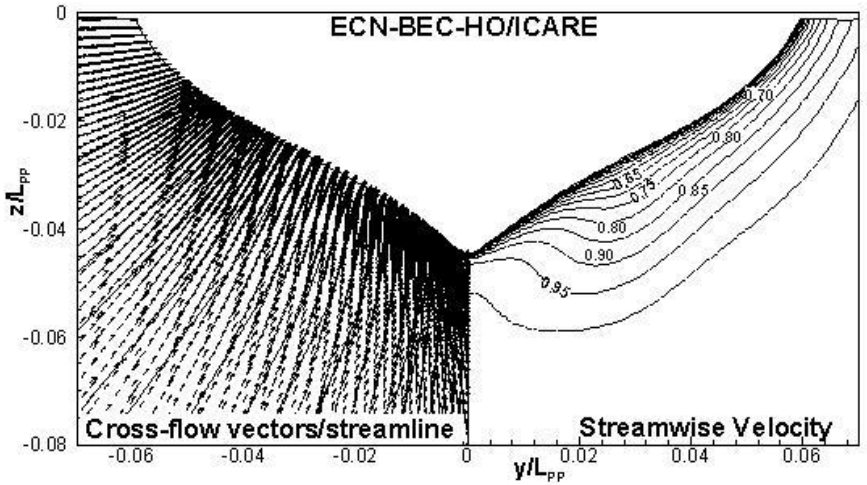

ECN/BEC/HO-Icare

Fig. 3.1a-5 Cross flow vectors and streamlines (left panel), U contours (right panel) at $x/L_{PP} = 0.8$ [$\Delta U = 0.05$]

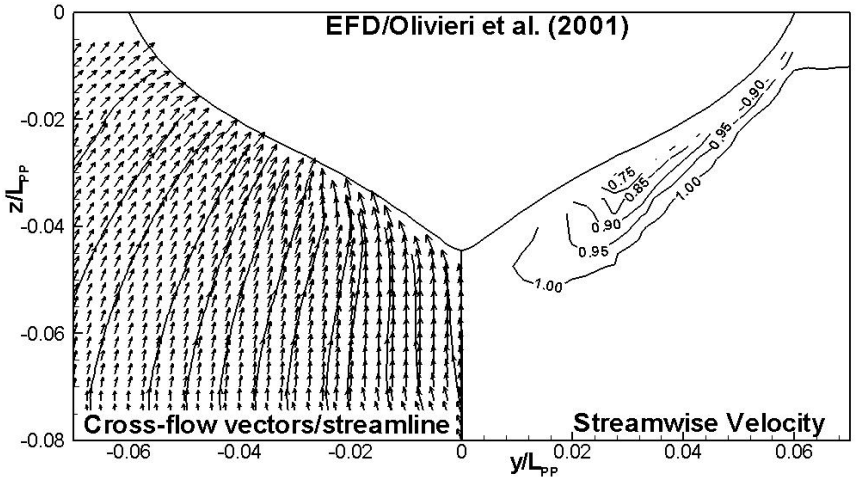

Experiment (INSEAN, Olivieri et al. 2001)

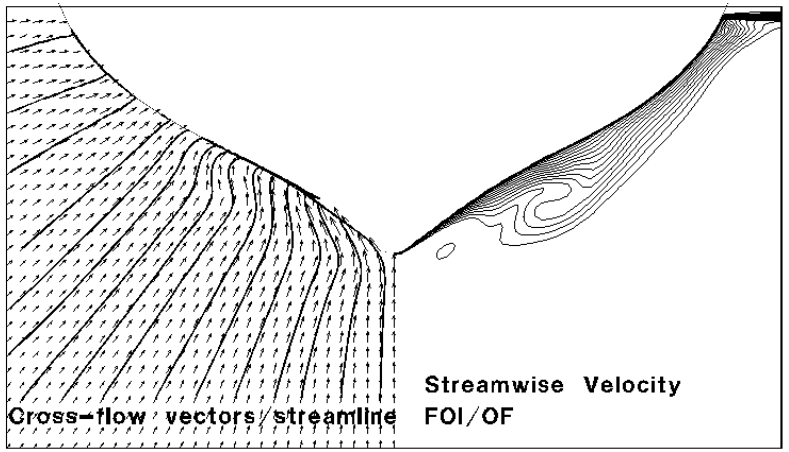

FOI-OF

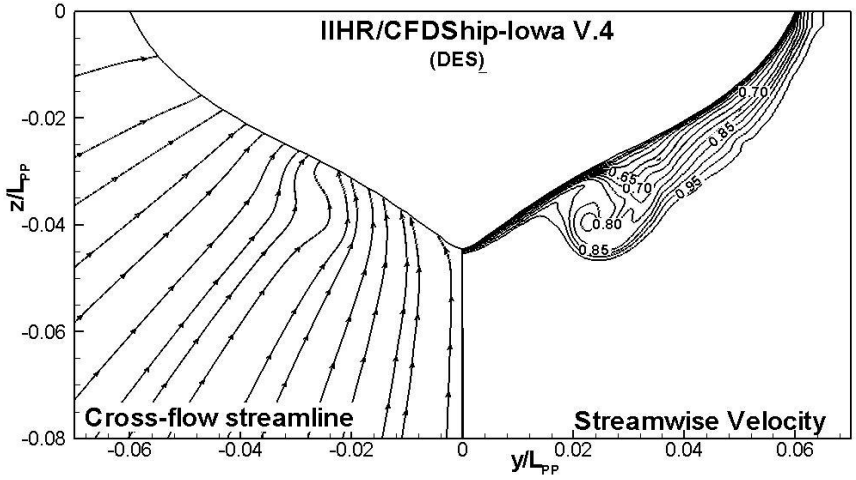

IIHR-CFDShip-IowaV4 (DES)

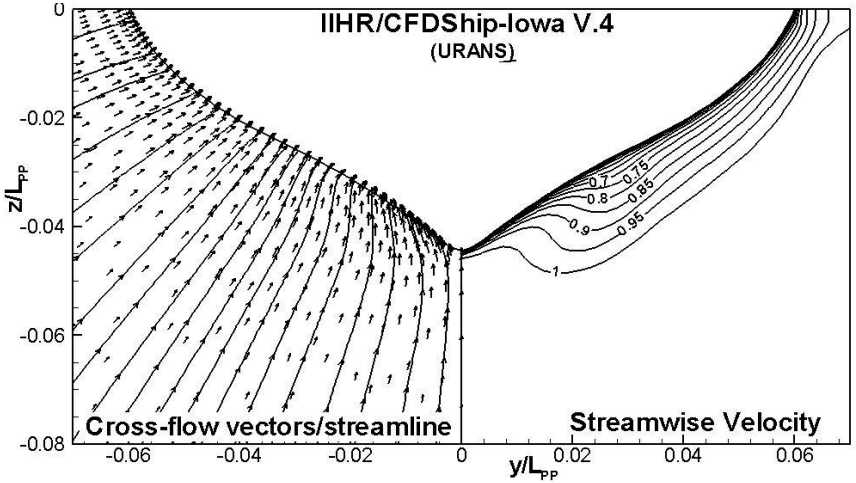

IIHR-CFDShip-IowaV4 (URANS)

Fig. 3.1a-5 Cross flow vectors and streamlines (left panel), U contours (right panel) at $x/L_{PP} = 0.8$ [$\Delta U = 0.05$]

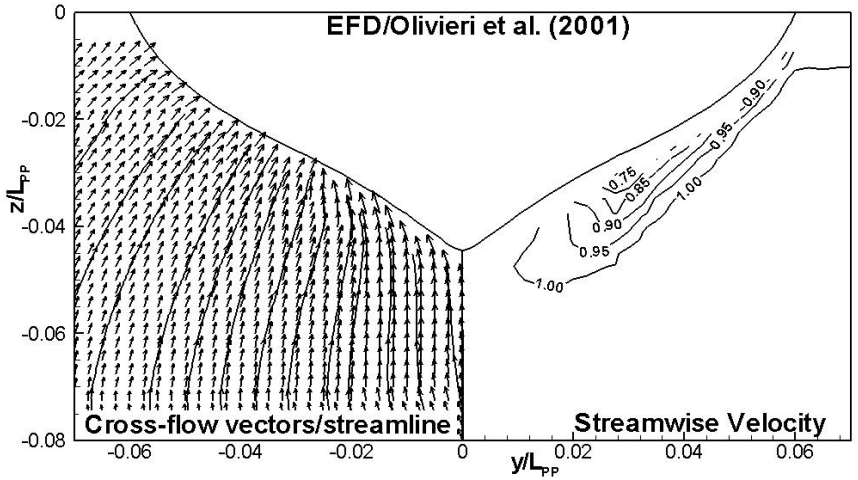

Experiment (INSEAN, Olivieri et al. 2001)

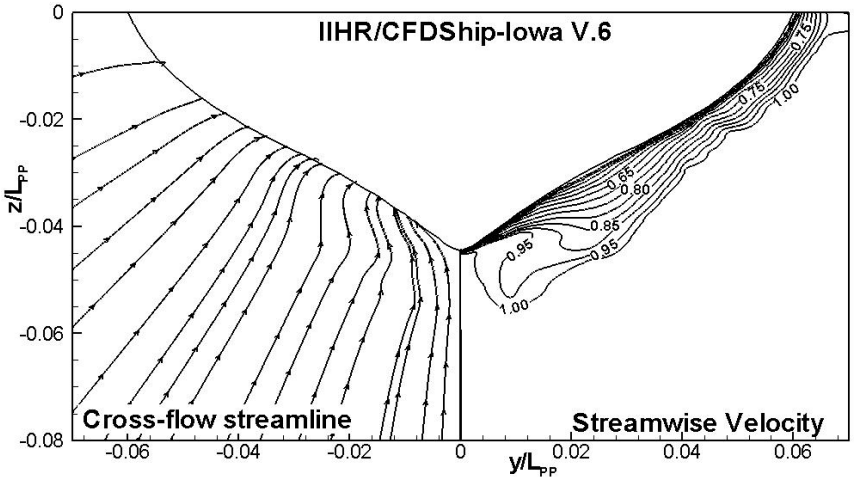

IIHR-CFDShip-IowaV6

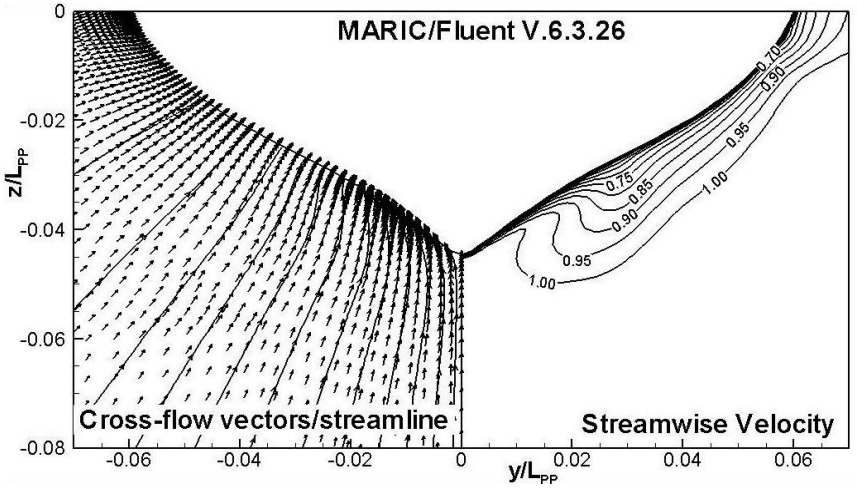

MARIC-FLUENT6.3.26

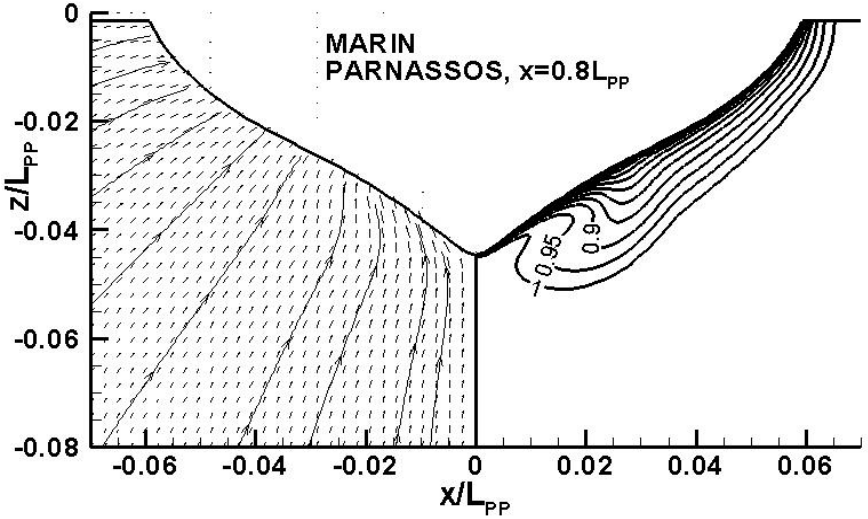

MARIN-PARNASSOS

Fig. 3.1a-5 Cross flow vectors and streamlines (left panel), U contours (right panel) at $x/L_{PP} = 0.8$ [$\Delta U = 0.05$]

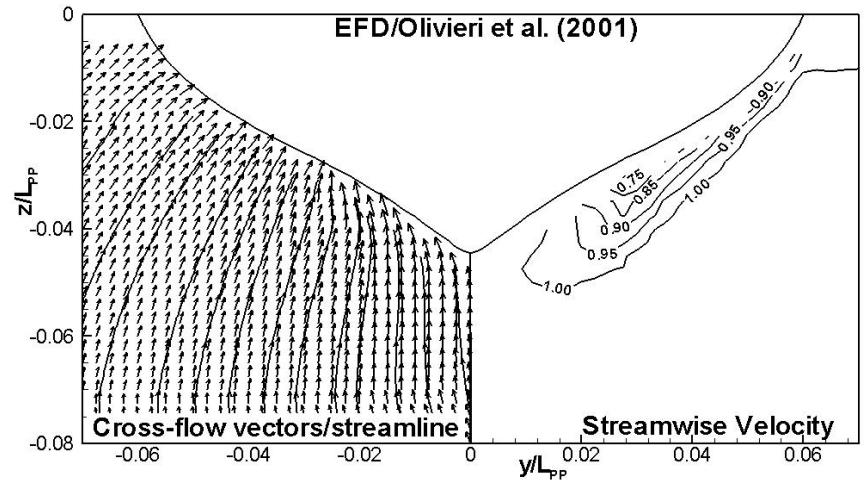

Experiment (INSEAN, Olivieri et al. 2001)

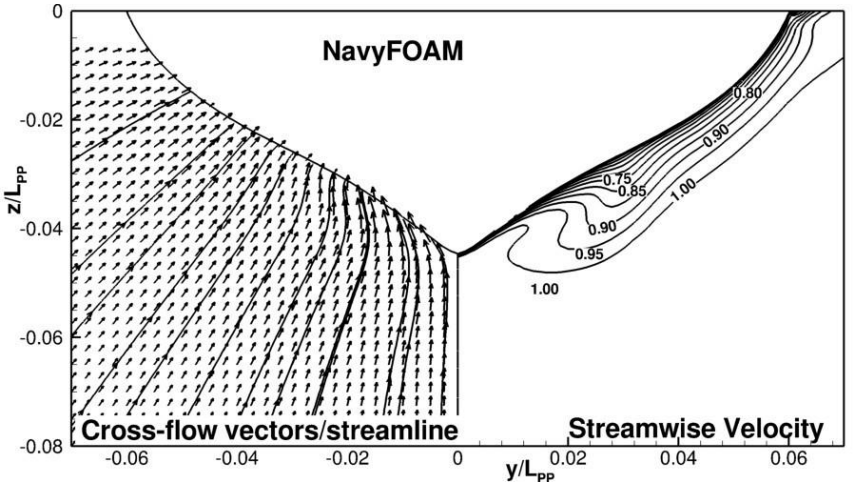

NavyFOAM-NavyFOAM

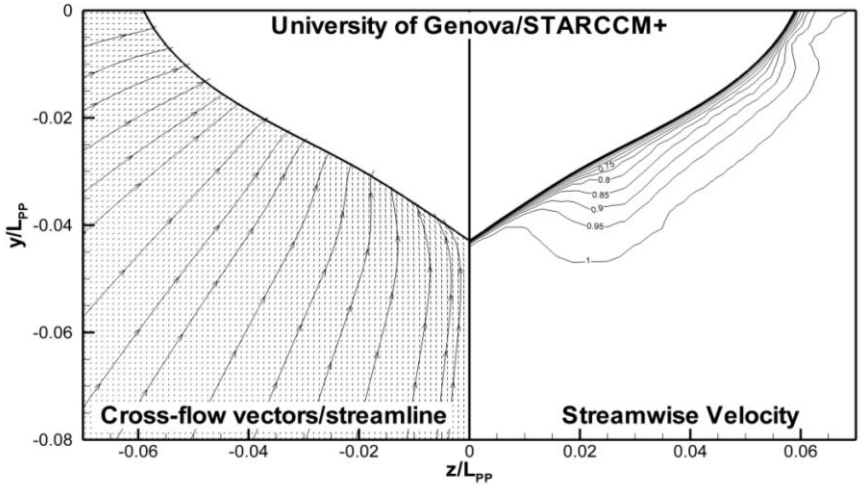

UoGe-STAR-CCM+

Fig. 3.1a-5 Cross flow vectors and streamlines (left panel), U contours (right panel) at $x/L_{PP} = 0.8$ [$\Delta U = 0.05$]

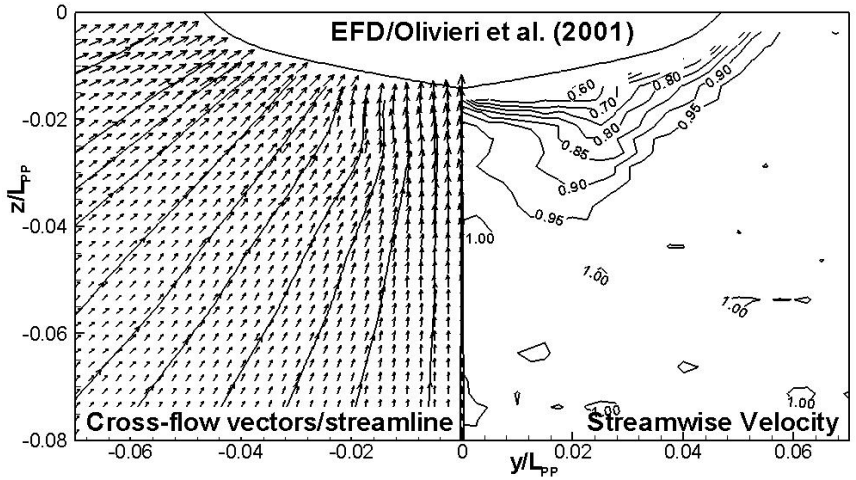

Experiment (INSEAN, Olivieri et al. 2001)

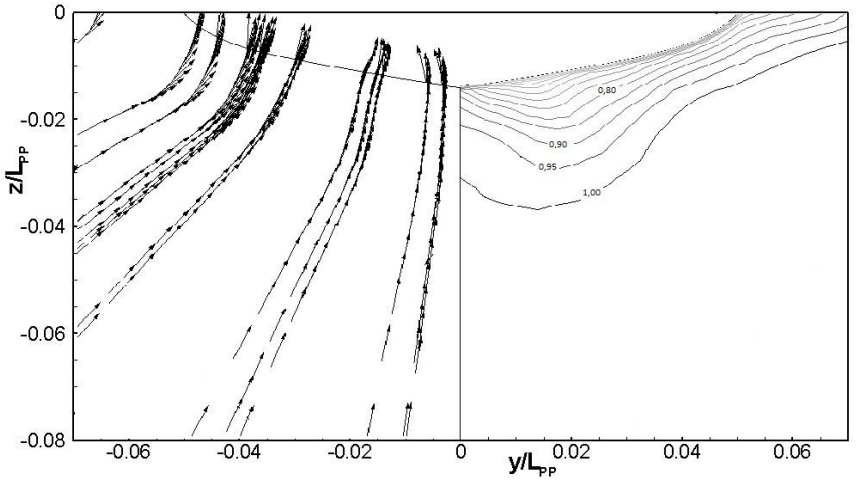

CEHINAV-STAR-CCM+

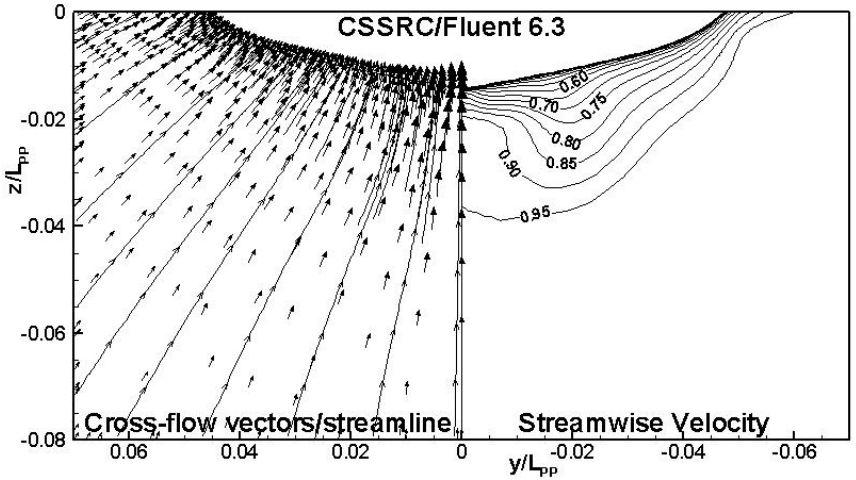

CSSRC-FLUENT6.3

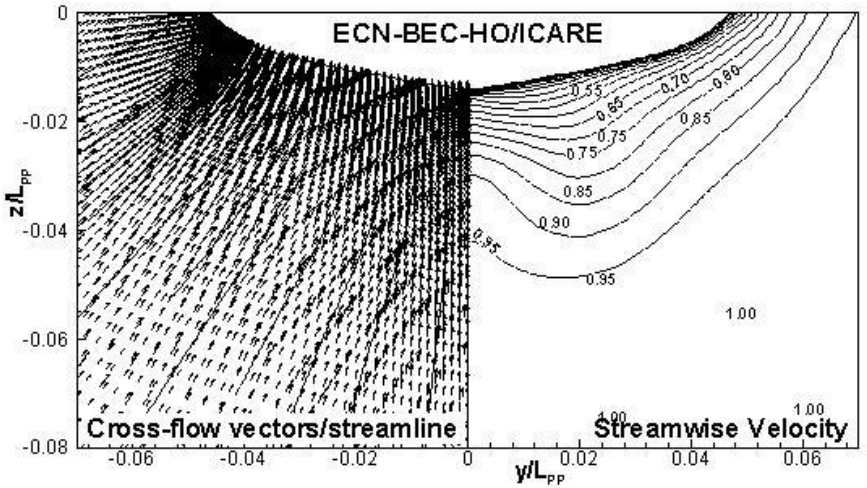

ECN/BEC/HO-Icare

Fig. 3.1a-6 Cross flow vectors and streamlines (left panel), U contours (right panel) at $x/L_{PP} = 0.935$ [$\Delta U = 0.05$]

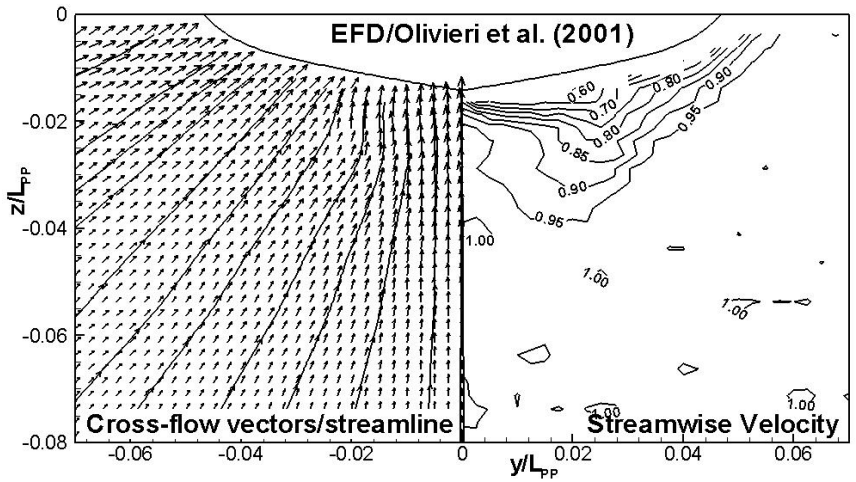

Experiment (INSEAN, Olivieri et al. 2001)

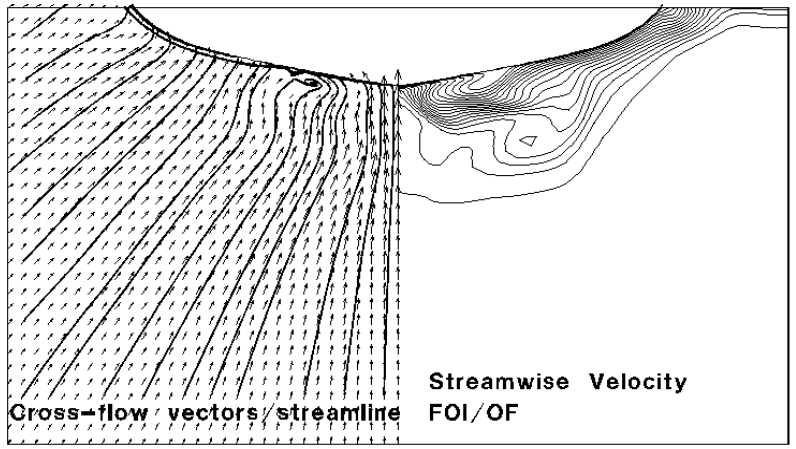

FOI-OF

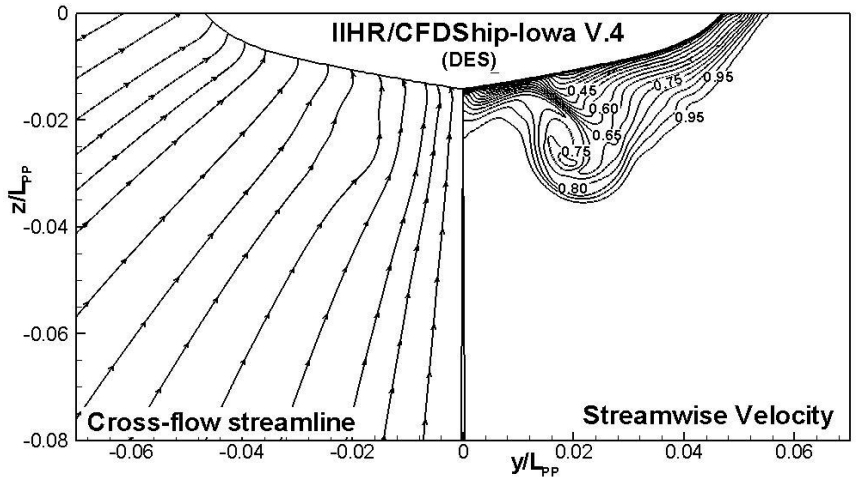

IIHR-CFDShip-IowaV4 (DES)

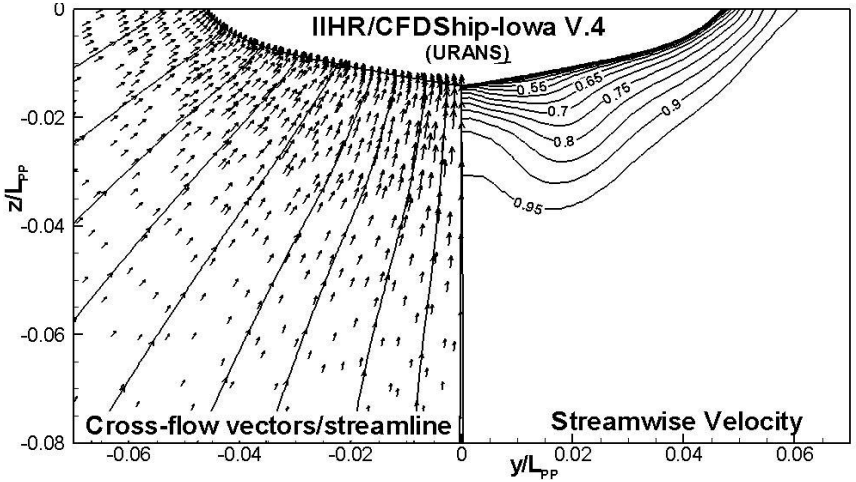

IIHR-CFDShip-IowaV4 (URANS)

Fig. 3.1a-6 Cross flow vectors and streamlines (left panel), *U* contours (right panel) at $x/L_{PP} = 0.935$ [$\Delta U = 0.05$]

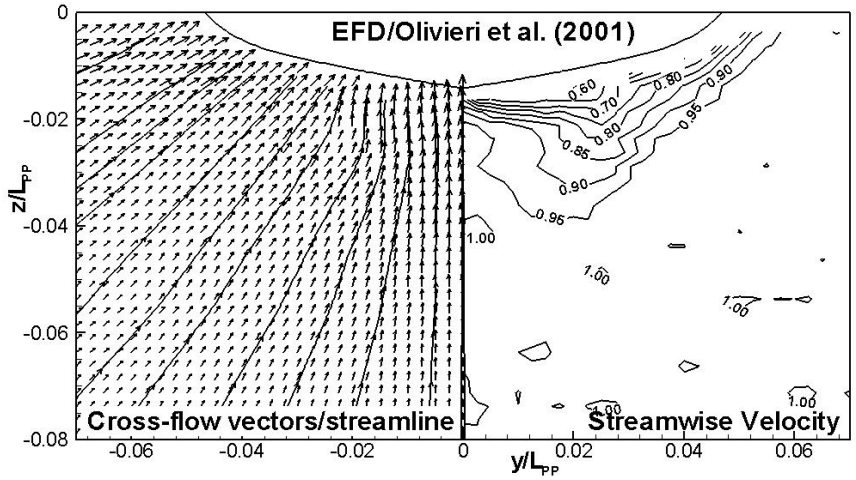

Experiment (INSEAN, Olivieri et al. 2001)

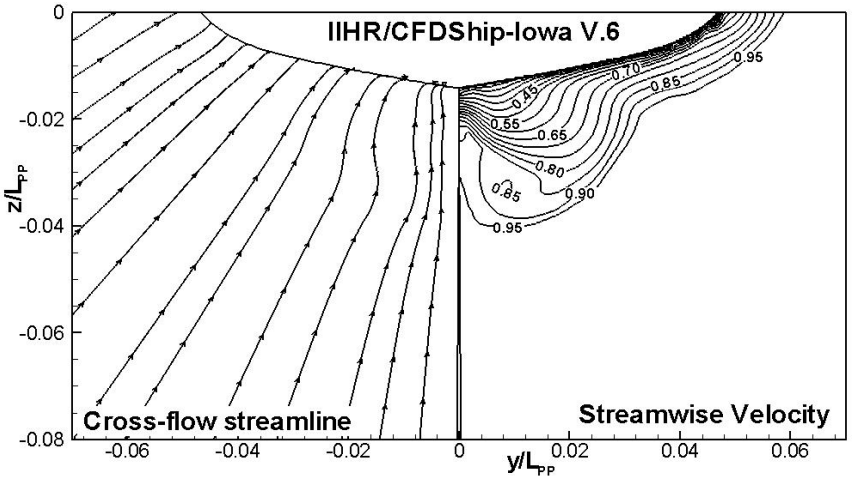

IIHR-CFDShip-IowaV6

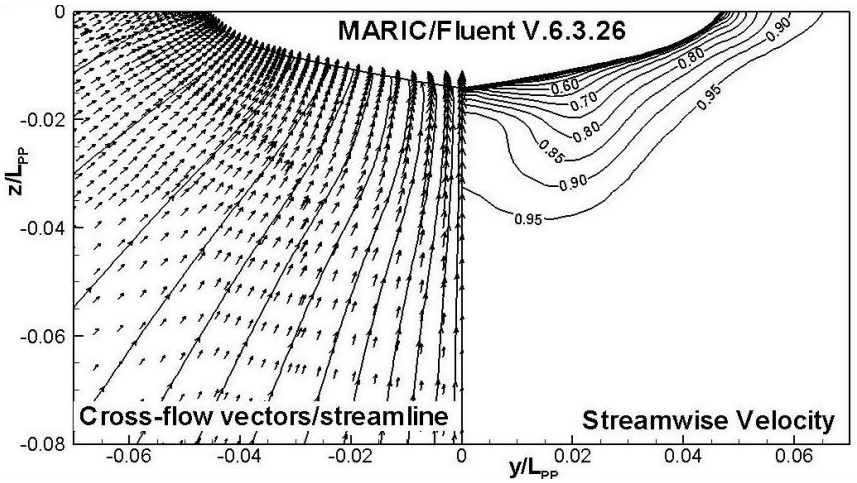

MARIC-FLUENT6.3.26

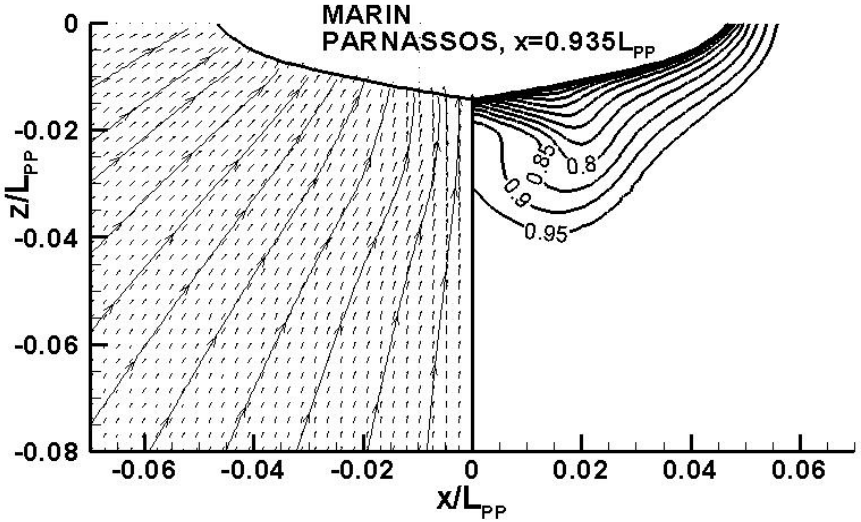

MARIN-PARNASSOS

Fig. 3.1a-6 Cross flow vectors and streamlines (left panel), *U* contours (right panel)
at $x/L_{PP} = 0.935$ [$\Delta U = 0.05$]

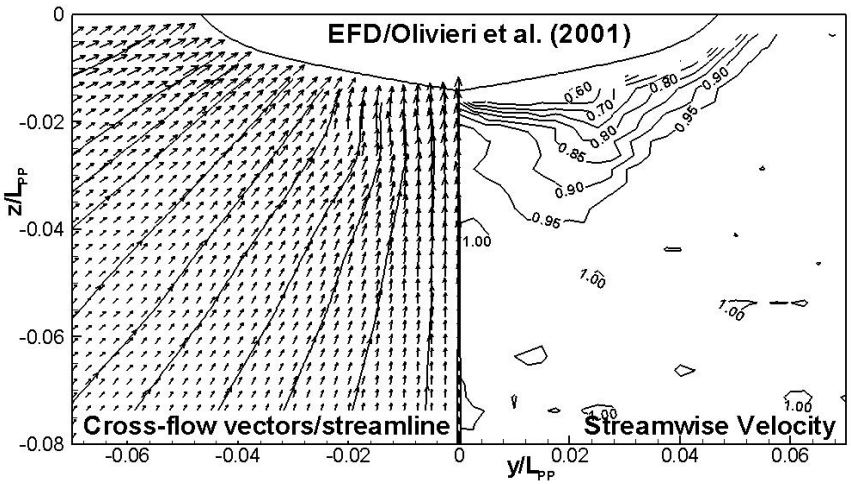

Experiment (INSEAN, Olivieri et al. 2001)

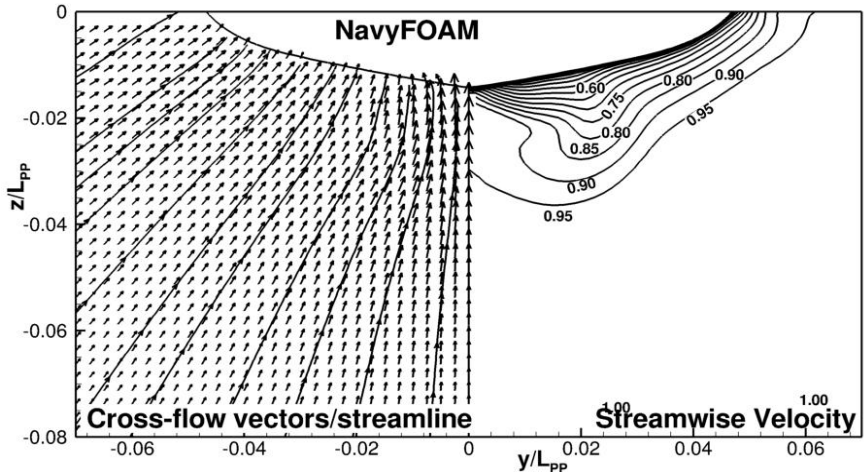

NavyFOAM-NavyFOAM

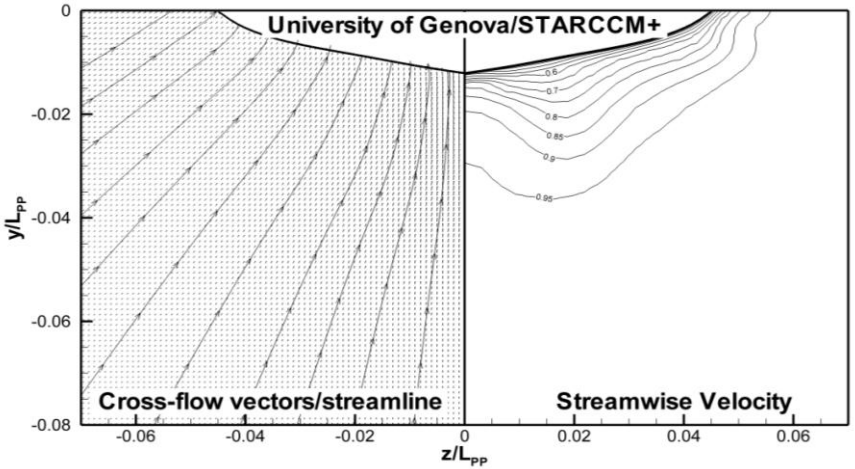

UoGe-STAR-CCM+

Fig. 3.1a-6 Cross flow vectors and streamlines (left panel), U contours (right panel) at $x/L_{PP} = 0.935$ [$\Delta U = 0.05$]

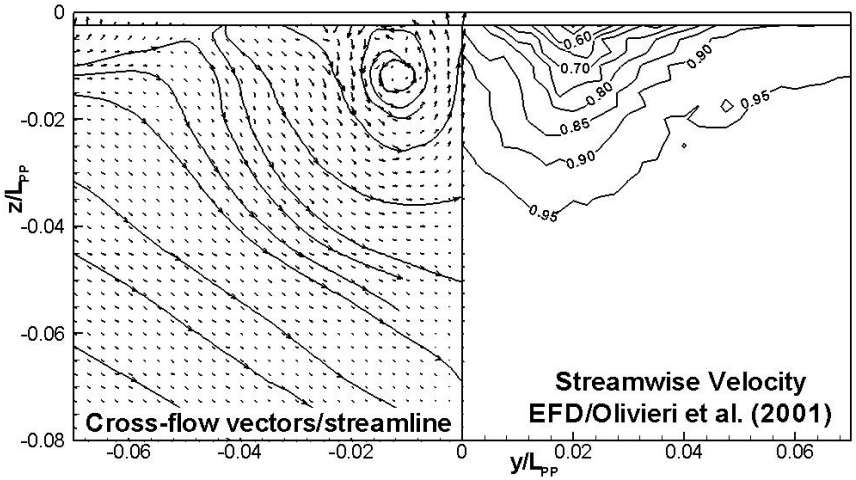

Experiment (INSEAN, Olivieri et al. 2001)

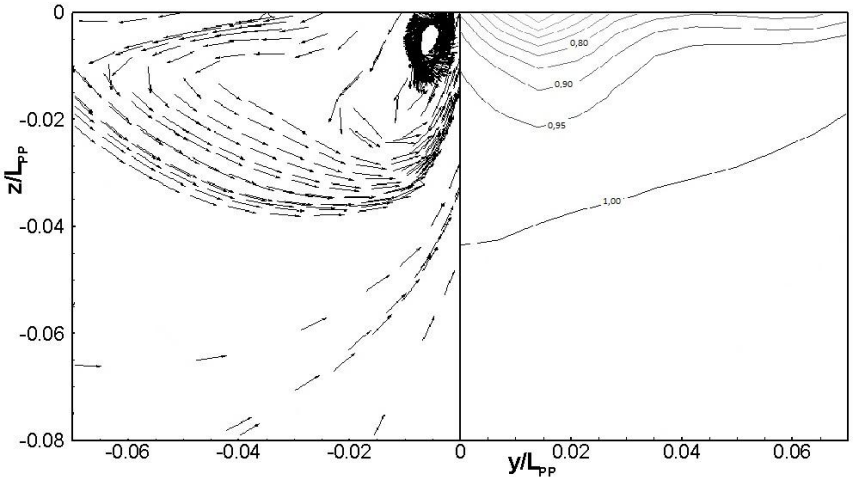

CEHINAV-STAR-CCM+

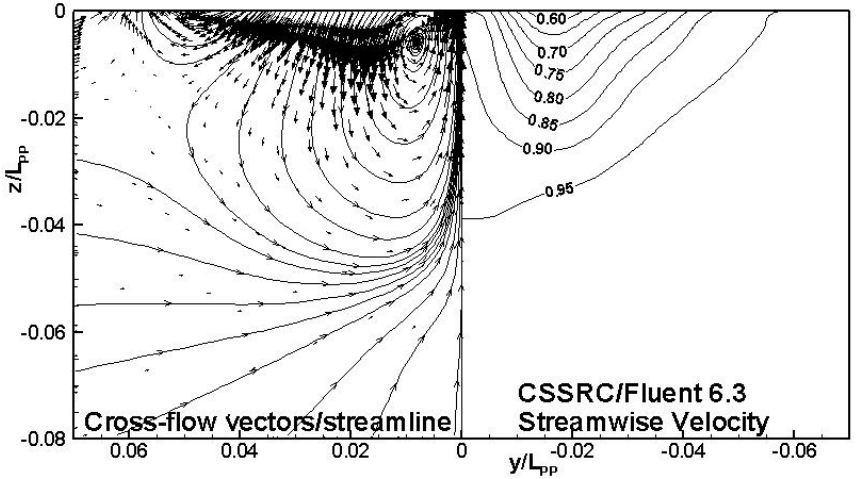

CSSRC-FLUENT6.3

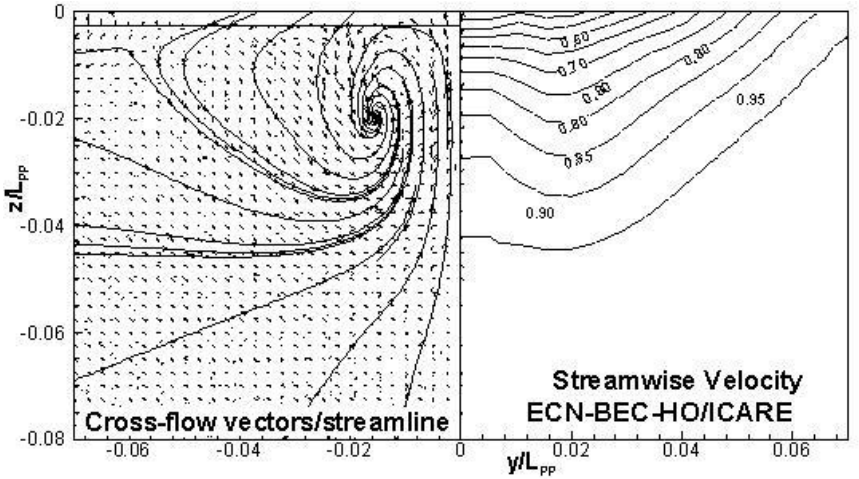

ECN/BEC/HO-Icare

Fig. 3.1a-7 Cross flow vectors and streamlines (left panel), U contours (right panel) at $x/L_{PP} = 1.1$ [$\Delta U = 0.05$]

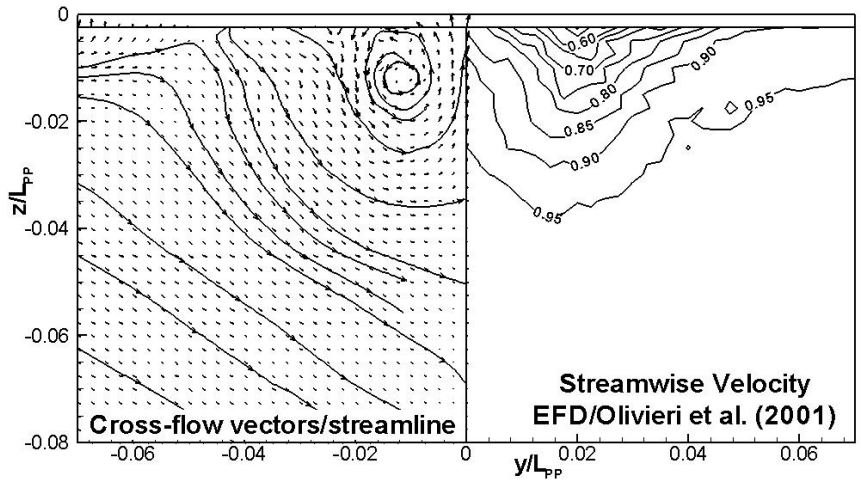

Experiment (INSEAN, Olivieri et al. 2001)

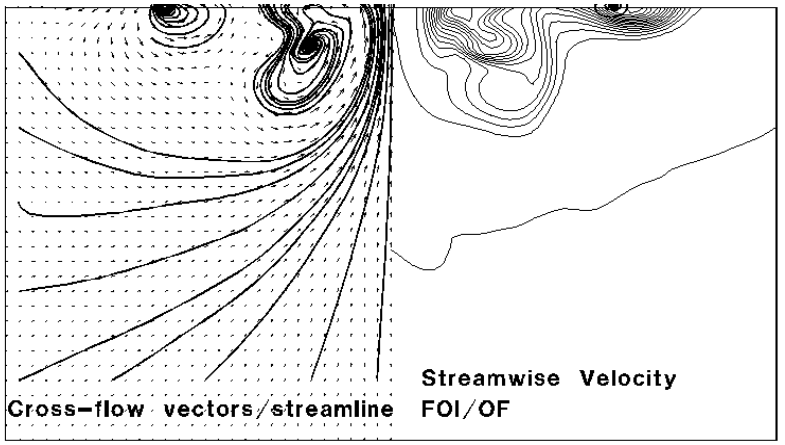

FOI-OF

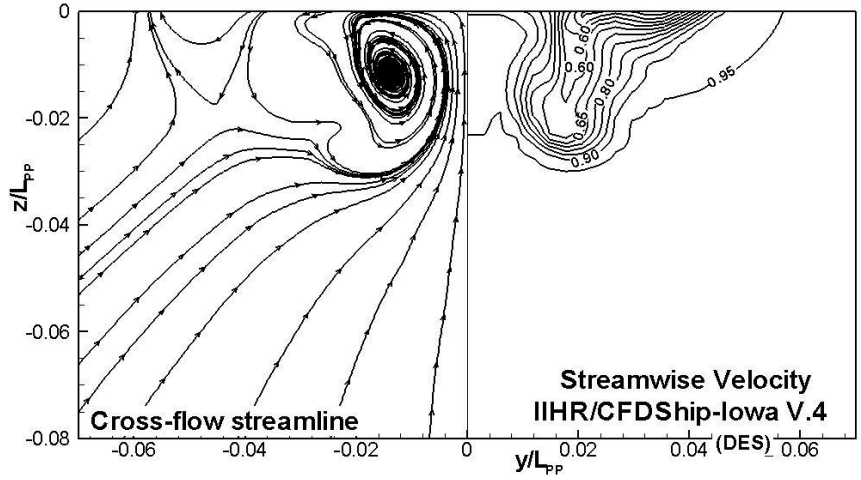

IIHR-CFDShip-IowaV4 (DES)

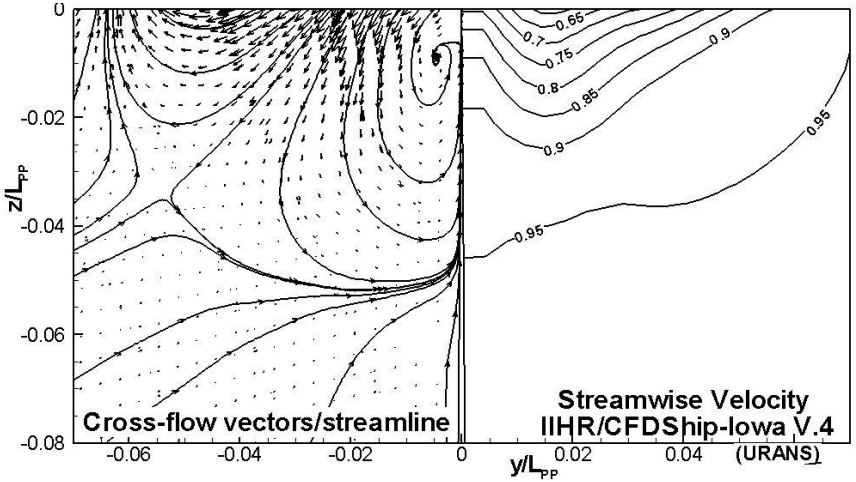

IIHR-CFDShip-IowaV4 (URANS)

Fig. 3.1a-7 Cross flow vectors and streamlines (left panel), U contours (right panel) at $x/L_{PP} = 1.1$ [$\Delta U = 0.05$]

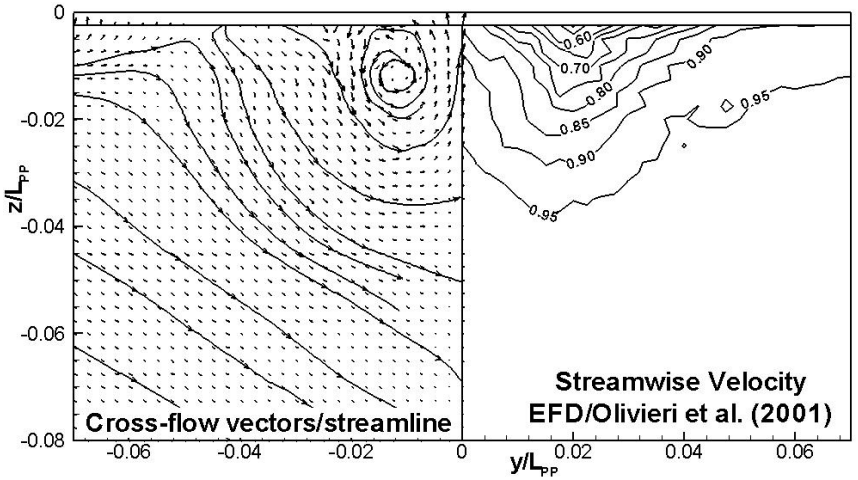

Experiment (INSEAN, Olivieri et al. 2001)

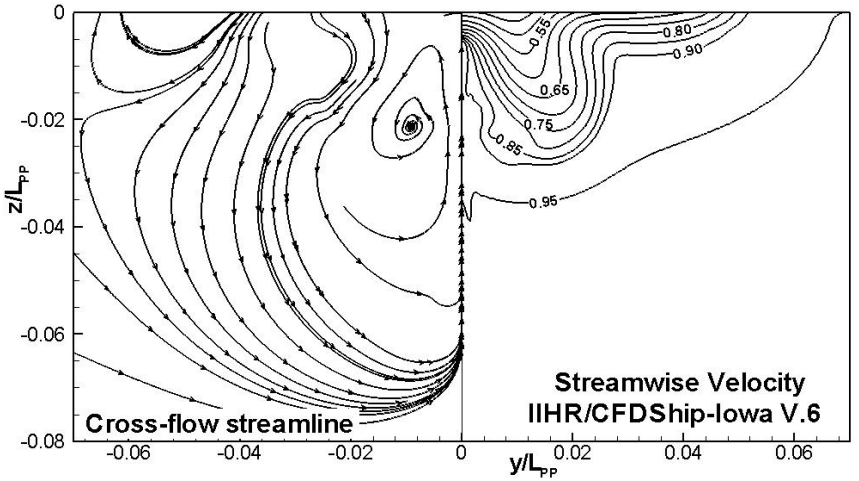

IIHR-CFDShip-IowaV6

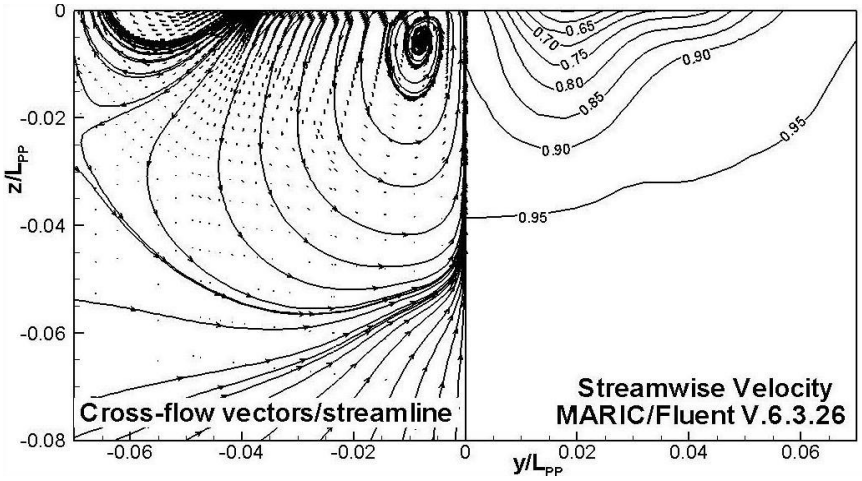

MARIC-FLUENT6.3.26

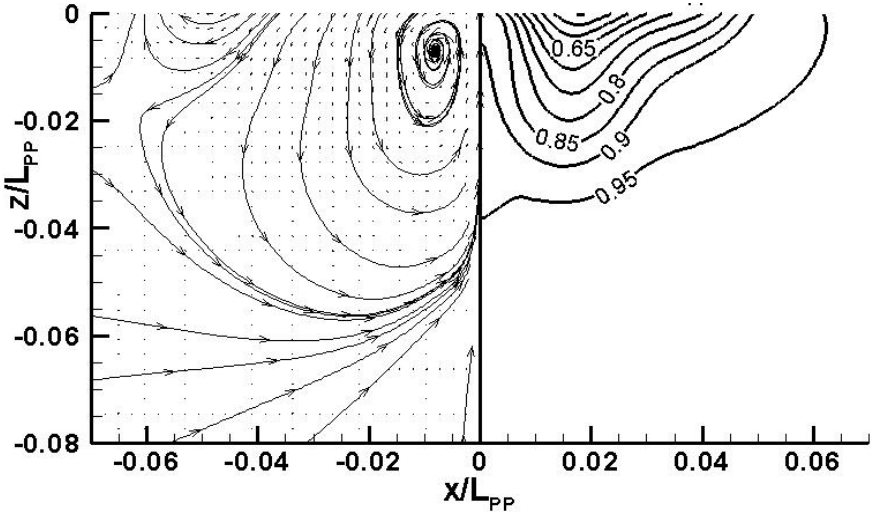

MARIN-PARNASSOS

Fig. 3.1a-7 Cross flow vectors and streamlines (left panel), *U* contours (right panel) at $x/L_{PP} = 1.1$ [$\Delta U = 0.05$]

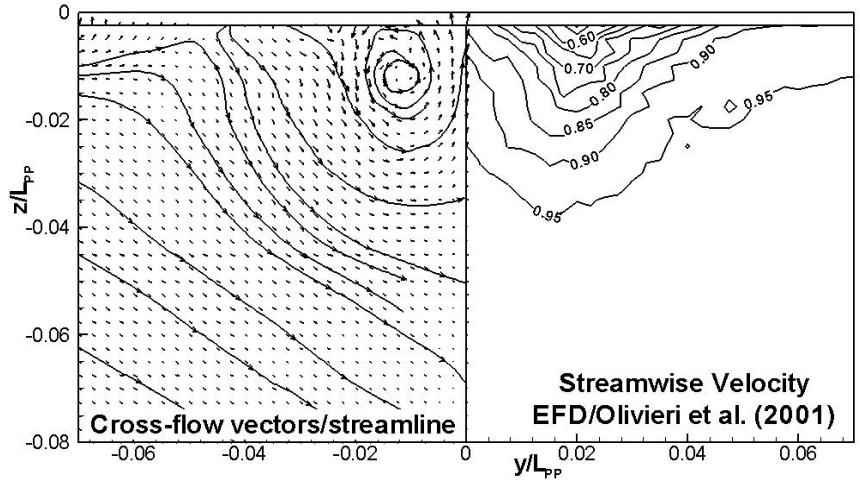

Experiment (INSEAN, Olivieri et al. 2001)

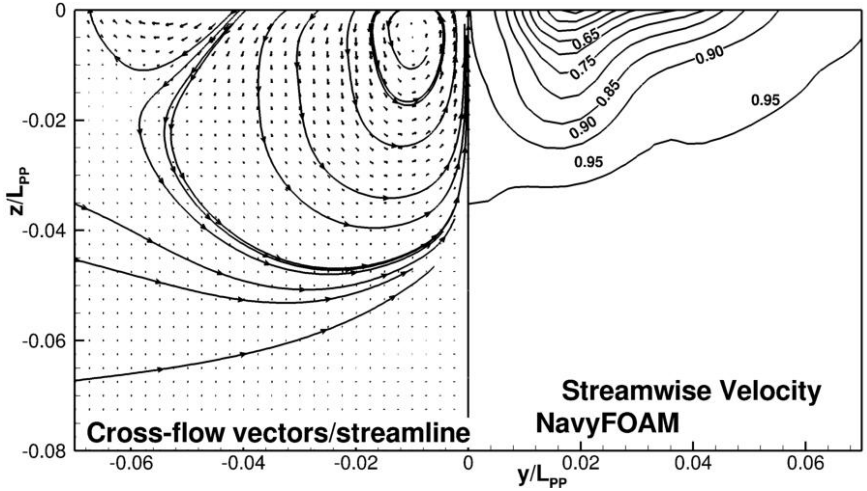

NavyFOAM-NavyFOAM

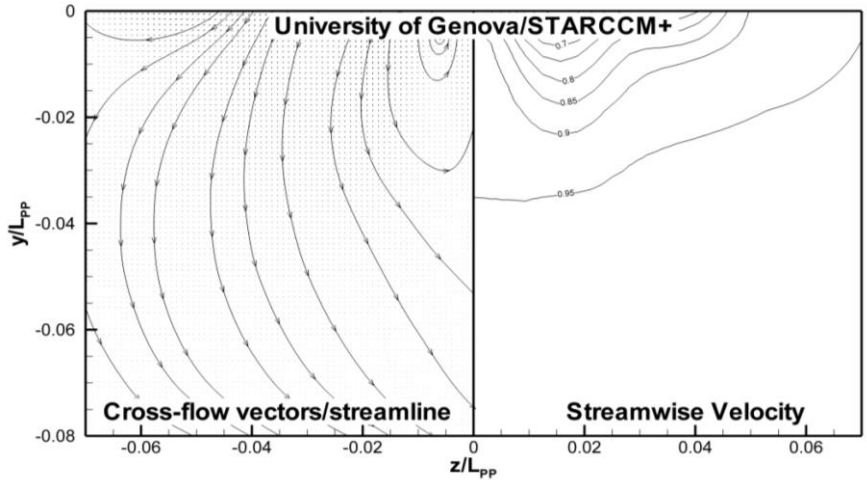

UoGe-STAR-CCM+

Fig. 3.1a-7 Cross flow vectors and streamlines (left panel), U contours (right panel) at $x/L_{PP} = 1.1$ [$\Delta U = 0.05$]

Test Case 3.1b

Table 3.1b-T-0 Computations information and V&V method
Table 3.1b-T-1 Computed C_T, C_F and C_R of different grid densities
Table 3.1b-T-2 V&V results for C_T, C_F and C_R

Figure 3.1b-1 Wave elevation contours
Figure 3.1b-1w-1 Longitudinal wave cut at $y/L_{PP} = 0.082$
Figure 3.1b-1w-2 Longitudinal wave cut at $y/L_{PP} = 0.0172$
Figure 3.1b-1w-3 Longitudinal wave cut at $y/L_{PP} = 0.0302$
Figure 3.1b-1w-4 Grid density distribution along the waterline (solid), and in transverse (dashed) and vertical (dotted) directions at mid-ship
Figure 3.1b-2 Streamwise velocity contour at $x/L_{PP} = 0.935$
Figure 3.1b-3 TKE contour at $x/L_{PP} = 0.935$
Figure 3.1b-4 $\overline{uu}$ contours at $x/L_{PP} = 0.935$
Figure 3.1b-5 $\overline{vv}$ contours at $x/L_{PP} = 0.935$
Figure 3.1b-6 $\overline{ww}$ contours at $x/L_{PP} = 0.935$
Figure 3.1b-7 $\overline{uv}$ contours at $x/L_{PP} = 0.935$
Figure 3.1b-8 $\overline{uw}$ contours at $x/L_{PP} = 0.935$

Table 3.1b-T-0: Computations information and V&V method

Organization (Code)	**V&V method (including the Determination of U_I)**
ECN/BEC/HO (Icare)	without V&V study
IIHR [CFDShip-IowaV4 (DES, URANS)]	without V&V study
IIHR (CFDShip-IowaV6)	without V&V study
MARIC (FLUENT6.3)	without V&V study
NavyFOAM (NavyFOAM)	3 grids
NMRI (SURF)	without V&V study
SSRC (FLUENT12.1)	without V&V study

Table 3.1b-T-1: Computed C_T, C_F and C_R of different grid densities

Organization (Code)	r_G		C_T ($\times 10^{-3}$)					C_F ($\times 10^{-3}$)					C_R ($\times 10^{-3}$)				
			Grid #5	Grid #4	Grid #3	Grid #2	Grid #1	Grid #5	Grid #4	Grid #3	Grid #2	Grid #1	Grid #5	Grid #4	Grid #3	Grid #2	Grid #1
EFD (IIHR)	-	*D*	4.61					3.38 (ITTC-57) *					1.23				
ECN/BEC/HO (Icare)	-	*S*	-	-	-	-	-	-	-	-	-	-	-	-	-	-	-
		E%D	-	-	-	-	-	-	-	-	-	-	-	-	-	-	-
IIHR (CFDShip-IowaV4) [DES]	-	*S*	-	-	-	-	4.730	-	-	-	-	3.470	-	-	-	-	1.260
		E%D	-	-	-	-	-2.60	-	-	-	-	-2.66	-	-	-	-	-2.44
IIHR (CFDShip-IowaV4) [URANS]	-	*S*	-	-	-	-	4.970	-	-	-	-	3.550	-	-	-	-	1.420
		E%D	-	-	-	-	-7.81	-	-	-	-	-5.03	-	-	-	-	-13.26
IIHR (CFDShip-IowaV6)	-	*S*	-	-	-	-	-	-	-	-	-	-	-	-	-	-	-
		E%D	-	-	-	-	-	-	-	-	-	-	-	-	-	-	-
MARIC (FLUENT6.3)	-	*S*	-	-	-	-	-	-	-	-	-	-	-	-	-	-	-
		E%D	-	-	-	-	-	-	-	-	-	-	-	-	-	-	-
NavyFOAM (NavyFOAM)	1.41	*S*	-	-	4.36	4.39	4.42	-	-	3.3	3.3	3.31	-	-	1.06	1.09	1.11
		E%D	-	-	5.42	4.77	4.12	-	-	2.37	2.37	2.07	-	-	13.82	11.4	9.76
NMRI (SURF)	-	*S*	-	-	-	-	4.820	-	-	-	-	3.540	-	-	-	-	1.280
		E%D	-	-	-	-	-4.56	-	-	-	-	-4.73	-	-	-	-	-4.07
SSRC (FLUENT12.1)	-	*S*	-	-	4.700	-	-	-	-	3.510	-	-	-	-	1.190	-	-
		E%D	-	-	-1.95	-	-	-	-	-3.85	-	-	-	-	3.25	-	-

* $C_F = 0.075 / \left(\log_{10} Re - 2\right)^2$ (ITTC 1957 Model-Ship Correlation Line)

E%D = (*D*-*S*)/*D*×100

Table 3.1b-T-2: V&V results for C_T, C_F and C_R

Organization (Code)	r_G	C_T						C_F						C_R					
		ε_{12} %S_1	$\frac{U_I}{\varepsilon_{12}}$	$\frac{P_G}{P_{G,th}}$	U_G %S_1	U_D %D	U_V%	ε_{12} %S_1	$\frac{U_I}{\varepsilon_{12}}$	$\frac{P_G}{P_{G,th}}$	U_G %S_1	U_D %D	U_V%	ε_{12} %S_1	$\frac{U_I}{\varepsilon_{12}}$	$\frac{P_G}{P_{G,th}}$	U_G %S_1	U_D %D	U_V%
ECN/BEC/HO (Icare)	-	-	-	-	-		-	-	-	-	-			-	-	-	-		
IIHR (CFDShip-IowaV4) [DES]	-	-	-	-	-		-	-	-	-	-			-	-	-	-		
IIHR (CFDShip-IowaV4) [URANS]	-	-	-	-	-		-	-	-	-	-			-	-	-	-		
IIHR (CFDShip-IowaV6)	-	-	-	-	-	0.63	-	-	-	-	-			-	-	-	-		
MARIC (FLUENT6.3)	-	-	-	-	-		-	-	-	-	-			-	-	-	-		
NavyFOAM (NavyFOAM)	1.41	0.679	-	-	-		-	-	-	-	-			-	-	-	-		
NMRI (SURF)	-	-	-	-	-		-	-	-	-	-			-	-	-	-		
SSRC (FLUENT12.1)	-	-	-	-	-		-	-	-	-	-			-	-	-	-		

$\varepsilon_{12}\%S_1 = |(S_1\text{-}S_2)/S_1| \times 100$; $U_{SN} = \sqrt{U_I^2 + U_G^2}$; $U_V = \sqrt{U_D^2 + U_{SN}^2}$

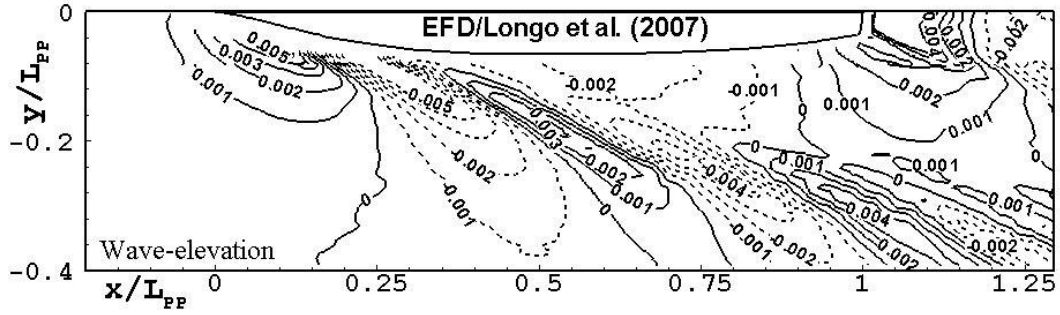

Experiment (IIHR, Longo et al. 2007)

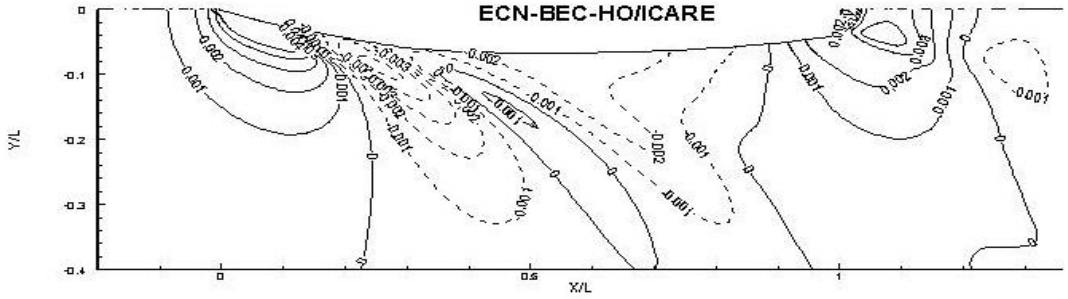

ECN/BEC/HO-Icare

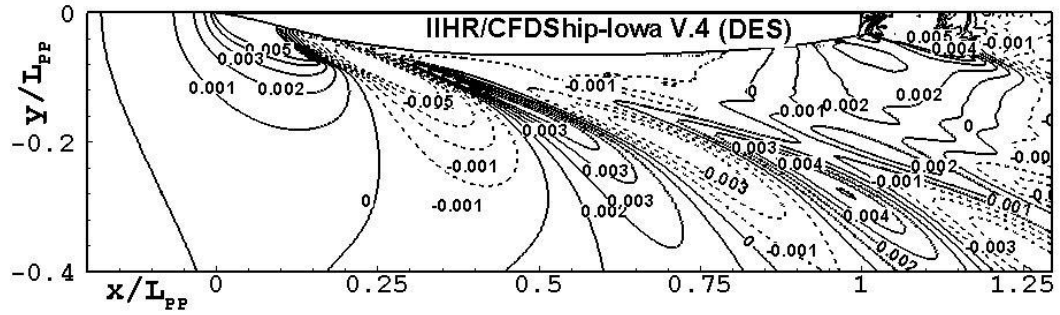

IIHR-CFDShip-IowaV4 (DES)

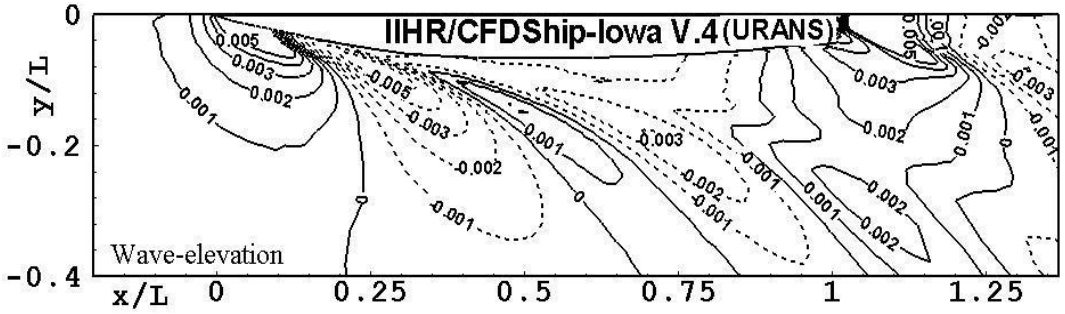

IIHR-CFDShip-IowaV4 (URANS)

Fig. 3.1b-1 Wave elevation contours [$\Delta z/L_{PP} = 0.001$]

(Solid lines: positive (+) values; Dashed lines: negative (-) values)

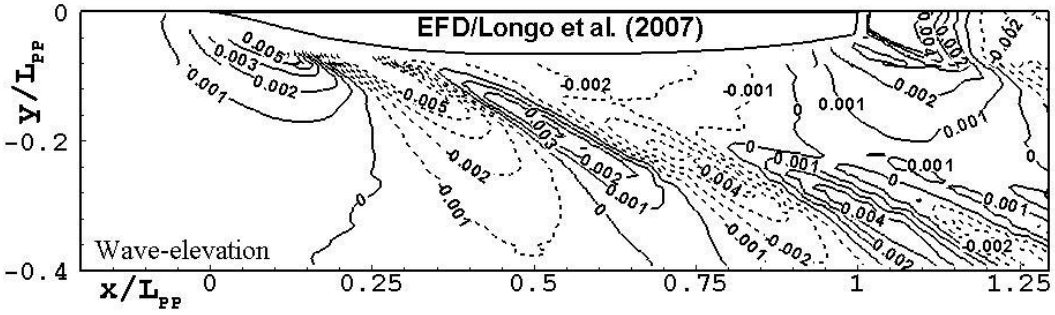

Experiment (IIHR, Longo et al. 2007)

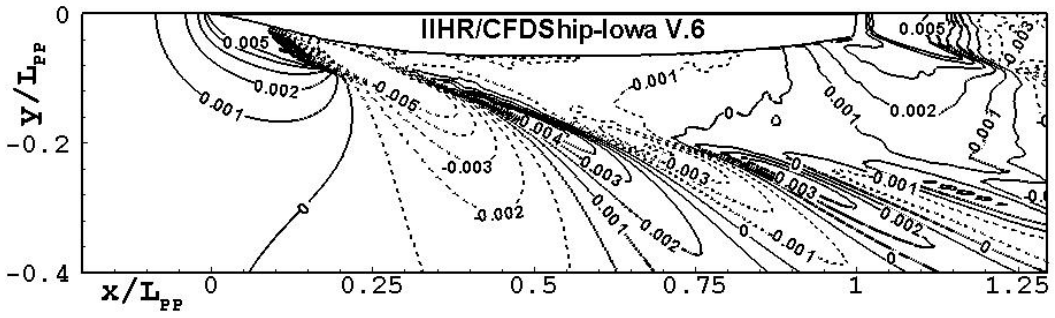

IIHR-CFDShip-IowaV6

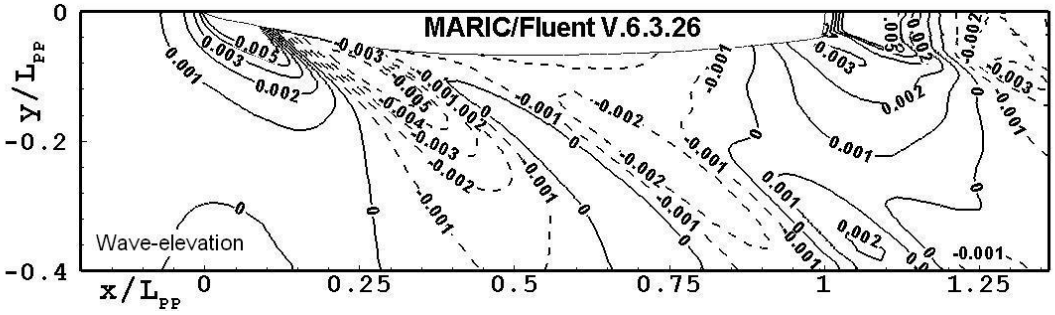

MARIC-FLUENT6.3.26

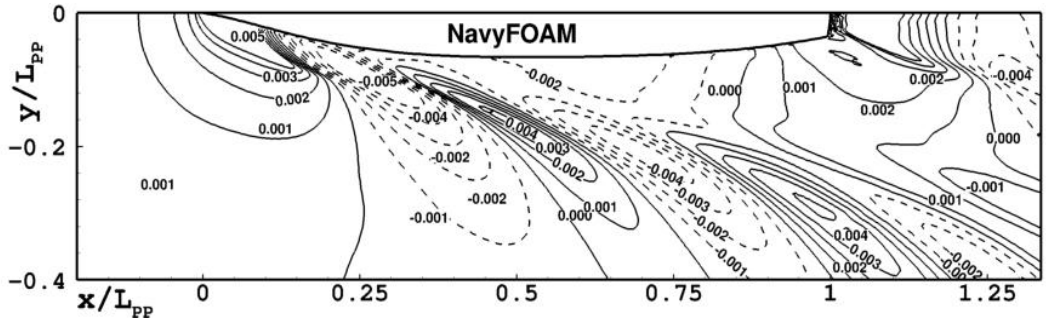

NavyFOAM-NavyFOAM

Fig. 3.1b-1 Wave elevation contours [$\Delta z/L_{PP} = 0.001$]

(Solid lines: positive (+) values; Dashed lines: negative (-) values)

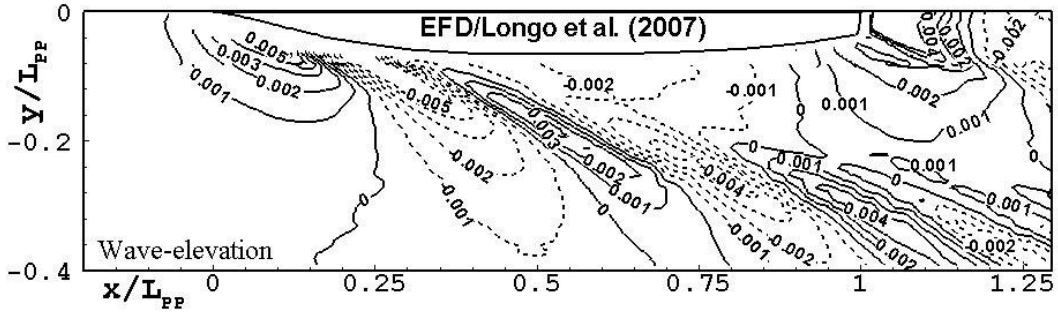

Experiment (IIHR, Longo et al. 2007)

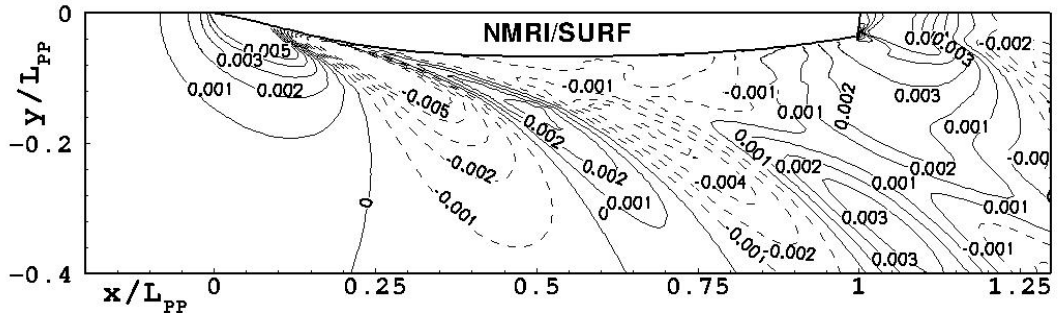

NMRI-SURF

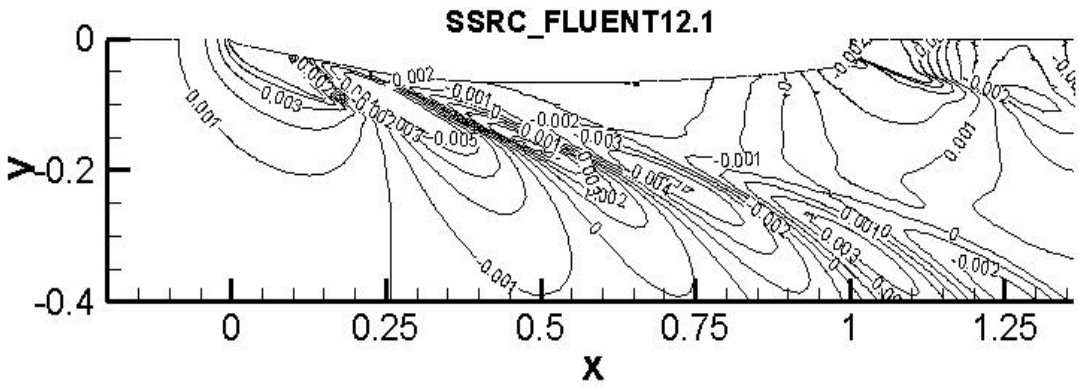

SSRC-FLUENT12.1

Fig. 3.1b-1 Wave elevation contours [$\Delta z/L_{PP} = 0.001$]

(Solid lines: positive (+) values; Dashed lines: negative (-) values)

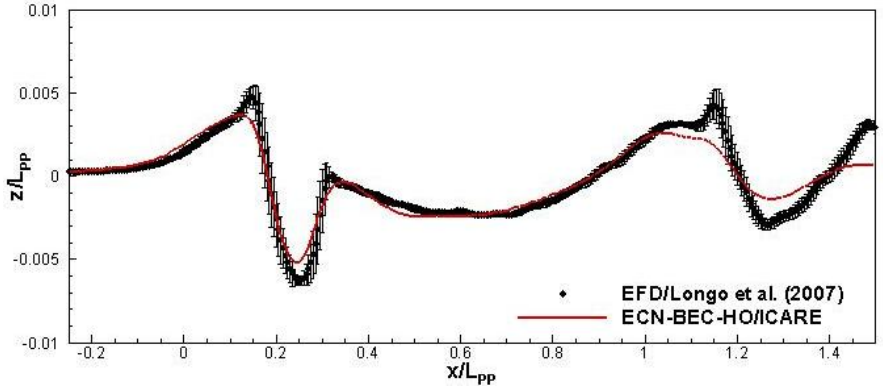

ECN/BEC/HO-Icare

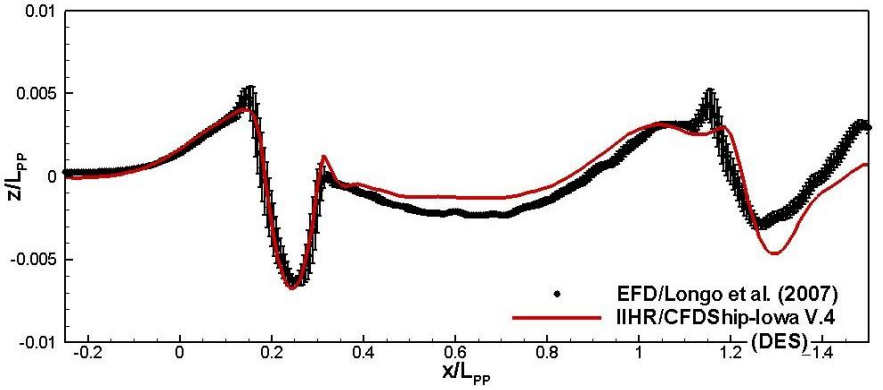

IIHR-CFDShip-IowaV4 (DES)

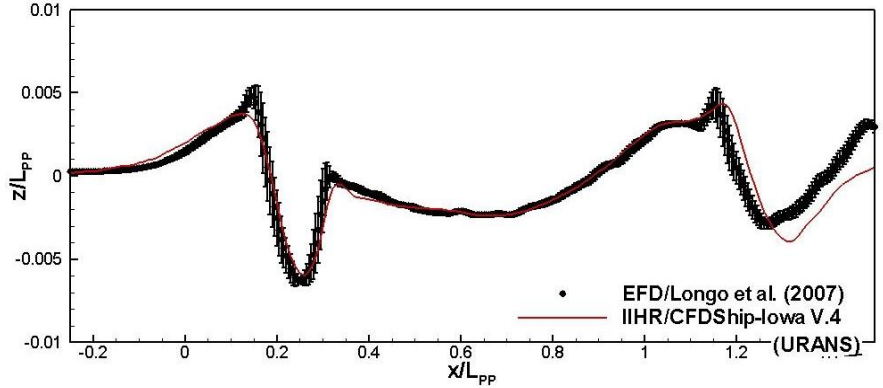

IIHR-CFDShip-IowaV4 (URANS)

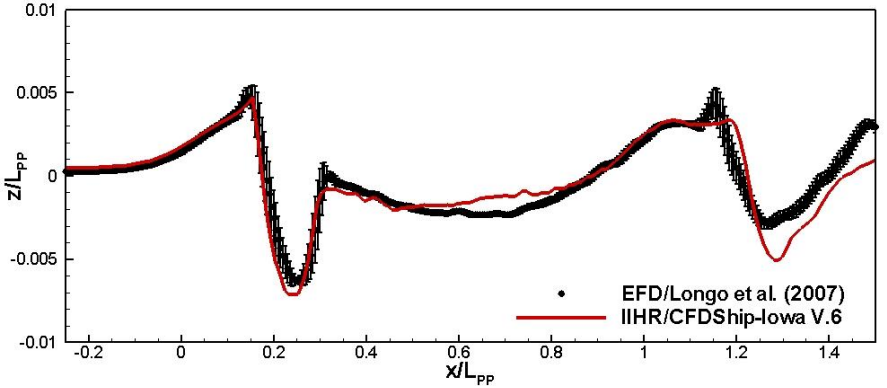

IIHR-CFDShip-IowaV6

Fig. 3.1b-1w-1 Longitudinal wave cut at $y/L_{PP} = 0.082$ (CFD: solid line; EFD: circles)

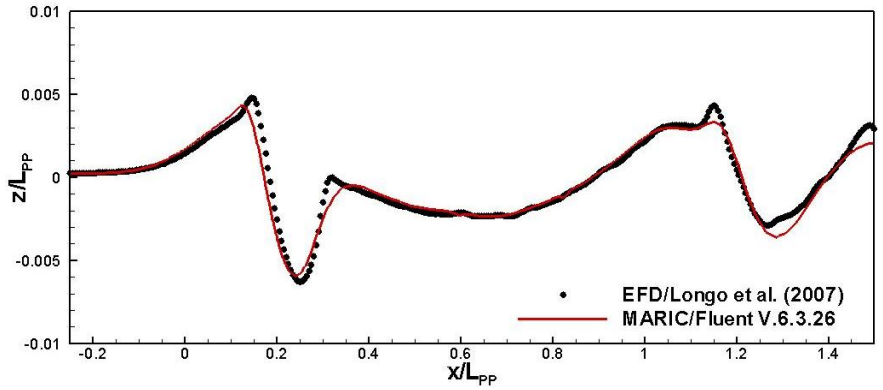

MARIC-FLUENT6.3.26

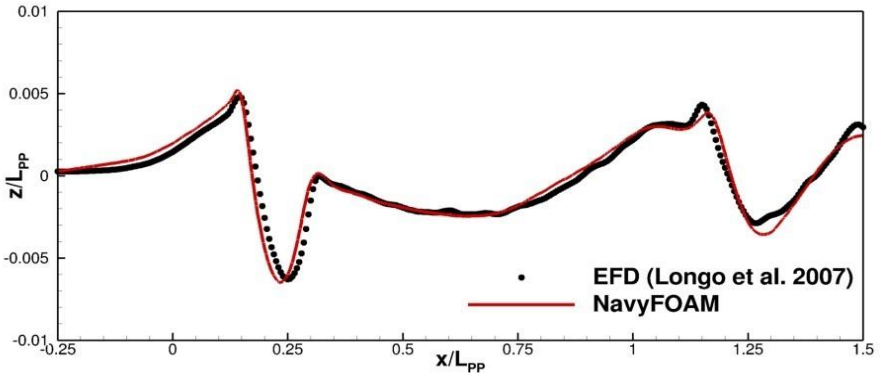

NavyFOAM-NavyFOAM

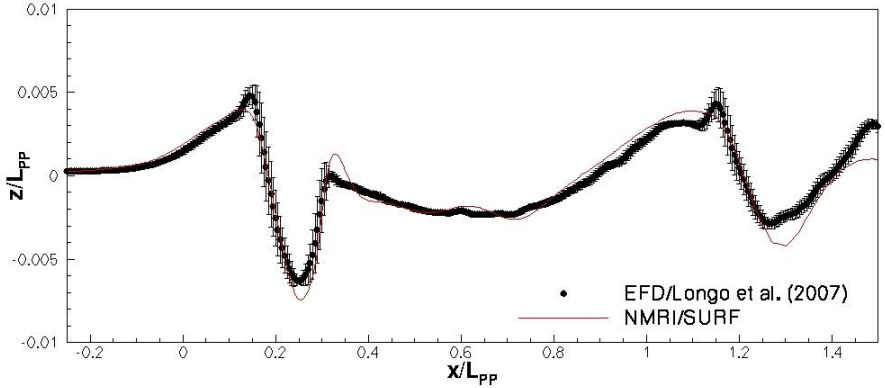

NMRI-SURF

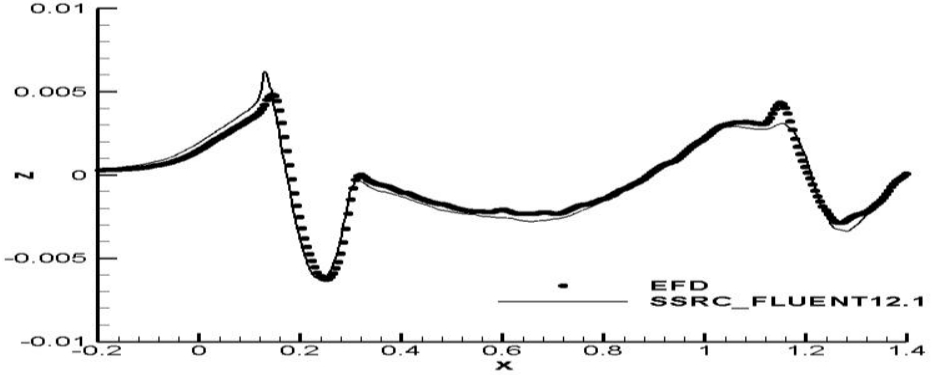

SSRC-FLUENT12.1

Fig. 3.1b-1w-1 Longitudinal wave cut at $y/L_{PP} = 0.082$ (CFD: solid line; EFD: circles)

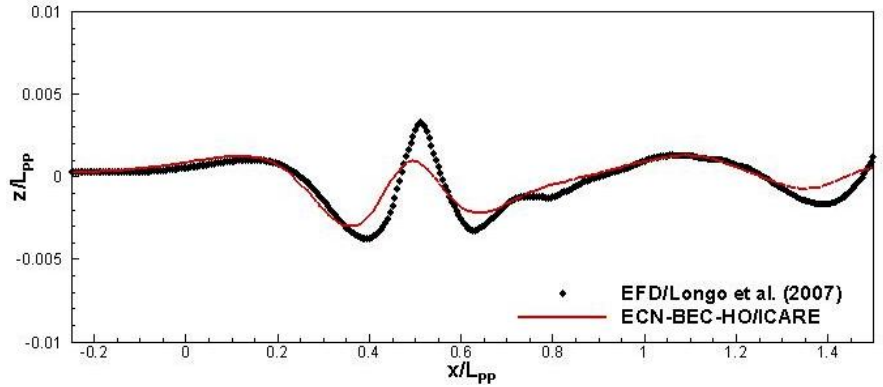

ECN/BEC/HO-Icare

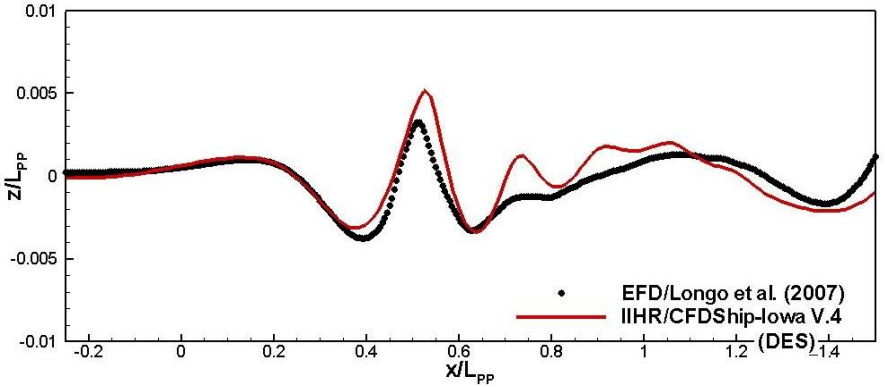

IIHR-CFDShip-IowaV4 (DES)

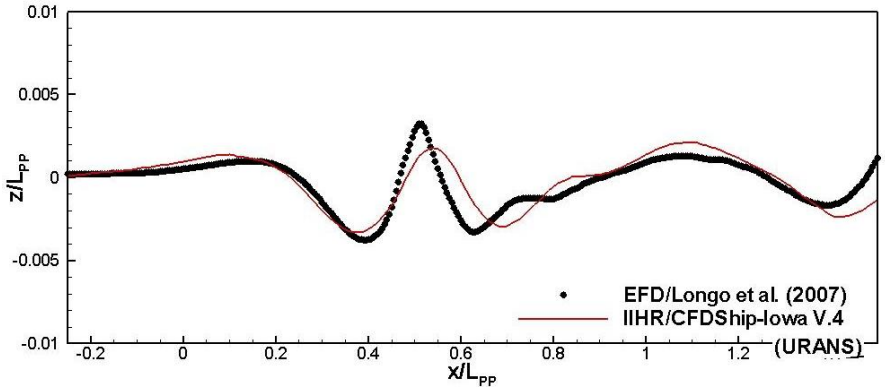

IIHR-CFDShip-IowaV4 (URANS)

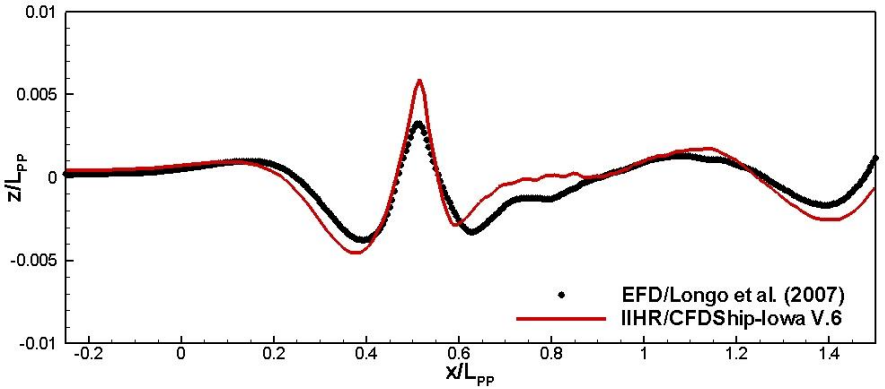

IIHR-CFDShip-IowaV6

Fig. 3.1b-1w-2 Longitudinal wave cut at $y/L_{PP} = 0.0172$ (CFD: solid line; EFD: circles)

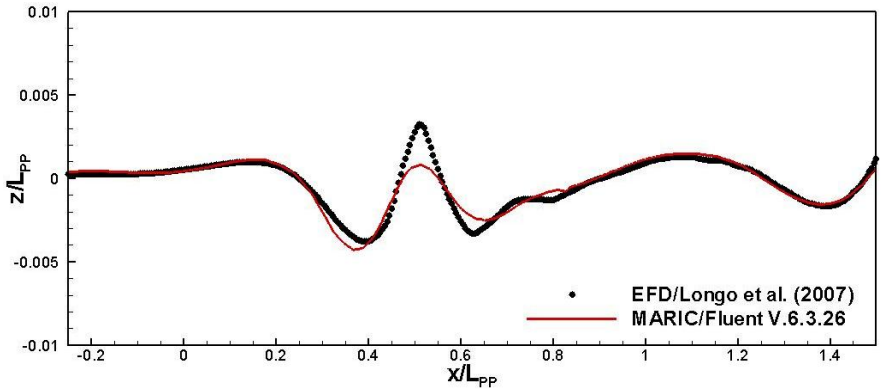

MARIC-FLUENT6.3.26

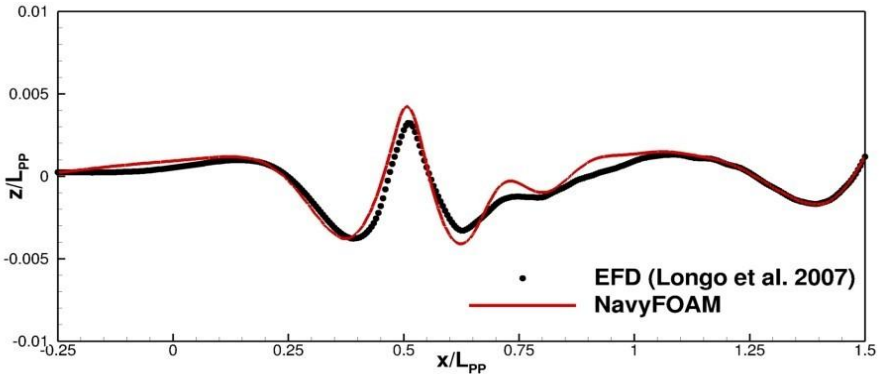

NavyFOAM-NavyFOAM

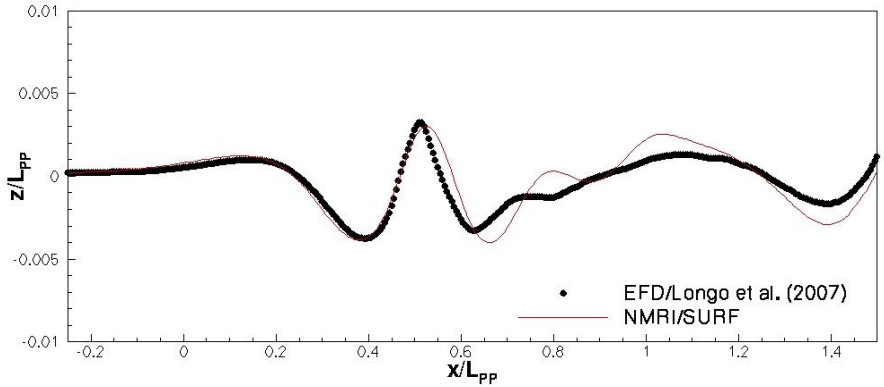

NMRI-SURF

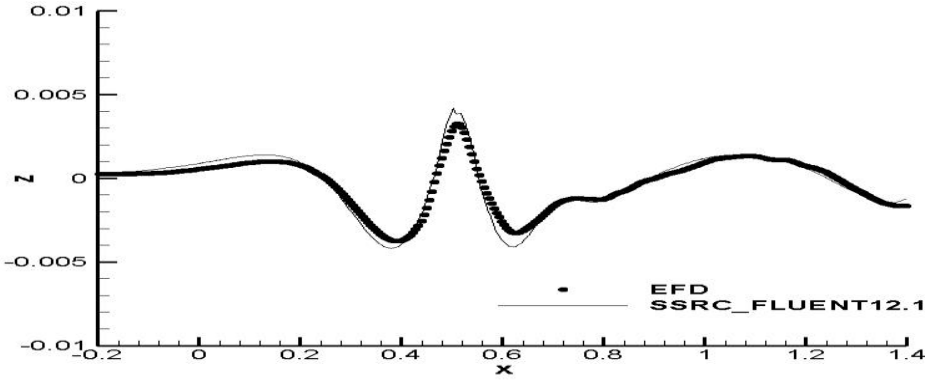

SSRC-FLUENT12.1

Fig. 3.1b-1w-2 Longitudinal wave cut at $y/L_{PP} = 0.0172$ (CFD: solid line; EFD: circles)

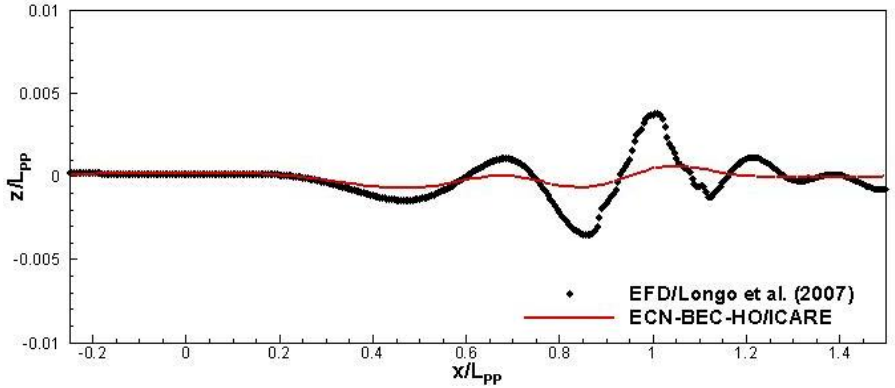

ECN/BEC/HO-Icare

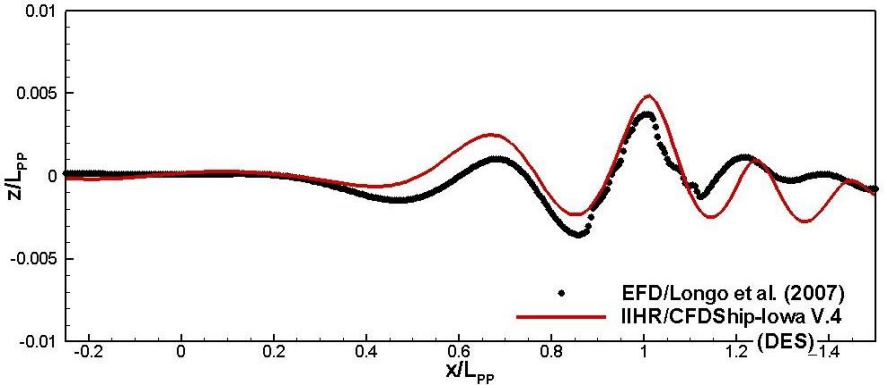

IIHR-CFDShip-IowaV4 (DES)

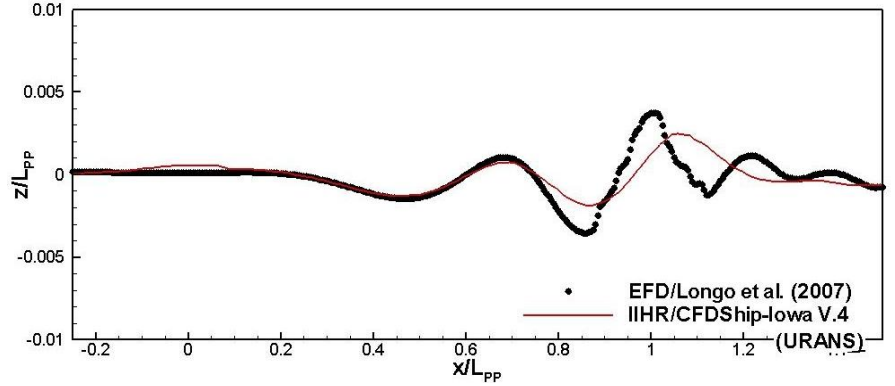

IIHR-CFDShip-IowaV4 (URANS)

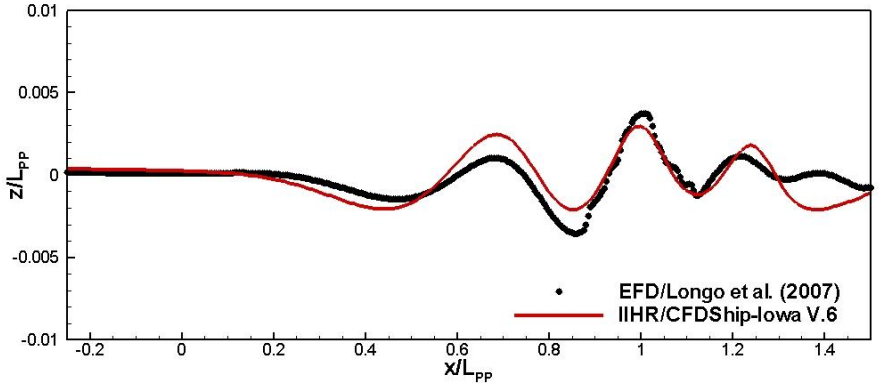

IIHR-CFDShip-IowaV6

Fig. 3.1b-1w-3 Longitudinal wave cut at $y/L_{PP} = 0.0302$ (CFD: solid line; EFD: circles)

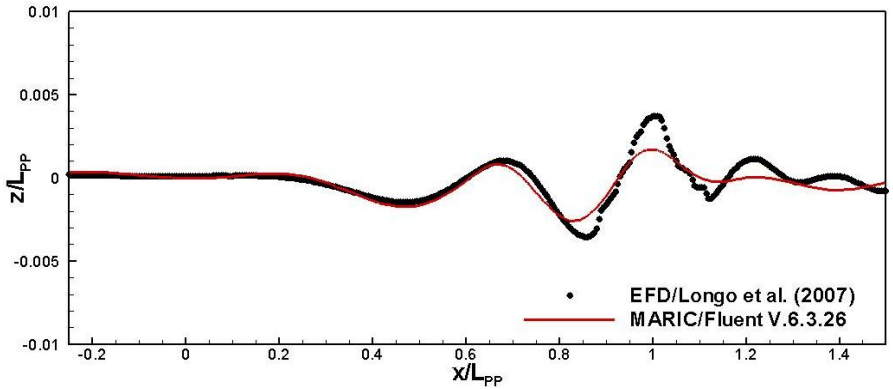

MARIC-FLUENT6.3.26

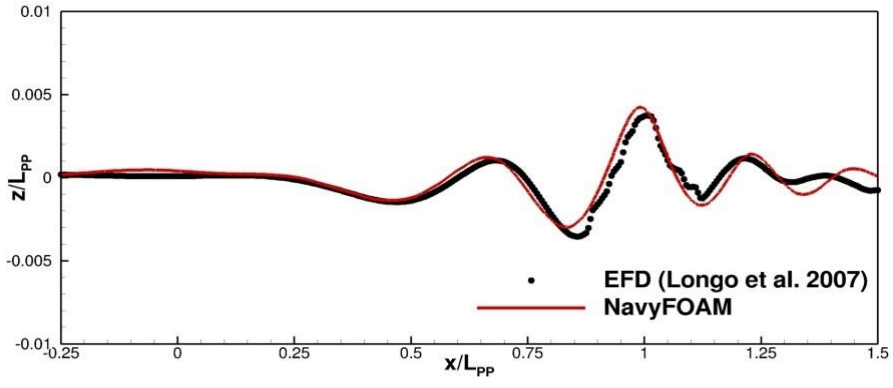

NavyFOAM-NavyFOAM

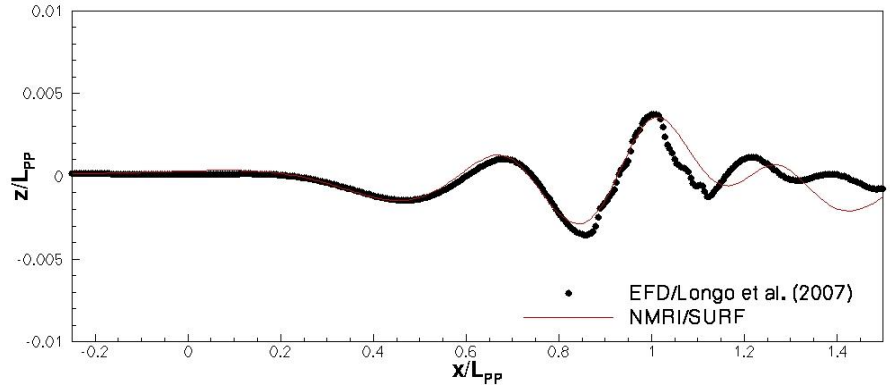

NMRI-SURF

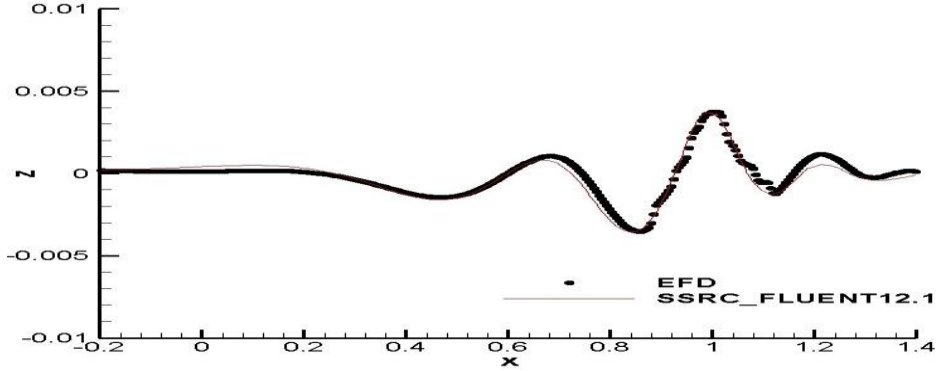

SSRC-FLUENT12.1

Fig. 3.1b-1w-3 Longitudinal wave cut at $y/L_{PP} = 0.0302$ (CFD: solid line; EFD: circles)

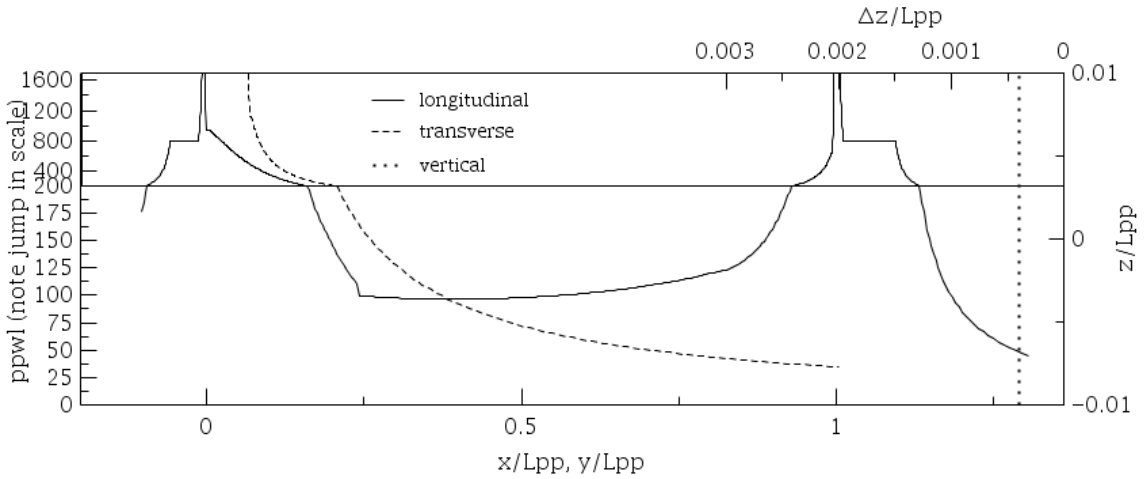

IIHR-CFDShip-IowaV4 (DES)

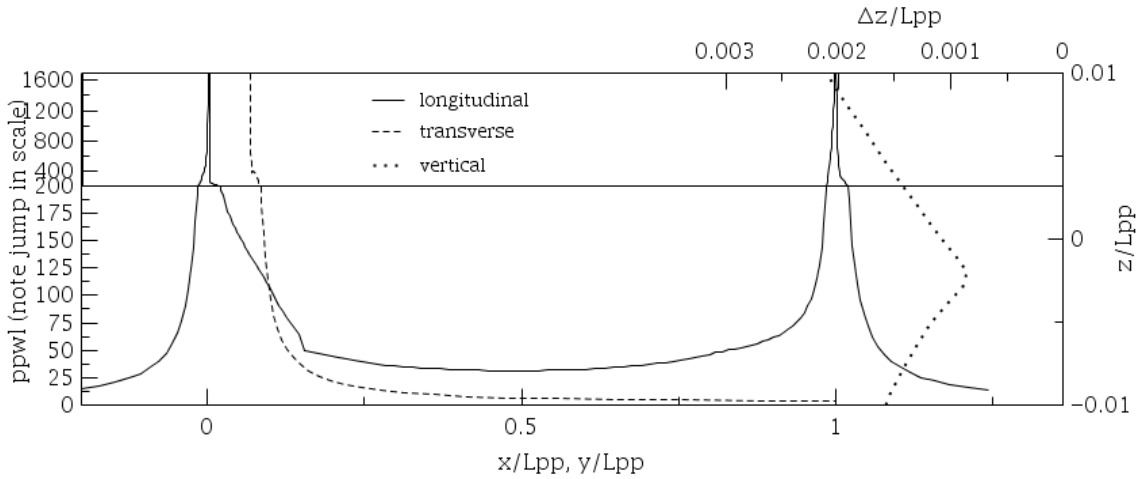

IIHR-CFDShip-IowaV4 (URANS)

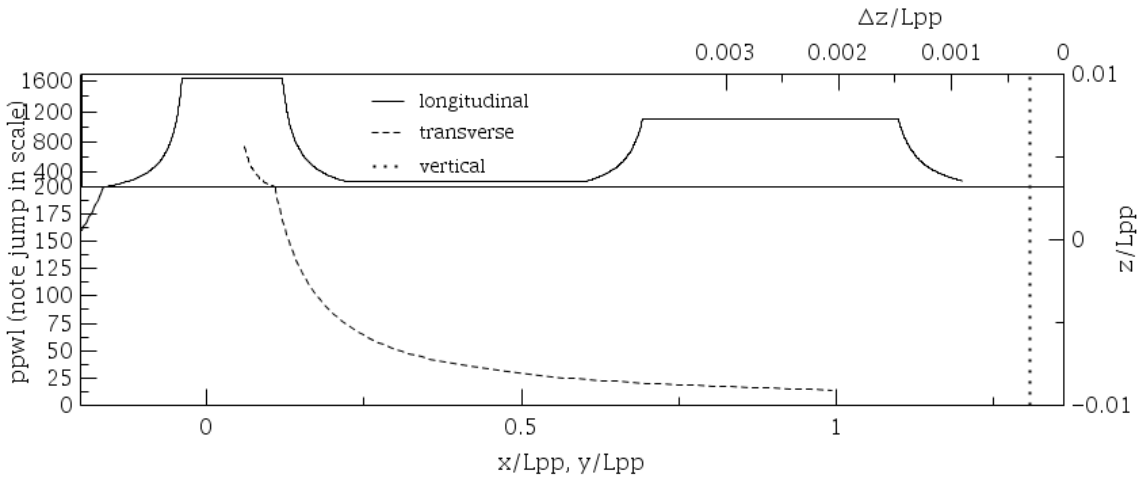

IIHR-CFDShip-IowaV6

Fig. 3.1b-1w-4 Grid density distribution along the waterline (solid), and in transverse (dashed) and vertical (dotted) directions at mid-ship

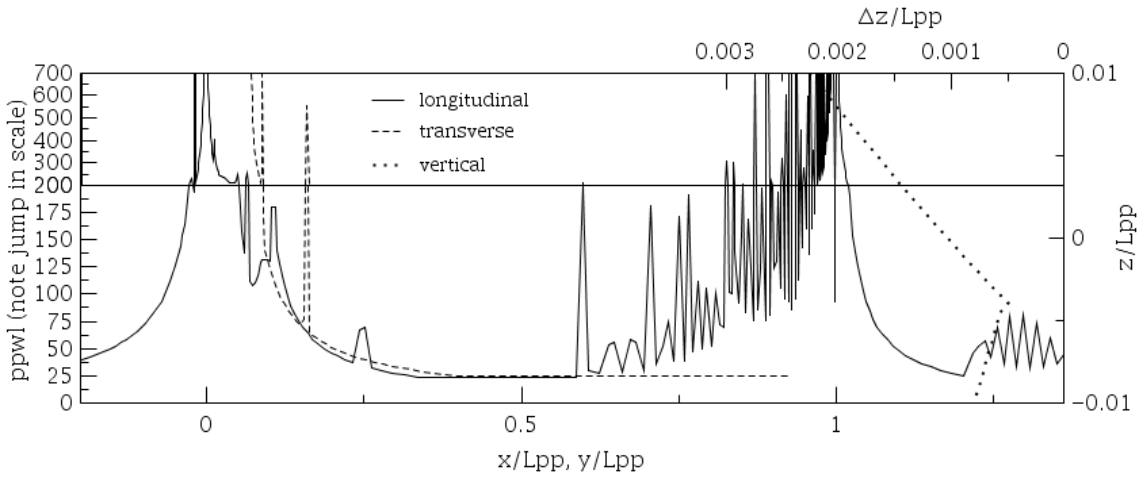

MARIC-FLUENT6.3.26

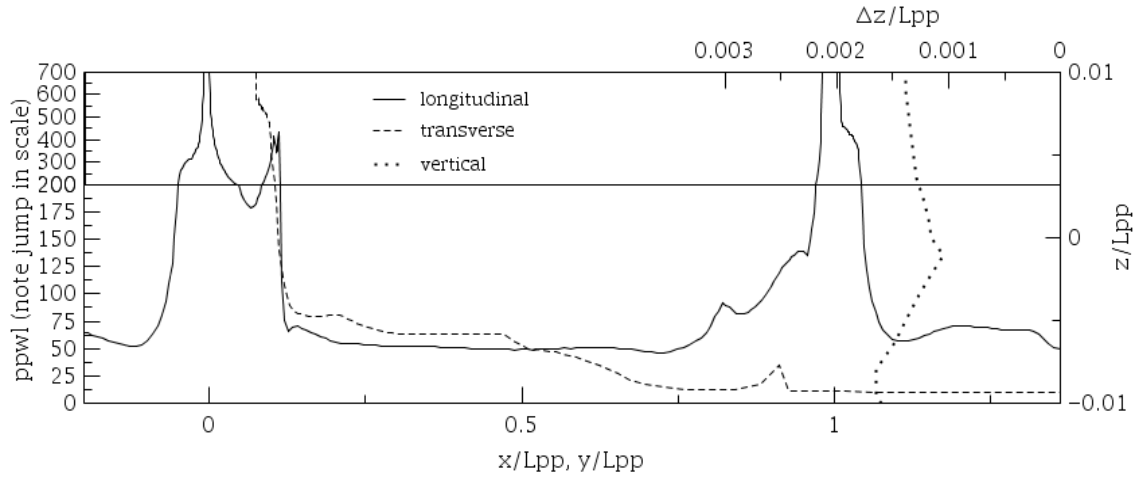

NavyFOAM-NavyFOAM

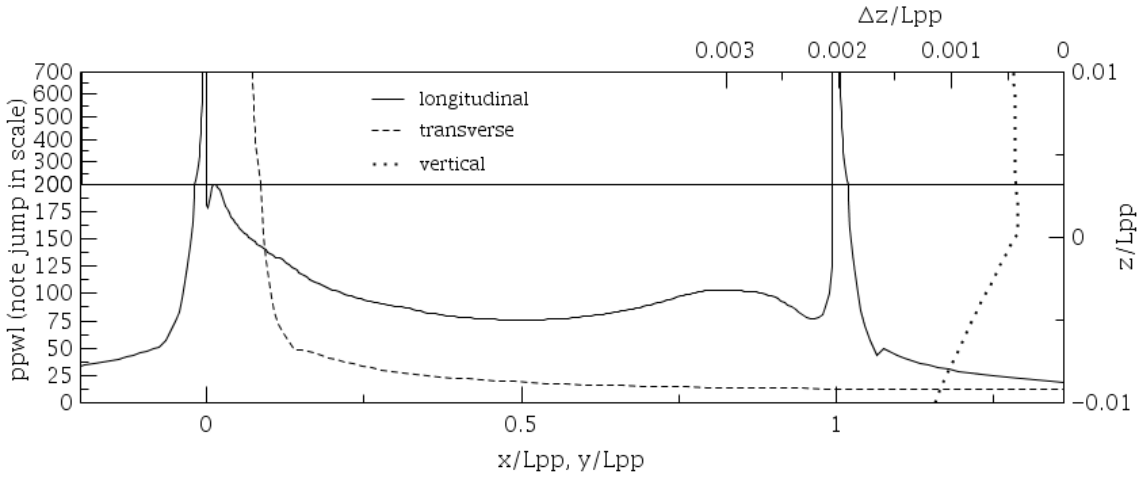

NMRI-SURF

Fig. 3.1b-1w-4 Grid density distribution along the waterline (solid), and in transverse (dashed) and vertical (dotted) directions at mid-ship

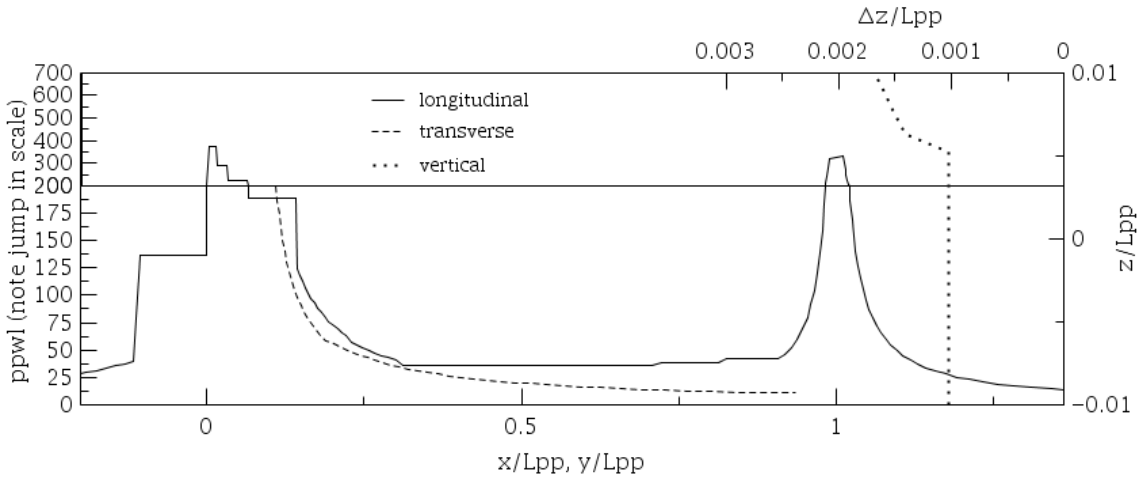

SSRC-FLUENT12.1

Fig. 3.1b-1w-4 Grid density distribution along the waterline (solid), and in transverse (dashed) and vertical (dotted) directions at mid-ship

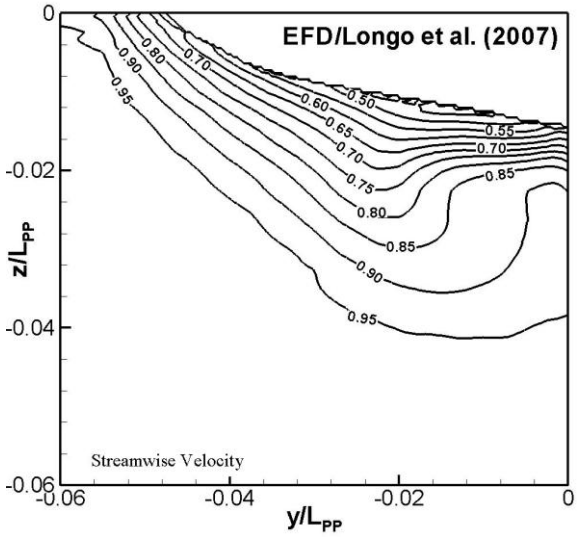

Experiment (IIHR, Longo et al. 2007)

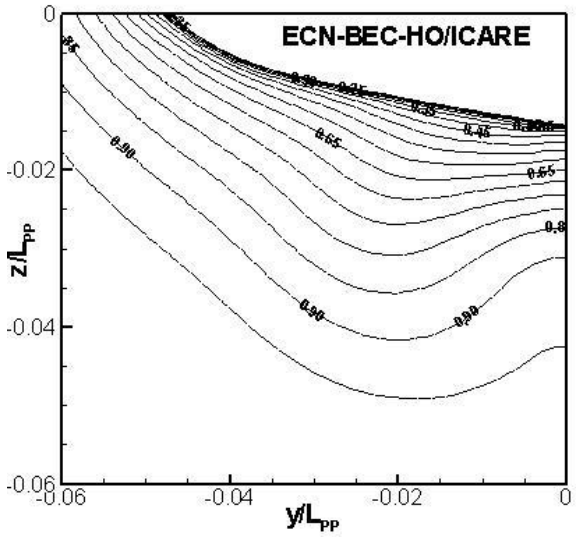

ECN/BEC/HO-Icare

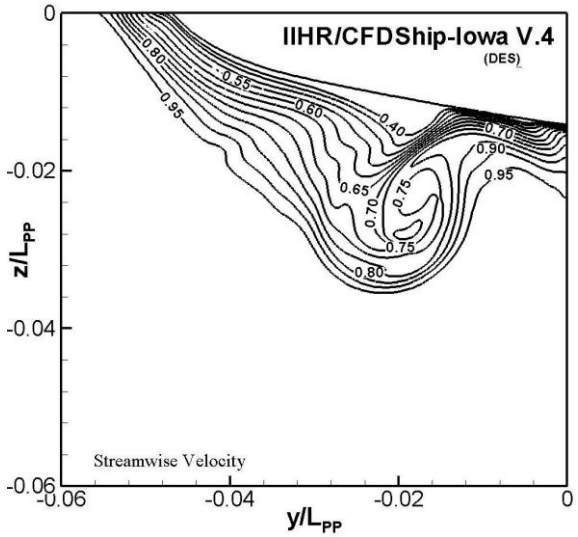

IIHR-CFDShip-IowaV4 (DES)

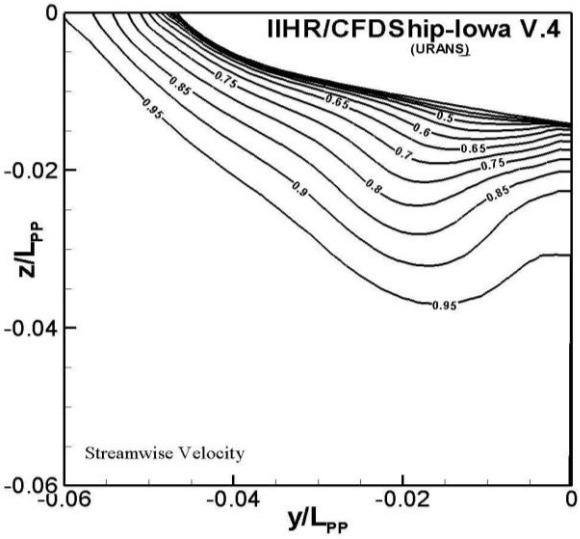

IIHR-CFDShip-IowaV4 (URANS)

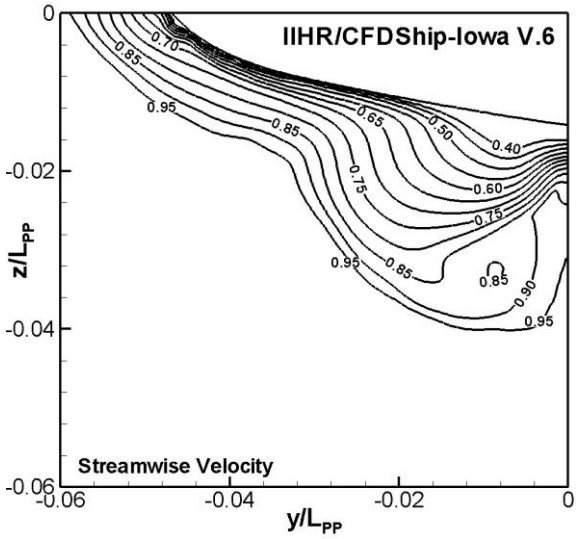

IIHR-CFDShip-IowaV6

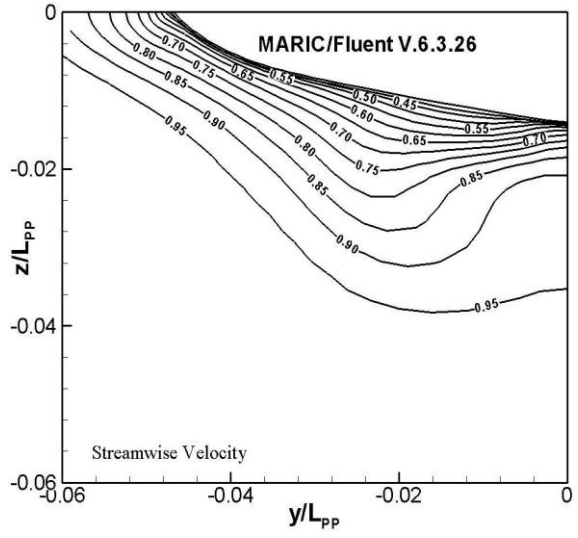

MARIC-FLUENT6.3.26

Fig. 3.1b-2 Streamwise velocity contour at $x/L_{PP} = 0.935$ [$\Delta U = 0.05$]

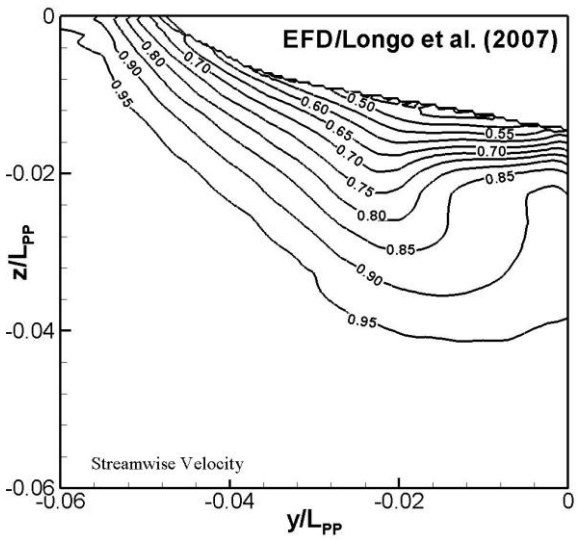

Experiment (IIHR, Longo et al. 2007)

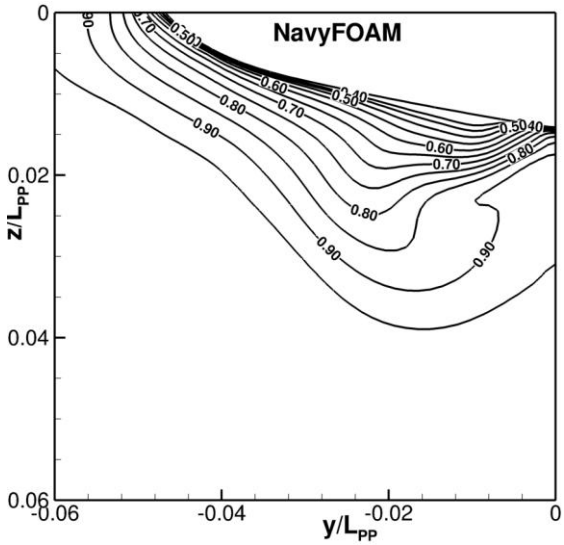

NavyFOAM-NavyFOAM

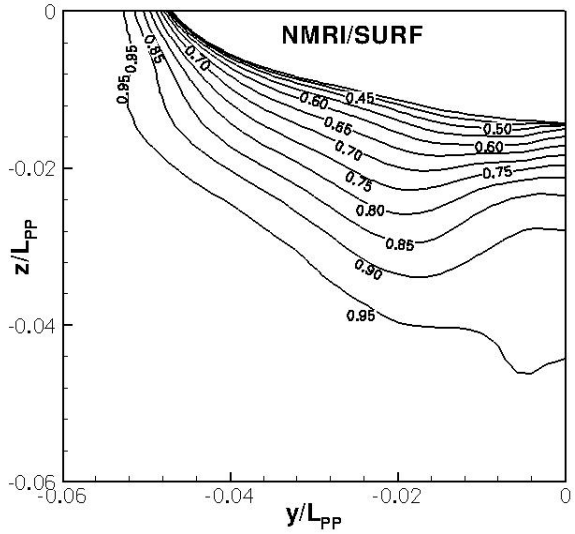

NMRI-SURF

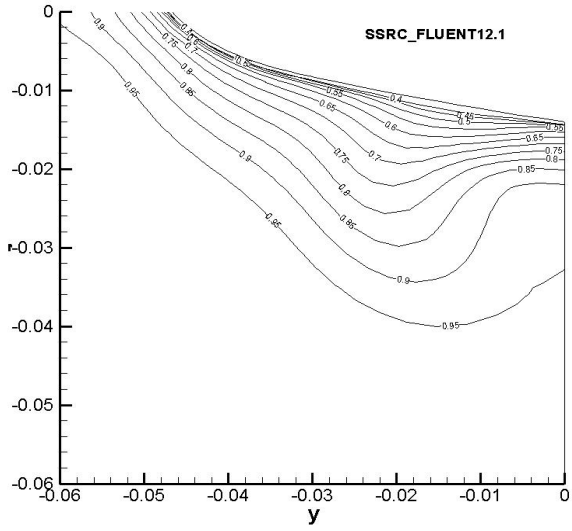

SSRC-FLUENT12.1

Fig. 3.1b-2 Streamwise velocity contour at $x/L_{PP} = 0.935$ [$\Delta U = 0.05$]

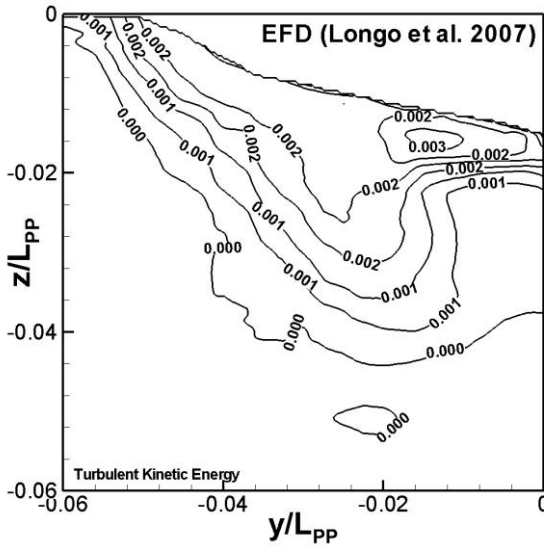

Experiment (IIHR, Longo et al. 2007)

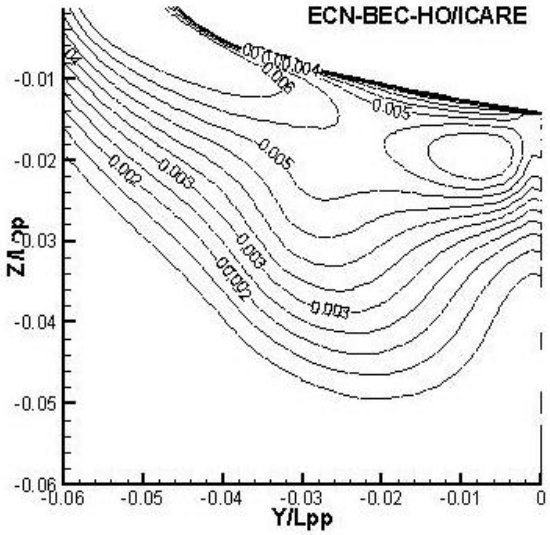

ECN/BEC/HO-Icare

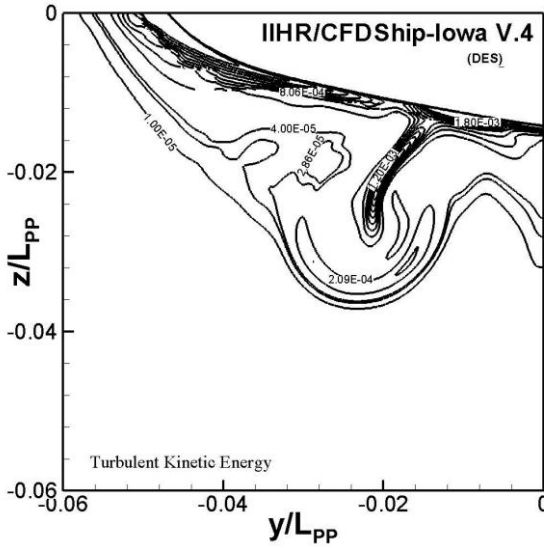

IIHR-CFDShip-IowaV4 (DES)

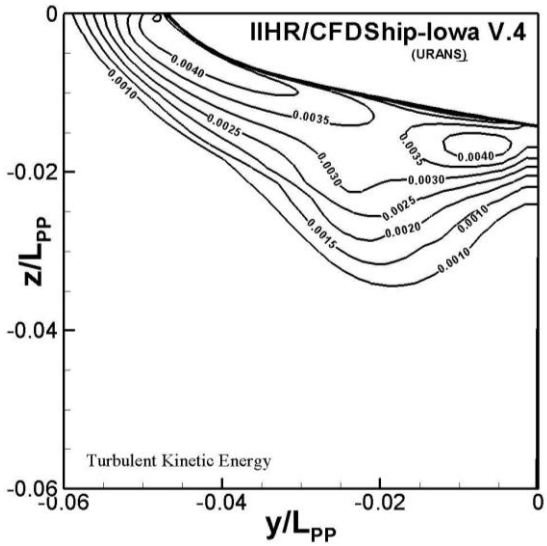

IIHR-CFDShip-IowaV4 (URANS)

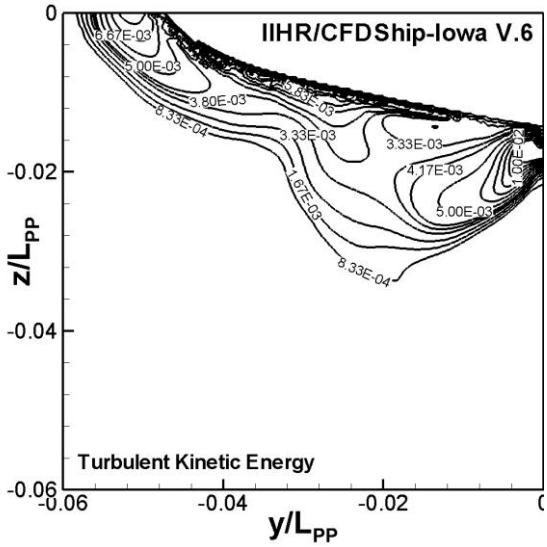

IIHR-CFDShip-IowaV6

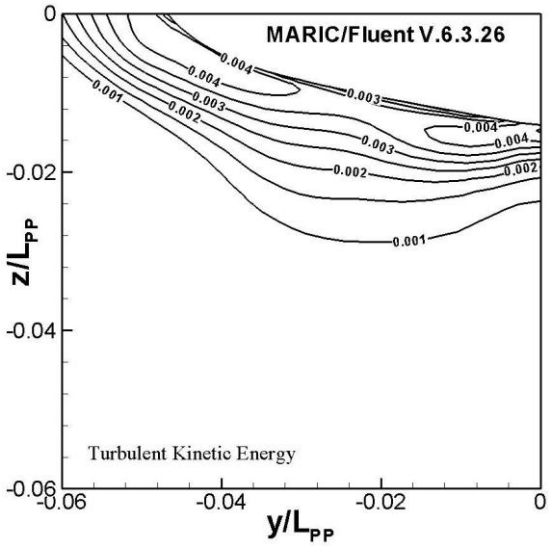

MARIC-FLUENT6.3.26

Fig. 3.1b-3 TKE contour at x/L_{PP} = 0.935 [ΔTKE = 0.0005]

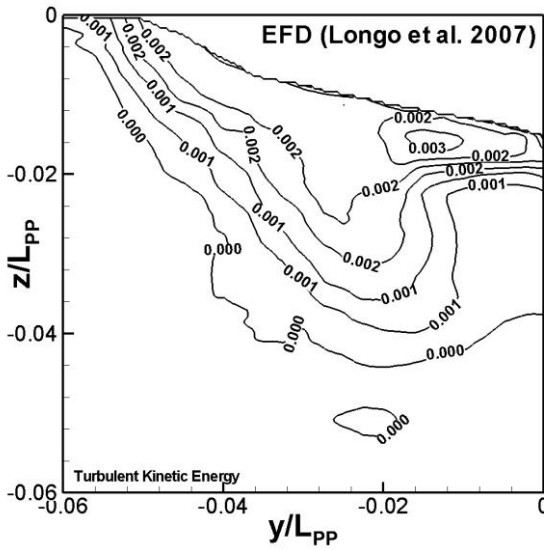

Experiment (IIHR, Longo et al. 2007)

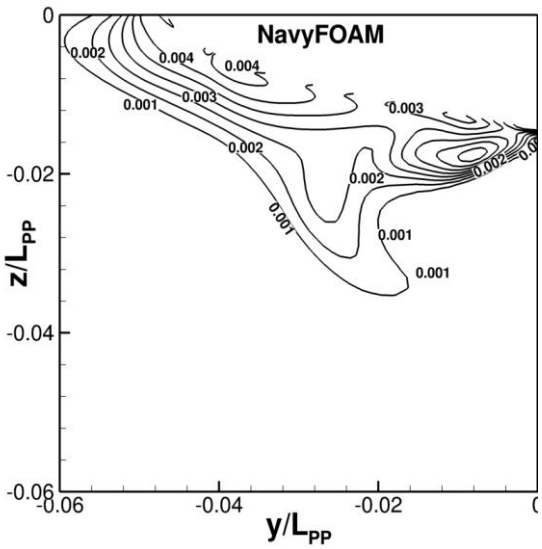

NavyFOAM-NavyFOAM

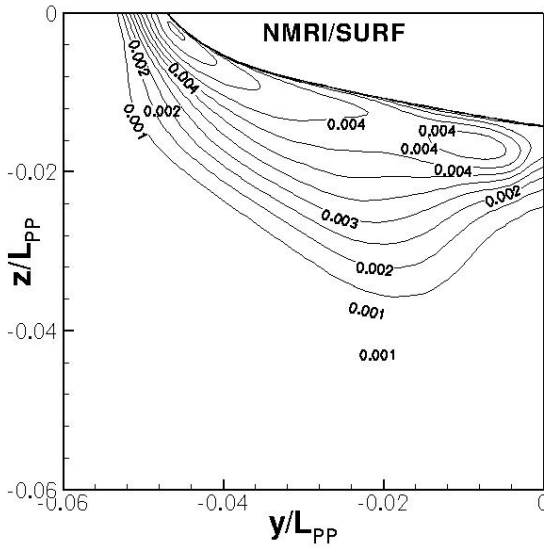

NMRI-SURF

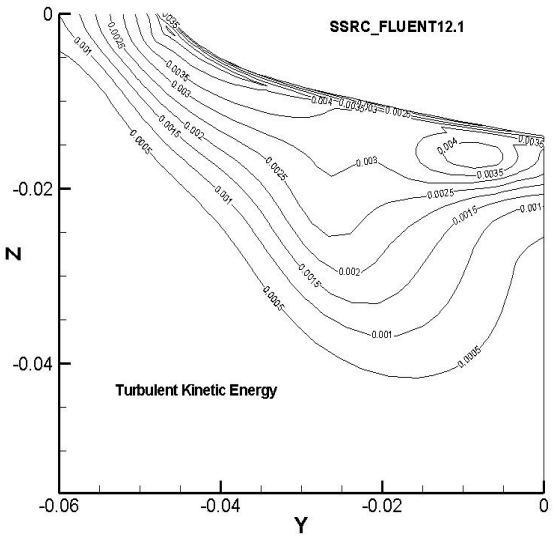

SSRC-FLUENT12.1

Fig. 3.1b-3 TKE contour at x/L_{PP} = 0.935 [ΔTKE = 0.0005]

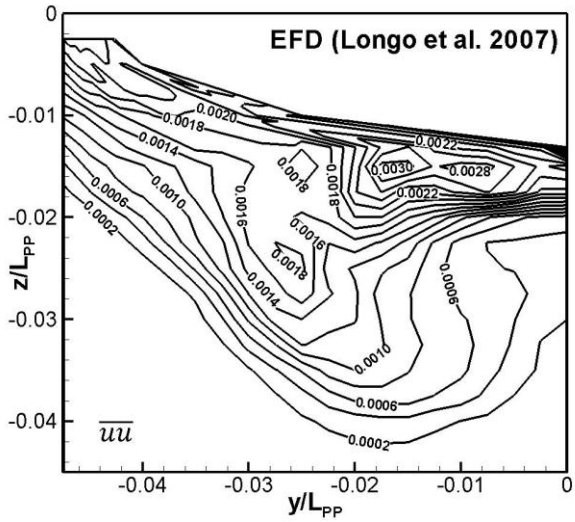

Experiment (IIHR, Longo et al. 2007)

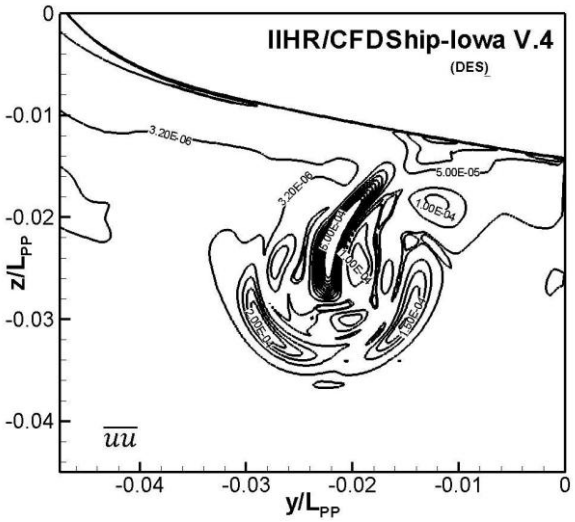

IIHR-CFDShip-IowaV4 (DES)

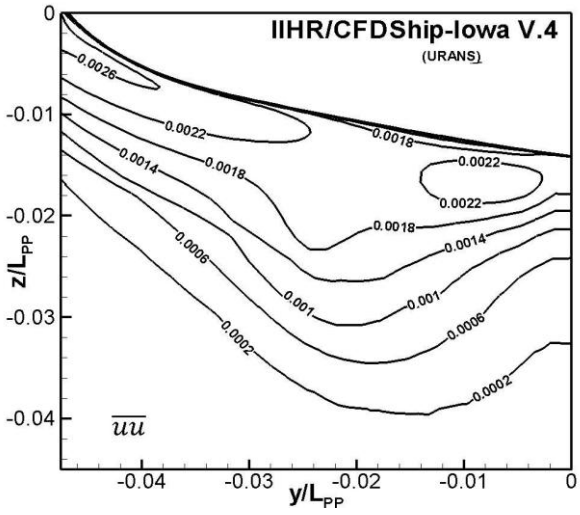

IIHR-CFDShip-IowaV4 (URANS)

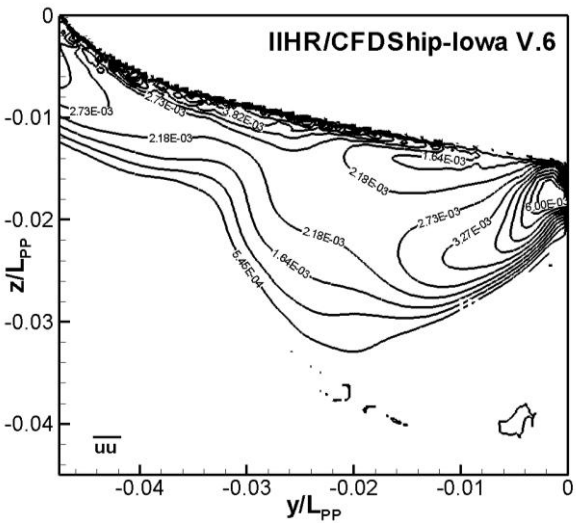

IIHR-CFDShip-IowaV6

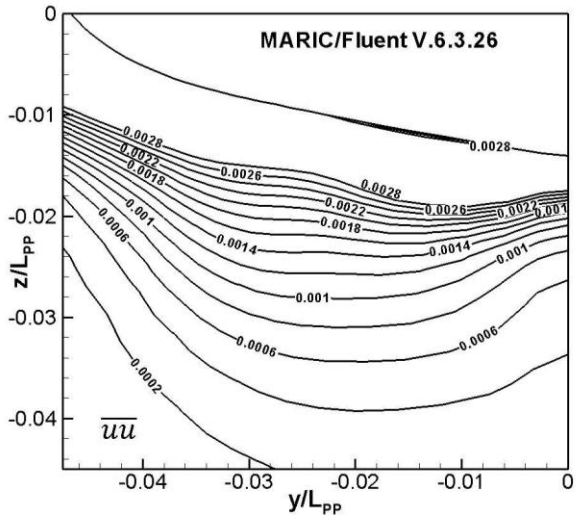

MARIC-FLUENT6.3.26

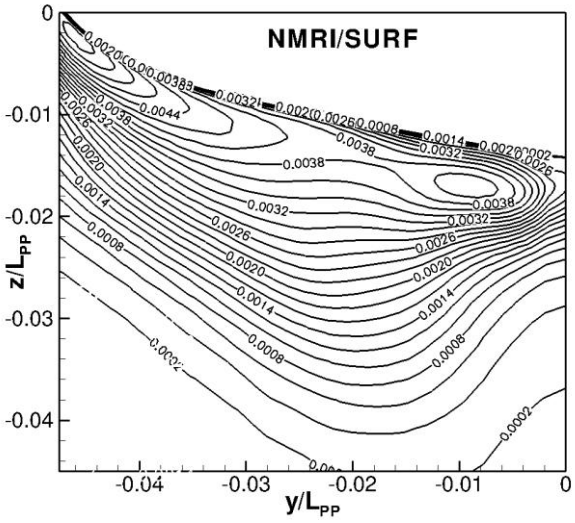

NMRI-SURF

Fig. 3.1b-4 $\overline{uu}$ contours at $x/L_{PP} = 0.935$ [$\Delta\overline{uu} = 2\times10^{-4}$]

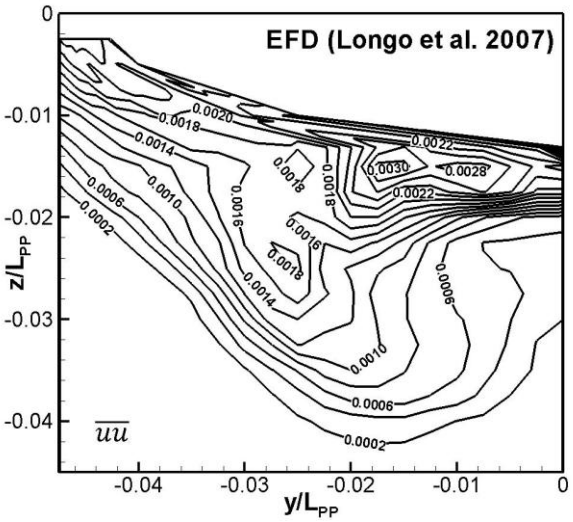

Experiment (IIHR, Longo et al. 2007)

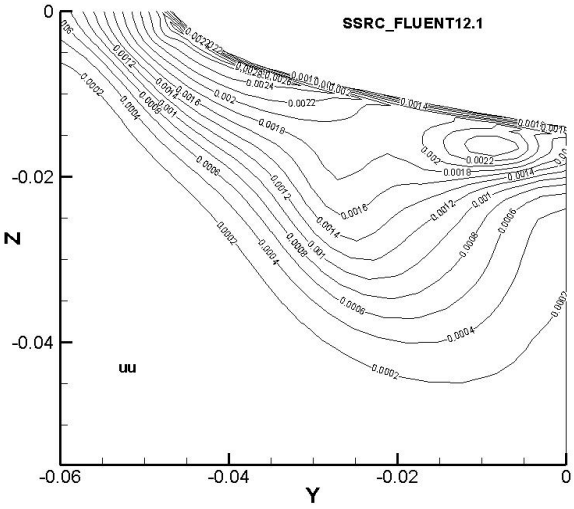

SSRC-FLUENT12.1

Fig. 3.1b-4 $\overline{uu}$ contours at $x/L_{PP} = 0.935$ [$\Delta\overline{uu} = 2\times10^{-4}$]

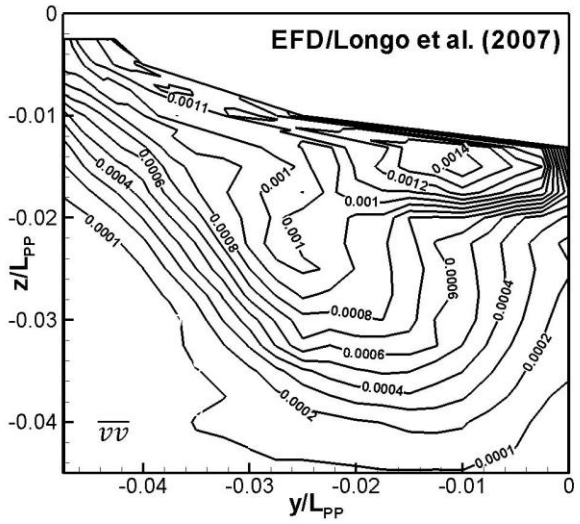

Experiment (IIHR, Longo et al. 2007)

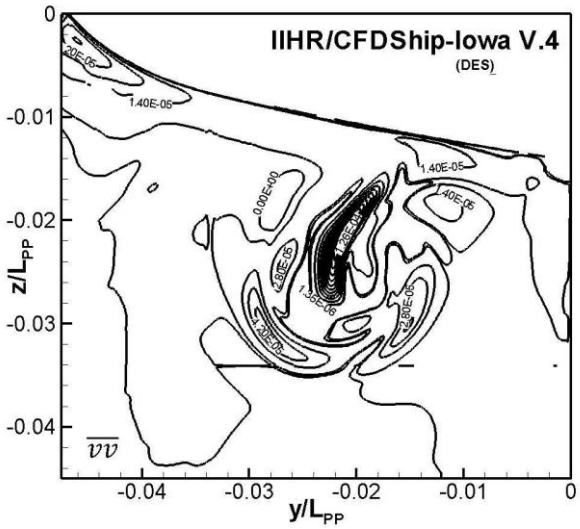

IIHR-CFDShip-IowaV4 (DES)

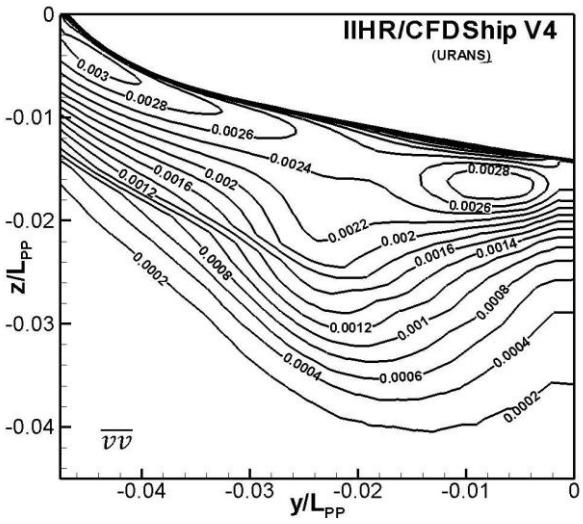

IIHR-CFDShip-IowaV4 (URANS)

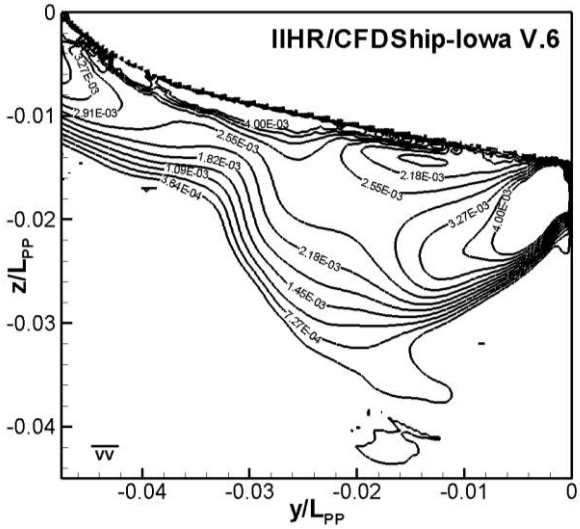

IIHR-CFDShip-IowaV6

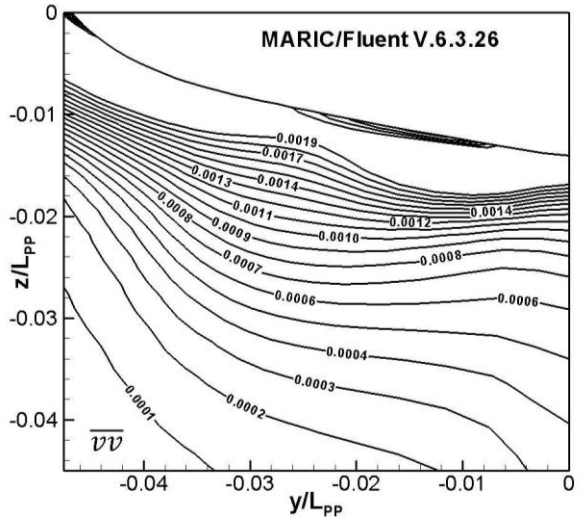

MARIC-FLUENT6.3.26

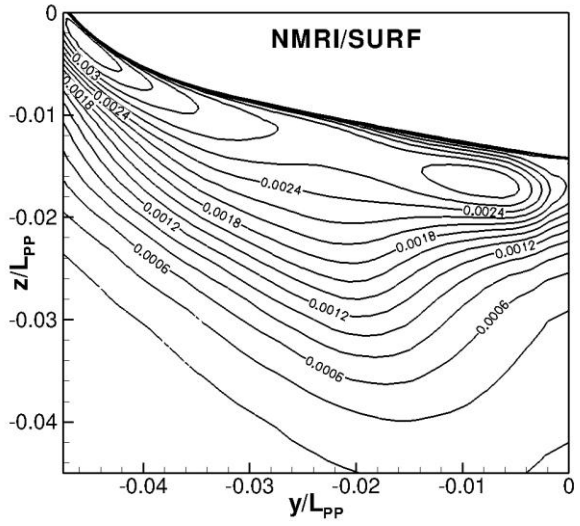

NMRI-SURF

Fig. 3.1b-5 $\overline{vv}$ contours at $x/L_{PP} = 0.935$ [$\Delta\overline{vv} = 1\times10^{-4}$]

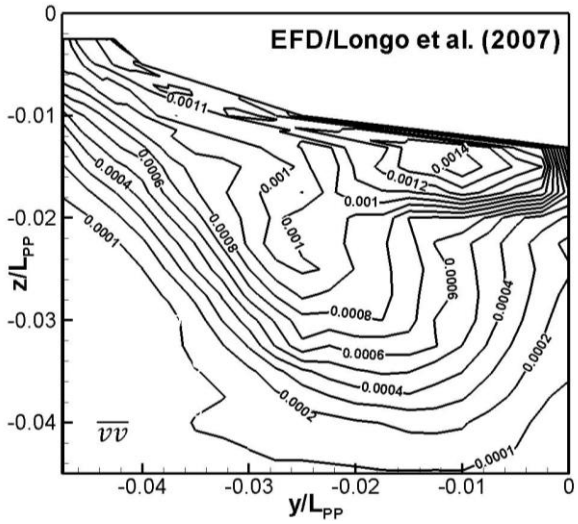

Experiment (IIHR, Longo et al. 2007)

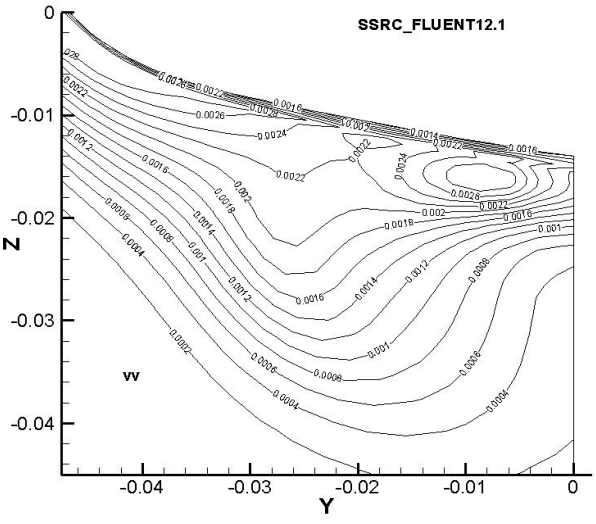

SSRC-FLUENT12.1

Fig. 3.1b-5 $\overline{vv}$ contours at $x/L_{PP} = 0.935$ [$\Delta\overline{vv} = 1\times10^{-4}$]

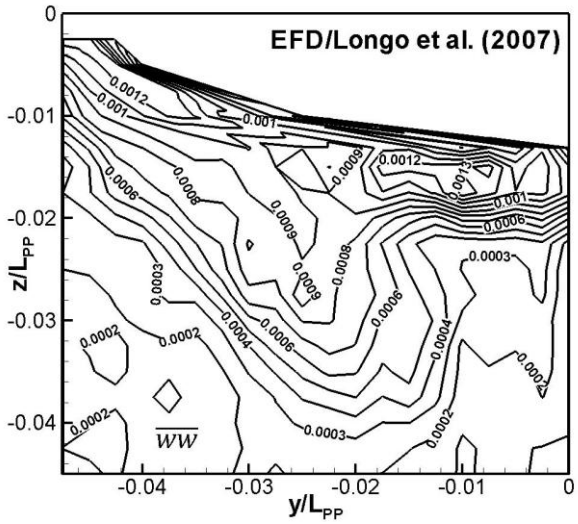

Experiment (IIHR, Longo et al. 2007)

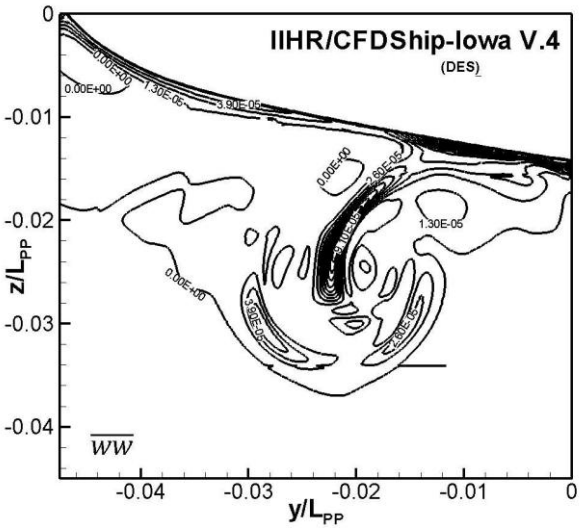

IIHR-CFDShip-IowaV4 (DES)

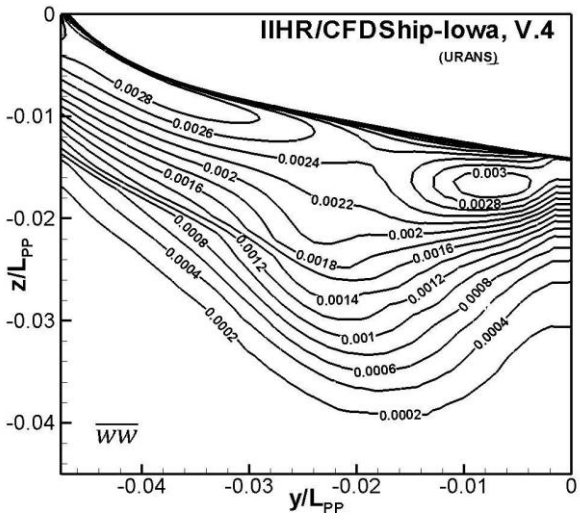

IIHR-CFDShip-IowaV4 (URANS)

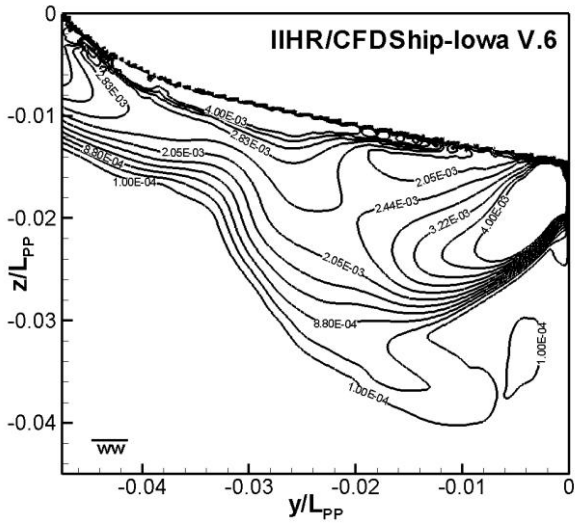

IIHR-CFDShip-IowaV6

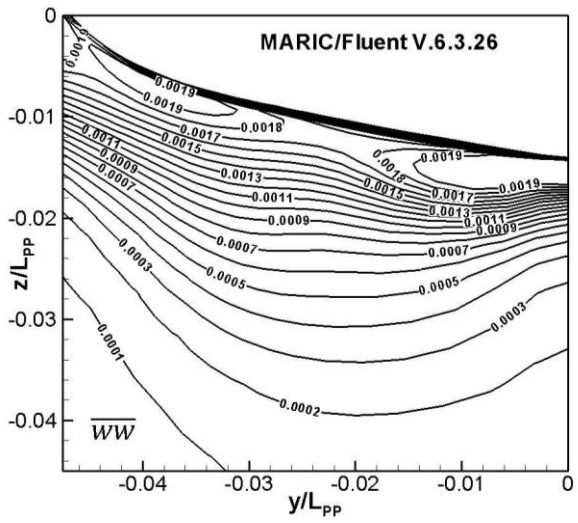

MARIC-FLUENT6.3.26

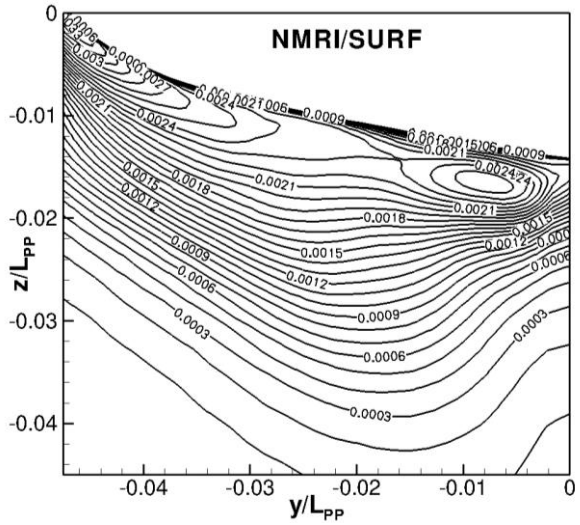

NMRI-SURF

Fig. 3.1b-6 $\overline{ww}$ contours at $x/L_{PP} = 0.935$ [$\Delta\overline{ww} = 1\times10^{-4}$]

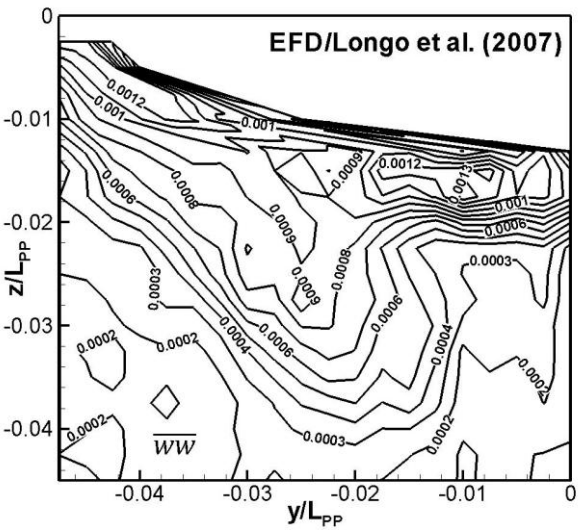

Experiment (IIHR, Longo et al. 2007)

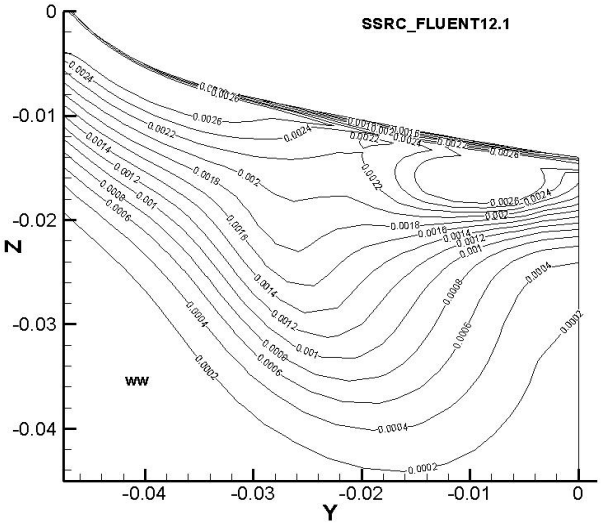

SSRC-FLUENT12.1

Fig. 3.1b-6 $\overline{ww}$ contours at $x/L_{PP} = 0.935$ [$\Delta\overline{ww} = 1\times10^{-4}$]

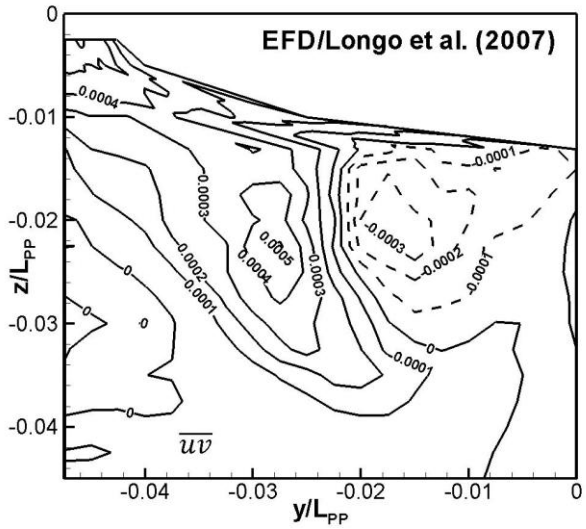

Experiment (IIHR, Longo et al. 2007)

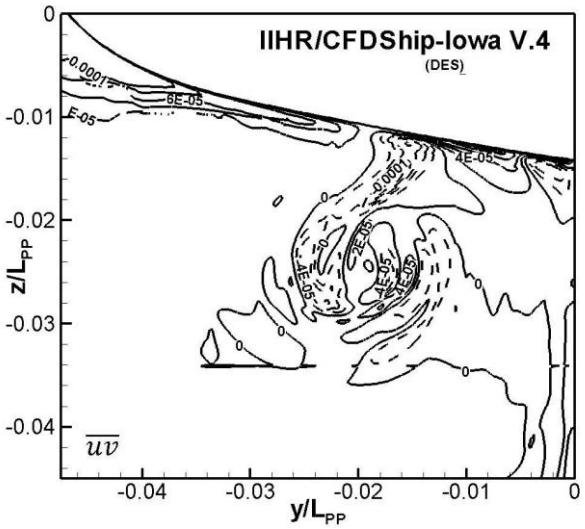

IIHR-CFDShip-IowaV4 (DES)

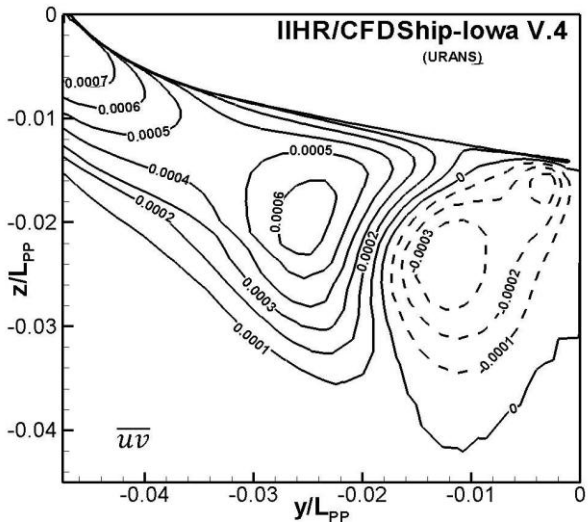

IIHR-CFDShip-IowaV4 (URANS)

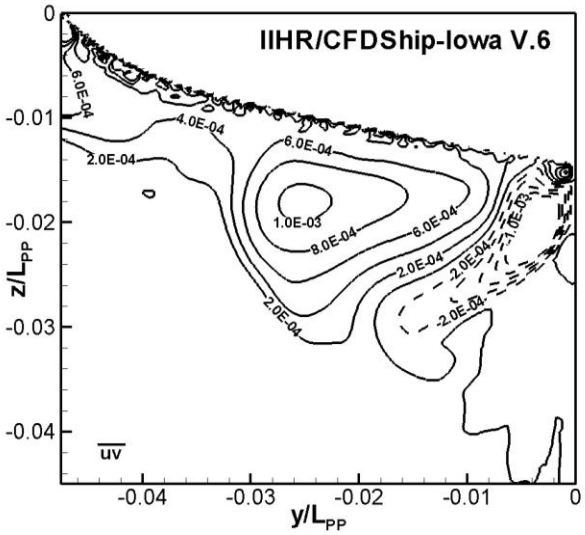

IIHR-CFDShip-IowaV6

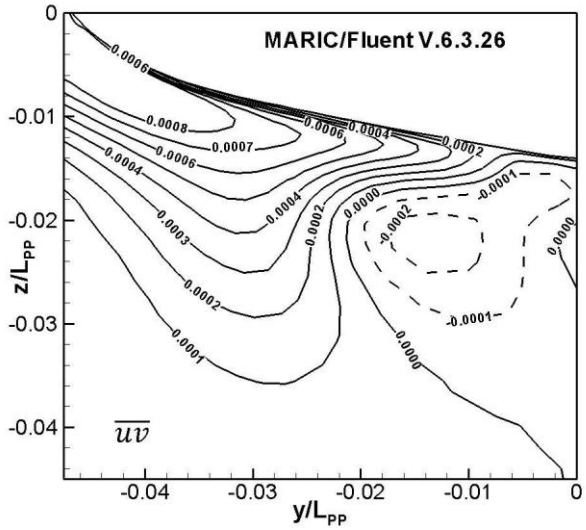

MARIC-FLUENT6.3.26

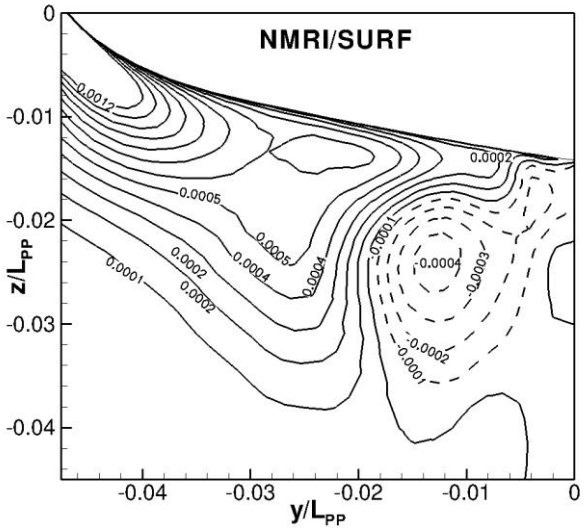

NMRI-SURF

Fig. 3.1b-7 $\overline{uv}$ contours at $x/L_{PP} = 0.935$ [$\Delta\overline{uv} = 1\times10^{-4}$]
(Solid lines: positive (+) values; Dashed lines: negative (-) values)

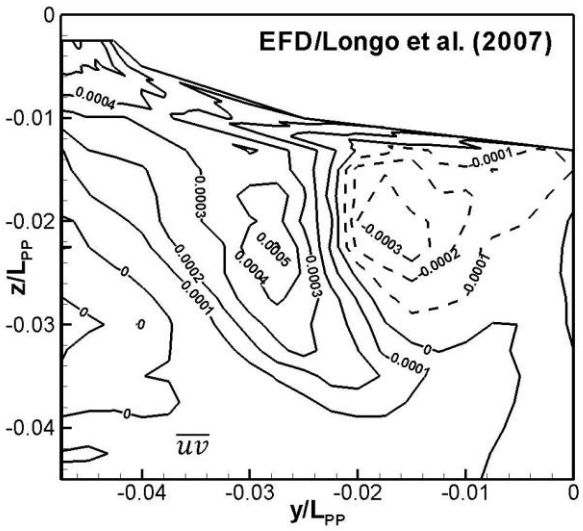

Experiment (IIHR, Longo et al. 2007)

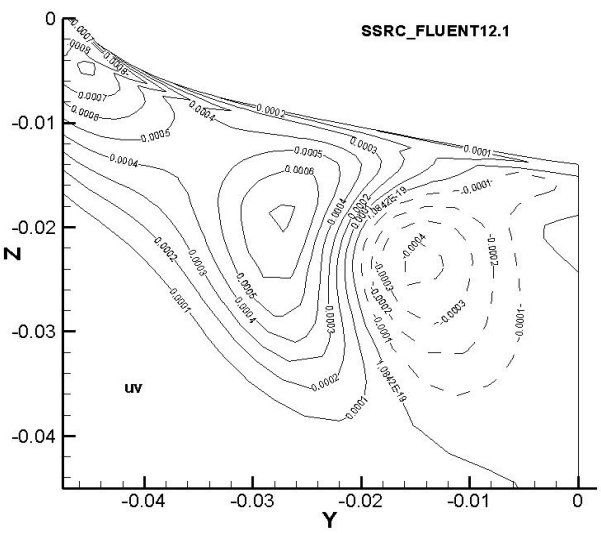

SSRC-FLUENT12.1

Fig. 3.1b-7 $\overline{uv}$ contours at $x/L_{PP} = 0.935$ [$\Delta\overline{uv} = 1\times10^{-4}$]
(Solid lines: positive (+) values; Dashed lines: negative (-) values)

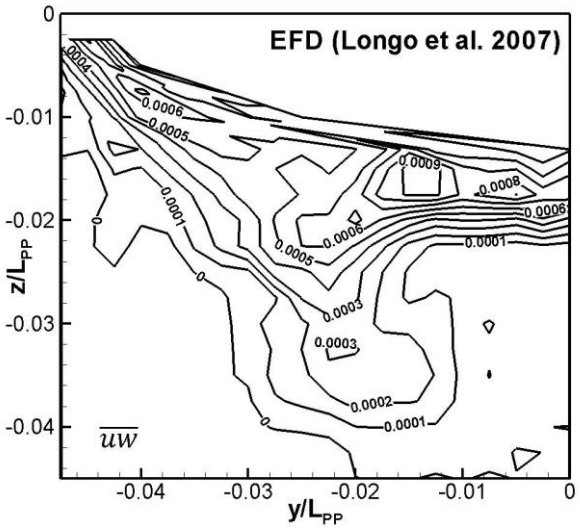

Experiment (IIHR, Longo et al. 2007)

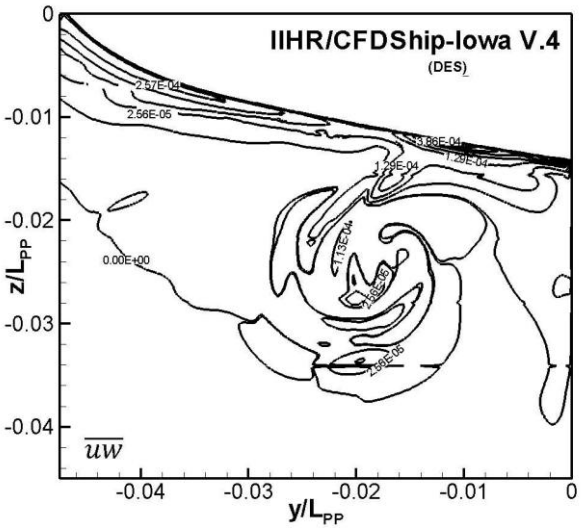

IIHR-CFDShip-IowaV4 (DES)

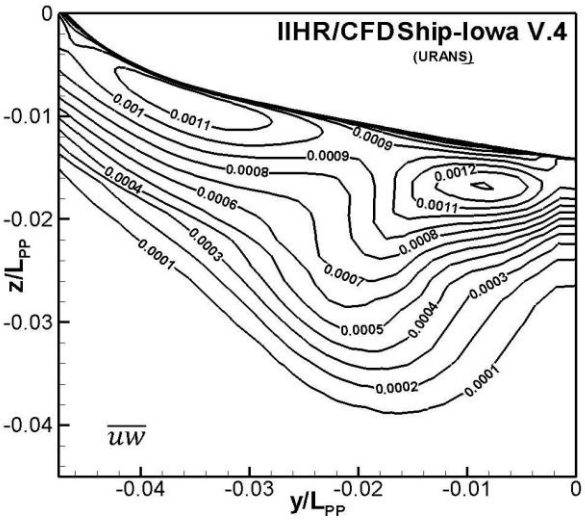

IIHR-CFDShip-IowaV4 (URANS)

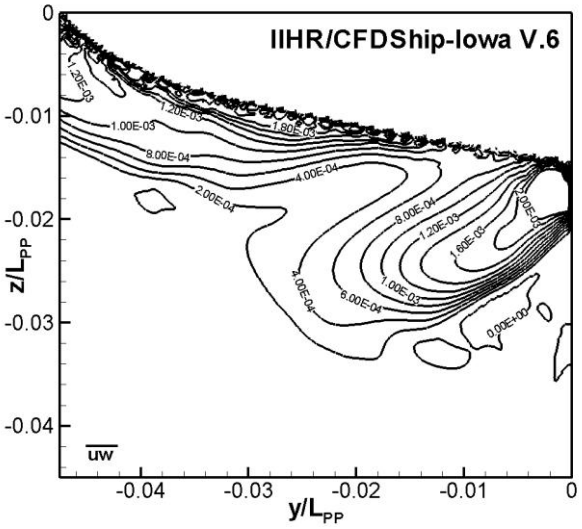

IIHR-CFDShip-IowaV6

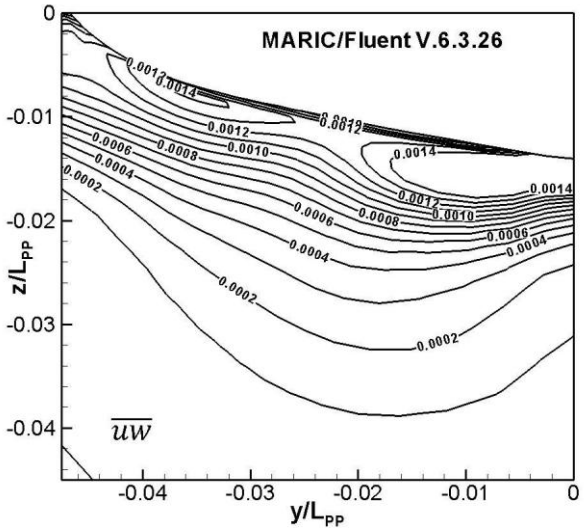

MARIC-FLUENT6.3.26

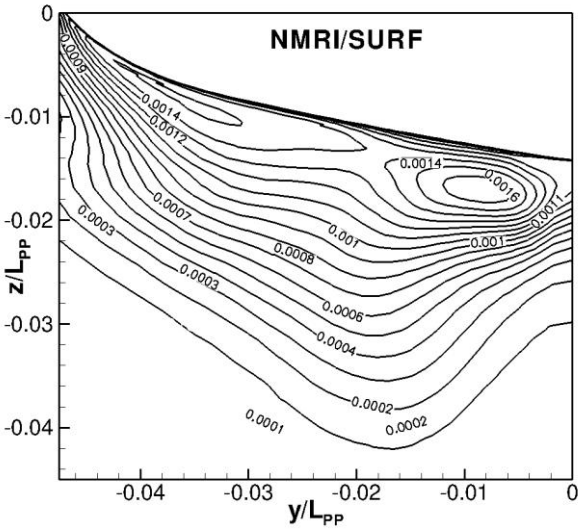

NMRI-SURF

Fig. 3.1b-8 $\overline{uw}$ contours at $x/L_{PP} = 0.935$ [$\Delta\overline{uw} = 1\times10^{-4}$]

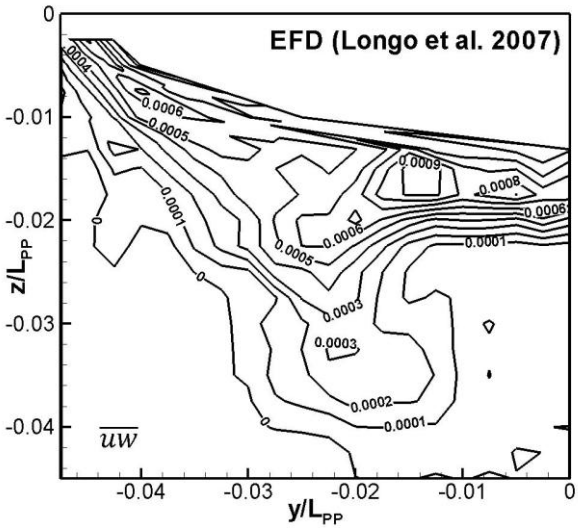

Experiment (IIHR, Longo et al. 2007)

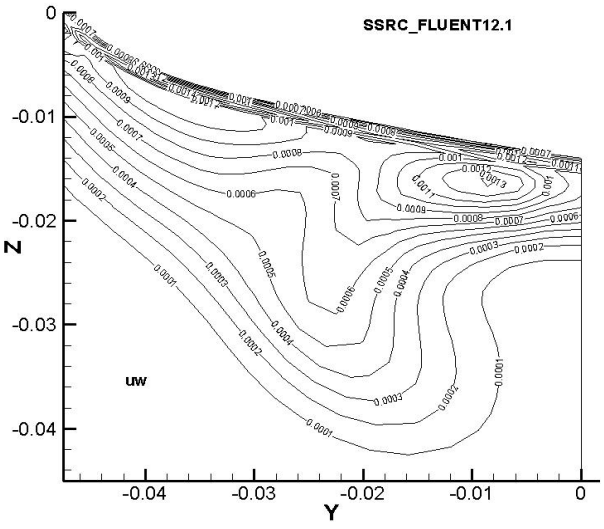

SSRC-FLUENT12.1

Fig. 3.1b-8 $\overline{uw}$ contours at $x/L_{PP} = 0.935$ [$\Delta\overline{uw} = 1\times10^{-4}$]

Test Case 3.2

Table 3.2-T123-0 Computations information and V&V method
Table 3.2-T123-1 Computed C_T, C_F, C_R of different grid densities at Fr = 0.138
Table 3.2-T123-2 V&V results for C_T, C_F and C_R at Fr = 0.138
Table 3.2-T123-3 Computed Sinkage (σ) and Trim (τ) of different grid densities at Fr = 0.138
Table 3.2-T123-4 V&V results for Sinkage (σ) and Trim (τ) at Fr = 0.138
Table 3.2-T123-5 Computed C_T, C_F, C_R of different grid densities at Fr = 0.28
Table 3.2-T123-6 V&V results for C_T, C_F and C_R at Fr = 0.28
Table 3.2-T123-7 Computed Sinkage (σ) and Trim (τ) of different grid densities at Fr = 0.28
Table 3.2-T123-8 V&V results for Sinkage (σ) and Trim (τ) at Fr = 0.28
Table 3.2-T123-9 Computed C_T, C_F, C_R of different grid densities at Fr = 0.41
Table 3.2-T123-10 V&V results for C_T, C_F and C_R at Fr = 0.41
Table 3.2-T123-11 Computed Sinkage (σ) and Trim (τ) of different grid densities at Fr = 0.41
Table 3.2-T123-12 V&V results for Sinkage (σ) and Trim (τ) at Fr = 0.41

Table 3.2-T123-0: Computations information and V&V method

Organization (Code)	**V&V method (including the determination of U_I)**
CSSRC (FLUENT6.3)	without V&V study
MARIC (FLUENT6.3)	without V&V study
MARIN (PARNASSOS)	V&V study for Fr=0.28 only
NavyFOAM (NavyFOAM)	without V&V study
NSWC-PC (CFDSHIPV4.5)	without V&V study
UoGe (STAR-CCM+)	without V&V study

Table 3.2-T123-1: Computed C_T, C_F, C_R of different grid densities at Fr = 0.138

Organization (Code)	r_G		C_T ($\times 10^{-3}$)					C_F ($\times 10^{-3}$)					C_R ($\times 10^{-3}$)				
			Grid #5	Grid #4	Grid #3	Grid #2	Grid #1	Grid #5	Grid #4	Grid #3	Grid #2	Grid #1	Grid #5	Grid #4	Grid #3	Grid #2	Grid #1
EFD (INSEAN)	-	*D*	3.89					3.29 (ITTC-57) *					0.605				
CSSRC (FLUENT6.3)	-	*S*	-	-	-	-	3.982	-	-	-	-	3.303	-	-	-	-	0.679
		E%*D*	-	-	-	-	-2.36	-	-	-	-	-0.39	-	-	-	-	-12.23
MARIC (FLUENT6.3)	-	*S*	-	-	-	-	3.880	-	-	-	-	3.217	-	-	-	-	0.663
		E%*D*	-	-	-	-	0.26	-	-	-	-	2.22	-	-	-	-	-9.59
MARIN (PARNASSOS)	-	*S*	-	-	-	-	-	-	-	-	-	-	-	-	-	-	-
		E%*D*	-	-	-	-	-	-	-	-	-	-	-	-	-	-	-
NavyFOAM (NavyFOAM)	-	*S*	-	-	-	-	4.17	-	-	-	-	-	-	-	-	-	-
		E%*D*	-	-	-	-	-7.20	-	-	-	-	-	-	-	-	-	-
NSWC-PC (CFDSHIPV4.5)	-	*S*	-	-	-	-	3.790	-	-	-	-	3.230	-	-	-	-	0.560
		E%*D*	-	-	-	-	2.50	-	-	-	-	1.80	-	-	-	-	7.40
UoGe (STAR-CCM+)	-	*S*	-	-	-	4.166	-	-	-	-	3.149	-	-	-	-	1.017	-
		E%*D*	-	-	-	-7.09	-	-	-	-	4.28	-	-	-	-	-68.05	-

* $C_F = 0.075 / \left(\log_{10} Re - 2\right)^2$ (ITTC 1957 Model-Ship Correlation Line)

E%*D* = (*D*-*S*)/*D*×100

Table 3.2-T123-2: V&V results for C_T, C_F and C_R at Fr = 0.138

Organization (Code)	r_G	C_T						C_F						C_R					
		ε_{12} %S_1	$\frac{U_I}{\varepsilon_{12}}$	$\frac{P_G}{P_{G,th}}$	U_G %S_1	U_D %D	U_V%	ε_{12} %S_1	$\frac{U_I}{\varepsilon_{12}}$	$\frac{P_G}{P_{G,th}}$	U_G %S_1	U_D %D	U_V%	ε_{12} %S_1	$\frac{U_I}{\varepsilon_{12}}$	$\frac{P_G}{P_{G,th}}$	U_G %S_1	U_D %D	U_V%
CSSRC (FLUENT6.3)	-	-	-	-	-	1.32	-	-	-	-	-			-	-	-	-		
MARIC (FLUENT6.3)	-	-	-	-	-		-	-	-	-	-			-	-	-	-		
MARIN (PARNASSOS)	-	-	-	-	-		-	-	-	-	-			-	-	-	-		
NavyFOAM (NavyFOAM)	-	-	-	-	-		-	-	-	-	-			-	-	-	-		
NSWC-PC (CFDSHIPV4.5)	-	0.05	-	-	-		-	0.0009	-	-	-			0.04	-	-	-		
UoGe (STAR-CCM+)	-	-	-	-	-		-	-	-	-	-			-	-	-	-		

$\varepsilon_{12}\%S_1 = |(S_1-S_2)/S_1|\times 100$; $U_{SN} = \sqrt{U_I^2 + U_G^2}$; $U_V = \sqrt{U_D^2 + U_{SN}^2}$

Table 3.2-T123-3: Computed Sinkage (σ) and Trim (τ) of different grid densities at Fr = 0.138

Organization (Code)	r_G		Sinkage $\sigma\times10^3$ (m)					Trim τ °				
			Grid #5	Grid #4	Grid #3	Grid #2	Grid #1	Grid #5	Grid #4	Grid #3	Grid #2	Grid #1
EFD (INSEAN)	-	*D*	-0.504					-0.028				
CSSRC (FLUENT6.3)	-	*S*	-	-	-	-	-0.441	-	-	-	-	-0.022
		E%D	-	-	-	-	12.50	-	-	-	-	21.43
MARIC (FLUENT6.3)	-	*S*	-	-	-	-	-0.320	-	-	-	-	-0.0225
		E%D	-	-	-	-	36.51	-	-	-	-	19.64
MARIN (PARNASSOS)	-	*S*	-	-	-	-	-	-	-	-	-	-
		E%D	-	-	-	-	-	-	-	-	-	-
NavyFOAM (NavyFOAM)		*S*	-	-	-	-	-0.2407	-	-	-	-	0.029
		E%D	-	-	-	-	52.24	-	-	-	-	203.57
NSWC-PC (CFDSHIPV4.5)	-	*S*	-	-	-	-	-0.435	-	-	-	-	-0.027
		E%D	-	-	-	-	13.60	-	-	-	-	3.80
UoGe (STAR-CCM+)	-	*S*	-	-	-	-0.291	-	-	-	-	0.133	-
		E%D	-	-	-	42.16	-	-	-	-	573.49	-

$E\%D = (D\text{-}S)/D\times100$

Table 3.2-T123-4: V&V results for Sinkage (σ) and Trim (τ) at Fr = 0.138

Organization (Code)	r_G	Sinkage σ						Trim τ °					
		ε_{12} %S_1	$\frac{U_I}{\varepsilon_{12}}$	$\frac{P_G}{P_{G,th}}$	U_G %S_1	U_D %D	U_V%	ε_{12} %S_1	$\frac{U_I}{\varepsilon_{12}}$	$\frac{P_G}{P_{G,th}}$	U_G %S_1	U_D %D	U_V%
CSSRC (FLUENT6.3)	-	-	-	-	-	6.57	-	-	-	-	-	7.64	-
MARIC (FLUENT6.3)	-	-	-	-	-		-	-	-	-	-		-
MARIN (PARNASSOS)	-	-	-	-	-		-	-	-	-	-		-
NavyFOAM (NavyFOAM)	-	-	-	-	-		-	-	-	-	-		-
NSWC-PC (CFDSHIPV4.5)	-	0.02	-	-	-		-	0.02	-	-	-		-
UoGe (STAR-CCM+)	-	-	-	-	-		-	-	-	-	-		-

$\varepsilon_{12}\%S_1 = |(S_1-S_2)/S_1|\times 100$; $U_{SN} = \sqrt{U_I^2 + U_G^2}$; $U_V = \sqrt{U_D^2 + U_{SN}^2}$

Table 3.2-T123-5: Computed C_T, C_F, C_R of different grid densities at Fr = 0.28

Organization (Code)	r_G		C_T ($\times 10^{-3}$)					C_F ($\times 10^{-3}$)					C_R ($\times 10^{-3}$)				
			Grid #5	Grid #4	Grid #3	Grid #2	Grid #1	Grid #5	Grid #4	Grid #3	Grid #2	Grid #1	Grid #5	Grid #4	Grid #3	Grid #2	Grid #1
EFD (INSEAN)	-	*D*	4.23					2.91 (ITTC-57) *					1.32				
CSSRC (FLUENT6.3)	-	*S*	-	-	-	-	4.235	-	-	-	-	2.911	-	-	-	-	1.324
		E%D	-	-	-	-	-0.12	-	-	-	-	-0.03	-	-	-	-	-0.3
MARIC (FLUENT6.3)	-	*S*	-	-	-	-	4.210	-	-	-	-	3.011	-	-	-	-	1.199
		E%D	-	-	-	-	0.47	-	-	-	-	-3.47	-	-	-	-	9.17
MARIN (PARNASSOS)	2	*S*	-	4.310	4.290	4.250	4.230	-	-	-	-	-	-	1.400	1.380	1.340	1.320
		E%D	-	-1.90	-1.40	-0.50	0.00	-	-	-	-	-	-	-6.10	-4.50	-1.50	0.00
NavyFOAM (NavyFOAM)	-	*S*	-	-	-	-	4.19	-	-	-	-	-	-	-	-	-	-
		E%D	-	-	-	-	0.95	-	-	-	-	-	-	-	-	-	-
NSWC-PC (CFDSHIPV4.5)	-	*S*	-	-	-	-	4.380	-	-	-	-	2.910	-	-	-	-	1.470
		E%D	-	-	-	-	-3.50	-	-	-	-	0.20	-	-	-	-	-11.30
UoGe (STAR-CCM+)	-	*S*	-	-	-	4.112	-	-	-	-	2.848	-	-	-	-	1.264	-
		E%D	-	-	-	2.79	-	-	-	-	2.12	-	-	-	-	4.27	-

* $C_F = 0.075 / (\log_{10} Re - 2)^2$ (ITTC 1957 Model-Ship Correlation Line)

$E\%D = (D\text{-}S)/D \times 100$

Table 3.2-T123-6: V&V results for C_T, C_F and C_R at Fr = 0.28

Organization (Code)	r_G	C_T						C_F						C_R					
		ε_{12} %S_1	$\frac{U_I}{\varepsilon_{12}}$	$\frac{P_G}{P_{G,th}}$	U_G %S_1	U_D %D	U_V%	ε_{12} %S_1	$\frac{U_I}{\varepsilon_{12}}$	$\frac{P_G}{P_{G,th}}$	U_G %S_1	U_D %D	U_V%	ε_{12} %S_1	$\frac{U_I}{\varepsilon_{12}}$	$\frac{P_G}{P_{G,th}}$	U_G %S_1	U_D %D	U_V%
CSSRC (FLUENT6.3)	-	-	-	-	-	0.64	-	-	-	-	-			-	-	-	-		
MARIC (FLUENT6.3)	-	-	-	-	-		-	-	-	-	-			-	-	-	-		
MARIN (PARNASSOS)	2	1.40	0.01%	-	1.40		1.54	-	-	-	-			-	-	-	-		
NavyFOAM (NavyFOAM)	-	-	-	-	-		-	-	-	-	-			-	-	-	-		
NSWC-PC (CFDSHIPV4.5)	-	0.03	-	-	-		-	0.0004	-	-	-			0.03	-	-	-		
UoGe (STAR-CCM+)	-	-	-	-	-		-	-	-	-	-			-	-	-	-		

$\varepsilon_{12}\%S_1 = |(S_1-S_2)/S_1|\times 100$; $U_{SN} = \sqrt{U_I^2 + U_G^2}$; $U_V = \sqrt{U_D^2 + U_{SN}^2}$

Table 3.2-T123-7: Computed Sinkage (σ) and Trim (τ) of different grid densities at Fr = 0.28

Organization (Code)	r_G		Sinkage $\sigma\times10^3$ (m)					Trim τ °				
			Grid #5	Grid #4	Grid #3	Grid #2	Grid #1	Grid #5	Grid #4	Grid #3	Grid #2	Grid #1
EFD (INSEAN)	-	*D*	-1.82					-0.108				
CSSRC (FLUENT6.3)	-	*S*	-	-	-	-	-1.920	-	-	-	-	-0.109
		E%D	-	-	-	-	-5.49	-	-	-	-	-0.93
MARIC (FLUENT6.3)	-	*S*	-	-	-	-	-1.490	-	-	-	-	-0.094
		E%D	-	-	-	-	18.13	-	-	-	-	12.96
MARIN (PARNASSOS)	2	*S*	-	-1.760	-1.750	-1.750	-1.760	-	-0.085	-0.089	-0.096	-0.092
		E%D	-	-3.30	-3.80	-3.80	-3.30	-	-21.30	-17.60	-11.10	-14.80
NavyFOAM (NavyFOAM)	-	*S*	-	-	-	-	-1.64	-	-	-	-	-0.045
		E%D	-	-	-	-	9.90	-	-	-	-	58.33
NSWC-PC (CFDSHIPV4.5)	-	*S*	-	-	-	-	-2.010	-	-	-	-	-0.116
		E%D	-	-	-	-	-10.40	-	-	-	-	-7.70
UoGe (STAR-CCM+)	-	*S*	-	-	-	-1.766	-	-	-	-	0.045	-
		E%D	-	-	-	2.99	-	-	-	-	141.80	-

$E\%D = (D\text{-}S)/D\times100$

Table 3.2-T123-8: V&V results for Sinkage (σ) and Trim (τ) at Fr = 0.28

Organization (Code)	r_G	Sinkage σ						Trim τ °					
		ε_{12} %S_1	$\frac{U_I}{\varepsilon_{12}}$	$\frac{P_G}{P_{G,th}}$	U_G %S_1	U_D %D	U_V%	ε_{12} %S_1	$\frac{U_I}{\varepsilon_{12}}$	$\frac{P_G}{P_{G,th}}$	U_G %S_1	U_D %D	U_V%
CSSRC (FLUENT6.3)	-	-	-	-	-	4.71	-	-	-	-	-	4.70	-
MARIC (FLUENT6.3)	-	-	-	-	-		-	-	-	-	-		-
MARIN (PARNASSOS)	2	0.50	0.01%	-	0.50		4.74	3.30	0.30%	-	3.30		5.74
NavyFOAM (NavyFOAM)	-	-	-	-	-		-	-	-	-	-		-
NSWC-PC (CFDSHIPV4.5)	-	0.01	-	-	-		-	0.008	-	-	-		-
UoGe (STAR-CCM+)	-	-	-	-	-		-	-	-	-	-		-

$\varepsilon_{12}\%S_1 = |(S_1\text{-}S_2)/S_1|\times 100$; $U_{SN} = \sqrt{U_I^2 + U_G^2}$; $U_V = \sqrt{U_D^2 + U_{SN}^2}$

Table 3.2-T123-9: Computed C_T, C_F, C_R of different grid densities at Fr = 0.41

Organization (Code)	r_G		C_T ($\times 10^{-3}$)					C_F ($\times 10^{-3}$)					C_R ($\times 10^{-3}$)				
			Grid #5	Grid #4	Grid #3	Grid #2	Grid #1	Grid #5	Grid #4	Grid #3	Grid #2	Grid #1	Grid #5	Grid #4	Grid #3	Grid #2	Grid #1
EFD (INSEAN)	-	*D*	6.67					2.73 (ITTC-57) *					3.94				
CSSRC (FLUENT6.3)	-	*S*	-	-	-	-	6.530	-	-	-	-	2.810	-	-	-	-	3.720
		E%D	-	-	-	-	2.10	-	-	-	-	-2.93	-	-	-	-	5.58
MARIC (FLUENT6.3)	-	*S*	-	-	-	-	6.410	-	-	-	-	2.952	-	-	-	-	3.458
		E%D	-	-	-	-	3.90	-	-	-	-	-8.13	-	-	-	-	12.23
MARIN (PARNASSOS)	-	*S*	-	-	-	-	-	-	-	-	-	-	-	-	-	-	-
		E%D	-	-	-	-	-	-	-	-	-	-	-	-	-	-	-
NavyFOAM (NavyFOAM)	-	*S*	-	-	-	-	6.30	-	-	-	-	-	-	-	-	-	-
		E%D	-	-	-	-	5.55	-	-	-	-	-	-	-	-	-	-
NSWC-PC (CFDSHIPV4.5)	-	*S*	-	-	-	-	6.370	-	-	-	-	2.704	-	-	-	-	3.660
		E%D	-	-	-	-	4.50	-	-	-	-	0.90	-	-	-	-	6.90
UoGe (STAR-CCM+)	-	*S*	-	-	-	6.301	-	-	-	-	2.811	-	-	-	-	3.491	-
		E%D	-	-	-	5.53	-	-	-	-	-2.96	-	-	-	-	11.40	-

* $C_F = 0.075 / \left(\log_{10} Re - 2\right)^2$ (ITTC 1957 Model-Ship Correlation Line)

$E\%D = (D\text{-}S)/D \times 100$

Table 3.2-T123-10: V&V results for C_T, C_F and C_R at $Fr = 0.41$

Organization (Code)	r_G	C_T						C_F						C_R					
		ε_{12} $\%S_1$	$\frac{U_I}{\varepsilon_{12}}$	$\frac{P_G}{P_{G,th}}$	U_G $\%S_1$	U_D $\%D$	$U_V\%$	ε_{12} $\%S_1$	$\frac{U_I}{\varepsilon_{12}}$	$\frac{P_G}{P_{G,th}}$	U_G $\%S_1$	U_D $\%D$	$U_V\%$	ε_{12} $\%S_1$	$\frac{U_I}{\varepsilon_{12}}$	$\frac{P_G}{P_{G,th}}$	U_G $\%S_1$	U_D $\%D$	$U_V\%$
CSSRC (FLUENT6.3)	-	-	-	-	-	0.61	-	-	-	-	-			-	-	-	-		
MARIC (FLUENT6.3)	-	-	-	-	-		-	-	-	-	-			-	-	-	-		
MARIN (PARNASSOS)	-	-	-	-	-		-	-	-	-	-			-	-	-	-		
NavyFOAM (NavyFOAM)	-	-	-	-	-		-	-	-	-	-			-	-	-	-		
NSWC-PC (CFDSHIPV4.5)	-	0.04	-	-	-		-	0.0009	-	-	-			0.03	-	-	-		
UoGe (STAR-CCM+)	-	-	-	-	-		-	-	-	-	-			-	-	-	-		

$\varepsilon_{12}\%S_1 = |(S_1-S_2)/S_1|\times 100$; $U_{SN} = \sqrt{U_I^2 + U_G^2}$; $U_V = \sqrt{U_D^2 + U_{SN}^2}$

Table 3.2-T123-11: Computed Sinkage (σ) and Trim (τ) of different grid densities at Fr = 0.41

Organization (Code)	r_G		Sinkage $\sigma\times10^3$ (m)					Trim τ °				
			Grid #5	Grid #4	Grid #3	Grid #2	Grid #1	Grid #5	Grid #4	Grid #3	Grid #2	Grid #1
EFD (INSEAN)	-	*D*	-4.7					0.421				
CSSRC (FLUENT6.3)	-	*S*	-	-	-	-	-4.530	-	-	-	-	0.395
		E%D	-	-	-	-	3.62	-	-	-	-	6.18
MARIC (FLUENT6.3)	-	*S*	-	-	-	-	-3.600	-	-	-	-	0.500
		E%D	-	-	-	-	23.40	-	-	-	-	-18.76
MARIN (PARNASSOS)	-	*S*	-	-	-	-	-	-	-	-	-	-
		E%D	-	-	-	-	-	-	-	-	-	-
NavyFOAM (NavyFOAM)	-	*S*	-	-	-	-	-4.23	-	-	-	-	0.45
		E%D	-	-	-	-	10.00	-	-	-	-	-6.89
NSWC-PC (CFDSHIPV4.5)	-	*S*	-	-	-	-	-5.380	-	-	-	-	0.448
		E%D	-	-	-	-	-14.40	-	-	-	-	-6.40
University of Genova (StarCCM+)	-	*S*	-	-	-	-4.228	-	-	-	-	0.502	-
		E%D	-	-	-	10.05	-	-	-	-	-19.13	-

$E\%D = (D\text{-}S)/D\times100$

Table 3.2-T123-12: V&V results for Sinkage (σ) and Trim (τ) at Fr = 0.41

Organization (Code)	r_G	Sinkage σ						Trim τ °					
		ε_{12} %S_1	$\frac{U_I}{\varepsilon_{12}}$	$\frac{P_G}{P_{G,th}}$	U_G %S_1	U_D %D	U_V%	ε_{12} %S_1	$\frac{U_I}{\varepsilon_{12}}$	$\frac{P_G}{P_{G,th}}$	U_G %S_1	U_D %D	U_V%
CSSRC (FLUENT6.3)	-	-	-	-	-	2.93	-	-	-	-	-	0.87	-
MARIC (FLUENT6.3)	-	-	-	-	-		-	-	-	-	-		-
MARIN (PARNASSOS)	-	-	-	-	-		-	-	-	-	-		-
NavyFOAM (NavyFOAM)	-	-	-	-	-		-	-	-	-	-		-
NSWC-PC (CFDSHIPV4.5)	-	0.002	-	-	-		-	0.004	-	-	-		-
UoGe (STAR-CCM+)	-	-	-	-	-		-	-	-	-	-		-

$\varepsilon_{12}\%S_1 = |(S_1\text{-}S_2)/S_1|\times 100$; $U_{SN} = \sqrt{U_I^2 + U_G^2}$; $U_V = \sqrt{U_D^2 + U_{SN}^2}$

Test Case 3.5

Table 3.5-T 0th and 1st harmonic amplitudes and 1st harmonic phase of the resistance and moment coefficients

Figure 3.5-1-1 Time histories of total resistance coefficient (C_T)
Figure 3.5-1-2 Time histories of heave force coefficient (C_H)
Figure 3.5-1-3 Time histories of pitching moment coefficient (C_M)
Figure 3.5-2-1 Wave-elevation ζ_T contours at t/Te = 0
Figure 3.5-2-2 Wave-elevation ζ_T contours at t/Te = 1/4
Figure 3.5-2-3 Wave-elevation ζ_T contours at t/Te = 1/2
Figure 3.5-2-4 Wave-elevation ζ_T contours at t/Te = 3/4
Figure 3.5-3 Wave-elevation ζ_T contours: 0th amplitude
Figure 3.5-4 Wave-elevation ζ_T contours: 1st amplitude
Figure 3.5-5 Wave-elevation ζ_T contours: 1st phase
Figure 3.5-6-1 U contours at x/L_{PP} = 0.935, t/Te = 0
Figure 3.5-6-2 U contours at x/L_{PP} = 0.935, t/Te = 1/4
Figure 3.5-6-3 U contours at x/L_{PP} = 0.935, t/Te = 1/2
Figure 3.5-6-4 U contours at x/L_{PP} = 0.935, t/Te = 3/4
Figure 3.5-7-1 V contours at x/L_{PP} = 0.935, t/Te = 0
Figure 3.5-7-2 V contours at x/L_{PP} = 0.935, t/Te = 1/4
Figure 3.5-7-3 V contours at x/L_{PP} = 0.935, t/Te = 1/2
Figure 3.5-7-4 V contours at x/L_{PP} = 0.935, t/Te = 3/4
Figure 3.5-8-1 W contours at x/L_{PP} = 0.935, t/Te = 0
Figure 3.5-8-2 W contours at x/L_{PP} = 0.935, t/Te = 1/4
Figure 3.5-8-3 W contours at x/L_{PP} = 0.935, t/Te = 1/2
Figure 3.5-8-4 W contours at x/L_{PP} = 0.935, t/Te = 3/4
Figure 3.5-9-1 U contours of 0th amplitude at x/L_{PP} = 0.935
Figure 3.5-9-2 U contours of 1st amplitude at x/L_{PP} = 0.935
Figure 3.5-9-3 U contours of 1st phase at x/L_{PP} = 0.935
Figure 3.5-10-1 V contours of 0th amplitude at x/L_{PP} = 0.935
Figure 3.5-10-2 V contours of 1st amplitude at x/L_{PP} = 0.935
Figure 3.5-10-3 V contours of 1st phase at x/L_{PP} = 0.935
Figure 3.5-11-1 W contours of 0th amplitude at x/L_{PP} = 0.935
Figure 3.5-11-2 W contours of 1st amplitude at x/L_{PP} = 0.935
Figure 3.5-11-3 W contours of 1st phase at x/L_{PP} = 0.935

Table 3.5-T 0th and 1st harmonic amplitudes and 1st harmonic phase of the resistance and moment coefficients

Organization (Code)		C_T			C_H			C_M		
		0th Amplitude	1st Amplitude	1st Phase°	0th Amplitude	1st Amplitude	1st Phase°	0th Amplitude	1st Amplitude	1st Phase°
EFD (IIHR)	*D*	0.00462	0.00608	-63.3	-0.0334	0.0357	-140	-6.08×10-4	0.0108	-58.8
ECN (Icare)	*S*	0.00475	0.00711	-20.0	-0.0275	0.0425	-100	-0.00065	0.0136	-18.0
	E%*D*	-2.81	-16.94	68.40	17.66	-19.05	28.57	-6.91	-25.93	69.39
IIHR (CFDShip-Iowa V4)	*S*	0.00460	0.00622	-46.5	-0.0338	0.0379	-127	-5.90×10-4	0.0117	-40.8
	E%*D*	0.43	-2.30	26.54	-1.20	-6.16	9.29	2.96	-8.33	30.61
NMRI (SURF)	*S*	0.00473	0.00739	-25.1	-0.0314	0.0412	-110	-9.6×10-4	0.0137	-22.7
	E%*D*	-2.38	-21.55	-60.35	5.99	-15.41	-21.43	-57.90	-26.85	-61.39
SSRC (FLUENT12.1)	*S*	0.00534	0.00771	-26.3	-0.0332	0.0421	-99.9	-0.00186	0.0136	-26.1
	E%*D*	-15.58	-26.81	58.45	0.60	-17.93	28.64	-205.92	-25.93	55.61

$E\%D = (D-S)/D \times 100$

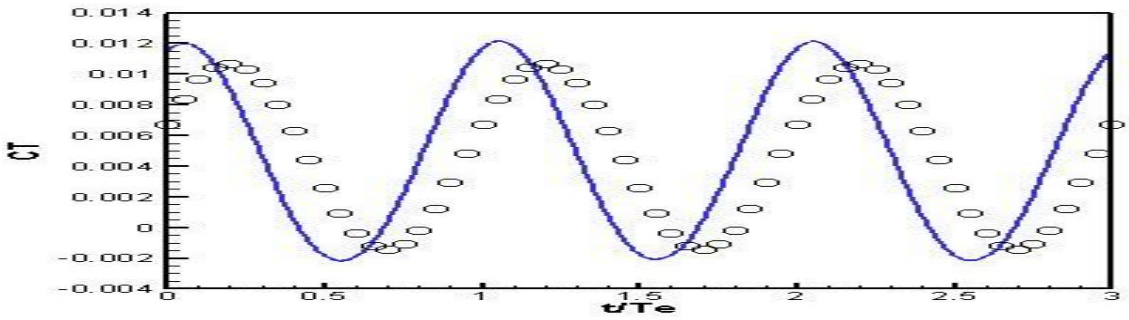

ECN-Icare

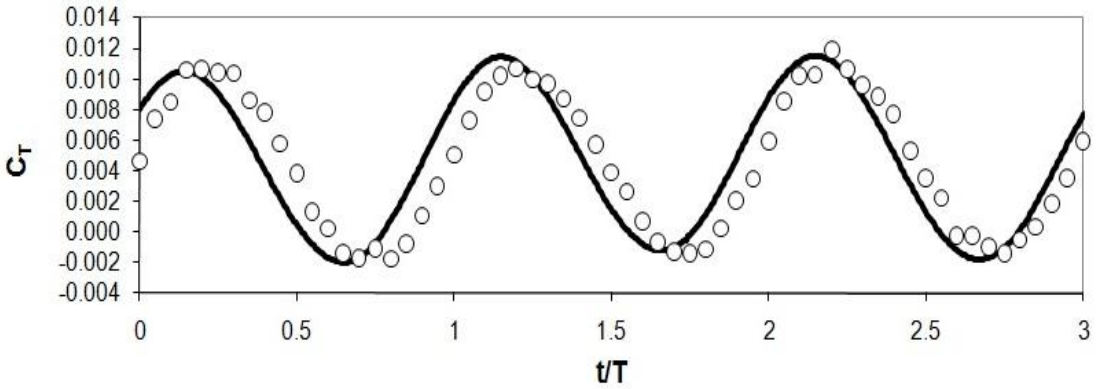

IIHR-CFDShipV4

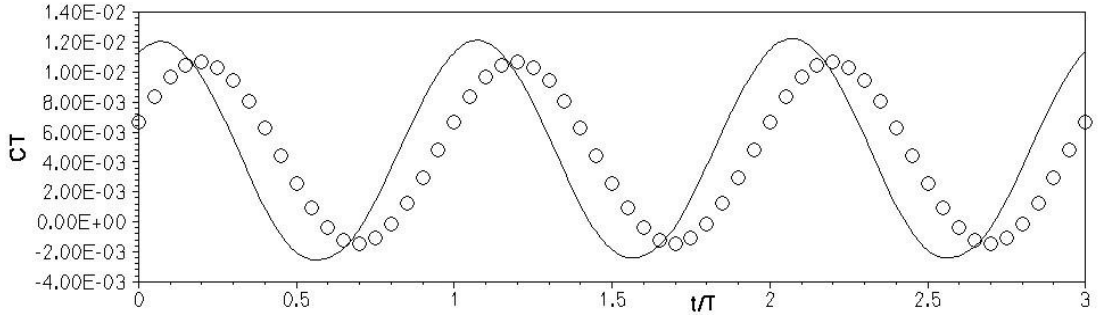

NMRI-SURF

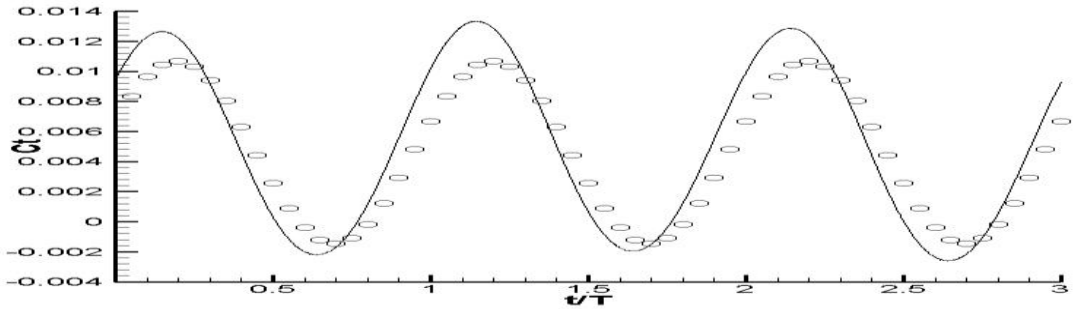

SSRC-FLUENT12.1

Fig. 3.5-1-1 Time histories of total resistance coefficient (C_T)
[CFD: solid line; EFD: open circles]

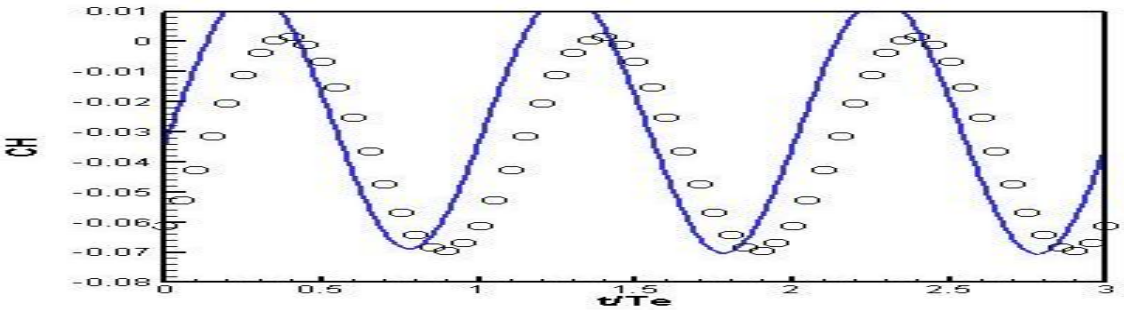

ECN-Icare

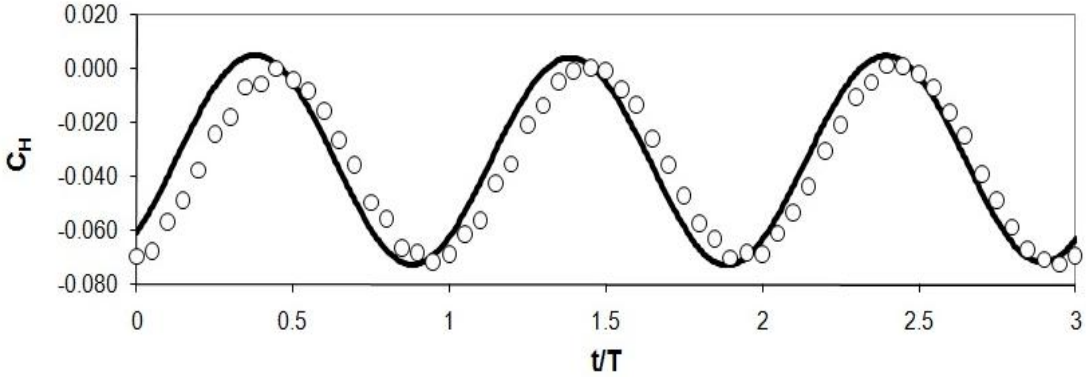

IIHR-CFDShipV4

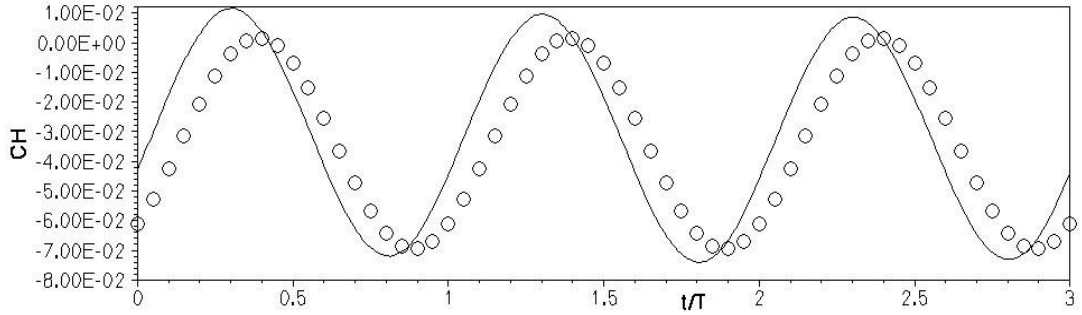

NMRI-SURF

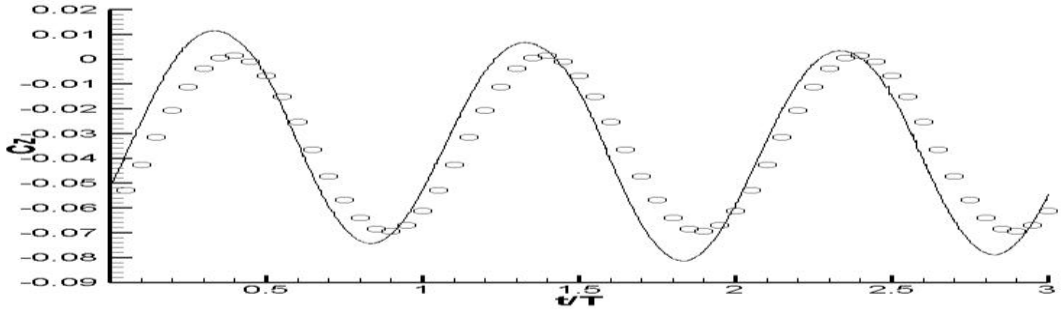

SSRC-FLUENT12.1

Fig. 3.5-1-2 Time histories of heave force coefficient (C_H)
[CFD: solid line; EFD: open circles]

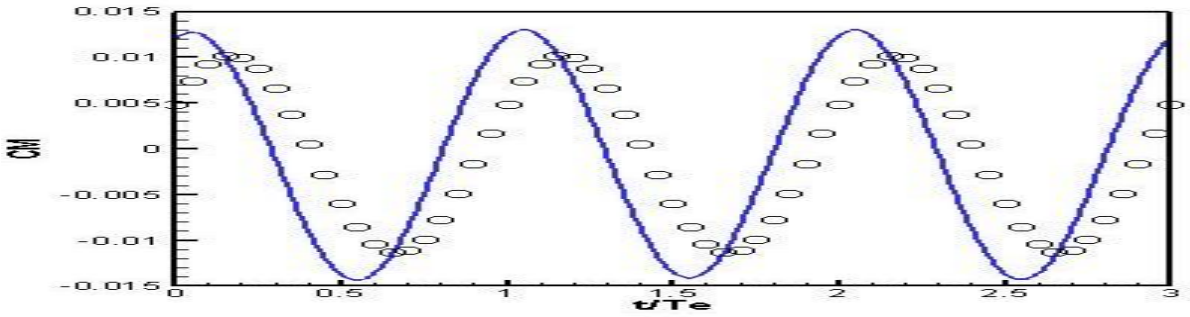

ECN-Icare

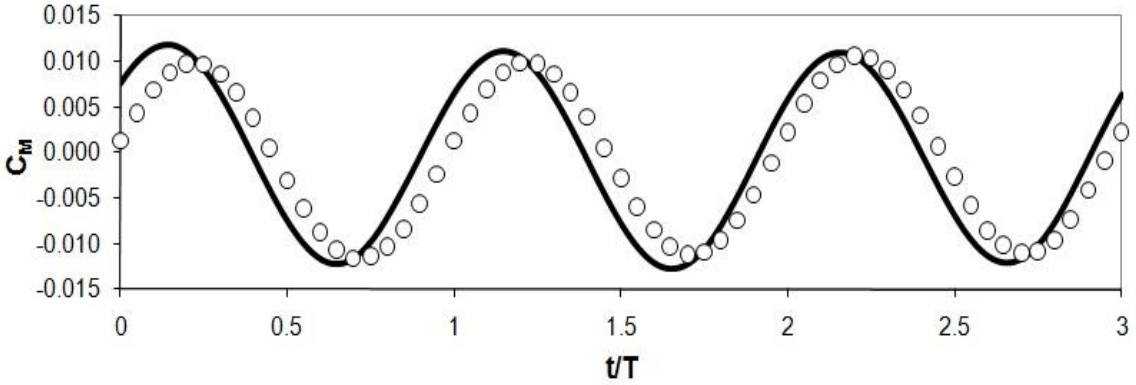

IIHR-CFDShipV4

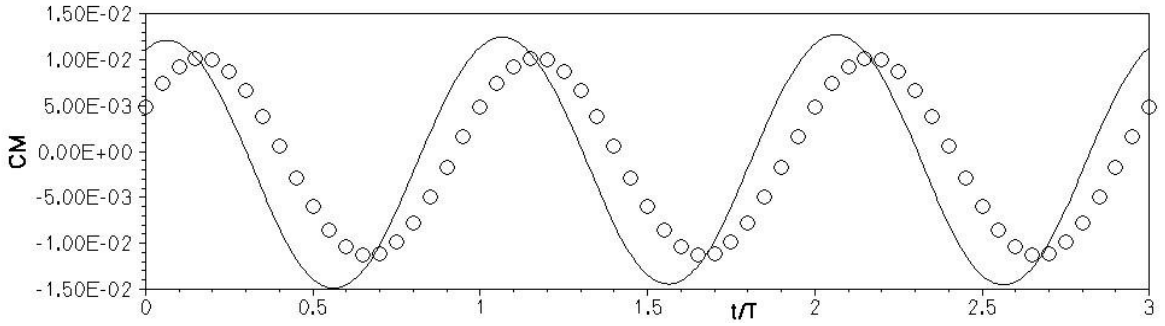

NMRI-SURF

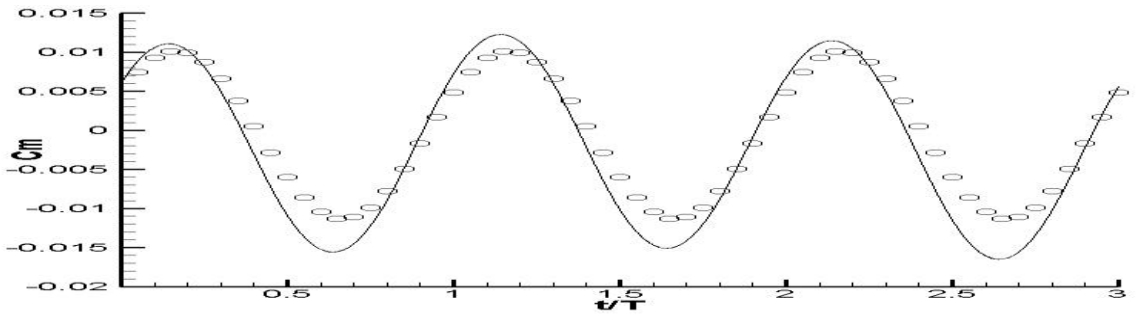

SSRC-FLUENT12.1

Fig. 3.5-1-3 Time histories of pitching moment coefficient (C_M)
[CFD: solid line; EFD: open circles]

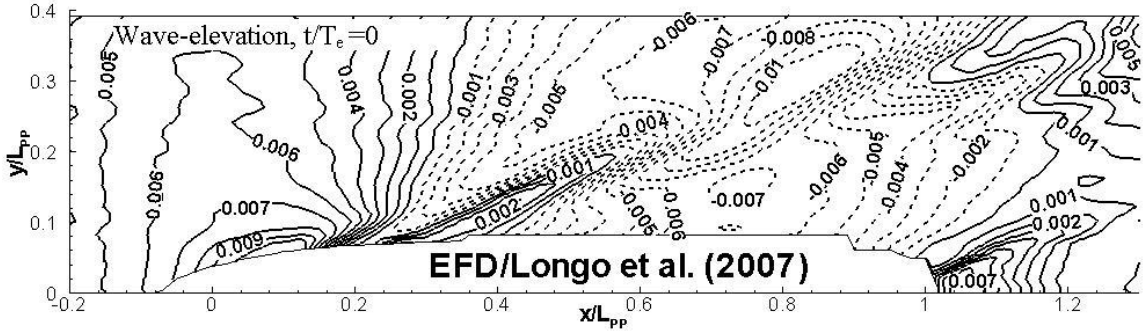

Experiment (IIHR, Longo et al. 2007)

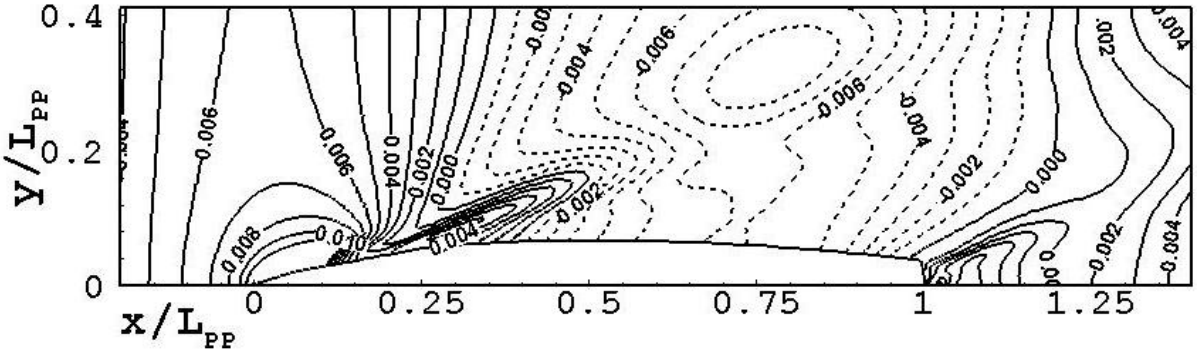

ECN-Icare

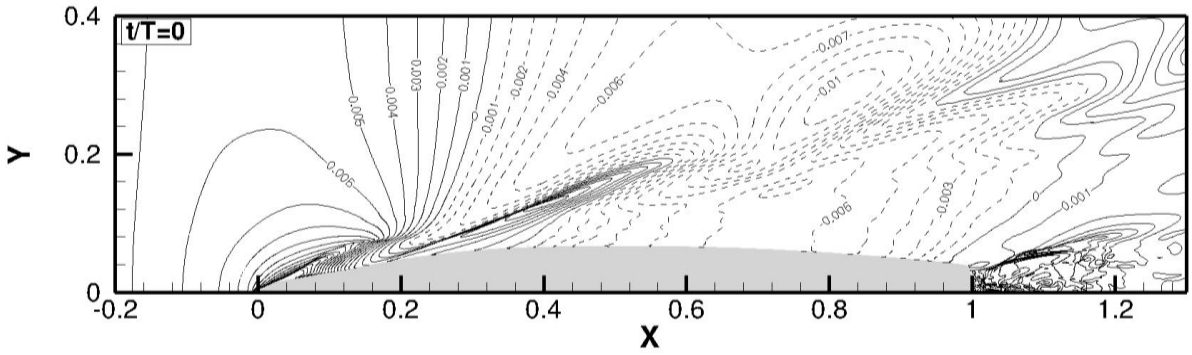

IIHR-CFDShipV4

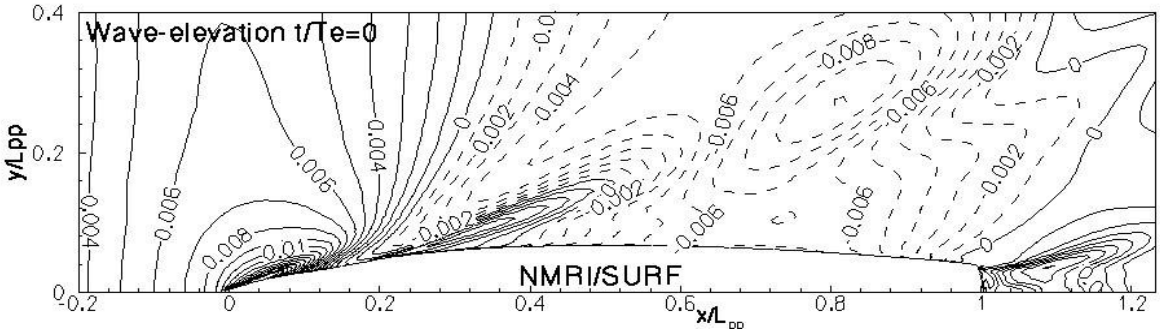

NMRI-SURF

Fig. 3.5-2-1 Wave-elevation ζ_T contours at $t/Te = 0$ [$\Delta z = 0.001$]
(Solid lines: positive (+) values; Dashed lines: negative (-) values)

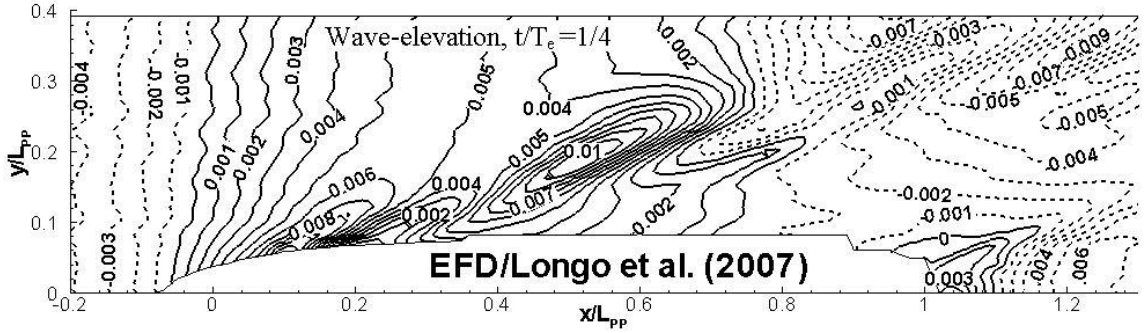

Experiment (IIHR, Longo et al. 2007)

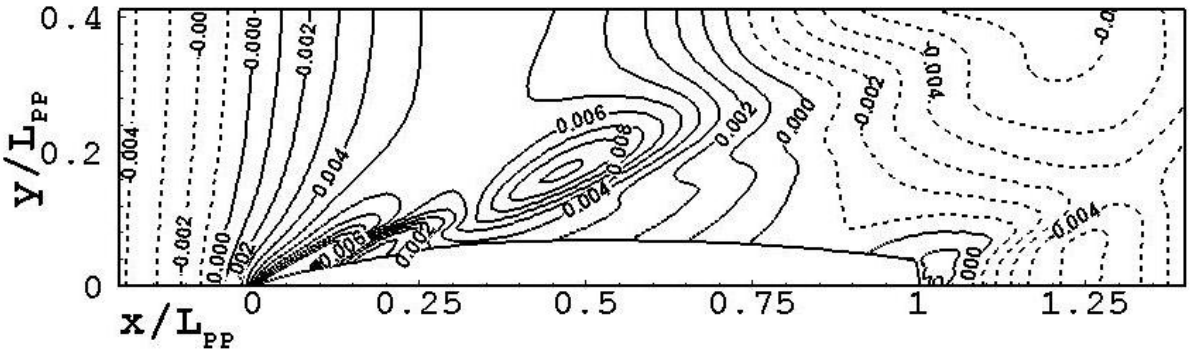

ECN-Icare

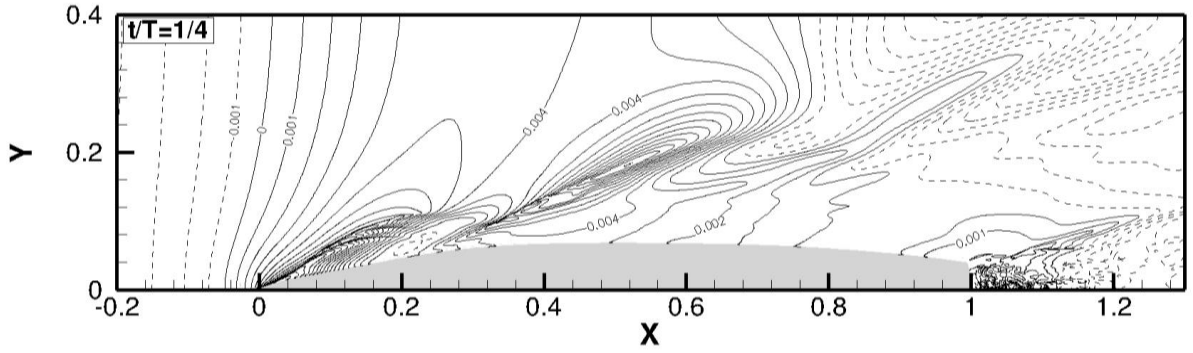

IIHR-CFDShipV4

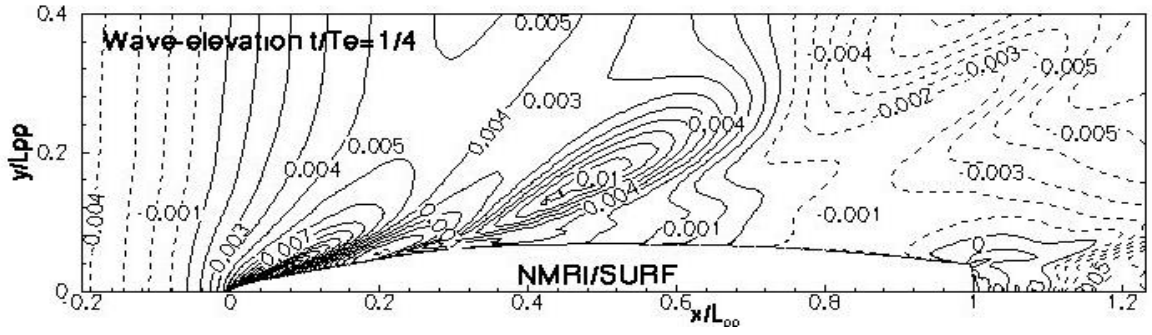

NMRI-SURF

Fig. 3.5-2-2 Wave-elevation ζ_T contours at t/Te = 1/4 [Δz = 0.001]
(Solid lines: positive (+) values; Dashed lines: negative (-) values)

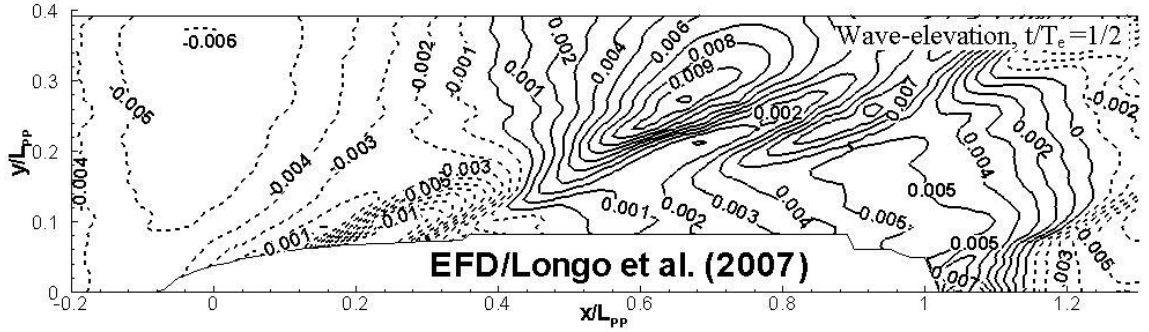

Experiment (IIHR, Longo et al. 2007)

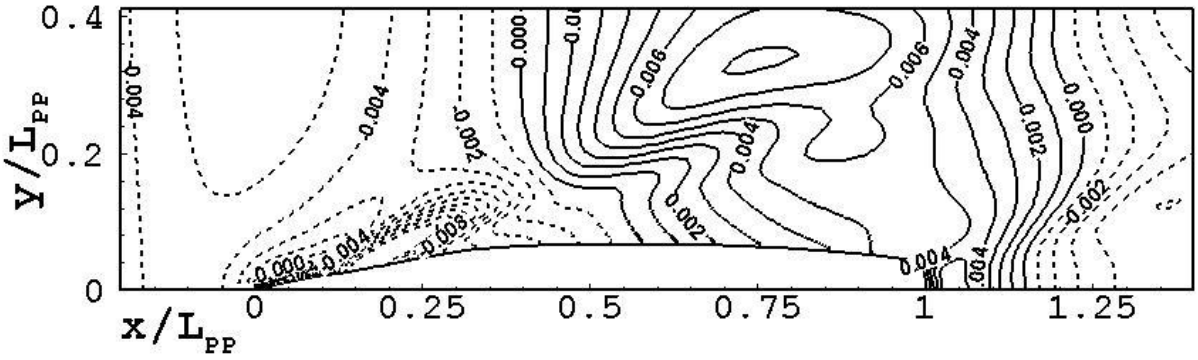

ECN-Icare

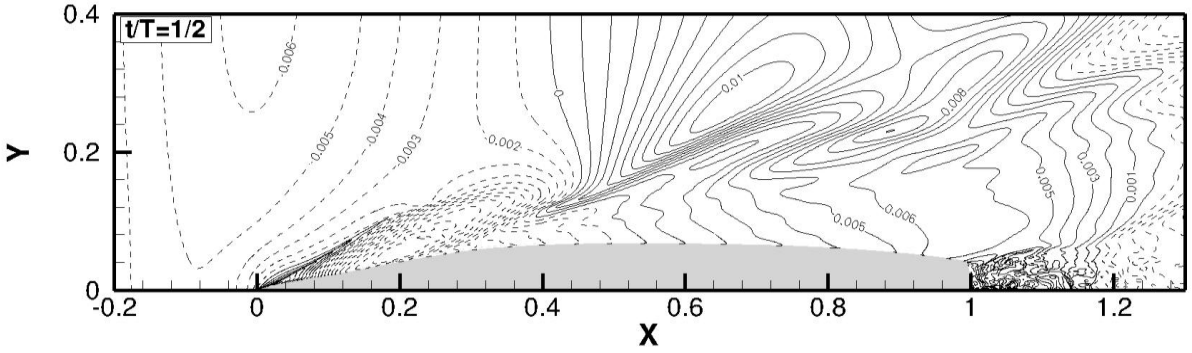

IIHR-CFDShipV4

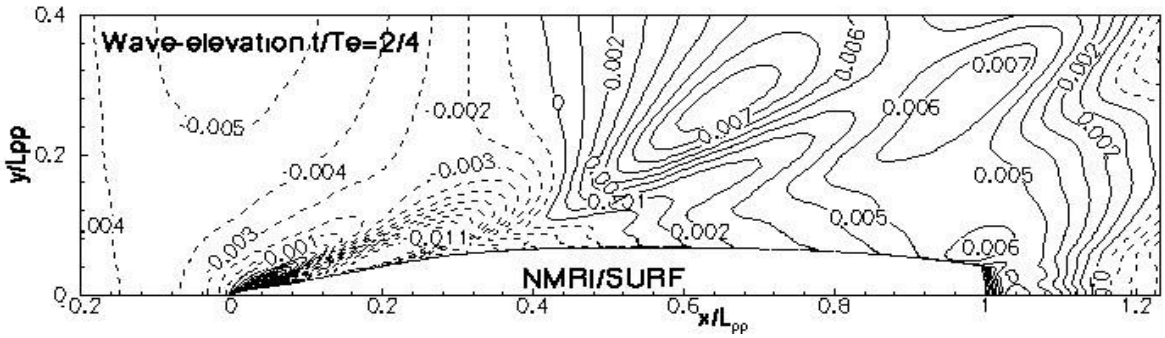

NMRI-SURF

Fig. 3.5-2-3 Wave-elevation ζ_T contours at t/Te = 1/2 [Δz = 0.001]
(Solid lines: positive (+) values; Dashed lines: negative (-) values)

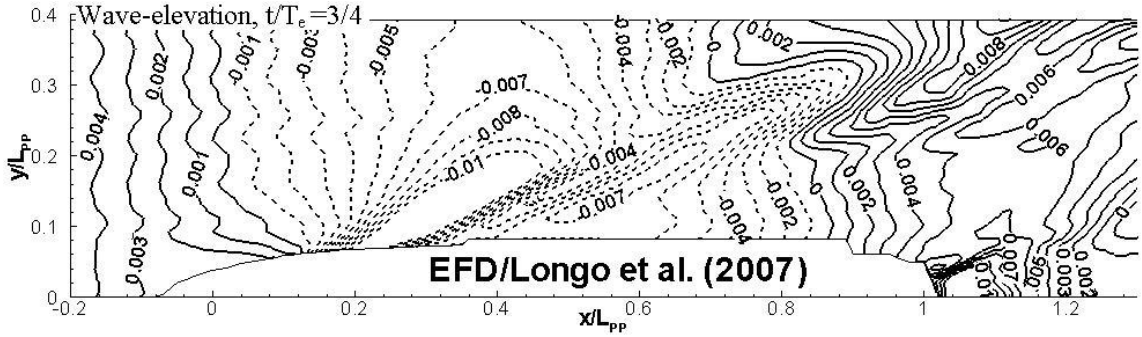

Experiment (IIHR, Longo et al. 2007)

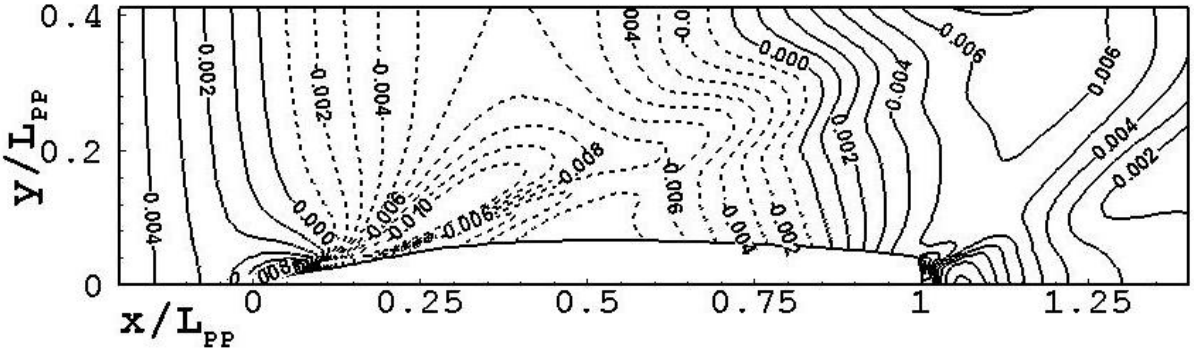

ECN-Icare

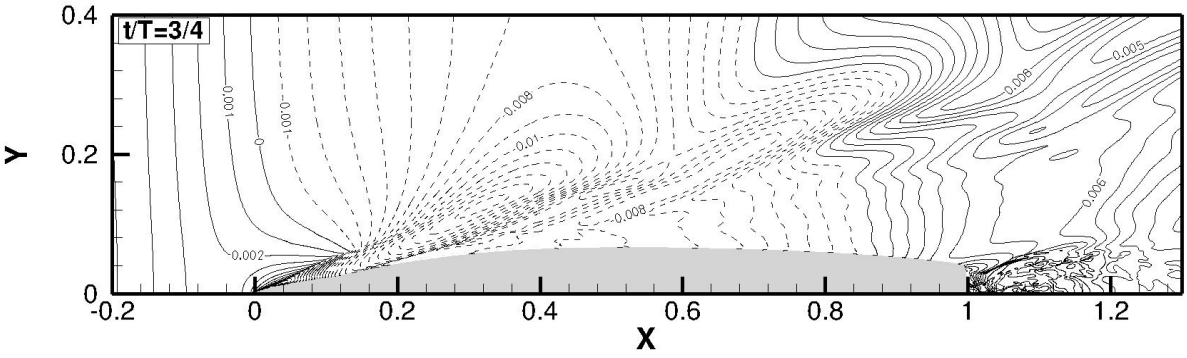

IIHR-CFDShipV4

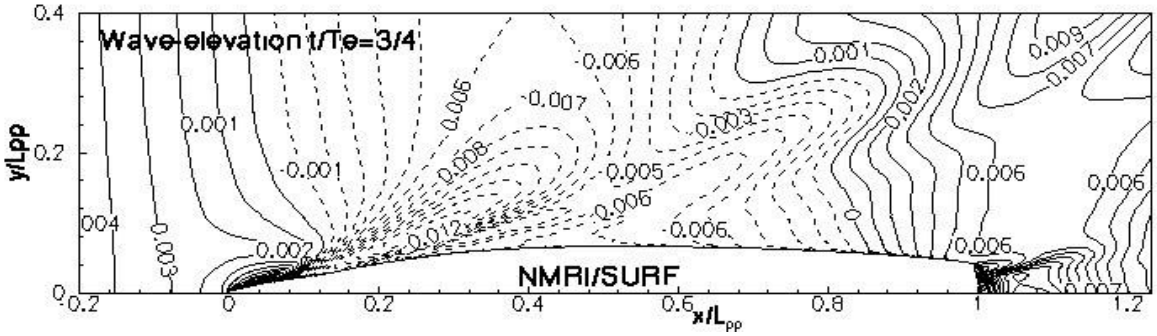

NMRI-SURF

Fig. 3.5-2-4 Wave-elevation ζ_T contours at t/Te = 3/4 [Δz = 0.001]
(Solid lines: positive (+) values; Dashed lines: negative (-) values)

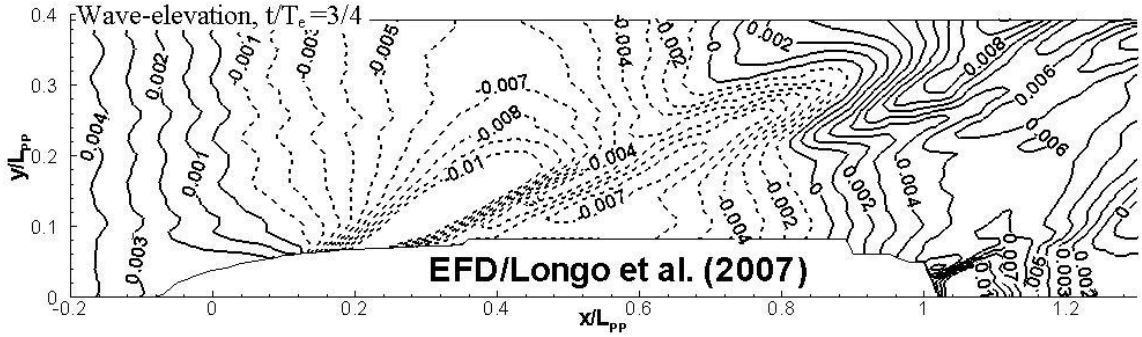

Experiment (IIHR, Longo et al. 2007)

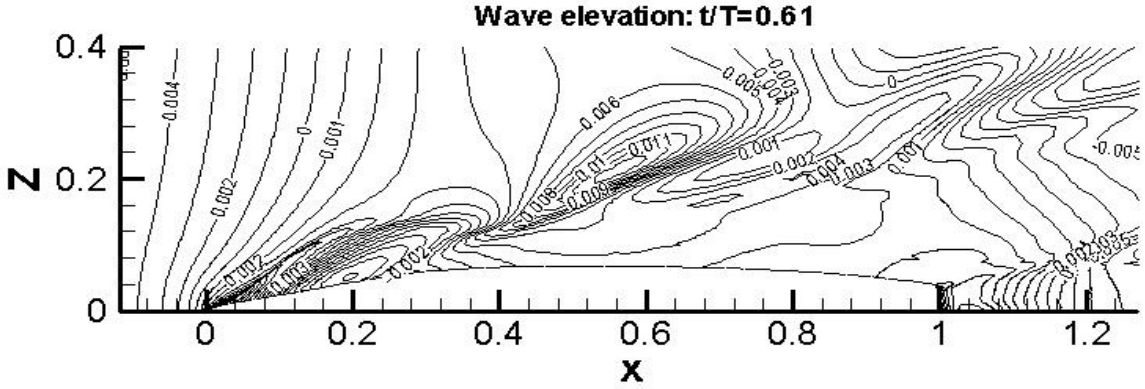

SSRC-FLUENT12.1 (t/T = 0.61)

Fig. 3.5-2-4 Wave-elevation ζ_T contours at t/Te = 3/4 [Δz = 0.001]
(Solid lines: positive (+) values; Dashed lines: negative (-) values)

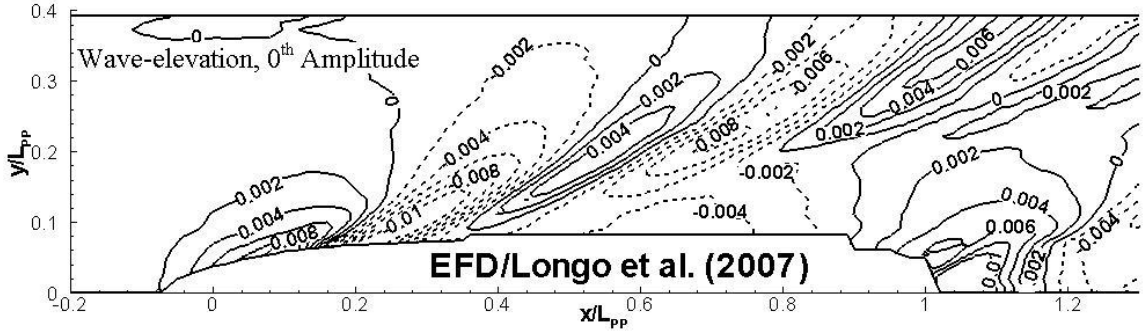

Experiment (IIHR, Longo et al. 2007)

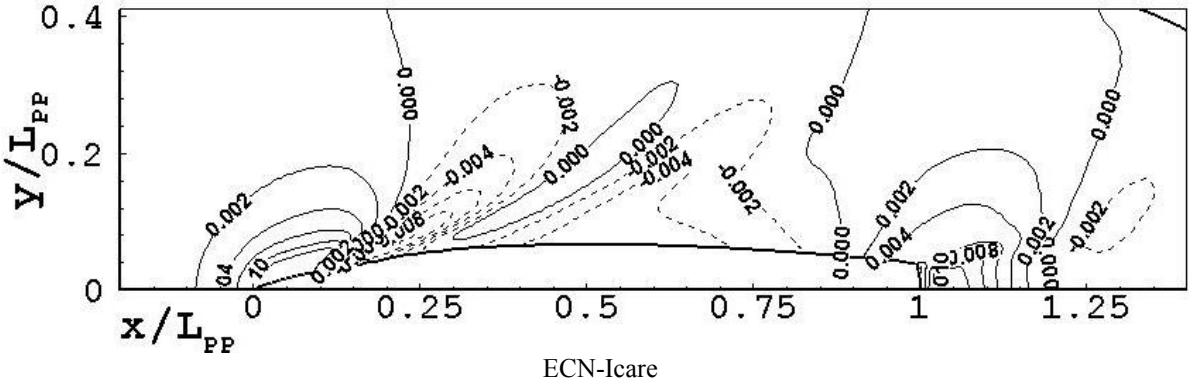

ECN-Icare

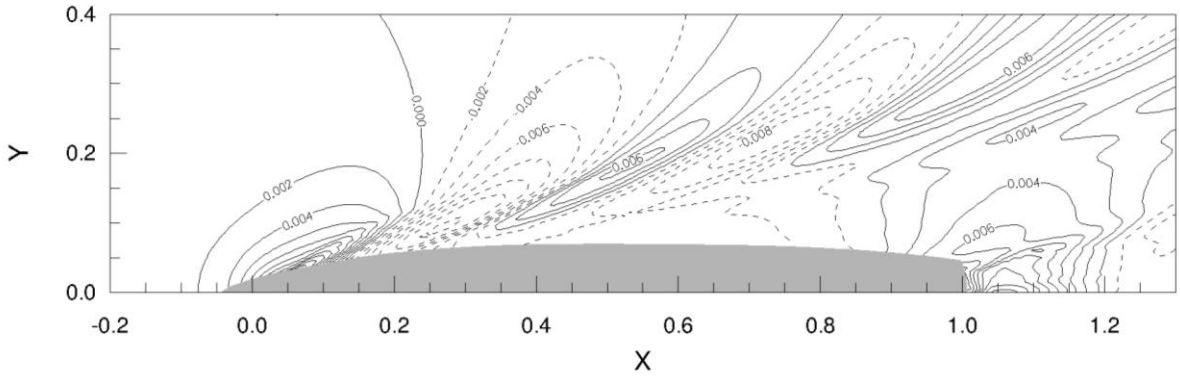

IIHR-CFDShipV4

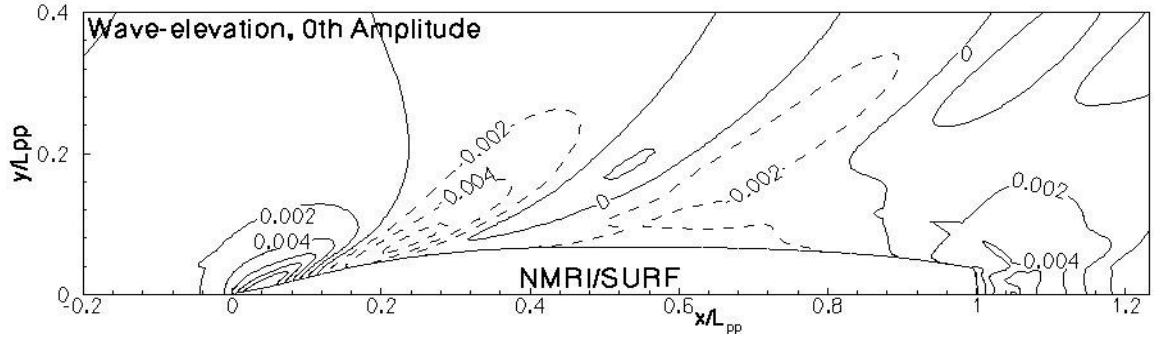

NMRI-SURF

Fig. 3.5-3 Wave-elevation ζ_T contours: 0th amplitude [$\Delta z = 0.002$]
(Solid lines: positive (+) values; Dashed lines: negative (-) values)

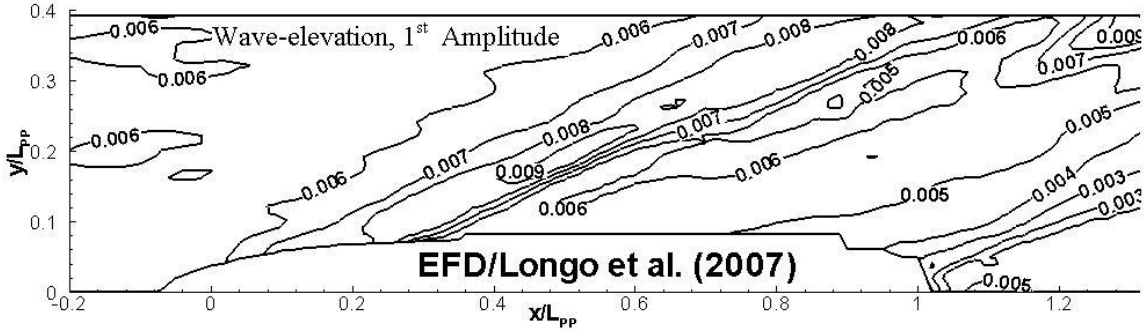

Experiment (IIHR, Longo et al. 2007)

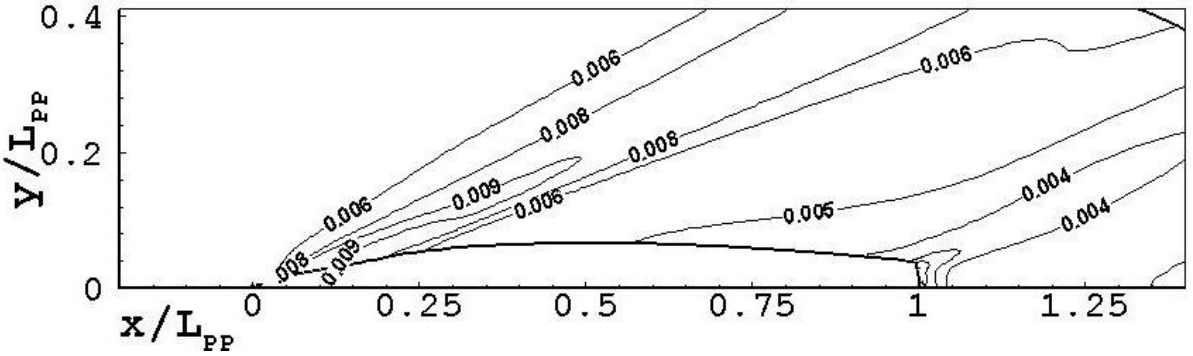

ECN-Icare

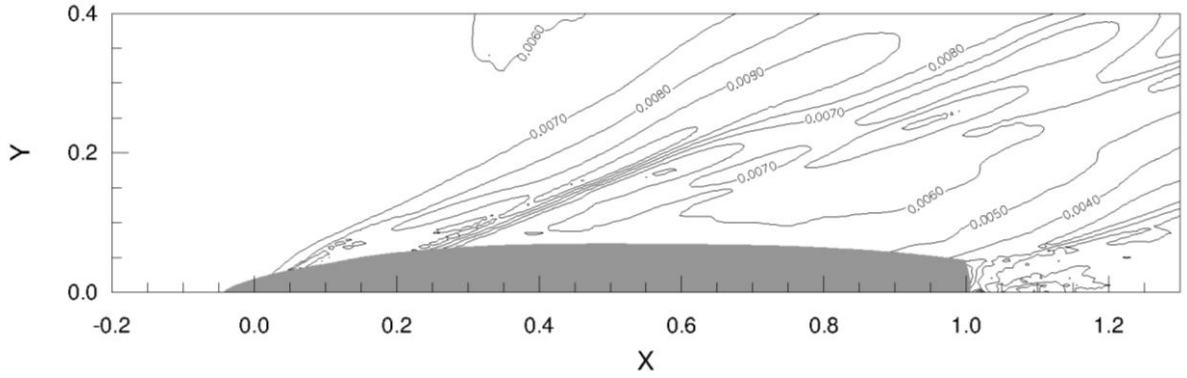

IIHR-CFDShipV4

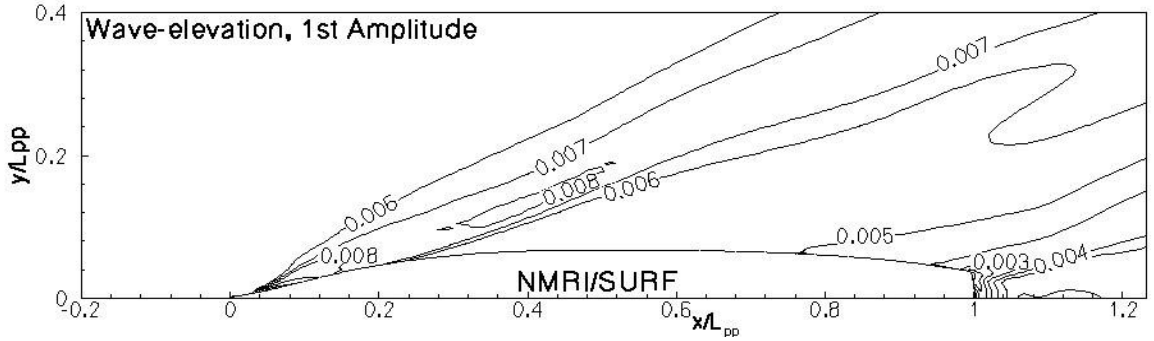

NMRI-SURF

Fig. 3.5-4 Wave-elevation ζ_T contours: 1st amplitude [$\Delta z = 0.001$]
(Solid lines: positive (+) values; Dashed lines: negative (-) values)

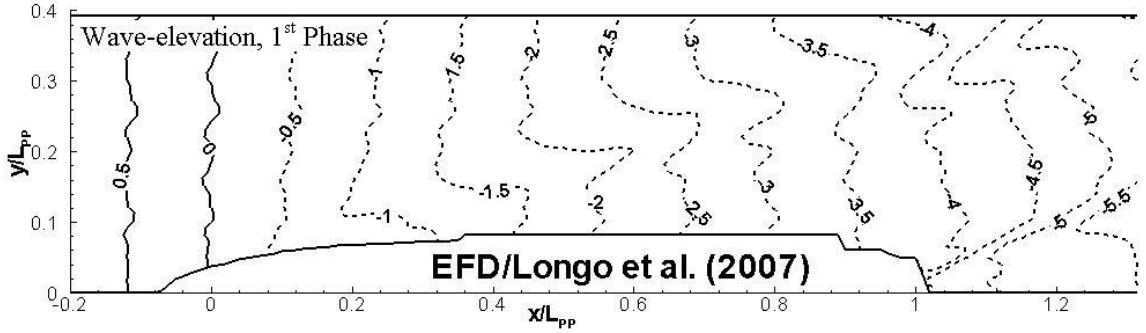

Experiment (IIHR, Longo et al. 2007)

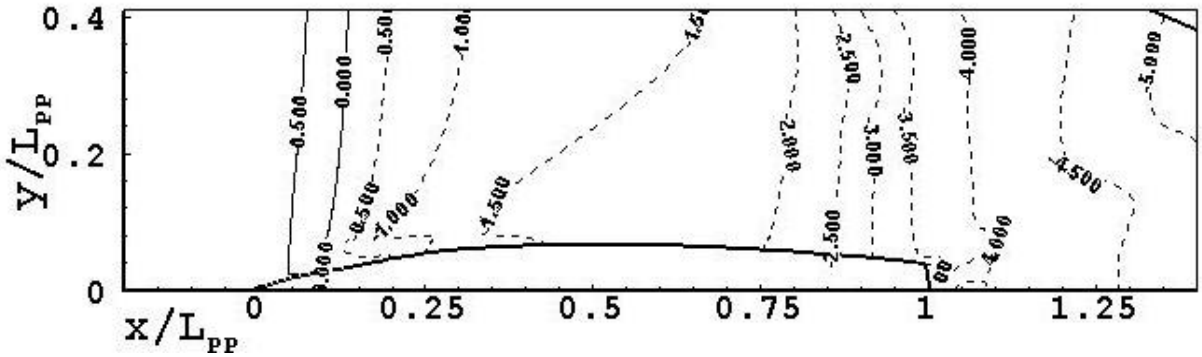

ECN-Icare

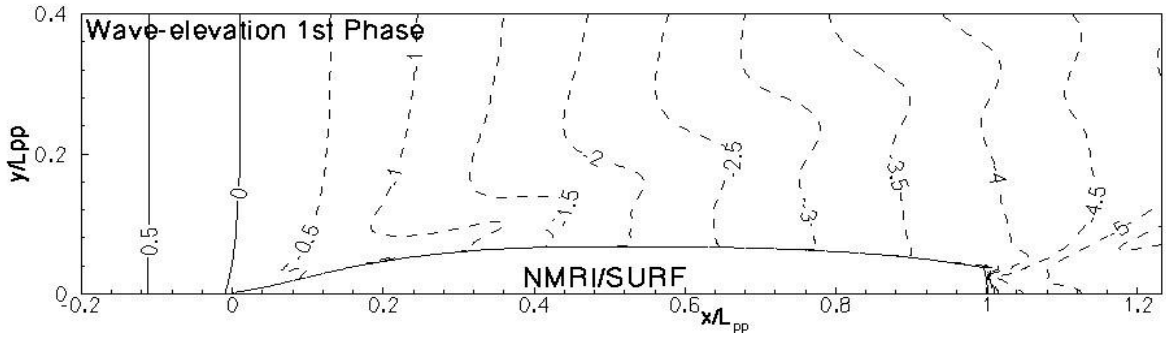

NMRI-SURF

Fig. 3.5-5 Wave-elevation ζ_T contours: 1st phase [Δg = 0.5]
(Solid lines: positive (+) values; Dashed lines: negative (-) values)

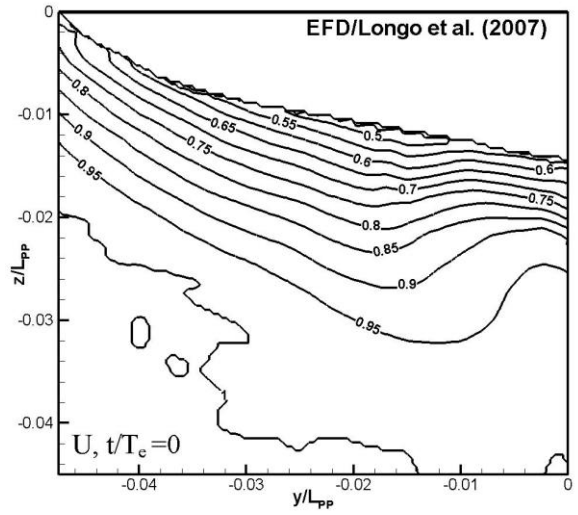

Experiment (IIHR, Longo et al. 2007)

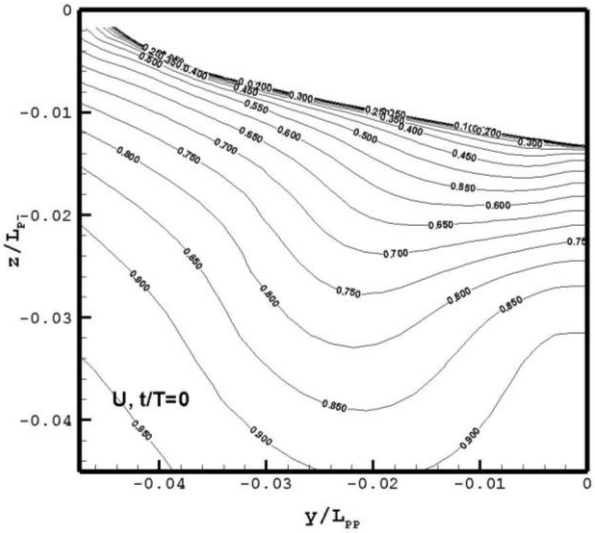

ECN-Icare

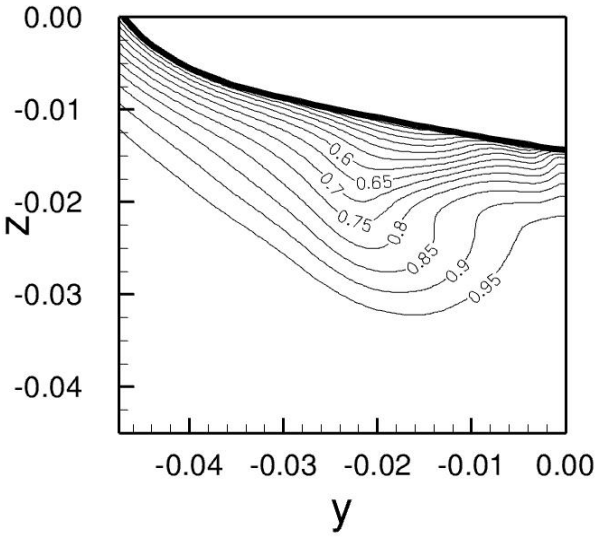

IIHR-CFDShipV4

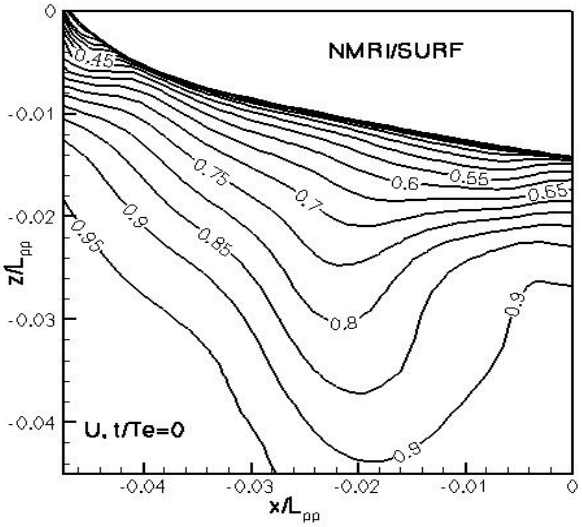

NMRI-SURF

Fig. 3.5-6-1 U contours at $x/L_{PP} = 0.935$, $t/Te = 0$ [$\Delta U = 0.05$]

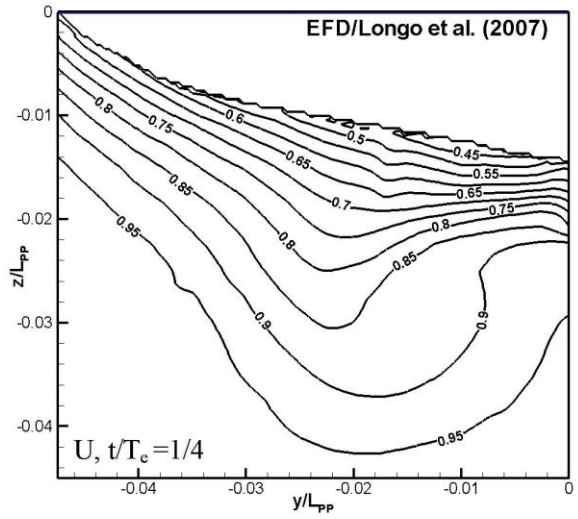

Experiment (IIHR, Longo et al. 2007)

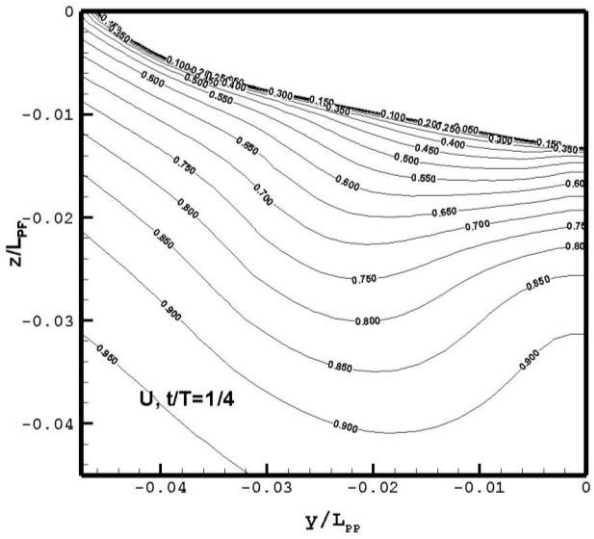

ECN-Icare

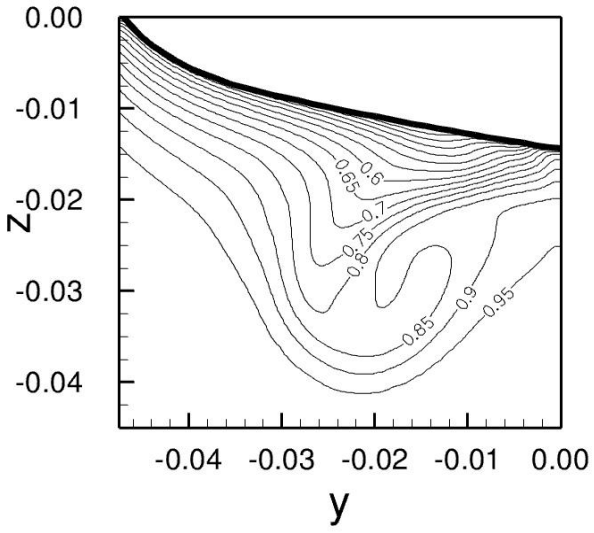

IIHR-CFDShipV4

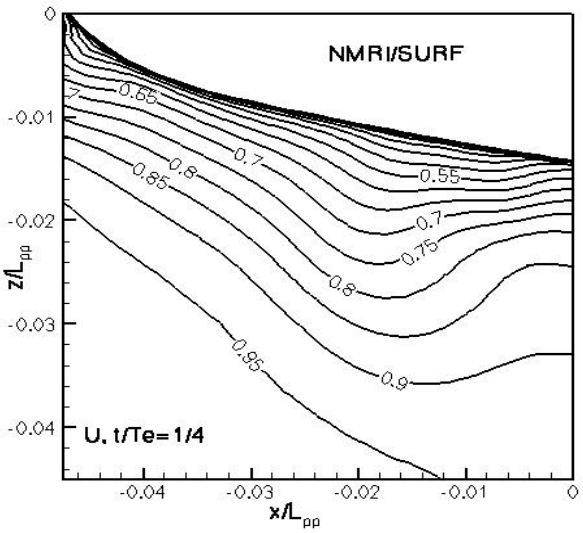

NMRI-SURF

Fig. 3.5-6-2 *U* contours at $x/L_{PP} = 0.935$, $t/Te = 1/4$ [$\Delta U = 0.05$]

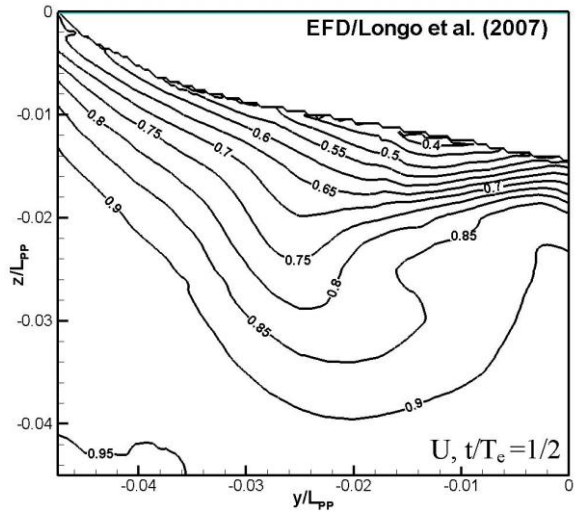

Experiment (IIHR, Longo et al. 2007)

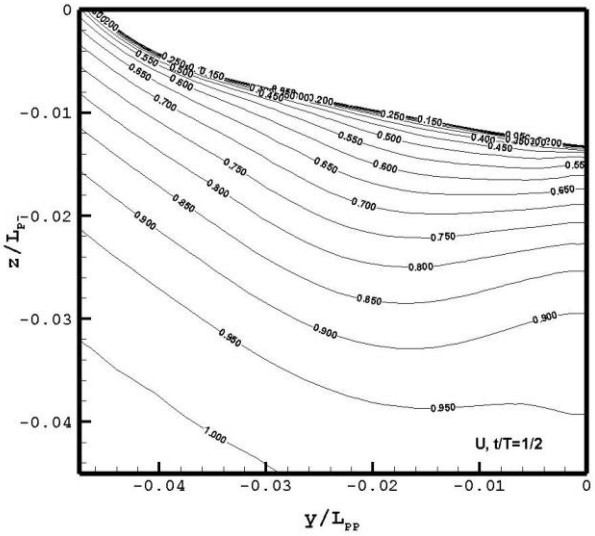

ECN-Icare

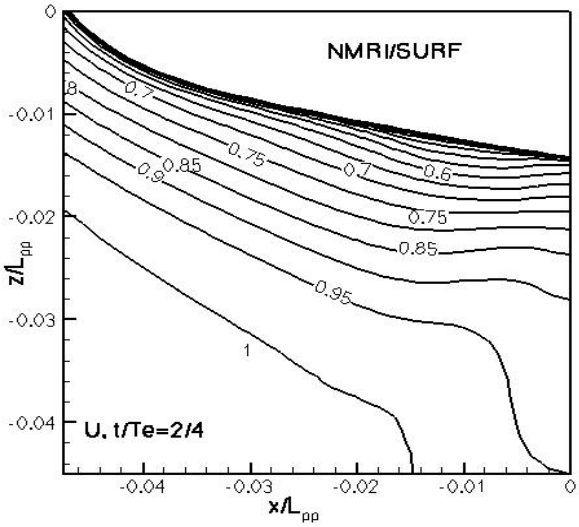

NMRI-SURF

Fig. 3.5-6-3 *U* contours at $x/L_{PP} = 0.935$, $t/Te = 1/2$ [$\Delta U = 0.05$]

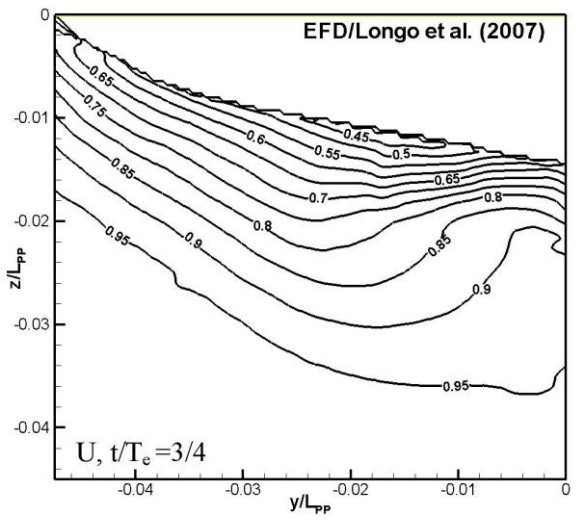

Experiment (IIHR, Longo et al. 2007)

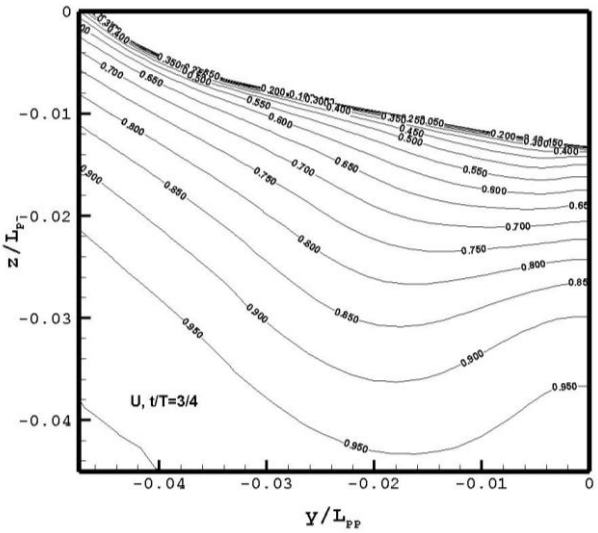

ECN-Icare

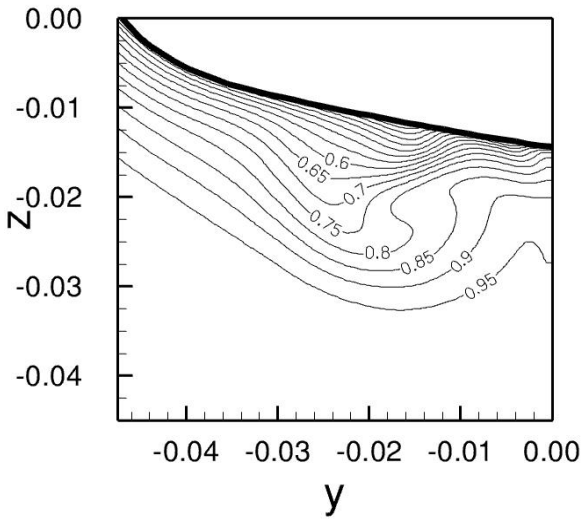

IIHR-CFDShipV4

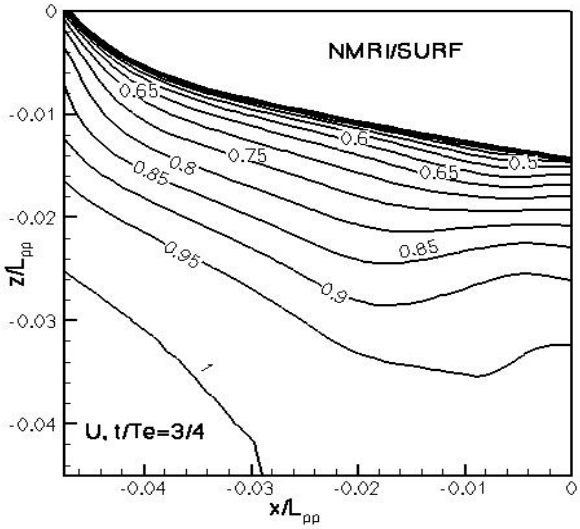

NMRI-SURF

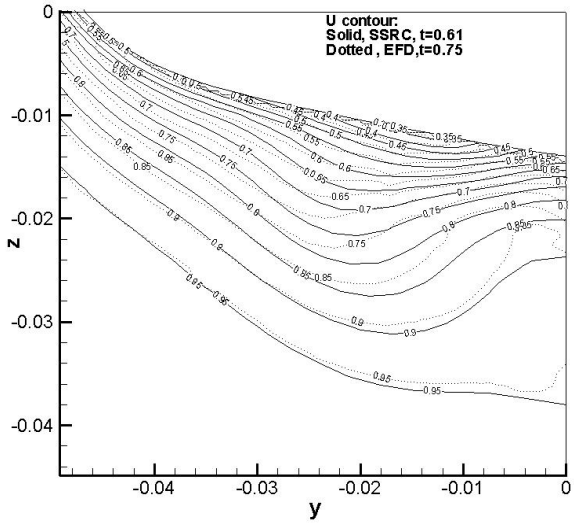

SSRC-FLUENT12.1 ($t/T = 0.61$)

Fig. 3.5-6-4 U contours at $x/L_{PP} = 0.935$, $t/Te = 3/4$ [$\Delta U = 0.05$]

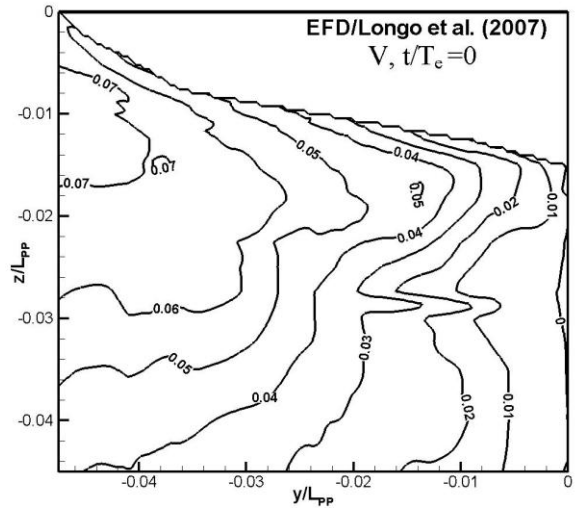

Experiment (IIHR, Longo et al. 2007)

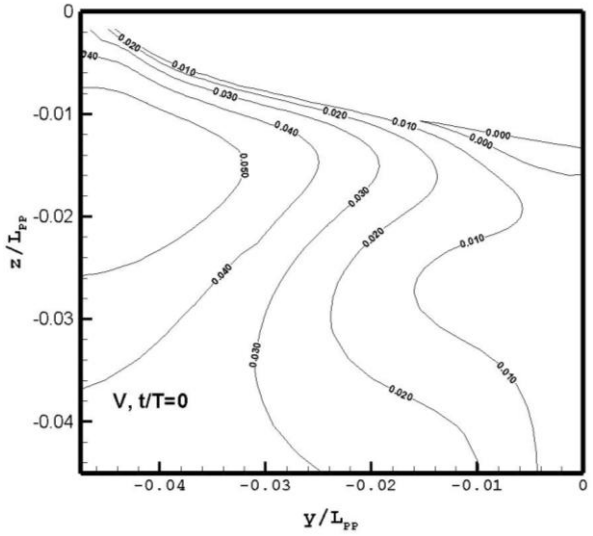

ECN-Icare

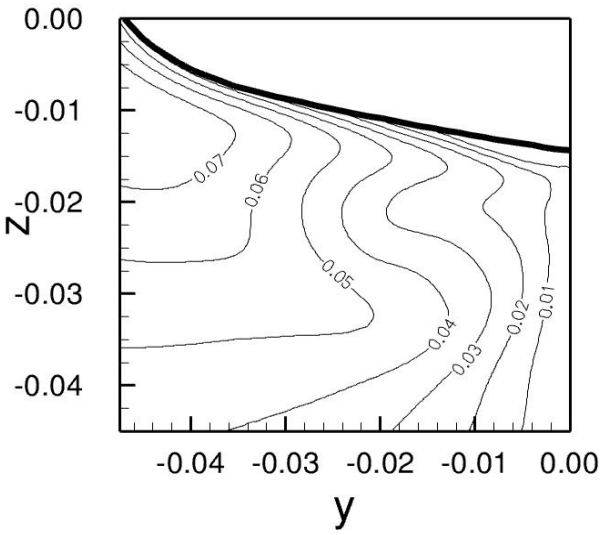

IIHR-CFDShipV4

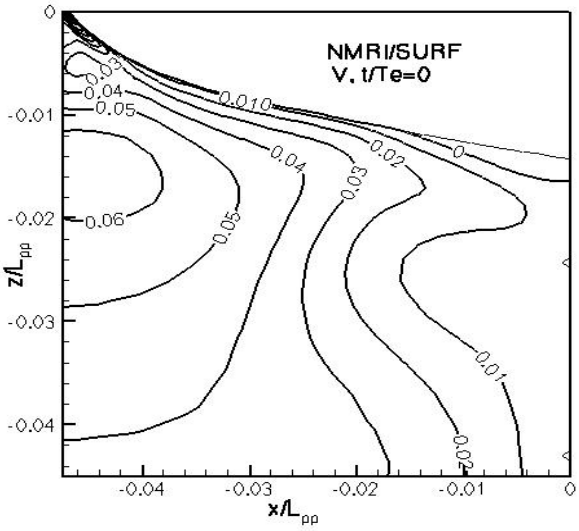

NMRI-SURF

Fig. 3.5-7-1 *V* contours at $x/L_{PP} = 0.935$, $t/Te = 0$ [$\Delta V = 0.01$]

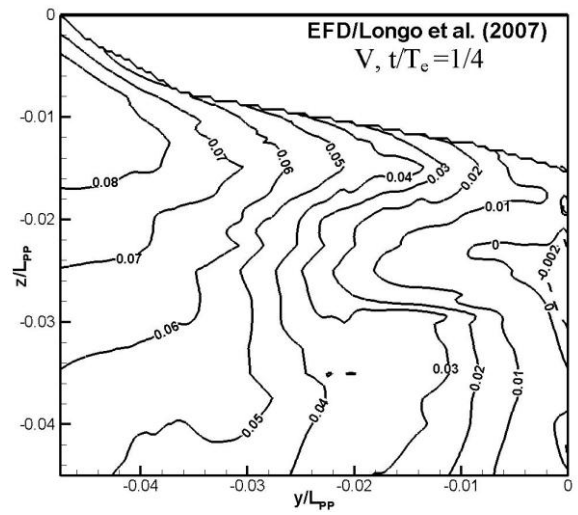

Experiment (IIHR, Longo et al. 2007)

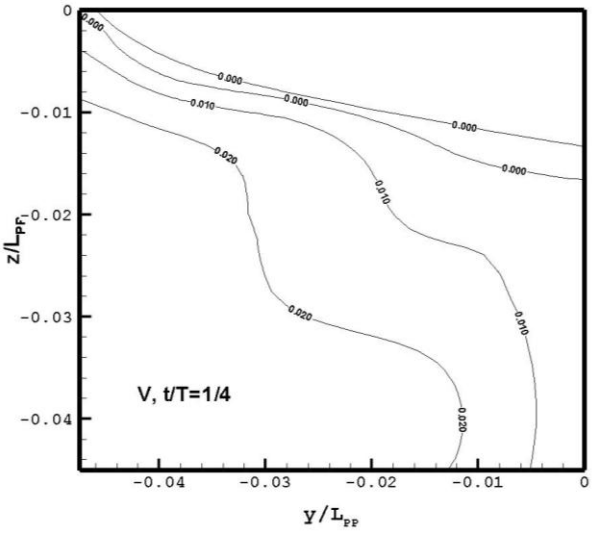

ECN-Icare

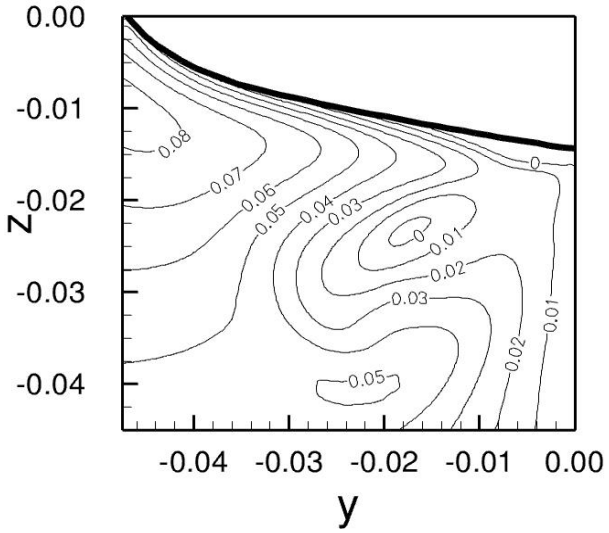

IIHR-CFDShipV4

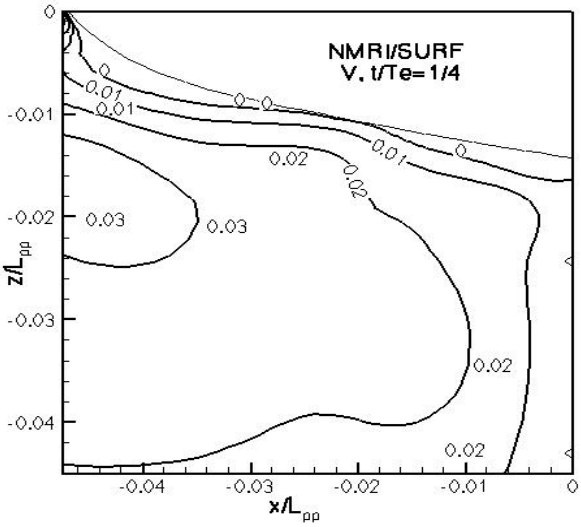

NMRI-SURF

Fig. 3.5-7-2 *V* contours at $x/L_{PP} = 0.935$, $t/Te = 1/4$ [$\Delta V = 0.01$]

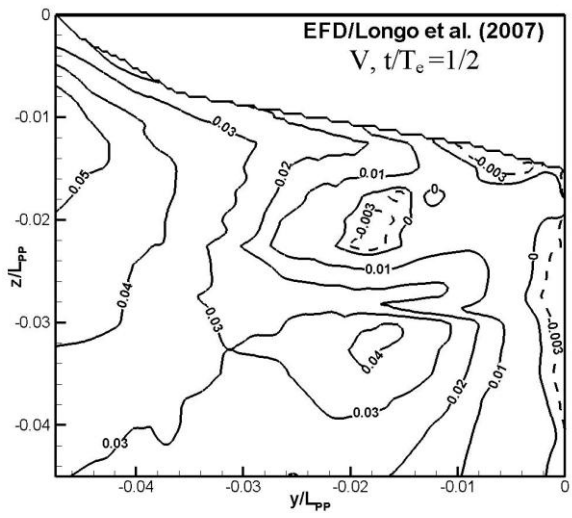

Experiment (IIHR, Longo et al. 2007)

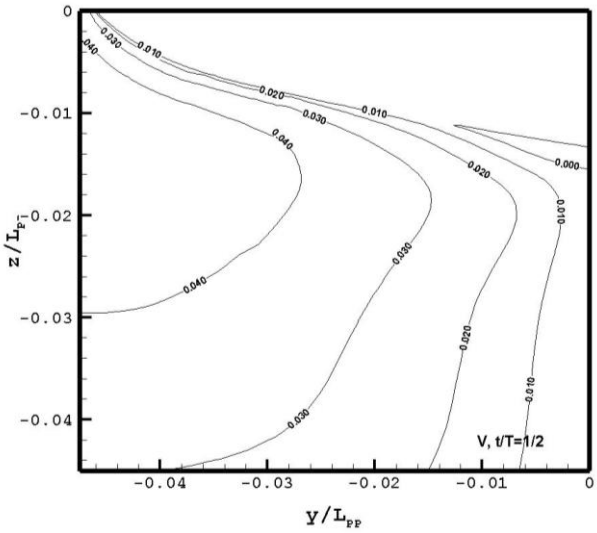

ECN-Icare

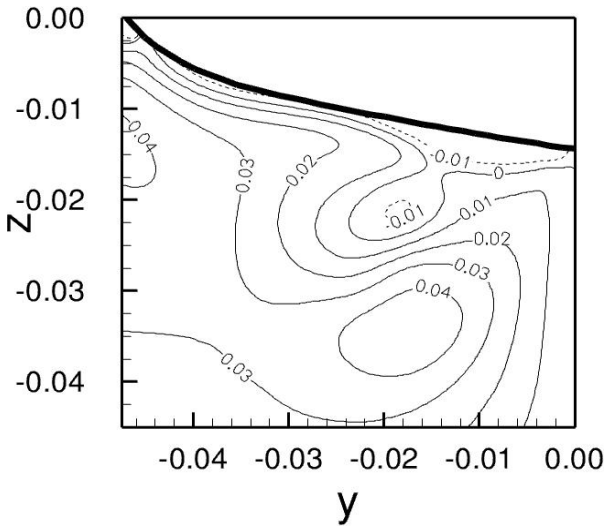

IIHR-CFDShipV4

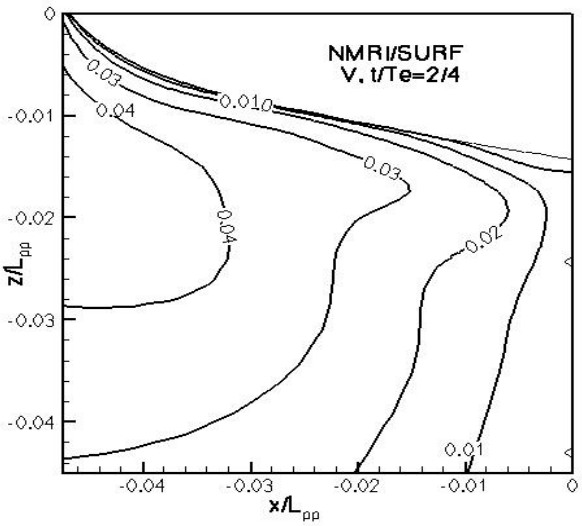

NMRI-SURF

Fig. 3.5-7-3 V contours at $x/L_{PP} = 0.935$, $t/Te = 1/2$ [$\Delta V = 0.01$]

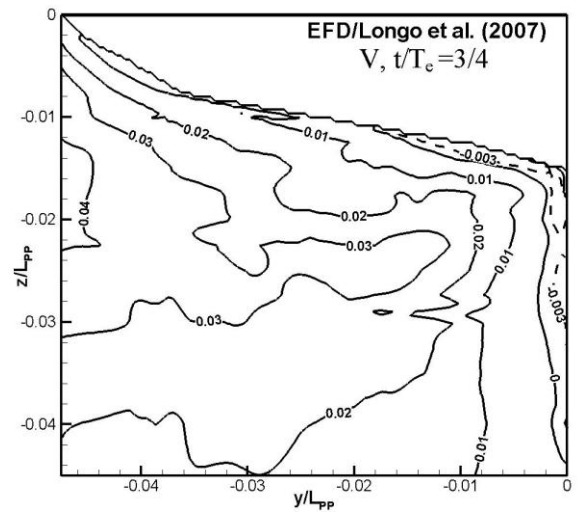

Experiment (IIHR, Longo et al. 2007)

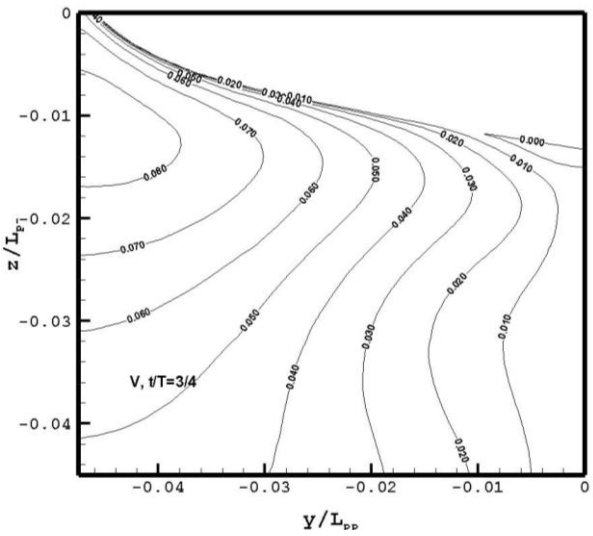

ECN-Icare

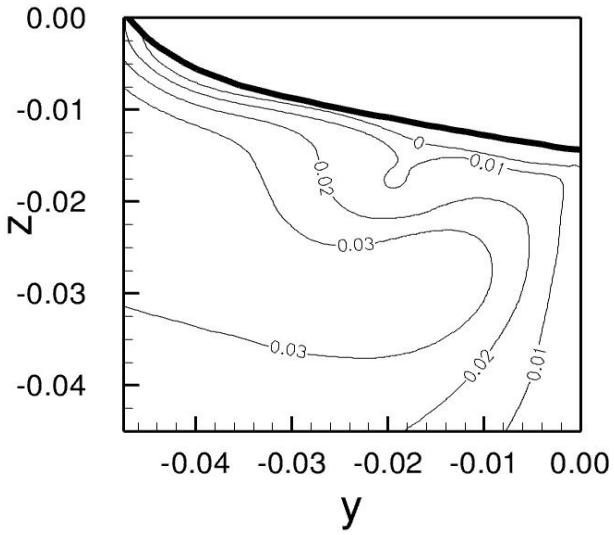

IIHR-CFDShipV4

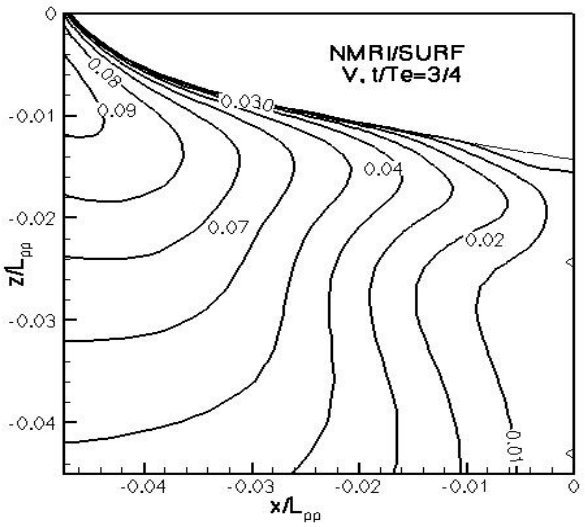

NMRI-SURF

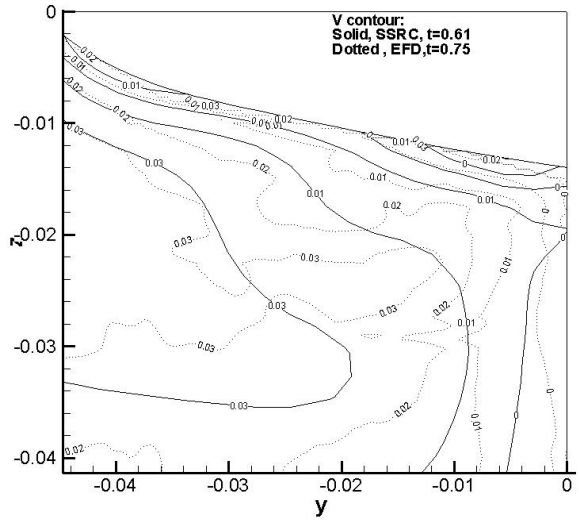

SSRC-FLUENT12.1 ($t/T = 0.61$)

Fig. 3.5-7-4 V contours at $x/L_{PP} = 0.935$, $t/Te = 3/4$ [$\Delta V = 0.01$]

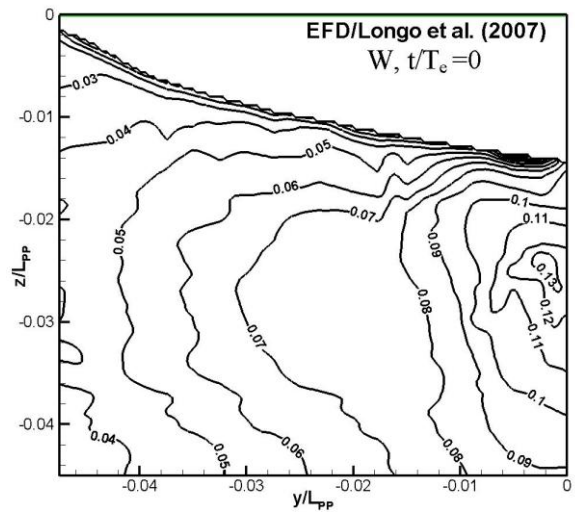

Experiment (IIHR, Longo et al. 2007)

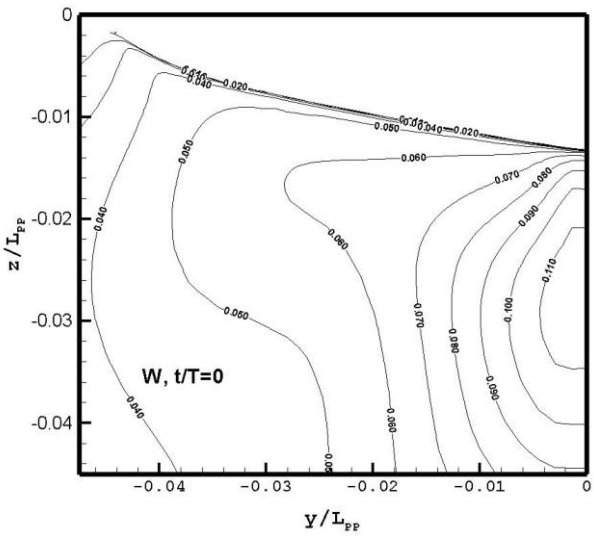

ECN-Icare

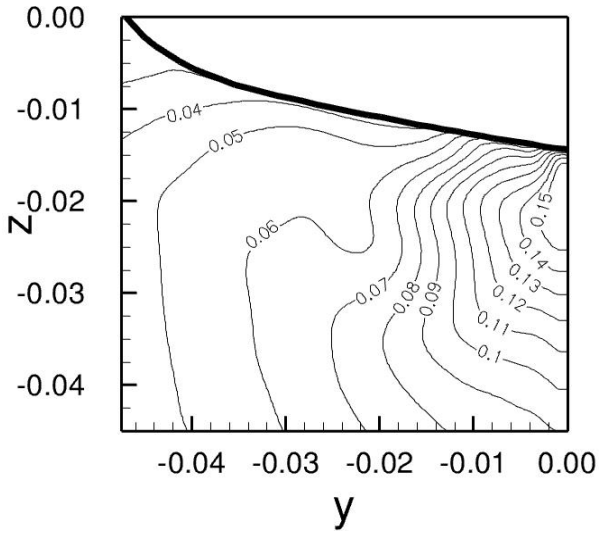

IIHR-CFDShipV4

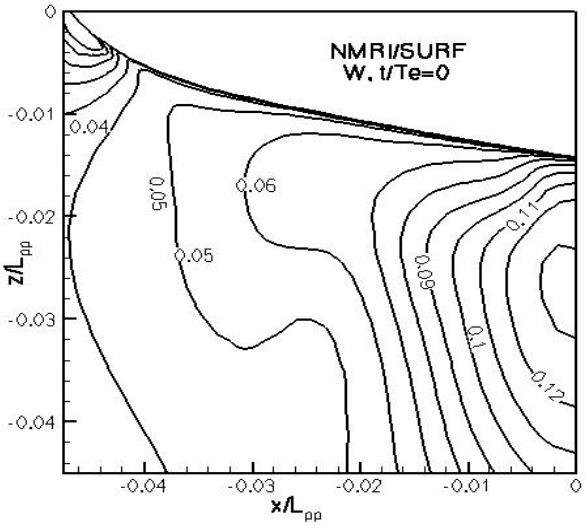

NMRI-SURF

Fig. 3.5-8-1 *W* contours at $x/L_{PP} = 0.935$, $t/Te = 0$ [$\Delta W = 0.01$]
(Solid lines: positive (+) values; Dashed lines: negative (-) values)

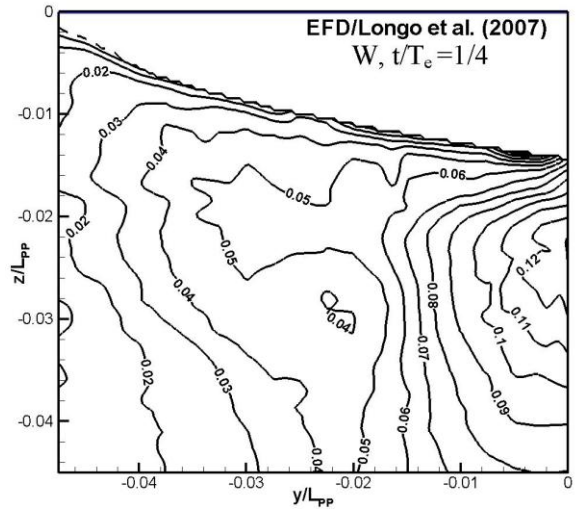

Experiment (IIHR, Longo et al. 2007)

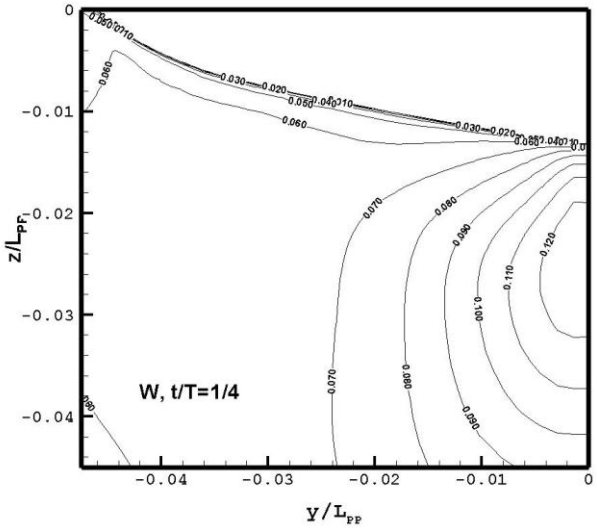

ECN-Icare

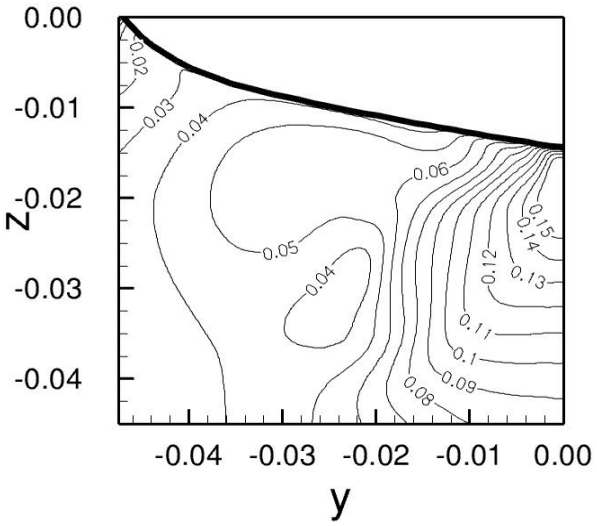

IIHR-CFDShipV4

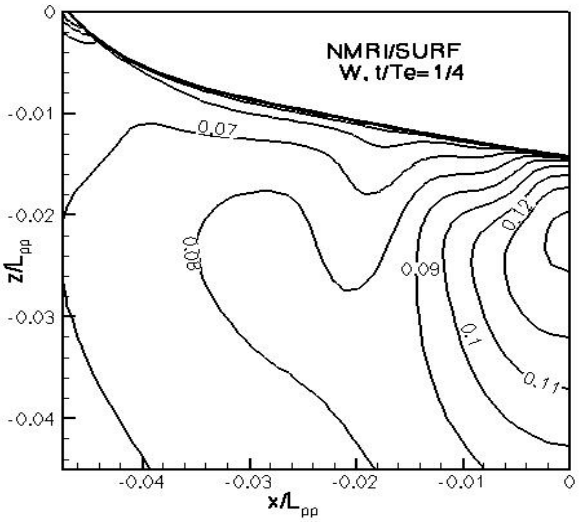

NMRI-SURF

Fig. 3.5-8-2 *W* contours at $x/L_{PP} = 0.935$, $t/Te = 1/4$ [$\Delta W = 0.01$]
(Solid lines: positive (+) values; Dashed lines: negative (-) values)

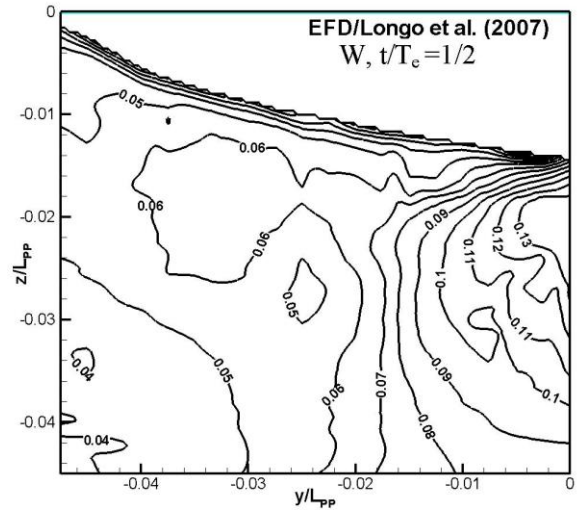

Experiment (IIHR, Longo et al. 2007)

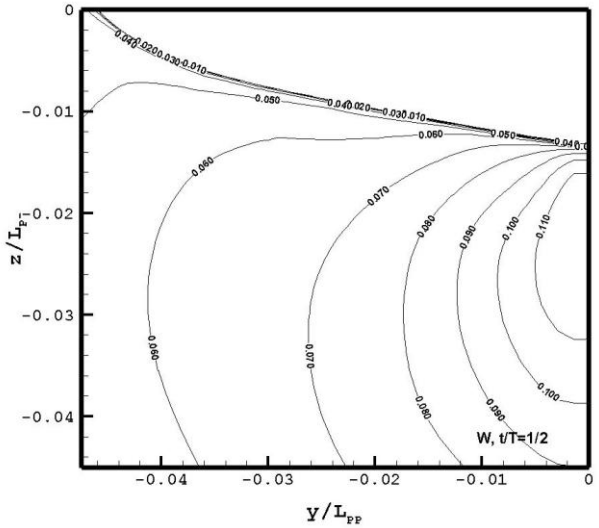

ECN-Icare

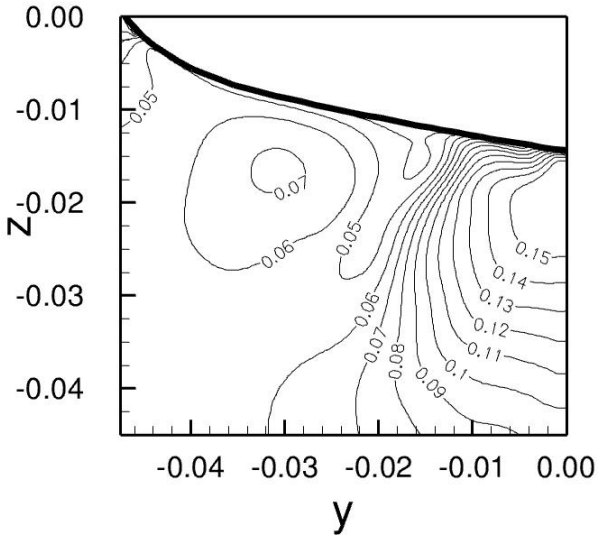

IIHR-CFDShipV4

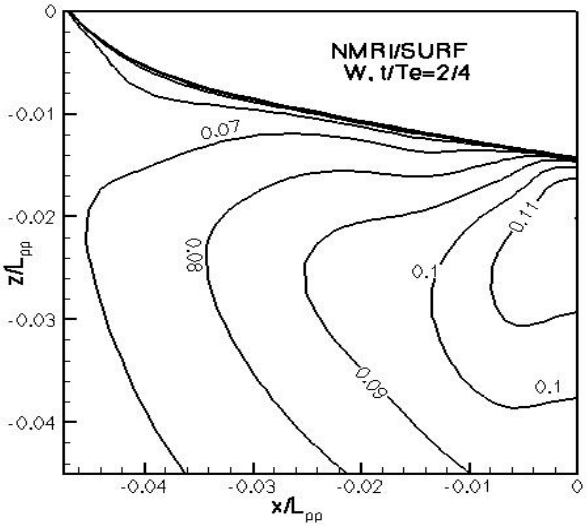

NMRI-SURF

Fig. 3.5-8-3 *W* contours at $x/L_{PP} = 0.935$, $t/Te = 1/2$ [$\Delta W = 0.01$]
(Solid lines: positive (+) values; Dashed lines: negative (-) values)

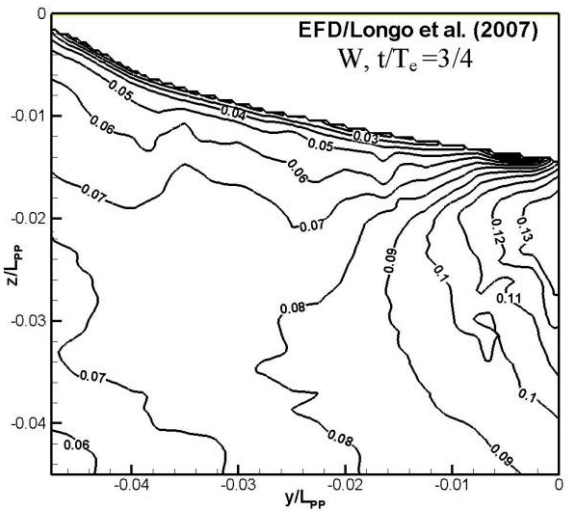

Experiment (IIHR, Longo et al. 2007)

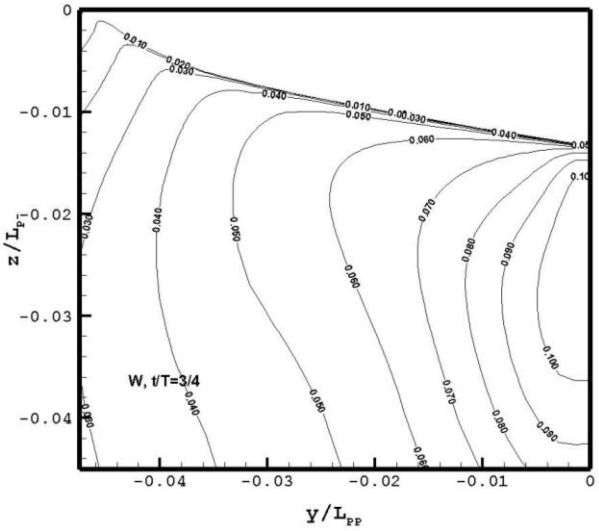

ECN-Icare

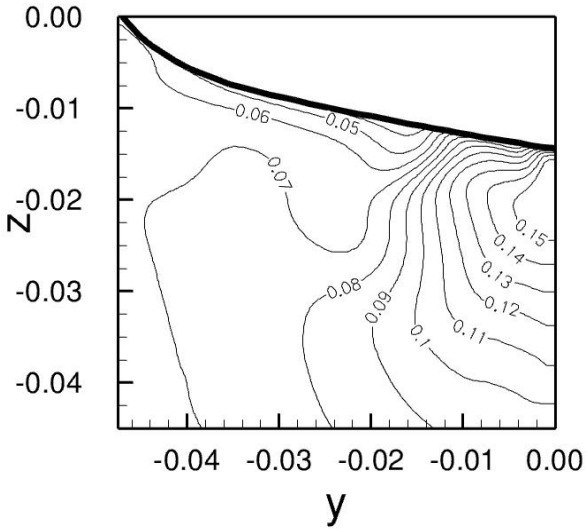

IIHR-CFDShipV4

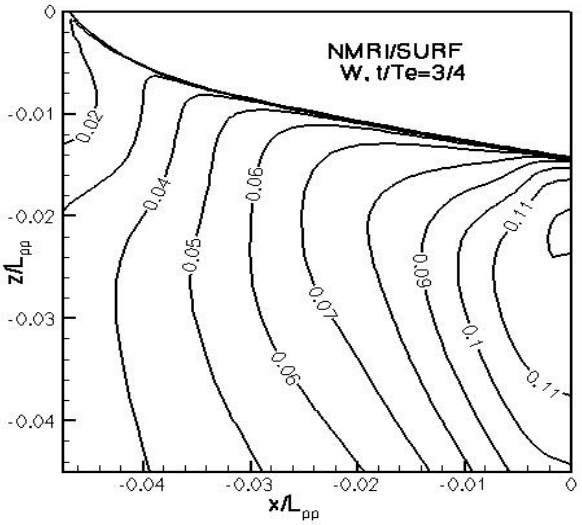

NMRI-SURF

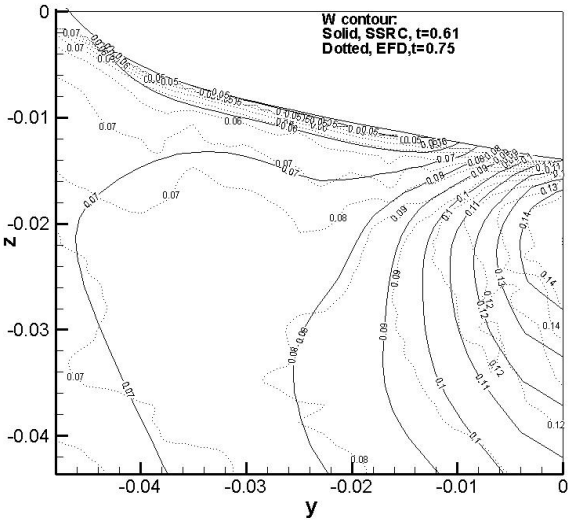

SSRC-FLUENT12.1 ($t/T = 0.61$)

Fig. 3.5-8-4 W contours at $x/L_{PP} = 0.935$, $t/Te = 3/4$ [$\Delta W = 0.01$]
(Solid lines: positive (+) values; Dashed lines: negative (-) values)

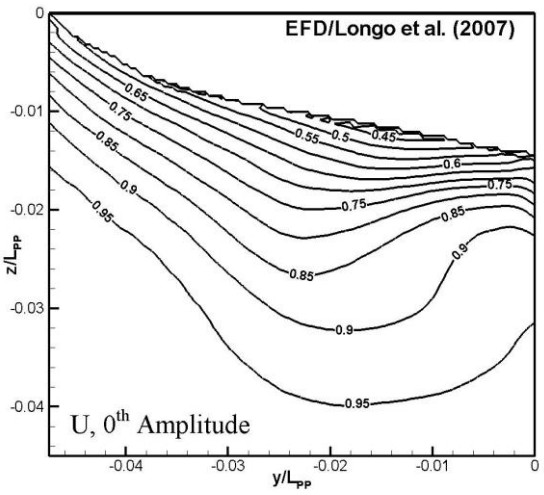

Experiment (IIHR, Longo et al. 2007)

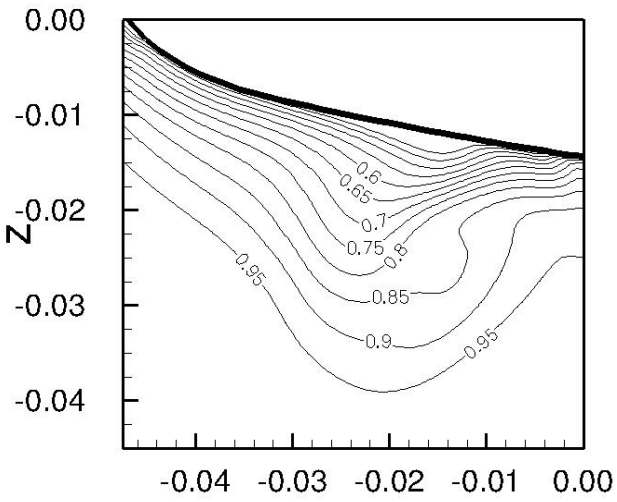

IIHR-CFDShipV4

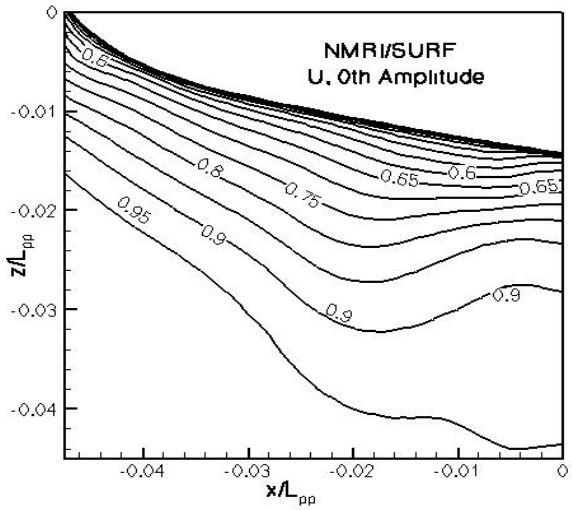

NMRI-SURF

Fig. 3.5-9-1 U contours of 0th amplitude at $x/L_{PP} = 0.935$ [$\Delta U = 0.05$]

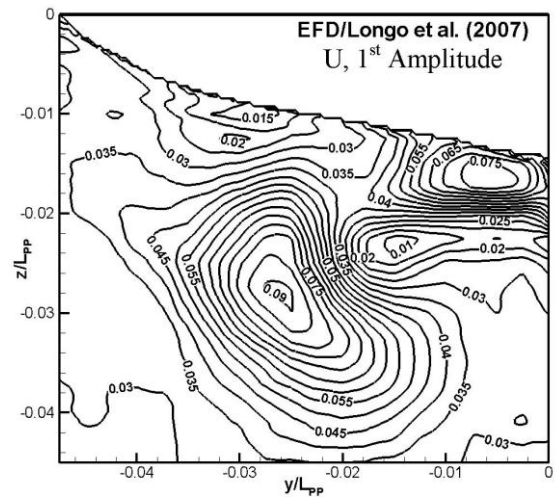

Experiment (IIHR, Longo et al. 2007)

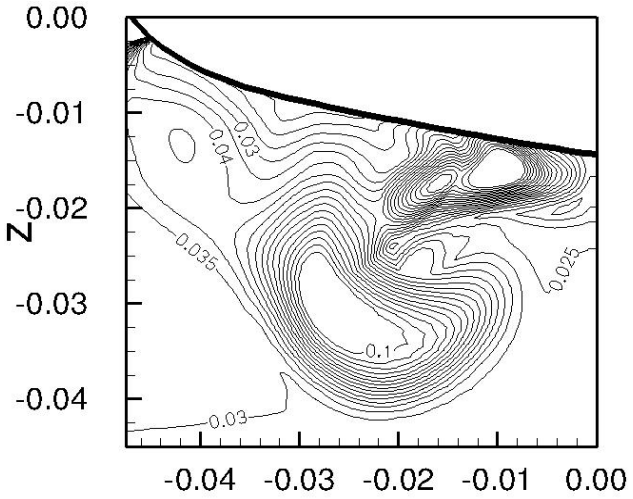

IIHR-CFDShipV4

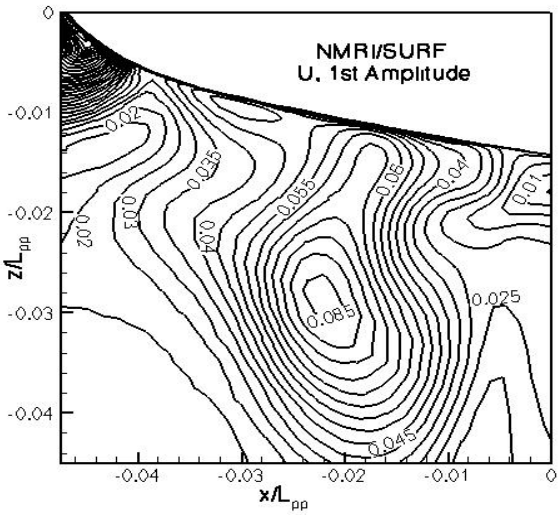

NMRI-SURF

Fig. 3.5-9-2 U contours of 1st amplitude at $x/L_{PP} = 0.935$ [$\Delta U = 0.005$]

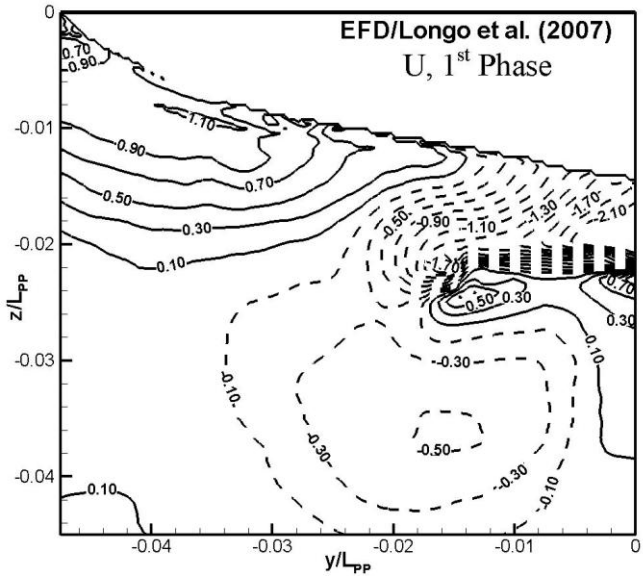

Experiment (IIHR, Longo et al. 2007)

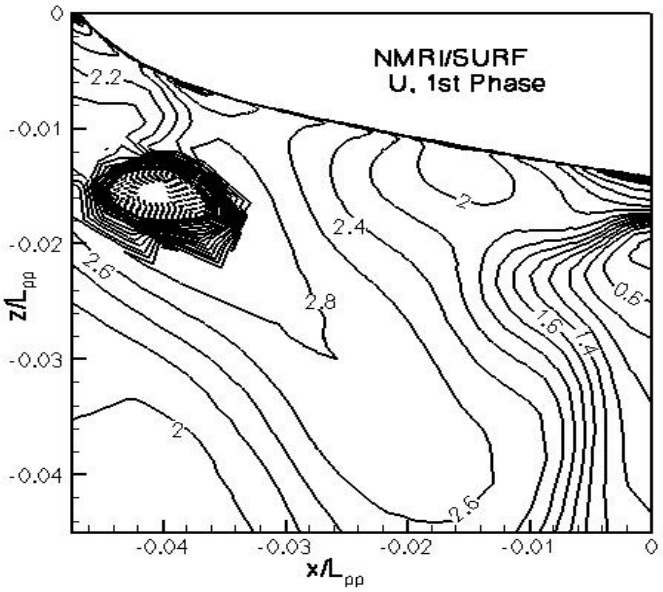

NMRI-SURF

Fig. 3.5-9-3 *U* contours of 1st phase at $x/L_{PP} = 0.935$ [$\Delta GU = 0.2$]
(Solid lines: positive (+) values; Dashed lines: negative (-) values)

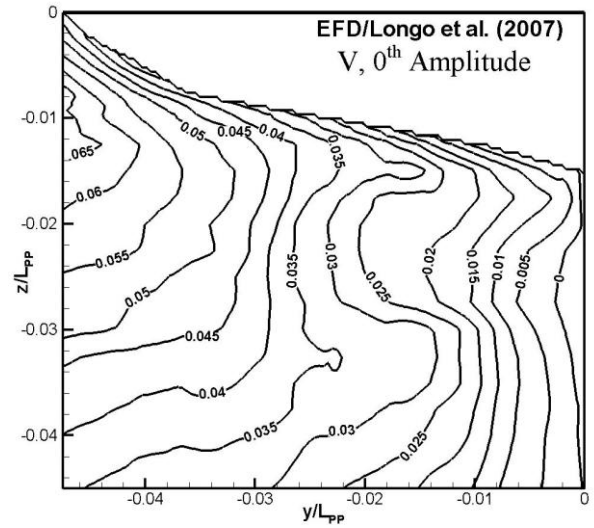

Experiment (IIHR, Longo et al. 2007)

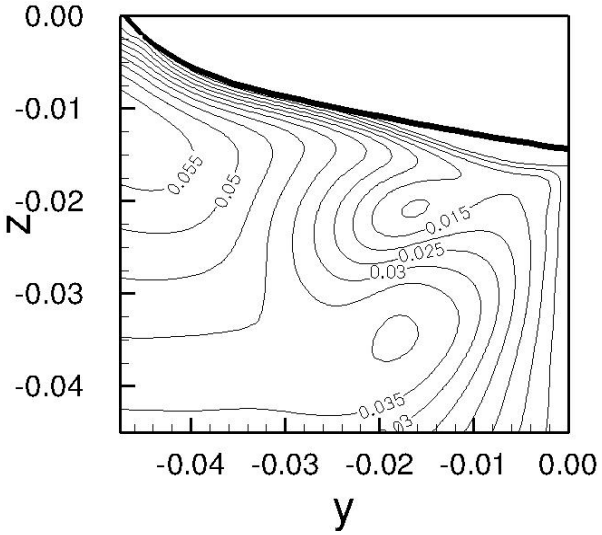

IIHR-CFDShipV4

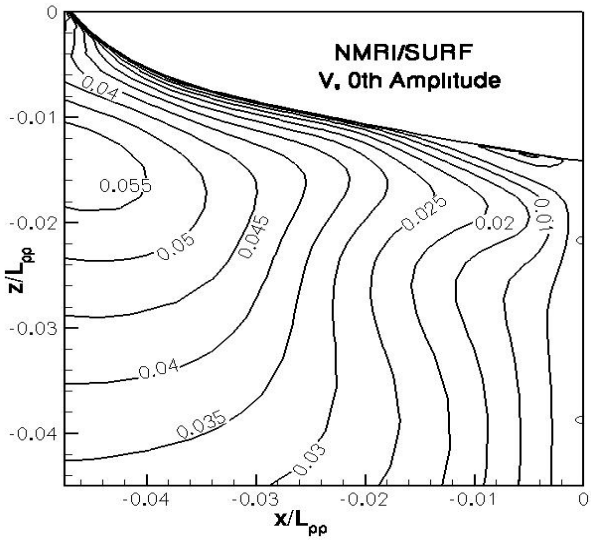

NMRI-SURF

Fig. 3.5-10-1 V contours of 0th amplitude at $x/L_{PP} = 0.935$ [$\Delta V = 0.005$]

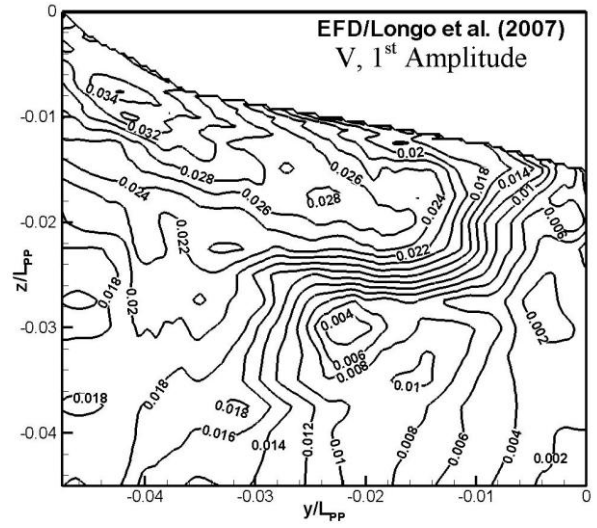

Experiment (IIHR, Longo et al. 2007)

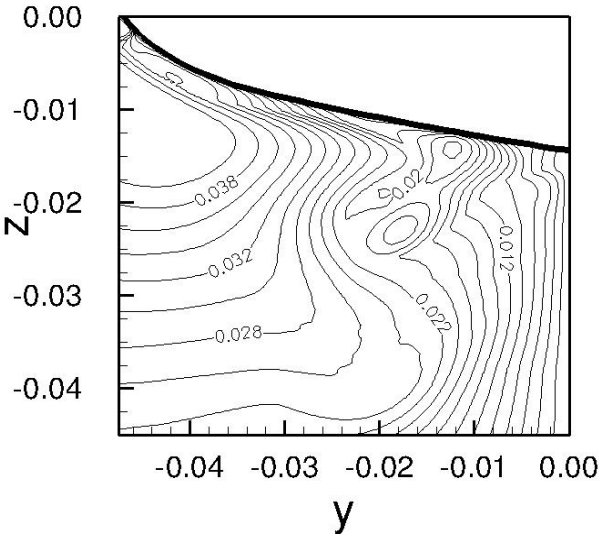

IIHR-CFDShipV4

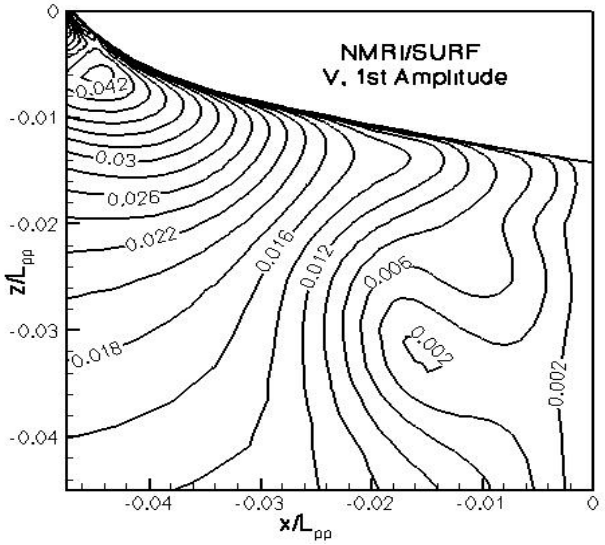

NMRI-SURF

Fig. 3.5-10-2 V contours of 1st amplitude at $x/L_{PP} = 0.935$ [$\Delta V = 0.002$]

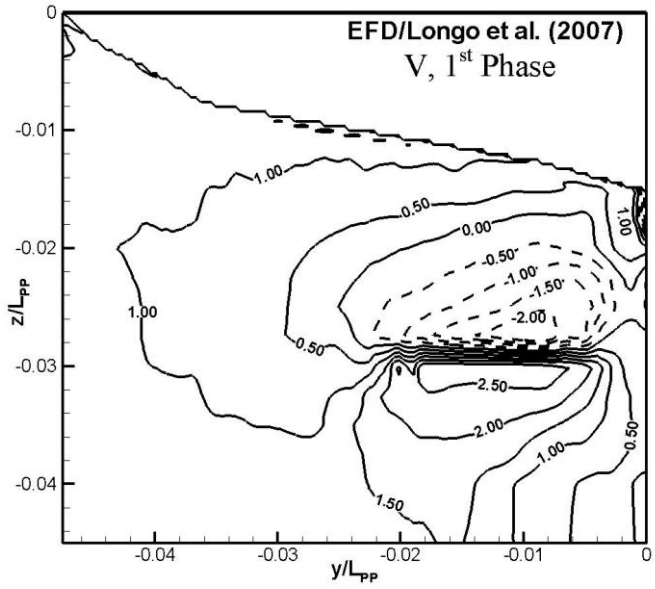

Experiment (IIHR, Longo et al. 2007)

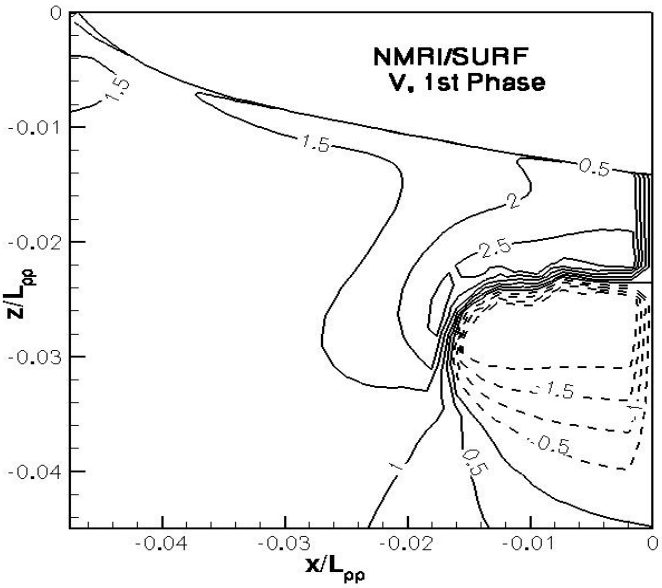

NMRI-SURF

Fig. 3.5-10-3 *V* contours of 1st phase at $x/L_{PP} = 0.935$ [$\Delta GV = 0.5$]
(Solid lines: positive (+) values; Dashed lines: negative (-) values)

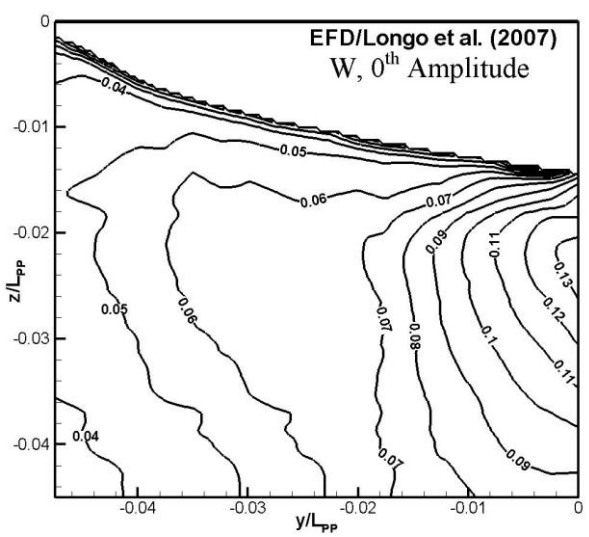

Experiment (IIHR, Longo et al. 2007)

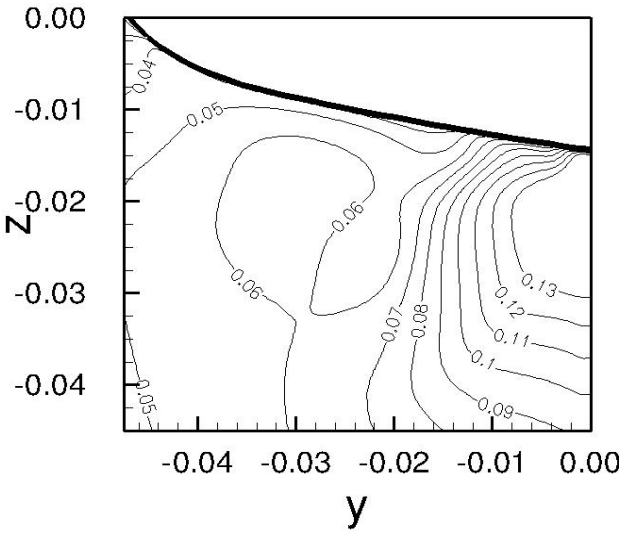

IIHR-CFDShipV4

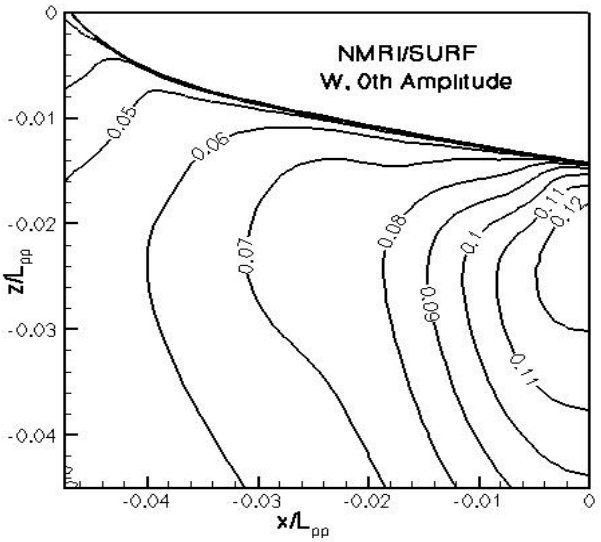

NMRI-SURF

Fig. 3.5-11-1 W contours of 0th amplitude at $x/L_{PP} = 0.935$ [$\Delta W = 0.01$]

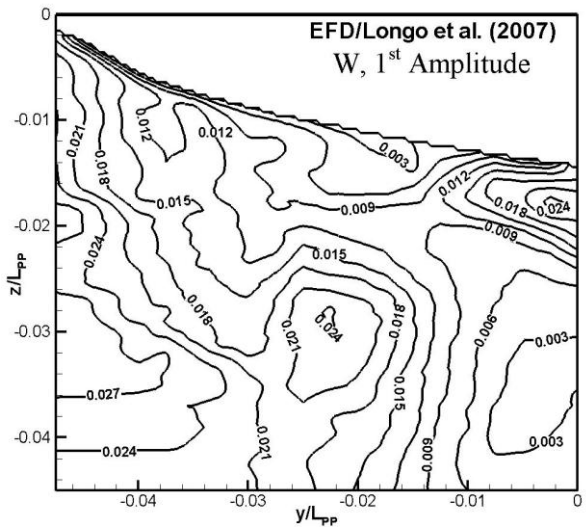

Experiment (IIHR, Longo et al. 2007)

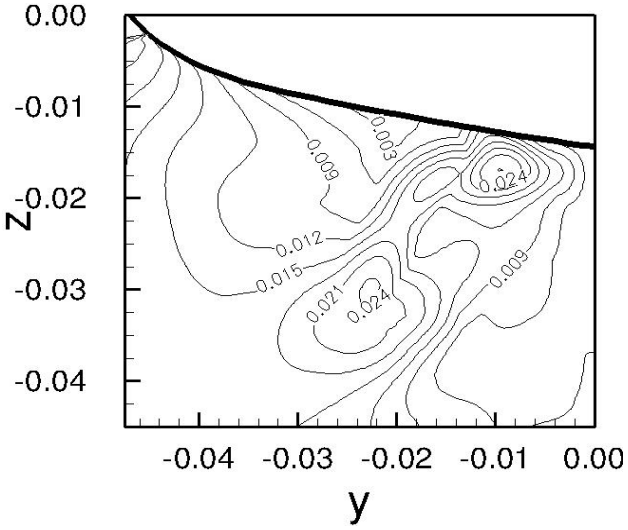

IIHR-CFDShipV4

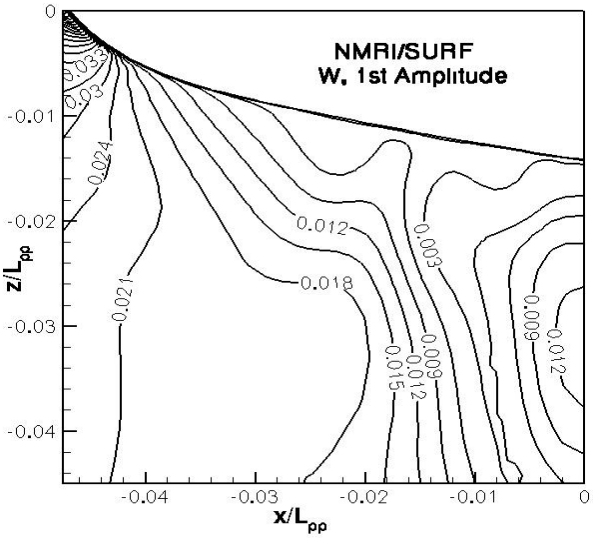

NMRI-SURF

Fig. 3.5-11-2 *W* contours of 1st amplitude at $x/L_{PP} = 0.935$ [$\Delta W = 0.03$]

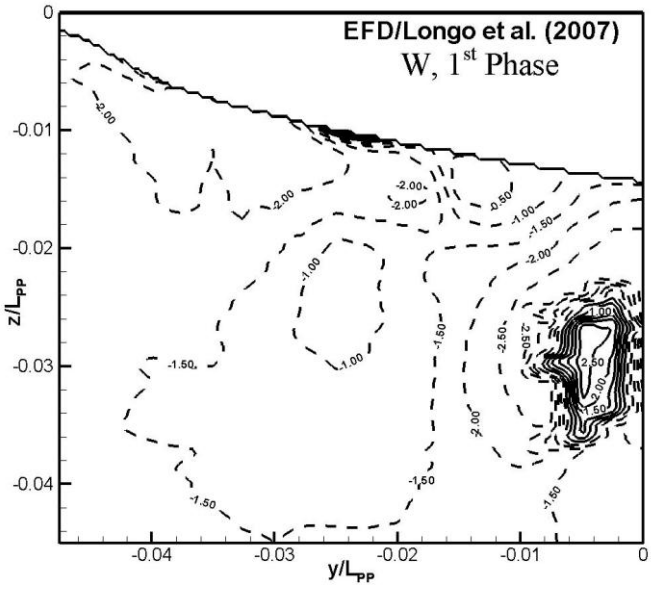

Experiment (IIHR, Longo et al. 2007)

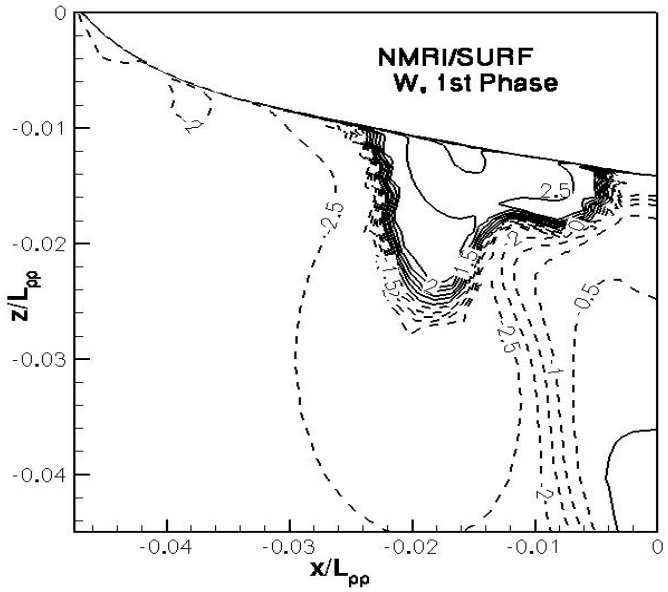

NMRI-SURF

Fig. 3.5-11-3 *W* contours of 1st phase at $x/L_{PP} = 0.935$ [$\Delta GW = 0.5$]
(Solid lines: positive (+) values; Dashed lines: negative (-) values)

Test Case 3.6

Table 3.6-T E_{RSS} for force and moment coefficients and roll angle time history

Figure 3.6-1 Time history of C_{TX}
Figure 3.6-2 Time history of roll angle
Figure 3.6-3 Mean wave-elevation ζ contours
Figure 3.6-4-1 Wave-elevation ζ_T contours during second cycle of roll decay (t/Te = 0)
Figure 3.6-4-2 Wave-elevation ζ_T contours during second cycle of roll decay (t/Te = 1/4)
Figure 3.6-4-3 Wave-elevation ζ_T contours during second cycle of roll decay (t/Te = 1/2)
Figure 3.6-4-4 Wave-elevation ζ_T contours during second cycle of roll decay (t/Te = 3/4)
Figure 3.6-5-1 Contours of U velocity at x/L_{PP}= 0.675 during second cycle of roll decay (t/Te = 0)
Figure 3.6-5-2 Contours of U velocity at x/L_{PP} = 0.675 during second cycle of roll decay (t/Te = 1/4)
Figure 3.6-5-3 Contours of U velocity at x/L_{PP} = 0.675 during second cycle of roll decay (t/Te = 1/2)
Figure 3.6-5-4 Contours of U velocity at x/L_{PP} = 0.675 during second cycle of roll decay (t/Te = 3/4)
Figure 3.6-6-1 Contours of V velocity at x/L_{PP} = 0.675 during second cycle of roll decay (t/Te = 0)
Figure 3.6-6-2 Contours of V velocity at x/L_{PP} = 0.675 during second cycle of roll decay (t/Te = 1/4)
Figure 3.6-6-3 Contours of V velocity at x/L_{PP} = 0.675 during second cycle of roll decay (t/Te = 1/2)
Figure 3.6-6-4 Contours of V velocity at x/L_{PP} = 0.675 during second cycle of roll decay (t/Te = 3/4)
Figure 3.6-7-1 Contours of W velocity at x/L_{PP} = 0.675 during second cycle of roll decay (t/Te = 0)
Figure 3.6-7-2 Contours of W velocity at x/L_{PP} = 0.675 during second cycle of roll decay (t/Te = 1/4)
Figure 3.6-7-3 Contours of W velocity at x/L_{PP} = 0.675 during second cycle of roll decay (t/Te = 1/2)
Figure 3.6-7-4 Contours of W velocity at x/L_{PP} = 0.675 during second cycle of roll decay (t/Te = 3/4)

Table 3.6-T E_{RSS} for force and moment coefficients and roll angle time history

Organization (Code)	E_{RSS}-C_{TX}	E_{RSS}-ϕ
ECN/CNRS (ISISCFD)	0.0920	0.00258
GL&UDE (OpenFOAM1.6libSixDoFv1.1.0)	-	0.0017

$$E_{RSS} = \frac{1}{N}\sqrt{\sum_{i=1}^{N}\left(E_i/\bar{C}\right)^2}\ ,\ E_i = EFD(t_i) - CFD(t_i)$$

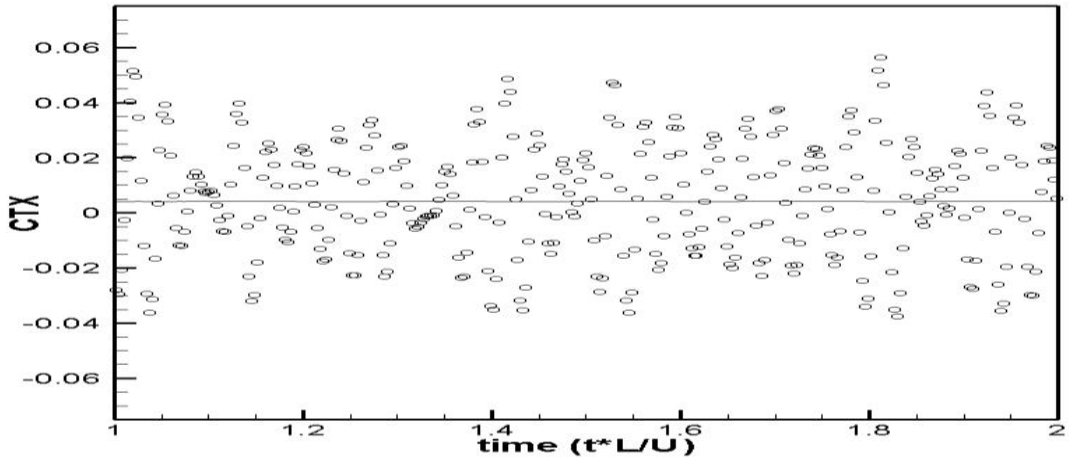

ECN/BEC/HO-Icare

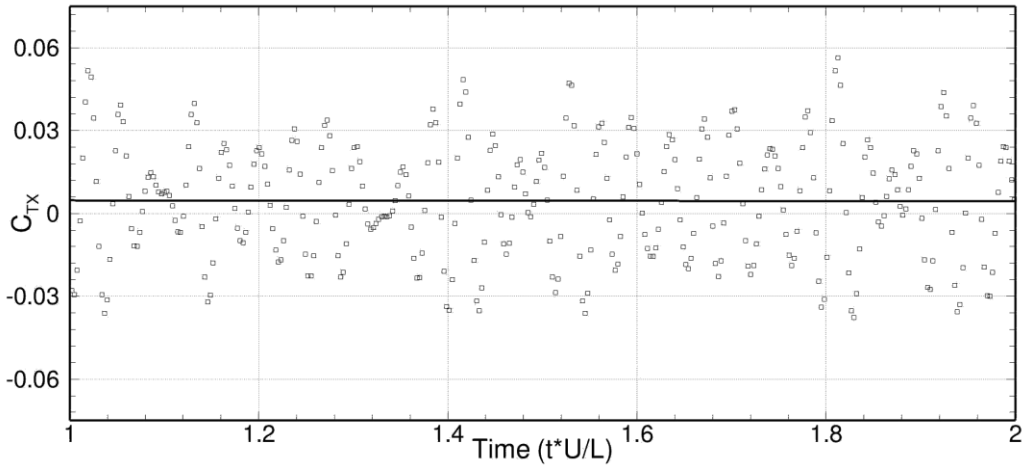

ECN/CNRS-ISISCFD

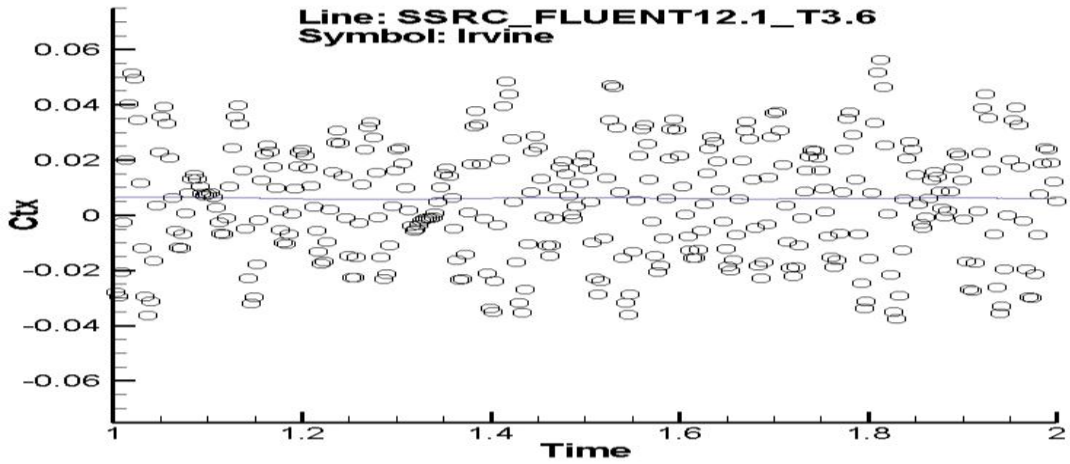

SSRC-FLUENT12.1

Fig. 3.6-1 Time history of C_{TX}
(EFD: Open circle; CFD: Solid black line)

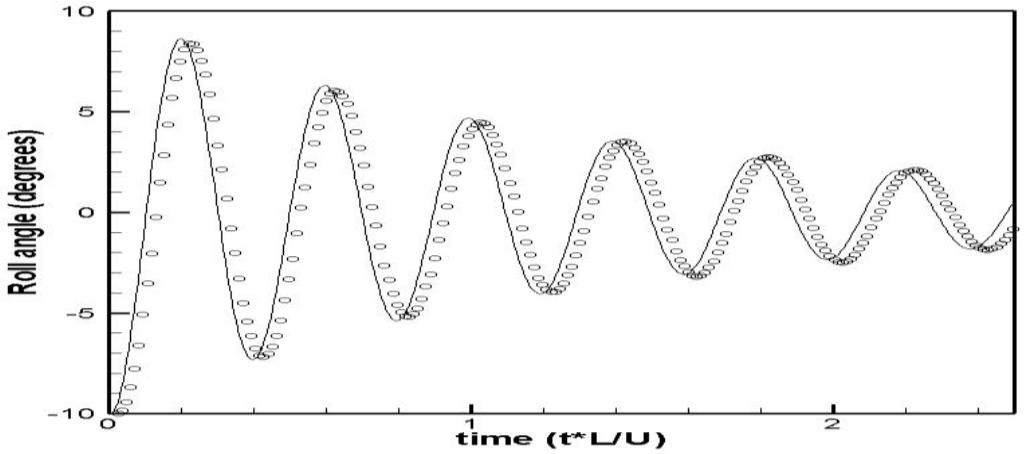

ECN/BEC/HO-Icare

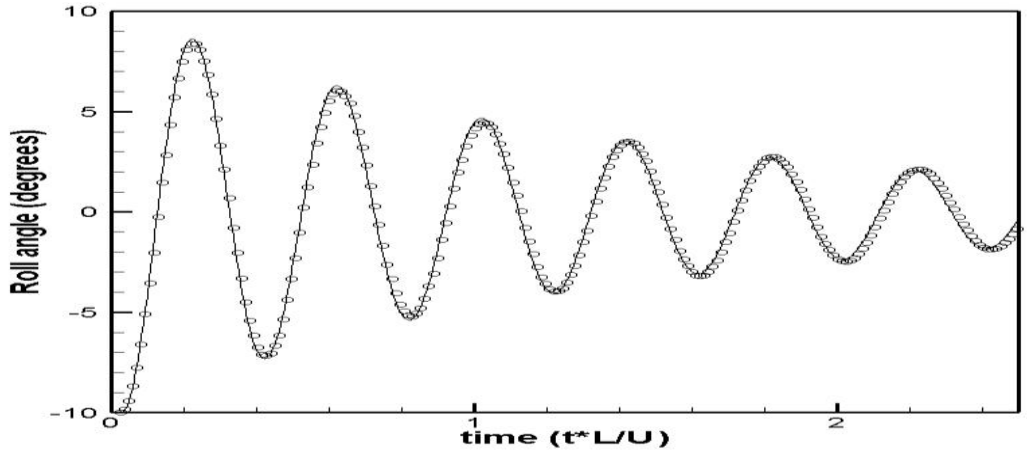

ECN/BEC/HO-Icare (recale)

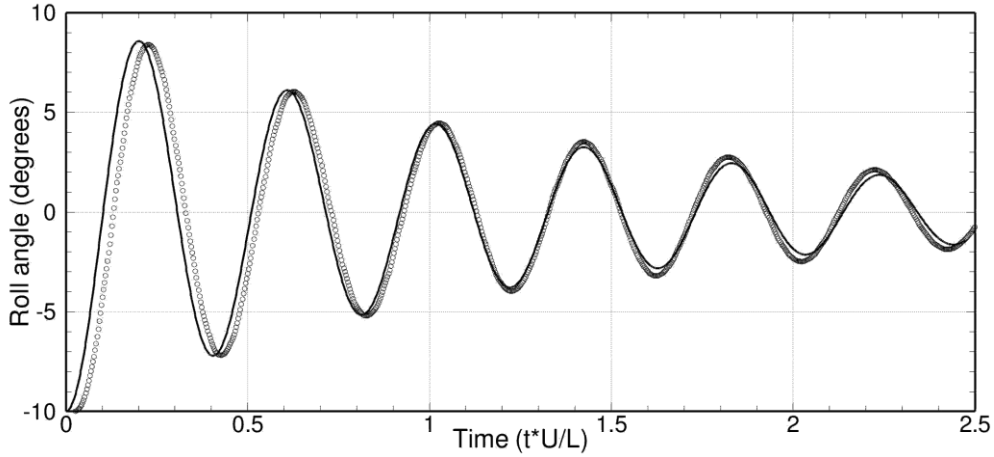

ECN/CNRS-ISISCFD

Fig. 3.6-2 Time history of roll angle
(EFD: Open circle; CFD: Solid black line)

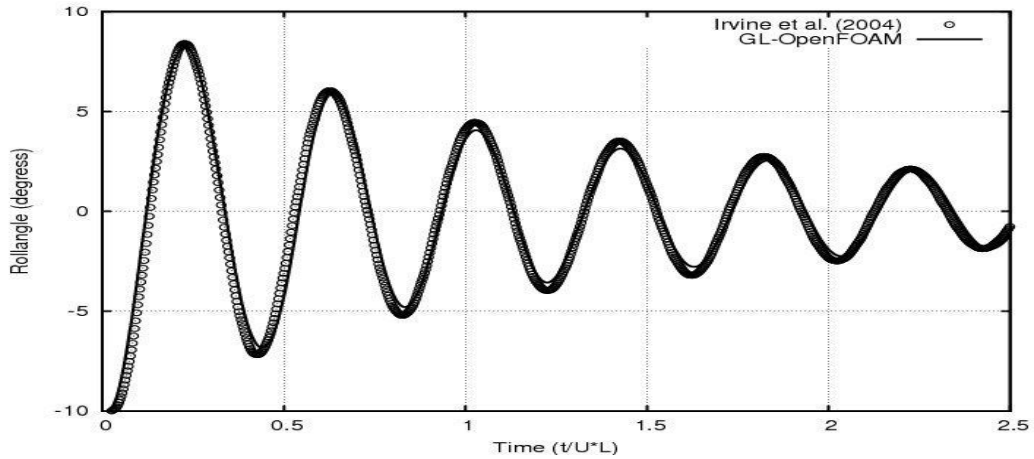

GL&UDE-OpenFOAM

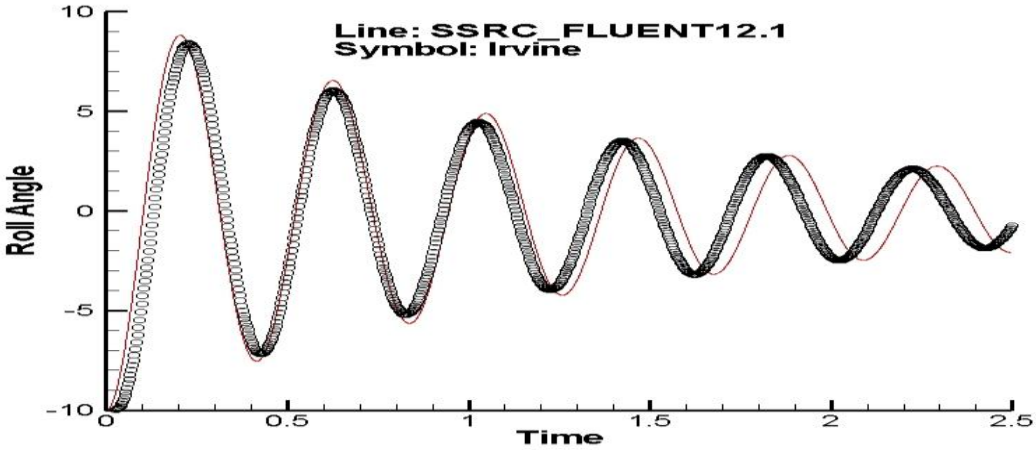

SSRC-FLUENT12.1

Fig. 3.6-2 Time history of roll angle
(EFD: Open circle; CFD: Solid black line)

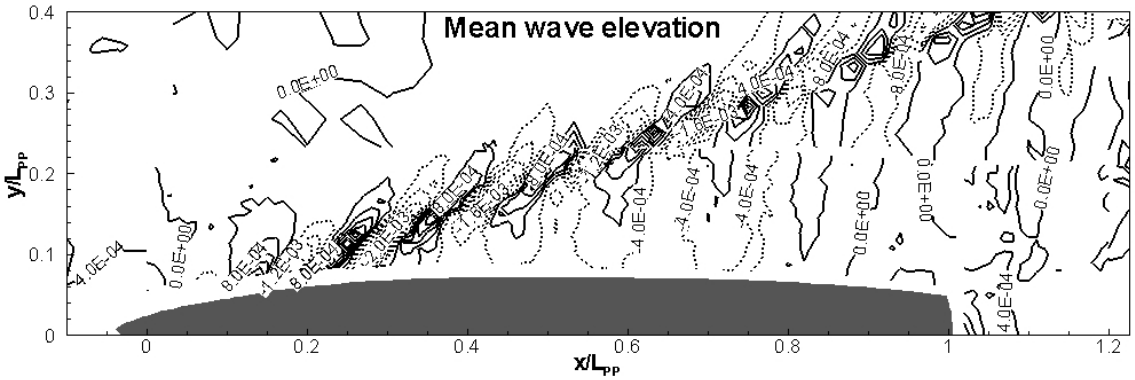

Experiment (IIHR, Irvine et al. 2004)

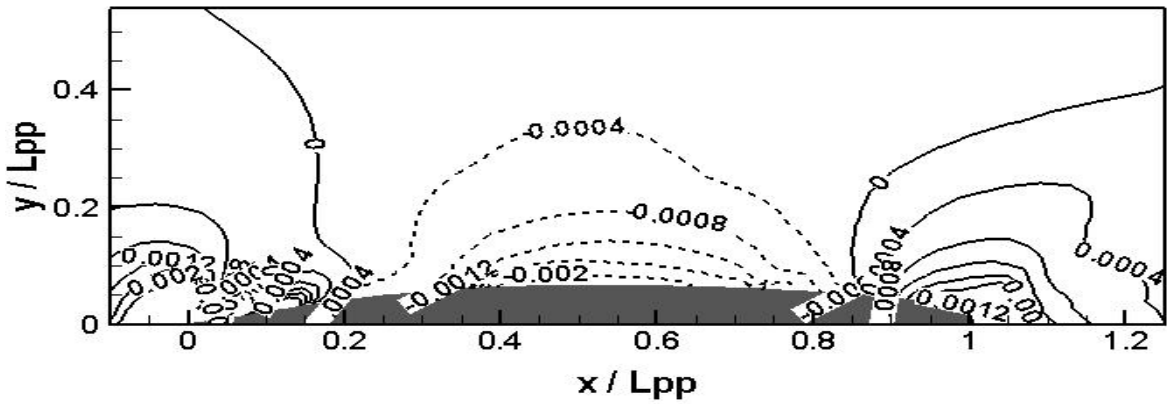

ECN/BEC/HO-Icare

Fig. 3.6-3 Mean wave-elevation ζ contours [$\Delta z = 0.004$]
(EFD: Open circle; CFD: Solid black line)

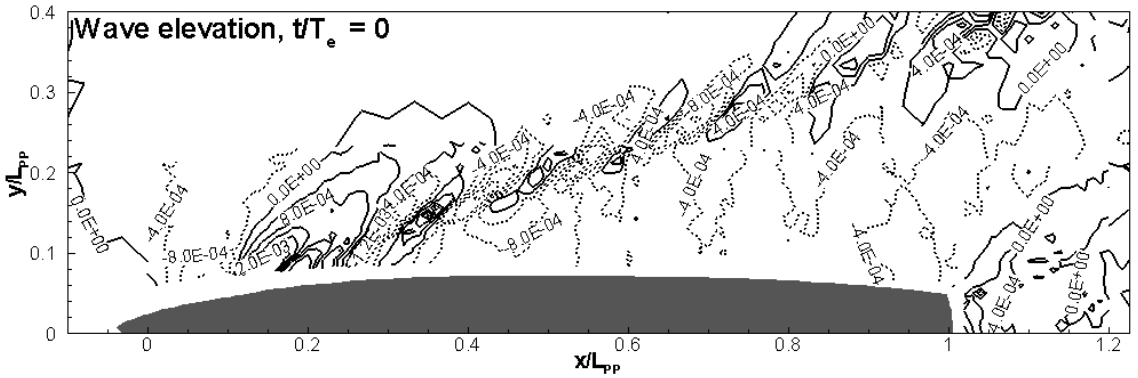

Experiment (IIHR, Irvine et al. 2004)

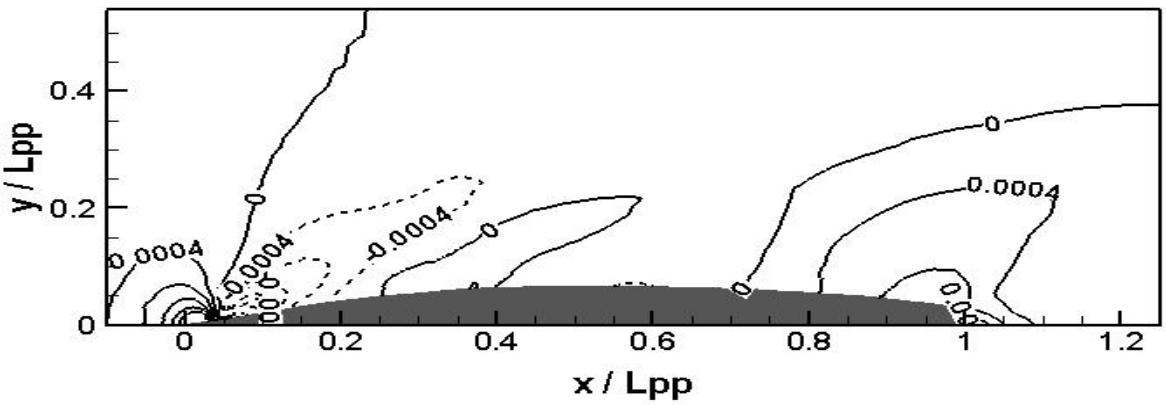

ECN/BEC/HO-Icare

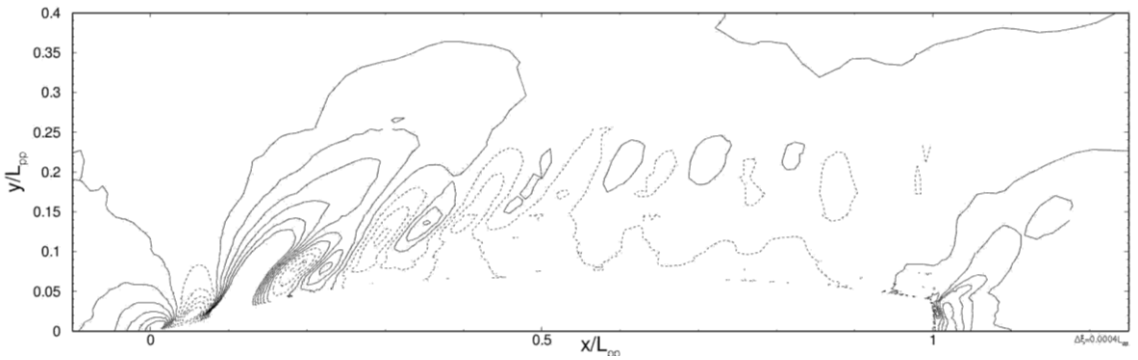

ECN/CNRS-ISISCFD

Fig. 3.6-4-1 Wave-elevation ζ_T contours during second cycle of roll decay (t/Te = 0) [Δz = 0.004]
(Solid lines: positive; broken lines: negative)

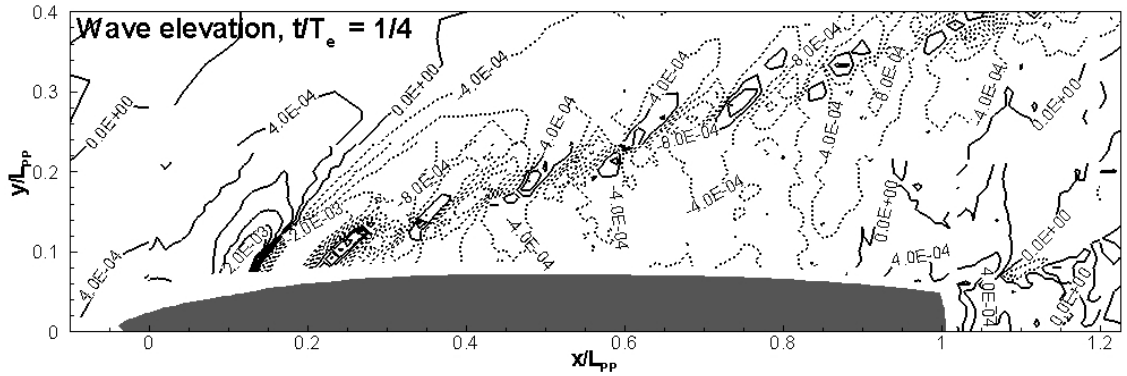

Experiment (IIHR, Irvine et al. 2004)

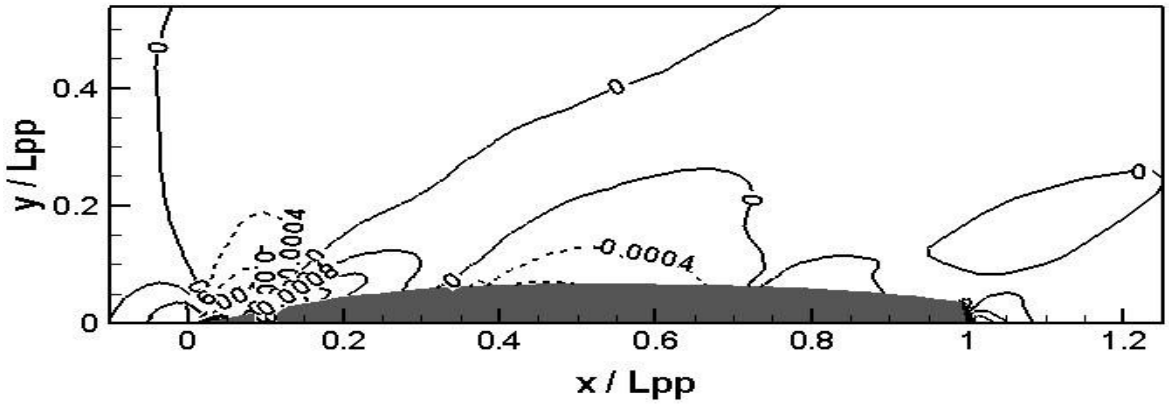

ECN/BEC/HO-Icare

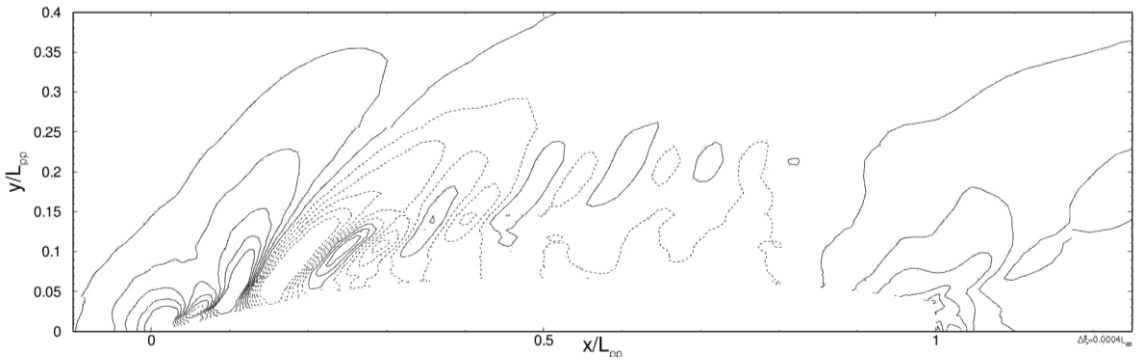

ECN/CNRS-ISISCFD

Fig. 3.6-4-2 Wave-elevation ζ_T contours during second cycle of roll decay (t/Te = 1/4) [Δz = 0.004]
(Solid lines: positive; broken lines: negative)

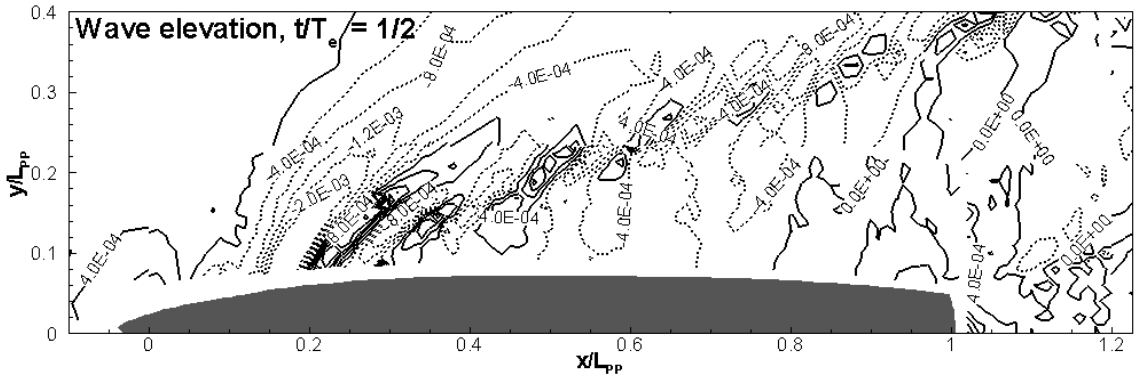

Experiment (IIHR, Irvine et al. 2004)

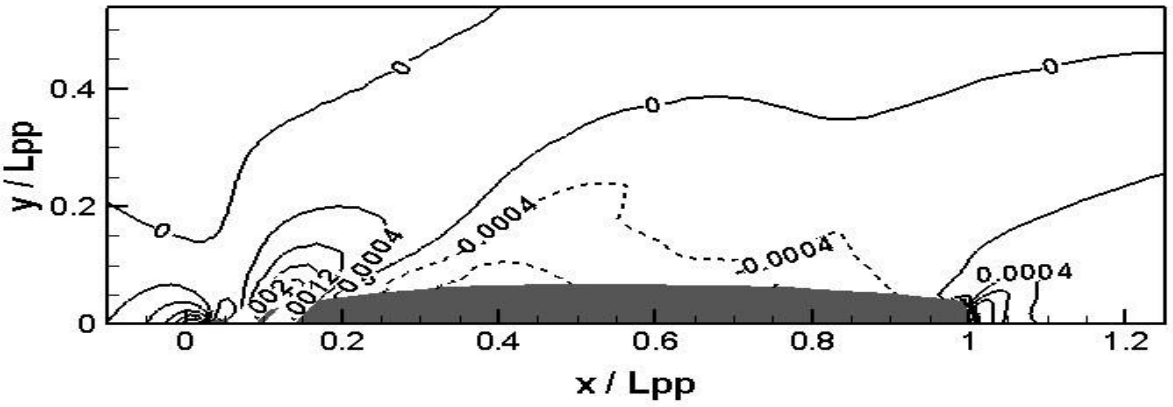

ECN/BEC/HO-Icare

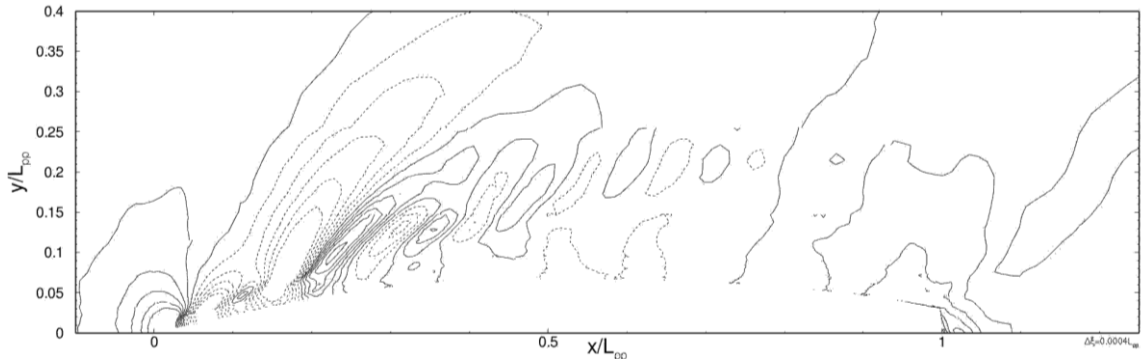

ECN/CNRS-ISISCFD

Fig. 3.6-4-3 Wave-elevation ζ_T contours during second cycle of roll decay (t/Te = 1/2) [Δz = 0.004]
(Solid lines: positive; broken lines: negative)

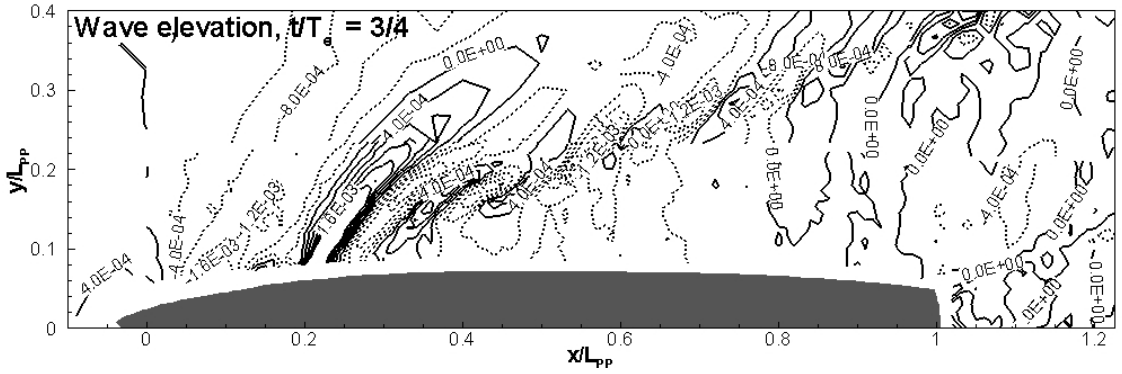

Experiment (IIHR, Irvine et al. 2004)

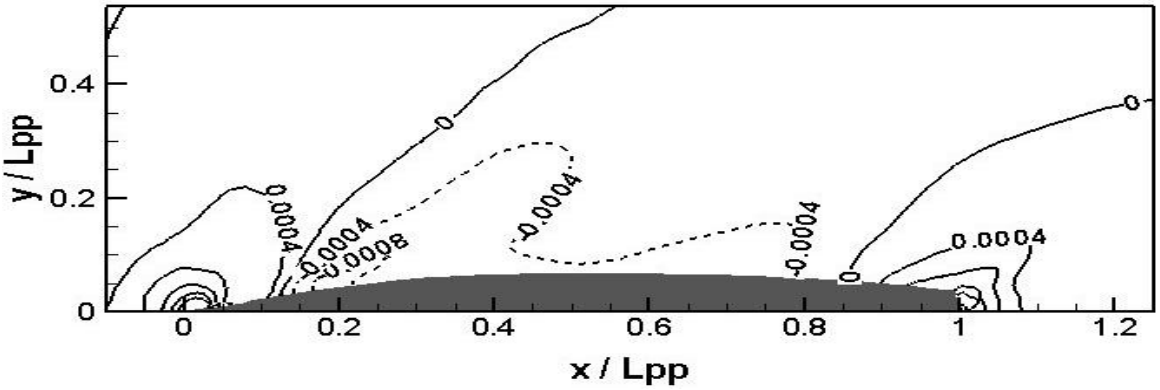

ECN/BEC/HO-Icare

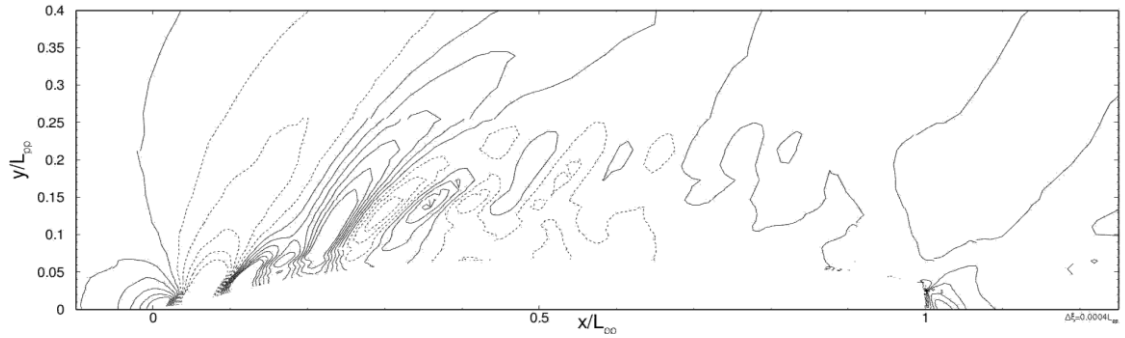

ECN/CNRS-ISISCFD

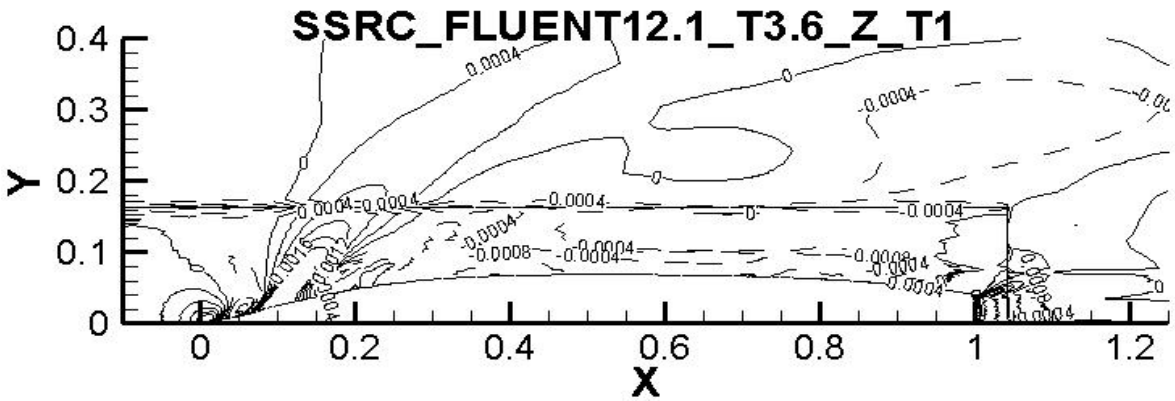

SSRC-FLUENT12.1

Fig. 3.6-4-4 Wave-elevation ζ_T contours during second cycle of roll decay (t/Te = 3/4) [Δz = 0.004]
(Solid lines: positive; broken lines: negative)

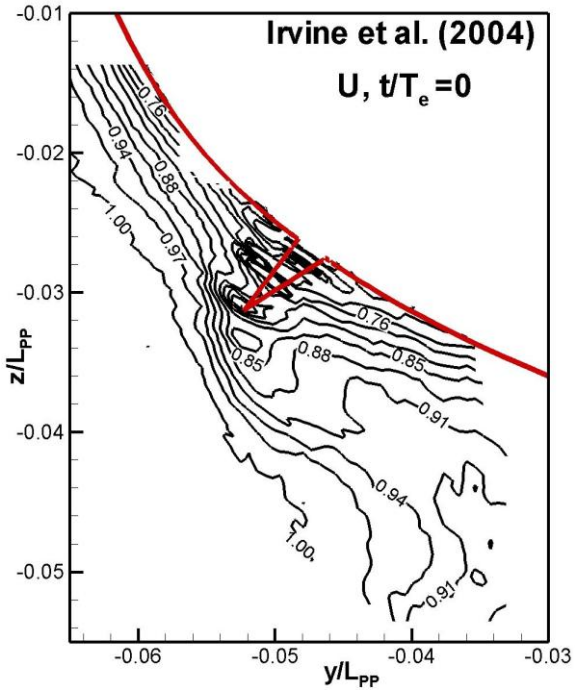

Experiment (IIHR, Irvine et al. 2004)

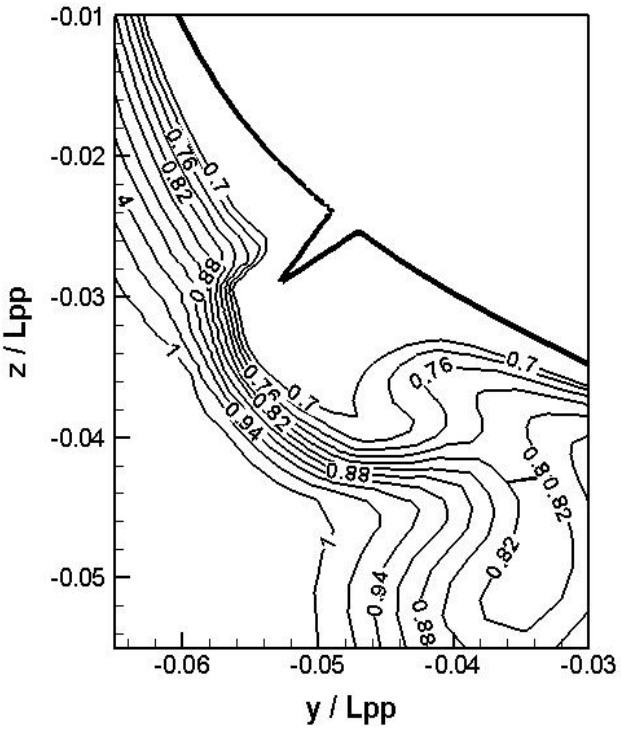

ECN/BEC/HO-Icare

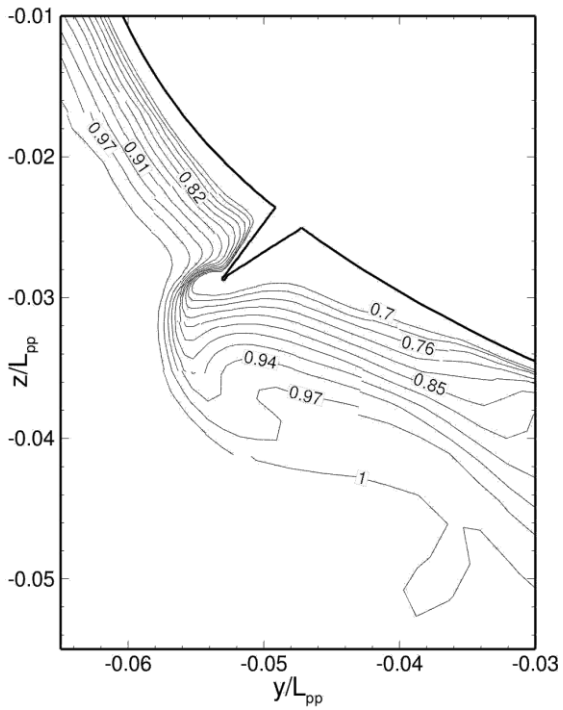

ECN/CNRS-ISISCFD

Fig. 3.6-5-1 Contours of U velocity at $x/L_{PP} = 0.675$ during second cycle of roll decay ($t/Te = 0$) [$\Delta U = 0.03$]

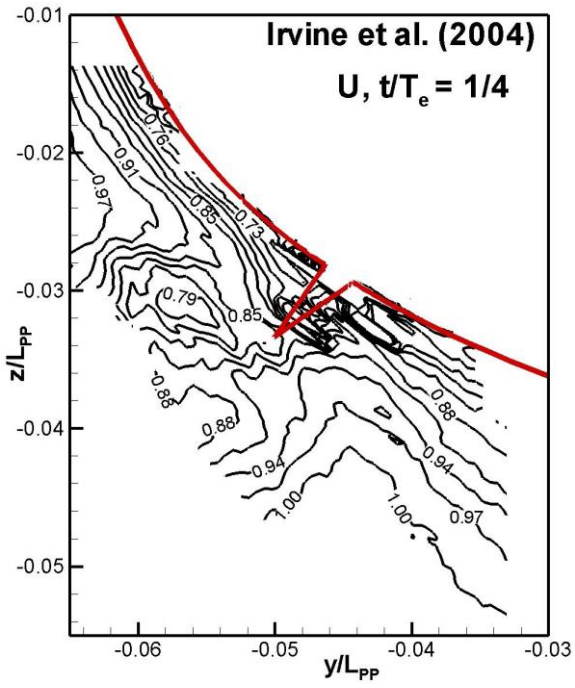

Experiment (IIHR, Irvine et al. 2004)

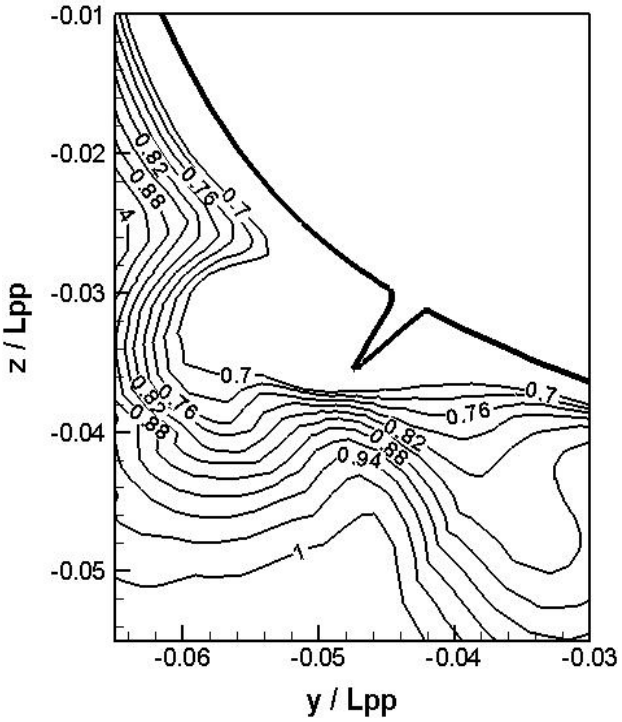

ECN/BEC/HO-Icare

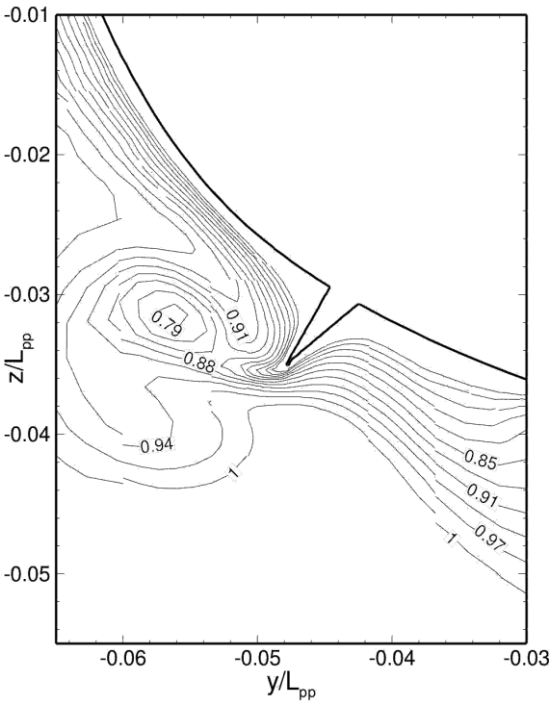

ECN/CNRS-ISISCFD

Fig. 3.6-5-2 Contours of U velocity at $x/L_{PP} = 0.675$ during second cycle of roll decay ($t/Te = 1/4$) [$\Delta U = 0.03$]

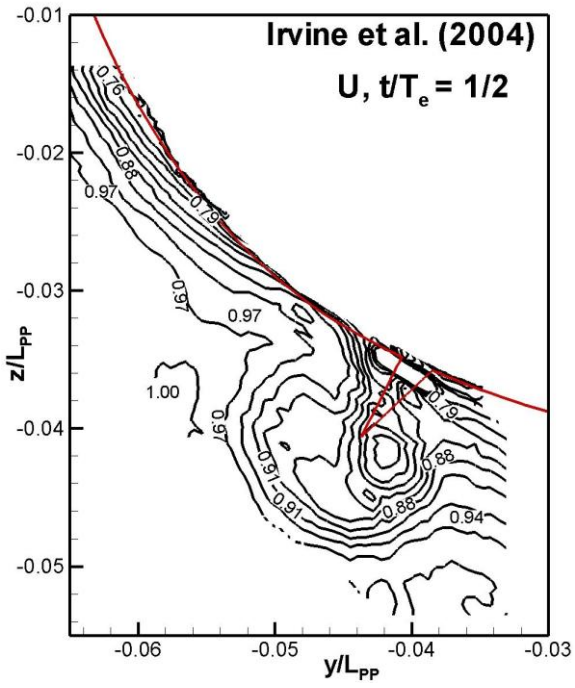

Experiment (IIHR, Irvine et al. 2004)

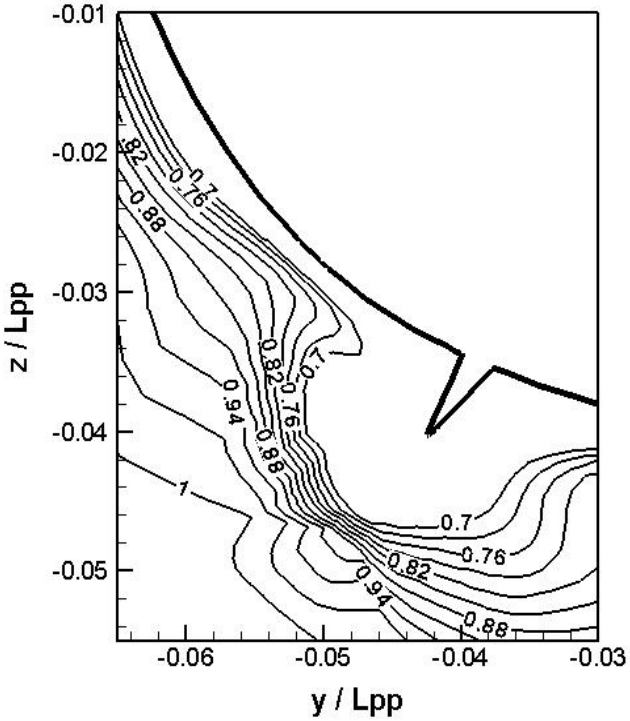

ECN/BEC/HO-Icare

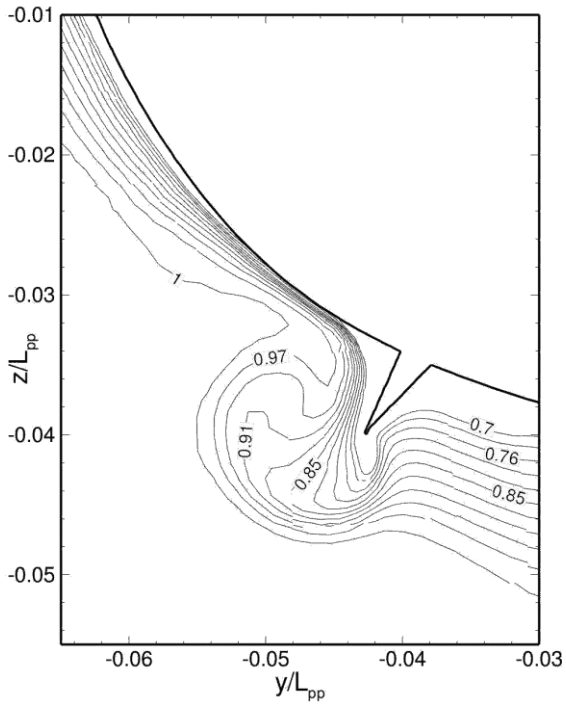

ECN/CNRS-ISISCFD

Fig. 3.6-5-3 Contours of U velocity at $x/L_{PP} = 0.675$ during second cycle of roll decay ($t/Te = 1/2$) [$\Delta U = 0.03$]

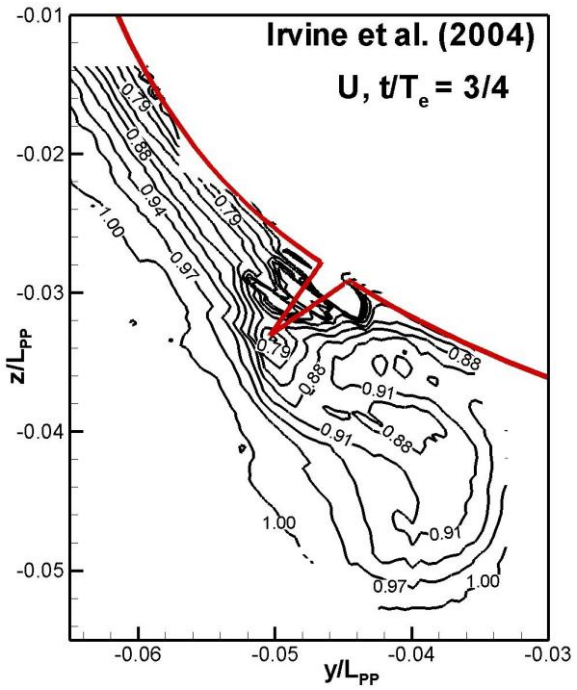

Experiment (IIHR, Irvine et al. 2004)

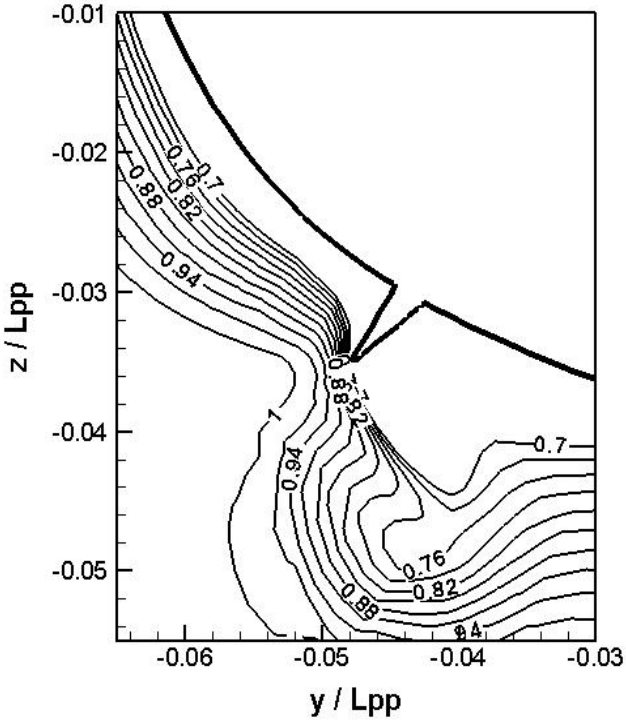

ECN/BEC/HO-Icare

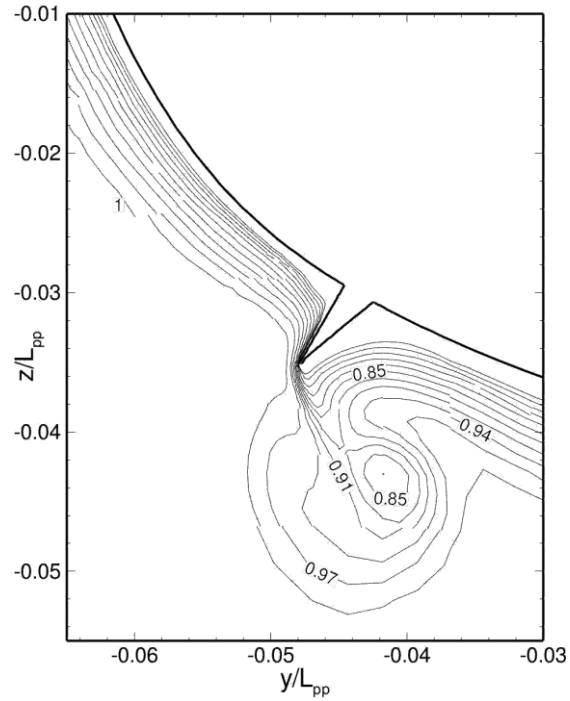

ECN/CNRS-ISISCFD

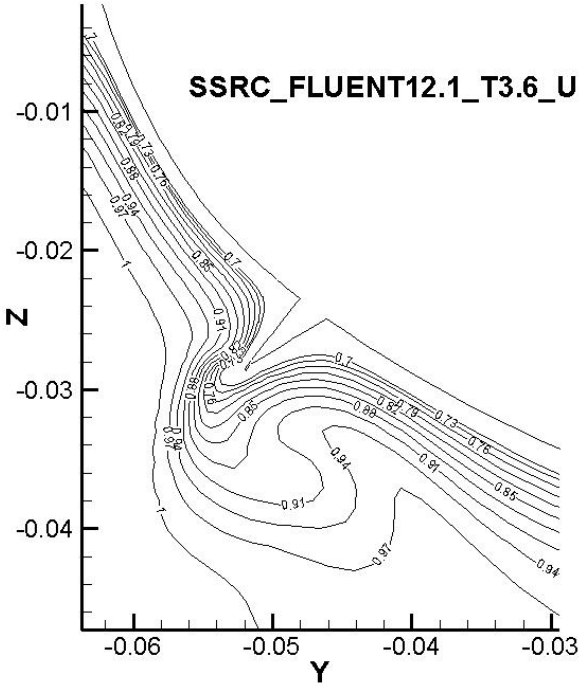

SSRC-FLUENT12.1

Fig. 3.6-5-4 Contours of U velocity at $x/L_{PP} = 0.675$ during second cycle of roll decay ($t/Te = 3/4$) [$\Delta U = 0.03$]

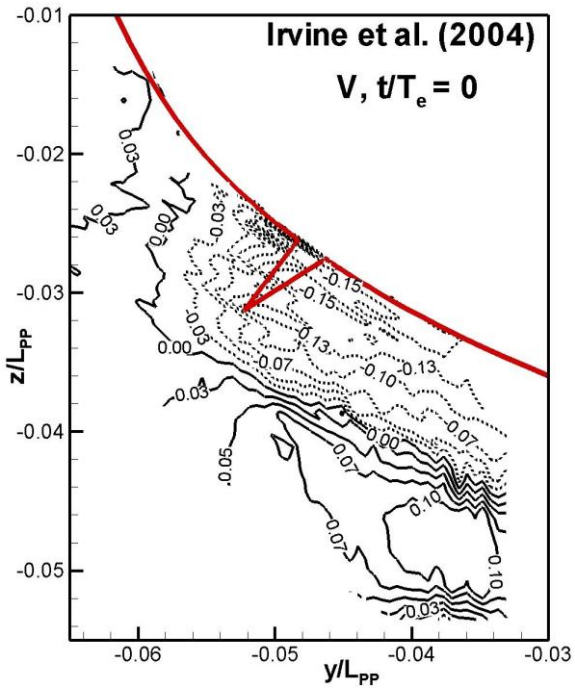

Experiment (IIHR, Irvine et al. 2004)

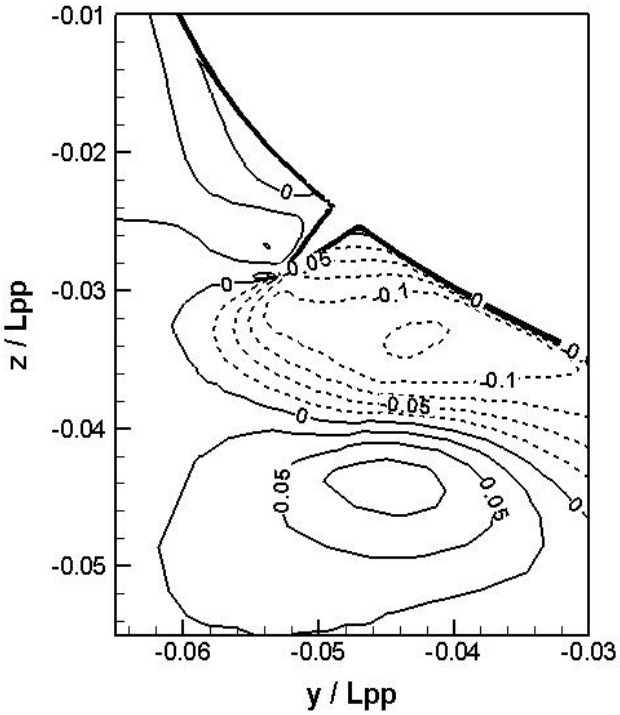

ECN/BEC/HO-Icare

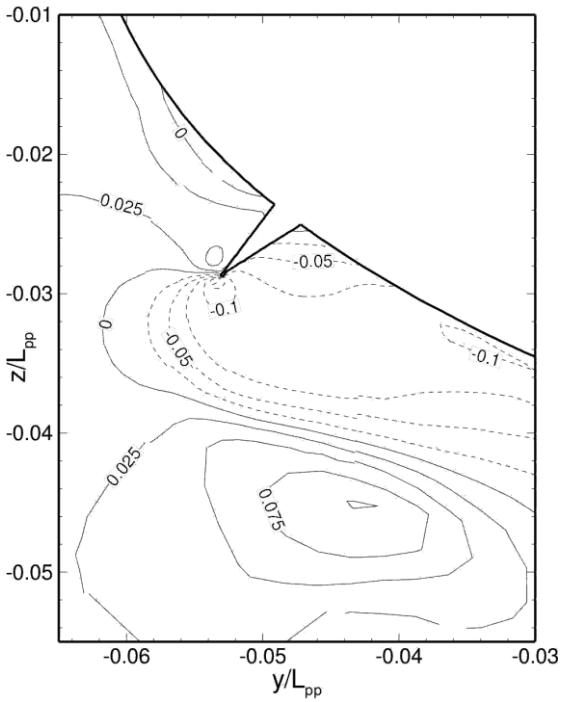

ECN/CNRS-ISISCFD

Fig. 3.6-6-1 Contours of V velocity at $x/L_{pp} = 0.675$ during second cycle of roll decay ($t/Te = 0$) [$\Delta V = 0.025$]
(Solid lines: positive; broken lines: negative)

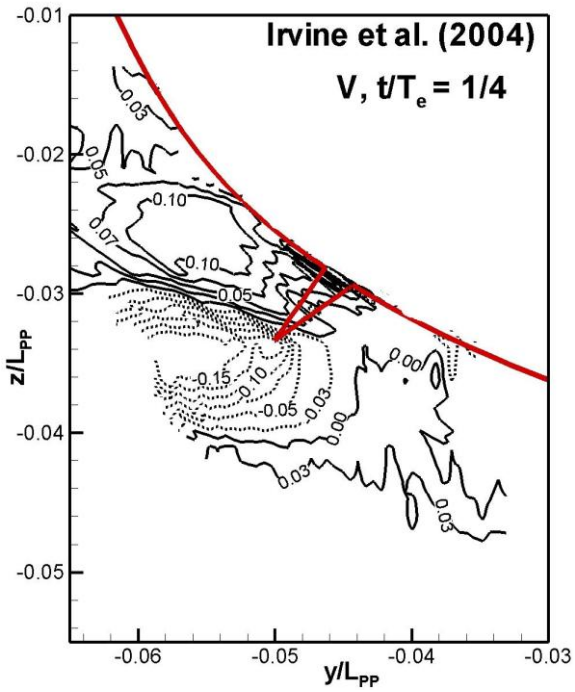

Experiment (IIHR, Irvine et al. 2004)

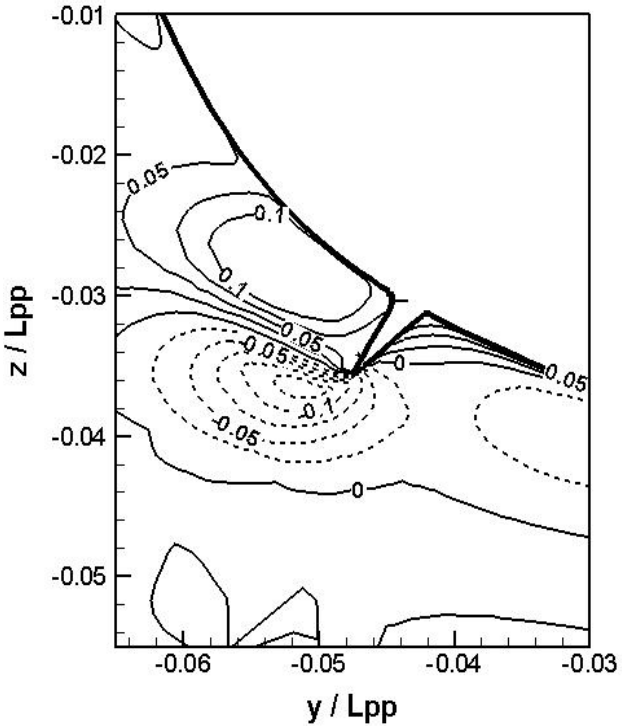

ECN/BEC/HO-Icare

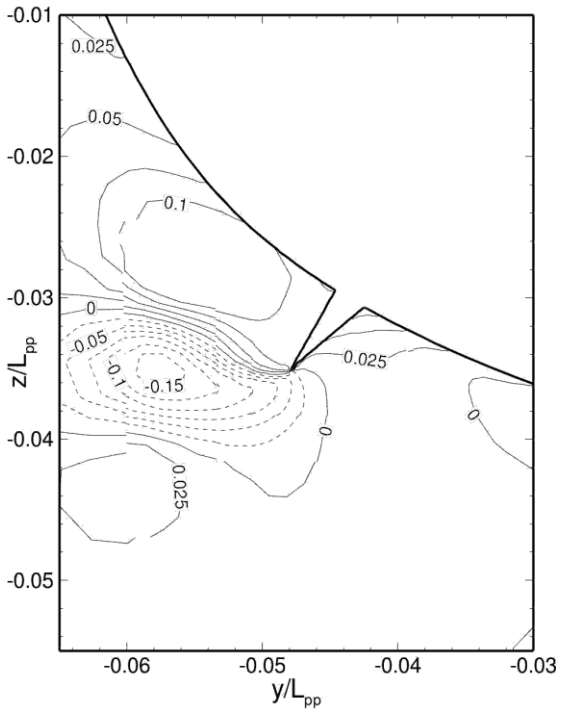

ECN/CNRS-ISISCFD

Fig. 3.6-6-2 Contours of V velocity at $x/L_{PP} = 0.675$ during second cycle of roll decay ($t/Te = 1/4$) [$\Delta V = 0.025$]
(Solid lines: positive; broken lines: negative)

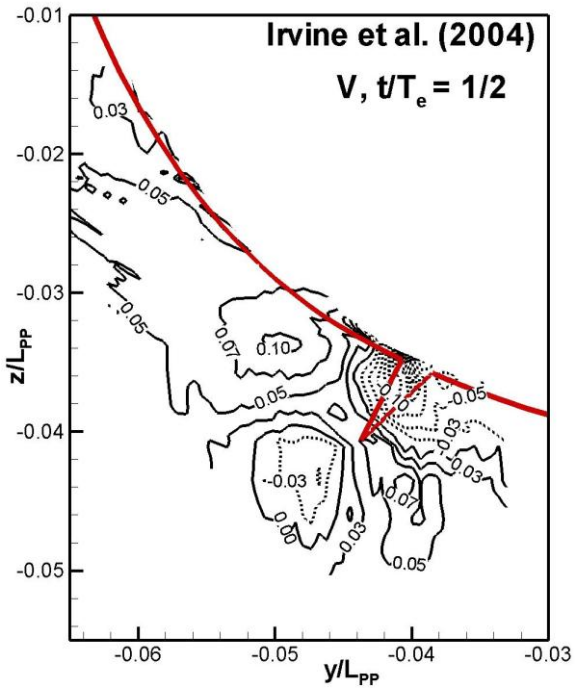

Experiment (IIHR, Irvine et al. 2004)

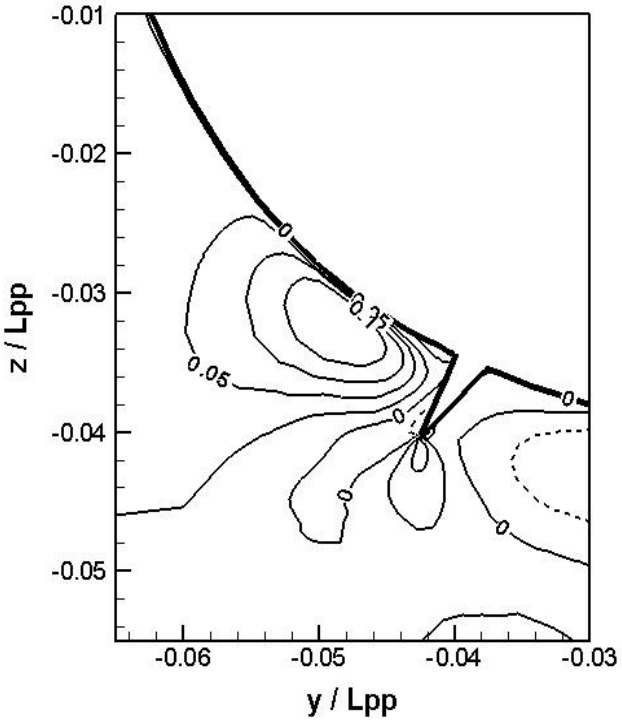

ECN/BEC/HO-Icare

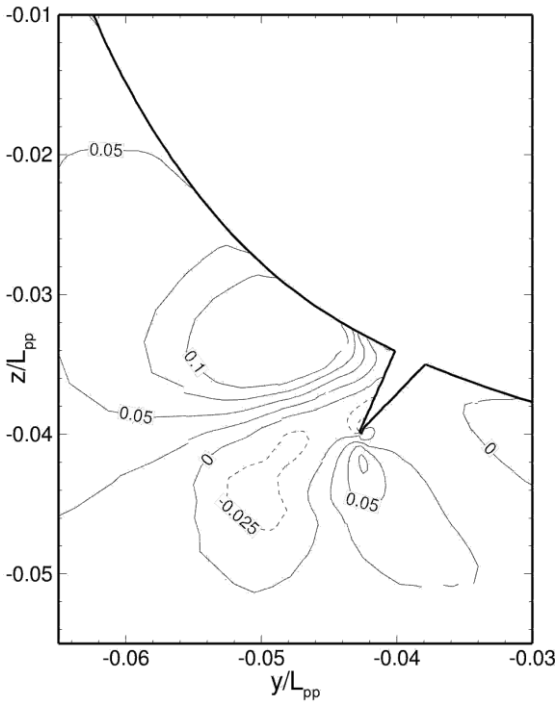

ECN/CNRS-ISISCFD

Fig. 3.6-6-3 Contours of V velocity at $x/L_{PP} = 0.675$ during second cycle of roll decay
($t/Te = 1/2$) [$\Delta V = 0.025$]
(Solid lines: positive; broken lines: negative)

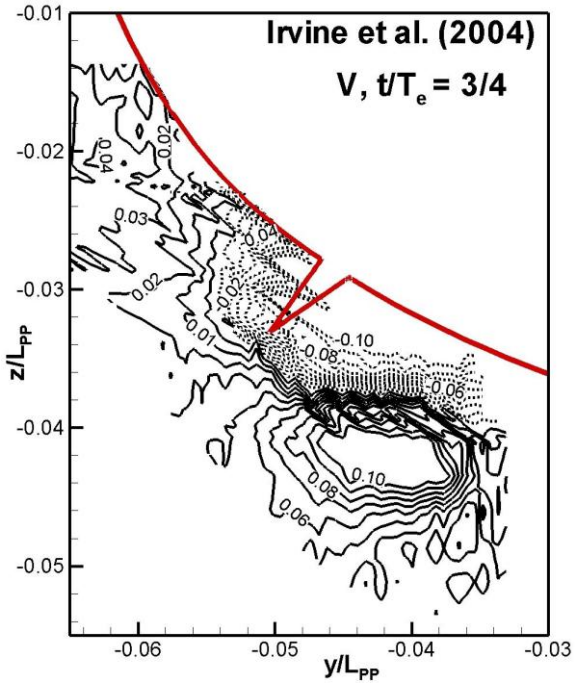

Experiment (IIHR, Irvine et al. 2004)

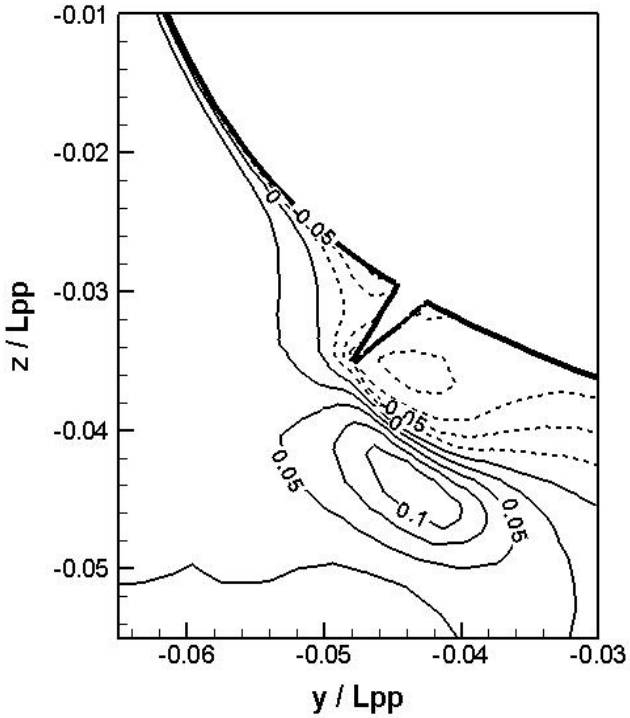

ECN/BEC/HO-Icare

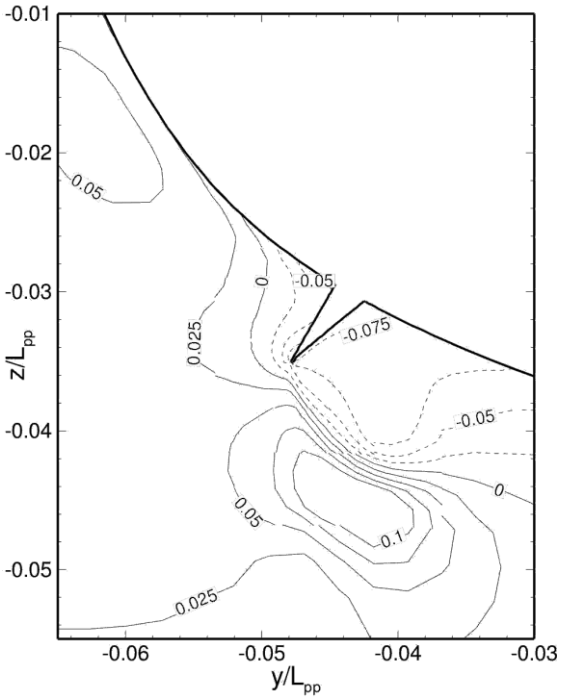

ECN/CNRS-ISISCFD

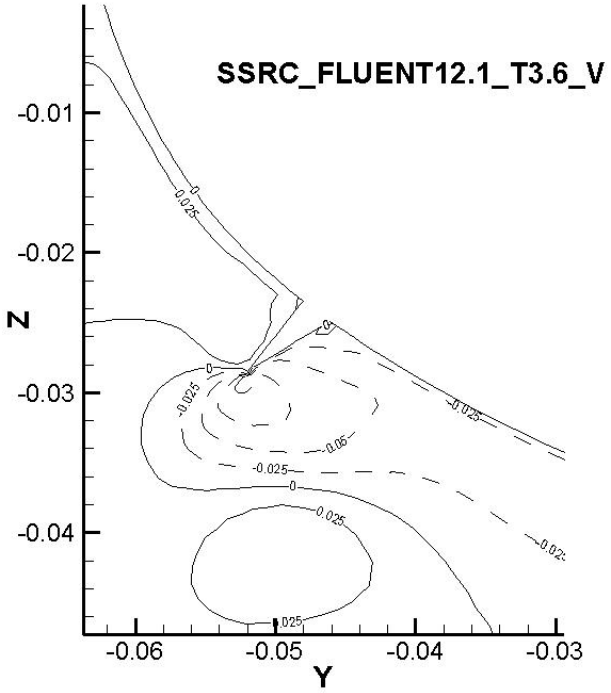

SSRC-FLUENT12.1

Fig. 3.6-6-4 Contours of V velocity at $x/L_{PP} = 0.675$ during second cycle of roll decay
($t/Te = 3/4$) [$\Delta V = 0.025$]
(Solid lines: positive; broken lines: negative)

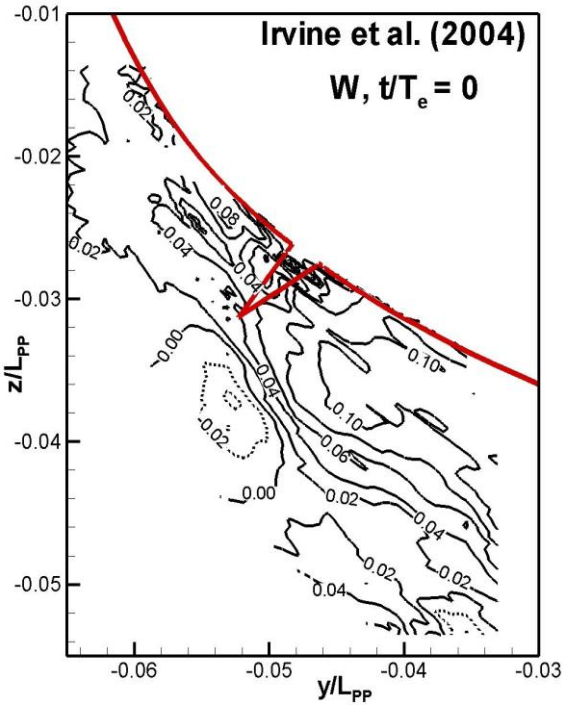

Experiment (IIHR, Irvine et al. 2004)

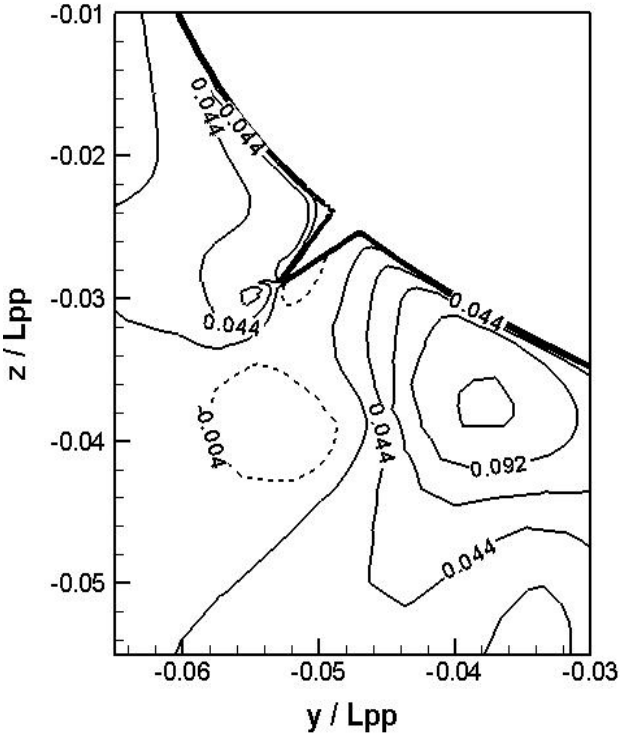

ECN/BEC/HO-Icare

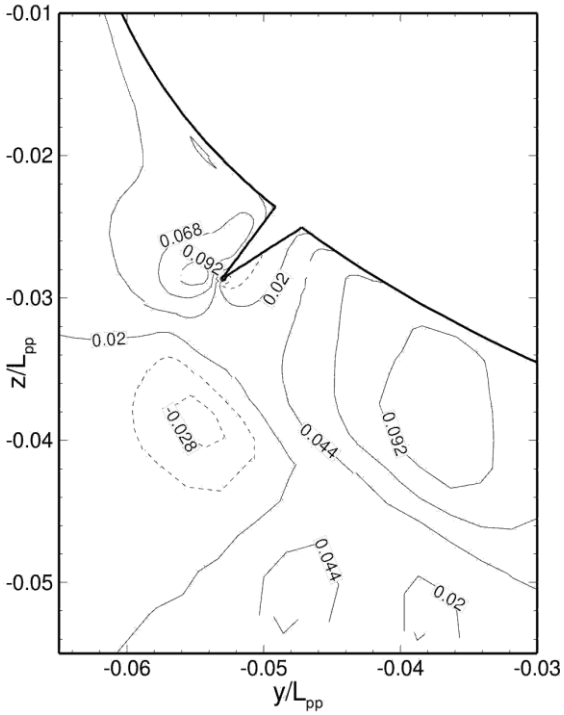

ECN/CNRS-ISISCFD

Fig. 3.6-7-1 Contours of W velocity at $x/L_{PP} = 0.675$ during second cycle of roll decay ($t/Te = 0$) [$\Delta W = 0.024$]
(Solid lines: positive; broken lines: negative)

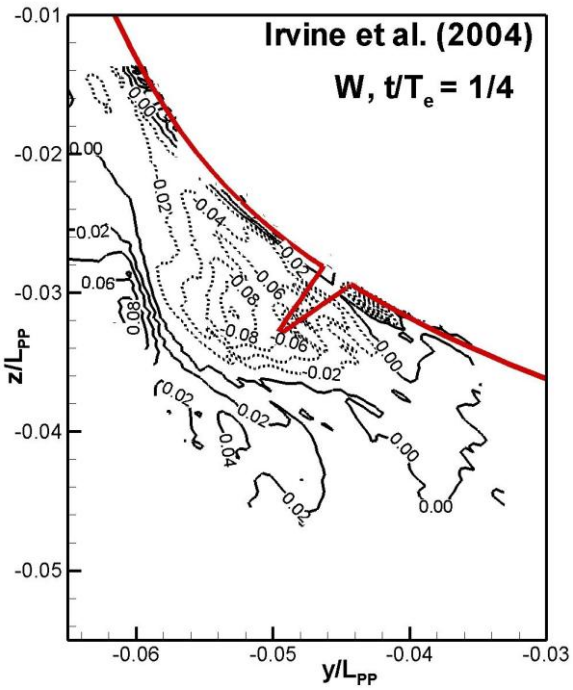

Experiment (IIHR, Irvine et al. 2004)

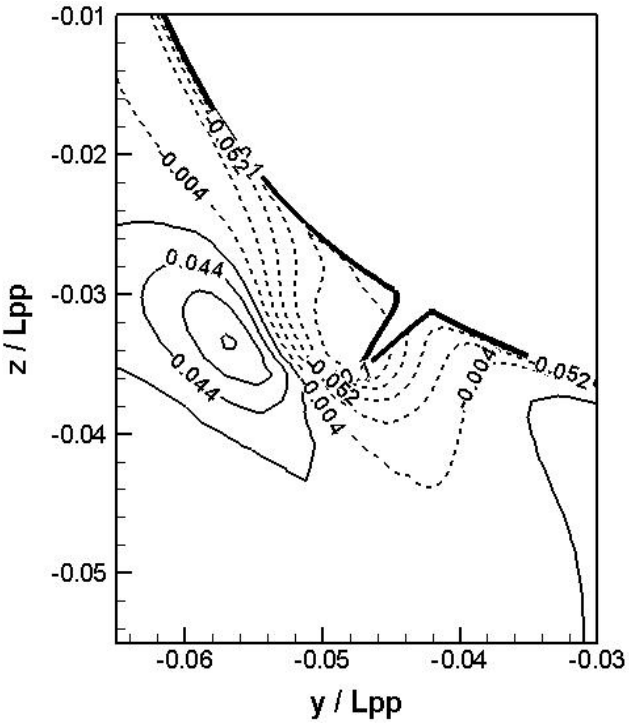

ECN/BEC/HO-Icare

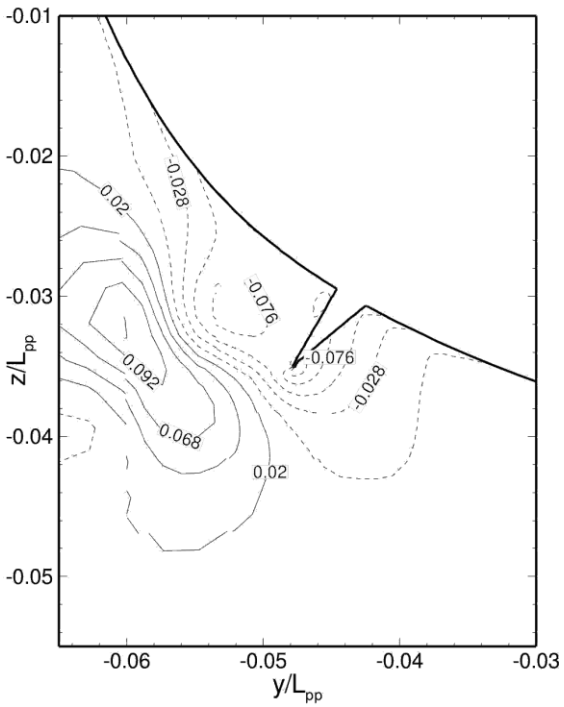

ECN/CNRS-ISISCFD

Fig. 3.6-7-2 Contours of W velocity at $x/L_{PP} = 0.675$ during second cycle of roll decay
($t/Te = 1/4$) [$\Delta W = 0.024$]
(Solid lines: positive; broken lines: negative)

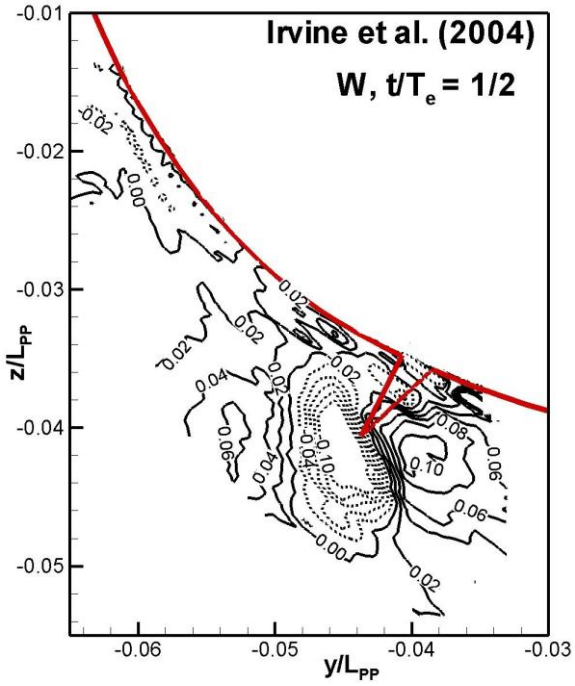

Experiment (IIHR, Irvine et al. 2004)

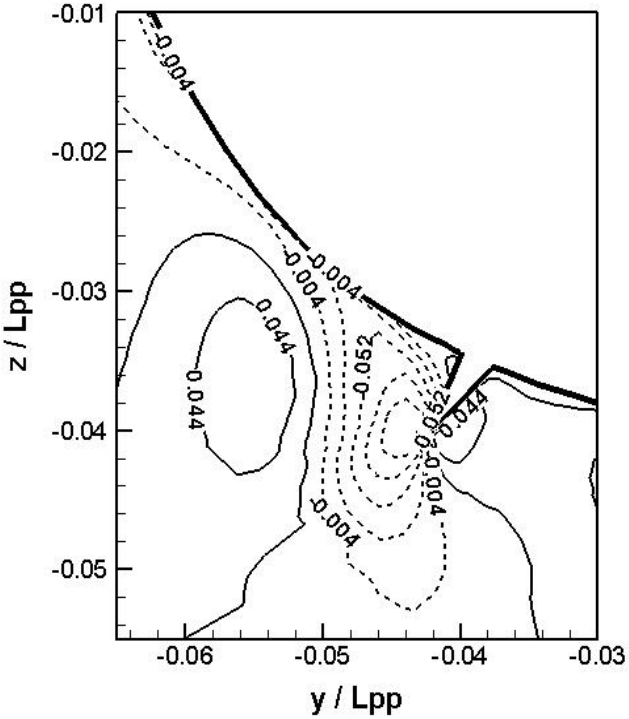

ECN/BEC/HO-Icare

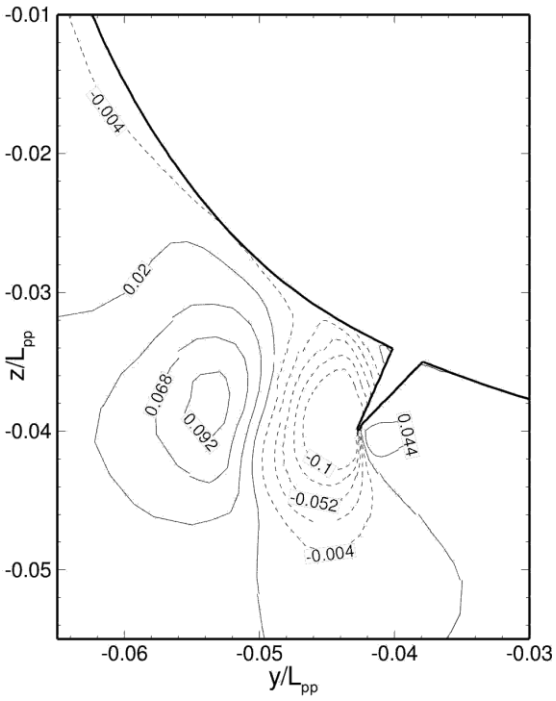

ECN/CNRS-ISISCFD

Fig. 3.6-7-3 Contours of W velocity at $x/L_{PP} = 0.675$ during second cycle of roll decay
($t/Te = 1/2$) [$\Delta W = 0.024$]
(Solid lines: positive; broken lines: negative)

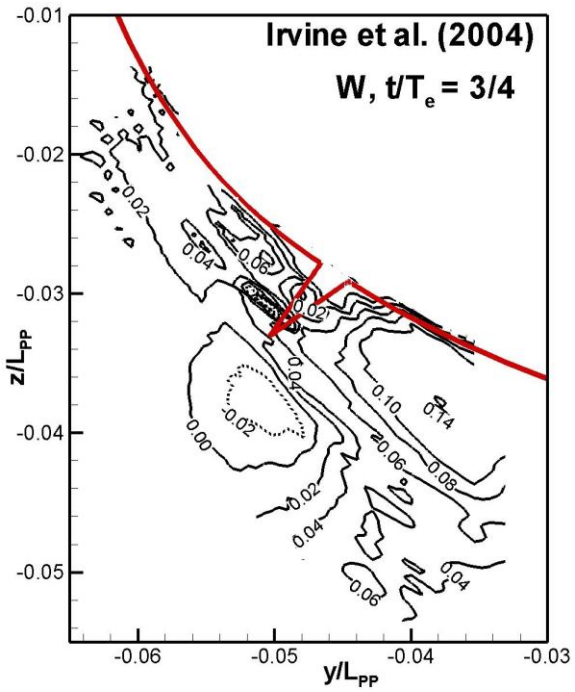

Experiment (IIHR, Irvine et al. 2004)

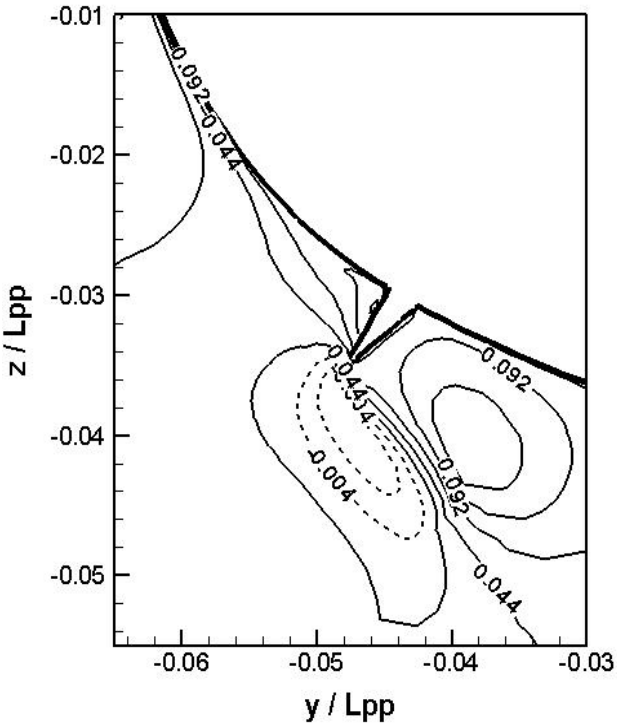

ECN/BEC/HO-Icare

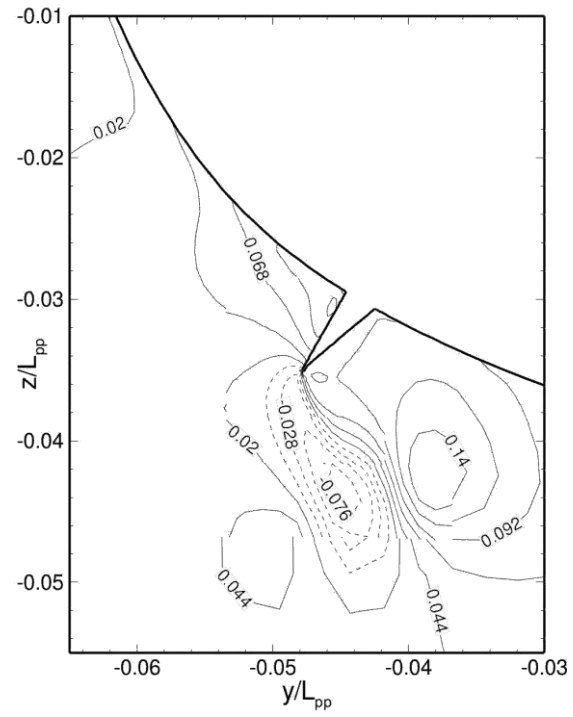

ECN/CNRS-ISISCFD

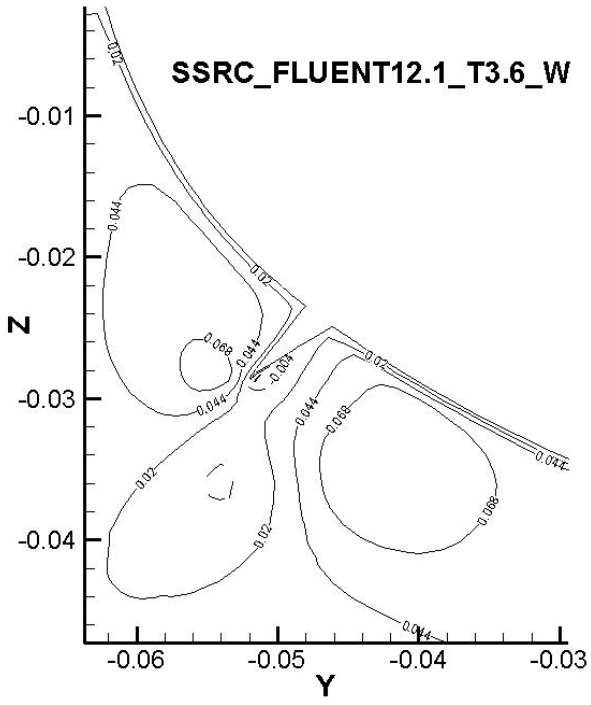

SSRC-FLUENT12.1

Fig. 3.6-7-4 Contours of W velocity at $x/L_{PP} = 0.675$ during second cycle of roll decay ($t/Te = 3/4$) [$\Delta W = 0.024$]
(Solid lines: positive; broken lines: negative)

PART 3: Papers

SIMULATION OF FLOW AROUND KCS-HULL

Sven Enger (CD-adapco, Germany)
Milovan Perić (CD-adapco, Germany)
Robinson Perić (University of Erlangen-Nürnberg, Germany)

1.SUMMARY

The paper describes results of computations of resistance, trim and sinkage for the KRISO Container Ship (KCS) at different Froude numbers in calm water. Unstructured trimmed grids with local refinement in zones of interest have been used to obtain maximum accuracy at low cell count. The solution method is of finite-volume type and uses mostly approximations of second order. Free surface is modeled using Volume-of-Fluid approach and a high-resolution interface-capturing scheme. It is demonstrated that acceptable accuracy can be achieved with grids containing around half a million cells for half of the geometry.

2. INTRODUCTION

Industrial use of Computational Fluid Dynamics (CFD) requires high level of automation, in order to provide sufficient accuracy at low effort (both in terms of manpower and computing time). Therefore the design of computational grid requires some effort, so that grid refinement and modifications to geometry can easily be done. All computations reported here were performed using the same grid topology described in the next section. All grids were created and all computations and post-processing were performed using STAR-CCM+ code.

The solution method is of finite-volume type and uses control volumes of arbitrary polyhedral shape. The conservation equations in integral form for mass and momentum, together with an equation for volume fraction of liquid and two or more equations describing turbulence quantities, are solved using a segregated iterative solution method based on SIMPLE-algorithm. Details on discretization and solution methods can be found in literature and will not be given here (see Ferziger and Perić, 2003; Demirdžić and Muzaferija, 1995; Weiss et al, 1999). All surface and volume integrals are approximated using midpoint rule; interpolation and gradient approximations are based on linear shape functions. Since time accuracy in the cases studied here is not of importance, first-order Euler implicit scheme is used for time integration.

The free-surface effects are modeled using the so called "Volume-of-Fluid" approach: the solution domain is assumed to be filled by a single effective fluid whose properties vary locally according to volume fraction of liquid. This equation contains only rate-of-change and convective term and its role is to track the deformation of the initially flat free surface. The convective terms are discretized using the HRIC-scheme (Muzaferija and Perić, 1999). It resolves the free surface typically with one cell when the interface is expected to be sharp.

In most computations, the standard k-ε turbulence model with wall functions was used to describe the effects of turbulence on the mean flow (Launder and Spalding, 1974). Some test calculations for the hull in fixed position and one Froude number were performed using two other two-equation turbulence models of edy-viscosity type and the full Reynolds-stress model, which requires the solution of 7 additional equations (6 for Reynolds stress tensor components and one for the dissipation rate). This was done to analyze the effects of turbulence models on the solution.

In addition, grid effects were analyzed by performing some simulations on a sequence of systematically refined grids. Grid spacing was reduced by a factor of 1.5 in the entire solution domain, except in the prism layer along walls, where the refinement was only in the directions tangential to wall. This was done in order to keep y^+ values at near-wall cell centers around 50, which was found in the past to produce best solutions (Azcueta, 2001). However, one simulation was perform with varying mesh spacing in prism layer in wall-normal direction to assess the influence of y^+ on the predicted resistance.

3. GRID GENERATION

In this study trimmed hexahedral grids with local refinements and prism layers along walls were used. The grid generation process is driven by specifying base mesh size, relative to which all spacings (prism layer thickness, cell size in various regions etc.) are defined. Finer meshes of the same topology are then automatically created by just reducing the base size. In order to avoid using fine grid where it is not necessary (in front of hull and at larger distance above, below, on each side and behind the hull), local volumes of different shape were created and assigned particular cell size, resulting in mesh structure shown in Fig. 1 for the coarsest mesh.

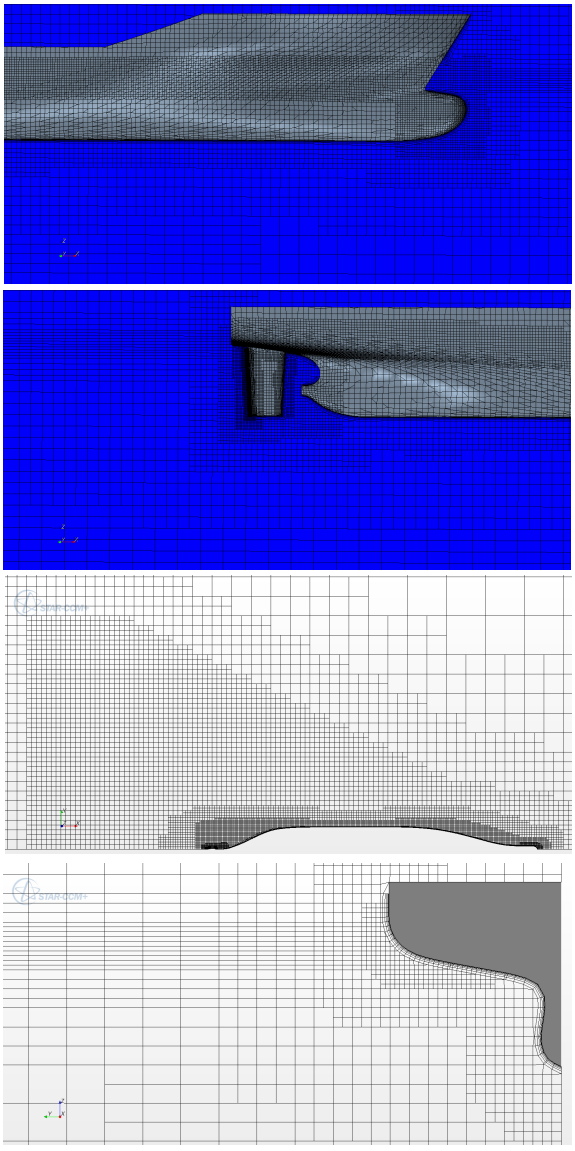

Fig. 1: The structure of the coarse mesh around KCS hull with rudder, showing local refinement regions near hull, near free surface, in the wake and in the wave zone.

Only half of the geometry was considered due to symmetry conditions. The solution domain extended from -18 m to 18 m in flow direction, from -18 m to 9 m in vertical direction and from 0 to 18 m in lateral direction, respectively. The hull length was about 7.7 m (L_{pp} = 7.2786, scale factor 31.6) and the coordinate origin was at aft perpendicular and still water surface (which was 0.341772 m above keel). In addition to the symmetry plane of the hull, the lateral boundary parallel to it was also treated as symmetry plane. At the downstream boundary, hydrostatic pressure corresponding to the undisturbed water surface was prescribed. Upstream, top and bottom boundaries were treated as inlets with prescribed velocity and volume fraction.

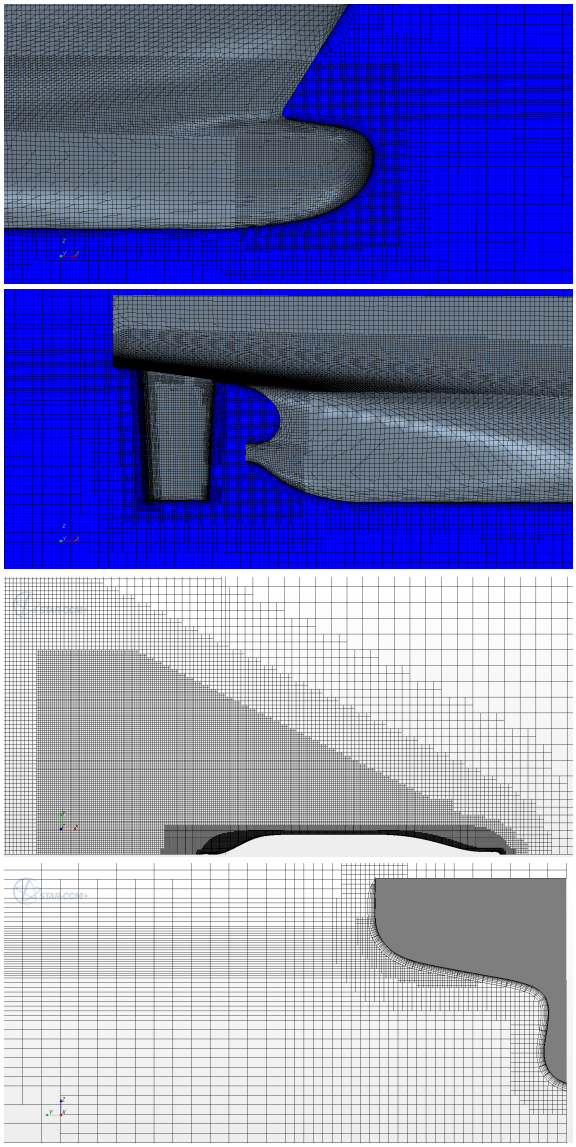

Fig. 2: The structure of the fine mesh around KCS hull with rudder, showing local refinement regions.

The coarse, medium and fine mesh had 544138, 1220966 and 2997355 control volumes, respectively.

There were 6 prism layers along walls (except for non-wetted walls) and the next-to-wall cells were 0.9 mm thick (prism layer was 20 mm thick, cell expansion ratio was 1.5). Figure 2 shows the fine mesh segments.

4. KCS, FIXED POSITION

This section contains results for the case of a hull fixed in its floating position at zero speed (even keel). The Froude number is 0.26. Computations were performed in a time-marching mode, starting with a flat water surface. The time step was 0.04 s and 4 iterations were performed at each time level. The standard k-ε turbulence model with wall functions was used. Figure 3 shows how forces on hull converge towards steady-state solution on the fine mesh. While shear force very quickly settles to a nearly constant value, pressure force oscillates around the steady-state value with a diminishing amplitude.

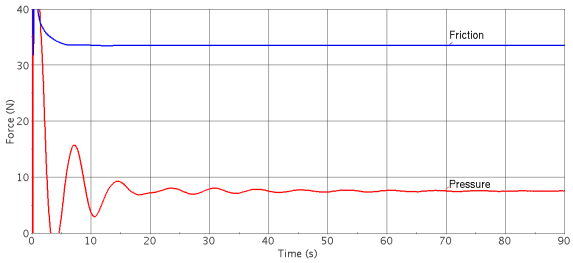

Fig. 3: Convergence of friction and pressure drag during computation.

Table 1 shows predicted resistance at each grid level. The measured value of C_T is $3.557 \cdot 10^{-3}$ (Van et al, 1998) and the numbers in parentheses show percentage difference to the experimentally obtained value (the + sign indicates that the value is over-predicted). The predicted total resistance is within 0.5% of measured value on all grids. The variation from one grid to another is not monotonic: the largest difference relative to measured value is obtained on medium grid. While the pressure drag reduces monotonically with grid refinement, the friction drag is largest on medium grid. It is not unusual that such variation is observed, especially when unstructured, locally refined grids are used.

Table 1: Predicted resistance coefficients on different grids

Grid	C_T ($\cdot 10^3$)	C_F ($\cdot 10^3$)	C_P ($\cdot 10^3$)
Coarse	3.568 (+0.31%)	2,873	0,695
Medium	3.574 (+0.48%)	2,911	0,663
Fine	3.561 (+0.11%)	2,909	0,652

Figure 4 shows predicted wave pattern, wall shear stress on the hull and the near-hull y^+ distribution. Only one half of the geometry was computed, but a mirror image of waves on the other side is also shown. The y^+ values vary between 40 and 60 over the largest part of the wetted hull surface, as desired when wall functions are used. The strong reduction of wall shear stress in the stern region is due to the diffusor effect in the absence of propeller.

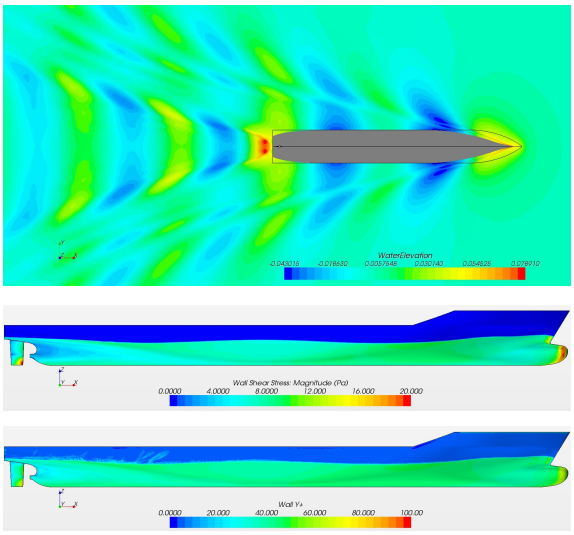

Fig. 4: Wave pattern (upper), wall shear stress (middle) and near-wall y+ (lower), computed on the finest mesh.

All three grids in these calculations had the same number of prism layers at walls: mesh refinement was done by reducing the cell size in all directions outside prism layer by a factor of 1.5, and within prism layer only in the two tangential directions, but not in the wall-normal direction. The idea here was to keep the same y^+ values at near-wall cells. In order to verify the effect of variable mesh spacing inside prism layer, another coarse grid was generated with 4 prism layers instead of 6. The expansion factor was the same, but now the near-wall cell was 2.46 mm thick (compared to 0.9 mm when 6 prism layers were created). This resulted in y^+ values between 100 and 120 over most of the hull surface. The total resistance computed on this mesh (which had 501342 cells, compared to 544138 cells with 6 prism layers) was $3.614 \cdot 10^{-3}$, which is 1.6% more than the measured value (compared with +0.31% more when 6 prism layers were used). Although this result is also acceptable for a relatively coarse mesh, the increase in accuracy resulting from adding two more prism layers is worth while.

We also looked at the effects of the choice of turbulence model on predicted resistance. This analysis was done using two grids provided by

Germanischer Lloyd; they were of a similar type as those presented earlier and one had 745434 cells while the finer one had 2680461 cells. The results are summarized in Table 2.

Table 2: Predicted resistance coefficients on two grids using different turbulence models

Grid	*k-ε* standard	*k-ε* two-layer	*k-ω* SST	RSM
Coarse	3.610 (+1.49%)	3.591 (+0.96%)	3.425 (-3.71%)	3.638 (+2.28%)
Fine	3.588 (+0.87%)	3.560 (+0.08%)	3.415 (-4.86%)	3.623 (+1.86%)

The structure of the meshes used here was less optimized, and hence the effect of mesh refinement is more visible. For all models but *k-ω*, the values computed on the finer mesh are closer to experimentally obtained value of $3.557 \cdot 10^{-3}$. The Reynolds-stress model (RSM) predicts slightly higher resistance than both versions of *k-ε* model, while the *k-ω* SST model under-predicts the measured value by almost 5%. The fact that for this model the deviation compared to experiment increases with grid refinement is due to the fact that modeling and discretization errors vary locally in both sign and magnitude; the finding that the *k-ε* model produces the best result is most probably due to the partial cancellation of the two error types. Also, the model which predicts resistance closest to the measured value may not necessarily give the best velocity distribution in the propeller plane (RSM is expected to do the best job in this respect).

5. KCS, HEAVE & PITCH

In the second set of simulations, the hull with rudder was free to heave and pitch. The same grids were again used, but the mesh was now moving with the hull as a rigid body. All simulations started with a flat water surface and hull's bottom parallel to free surface. The mass of the half hull with rudder was set to 823.0451 kg, the center of gravity was at x = 3.5315 m (relative to coordinate origin in CAD-file, which was at aft perpendicular) and 0.1113924 m below free surface. The moment of inertia for rotation around y axis, needed for prediction of pitching motion, was set to 2725.117 kg m^2. Simulations were performed for four Froude numbers: 0.1949, 0.2274, 0.2599 and 0.2816. For the two smaller Froude numbers, computations were performed only on the coarsest grid, while for the two highest Froude numbers, all three grids were used. The time step was set to 0.04 s for the Froude number 0.2599, and for other Froude numbers it was scaled according to velocity variation. For body motion, 4 to 5 iterations per time steps were performed, while for the flow computation, 8 to 10 iterations were performed. The time step was the same for all grids, since temporal accuracy is not of interest – only the final steady-state solution is sought.

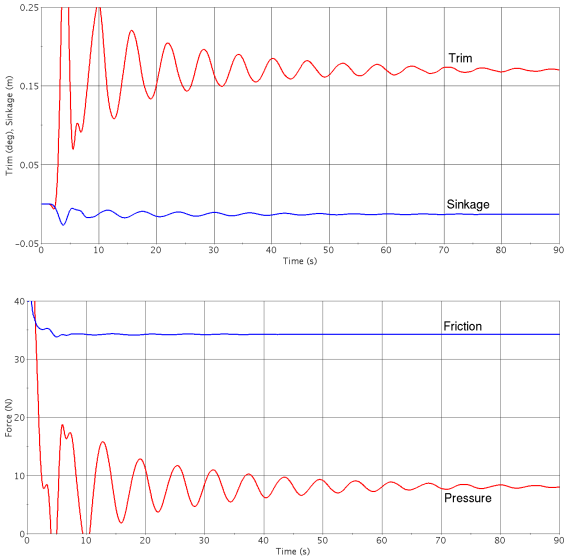

Fig. 5: Convergence of pitch and heave motion (upper) and friction and pressure forces (lower) for Fn = 0.2599 and the finest mesh.

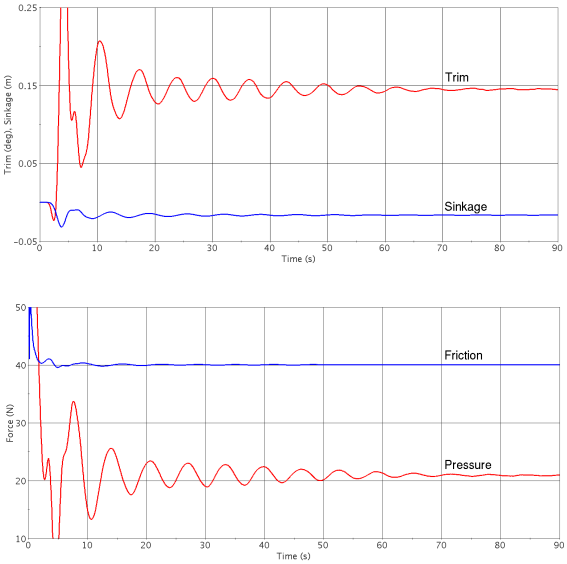

Fig. 6: Convergence of pitch and heave motion (upper) and friction and pressure forces (lower) for Fn = 0.2816 and the finest mesh.

Figures 5 and 6 show convergence of ship motion and forces acting on it during simulation on the finest mesh for the two largest Froude numbers. Both the amplitude and frequency of oscillations are

higher for lower Froude number. This behavior has been observed in other applications of the solution methods to similar problems. No attempts were made here to vary the parameters in the simulation to minimize the computing effort needed to obtain the steady-state solution.

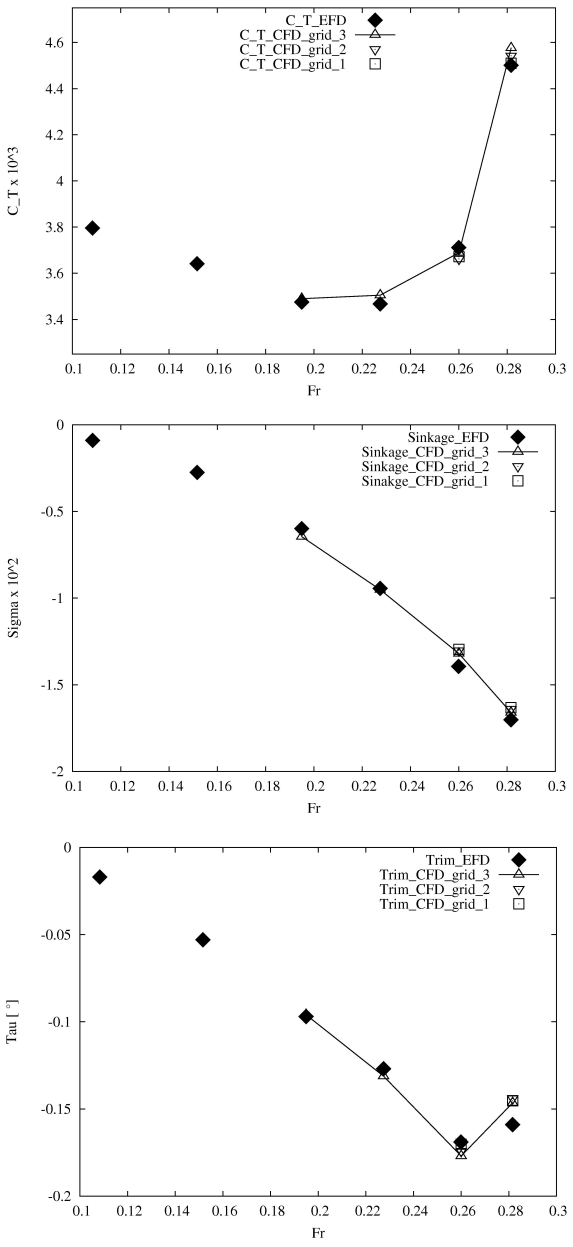

Fig. 7: Comparison of predicted and measured total resistance (upper), sinkage (middle) and trim (lower)

Figure 7 shows comparison of predicted and measured total resistance, sinkage and trim. The predicted drag agrees well with experimental data: the largest discrepancy is 1.66% on the coarsest grid for Fn = 0.2816. For other Froude numbers, already on the coarsest grid the error is of the order of 1% or less (0.4%, 1.1% and 0.6% in the order of increasing Froude number). For Fn = 0.2816, the error is reducing with grid refinement to 0.2% on the finest mesh. However, for Fn = 0.2599, the error first increases to 1.3% and then drops to 1% on the finest mesh. It is also interesting that the predicted friction resistance slightly reduces with increasing Froude number (from 3.035 to 2.985, 2.071 and 2.961), while the pressure drag increases (from 0.455 to 0.520, 0.701 and 1.549, in the order of increasing Froude number). The contribution of pressure drag to total resistance increases sharply from 19.1% at Fn = 0.2599 to 34.3% at Fn = 0.2816.

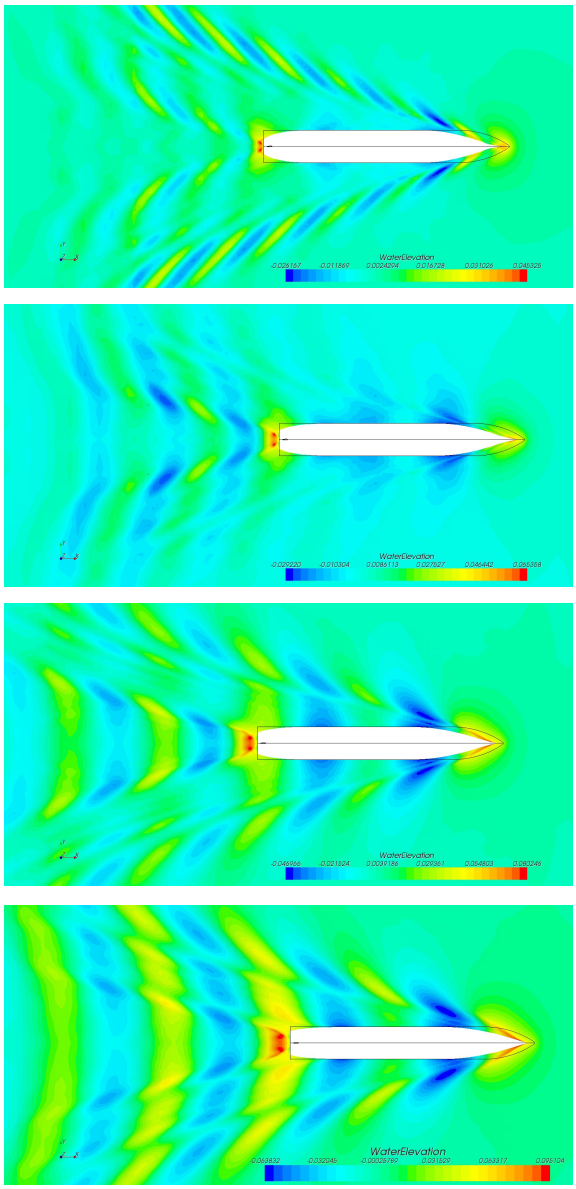

Fig. 8: Computed wave pattern around KCS-hull for Froude numbers 0.1949, 0.2274, 0.2599 and 0.2816 (from top to bottom; first two computed on the coarsest, last two on the finest grid).

The trim and sinkage differ more from experimental data. The discrepancies in sinkage are 7.7%, 0.8%, 7.0% and 4.1% in the order of increasing Froude numbers, respectively (the last two values correspond to the finest mesh). Grid refinement did not result in improvement: the error increased from 5.3% to 7% for Fn = 0.2599, and from 2.5% to 4.1% for Fn = 0.2816. The errors in trim angle are 1%, 3.3%, 0.7% and 8.6% (from the lowest to the highest Froude number). At Fn = 0.2599, the discrepancy reduced from 4.7% to 0.7% with grid refinement, but for Fn = 0.2816, the discrepancy to experiment increased slightly from 7.5% to 8.6%.

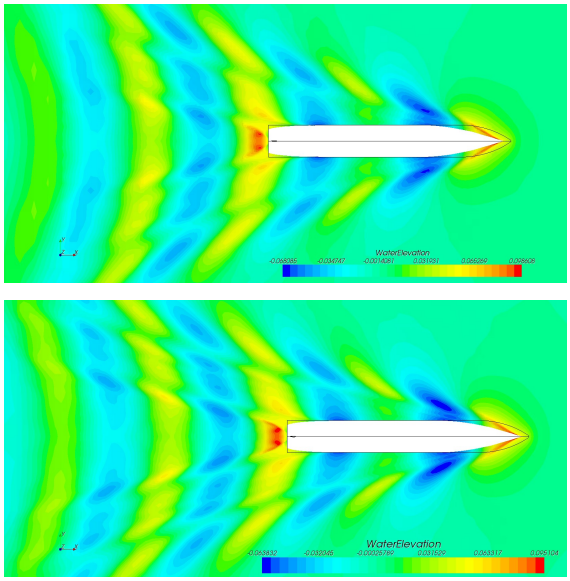

Fig. 9: Wave pattern around KCS-hull for Froude number 0.2816 computed on the coarse (upper) and fine (lower) grid.

Figure 8 shows predicted wave patterns for the four Froude numbers. The highest water elevation is always just behind ship stern, ranging from 45 mm at Fn = 0.1949 to 95.1 mm at Fn = 0.2816. The minimum water level is always at hull shoulder, ranging between -26 mm at Fn = 0.1949 to -64 mm at Fn = 0.2816. Water elevation is over-predicted on coarse grids. Figure 9 shows a comparison of wave pattern at Fn = 0.2816 computed on the coarse and the fine grid, respectively. The maximum predicted water elevation on the coarse grid was 98.6 mm, which dropped to 95.1 mm on the finest mesh (3.7% change). The lowest predicted point on water using coarse mesh was at -68.1 mm, which changed to -63.8 mm on the finest mesh (6.7% change). The change in resistance, however, was just below 1.5%.

Finally, Fig. 10 shows the resolution of free surface in the symmetry plane and along hull in the stern region on coarse grid. Almost everywhere the interface falls into one cell, which is the maximum possible resolution by interface-capturing schemes.

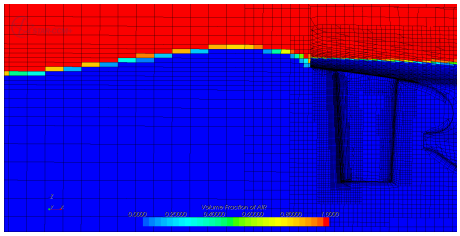

Fig. 10: Resolution of free surface by HRIC scheme.

6. CONCLUSIONS

The presented results of simulations show that one can obtain a reliable prediction of resistance of container vessels using relatively coarse grids with about half a million cells (for half of the geometry) when the grid is well designed and locally refined in critical zones. The standard k-ε turbulence model with wall functions is adequate for this purpose and for optimum results, the prism layers near wall should be arranged so that y^+ values around 50 are obtained. While the k-ε and Reynolds-stress model over-predict resistance by up to 2%, the k-ω SST model under-predicts the measured value by almost 5%.

REFERENCES

[1] Ferziger, J.H. and Perić, M. (2003): "*Computa-tional Methods for Fluid Dynamics*", 3rd Ed., Springer Verlag, Berlin, Heidelberg.

[2] Demirdžić, I., Muzaferija, S. (1995): Numerical method for coupled fluid flow, heat transfer and stress analysis using unstructured moving meshes with cells of arbitrary topology, *Comput. Methods Appl. Mech. Engrg.*, **125**, 235-255.

[3] Weiss, J., Maruszewski, J.P., Smith, W.A. (1999): Implicit solution of preconditioned Navier-Stokes equations using algebraic multigrid. *AIAA J.*, **37**, 29-36.

[4] Muzaferija, S., Perić, M. (1999): Computation of free surface flows using interface-tracking and interface-capturing methods, In O. Mahrenholtz, M. Markiewicz (eds.), *Nonlinear Water Wave Inter-action*, Chap. 2, 59-100, WIT Press, Southampton.

[5] Launder, B.E., and Spalding, D.B. (1974): The numerical computation of turbulent flows, *Comput. Meth. Appl. Mech. Eng.*, **3**, 269–289.

[6] Azcueta, R. (2001): *Computation of turbulent free-surface flows around ships and floating bodies,* PhD Thesis, Technical University of Hamburg-Harburg, Germany.

[7] Van, S.H., Kim, W.J., Yim, G.T., Kim, D.H., and Lee, C.J. (1998): Experimental Investigation of the Flow Characteristics Around Practical Hull Forms, Proc. 3rd *Osaka Colloquium on Advanced CFD Applications to Ship Flow and Hull Form Design*, Osaka, Japan.

URANS COMPUTATIONS OF A DTMB 5415

Jorge Izquierdo (CEHINAV Universidad Politécnica de Madrid, Spain)
Leo M. González (CEHINAV Universidad Politécnica de Madrid, Spain)

1. SUMMARY

This paper presents the results of the computations performed in the Canal de Ensayos Hidrodinámicos de ETSI Navales (CEHINAV) for the US Navy Combatant DTMB 5415 [Larsson et al. 2003] at model scale with the URANS free surface commercial solver StarCCM+. In this context we focused on the results required to complete the case 3.1a. In this situation the bare hull ship is fixed in a specified position and sails in still water. These computational results are validated against experimental data [Olivieri et al. 2001] in terms of various global and local quantities.

2. INTRODUCTION

The StarCCM+ code is based on a finite volume discretization [Demirdzic et al. 1995, Weiss et al. 1999, Muzaferija et al. 1999]. In the finite volume method the solution domain in divided into a finite number of small control volumes corresponding to the cells of the computational grid. Discrete versions of the integral form of the continuum transport equations, mass and momentum conservation are applied to each control volume. The objective is to obtain a set of linear algebraic equations, with the total number of unknowns in each equation system corresponding to the number of cells in the grid. In the case presented in this paper, the Navier-Stokes equations present a dominant non-linearity and iterative techniques that rely on suitable linearization strategies must be employed [Ferziger et al. 2002].

The turbulence model used in the calculations was the SST (Shear Stress Transport) based on two equation blended k-ω model [Menter 2003]. The use of a blending function, which includes functions of wall distance, also implements the cross diffusion term far from the walls, but not near the walls. This approach effectively blends the k-epsilon model in the far-field with the k-Omega model near the wall. This approach cures the biggest drawback to applying the k-Omega model to practical flow simulations.

The volume of fluid method technique (VOF) is used to model the free-surface flow. The VOF method seems to be one of the most promising for free surface calculations, but it still requires some improvement [Kleefsman, 2005].
The two-phase Unsteady Reynolds Averaged Navier-Stokes (URANS) equations are solved in relative inertial coordinates, where no relative movement is allowed between the grid and the ship [Ghia et al. 1982]. An implicit unsteady Euler predictor-corrector scheme is used for time discretization scheme. The Euler method is not as accurate as the Newmark second order method, so a smaller time step is required to obtain the same accuracy. For a given time step, the Euler method incurs more numerical damping than the second order version for modes which are at a higher frequency than a time-step can resolve. However, our experience was that we found the Euler method more stable and useful for damping out high frequency and small wavelength oscillations. It is important to remark that in stationary cases as the one studied here, the time dependant part of the simulation has a minor role in the final result. Convection term is discretized using a 1st-order upwind scheme and diffusion term using 2nd-order central difference scheme. The Segregated Flow solver controls the solution update according to the SIMPLE algorithm. A segregated flow solver computes the flow equations, one for each velocity components and one for the pressure in a uncoupled manner. The linkage between the momentum and continuity equation is achieved with a predictor-corrector approach. The complete formulation of this algorithm uses a collocated variable arrangement and Rhie-Chow pressure velocity coupling combined with a SIMPLE model. The SIMPLE solver algorithm can be described by the following steps:

1-Solve the discretized momentum equation to create an intermediate velocity $\mathbf{v}^*$.
2-Solve the pressure correction equation to produce cell values of the pressure correction p*. The pressure correction equation is linearized and solved by an algebraic multigrid iterative solver.
3-Update the pressure field $p^{n+1} = p^n + \omega\, p^*$, where ω is a under-relaxation factor for pressure.
4- Correct the cell velocities.

The Message Passing Interface (MPI) library is used in order to handle the domain decomposition, where each decomposed block is mapped to a single processor.
Parallel computation on 3 processors was adopted to reduce the required computational time. The grid is formed by 300k elements for a physical time equivalent to $20L/U_0$. Each simulation took 10 hours of clock time and 30 hours of CPU time.
The platform used in the computations is a PowerEdge cluster 2950 which consist of 4 CPUs/node with 8 cores per node. Each core has 1GB memory.

3. GEOMETRY, GRIDS AND BOUNDARY CONDITIONS USED.

Due to the symmetry of the problem, the simulation was carried out using half domain and using the plane Y=0 as the symmetry plane, see figure 1. The domain size in [X,Y, Z] is given by [-1.0-3.0L, 0-2L, -1.5-0.75L], where L is main dimension of the ship.

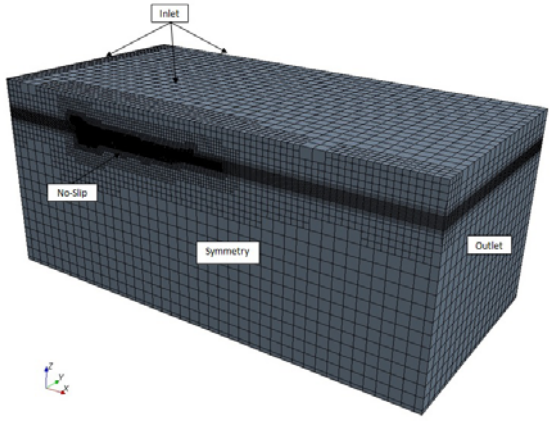

Fig 1. Domain and grid S1 used for the simulation. Boundary conditions are labeled in the corresponding boundary planes.

Three grids have been used for this model. First a coarse grid, mesh S1, of 300k elements was initially used. Later, this initial mesh was systematically refined in order to obtain converged results. Consequently, the first mesh was globally refined with a refinement ratio r_G=5/3 obtaining a medium mesh S2 with 1.1 M elements. Finally this second mesh was also refined with a refinement ratio of r_G=6/5 giving the finest mesh S3 which is a 2M element grid. The mesh is formed by hexahedral and tetrahedral cells and it also has a prism layer around the hull. In order to capture more accurately the wave formation, the mesh has also been refined around the free surface.

The boundary conditions used in these simulations are the following: the hull has no-slip boundary condition, this means that the velocity is explicitly set to zero and the boundary face static pressure is extrapolated from the adjacent cells using reconstruction gradients. Due to the turbulence model used, a wall treatment has been used in the simulation trying to keep the non dimensional parameter y^+>30. A wall treatment in STAR-CCM+ is the set of near wall modeling assumptions for each turbulence model. In figure 2 the y^+ has been plotted along the ship hull and we can observe that when the grid size is reduced the value of the non dimensional y+ is kept below the recommended value. The inflow (X_{min}) plane has a uniform velocity U_0 and the pressure follows an hydrostatic distribution, and for the outflow (X_{max}) plane extrapolated velocity and hydrostatic pressure are imposed. As it was written before, a symmetry condition is used for the plane Y=0, this means that the face values of the velocity and pressure is computed by extrapolating the parallel component of velocity in the adjacent cells using reconstruction gradients. For the rest of the planes: Y-max, Z-max and Z-min, inlet velocities U_0 are imposed and a zero-gradient boundary condition is used for pressure.

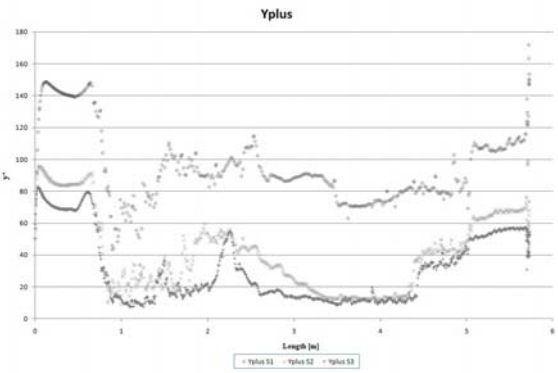

Fig 2. Values of y^+ along the ship hull for the three different meshes used.

4. SHIP RESISTANCE

During the simulation the ship resistance parameters were calculated and these numbers were used as stopping criteria for the time marching problem. The force on the hull surface is computed as the global action of the viscous shear force and the pressure force. The pressure used in each surface is the result of the face pressure minus the reference pressure. In our case the reference pressure is fixed and equal to the atmospheric pressure. As can be observed in Table 1, the grid refinement affects quantitatively the computation of the resistance parameters. In the case of the coarsest grid S1 the total resistance coefficient C_T has been calculated with an error of less than 1%. The contribution of the viscous and pressure forces to this global resistance is over predicted for the viscous prediction while the pressure contribution is under predicted. In one hand, the viscous case, the coefficient C_F was computed with an error that is less than 2% for all the grids used. On the other hand, the coefficient C_R was computed with an error that is just less than 7% for the coarsest grid S1. The V&V study of these results reveals that the only mesh that verifies that the total error of the drag prediction, 0.55%D is less than U_V=3.57%D, is the coarsest grid S1.

This fact confirms that our prediction is validated with the mesh S1, anyway systematic mesh refinements were performed to improve other computed results as the wave contour elevation.

Parameters	*EFD*	ITTC	Grid S3	Grid S2	Grid S1
$C_T \times 10^3$	**4.23**		4.04	4.06	4.21
$C_F \times 10^3$		**2.91**	2.93	2.93	2.97
$C_R x 10^3$	**1.32**		1.10	1.13	1.24

Table 1. Summary of the ship resistance prediction for the conditions of the case 3.1.a.

5. WAVE PROFILE CALCULATIONS.

When resistance coefficients were finally converged in time the wave profiles has been plotted at different distances from the symmetry plane. In figure 3 the global wave contour elevation can be appreciated when the finest mesh S3 has been used. In figures 4, 5 and 6 we can see different wave cuts computed with meshes S1 and S3 at $y/L_{PP}=0.082$, 0.172 and 0.301. These plots are compared with the EFD results, see Olivieri et al. 2001 and the agreement is reasonable. Although the predictions are accurate, it is important to remark that the error in the maximums of wave profile grows when the wave cut increases, this fact can be observed in Figure 6 for the peaks at x=1.0 and x=1.2 where the maximums and the minimums of the wave profile are slightly over predicted. In figures 4, 5 and 6 we can observe that the accuracy of the wave cut improves when the finest grid S3 is used.

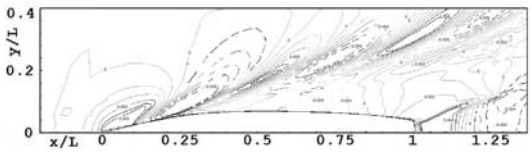

Fig 3. Wave contour elevation .Mesh S3

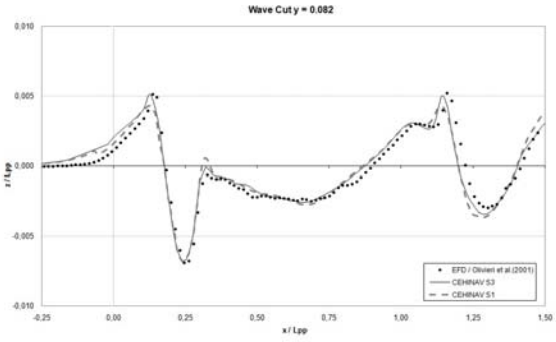

Fig 4. Wave cut, $y/L_{PP}=0.082$.

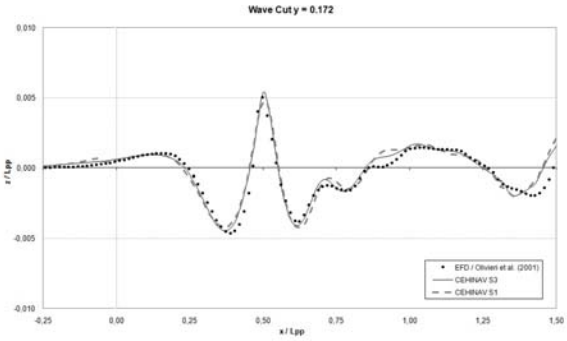

Fig 5. Wave cut, $y/L_{PP}=0.172$.

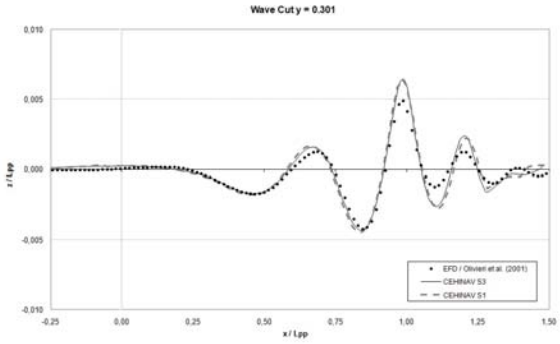

Fig 6. Wave cut, $y/L_{PP}=0.301$.

6. VELOCITY FIELDS

Once the simulation has reached the steady state, the velocity field has been plotted at different planes normal to the X direction. The velocity fields have been plotted in five different normal planes, these planes are set at X/L_{PP} =0.1, 0.2, 0.6, 0.8, 0.935 and 1.1

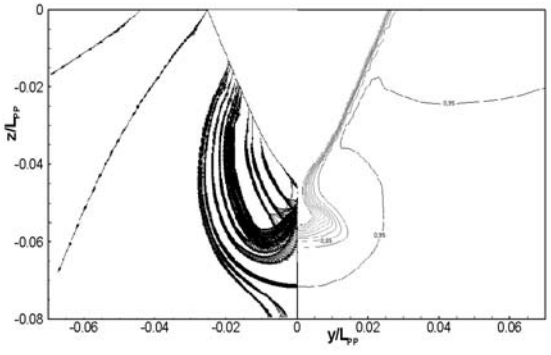

Fig 7. U contour lines (right panel), cross flow streamlines (left panel) at $x/L_{PP}=0.1$.

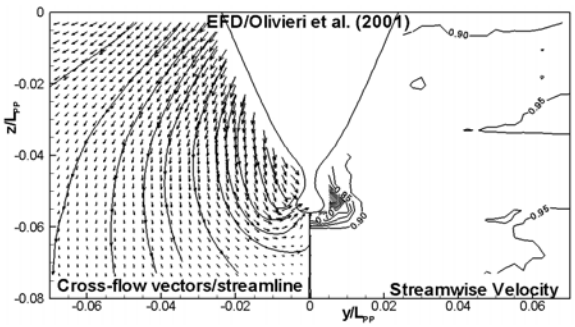

Fig 8. Experimental results at $x/L_{pp}=0.1$. As before, U contour lines (right panel), cross flow streamlines (left panel).

In the left panel of Figure 7 and 9 the boundary layer attached to the ship hull can be easily appreciated. In Figure 7, the streamlines plotted in the right panel are clearly influenced by the presence of the bulb that divides the flow in two different parts. The first part is formed by the streamlines that start in a hull point and finish far away of the ship and the second part are streamlines that also start in a hull point but keep themselves inside a fluid bubble where the streamlines are finally reattached close to the bulb. This velocity distribution has a remarkable agreement with the one shown in Figure 8 where the reattached streamlines are also present on the right panel.

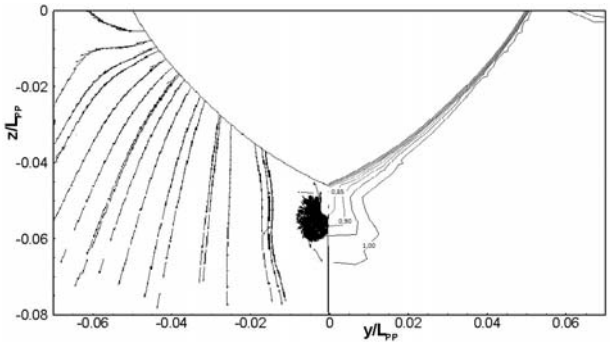

Fig 9. U contour lines (right panel), cross flow streamlines (left panel) at $x/L_{pp}=0.2$.

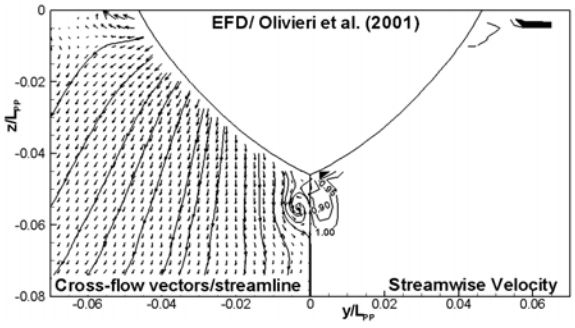

Fig 10. Experimental results at $x/L_{pp}=0.2$. As before, U contour lines (right panel), cross flow streamlines (left panel)..

In figure 9 the projection of the vortex detached because of the presence of the bulb is clearly appreciated. Most of the streamlines that are plotted on the right panel of Figure 9 just show how the flow feels the section of the boat is increasing towards the X direction. The equivalent experimental result is shown in Figure 10 where the vortex is also present at the bottom of the hull. This situation is clearly changed in Figures 11, 12 and 13, the sections presented in these cases have $x/L_{pp} > 0.5$, this means that the section is decreasing towards the X direction, this changes drastically the direction of the flow.

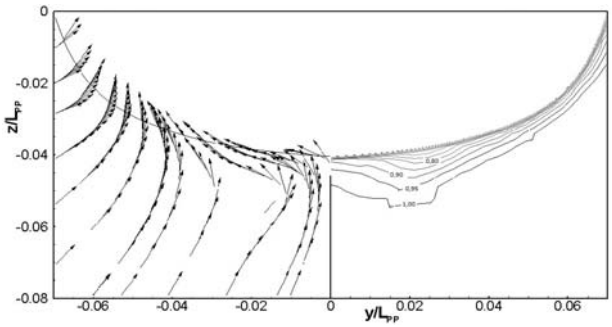

Fig 11. U contour lines (right panel), cross flow streamlines (left panel) at $x/L_{pp}=0.6$.

In Figures 14 and 15, the section represented is just behind the ship $X/L_{PP}=1.1$, consequently the wake of the flow can be perfectly appreciated. It is important to remark that the central vortex coming out of the wake is well captured by the simulation. In the right panel of Figure 14 the recirculation of the flow is clearly visible. Comparing these results to the ones coming from the experimental study some differences can be noticed. First, the centre of the vortex is set in a slight different position, closer to the central axis in the computational case. Second, the streamlines at the bottom of the Figures 14 seem to follow the behavior of the central vortex, while those streamlines are out of the vortex bubble as can be seen in Figure 15. The consequence of this is that the streamlines of the computational version are more influenced by the presence of the vortex than the ones obtained by the experimental measurements.

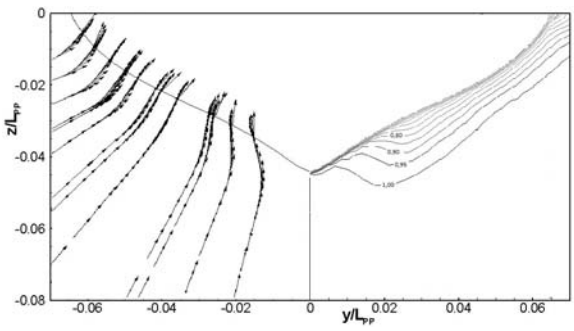

Fig 12. U contour lines (right panel), cross flow streamlines (left panel) at $x/L_{pp}=0.8$.

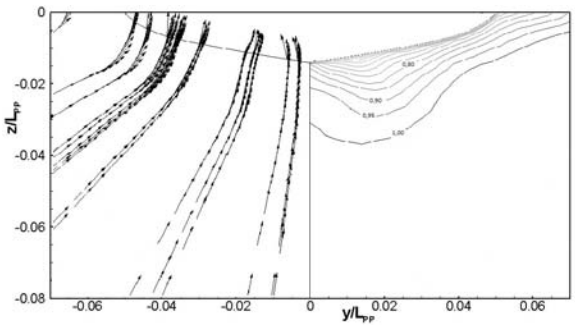

Fig 13. U contour lines (right panel), cross flow streamlines (left panel) at x/L_{pp}= 0.935.

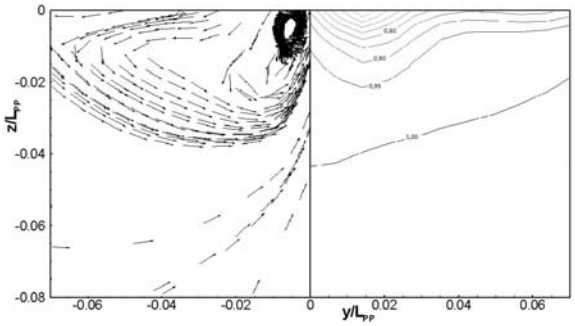

Fig 14. U contour lines (right panel), cross flow streamlines (left panel) at x/L_{pp}= 1.1.

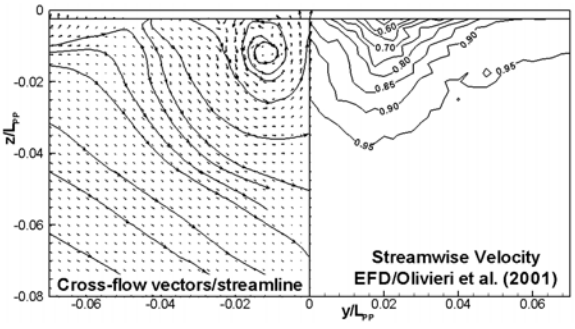

Fig 15. Experimental results at x/L_{pp}= 1.1. As before, U contour lines (right panel), cross flow streamlines (left panel).

7. CONCLUSION

This paper has presented the results of the required computations for the case 3.1a performed in the CEHINAV for the US Navy Combatant DTMB 5415 at model scale. For this task the URANS equations were solved using the commercial solver StarCCM+. In this case the bare hull ship is fixed in a specified position and sails in still water. The comparison is done in terms of global quantities as resistance coefficients and also comparing wave cuts and velocity fields where local differences could be appreciated. Three different grids have been used for the computations and the V&V test has been used to validate our predictions. The coarsest mesh obtained accurate enough results, but more refined meshes were used to improve the wave cut calculation. The relative error obtained in the ship total resistance with the coarsest grid was less than 1%. The comparison of the wave cuts and velocity fields of the computational results to experimental data given by the organizers of the Workshop presents a remarkable agreement. Consequently, the code Star CCM+ has shown that is a useful tool for the prediction of the fluid quantities in ship hydrodynamics.

ACKNOWLEDGMENTS

The research has been funded by the Spanish Administration included in the project TRA 2005 – 08866 – C02-01.

REFERENCES

Larsson, L., Stern, F. and Bertram, V., (2003), "Benchmarking of Computational Fluid Dynamics for Ship Flows: the Gothenburg 2000 Workshop", *Journal of Ship Research*, Volume 47, No 1, March

Ferziger, J.H. and Peric, M., (2002), "*Computational Methods for Fluid Dynamics*", 3rd Ed., Springer Verlag, Berlin, Heidelberg

Van, S.H., Kim, W.J., Yim, G.T., Kim, D.H., and Lee, C.J., (1998b), "Experimental Investigation of the Flow Characteristics Around Practical Hull Forms," Proceedings 3rd Osaka Colloquium on Advanced CFD Applications to Ship Flow and Hull Form Design, Osaka, Japan

Olivieri, A., Pistani. F., Avanaini, A., Stern, F., and Penna, R. (2001), "Towing Tank Experiments of Resistance, Sinkage and Trim, Boundary Layer, Wake, and Free Surface Flow Around a Naval Combatant INSEAN 2340 Model," Iowa Institute of Hydraulic Research, The University of Iowa, IIHR Report No. 421, 56 pp.

K.M.T. Kleefsman, G. Fekken, A.E.P. Veldman, B. Iwanowski, B. Buchner, A Volume-of-Fluid based simulation method for wave impact problems, Journal of Computational Physics, Volume 206, Issue 1, 10 June 2005, Pages 363-393, ISSN 0021-9991, DOI: 10.1016/j.jcp.2004.12.007.

Menter, F.R. "Two-equation eddy-viscosity turbulence models for engineering applications" AIAA-Journal, 32(8), 1994.

Industries Inc., 1993. 460pp.

U. Ghia, K. N. Ghia, C. T. Shin, High-Re solutions for incompressible flow using the Navier-Stokes equations and a multigrid method, Journal of Computational Physics, Volume 48, Issue 3, December 1982, Pages 387-411

Demirdzic, I., Muzaferija, S. "Numerical method for coupled fluid flow, heat transfer and stress analysis using unstructured moving meshes with cells of arbitrary topology", Comput. Methods Appl. Mech. Engrg., Vol. 125 pp. 235-255 (1995).

Weiss, J., Maruszewski, J.P., Smith, W.A "Implicit solution of preconditioned Navier-Stokes equations using algebraic multigrid", AIAA J., Vol. 37, pp. 29-36 (1999).

Wilcox D. C.."Turbulence Modelling for CFD". By DCW

Muzaferija, S., Peric, M. "Computation of free surface flows using interface-tracking and interface-capturing methods", In O. Mahrenholtz, M. Markiewicz (eds.), Nonlinear Water Wave Interaction, Chap. 2, pp. 59-100, WIT Press, Southampton, 1999.

CD-Adapco "Star-CCM+ User Guide" version 5.02.009, 2010.http://www.cd-adapco.com/products/STAR-CCM_plus/

CFD PREDICTION OF THE LOCAL FLOW AROUND THE KVLCC2 TANKER IN FIXED CONDITION

Lu Zou (Chalmers University of Technology, Sweden)
Lars Larsson (Chalmers University of Technology, Sweden)

1. SUMMARY

This paper presents an investigation on the local flow around a tanker hull in fixed condition. This is one of the test cases in the 2010 Workshop on CFD in Ship Hydrodynamics. A steady state Reynolds Averaged Navier-Stokes solver was used to solve the viscous flow around the hull. To figure out a way predicting the local wake flow as accurately as possible, several possibilities have been tested in terms of the turbulence model and the approach dealing with the computational domain.

2. INTRODUCTION

From the point of view of ship propulsion, the prediction of the wake field behind the hull is of great interest and importance as the predicted wake flow decides the accuracy of the inflow to the propeller plane and affects the prediction of propulsion performance. On account of this, in the whole history of the series of international Workshops on CFD in Ship Hydrodynamics, the local flow computation has always been one of the subjects in each workshop with the purpose of estimating the state of the art in the local/wake flow prediction by means of CFD methods. For instance, the first local flow test case in the series of CFD Workshop for the KRISO (Korea Research Institute of Ships and Ocean Engineering) VLCC (Very Large Crude-oil Carrier) tanker hull can be traced back to 2000 (Larsson et al. 2000) and the same case appeared in 2005 (Hino 2005).

The present work intended to investigate this 'traditional' test case under the frame of the recent workshop in 2010. The test case is local flow investigation for a double model KVLCC2 tanker hull in fixed condition. This case mainly aims to evaluate the predicted wake flow, the turbulent quantities behind the hull, as well as the pressure distribution and limiting streamlines on the hull surface. Actually in the past two decades, plenty of investigations for the local flow characteristics around the VLCC hull have been carried out in different aspects, both experimentally (such as: Van et al. 1998, Kim et al. 2001, Lee et al. 2003, Van et al. 2006) and numerically (such as: Larsson et al. 2000, Kim et al. 2002, Hino 2005, Deng et al. 2005), so that the flow characteristics in the experiments were documented in detail and used as validation resource for numerical solutions. Meanwhile, several potentials to improve the numerical methods have been considered, studied and reported with more and more promising results. Looking back upon the previous wake predictions, the accuracy has been enhanced by means of increased grid points, more advanced turbulence models, and so on. And together with the expanded computer resource/ability over last five years, it would be still interesting to evaluate the recent accuracy of local flow prediction.

It should be mentioned that the hull geometry in the 2010 workshop is slightly different from the original KVLCC2 geometry: a semi-spherical cap was attached at the location of hub to make the flow around the shaft center line smooth, and the propeller plane is placed behind the cap. The entire KVLCC2 hull geometry is given in Fig. 1 and the detail of dummy hub can be found in Fig. 2.

Fig. 1 Geometry of KVLCC2 tanker

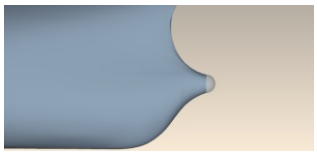

Fig. 2 Sketch of the dummy hub

To carry out the investigation, the efforts have been placed on the computations through different approaches and the comparisons among obtained results thereafter indicate which method gives the best prediction with respect to mean velocities and wake fraction. In the present study, the computations/investigations were executed as follows: In the first place, the effect of turbulence modeling was investigated. Two turbulence models were involved in the computations and the one giving the best results was used in the following investigation; then, two approaches dealing with the computational domain differently were investigated, one was the popular global approach and the other was the zonal approach.

3. GLOBAL APPROACH VERSUS ZONAL APPROACH

With the capability of handling both global and zonal approaches in the ship hydrodynamic CFD software SHIPFLOW (V4.3) (Regnström et al. 2005), the local flow can be computed by these two methods. This section presents the different treatment of the computations (domain, etc.) in the global and zonal approach and the following section will exhibit the comparisons of the results from all the computations.

3.1 Method Description

In the widely applied global approach, the selected domain covers the whole flow field around the hull which is a single block H-O grid topology in the present work. Assuming that the viscous flow around the KVLCC2 tanker is incompressible, the numerical problem can be described by the following steady Reynolds Averaged Navier-Stokes (RANS) equations:

$$\frac{\partial}{\partial x_j}(\overline{u}_i\overline{u}_j) = -\frac{1}{\rho}\frac{\partial \overline{p}}{\partial x_i} + F_i + \frac{1}{\rho}\frac{\partial}{\partial x_j}\left(\overline{\sigma}_{ji} + R_{ji}\right) \quad (1)$$

$$\frac{\partial \overline{u}_i}{\partial x_i} = 0 \quad (2)$$

here $\overline{u}_{i(j)}$, $\overline{p}$ and $\overline{\sigma}_{ij}$ denote the average velocity, pressure and stress; ρ is the water density; F_i represents the body force, which is regarded as a constant term; and $R_{ji} = R_{ij} = -\rho\overline{u_i'u_j'}$ is the Reynolds stresses.

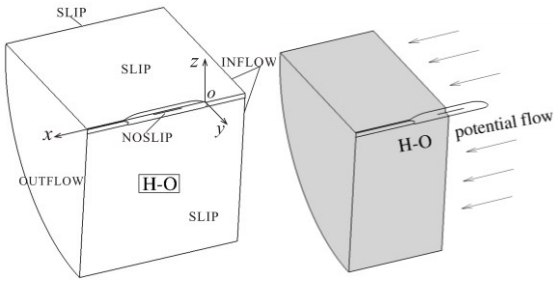

Fig. 3 Comparison of the computational domain in global and zonal approach
(Left: Global approach; Right: Zonal approach)

However, the zonal approach handles the domain in a separate way: to compute the turbulent flow over the aft body of the hull, it only uses RANS equations for the second half of the H-O grid topology starting from the mid-ship where the inflow information is given by the boundary layer/potential flow method which solve the flow around the fore body part beforehand. On the inlet plane of the H-O grid, the velocity profiles from the boundary layer/potential flow method are applied at the radial grid points. As only about half of the H-O grid is needed in the computation, lower computation expense can be expected, or in other words, more grid points can be saved to the hull stern region which may improve the resolution of the flow/wake field around the stern. The coordinate system and the comparison of the computational domain in global and zonal approach are shown in Fig. 3.

3.2 Computation Setup and Boundary Conditions

As mentioned above, the H-O grid topology is used in the global approach. It is composed of six boundaries: inflow plane, outflow plane, outer boundary, hull surface as well as symmetry plane at y=0 and the flat free surface z=0 as double model was investigated in this test case. The inflow and outflow plane are located at $0.5L_{PP}$ in front of and behind the hull respectively. The cylindrical outer boundary extends to $2.0L_{PP}$ from the hull surface. In the zonal approach, the inlet plane of the H-O grid topology is located at the mid-ship x=$0.5L_{PP}$, the outlet plane is a bit more extended to x=$1.8L_{PP}$ and the position of the outer boundary is the same as in the global approach.

As for the adopted boundary conditions in the computations (as indicated in Fig. 3), in the global approach a fixed velocity, k, ω and zero pressure gradient are set at the inflow boundary; zero gradient of velocity, k, ω and fixed pressure are set at the outflow boundary; slip condition (normal velocity component, normal gradient of all other flow quantities are zero) is used at the outer boundary, symmetry plane (y=0) and flat free surface (z=0); no-slip condition (velocity components, k and pressure gradient are zero) is fulfilled on the hull. In the zonal approach, the velocity, k, ω profiles from the boundary layer/potential flow solution and zero pressure gradient are distributed at the inlet plane to the H-O grid; same condition as in the global approach is set on the downstream outflow plane; same no-slip condition and slip condition is put on the hull surface and symmetry planes respectively; at the far-field outer boundary, zero gradient of tangential velocity, k, ω is applied and the pressure and normal velocity are set to zero.

All the body fitted H-O grids were generated by an in-house module XGRID in SHIPFLOW, no wall function was introduced and thus y^+=0.8 was employed instead. About 4.37M grid points were used in the global approach and 2.97M grid points in the zonal approach. The finite volume solver XCHAP in SHIPFLOW (Regnström 2007) was applied to solve the RANS equations. In the solver, the discretization of convective terms is implemented by a Roe scheme and for the diffusive fluxes central differences are applied. To approach second order accuracy, a flux correction is adopted. An ADI (Alternating Direction Implicit scheme) is utilized to solve the equations.

In the present work, before the computations of global and zonal approach, two different turbulence models were tested first in the global approach to figure out which one performed better in the local flow prediction and it would be used in the subsequent investigation. That is, at the beginning of the work, two available turbulence models in SHIPFLOW, the Menter k-ω SST model (Menter 1993) and EASM (Explicit Algebraic Stress Model) (Deng et al. 2005) were used in the global approach computation; after

that, one of them was used in the global and zonal approach to ensure parallel comparison.

4. RESULTS

This section shows the CFD results of the computations with different turbulence models and based on different approaches. First part is the results produced by turbulence model k-ω SST and EASM. To evaluate the results, here take the predicted axial velocity at the propeller plane (x/L_{PP}=0.9825) as an example as it is the most significant section in terms of the wake prediction. The results are presented in Fig. 4 compared with the wind tunnel measurement (Lee et al. 2003) at Pohang University of Science and Technology. It is shown that at the propeller disc (inside the dashed line region) the axial velocity is over-predicted by the k-ω SST model and the distortion of the axial velocity, namely the so-called 'hook-like' bilge vortex is not so pronounced by the k-ω SST. This phenomenon was also identified in the 2005 Workshop (Hino 2005). Although the result from the EASM model is better, still it is barely satisfactory as the predicted 'hook' shape is very small. Therefore, the interest was moved to the next investigation: global approach versus zonal approach. The EASM model was adopted in both approaches as it had an advantage over the k-ω SST in the wake prediction.

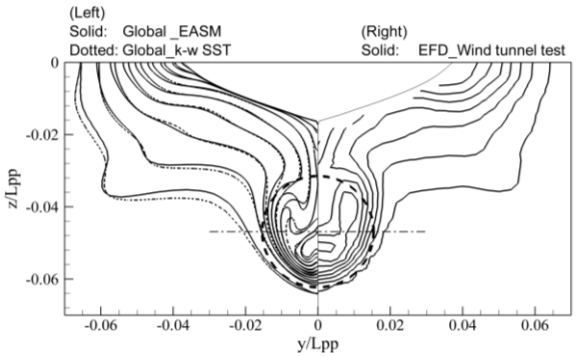

Fig. 4 Axial velocity on the propeller plane (x/L_{PP}=0.9825) ((Left) k-ω SST model: dotted line; EASM: solid line)

At the second stage, the results from the global and zonal approach were compared with two sets of available experimental measurements, one was from the wind tunnel test, and the other was from the towing tank test (Kim et al. 2001) at KRISO. Both experiments were carried out in the fixed condition, namely no sinkage and trim was allowed. The main differences between them lie in that the wind tunnel test was performed with a double model and the spatial distribution of the mean velocities and the turbulence statistics were measured, while the hull was towed in the towing tank test at the Froude number Fr=0.142 and the global force, wave pattern and local velocity field were measured. The Reynolds number was the same in both tests: Re=4.6x10^6. Fig. 5 gives a comparison of measured axial velocity at the propeller plane (x/L_{PP}=0.9825) in the wind tunnel and towing tank test. Two obvious differences can be observed: first the wind tunnel test provides a higher velocity outside of the propeller disc, which may be due to the fact that the wind tunnel test had a high blockage ratio: 6.6%, which is much larger than the one in the towing tank test (0.35%) and thus introduced more blockage to the flow; second the velocity contour level 0.4 above the shaft center line do not coincide. The one in the wind tunnel test turns out to be horizontal near y/L_{PP}=0 but the one in the towing tank goes upwards. The reason behind this is unknown so far, it may attribute to the difference in the test setup.

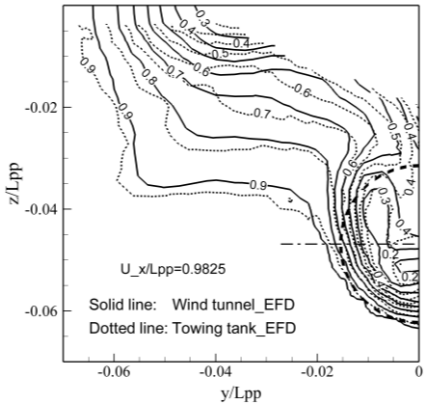

Fig. 5 Comparison of measured axial velocity on the propeller plane (Wind tunnel test versus Towing tank test)

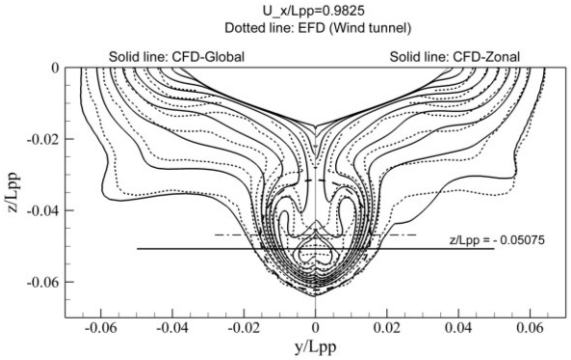

Fig. 6 Axial velocity on the propeller plane (Compared with Wind tunnel test)

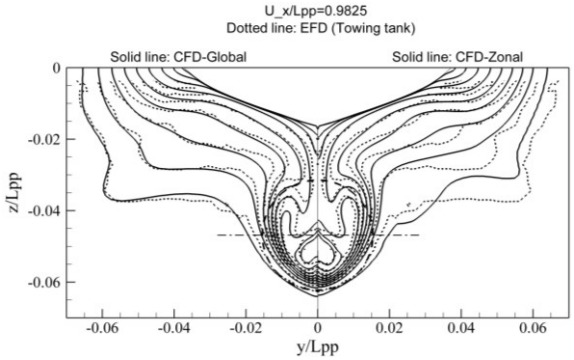

Fig. 7 Axial velocity on the propeller plane (Compared with Towing tank test)

Fig. 6 exhibits the predicted axial velocity on the propeller plane through the global and zonal approach. The results are placed to two sides, and each result is presented coupled with the experimental data from wind tunnel test for parallel comparison. From the comparison, it is observed that the zonal approach provides fairly good wake results especially

at the propeller disc, where the 'hook-like' shape shows up clearly in the prediction and the velocity contours agree with the experimental ones well; while the global approach over-predicts the velocities at the propeller disc as it presents a much smaller 'hook-like' contour.

To further evaluate the computed axial velocity, the computed results from the global and zonal approaches were compared with the towing tank measurement as well. Interesting comparisons are shown in Fig. 7, where more promising agreements with the towing tank data are indicated in both results. This is so, since the blockage in the computations is quite small, 0.27%, i.e. close to that of the towing tank and much smaller than that of the wind tunnel. At the propeller disc, the wake profile and the magnitudes of the predicted axial velocity contours by the zonal approach are almost in accordance with the measured ones. Although not as good as the zonal approach results, the result from the global approach also correspond better with the towing tank data and this holds particularly for the region outside of the propeller disc, where the global approach result corresponds to the towing tank measurement very well, but the zonal approach surprisingly gives the result with lower accuracy.

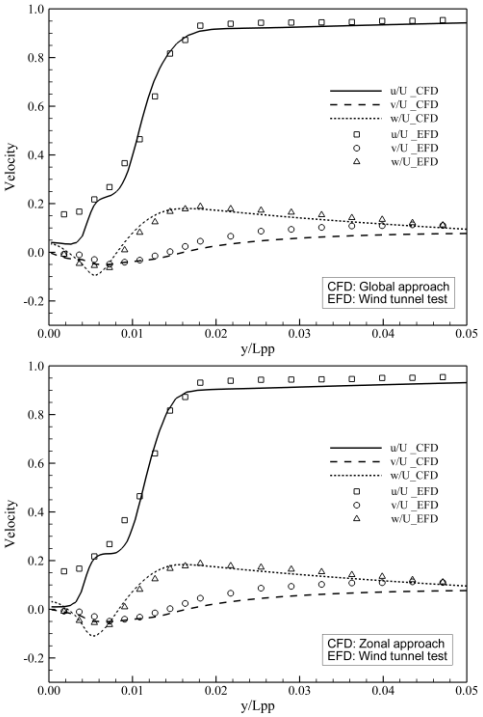

Fig. 8 [*u*, *v*, *w*] profile at z/L_{PP}= -0.05075 on the propeller plane (upper: Global approach; lower: Zonal approach)

The velocity components (*u*, *v*, *w*) profile along a horizontal line z/L_{PP}= -0.05075 (illustrated in Fig. 6) at the propeller plane offers more insight into the predicted velocity close to the shaft center line. Results from the global approach and zonal approach are presented in Fig. 8. Both are compared with the wind tunnel measurement. The figures indicate that in the range between y/L_{PP}=0.0 and 0.005 which is inside the lower part of the bilge vortex, both methods under-predict the axial velocities and the zonal approach is even slightly worse. As this region is very close to the hub cap, the difference in hub cap geometry used in the experiment and the computations may explain the difference between the measurement and the CFD prediction.

More details of the velocity/wake at the propeller disc can be revealed by the circumferential distribution of total wake fraction w_T as the wake (fraction) is always an important factor (parameter) for propulsion efficiency. In the present study, four radii (*r*) inside the propeller disc (specified by Fig. 9) were selected, and non-dimensionalized by the propeller radius *R*: *r*/*R*= 1.0, 0.8, 0.6 and 0.4. The predicted total wake fractions at the circumferential angles from ϕ=0° to 360° are plotted for each radius.

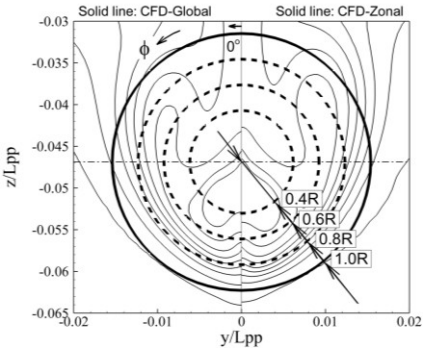

Fig. 9 Radii at the propeller disc (thick solid line area)

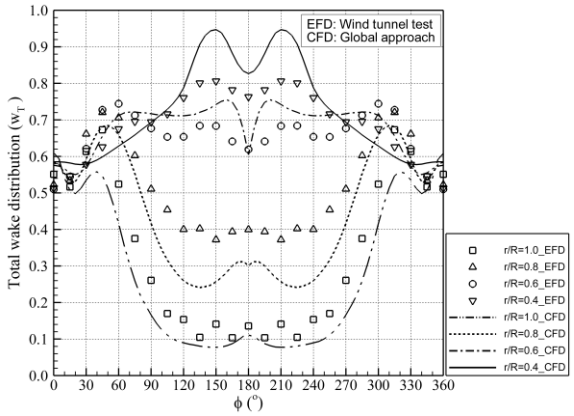

Fig. 10 Circumferential distribution of total wake fraction w_T at the propeller disc
(Global approach results compared with Wind tunnel test data)

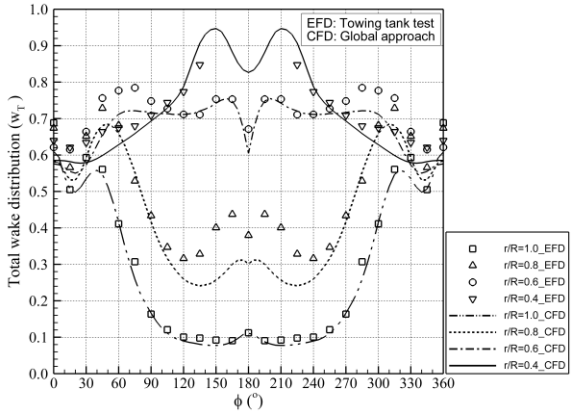

Fig. 11 Circumferential distribution of total wake fraction w_T at the propeller disc
(Global approach results compared with Towing tank test data)

Fig. 10 and 11 present the produced circumferential distribution of w_T from the global approach compared with the wind tunnel test and the towing tank test. Somewhat different w_T results are shown in Fig. 12 and 13, which were predicted through the zonal approach and are compared with two tests as well. In general, the two results match the towing tank data best, and the results from the zonal approach are most satisfactory, especially at r/R=1.0; while most of w_T values are under-predicted at r/R=0.8 and over-predicted at r/R=0.6 and 0.4. It should be noted that some of the wake fractions at r/R=0.4 (in the angle range 135° to 225°) in towing tank test are missing (see Fig. 11, 13). The reason is that in the test this region was below the stern cap where the local flow angle was out of the calibration range so that the velocities could not be determined (Kim et al. 2001).

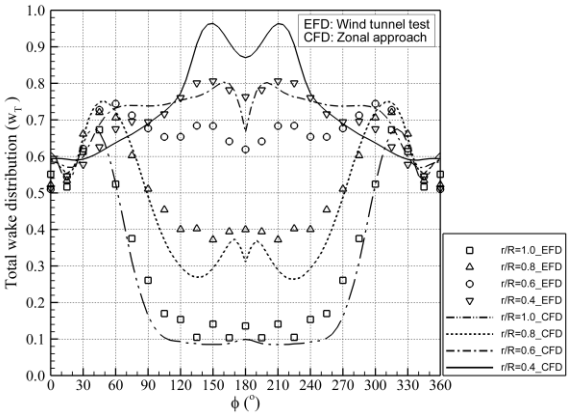

Fig. 12 Circumferential distribution of total wake fraction w_T at the propeller disc
(Zonal approach results compared with Wind tunnel test data)

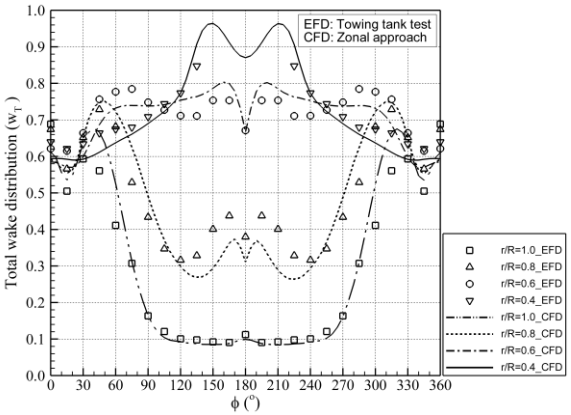

Fig. 13 Circumferential distribution of total wake fraction w_T at the propeller disc
(Zonal approach results compared with Towing tank test data)

In addition, the quantitative differences in the predicted wake fraction by the zonal approach are demonstrated by the errors E given in Table 1 and 2. E is defined as: E = (S-D) % D, here S is the w_T solution and D is the test data from the two measurements. Only half of the wake field (0° to 180°) is considered as the flow field is symmetric in this test case. The tables further confirm the observation in the results for the axial velocity on the propeller plane (Fig. 6, 7 and 8) and circumferential distribution of w_T (Fig. 12 and 13) that lower errors are exhibited in the comparison with the towing tank measurement as the mean value of the absolute errors in w_T at the circles of r/R=1.0, 0.8, 0.6 and 0.4 are smaller in Table 2.

Table 1 Errors in predicted w_T (versus Wind tunnel test)

% / ϕ(°)	r/R = 1.0 E_w_T	r/R = 0.8 E_w_T	r/R = 0.6 E_w_T	r/R = 0.4 E_w_T
0	10.79	13.23	14.76	15.76
15	3.71	3.74	4.71	8.40
30	3.66	-1.57	-3.63	2.53
45	-0.91	4.00	-5.58	-2.31
60	0.29	2.46	-1.59	-5.58
75	-16.61	3.76	3.78	-4.99
90	-37.27	-3.89	9.05	-0.64
105	-38.67	-18.30	13.48	0.97
120	-39.25	-25.24	15.34	1.67
135	-16.32	-33.02	11.64	13.35
150	-39.48	-21.01	15.08	19.58
165	-14.94	-7.95	24.69	16.59
180	-27.00	-22.09	7.74	14.04
mean $\|E\|$	19.15	12.33	10.08	8.19

Table 2 Errors in predicted w_T (versus Towing tank test)

% / ϕ(°)	r/R = 1.0 E_w_T	r/R = 0.8 E_w_T	r/R = 0.6 E_w_T	r/R = 0.4 E_w_T
0	-11.31	-12.26	-5.80	-7.15
15	6.07	-2.05	-7.25	-4.67
30	7.17	-0.08	-9.86	-6.59
45	18.87	2.86	-9.17	-7.90
60	27.83	6.09	-5.75	-5.48
75	1.85	18.20	-5.78	-2.80
90	0.06	13.20	-1.35	-2.63
105	-13.75	6.87	1.97	-2.81
120	-7.26	-5.41	5.98	-0.05
135	-10.35	-17.97	7.44	7.10
150	-7.47	-26.67	4.37	-
165	-2.74	-17.10	6.11	-
180	-11.58	-18.00	-0.64	-
mean $\|E\|$	9.71	11.29	5.50	3.63

5. CONCLUSION

The local/wake flow investigations for the KVLCC2 tanker were performed in the present work. The evaluations were done comparing two different turbulence models and two possibilities for handling the computational domain in the ship hydrodynamic CFD software SHIPFLOW. Some interesting phenomena have been observed through comprehensive comparisons between the CFD approaches and two experimental measurements:

Firstly, measurements from the wind tunnel test and towing tank test differ in some respects although the tests were under similar test conditions. Attention should be paid to these differences in the validation of CFD solutions.

Secondly, the 'hook-like' velocity contour was clearly predicted with the EASM turbulence model in the global approach, which is in accordance with the recommendations in 2000 and 2005 Workshop, but with accuracy deficiency problem. The zonal approach coupled with the EASM model produced the most accurate wake flow in the present study. These results further confirm the accuracy of EASM model in the wake prediction.

Finally, although the computational setup in the zonal approach is more complicated, it did provide slightly better results and also saved computing expense (2.97M versus global 4.37M grid points) in this work. A grid dependence study could give more information about the relationship between accuracy and grid density, but this was not done in the present work.

REFERENCES

Larsson, L., Stern, F., and Bertram, V., (2000), Proceedings of A Workshop on Numerical Ship Hydrodynamics, Gothenburg, Sweden

Hino, T., (2005), Proceedings of CFD Workshop Tokyo 2005, Tokyo, Japan

Van, S.H., Kim, W.J., Yim, G.T., Kim, D.H., and Lee, C.J., (1998), "Experimental Investigation of the Flow Characteristics Around Practical Hull Forms", Proceedings 3rd Osaka Colloquium on Advanced CFD Applications to Ship Flow and Hull Form Design, Osaka, Japan

Kim, W.J., Van, S.H. and Kim, D.H., (2001), "Measurement of flows around modern commercial ship models", Exp. in Fluids, Vol. 31, pp 567-578

Lee, S.J., Kim, H.R., Kim, W.J., and Van, S.H., (2003), "Wind tunnel tests on flow characteristics of the KRISO 3,600 TEU containership and 300K VLCC double-deck ship models", J. Ship Res., Vol. 47, No 1, pp. 24-38

Van, S.H., Kim, J.W., Yoon, H.S., Lee, Y.Y., Park, I.R., (2006), "Flow measurement around a model ship with propeller and rudder", Experiments in Fluids 40(4): 533-545

Kim, W. J., Kim, D. H., Van, S. H., (2002), "Computational study on turbulent flows around modern tanker hull forms", International Journal for Numerical Methods in Fluids 38(4): 377-406

Deng, G.B., Queutey, P., and Visonneau, M., (2005), "Three-Dimensional Flow Computation with Reynolds Stress and Algebraic Stress Models", Engineering Turbulence Modeling and Experiments 6, Rodi, W., and Mulas, M., eds. ELSEVIER, 389-398

Regnström, B., Broberg, L., Östberg, M., Bathfield, N. and Larsson, L. (2005), "Drag Prediction for the KVLCC2M Hull", Proceedings of CFD Workshop Tokyo 2005

Regnström, B., (2007), SHIPFLOW theoretical manual, FLOWTECH International AB, Gothenburg, Sweden

Menter, F.R., (1993), "Zonal Two Equation k-ω Turbulence Models for Aerodynamic Flows", 24th Fluid Dynamics Conference, Orlando, AIAA paper 93-2906

NUMERICAL SIMULATION OF FREE SURFACE FLOW OF KCS AND THE INTERACTION BETWEEN PROPELLER AND HULL

Zhirong Zhang (CSSRC, China)
Chengsheng Wu (CSSRC, China)
Shaofeng Huang (CSSRC, China)
Feng Zhao (CSSRC, China)
Zhenping Weng (CSSRC, China)

1. SUMMARY

Computational Fluid Dynamics (CFD) has made remarkable progress in the past few decades in the field of ship hydrodynamics. Today, although ship model tests still provide the most accurate predictions of the required power and other overall results. However, serious scale effects are present in viscous flow phenomena. Moreover, the time and cost needed, mainly for model manufacture, make model testing impractical for hydrodynamics optimization studies. CFD method is applying to practical ship design and performance prediction more often now. It can provide insight in the local flow characteristics which may often enable the designer to develop or improve their design. The cost and time required for the computation are much lower than for model tests. CFD approach is very suitable for predicting trends and optimizing in ship hydrodynamics.

Precise prediction of the ship resistance and the flow field on propeller disk using CFD are very crucial in ship hydrodynamics design. In the present paper the free surface flow of a modern container ship KCS without propeller was firstly simulated using three sets of grids to study the grid convergence. The computed results including resistance, wave elevation and flow field on propeller disk were compared with the experimental data in detail. Then the flow fields of KCS free to heave and pitch were also calculated. Total resistance, sinkage and trim at various Froude number are provided.

Propellers are always operating behind ship hull. The interaction between hull and propeller is very important for the designer. In this paper, the viscous flow around KCS with operating propeller behind was also simulated. The actual propeller was modeled and sliding mesh technique was used. The sliding mesh technique is the most accurate method for simulation of propeller/hull interaction but also the most computationally demanding. The calculated results were also compared with the experimental data and it demonstrated that this approaches is appropriate for applying to the study of hull/propeller interaction.

1.1 Solver

The commercial CFD software FLUENT6.3.26 was used in the present study. It solves the RANS equations using a cell-centered finite-volume method.

1.2 Turbulence Model

The SST (Shear Stress Transport) k-ω turbulence model was used for turbulence closure in present study. The SST k-ω model is one of the most widely used turbulence models for external aero- and hydrodynamics. The SST k-ω model was developed by Menter (1994) to effectively blend the robust and accurate formulation of the k-ω model in the near-wall region with the free-stream independence of the k-ε model in the far field. This model has reportedly better computational performance in flows involving separation, which is an important issue in the analysis of ship flow, where separation always occurs in the region of ship stern.

1.3 Free Surface Treatment

In the present study the free surface was included. The VOF method was applied to deal with water-air two phase free surface interface. The VOF model is a fixed grid technique designed for two or more immiscible fluids where the position of the interface between the fluids is part of the unknown to be found through the solution procedure. In the VOF model, the fluids share a single set of momentum equations, and the volume fraction of each of the fluids in each computational cell is tracked throughout the domain.

1.4 Ship Motion Treatment

In the case of ship model free to heave and pitch, the ship

motion and the flow field around it are simulated coupled. While the ship motion is determined by the resulting vertical force and pitch moment acting on it. The couple of ship motion and flow field is demonstrated as in the Fig. 1 below.

The ship motion is analyzed in the Earth-fixed frame. The motions of ship model were realized by moving the (overall) grid during the numerical simulations. A multi-step method with 2nd order of accuracy is used for the temporal discretization.

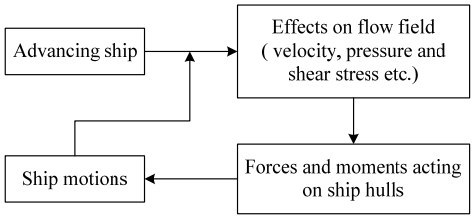

Fig.1 Couple of ship motion and flow

1.5 Rotating Propeller

For modeling the propeller effects, there are many techniques can be used including body force method, pressure jump method and actual propeller method. In this paper the actual rotating propeller was included in the numerical computation. To obtain the time-accurate solution for propeller/hull interaction (rather than a time-averaged solution), the sliding mesh method to compute the unsteady flow field has been used. The sliding mesh model is the most accurate method for simulating flows in which there exists relative motion of propeller and ship hull, but also the most computationally demanding.

In the sliding mesh approach two or more cell zones are used. Each cell zone is bounded by at least one interface zone where it meets the opposing cell zone. The interface zones of adjacent cell zones are associated with one another to form a grid interface. The two cell zones will move relative to each other along the grid interface. During the calculation, the cell zones slide relative to one another along the grid interface in discrete steps. (See Fig. 2 for schematic of sliding mesh model)

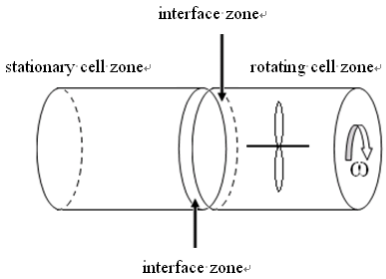

Fig.2 Schematic for sliding mesh model

1.6 Numerical Method

The governing equations of RANS are solved using a cell-centered finite-volume method. Convection terms in the RANS equations are discretized using a second order upwind scheme, while diffusion terms are discretized using a second order central scheme. Overall solution procedure is based on a SIMPLE-type segregated algorithm. The discretized equations are solved using the Gauss-Seidel iterative procedure, and the algebraic multi-grid method is used to accelerate the solution convergence.

2. KCS WITHOUT PROPELLER

The grid convergence study for KCS without propeller and rudder has been performed in this paper. It is assumed that as the number of grid point increases and the grid spacing tend to zero, the discretization error should tend to zero as well. As the grid is refined the solution should approaches the solution of the continuous equations. Grid convergence study is useful for deciding the level of discretization error existing in the CFD solution.

In the present study, three sets of systematically refined grids were generated (Fig. 3). The multi-block structured mesh was used. And the number of numerical mesh is list in Table 1 for all three sets of grids. In the calculations, the Reynolds number based on ship length and ship velocity is 1.4×10^7. And the Froude number is Fr=0.26.

Table 1 Number of mesh for systematically refined grids

Coarse mesh	Medium mesh	Fine mesh
0.148 M	0.423 M	1.247 M

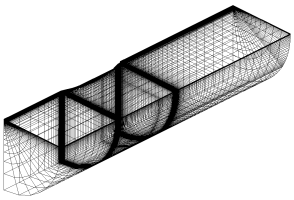

Coarse mesh

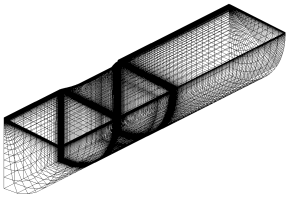

Medium mesh

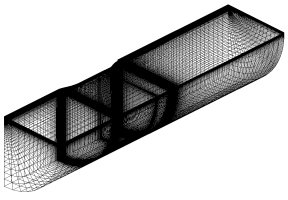

Fine mesh

Fig.3 Three sets of systematically refined grids

The results from the grid convergence study for total resistance C_T are summarized in Table 2. Fig.4 is the wave contour from the three sets of grids. It is seen that as the number of grid points increased, the wave pattern is refined especially in the far field and Fig.5 is the test results of wave contour. The agreement between calculated and tested wave contour is very good.

Table 2 Grid convergence study for total C_T

	Coarse 3	Medium 2	Fine 1	Data (D)
C_T	3.756	3.639	3.625	3.557 (with rudder)

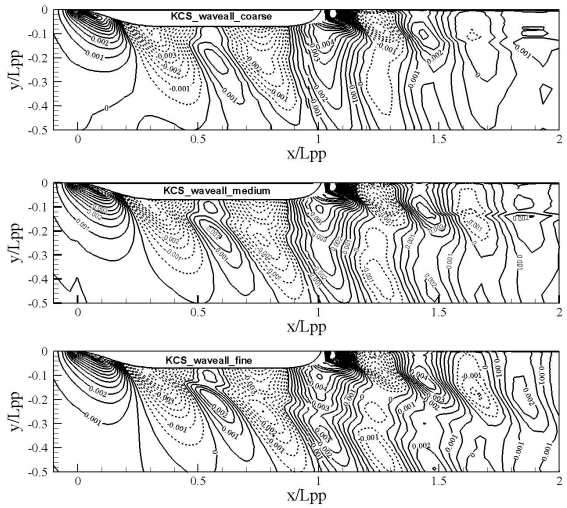

Fig.4 Wave elevation contour for three sets of grids

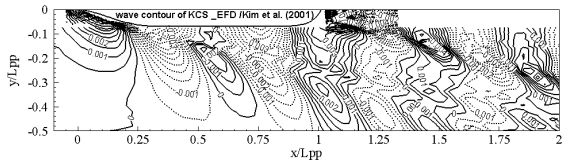

Fig.5 Wave elevation contour from test

Fig.6 is the result of grid convergence study for wave profile on the hull. The agreement with the experimental result is also very good.

Fig.7 is the result of grid convergence study for longitudinal wave cut at y/Lpp=0.1509. With the number of grid point increases, the result is closer to the test data. And the far field wave profile can be well simulated by the fine grid than the coarse grid.

The comparison of velocity field on propeller plane between calculated and measured results for the three sets of grid are shown in Fig.8. The right half of each figure is the calculated result while the left half is the measured result. When the grid is fined the velocity at propeller plane changes a little and they all agree well with the experimental results.

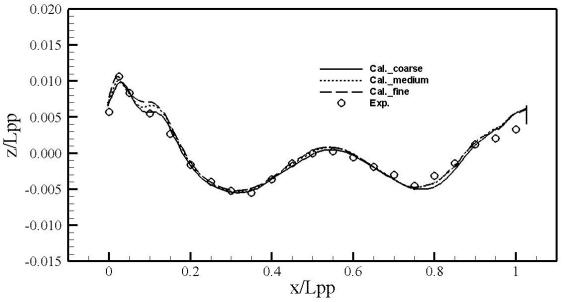

Fig.6 Grid convergence study for wave profile on hull

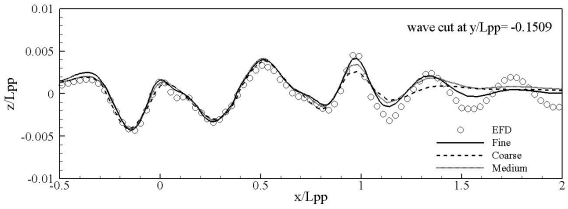

Fig.7 Grid convergence study for longitudinal wave cut at y/Lpp=0.1509

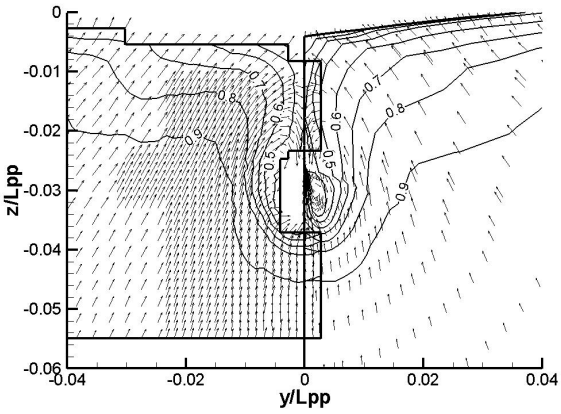

Coarse mesh（Left:Exp., right: Cal.）

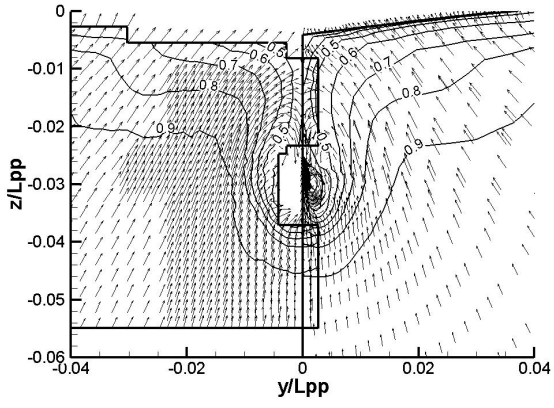

Medium mesh（Left:Exp., right: Cal.）

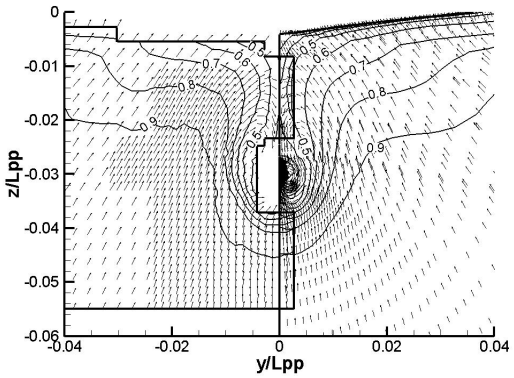

Fine mesh（Left:Exp., right: Cal.）

Fig.8 Grid convergence study for velocity at propeller plane

3. KCS FREE TO HEAVE AND PITCH

CFD simulation of KCS ship model (without rudder) free to heave and pitch in calm water with different speed is also carried out in this paper. The Reynolds number (Re) varies from 5.2×10^6 to 1.4×10^7 with Froude number (Fr) 0.1083 to 0.2816.

The computed total resistance coefficient (calculated based on wetted surface area without rudder) is summarized in Table 3 and Fig. 9. The results of model test are also presented. The comparison shows quite good agreement even if the difference between the computation and model test is taken into consideration.

Table 3 Computed total resistance coefficient CT

Fr	$Re\times10^{-6}$	$C_T\times10^3$	
		CFD	Exp
0.1083	5.2×10^6	3.777	3.796
0.1516	7.3×10^6	3.646	3.641
0.1949	9.4×10^6	3.506	3.475
0.2274	1.1×10^7	3.481	3.467
0.2599	1.3×10^7	3.720	3.711
0.2816	1.4×10^7	4.532	4.501

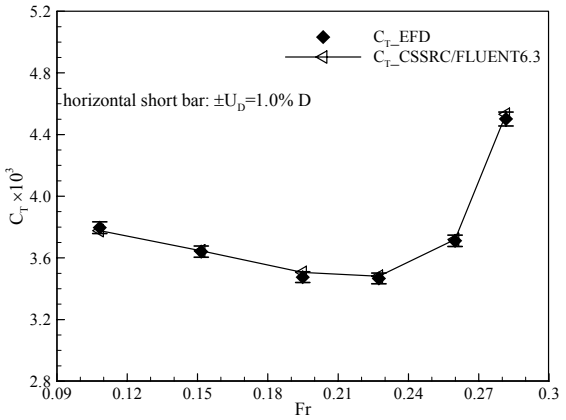

Fig.9 Computed total resistance coefficient C_T

The computed results of sinkage and trim of the model is summarized in Table 4, Fig. 10 and Fig. 11. The results of model test are also given out in the table and figures. The comparison between them shows rather good agreement. The differences between the computed and experimental results are relatively big for low speeds. This is because the values of sinkage and trim are very small in these cases which are quite difficult to compute accurately.

Table 4 Computed sinkage σ and trim τ

Fr	$\sigma\times10^2$ (m)		τ (°)	
	CFD	Exp	CFD	Exp
0.1083	-0.15	-0.090	-0.023	-0.017
0.1516	-0.38	-0.275	-0.052	-0.053
0.1949	-0.66	-0.599	-0.100	-0.097
0.2274	-1.00	-0.944	-0.135	-0.127
0.2599	-1.43	-1.394	-0.180	-0.169
0.2816	-1.83	-1.702	-0.160	-0.159

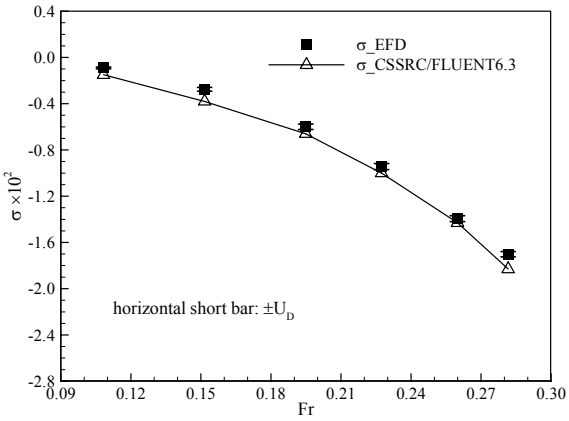

Fig.10 Computed sinkage σ for KCS model

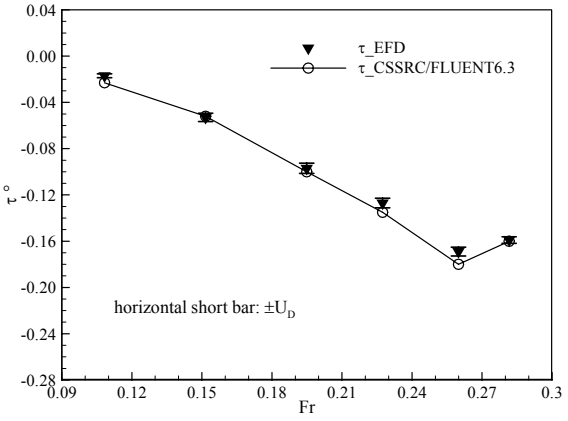

Fig.11 Computed trim τ for KCS model

4. FLOW SIMULATION OF KCS WITH PROPELLER

It is most important for ship and propeller designers to have a good understanding of the interaction between hull and propeller. In this paper, CFD method has been

used to predict flow fields around ship with propeller. And this method may become an important tool for study propeller/hull interaction.

For modeling the propeller effects, Sliding mesh technique has been used in this paper. In this approach, actual rotating propeller was included in the numerical computation. It's the most accurate but also the most computationally demanding approach. This approach should able to deal with the different time scales of ship flow and the propeller flow. In addition, when actual propeller was included. The proper selection of grid topology around ship became more challenging.

Flow field of KCS with Propeller KP505 in calm water was calculated. The rudder was not included. The velocity of ship motion is 2.196m/s and the rotating speed of propeller is 9.5rps. The Self propulsion tests were carried out at the Ship Research Institute (now NMRI) in Tokyo and are reported in the Proceedings of the CFD Workshop Tokyo in 2005 (Hino, 2005).

Fig. 12 is the calculated axial velocity contour downstream of propeller (0.25D behind the propeller plane) by using sliding mesh technique. And Fig. 13 is the experimental result. It can be seen that the axial velocity is relatively well predicted by the rotating propeller approach.

Fig. 14 and Fig. 15 is the cross flow vector obtained from sliding mesh approach and experiment respectively. The cross flow is also well predicted by the rotating propeller approach.

Fig. 16 is the comparison of velocity downstream of propeller at z/Lpp=-0.03 between CFD results and experimental results.

Fig. 17 is the hull surface pressure contour (port-side view) from sliding mesh approach and Fig. 18 is the experimental result.

Table 5 listed the comparisons of thrust and torque coefficients between measured results and calculated results. It is shown that the sliding mesh technique can predicted K_T and K_Q very good for propeller behind hull.

These numerical investigation shows that accurate prediction of propeller/hull interaction using CFD method is feasible. With increasing computing power and improved grid generation techniques the CFD will be a valuable tool for the optimization of integrated hull-propeller configurations.

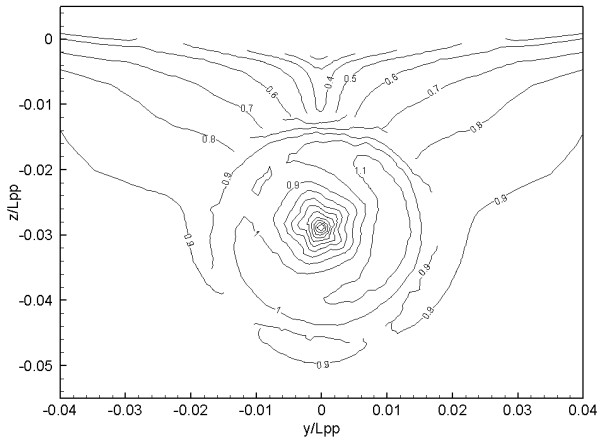

Fig.12 Axial velocity contours downstream of propeller plane from sliding mesh modeling

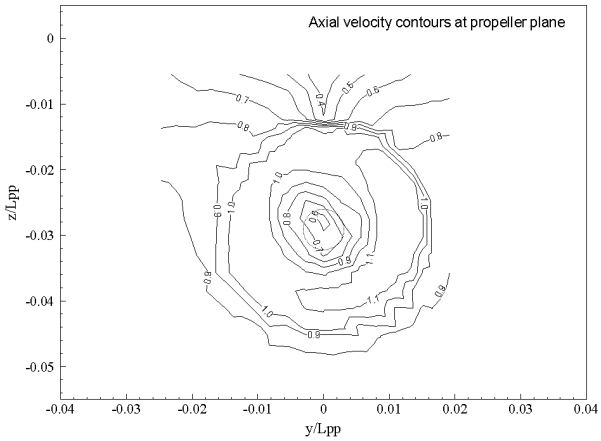

Fig.13 Axial velocity contours downstream of propeller plane from test

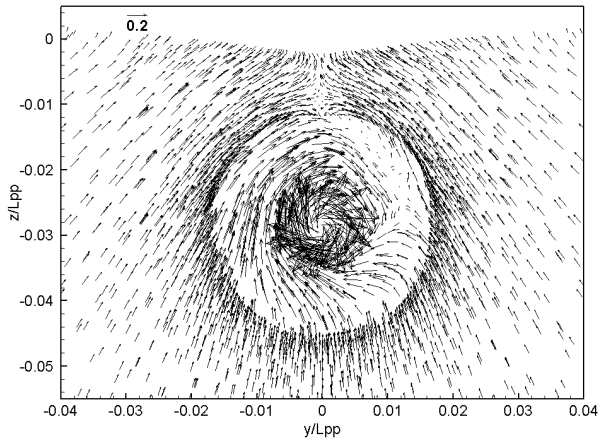

Fig.14 Cross flow vector downstream of propeller plane from sliding mesh modeling

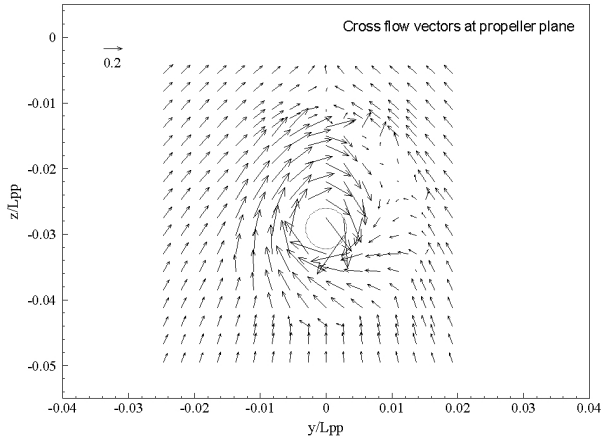

Fig.15 Cross flow vector downstream of propeller plane from test

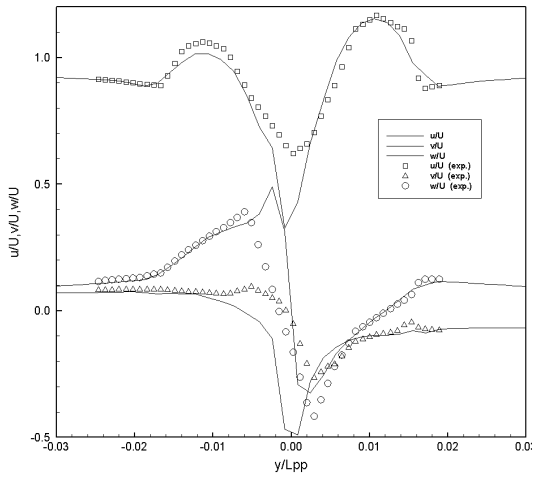

Fig.16 Velocity downstream of propeller plane (x/LPP=0.9911) at z/LPP=-0.03 (by sliding mesh method)

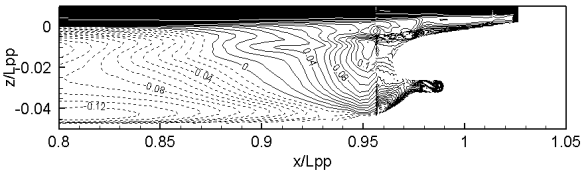

Fig.17 Hull surface pressure contour from sliding mesh modeling

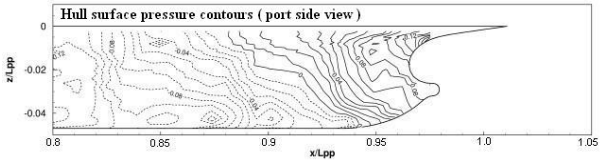

Fig.18 Measured surface pressure contour

Table 5 Comparisons between measured and calculated K_T and K_Q

	K_T	K_Q
Measured results	0.1703	0.0288
Sliding mesh results	0.1699	0.0292

5. CONCLUSION

The flow around container ship KCS using three grids are computed in this paper and the grid convergence study was performed.

Then the flow fields of KCS free to heave and pitch were also calculated. Total resistance, sinkage and trim at various Froude number are provided. Good agreement with experimental data has been observed.

CFD simulations of KCS with propeller are also performed using actual propeller. Accurate prediction of propeller/hull interaction using CFD method is feasible.

And the huge potentials of CFD application in ship hydrodynamics performance prediction as well as in ship engineering design practice are demonstrated.

REFERENCES

Menter, F.R. (1994), "Two-Equation Eddy-Viscosity Turbulence Models for Engineering Applications", *AIAA Journal*, Volume32, No 8:1598-1605.

Van, S.H., Kim, W.J., Yim, G.T., Kim, D.H., and Lee, C.J., (1998), "Experimental Investigation of the Flow Characteristics Around Practical Hull Forms", Proceedings 3rd Osaka Colloquium on Advanced CFD Applications to Ship Flow and Hull Form Design, Osaka, Japan

Kim, W.J., Van, D.H. and Kim, D.H., (2001), "Measurement of flows around modern commercial ship models" *Exp. in Fluids*, Vol. 31, pp 567-578

Hino, T., "Proceedings of CFD Workshop Tokyo 2005", NMRI report 2005

Zhirong Zhang, (2009) Numerical simulation of flow field around container ship KCS and its uncertainty analysis. CSSRC Report No. 09691 (In Chinese)

CFD SIMULATION OF SHIP MODEL FREE TO SINKAGE AND TRIM ADVANCING IN CALM WATER

Chengsheng Wu (CSSRC, China)
Lei Yang (CSSRC, China)
Zhirong Zhang (CSSRC, China)
Feng Zhao (CSSRC, China)
Kai Yan (CSSRC, China)

1. SUMMARY

A great deal of work has been done by ship hydrodynamic researchers to predict the resistance accurately for ship/model by CFD method, including studies on computational domain, grid generating, turbulence model, free surface treatment and so on. One of the main characteristics of numerical simulation of free surface flow around surface ship/model is that the ship/model will have dynamic sinkage & trim while advancing in sea or towing tank, which is neglected in former simulation for a long time. However, for ship with medium or high speed, the sinkage & trim are considerable and will bring remarkable effect to the resistance. So in recent years, sinkage and trim are taken into consideration in more and more CFD simulations of free surface flow around surface ships.

In this paper, numerical simulation of free surface flow around naval combatant model DTMB5415 with fixed sinkage and trim was carried out firstly. Then the free surface flow around DTMB5415 free to sinkage and trim with different speeds was simulated. The computed results of resistance, wave elevation, velocity field, sinkage and trim are presented and compared with the experimental data in detail. Quite good agreement is shown in the comparison.

1.1 Solver

The commercial CFD software FLUENT6.3.26 was used in present study. The RANS equations are solved by using a cell-centered finite-volume method in the solver.

1.2 Turbulence Model

The Renormalization group (RNG) k-ε two-equation turbulence model, an upgrading version of standard k-ε two-equation turbulence model, is used in present study. The model was developed by Yakhot etc. and was applied successfully in the simulation of many turbulent flows. It is also used widely in numerical simulation of ship hydrodynamics.

1.3 Free Surface Treatment

In present study, the free surface is included. The free surface flow is treated as two-phase flow, i. e. water and air, free surface is the interface between air and water, and volume of fluid (VOF) method is adopted to deal with it. The VOF model is a fixed grid technique designed for two or more immiscible fluids where the location of the interface between the fluids is part of the unknown to be found through the solution procedure. In the VOF model, the fluids share a single set of momentum equations, and the volume fraction of each of the fluids in each computational cell is tracked throughout the domain.

1.4 Ship Motion Treatment

In the case of ship model free to sinkage and trim, the motions are determined by the resulting vertical force and pitch moment acting on the model by the flow. However, the flow is influenced by ship motion as well and both problems have to be considered simultaneously. The couple of ship motions and flow field is demonstrated in Fig.1.

The ship motions are analyzed in the Earth-fixed frame. The motions of ship model were realized by moving the overall grid during the numerical simulations. A multi-step method with 2nd order of accuracy is used for the temporal discretization.

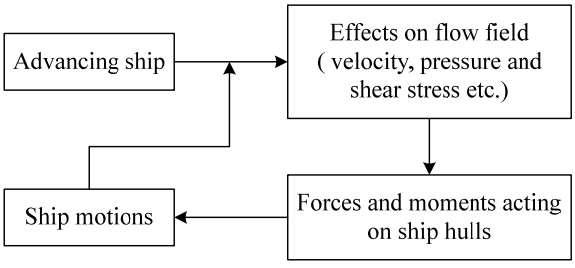

Fig.1 Couple of ship motions and flow field

1.5 Numerical Method

The governing equations of RANS are solved using a cell-centered finite-volume method. Convection terms in the RANS equations are discretized using a second order upwind scheme, while dissipation terms are discretized using a second order central scheme. Overall solution procedure is based on a SIMPLE-type segregated algorithm. The discretized equations are solved using the Gauss-Seidel iterative procedure, and the algebraic multi-grid method is used to accelerate the solution convergence.

2. MODEL WITH FIXED SINKAGE AND TRIM

Numerical simulation of free surface flow around DTMB5415 with fixed sinkage (σ=-1.82×10-3) and trim (τ=-0.108°) was carried out firstly. The Reynolds number based on model length and model speed is 1.19×107 and the Froude number is Fr=0.28.

2.1 Computational Domain and Mesh

The origin of the coordinate for the computational domain locates on the intersection of free-surface of calm water, symmetric plane and vertical-transverse mid-plane of the hull. The computational domain extents are: -1.2L~2.4L in x-direction, -1.2L~1.2L in y-direction and -1.2L~0.3L in z-direction, where L denotes the model length. The outline of the computational domain is shown in Fig. 2. Because of the symmtry of problem solved in present study, only half of the computational domain need to be simulated.

Multiblock structural mesh of H-O type (Fig. 2) with 660,500 cells (L230×V55×R50) was used in the simulation. Grids are congregated in the regions of the bow, stern of the model, near the hull surface and free surface. The near wall mesh grids located within log-law region with averaged y^+≈60. The mesh on the hull surface (L150×V50) is shown in Fig. 3.

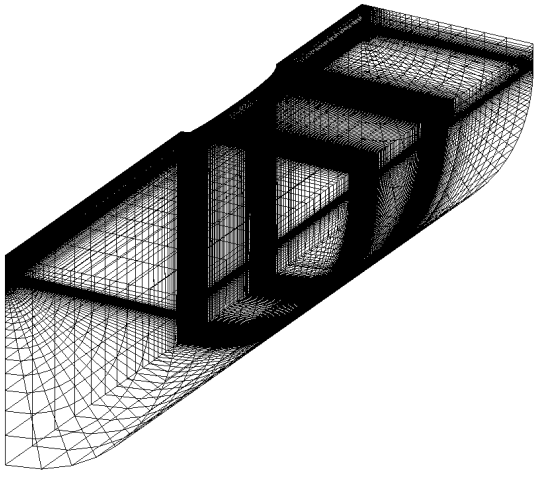

Fig.2 Computational mesh

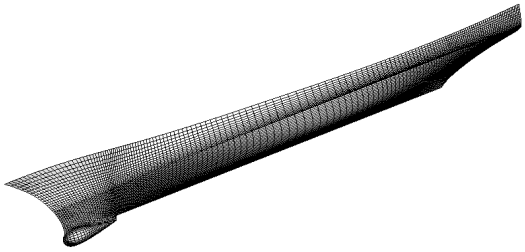

Fig.3 Mesh on hull surface

2.2 Computational Results

a. Resistance

The computational results of resistance for the ship model in this case are summarized in table 1. The experimental results are also given in the table, where the frictional coefficient CF is calculated by ITTC'57 formulation (CF=0.075/(logRe-2)2). It can be seen from the table that the computational results of resistance agree quite well with the experimental ones.

Table 1 Computational results of resistance

	$C_T\times10^3$	$C_F\times10^3$	$C_R\times10^3$
CFD	4.238	2.908	1.330
EFD	4.23	2.91	1.32
Err (%D)	-0.19	0.07	-0.76

b. Wave elevation

The computational result of wave elevation contour is plotted in Fig. 4 (upper part), the experimental result is also presented in the figure (lower part). It can be seen from the figure that the simulated wave pattern agrees rather well with the experimental result especially in the near field. In the far field, the wave attenuates a lot in CFD simulation because of the grids there are getting sparser, so the agreement between the computational and experimental results will be worse than in the near field. More detailed comparisons will be shown in Fig. 5~7.

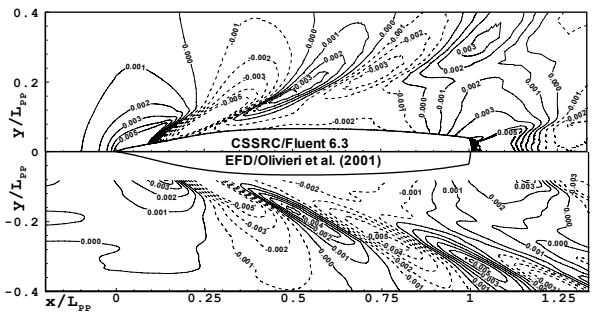

Fig.4 Computational wave pattern

The simulated results of wave cut at y/LPP=0.082, 0.172 and 0.301 are plotted in Fig. 5 to Fig. 7. The experimental results are also plotted in the figures.

It can be seen from Fig. 5 that the simulated wave cut at y/L_{PP}=0.082 agrees quite well with the experimental data. The peaks, troughs and amplitude of the wave cut are all predicted quite well.

For wave cut at y/L_{PP}=0.172, the simulated result also agrees rather well with the experimental data, while a few minor discrepancies for short wave components between them can be seen in Fig. 6. The peaks, troughs and amplitude of the wave cut are all predicted quite well on the whole.

As can be seen in Fig.7, for wave cut at y/L_{PP}=0.301, the agreement between the simulated result and experimental data is not very good. The wave attenuates a lot as compared with EFD result and some wave components with short wave length disappeared in the CFD results. This is because of the grids here are getting sparser and are not enough to simulate the short wave components.

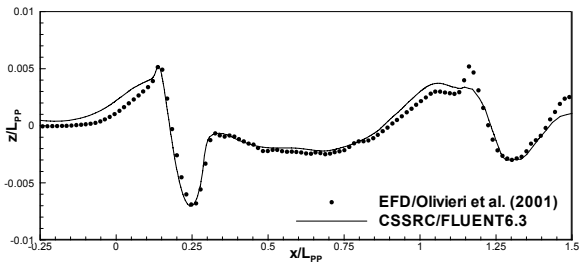

Fig.5 Wave cut at y/L_{PP}=0.082

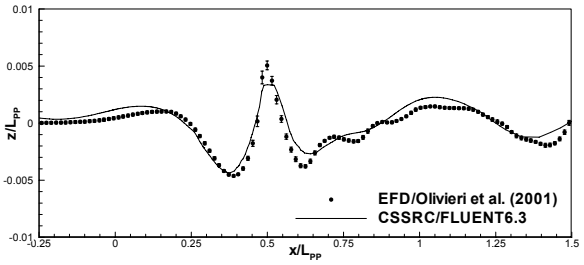

Fig.6 Wave cut at y/L_{PP}=0.172

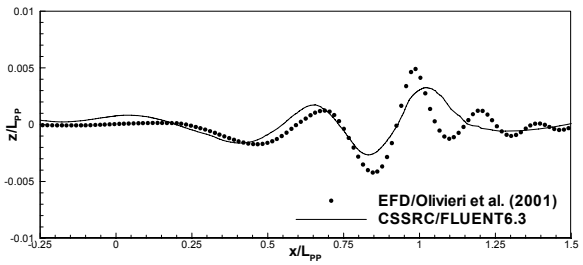

Fig.7 Wave cut at y/L_{PP}=0.301

c. Velocity field

The computational results of velocity field near the model hull are presented in the figures listed below.

The computational results of streamwise velocity contour (right side) and cross-flow vectors/streamline (left side) at x/L_{PP}=0.2 are plotted in Fig. 8. The experimental results are presented in Fig. 9. It can be seen from the figures that the computational results agree quite well with the experimental results both for the streamwise velocity contour and cross-flow vectors/streamline, the vortex behind the sonar dome is also predicted quite accurately.

Fig. 10 shows the computational results of velocity field at x/L_{PP}=0.6. The corresponding experimental results are presented in Fig. 11. From the figures we can see that for streamwise velocity contour, the computational result agree rather well with the experimental result. But for cross-flow vectors/streamline, the agreement between them is not very good, the direction of the vector/ streamline for CFD simulation differs a lot from that of EFD result and the two vortexs right below the hull is not resolved well.

The computational results of streamwise velocity contour and cross-flow vectors/streamline at x/L_{PP}=0.935 are presented in Fig. 12. The experimental results are plotted in Fig. 13. It can be seen from the figures that the computational results agree quite well with the experimental results both for the streamwise velocity contour and cross-flow vectors/streamline.

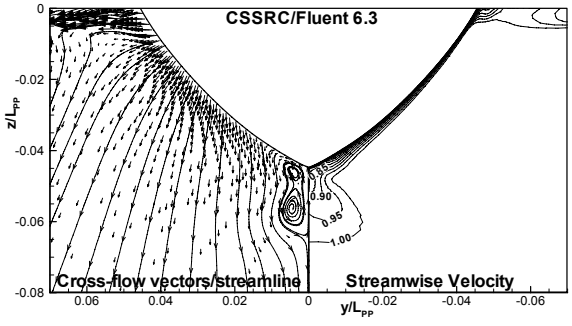

Fig.8 Velocity field at x/L_{PP}=0.2 (CFD)

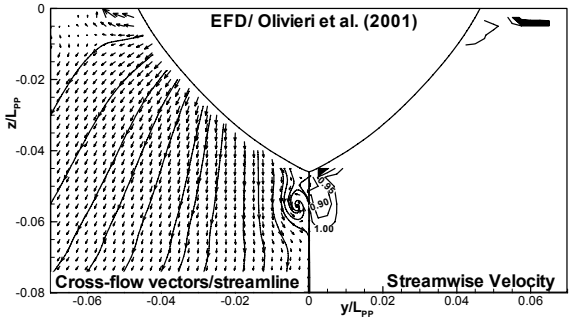

Fig.9 Velocity field at x/L_{PP}=0.2 (EFD)

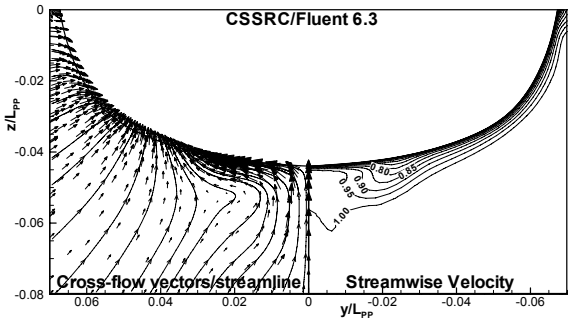

Fig.10 Velocity field at x/L_{PP}=0.6 (CFD)

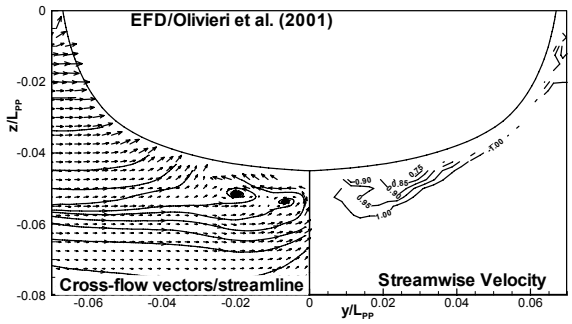

Fig.11 Velocity field at x/L_{PP}=0.6 (EFD)

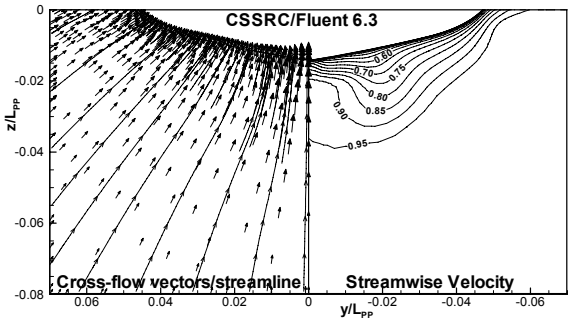

Fig.12 Velocity field at x/L_{PP}=0.935 (CFD)

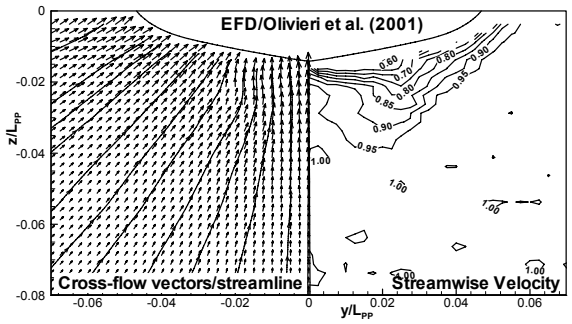

Fig.13 Velocity field at x/L_{PP}=0.935 (EFD)

From the computational results for DTMB5415 with fixed sinkage and trim include resistance, wave elevation and velocity field summarized hereinbefore, it can be seen that the overall agreements between them and the experimental results are quite good, most of them are predicted quite well by CFD simulation.

3. MODEL FREE TO SINKAGE AND TRIM

3.1 Introduction to CFD Simulation

Numerical simulation of free surface flow around DTMB5415 free to sinkage and trim advancing in calm water with different speeds is carried out in this section. The Froude numbers based on model length and model speed are 0.138, 0.28 and 0.41 with Reynolds numbers 5.96×106, 1.19×107 and 1.75×107.

The extents of the computational domain used here is the same as that used in the simulation of DTMB5415 with fixed sinkage and trim. Multiblock structural mesh of H-O type with about 450,000 cells (L180×V52×R45) was used in the simulation of DTMB5415 free to sinkage and trim.

3.2 Computational Results

a. Resistance

The computed resistance coefficients are summarized in table 2. The results of model test is also presented in the table. The comparison between them shows quite good agreement for total resistance and frictional resistance. For the residual resistance, the relative difference between the computation and experiment is bigger in the case of Fr=0.138 than in the other two cases. This is because of the value of residual resistance is quite small in this case which is rather difficult to predict accurately.

Table 2 Computed resistance coefficients

	Fr	$C_T\times10^3$	$C_F\times10^3$	$C_R\times10^3$
CFD	0.138	3.982	3.303	0.679
EFD		3.89	3.29	0.605
Err (%D)		-2.36	-0.39	-12.23
CFD	0.28	4.235	2.911	1.324
EFD		4.23	2.91	1.32
Err (%D)		-0.12	-0.03	-0.3
CFD	0.41	6.53	2.81	3.72
EFD		6.67	2.73	3.94
Err (%D)		2.1	-2.93	5.58

The computed resistance coefficients for DTMB5415 free to sinkage and trim advancing in calm water over a wide range of speed with Fr=0.10~0.45 are plotted in Fig. 14. The results of model tests carried out in IIHR and CSSRC are also presented in the figure. It can be seen from the figure the overall agreement between them is quite good especially within the range of medium speed with Fr=0.25~0.35.

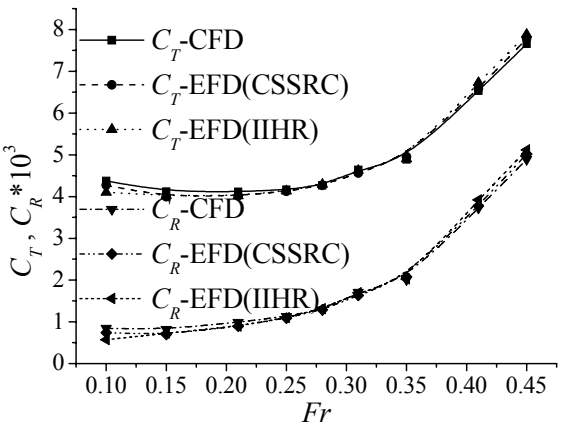

Fig.14 Computed resistance coefficients

b. Sinkage and trim

The computed sinkage and trim for the ship model are summarized in table 3. The results of model test is also presented in the table. The comparison between them shows rather good agreement especially for medium and high speed (Fr=0.28, 0.41). In the case of low speed (Fr=0.138), the relative differencies between the results of CFD simulation and model test are more obvious than in the other two cases. This is also because of the values of sinkage and trim are very small in this case which are quite difficult to predict accurately.

Table 3 Computed sinkage σ and trim τ

	Fr	σ×10^3	τ (°)
CFD	0.138	-0.441	-0.022
EFD		-0.504	-0.028
Err (%D)		12.50	21.43
CFD	0.28	-1.92	-0.109
EFD		-1.82	-0.108
Err (%D)		-5.49	-0.93
CFD	0.41	-4.53	0.395
EFD		-4.70	0.421
Err (%D)		3.62	6.18

The computed sinkage and trim for DTMB5415 free to sinkage and trim advancing in calm water over a wide range of speed with Fr=0.20~0.45 are plotted in Fig. 15 and Fig. 16. The results of model tests carried out in IIHR and CSSRC are also presented in the figures. It can be seen from the figures the overall agreement between them is quite good. And the tendencies of computed sinkage and trim vary with model speed (Fr) is the same as that of model test.

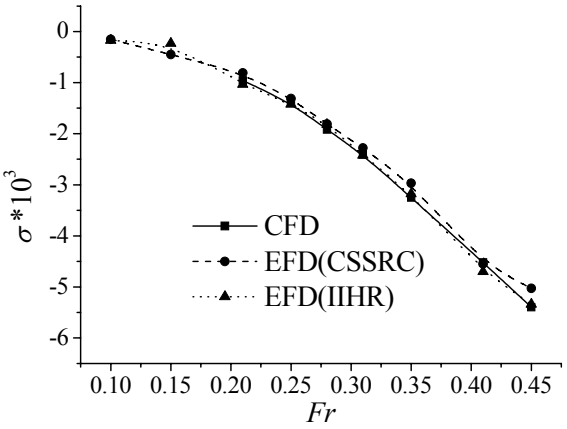

Fig.15 Computed sinkage for DTMB5415

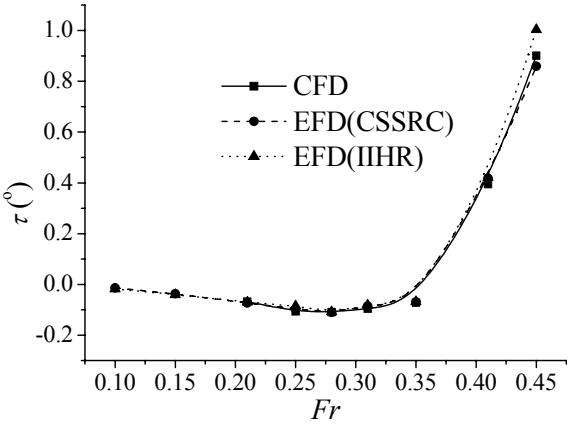

Fig.16 Computed trim for DTMB5415

From the computational results for DTMB5415 free to sinkage and trim advancing in calm water with different speeds include resistance, sinkage and trim summarized hereinbefore, it can be seen that the overall agreements between them and the experimental results are quite good, most of them are predicted quite well by CFD simulation.

4. CONCLUSION

Numerical simulations of free surface flow around naval combatant model DTMB5415 with fixed sinkage & trim and free to heave & pitch are carried out in this paper. The computed results of resistance, wave elevation, velocity field, sinkage and trim are presented and compared with the experimental data in detail.

For the simulation of ship model with fixed sinkage and trim, the computed results of resistance agree quite well with the experimental data, the wave elevation is simulated quite well in the near field while in the far field the wave attenuates a lot because of the grids there are getting sparser, the prediction of velocity field in the region of bow and stern is rather good while the direction of the cross-flow vector/streamline differs a lot from that of EFD result in the region of mid-ship.

For the simulation of ship model free to sinkage and trim, the computed results of resistance, sinkage and trim agree quite well with the experimental data in the cases of medium and high speed. While in the case of low speed (Fr=0.138), the relative differences between the results of residual resistance, sinkage and trim of CFD simulation and model test are more obvious. This is because of the values of them are quite small in this case and rather difficult to predict accurately.

In general, rather good agreement has been observed between the computed results and experimental data. It is recommended that in the prediction of resistance for surface ship with medium and high speed by CFD simulation, the ship/model should be free to sinkage and trim (or the sinkage and trim should be taken into consideration).

REFERENCES

Olivieri, A., Pistani. F., Avanaini, A., Stern, F., and Penna, R. (2001), "Towing Tank Experiments of Resistance, Sinkage and Trim, Boundary Layer, Wake, and Free Surface Flow Around a Naval Combatant INSEAN 2340 Model," Iowa Institute of Hydraulic Research, The University of Iowa, IIHR Report No. 421, 56 pp.

Yang, L. (2008), "Resistances, Sinkage and Trim, Wave Elevations Tests Report for the ITTC Benchmark Model DTMB5415", China Ship Scientific Research Center, CSSRC Report No. 08206 (in Chinese), 76pp.

Yang, L. (2008), "Resistances, Sinkage and Trim Uncertainty Analysis for the ITTC Benchmark Model DTMB5415", China Ship Scientific Research Center, CSSRC Report No. 08587 (in Chinese), 50pp.

Hino, T., "Proceedings of CFD Workshop Tokyo 2005" , NMRI report 2005

NUMERICAL SIMULATION OF THE INTERACTION BETWEEN SHIP HULL AND ROTATING PROPELLER

Tomasz Bugalski and Paweł Hoffmann
(Ship Design and Research Centre S.A., Poland)

1. SUMMARY

One of the current research projects of Ship Design and Research Centre S.A. (CTO) is focused on investigation of flow around ship hull and rotating propeller. The goal of the project is to test and demonstrate the capabilities of Reynolds-averaged Navier –Stokes equations (RANSE) solver in connection with complex ship flows. Focus is on a complete numerical model for hull, propeller and rudder, which can account for the mutual interaction between the components when the flow field is computed. In the present work the real propeller geometry is modeled.

The computations required to use "sliding grid" method – a mesh divided into two regions connected with an interface surface. The first region was a cylinder built around the propeller. The second one contained the rest of computational domain. The mesh around the propeller rotates relative to a fixed mesh connected with the hull. In order to check the performance of the numerical model, the calculated results are compared with experimental data.

The paper presents the results of preliminary investigation of the flow computations around ITTC KRISO Container Ship (KCS).

Meshing and flow simulations are conducted with StarCCM+ from CD-adapco.

2. INTRODUCTION

Hydrodynamic aspects play a significant role in the quality of a ship. Dominant criteria in the hull form design are often the resistance and powering performance; in addition, the occurrence of noise and vibrations, important for the comfort level of crew and passengers, often has a hydrodynamic cause, stemming from the operation of the propeller in the flow field behind the ship hull. Therefore, the detailed knowledge of the flow around the aft-part of a ship is critical: In this area, flow separation may occur, with important consequences for the resistance and power; and the flow field felt by the propeller should be determined. Unfavorable characteristics of this flow field (e.g. large spatial variations of the velocity) may result in performance loss, propeller cavitation leading to noise, vibrations and erosion, etc. The viscous flow computed using RANSE solvers becomes a common component in the ship design process, and satisfactory agreement with model-scale wake field measurements can be achieved today.

The real purpose is to predict the hull/propeller interaction, wake field and finally full-scale flow about ship hull. RANSE computations offer that possibility, and such viscous-flow computations become progressively used in the practical ship design; but how accurate these predictions are, and to what extent they depend on the turbulence modeling used, is not really known. A validation of the full-scale ship viscous flow predictions has been generally insufficient so far, mainly due to the virtual absence or difficult availability of the suitable full-scale experimental wake field data.

For thirty years the CFD methods are used in Poland for studies on the nature of propeller-hull interaction. The methods developed during this time can be found in Bugalski & Jaworski (1984), Bugalski (1997), Bugalski & Szantyr (1998). These studies change their character in view of the dynamic development of the CFD methods, but the original approach to the interaction phenomena still remains essential.

The results of preliminary numerical simulation of the flow around ship and rotating propeller are presented below. The computations were carried out in model scale, to enable direct comparison of the CFD results with the experimental results.

3. MODEL GEOMETRY AND SIMULATION CONDIDTIONS

The KCS was conceived around 1997 to provide data for both explication of flow physics and CFD validation for a modern container ship with a bulbous bow. The Korea Research Institute for Ships and Ocean Engineering (now MOERI) performed towing tank experiments to obtain resistance, mean flow data and free surface waves (Van et al,

1998, Kim et al., 2001). Self propulsion tests were carried out at the Ship Research Institute (now NMRI) in Tokyo and are reported in the Proceedings of the CFD Workshop Tokyo in 2005 (Hino, 2005). Data for pitch, heave, and added resistance are also already available from Force/DMI measurements reported in Simonsen et al. (2008). No full scale ship exists.

Table 1 Main particulars of KCS and KP505 propeller

Ship	KCS
Length b.p. [m]	230,00
Length of waterline [m]	232,50
Breadth [m]	32.20
Draught [m]	10,80
Displacement [m3]	52030
Wetted surface area [m2]	9424
Block coefficient	0,651
Midship section coeff.	0,985
Service speed [kn]	24,0
Propeller	KP505
Direction of rotation	right
Diameter [m]	7,90
Number of blades	5
Expanded area ratio	0,7963
Pitch ratio	1,1740
Blade rake /Skew back [deg]	0/16,8
Profile	NACA66/0.8

Table 2 Scale factor and speed in model scale

Scale factor	31.60
Model speed V_m [m/s]	2.196
Froude number F_N	0.260
Model Reynolds number R_N	$1.4 \cdot 10^7$

As mentioned above, the computations were carried out at model scale. The scale factor was the same as for the model used for towing tank experiments. The scaled value of speed and dimensionless numbers are listed in Table 2.

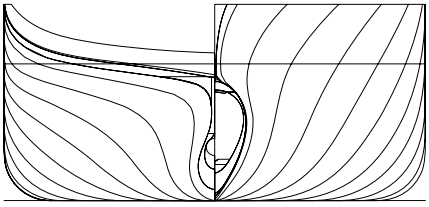

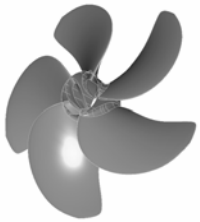

Fig.1 Geometry of the KCS hull and KP505 propeller.

4. NUMERICAL SIMULATION METHOD OF HULL –PROPELLER INTERACTION

The computations are performed with the Reynolds Averaged Navier-Stokes (RANSE) solver StarCCM+ from CD-adapco. The code solves the RANSE and continuity equations in integral form on a polyhedral mesh by means of the finite volume technique. Both steady state and transient calculations are considered. The Reynolds stress problem is solved by means of k-ε turbulence model. The rotating propeller is treated in the following different ways. For open-water calculations the propeller inflow is uniform, so the moving reference approach is applied. For the propeller rotating behind a ship, a rigid body approach is applied. The free surface is modeled with the two phase volume of fluid technique (VOF).

The RANSE method is based on the fundamental conservation equations however they are solved for the values averaged in a time range longer then the period of velocity and pressure fluctuations due to turbulence. Accurate numerical flow modeling requires excessive computational effort due to requirement of very dense discretization of computational domain and use of very short time step. It is assumed that the influence of turbulence on the flow is derived with sufficient accuracy based on the averaged flow parameters. Therefore there are introduced the additional, partly empirical, relationships between factors characterizing the turbulence – so called Reynolds stress, and averaged flow parameters. They are referred to as so called turbulence models. Because turbulence modeling is by design a kind of simplification and universal relations for proper turbulence modeling of all flow types have not been formulated yet, different turbulence models are applied, depending on a requested accuracy and a flow type. In case of present computations, "k-epsilon" model is applied; it is a standard model of high stability and accuracy level, sufficient for most of engineering works. There are many variants of this model; "realizable k-epsilon" is used here.

Equations of the fluid motion are solved numerically using the finite volume method. This method can be described in brief as follows.

The flow domain is divided into small cells called finite volumes. The fluid motion equations are integrated numerically for each finite volume having the values of flow parameters attributed to its centre. Equations of the

fluid motion integrated for all the finite volumes compose a system of algebraic equations which is solved iteratively. The transformation of analytical equations into algebraic equations for a finite number of points in the space is called their discretization. The aim of the discretization is to set up the equations in such way that unknowns are values in central points of cells, therefore it is required to express the values on the cells' faces as a function of their central points.

There are many ways for calculation of values on faces based on the cell's central point values. In the current instance the so called Second-Order Upwind scheme is used.

The following jobs were conducted within the reported research project:

- development of discretization method for "hull – propeller" system,
- development of propeller hydrodynamic characteristics computations using „moving reference frame",
- comparative computations of open water propeller (equivalent for open water propeller test) and flow around ship hull without propeller (equivalent to resistance test),
- computation of the flow around ship with working propeller (equivalent to propulsion test).

The basic assumptions for the simulation were as follows: the dynamic trim and sinkage of the hulls were neglected, propeller operation was modeled.

The unstructured computational mesh of hexahedral and polyhedral cells was used for the computations. The total number of grid elements used in the calculation was approximately 2, million. The visualizations of mesh details are presented in figures 2 and 3.

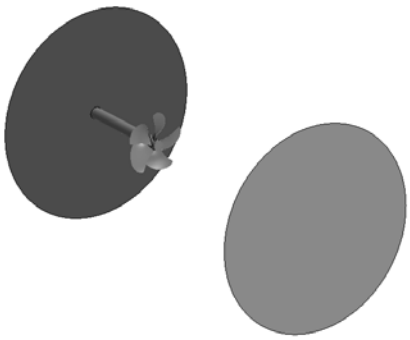

Fig.2 Computational domain in open water propeller test.

Computational domain consists of two parts – the cylindrical volume in which there is a propeller (Fig. 3) with a separate sub-domain for propeller calculations (semi-transparent outer wall) and the rest of the volume - separated by the intermediate surface (interface) that is providing a connection between boundaries during the simulation. A larger volume is divided into a grid of hexahedral cells, which size and number are adjusted according to the complexity of the flow in the area. The area near the propeller is of particular interest, therefore the mesh has been refined there. A smaller cylindrical region connected to propeller is generated as a grid of polyhedral cells which is more suitable for mapping the shape of a rotating propeller.

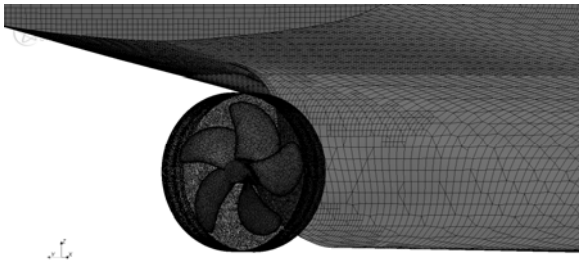

Fig.3 Mesh in the aft part of the ship hull with propeller

The solver settings for the simulation were as follows: turbulence model: k –epsilon, time step: 0.001 s; number of iterations per time step: 4.

5. RESULTS OF NUMERICAL SIMULATION OF SELF –PROPULSION TEST

The numerical simulation of self –propulsion test was developed in three steps: simulation of the open water propeller test, computations of flow around ship hull without propeller (equivalent to resistance test) and computation of the flow around ship with working propeller (equivalent to propulsion test).

The open water calculation was carried out at the same running conditions as used in the experimental set up at KRISO. The solution domain was chosen to extend 10 propeller diameters in front of the propeller, 3 diameters in the radial direction and 5 diameters behind the propeller. The flow solver was run in steady mode and the rotation of the propeller was accounted for by using the moving reference frame approach. This approach works fine in open water, where the propeller experiences a completely uniform inflow field. The calculations were carried out for advance coefficients in the range from J=0.0 to J=1.0. Similar to the experiment the computed thrust and torque on the propeller were converted into the dimensionless thrust coefficient, torque coefficient and the efficiency was calculated.

The study of the flow field shows that the propeller accelerates the flow over the blades and introduces swirl in the flow downstream of the propeller, as expected. The pressure field on the blades shows low pressure on the suction side and high pressure on the pressure side.

The comparison between the calculated and measured data for P505 –KCS propeller, shown in the Fig. 4 proves that fairly good agreement is achieved. Particularly in the region around J=0.6-0.8, which corresponds to the usual propeller operation.

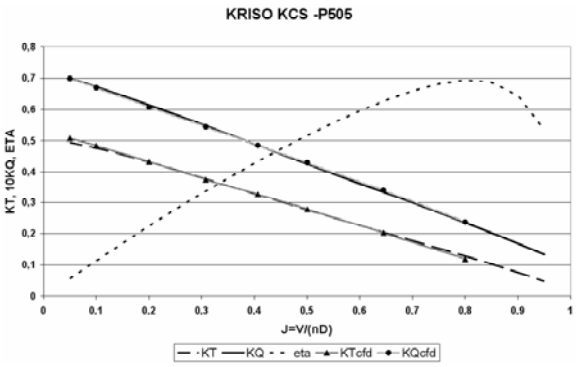

Fig.4 Comparison of open water hydrodynamic characteristics of KP505 propeller computed and obtained from experiment.

The results of study of grid size and turbulence model influence on ship hull without propeller resistance are presented in Table 3.

Table 3 Influence of grid size & turbulence models on KCS ship model resistance

Grid type	Turbulence model	Resistance [N]
Rough (950k)	k-ω	41,0
	k-ε	41,8
	RSM	42,0
Medium (1,7M)	k-ε	41,8
Fine (2,6M)	k-ε	41,8

The goal of the present project is to simulate numerically the flow about ship hull and propeller including the free surface around the ship. The calculations have been performed for the ship without rudder in fixed conditions FX_0 (suppressing dynamic sinkage and trim).

The self propulsion computation has been carried out at the ship point following the experimental procedure. Thus, the rate of revolutions of the propeller *n* has been adjusted to obtain force equilibrium in the longitudinal direction considering the applied towing force (Skin Friction Correction, SFC), i.e.

$$T = R_{T(SP)} - SFC$$

where T is the computed thrust, $R_{T(SP)}$ is the total resistance at self propulsion and SFC = 30.3 N (from the tests). The simulation with the propeller behind the ship must be run in transient mode, i.e. time accurate.

The computational results for the ship hull and rotating propeller are listed in Table 4.

Table 4 V&V study for FX0, KCS self propulsion prediction, Re = 1.4×107, Fr = 0.26.

Parameters		EFD(D)	V&V Study
C_T*10^3	Value	**3,966**	**3,804**
	E%D		4,08%
C_F*10^3	Value		2,676
	E%D		
C_P*10^3	Value		1,128
	E%D		
K_T	Value	**0,1700**	**0,1502**
	E%D		11,65%
K_Q	Value	**0,0288**	**0,0283**
	E%D		1,77%
n (rps) (for given SFC)	Value	**9,50**	**9,80**
	E%D		-3,16%
(RT(SP)-T) [N] (for given n)	Value	**30,25**	**30,20**
	E%D		0,17%

The axial velocity contours and cross flow vectors downstream of propeller plane (x/LPP=0.9911) are compared with the experimental data (Hino 2005), as shown in Fig. 5 and 6.

The comparison of the transverse distribution of all three velocity components downstream of plane of propeller is presented in Fig.7.

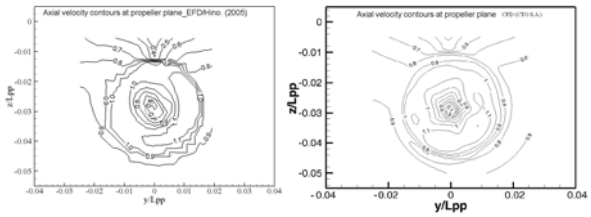

Fig.5 Comparison of axial velocity contours downstream of propeller plane (x/LPP=0.9911) EFD –left figure, CFD –right figure

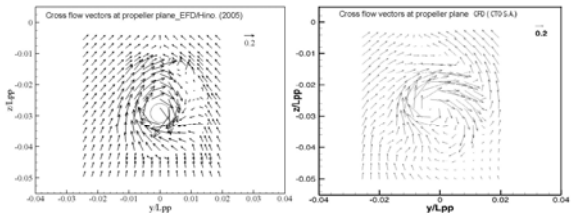

Fig.6 Comparison of cross flow vectors downstream of propeller plane (x/LPP=0.9911) EFD –left figure, CFD –right figure

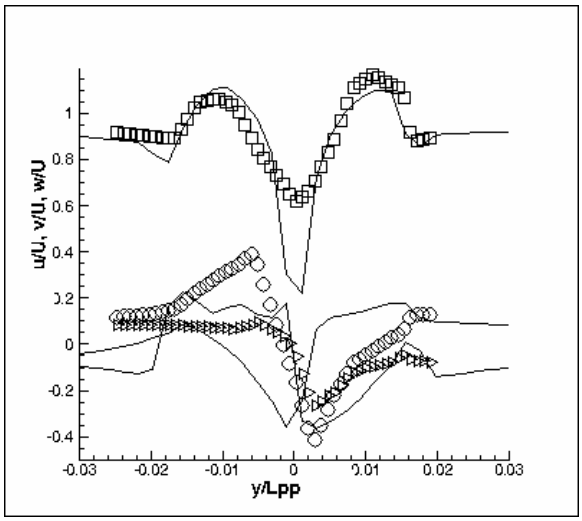

Fig.7 Velocity downstream of propeller plane (x/LPP=0.9911) at z/LPP=-0.03

The pressure distribution on the hull surface is presented in Fig.8.

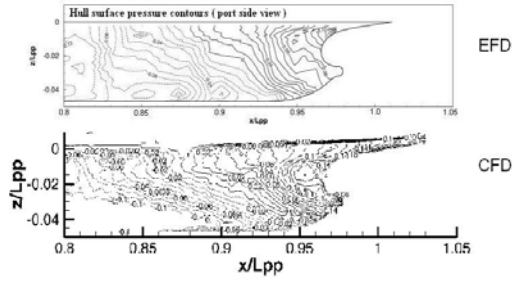

Fig.8 Hull surface pressure contours (port side view)

As it can be seen the wake of the ship strongly influences the propeller, but the propeller also influences the ship flow. The influence is most clearly seen in the pressure field. Upstream of the propeller the hull experiences suction, which reduces the pressure and increases the resistance. The effect is usually expressed as the thrust deduction. Another region of the hull that feels the presence of the propeller is the region above the propeller. In this region the passing blades will introduce pressure pulses on the hull, which in critical case may lead to noise and the ship structure vibration.

6. CONCLUSION

The planned results of research including: development of discretization method for rotating propeller using STAR-CCM+ solver, development of computation method for hull – propeller system and obtaining reliable results of the calculation of flow around a rotating propeller and viscous flow around a model ship with working propeller have been achieved.

Computations of flow around the ship hull with rotating propeller simulating propulsion tests have an unsteady character and therefore need more time to obtain convergent result. Calculations using sliding grids as in hull –propeller system are characterized by lower stability compared to simple flow computations, hence using lower relaxation factors and higher number of iterations per time step is necessary. As a result the calculation time increases significantly and the convergent result is more costly to obtain. At the same time the opportunity arises to analyze the phenomena occurring temporarily in the time domain. For the method to be practically useful the accuracy of the calculated suction coefficient should be close to accuracy of the resistance determination. At the present stage of development the method is sufficiently accurate in prediction of the ship hull resistance and of the propeller open water characteristics. However, the interaction phenomena are not predicted accurately enough. Further development work is planned in this area, involving modification of the grid structure, increasing grid density and application of other turbulence models.

ACKNOWLEDGMENT

This research was supported by the Polish National Centre for Research and Development (NCBiR), grant No. N R10 0039 06/2009) and Ministry of Sciences and Higher Education (MNiSW), grant No. A3:800-14/2009.

REFERENCES

Bugalski T., Jaworski S., (1984), "Computer analysis of the interaction between the propeller and an axisymmetrical body", XIII Seminar on Ship Hydrodynamics, Varna, Bulgaria.

Bugalski T., (1997), "Modern Methods for Investigation of Hull -Propeller Interaction Phenomena using CFD", NAV&HSMV International Conference , Sorrento, Italy, pp. 2.3-2.8.

Bugalski T., Kraskowski M., (2006), "Validation of the RANSE wake computations for the training ship Nawigator XXI and the dredger Uilenspiegel", Proceedings of 9th Numerical Towing Tank Symposium (NuTTS), Le Croisic, France, pp.4.1-4.6.

Bugalski T., Szantyr J., (1998), 'Application of CFD for Analysis of the Ship and Propeller Flow'. TASK Quarterly 2/98 Scientific Bulletin of the Academic Computer Centre, Gdansk, Poland.

Chao K., (2005), "Numeric Propulsion Simulation for the KCS Container Ship", Proceedings of CFD Workshop Tokyo, Tokyo, Japan, pp.539-545.

Hino, T., (2005 ed.), "Proceedings of CFD Workshop Tokyo 2005", NMRI report 2005, Tokyo, Japan.

Kim W.J., Van D.H., Kim D.H., (2001). „Measurement of

flows around modern commercial ship models", Exp. In Fluids, Vol.31, pp. 567-578.

Simonsen C.D., Carstens R., (2008), "RANS Simulation of the Flow around a Ship Appended with Rudder, Ice Fins and Rotating Propeller", Proceedings of 11th Numerical Towing Tank Symposium (NuTTS), Brest, France.

Van, S.H., Kim, W.J., Yim, G.T., Kim, D.H., and Lee, C.J., (1998b), "Experimental Investigation of the Flow Characteristics Around Practical Hull Forms", Proceedings 3rd Osaka Colloquium on Advanced CFD Applications to Ship Flow and Hull Form Design, Osaka, Japan

VERIFICATION AND VALIDATION FOR UNSTEADY COMPUTATION

G.B. Deng, A. Leroyer, E. Guilmineau, P. Queutey, M. Visonneau and J. Wackers
E.M.N, L.M.F.-UMR6598, Ecole Centrale de Nantes
1, Rue de la Noe, Nantes, France

SUMMARY

This paper is devoted to the verification and validation exercises with the ISIS-CFD code conducted for the Gothenburg 2010 Workshop. We mainly focus on unsteady computation, namely seakeeping test case 1.4a, 1.4b and roll decay test case 3.6. A simpler wave pattern test case 1.1b has also been performed for the validation of the newly implemented automatic grid refinement approach.

1. INTRODUCTION

With recent progress made in software development, CFD can be considered a mature tool for steady state ship hydrodynamic applications such as resistance and wake flow computations. Accurate enough predictions can be obtained with reasonable resources even for fully appended hulls, both for model and for full scale. However, for unsteady computations, due to still limited computer resources, the reliability of CFD computations remains to be proven. Our contribution to the Gothenburg 2010 Workshop focuses mainly on the verification and validation of unsteady flow computation. Sea keeping test cases 1.4a, 1.4b and roll decay test case 3.6 have been performed. Wave pattern test case 1.1b is also selected as a validation exercise of a newly implemented adaptive grid refinement approach.

2. NUMERICAL APPROACH

Computation has been performed with the ISIS-CFD flow solver developed by EMN (Equipe Modélisation Numérique, i.e. CFD Department of the Fluid Mechanics Laboratory). Turbulent flow is simulated by solving the incompressible Reynolds-averaged Navier-Stokes equations (RANS). The flow solver is based on finite volume method to build the spatial discretization of the transport equations. The velocity field is obtained from the momentum conservation equations and the pressure field is extracted from the mass conservation constraint, or continuity equation, transformed into a pressure-equation. In the case of turbulent flows, additional transport equations for modeled variables are discretized and solved using the same principles. The gradients are computed with an approach based on Gauss's theorem. Non-orthogonal correction is applied to ensure a formal first order accuracy. Second-order accurate results can be obtained on a nearly symmetric stencil. Inviscid fluxes are computed with a piecewise linear reconstruction associated with an upwinding stabilizing procedure which ensures a second order formal accuracy for smooth flow. Viscous fluxes are computed with a central difference scheme which guarantees a first order formal accuracy. We have to rely on mesh quality to obtain a second order discretization for the viscous terms. Free-surface flow is simulated with a multi-phase flow approach. Incompressible and non-miscible flow phases are modeled through the use of conservation equations for each volume fraction of phase/fluid. An implicit scheme is applied for the time discretization. A second order three-level time scheme is employed for time-accurate unsteady computation. Velocity-pressure coupling is handled with a SIMPLE like approach. Ship free motion can be simulated with a 6 DOF module; some degrees of freedom can be fixed as well. An analytical weighting mesh deformation approach is employed when free-body motion is simulated. Several turbulence models ranging from one-equation model to Reynolds stress transport model are implemented in ISIS-CFD. Most of the classical linear eddy-viscosity based closures like the Spalart-Allmaras one-equation model, the two-equation k-w SST model by Menter, for instance are implemented. Two more sophisticated turbulence closures are also implemented in the ISIS-CFD solver, an explicit algebraic stress model (EASM) and a Reynolds stress transport model. The EASM model is employed in the present study for the sea keeping cases, the k-w SST model is used in the roll

decay study. A wall function is implemented for two-equation turbulence models.

3. TEST CASES

3.1 Sea keeping test case 1.4a

The test case condition is given on the web site of the Workshop and will not be repeated here. The depth of the original KVLCC2 model with a scale factor of 100 is 0.3m. With a draft T=0.208m, green water on deck is observed in the measurement for the case with long wave length. To avoid such undesirable effect, the deck of the ship model is extended to 0.35m in the measurements performed by INSEAN. The same modification of the ship geometry is applied in numerical simulation. However, no information is given concerning the center of gravity and the inertial matrix of the modified hull. We keep the parameters of the original hull for our computation. Since the sway, yaw and roll motion is fixed, only half the boat is simulated by using a mirror plane. The computational domain is extended to about 1Lpp before the ship where a wave boundary condition is applied. Up and down boundaries are located at about 0.5LPP and 1.5 LPP respectively where a pressure boundary condition is applied. The side boundary is also treated as a mirror plane and is located at about 1.8Lpp. The downstream boundary is located at about the same distance after the boat where a classical exit boundary condition is applied. An unstructured hexahedral mesh is generated with the commercial software Hexpress. Three different meshes are generated for each case to assess the spatial discretization error. Based on the parameter used for mesh generation, the refinement ratio from the coarse grid to the medium grid and from the coarse grid to the fine grid are about 1.33 and 1.67 respectively. The grid is refined in the longitudinal direction near the free surface such that there is about 60 nodes per wave length and 10 nodes in wave height on the coarse grid. Based on our experiences, with such a spatial resolution, incident waves can be captured with sufficient accuracy.

Computations have been first performed for calm water to evaluate the spatial discretization error. Table 1 gives the predicted resistance in Newton obtained on three different grids. The number of cells for each grid is also given in the table. The last line gives the extrapolated value and the observed order of convergence based on the grid refinement ratio mentioned above. Based on the extrapolated value, numerical uncertainty is about 1%, 2% and 3% respectively for the fine grid, the medium grid and the coarse grid without taking into account any safety factor. This is a typical range of uncertainty levels for resistance prediction using the ISIS-CFD code with a recommended setup. The medium grid is the grid density commonly used for routine applications. The predicted resistance coefficient Ct=0.00463 is 10% lower than the available measurement data Ct=0.00514 possibly obtained by INSEAN. But the deduced form factor 1+k=1.199 is in very good agreement with the form factor 1+k=1.191 deduced from the measurement data obtained at the same Froude number, but higher Re=4.6e6, by MOERI.

Table 1. Resistance prediction in calm water

Grid	Nb. of cells	Resistance (N)
Coarse	437283	4,0749
Medium	823193	4,0199
Fine	1395610	3,9943
Extrapolated	-	3,9478/2.0

Uncertainty estimation for resistance in waves prediction is much more difficult. In addition to the usual time and spatial discretization error of the Navier-Stokes equation, additional sources of error exist such as the time discretization error for the resolution of the free body motion, additional errors induced by the treatment of deforming grids, sampling uncertainty, etc. We first examine the time discretization error by performing a computation with the same grid using different time steps. Data sampling is performed over the same time interval to reduce sampling uncertainty. Figures 1 and 2 display the relative error for 0^{th} and first harmonic amplitudes for the case with wave length 1.1Lpp. Assumed second order time accuracy is used for the uncertainty estimation. It can be seen that for a given time step, the numerical error increases as we refine the grid. To reduce the error to an acceptable level (<4%), at least 250 time steps per period are needed. The result for the case with wave length 1.6Lpp is similar. Both cases are characterized by a relatively large-amplitude ship motion. For the case with wave length 0.6Lpp, the ship motion amplitude becomes very small. For more than 100 time steps per period, the numerical solution becomes almost time-step independent.

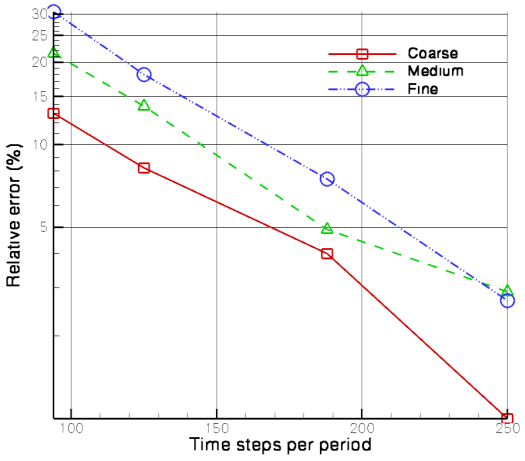

Fig.1 Relative error for the 0th harmonic amplitude for the case with wave length=1.1Lpp

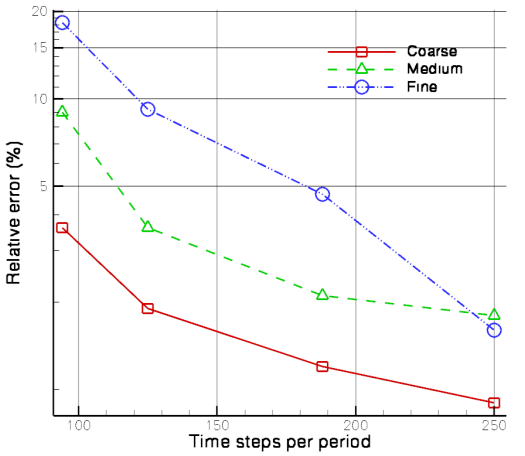

Fig.2 Relative error for the 1st harmonic amplitude for the case with wave length=1.1Lpp

For each case, we attempt to assess the spatial discretization error by using the finest time step solution obtained with three different grids. Such attempt is not so successful. A poor convergence behavior is observed, which makes uncertainty estimation difficult. Such result is due to the fact that time discretization error (about 2-4%) is more important than spatial discretization error (about 1%). Nevertheless, data difference between the medium and the fine grid is smaller than 4% almost for all cases. We believe that the numerical uncertainty of our computation is smaller than 5%. Detailed results for this verification exercise can be found in Deng et al. [2010].

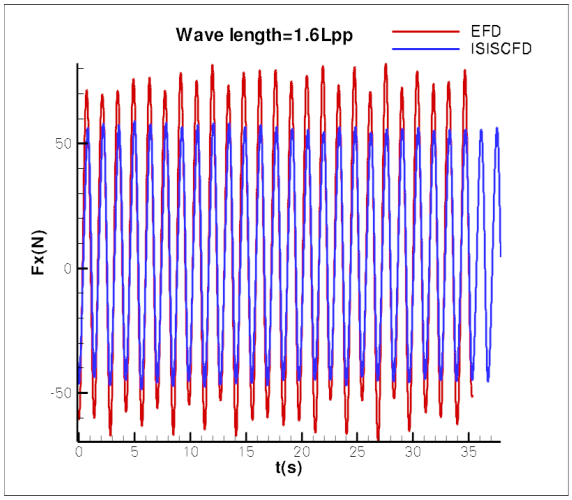

Fig.3 Time evolution of resistance for the case with wave length 1.6Lpp

A comparison of the time evolution of the resistance with measurement data is shown in figures 3 and 4. The 1st harmonic amplitude is clearly under-estimated. The difference (28% for the case with 1.6Lpp and 48% for the case with 1.1Lpp) is much higher than the numerical uncertainty. Moreover, for the case with wave length 1.1Lpp, bow wave breaking is observed in the computation resulting in a non-linear response, while in the measurement, a nearly linear response is observed. It is quite unexpected that for this case, even with so much difference in the time evolution behavior, the mean value of the resistance agrees well between the computation and the measurement data obtained by INSEAN and by OSAKA University.

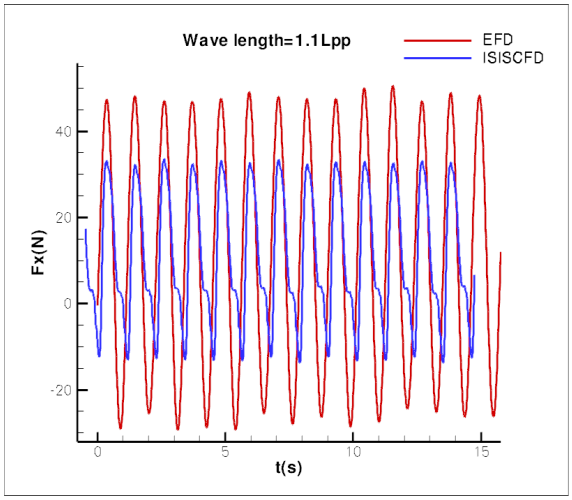

Fig.4 Time evolution of resistance for the case with wave length 1.1Lpp.

3.2 Sea keeping test case 1.4b

Due to the higher waves, the depth of the ship model is extended to 0.7m in agreement with the

measurement. Since the geometry is the same as the previous test case, the grid independence study was not performed. A fine grid with a similar grid density as the fine grid of the test case 1.4a is employed. With this grid, the predicted calm water resistance coefficient Ct=0.00407 at Froude number 0.142 is more than 10% lower than the measurement data obtained by NTNU (Ct=0.004556). But it is in good agreement with the measurement result obtained by MOERI (Ct=0.004056) at the same Froude number and Reynolds number, but with rudder included. At the higher Froude number Fr=0.182, numerical prediction gives Ct=0.004208, while measurement data obtained by NTNU gives Ct=0.004623. For both cases, the numerical prediction is outside the uncertainty range when compared with experimental result obtained by NTNU. For each case, care has been taken to ensure that the time discretization error is small enough (lower than a few percents), both for the 0^{th} harmonic amplitude and for the first harmonic amplitude. Numerical uncertainty is expected to be of the same order as the previous test case. Special attention needs to be paid to test case C1 with zero advancing speed. The time evolution of the resistance shown in figure 5 indicates that the transitional period is quite long. Data sampling is started at about t=100s. Except the case with zero advancing speed, the predicted 0^{th} harmonic amplitude agrees with measurement data within the uncertainty range.

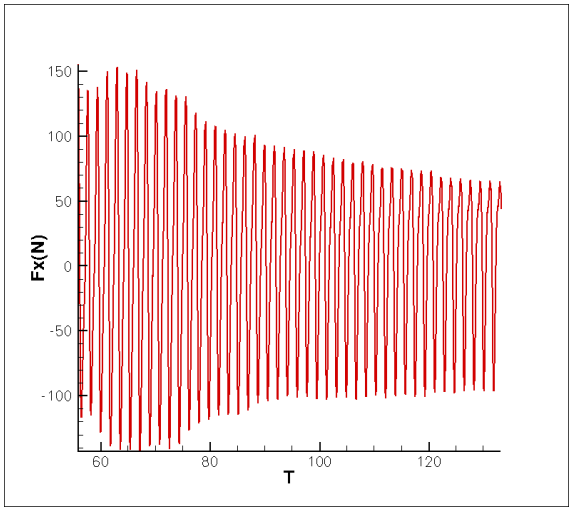

Fig.5 Time evolution of resistance for test case 1.4b-C1.

3.3 Wave pattern test case 1.1b

This test case is selected to validate the newly implemented adaptive grid refinement procedure. Details of the grid refinement approach can be found in Wackers et al. [2010]. Resistance prediction for such low Froude number is not difficult. However, accurate prediction of the free-surface elevation is a challenging task for a CFD computation due to the very small amplitude of the Kelvin wave. The free surface varies from -0.004Lpp to 0.01Lpp. The characteristic height of the Kelvin wave is only about 0.0008Lpp. If we consider that at least 5 grid nodes are necessary to capture the wave in the Z-direction, a systematic grid refinement to cover the entire free-surface elevation region would require more than 80 grid nodes in the normal direction, which will require excessive computer resources, even without taking into account the refinement in the X-Y plane, which is also necessary.

The unstructured hexahedral mesh generator Hexpress is used to generate the mesh. The initial mesh size normal to the free surface is about 0.0014Lpp, which is almost two times higher than the Kelvin wave height. We expect to use 3 levels of grid refinement to capture correctly the Kelvin wave. The wave length of the Kelvin wave is about 0.1Lpp. If the mesh is not pre-refined in the X-Y plane, the initial mesh size in X and Y direction is about 0.016Lpp, namely, with only about 6 nodes per wavelength. Such initial grid resolution is not enough. Moreover, there is a grid refinement interface in the region where the Kelvin wave is expected, which will affect the accuracy of the numerical prediction. To achieve better numerical accuracy, the initial mesh is pre-refined in the region where the Kelvin wave is expected. The mesh size in the X-Y plane near the target region is about 0.008Lpp, namely about 12 nodes per wave length.

A first computation has been done without grid refinement (noted as refinement 0 here after). 4 other computations with different target mesh size have been performed. In the first computation, noted as refinement 1 here after, the target mesh size is the same as the initial mesh size (0.0014Lpp). With such a setup, the mesh will not be refined unless the free-surface is located outside the region where the mesh is initially refined. In the subsequent computations (refinement 2, 3 and 4), the target mesh size is divided by 2 each time. The initial mesh contains about 1.79M cells. With grid refinement, the number of cell increases to 1.80M, 1.95M, 2.71M and 5.47M for refinement 1-4, respectively. Comparison of wave cuts at y=0.2993Lpp (figure 6) reveals that a grid-independent solution is obtained with refinement 3 with about 2.71M nodes where the target cell size near free surface is divided by 4, resulting in a mesh with only about 3 cells per wave height. As expected, the predicted resistance is almost the same whatever the refinement. The predicted resistance coefficient Ct=0.00406 is in good agreement with the measurement data.

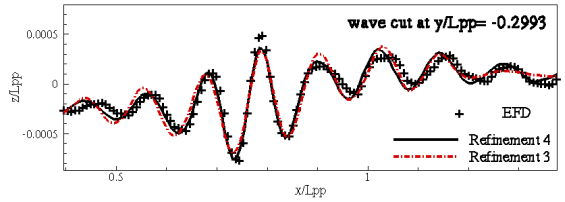

Fig.6 Wave cuts at y=0.2993Lpp

3.4 Roll decay test case 3.6

For this test, the DTMB 5512 geometry with bilge keels fitted is used. The rolling motion is taken into account with weighted mesh deformation; the particularity of rolling motion is that the mesh at a distance from the ship moves much more than the mesh close to the ship (figure 6). To keep a sufficiently fine grid at the water surface for all roll angles, a bow-tie shaped zone of fine cells in Z-direction is created around the ship. Strong refinement is also applied round the bilge keels, and especially at their tips. No formal grid convergence study is done for this case; instead, two grids have been generated. Both grids have the same mesh spacing in Z-direction at the water surface: 0.001Lpp. On the fine grid, the cell sizes on the hull are halved with respect to the coarse grid. However, cell size diffusion is less on the fine grid so it is not two times finer everywhere. The grids have 4885774 and 9036329 cells respectively. All results presented to the Workshop are computed on the coarse grid.

The main difficulty in this simulation comes from the movement of the grid at the water surface. As the surface itself is hardly moving, grid motion due to rolling causes the surface to move through the grid. This causes a restriction on the time step. It was found that, when the surface moves more than about 0.5 cell size during one time step, numerical waves are created due to the mesh motion which perturb the computed roll damping and frequency. On the coarse grid, the dependence on the time step is checked during the first two roll periods.

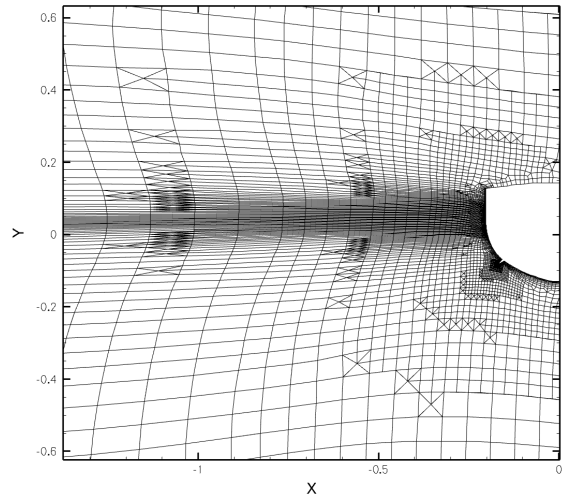

Fig.7 Cut through coarse mesh in maximally rolled position (10 deg), for test case 3.6.

The baseline computation is performed with 327 time steps per roll period. Another computation is performed on the same mesh, with a time step that was chosen 2.5 times smaller. The difference in roll angle after one oscillation is about 0.3%.

Then a computation was performed on the fine grid. While the grid around the water surface has the same size as for the coarse grid, the mesh deformation law had to be adjusted in order to keep a good grid quality in the small cells near the hull. As a consequence, the grid away from the hull has a stronger motion, so the time step had to be reduced. It was set to a value four times smaller than for the baseline coarse grid computation. With this setup, the difference in roll angle between the two solutions, after one period of roll, is about 1.0%. This difference is less than the difference with the experimental values from IIHR, even when taking into account the reasonable assumption that the mesurements should be slightly displaced in time (figure 7).

Finally, the influence of the turbulence model is tested. The baseline computation was performed with the standard k-w SST model. Another computation was done on the coarse grid with the EASM turbulence model. For ship flows, the most important property of this turbulence model is that it causes reduced turbulent viscosity in elongated streamwise vortical structures, thus preserving the strength of bilge vortices. For the case 3.6, the most important vortex generation takes place at the bilge keels. It appears that turbulent damping is of minor

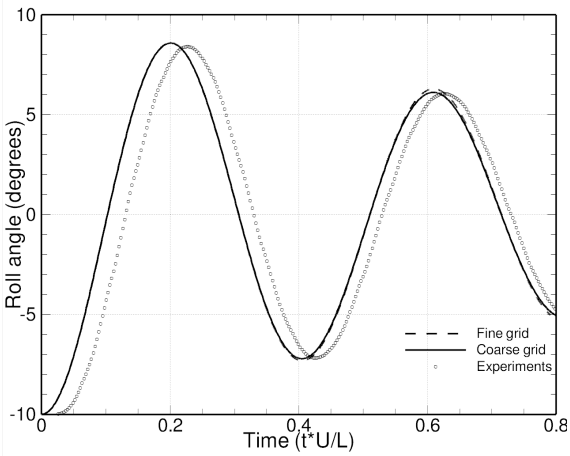

Fig.8 Time evolution of roll angle for test case 3.6.

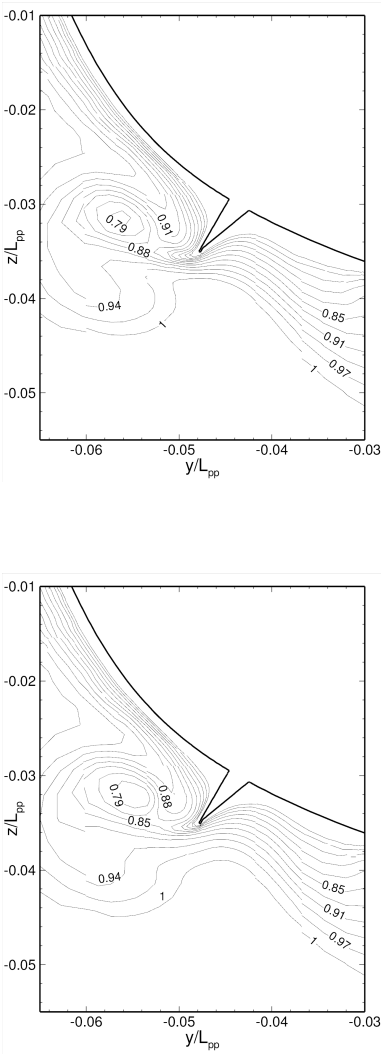

Fig.9 Axial velocity around a bilge keel (X/Lpp=0.675) at t/T=1/4 during the second period of roll, for the test case 3.6. k-w SST turbulence model (top) and EASM model (bottom).

importance for the vortex influence on the keels, as the difference in the solutions for the two turbulence models is very small (figure 8). The difference in roll angles after one period is 0.4%.

Concluding, even though no formal grid convergence test was done, the numerical and modelling uncertainty seems to be acceptable for this case, in the order of a few %.

4. CONCLUSION

Verification and validation for sea keeping computations remains a difficult task. Although the 0th harmonic amplitude is validated for most of the cases, considerable discrepancies are observed for the prediction of the 1st harmonic amplitude. Detailed experimental conditions such as the position of the center of gravity, the location of the towing point, the moment of inertia, a description of the flexible connection system between the carriage and the ship model, etc... should be given so that measurement conditions can be correctly reproduced in numerical computations. Careful verification of experimental work is also required. Calm water resistance result differs by more than 10% between different measurements. Such level of difference is higher than the numerical uncertainty of CFD computations. Hence, validation of CFD computational results with such measurement data is questionable.

REFERENCES

Deng, G.B., Queutey, P. and Visonneau, M., (2010), "RANSE Prediction of the KVLCC2 Tanker in Head Waves", Proceedings 9th International Conference on Hydrodynamic, Shanghai, China

Wackers, J., Ait Said, K., Deng, G.B., Queutey, P. and Visonneau, M., (2010) "Adaptive Grid Refinement Applied to RANS Ship Flow Computation", Proc. 28th ONR Symposium on Naval Hydrodynamics, Pasadena, California, USA

NUMERICAL SIMULATION OF SHIP SEAKEEPING BY THE SWENSE FUNCTIONAL DECOMPOSITION METHOD

L. Gentaz[1], A. Drouet[1&2], P.-E. Guillerm[1], R. Luquet[3], C. Monroy[1], O. Payen[2], G. Reliquet[1&2], B. Alessandrini[1], P. Ferrant[1], E. Jacquin[2]
[1]Ecole Centrale Nantes*, Equipe HGO (Hydrodynamique et Génie Océanique), France
[2]HydrOcean, Nantes, France
[3]DGA Techniques Hydrodynamiques, Val de Reuil, France

ABSTRACT

This paper presents the main principles of the SWENSE (Spectral Wave Explicit Navier-Stokes Equations) approach dedicated to the simulation of wave-body interactions under viscous flow theory. This work has been motivated by the accuracy and efficiency requirements for long time calculations of hulls in regular and irregular waves. Some results are presented for the DTMB 5415 hull in regular waves (one of the cases of the CFD Workshop 2010) and for a ship in irregular waves.

1. INTRODUCTION

The complexity of simulating the behavior of a ship in waves has been historically overcome by separating the problem in simpler uncoupled problems : resistance, propulsion, maneuvering or seakeeping. On a numerical point of view, these problems have been solved through potential flow theory neglecting viscosity, turbulence of flow separation effects, these effects being considered through simplified tools or empirical formulas. Some important problems for ship design or naval engineering have been solved by this way.
During last decades, use of RANS (Reynolds Averaged Navier-Stokes Equations) Equations for simulation of classical ship problems under viscous flow theory has known a great development. Today with improvement of numerical methods or algorithms and development of parallel computing capabilities (now grids of one to ten millions nodes are generally used ; the use of a one billion nodes can be noticed in Fu & al., 2010), CFD (Computational Fluid Dynamics) for viscous flows is more and more used as a practical tool for naval engineering and ship design. Nevertheless it still takes non negligible effort to have a confidence in RANS codes that currently exists with experimental model tests in bassin.
Concerning the problem of the resistance on a ship with rectilinear motion in calm water viscous softwares are now well adapted to achieve computations accuratly and quite quickly (a few hours for a given forward velocity). Due to use of multi block-structured or multiblock grids, block overlapping methods, real and complex geometries with appendages, rudder, shaft, struts (see Bull *et al.*, 2002 among others ...) can now be successfullly treated. Results concerning pressure and viscous drag forces, free surface elevation on or near the hull, pressure and velocity fields near the location of propulsor are in good agreement with experimental data (see Hino, 2005) provided grids are carefully defined and turbulence models are well chosen (two-equations k-ω or k-ω SST models which are the most popular models seem to give good results; Reynolds Stress models can be necessary especially at scale models, see Duvigneau *et al*., 2003). Moreover use of free surface capturing methods (Volume Of Fluid or Level Set algorithms) lead to a good capture of the bow wave breaking and flow at the transom stern for cases at high Frounde number.
Studies concerning propulsion can now be undertaken by using actuator disk models or by using the real geometry of the propeller (see Burg *et al.* 2002 among others ..) connected to Chimera or block-gliding algorithms. It must be noticed that self-propulsion problems are now treated by a numerical way that emphasizes attractivity and capabilities of CFD by viscous flow solvers.
Finally cases of maneuvering with drift in translation or rotation motion can be now successfully treated (Jacquin *et al*., 2006).

Concerning simulation of seakeeping under viscous flow theory some tests have been successfully undertaken especially for codes using free surface capturing methods : for a ship advancing in head waves, one can refer to Weymouth et al. (2005) or Carrica *et al*. (2006).
The usual method to define an incident wavetrain in the computational domain is to impose an incident wave field at the inlet boundary or to simulate the action of a wave paddle.
However such simulations require very large computing resources because grids must be very refined between the location of the structure (at the centre of the computational domain) and the location of the wave generation system to ensure a good propagation of incident waves with no noticeable damping. Moreover if long time simulations are performed successive wave reflections on the body or on the paddle can affect the incoming wavetrain and reduce the useable duration simulation : it is indeed very complicated to damp the diffracted field near outer boundaries without modifying the incident waves (except if active absorption is used for the paddle).

Furthermore, it seems to us that the generation of complex wave systems –irregular or focused waves- will be very problematic with this method, especially for 3D sea states.
To overcome these difficulties an original formulation has been proposed a few years ago using a functional decomposition of dependent variables of the problem in incident and diffracted parts. This approach has been used previously in the frame of the potential flow theory, by Di Mascio *et al*. (1994) or Ferrant (1996) in 3D seakeeping cases. They split unknowns of the problem (potential and free-surface elevation) into the sum of an incident term and a diffracted term. The incident terms (ie incoming waves) are described explicitly using a nonlinear potential flow model. Only the diffracted part is solved implicitly under potential flow theory.

2. THE SWENSE APPROACH

In the SWENSE (Spectral Wave Explicit Navier Stokes Equations) method presented here incident wave terms are calculated with a potential flow model and are then introduced explicitly in a RANSE solver from which equations have been modified (by decomposing each physical variable in a sum of an incident variable and a diffracted one). This solver solves the diffracted field only.
Finally incident and diffracted fields are summed at each time step to obtain the total fields (figure 1).

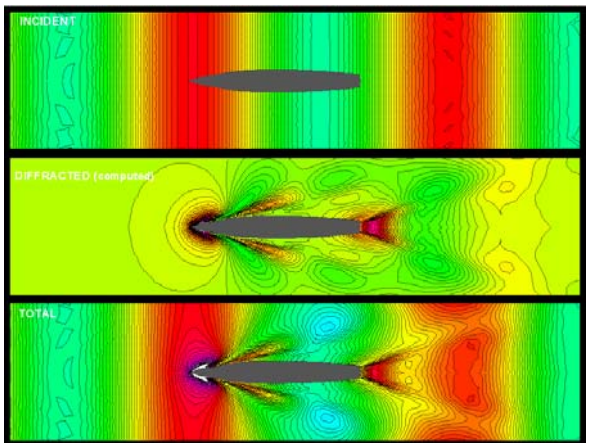

Figure 1: Three steps of the SWENSE approach.

This splitting is theoretically warrantable because nonlinear potential models are very accurate and efficient to model nonlinear waves propagation (if we except wave breaking effects).
According to us, advantages of this method are numerous :
- precision of the incident wavefield is not grid dependant
- only the part of the grid in the vicinity of the ship has to be refined. Far from the body a stretched grid allows an efficient damping of the diffracted flow
- real sea states, irregular or focused waves can easily be considered through HOS (High Order Spectral) models
- the duration time of the simulations becomes practically unlimited because the incident waves and the diffracted field are separated so it is quite simple to damp the diffracted field only at the boundaries of the domain
- CPU time is largely reduced due to less requirements in grid refinement far from the body compared to classical approachs for seakeeping in viscous flow (see Hino, 2005).

The SWENSE decomposition has been implemented in the free surface RANS solver ICARE (Alessandrini & Delhommeau, 1995 & 1999) developed at Ecole Centrale Nantes by the Hydrodynamic group since 1993. Thus cases of ship in regular head waves (Luquet *et al*., 2004 & 2005) have been successfully simulated; more recently, cases of a ship with no speed in irregular 2D waves (Monroy *et al*., 2009) and a cylindrical buoy with a horizontal skirt in irregular 3D waves (Monroy *et al*., 2010) have been computed with a fairly good agreement between computations and experimental data.

3. SWENS EQUATIONS

The original RANS Equations solver ICARE used for the implementation of the SWENSE scheme was initially developed to solve the viscous, turbulent and free surface flow around a ship with a forward speed. It is based on 2nd order finite difference schemes for discretisation of equations, a free surface tracking method and a fully-coupled linear system in velocity, pressure and free surface elevation solved by a bi-CGSTAB algorithm.
Capabilities for use of multiblock grids and parallel computing have been implemented recently.

The classical set of RANS Equations has been rewritten in order to formulate a problem for the nonlinear, viscous diffracted flow. Primitive unknowns (cartesian components of velocity (U^α) with , pressure P (including gravity and turbulent terms) and free-surface elevation h) are decomposed as follows:

$$\begin{cases} U^i = U_I^i + U_D^i \\ P = P_I + P_D \\ h = h_I + h_D \end{cases} \qquad (1)$$

Variables with the subscripts I and D represent incident and diffracted variables respectively.

3.1. Continuity and momentum equations

The previous decomposition is then introduced in the set of initial RANS equations in Cartesian coordinates assuming that the incident wave flow fulfils potential flow equations (perfect fluid flow with no rotational):

$$\frac{\partial U_D^i}{\partial x_i} = 0 \qquad (2)$$

$$\frac{\partial U_D^i}{\partial t} + \left(U_I^j + U_D^j - \frac{\partial \nu_t}{\partial x^j} \right) \frac{\partial U_D^\alpha}{\partial x_j} - (\nu + \nu_t) \frac{\partial^2 U_D^\alpha}{\partial x_j{}^2} + \frac{1}{\rho} \frac{\partial P_D}{\partial x_\alpha}$$
$$= -U_D^j \frac{\partial U_I^\alpha}{\partial x_j} + (\nu + \nu_t) \frac{\partial^2 U_I^\alpha}{\partial x_j{}^2} + \frac{\partial \nu_t}{\partial x^j} \frac{\partial}{\partial x_\alpha} \left(U_I^j + U_D^j \right) \qquad (3)$$

Then these equations are written through partial transformation from Cartesian space (x^1, x^2, x^3) to curvilinear space (ξ^1, ξ^2, ξ^3) fitted to the hull and the free surface at each time. We obtain finally:

$$a_i^k \frac{\partial U^i}{\partial \varepsilon_k} = 0 \qquad (4)$$

$$\frac{\partial U_D^\alpha}{\partial t} + \left(a_i^j \left(U_I^j + U_D^j - v_g{}^i \right) - f^j - a_k^i \frac{\partial \nu_t}{\partial \varepsilon_i} a_k^j \right) \frac{\partial U_D^\alpha}{\partial \varepsilon_j}$$
$$- g^{kk} \frac{\partial^2 U_D^\alpha}{\partial \varepsilon_k{}^2} + a_\alpha^k \frac{1}{\rho} \frac{\partial P_D}{\partial \varepsilon_k}$$
$$= g^{jk} \left. \frac{\partial^2 U_D^\alpha}{\partial \varepsilon_j \varepsilon_k} \right|_{k \neq l} + a_k^i \frac{\partial \nu_t}{\partial \varepsilon_i} a_\alpha^j \frac{\partial}{\partial \varepsilon_j} \left(U_I^k + U_D^k \right)$$
$$+ \left(g^{jk} \frac{\partial^2 U_I^\alpha}{\partial \varepsilon_j \varepsilon_k} + f^j \frac{\partial U_I^\alpha}{\partial \varepsilon_j} \right) - a_j^k \left(U_D^j - a_j^i \frac{\partial \nu_t}{\partial \varepsilon^i} \right) \frac{\partial U_I^\alpha}{\partial \varepsilon_k} \qquad (5)$$

where $\left(a_{ij}\right)$ and $\left(a_i^j\right)$ are the covariant and contravariant coefficients respectively,

$g^{ij} = a_k^i a_k^j$ is the contravariant metric tensor,

$f^j = \frac{1}{J} \frac{\partial}{\partial \varepsilon^i} \left(J g^{ji} \right)$ the control grid functions,

$v_g{}^i = \frac{\partial x_i}{\partial t}$ the grid velocities.

In the transport equations above, incident terms (pressure, velocities and their gradients) are explicitly and directly computed at each time step using a nonlinear potential wave model described further.

Then the diffracted variables are the only remaining unknowns of the problem and are discretised under implicit form (for the equation (5) only left hand side terms are considered under implicit form).

3.2 Free surface boundary conditions

The nonlinear free surface boundary conditions are developed using decomposition given in (1) :

- kinematic condition :

$$\frac{\partial h_D}{\partial t} + \left(\frac{\partial h_D}{\partial x_1} + \frac{\partial h_I}{\partial x_1} \right) U_D^1 + \left(\frac{\partial h_D}{\partial x_2} + \frac{\partial h_I}{\partial x_2} \right) U_D^2 - U_D^3$$
$$= U_I^3 - \frac{\partial h_I}{\partial t} - \left(\frac{\partial h_D}{\partial x_1} + \frac{\partial h_I}{\partial x_1} \right) U_I^1 - \left(\frac{\partial h_D}{\partial x_2} + \frac{\partial h_I}{\partial x_2} \right) U_I^2 \qquad (6)$$

- normal dynamic condition (only capillarity term is neglected) :

$$P_D - \rho g h_D = \rho g h_I - P_I - 2\rho(\nu + \nu_t) \frac{\partial \left(U_I^i + U_D^i \right)}{\partial x_j} n_i n_j \qquad (7)$$

- tangential dynamic conditions :

$$\begin{cases} \left(n_j t_{1i} + n_i t_{1j} \right) \frac{\partial U_D^i}{\partial x^j} = -\left(n_j t_{1i} + n_i t_{1j} \right) \frac{\partial U_I^i}{\partial x^j} \\ \left(n_j t_{2i} + n_i t_{2j} \right) \frac{\partial U_D^i}{\partial x^j} = -\left(n_j t_{2i} + n_i t_{2j} \right) \frac{\partial U_I^i}{\partial x^j} \end{cases} \qquad (8)$$

Once again, the free surface boundary equations are rewritten as functions of curvilinear space variables. Then all incident terms are explicitly computed. Left hand side terms are discretised under implicit form in equations (6), (7) and (8) (with linearisation of nonlinear terms in the kinematic condition).

3.3 No-slip boundary condition

As previously, the equation (1) is used to obtain :

$$U_D^i = -U_I^i \qquad (9)$$

On the farfield, the cancellation of the diffracted velocities is progressively imposed. This modified condition combined with a stretching of the grid, in order to create a so-called *numerical beach*, prevents efficiently from diffracted wave reflections and verifies the decay of the diffracted field far from the body.

3.4. Turbulence model

To close the equations set we use a classical *k-ω* turbulence model proposed by Wilcox (1988) or the SST variant (Menter, 1994).

To summarize, the viscous solution for the diffracted fields is the solution of a modified problem defined by previous equations where incident terms are known at each time step and of which values are replaced in the SWENS Equations.

The global structure of the modified viscous code concerning location of unknowns, use of boundary conditions or velocity-pressure coupling remains unchanged.
It must be noticed that there are no specific assumptions and the diffracted solution summed with the incident fields gives the total velocity, pressure and free surface elevation fields at each time step.

4. COMPUTATION OF THE INCIDENT WAVE FLOW

In order to apply the SWENSE method it is necessary to be able to know at each time step all the characteristics of the incident field (velocities, pressure, free surface elevations).

4.1. Regular incident waves

An algorithm based on the stream function theory (Rienecker & Fenton, 1981) has been implemented. This algorithm has been chosen as it can generate the solution of steadily progressing periodic waves of a irrotational flow over a horizontal bed for a wide range a wide range of depths (but not for the solitary wave limit), amplitudes and wavelengths (in the limit of breaking waves) with high accuracy (computer accuracy in fact).

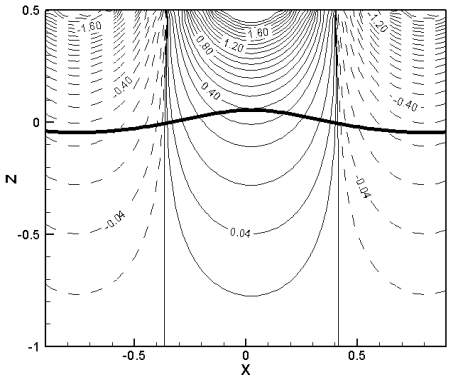

Figure 2 : contours of the axial velocity in the whole space for $2A = 0.1$, $\lambda = 1.5$ (nondimensional values). The bold line represents the free surface.

It must be noticed that the computational time needed to obtain the solution of the incident field at each time step is negligible comparing to a RANSE iteration.
Figure 2 shows the axial velocity field to demonstrate the continuity of the wave field under, through and also upon the incident free surface. This continuity is necessary because values of incident wave fields are required sometimes upon the incident free surface (because the total free surface elevation can locally be located upon the incident free surface elevation).

4.2. Irregular incident waves

The model used for propagation of irregular incident waves belongs to the family of Higher Order Spectral (HOS) schemes initiated by West *et al*. (1987) and Dommermuth & Yue (1987). This algorithm has been chosen as it can generate the solution of almost all the existing waves profiles on irrotational flow over a horizontal bed for any depth (in the limit of breaking waves) with high accuracy and fast computations.
It is based on potential theory with nonlinear free-surface boundary conditions rewritten (following Zakharov, 1968) in terms of surface quantities, namely the single-valued free surface elevation $\eta(x,y,t)$ and the surface potential $\phi^S(x,y,t) = \phi(x,y,\eta,t)$:

$$\frac{\partial \phi^S}{\partial t} = -g\eta - \frac{1}{2}\left|\nabla \phi^S\right|^2 + \frac{1}{2}\left(1+\left|\nabla \eta\right|^2\right)W^2 \quad (10)$$

$$\frac{\partial \eta}{\partial t} = \left(1+\left|\nabla \eta\right|^2\right)W - \nabla \phi^S \nabla \eta \quad (11)$$

on $z = \eta(x,y,t)$.

$W = \frac{\partial \phi}{\partial z}$ is the vertical velocity. The unknowns, $\eta(x,y,t)$ and $\phi^S(x,y,t)$, expressed at collocation points are time-marched once the vertical velocity has been obtained through the solution of a Dirichlet problem for the potential. The latter is solved by the HOS expansion of the potential in orders of the wave elevation in parallel with the order consistent formulation of West *et al.* (1987). Right Hand Sides of equations (32) and (33) contain nonlinear products that are computed in the spatial domain by means of a pseudospectral method. Rapid conversion between spectral and spatial space are made thanks to Fast Fourier Transforms (FFT). This leads us to a fully-spectral technique with FFT-based resolution with computational cost in $O(N\log(N))$ with N, the number of collocation points which is equal to number of modes used. Thus, the proposed method exhibits fast-convergence properties with very low computational time.
A periodic formulation has been implemented as well as a new non-periodic one. The former gives the solution at large scale and the latter is useful to model a wave tank.
Details concerning time domain simulations of nonlinear water waves using spectral methods can be found in Ducrozet *et al.* (2006) or Bonnefoy *et al.* (2009).

5. RESULTS

5.1. DTMB 5415 in regular head waves

This problem is the case (3.5) of the 2010 CFD Workshop in Gothenburg. Computations have been made with a grid of 800000 nodes and 150 time steps per wave encounter period (equal to 1.83 s).
Froude and Reynolds numbers are equal to Fn=0.28 and Re=4.86.10^6 respectively. Head waves are defined by non-dimensional wavelength λ/L_{PP}=1.5 (L_{PP} at full scale is 142 m) and wave stepness Ak=0.025.
Computations have been made with 16 AMD Opteron processors 250 (2.4 GHz). 4000 time iterations (about 26 encounter wave periods) have been computed in 65 hours (that is a CPU time of 1040 hours) that leads to 1.17 10^{-3} s of CPU time per time iteration and per node.
We present here some comparisons of harmonic components of the free surface elevation calculated by a Fourier analysis on a moving window of one period long (for each node of the free surface grid).

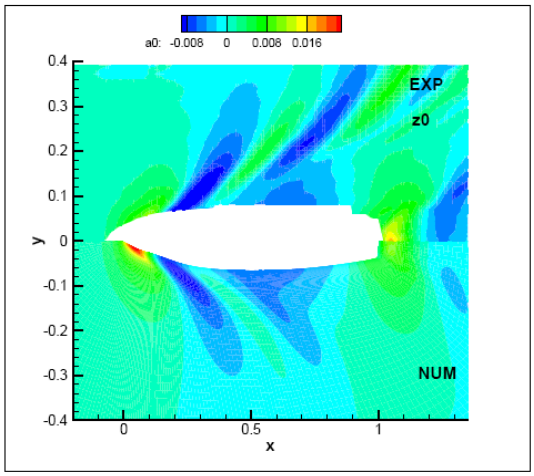

Figure 3 : average amplitude of the free surface elevation; top: experiments; bottom: numerics.

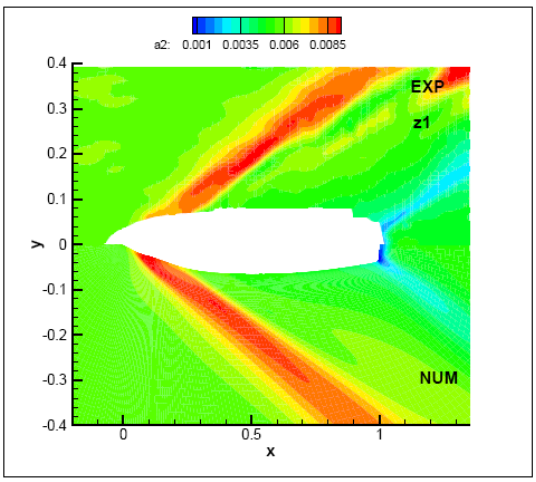

Figure 4 : 1st harmonic amplitude of free surface elevation; top: experiments; bottom: numerics.

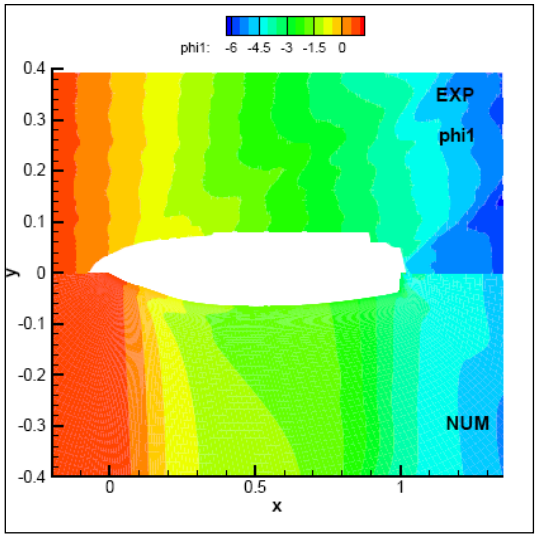

Figure 5 : angle phase of the 1st harmonic term; top: experiments; bottom: numerics.

Numerical average amplitude (figure 3), 1st harmonic amplitude and phase (figures 4 and 5) of free surface elevations are in good agreement with experimental data near the hull. The discrepancy far from the hull is due to the lack of refinement of the grid in this region.

5.2. Ship with no forward motion in 2D irregular head waves

This purpose of this case is to show capabilities of the SWENSE method for computation of seakeeping in 2D irregular head waves and for long time simulations. The studied ship is a heavy-lift vessel used in offshore engineering. Experimental data used for comparison have been obtained at the wave tank of Ecole Centrale Nantes (see Roux de Reilhac *et al.*, 2008).

total length (m)	3.83
length between perpendiculars (m)	3.61
beam (m)	0.90
Draft (m)	0.10
mass (kg)	272
longitudinal location of the gravity center* (m)	1.44
vertical location of the gravity center* (m)	0.15

*with respect to the after perpendicular and the base line respectively
Table 1: Geometric characteristics of the model

During experiments, the model (see table 1) is retained in longitudinal motion by 3 mooring lines which ensure an elastic fastening. In the numerical simulation, the model is supposed to be fixed in surge motion and free in roll and pitch motions.
A Bretschneider spectrum defined by a peak

frequency $f_P = 0.65$ Hz and a significant wave height $H_S = 0.02$ m is used for experiments. The time history of the wavemaker motions being experimentally known it is possible to compute time history of the incident wavetrain with the HOS method described previously.

A 250000 nodes grid for the half domain has been used (the incoming waves are head waves) and 600 s of wave-body interaction have been simulated with a time step of 0.01 s (about 150 time step for the average period of 1.54 s). With a single processor AMD Opteron 250 (2.4 GHz), 2 months of CPU time have been required.

As the irregular head sea experiment was made in the ECN basin, we have the historics of the wavemaker motions, therefore we can reproduce the exact elevation of the incident wave field everywhere in the basin with the HOS method.

By this way, our simulation has a deterministic character and it is possible to compare at every time step the results of the simulation against the experiment. For example, figure 6 shows time comparison of numerical and experimental signals between 140 and 170 s for the wave elevation of a point P (located at x=2.98 m and y=2.40 m relatively to the model center of gravity), as well as for heave and pitch motions. The agreement is quite correct, even if we fail to reproduce with precision some extrema of the heave and pitch signals. Nevertheless it shows the efficiency of the damping of diffracted waves near the external boundaries during the computation and the capability of the SWENSE method to simulate long time simulations (about 110 average incident periods at t=170 s) correctly.

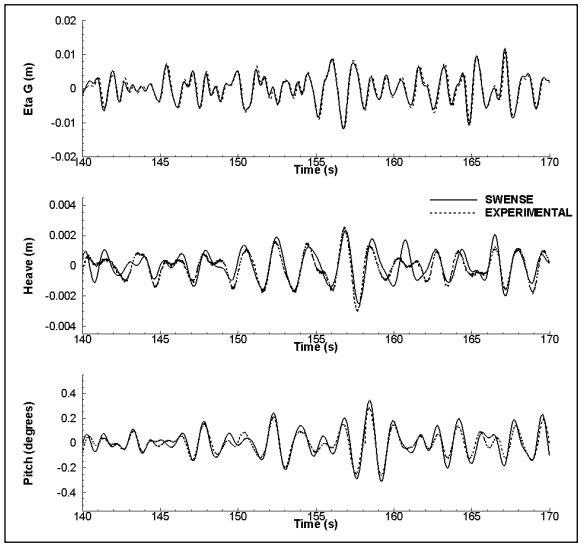

Figure 6 : Comparison numerics (solid line)-experiments (dotted line) of time history signals :
at the top : wave elevation for a wave probe at 3.83m from the ship center of gravity
middle : heave motion of the center of gravity
bottom : pitch motion of the center of gravity.

For the calculation of spectra of heave and pitch motions we choose a window corresponding to the repetition period of the wavemaker (512 seconds) and starting after the wave front encounter. Then we use the Welch method (the signal is split up into 16 segments of 32 seconds with an overlap of 50%) and a Hann window is applied to the overlapping segments. Figures 7 and 8 show comparison of numerical and experimental motions spectra.

This example sheds light on an important potentiality of the SWENSE method. Since it is now proven possible to compute an entire repetition period of the wavemaker (512 seconds from the wave front encounter in the present case), it permits the wave target spectrum full establishment. Therefore it allows to determine the motion response spectrum of a ship for a wave spectrum of which we do not know the historics of the wavemaker motion.

Thus, the simulations get also a statistical interest.

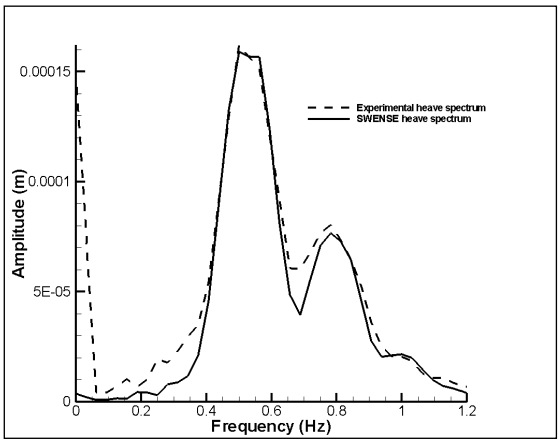

Figure 7 : Comparison of experimental (dotted line) and numerical (solid line) spectra for the heave motion.

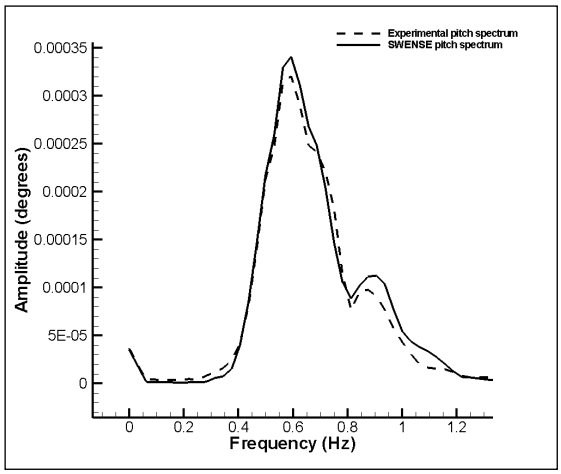

Figure 8 : Comparison of experimental (dotted line) and numerical (solid line) spectra for the pitch motion.

Finally, In order to evaluate the difference between experimental and numerical spectra, we define an error rate ε as :

$$\varepsilon = \frac{\int_f \left| a_{num} - a_{exp} \right| df}{\int_f a_{exp}\, df} \qquad (12)$$

In the frequency domain between 0.3 Hz and 1.2 Hz, it represents the area located between the experimental and the SWENSE curves, normalised by the area beneath the experimental curve. During the computation this error rate for heave and pitch spectra (see figure 9 for the heave case) is about 10 %.

As a tool of comparison, we used a commercial seakeeping code based on a linear potential solver. For the same wave spectrum, we proceeded to the resolution in the frequential domain, with a surface mesh of 2500 nodes for a half ship, and we found an error rate equal to 20% for heave and 9% for pitch.

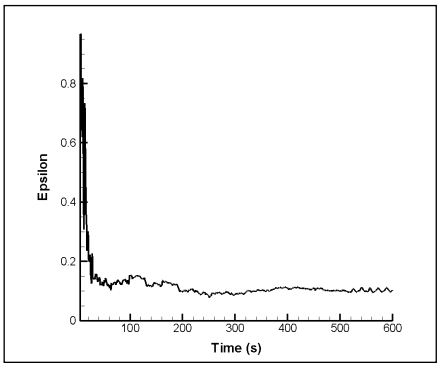

Figure 9 : Time history of the error rate for heave motion during computation.

CONCLUSION

The SWENSE formulation presented here has been developed for numerical simulation of ship and offshore structures seakeeping under viscous flow theory.

The main advantages of this method is the capabality to take incident real sea states into account with no difficulty and to be able to simulate long time wave-body interactions with a good accuracy. In particular discrepancies due to reflection of waves on the external boundaries are quite negligible here. Moreover the SWENSE procedure permits to keep quite low CPU time compared to classical simulations of seakeeping problems using RANS Equations.

The next purpose is to implement a free surface capturing Level-Set procedure in the ICARE-SWENSE solver in order to simulate wave breaking and complex shapes of interface in seakeeping problems.

REFERENCES

Alessandrini, B., Delhommeau, G. (1995). “A multigrid velocity-pressure-free surface elevation fully coupled solver for calculation of turbulent incompressible flow around a hull”, Proceedings of the 9th International Conference on Numerical Methods in Laminar and Turbulent Flows, Atlanta, United States, pp. 1173-1184.

Alessandrini, B., Delhommeau, G. (1999). "A fully coupled Navier-Stokes solver for calculations of turbulent incompressible free surface flow past a ship hull", International Journal for Numerical Methods in Fluid, Vol. 29, pp. 125-142.

Bonnefoy, F., Ducrozet, G., Le Touzé, D., Ferrant, P., (2009). "Time domain simulation of nonlinear water waves using spectral methods", Advances in Numerical Simulation of Nonlinear Water Waves

Bull, P., Verkuyl, J.B., Ranocchia, D., Di Mascio, A., Dattola, R., Merle, L., Cordier, S. (2002). "Prediction of high Reynolds number flow around naval vessels", Proc. 24th Symp. Naval Hydrodynamics, Fukuoka, Japan.

Burg, C.O.E., Sreenivas, K., Hyams, D.G., Mitchell, B. (2002). "unstructured nonlinear free surface simulations for the fully-appended DTMB 5415 Series hull including rotating propulsors", Proc. 24th Symposium Naval Hydrodynamics, Fukuoka, Japan.

Carrica, P.M., Wilson, R.V., Stern, F. (2006). "Unsteady RANS simulation of the ship forward speed diffraction problem", Computers & Fluids Vol 35, Issue 6, pp. 545-570.

Di Mascio, A., Landrini, M., Lalli, F., Bulgarelli, U. (1994). "Three Dimensional non linear diffraction around fixed structures", Proceedings of the 20th Symposium on Naval Hydrodynamics.

Dommermuth, D., Yue, D. (1987), "A high-order spectral method for the study of nonlinear gravity waves", J. Fluid Mech., vol. 184, pp. 267-288.

Ducrozet, G., Bonnefoy, F., Le Touzé, D., Ferrant, P. (2006). "Implementation and validation of nonlinear wave maker models in a HOS Numerical Wave Tank", *Int. J. Offshore Polar Eng.*, Vol.3, pp161-167.

Duvigneau, R., Visonneau, M., Deng, G.B. (2003). "On the role Played by Turbulence Closures in Hull Shape Optimization at Model and Full Scale", J. Mar. Sci. Technology, Vol. 8, pp. 11-25.

Ferrant, P. (1996). "Simulation of strongly non-linear wave generation and wave-body interaction using a 3D MEL model", Proceedings of 21st Symposium on Naval Hydrodynamics, Trondheim, Norway.

Fu, T.C., Ratcliffe, T., O'Shea, T.T., Brucker, K.A., Graham, R.S., Wyatt, D.C., Dommermuth, D.G. (2010). "A Comparison of Experimental Measurements and Computational Predictions of a Deep-V Planing Hull", Proc. of 28th Symposium on Naval Hydrodynamics, Pasadena, United States.

Jacquin, E., Guillerm, P.E., Drouet, A., Perdon, P. (2006). "Simulation of unsteady ship maneuvering using free-surface RANS solver", Proc. 26th Symposium on Naval Hydrodynamics, Rome, Italy.

Hino, T. (2005). Editor. Proceedings of CFD Workshop, Tokyo, Japan, National Maritime research Institute.

Luquet, R., Gentaz, L., Ferrant, P., Alessandrini, B. (2004). "Viscous flow simulation past a ship in waves using the SWENSE approach", Proceedings of the 25th Symposium on Naval Hydrodynamics, St John's, Canada.

Luquet, R., Jacquin, E., Guillerm, P.E., Gentaz, L., Ferrant, P., Alessandrini, B. (2005). "RANSE with free surface computations around fixed and free DTMB 5415 model, in still water and in waves", Proceedings of the CFD Workshop, Tokyo, Japan.

Menter, F.R. (1994). "Two-Equation Eddy-Viscosity Turbulence Models for Engineering Applications", AIAA Joournal, Vol. 32, No. 8, pp. 1598-1605.

Monroy, C., Ducrozet, G., Roux de Reilhac, P., Gentaz, L., Ferrant, P., Alessandrinin, B. (2009) "RANS Simulations of ship motions in Regular and Irregular Head Seas using the SWENSE Method", Proc. of 19th ISOPE Conference, Osaka, Japan.

Monroy, C., Ducrozet, G., Bonnefoy, F., Babarit, A., Gentaz, L., Ferrant, P. (2010). "RANS Simulations of a Calm Buoy in Regular and Irregular Seas using the SWENSE Method", Proc. of 20th ISOPE Conference, Beijing, China.

Rienecker, M.M.; Fenton, J.D. (1981). "A Fourier approximation method for steady water waves", Journal of Fluid Mechanics, Vol. 104, pp. 119-137.

Roux de Reilhac, P., Rousset, J.-M., Gentaz, L., Bonnefoy, F., Alessandrini, B., Ferrant, P., (2008). "Experimental and numerical analysis of the response of a moored barge to focused waves", Proc. of the 8th International Conference on Hydrodynamics, Nantes, France.

Weymouth, G.D., Wilson, R.V., Stern, F. (2005). "RANS Computational Fluid Dynamics Predictions of Pitch and Heave Ship Motions in Head Seas", J. Ship Research, Vol. 49, N°2, pp.80-97.

West, B., Brueckner, K., Janda, R., Milder, M., Milton, R. (1987), "A new numerical method for surface hydrodynamics", J. Geophys. Res., Vol. 92.

Wilcox, D., C. (1988). "Reassessment of the scale-determining equation for advanced turbulence models", AIAA journal, Vol. 26, pp. 1299-1310.

Zakharov., Z. (1968). "Stability of periodic waves of finite amplitude on the surface of a deep fluid" , J. Appl. Mech. Tech. Phys., pp. 190–194.

VISCOUS FREE SURFACE CALCULATIONS FOR THE KCS HULL

Michał Orych (FLOWTECH Int. AB, Sweden)
Lars Larsson (Chalmers University of Technology, Sweden)
Björn Regnström (FLOWTECH Int. AB, Sweden)

1. SUMMARY

This paper describes computations of the flow around the KRISO Container Ship (KCS) with focus on wave pattern predictions. A steady state RANS code with a volume-of-fluid (VOF) free surface capturing method is used. The calculations are performed with block structured grids with H-O topology and around 4 million cells. The results obtained show a satisfactory correlation with the measurements.

2. INTRODUCTION

The main purpose of the work is the validation of the numerical predictions with respect to free surface flows. A wave pattern, wave profile and longitudinal cuts are compared with the measurements. Additionally a comparison of two discretization schemes for water fraction transport equation is made and the effect on interface thickness and wave patern details is discussed.

The computations are performed with the SHIPFLOW code developed at Flowtech International AB. The free surface capability is being developed as a part of PhD project supported by Chalmers University of Technology. The numerical method is based on RANS equations supplemented with a water fraction transport equation for the free surface location computation.

3. NUMERICAL METHOD

The solver is based on the steady RANS equations. The closure terms are modeled with the Menter $k-\omega SST$ turbulence model. The model is valid all the way to the solid walls, so there is no need for wall functions. Also no special treatment for the turbulence modeling was applied near the free surface interface.

In addition to the RANS and turbulence model equations, a water fraction transport equation is introduced. A scalar function describes the amount of water in each cell of the computational domain and takes values from 0 in the air to 1 in the water. The intermediate values indicate the location of the free surface. The transition band has to be thin, which usually means around 3 cells. Therefore, the discretization scheme needs to be able to represent a step discontinuity in the best possible manner. The density and dynamic viscosity are constant except in the transition band, where a simple mixing rule is used to describe them.

The partial differential equations are discretized to algebraic equations with the Finite Volume Method (FVM). The averaged values in each cell volume surrounding the centers are calculated from face fluxes. The variations of the flow properties between the cells is approximated with appropriate differencing schemes which are chosen to support the physical behavior of the flow. The diffusion terms are discretized with central differences while hybrid schemes are used for the convection. All convective terms use the Monotonic Upwind Scheme for Conservation Law (MUSCLE) scheme, except those of the water fraction equation which use either the SuperBee or Superbee-C, Orych et al (2009) scheme.

A source balancing method is used to introduce gravity, Leveque (1998), Hubbard and Garcia-Navarro (1999). The body forces that arise from the gravity are incorporated into the approximate Riemann solver and the Roe type discretization. The pressure gradient due to gravity is subtracted from the input states for the solver. Thus, only the perturbations from the steady state are seen, not the large hydrostatic pressure gradient that would otherwise create spurious accelerations of the fluid particles due to strong coupling of pressure and velocity. The boundary conditions are implemented using two layers of ghost cells, Broberg et al (2007).

The initial conditions are specified to uniform flow with an undisturbed free surface and an approximate boundary layer profile. The hydrostatic pressure and void fraction fields are prescribed accordingly.

Another aspect of the work that can be considered as an interesting feature of the implementation is that the free-surface solution is computed with an artificial time step as opposed to other well established codes which use time dependent techniques to advance the computations and acquire the average wave height. The local artificial time-step is added to the equations and the discrete coupled equations are solved with the Alternating Direction Implicit (ADI) method. For each sweep a local artificial time-step is calculated based on the CFL and von Neumann numbers.

The convective flux discretization is based on the first order Roe type flux difference splitting algorithm, Roe (1981). Higher order accuracy is achieved by the explicit defect correction with flux extrapolation based on the work presented by Dick and Linden (1992), which stems from the Chakravarthy and Osher (1985) formulation. High resolution schemes are composed by applying limiters to the correction terms and blending of basic schemes. The limiter functions select an appropriate correction term based on the relations of flux differences in the computational stencil. High resolution composite schemes have been developed to overcome problems with non-physical oscillations and overshoots of a solution.

It should be noted that in case of the current implementation the recognition of the flow direction is taken care of by the underlying Roe discretization scheme that is inherently upwind. In the present method the base for the momentum and continuity equations is the MUSCL scheme. In order to keep the air and water interface sharp a certain amount of anti-diffusion is required. A scheme that can sharpen the step discontinuity of the fluid density should be used. Therefore, the transport equation for the volume fraction utilizes either the SuperBee or the SuperBee-C scheme.

A scheme called SuperBee developed by Roe (1985) is one of the most compressive schemes. The scheme is constructed with central differences and second-order upwind and first-order downwind basic schemes. It is able to represent step changes in the computed flow quantities which makes it very suitable for free surface applications.

The second scheme used in the computations is SuperBee-C which is a combination of SuperBee and Super-C. The Super-C itself, Leonard (1988), is ”super compressive” and indeed the step changes are represented with steeper gradients than in case of SuperBee. In the Superbee-C a parameter was introduced to control the amount of central differencing. The parameter was set based on test calculations and a good compromise turned out to be closer to the Super-C scheme, Orych et al (2009).

4. COMPUTATIONAL GRID

The computations were carried out with structured, H-O type multi-block grid. One block constituted the main part and was covering the whole hull except the volume behind the flat transom where an additional block was fitted. The domain extended 1.5 length between perpendiculars (Lpp) upstream of the forward perpendicular and 3.0 Lpp behind the aft perpendicular. The outer boundary had a radius of 1 Lpp and the top was about 0.1 Lpp above the water plane. The cells were stretched in the normal direction to the hull down to $y+ \sim 1$, in order to satisfy requirements of the turbulence model. In the vertical direction the grid was refined close to the free surface, where the cells had the thickness Δz of 0.001 Lpp and the cell faces were aligned with the undisturbed free surface for the layers in a range from -0.01 to 0.015 Lpp in z-direction, see Figure 1 and 2.

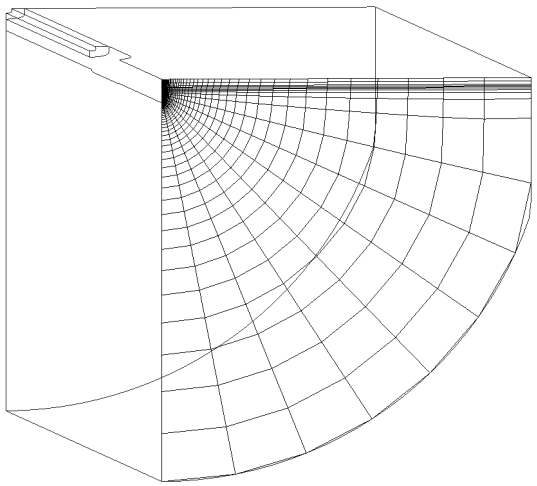

Figure 1: H-O volume grid with visible surface mesh at the inlet (grid was coarsened for the picture clarity).

Along the hull there were 240 cells with stretching applied near the bow and stern. The cell length Δx varied from 0.0045 Lpp at the bow, 0.0057 Lpp at the midship to 0.0022 Lpp at the stern which corresponded to 93, 74 and 188 cells per wave length respectively. Figure 4 shows the distribution of the cells in longitudinal direction along the undisturbed waterline and in the transverse and vertical directions at midship. Behind the hull the cell size increased for wave damping purposes to avoid reflections from the outlet and therefore the waves became less pronounced shortly behind the transom. In total 4.6 million grid cells were used.

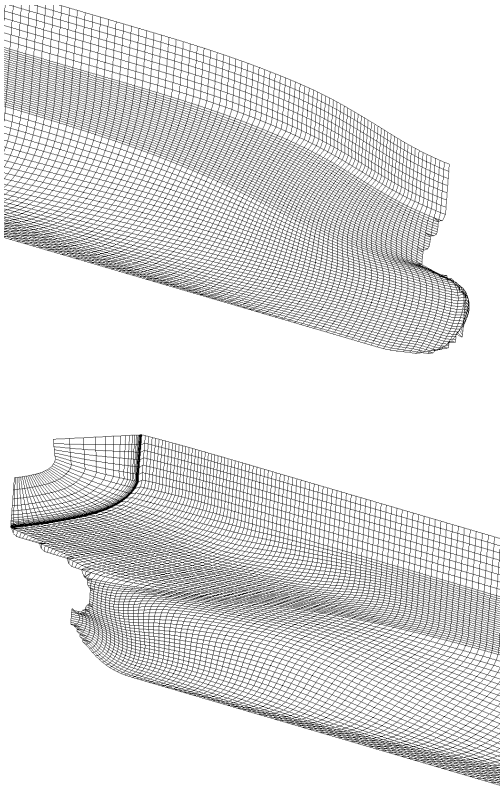

Figure 2: Surface grid on hull with visible fine region near free surface level, bow and stern part.

5. CASE SETUP

The computations were set up to resemble the conditions of the experiments carried out at MOERI, Kim et al (2001). The model was towed at a Froude number of 0.26 and a corresponding Reynolds number was $1.4*10^7$. A bare hull was considered in model-fixed conditions, without effects of dynamic sinkage and trim.

The simulations were performed with the Courant number of 0.4 at the beginning of the computations and was increased up to 0.6 after several hundred iterations. The computations were stopped when the averaged pressure residual dropped three orders of magnitude.

6. RESULTS

The computed free surface was compared to measurements. The longitudinal wave cuts at -0.0741, -0.1509, -0.4224 and the wave profile along the hull are presented in Figure 3. It can be seen that the stern wave is slightly overestimated. That concerns mainly the diverging stern wave system. The waves behind the the hull where the grid is coarsened rapidly are damped out and also loose the correct phase.

The wave profile at the hull surface follows the measured height well. The largest deviations are at the bow and stern. The bow wave crest is underestimated while the trough at the aft shoulder and the crest at the stern are overestimated.

The wave pattern in general corresponds well with the measurements, see Figure 4 (after the References). However, due to the inadequate grid stretching in both longitudinal and transverse directions the diverging waves loose their details when going away from the hull. This is mostly visible looking at the wave features that should appear between diverging bow and stern wave systems.

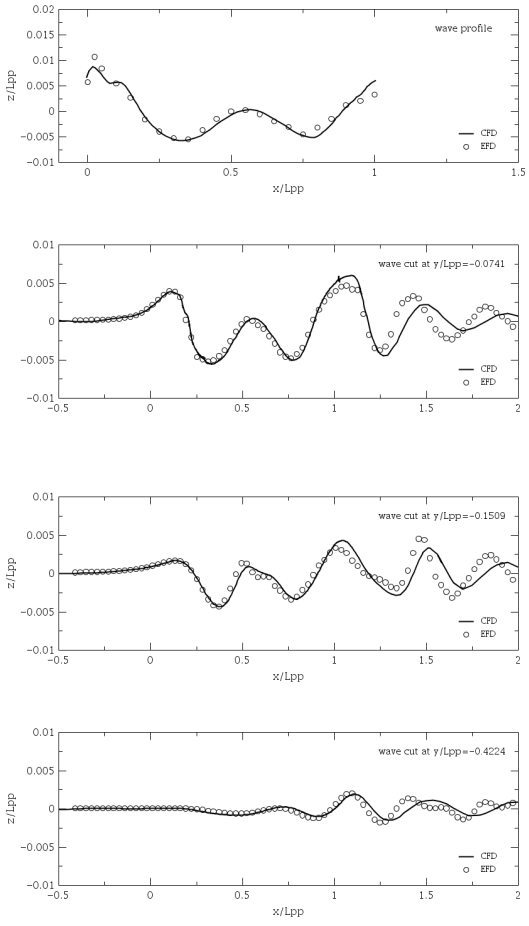

Figure 3: Wave profile and longitudinal wave cuts.

The current investigation includes also a comparison between the SuperBee and SuperBee-C schemes for the water fraction equation. The focus was put on the wave pattern and interface thickness.

From the wave pattern comparison in Figure 5 it is not obvious that there is any significant difference between the computations. The wave details and numerical damping are at a very similar level.

The most visible effect can be noticed for the interface thickness. By analysing the water fraction distribution at the hull surface we can clearly see that the SuperBee-C keeps the interface sharper along the hull. Additionally a small air bubble that appeared near the stern for the SuperBee was not present for the other scheme, see Figure 6.

7. CONCLUSIONS

The code capability was examined with respect to the wave pattern prediction for a container vessel. The RANS simulations with free surface modelled with a water fraction equation showed good overall agreement for the KCS hull. One of the most visible difficulties is a small phase shift of the waves behind the ship which was not present in the earlier simulations performed on the Wigley and Series 60 hulls. Moreover, the grid distribution is not adequate to achieve better quality results. Further efforts will be focused on improving efficiency of the code as well as on accuracy of the wave resistance prediction.

REFERENCES

BROBERG, L., REGNSTRÖM, B., ÖSTBERG, M. (2007): XCHAP – Theoretical Manual, FLOWTECH International AB.

CHAKRAVARTHY, S. & OSHER, S. (1985): A New Class of High Accuracy TVD Schemes for Hyperbolic Conservation Laws, AIAA paper-85-0363 .

DICK, E., LINDEN, J. (1992): A Multigrid Method for Steady Incompressible Navier-Stokes Equations Based on Flux Difference Splitting, International Journal for Numerical Methods in Fluids, Vol.14, 1311-1323

HUBBARD, M. E., GARCIA-NAVARRO, P. (2000): Flux Difference Splitting and the Balancing of Source Terms and Flux Gradients . Journal of Computational Physics, Vol. 165(1), pp. 89-125

KIM, W. J., Van, D.H. and Kim, D.H., (2001): Measurement of flows around modern commercial ship models, Exp. in Fluids, Vol. 31, pp 567-578

LEONARD, B. P. (1991): The ULTIMATE conservative difference scheme applied to unsteady one-dimensional advection. Computer Methods in Applied Mechanics and Engineering, 88, 17-74.

LEVEQUE, R. J. (1998): Balancing Source Terms and Flux Gradients in High-Resolution Godunov Methods: The Quasi-Steady Wave- Propagation Algorithm. Journal of Computational Physics, 146, 346-365.

ORYCH, M., REGNSTRÖM, B., LARSSON, L. (2009): A Surface Capturing Method in the RANS Solver SHIPFLOW. 12th Numerical Towing Tank Symposium, Cortona, Italy 4-6 October 2009.

ROE, P. L. (1981): Approximate Riemann Solvers, Parameter Vectors, and Difference Schemes, Journal of Computational Physics, Vol. 43, 357

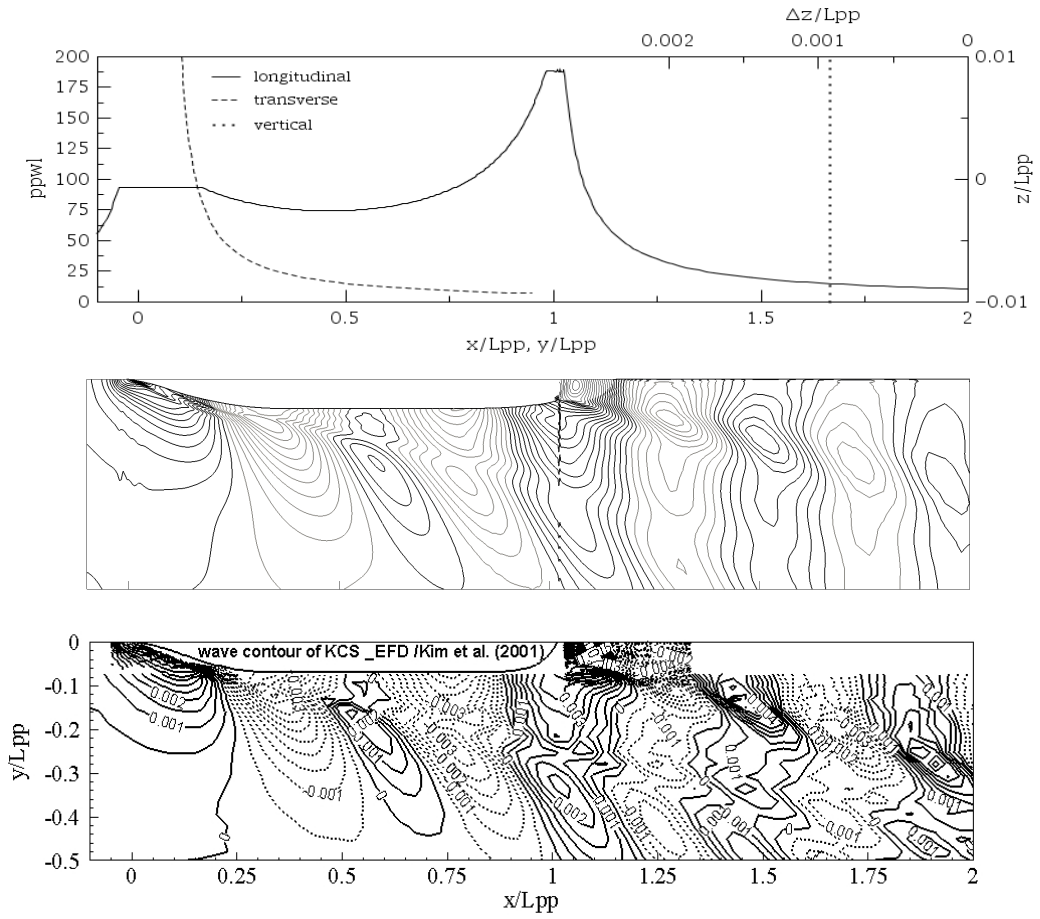

Figure 4: Grid density distribution (top), computed (middle) and measured wave pattern (bottom). Spacing between contour lines 0.0005 L.

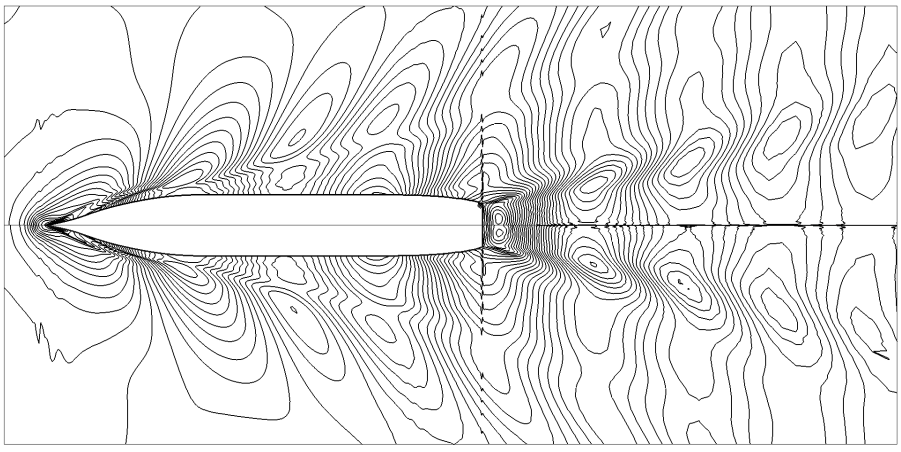

Figure 5: Wave pattern comparison, top: SuperBee, bottom: SuperBee-C. Spacing between contour lines 0.0005 L.

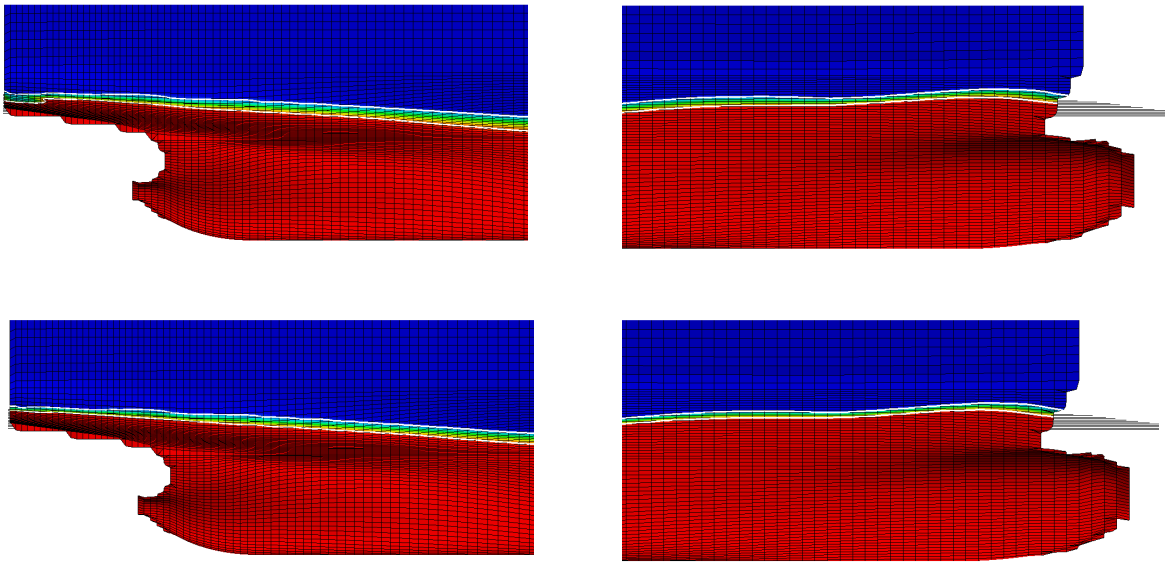

Figure 6: Water fraction at the hull surface for SuperBee (top) and SuperBee-C (bottom) schemes.

LARGE EDDY SIMULATION OF THE FLOW PAST THE DTMB 5415 SURFACE COMBATANT HULL

C. Fureby[†,‡], N. Alin[†] & M. Liefvendahl[†]
[†]Defense Security Systems Technology, The Swedish Defense Research Agency – FOI,
SE 147 25 Tumba, Stockholm, Sweden
[‡]Dept. of Shipping and Marine Technology, Chalmers
University of Technology, SE-412 96, Göteborg, Sweden

Summary

In this study the flow and wave patterns around the DTMB 5415/INSEAN2340 model hull are investigated using Large Eddy Simulation (LES) models and compared with available experimental data. The aim of the study is to evaluate the capabilities and cost of LES in predicting the flow and wave pattern around surface ships and to investigate and further elucidate the relevant flow physics. Transient simulation methods like LES provide more information about the flow than steady simulation methods such as Reynolds Average Navier Stokes (RANS) models but at a higher cost. RANS and LES can therefore be viewed as complementary tools in e.g. a design process. When compared with the experimental data, it can be concluded that the LES predictions are in good overall agreement with the data, suggesting that LES have reached sufficient maturity to be used to predict details of the flow past a ship hull.

1. Introduction and Background

In the present study we aim at investigating the predictive capabilities of Large Eddy Simulation (LES), [1-4], for surface ship hydrodynamics by computing and analyzing the unsteady flow past the DTMB 5415 surface combatant hull. The flow past a surface ship hull is complicated due to the flow features induced by the shape of the hull, including developing boundary layers, vortex structures from appendages, such as bilge keels, sonar domes, struts and shafts, high Reynolds (Re) number turbulence and the free water surface on which wave structures develop as a consequence of the ship making speed through the water. In the past, potential flow methods, e.g. [5], proved useful in predicting the gross features of the flow including the pressure distributions and wave-pattern, but more recently these methods have started to be replaced by Reynolds Averaged Navier-Stokes (RANS) models, [6-7], which have the ability to predict the mean pressure, velocity and free-surface distribution around the hull together with estimates of the turbulence – even for full scale ship hulls, [8]. In RANS all of the turbulence is represented by a turbulence model, [6], the intrinsic features of which are crucial for accurate predictions. RANS can give acceptable predictions of drag and mean velocities but towards the stern, where the flow becomes extremely complicated, RANS is not always able to predict the mean flow, and certainly not the unsteady coherent flow structures, that may trigger intermittent separation, being transported into the propulsor causing vibrations, cavitation and noise. It is therefore natural to also consider even more advanced Computational Fluid Dynamic (CFD) models such as Detached Eddy Simulation (DES), [9-10], and LES, [10-11], models that have the ability to predict the unsteady coherent vortex structure dynamics, but at the cost of more expensive computations. Only a few DES and LES type computations of surface ship hydrodynamics have so far been presented in the open literature, [9-11], but these results indicate that the DES/LES approaches have the capability to capture essential features that RANS cannot capture provided that the computations are performed with great care and on sufficiently fine and smooth computational grids.

Here we present an LES methodology developed for ship hydrodynamics with or without a free water surface, and use this method to compute the flow and wave pattern developing around the DTMB 5415 surface combatant hull, [12-14]. Comparisons of velocity profiles along the hull as well as the wave pattern will here be presented to assess the predictive capabilities of the LES model. Results from computations on two grids will be reported to study the sensitivity of the predictions to these potentially very important simulation parameters.

2. Mathematical Formulation of Free Surface LES

The flow physics involved in surface ship hydrodynamics consists primarily of high Re-number boundary layer dominated incompressible flow around the hull, the generation and evolution of the surface wave pattern, and the wake stretching far astern of the ship. The governing equations are the incompressible Navier Stokes Equations (NSE), [15], modeling the flow of air and water, and an additional equation for the evolution of the interface between these two immiscible fluids. Different approaches can be used for tracking the air-water interface, [16], and here we use the Volume of Fluids (VoF) approach, [17-18], in which a volume fraction, α, taking the value 0 in air, 1 in water and $0<\alpha<1$ in regions where the two fluids co-exists, is employed to represent the air-water interface. The governing equations are thus,

$$\begin{cases}\partial_t(\rho\mathbf{v})+\nabla\cdot(\rho\mathbf{v}\otimes\mathbf{v})=-\nabla p+\nabla\cdot\mathbf{S}+\rho\mathbf{f},\ \nabla\cdot\mathbf{v}=0,\\ \partial_t(\alpha)+\nabla\cdot(\alpha\mathbf{v})=0,\end{cases} \quad (1)$$

where $\mathbf{v}$ is the velocity, $\rho=\alpha\rho_1+(1-\alpha)\rho_2$ the density, p the pressure, $\mathbf{S}=2\mu\mathbf{D}$ the viscous stress tensor, $\mu=\alpha\mu_1+(1-\alpha)\mu_2$ the viscosity, $\mathbf{D}=\frac{1}{2}(\nabla\mathbf{v}+\nabla\mathbf{v}^T)$ the rate-of-strain tensor, $\nabla\mathbf{v}$ the velocity gradient, and $\mathbf{f}$ the specific body force consisting of the gravitational acceleration and surface tension. In the above expressions indices 1 and 2 refers to the water and the air phase, respectively, whereas for free-surface ship hydrodynamics the surface tension is neglected.

The motivation behind LES was to establish a simulation framework that properly resolves the coherent structure dynamics, modeling the residual flow in a manner consistent with the cascade process, [19], and thus being more accurate than RANS and less expensive than DNS. For LES to work as intended the coherent structure dynamics needs to be resolved on the grid together with the large-scale part of the energy cascade, resulting in carefully designed grids with good resolution in regions of coherent structure activity. The equations governing the large-scale flow features are then obtained by applying a spatial filter, having a width of Δ, to (1) in order to eliminate the small-scale flow features. After spatial filtering and rearranging terms the governing equations for the large (resolved) scales then becomes,

$$\begin{cases}\partial_t(\rho\bar{\mathbf{v}})+\nabla\cdot(\rho\bar{\mathbf{v}}\otimes\bar{\mathbf{v}})=-\nabla\bar{p}+\nabla\cdot(\bar{\mathbf{S}}-\mathbf{B})+\rho\bar{\mathbf{f}},\ \nabla\cdot\bar{\mathbf{v}}=0,\\ \partial_t(\bar{\alpha})+\nabla\cdot(\bar{\alpha}\,\bar{\mathbf{v}})=-\nabla\cdot\mathbf{b},\end{cases} \quad (2)$$

where overbars denote spatially filtered variables, $\mathbf{B}=\rho(\overline{\mathbf{v}\otimes\mathbf{v}}-\bar{\mathbf{v}}\otimes\bar{\mathbf{v}})$ the subgrid stress tensor and $\mathbf{b}=\overline{\alpha\mathbf{v}}-\bar{\alpha}\,\bar{\mathbf{v}}$ the subgrid flux vector which both must be modeled in order to close (2). The demands on the subgrid models are expected to be less severe compared to RANS since a substantial fraction of the coherent structure dynamics is resolved. However, as the hull is approached, the flow structures change character, and the flow becomes dominated by longitudinal vortices with a characteristic length and spacing, which form Ω-shaped vortex structures that interacts with the bulk flow. The scales dominating the near wall flow varies with the Re-number, and are much smaller than those of the detached or free flow, requiring either grid refinement as the wall is approached, or the use of an LES wall model.

The subgrid stress tensor $\mathbf{B}$ and subgrid flux vector $\mathbf{b}$ are here both modeled by structural models, [1], designed to retain as much as possible of the physics embedded in these terms, but at the expense of some numerical stability that may lead to ripples in e.g. the computed free surface wave field. Following Bardina *et al*, [20], and Fureby & Bensow, [21], we here use a Mixed Model (MM) that is composed of a scale similarity term $\rho(\overline{\bar{\mathbf{v}}\otimes\bar{\mathbf{v}}}-\bar{\bar{\mathbf{v}}}\otimes\bar{\bar{\mathbf{v}}})$, responsible for modeling the flow physics at barely resolved scales, and a subgrid viscosity term, $-2\rho\nu_k\bar{\mathbf{D}}$, representing the subgrid dissipation. The model then consists of $\mathbf{B}\approx\rho(\overline{\bar{\mathbf{v}}\otimes\bar{\mathbf{v}}}-\bar{\bar{\mathbf{v}}}\otimes\bar{\bar{\mathbf{v}}})-2\rho\nu_k\bar{\mathbf{D}}$ and $\mathbf{b}\approx(\overline{\bar{\mathbf{v}}\bar{\alpha}}-\bar{\bar{\alpha}}\,\bar{\bar{\mathbf{v}}})-\nu_k\nabla\bar{\alpha}$, in which the subgrid viscosity, ν_k, is estimated as $\nu_k=c_k\Delta k^{1/2}$, in which the subgrid kinetic energy, k, is assumed to evolve according to the following (modeled) transport equation, [21],

$$\partial_t(k)+\nabla\cdot(k\bar{\mathbf{v}})=2\nu_k\|\bar{\mathbf{D}}\|^2+\nabla\cdot(\nu_k\nabla k)-c_\varepsilon k^{3/2}/\Delta, \quad (3)$$

where $\varepsilon=c_\varepsilon k^{3/2}/\Delta$ is the subgrid dissipation, [1]. The model coefficients $c_k=0.07$ and $c_\varepsilon=1.03$ are obtained from an expected inertial sub-range behaviour. To alleviate the extreme resolution requirements close to the hull the subgrid model is adjusted as the hull is approached. More precisely, adjacent to the hull the total viscosity, $\nu+\nu_k$, is replaced by $\tau_w/(\partial v_y/\partial y)|_w$, in which τ_w has been computed from an assumed log-law behavior of the velocity.

3. Numerical Methods

The governing equations (2) and (3) are here discretized using an unstructured collocated Finite Volume (FV) method based on the OpenFoam C++ library, [22]. The dependent variables are re-presented by control volume averages $f_P=\frac{1}{\delta V_P}\int_{\Omega_P}f(\mathbf{x},t)dV$, formally defining the spatial filtering in (2), and by using Reynolds transport theorem together with a multi-step time integration procedure the LES equations (2) can be discretized, resulting in,

$$\begin{cases}\frac{\beta_i\Delta t}{\delta V_P}\sum_f[\,\mathbf{F}_f^{C,\rho}\,]^{n+i}=0,\\ \sum_{i=0}^m(\alpha_i(\bar{\rho}\bar{\mathbf{v}})_P^{n+i}+\frac{\beta_i\Delta t}{\delta V_P}\sum_f[\,\mathbf{F}_f^{C,v}+\mathbf{F}_f^{D,v}+\mathbf{F}_f^{B,v}\,]^{n+i})=\\ \qquad -\beta_i(\nabla\bar{p})_P^{n+i}\Delta t+\beta_i(\bar{\mathbf{f}})_P^{n+i}\Delta t,\\ \sum_{i=0}^m(\alpha_i(\alpha)_P^{n+i}+\frac{\beta_i\Delta t}{\delta V_P}\sum_f[\,\mathbf{F}_f^{C,\alpha}\,]^{n+i})=0,\end{cases} \quad (4)$$

where m, α_i and β_i are parameters of the multi-step time-integration scheme whereas $\mathbf{F}_f^{C,\rho}=(\bar{\mathbf{v}}\cdot d\mathbf{A})_f$, $\mathbf{F}_f^{C,v}=(\bar{\mathbf{v}}\cdot d\mathbf{A})_f\bar{\mathbf{v}}_f$, $\mathbf{F}_f^{D,v}=(\nu\nabla\bar{\mathbf{v}})_f d\mathbf{A}$, $\mathbf{F}_f^{C,\alpha}=(\bar{\mathbf{v}}\cdot d\mathbf{A})_f\bar{\alpha}_f$ as well as $\mathbf{F}_f^{B,v}=(\mathbf{B})_f d\mathbf{A}$ and $\mathbf{F}_f^{b,\alpha}=(\mathbf{b})_f\cdot d\mathbf{A}$ are the fluxes. To close the FV-discretization the fluxes (at face f) need to be reconstructed from the variables at neighboring cells. Linear *interpolation* is used for the convective terms in the momentum equation and linear *approximations* are used to evaluate the inner derivatives in the viscous and subgrid fluxes. For the momentum equation this results in second order accurate schemes, respectively, whereas a specific treatment is used to handle the reconstruction of the fluxes in the α-equation, since the interface is required to be as sharp as possible. The pressure velocity system is here decoupled by combining (4_1) and (4_2) into a Poisson equation for $\bar{p}$ that is solved together with (4_2) and (4_3) using a PISO (Pressure Implicit with Splitting of Operators) algorithm with a modified Rhie & Chow interpolation for cell-centered data, [23]. The equations are solved sequentially with iteration over the coupling terms to obtain rapid convergence. The convective fluxes of the α-equation (4_3) are recon-

structed using a novel flux reconstruction formulation $F_f^{C,\alpha} \approx [F_f^{C,\rho}\alpha_f^{R1} + |F_f^{C,\rho}|/|d\mathbf{A}_f|\mathbf{n}(1-\alpha_f^{R2})\alpha_f^{R2}]$, in which **n** is the unit normal vector to α, and the superscripts R1 and R2 denotes two different flux reconstruction algorithms. For the simulations presented here the two flux reconstruction schemes R1 and R2 are chosen to be the conventional bounded linear scheme and the van-Leer scheme, respectively.

4. The DTMB 5415 Surface Combatant Model

The case under consideration the bare hull version of the DTMB 5415 or INSEAN 2340 model hull, [12-14, 24], as shown in figure 1. A unique aspect of this hull is that is has been used in a collaborative effort between David Taylor Model Basin, Iowa Institute of Hydraulic Research, and the Italian Ship Model Basin in order to obtain a complete data set at various conditions and to provide information on facility biases as there were repeated runs between the facilities, [24]. Here, the DTMB 5415 hull, figure 1, with a length of L=5.72 m is sunk and trimmed by amounts given from the experiment and was run straight ahead at a speed of 4.0 knots (2.06 m/s) for a corresponding model scale Re number of 12 million, based on L and a Fr number of 0.277. The computational domain has an overall length of 4L and an overall width of 4L, including the external sponge region of width L, with the hull positioned at y/L=0.0, with the forward perpendicular at x/L=1.0 downstream of the inlet plane. The height of the computational domain is 2.5L, with the nominal free water surface being located 2.0L above the lower computational boundary. Representative physical values for densities and viscosities are selected for water and air.

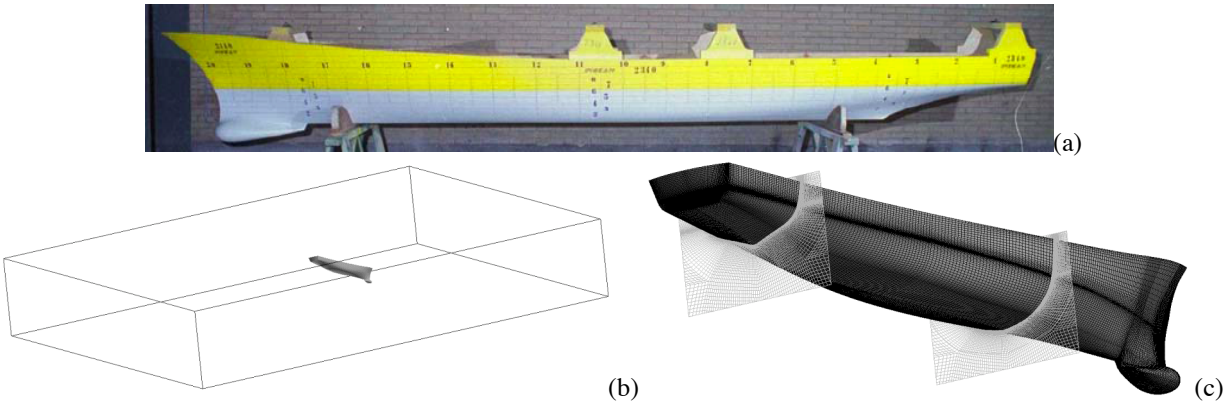

Figure 1. DTMB 5415 surface combatant model. (a) DTMB 5415 model from [25], (b) overview of computational domain and (c) typical surface and volumetric grid.

Table 1 summarize the different computations performed, including grids, subgrid models and numerical features. Two multi-block structured grids of 7.2 and 57.6 million hexahedral control volumes have been generated in order to analyze the sensitivity of the LES predictions to the grid size. Both grids have the same topology, with most of the cells concentrated in the inner do-main of size 2L by 2L, which is surrounded by a sponge region of size L in which the grid resolution is successively coarsened towards the boundaries. The velocity and undisturbed free surface location are prescribed on the inflow plane, and at the outflow Neumann conditions are used for all quantities except the pressure, which is set to a constant value. On the hull, no-slip conditions are used, as facilitated by the use of subgrid wall models. A uniform velocity, a constant pressure and the domain divided into air and water through the α–field serves as initial conditions.

Table 1. Calculations performed for the DTMB5415/INSEAN 2340 model hull.

Case	*Conditions*	*Grid*	*CFD model*	*SGS model*	*Numerics*
1	Full hull	7.2	LES	MM+wall model	2nd CD+VoF
2	Full hull	57.6	LES	MM+wall model	2nd CD+VoF

5. Results for the Surface Combatant Model DTMB 5415/INSEAN 2340

Figure 2 presents the flow beneath the DTMB 5415 hull in terms of vortical structures, represented by iso-surfaces of the second invariant of the velocity gradient, and contours of the axial velocity at eight cross-sections. The flow at the bow has a large downward component on each side of the bow, growing in size and strength as it is advected downstream whilst interacting with the hull boundary layer. At the edge of the sonar dome this results in a counter-rotating bow dome vortex pair detaching from the trailing tip of the sonar dome, and becomes enhanced by the inward and downward flow over the forward bilge after

which it continues downstream beneath hull close to the keel at some distance from the hull. Furthermore, the flow over the upper part of the sonar dome and lower part of the bow, roll-up and form a strong vortex on each side of the keel, the so-called bilge vortex that is partially located within the hull boundary layer and further away from the keel. While the sonar dome vortex pair is relatively stable, the bilge vortex system is unsteady as it interacts with the evolving hull boundary layer, resulting in new vortical structures, whilst being advected downstream. Towards the transom stern, the hull boundary layer thickens, and the bilge vortex system partly detaches from the hull boundary layer and becoming rounder and weaker, as well as giving birth to multiple vortices. The sonar dome vortex pair is less affected by the pressure difference due to the transom stern and is therefore also less vertically deflected.

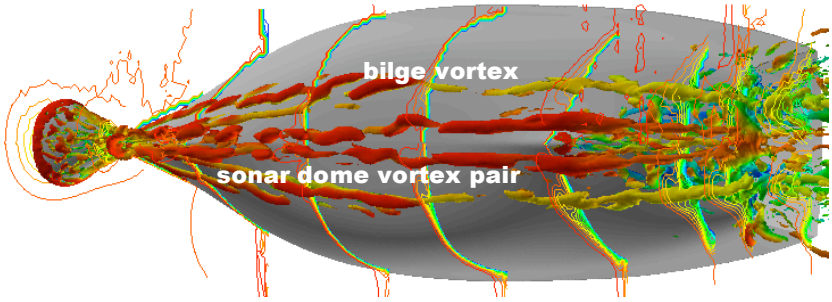

Figure 3. Instantaneous flow structures beneath the hull in terms of iso-contours of the second invariant of the velocity gradient together and velocity contours in cross-planes from the fine grid LES.

In figure 3 we compare predicted and measured stereoscopic views of the wave pattern to get an overview of the wave pattern developing around the DTMB 5415 hull and to obtain a first assessment of the predictive capabilities of the LES model. Wave crests form along the Kelvin envelope at 18.35º, close to the theoretically estimated value of 18.28º, [26]. The predicted amplitude of all wave crests, however, seems to be somewhat underpredicted, but this may also be related to the value of α used to represent the interface, and the amount of foam produced along the crests and valleys. The transverse stern (or Kelvin) waves are equally well predicted, as is the so-called initial spreading region, just behind the transom stern, and the interactions between the diverging and transverse waves. An interesting feature of the wave pattern captured by the LES is the decrease in wave elevation along the midship section inside of the Kelvin envelope with its associated wave crests and valleys. A reason for underpredicting the wave elevation may be that the bow-wave at Fr≈0.28 is only 0.12 m high, as compared to the length of the hull which is 5.70 m. The resolution of the wave pattern requires a rather fine computational grid, in all three directions, in the region of the Kelvin waves, which covers largely the entire computational domain. Some smearing of the diverging and transverse waves, due to numerical diffusion, can be observed.

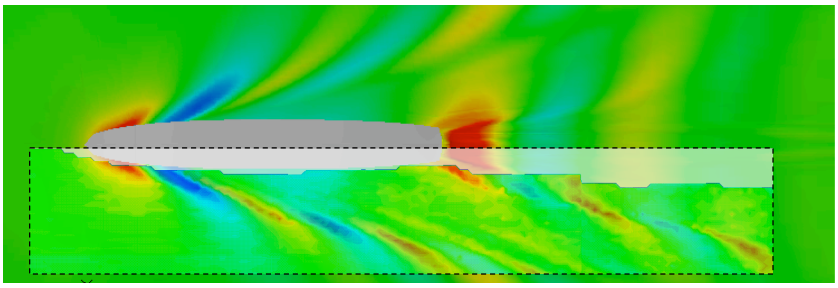

Figure 3. Comparison of computed and predicted free-surface elevation as a steroscopic view with the experimental data superimposed below from the fine grid LES.

In figure 4 we show time-averaged axial velocity, $\langle \overline{v}_x \rangle$, profiles along the hull at x/L=0.2, 0.4, 0.6, 0.8, 0.935 and 1.2 from the measurements [12] and the LES. Comparing predicted and measured $\langle \overline{v}_x \rangle$ contours shows good qualitative and quantitative agreement, with the most peculiar flow features well represented both experimentally and computationally. The flow past the sonar dome give rise to high cross flow, in particular close to the keel, which in turn create the rotating streamwise sonar dome vortex pair upstream of x/L=0.2. At x/L=0.4 the vortex motion from to this sonar dome vortex pair results in that a patch of low momentum fluid is lifted away from the hull boundary layer, thickening the boundary layer. Close to x/L=0.2 a bilge vortex, rotating in the same direction as the sonar dome vortex, develops on the upper side of the sonar do me. This bilge vortex develops substantially between x/L=0.2 and

0,6, as can be seen in figure 2, and results in the low speed regions near the girth-length at x/L=0.4 and 0.6. At x/L=0.8, the $\langle \overline{v}_x \rangle$ contours indicates a wider low speed region due to the unsteady nature of the bilge vortex, which in turn creates new vortex structures, cf. figure 2. Furthermore, the boundary layer thickens, and its shape manifests a well-known feature, developing a bulge around girth-length. Between x/L=0.8 and 0.935 the two vortex systems combine and result in a complicated $\langle \overline{v}_x \rangle$ distribution, with a low-speed streak found close to the air-water interface as indicated already by the color of the air-water interface in figure 3. Further downstream, at x/L=1.2, two weak but large and unsteady, longitudinal counter-rotating vortices have developed, being somewhat further apart in the LES predictions than in the experimental data.

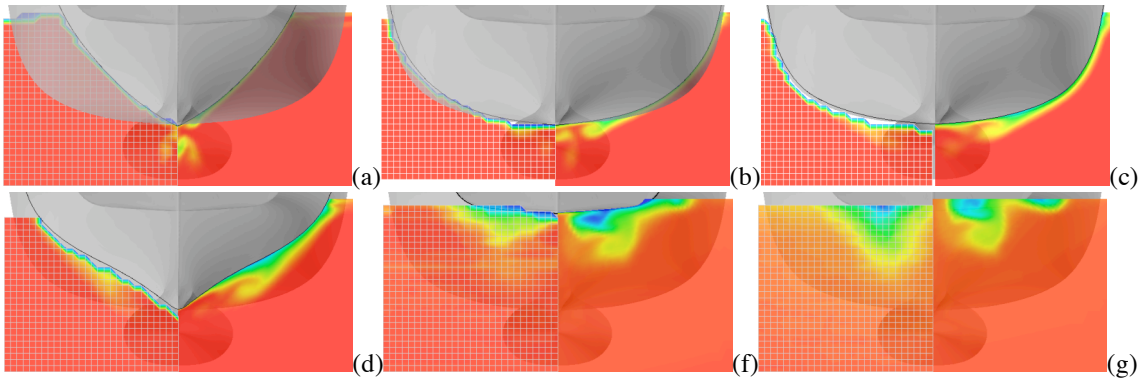

Figure 4. Comparison of the predicted and measured mean axial velocity components at x/L=0.2, 0.4, 0.6, 0.8, 0.935 and 1.2 along the hull. Experimental data is obtained from [18] and is presented to the left together with the measurement grid whereas the fine grid LES results are presented to the right.

Figures 5a, 5b and 5c show wave cuts at fixed distances y/L=0.096, 0.172 and 0.324 from the hull centerline for both the coarse and fine grid LES and the experimental data. At all cross-sections the wave profile predictions agree reasonably well with the experiments but are missing some crests and troughs as indicated already in figure 3. Best agreement between LES predictions and experimental data is obtained close to the hull at x/L=0.096, whereas further away from the hull the accuracy of the predictions decreases, in particular with respect to wave amplitude and wave profile sharpness. One reason for this is that the grid is probably not sufficiently fine in this region to allow these wave profiles to be sufficiently well resolved. An additional factor may be that the numerical algorithm used to capture the air-water interface is not sufficiently accurate. It is well known that this is a challenging aspect of such simulations, and it is not obvious wheather LES will simplify this issue. The accuracy of these predictions are however comparable with the results from the Gothenburg 2000 workshop, [14], where advanced RANS models were used together with different interface capturing methods.

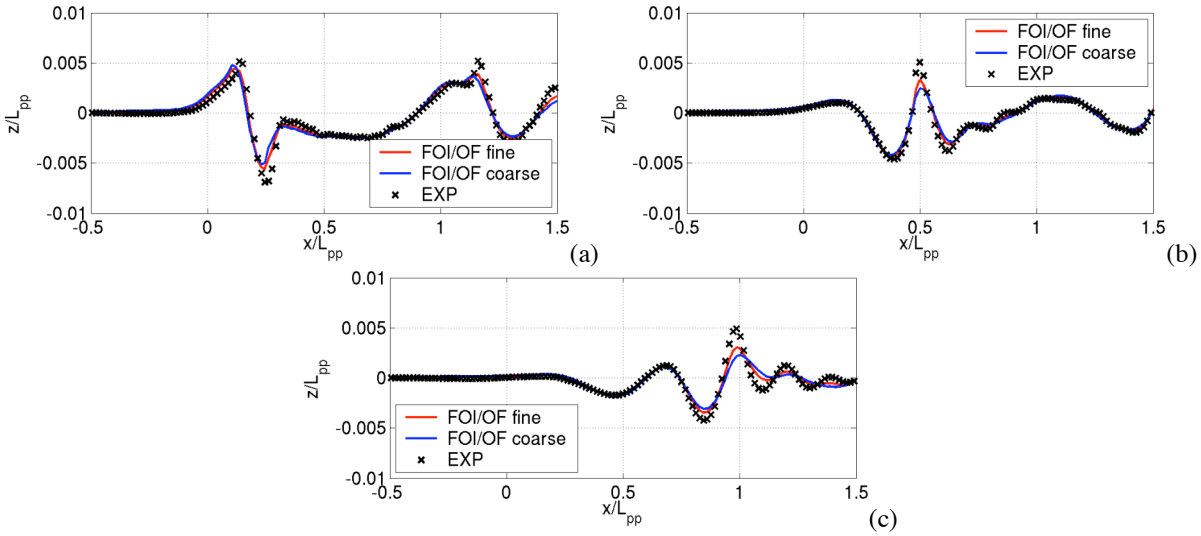

Figure 5. Comparison of the computed and predicted free-surface elevation as wave cuts at different distances from the hull at (b) y/L=0.096, (c) y/L=0.172 and (d) y/L=0.324 from both LES.

6. Concluding Remarks

LES has been applied to study the flow past the DTMB 5415 surface combatant model under the experimentally investigated conditions $Re=12\cdot10^6$ and Fr=0.277. Comparisons between predicted wave profiles and velocity contours at different cross-section beneath the hull have been performed to assess the accuracy of the LES model. In addition have the LES results been used to elucidate the flow underneath the hull and in some aspects also the wave pattern developing around the hull. The predicted flow agrees very well with the experimental results, and suggests a more complicated flow pattern than previously described. In particular do we find that several vortex systems interact with each other to form the observed velocity distributions beneath the hull. The vortex interactions appears to be unsteady and are presumably driven by helical shear layer instabilities developing at the outer edges of these vortical structures. The wave pattern is also in reasonable agreement with the experimentally measured wave field. We find however an underprediction of the wave amplitudes. This is likely to be the result of a somewhat too coarse grid and an interface capturing scheme that requires improvement to provide good predictions on computational grids of less than optimal quality.

References

[1] Sagaut P.; 2001, "Large Eddy Simulation for Incompressible Flows", Springer Verlag.

[2] Grinstein F.F., Margolin L. & Rider B.; 2007, "Implicit Large Eddy Simulation: Computing Turbulent Fluid Dynamics", Cambridge University Press.

[3] Fureby C.; 2008, "Towards Large Eddy Simulation in Engineering", Prog. Aerospace Science, **44**, p 381.

[4] Fureby C.; 2008, "Large Eddy Simulation of Ship Hydrodynamics", 27th Symp. on Naval Hydrodynamics, Seoul, Korea.

[5] Larsson L. & Baba E.; 1996, "Ship Resistance and Flow Computations", In Advances in Marine Hydrodynamics, Comp. Mech. Publ. Boston, USA.

[6] Wilcox D.C.; 1998, "Turbulence Modelling for CFD", DCW Industries.

[7] Paterson E., Hyman M., Stern F., Bonetto F., Drew D., & Lahey R.; 1996, "Near and Farfield CFD for a Naval Combatant including Thermal Stratification and Two-fluid Modeling", 21st Symp. on Naval Hydrodynamics, Trondheim, Norway, p 102.

[8] Gorski J., Miller R.W. & Coleman R.M.; 2004, "An Investigation of Propeller Inflow for Naval Surface Combatants", 25th Symp. on Naval Hydrodynamics, St. Johns, Canada, Vol. 2, p 151.

[9] Nikitin N.V., Nicoud F. Wasistho B. Squires K.D. & Spalart P.R.; 2000, "An Approach to Wall Modeling in Large Eddy Simulation", Phys. Fluids, **12**, p. 1629.

[10] Yang J. Bhushan S., Suh J.S., Wang Z., Koo B., Sakamoto N., Xing T. & Stern F.; 2008, "Large Eddy Simulation of Ship Flows with Wall Layer Models on Cartesian Grids", 27th Symp. on Naval Hydrodynamics, Seoul, Korea.

[11] Alin N., Fureby C., Parmhed O. & Svennberg U.; 2008, "Large Eddy Simulation Past the DTMB 5415 Hull", 27th Symposium on Naval Hydrodynamics, p 217.

[12] Olivieri A., Pistani F., Avanzini A., Stern F., & Penna, R.; 2001, "Towing Tank Experiments of Resistance, Sinkage and Trim, Boundary Layer, Wake, and Free Surface Flow Around a Naval Combatant INSEAN 2340 Model", IIHR Report No. 421, Iowa Institute of Hydraulic Research, University of Iowa, USA.

[13] Longo J., Shao J., Irvine M., & Stern F.; 2007, "Phase-Averaged PIV for the Nominal Wake of a Surface Ship in Head Waves", J. Fluids Eng., **129**, p 524.

[14] Larsson L., Stern F. & Bertram V.; 2003, "Benchmarking of Computational Fluid Dynamics for Ship Flows: The Gothenburg 2000 Workshop", J. Ship Res., **47**, p 63.

[15] Gurtin M.. E.; 1981, "An Introduction to Continuum Mechanics", Academic Press, Orlando.

[16] Ubbink O.; 1997, "Numerical Prediction of Two Fluid Systems with Sharp Interfaces", PhD Thesis, London University.

[17] Hirt C.W. & Nichols B.D.; 1981, "Volume of Fluid (VOF) Method for the Dynamics of Free Boundaries", J. Comp. Phys., **39**, p 201.

[18] Ubbink O.; 1997, "Numerical Prediction of Two Fluid Systems with Sharp Interfaces", PhD Thesis, London University.

[19] Pope, S.B.; 2000, "Turbulent Flows", Cambridge University Press.

[20] Bardina J., Ferziger J.H. & Reynolds W.C.; 1980, "Improved Subgrid Scale Models for Large Eddy Simulations", AIAA Paper 80-1357.

[21] Bensow R. & Fureby C., 2007, "On the Justification and Extension of Mixed Models in LES", J Turb. **8**, N54 .

[22] Weller H.G., Tabor G., Jasak H. & Fureby C.; 1997, "A Tensorial Approach to CFD using Object Oriented Techniques", Comp. in Physics, **12**, p 629.

[23] Issa R.I.; 1986, "Solution of the Implicitly Discretized Fluid Flow Equations by Operator Splitting", J. Comp. Phys., **62**, p 40.

[24] Stern F., Longo J., Penna R., Olivieri A., Ratcliffe T., & Coleman H.; 2000, "International Collaboration on Benchmark CFD Validation Data for Surface Combatant DTMB Model 5415", 23rd Symp. on Naval Hydrodynamics, Val de Reuil, France.

[25] http://www.dt.navy.mil/hyd/sur-shi-mod/index.html

[26] Maver K. & Podgornik R.; 2004, "Kelvin Ship Waves", Report, Faculty for Mathematics and Physics, Department of Physics, University of Ljubljana, Croatia.

CFD SIMULATION OF KCS SAILING IN REGULAR HEAD WAVES

Claus D. Simonsen (FORCE Technology, Denmark)
Fredrick Stern (IIHR, University of Iowa, USA)

1. SUMMARY

The KCS container ship is investigated in regular head seas by means CFD. The CFD study was conducted using the RANS code CFDSHIP-IOWA. The ship was sailing at service speed in a wave corresponding to resonance condition. The heave and pitch motions and the resistance have been computed. The results show that the ship responds strongly, when the resonance condition is met. The computation shows a very complex and time varying flow pattern. With respect to the integral quantities, a comparison between EFD and CFD shows that the computed heave and pitch motions are in fair agreement with the measurement. For the resistance the mean value is predicted reasonably well, but the first order amplitude of the resistance time history is significantly under predicted by the computation. Possible reasons may be difference in the towing setup between the experiment and the CFD simulation and grid resolution.

2. INTRODUCTION

Over the past years IIHR and FORCE Technology have worked together on projects related to RANS simulations of ships in maneuvering conditions in calm water. However, since many maneuvers are done in waves it is interesting to investigate if CFD simulation can be used for this purpose. Instead of doing complex maneuvers in waves, it was decided to start with a simpler case with a ship sailing in head seas. The work is based on the KCS container ship, Fig. 1, which besides being one of the benchmark ships for G2010 also is one of the benchmark ships used within the maneuvering community. The number of RANS based CFD and EFD studies of ships sailing in waves are quite limited. Examples of CFD calculations are found in Simonsen et al. (2010), Carrica et al. (2007) and Weymouth et al. (2005) who performed simulations of ships sailing in regular head seas. For EFD Irvine et al. (2008), O'Dea et al. (1992) and Otzen and Simonsen (2008) present heave and pitch results including uncertainty assessment for ships sailing in head waves.
The flow in this work is calculated by means of URANS solver CFDSHIP-IOWA and the motions of the ship are solved for in heave and pitch by a 6 DOF module, which is implemented in the RANS code.

3. GEOMETRY AND CONDITIONS

Fig. 1 KCS container ship geometry.

The appended hull of the 230m KCS container ship, Fig. 1, is considered in model scale 1:52.667, which gives a model length of L_{PP} =4.3671m. The ship is considered at a speed corresponding to service speed of 24 knots which corresponds to a Froude number of 0.26. In model scale the speed is U_0=1.701m/s and the Reynolds number Re=6.517·106. The wave parameters, Table 1, are chosen in order to have a resonance condition where the frequency of encounter $f_e = \sqrt{g/(2\pi\lambda)} + U_0/\lambda$ is close to the natural frequency of the ship in heave and pitch, f_n≈0.9 Hz.

Table 1 Wave condition considered in calculation.

Test in Regular Head Waves				
Froude number	wave/ship length	Steepness λ/H	Height H [m]	Encounter frequency [Hz]
0.26	1.15	60	0.084	0.90

4. COMPUTATIONAL METHOD, GRIDS, SIMULATED CONDITIONS AND VERIFICATION APPROACH

CFDSHIP-IOWA is an unsteady general-purpose, multi block, parallel computing URANS code, which models the free surface by the single-phase level set method. It solves the continuity equation and the unsteady RANS equations, which are derived and solved in absolute inertial earth-fixed coordinates (X,Y,Z) for an arbitrary moving and non-deforming control volume and solution domain, respectively.
The method works in the following way: The flow field is solved and the forces and moments acting on the ship are calculated in the earth-fixed coordinate system. Then the forces and moments are transformed into a non-inertial ship-fixed coordinate system, which has its origin O in the ships center of gravity. Here the equations of motion are solved to find the ship's translational and angular velocities. These velocities are then transformed back to the earth-fixed coordinate system where they are integrated to find the new position of the ship and grid system. The complete grid

system is moved after each time step. The positions are corrected during the inner iterations until convergence of the motion is obtained. For the present simulation minimum 5 inner iterations are applied on each time step. The non-dimensional time step is set to Δt=0.005, which gives 85 time steps per period of encounter. The isotropic blended k-ω/k-ε SST turbulence model without wall functions is used. The code is based on finite differences and applies 2nd order upwind differences for convective terms and central differences for diffusive terms. Temporal discretization is done with a 2nd order backward difference scheme. Pressure and velocities are coupled via the PISO method. Finally, the governing equations are non-dimensionalized with U_0, ρ, μ and L_{pp} and transformed into non-orthogonal curvilinear coordinates. More details can be found in Carrica et al. (2007) and Xing et al. (2008).

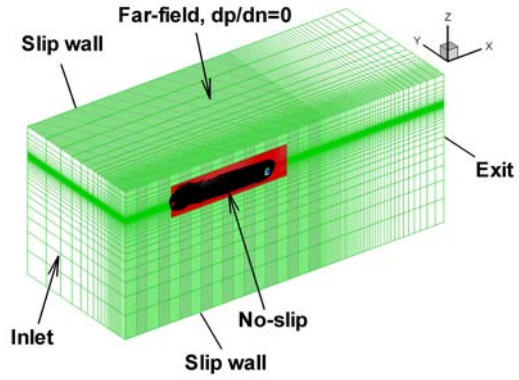

Fig. 2 Chimera Grid applied in CFDSHIP-IOWA. Only starboard side mesh is shown.

CFDSHIP-IOWA uses overset multi block chimera grids generated with Gridgen and dynamically overset with Suggar, Noack (2005). The applied grid consists of 8 blocks and 4,351,785 cells, Fig. 2. In the wave zone the incoming waves are resolved with 100 points per wave length and 10 points for the wave height. For the present application different parts of the domain moves with different degrees of freedom. All blocks are translated with the ship speed in surge. But, the rudder and hull domains are also moving in heave and pitch to capture the wave induced motions. This approach maintains the fine grid resolution in the wave region and hereby helps carrying the wave through the domain without too much dissipation.

For boundary conditions, a no-slip condition is applied on the hull and rudder surfaces, Fig. 3. The velocity on these surfaces corresponds to the calculated velocity of the ship. Due to application of turbulence modelling without wall functions the near wall spacing is designed so the wall distance equals $Y^+ \approx 1$.

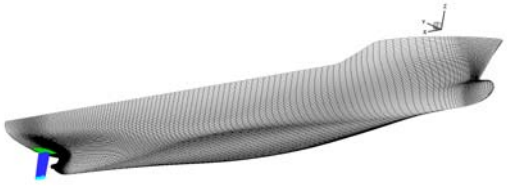

Fig. 3 Surface mesh on hull and rudder.

The outer boundaries upstream, next to and behind the ship are located within distances of approximately 0.6, 1.5 and 2.0 ship lengths from the ship, respectively. The width and depth of the domain match the dimension of the towing tank where the data for validation was measured. The inlet boundary condition describes the regular incoming wave in order to prescribe the wave elevation ζ, the inlet velocities (u, v, w) and the pressure p. Finally, free stream turbulence for k and ω is set to 10^{-7} and 9, respectively. On the sides and on the bottom of the domain, an impermeable slip surface condition is applied. Behind the ship a zero-gradient exit condition is applied for all variables and finally on the top of the domain a zero pressure gradient condition is applied.

For the verification the grid study was conducted without rudder since it was not possible to obtain valid interpolation stencils for the overlapping meshes in the rudder region for the coarser grids. However, for the overall integral quantities it is assumed that the bare hull model gives results that are representative for the appended hull case. With a refinement ratio of $r_G = \sqrt[4]{2}$ the applied fine, medium and coarse grids consist of 3,768,044, 2,502,605 and 1,762,189 points, respectively. To be able to carry the wave through the domain all three grids use the same fine background grid.

In the verification, the following have been investigated: Statistical convergence, time step, sensitivity to location of the vertical position of the centre of gravity and grid size. Statistical convergence is investigated based on running means of the time series while sensitivity of time step and center of gravity are studied based on small changes in these quantities. The grid uncertainty U_G is estimated based on method in Stern et al. (2001), Wilson et al. (2004) and Xing and Stern (2008), where U_G is estimated based on three systematically refined grids and factors of safety are used to include the proximity to the asymptotic range in the estimate.

To estimate the grid uncertainty the above verification approach was applied to the considered quantity at each time step, for instance if F_X is calculated at t=0,

$t=t_1$, $t=t_2$ etc., then for each time step it is decided whether grid convergence, oscillatory convergence or divergence is obtained and the uncertainty is estimated if possible. However, as will be shown later a mix of converging, oscillatory and diverging conditions were found. One of the reasons is that the applied refinement ratio is fairly small, which means that the changes between solutions get small. This influences the convergence ratio, which sometimes becomes ill-defined in cases where the solution changes go to zero. Finally, for the time step study, the time step was set to half the size used for the grid study. To study the vertical position of the center of gravity, the position was changed 30% of the draft. The two latter investigations were done with the coarse grid. The results of the verification are described below.

5. RESULTS FOR CFD

The CFD study covers verification of the numerical method, a comparison of CFD and EFD quantities and a brief discussion of the flow field around the model.

5.1 Flow field

Fig. 4 shows the incoming regular wave and the waves generated by the ship. At t/T_e=0 the bow is deeply submerged in the wave and the flare of the ship generates a wave on top of the incoming wave. As the wave moves on, t/T_e=1/4, the bow starts to come out of the water again and the wave formation is reduced in this region.

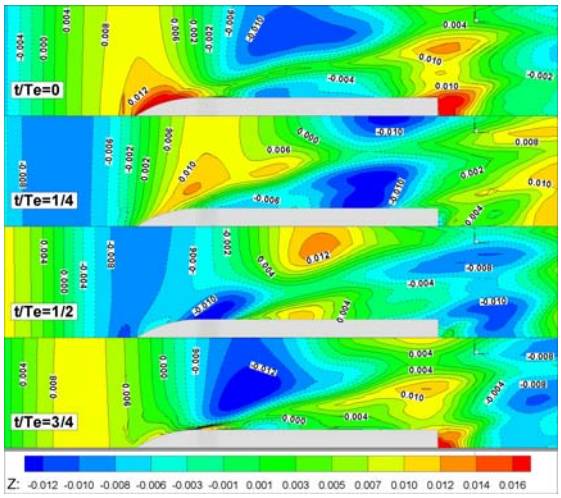

Fig. 4 Free surface elevations over one period of encounter, T_e.

At t/T_e=1/2 the bow reaches the wave trough and most of the fore ship comes out of the water, which reduces the wave making of the ship. Next the new wave is coming in towards the bow, t/T_e=3/4, which starts to dive into the wave where the flared shape again starts to generate waves around the fore body. As t/T_e=1 is reached the periodic behavior of problem leads to a wave pattern similar to t/T_e=0.

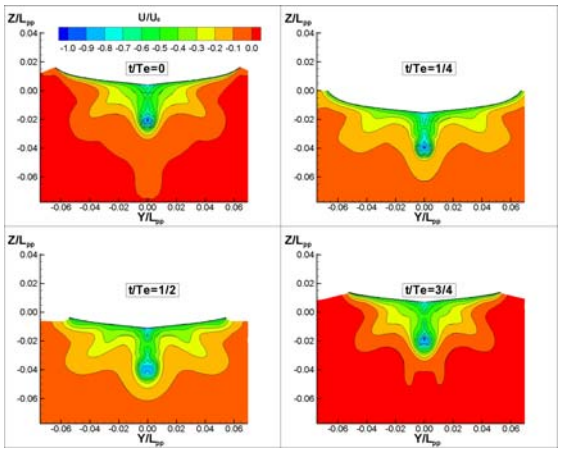

Fig. 5 Axial velocity contours at propeller plane over one period of encounter, T_e.

Fig. 5 shows the axial velocity contours at AP. The wake field behind a ship in waves is more complex than in calm water. The figure shows that the combination of the ship motion and the wave changes the shape of the wake field throughout the period of encounter. The resulting wake contours are “squeezed” towards the hull and centre plane as the wave crest passes, while the contours are “expanding” when the water retrieves in the wave trough. The complex wake field is a combination of the normal wake deficit behind the ship, the orbital velocities in the wave and the relatively strong fluctuations in the stern region pressure.

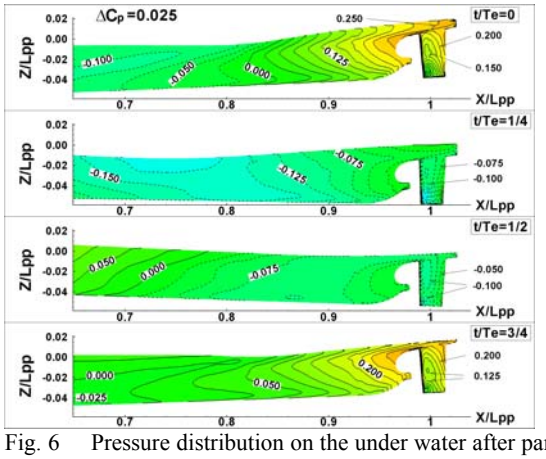

Fig. 6 Pressure distribution on the under water after part of the hull over one period of encounter, T_e.

Figs 6 and 7 show the pressure distribution on the wetted part of the stern and bow, respectively. In the stern it is characteristic that the pressure increases

when the wave crest passes, while it decreases in the trough. In the bow the pressure variations over the period of encounter are also significant. The pressure increases, primarily due to stagnation, when the bow dives into the wave. The result of the large changes in pressure and wetted surface area is reflected in the resistance, which varies significantly through out the period of encounter. This is discussed later.

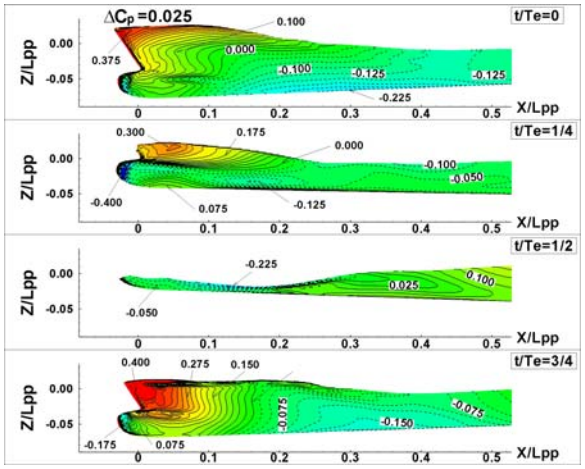

Fig. 7 Pressure distribution on the underwater fore-part of the hull over one period of encounter, T_e.

5.2 Verification of integral quantities

The computational method was verified based on three systematically refined grids. Figs 8 to 10 show time series and running mean for heave, pitch and resistance. Latter is non-dimensionalized with ρ, U and S. The verification gives a combination of converging, oscillatory and diverging conditions through time.

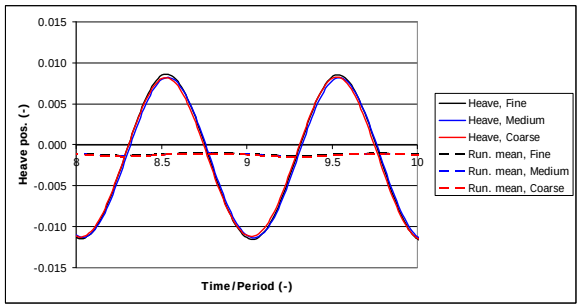

Fig. 8 Calculated heave position from grid study. Time is non-dimensionalized with period of encounter.

This may be explained by the relatively small changes between grids caused by the small refinement ratio. Consequently, it is not possible to use Richardson extrapolation, to estimate the grid uncertainty. Instead the maximum change between grids Δ_G over the considered period of time is used. The results are summarized in Table 2.

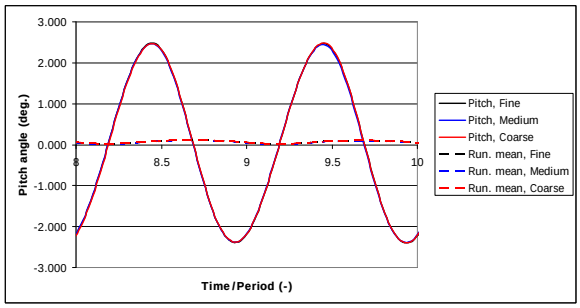

Fig. 9 Calculated pitch angle from grid study.

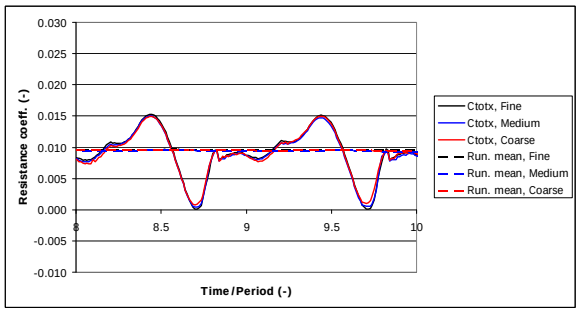

Fig. 10 Calculated resistance coeff. from grid study.

Table 2 Grid uncertainty and statistical convergence.

	Heave	Pitch	Resist.
Δ_G	0.00089	0.0645	0.00028
Δ_{SC}	0.00038	0.0901	0.00022
Δ_G / S_U [%]	10.3	2.6	1.5
Δ_{SC} / S_U [%]	4.4	3.6	1.4

The statistical convergence represented by Δ_{SC} in Table 2 is found as the difference between the maximum and minimum values running mean envelope. Δ_G and Δ_{SC} are of the same order of magnitude.

The grid study was done with dt=0.005. The time step check was run with dt=0.0025. Fig. 11 shows the calculated pitch angle with dt=0.005 and dt=0.0025. The amplitudes are slightly reduced, while the phase seems to be the same. Same thing is observed for heave and resistance.

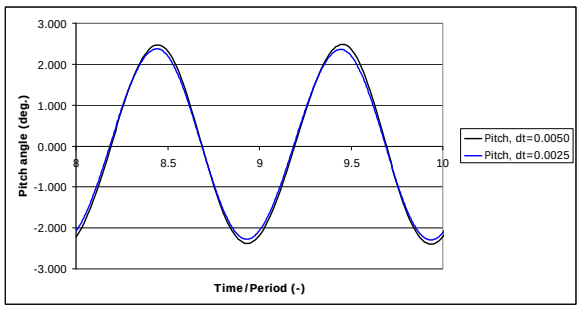

Fig. 11 Pitch angle calculated with different time steps.

The sensitivity of the position of the VCG was studied by moving VCG upwards as described earlier. Fig. 12 shows the calculated pitch angle and it is seen that the effect is very limited. Same is observed for heave and resistance.

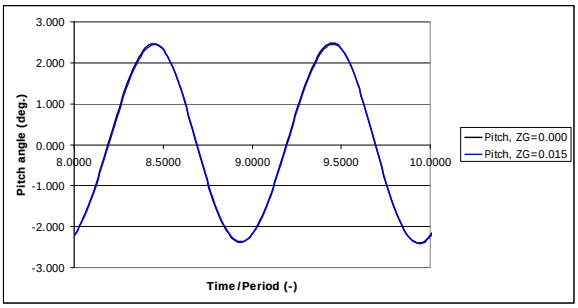

Fig. 12 Pitch angle calculated with different VCG.

5.3 Discussion of forces and moments

The integral quantities are presented in terms of time series, zero order coefficients, i.e. average levels, first order coefficients and phases for heave, pitch and resistance signals. All quantities are given in earth fixed coordinates. Concerning wave height, it should be noted that the CFD calculation was done with the nominal wave height of H=84mm from the test program, but the wave for the measured wave ended up being slightly different, namely H=82.55mm. This will influence the comparison between EFD and CFD, but the calculation was done before the model test and due to time limitations calculations could not be redone.

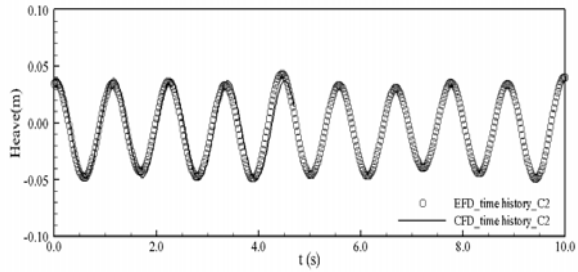

Fig. 13 Heave position. EFD and CFD.

Figs 13 to 15 show the time series for heave, pitch and resistance, respectively. Both computed heave and pitch signals are in quite good agreement with the measurement. Though, a small phase shift between EFD and CFD are observed for both cases and the pitch amplitude seems to be slightly over predicted by CFD.

The comparison between the measured and calculated resistance signal is worse. In Fig. 15 it is observed that signals form EFD and CFD are quite different. The mean levels are approximately the same, but the amplitudes are much higher in the experiment.

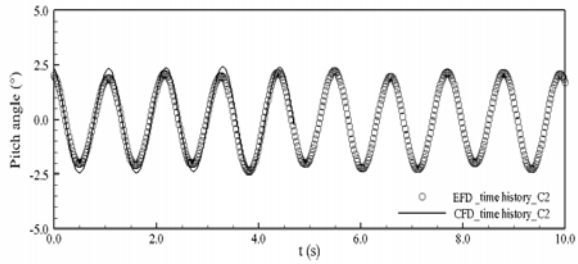

Fig. 14 Pitch angle. EFD and CFD.

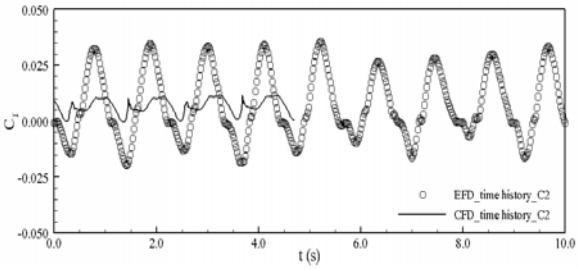

Fig. 15 Resistance coefficient. EFD and CFD.

To quantify the comparison between EFD and CFD the time series were analyzed with Fast Fourier Transformation. The mean levels and first order amplitudes are shown in Table 3 for heave, pitch and resistance coefficients, respectively, while the phase angles between the incoming wave and the heave, pitch and resistance signals are shown in Table 4.

Table 3 Fourier coefficients. EFD and CFD

	Mean Heave [mm]	1st Amplitude Heave [mm]
EFD	5.436	39.544
CFD	5.714	43.541
E % EFD	-5.1	-10.1
	Mean Pitch [deg]	1st Amplitude Pitch [deg]
EFD	0.064	2.095
CFD	-0.028	2.389
E % EFD	143.4	-14.0
	Mean Resistance [-]	1st Amplitude Resistance [-]
EFD	0.00716	0.02043
CFD	0.00676	0.00361
E % EFD	5.6	82.3

The tables show the same as the time series did, namely fair agreement between EFD and CFD for heave and pitch, over prediction of the resistance amplitude. Finally, the phase shifts between EFD and CFD can also be observed in Table 4.

Table 4 1st order phase shifts relative to wave.

	1st phase heave (deg/s)	1st phase pitch (deg/s)	1st phase resistance (deg/s)
EFD	-20.57	8.49	81.87
CFD	-11.35	22.98	77.89

The reason for the large difference in the amplitude could be found in the way the model is towed. In the experiment, the model is mounted in two posts. The system is not completely stiff, so the ship may surge a little when it moves through the waves, so the system will act like being towed in a spring. In the CFD setup, the model is towed in an ideal stiff setup, which means that the model is towed through the waves without any flexibility. The result could be that the shape of the time series for the resistance obtained with the different systems could be different and that the signals therefore cannot be directly compared at a given instant of time.

5. CONCLUDING REMARKS

In the present work the KCS container ship is investigated in regular head seas by means of CFD. The CFD study including verification was conducted using the RANS code CFDSHIP-IOWA. A study of the flow field reveals a quite complex time varying flow pattern caused by the combination of the incoming waves, the ship motions and the hull form. With respect to the comparison between the motions and forces from EFD and CFD, reasonable good agreement is found for heave and pitch motions. For the resistance the mean resistance or 0th harmonic in waves is predicted reasonably well but the first order amplitude of the resistance time series is much more difficult to capture and CFD under predicts the amplitude.

The observed deviations between measured and calculated resistance time series cannot be explained by the simulation or measurement uncertainty alone, since the uncertainty levels are quite smaller compared to the difference between the EFD and CFD data. The reason for the large difference in the amplitude is believed to be found in the way the model is towed. While the ship is towed in a stiff connection in CFD, the EFD model is mounted in a two gauge system via two trim holders. The system is not completely stiff and may allow small surge motions while the ship moves through the waves. The result is that the shape of the time series for the resistance obtained with the different systems may be different and that the signals therefore cannot be directly compared at a given instant of time.

ACKNOWLEDGEMENT

This research is sponsored by FORCE Technology, Office of Naval Research (ONR) contract N00014-07-C-0035 and grant N00014-09-1-1055 under the Naval International Cooperative Opportunities in Science and Technology Program (NICOP).

REFERENCES

Otzen, J.F. and Simonsen, C.D. (2008) "Uncertainty assessment for KCS resistance and propulsion tests in waves," FORCE Technology report no. ONRIII187 01, Lyngby, Denmark, 2008. Under preparation.

Irvine, M. Jr., Longo, J. and Stern, F. (2008) "Pitch and Heave Tests and Uncertainty Assessment for a Surface Combatant in Regular Waves," Journal of Ship Research, Vol. 52, No. 2, 2008, pp. 146-163.

O'Dea, J., Powers, E. and Zselecsky, J. (1992) "Experimental determination of non-liniarities in vertical plane ship motions," Proceedings of 19th ONR Symposium on Naval Hydrodynamics, Seoul, Korea, 1992.

Carrica, P.M., Wilson, R.W., Noack, R.W. and Stern, F. (2007) "Ship Motions using Single-Phase Level Set with Dynamic Overset Grids," Computers & Fluids, Vol. 36, 2007, pp. 1415-1433.

Xing, T., Carrica, P.M. and Stern, F. (2008) "Computational Towing Tank Procedure for Single Run Curves of Resistance and Propulsion" Journal of Fluids

Stern, F., Wilson, R.V., Coleman, H.V. and Paterson, E.G., (2001) "Comprehensive approach to verification and validation of CFD simulations-Part 1: methodology and procedures," ASME J Fluids Engineering 2001; 124(4): 793-802.

Wilson, R., Shao, J. and Stern, F., (2004) "Discussion: Criticism of the "Correction Factor" Verification Method," ASME J Fluids Engineering 2004; 126:704-706.

Xing, T. and Stern, F. "Factor of Safety for Richardson Extrapolation for Industrial Application" (2008) Journal of Fluids Engineering, Under preparation.

Simonsen, C.D. Otzen J. F. and Stern, F. (2010) "EFD and CFD for KCS heaving and pitching in regular head waves," Submitted to J. of Marine Science and Technology.

Noack, R. (2005) "SUGGAR: a general capability for mowing body overset grid assembly", AIAA paper 2005-5117, 17th AIAA Computational Fluid Dynamics Conf., Toronto, Ontario, Canada, 2005.

Weymouth, G., Wilson, R. and Stern, F., (2005) "RANS CFD predictions of pitch and heave ship motions in head seas", J. of Ship Research, 2005;49:80-97.

PREDICTION OF SHIP RESISTANCE AND SHIP MOTIONS USING RANSE

B. el Moctar[1,2], J. Kaufmann[2], J. Ley[1], J. Oberhagemann[1], V. Shigunov[2], T. Zorn[2]
([1]University Duisburg-Essen, [2]Germanischer Lloyd, Germany)

Nomenclature

B_{WL}	waterline breadth of the ship
C_T	coefficient of the total resistance
C_F	coefficient of the frictional resistance
C_P	coefficient of the pressure resistance
$\vec{F}$	force vector
Fn	Froude number
G	ship centre of mass
I_L	inertia tensor of the ship in the ship-fixed reference frame
h_w	wave height
k_{xx}	central longitudinal radius of inertia
k_{yy}	central transversal radius of inertia
k_{zz}	central transversal radius of inertia
L_{CB}	longitudinal position of the buoyancy centre
L_{pp}	length between perpendiculars
L_{WL}	length of waterline
$\vec{M}$	moment vector with respect to G
m	ship mass
Rn	Reynolds number
S	transformation matrix
S_W	water plane area
S_R	rudder area
T	draught of the ship
x,y,z	axis of the Newtonian coordinate system
z	heave motion
Δ	volume displacement of the ship
λ	wave length; model scale
$\vec{\xi}$	rotational position vector
ξ	ship-fixed reference frane
η	ship-fixed reference frane
ζ	ship-fixed reference frane
θ	pitch angle
$\vec{\omega}$	angular velocity vector

Abstract

The paper compares numerical and experimental results for calm water resistance, added resistance and motions in waves, and roll damping of various ship types in different conditions. Resistance in calm water was evaluated with and without the influence of dynamic trim and sinkage; Ship motions and added resistance were measured in regular waves; roll damping was defined from roll decay history in calm water. The numerical methods used, Comet [1] und OpenFOAM [2], are based on the solution of the Reynolds-averaged Navier-Stokes equations (RANSE) with finite-volume approach. The free surface is modelled in the both methods with a volume of fluid-like approach. Both solvers were extended with a model of ship motions coupled with the solution of the flow equations. The studied ships include a Panmax container ship, a tanker and a destroyer. In general, computed resistance and ship motions agree well with the measurements. The study was undertaken in a cooperation between Germanischer Lloyd (GL) and University Duisburg-Essen (UDE).

1. INTRODUCTION

The Gothenburg Workshop 2000 [3] has shown already ten years ago, that RANSE-methods are capable of the computation of ship resistance with a sufficient accuracy. Since then, no significant developments were undertaken in the numerical models of the free surface or turbulence; most developments were devoted to efficiency and robustness of grid generation and flow solution. In addition, significant progress was achieved in the prediction of ship motions and loads in seaway, as well as fluid-structure interaction.

Nevertheless, the required power of ships was determined as before from model tests. Interest to numerical power prediction might increase in the near future due to the growing importance of ship energy efficiency and demand for the corresponding hull form optimisation.

2. NUMERICAL METHODS

2.1 Flow Solvers

The applied numerical methods solve the conservation equations for mass and momentum in their integral form. The fluid is assumed viscous and incompressible, and the

flow turbulent, satisfying the Reynolds-averaged Navier-Stokes (RANS) equations. The solution domain is subdivided into a finite number of control volumes of arbitrary shape. The integrals over control volumes and their faces are numerically approximated using the midpoint rule. The mass flux through the cell face is taken from the previous iteration, following a simple Picard iteration. The free surface dynamics is computed employing Eulerian interface-capturing techniques of the volume-of-fluid (VoF) type.

The unknown variables at cell face centres are determined in COMET by combining central- (CDS) and upwind- (UDS) differencing schemes, blended to obtain a good compromise between accuracy and stability. Near the ship hull, the blending factor is chosen between 0.8 and 0.9. The transport equations for the turbulent kinetic energy and its dissipation rate were discretised with upwind differences. The three time level methods are used to integrate in time. Pressure and velocity are coupled by a variant of the SIMPLE algorithm [2]. All equations except the pressure correction equations are under-relaxed using a relaxation factor of 0.8, while the pressure-correction equation is under-relaxed with a factor between 0.2 and 0.4 for unsteady simulations, finding in each case a suitable compromise between stability and convergence speed.

In OpenFOAM, the convection terms in the momentum equations are approximated using a TVD-limited linear second-order scheme. The pressure-velocity coupling follows the PISO method. Integration in the time domain relied on the use of the implicit Euler or Runge Kutta scheme. To ensure numerical stability, the exciting forces are under-relaxed. Although the PISO scheme for pressure-velocity coupling does not require outer iterations, for implicit coupling of flow equations and rigid-body motions such iterations were introduced. At the end of each outer iteration, the force equilibrium is checked. The normalised difference between fluid and mass forces serves as criterion to stop outer iterations. Since the first rigid body motions in the current time step can be predicted well based on the previous time steps, the approach converges rapidly. For quickly changing hydrodynamic added masses (e.g. slamming), more outer iterations are needed.

In the both methods, the two-fluid system is modelled following a two-phase formulation of the governing equations. The spatial distribution of each of the two fluids is obtained by solving an additional transport equation for the volume fraction of one of the fluids. Because no explicit treatment for the free surface is required, overturning (breaking) waves as well as effects of trapped air can be modelled. In order to avoid numerical smearing of the interface, COMET employs a high-resolution interface-capturing (HRIC) scheme [4], while OpenFOAM employs the explicit MULES scheme.

2.2 Coordinate system and rigid body motions

The nonlinear ship motion equations are coupled with the flow solver. The equations of motion are solved in the Newtonian reference frame *Gxyz* fixed with respect to the mean position of the ship; its origin is located at the centre of gravity of the ship *G* and the *x*-, *y*- and *z*-axes point horizontal forward, horizontal to the port and vertically upwards, respectively.

In COMET, the coordinate transformation between the Newtonian and the ship-fixed reference frame $G\xi\eta\zeta$ is defined as

$$\vec{x} = \vec{x}_G + S\vec{\xi} \tag{1}$$

where *S* denotes the transformation matrix and $\vec{\xi}$ the rotational position vector. Following the definition of Euler angles, the transformation matrix resulted from consecutive rotations about the vertical *z*-axis (yaw), the new transverse η-axis (pitch), and the new longitudinal ξ-axis (roll). The governing equations of motions are expressed as follows:

$$\vec{F} = m\ddot{\vec{x}}_G \tag{2}$$

$$\vec{M} = S\, I_L S^T \dot{\vec{\omega}} + \vec{\omega} \times S\, I_L S^T \vec{\omega} \tag{3}$$

where $\vec{F}$ denotes the resulting force vector, m the mass of the ship, $\ddot{\vec{x}}_G$ the translational acceleration vector of G, $\vec{M}$ the resulting moment vector with respect to *G*, I_L the inertia tensor of the ship about the axes of the ship-fixed (local) reference frame, and $\vec{\omega}$ the angular velocity vector. Integration in the time domain applied an implicit trapezoidal method [5].

In OpenFOAM, quaternions [6] are used for transformations between coordinate systems to avoid singularities.

3. REFERENCE SHIPS AND TEST CASES

3.1 Test Ships

The study was undertaken for three ship types, a Panmax container ship (KCS), an oil tanker (KVLCC2) and a destroyer (DTMB 5415); the main dimensions are shown in Table 1. A series of model measurement results at different institutes was provided to the participants of the workshop (http://www.gothenburg2010.org). In this study, computations of resistance and motions in waves were carried out for the container ship and the oil tanker, as well as roll decay simulations for the destroyer, Tables 2 to 4.

Table 1 Full scale dimensions of the used geometries

	KCS	KVLCC2	DTMB
L_{pp}, m	230.0	320.0	142.0
L_{WL}, m	232.5	325.5	142.18
B_{WL}, m	32.2	58.0	19.06
T, m	10.8	20.8	6.15
Δ, m^3	52030	312622	8424.4
c_B	0.6505	0.8098	0.5070
S_W, m^2	9424	27194	2972.6
S_R, m^2	115.0	273.3	30.8
L_{CB}, %L_{pp} fwd	-1.48	-1.48	-0.683
k_{xx}/B	0.40	0.40	0.37
k_{yy}/L_{pp}, k_{zz}/L_{pp}	0.25	0.25	0.25

3.2 Calm Water Resistance Test Cases

Calm water resistance was calculated only for the container ship; test cases are shown in Table 2.

Table 2 Resistance test cases for container ship KCS

Case	2.2a	2.2b
Fn	0.26	0.1083[(1)], 0.2274, 0.2816
$Rn \cdot 10^{-7}$	1.4	0.52, 1.1, 1.4
Rudder	yes	Yes
Experimental data	resistance	resistance, sinkage, trim
Experiments	MOERI	MOERI

(1) OperFOAM computations were not carried out for this case

3.3 Ship Motions and Added Resistance in Waves

The model tests were performed in head waves. Measurements and simulations concern heave and pitch of the container ship and tanker, as well as the added resistance of the tanker, see Tables 3 to 4.

Table 3 Test Case 2.4a for container ship KCS

	C1	C2	C3	C4
Fn	0.26	0.26	0.26	0.33
$Rn \cdot 10^{-6}$	6.52	6.52	6.52	8.27
scale	52.667	52.667	52.667	52.667
λ/L_{pp}	0.50	1.15	2.00	1.33
h_w, mm	36	84	146	97

Table 4 Test cases in regular waves for the tanker

	Cases 1.4a and c			Case 1.4b				
	C1	C2	C3	C1	C2	C3	C4	C5
Fn	0.142	0.142	0.142	0.000	0.142	0.142	0.142	0.182
$Rn \cdot 10^{-6}$	2.55	2.55	2.55	0.0	5.4	5.4	5.4	6.9
scale	100	100	100	58	58	58	58	58
λ/L_{pp}	0.6	1.1	1.6	0.9171	0.6364	0.6364	0.9171	0.6364
h_w, mm	60	60	60	122.66	27	140	138	150

For Cases 1.4a and b, surge motion was restrained, while for Case 1.4c, it was additionally modelled. Two linear springs are modelled, attached to the model at the centre of gravity and acting horizontally in Newtonian coordinate system.

3.4 Roll Damping for DTMB

Simulation of the roll decay test was performed for destroyer DTMB with the roll axis fixed at G for Fn=0.138, Rn=2.56·10^6 in model scale λ=46.59; initial roll angle 10°.

4. COMPUTATIONS

4.1 Numerical Grids

The numerical grids consist of predominantly hexahedral control volumes and are fully unstructured. The grids are refined around the wetted hull surface and expected free surface position. Sufficiently far away from the ship, the grids were coarsened in order to dampen the waves and thus avoid reflection from the boundaries. An example of the grid around the containership is shown in Figures 1 and 2. The innermost cell thickness was chosen so that, on average, the dimensionless distance from the wall y^+ was between 25 and 50. For calm water and head wave conditions, only half ship was modelled by setting a symmetry plane at the centre line. To avoid disturbances at outer grid boundaries, these boundaries were located at a distance of one (for seakeeping analyses) to three (calm water analyses) ship length ahead of the bow, two (seakeeping) to six (calm water) ship lengths aft of the stern, one (seakeeping) to three (calm water) ship length beneath the keel and two (seakeeping) to three (calm water) ship length to the side. The top grid boundary was located above the deck at a distance equal to half length of the ship.

The numerical grids were generated with an open source grid generator SnappyHexMesh [7]; only for the KCS Test Cases 2.2a and 2.2b the grids for COMET computations were produced with a commercial program StarCCM+. For seakeeping analyses, the same or similar grids were usually used for the computations with OpenFOAM and COMET. The grid resolution depends on the wave length and Froude number; significantly more cells were used for the simulations with short waves and small Froude numbers in order to resolve incoming, radiated and diffracted waves.

The rigid body motions were accounted for by grid deformation. The solution of the motion equations yields the displacement of the vertices on the ship hull, while vertices on the water bottom, inlet and outlet are fixed. The displacement of the cell vertices inside the computational domain is determined using a grid deformation algorithm. For the estimation of the spatial discretisation error, grids of varying density were used. Table 5 indicates the numbers of cells used.

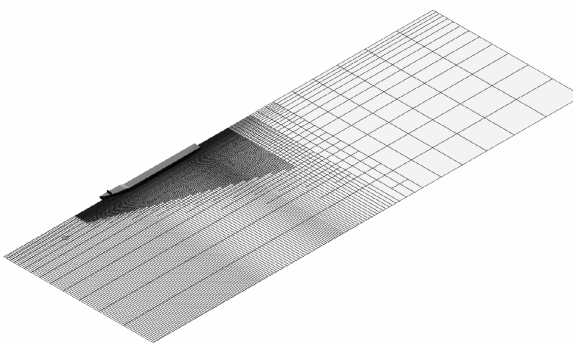

Fig.1 Example of grid at the free surface for the KCS

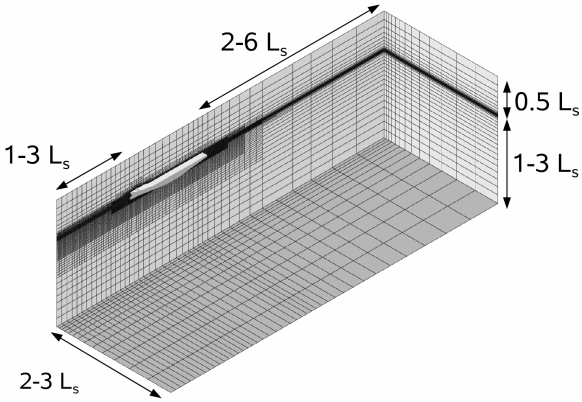

Fig.2 Domain extensions for KCS

Table 5 Number of finite volumes

		Number of cells $\times 10^{-3}$		
Ship	Condition	coarse	Medium	Fine
KCS	calm water	70(2)	750(1), 700(2)	2700(1), 1000(2)
	regular waves	100-200(3)	200-500(3)	600-1200(3)
KVLCC	calm water	–	–	–
	regular waves	100-200(3)	200-500(3)	600-1200(3)
DTMB	roll decay	70(2)	500(2)	1000(2)

(1) Grid used for COMET
(2) Grid used for OpenFOAM
(3) larger numbers of cells correspond to shorter waves

4.2 Boundary Conditions

The front boundary of the computational domain was specified as inlet with known velocities (reversed ship speed for calm water conditions or a superposition of reversed ship speed and orbital particle velocities of the linear Airy wave for incoming wave conditions), volume fraction, turbulent kinetic energy and its dissipation rate. A slip boundary condition was specified on the side and bottom boundaries. A no-slip condition with specified velocities due to ship motions was enforced on the hull surface. Hydrostatic pressure boundary condition was imposed at the outlet and (for OpenFOAM) also top boundaries. Numerical diffusion caused by the coarse grid aft of the ships damped the incident wave and the ship waves to such an extent that no significant wave reflection occurred at the outlet boundary.

k-ε and k-ω SST turbulence models with wall functions were used in COMET and OpenFOAM, respectively.

4.3 Initial conditions

Initial flow velocities were calculated from the ship speed (for calm water conditions) or from the superposition of ship speed with orbital particle velocities of a linear Airy wave (for incoming wave conditions). Volume fractions were initialised taking into account a linear Airy wave for seakeeping computations. At the beginning of simulations, the ship was set without trim and heel; only in the roll decay simulation an initial heel of 10° was used.

4.4 Convergence

Calm water conditions

OpenFOAM computations were started on the coarse grid. The flow variables were then interpolated onto the next fine grid and the simulation continued; this procedure leads to a quicker convergence. Simulation of the flow continued until a stationary or a periodic solution was reached. Figures 3 and 4 show examples of convergence histories in time for Case 2.2b obtained with OpenFOAM and COMET, respectively (the model was fixed until time 10.0 s and then unrestrained).

Incoming wave conditions

For incoming waves longer than about one ship length, the numerically predicted ship motions become periodic in few wave periods. However, for shorter incoming waves, the disturbances due to the initial condition remain relatively long. In such cases, more than 10 periods were usually required until periodic ship motions are achieved.

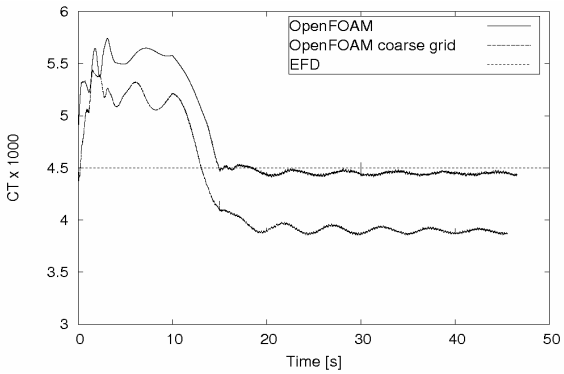

Fig.3 Convergence in time of resistance on coarse and fine grids (OpenFOAM for 2.2b, *Fn*=0.2816); the model is released at 10.0 s

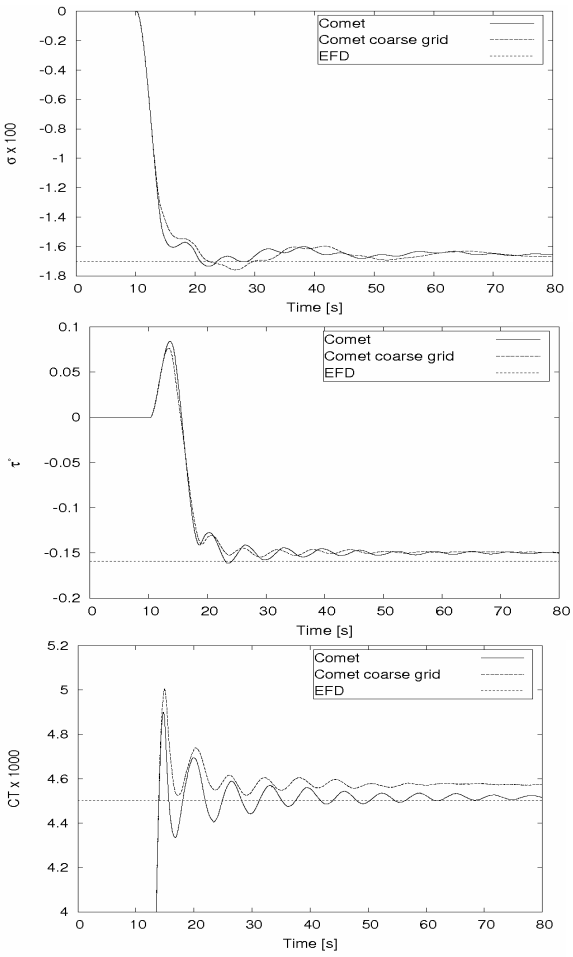

Fig.4 Convergence in time of sinkage (top), trim (middle) and resistance (bottom) on coarse and fine grids (COMET simulations for the same case as in Fig.3)

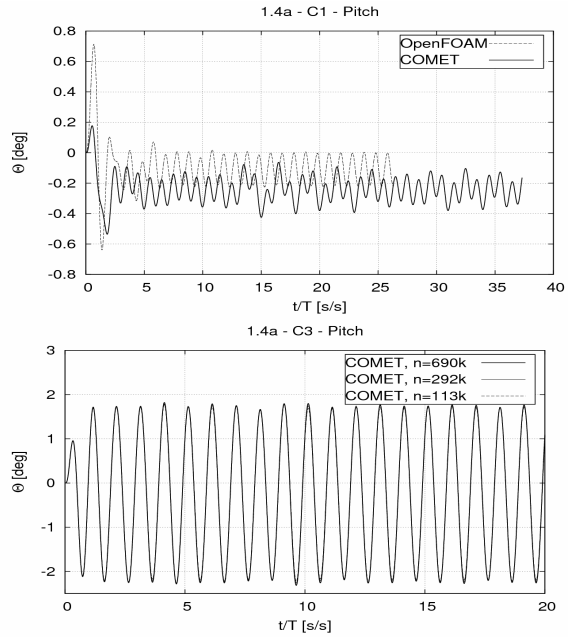

Fig.5 Time series of trim for Test Cases 1.4a C1 for COMET and OpenFOAM (top) and C3 for COMET on different grids (bottom); n is the number of cells, k=10^3

5. RESULTS

5.1 KVLCC2

Test Case 1.4a

No measurements were available for this test case. Computations were performed with OpenFOAM and COMET. Figures 6 to 8 show time histories of heave and pitch motions and total resistance coefficient; Table 6 shows the amplitude and the phase of the first Fourier harmonic, derived from the time histories. OpenFOAM shows on the average larger motions than COMET.

Table 6 Computational results for Case 1.4a

		Heave		Pitch	
		ampl., mm	phase, deg.	ampl., deg.	phase, deg.
C1	COMET	1.28	102.13	0.09	-172.78
	OpenFOAM	1.63	103.59	0.11	-167.69
C2	COMET	17.70	151.61	1.42	-142.67
	OpenFOAM	21.62	156.41	1.81	-135.47
C3	COMET	27.04	-103.00	2.00	-50.33
	OpenFOAM	27.75	-101.30	2.24	-46.84

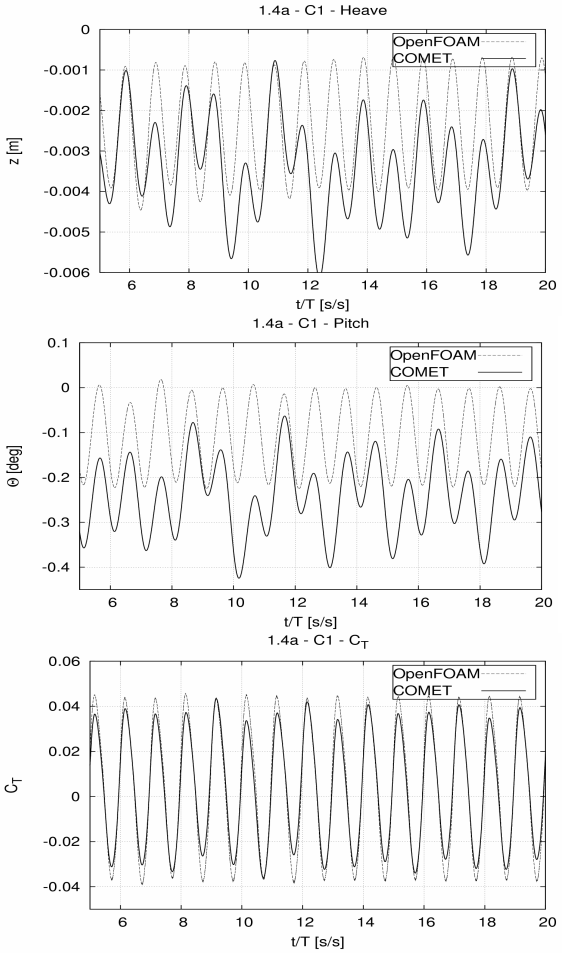

Fig.6 OpenFoam and COMET heave (top), pitch (middle) and total resistance (bottom) for case 1.4a condition C1

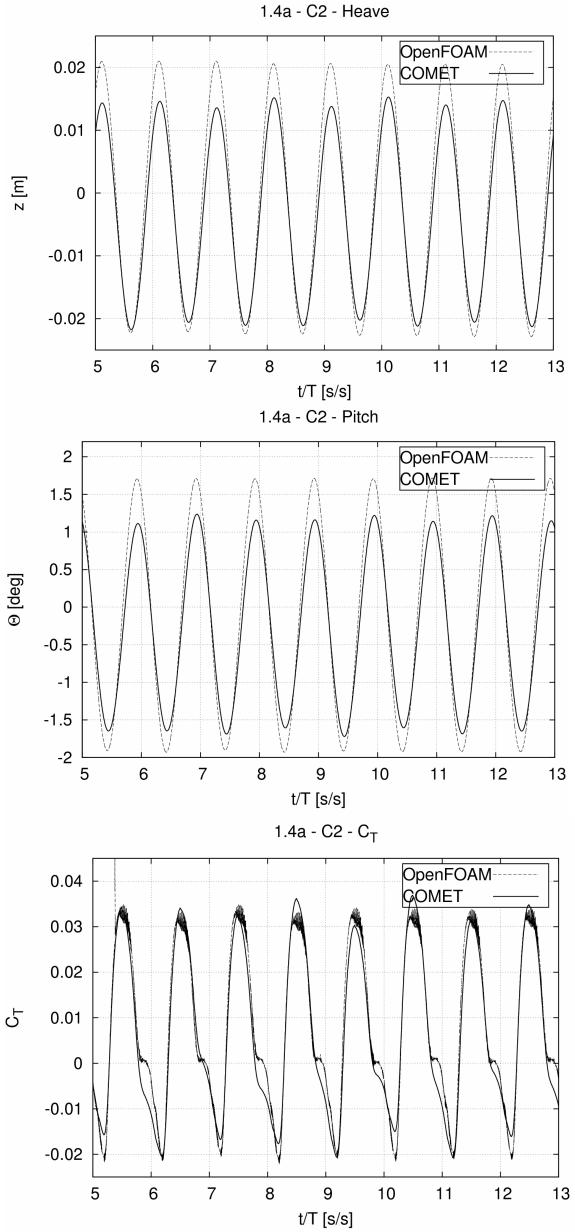

Fig.7 OpenFoam and COMET heave (top), pitch (middle) and total resistance (bottom) for case 1.4a condition C2

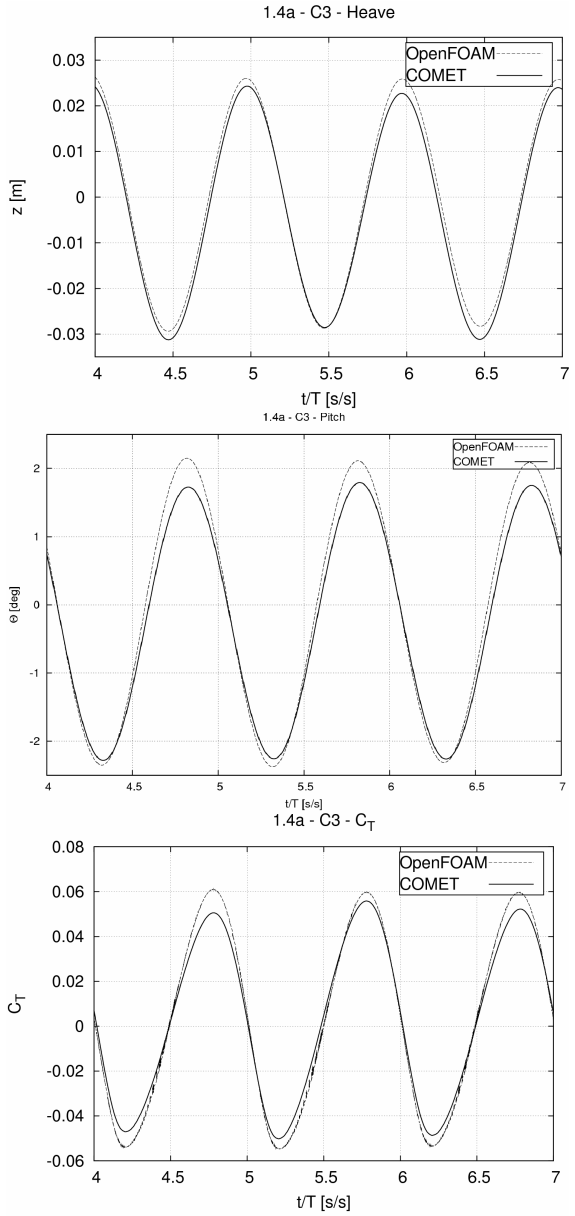

Fig.8 OpenFoam and COMET heave (top), pitch (middle) and total resistance (bottom): case 1.4a condition C3

Test Case 1.4b

Computations were performed with OpenFOAM and COMET; Table 7 shows a summary of the results. Fig.9 shows examples of time histories of heave and pitch motions and total resistance coefficient for one of the test conditions, C4.

Computational results for short waves (conditions C2, C3 and C5) show small ship motions and small added resistance; however, the transient phase is long in comparison to the oscillation period and thus requires large simulation time until a periodic solution is achieved.

Table 7 Computational results for Case 1.4b

		Heave, mm		Pitch, deg.	
		0th ampl.	1st ampl.	0th ampl.	1st ampl.
C1	COMET	0.223	18.439	-0.091	1.541
	OpenFOAM	-2.315	15.491	-0.004	1.414
	EFD	-0.130	13.378	-0.023	1.638
C4	COMET	-6.100	12.482	-0.191	1.323
	OpenFOAM	-3.427	13.079	-0.188	1.358
	EFD	-5.625	11.081	-0.137	1.357

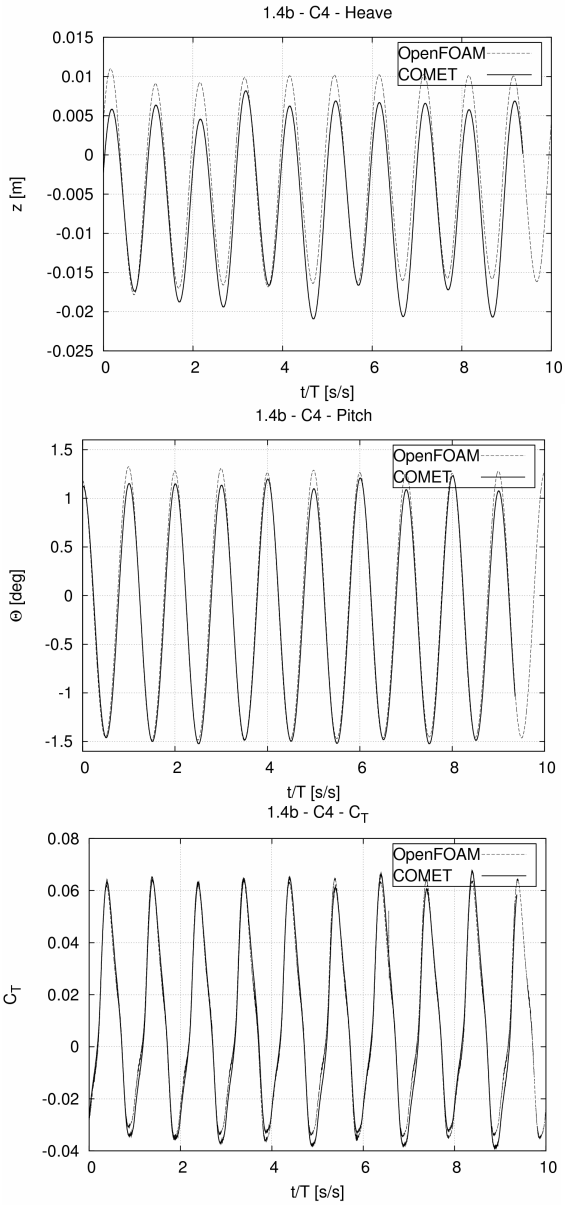

Fig.9 OpenFoam and COMET heave (top), pitch (middle) and total resistance (bottom) for case 1.4b condition C4

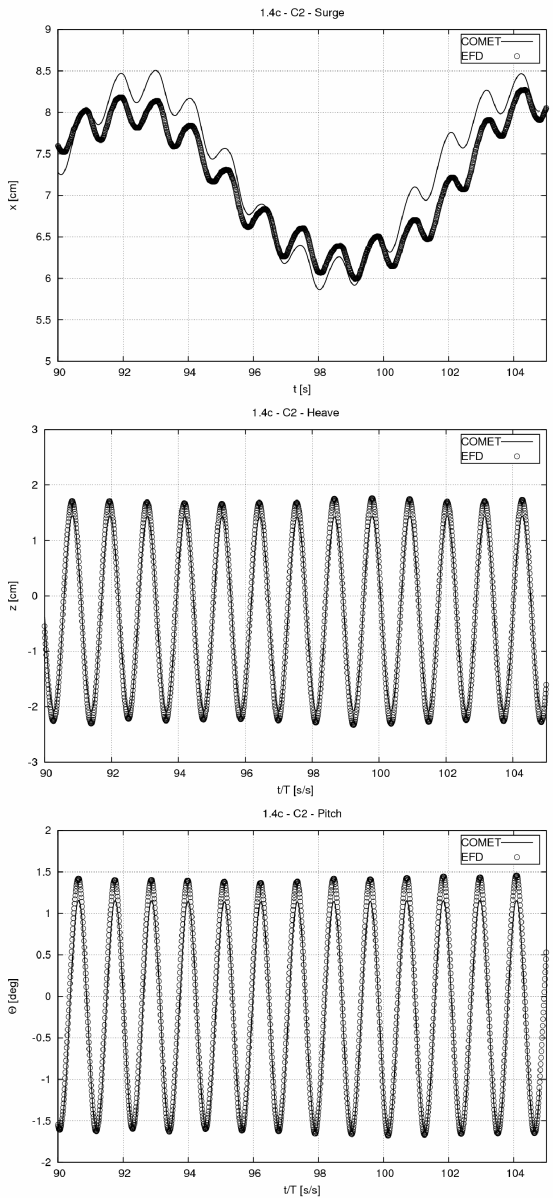

Fig.10 Surge motion x, heave motion z and pitch angle θ (OpenFoam and COMET for case 1.4c condition C2)

Test Case 1.4c: COMET

This test case concerns ship motions and added resistance in head waves for a model attached to the carriage by the means of springs. The springs were modelled as a horizontal force proportional to the relative displacement between the model and the carriage; thus, surge motion was also taken into account.

Computations were performed with COMET; Table 8 shows the amplitudes of the 0th and 1st harmonics for surge, heave and pitch motions and Fig.10 shows time histories of surge, heave and pitch for test condition C2.

Table 8 Computational results for Case 1.4c

		surge	heave		pitch	
		1st ampl., mm	0th ampl., mm	1st ampl., mm	0^{th} ampl., °	1st ampl.,°
C1	COMET	1.49	-3.516	1.316	-0.241	0.085
	EFD	1.73	-3.200	1.900	-0.090	0.110
C2	COMET	2.14	-3.300	17.615	-0.243	1.396
	EFD	2.08	-2.880	1.990	-0.130	1.510
C3	COMET	5.68	-3.188	26.753	-0.243	1.958
	EFD	7.88	-2.800	26.600	-0.180	1.790

5.2 KCS

Test Case 2.2a: COMET

Calculations were performed with COMET for *Fn*=0.26 with restrained trim and sinkage; Fig.11 shows converged free surface elevation and Table 9 shows the total resistance coefficient, as well as coefficients of friction and pressure forces for the two grids used in comparison with the measured resistance.

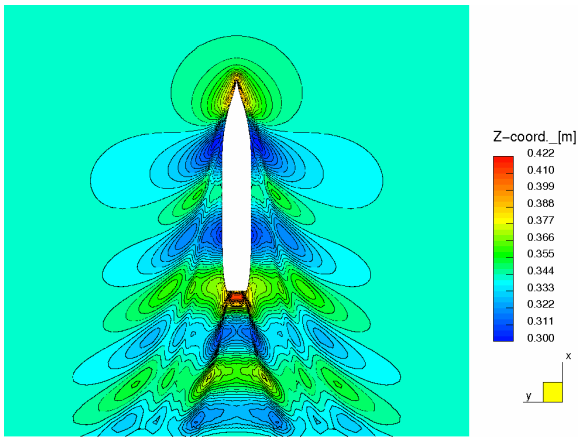

Fig.11 Free surface computed by COMET for Case 2.2a

Table 9 COMET results for Case 2.2a

	$C_T \cdot 10^3$	$C_F \cdot 10^3$	$C_P \cdot 10^3$
Medium	3.706	2.872	0.834
Fine	3.618	2.879	0.739
Difference fine vs. med., %	2.43	-0.24	12.86
EFD	3.557	–	–
Difference fine vs. EFD, %	-1.71	–	–

Test Case 2.2a: OpenFoam

Calculations were performed with OpenFOAM for *Fn*=0.26 with restrained trim and sinkage; Table 10 shows the resistance coefficient in comparison with measurements.

Table 10 OpenFOAM results for Case 2.2a

	$C_T \cdot 10^3$	$C_F \cdot 10^3$	$C_P \cdot 10^3$
Medium	4.000	2.842	1.158
Fine	3.544	2.856	0.688
Difference fine vs. med., %	12.867	0.49	68.314
EFD	3.557	–	–
Difference fine vs. EFD, %	0.365	–	–

Test Case 2.2b: COMET

Calculations performed with COMET for *Fn*=0.1083, 0.2274 and 0.2816 with unrestrained trim and sinkage. Fig.12 shows converged free surface elevation for the Froude number 0.1083 and Table 11 shows the total resistance coefficient for the Froude numbers 0.1083, 0.2274 and 0.2816, as well as the coefficients of resistance components for the two grids used, in comparison with the measurements.

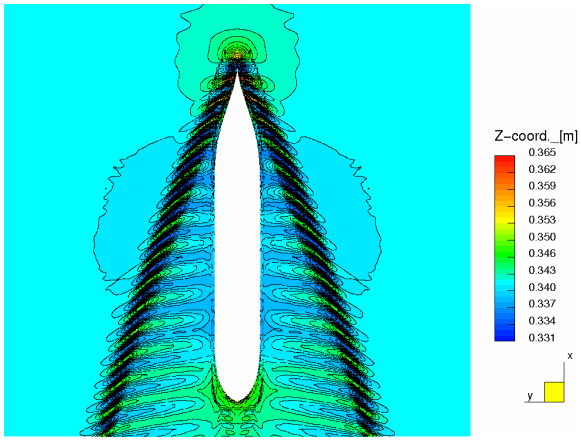

Fig.12 Comet free surface for case 2.2b, *Fr*=0.1083

Table 11 COMET results for Case 2.2b

	$C_T \cdot 10^3$	$C_F \cdot 10^3$	$C_P \cdot 10^3$	Sinkage, m	Trim, deg.
Fn=0.1085					
Medium	3.836	3.293	0.543	-0.145	-0.033
Fine	3.691	3.297	0.394	-0.145	-0.034
Fine vs. med., %	-3.93	0.12	-37.82	0.00	2.94
EFD	3.796	–	–	-0.090	-0.017
Fine vs. EFD, %	2.77	–	–	-61.11	-100.00
Fn=0.2276					
Medium	3.577	2.979	0.598	-0.947	-0.130
Fine	3.493	2.990	0.503	-0.945	-0.132
Fine vs. med., %	-2.40	0.37	-18.89	-0.21	1.29
EFD	3.467	–	–	-0.944	-0.127
Fine vs. EFD, %	-0.75	–	–	-0.11	-3.78
Fn=0.2818					
Medium	4.574	2.925	1.649	-1.655	-0.149
Fine	4.517	2.945	1.572	-1.656	-0.150
Fine vs. med., %	-1.26	0.68	-4.90	0.06	0.67
EFD	4.501	–	–	-1.702	-0.159
Fine vs. EFD, %	-0.36	–	–	2.70	5.66

Test Case 2.2b: OpenFoam

Calculations performed with OpenFOAM for Froude numbers 0.2274 and 0.2816 with unrestrained trim and sinkage. Table 12 shows the total resistance coefficient for the Froude numbers 0.2274 and 0.2816 in comparison with the measured resistance, as well as the coefficients of resistance components for the two grids used.

Table 12 OpenFOAM results for Case 2.2b

	$C_T \cdot 10^3$	$C_F \cdot 10^3$	$C_P \cdot 10^3$	Sinkage, m	Trim, deg.
Fn=0.2274					
Medium	3.583	2.876		-0.986	-0.121
Fine	3.505	2.995			
Fine vs. med., %	2.23	3.97			
EFD	3.467	–	–	-0.944	-0.127
Fine vs. EFD, %	-1.10	–	–		
Fn=0.0.2816					
Medium	3.9	2.86	1.04	-1.63	-0.201
Fine	4.45	2.92	1.53	-1.78	-0.161
Fine vs. med., %	12.36	2.05	32.03	8.43	24.84
EFD	4.501	–	–	-1.702	-0.159
Fine vs. EFD, %	1.13	–	–	-4.58	-1.26

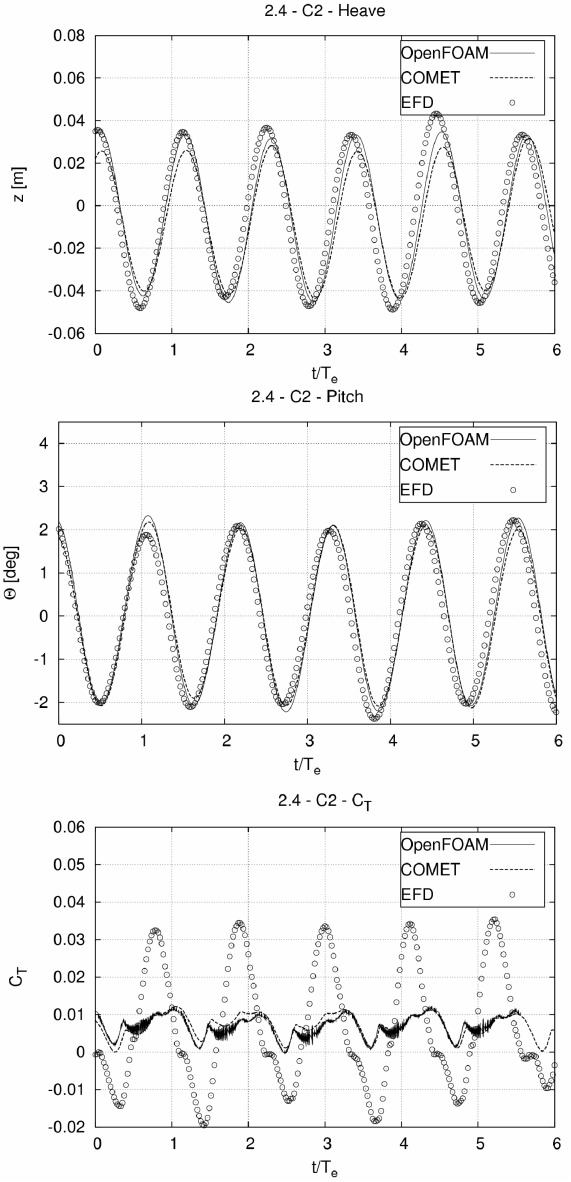

Fig.13 OpenFoam and Comet heave (top), pitch (middle) and total resistance (bottom) time histories for case 2.4, condition C2

Test Case 2.4: COMET and OpenFOAM

Simulations were performed with COMET and OpenFOAM in head waves for a model unrestrained in heave and pitch and moving with a prescribed forward speed. Figures 13, 14 and 15 show time histories of ship motions and total resistance for the conditions C2, C3 and C4, respectively; Table 13 shows a summary of computational results (OF denotes OpenFOAM; A_0 and A_1 are the amplitudes of the 0th and 1st harmonics, respectively) in comparison with the measurements.

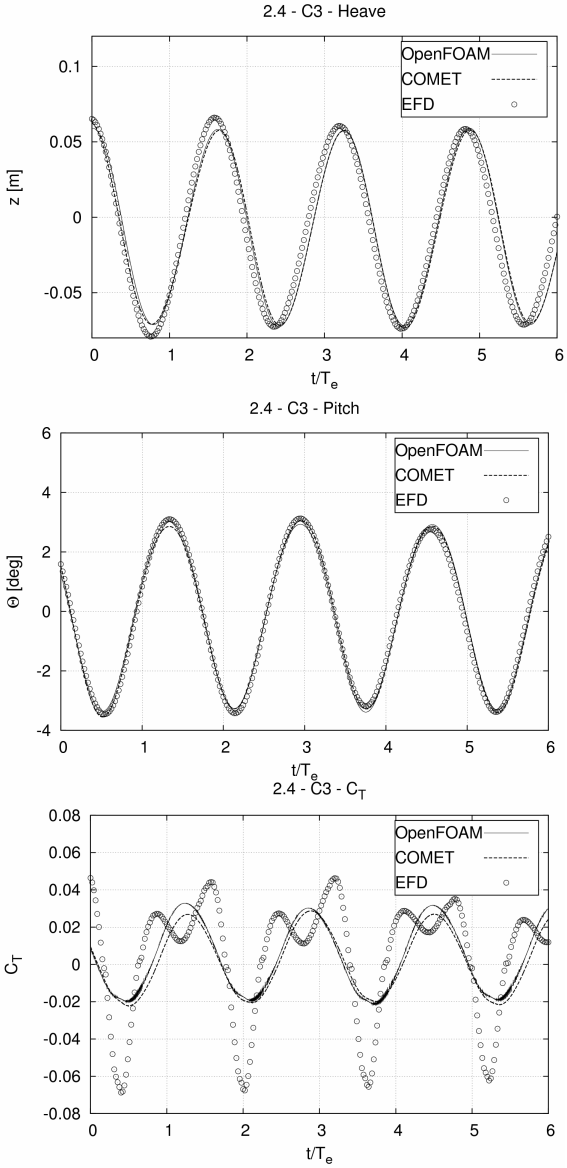

Fig.14 OpenFoam and Comet heave (top), pitch (middle) and total resistance (bottom) time histories for case 2.4, condition C3

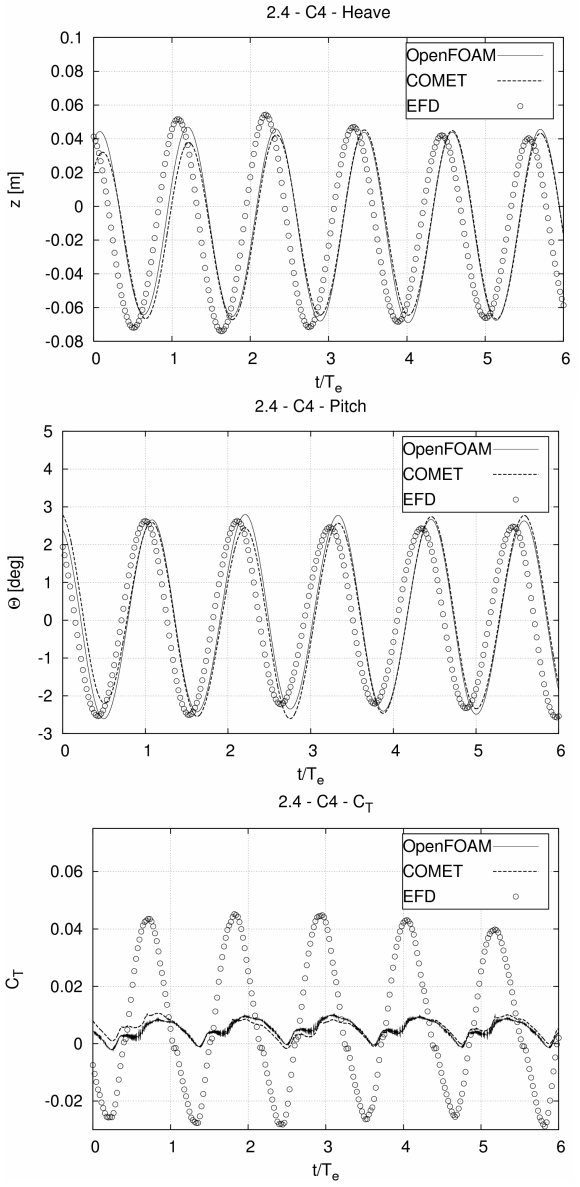

Fig.15 OpenFoam and Comet heave (top), pitch (middle) and total resistance (bottom) time histories for case 2.4, condition C4

Table 13 OpenFOAM and COMET results for Case 2.4

		heave			pitch			$C_T \times 10^3$		
		A0, mm	A1, mm	phase,°	A0,°	A1,°	phase,°	A0, N	A1, N	phase,°
C1	COMET	-8.421	0.943	20.071	-0.128	0.054	102.50	1.794	1.779	-71.40
	OF	-8.488	1.048	22.164	-0.151	0.058	104.99	3.922	2.137	285.365
	EFD									
C2	COMET	-6.496	37.808	-21.126	0.019	2.122	12.89	7.344	3.440	66.94
	OF	-5.869	38.819	-19.770	0.023	2.165	14.052	6.817	3.343	62.849
	EFD	-5.436	39.544	-20.57	0.064	2.095	8.485	7.160	20.420	81.870
C3	COMET	-6.540	65.020	-1.136	-0.037	3.129	63.80	2.982	24.271	75.41
	OF	-7.074	65.088	0.764	-0.080	3.141	65.089	4.880	25.956	80.878
	EFD	-6.573	67.328	-3.1	0.062	3.156	50.270	6.033	32.070	70.810
C4	COMET	-11.905	55.334	-26.048	0.141	2.548	16.44	5.558	3.843	89.22
	OF	-11.278	55.999	-24.616	0.117	2.573	17.661	8.090	4.155	92.399
	EFD	-12.274	61.811	-18.28	-0.067	2.523	46.097	8.716	35.390	-260.210

5.3 DTMB5415

Test Case 3.6

For the destroyer DTMB, only roll decay was simulated. Time history of roll angle is shown in Fig.16. Fig.17 shows logarithmic decrement of roll amplitude vs. roll amplitude for two OpenFOAM simulations (medium and fine grids) and measurements.

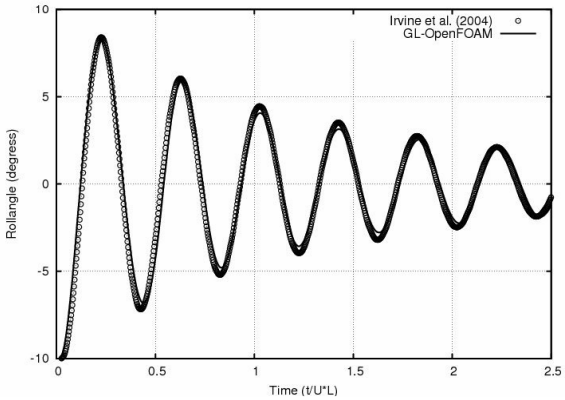

Fig.16 GL OpenFoam roll decay results for case 3.6b

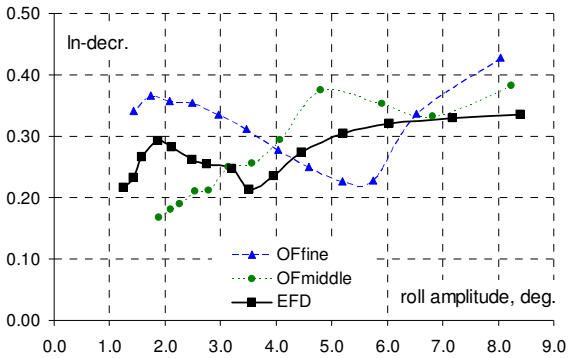

Fig.17 Logarithmic decrement ($\ln\varphi_i/\varphi_{i+1}$) vs. roll amplitude φ_i for roll decay test 3.6b; OF denotes OpenFOAM results, 'fine' and 'middle' fine and medium grid size, respectively

6. CONCLUSION

Computational results agree well with the measurements for almost all studied test cases, especially for heave and pitch amplitudes (1st harmonics) for the wave lengths relevant for the excitation of ship motions, as well as calm water resistance, trim and sinkage. A significant difference is noticed between the computed and measured amplitude of the longitudinal force in waves; the authors suggest shortcomings in the measurements or their post-processing, because the reference measured amplitudes of the longitudinal force in waves appear unrealistically high.

Further, differences are noticed between measurements and computations for shorter waves (wave length of about 0.6 L_{pp} or less). Note however that the corresponding ship motions are relatively small and, therefore, are sensitive to small disturbances in the computations and measurements on the one hand, and less relevant for the practice on the other.

Moreover, marginal differences are found between the measured and computed average values of all ship motions (0th harmonics). These values are extremely small because of the almost linear ship motions (heave and pitch) for the studied relatively small wave heights, therefore their comparison cannot be done here with confidence.

Comparison of the measured and computed phases of motions appears challenging. To the opinion of the authors, small uncontrollable uncertainties can lead to large changes in the measured phases.

Simulated roll decay test agrees well with the measurements with respect to both amplitude and period of the motion.

The influence of the grid density on the computed ship motions is remarkably small. The computed motions hardly change for the cell numbers already above 10^5, Fig.5. This is because the dominating Froude-Krylov forces can be accurately resolved with relatively coarse grids.

On the other hand, the influence of the grid density on the calm water resistance is significant, because for the Froude numbers studied here (below 0.28) viscous effects are dominating. At the same time, the influence of the grid density on the calm-water trim and sinkage is again insignificant, because these are defined mostly by the primary wave system of the ship, which can be accurately resolved with relatively coarse grids.

Computed ship motions for long waves become periodic very quickly (after about two wave encounter periods) with a suitable initialisation of the flow velocities including ship speed and the orbital velocities due to the wave and the corresponding pressure field. For shorter waves, the ship motions become periodic only after many encounter periods (usually more than 5). The reason is the initial disturbance of the flow field, which require much more time in short waves.

In general, the results of COMET and OpenFOAM agree well, although the solvers use different pressure-velocity coupling (SIMPLE vs. PISO) as well as different interpolation schemes.

The application of deforming grids for the implementation of ship motions proved robust and efficient for both solvers.

The experience with OpenFOAM shows that computation of calm-water resistance on a coarse grid and extrapolation onto a finer one significantly accelerates convergence.

REFERENCES

[1] Larsson, L., Stern, F. and Bertram, V., (2003), "Benchmarking of Computational Fluid Dynamics for Ship Flows: the Gothenburg 2000 Workshop", Journal of Ship Research, Volume 47, No 1, March

[2] Ferziger, J.H. and Peric, M., (2002), "*Computational Methods for Fluid Dynamics*", 3rd Ed., Springer Verlag, Berlin, Heidelberg

[3] Van, S.H., Kim, W.J., Yim, G.T., Kim, D.H., and Lee, C.J., (1998b), "Experimental Investigation of the Flow Characteristics Around Practical Hull Forms," Proceedings 3rd Osaka Colloquium on Advanced CFD Applications to Ship Flow and Hull Form Design, Osaka, Japan

[4] Muzaferija, S. and Peric, M., Computation of Free Surface Flows Using Interface-Tracking and Interface-Capturing Methods. Proc. Nonlinear Water Wave Interaction, O. Marenholtz and M. Markiewicz, Eds., Computational Mechanics Publ., Southampton, 1998, Ch. 3.

[5] Brunswig, J. and El Moctar, O., Prediction of Ship Motions in Waves using RANSE. Proc. 7th Numerical Towing Tank Symposium (NUTTS), Hamburg, 2004

[6] Shivarama, R. and Fahrenthold, E. P. (2004) Hamilton's equations with Euler parameters for rigid body dynamics modeling, ASME J. of Dynamics Systems, Measurement, and Control **126,** 124-30.

[7] Mesh generation with the SnappyHexMesh utility, http://www.openfoam.com

RANS Simulation of the Flow around the KVLCC2 Tanker using the FreSCo$^+$ Code

Marco Schneider
CFD Department, Hamburg Ship Model Basin (HSVA),
Hamburg, Germany

SUMMARY

The flow around the KVLCC2 tanker was computed using the RANS solver FreSCo$^+$. The wake field was analysed and compared with experimental data. The resistance was computed and a grid sensitivity study with five systematically refined grids was conducted.

INTRODUCTION

The present paper reports the numerical results of the KVLCC2 test case, proposed by the Gothenburg 2010 Workshop on CFD in ship hydrodynamics. Purpose of the work was the validation of the RANS solver FreSCo+ that is jointly developed by the TUHH (Technical University of Hamburg-Harburg) and the HSVA (Hamburg Ship Model basin). The wake field was computed with steady state RANS computations using the two equation k-ω turbulence model.

NUMERICAL METHOD

The FreSCo code solves the incompressible, unsteady Navier-Stokes-equations (RANSE) (Schmode and Hafermann 2006, Schmode et. al. 2006, Hafermann 2007). The transport equations are discretized with the cell-centered finite volume method. Using a face-based approach, the method is applied to fully unstructured grids using arbitrary polyhedral cells. Therefore the code can use grids from different grid generators like the fully unstructured, automatic grid generator HEXPRESS. This reduces the time needed for generating typical grids from several days to hours. The governing equations are solved in a segregated manner, utilizing a volume-specific pressure correction scheme to satisfy the continuity equation (Ferziger and Peric, 2002). To avoid an odd-even decoupling of pressure and velocity, a third-order pressure smoothing is employed along the way outlined by Rhie and Chow (1983). The fully implicit algorithm is second-order accurate in space and time. The approximation of integrals is based on the mid-point rule. Diffusion terms are approximated using second-order central differences, whereas advective fluxes are approximated based on blends between high-order upwind-biased schemes (e.g. QUICK), first order upwind and second order central differences schemes. The resulting linear equation systems are solved iteratively using Krylov subspace methods. The respective solvers are provided by the PETSc library (Balay et al. 2010). The code is efficiently parallelized in space using the message passing interface (MPI). To account for turbulent flows, additional transport equations are solved for turbulent quantities. Several turbulence models are implemented in the code: k-ε (Standard, RNG, and Chen), k-ω (Standard, BSL, SST), Menter's One Equation model and the Spalart-Allmaras turbulence model.

VERIFICATION AND VALIDATION

The uncertainty in numerical predictions can be categorised into numerical and modelling uncertainties. In this study only the numerical uncertainty was investigated and the modelling uncertainty arising from turbulence or free surface model etc. were not considered. Thus the numerical uncertainty with the given models was investigated. The numerical uncertainty can be broken down into the iterative uncertainty, the grid uncertainty, the time step uncertainty and other parameter uncertainties. Since the simulations are steady state calculations the time step uncertainty vanishes and it is assumed that the uncertainty of other parameters is negligible. The iterative uncertainty was reduced to a minimal effect by using an excessive number of iterations. However a curve fit of an exponential function for the convergence target value was used to estimate the iterative uncertainty. This estimated confirmed the assumption that the iterative error is negligible.

The grid uncertainty was investigated by using a systematic grid refinement study with Richardson extrapolation. The grids were generated using the commercial software package HEXPRESS. The uniform coarse hexahedral background meshes are split into finer hexahedral elements near the walls. The size of the fine cells at the wall is kept constant in the volume for a given amount of cells and is increased stepwise until the size of the background mesh is reached. The meshes are projected on the geometry afterwards. At the wall sub-layers are applied for the proper resolution of the boundary layer. Figure 1 and Figure 2 show examples of the resulting meshes.

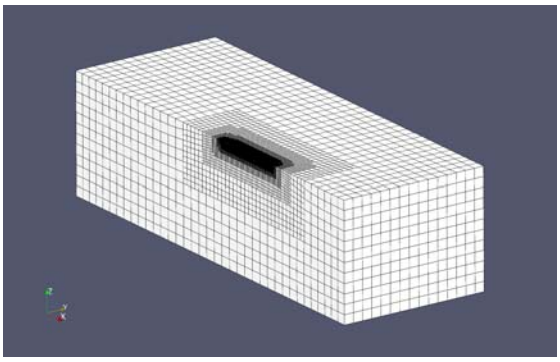

Figure 1: Refinement levels of Grid 3

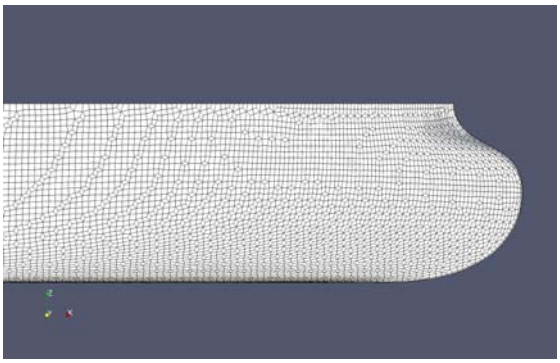

Figure 2: Surface mesh at the bow of Grid 3

With this approach the systematically refined grids where created using only the number of splits of the background mesh at the wall and the resolution of the sub-layer as parameters. Table 1 shows the resulting grid sizes and the parameters. Wall functions are used for all simulations. The y^+ value of the first cell near the wall was increased with the same ratio as the grid refinement ratio.

	Y+	Number of Cells	Expansion Factor	Sublayers	Refinement levels
Grid 1	15	10191729	1.13	12	8
Grid 2	30	2175181	1.13	8	7
Grid 3	60	550997	1.13	6	6
Grid 4	120	162588	1.13	4	5
Grid 5	240	64704	1.13	2	4

Table 1: Grid sizes and parameters

The numerical simulation uncertainty estimated with the above procedure is approximately 0.16 % of the solution on the finest grid. Table 2 shows the friction, pressure and total resistance and the error compared to the measurements for the different grids.

	$C_F \times 10^3$	$C_P \times 10^3$	$C_T \times 10^3$	E%D
Grid 1	3.447	0.692	4.140	-0.719
Grid 2	3.515	0.682	4.198	-2.131
Grid 3	3.538	0.678	4.215	-2.567
Grid 4	3.495	0.731	4.226	-2.825
Grid 5	3.252	1.287	4.539	-10.437

Table 2: Resistance coefficients

COMPARISON OF THE COMPUTED AND MEASURED WAKE FIELD

Figure 3 shows the computed results of the wake field using the two equation k-ω turbulence model and Figure 4 the measured results. The agreement is quite satisfactory. The hook shape of the wake field is slightly underestimated in the numerical simulations. The workshops from the VIRTUE project revealed that a better resolution of the hook shape requires higher order turbulence models like Reynolds stress models or even more expensive DES simulations. The mesh used for the simulation had the grid resolution of "Grid 2" from systematically grid refinement study with an additional refinement box at the stern. Figure 5 and Figure 6 show the direct comparison of the computed and measured wake field

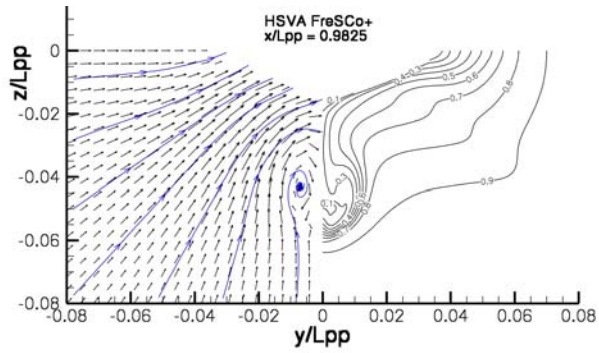

Figure 3: Computed wake field in the propeller plane

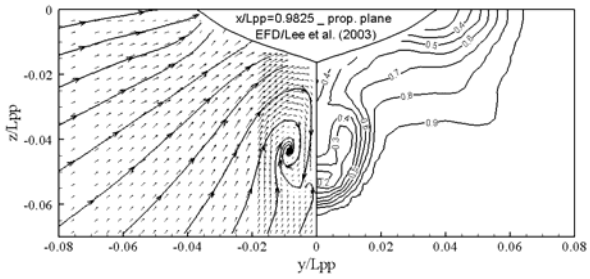

Figure 4: Measured wake field in the propeller plane

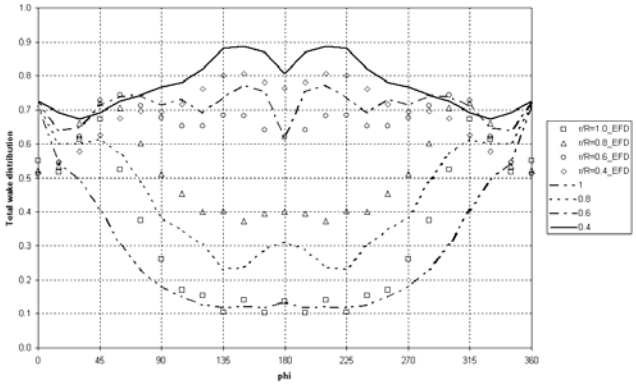

Figure 5: Comparison of the total wake distribution

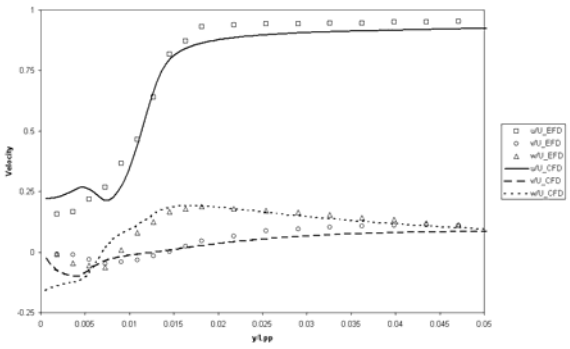

Figure 6: Comparison of the velocity in the propeller plane at z/LPP = -0.05075

CONCLUSIONS

The numerical results of the simulation of the ship flow around the KVLCC2 tanker using the RANS solver FreSCo$^+$ were compared with experimental data. The flow features and the resistance were predicted more than adequate for all practical purposes. A grid resolution study has been carried out.

REFERENCES

Rhie, C.M. and Chow, W. L. (1983), "A numerical study for the turbulent flow an isolated airflow with trailing edge separation" ,AIAA Journal,1983(17), pp. 1525

Schmode, D. and Hafermann,D (2006). "Comparison of Wind Tunnel Measurements and Computations with RANS Solver FreSCo", NuTTS symposium, Varna, Bulgaria (2006)

Ferziger, J. H. and Peric, M. (2002), "Computational Methods for Fluid Dynamics", 3rd Ed., Springer Verlag, 2002

Hafermann, D. (2007): "The New RANSE Code FreSCo for Ship Application", STG Jahrbuch 2007

Stern F., Wilson R.V. Coleman H.W. and Paterson E.G. "Comprehensive Approach to Verification and Validation CFD Simulations", Journal of Fluid Engineering, Vol. 123, 2001

NUMERICAL SIMULATION OF KCS CONTAINER CARRIER IN HEAD WAVE CONDITION

Hiromichi Akimoto (The University of Tokyo, Japan)
Takuya Omori (IHI Corporation, Japan)
Hiroyuki Saito (IHI Corporation, Japan)
Rahaman Md. Masiur (The University of Tokyo, Japan)

1. SUMMARY

Head sea condition of MOERI container ship, KCS model, is simulated using CFD code WISDAM-X. The simulation includes heave and pitch motion on KCS hull geometry without rudder. Four conditions from C1 to C4 with variations of wavelength, wave height and Froude number are numerically tested and are compared with provided experimental data except C1. It showed good agreement in pitch and heave (see submitted data of workshop). However, prediction of total resistance is not in a satisfactory level yet. In remaining condition C1 (EFD data not provided), our CFD result show long transitional behavior of ship motion. The paper describes additional information of the code and discussion of the results.

2. INTRODUCTION

A ship in operation shows unsteady motion under the oscillatory load of waves. However, obtaining realistic motion and performance data of the ship in the condition is not an easy task. Although we can obtain heave and pitch motion of the ship on head waves in towing tanks, asymmetric motion of yaw, roll and sway in oblique waves is only available in maneuvering tank with lower accuracy.

Since target of our R&D is on the performance of ship in actual operating conditions, i.e., oblique wave and asymmetric motions, development of the tool for obtaining performance data in them is important. At present, evaluation of ship performance by CFD is usually less accurate than EFD. However, since CFD does not have mechanical restriction that exists in tank tests, it has good potential for the evaluation of real ship performance in operating conditions.

Orihara and Miyata (2003) developed a RaNS simulator WISDAM-X for solving unsteady heave and pitch motion in head sea and oblique wave conditions. We are continuously improving the code for better stability and efficiency of simulations. The present paper describes the numerical evaluation of KCS container ship in head sea conditions with heave and pitch motion.

3. NUMERICAL METHOD

Governing equations of the code are RaNS equation and continuity equations. Spatial descretization is Finite Volume Method (FMV). Definition of physical values in a control volume is staggered manner, i.e., velocity components are separately defined on the face centers of primary hexahedral control volume while pressure is defined at the center of volume. Free surface capturing is marker density method (Miyata et al. 1988). Turbulence model is blending of Baldwin-Lomax model (Baldwin and Lomax, 1978) and dynamic subgrid scale (DSGS) model (Germano et al., 1991). Local turbulent viscosity is determined by weighted average of two models.

WISDAM code is applicable to the ship motion of six degrees of freedom and deformation of hull surface (Akimoto and Miyata, 2002 and Sato et al., 1999) and non-linear free surface phenomena including planing (Orihara and Miyata, 2000). To provide spatial resolution on both around the free surface and hull surface in motion, we employ overset grid technique (Orihara and Miyata, 2003). Fig. 1 shows the two grid systems used in our simulation. The outer domain is rectangular mesh with fine resolution around the free surface. The inner domain has a body boundary fitted curvilinear structured mesh. Simulation in the inner domain is on the moving coordinates fixed on the center of gravity of the ship. The outer mesh is also on the moving coordinates. However, its motion is restricted in planer ones. On the exterior surface of the inner domain, tri-linear interpolation of outer flow variables provides the boundary condition of inner domain and the interpolation of the inner values determines the boundary values for outer domain, vice versa.

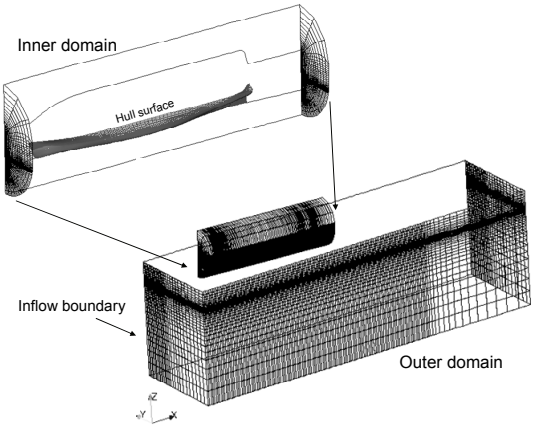

Fig.1 Overset grids: outer rectangular and inner curvilinear mesh.

Coefficients of interpolation between domains are updated at each time step (Orihara and Miyata, 2003). To obtain consistency between the motion of ship and the flow field, flow solution of the inner domain and the equation of motion of the ship require iteration. In the tested conditions, we conducted two pressure iterations before and after the integration of the equation of motion.

4. MESHING

Fig. 2 shows the distribution of grid points on the hull surface of KCS. For the green water was not in the focus of present analysis, hull surface is extended upward to cover the deck. However, simulated results show that green water occurs in the given conditions C3 and C4. Further improvement of the mesh requires detailed information of deck geometry in the experiments. Type of the inner mesh is single O-H type structured grids generated by Gridgen. On the hull surface, number of grid points is 90x70 (in longitudinal and girth direction) including dummy covering over the deck.

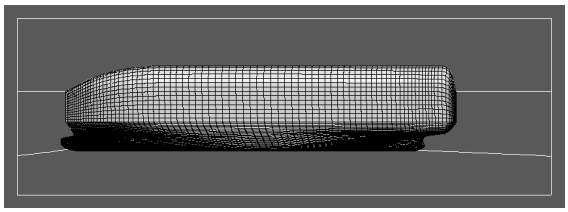

Fig.2 Grid distribution on the hull surface; dummy covering over deck, .

5. ADDITIONAL DISCUSSION OF RESULTS

We conducted simulations of KCS container ship with pitch and heave motion in head waves. Tested conditions are four conditions C1, C2, C3 and C4 of Case 2-4. All conditions showed steady oscillation except C1. Since C1 did not show steady oscillation in our standard simulation time, we extend simulation time until it reaches steady state. Fig. 3 shows the time history of pitch angle from the start of incident wave to t=160 second. It shows slow growth of low frequency mode.

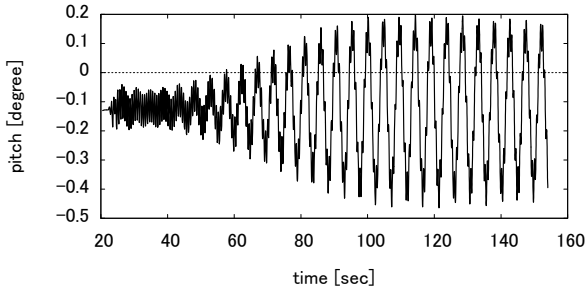

Fig.3 Time history of pitch angle; condition C1, Case 2-4.

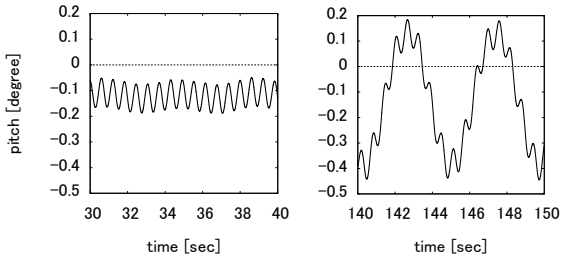

Fig.4 Time history of pitch angle; condition C1, from t=30 – 40 sec (left) and t=140 -150 sec (right).

Fig.5 Side view of pressure distribution; condition C1, Case 2-4.

Fig. 4 shows two parts of the time history, the first is from t=30 to 40 sec (before the development of low frequency mode), and t=140 to 150 sec (after the development of the mode). Fig. 5 shows pressure distribution after the development of low frequency mode. However, pitching motion is not significant in the visualization because of its small amplitude. The result implies that the growth of the mode is very slow, or that there are two possible oscillation modes in the given condition. However, even if the present result is accurate, such a long measurement time might be difficult to obtain in a towing tank.

Fig. 6 shows the visualization sample of condition C4. Since Froude number of the condition is high, the bulb of KCS protrudes from the wave surface in the peak of bow up motion.

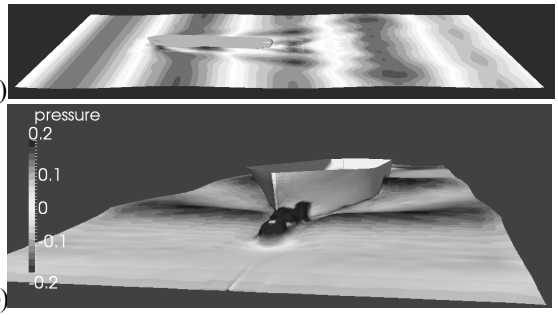

Fig.6 Pressure distribution and free surface deformation; entire domain (a) and close up of bow in the inner domain (b); condition C4, t=0.82T

Fig. 7 shows side views of bow part and the pressure distribution and free surface shape. Although the bulb protrudes from the wave surface, it is still covered with water (Fig.7 (a)). When pitch goes down to almost even-trim level, local wave elevation occurs over the bulb and shows wave breaking in front of FP (Fig. 7 (b)). At the peak of bow-down, the position of the deck is under the wave surface. It indicates that green water occurs in the condition. However, since the computational mesh in the analysis has dummy coverings on the deck, the simulation does not provide green water phenomena. The load of water on the deck (it might exist in the experiment) is not included in the evaluation of motion.

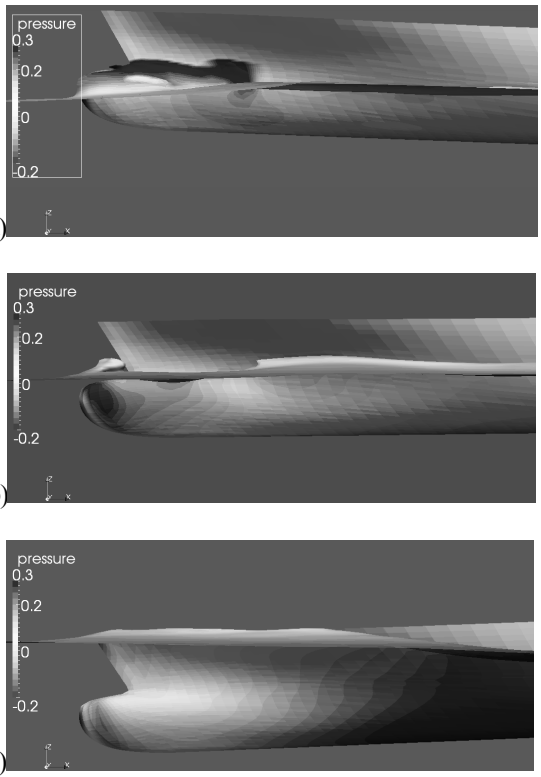

Fig.7 Side views of bow part from the peak of bow-up to bow-down, condition C4, Case 2-4, (a): t=0.82T, (b): t=1.07T, (c): t=1.32T.

6. CONCLUDING REMARKS

The authors numerically tested pitch and heave motions of KCS ship in head wave conditions (Case 2-4) using RaNS simulation code WISDAM-X. It showed accurate prediction of heave and pitch time history in the provided EFD data of conditions C2, C3 and C4. However, prediction of drag needs improvement. Since our numerical results show that green water occurs in conditions C3 and C4, a part of discrepancy in drag might be attributable to the green water load that is not included in the present simulation. In the condition C1, simulation results show the slow development of low frequency oscillation mode or slow transition between two possible modes of motion. However, it might be difficult to validate in towing tank experiments because of long measurement time required for the phenomena.

REFERENCES

Orihara, H. and Miyata, H. (2000), "Numerical simulation method for flows about a semi-planing boat with a transom stern", *Journal of ship research*, Vol. 4, No. 3, pp. 170-185.

Orihara, H. and Miyata, H. (2003), "Evaluation of added resistance in regular incident waves by computational fluid dynamics motion simulation using an overlapping grid system", *Journal of Marine Science and Technology,* Vol. 8, No 2, pp. 47-60

Akimoto, H. and Miyata, H., "Finite-volume simulation method to predict the performance of a sailing boat", Journal of Marine Science and Technology, Vol.7, No.1, pp. 31-42, 2002.

Miyata, H., Katsumata, M., Lee, Y. G. and Kajitani, H. (1988), "A finite-difference simulation method for strongly interacting two-layer flow," *Journal of Society of Naval Architects of Japan*, Vol. 163, pp. 1-16.

Sato, Y., Miyata, H., and Sato, T.(1999), "CFD simulation of 3-dimensional motion of a ship in waves: application to an advancing ship in regular head waves", *Journal of Marine Science and Technology*, Vol.4, No.3, pp. 108-116.

Baldwin, B. S. and Lomax, H. (1978), "Thin layer approximation and algebraic model for separated turbulent flow," *AIAA Paper,* 78-257

Germano, M. (1991), "A dynamic subgrid-scale eddy viscosity model," *Physics of Fluids A*, Vol. 3, No. 7, pp. 1760-1765

LARGE-SCALE RANS AND DDES COMPUTATIONS OF KVLCC2 AT DRIFT ANGLE 0 DEGREE

Tao Xing (Department of Mechanical Engineering, Tuskegee University, U.S.A.)
Pablo Carrica (IIHR-Hydroscience & Engineering, The University of Iowa, U.S.A.)
Frederick Stern (IIHR-Hydroscience & Engineering, The University of Iowa, U.S.A.)

1. SUMMARY

The objective of this study is to obtain numerical benchmark solutions for KVLCC2 at drift angle 0 deg. on a 305M points grid using both ARS and Delayed DES methods with quantitative verification and validation. The behavior of different numerical schemes and turbulence models on different grid resolutions are evaluated. Overall, differences between a TVD scheme and a hybrid 4th order scheme is negligible on such a fine grid. ARS is less dependent on grid resolution than DES. Compared to RANS, DES improves the prediction of the total resistance and velocity distribution for most regions at the propeller plane; however, DES tends to over-predict the velocity near the symmetry plane and the Reynolds stresses at the propeller plane. The grid induced separation using DES model is resolved by the DDES model, but both show modeled stress depletion inside the boundary layer.

2. COMPUTATIONAL METHOD

The three-dimensional (3D) unsteady two-phase CFD solver, CFDShip-Iowa V4.5 (Huang et al. 2008) is used. CFDShip-Iowa 4.5 is developed on top of CFDShip-Iowa V4.0 (Carrica et al. 2007a, 2007b, 2010), which was originally designed for ship hydrodynamics applications based on the single-phase level set method. CFDShip-Iowa has dynamic overset grids for large-amplitude motions including parent/children objects and controllers for multiple moving bodies. CFDShip-Iowa has been demonstrated for applications of up to 300 million grid points (Stern et al. 2009). Overset connectivity is obtained from the code Suggar (Noack 2009), which allows dynamic interpolations and has been recently optimized for large-scale computations (Carrica et al. 2010). The solver allows for detached eddy simulation (DES), delayed DES (DDES), has robust and accurate numerical schemes, and is geared for industrial CFD applications. The readers can refer to the corresponding references for details of models and numerics.

2.1 Numerical Methods

The equations are discretized using finite differences with body-fitted curvilinear grids. Unless otherwise stated, all simulations used TVD 2nd order with super bee limitation for the convection terms in the momentum equations. The other scheme used is the hybrid 4th order scheme (FD4). Both methods are documented in (Ismail et al. 2009). A projection algorithm is used to obtain a pressure equation and satisfy continuity (cf. Carrica et al. 2007b for details). The pressure Poisson equation is solved using the PETSc toolkit (Balay et al. 2002). All the other systems are solved using an alternating direction implicit (ADI) method. Suggar runs as a separate process from the flow solver and exchanges information with CFDShip-Iowa through MPI directives. All simulations on Grid 0 are conducted on the Navy's Cray XT5 using 1,728 processors. Simulations on other grids are performed on the Navy's IBM P6 using a number of processors ranging from 36 for Grid 4 to 128 for Grid 1.

2.2 Turbulence Models

Both RANS and DES models are used, including Algebraic Reynolds stress model (ARS), ARS-DES model, blended k-ω/k-ε-DES (BKW-DES), and BKW based DDES (BKW-DDES). The DDES formulation follows (Sainte-Rose et al. 2008). The readers can refer to (Xing et al. 2007) for formulations for other models. The destruction term in the equation of the turbulent kinetic energy of the SST model is modified:

$$\frac{Dk}{Dt} = \mathrm{Prod}_k - \frac{k^{3/2}}{l_{DDES}} + \mathrm{Diff}_k \tag{1}$$

where l_{DDES} is a modification of l_{DES} proposed by Strelets and Prod_k, Diff_k are respectively the production and diffusion term,

$$l_{DES} = \min\left(C_{DES}\Delta, l_{RANS}\right) \tag{2}$$

$$l_{DDES} = l_{RANS} - f_{DDES} \times \max\left(0, l_{RANS} - C_{DES}\Delta\right) \tag{3}$$

$$l_{RANS} = \frac{\sqrt{k}}{\beta^* \omega} \tag{4}$$

where Δ is the mesh scale.

2.3 Geometry, Flow Conditions and Complementary EFD

Case 1.1a in Gothenburg 2010 CFD Workshop is simulated. The geometry is a double model for KVLCC2 without rudder in straight ahead condition. KVLCC2 is the second variant of the MOERI tanker with more U-shaped stern frame-lines (Van et al. 1998a,b). The length between perpendiculars is Lpp=320m. The ship is fixed at zero sinkage and trim. Reynolds number is Re = 4.6×10^6. Simulations are compared with the EFD data by Van et al. (1998a) and Lee et al. (2003).

2.4 Computational Domain, Grid Topology and Boundary Conditions

The solution domain used in this study extends (-1.5L, 3.5L) in the streamwise direction (X), (-2L, 2L) in the transverse direction (Y), and (-2L, -1L) in the vertical direction (Z). The negative Z ensures that the code will not solve the level set transport equation. The top boundary is specified as "symmetry" boundary to mimic the "double-tanker" model in the experiments.

Grids 1, 2, 3, and 4 are systematically refined as shown in Table 1. Each grid consisted of a boundary layer grid for the ship hull and a background grid. Grid 0 (Table 2) is not systematically related to Grids 1 to 4 as it has additional refinement blocks for the boundary layer, wake region (Fairing Star/Port), and propeller region (Stern Star/Port).

Table 1. Grid dimensions for verification and validation

Grid	1	2	3	4
Ship	406×244×98 =9,708,272	287×174×69 =3,445,722	203×122×49 =1,213,534	144×88×35 =443,520
Back-ground	214×132×116 =3,276,768	152×93×82 =1,159,152	107×66×58 =409,596	76×47×41 =146,452
Total	12,985,040	4,604,874	1,623,130	589,972
y^+	0.40	0.56	0.80	1.13

Table 2. Finest Grid 0 dimension

Grids	Dimension
Boundary layer Star	421×101×251= 10,672,771
Boundary layer port	421×101×251= 10,672,771
Boundary layer refinement	491×301×151= 22,316,441
Fairing Star 1	281×301×301= 25,458,881
Fairing Star 2	351×301×301= 31,800,951
Fairing Port 1	281×301×301= 25,458,881
Fairing Port 2	351×301×301= 31,800,951
Stern Star 1	351×151×601= 31,853,601
Stern Star 2	351×151×601= 31,853,601
Stern Port 1	351×151×601= 31,853,601
Stern Port 2	351×151×601= 31,853,601
Background	421×301×151= 19,134,871
Total	304,730,922

2.5 Analysis Method

The Q-criterion (Hunt 1988) is used to identify the vortical structures. The Q-criterion is based on the second invariant of velocity gradient tensor $\nabla\mathbf{u}$. However, Q-criterion cannot be used to visualize the orientation of the vortex detected. To overcome this disadvantage, the normalized helicity density is proposed as follows and will be applied to color-code the Q-isosurfaces in the current study (Levy et al. 1990):

$$H_n = \frac{\mathbf{V}\cdot\boldsymbol{\omega}}{|\mathbf{V}||\boldsymbol{\omega}|} \tag{5}$$

Where $\mathbf{V}$ and $\boldsymbol{\omega}$ are the velocity and vorticity vector at the same point. The normalized helicity density H_n represents the directional cosine between the vorticity vector and the velocity vector, $-1 \le H_n \le 1$. The sign of H_n indicates the direction of swirl of the vortex relative to the streamwise velocity component.

The methodology and procedure for verification and validation follow the quantitative procedures proposed by Xing and Stern (2010).

TKE, or the total TKE, consists of resolved TKE and modeled TKE (Hedges et al. 2002). The resolved TKE $k_R(\mathbf{x})$ is evaluated using the resolved unsteady velocity components $u_i(\mathbf{x},t)$:

$$k_R(\mathbf{x}) = \frac{1}{2}\overline{u_i^2(\mathbf{x},t)} \tag{6}$$

where

$$u_i(\mathbf{x},t) = U_i(\mathbf{x},t) - \overline{U_i}(\mathbf{x}) \tag{7}$$

represent the unsteadiness caused by organized oscillations and random fluctuations and $\overline{U_i}(\mathbf{x})$ represent the time-averaged velocity components. $\overline{U_i}(\mathbf{x})$ are evaluated using:

$$\overline{U}(\mathbf{x}) = \overline{U(\mathbf{x},t)} = \frac{1}{T_0}\int_t^{t+T_0} U(\mathbf{x},t)dt \tag{8}$$

where T_0 is the averaging time. The resolved Reynolds stresses $\overline{u_iu_j}\big|_R$ are evaluated using:

$$\overline{u_iu_j}\big|_R = \frac{1}{T_0}\int_t^{t+T_0} u_i(\mathbf{x},t)u_j(\mathbf{x},t)\,dt \tag{9}$$

The time-averaged modeled TKE $\overline{k_M(\mathbf{x})}$ is calculated by time-averaging $k_M(\mathbf{x},t)$ evaluated by the two-equation turbulence model. The modeled Reynolds stresses for ARS model are output at each time step using

$$\overline{u_iu_j} = -\nu_T\left(\frac{\partial U_i}{\partial x_j}+\frac{\partial U_j}{\partial x_i}\right)+\frac{2}{3}k\delta_{ij}+a_{ij}^{(ex)}k \tag{10}$$

The modeled Reynolds stresses for DES and DDES uses the same equation except the last term account for the effect of the extra anisotropy is zero. DES and DDES resolve about 94% of the total TKE and Reynolds stresses. The modeled turbulent statistics show similar trends as the resolved in the region where LES is activated. For steady flow results (e.g. ARS), only the modeled TKE and Reynolds stresses are shown. For unsteady flow results (e.g. DDES), the total TKE and Reynolds stresses are shown.

3. RESULTS AND DISCUSSION

Complete results are presented in the supplemental materials available upon request. Herein, all tables and selected figures are extracted and discussed with special focus on RANS and DDES on Grid 0.

3.1 Verification and Validation

ARS-DES on Grids 1, 2, 3, 4 show that C_X only exhibits monotonic convergence on the three coarsest grids (2, 3, 4) whereas C_{XF} shows monotonic convergence on (1, 2, 3) and (2, 3, 4). This is due to the fact that ARS-DES on Grid 1 shows unsteady flow whereas all other grids predict steady flows and thus they are resolving different flow physics.

Table 3. Verification and validation for ARS-DES (*δ%ITTC for C_{XF})

Variables	Grids	R_G	P_G	U_G%	E%*	U_V%	U_D%
C_X	2,3,4	0.125	3.00	1.716	2.15	1.88	0.78
C_{XF}	1,2,3	0.059	4.09	0.228	22.54	—	—
C_{XF}	2,3,4	0.447	1.16	4.07	22.63	—	—

Table 4. Validation of resistance coefficients on different grids

Case	$C_{XF}\times10^{-2}$ (ITTC: -1.476)	C_{XF} (δ%ITTC)	$C_{XI}\times10^{-3}$	$C_X\times10^{-2}$ (EFD: -1.756)	C_X (E%D)
ARS-G1	-1.449	1.8%	-2.648	-1.714	2.4%
ARS-G0	-1.401	5.1%	-3.004	-1.702	3.1%
BKW-DDES-FD4-G0	-1.390	5.8%	-2.993	-1.692	3.6%
ARS-DES-G1	-1.434	2.9%	-2.993	-1.732	1.4%
ARS-DES-G2	-1.432	3.0%	-2.868	-1.719	2.1%
ARS-DES-G3	-1.415	4.1%	-2.980	-1.713	2.4%
ARS-DES-G4	-1.377	6.7%	-2.879	-1.665	5.2%

3.2 Iterative and Statistical Convergence

Parametric studies on the sub iterations (velocity and momentum coupling) for each time step ensure iterative convergence at each time step. The simulation is then advanced to the next time step. Simulations used five iterations. Statistical convergence of the running mean on the time history of C_{TX} establishes statistically stationary unsteady solutions. The criterion for statistical convergence of C_{TX} is that the oscillations/fluctuations of the running mean are less than 1% of the mean value, which is ensured for all cases run in this study. Based on this criterion, C_{TX} converges after 2 flow times for BKW-DDES-FD4-G0. An additional 4.8 flow times (T_0) after convergence was calculated in order to perform the statistical analysis for the mean velocities and all the turbulence structure analysis.

3.3 Force Convergence

Figure 1 shows the time history and running mean for C_{TX} for BKW-DDES-FD4-G0. All ARS simulations are steady state and thus not shown.

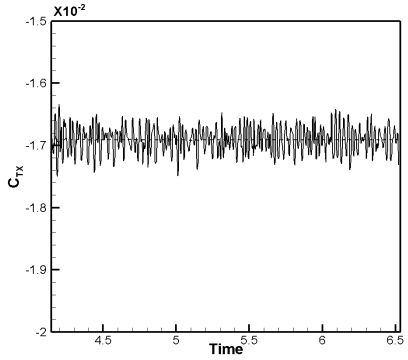

Figure 1. Time history and running mean of C_{TX} for BKW-DES-FD4-G0.

3.4 Vortical Structures, Velocities and Wake Fractions

Figure 2 shows the vortical structures for ARS on Grid 1, ARS-DES on Grid 1, and BKW-DDES-FD4 on Grid 0. ARS-G1 shows two main steady vortices with opposite rotation with respect to the symmetry plane at $y = 0$. These two vortices are dissipated very quickly downstream from the ship hull. ARS-DES-G1 predicts more complicated vortical structures that extend much longer distance downstream. BKW-DDES-FD4-G0 presents the broadest range of frequency content and vortical structures. Streamwise velocity contours, cross flow vectors and streamlines at the propeller plane are shown in Figure 3. DDES resolves the grid induced separation inside the boundary layer occurring with DES (not shown). Compared to ARS, the area enclosed by the contour line 0.9 and the distribution of the contour line 0.3 are improved using DDES. Total wake fraction w_T= 1-u/U and velocity on the propeller plane at z/Lpp = -0.05075 are shown in Figures 4 and 5, respectively. Compared to ARS, DDES improved the prediction of w_T at r/R=1.0 and 0.8 but over-predicts w_T at r/R=0.6 and 0.4, especially near the symmetry plane (ϕ=180°). No significant differences are shown in Figure 5 between ARS and DDES except near y=0 where ARS agrees better with EFD, which is consistent with Figure 4. Tables 5 and 6 show the L2 norm for the comparison error E for all the simulations shown in the supplemental materials. The minimum value for the error in each row is shown in bold face. Overall ARS-TVD-Grid0 predicts the best RANS results and BKW-DDES-FD4-Grid0 gives the best DES results. None of the methods is consistently better than any other method.

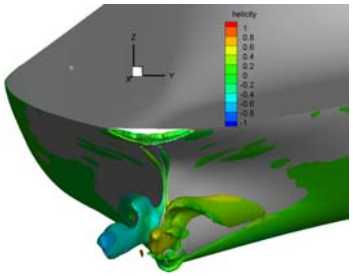

(a)

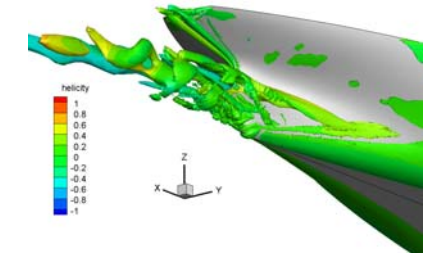

(b)

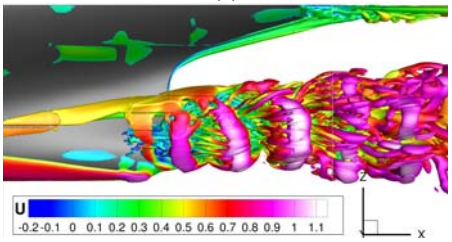

(c)

Figure 2. Instantaneous vortical structures (Iso-surface of Q=400 colored by helicity for a and b and axial velocity for c): (a)ARS-G1, (b)ARS-DES-G1, (c)BKW-DDES-FD4-G0.

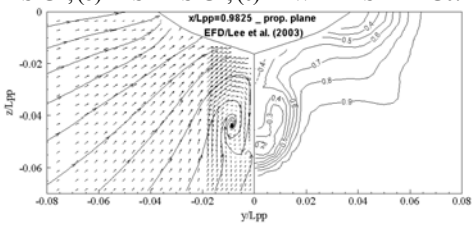

(a)

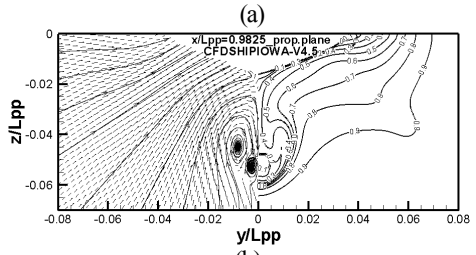

(b)

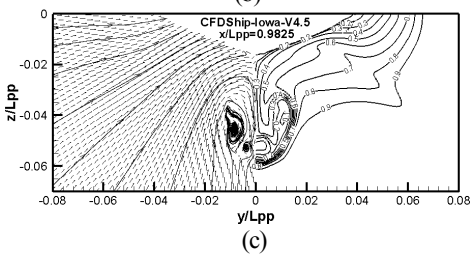

(c)

Figure 3: U contours (right panel), cross flow vectors and streamlines (left panel) at x/Lpp=0.9825: (a) EFD, (b) ARS-G0, (c) BKW-DDES-FD4-G0

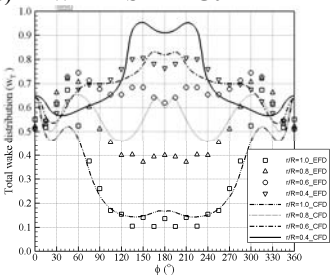

(a)

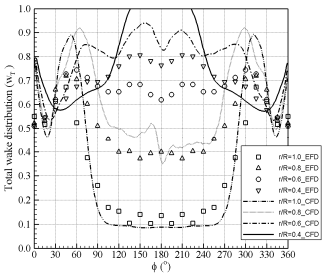

(b)

Figure 4: Total wake fraction (w_T) on the propeller plane (x/Lpp=0.9825): (a) ARS-G0, (b) BKW-DDES-FD4-G0.

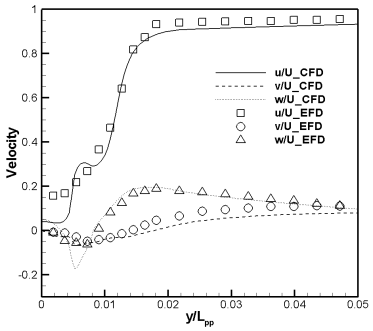

(a)

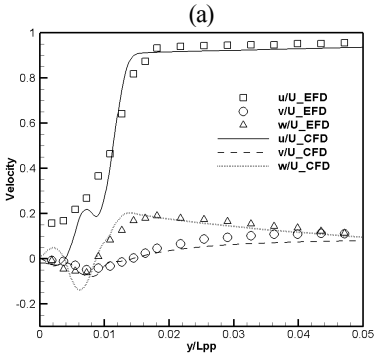

(b)

Figure 5: Velocity on the propeller plane (x/Lpp=0.9825) at (z/Lpp=-0.05075): (a) ARS-G0, (b) BKW-DDES-FD4-G0.

Table 5. *L2* Norm of the comparison error *E* for the total wake fraction w_T shown in Figure 4 (values are percentages based on maximum w_T=1 in the free stream).

w_T	ARS-G1	ARS-G0	ARS-DES-G1	BKW-DES-FD4-G0	BKW-DDES-FD4-G0
r/R = 1.0	12.5	**12.5**	27.6	26.3	36.0
r/R = 0.8	79.8	**32.3**	108.2	69.6	41.8
r/R = 0.6	46.1	**22.9**	59.8	26.8	69.2
r/R = 0.4	31.0	23.8	41.5	**12.4**	55.1

Table 6. *L2* Norm of the comparison error *E* for the velocity on the propeller plane shown in Figure 5 (values are percentages based on maximum free stream velocity U_∞=1).

Velocity	ARS-G1	ARS-G0	ARS-DES-G1	BKW-DES-FD4-G0	BKW-DDES-FD4-G0
u/U	26.7	**22.1**	31.9	30.5	36.4
v/U	13.6	13.3	14.3	11.3	**11.1**
w/U	**9.6**	13.9	14.9	17.9	14.2

3.5 Turbulent Structures

DES tends to over-predict the velocity and the Reynolds stresses near the symmetry plane at the propeller plane. Grid induced separation, i.e., LES is activated inside the boundary layer, is found for BKW-DES-FD4-G0. This was resolved by BKW-DDES-FD4-G0. However, compared to RANS, DES and DDES on Grid 0 exhibit modeled stress depletion (MSD) (Haase et al., 2009), i.e., modeled Reynolds stress inside the boundary layer is very small due to a very low value of turbulent eddy viscosity. This issue is less apparent on a coarser grid (see ARS-DES-Grid 1 in supplemental materials).

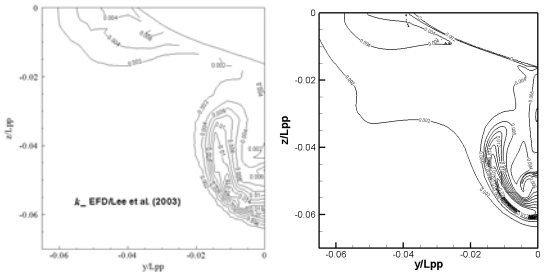

(a) (b)

(c)

Figure 6: Turbulent Kinetic energy (k) contours at (x/Lpp=0.9825): (a) EFD, (b) ARS-G0, (c) BKW-DDES-FD4-G0.

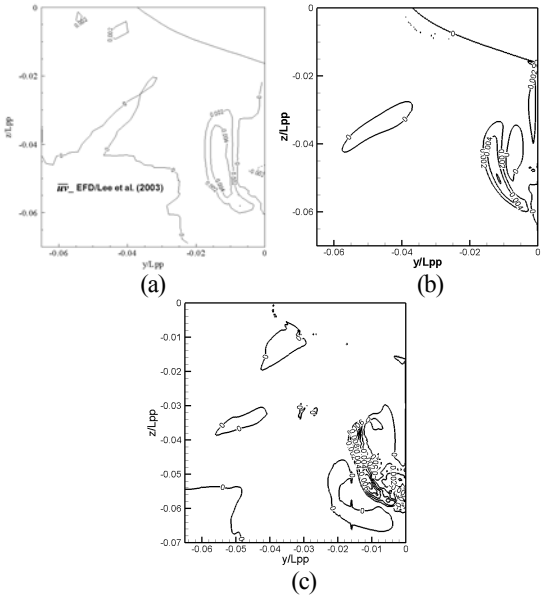

(a) (b)

(c)

Figure 7: $\overline{uv}$ contours at (x/Lpp=0.9825): (a) EFD, (b) ARS-G0, (c) BKW-DDES-FD4-G0.

3.6 Pressure Contours and Limiting Streamlines

Pressure contours and limiting streamlines for the ship hull are shown in Figures 8 and 9, respectively. Before the separation, there are no noticeable differences between ARS and BKW-DDES. Compared to ARS, BKW-DDES has an additional secondary separation line, which forms the vortices shown in Figure 2(c).

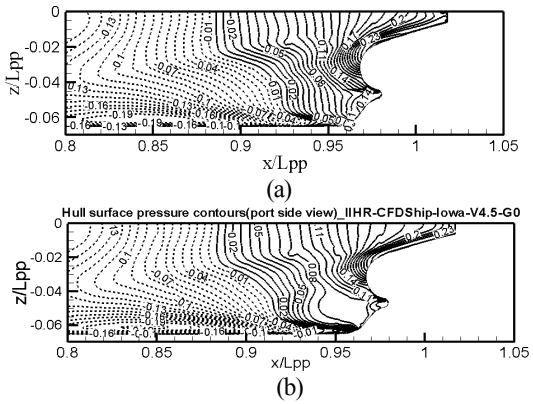

(a)

(b)

Figure 8: Hull surface pressure contours (port side view): (a) ARS-G0, (b) BKW-DDES-FD4-G0.

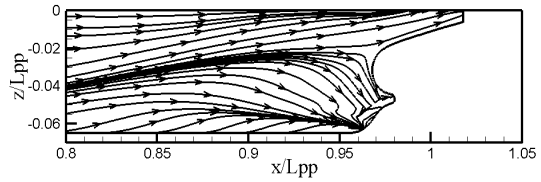

(a)

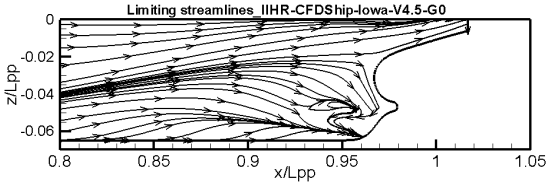

(b)

Figure 9: Limiting streamlines (port side view): (a) ARS-G0, (b) BKW-DDES-FD4-G0.

4. CONCLUSIONS AND FUTURE WORK

All simulations are steady except ARS-DES-Grid1, BKW-DES-FD4-Grid0, and BKW-DDES-FD4-Grid0. Compared to EFD, ARS-TVD-Grid0 predicts the best RANS results and BKW-DDES-FD4-Grid0 predicts the best DES results. None of the methods is consistently better than any other method. Ismail et al. (2009) identified that the TVD scheme is better than the FD4 and 2nd order upwind scheme on Grid 3. Herein, differences between the results of ARS-TVD-Grid0 and ARS-FD4-Grid0 are negligible, i.e., truncation error differences between different numerical schemes are negligible on the very fine grid.

ARS shows less dependence on grids than ARS-DES. Compared to RANS, DES improves the prediction of the total resistance and velocity distribution for most regions at the propeller plane; however, DES tends to over-predict the velocity near the symmetry plane and the Reynolds stresses at the propeller plane. Grid induced separation, i.e., LES is activated inside the boundary layer, is found for DES on Grid 0. This was resolved by the Delayed DES model on Grid 0. However, compared to RANS, DES and DDES on Grid 0 exhibit the modeled stress depletion, i.e., modeled Reynolds stress inside the boundary layer is very small due to a very low value of turbulent eddy viscosity. This issue is less apparent for a coarser grid (ARS-DES-Grid 1). The MSD could be resolved using the improved DDES (Shur et al., 2008), which is planned for future work.

REFERENCES

Balay, S., Buschelman, K., Gropp, W., Kaushik, D., Knepley, M., Curfman, L., Smith, B., and Zhang, H., (2002), "PETSc User Manual," Argonne National Laboratory, ANL-95/11-Revision 2.1.5

Carrica, P.M., Huang, J., Noack, R.W., Kaushik, D., Smith, B., Stern, F., (2010), "Large-scale DES Computations of the Forward Speed Diffraction and Pitch and Heave Problems for a Surface Combatant," *Computers & Fluids*, Volume 39, No. 7, pp.1095-1111

Carrica, P.M., Wilson, R.V., Noack, R.W., Stern, F., (2007), "Ship Motions Using Single-phase Level Set with Dynamic Overset Grids," *Computers & Fluids*, Volume 36, No. 9, pp. 1415-1433

Carrica, P.M., Wilson, R.V., Stern, F., (2007), "An Unsteady Single-phase Level Set Method for Viscous Free Surface Flows," *International Journal for Numerical Methods in Fluids*, Volume 53, No. 2, pp. 229-256

Haase, W., Braza, M., Revell, A., (2009), "*DESider-A European Effort on Hybrid RANS-LES Modelling*," Springer-Verlag Berlin Heidelberg

Hedges, L.S., Travin, A.K., Spalart, P.R., (2002), "Detached-Eddy Simulations over a Simplified Landing Gear," *Journal of Fluids Engineering, Transactions of the ASME*, Volume 124, pp. 413-423

Huang, J., Carrica, P.M., Stern, F., (2008), "Semi-coupled Air/Water Immersed Boundary Approach for Curvilinear Dynamic Overset Grids with Application to Ship Hydrodynamics," *International Journal for Numerical Methods in Fluids*, Volume 58, No. 6, pp. 591-624

Hunt, J.C.R., Wray, A.A., and Moin, P., (1988), "Eddies, Stream, and Convergence Zones in Turbulent Flows," Center for Turbulence Research, Report CTR-S88

Ismail, F., Carrica, P.M., Xing, T., Stern, F., (2009), "Evaluation of Linear and Nonlinear Convection Schemes on Multidimensional Non-orthogonal Grids with Applications to KVLCC2 Tanker," *International Journal for Numerical Methods in Fluids*, DOI: 10.1002/fld.2174

Lee, S.-J., Kim, H.-R., Kim, W.-J., and Van, S.-H., (2003), "Wind Tunnel Tests on Flow Characteristics of the KRISO 3,600 TEU containership and 300K VLCC Double-deck Ship Models," *Journal of Ship Research*, Vol. 47, No. 1, pp. 24-38

Levy, Y., Degani, D., Seginer, A., (1990), "Graphical Visualization of Vortical Flows by Means of Helicity," *AIAA Journal*, Volume 28, pp. 1347-1352

Noack, R., Boger, B., (2009), "Improvements to SUGGAR and DiRTlib for Overset Store Separation Simulations," 47th AIAA Aerospace Sciences Meeting Including the New Horizons Forum and Aerospace Exposition, AIAA paper 2009-340

Sainte-Rose, B., Bertier, N., Deck, S., (2008), "Delayed Detached Eddy Simulation of a Premixed Methane Air Flame behind a Backward Facing Step," 44th AIAA/ASME/SAE/ASEE Joint Propulsion Conference & Exhibit, AIAA 2008-5134

Shur, M., Spalart, P., Strelets, M., Travin, A., (2008), "A Hybrid RANS-LES Approach with Delayed-DES and Wall-modelled LES Capabilities," *International Journal of Heat and Fluid Flow*, Volume 29, No. 6, pp. 1638-1649

Stern, F., Bhushan, S., Carrica, P.M., and Yang, J.M., (2009), "Large Scale Parallel Computing and Scalability Study for Surface Combatant Static Maneuver and Straight Ahead Conditions Using CFDShip-Iowa," Invited paper in ParCFD 2009 Special Session "Parallel CFD in Ship Aero and Hydrodynamics."

Van, S.H., Kim, W.J., Yim, D.H., Kim, G.T., Lee, C.J., and Eom, J.Y., (1998a), "Flow Measurement around a 300K VLCC Model," Proceedings of the Annual Spring Meeting, SNAK, Ulsan, pp. 185-188

Van, S.H., Kim, W.J., Yim, G.T., Kim, D.H., and Lee, C.J., (1998b), "Experimental Investigation of the Flow Characteristics Around Practical Hull Forms," Proceedings 3rd Osaka Colloquium on Advanced CFD Applications to Ship Flow and Hull Form Design, Osaka, Japan

Xing, T., Shao, J., and Stern, F., (2007), "BKW- RS-DES of Unsteady Vortical Flow for KVLCC2 at Large Drift Angles," the 9th international conference on Numerical Ship Hydrodynamics, Ann Arbor, Michigan

Xing, T., Stern, F., (2010), "Factors of Safety for Richdson Extrapolation," *Journal of Fluids Engineering, Transactions of the ASME*, Volume 132, No. 6, DOI: 061403.

URANS SIMULATION AND VALIDATION OF ADDED RESISTANCE AND MOTIONS OF THE KVLCC2 CRUDE CARRIER WITH FIXED AND FREE SURGE CONDITIONS

Hamid Sadat-Hosseini (IIHR-Hydroscience and Engineering, The University of Iowa, USA)
Pablo M. Carrica (IIHR-Hydroscience and Engineering, The University of Iowa, USA)
Ho Kim (Department of Naval Architecture & Ocean Engineering, Osaka University, Japan)
Toda Yasuyuki (Department of Naval Architecture & Ocean Engineering, Osaka University, Japan)
Frederick Stern (IIHR-Hydroscience and Engineering, The University of Iowa, USA)

1. SUMMARY

CFD is used to study the KVLCC2 commercial tanker ship responses advancing at Froude number 0.142 in head waves and calm water. The simulations are performed for both free and fixed surge conditions and for a range of wave lengths. The free surge condition is achieved by using a spring to attach the model to the towing carriage. The responses for heave, pitch, and surge motions and added resistance are discussed and compared with the available experimental data. The maximum response conditions for KVLCC2 and nonlinearities in motions and added resistance are also investigated. For calm water, CFD closely agrees with EFD for resistance, surge, sinkage, and trim. CFD predicts very well amplitude and phase responses for heave, pitch, surge, and added resistance in waves. Nonlinearities and harmonics at the spring frequency are observed only for surge motion and resistance. The maximum responses for vertical motions occur when the encounter frequency is close to the heave and pitch natural frequencies while the maximum surge motion was for the longest wave. The amplitude of added resistance is highest for $\lambda/L=1.1$. Overall, the comparison of free with fixed surge results indicate no significant differences for heave, pitch and added resistance.

2. INTRODUCTION

The study of the behavior and performance of the ships in sea waves are one of the essential aspects of ship design. Ship responses and motions are significantly important from a safety point of view. On the other hand, added resistance and speed loss, which are due to diffraction of incident waves on the bow, are important from an economic point of view. Since accurate estimation of ship responses and added resistance are critical, many researchers have investigated ship behavior in waves. Recent efforts have focused on using CFD for different test cases. Simonsen et al. (2008) presented RANS simulation of the KCS container ship in regular head waves, showing good agreement for pitch and heave motions, but resistance was under predicted. Paik et al. (2009) performed simulations for pitch and heave computations of the S175 considering fluid-structure interactions. Predicted heave and pitch matched well with the experimental values. The elastic models predicted well the ringing of the structure and showed that the ringing was mainly triggered by bow flare slamming. Castiglione et al. (2009) studied the response of high speed DELFT catamaran in regular head waves for a range of wavelengths and several Froude numbers, focusing on the maximum response conditions. The peak heave and pitch responses occurred at the resonant frequency for all Froude numbers simulated. The response amplitude peaks increased with the Froude number, reaching their maximum at the highest speed. Carrica et al. (2008) demonstrated full 6DOF simulation capability in irregular waves with a steered rudder using a body force model propeller model. Sadat-Hosseini et al. (2010a,b) studied extreme motions due to broaching and parametric rolling in regular waves for surface combatant ONR Tumblehome. The results compare reasonably well with the experimental data. Mousaviraad (2010) developed a harmonic wave group single run procedure for seakeeping computations, and compared with experiments and regular wave and transient wave group procedures.

This paper discusses the results of simulations for KVLCC2 crude carrier advancing at Fr=0.142 in regular head waves. The simulations are carried out for fixed and free surge conditions for wave amplitude A/L=0.009375 and for a range of wave length. The free surge condition is achieved using a spring to attach the model to the towing carriage.

3. EFD SETUP AND CONDITIONS

Model tests were conducted for KVLCC2, a modern commercial tanker ship with bulbous bow and stern bulb, as shown in Fig.1. The model has no appendages, rudders

or propellers. The coordinate system is located at centre of gravity, with *x* pointing toward the aft (positive downstream), *y* to starboard and *z* upwards.

The free surge tests were conducted in the Osaka University's towing tank for a 1/100 scaled model (L=3.2 m) while the fixed surge tests were conducted with the same model in the INSEAN 220x9x3.5 m towing tank. For the free surge tests, the model was towed with a light weight carriage connected to the main carriage by a spring, allowing the model to surge freely, while a gimbal permits heave and pitch, as shown in Fig 2. An external force F_0 was used to avoid excessive spring stretching and was chosen roughly as the total resistance in waves. The mass of the model including hull and gimbal (shown in red in Fig. 2) was m_1=306.2 Kg. The mass of the dynamometer (in blue) and light weight carriage (in green) were m_2=6.4 Kg and m_3=2.5 Kg, respectively.

The model was towed at Froude number 0.142 in head waves with A/L=0.009375 and λ/L=0.6-2.0, and in calm water. The wave signal, surge, heave, pitch, and F_x were recorded for all cases. Some extra tests were also performed to check repeatability.

Fig.1 KVLCC2 hull from.

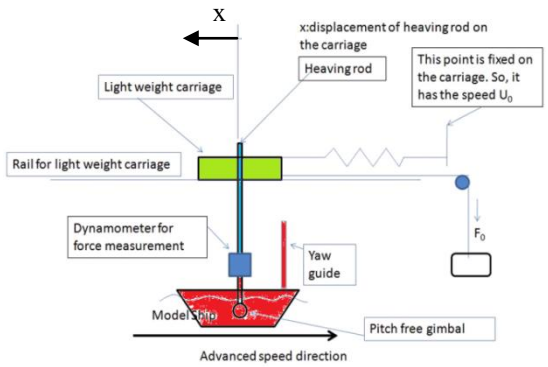

Fig.2 Test setup for free surge condition.

4. CFD SETUP

CFDShip-Iowa v4.5, see Carrica et al. (2008) and references therein, is used for the CFD computations. CFDShip-Iowa is an overset, block structured CFD solver using non-orthogonal curvilinear coordinate system for arbitrary moving control volumes. Turbulence models include blended k-ω/k-ε and DES approaches. A single-phase level set method is used for free-surface capturing. Captive, semi-captive, and full 6DOF capabilities for multi-objects with parent/child hierarchy are available. Numerical methods include advanced iterative solvers, higher order finite differences with conservative formulation, PISO or projection methods for pressure-velocity coupling, and parallelization with MPI-based domain decomposition.

The computational domain extends from -0.8<x<2, 0<y<1, -1<z<0.2 in dimensionless coordinates based on ship length. Only half of the ship is modeled due symmetry of the test cases. The ship axis is aligned with x with the bow at x=0 and the stern at x=1. The y axis is positive to starboard with z pointing upward. The free surface at rest lies at z=0. The computational grids are overset, with independent grids for the boundary layer, shaft, stern bulb, refinement, and background, and then assembled together to generate the global grid. A Cartesian grid is used to impose the far-field boundary conditions and to resolve the flow far from the hull, with a refinement Cartesian block closer to the ship. The total number of grid points is 4.73 M.

The validation was performed at model scale based on comparison error E for heave, pitch, and surge motions and added resistance, for fixed and free surge conditions in calm water and head waves with A/L=0.009375, λ/L=0.6-2.0, and Fr=0.142 ($Re=2.55\times10^6$).

5. RESULTS

5.1 Resistance Test and Heave and Pitch Natural Frequencies

Table 1 shows EFD and CFD results in calm water with free surge. EFD dynamic sinkage and trim are -0.31783 cm and -0.129 deg, respectively. The EFD resistance is 4.3844 N, corresponding to a resistance coefficient C_T=0.0051. The EFD surge is 1.24 cm, for an external force F_0=3.16 N ($x=(R-F_0)/K$). EFD data for fixed surge is also given in Table 1. The free and fixed condition should not change the steady state values of motions and resistance but the transient values. EFD for fixed surge shows fairly similar value for resistance but sinkage and trim are different most probably due to discrepancies in the static condition. CFD predicts sinkage and trim by E=-2.13%D and 4.04 %D, respectively. The error is in the same order of previous CFD simulations errors reported by Sadat-Hosseini et al. (2010a,b). CFD over predicts the resistance by 7.8%D. CFD shows that 69% of the resistance is due to friction, R_F=3.28 N, 3% lower than the ITTC prediction R_F=3.38 N. The surge agrees well with EFD with -4.5%D.

Table 1 Comparison of CFD and EFD resistance force and motions for resistance test in calm water.

	EFD (Free Surge)	EFD (Fixed Surge)	CFD (Free Surge)	E%D
Sinkage (cm)	-0.3178	-0.259	-0.3246	-2.13
Trim (deg)	-0.1290	-0.142	-0.1238	4.04
x (cm)	1.2426	-	1.2992	-4.55
X (N)	4.3844	4.425	4.7268	-7.8

5.2 Time Histories of Added Resistance and Motions

The time histories of sinkage and trim, not shown here, indicate that EFD sinkage and trim oscillate at $f_n \approx 0.72$

HZ. This frequency should be equivalent to the coupled heave and pitch natural frequency at Fr=0.142. The coupled heave and pitch natural frequency neglecting speed effects can also be estimated using the empirical formula derived by Irvine et al. (2008) resulting in $f_n \approx$ 0.81 HZ. Herein, the heave and pitch natural frequency is assumed to be the average of these two values, $f_n \approx$ 0.765.

Figure 3 shows comparisons of motions and axial force for λ/L=0.6. EFD data is only available for free surge condition while CFD simulations are performed for both free and fixed surge conditions. EFD heave and pitch respond with the encounter frequency as expected but with low frequency oscillations, probably due to variations on the incident waves. The mean values of heave (-0.3147 cm) and pitch (-0.124 deg) are close to the values for calm water. The heave and pitch amplitudes are 0.06A and 0.017Ak, respectively, with about 100 deg phase lag between them. FFT results indicate no nonlinearity or higher order harmonics in heave and pitch responses. The surge motion and axial force oscillate at encounter frequency and at the spring natural frequency $f_{spring} = 1/2\pi\sqrt{K/m} = 0.09\,Hz$, as shown in Fig. 3. The EFD test was not carried out for long enough time to include multiple spring periods such that the surge motions behaves barely periodic. The amplitudes of surge harmonics at f_e and f_{spring} are about 0.055A and 0.18A, respectively, which is almost the same order as heave motion. The mean value of surge motion is unimportant as it is shifted by an arbitrary F_0 used in the experiment. The EFD setup has measured the hydrodynamic force excluding inertial component such that $F_x = F_{hydro} - m\ddot{x}$. Thus, the amplitude of measured force F_x is much smaller than that of hydrodynamic force. Yet, the mean values for F_x and F_{hydro} are the same and can be used to estimate resistance in waves and added resistance. The mean value of EFD axial force is 6.85 N. This is 2.47 N larger than for calm water, which represents the added resistance at wave length λ/L=0.6 and Fr=0.142. For free surge condition, CFD heave and pitch show close agreement with EFD in terms of mean value, amplitude, and phase. CFD heave and pitch amplitudes are about 0.054A and 0.0198Ak, respectively. Thus, the heave amplitude is under predicted by 10%D and the pitch amplitude is over predicted by the same amount. CFD results show no higher harmonics similar to EFD. The mean values of heave and pitch are predicted within 6%D. The errors in mean values are probably due to discrepancies on EFD and CFD static sinkage and trim. The CFD surge motion is shifted to match the mean value to that of EFD, as CFD was blind in that EFD F_0 was unknown. The surge oscillates at encounter and spring frequency with the amplitude of 0.056A at f_e, very similar to the EFD values. For F_x, the mean value is under predicted by 7%D suggesting added resistance is under predicted as well.

Comparisons with fixed surge results indicate no significant differences for heave and pitch responses. This emphasizes that there is no strong coupling between heave/pitch and surge motion. F_x shows very large amplitude for fixed surge condition, as x is zero and F_x is not subtracted by the inertial force. The mean value is five percent larger than that for free surge condition and consequently would show to some extent larger added resistance.

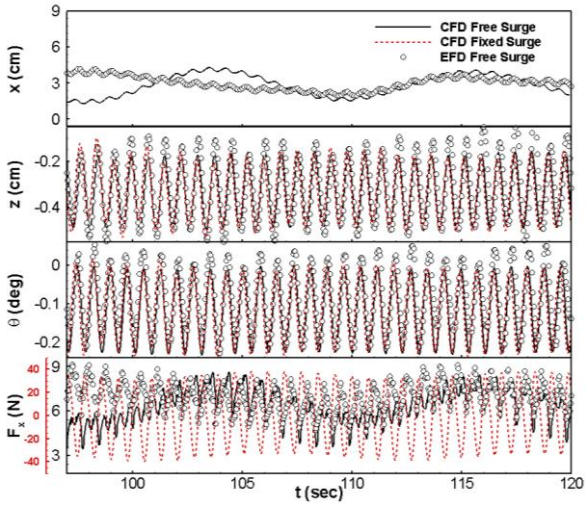

Fig.3 Time histories for λ/L=0.6.

Figure 4 shows results for λ/L=1.1. For free surge EFD heave and pitch show that the ship motions just follow the sinusoidal incident wave pattern with a period corresponding to the encounter frequency. The amplitudes of heave and pitch are 0.66A and 0.50Ak, respectively. These motions are very significant compared to those for λ/L=0.6 as the encounter frequency for the current wave length and Fr=0.142 is closer to heave and pitch natural frequency. Yet, higher harmonics and nonlinearities are not observed. The phase lag between these motions is about 60 deg. The mean values are -0.32 cm and -0.134 deg suggesting that the ship is oscillating around a bow down position while it is sank. The EFD surge motion oscillates at high frequency due to wave and low frequency due to spring. The surge amplitude for high frequency oscillations is about 0.073A, much smaller than heave amplitude, and the amplitude at f_{spring} is 0.319A. Note that the restoring force for surge motion is the spring force so that the surge resonance could only occur if wave encounter frequency reaches to the spring natural frequency. The surge mean value is about 7.08 cm which is induced by the incident wave force and F_0. The EFD axial force has the same pattern as the surge motion, oscillating at both encounter and spring frequencies. The mean axial force is 10.39 N which compared to the resistance in cam water results in 58% of the mean value due to added resistance. The axial force for high frequency oscillations show first and second harmonics with amplitudes 0.786 N at f_e and 0.15 N at $2f_e$. The amplitude due to the spring oscillation is about 0.88 N. CFD shows remarkably good agreement with EFD heave and pitch motions, both showing essentially linear behavior. The heave and pitch amplitudes are 0.65A and 0.51Ak, respectively, yielding prediction errors of less

than 3%D for heave and pitch. Moreover, the errors for mean values are also less than 3%D. The CFD surge motion oscillates at the encounter and spring frequencies, as observed in EFD. The amplitude of the high frequency oscillation is over predicted by 8%D, whereas the amplitude of low frequency oscillations is under predicted by nearly same amount. The mean value of CFD surge is shifted to match that of EFD, as discussed earlier. The CFD axial force presents harmonics at f_e and f_{spring}. The amplitude of the first harmonic at f_e is 0.563 N, under predicted by 28%D. Nevertheless, the mean value is over predicted by only 3%D resulting in a good prediction of added resistance.

For fixed surge condition, there was no phase reference provided for EFD waves so all EFD time histories, shown in Fig. 4, are shifted manually to fit roughly on the data for free surge condition. This limits phase comparison and makes time histories for fixed surge condition only useful to evaluate the amplitudes and relative phases between heave and pitch motions. EFD shows sinusoidal pattern for heave and pitch motions with amplitudes z=0.66A and θ=0.56Ak, same heave but larger pitch amplitude compared to free surge condition. The mean values are -0.357 cm and -0.183 deg, different with those values for free surge condition. The EFD axial force oscillates at f_e with mean value of 10.74 N and amplitude of 37.17 N. As shown in Fig 4, the amplitude of F_x for fixed surge is much larger than that for free surge, as expected. However, the mean values are fairly close and thus the added resistance should be nearly similar for both conditions. The CFD results for fixed surge condition show less than 3% deviation in heave and pitch mean values or amplitudes compared to values for free surge conditions. The amplitude of axial force increases to 23.5 N for fixed surge. Also, the mean value is 11.28 N showing a 5% increase for fixed surge condition.

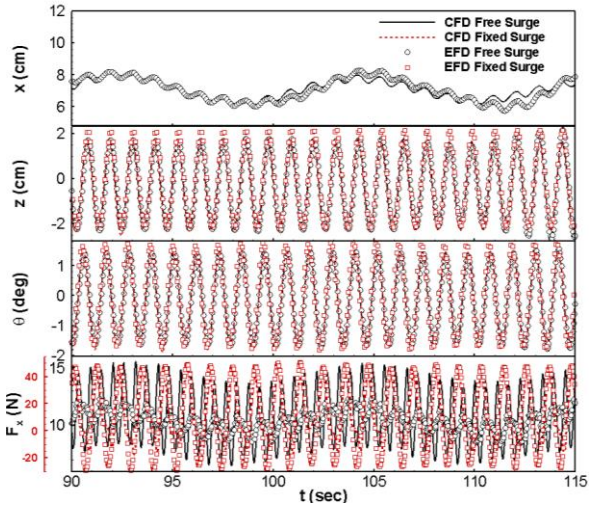

Fig.4 Time histories for λ/L=1.1.

The results for λ/L=1.6 are shown in Fig. 5. For free surge condition, the experimental heave and pitch show similar pattern to those for case λ/L=1.1 but with larger amplitude such that heave and pitch oscillate at 0.88A and 0.85Ak, respectively. Also, the mean value errors increase to about 10%D. The EFD surge motion shows clearly harmonics at spring and wave encounter frequencies. The amplitude of the oscillations at f_e and f_{spring} are 0.24A and 0.31A, respectively. The EFD axial force oscillates tightly with surge motion. The mean value of axial force is 5.98 N, introducing 1.6N added resistance for λ/L=1.6 and Fr=0.142. The added resistance is less than that for λ/L=1.1, indicating that the wave condition is beyond the point of maximum resistance on the ship. The resistance has a mean value of 5.99 N with amplitudes of 1.82 N at f_e and 0.7 N at f_{spring}. Also, there is a weak second harmonic at $2f_e$ with amplitude of 0.07 N. The CFD heave and pitch responses show fairly close agreement with EFD. The amplitudes of heave and pitch motions are 0.84A and 0.94AK, respectively, and thus under and over predicted by 4%D and 10%D, respectively. CFD predicts surge motion with similar harmonics observed for EFD. The amplitude of surge at f_e is under predicted by less than 1%D exhibiting a remarkable agreement with EFD. CFD over predicts the mean value of axial force by 40%D and accordingly also the added resistance.

For fixed surge condition, EFD amplitudes of heave and pitch are z=0.90A and θ=1.2Ak, similar to the free surge condition for heave but 40% larger for pitch.. The mean value of axial force is 7.1 N compared to 5.9 N for free surge condition showing that the added resistance is larger for fixed surge condition. CFD shows good agreement for pitch, heave, and axial force. The heave and pitch amplitudes are under predicted by 5%D and 20%D, respectively. F_x mean value is 8.06 N, over predicted by 13%D, while the amplitude is under predicted.

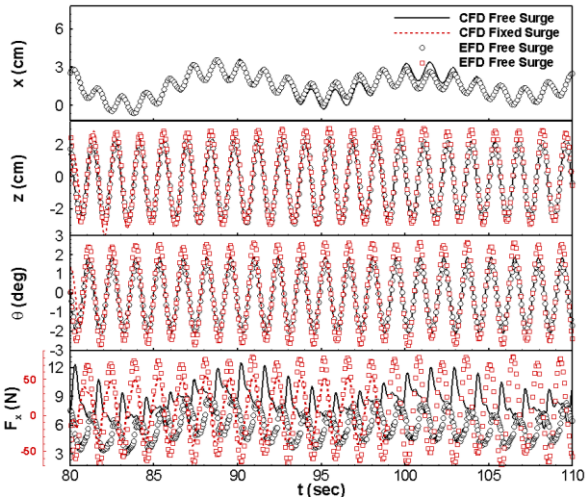

Fig.5 Time histories for λ/L=1.6.

5.3 Amplitude and Phase Responses of Added Resistance and Motions

Figure 6 shows heave amplitude and phase for CFD compared with EFD data for both free and fixed surge. EFD data for free surge condition are available for 0.6<λ/L<2 and include repeated tests. Fixed surge data is presented for only λ/L=1.1 and 1.6. For free surge

condition, the EFD heave amplitude is fairly small for short waves and reaches to about wave amplitude *A* for long waves as the ship just moves up and down with the amplitude of wave at large wave length. The heave response increases dramatically for λ/L>1 and the maximum response is observed for λ/L=1.4, where the encounter frequency is f_e=0.768, close to the natural frequency. The heave phase indicates no phase lag between heave response and wave at large wave length underlining that heave is synchronized with incident wave. The maximum phase lag is 90 deg which occurs at λ/L=1 i.e. the heave response is close to zero when wave crest is located on center of gravity and λ/L=1. The average CFD prediction error for heave amplitude is 7.06%D for the whole range of wave lengths. The maximum error is for the shortest wave length and is 1.5 times the average error. To avoid the meaningless large phase errors for phases close to zero, the phases are added by 180 deg before being used to evaluate the error of CFD phase prediction. CFD predicts the phase by 3.7%D with the maximum error of 14.22%D for the shortest wave. Overall, CFD simulations predict remarkably well the trends and the values for both heave amplitude and the phase. The results for fixed surge condition show no significant changes.

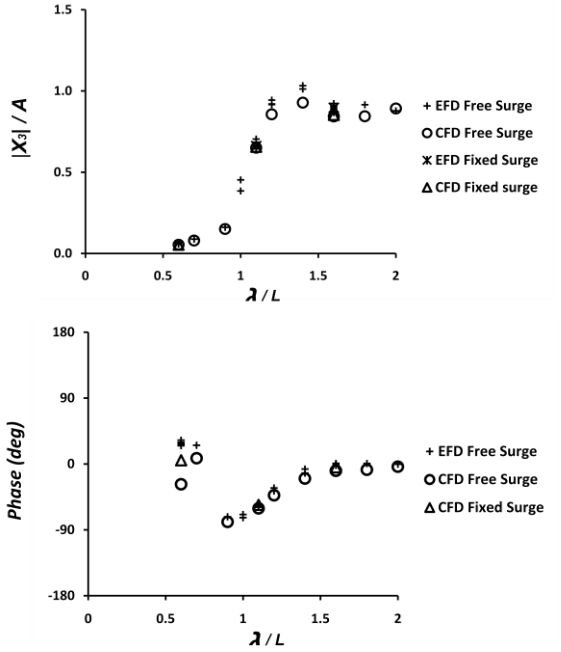

Fig.6 Heave amplitude and phase responses at Fr=0.142.

The pitch amplitude and phase are plotted in Fig. 7. For free surge condition, the pitch amplitude increases with wave length to slightly more than 1.0 at long waves. The rate of pitch amplitude increase is fairly constant from λ/L=0.9 to λ/L=1.4. The pitch phase indicates that the ship reaches an asymptotic behavior for long waves, where the pitch response leads 90 deg the incoming waves, indicating that the pitch is in phase with the wave slope. The minimum phase lag is -90 deg observed for λ/L=0.7. This means that the ship is in bow up position while the center gravity of ship is located on the wave downslope. CFD shows very good agreement with EFD. The average error of pitch amplitude is 4.2%D for the current range of wave lengths. The maximum prediction error is for the maximum wave length, 13%D. The CFD phase also shows good prediction with average error 5.29%D and maximum 17.6%D for λ/L=0.7. For fixed surge condition, CFD and EFD show similar trends to those for free surge condition except that the EFD pitch for λ/L=1.6 is notably different.

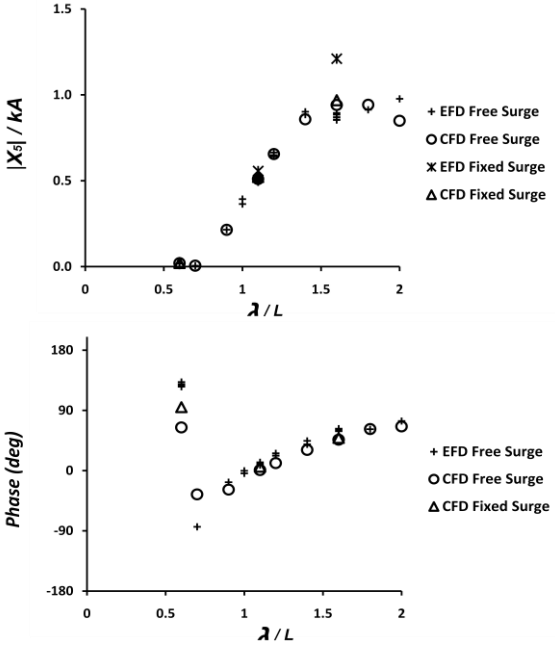

Fig.7 Pitch amplitude and phase responses at Fr=0.142.

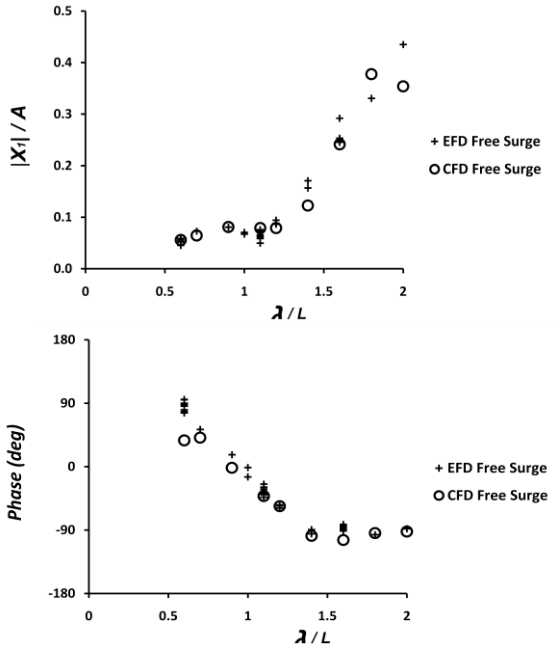

Fig.8 Surge amplitude and phase responses at Fr=0.142.

The surge amplitude and phase are shown in Fig. 8. The surge amplitude indicates that maximum response is for the largest wave in which surge amplitude is about 50%

of the wave amplitude. The phase shows that the surge amplitude is maximum when the ship is located on wave downslope in long waves or on wave upslope in short waves. CFD predicts similar trends for surge amplitude and phase. The average error of CFD simulation is 12.3 and 3.5%D for amplitude and phase, respectively. The maximum errors are about twice the average errors which take place at λ/L=1.4 for amplitude and λ/L=0.6 for phase .

The added resistance is shown in Fig. 9. The EFD repeated tests do not show good repeatability. In particular, the added resistance at λ/L=1.1 is scattered around ±10% of its average value. The maximum added resistance occurs around λ/L=1.1. The CFD simulation under predicts the added resistance for short waves and over predicts it for long waves. The average error is 42%D with maximum error for the longest wave. Fixed surge condition results display fairly similar values for λ/L=1.1 but slightly different for λ/L=1.6.

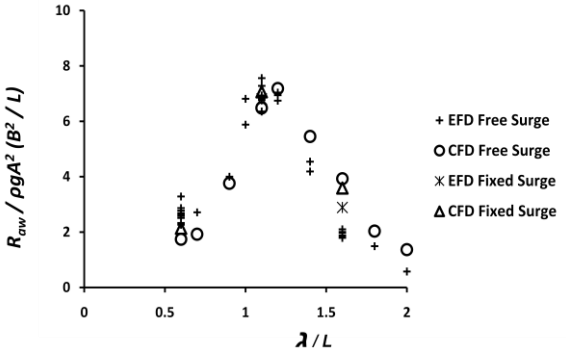

Fig.9 Added resistance at Fr=0.142.

6. CONCLUSIONS

CFD is used to study the KVLCC2 tanker ship responses advancing at Froude number 0.142 in head waves and calm water. The simulations are performed for both free and fixed surge conditions and for a range of wave lengths.

For calm water, EFD for fixed and free surge show fairly similar values for resistance but sinkage and trim are different, most probably due to discrepancies in the static conditions. CFD closely agrees with EFD for resistance, surge, sinkage, and trim with the average error of 4.6%D. The natural coupled heave and pitch frequency is estimated at 0.765 Hz, suggesting resonance in head waves will occur around λ/L=1.4 at Fr=0.142, where the wave encounter frequency is 0.768 HZ.

For head waves, CFD and EFD heave and pitch respond linearly with a period corresponding to the encounter frequency, showing no nonlinearities or higher order harmonics. Surge motion and axial force oscillate at the encounter frequency and at a lower frequency corresponding to the resonance frequency of the spring-ship system. Higher order harmonics are observed for surge motion and axial force. The comparison with fixed surge results indicates that there is no strong coupling between heave/pitch and surge motion. CFD predicts remarkably well the amplitudes and phases for heave, pitch, surge, and added resistance. The average CFD prediction error for all the amplitudes and phases of motions are 7.85%D and 4.16%D, respectively, for the whole range of wave lengths. CFD predicts well the trend for added resistance with a maximum around λ/L=1.1. The CFD simulation under predicts the added resistance for short waves and over predicts it for long waves. Fixed surge condition results illustrate fairly similar values for λ/L=1.1 but slightly different for λ/L=1.6 for pitch amplitude and added resistance.

ACKNOWLEDGEMENTS

This research was sponsored by the US Office of Naval Research, grants N00014-10-1-0017 and N000140-91-09-5-4 under administration Dr. Patrick Purtell.

REFERENCES

Carrica, P.M., Paik, K.J., Hosseini, H.S., and Stern, F., (2008), "URANS analysis of a broaching event in irregular quartering seas", J Marine Sci and Tech, 13, p395-407.

Castiglione, T., Stern, F., Kandasamy, M., Bova, S., (2009), "Unsteady RANS simulations for a catamaran advancing in regular waves", 10th International Conference on Fast Sea Transportation, Athens, Greece.

Irvine, M., Longo, J. & Stern, F., (2008). "Pitch and heave tests and uncertainty assessment for a surface combatant in regular waves", J. Ship Research, 52, p146-163.

Mousaviraad, M.S., Carrica, P. & Stern, F., (2010). "Development and validation of harmonic wave group single-run procedure for RAO with comparison to regular wave and transient wave group procedures using URANS", Ocean Engineering 37, p653-666.

Paik, K., Carrica, P.M., Lee, D., Maki, K., (2009), "Strongly coupled fluid–structure interaction method for structural loads on surface ships", Ocean Engineering, 36, p1346-1357.

Sadat-Hosseini, H., Carrica, P., Stern, F., Umeda, N., Hashimoto, H., Yamamura, S., Mastuda, A., (2010), "CFD, system-based and EFD study of ship dynamic instability events: surf-riding, periodic motion, and broaching", Journal of Ocean Engineering, In Press.

Sadat-Hosseini, H., Stern, F., Olivieri, A., Campana, E., Hashimoto, H., Umeda, N., Bulian, G., Francescutto, A., (2010), "Head-waves parametric rolling of surface combatant", Ocean Engineering, 37, p859-878.

Simonsen, C., Otzen, J. & Stern, F., (2008), "EFD and CFD for KCS heaving and pitching in regular head waves", Proc. 27th Symp. on Naval Hydro., Korea.

Wilson, R.V., Ji, L., Karman, S.L., Hyams, D.G., Sreenivas, K., Taylor, L.K., Whitfield, D.L., (2008), "Simulation of large amplitude ship motions for prediction of fluid–structure interaction", Proc. 27th Symp. on Naval Hydro., ONR, . Korea.

FULL SCALE SELF-PROPULSION COMPUTATIONS WITH DISCRETIZED PROPELLER ON KRISO CONTAINER SHIP KCS

Alejandro M. Castro (IIHR-Hydroscience and Engineering, USA)
Pablo M. Carrica (IIHR-Hydroscience and Engineering, USA)
Frederick Stern (IIHR-Hydroscience and Engineering, USA)

1. SUMMARY

Self-propulsion computations of the KCS containership are performed in full-scale with discretized propeller. The self-propulsion point is obtained following the procedure of Carrica et al. (2010), in which a controller is used to modify the propeller RPS until a target speed is reached. To obtain propulsion coefficients the open-water curves of the propeller and a towed case are also computed. Results are comparable with those obtained in model scale at the ship point.

2. INTRODUCTION

CFD has been used in attempts to predict self-propulsion and powering characteristics, with good success. Due to the small time steps and high-cost required in a discretized propeller approach, most self-propulsion simulations are performed using a body force model of the propeller. The level of complexity of these body force approaches vary from a prescribed body force (Choi et al. 2010), to coupling with a potential flow solver of some kind to account for the non-uniform inflow at the propeller plane (Kim et al. 2006, Vogt and Hochbaum 2008).

Fully discretized propeller computations in ships are reported in the literature. Lübke (2005) computed the container KCS under self-propelled conditions using the commercial code CFX. Pankajakshan et al. (2004) performed RANS calculations the radio-controlled submarine ONR Body 1, but no free surface was modeled in this case. Turn and zigzag maneuvers for a KVLCC1 tanker with moving rudder and rotating propeller have been reported by Carrica et al. (2008) using overset grids and solving for the free surface. The most comprehensive self-propulsion computations to date have been performed by Carrica et al. (2010), who studied a tanker (KVLCC1) a containership (KCS) and a surface combatant (ONR Tumblehome). All those computations were performed at model scale, though KCS is extrapolated to ship point using ITTC procedures.

In this work computations are performed directly in full scale. In order to carry a simulation fully independent from experimental results three cases are run: a towed simulation, an open water curve for the propeller, and the self-propulsion simulation itself with discretized propeller.

3. MATHEMATICAL AND NUMERICAL MODELING

The computations are performed with CFDShip-Iowa v4.5. CFDShip-Iowa employs a single-phase level set approach to solve the viscous flow with free surface, using either RANS or DES models for turbulence, both based on a blended $k-\omega/k-\varepsilon$ model with SST (Carrica et al. 2007a). Multiblock structured grids with dynamic overset capabilities allow handling of complex geometries and large-amplitude motions, as described in Carrica et al. (2007b). The overset interpolations are performed at run time using the code Suggar (Noack 2005), and the surface weights to compute forces and moments as a preprocessing step using Usurp (Boger and Dreyer 2006). A PI speed controller is used to act on the propeller RPS to achieve the target speed. The error is defined as the difference between the instantaneous ship speed and target speed

$$e_U = U_{ship} - U_{target} \tag{1}$$

and the instantaneous RPS is

$$n = P\, e_U + I \int_0^t e_U\, dt \tag{2}$$

where P and I are the proportional and integral constants of the controller. For details refer to Carrica et al. (2010).

3.1 Hull Roughness Modeling and Sand Grain Equivalent

Ship point experiments or computations require the addition of the Skin Correction Factor (SFC), estimated by

$$SFC = \frac{1}{2}\rho U_0^2 S_0 \times \{(1+k)(C_{F0M} - C_{F0S}) - \Delta C_F\} \quad (3)$$

where C_{F0M} and C_{F0S} are computed from the ITTC'57 frictional line at model and full scale Reynolds numbers respectively. ΔC_F is the roughness allowance and depends on the ship hull roughness,

$$\Delta C_F = 0.044\left[(k_s / L_{PP})^{1/3} - 10\,\mathrm{Re}^{-1/3}\right] + 2.5\times10^{-4} \quad (4)$$

where Re is the Reynolds number and k_s is the roughness ($k_s = 208\mu$m in the Tokyo 2005 Workshop, Hino 2005). Notice that k_s is a roughness obtained by the Hull Roughness Analyzer as explained in the 19th ITTC (1990). Turbulent boundary layers are modeled in CFD with the use of wall functions. The roughness appearing in the functional form of these wall functions are sand grain roughnesses, i.e. these were calibrated with this kind of measurements. Hence it is necessary to find a sand grain equivalent roughness and use this in the CFD simulations. To do that the ITTC'57 frictional line is compared to flat plate correlations where the roughness is sand grain roughness. For instance, from White (2001)

$$C_D = \left(1.89 + 1.62\log_{10}(L / k_{sg})\right)^{-2.5} \quad (5)$$

The same friction drag obtained in Eq. (4) with $k_s = 208\mu$m is obtained in Eq. (5) with $k_{sg} = 32\mu$m. This is the roughness value used in the computations.

4. GEOMETRIES AND GRIDS

The grid system for the self-propelled KCS is shown in Fig. 1, and details are listed in Table 1. It consists of 24 multiblock/overset grids of which 11 form the propeller itself and about 2/3 of the total number of grid points are refinements to resolve the flow around the propeller and in the stern. The whole domain is distributed among 144 processors. The grid system used for the open water test of the propeller is composed of the 11 grids described in Table 1 plus a refinement and a background grid. This results in a total of 8.58 million grid points distributed in 72 processors. Table 2 summarizes the open water grid system. Figure 2 sketches the system setup. The refinement extends 0.5 diameters upstream and 2.5 diameters downstream of the propeller while the background grid extends 5.0 and 38.5 diameters upstream and downstream the propeller plane, respectively. Finally, the system of grids used for the towed case comprises the same grids used for the self-propelled case but removing the propeller and propeller refinement, and using only the starboard side. Then a total of 8 multiblock/overset grids are used resulting in 6.87 million points distributed among 47 processors.

5. PROPELLER OPEN WATER CURVE

To obtain a full CFD prediction of the self-propulsion factors, a full scale open water test was carried out. This test also evaluates the ability of the code to perform full-scale predictions of propeller open water characteristics. The propeller surfaces are assumed to be smooth for these computations. The $k-\omega/k-\varepsilon$ based DES model of turbulence is used.

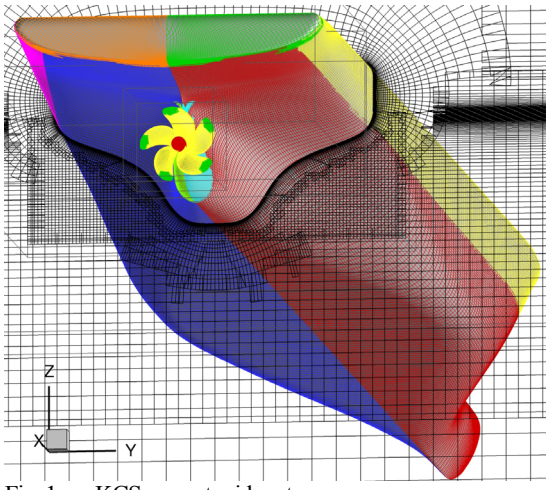

Fig. 1 KCS overset grid system.

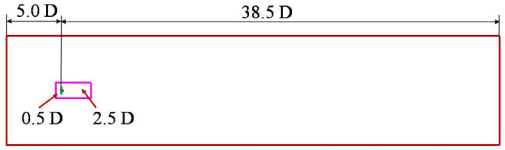

Fig. 2 Refinement and background for the KP 505

The variables are non-dimensionalized with the KCS service speed $U_0 = 12.35$ m/s (24 knots) as the velocity scale and the KCS length between perpendiculars $L_{PP} = 232.5$ m as the length scale.

Four cases with four different advance coefficients are run. In three of them, with $J = 0.6$, 0.7 and 0.8, the advance coefficients are chosen to be near the expected self propulsion point and a fourth case with a low advance coefficient of $J = 0.05$ is included in order to evaluate the ability of the code to predict the open water characteristics in a regimen of high propeller load. The advance coefficients are varied by keeping fixed the rotational speed and by changing the advance velocity V_a. The rotational speed is chosen by scaling to full scale the sell-propulsion point rotational speed from the experiments reported on the Tokyo 2005 CFD Workshop. Hence, the dimensionless rotational speed is $n = 31.82$, and the Reynolds number is $\mathrm{Re}_{L_{PP}} = 2.487\times10^9$.

The computations are performed on a Cray XT5 using 72 processors. The overset solver is not called on these simulations since all the grids rotate together as a rigid body and hence the overset interpolation coefficients can be computed in a pre-processing step. For all of the simulations 10 propeller revolutions are run. This provides

enough time for the computations to develop a periodic solution over which statistics are computed. The time step is set such that 200 time steps are run per revolution of the propeller, thus $\delta t = 1.572 \times 10^{-4}$. Every run took about 24 hours wall clock time. Results show that for the range $J \in (0.6; 0.8)$ 6 propeller revolutions are enough to obtain converged forces and moments on the propeller and hence these computations could have been carried out in about 14.4 hours.

Fig. 3 shows the open water curves, both computed and experimental results obtained by KRISO. These experiments were performed in model scale and hence this is not a fair comparison a priori. The assumption in these experiments is that there is a minimum propeller size to use in the experiments such that the open water characteristics become independent of Reynolds number. Hence, is not surprising to find that the CFD results lie on top of the EFD and they even provide evidence to the validity of this assumption.

Table 1 Grid system for the self-propelled computations of KCS

Grid	Points	Type	Processors	Moves with ship	Rotates with propeller
B. layer lower starboard	1,179,695	O on bow	9	Yes	No
B. layer upper starboard	740,834	O on bow	5	Yes	No
B. layer stem starboard	149,328	Wrap	1	Yes	No
B. layer transom starbrd	148,461	O with pole	1	Yes	No
B. layer lower port	1,179,695	O on bow	9	Yes	No
B. layer upper port	740,834	O on bow	5	Yes	No
B. layer stem port	149,328	Wrap	1	Yes	No
B. layer transom port	148,461	O with pole	1	Yes	No
Propeller hub	580,752	O with pole	4	Yes	Yes
Propeller blades	5x298,146	O no pole	2x3+3x2	Yes	Yes
Propeller blade tips	5x148,461	Wrap	5x1	Yes	Yes
Propeller refinement	3,853,369	Cartesian	27	Yes	No
Refinement stern	582,063	Cartesian	4	Yes	No
Refinement transom	1,152,713	Cartesian	8	No	No
Refinement free surface	4,600,449	Cartesian	32	No	No
Background	2,899,806	Cartesian	20	No	No
Total	**20,338,823**		**144**		

Table 2 Grid system used for the open water computations of the KP 505.

Grid	Points	Type	Processors	Rotates with propeller
Propeller hub	580,752	O with pole	4	Yes
Propeller blades	5x298,146	O no pole	5x2	Yes
Propeller blade tips	5x148,461	Wrap	5x1	Yes
Refinement	6,407,081	Cartesian	45	Yes
Background	1,142,919	Cartesian	8	Yes
Total	**8,577,359**		**72**	

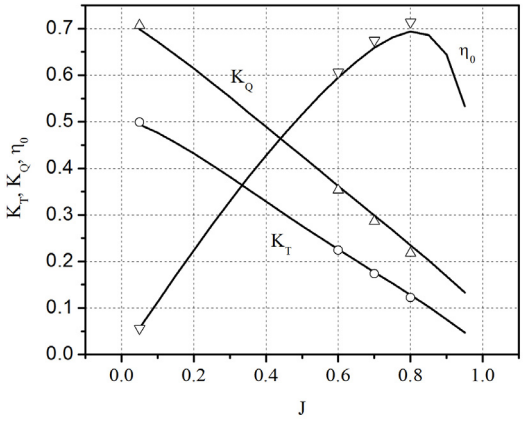

Fig. 3 Open water characteristics for KP 505.
Symbols: CFD. Solid lines: KRISO EFD.

Isosurfaces of the second invariant of the rate of strain tensor $Q = 10000$ colored with velocity for 4 different advance coefficients are shown in Fig. 4. On this figure these velocities are normalized with the advance velocity V_a except for Fig. 4d where this is left unchanged. The vortex shedding pitch increases as a result of the increase on the advance velocity. Vortex pairing, i.e. when two vortices merge to form a stronger one, can be observed for $J = 0.6$ and 0.7 and it is delayed further downstream as the advance coefficient increases. This phenomena was previously reported in the work by Carrica et al. (2010).

6. SELF-PROPULSION

Computations for self-propulsion were compared with those carried out in model scale (Carrica et al. 2010). The computation at model scale was performed at the ship point by adding the skin friction correction force (SFC) as outlined in detail in Carrica et al. 2010. Details on the model scale simulation can be found in the cited references.

While the model scale simulation was started with the ship at rest, the full scale computation was started from the model scale simulation. The controller was let to adjust the RPS accordingly in order to achieve cruise speed. The proportional and integral constants were set to $P = I = 40$. The mass of the ship was artificially reduced by a factor of 40 in order to achieve steady state faster and hence reduce the computational time. The time step was set to $\delta t = 2.5 \times 10^{-4}$. 27,140 time steps were run (the model scale simulation took 42,000 time steps) until the target cruise velocity was reached.

Originally the system of grids for the propeller was designed in order to partition the blades in 2 blocks each. As shown in Table 1 two of the blades were partitioned in three blocks and the rest in two blocks. This uneven partition was imposed in order to have a total number of processors multiple of 8 and to allow requesting for a whole computer node for each of the overset solver processors which require a large amount of memory. This case was run on a Cray XT5 machine with 8 processors and 16 GBytes of memory per node. In total, the case was run with 168 processors of which 144 were for the CFD solver and 24 processors for the overset solver (3 groups times 8 processors in each of three different nodes). 19 days were needed to perform the computation.

The towed case was run from rest on the same Cray XT5 computer with a time step $\delta t = 5 \times 10^{-3}$. A long run of 50 ship lengths was performed, the objective being twofold. First, to dump out transient waves and get as close as possible to a steady state. Second, to assess the effect of surface roughness on the computed total resistance. Figure 5 shows the total resistance versus nondimensional time for different roughnesses. Each solution was restarted from the previous one. It is important to observe that this is sand grain roughness.

The last run was performed with the sand grain equivalent of $k_s = 32\mu$m obtained with the procedure described in Section 2.1

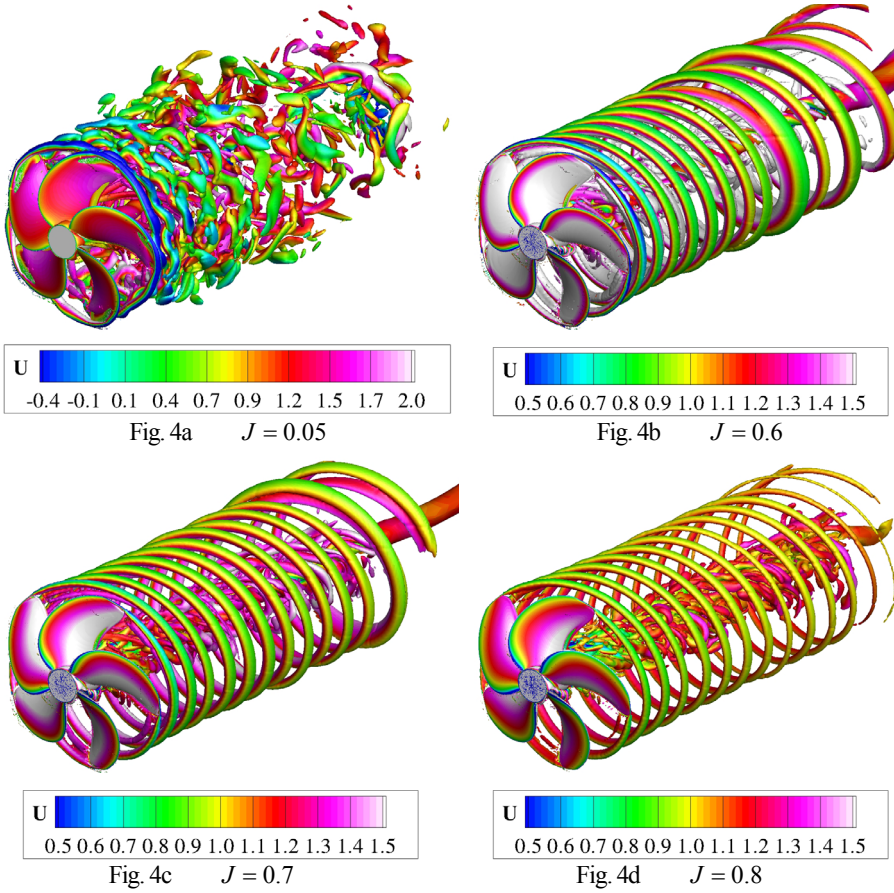

Fig. 4a $J = 0.05$ Fig. 4b $J = 0.6$

Fig. 4c $J = 0.7$ Fig. 4d $J = 0.8$

Fig. 4 KP505 isorsurfaces of $Q = 10000$ for different advance coefficients

With this value of roughness the computed total resistance was found to be $C_T = 2.33\times10^{-3}$ which is 5.1% larger than the predicted value computed with the ITTC correlations. Results for towed KCS are summarized for both model and full scale in Table 3. Percent differences with the experiments are shown in brackets. The large error in the pressure coefficient is due to the fact that the experimental value is estimated as the subtraction of two numbers and this adds up the errors. The SFC can be obtained as a result from these computations. The SFC is the difference between the total resistances at model and full scale

$$SFC = C_T(\text{Model}) - C_T(\text{Full}) \qquad (6)$$

This value differs 6.65% from the estimated SFC according to the 19th ITTC.

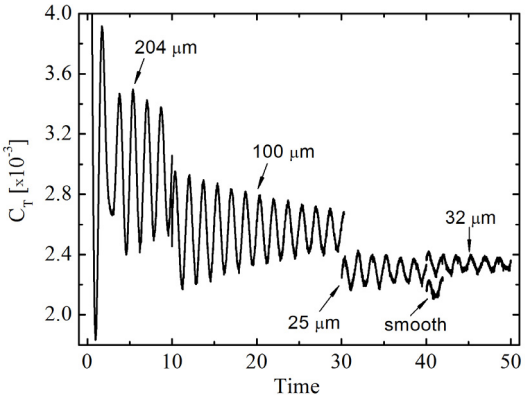

Fig. 5 Total resistance vs. time. Roughness is changed throughout the simulation

Table 3 Resistance coefficients for towed KCS.

		C_T	C_P	C_F	SFC
Model scale	EFD	3.55	0.718[b]	2.832[a]	
	CFD	3.575 (+0.7)	0.737 (+2.6)	2.838 (+0.2)	
Full scale	EFD	2.221[c]	0.578[b]	1.643[d]	1.3294[e]
	CFD	2.334 (+5.1)	0.850 (+47.2)	1.570 (-4.4)	1.241 (+6.65)

[a] ITTC 1957 friction line, $C_{F0} = 0.075 / (\log_{10}\text{Re} - 2)^2$.

[b] Computed as $C_P = C_T - C_F$.

[c] Estimated by $C_T = C_T(\text{Exp.}) - SFC$

[d] According to ITTC 1957 friction line $C_F = C_{F0} + C_a + \Delta C_f$

[e] Computed according to the 19th ITTC and the Tokyo 2005 CFD Workshop

Fig. 6 shows the computed ship speed and propeller rotational velocity. The computation started from a previous model scale simulation and after 7 ship lengths the ship speed and rotational velocity approached an asymptotic value. At $t = 12.77$ the mass was changed from a twentieth of the real mass to a fortieth of it in order to speed up the convergence to the stationary solution.

Fig. 7 shows isosurfaces of $Q = 10^4$ colored with velocity. Tip vortices are well resolved in the refinement region and only the strong hub vortex survives the transition to a coarser grid.

Table 4 summarizes the self-propelled KCS results and also includes the model scale results from Carrica et al. (2010). The self-propulsion factors shown in Table 4 at model scale were obtained using the experimental open water curves for the KP505 propeller measured at MOERI (available at the G2010 website). For the full scale self-propulsion factors these were obtained using the open water characteristics at full scale computed in this work. Self-propulsion factors are computed according to ITTC procedures 7.5-02-03-01.1 (2002).

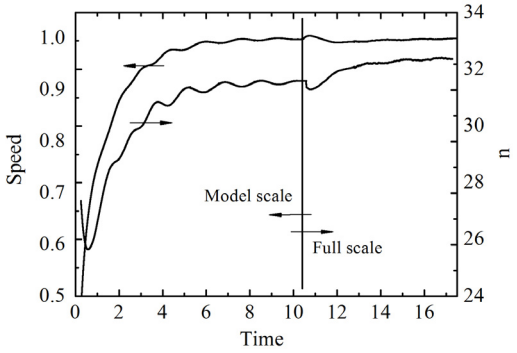

Fig. 6 Ship speed and propeller rotational speed.

Table 4 Resistance coefficients for self-propelled KCS.

	EFD	CFD (model)	CFD (full)
C_T		4.011x10^3	2.773x10^3
C_P		1.172x10^3	1.145x10^3
C_F		2.847x10^3	1.577x10^3
SFC		1.3294[a]	1.238[b] (-6.9)
K_T	0.17	0.1689 (-0.6)	0.166 (-2.4)
K_Q	0.0288	0.0296 (+2.8)	0.0261 (-9.2)
n	31.48	31.88 (+1.27)	32.35 (+2.8)
$1-t$	0.853	0.8725 (+2.29)	0.8417 (-1.3)
$1-W_t$	0.792	0.785 (-0.88)	0.7935 (+0.2)
η_0	0.682	0.6684 (-1.99)	0.6827 (+0.1)
η_r	1.011	0.9738 (-3.68)	1.0573 (+4.6)
J	0.728	0.717 (-1.51)	0.7142 (-1.9)
η	0.74	0.7234 (-2.24)	0.7656 (+3.5)

[a] Computed according to the 19th ITTC and the Tokyo 2005 CFD Workshop

[b] $SFC = C_T(\text{Model}) - C_T(\text{Full})$

The percent difference with the experiments is shown in parenthesis. The SFC in Table 4 is again computed using Eq. 3 and differs by 6.9% from the ITTC estimate. Self-propelled factors are mostly within 2% of the experimental values computed in model scale at the ship point. Exceptions are the torque coefficient K_Q, off by 9.2%, and the relative rotative efficiency η_r off by 4.6%. The difference in the relative rotative efficiency is expected since it is a number close to 1 and hence difficult to predict numerically and by

measurements. Recall that these experiments were performed in model scale and direct comparison may not be valid.

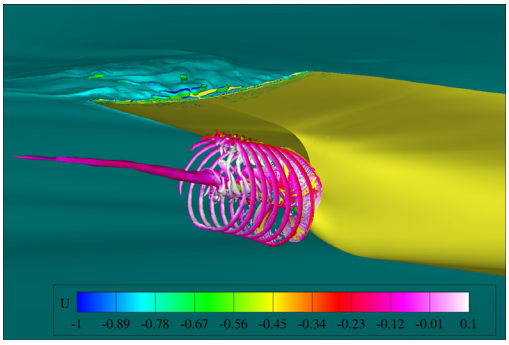

Fig. 7 Isosurfaces of $Q = 10^4$ colored with velocity for self propelled KCS in full scale

6. CONCLUSIONS

This work shows the feasibility of a full CFD prediction of self-propulsion characteristics in full scale. The only input in the methodology is the hull roughness. The procedure to follow to find a sand grain equivalent roughness compatible with CFD wall functions models is presented. The complete process requires finding the sand grain equivalent roughness and running three different simulations, all in full scale: an open water test, a towed case and finally the full self-propelled case. The new methodology is then applied to the self-propulsion computations for the KRISO container ship KCS. It is shown that the SFC can be naturally obtained as the difference of the model and full scale total resistances. Self propulsion coefficients are in good agreement with the available data. Even when these experiments are in model scale the comparison shows that the approximations made in the model scale computations are consistent with full-scale computations.

7. ACKNOWLEDGEMENTS

This work is sponsored by the US Office of Naval Research through research grants N00014-01-1-0073 and N00014-06-1-0474. Dr. Patrick Purtell is the technical manager. Computations were performed on NAVY DSRC Cray XT5 supercomputer Einstein.

REFERENCES

Boger DA, Dreyer JJ (2006), "Prediction of Hydrodynamic Forces and Moments for Underwater Vehicles Using Overset Grids", AIAA paper 2006-1148, 44th AIAA Aerospace Sciences Meeting, Reno, NV, USA.

Carrica PM, Wilson R, Stern F (2007a), "An unsteady single-phase level set method for viscous free surface flows", *Int J Num Meth Fluids* 53:229-56.

Carrica PM, Wilson RV, Noack R, Stern F (2007b), "Ship motions using single-phase level set with dynamic overset grids", *Comput Fluids* 36:1415-33

Carrica PM, Stern F (2008), "DES simulations of KVLCC1 in turn and zigzag maneuvers with moving propeller and rudder", SIMMAN 2008, Copenhagen, Denmark.

Carrica PM, Castro AM and Stern F, (2010), "Self-Propulsion Computations Using Speed Controller and Discretized Propeller with Dynamic Overset Grids", *J. Mar. Sci. Technol.*, In press, available on line DOI 10.1007/s00773-010-0098-6.

Choi JE, Kim JH, Lee HG, Choi BJ and Lee DH, (2010), "Computational predictions of ship-speed performance", *J Mar Sci Technol* 15:64-77

Cura Hochbaum A. and Vogt M., (2008), "Manoeuvring prediction for two tankers based on RANS calculations", SIMMAN 2008, Copenhagen, Denmark

Hino T., Editor (2005) CFD Workshop Tokyo 2005, National Maritime Research Institute, Japan. http://www.nmri.go.jp/cfd/cfdws05/index.html

Kim J, Kim KS, Kim GD, Park IR, Van SH (2006), "Hybrid RANS and Potential Based Numerical simulation for self-propulsion performances of the practical container ship", *J Ship Ocean Tech* 10(4):1-11

Lübke L.O., (2005), "Numerical simulation of the flow around the propelled KCS", CFDWS05, Tokyo, Japan.

Noack R., (2005), "SUGGAR: a general capability for moving body overset grid assembly", AIAA paper 2005-5117. 17th AIAA Computational Fluid Dynamics Conf. Toronto, Ontario, Canada.

Pankajakshan R., Remotigue S., Taylor L., Jiang M., Briley W. and Whitfield D., (2004), "Validation of control-surface induced submarine maneuvering simulations using UNCLE," Proc 24th Symp Naval Hydrodynamics, Fukuoka, Japan.

White F.M., (2001), *Fluid Mechanics*, Mc Graw Hill, NY

G2010, http://www.gothenburg2010.org/kcs_gc.html

ITTC Recommended Procedures and Guidelines (2002) Testing and extrapolation methods, performance propulsion test. Report 7.5-02-03-01.1.

19th ITTC Report of the Powering Performance Committee (1990), 19th International Towing Tank Conference, Madrid, Spain.

SELF-PROPULSION FREE TO SINK AND TRIM AND PITCH AND HEAVE IN HEAD WAVES OF A KCS MODEL

Pablo M. Carrica (IIHR-Hydroscience and Engineering, The University of Iowa, USA)
Huiping Fu (School of Naval Architecture, Ocean and Civil Engineering, Shanghai Jiao Tong University, China)
Frederick Stern (IIHR-Hydroscience and Engineering, The University of Iowa, USA)

1. SUMMARY

Two computations of the KCS containership model with motions are presented. Predictions of self propulsion point in model scale free to sink and trim with the rotating discretized propeller from the Hamburg Model Basin (HSVA) are performed for Fr=0.26. The second case involves pitch and heave in regular head waves, for which the model is modified to include a superstructure to prevent wet deck conditions. Computations were performed with CFDShip-Iowa version 4.5, a RANS/DES CFD code designed for ship hydrodynamics. The self-propulsion computations were carried out following the procedure described in Carrica et al. (2010b), in which a speed controller is used to find the propeller rotational speed that results in the specified ship velocity. The rate of revolutions n, sinkage, trim, thrust and torque coefficients K_T, K_Q and resistance coefficient $CT_{(SP)}$ are thus obtained. Comparisons between CFD and EFD show that the rate of revolutions n, thrust and torque coefficients K_T and K_Q have higher prediction accuracies than sinkage and trim. For the simulation of pitch and heave in head waves, the geometry includes KCS hull and rudder under three conditions with two Froude numbers and three wave length and amplitude combinations. 0th, 1st, 2nd, 3rd harmonic amplitudes and phases are computed for total resistance coefficient C_T, heave motion z and pitch angle θ. Comparisons between CFD and EFD show that pitch and heave are much better predicted than the resistance.

2. INTRODUCTION

Except for a handful of applications, like resistance, drift and steady turn, most ship tests require motions. This requires modern CFD or EFD to reproduce ship motions as realistically as possible. Conventional research methods of ship maneuvering and sea-keeping are based on Systems Based Simulators (SBS) and potential flow codes. Both of these methods are generally flexible, but they also have limitations. The SBS method is based on integral quantities, i.e. the equations of motion (EOM) are solved based on large sets of force data obtained from empirical, experimental or numerical methods. Relative forces and moments are treated separately, and interaction among hull and appendages is hard to include. Not being a physics-based approach, no information on the flow field is obtained. As for ship motions in waves, sea-keeping codes based on potential theory also have some obvious limitations. They are inviscid and frequently linearized. Forces due to waves are approximate. Because CFD solvers are based on more realistic physics, the results are typically better and require no empirical input. This comes, however, with a considerable increase in cost in computational time and problem setup complexity.

The application of URANS (unsteady Reynolds averaged Navier-Stokes) CFD solvers to ship motion problems is relative new, but the technique has shown promising results in connection with calculation of hydrodynamic forces and studies of the complex vortical flow field around ships in calm water (Sakamoto et al. 2008, Carrica et al. 2008a) or in waves (Weymouth et al. 2005, Carrica et al. 2007a, Carrica et al. 2008b, Mousaviraad et al. 2009, Carrica et al. 2010a).

The objective of the current work is to study motions, resistance and flow field for the KCS containership appended with rudder either a) self-propelled in calm water with a discretized propeller or b) sailing in regular head seas without propeller. The computations are performed using the DES capability in CFDShip-Iowa version 4.5.

3. MATHEMATICAL AND NUMERICAL MODELING

CFDShip-Iowa version 4.5 solves the RANS/DES equations using a blended k–ε/k–ω model for turbulence modeling. The free surface is modeled using a single phase

level-set approach, in which the air/water interface is the zero level set of the level-set distance function. The domain is discretized using multiblock/overset structured grids. The overset capabilities are fully dynamic, which allows the code to simulate large-amplitude motions. Numerical methods include finite differences discretization, with second- to fourth-order upwind (for DES) discretization of the convection terms and second-order centered scheme for the viscous terms. The temporal terms are discretized using a second order backwards Euler scheme. Incompressibility is enforced by a strong pressure/velocity coupling, achieved using Pressure Implicit Split Operator (PISO) or projection algorithms. The equations of motion are solved only on the water side, while quantities are extended into the air to satisfy the proper boundary conditions at the interface. Regular waves are implemented through initial and boundary conditions. 6DoF capabilities are enabled in a hierarchy of bodies. The ship (parent object) and appendages move together with respect to static grids, while propellers, rudders and other control surfaces follow the ship but add motion relative to it (children objects). The fluid flow equations are solved in an Earth-fixed inertial reference system, while the rigid-body equations are solved in the ship system, so forces and moments are projected appropriately to perform the integration of the rigid-body equations of motion, which are solved iteratively. The overset connectivity is obtained at run time using the code Suggar (Noack, 2005). Waves are introduced as initial and boundary conditions, with regular and irregular waves of any direction implemented, including JONSWAP, Bretschneider, Hurricane and Pierson-Moskowitz spectra. Passive and feedback controllers are implemented for speed, heading, course and roll control. Details of mathematical formulation, numerical methods, and implementation of these features in CFDShip-Iowa version 4 can be seen in the cited references (Carrica et al. 2007a, 2007b, 2008b, 2010a, 2010b) and the literature therein.

4. SIMULATION CONDITIONS

4.1 Geometry

The KCS containership was conceived to provide data for both exploration of flow physics and for CFD validation for a modern container ship with a bulbous bow. Data for pitch, heave, and added resistance are available from Force Technology in Denmark (Otzen and Simonsen 2008), as well as self-propulsion tests, in both cases using the model from HSVA. The KCS geometry is shown in Fig. 1, and details of the dimensions and geometrical properties are listed in Table 1. The ship's reference system follows the customary CFD standard, with the origin located on the centerline at the bow where it meets the design water line. The *x*-axis lies in the center plane and water plane, being the longitudinal axis pointing to stern. The *y*-axis points from port to starboard, and *z*–axis points upwards. The Earth system is coincident with the ship system at rest and is denoted by (X_e, Y_e, Z_e).

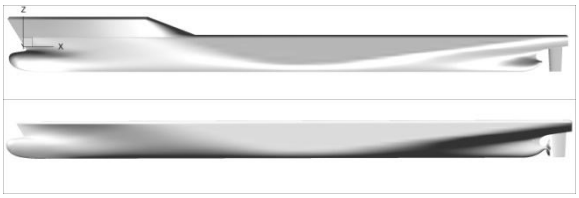

Fig.1 KCS geometry for pitch and heave in head waves (top) and self-propulsion in calm water (bottom).

Two cases are studied. Case 1 is a self-propulsion test at model point in calm water but free to sink and trim with rudder and propeller appended to hull, corresponding to case 2.3b in G2010. Case 2 includes 4 conditions of pitch and heave motions in head waves with rudder appended to hull, corresponding to case 2.4 in G2010. Details of the simulation conditions are listed in Table 2.

Table 1 Geometrical properties of KCS.

Main particulars		Full scale
Length between perpendiculars	L_{PP} (m)	230.0
Length of waterline	L_{WL} (m)	232.5
Maximum beam of waterline	B_{WL} (m)	32.2
Depth	D (m)	19.0
Draft	T (m)	10.8
Displacement	Δ (m^3)	52030
Wetted area w/o rudder	S_W (m^2)	9424
Wetted surface area of rudder	S_R (m^2)	115.0
Block coefficient (CB)	$\Delta/(L_{PP}B_{WL}T)$	0.6505
Midship section coefficient (CM)		0.9849
LCB (%L_{PP}), fwd+		-1.48
Vertical Center of Gravity (from keel)	KG (m)	7.28
Metacentric height	GM (m)	0.60
Moment of Inertia	K_{xx}/B	0.40
Moment of Inertia	K_{yy}/L_{PP}, K_{zz}/L_{PP}	0.25
Propeller center, long. location (from FP)	x/L_{PP}	0.9825
Propeller center, vert. location (below WL)	$-z/L_{PP}$	0.02913

Table 2 Simulation conditions. Conditions corresponding to the higher speed are indicated in parenthesis.

Case	1 (G2010 2.3b)	2 (G2010 2.4)
Type of data	Self propulsion, sinkage and trim at model point	Pitch, heave, added resistance
Scale factor	52.667	52.667
Lpp(m)	4.3671	4.3671
Speed(m/s)	1.701	1.701, (2.151)
Froude number	0.26	0.26, (0.33)
Reynolds number	6.52×10^6	6.52×10^6 (8.27×10^6)
Rudder	Yes	Yes
Wave direction	-	Head sea
Wave lengths/Lpp	-	1.15, 2.00, (1.33)
Wave heights(m)	-	0.084,0.146, (0.097)

4.2 Grid design

Since the code supports overset grids, the general strategy is to generate a background grid which extends to the far field and is appropriate to define the boundary conditions on that region. The background grid is a box that extends from -1 to 2 in *x*, from -1 to 1 in *y* and from -1 to about 0.2 in *z*, all in non-dimensional coordinates. Refinements blocks are

added near the propeller and rudder regions and on the wake. Appendages are added by use of overset grids. These grids have a collar surface grid that conforms to the hull, and other surface grids that conform to the appendage itself. From these surface grids volume grids are generated. Figure 2 shows the mesh at the hull, propeller and rudder on the wall boundary for case 1. The grid is comprised of 26 base blocks with a total of 23.2 million points, split for parallel processing in 160 domains. This includes 4.4 million points for the hull grids, 9.35 million points for the propeller, 0.75 million points for the rudder and 8.7 million points for background and refinements on the free surface.

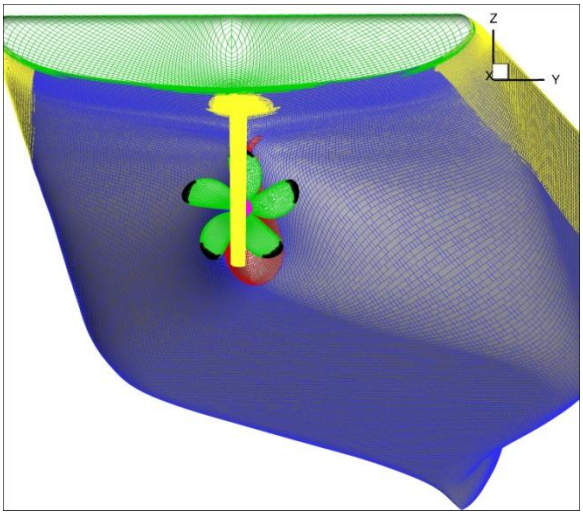

Fig.2 Mesh on the wall boundaries for the KCS self-propulsion computation.

The grid used for case 2 takes advantage of the absence of the propeller and the symmetry of the problem, computing only the starboard side of the ship. A superstructure is added to the bow area to avoid wet deck condition under heavy pitching, mimicking the experimental condition (see Fig. 1). This results in a total of 7.6 million grid points, with 2.2 corresponding to the hull grids, 0.3 million for the superstructure, 0.44 million for the rudder and 4.66 million for background and refinements, for a total of 10 base blocks split into 48 processors.

In this grid system we can identify three grid levels. The background and refinement grids are not subject to ship motions, but follows the ship by surging with it (only for case 1, it is static for case 2). Since the background grid is refined about the free surface, this assures that a reasonable refinement is available everywhere independently of the motions that the ship undergoes. All the other grids form the ship object and move with it following the surge, pitching and heaving motions computed for the object. The propeller is a child object and follows the ship but also rotates at the rotational speed imposed by the controller.

4.3 Propeller and controller for self-propulsion computations

Following the experimental conditions for case 1, self-propulsion of KCS, the SVP1193 propeller from HSVA is used. The propeller has 5 blades of variable pitch and diameter 150mm. In this case the pitch to diameter ratio is 1. The rotational speed of the propeller is determined by a PID controller that modified the propeller rotational speed n in revolutions per second (RPS) to achieve the target speed. Details of these controllers and how they are used to achieve the self-propulsion point are provided in Carrica et al. (2010b). In this case a small gap between the hull hub and the propeller hub is used to allow grids to rotate and still obtain a valid overset interpolation.

4.4 Waves

For case 2 in head waves three conditions are studied, listed in Table 3. For all conditions $ak = 0.0525$.

Table 3 Head wave conditions

Condition No.	C1	C2	C3
Speed (m/s)	1.701	1.701	2.151
Froude number (Fr)	0.26	0.26	0.33
Reynolds number (Re)	6.52×10^6	6.52×10^6	8.27×10^6
wave length λ/L_{PP}	1.15	2.00	1.33
wave height H_S (mm)	84	146	97

Heave and pitch motions are evaluated at midships ($L_{pp}/2$) and the phase is defined such that the wave crest is at midships at $t = 0$.

5. RESULTS AND DISCUSSION

Case 1 was run using a total of 184 processors, 160 for the flow computation and 24 for the overset connectivity calculation. Case 2 required 48 processors for the flow solver and 8 for the overset solver.

5.1 Case 1: KCS self-propulsion at model point

The wall clock time for this case was about three weeks, for a total of about 93,000 CPU hours, Once the controller reaches the self-propulsion point, the rotational speed n, thrust and torque coefficients K_T, K_Q and resistance coefficient $CT_{(SP)}$ are obtained.

Time histories of the rate of revolutions n, sinkage and trim during self-propulsion simulation are shown in Fig. 3. Notice that the self-propulsion point is reached in an oscillatory fashion, showing reflected waves from the exit boundary. These oscillations have an amplitude of less than 0.1 RPS, and are thus of the same order of magnitude of the experimental errors. Results of the computation are condensed in Table 4. Here, resistance coefficient is based on wetted surface area (S/L_{pp}^2) = 0.1803 with rudder for static orientation in calm water. The comparison error is defined as E%D=(S-D)/D×100, where D is the EFD value and S is the simulation value. From Table 4, comparisons between CFD and EFD show that the rate of revolutions n, thrust and torque coefficients K_T and K_Q have higher prediction accuracies than motions of sinkage and trim.

The error in the prediction of the resistance is small, increasing to 5~6% for the thrust and torque coefficients, mostly due to the overprediction of the propeller rotational speed. These errors are comparable to those for other self-propulsion computations with resolved rotating propellers (Carrica et al. 2010b). Notice that the experiment by Otzen and Simonsen (2008) exhibits an error of 2.0%, and that self-propulsion is off by 1.6%. The predicted values for sinkage and trim are around 15%, consistent also with other simulations.

Figure 4 shows a rear view of the free surface and isosurfaces of $Q = 5000$, the second invariant of the rate of strain tensor. The propeller blade tip vortices are clearly identified as they interact with the rudder. A very strong hub vortex is also observed. Notice that the propeller creates a flow field strong enough to break the symmetry of the free surface.

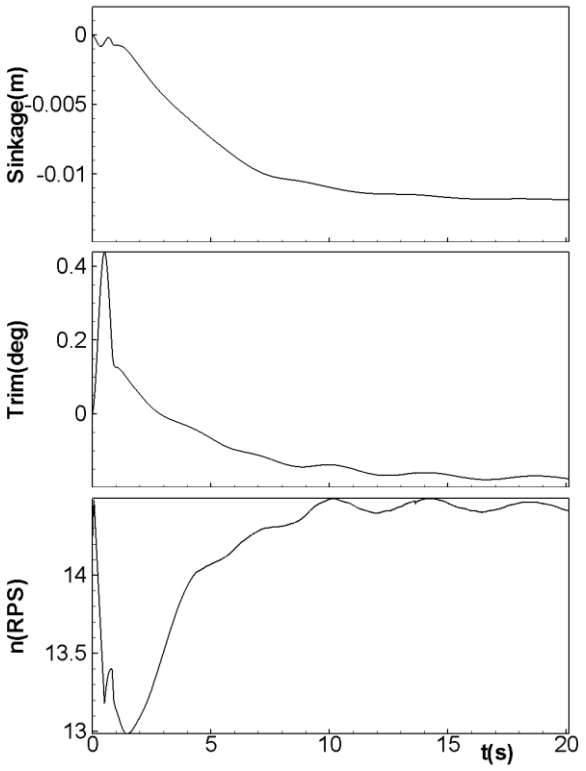

Fig.3 Time histories of sinkage, trim and rate of revolutions, for KCS self-propelled.

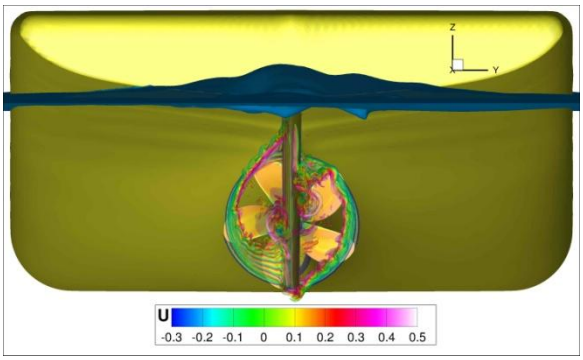

Fig.4 Free surface and vertical structures as isosurfaces of $Q = 5000$ for case 1.

Table 4 Self-propulsion results for KCS

	C_T ×10³	σ ×10²(m)	τ(°)	K_T	$10K_Q$	n
EFD(D)	5.14	-1.0	-0.155	0.252	0.408	14.15
CFD(S)	5.01	-1.183	-0.172	0.236	0.387	14.44
E%D	-2.5	18.3	11.0	-6.3	-5.1	2.0

5.2 Case 2: KCS pitching and heaving in head waves

As described in Table 3, three conditions C1, C2 and C3 with three wave lengths and two velocities were studied with the ship free to pitch and heave. Time histories of the total resistance coefficient C_T, heave motion z and pitch angle θ are obtained from the computation.

As an example of the type of flow generated by the ship pitching and heaving, free surface and vertical structures obtained as isosurfaces of $Q = 100$ are shown in Fig. 5 for condition C1. Notice the bilge vortices coming off the stern, modulated by the motion of the ship. Time histories of C_T, z and θ for conditions C1 to C3 are shown in Figs 6 through 8. Results of the 0th harmonic amplitude of C_T, z and θ are given in Table 5, with the resistance coefficient based on the same wetted surface area used for case 1.

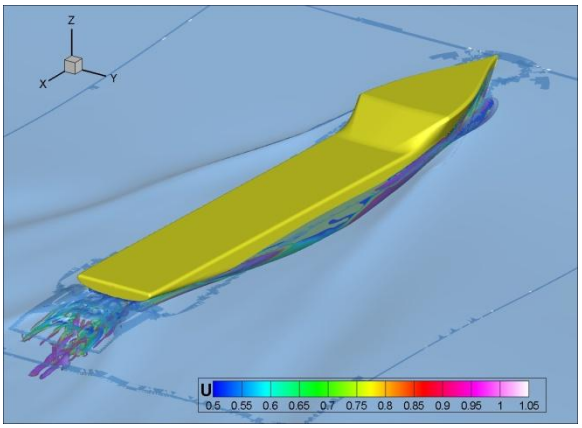

Fig.5 Free surface and vertical structures for case 2, C1.

Comparisons between CFD and EFD show that the 0th harmonic amplitude of the resistance coefficient is generally well predicted, with under prediction of the forces ranging from 1% to 7% for all conditions, see Table 5. Heave is predicted within 5% of error for all conditions except C1, in which the over prediction reaches 18%. The pitch average is very small, in the order 0.06 degrees for all cases, and thus large errors are observed when compared with EFD even though CFD also predicts small pitching average angles.

The motions observed are mostly linear, but the forces are not with the exception of condition C2. The first harmonic amplitude and phases for pitch and heave are in excellent agreement, with the heave amplitude a bit under predicted for conditions C1 and C3. The resistance coefficient is completely off respect to the experiments. The strong non-linear behavior observed in the experimental forces in conditions C1 and C3 are somewhat captured by CFD,

but the amplitude of the fluctuations is grossly underestimated while the phase is also off. The reasons for these discrepancies are not clear, and need further investigation. Results from Simonsen et al. (2008) are also in strong disagreement with resistance data for this same experiment, suggesting that the data may be deficient.

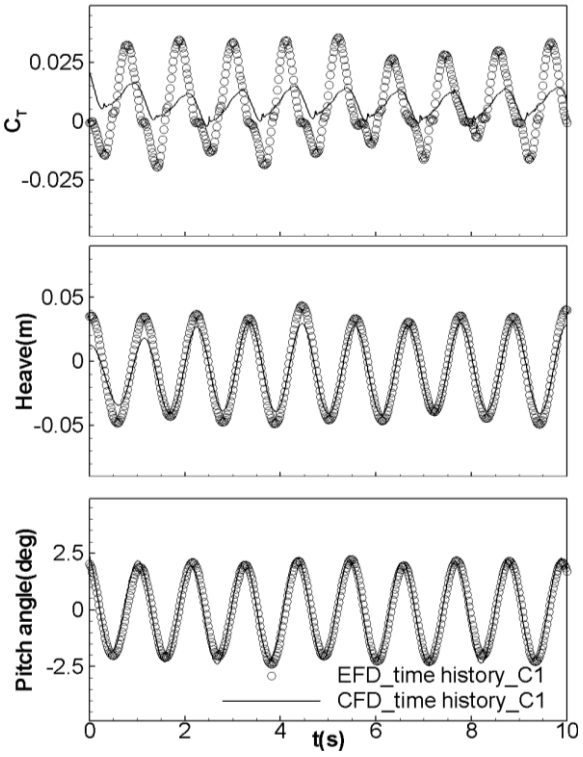

Fig.6 Time histories of C_T, z and θ, case 2, C1.

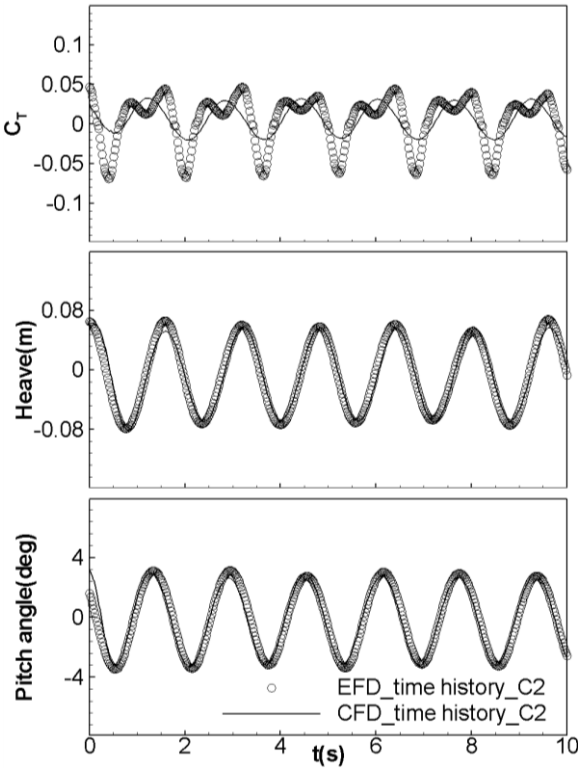

Fig.7 Time histories of C_T, z and θ for case 2, C2.

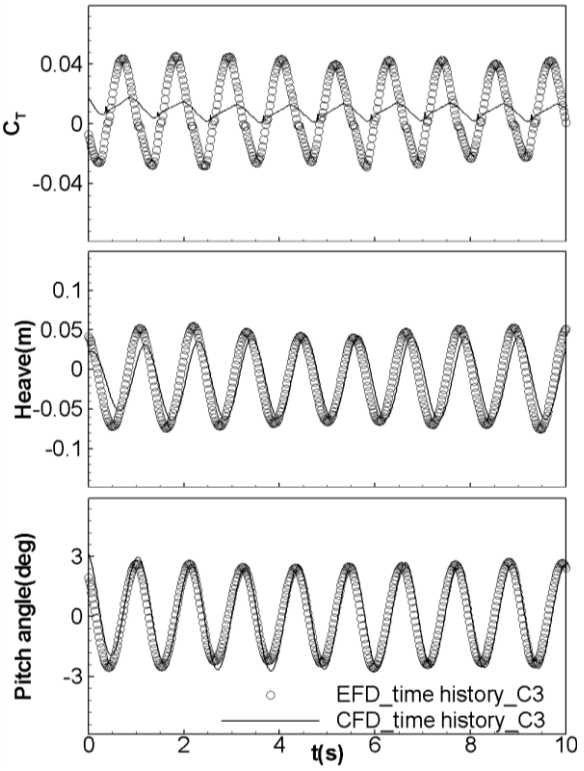

Fig.8 Time histories of C_T, z and θ, case2, C3.

Table 5 Amplitudes and phases of C_T, z and θ for case2.

	$C_T \times 10^3$	z(mm)	θ°
C1			
0th EFD	7.159	-4.89	-0.058
0th CFD (E%D)	6.971 (-2.6)	-6.37 (30.0)	-0.077 (32.7)
1st EFD	20.42	40.04	2.11
1st CFD (E%D)	6.03 (-70.4)	33.97 (-15.1)	2.21 (4.7)
1st φ EFD	82	4.7	34
1st φ CFD (E%D)	67 (-8.3)	-7.5 (-6.8)	30 (-2.2)
C2			
0th EFD(D)	6.033	-6.52	-0.13
0th CFD (E%D)	5.599 (-7.2)	-6.49 (-0.4)	-0.21 (61.5)
1st EFD	32.07	65.8	3.12
1st CFD (E%D)	25.2 (-21.4)	62.4 (-5.2)	2.99 (-4.2)
1st φ EFD	70.8	9.0	61.0
1st φ CFD (E%D)	82.3 (6.4)	2.0 (-3.9)	70.0 (5.0)
C3			
0th EFD(D)	8.716	-11.4	0.075
0th CFD(S)	8.189 (-6.0)	-11.8 (3.5)	0.04 (87.5)
1st EFD	35.4	58.1	2.43
1st CFD (E%D)	5.09 (-85.6)	51.0 (-12.2)	2.59 (6.6)
1st φ EFD	99.8	21.0	45.0
1st φ CFD (E%D)	86.4 (-7.4)	-14.0 (-19.4)	21.0 (-13.3)

Irvine et al. (2008) suggest that the maximum response of the ship will occur when $f_e=f_n$ and $\lambda/L_{pp}=1.33$ at the same time, with f_e is the encounter frequency and f_n the natural frequency of the pitching and heaving system in wet condition. For the present model the natural frequencies in heave and pitch are close to $f_n \approx 0.9$ Hz. Conditions C1 and C3 have frequencies of encounter of 0.896 and 0.8885, respectively, both very close to the natural frequency of the system. The wavelength in condition C2 is very large ($\lambda/L_{pp}=2.0$) and thus exhibits a very linear behavior with

amplitudes and phases as expected from a long wave: the amplitude of heave the same as the waves and in phase with them, and the amplitude of pitch the slope of the wave with 90 degrees lead in phase. Condition C3 also has the maximum response wavelength λ/L_{pp}=1.33, with resonance occurring as shown in Fig. 9, where a small amount of green water can be observed in the bow.

Notice in the data for pitch and heave a significant low frequency content, which is not reproduced by CFD. This could be due to wave reflections or direct low frequency content in the carrying wave. This generates inaccuracies in the calculation of the 0th and 1st harmonics of the experimental data.

6. CONCLUSIONS

High-performance computations of self-propulsion and pitch and heave in waves for KCS appended with rudder in model scale are presented. The self-propulsion results, computed with a discretized propeller, are in very good agreement with the data for forces, sinkage and trim, and consistent in accuracy with other simulations of self-propulsion using discretized propellers. Pitch and heave motions agree well with data for all three wave and Froude number conditions evaluated, as does also the 0th harmonic of the forces. The predicted amplitude and 1st harmonic amplitude and phase of the force are considerably off, in agreement with reported results by Simonsen et al. (2008), raising questions about the accuracy of the experimental data.

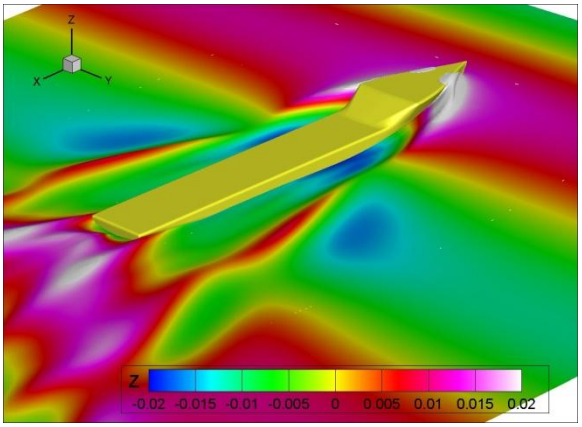

Fig.9 Green water occurs when f_e=f_n and λ/L_{pp}=1.33 in C3.

ACKNOWLEDGMENTS

This research was sponsored by the US Office of Naval Research under the administration of Dr. Patrick Purtell. Discussions and help by H. Hosseini are appreciated. Computations were performed on ARSC and NAVO machines, from the HPCMP of the US DoD.

REFERENCES

Carrica PM, Wilson RV, Stern F (2007a) "An Unsteady single phase level set method for viscous free surface flows," Int. J. Num. Meth. Fluids 53, 229–256.

Carrica PM, Wilson RW, Noack R, Stern F (2007b) "Ship Motions using Single-Phase Level Set with Dynamic Overset Grids," Comput. Fluids 36, 1415-1433.

Carrica PM, Ismail F, Hyman M, Bhushan S, Stern F (2008a) "Turn and zigzag maneuvers of a surface combatant using a URANS approach with dynamic overset grids", SIMMAN 2008, Copenhagen, Denmark.

Carrica PM, Paik K, Hosseini H, Stern F (2008b) "URANS Analysis of a Broaching Event in Irregular Quartering Seas," J. Marine Sci. Technol. 13, 395-407.

Carrica PM, Huang J, Noack R, Kaushik D, Smith B, Stern F (2010a) "Large-Scale DES Computations of the Forward Speed Diffraction and Pitch and Heave Problems for a Surface Combatant," Comput. Fluids 39, 1095-1111.

Carrica PM, Castro AM, Stern F (2010b) "Self-Propulsion Computations Using Speed Controller and Discretized Propeller with Dynamic Overset Grids," J. Marine Sci. Technol. (in press, doi:10.1007/s00773-010-0098-6).

Irvine M Jr., Longo J, Stern F (2008) "Pitch and Heave Tests and Uncertainty Assessment for a Surface Combatant in Regular Waves," J. Ship Res. 52, 146-1.

Mosaviraad M, Carrica PM, Stern F (2010) "Development and Validation of Harmonic Wave Group Single-Run Procedure for RAO with Comparison to Regular Wave and Transient Wave Group Procedures Using URANS," Ocean Eng. 37, 653-666.

Noack R (2005) SUGGAR: a general capability for moving body overset grid assembly. AIAA paper 2005–5117, 17th AIAA CFD Conf., Toronto, Canada

Otzen J, Simonsen C (2008) "Uncertainty assessment for KCS resistance and propulsion tests in waves," Force Technology report ONRIII187-01.

Sakamoto N, Carrica P, Stern F (2008) "URANS Simulations of Static and Dynamic Maneuvering for Surface Combatant," SIMMAN 2008, Copenhagen, Denmark.

Simonsen C, Otzen J, Stern F (2008) "EFD and CFD for KCS heaving and pitching in regular head waves," Proc. 27th Symp. Naval Hydrodynamics, Seoul, Korea.

Weymouth G., Wilson R, Stern F, (2005) "RANS CFD predictions of pitch and heave ship motions in head seas," J. Ship Res. 49, 80-97.

FIXED SINKAGE AND TRIM BARE HULL 5415 SIMULATIONS USING CFDSHIP-IOWA

Shanti Bhushan, Thad Michael, Jianming Yang, Pablo Carrica, and Frederick Stern
IIHR-Hydroscience and Engineering, The University of Iowa, Iowa City, IA 52242-1585

1. SUMMARY

Simulations are performed using CFDShip-Iowa toolbox curvilinear (V4) and Cartesian (V6) grid solvers for straight ahead bare hull 5415 at Reynolds number Re = 5.13×10^6 and Froude number (Fr) = 0.28 corresponding to the flow conditions for Case 3.1b in this workshop. The boundary layer and wake profiles are also compared with the higher Re experimental data for Case 3.1a. V4 simulations include DES on a 300M grid and URANS on a 615K grid. V6 simulations are performed using wall-function wall-layer model on grids up to 276M points. The large grid V4-DES simulation provides significantly better resistance and wave elevation predictions than the coarse grid URANS simulations. V4-DES provides a plausible description of the vortical structures and mean flow patterns observed in the sparse experimental data. However, the vortex strengths are over predicted and the turbulence is not resolved which suggests the need for advance turbulence model. V6 provides good predictions for the wave elevation pattern, but predicts diffused vortical structures due to poor wall-layer predictions. An approximate domain method for the immersed boundary is investigated to address the limitations of the wall-function implementation.

2. INTRODUCTION

Bare hull 5415 in straight ahead condition at fixed sinkage and trim for Fr = 0.28 is a well documented validation case for ship hydrodynamics. This case has been previously used at the CFD Workshops Gothenburg 2000 (Larsson et al., 2000) and Tokyo 2005 (Hino, 2005) to assess the state of the art in viscous ship flow computations. The available experimental datasets for this test case include resistance, wave elevation and boundary layer and wake profiles at several axial cross planes at Re = 1.2×10^7 (Olivieri et al., 2001) which are used for case 3.1a in this workshop, and resistance, wave elevation, velocity and turbulence profiles at the nominal wake plane x/L = 0.935 at Re = 5.13×10^6 (Longo et al., 2007) which are used for case 3.1b.

Previously, Wilson and Stern (2002) performed simulations at Re = 5.13×10^6 using CFDShip-Iowa V3, which uses surface-tracking method for free-surface modeling. The study focused on the verification and validation using grids up to 1.78 million (M) points. The averaged comparison error (E = D-S) between the experimental data (D) and the solution (S) was 4.2%D for the resistance and was validated at U_V = 8%D interval, where U_V=$\sqrt{(U_G^2+ U_D^2)}$, U_G and U_D are validation, grid and experimental uncertainties, respectively. The wave elevation and the boundary layer profiles at the nominal wake plane were validated at U_V = 6.4%D and 5.7%D intervals, respectively. Recently, Sakamoto et al. (2009) studied the effect of turbulence models and convection schemes on CFDShip-Iowa V4 (Carrica et al., 2007) resistance prediction using a 1.27M grid. The anisotropic Reynolds stress (ARS) model showed significant improvement over the blended k-ω/k-ε (BKW) model. However the total variation diminishing (TVD) convective scheme did not show significant improvement over the upwind scheme.

Even though the flow pattern for this case is well studied, the vortical structures and their interaction with the hull boundary layer are not yet completely understood. The sparse experimental data documents the flow pattern at several axial cross planes, but is not sufficient to identify the evolution of the vortical structures. Herein, a large grid V4-DES simulation using BKW is performed to evaluate the capability of DES in predicting integral variables, vortical structures and resolved turbulence. A coarse grid URANS using ARS and wall-function (WF) models are also presented for comparison purposes.

The near-wall resolution using immersed boundary method (IBM) is prohibitively expensive for high Re ship flows. A WF wall-layer model helps in alleviating the grid resolution requirements, but requires large grids compared to curvilinear grid solvers to achieve the ideal near-wall distance y^+ = 30. Herein, simulations are performed using CFDShip-Iowa V6 (Yang et al., 2008; Yang and Stern, 2009) to evaluate the WF wall-layer modeling with the immersed boundary method.

3. NUMERICAL METHODS

CFDShip-Iowa toolbox includes curvilinear (V4) and Cartesian (V6) grid solvers. V4 is currently the work-horse code for ship resistance, propulsion, seakeeping and maneuvering simulations. V6 is a research code which is being turned into a ship hydrodynamics code, and has been previously applied to several fundamental problems such as wave breaking, bubble entrainment and air layer drag reduction. The modeling, numerical methods and HPC of both solvers are discussed below. Readers are referred to Bhushan et al. (2010) for a complete list of the references.

3.1 CFDShip-Iowa V.4

Modeling: The general-purpose code V4 solves the URANS/DES equations in the liquid phase of a

free-surface flow. The governing equations are solved in absolute inertial earth-fixed or relative inertial coordinates for an arbitrary non-deforming control volume. The turbulence modeling is performed using BKW or ARS models and has DES and WF options. The interface modeling is performed using level-set methods. A multi-block dynamic overset grid approach is used to allow relative motions between the grids for 6DoF ship motions. The overset grid interpolation is performed using SUGGAR. The code provides propeller modeling using simplified body-force or direct discretization, and has a proportional-integral-differential controller to allow self-propulsion or auto-piloted simulations. A semi-coupled two phase flow version of the code with thermal and solute transport capability is also available, where the air flow is solved using the water velocity as boundary condition. (Huang et al., 2008).

Numerical Methods: The governing equations are discretized using node-centered finite difference schemes on body-fitted curvilinear grids and solved using a predictor-corrector method. The time marching is done using a second-order backward difference scheme, the convection terms are discretized using a hybrid second/fourth-order linear scheme, and a hybrid first/second-order TVD scheme is used for the level-set equation. First and second-order schemes are also available, but are not used in this study. The equations are solved using implicit schemes. The pressure Poisson equation is solved using the PETSc toolkit and projection algorithms are used to satisfy continuity.

High Performance Computing: MPI-based domain decomposition is used for parallelization, wherein each grid block is partitioned into sub-blocks by the user by specifying the number of times the grid needs to be split in the I, J and K directions. Then each sub-block is mapped to a processor. An exact load balance cannot be achieved for a general application, as the number of grid points in a direction may not be divisible by the number of splits or due to the differences in the grid block size. However, the load balance is achieved within 5% on each processor. Recently, Carrica et al. (2010) performed an extensive profiling using the PETSc user-defined events to identify bottlenecks of the in-processor and inter-processor procedures. The HPC performance was improved by optimizing the serial and parallel execution of routines and overset grid assembly resulting in up to 10 times speedup for large grids. The memory usage was improved to avoid the use of shared memory for better scalability on distributed memory machines. For this purpose a scalable partial differential equation-based reinitialization was added as an alternative to the geometrical reinitialization. The most important improvements for the overset assembly included, implementation of SUGGAR as a library to be executed on a dedicated MPI rank and limiting the grid search by using preassembly for motions. The solver shows good scalability up to 2048 processors where the speedup drops 37% below the ideal scaling (Bhushan et al., 2010). The scalability bottlenecks are identified to be the pressure Poisson solver which requires 72% of the CPU time and SUGGAR interpolation for motions. Based on the scalability studies it was estimated that the largest simulation using V4 on current 2Gb/core HPC systems can be performed using 490M grid points with 2048 processors. The ability to use even larger grids is expected as machines with better memory and cache become available and the code memory usage is further optimized.

3.2 CFDShip-Iowa V.6

Modeling: The URANS/DES/LES equations for two-phase turbulent flows are solved in absolute inertial earth-fixed coordinates using IBM on Cartesian grids. Turbulence is modeled using either BKW or k-g/k-ε (BKG) models with WF for URANS or a dynamic Smagorinsky SGS model for LES. The WF model include a multi-layer model implemented using a two-point approach (Bhushan et al., 2009). The WF provides the boundary conditions at the immersed boundary using the velocities at a selected probe point. The probe point is selected in the fluid phase along the wall normal direction located at least twice the wall distance of the immersed boundary point or one cell size. The interface is modeled using level-set, particle level-set or coupled level-set and volume-of-fluid (Wang et al., 2009) methods. The level-set model is used in this study

Numerical Methods: The governing equations are discretized using finite differences on a non-uniform staggered Cartesian grid and solved using a four-step fractional-step method. Time marching is performed with a second-order Adams-Bashforth scheme; the convection term is discretized using the QUICK or high-order (third or fifth) WENO schemes. The fifth-order schemes are used in this study. The level set evolution and reinitialization equations are solved using the third-order TVD Runge-Kutta and fifth-order HJ-WENO schemes. A semi-implicit scheme can be used for the time marching, but the explicit schemes are used here. The pressure Poisson equation is solved using the Krylov subspace based multi-grid solver in PETSc or the semi-coarsening multi-grid solver in the HYPRE library, and the latter is used herein.

Recently, the immersed boundary approximate domain method (ADM) (Kang et al., 2009) was incorporated to improve the pressure solution near the immersed boundary. For this purpose the ADM boundary was located one cell away from the body as shown in Fig. 1, the cells intersected by the body were removed from the pressure Poisson solver and zero net flux was enforced through the boundary. The implementation of ADM is expected to improve WF predictions as the coupled fluid-solid pressure field with a velocity jump from WF at the immersed boundary causes unphysical large flux near the boundary.

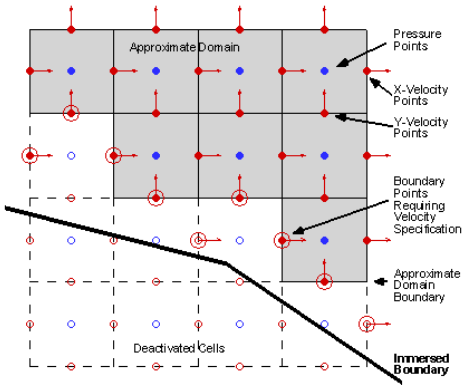

Fig.1 Illustration of the grid, body, active and deactivated cells for the approximate domain immersed boundary pressure solver.

High Performance Computing: The code uses MPI-based domain decomposition and MPI-I/O for solution on HPC platforms. Recent HPC developments were performed by Yang et al. (2008), where the one-dimensional slab decomposition was extended to three directions for parallelization. The solver allows only even splitting of the grids such that an exact load balance can be achieved on each processor. However, the load balance is affected by the uneven distribution of the air-water interface and IBM overhead. The inter-processor communications for the ghost cell information exchange were changed into non-blocking mode. A parallel I/O using MPI2 was implemented such that all the processors read from and write to a single file simultaneously. The solver shows good scalability up to 2048 processors where the speedup drops 25% below the ideal scaling (Bhushan et al., 2010). The scalability bottleneck is identified to be the pressure Poisson solver, which requires 91% of the CPU time. The scalability studies suggest that the largest grid that can be used on current HPC systems is about 1 Billon points. The code has not yet undergone an extensive optimization process similar to V4, thus further improvements are expected. Overall, V6 has advantages over V4 for numerical accuracy and scalability, requires 50% less memory and 20-25% less CPU time per time step per grid point than V4, which makes it better suited for large grid computations.

3.3 Domain, Grids, Boundary and Simulation Conditions

The simulations are performed for half hull only as shown in Fig. 2. The domain sizes are X/L_{PP}= [-1, 3], Y/L_{PP} = [0,3] and Z/L_{PP} = [0.25, -1] in the streamwise, spanwise and normal directions, respectively. The V4-DES simulation is performed using a 300M grid on 1461 processors with time step size of 5×10^{-4} for 4 flow times. This required about 110 hours of clock time and a total of 160K CPU hours. The V4-ARS and -WF simulations are performed on a 615K grid on 8 processors with time step size of 2×10^{-3} for 4 flow times. This required 16 hours of clock time and a total of 128 CPU hours. V6-WF simulations are performed on three grids consisting of 34M points with y^+ =150, 92M points with y^+ = 60 and 276M points with y^+ = 30. The 276M grid simulation is performed using 384 processors with a time step size of 1.75×10^{-5} with periodic time striding, i.e., time step size is increased to 8.75×10^{-5} every 10^{th} time step. The simulation is performed for 1.53 flow times, which required about 900 hours of clock time and a total of 350K CPU hours. The V6-WF with ADM simulation is performed using the 276M grid restarting from the V6-WF simulation. The simulation is performed for 1 flow time.

A uniform inlet and convective exit boundary conditions are applied at the X-Min and X-Max planes, respectively. A symmetry boundary condition is applied at Y/L_{PP} = 0 and far-field conditions at rest of the boundaries. The near-wall simulations use no-slip boundary conditions at the wall, i.e., J=1. In the WF simulations a multi-layer model used to specify velocities and turbulence quantities at J=2 plane or at immersed boundary points in V4 and V6, respectively. The simulations are performed for Case 3.1b conditions, i.e., $Re = 5.13\times10^6$, Fr = 0.28, sinkage = 1.92×10^{-3} and trim = 0.136°.

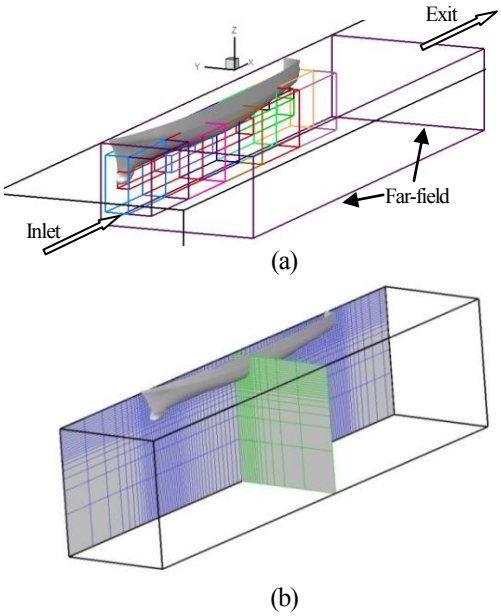

Fig.2 The domains for (a) V4-DES and (b) V6-WF simulations.

4. FIXED SINKAGE AND TRIM 5415

4.1 CFDShip-Iowa V.4

The grid verification study is not performed, thus the validation study includes only the comparison errors. The resistance predictions show E = 2.6%D, 7.8%D and 4.2%D for V4-DES, V4-ARS and V4-WF, respectively. V4-DES predictions are better than those reported by Wilson and Stern (2002), whereas the poor V4-ARS predictions are likely due to coarse grid resolution.

The measured wave elevation displays the so-called Kelvin wave pattern consisting of diverging and transverse waves within a half envelope angle α = 19°. Both V4-DES and -URANS predict the Kelvin wave half envelop angle well,

however in URANS the waves are diffused and dissipated away from the hull. V4-DES predicts the peaks and troughs in the wave-cuts well. The peaks compare well with the Olivieri et al. (2001) data, but are over predicted compared to Longo et al. (2007) data. V4-URANS predicts lower peaks than the experiments and fails to predict the peaks and troughs for the farthest wave-cut location. Overall, averaged E = 3%D and 8%D for V4-DES and -URANS predictions, respectively.

The vortical structures predicted by V4-DES are shown in Fig. 3a using iso-surfaces of normalized helicity Q = 100 on the starboard side. Symmetric vortices with opposite axial vorticity are predicted on the port side. The results show dominant sonar dome and fore-body keel vortices and relatively weak after-body keel, after-body counter rotating and transom vortices. The sonar dome vortex initiates on the side of the sonar dome surface and evolves in the wake below the hull boundary layer aligned with the center-plane. The fore-body keel vortex initiates at the intersection of sonar dome trailing edge and the keel, and interacts with the hull boundary layer causing a bulge in the boundary layer profile. The sonar dome vortex lifts toward the hull and both the sonar dome and fore-body keel vortices drift away from the center-plane around mid-girth x/L = 0.6. The sonar dome vortex wraps around the fore-body keel vortex at x/L = 0.8, which generates the after-body counter-rotating vortex. The merged sonar dome/fore-body keel and the after-body counter-rotating vortices interact with the hull boundary layer causing a bulge in the boundary layer profile at the nominal wake plane. The after-body keel vortex is formed from the keel at x/L = 0.8 and evolves aligned with the hull. The transom vortices are predicted aft of the partially wetted transom stern. As shown in Fig. 3b, V4-ARS predicts the inception of sonar dome and fore-body keel vortices well, but they dissipate quickly downstream and the vortical structures are not captured after x/L = 0.4. V4-WF predictions are similar to those of V4-ARS, but shows slightly higher diffusion and dissipation.

The sparse experimental data axial vorticity contours and cross flow streamlines at selected axial cross planes in Fig. 4 show a dominant sonar dome and poorly resolved fore-body keel vortices at x/L = 0.2, sonar dome and fore-body keel vortices at mid girth, and a diffused merged sonar dome/fore-body keel vortex and poorly resolved weak after-body keel and after-body counter-rotating vortices at the nominal wake plane. V4-DES provides a plausible description of the vortical structures observed in the experiment. However, the vortex strengths are higher due to lower dissipation as the turbulence is not resolved, which is discussed later. Both V4-ARS and -WF fail to predict the closed streamlines at the mid-girth and the vortex strengths are significantly weak due to excessive diffusion and dissipation.

Longo et al. (2007) identified that the mean axial and turbulent flow pattern at the nominal wake plane are similar to the boundary layer and turbulence structure in the presence of common-down axial vortex pair. V4-DES helps identify the vortex pair to be the starboard and port side merged sonar dome/fore-body keel vortices. The vortex pair transports high momentum fluid towards the center plane thinning the boundary layer, whereas the low momentum fluid is transported away from the hull causing a bulge in the boundary layer. V4-DES over predicts the boundary layer bulge due to the over prediction of vortex strength. Both V4-ARS and -WF perform relatively well with slightly thicker boundary layer and under predicted bulge even though the vortices are excessively diffused and dissipated.

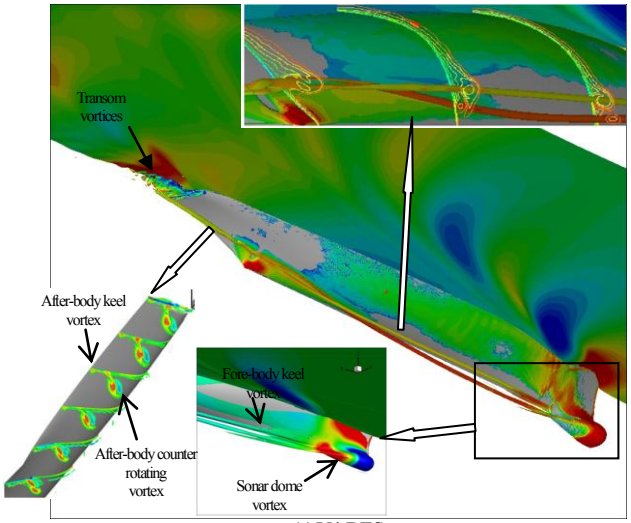

(a) V4-DES

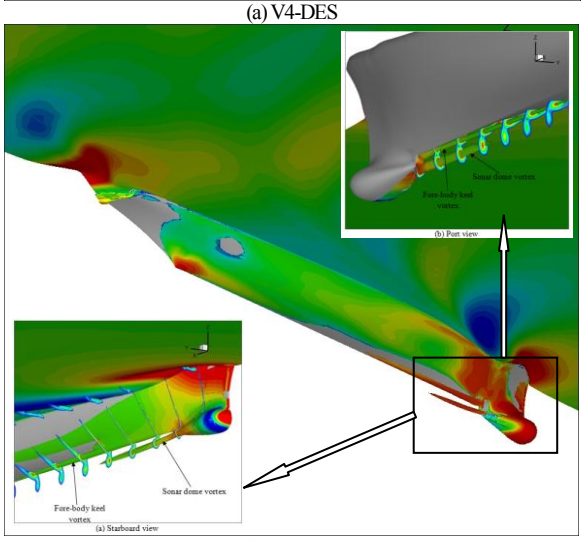

(b) V4-ARS

Fig.3 Isosurface of normalized helicity Q = 100 obtained using (a) V4-DES and (b) V4-ARS.

V4-DES does not predict the turbulence structures well, as the turbulent fluctuations are not activated, i.e., resolved TKE is 25% of the total TKE. The absence of turbulent fluctuations (or turbulent eddy viscosity) explains the lower vortex dissipation. V4-ARS TKE and stress predictions compare qualitatively well with the experiments, however only the TKE, axial normal and uv shear stresses are predicted quantitatively well. The normal stresses in the other directions and uw shear stresses are over predicted by

as much as 60%*D*. V4-WF shows a penalty in the turbulence prediction both qualitatively and quantitatively.

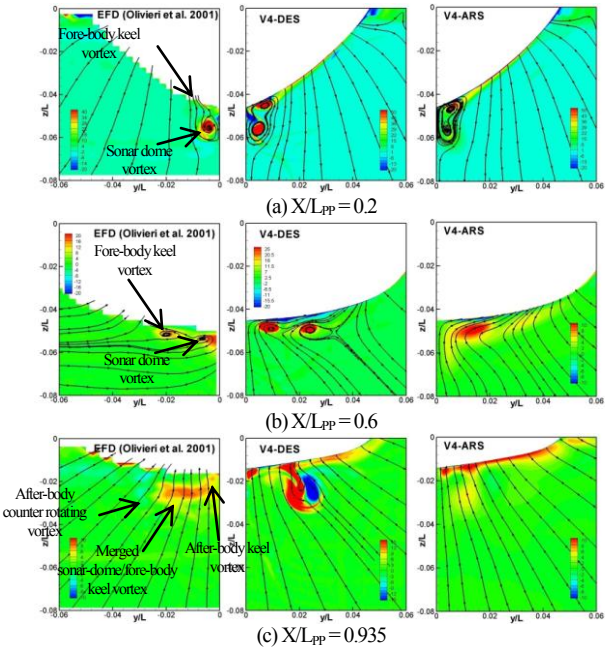

(a) $X/L_{PP} = 0.2$

(b) $X/L_{PP} = 0.6$

(c) $X/L_{PP} = 0.935$

Fig.4 Contour of axial vorticity and cross flow streamlines obtained using V4-DES and V4-ARS are compared with experimental data.

4.2 CFDShip-Iowa V.6

In V6, the resistance calculations are not yet possible, thus resistance coefficients are not validated. The Kelvin wave predictions are in good agreement with the experiments for all the grids. However, the transom wave predictions improve with the decrease in y^+. V6-WF with ADM does not show significant influence on the wave elevation predictions. V6-WF with y^+=30 wave-cut predictions show slightly better agreement with Olivieri et al. (2001) data than V4-DES. The averaged E = 3%D for the entire wave elevation is comparable to those obtained for V4-DES.

V6-WF with y^+ = 150 fails to predict the fore-body keel vortex and predicts a significantly diffused sonar dome vortex. The fore-body keel and sonar dome vortex predictions improve with the decrease in y^+. As shown in Figs. 5a and 6a, V6-WF with y^+ = 30 predicts all the vortical structures observed in V4-DES. However the fore-body keel vortex merges with the sonar dome vortex even before the mid-girth. The after-body keel vortex strength is higher than V4-DES, and merges with the merged sonar dome/fore-body keel vortex. Overall, V6-WF predicts diffused vortical structures and the merged sonar dome/fore-body keel vortex is closer to the center-plane compared to V4-DES. V6-WF with ADM in Fig. 5b shows a massive separation from the sonar dome surface, which drifts away from the hull. Thus a well defined sonar dome vortex is not predicted at $X/L_{PP} = 0.2$ in Fig. 6b. A fore-body keel vortex is observed close to the hull aligned with the center plane both at the inception and mid girth. The poor predictions of the vortical structures and their evolution are probably due to the poor prediction of the sonar dome vortex. The sonar dome vortical structure resembles vortices shed by a blunt body at low *Re*, which suggests that the ADM boundary is located quite far from the body, thus the geometry is not properly resolved.

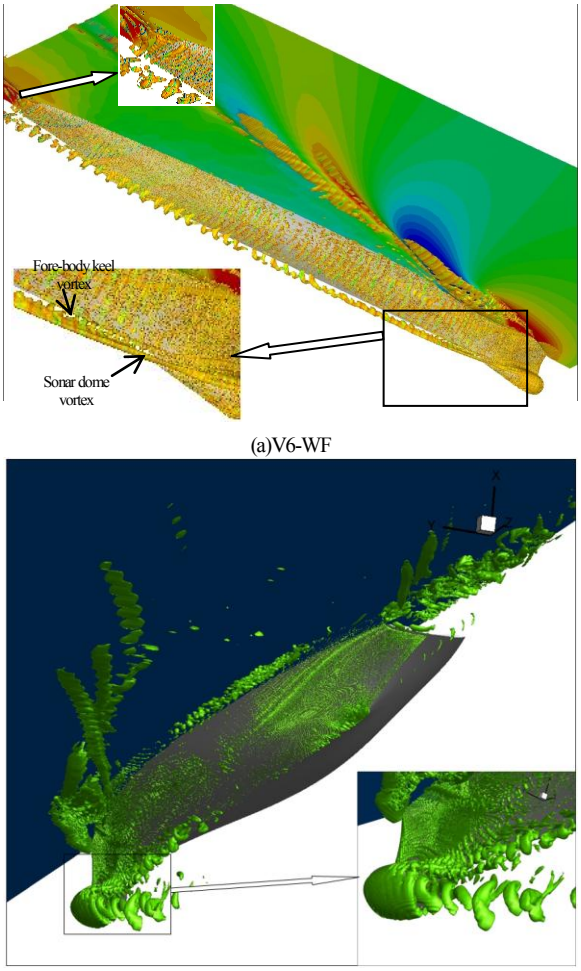

(a)V6-WF

(b) V6-WF with ADM

Fig.5 Isosurface of normalized helicity Q = 100 obtained using (a) V6-WF and (b) V6-WF with ADM using 276M grid.

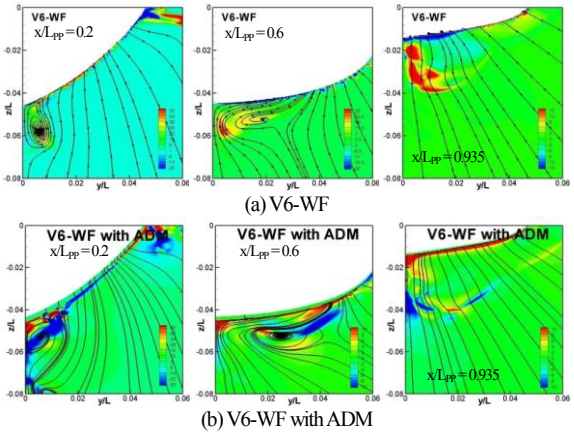

(a) V6-WF

(b) V6-WF with ADM

Fig.6 Contour of axial vorticity and cross flow streamlines obtained using V6-WF and V6-WF with ADM using 276M grid.

V6-WF boundary layer predictions improve with the decrease in y^+, but even with y^+= 30 the boundary layer bulge is over predicted and is closer to the center-plane compared to the experiments. The latter predicts TKE and stress profiles similar to the experiments, but the peak TKE and the shear stress minima are closer to the center-plane and their magnitudes are over predicted by 40-60%*D*.

5. CONCLUSION

The large grid V4-DES and the coarse grid URANS resistance predictions compare within 2.6%*D* and 6%*D* of the experimental data, respectively. V4-DES also shows significant improvements in the wave elevation predictions over URANS, where the comparison errors are 3%*D* and 8%*D*, respectively. V4-DES provides a plausible description of the vortical structures and mean flow patterns observed in the sparse experimental data, and helps identify the common-down axial vortex pair at the nominal wake plane to be the port and starboard merged sonar dome/ fore-body keel vortices. However, the vortex strengths are over predicted compared to the experiment as the turbulence is not resolved. Further investigation using finer grids are required to understand the resolved turbulence issue, which may lead to the need for advanced turbulence models such as the delayed DES or synthetic turbulence forcing at the inlet or the interface of URANS and LES. The coarse grid URANS performs quite well in predicting the boundary layer and turbulence structures at nominal wake plane, but fails to capture the evolution of vortical structures. Further simulations need to be performed on finer grids to obtain benchmark URANS results. Experiments with even higher resolution are required to capture the inception of the fore-body keel vortex and the vortical structures at the nominal wake plane.

V6-WF wave elevation predictions are within 3%*D* of the experiment and perform slightly better than V4-DES for the wave-cuts. The vortical structure and boundary layer predictions for 5415 in the straight ahead condition improve with the decrease in y^+ due to the reduction in modeling error. However, even with the ideal WF resolution of y^+ = 30 the vortical structures are diffused, the boundary layer bulge in over predicted and the turbulence quantities are over predicted by 40-60%*D* compared to the experiments. V4 results show that the WF have some limitations in predicting turbulence quantities, but does not explain the significantly higher turbulence predictions in V6-WF. However, the poor fore-body keel vortex prediction suggests that the wall-layer is not properly resolved probably due to the limitations of WF implementation with immersed boundaries. An approximate domain pressure solver is implemented to decouple the pressure solutions across the immersed boundary to improve the WF predictions. Some preliminary results using ADM suggests that the approximate domain boundary is not specified properly, which results in loss of geometry information. Further study using simple geometries, such as Wigley hull, is required to validate approximate domain method implementation. Future work will also focus on the implementation of force calculations which may provide additional insight in the boundary layer predictions.

ACKNOWLEDGEMENT

This research is sponsored by the Office of Naval Research under grants N00014-01-1-0073 and N00014-06-1-0420, administered by Dr. Patrick Purtell. The computations were performed at DoD Navy HPC systems Einstein (XT5) and DaVinci (IBM P6).

REFERENCES

Bhushan, S., Xing, T., Carrica, P.M., and Stern, F, (2009), "Model- and full-Scale URANS simulations of Athena resistance, powering and seakeeping, and 5415 maneuvering," *Journal of Ship Research*, 53(4):179-198.

Bhushan, S., Carrica, P., Yang, J. and Stern, F., (2010), "Scalability studies and large grid computations for surface combatant using CFDShip-Iowa," submitted to *The International Journal of High Performance Computing Applications*

Carrica, P. M., Wilson, R. V., and Stern, F, (2007), "An Unsteady Single-phase Level Set Method for Viscous Free Surface Flows," *International Journal of Numerical Methods in Fluids*. 53(2): 229-256.

Carrica, P. M. Huang, J., Noack, R., Kaushik, D., Smith, B., and Stern, F., (2010), "Large-scale DES computations of the forward speed diffraction and pitch and heave problems for a surface combatant," *Computers and Fluids*. 39(7), 1095-1111.

Hino, T, (2005), Proceedings of the CFD Workshop Tokyo 2005, National Maritime Research Institute, Tokyo, Japan.

Huang, J., Carrica, P. M., and Stern, F, (2008), "Semi-coupled air/water immersed boundary approach for curvilinear dynamic overset grids with application to ship hydrodynamics," *International Journal Numerical Methods Fluids*. 58: 591–624.

Seongwon Kang, S., Iaccarino, G., Ham, F. and Moin, P, (2009), "Prediction of wall-pressure fluctuation in turbulent flows with an immersed boundary method," *Journal of Computational Physics*, 228, 6753–6772.

Larsson, L., Stern, F. and Bertram, V, (2000), Proceedings of Gothenburg 2000- A workshop on numerical ship hydrodynamics, Chalmers University of Technology, Gothenburg, Sweden.

Sakamoto, N., (2009), "URANS and DES simulations of static and dynamic maneuvering for surface combatant," *Ph.D. Thesis*, The University of Iowa.

Wilson, R. and Stern, F., (2002), "Verification and Validation for RANS Simulation of a Naval Surface Combatant," *AIAA 2002-0904 Aerospace Sciences Meeting*, Reno, Nevada.

Wang, Z., Yang, J., Koo, B., and Stern, F. (2009). "A coupled level set and volume-of-fluid method for sharp interface simulation of plunging breaking waves," *International Journal of Multiphase Flow*. 35 (3): 227-246.

Yang, J., Bhushan, S., Suh, J. S., Wang, Z., Koo, B., Sakamoto, N., Xing, T. and Stern, F, (2008), "Large-eddy simulation of ship flows with wall-layer models on Cartesian grids," 27th Symposium on Naval Hydrodynamics, October 5-10, Seoul, Korea.

Yang, J. and Stern, F. (2009), "Sharp interface immersed-boundary/level-set methods for wave-body interactions," *Journal of Computational Physics*. 228(17):6590-6616.

A METHOD TO PERFORM SELF-PROPULSION COMPUTATIONS WITH A SIMPLIFIED BODY-FORCE PROPELLER MODEL

Huiping Fu (School of Naval Architecture, Ocean and Civil Engineering, Shanghai Jiao Tong University, China)
Thad Michael (Naval Surface Warfare Center, Carderock Division, West Bethesda, Maryland, USA)
Pablo M. Carrica (IIHR-Hydroscience and Engineering, The University of Iowa, USA)

1. SUMMARY

A method to perform self-propulsion computations using simple non-interactive body force models is presented. In order to predict self-propulsion factors, a procedure to obtain the propeller operating point advance coefficient using the body force model is developed. The method is intended for quick computations and educational purposes, though it has proven notably accurate for its simplicity. To test the methodology, the viscous free surface flow field around the model-scale KRISO container ship KCS at the self propulsion operating point in full scale is numerically simulated with the student version of the general CFD code FLUENT 12.0.16. All of the predicted propulsion coefficients are within 3% of the experimental values and the flow details also compare well with experimental data. The relatively small 330,000 cell hexahedral mesh created for the student version proved to be highly effective. Both the model ship towed resistance and self-propulsion tests in still water are numerically simulated. For the self-propulsion computation, cases with and without propeller torque are evaluated. It is shown that accounting for torque improves the accuracy of the computation and captures the flow features better, but with significant additional computational expense. Since this methodology and case present most of the features involved in a self-propulsion computation with little cost using widely available academic versions of Fluent or other commercial packages, it is very attractive for use in classes teaching computational ship hydrodynamics.

2. INTRODUCTION

The development of computational fluid dynamics (CFD) and parallel, high-speed computer technology makes it possible to numerically simulate almost all of the complex ship flow features at both model and full scale, including moving rudders and rotating propellers (Carrica et al. 2008). However, previously limited by available computer hardware, CFD researchers aimed to create computational models for complex flows. For example, in the field of computational ship hydrodynamics, to solve the interaction problem between the hull and propeller, earlier researchers separated them and computed them independently. Generally, the hull was computed by solving the RANS equations, and the propeller was solved using a lifting surface method. The interaction between them was simulated through an iterative procedure, as in Stern et al. (1988) and Xu et al. (1999).

Self-propulsion computations can be accomplished with a hierarchy of CFD methods and modeling. The most accurate approach, but also the most expensive, is to use CFD gridding the hull, appendages, and rotating propellers to find the propeller rotational speed (RPS) for self-propulsion at a given speed. The first computation of this kind was performed for the KCS containership by Lubke (2005), though it was not a truly self-propulsion case since both the propeller RPS and ship speed were imposed. Carrica et al. (2010a) used a controller to obtain the self-propulsion model point for the KVLCC1 tanker and the ONR Tumblehome surface combatant free to sink and trim, and for self-propulsion at full scale for the KCS containership at even keel. Though very detailed information is obtained, these computations are very resource intensive, and can only be performed with high-performance computers. The main limitation comes from the extremely small time step due to restrictions imposed by explicitly solving the propeller.

The next level of complexity consists of coupling a potential flow propeller solver with a CFD solver, which alleviates the time step restrictions. This approach is frequently used, most recently Hino (2006), Kim et al. (2006), Tahara et al. (2006) and Choi et al. (2009, 2010). Though the degree of accuracy of these approaches is satisfactory, the complexity is still significant and access to both propeller and CFD codes is necessary.

The third and simplest level of complexity is to use a non-interactive body force propeller model. In this case, a

body force distribution resembling the propeller radial load distribution in axial flow, for instance the Hough and Ordway (1965) distribution, is imposed in the CFD code to obtain an approximation of the flow field caused by an actual propeller. Though simple, this approach is very attractive because no propeller code is needed; the propeller is not explicitly modeled. This, of course, is also its main weakness: since the propeller is not resolved, it is usually impossible to obtain the self-propulsion factors using simple prescribed body force models.

In this paper, a methodology to compute most of the self-propulsion factors using a simple prescribed body force model for the propeller is presented. In order to obtain self-propulsion factors, a method is proposed to obtain the advance velocity at the self-propulsion point. The application to the KCS containership self-propelled at the full-scale operating point is described, stressing the educational value of the approach.

3. GEOMETRY AND CONDITIONS

The subject to compute is the KCS model (Figure 1). The KCS is a generic container ship model commonly used as benchmark for computational ship hydrodynamics (Larsson 2003, Hino 2005). Experimental data are available from Kim et al. (2001) and from the Tokyo 2005 Ship Hydrodynamics CFD Workshop (Hino 2005).

Fig.1 KCS geometry and free surface on the hull.

The main particulars of the ship model and computational conditions are L_{pp}=7.2786m, D=0.342m, S_W=9.4379m^2, U=2.196m/s, Re=1.4×10^7, Fr=0.26, where L_{pp} is the length between perpendiculars, S_W is the static wetted surface area for the given draft D, U is the ship speed, and Re and Fr are the Reynolds and Froude numbers.

The origin of the CFD coordinate system is located on the centerline at the bow where it meets the design water line. The x-axis lies in the center plane and water plane, positive toward the stern. The y-axis is positive to starboard and the z-axis upward.

4. MESH

Fine meshes for KCS have been presented by Fu and Yang (2009), who used two meshes with up to 3.5 million cells to compute resistance and wake KCS, and by Carrica et al. (2010a), who performed a self-propulsion computation of KCS with discretized propeller using overset grids with 21 million grid points. In this work the aim is instead to design a coarse grid that provides meaningful results but still fits the limit of maximum cells imposed by the academic version of Fluent.

The required mesh size at the hull surface, Δy_p, can be estimated using the formula in Fu and Ma (2009). Since the resistance is dominated by friction, it is important to design the grid to meet the requirement of the numerical approach followed. Accurate simulation of the wall boundary layer with wall functions requires that the local y^+ be in the range of 30~300. In this paper, the mesh is designed to have $y^+ \cong 60$, resulting in Δy_p=0.002m.

The Kelvin wavelength produced by the ship, λ, is estimated with the formula from Sheng and Liu (2003)

$$\lambda = \frac{2\pi}{g} U^2 \qquad (1)$$

where g is gravitational acceleration. With U=2.196m/s the Kelvin wavelength is λ=3.09m. For accurate calculation of the wave resistance the wave profile at the hull must be captured, which requires the near-hull wave field to be properly resolved. For surface capturing approaches, a minimum of 40 points per wavelength is recommended to resolve the wave (Carrica et al. 2006), justifying the use of 100 grid points along the hull length.

The mesh in the vertical direction near the free surface must be as orthogonal as possible, with no less than 20 grid points to capture the surface of the waves. The wave height is estimated with $H \cong \lambda/20$=0.1545m, so that ΔH<0.007m near the free surface. In this work a spacing of 0.005 m was used near the free surface.

The grid generation software Gridgen 15.11 was used to mesh the bare hull KCS model geometry using a fully structured grid with double-O topology. Since the flow is symmetric about the center plane when the torque of the propeller is not included, only one half of the hull is modeled. The final mesh contains 330,000 hexahedral cells. When torque is accounted for, the mesh is mirrored about the center plane to compute the whole flow field.

5. SELF-PROPULSION COMPUTATION PROCEDURE

The methodology to compute self propulsion at the full-scale operating point follows partly the ITTC (2002) procedures and those recommended in the CFD Workshop at Tokyo 2005 (Hino 2005). Differences arise from the use of a non-interactive body force, discussed in detail in this section.

All governing equations in Fluent are discretized with the finite volume method. For incompressible flow, the segregated solver is used. The SIMPLE method is used to couple velocity and pressure. Convective terms in the momentum equations are discretized by a third-order MUSCL (Monotone Upstream-Centered Scheme for Conservation Laws) scheme, which is a blending of a central differencing scheme and a second-order upwind scheme. Turbulence is simulated with the realizable k-ε two-equation model discretized with a first-order upwind scheme with non-equilibrium wall functions. The volume of fluid (VOF) multiphase method is used to capture the

free surface, where volume fraction is spatially discretized with the third-order QUICK scheme.

A no-slip wall boundary condition is applied on the hull. On the center plane, a symmetry condition is applied. The outer boundaries are comprised of a constant pressure condition on the top of the domain and a two-level velocity inlet on the surrounding quarter of spherical surface, which is separated into an air velocity inlet and a water velocity inlet along the design water line. The radius of the spherical surface is about one ship length. A time step of Δt=0.002s is used. A minimum of 10 inner iterations are applied on each time step. A fully converged simulation takes about 60,000 time steps, taking about 48 hours on a four core Xeon Linux workstation.

5.1 Towed Condition

In order to obtain self-propulsion factors, a towed computation at the operational speed is needed. Table 1 shows a comparison between the CFD predictions and the experimentally measured ship resistance components and nominal wake coefficient. The results show that the CFD prediction errors for the frictional resistance coefficient, C_F, and total resistance coefficient, C_{Tot}, are about -2.6% (compared to the ITTC friction line) and -0.4%, respectively. The CFD prediction error for the nominal wake coefficient 1-w_n is +3.6%. These results compare very favorably with the computations presented by 11 groups of CFD researchers for case 1.1 in Hino et al. (2005). To evaluate grid convergence, two additional grids were run, with a coarsening factor of $\sqrt{2}$, resulting in 117,000 and 41,000 cells, respectively. Table 2 shows results of the grid study.

Table 1 Comparison of predicted resistance coefficients ($\times 10^{-3}$) and nominal wake coefficient.

	EFD	CFD	E (%)
C_{Tot}	3.554	3.541	-0.4
C_P		0.782	
C_F	C_{F0}=2.832 (ITTC)	2.759	-2.6
1-w_n	0.686	0.711	+3.6

Table 2 V&V study of the resistance coefficient C_{Tot}.

G3(S_3)	G2(S_2)	G1(S_1)	U_I/ε_{12}	$p_G/p_{G,th}$	U_G % S_1
3.851 (8.36%)	3.634 (2.25%)	3.541 (-0.37%)	0.22	1.18	3.28

5.2 Self-propulsion Computations

For the self-propulsion computations, a body-force, $\overline{fb}$, is added to the momentum equations to represent the propeller. Herein the Hough and Ordway (1965) load distribution is used. The distribution was obtained analytically under the assumption that the radial thrust and torque distributions are similar to the radial circulation distribution which is assumed to be proportional to $r^*\sqrt{1-r^*}$, where $r^* = (Y - Y_h)/(1 - Y_h)$ and $Y_h = R_h/R_p$. R_p and R_h are the radii of the propeller tip and hub, respectively. Using these assumptions, the body forces in the axial and angular directions are

$$fb_x = \frac{\rho U^2}{L} A_x r^* \sqrt{1-r^*} \tag{2}$$

$$fb_\theta = \frac{\rho U^2}{L} A_\theta \frac{r^* \sqrt{1-r^*}}{(1-Y_H) r^* + Y_h} \tag{3}$$

$$A_x = \frac{C_T}{\Delta x} \frac{105}{16(4+3Y_H)(1-Y_H)} \tag{4}$$

$$A_\theta = \frac{K_Q}{\Delta x J^2} \frac{105}{16(4+3Y_H)(1-Y_H)} \tag{5}$$

$$C_T = \frac{32 n^2 R_p^2 K_T}{\pi U^2} \tag{6}$$

and Δx is the dimensionless axial extent of the volume where the propeller forces are imposed, usually the thickness of the propeller. Note that Eqs. (2) and (3) are in cylindrical coordinates and implementation in Fluent through user-defined functions requires transformation to Cartesian coordinates. $C_T = 2T/(\rho U^2 \pi R_p^2)$ and $K_T = T/(\rho n^2 D_p^4)$ are the propeller thrust coefficients, $K_Q = Q/(\rho n^2 D_p^5)$ is the propeller torque coefficient, n is the propeller rotational speed in RPS, and $J=V_a/(nD_p)$ is the advance coefficient, with V_a the advance velocity.

5.2.1 Computations neglecting the torque

In this section, the torque is neglected, including only the axial body-force component Eq. (2). This simplification is expected to have little effect on most of the self-propulsion factors at the ship's operational point, though the effects on the propeller wake will be dramatic.

Note that in non-interactive body force models the force distribution is independent of the wake velocity distribution or propeller advance coefficient. Thus the self-propulsion point is obtained by varying the thrust, through the thrust coefficient, C_T, until resistance and thrust are balanced, see Eqs. (2), (4) and (6), irrespective of RPS or propeller thrust coefficient, K_T. One way to do this is to mimic the way an experiment is performed, changing the RPS until self-propulsion is achieved in Eq. (6) for an imposed fixed thrust coefficient, K_T. This combination of K_T and RPS provides the thrust for self propulsion, but are not the right values for self propulsion.

The computations are performed at the full-scale (ship) point, thus at self propulsion the resistance, thrust, and skin friction correction balance:

$$R_{T,SP} - T - SFC = 0 \tag{7}$$

where T is the propeller thrust, $R_{T,SP}$ is the total resistance

at self-propulsion integrated from forces on the hull, and *SFC* is the skin friction correction. The skin friction correction accounts for the difference in viscous drag due to different Reynolds numbers at model and full scale; we use the same value as in the experiments, 30.25 N.

The self propulsion is thus obtained by imposing K_T=0.17 and changing the rotational speed of the propeller, starting with *n*=9.5RPS, until the excess thrust,

$$T_e = T - R_{T,SP} + SFC \tag{8}$$

is zero. After the initial computation is converged with *n*=9.5RPS, the resistance and excess thrust are evaluated, and a second computation is performed with a different thrust. For a positive T_e, a smaller *n* is used, or a larger *n* otherwise. After this, linear interpolation with iteration as necessary can be used to find the value of *n* to eliminate the excess thrust. In this case *n*=9.5RPS resulted in an excess thrust of about 2N, and the next guess of *n*=9.0RPS yielded $T_e \cong -3.5\ N$. Linear interpolation between these values resulted in *n*=9.308RPS, which after convergence provided a thrust *T*=57.534N and a negligible excess thrust, as shown in Fig. 2. Using the computed self-propelled resistance $R_{T,SP}$, the thrust deduction factor is computed with

$$1-t = \frac{T-\left(R_{T,Tow}-SFC\right)}{T} = 1-\frac{R_{T,SP}-R_{T,Tow}}{T} \tag{9}$$

In the experimental procedure, the measured rotational speed, *n*, and thrust coefficient, K_T, are used with the propeller open water characteristics to obtain the advance ratio based on the speed of advance, *J*, and corresponding Taylor wake fraction, w_T, through the thrust identity method (ITTC 2002). Finally, the delivered propulsive efficiency, η_D, is determined. In a non-interactive body force method this procedure cannot be followed because only the thrust is obtained; K_T and *n* are not known.

To overcome this limitation, a method is proposed to obtain the advance velocity. The idea is to find the far-field velocity in an "open water" computation that is performed using the body force propeller with the thrust determined in the self propelled calculation. The inlet velocity for this calculation is iterated to obtain the same integral of axial velocity squared on the propeller disk that was obtained in the above self propelled computation. This will provide the same momentum flux through the disk at the same thrust, like the similarity condition used for the thrust identity method used in the experimental procedure. This essentially implies two steps: 1) find the average of the velocity squared at the propeller disk in the self-propulsion final condition, which in this case results in $\overline{V}^2_{disk} = 3.876\ m^2/s^2$; 2) compute the flow for the propeller only, operating at the same thrust as in self propulsion, and vary the far-field velocity until the average of the velocity squared at the propeller disk equals the value found in step 1). The iterations for step 2) are shown in Fig. 3. Since the open water problem is simple, with no free surface, it converges very fast. The value obtained is V_a/U=0.775. The advance velocity is then used to calculate the effective wake, $1\text{-}w_T = V_a/U$. Using the definitions of the advance and thrust coefficients the ship curve is obtained

$$K'_T = \frac{TJ^2}{\rho V_a^2 D_p^2} \tag{10}$$

Eq. (10) and the experimental open water curves are plotted as a function of *J* in Fig. 4. The intersection of the ship curve K'_T with the propeller open water curve K_T determines the *J* of the propeller operating point. As shown in Fig. 4, the predicted values are *J*=0.722, K_T=0.166, and $K_{Q(O)}$=0.0285. Finally, from *J* and V_a, the rate of rotation is found to be *n*=9.429RPS.

Table 3 lists the computational results for self-propulsion and compares the predictions with EFD data. When using this method with the body-force propeller, the torque coefficient, K_Q, cannot be resolved. Here, it is assumed that $K_Q = K_{Q(O)}$ as determined from the open water curve. The largest difference between the CFD and EFD coefficients is 2.9%.

Table 3 Computational results and error analysis

Self-Propelled	EFD	CFD	*E*(%)
Thrust coefficient, K_T	0.170	0.166	-2.4
Torque coefficient, K_Q	0.0288	0.0285	-1.0
Thrust deduction, (1-*t*)	0.853	0.878	+2.9
Effective wake, (1-w_T)	0.792	0.775	-2.1
Open water efficiency, η_o	0.682	0.669	-1.9
Relative rotative eff., η_R	1.011	1.0	-1.1
Advance ratio, *J*	0.728	0.722	-0.8
Revolution rate, *n*(RPS)	9.5	9.429	-0.7
Propulsive efficiency, η	0.74	0.758	+2.4

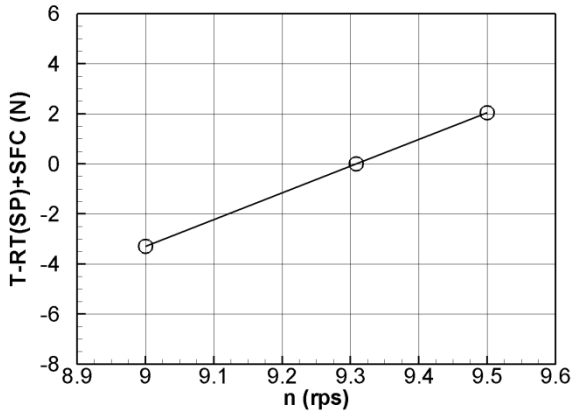

Fig.2 Excess thrust at three rates of rotation.

5.2.2 The influence of torque

The introduction of the rotational body force produced by the torque, Eq. (3), breaks the symmetry of the problem, forcing the use of both sides of the ship. Though the grid is still fairly coarse, the academic version of Fluent cannot be used for this case. The induced flow field of the complete case is of course much more realistic.

Axial velocity contours and cross flow vectors $0.25D_p$ behind the propeller plane are shown in Figures 5 and 6, respectively. There is no symmetry plane; the rotation of

the flow is fully simulated. Velocity components on the line $0.25D_p$ behind the propeller plane and at z/L_{pp}=-0.03 are shown in Fig. 7. The predictions are obviously improved compared to the results without torque, especially for the velocity components u and w, though the differences with EFD are still large. It is known that predicting the forces and moments, and therefore the self-propulsion point, is much easier than predicting flow field features (Carrica et al. 2010b). Usually, fairly coarse grids do a good job predicting overall forces and moments in relatively streamlined ships if the free surface profile over the hull is properly resolved and if the turbulence model is applicable to the problem.

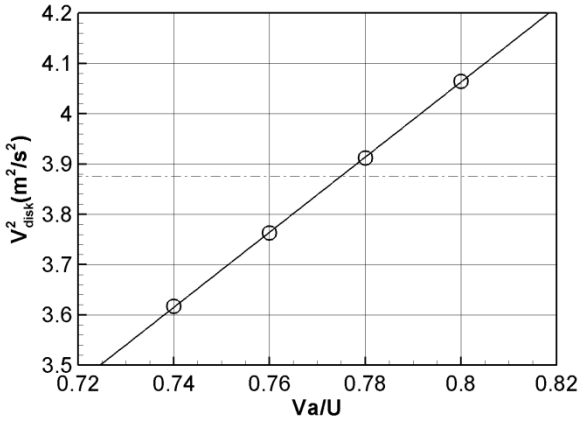

Fig.3 Area-weighted average of axial velocity squared on the propeller disk.

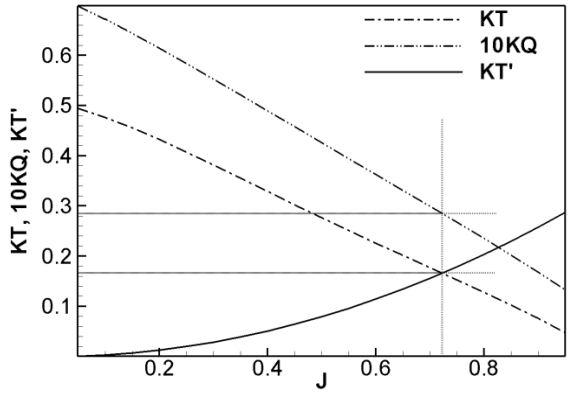

Fig.4 Propeller open water curves with predicted self-propulsion point.

Hull surface pressure contours, the free surface, and streamlines are shown in Fig. 8. Notice the swirl introduced by the propeller rotational body force on the flow field. Table 4 lists the self-propulsion computational results for the simulation including the torque body force. As in the previous section, it is assumed that $K_Q = K_{Q(O)}$, determined using the open water curves. Comparison of Tables 3 and 4 shows that most of the computed errors are slightly smaller when the effect of torque is included. The relatively minor improvements in error demonstrate that the self-propulsion method neglecting torque is effective to obtain quick self-propulsion factors, and allows the use of a symmetry plane to reduce the computational expense.

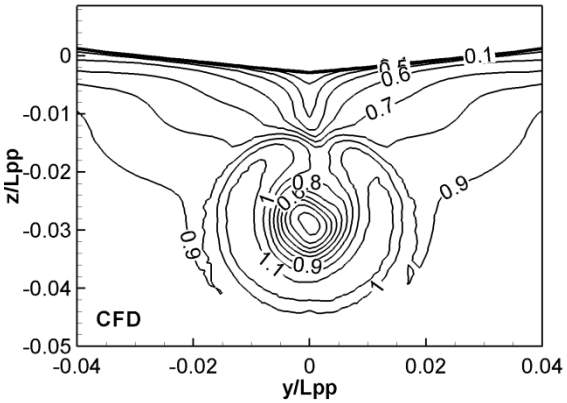

Fig.5 Axial velocity contours $0.25D_p$ behind the propeller plane, $\Delta u/U$=0.1.

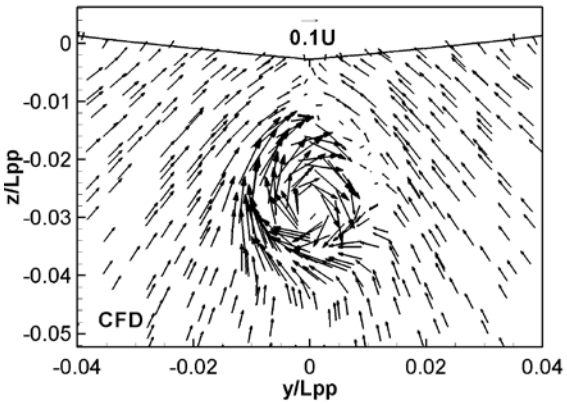

Fig.6 Cross flow vectors $0.25D_p$ behind the propeller plane.

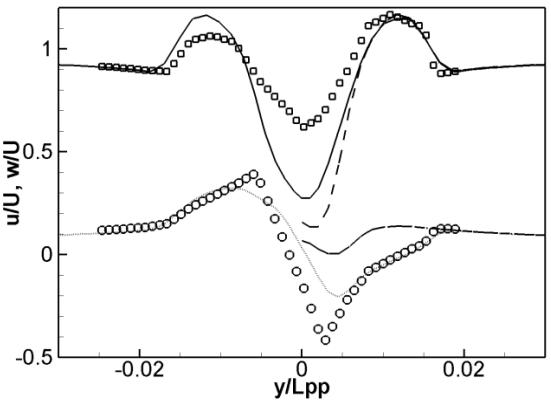

Fig.7 Velocity $0.25D_p$ behind the propeller plane at z/L_{pp}=-0.03. (u/U: EFD open square, CFD with K_Q solid line, CFD without K_Q dashed line. w/U: EFD open circles, CFD with K_Q dotted line, CFD without K_Q dashed line)

6. CONCLUSIONS

A method to simulate self-propulsion using a non-interactive body force propeller model has been presented. The effective wake coefficient is computed by matching the momentum flux through the propeller disk

in open water with the flux in the self-propelled condition. This method is similar to the thrust identity method used in experiments. When the torque body force and asymmetry are neglected, self-propulsion coefficients are within 2.9% of experimental measurements.

The influence of torque was also investigated. It has been shown that accounting for torque is advantageous and improves the flow simulation and predicted coefficients. However, the improvements are relatively small, justifying the use of the half-ship computation when the size of the problem must be minimized.

Comparisons of wave elevations, wake velocities, and hull surface pressures between CFD and EFD have shown that this hexahedral mesh, comprised of 330,000 cells for the symmetric mesh and 660,000 cells for the whole hull, is sufficient to capture the main flow features affecting resistance.

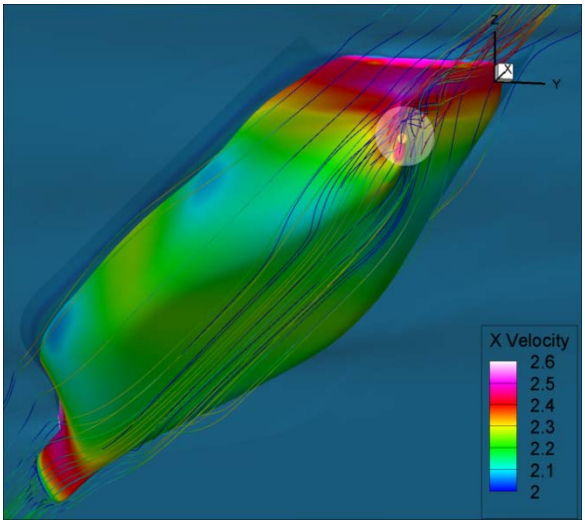

Fig.8 Hull surface pressure contours and streamlines.

Table 4 Computational results with torque

Self-Propelled	EFD	CFD	E(%)
Thrust coefficient, K_T	0.170	0.167	-1.8
Torque coefficient, K_Q	0.0288	0.0286	-0.7
Thrust deduction, (1-t)	0.853	0.878	+2.9
Effective wake, (1-w_T)	0.792	0.778	-1.8
Open water efficiency, η_o	0.682	0.670	-1.8
Relative rotative eff., η_R	1.011	1.0	-1.1
Advance ratio, J	0.728	0.721	-1.0
Revolution rate, n(RPS)	9.5	9.476	-0.3
Propulsive efficiency, η	0.74	0.756	+2.2

REFERENCES

Carrica PM, Wilson RV, Stern F (2006). Unsteady RANS Simulation of the Ship Forward Speed Diffraction Problem. *Comput. Fluids* **35**, 545-570.

Carrica PM, Stern F (2008). DES simulations of KVLCC1 in turn and zigzag maneuvers with moving propeller and rudder. *SIMMAN 2008*, Copenhagen, Denmark.

Carrica PM, Castro AM, Stern F (2010a). Self-Propulsion Computations Using Speed Controller and Discretized Propeller with Dynamic Overset Grids. *J. Mar. Sci. Technol.* (in press)

Carrica PM, Huang J, Noack R, Kaushik D, Smith B, Stern F (2010b). Large-Scale DES Computations of the Forward Speed Diffraction and Pitch and Heave Problems for a Surface Combatant. *Comput. Fluids* **39**, 1095-1111.

Choi JE, Kim JH, Lee HG, Choi BJ, Lee DH (2009). Computational predictions of ship-speed performance. *J. Mar. Sci. Technol.* **14**, 322-333.

Choi JE, Min KS, Kim JH, Lee SB, Seo HW (2010). Resistance and propulsion characteristics of various commercial ships based on CFD results. *Ocean Eng.* **37**, 549-566.

Fu H, Yang C (2009). Effects of Reynolds number on resistance and wake of ship. *J. Shanghai Jiao Tong Univ.* **43**, 1555-1558 (in Chinese).

Fu H, Ma N (2009). Demands of free surface and wake computation on mesh. *J. Shanghai Jiao Tong Univ.* **43**, 1573-1576 (in Chinese).

Hino T, Editor (2005). *CFD Workshop Tokyo 2005*. Tokyo, Japan.

Hino T (2006). CFD-based estimation of propulsive performance in ship design. Proc. *26th Symp Naval Hydrodynamics*, Rome, Italy

Hough GR, Ordway DE (1965). The generalized actuator disk. *Developments Theoretical Appl. Mech.* **2**, 317–336.

Kim WJ, Van SH, Kim, DH (2001). Measurement of flows around modern commercial ship models. *Exp. Fluids* **31**, 567-578.

Kim J, Kim KS, Kim GD, Park IR, Van SH (2006). Hybrid RANS and Potential Based Numerical simulation for self-propulsion performances of the practical container ship. *J. Ship Ocean Tech.* **10**, 1-11.

Larsson L, Stern F, Bertram V (2003). Benchmarking of computational fluid dynamics for ship flows: the Gothenburg 2000 workshop, *J. Ship Res.* **47**, 63-81.

Lübke LO (2005) Numerical simulation of the flow around the propelled KCS. *CFD Workshop Tokyo 2005*, Tokyo, Japan.

Sheng Z, Liu Y (2003) *Principles of Naval Architecture*. Shanghai Jiao Tong University, Shanghai, China.

Stern F, Kim HT, Patel VC, Chen HC (1988). A viscous-flow approach to the computation of propeller-hull interaction, *J. Ship Res.* **32**, 246-262.

Tahara Y, Wilson RV, Carrica PM (2006). RANS simulation of a container ship using a single-phase level set method with overset grids and prognosis for extension to self-propulsion simulator. *J. Mar. Sci. Technol.* **11**, 209-228.

Xu J, Gao Q, Zhou L (1999). Numerical simulation of Reynolds number effect on effective wake, *Journal Ship Mech.* **3**, 13-20 (in Chinese).

CALCULATION OF THE FLOW AROUND THE KVLCC2 TANKER: CASE 1.1.a

L. Eça (IST, Portugal)
M. Hoekstra (MARIN, The Netherlands)
H.C. Raven (MARIN, The Netherlands)

1. ABSTRACT

This paper describes the calculations performed with the RANS solver PARNASSOS (van der Ploeg *et al.*, 2000) for the double-body flow (no gravity waves) around the KVLCC2 tanker. The aim of this study is twofold: assess the numerical (iterative and discretization) uncertainty of the predictions in H-O grids with up to about 6 million cells; demonstrate (by graphical comparisons with experimental data) the quality of the predictions with two-equation eddy-viscosity models using empirical corrections for rotation and streamline curvature effects.

It must be stated that the flow settings used in the numerical calculations (unbounded flow) are not identical to those used in the experiments (wind tunnel, bounded flow). Furthermore, we have not found any information about the experimental uncertainty. Therefore, it is not possible to make a proper validation study.

1.1 Numerical uncertainty

Two contributions to the numerical uncertainty have been addressed: iterative and discretization errors. Although we have demonstrated previously that the influence of the iterative error is often underestimated (Eça *et al.*, 2006, 2009, 2010b), we have performed a small exercise using different convergence criteria for the iterative solution of the flow. The iterative error again turns out to be larger than what the normalized residuals or maximum differences between iterations of the dependent variables suggest. Grid refinement studies in sets of nearly geometrically similar grids have been performed to estimate the discretization error contribution to the numerical uncertainty. The procedure described in (Eça *et al.*, 2010a) has been applied to several flow quantities obtained with an iterative convergence criterion guaranteeing that the iterative error is negligible compared to the discretization error.

1.2 Comparison of numerical predictions with measurements

Two eddy-viscosity two-equation models have been selected: the Shear-Stress Tranport k-ω(SST) model (Menter, 1994) and the $k-\sqrt{k}L$ (KSKL) model (Menter *et al.*, 2006). In both cases, we have explored the use of simple corrections that take into account the effects of rotation and streamline curvature (Dacles-Mariani *et al.*, 1995, Schweighofer and Hellsten, 1999).

Although the results requested by the Workshop organization are restricted to three cross-stream sections, we have compared the predictions and measurements at all locations with experimental data available. Unfortunately, many of these are simple graphical comparisons of isolines of a given flow variable without any information about the numerical and experimental uncertainties. Nevertheless, we have interpolated the numerical solution to the measured points to guarantee that the isolines are obtained with an equivalent amount of information. Furthermore, we have included the estimated numerical uncertainties in all the comparisons along lines (horizontal or circumferential) in the propeller plane.

2. CALCULATION DETAILS

PARNASSOS solves the Reynolds-averaged momentum (RANS) and continuity equations in a general non-orthogonal curvilinear coordinate system using eddy-viscosity turbulence models. The equations are written in contravariant form and discretized with finite-difference approximations without any transformation of the continuity equation. All metric and diffusion terms are approximated with second-order central differences. Pressure derivatives are discretized with four-point third-order schemes and velocity derivatives in the continuity equation with at least second-order schemes. All convective terms (including turbulence quantities) are approximated with four-point upwind schemes with limiters. This means that the code is second-order accurate.

2.1 Turbulence models

The SST and KSKL eddy-viscosity models are both proposed by Menter and their description is given in (Menter, 1994) and (Menter *et al.*, 2006). The alternative formulations tested in this study include corrections to the production and/or dissipation terms of the turbulence quantities to account for the effects of rotation and curvature (RC). The RCSST model includes a damping function, f_ω, in the dissipation term of the ω equation (Schweighofer and Hellsten, 1999) given by

$$f_\omega = \min\left(1, \frac{1}{1+3.6\frac{\Omega}{S}\left(\frac{\Omega}{S}-1\right)}\right), \quad (1)$$

where Ω is the vorticity magnitude and S the mean strain rate. A second alternative, RC1SST, was also tested multiplying the production term of k by f_ω. For the KSKL model, we have modified the production term of the two transport equations using f_ω and the corrected strain rate proposed in (Dacles-Mariani *et al.*, 1995) to obtain the RCKSKL model. In both equations, S^2 is replaced by $f_\omega\left(S+4\min\left(0,S-\Omega\right)\right)^2$.

2.2 Computational domain and grid sets

For the flow around the KVLCC2 tanker at model scale Reynolds number, 4.6×10^6, we have selected a computational domain with a cylindrical shape. The boundaries of the domain are two *x=constant* planes at the inlet and outlet, the planes *y=0* (symmetry plane of the ship) and *z=0* (still water plane), the surface of the ship and a cylindrical surface (external boundary) with the axis along the x direction at the intersection of the symmetry plane of the ship and the still water plane. The inlet and outlet planes are located one ship length (L_{PP}) upstream and downstream of the forward and aft perpendiculars, respectively. The radius of the external boundary is equal to L_{PP}.

We have tested three sets, A, B and C, of six nearly geometrically similar grids in the computational domain described above. All the grids are single-block H-O grids that differ essentially in the streamwise and girthwise node distributions. The coarsest grids have 0.7 to 0.8 million cells and the finest 5.3 to 6.1 million cells, covering a grid refinement ratio of 2. Figure 1 illustrates the coarsest grids of each set at the bow and stern regions.

Table 1 Maximum y^+ at the first node away from the wall

Grid Set	G1	G2	G3	G4	G5	G6
A	0.33	0.34	0.37	0.43	0.45	0.55
B	0.46	0.49	0.54	0.59	0.66	0.76
C	0.38	0.41	0.46	0.50	0.57	0.66

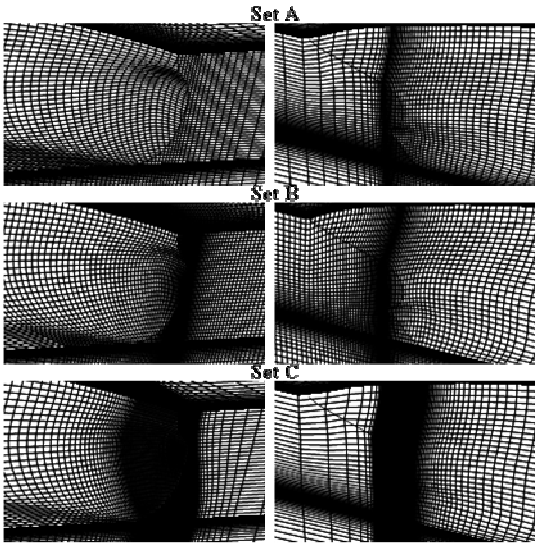

Fig.1 Illustration of the grids at the bow and stern regions.

The maximum y^+ obtained in the first grid node away from the wall, $(y_2^+)_{max}$, for the calculations performed with the SST model are given in table 1. All the values of $(y_2^+)_{max}$, are clearly below 1 and most of them are even below 0.5.

The results obtained in the three sets are perfectly consistent, i.e. there is overlap of the uncertainty intervals of all the selected flow quantities. However, the grid set that leads to the smallest numerical uncertainty depends on the selected flow quantity. In general, the smallest uncertainties at the propeller plane were obtained for set A that has the smallest grid line spacing in the girthwise direction. Therefore, in this paper, we will present only results obtained in set A.

2.3 Boundary conditions

The following boundary conditions are applied at the boundaries of the computational domain:

- Velocity components specified from a potential flow solution and pressure extrapolated from the interior of the domain at the inlet; the eddy-viscosity is set equal to 0.01 of the kinematic viscosity, $\nu_t=0.01\nu$ and the non-dimensional value of ω is set equal to 10, $\omega=10U_\infty/L_{PP}$. Any other turbulence quantities are derived from ν_t and ω

- At the outlet, zero streamwise derivatives are assumed for all flow variables.

- At the symmetry plane of the ship, the normal velocity component is set equal to zero. Tangential velocity components and pressure are obtained from the solution of the momentum equations with the symmetry conditions applied at virtual nodes, when the symmetry plane of the

ship coincides with the bottom of the computational domain (extreme of the normal grid lines). Otherwise, the symmetry conditions are applied directly to the tangential velocity components and to the pressure. Symmetry conditions are applied directly to all turbulence quantities.

- At the still water plane, girthwise velocity is set equal to zero and tangential velocity components and pressure are obtained from the solution of the continuity, streamwise and normal momentum equations with the symmetry conditions applied at virtual nodes. Girthwise derivatives are set equal to zero for all turbulence quantities.

- Tangential velocity components and pressure are imposed from a potential flow calculation at the external boundary. Normal derivatives of turbulence quantities are assumed to be zero.

- Direct application of the no-slip condition at the wall, i.e. velocity components set equal to zero and wall shear-stress computed from the normal velocity derivative at the ship surface. Normal pressure derivative equal to zero and all turbulence quantities equal to zero, except ω that is specified at the first grid node away from the wall (Eça and Hoekstra, 2004).

2.4 Convergence criteria

In PARNASSOS, the convergence criterion is based on the maximum pressure coefficient difference between consecutive iterations, $(\Delta C_p)_{max}$. Each iteration includes a complete update of the turbulence flow quantities and of the mean flow field. Changes between consecutive iterations are equivalent to residuals normalized by the main-diagonal of the discretized system, which are also checked at the end of the calculation. We note that in PARNASSOS there is no implicit under-relaxation and local time stepping is only used at the initial iterations of the solution procedure. As we will discuss below four different levels were tested for $(\Delta C_p)_{max}$.

Table 2 Maximum iterative errors of u_x, u_y, u_z

$(\Delta C_p)_{max}$	u_x	u_y	u_z
2×10^{-3}	5.3×10^{-2}	2.6×10^{-2}	1.0×10^{-1}
2×10^{-4}	3.1×10^{-2}	1.0×10^{-2}	1.6×10^{-2}
2×10^{-6}	5.0×10^{-4}	2.0×10^{-4}	3.9×10^{-4}

Table 3 RMS iterative errors of u_x, u_y, u_z

$(\Delta C_p)_{max}$	u_x	u_y	u_z
2×10^{-3}	3.5×10^{-3}	6.4×10^{-4}	1.1×10^{-3}
2×10^{-4}	7.1×10^{-4}	1.9×10^{-4}	2.7×10^{-4}
2×10^{-6}	1.1×10^{-5}	2.3×10^{-6}	3.1×10^{-6}

3. NUMERICAL UNCERTAINTY

3.1 Iterative error assessment

Four different convergence criteria were tested in grid set A with the SST turbulence model: $(\Delta C_p)_{max}<2\times10^{-3}$, $(\Delta C_p)_{max}<2\times10^{-4}$, $(\Delta C_p)_{max}<2\times10^{-6}$ and $(\Delta C_p)_{max}<2\times10^{-8}$. These results correspond approximately to a drop of 3, 4, 6 and 8 orders of magnitude in the maximum normalized residuals. The flow field obtained with the most demanding criterion was used as a reference to estimate the iterative error of the remaining three solutions. Tables 2 and 3 present the maximum and root mean squared (RMS) iterative errors of the Cartesian velocity components, u_x, u_y, and u_z in the finest grid of the set, G1.

It is obvious that reducing the residuals 3 orders of magnitude is not sufficient to have a negligible iterative error. As we have observed in previous exercises (Eça et al., 2006, 2009, 2010b), the maximum iterative errors can be two orders of magnitude higher than the maximum normalized residual (or change between consecutive iterations). Furthermore, even the RMS values of the iterative error are larger than the tolerance assumed for the convergence criteria.

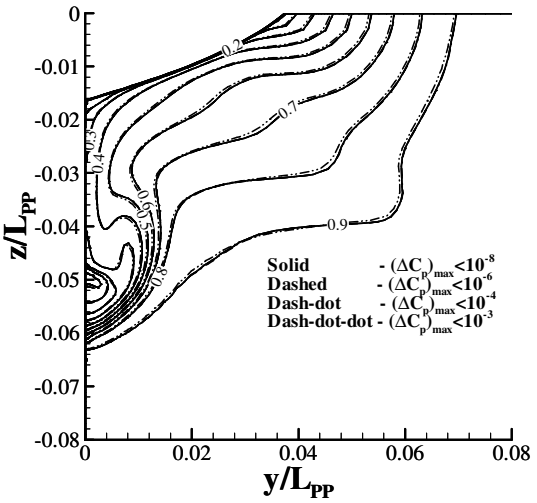

Fig.2 Axial velocity isolines at the propeller plane for four different convergence criteria.

It must also be emphasized that graphical comparisons are not reliable to make quantitative judgments about iterative errors. As an example, figure 2 presents the u_x isolines at the propeller plane for the calculations performed with the SST model in the finest grid using the four different values of the convergence criteria. The maximum values of the estimated iterative error for the three highest values of $(\Delta C_p)_{max}$ (difference to the $(\Delta C_p)_{max}$ <2×10^{-8} solution) are 3.6×10^{-2}, 4.4×10^{-3} and 6.7×10^{-5}, respectively. This means that even the solution obtained with four orders of magnitude reduction of the maximum normalized residual (changes

between consecutive iterations) exhibits an iterative error that is not negligible when compared to the discretization error. On the other hand, the isolines plotted in figure 2 show small differences and it can even be argued from the qualitative point of view that the least demanding convergence criterion is a "well established" solution (whatever that means). Therefore, it is not possible to make reliable quantitative judgments about iterative errors from simple graphical comparisons.

For all the remaining results presented in this paper, the convergence criterion requires $(\Delta C_p)_{max}<2\times10^{-6}$, which guarantees a negligible iterative error compared to the discretization error.

3.2 Discretization error

The contribution of the discretization error to the numerical uncertainty was estimated for integral and local flow quantities. Although not requested by the Workshop organization, it is interesting to check the accuracy of the computed friction, C_F, and pressure resistance coefficients, C_P. Both quantities are plotted in figure 3 as a function of the grid refinement ratio for the five turbulence models tested.

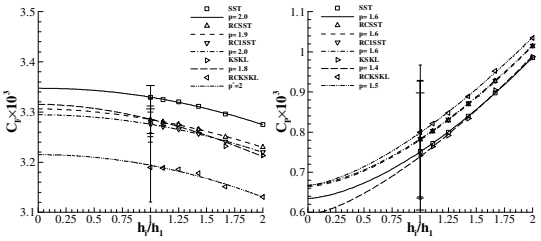

Fig.3 Convergence of the friction (C_F) and pressure (C_P) coefficients with the grid refinement.

The numerical accuracy obtained for C_F is close to 1% of the viscous resistance coefficient, C_V, and 4.5% of C_V for the pressure resistance. This latter result must be a consequence of having grid lines that do not match the exact ship geometry at the bow and stern regions.

The convergence properties obtained with the five turbulence models tested are similar. However, the $k-\sqrt{k}L$ models lead to more scatter in the data than the k-ω models. This is likely to be caused by the limiters used in the definition of the length scale in the $k-\sqrt{k}L$ models (Menter et al., 2006). Nevertheless, it is possible to estimate the observed order of accuracy of C_F and C_P for the five turbulence models.

The discrepancies between the solutions of the five turbulence models are within the numerical uncertainty for C_P, but for C_F the five estimated error bars do not overlap. Although the KSKL model tends to give a too low level of friction resistance (Eça and Hoekstra, 2008), the RC corrections exhibit the same trend in the two eddy-viscosity

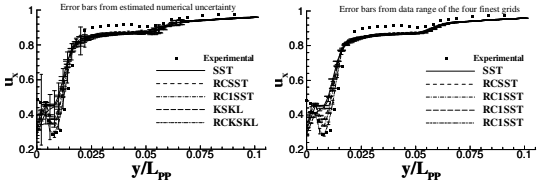

Fig.4 Axial velocity component at the propeller plane for z=-0.03625L_{PP}.

models: decrease of C_F and increase of C_P. These results are a consequence of the increase of the streamwise flow separation region at the end of the stern with the inclusion of the RC corrections.

The numerical uncertainty of the mean flow quantities is illustrated in figure 4 for u_x along an horizontal cut located at z=-0.03625L_{PP}. The figure presents two plots: the left graph contains error bars obtained from the procedure proposed in (Eça et al., 2010a), whereas the right figure includes the error bars equal to the data range of the four finest grids. With this information it is possible to check if large numerical uncertainties are a consequence of poor convergence properties or of a non-negligible grid dependency of the data. The plots also include the experimental data, but the comparison of predictions with measurements is only discussed in the next section

Although the estimated numerical uncertainties depend on the selected turbulence model, it is clear that the estimated uncertainties are larger close to the symmetry plane than at the outer region. The right graph shows that poor convergence properties (uncertainty from the data range of the six grids and safety factor of 3) are responsible for many of the large error bars observed in the left plot. However, the data range close to the symmetry plane shows that the grid dependency is not negligible in the bilge vortex region.

Figure 5 presents the predicted values of k along the same line together with the experimental data. The numerical uncertainty obtained for k is larger than that of u_x. There are still some larger estimated uncertainties due to poor convergence properties, but the data range of the four finest grids confirms that for the present level of grid refinement there is still a significant grid dependency in the turbulence flow quantities.

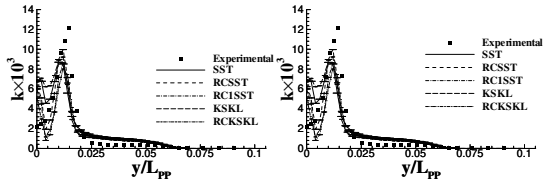

Fig.5 Turbulence kinetic energy at the propeller plane for z=-0.03625L_{PP}.

4. COMPARISON OF PREDICTIONS AND MEASUREMENTS

The best agreement between numerical predictions and experimental data is obtained for the RCKSKL model. Figure 6 presents the isolines of u_x and the transverse velocity vectors at the six cross-stream sections with experimental data available. The correlation between predictions and experiments is excellent at five of the six cross-sections. The exception is the last section at x=1.1L_{PP}, where a significant mismatch in the location and strength of the bilge vortex occurs. RCSST and RC1SST also show a reasonable agreement with the experiments. However, as is well-known, the standard versions of the models, SST and KSKL, are not able to capture correctly the axial velocity reduction at the propeller plane, as illustrated in figure 7.

The deterioration of the correlation between predictions and experiments at x=1.1L_{PP} is observed for all five turbulence models tested. Furthermore, there are other systematic differences to the experimental data for several flow details: at the outer region, the level of the axial velocity in the measurements is higher than in the predictions (figure 4); the measured horizontal velocity component at the propeller plane is larger than in the predictions, especially below the bilge vortex. This latter result is somehow strange, because the experiments exhibit a nonzero normal velocity at the symmetry plane of the ship.

It is hard to believe that some of these discrepancies are a consequence of shortcomings in the turbulence model (mathematical model). Due to the lack of experimental uncertainties and the different settings used in experiments and predictions it is not possible to explain these discrepancies convincingly.

Similar comparisons were also performed for the turbulence quantities. Although the trends observed for the five turbulence models are similar to those obtained for the mean velocity field, the comparison between measurements and predictions is better for the mean velocity field than for the turbulence flow quantities (turbulence kinetic energy and Reynolds stresses). Nonetheless, for the RCKSKL model solution, only one of the tangential stresses ($-\rho\overline{uw}$) shows a poor correlation between predictions and measurements.

5. CONCLUSION

Although the present exercise is the simplest proposed for the 2010 Gothenburg Workshop, it remains a challenging one for CFD. Achieving an acceptable numerical accuracy for a RANS solution of a ship viscous flow is not an easy task. It involves careful choices to avoid significant iterative and/or discretization errors.

We have demonstrated once more, that a drop of three orders of magnitude in the normalized residual does not guarantee negligible iterative errors. Furthermore, we have

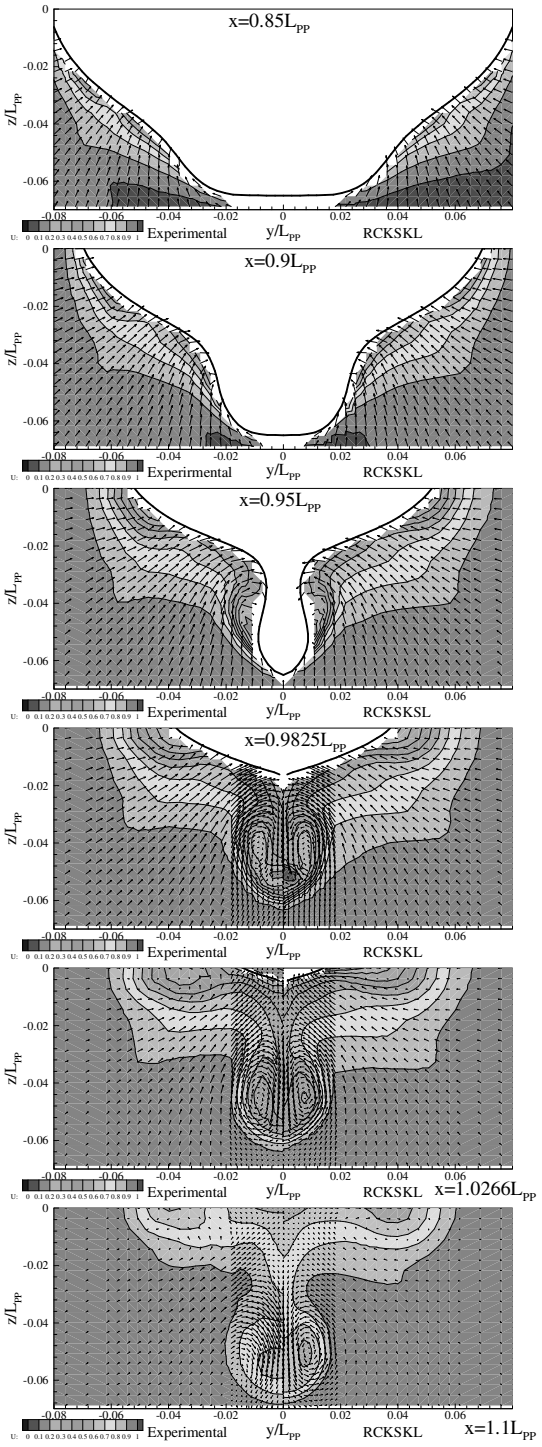

Fig.6 Comparison of velocity fields obtained with the RCKSKL turbulence model and the experimental data at six cross-stream sections.

shown that graphical comparisons are not sufficient to make quantitative judgments about the iterative error. This is an important topic for more complex CFD applications, because in many CFD solvers the iterative convergence tends to deteriorate with the increase of the grid size.

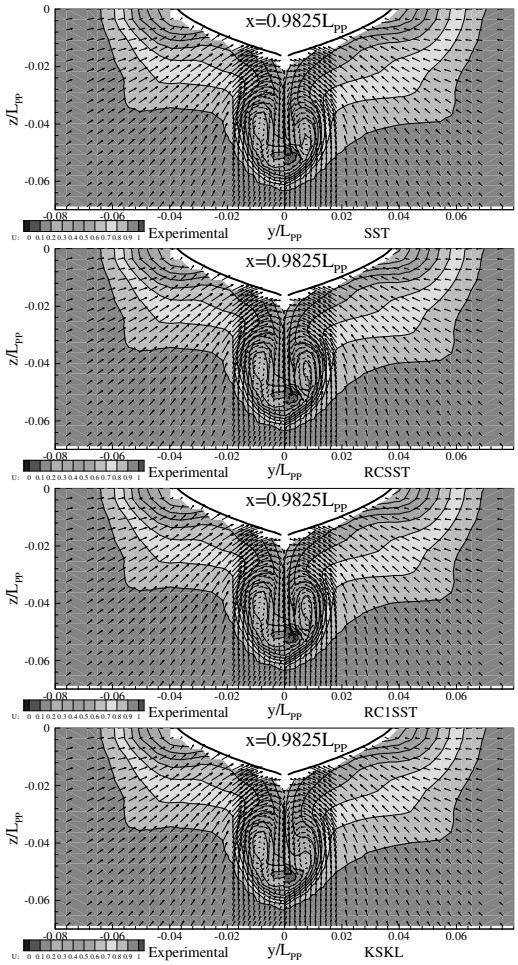

Fig.7 Comparison of velocity fields obtained with the SST, RCSST, RC1SST and KSKL turbulence models and the experimental data at the propeller plane.

Eddy-viscosity models lead to robust RANS solvers, i.e. the iterative error may be reduced to negligible levels with all terms of the transport equations (including turbulence models) discretized with at least second-order schemes. However, for the present grid refinement level, the contribution of the discretization error to the numerical uncertainty in the near-wake (pointwise determination) is still comparable to the differences obtained with predictions performed with different turbulence models, i.e. the noise is still too high to quantify modeling errors. This limitation becomes worse for the turbulence quantities, because they have a larger numerical uncertainty than the mean flow quantities.

Qualitatively, it is clear that the inclusion of rotation and streamline curvature corrections in the SST and KSKL eddy-viscosity models improves significantly the comparison of the predicted flow fields with the experimental data (comparison of shape of isolines). The correlation between experiments and predictions is better for the mean flow quantities than for the turbulence quantities. However, the noise in this comparison (numerical uncertainty, unknown experimental uncertainty, mismatches in the flow settings) precludes a quantitative judgment of the modeling accuracy of the flow predictions.

We must be aware that in order to quantify modeling errors, it is not enough to improve the "numerical side" of the problem. The experimental information available for this flow is clearly insufficient to reach that goal.

REFERENCES

Dacles-Mariani J. Zilliac G.G., Chow J.S., Bradshaw P., (1995), "Numerical/experimental study of a wing tip vortex in the near field", *AIAA Journal*,Volume 33, pp. 1561-1568.

Eça L, Hoekstra M., (2004), "On the Grid Sensitivity of the Wall Boundary Condition of the k-ω model", *Journal of Fluids Engineering,* Volume 126, Nº 6, pp. 900-910.

Eça L, Hoekstra M., (2006), "On the Influence of the Iterative Error in the Numerical Uncertainty of Ship Viscous Flow Calculations", Proceedings of 26th Symposium on Naval Hydrodynamics, Rome, Italy.

Eça L., Hoekstra M., (2008), "The Numerical Friction Line", *Journal of Marine Science and Technology*, Volume 13, Number 4, pp-328-345.

Eça L., Hoekstra M., (2009), "Evaluation of Numerical Error estimation based on Grid Refinement Studies with the Method of the Manufactured Solutions", *Computers and Fluids*, Volume 38, Issue 8, September, p.p. 1580-1591.

Eça L., Vaz G., Hoekstra M., (2010a) "Code Verification, Solution Verification and Validation in RANS Solvers", Proceedings of ASME 29th International Conference OMAE2010,, Shanghai, China.

Eça L., Vaz G., Hoekstra M. (2010b), "A Verification and Validation Exercise For The Flow Over A Backward Facing Step", Proceedings of V European Conference on Computational Fluid Dynamics, ECCOMAS CFD 2010, Lisbon, Portugal.

Menter F.R., (1994), "Two-Equation Eddy-Viscosity Turbulence Models for Engineering Applications", *AIAA Journal*, Volume 32, August, pp. 1598-1605.

Menter F.R., Egorov Y., Rusch D., (2006), "Steady and Unsteady Flow Modelling Using the $k-\sqrt{k}L$ Model", Proceedings Turbulence Heat and Mass Transfer, Volume 5, 2006.

van der Ploeg A., Eça L., Hoekstra M., (2000), "Combining Accuracy and Efficiency with Robustness in Ship Stern Flow Computation", Proceedings 23rd Symposium on Naval Hydrodynamics, Val de Reuil, France.

Schweighofer J., Hellsten A., (1999), "Computations of the Viscous Flow around the HSVA Tanker using Two Versions of the k-ω Turbulence Model", Report B51, Helsinki University of Technology.

CIP BASED CARTESIAN GRID METHOD FOR PREDICTION OF NONLINEAR SHIP MOTIONS

Changhong Hu (Research Institute for Applied Mechanics, Kyushu University, Japan)
Masashi Kashiwagi (Graduate School of Engineering, Osaka University, Japan)

1 INTRODUCTION TO THE CIP BASED CARTESIAN GRID METHOD

A Cartesian grid method with CIP (Constraint Interpolation Profile, Yabe et al, 2001) based flow solver has been developed in Research Institute for Applied Mechanics (RIAM), Kyushu University, by Hu and his colleagues for numerical simulation of strongly nonlinear free surface problems, such as violent sloshing inside a liquid tank, slamming, water on deck, wave impact by green water, large amplitude motions of ships or ocean structures, and so on (Hu et al., 2004, 2007, 2009, 2010) .

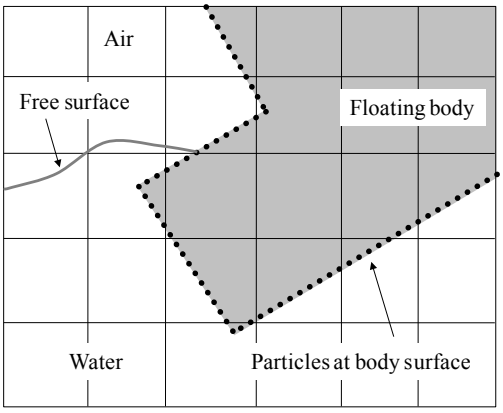

Fig.1 Multi-phase computation of wave-body interactions.

The concept of our Cartesian grid method is shown in Fig. 1. The wave-body interaction problem is viewed as a multiphase flow, which includes a liquid phase (water), a gas phase (air) and a solid phase (floating body). A Cartesian grid that covers the whole computation domain is adopted for numerical calculation. The free surface and the body boundary are treated as immersed interfaces. To recognize different phases we define a density function ϕ_m, in which m=1, 2, 3 denotes the liquid, gas, and solid phase, respectively. The density function for each computational cell has the relation of $\sum \phi_m = 1.0$ and follows the equation:

$$\frac{D\phi_m}{Dt} = 0 \tag{1}$$

where $D/Dt = \partial/\partial t + (\mathbf{u} - \mathbf{U}_0)\cdot\nabla$, $\mathbf{U}_0$ is the velocity of the grid.

For the flow solver, the fluid is considered as viscous and incompressible, and the following governing equations are used.

$$\nabla \cdot \mathbf{u} = 0 \tag{2}$$

$$\frac{D\mathbf{u}}{Dt} = -\frac{1}{\rho}\nabla p + \frac{1}{\rho}\nabla\cdot\mathbf{T} + \mathbf{f} \tag{3}$$

where **T** is the stress tensor, **f** is the body force. Time evaluation of Eq. (3) is performed by a fractional step method in which the equation is divided into an advection step and two non-advection steps. In the advection step, the CIP scheme is used.

The CIP method is a third order upwind scheme with compact structure, which can efficiently increase the computation accuracy in the vicinity of the inner interfaces for a Cartesian grid method.

For the interface capturing scheme, the THINC (Tangent of Hyperbola for Interface Capturing, Xiao, et al, 2003) has been improved and implemented in our CFD code.

The floating body is immersed in the Cartesian grid. In the current numerical model, only rigid bodies are considered. A weekly coupling procedure has been developed to treat the wave-ship interactions. In each time step, first the flow field is solved with the body motion approximated by adding a body force to the relevant Cartesian cells. The hydrodynamic forces on the body surface are then obtained which are used to calculate the translational and rotational velocities at the body gravity center. In order to treat

large-amplitude ship motions, e.g., capsizing, the rotation of the body is solved by using quaternion representation.

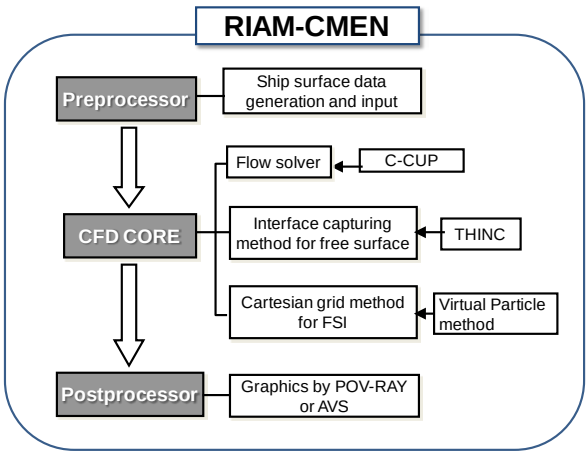

Fig. 2 Diagram of RIAM-CMEN

Such CIP based Cartesian grid method has been developed and improved for several years, to make it not only be able to handle complicated flow phenomena but also be efficient enough to perform three-dimensional simulations in an acceptable spatial and temporal resolution at reasonable cost.

The CFD code called RIAM-CMEN (Computation Method for Extremely Nonlinear hydrodynamics, see Fig.2) is based on the CIP-Cartesian grid method, and is now being developed and validated for various kinds of engineering applications. We have checked the performance of RIAM-CMEN for some 2-D problems such as dam breaking, violent sloshing in a rectangular tank, wave generation and interaction between waves and a floating body (Hu et al., 2004, 2009), and 3-D problems on ship motions and wave loads for a mathematical ship model or a real ship model in large-amplitude waves (Hu et al., 2007, 2010). The numerical simulations presented in this paper are carried out using RIAM-CMEN.

2 THREE DIMENSIONAL NUMERICAL WAVE TANK

The 2-D numerical simulation by the CIP based Cartesian grid method can be performed by using a numerical wave tank that simulates a real wave channel as shown in Fig. 3, in which the wave maker can be included in the computation. However, for a 3-D numerical simulation of wave-ship interactions, the size of computation domain has to be reduced due to the restriction of available computer resources. The concept of our 3-D NWT is also shown in Fig.3, in which the computation domain is a rectangular space around the ship. A Cartesian grid is used for discretization of the domain and the whole computation grid is moving with the advancing ship speed $\mathbf{U}_0$.

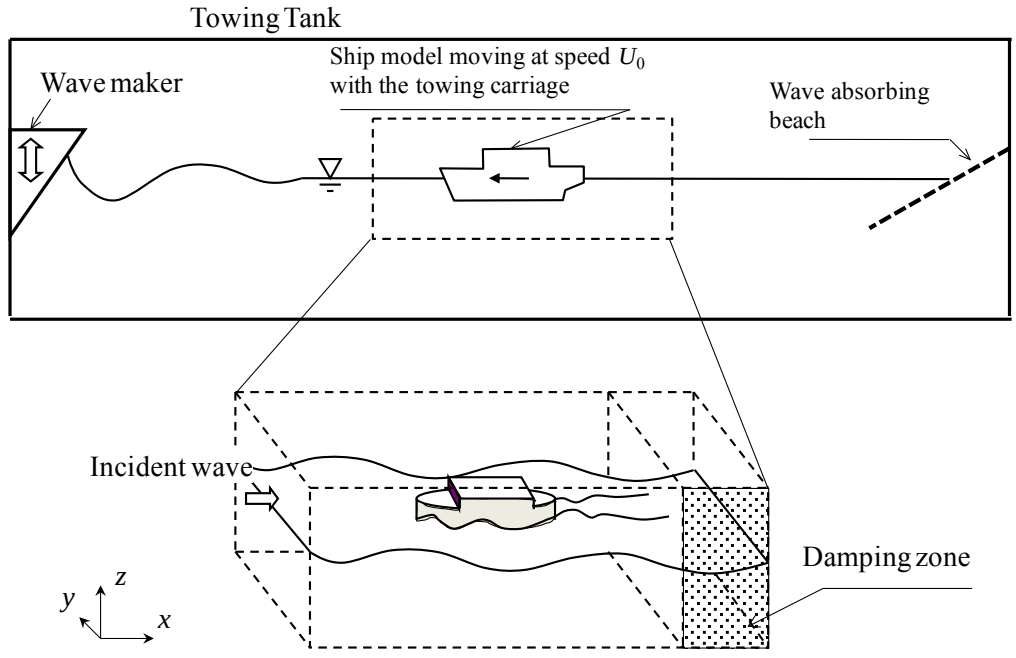

Figure 3: 3-D NWT moving at speed U_0

3 NUMERICAL RESULTS

The test case 1.4b is chosen for RIAM-CMEN computation. The experiment with a model of MOERI (Maritime & Ocean Engineering Research Institute) KVLCC2 tanker was conducted at MARINTEK. The numerical results for the case of Fn=0.142 and H=150mm are shown below. In the computation, surge motion is restricted. The number of cells is $240 \times 100 \times 150$. The minimum grid spacing is $\Delta x_{\min} = \Delta y_{\min} = 0.005L$ around the ship and $\Delta z_{\min} = 0.004L$ near the free surface. The time step size is taken equal to $\Delta t / T_e = 1/2000$, and adjusted automatically according to CFL condition in the computation. Here, T_e is the encounter period. The computations are performed by using a personal computer (Pentium4 3.4G, Memory DDR 2G), and the CPU time for the case shown in Fig.4 is about 34 hours.

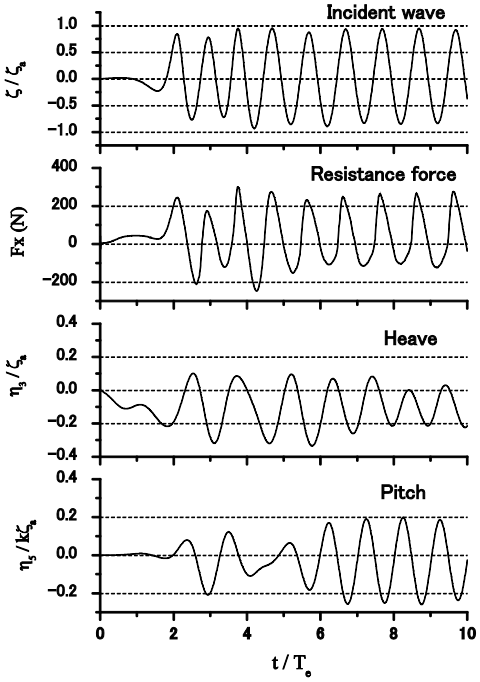

Fig.4 Time series for Fn=0.142, $\lambda/L = 0.9171$ and H=150mm.

The time series of computed wave elevation at the ship bow, resistance force, heave and pitch motions are shown in Fig.4. Physical time of 10 encounter periods is computed. It seems that the computation has reached periodic state and the data of last two periods are used for obtaining Fourier coefficients. The frequency response characteristics of the total resistance and wave-induced motions are shown in Figs. 5-7.

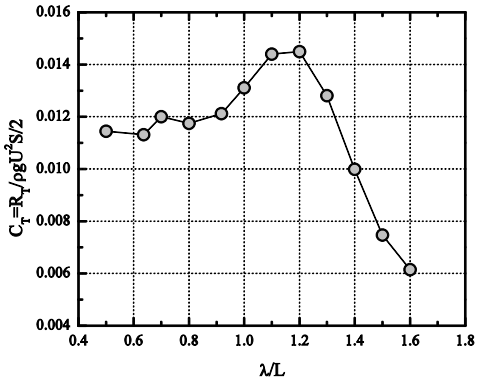

Fig.5 ROA of total resistance coefficient for Fn=0.142 and H=150mm.

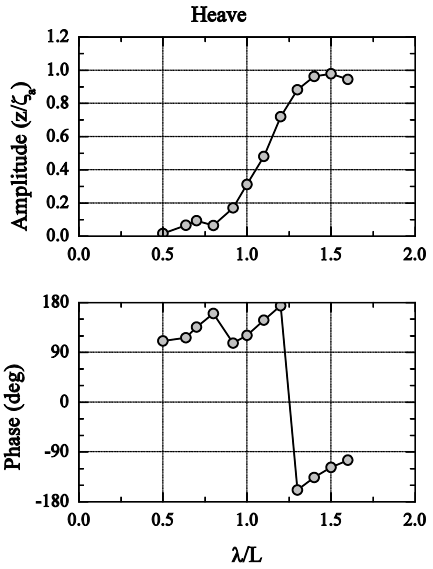

Fig.6 ROA of heave for Fn=0.142 and H=150mm.

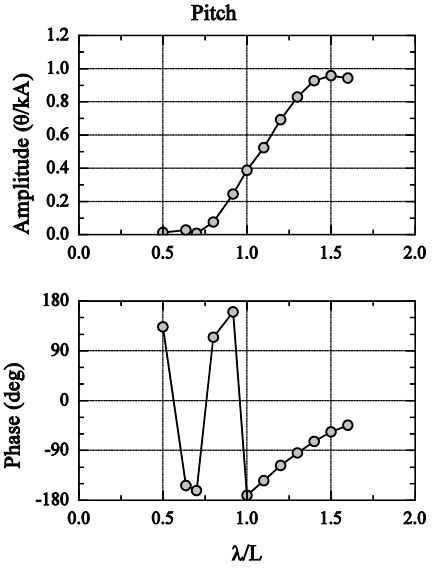

Fig.7 ROA of pitch for Fn=0.142 and H=150mm.

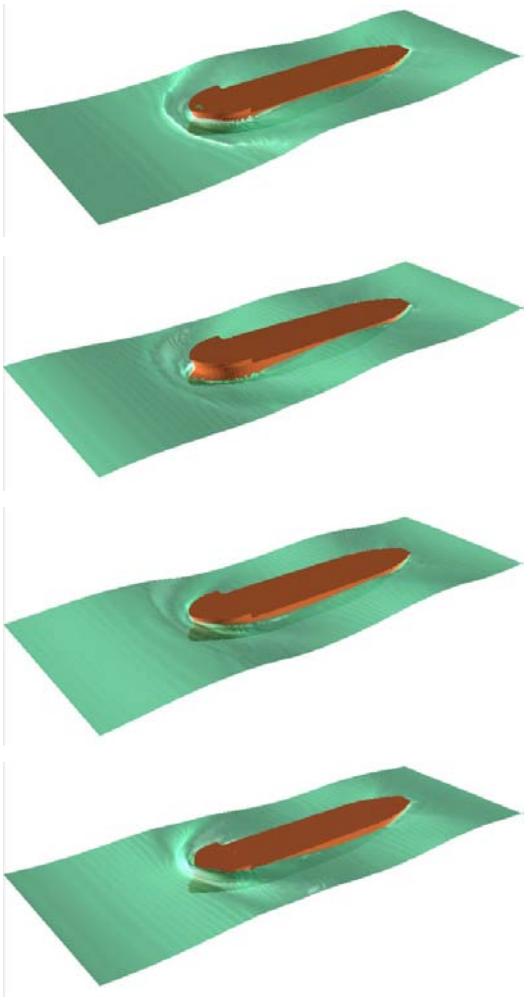

Fig.7 Snapshots of computation for Fn=0.142, $\lambda/L = 0.9171$ and H=150mm. From top: t/Te = 9.00, 9.25, 9.50, 9.75.

In Fig.7, computed snapshots in one encounter period to show the interaction between the ship and the free surface are shown for the case of Fn=0.142, $\lambda/L = 0.9171$ and H=150mm.

4 CONCLUSIONS

We have carried out numerical simulation on the KVLCC2 model for prediction of heave and pitch motions in waves by using our in-house CFD code RIAM-CMEN. The CFD code is a Cartesian grid based code which has been developed for strongly nonlinear wave-ship interactions, with the emphasis on the simulation of violent free surface phenomena such as bow slamming, water on deck, etc. The test cases provided in this workshop are for moderate conditions, the numerical simulations of which require enough boundary layer resolution and high accuracy of wave scattering calculation. We have to point out, however, that such numerical simulation is not a strong point of our Cartesian grid code. Therefore, the purpose of our participation of this conference is to show how accuracy a Cartesian grid method can achieve for such a moderate problem by submitting our numerical results without special treatments and turbulence modeling. Turbulence effect is considered in part by the use of upwind difference scheme in our code. The computed amplitudes of the ship motions are reasonably good.

REFERENCES

Hu, C. and Kashiwagi, M. (2004) A CIP-Based Method for Numerical Simulations of Violent Free Surface Flows, J. Marine Science and Technology, 9: 143-157

Hu, C. and Kashiwagi, M. (2007). Numerical and Experimental Studies on Three-Dimensional Water on Deck with a Modified Wigley Model, Proc. 9th Int. Conf. on Numerical Ship Hydrodynamics, Michigan, USA, V1, 159-169.

Hu, C., and Kashiwagi, M. (2009): Two-dimensional numerical simulation and experiment on strongly nonlinear wave–body interactions, Journal of Marine Science and Technology, 9, 143-157

Hu, C., Sueyoshi, M., Miyake, R., Zhu, T. (2010). Computation of Fully Nonlinear Wave Loads on a Large Container Ship by CIP based Cartesian Grid Method, Proc. 29th Int. Conf. on Ocean, Offshore and Arctic Engineering (OMAE2010), June 6-11, 2010, Shanghai, China, CD-ROM, Paper No.: OMAE2010-20826

Xiao, F, Ikebata, A (2003) – An Efficient Method for Capturing Free Boundaries in Multi-fluid simulations, Int J Num Methods Fluids, Vol 42, pp 187-210

Yabe, T., Xiao, F. and Utsumi, T. (2001) The Constrained Interpolation Profile Method for Multiphase Analysis, J. Comput. Phys., 169: 556-593

Prediction of Ship Resistance and Wake using Multi-Block Structural Grid

H. Yu X-M. Feng Q. Wu J-B. Wang and R-Q. Cai
Marine Design and Research Institute of China, Shanghai, China.

X-L. Chen
Shanghai Supercomputer Center, Shanghai, China.

1. ABSTRACT

In this paper, numerical simulation of resistance and wake of KVLCC was performed using computational fluid dynamics (CFD) techniques, where a Reynolds-averaged Navier-Stokes equations solver was employed. Reynold stress model(RSM) is used for wake simulation and shear stress transport (SST) $\kappa-\omega$ model was used for resistance prediction . Multi-block structured meshes were used in the whole calculation domain for case 1.1a,1.1b and 1.2a. Free-surface effects were taken into account by adopting the volume of fluid(VOF) method for multi-phase flows for case 1.1b and 1.2a. The computational results were validated by comparing with the test data.

2. INTRODUCTION

With the rapid development of both soft and hard ware, it has become quite common to carry out ship's resistance and wake calculation using CFD technique. However, to get the right wake distribution, reasonable resistant component together with right wave pattern, still needs joint effort and exploration. In this paper, multi-block structural grid and different mesh model was used for different cases. The optimization of various parameter combination was studied to speed up convergence.

3. COMPUTATIONAL MODEL AND CONDITION

KRISO very large crude carrier (KVLCC) was the object ship . The main particulars are described in Tables 1.

Table 1 Principal particulars of KVLCC

case	1.1a	1.1b	1.1c
Fluid Material	air	water	water
Scale ratio	116	58	58
Lpp (m)	2.7586	5.5172	5.5172
Beam(m)	0.5	1	1
Draft(m)	0.1793	0.3586	0.3586
rudder	no	no	yes
Speed (m/s)	25	1.047	1.047
Froude number	4.808	0.142	0.142
Reynolds number	4.6×10^6	4.6×10^6	4.6×10^6

4. COMPUTATIONAL METHOD

4.1 Mathematical modeling and Numerical Method

The governing equations are written as follows.

$$\frac{\partial \rho}{\partial t} + \nabla \cdot (\rho \vec{v}) = 0 \qquad (1)$$

$$\frac{\partial (\rho \vec{v})}{\partial t} + \nabla \cdot (\rho \vec{v}\vec{v}) = -\nabla p + \nabla \cdot \bar{\bar{\tau}} + \rho g \qquad (2)$$

where $\vec{v}$ is the velocity vector in the Cartesian coordinate system, p the static pressure, and $\bar{\bar{\tau}}$ the stress tensor given by

$$\bar{\bar{\tau}} \equiv \mu[(\nabla \vec{v} + \nabla \vec{v}^T) - \frac{2}{3}\nabla \cdot \vec{v} I] \qquad (3)$$

where μ is the molecular viscosity, I the unit tensor, and the second term on the right hand sifactode the effect of volume dilation. The Reynolds averaged Navier-Stokes equations can be written in Cartesian tensor form as

$$\frac{\partial \rho}{\partial t} + \frac{\partial}{\partial x_i}(\rho \vec{v}_i) = 0 \qquad (4)$$

$$\frac{\partial}{\partial t}(\rho u_i)+\frac{\partial}{\partial x_j}(\rho u_i u_j)$$
$$=-\frac{\partial p}{\partial x_i}+\frac{\partial}{\partial x_j}[\mu(\frac{\partial u_i}{\partial x_j}+\frac{\partial u_j}{\partial x_i}-\frac{2}{3}\delta_{ij}\frac{\partial u_l}{\partial x_l})] \quad (5)$$
$$+\frac{\partial}{\partial x_j}(-\rho\overline{u'_i u'_j})$$

where δ_{ij} is the Kronecker delta, $-\rho\overline{u'_i u'_j}$ and the Reynolds stresses. These Reynolds stresses must be modeled to close equation (5), i.e., for turbulence closure. The VOF method is employed to handle the free-surface wave flow around the ship. Based on the local volume fraction of the q-th fluid, α_q, the appropriate variables and properties are assigned to each cell within the domain. The tracking of the interfaces between the phases is accomplished by the solution of a continuity equation for the volume fraction of phases. For the q-th phase, this equation has the following form.

$$\frac{\partial \alpha_q}{\partial t}+\vec{v}\cdot\nabla\alpha_q=0 \quad (6)$$

$$\sum_{q=1}^{n}\alpha_q=1 \quad (7)$$

$$\rho=\sum_{q=1}^{n}\alpha_q\rho_q \quad (8)$$

In the case of turbulence quantities, a single set of transport equations is solved, and the turbulence variables are shared by the phases throughout the field.

The computations were carried out using FLUENT v6.3. The governing equations were resolved using steady method. The second order accurate upwind scheme was selected for the convection terms, while the second order accurate central scheme was for the diffusion terms and the volume fraction equation. The equations of the continuity and momentum were solved sequentially (Weiss and Smith, 1995). The RSM and SST $\kappa-\omega$ model was used for turbulence closure. Residual was used as criterion for convergence and all the residual was set to 10^{-6}. Also, the constancy of the total force on the ship was chosen as another standard for convergence criterion.

4.2 Computational Mesh and Boundary Conditions for Wake Calculation

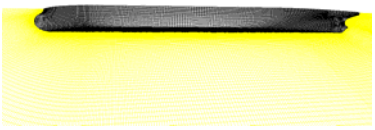

Fig.1 Computational grid for wake simulation

The computational grid is shown in Fig.1. The computational domain [X, Y, Z] was [-10-20L, 0.0-10L, -10L-0L].

The no-slip condition was applied on the hull surface. On inlet and side face, uniform velocity of U_0 is imposed as boundary condition. The symmetric condition is applied on the top boundary and at y=0.

Structured mesh was used in the whole region, and more grids are put near wall, fore and aft parts of hull. The total number of cells was about 2.54 million

4.3 Computational Mesh and Boundary Conditions for Resistance Calculation

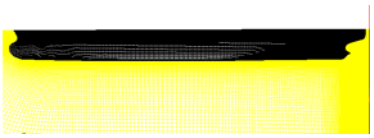

Fig.2 Computational grid for resistance test

The computational grid is shown in Fig.2. The computational domain [X, Y, Z] was [-1.0-2.5L, 0.0-1.0L, -0.1L-0.0225L], in which Z=0~0.0225L is used to capture free surface.

The no-slip condition was applied on the hull surface. On inlet and side face, uniform velocity of U_0 is imposed as boundary condition, while on outlet face, pressure-outlet is applied. The symmetric condition is applied on the top boundary and at y=0.

Structured mesh was used in the whole region, and more grids are put near wall, fore and aft parts of hull and free surface. The total number of cells used for resistance calculation was about 2.846 million

4.4 Wind Tunnel test

The wake distribution at X/L_{pp}=0.9825 was compared with the experimental data, as shown in Fig. 3. The upper one is the experimental data and lower one is the present study results. The right panel of each figure shows axial velocity contours and the left panel shows the cross flow vector and streamlines. The overall trend as well as distribution was well reproduced. As seen in the figures, the characteristic feature of the axial velocity contours, namely "hook" or "rabbit's ear", is captured exactly.

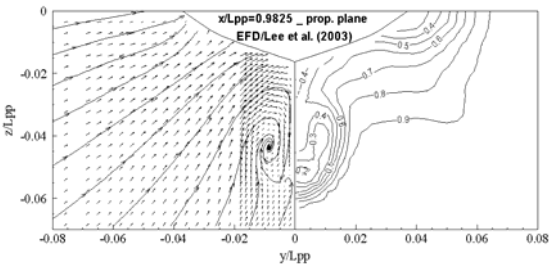

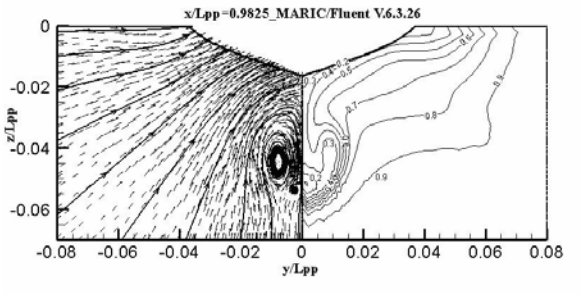

Fig.3 Comparison of wake at X/L_{pp}= 0.9825

Fig.4 is comparison of the circumferential wake distribution of different radius between CFD and test. It can be seen that CFD results agree with the test one well.

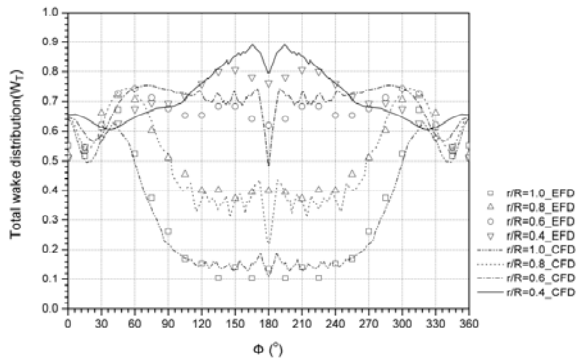

Fig.4 Wake compared with EFD data at x/L=0.9825

4.5 Resistance test

The wave pattern from CFD is compared with the experimental data (Kim et al 2001),see Fig.5. The lower part of the figure is from the experiment. The upper part is from CFD. The most obvious difference between CFD and test is prediction of the diverging wave from the fore part in the test. However, CFD failed to capture this feature. One possible reason may be more grid is needed.

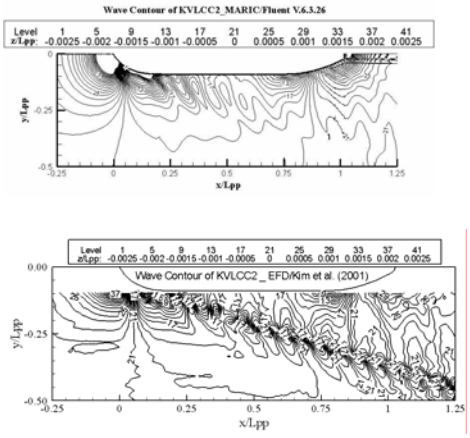

Fig.5 Comparison of Wave Patterns

From Fig.6 to 8, the comparison of wave cut at Y/L_{pp}= -0.0964, -0.1581 and -0.2993 are presented. The free-surface wave solution shows good agreement with the experimental data. However, numerical prediction of free-surface wave solution is more damped far from the hull for given Fn=0.142.

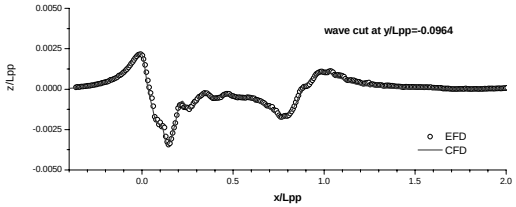

Fig.6 Comparison of Wave cut at Y/L_{pp}= - 0.0986

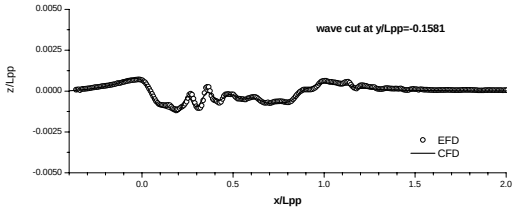

Fig.7 Comparison of Wave cut at Y/L_{pp}= - 0.1581

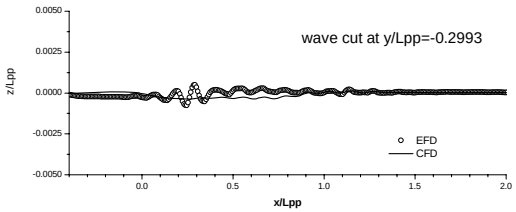

Fig.8 Comparison of Wave cut at Y/L_{pp}= - 0.2993

5. VALIDATION

Verification study is performed to obtain grid convergence uncertainties (*UG*) following the quantitative methodology and procedures proposed by Stern et al. (2006). *UI*/ε12=0.125 for Ct. Monotonic convergence is obtained for the resistance coefficients. pG/pG,th is 1.354 for Ct. UG =2.03%*D* for Ct . E for Ct on fine grid =3.431 %*D* > UV=2.317%*D*. Thus Ct prediction is not validated.

Table: V&V study for FXτσ Kvcll resistance prediction, Re = 4.6×106, Fr = 0.142.

Parameters		EFD (D)	V&V Study									
			Grid#3 (S_3)	Grid#2 (S_2)	Grid#1 (S_1)	r_G	ε_{12}%S_1	U_I/ε_{12}	$p_G/p_{G,th}$	U_G%S_1	U_D%D	U_V%
$C_T\times10^3$	Value	4.110	4.475	4.314	4.251	1.414	1.482	0.125	1.354	2.013	1.0	2.317
	E%D		-8.88	-4.96	-3.43							
$C_F\times10^3$	Value											
	E%D											
$C_{PV}\times10^3$	Value											
	E%D											

6. CONCLUSION

In this article, structural grid is used for ship wake and resistance calculation. The computational results were compared with experimental data and agreed well generally. However, it still seems difficult to get diverging waves unless more dense grid is used for given Fn=0.142.

REFERENCES

[1] LARSSON L, STERN F, BERTRAM V. Benchmarking of computational fluid dynamics for ship flows: the Gothenburg 2000 Workshop[J]. Journal of Ship Research, 2003, 47(1): 63-81

[2] ZHANG Z R, LIU H, ZHU S P, et al. Application of CFD in ship engineering design practice and ship hydrodynamics[C]. Conference of Global Chinese Scholars on Hydrodynamics (CCSH'06)，Shanghai, China, 2006. 315-322.

[3] KERKHOF R. Model test for a VLCC[R]. MARIN report, 2006. 21009-1-DT.

[4] Menter, F.R. 1994, "Two Equation Eddy Viscosity Turbulence Models for Engineering Applications," AIAA Journal, 32(8), 1598-1605.

[5] ITTC - Quality Manual 7.5-03–01 – 01，CFD General "Uncertainty Analysis in CFD Verification and Validation Methodology and Procedures".

[6] Stern, F., Wilson, R. and Shao, J., 2006, "Quantitative approach to V&V of CFD simulations and certification of CFD codes," International Journal of Numerical Methods in Fluids, 50, 1335-1355.

[7] Launder, B.E., Reece, G.J. and Rodi, W. 1975, "Progress in the Development of a Reynolds-Stress Turbulence Closure," J. Fluid Mech., 68(3), 537-566.

Prediction of Ship Resistance and Propulsion Performance using Multi-Block Structural Grid

Q. Wu X-M Feng H. Yu J-B. Wang and R-Q. Cai
Marine Design and Research Institute of China, Shanghai, China.

X-L. Chen
Shanghai Supercomputer Center, Shanghai, China.

1. ABSTRACT

In this paper, numerical simulation of resistance and self-propulsion on KCS was performed using computational fluid dynamics (CFD) techniques, where a Reynolds-averaged Navier-Stokes equations solver was employed and Realizable k - ε turbulence model is used. Multi-block structured meshes were used in the whole calculation domain for case 2.1 and 2.2a. While the domain was subdivided into two parts for 2.3a, where a sliding mesh technique was introduced for the rotating propeller in self-propulsion calculation. Free-surface effects were taken into account by adopting the volume of fluid(VOF) method for multi-phase flows. The computational results were validated by comparing with the test data.

2. INTRODUCTION

With the rapid development of both soft and hard ware, it has become more and more common to carry out ship's resistance calculation using CFD technique. And also it has become possible to perform propulsion simulation for design purpose. However, during the process of actual application, mesh generation for propulsion is still the most difficult issue which takes much patience. On the other hand, calculation strategy is also very important to speed up convergence. In this paper, multi-block is used for above 3 cases. To shorten time to stability, steady calculation with free surface is performed first as the initial condition for unsteady calculation.

3. COMPUTATIONAL MODEL AND CONDITION

KRISO container ship (KCS) was selected as the object ship, and KP505, the propeller designed for KCS, was selected as the object propeller. The principal particulars are described in Tables 1 and 2.

Table 1 Principal particulars of KCS

Length between perpendiculars	7.2786 (m)
Beam	1.019 (m)
Draft	0.3418 (m)
Wetted surface area (without rudder)	9.4376 (m^2)
Speed	2.196 (m/s)
Rotation speed	9.27rpm
Reynolds number	1.4 x 10^7

Table 2 Principal particulars of KP505

Diameter	250.0 (mm)
A_e/A_0	0.800
Hub ratio	0.180
No. of blades	5
Blade section	NACA66 Thickness form + a=0.8 mean line Camber

4. COMPUTATIONAL METHOD

4.1 Mathematical modeling and Numerical Method

The governing equations are written as follows.

$$\frac{\partial \rho}{\partial t} + \nabla \cdot (\rho \vec{v}) = 0 \quad (1)$$

$$\frac{\partial (\rho \vec{v})}{\partial t} + \nabla \cdot (\rho \vec{v}\vec{v}) = -\nabla p + \nabla \cdot \bar{\bar{\tau}} + \rho g \quad (2)$$

where $\vec{v}$ is the velocity vector in the Cartesian coordinate system, p the static pressure, and $\bar{\bar{\tau}}$ the stress tensor given by

$$\bar{\bar{\tau}} \equiv \mu[(\nabla\vec{v} + \nabla\vec{v}^T) - \frac{2}{3}\nabla\cdot\vec{v}I] \quad (3)$$

where μ is the molecular viscosity, I the unit tensor, and the second term on the right hand side the effect of volume dilation. The Reynolds averaged Navier-Stokes equations can be written in Cartesian tensor form as

$$\frac{\partial\rho}{\partial t} + \frac{\partial}{\partial x_i}(\rho\vec{v}_i) = 0 \quad (4)$$

$$\frac{\partial}{\partial t}(\rho u_i) + \frac{\partial}{\partial x_j}(\rho u_i u_j) = -\frac{\partial p}{\partial x_i} + \frac{\partial}{\partial x_j}[\mu(\frac{\partial u_i}{\partial x_j} + \frac{\partial u_j}{\partial x_i} - \frac{2}{3}\delta_{ij}\frac{\partial u_l}{\partial x_l})] + \frac{\partial}{\partial x_j}(-\rho\overline{u'_i u'_j}) \quad (5)$$

where δ_{ij} is the Kronecker delta, $-\rho\overline{u'_i u'_j}$ and the Reynolds stresses. These Reynolds stresses must be modeled to close equation (5), i.e., for turbulence closure. The VOF method is employed to handle the free-surface wave flow around the ship. Based on the local volume fraction of the q-th fluid, α_q, the appropriate variables and properties are assigned to each cell within the domain. The tracking of the interfaces between the phases is accomplished by the solution of a continuity equation for the volume fraction of phases. For the q-th phase, this equation has the following form.

$$\frac{\partial\alpha_q}{\partial t} + \vec{v}\cdot\nabla\alpha_q = 0 \quad (6)$$

$$\sum_{q=1}^{n}\alpha_q = 1 \quad (7)$$

$$\rho = \sum_{q=1}^{n}\alpha_q\rho_q \quad (8)$$

In the case of turbulence quantities, a single set of transport equations is solved, and the turbulence variables are shared by the phases throughout the field.

The computations were carried out using FLUENT v6.3. The governing equations were resolved using implicit unsteady method. The second order accurate upwind scheme was selected for the convection terms, while the second order accurate central scheme was for the diffusion terms and the volume fraction equation. The equations of the continuity and momentum were solved sequentially (Weiss and Smith, 1995). The Realizable k-ε turbulence model with non-equivalent wall function was used for turbulence closure. Residual is used as criterion for convergence and all the residual was set to 10^{-6}. Also, the constancy of the total force on the ship or propeller was chosen as another standard for convergence criterion.

4.2 Computational Mesh and Boundary Conditions for Resistance Test

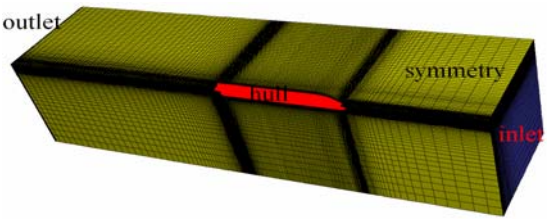

Fig.1 Computational domain for resistance test

The computational domain is shown in Fig.1. Domain [X, Y, Z] was [-1.0-3.0L, 0.0-1.0L, -0.87L-0.028L], in which Z=0~0.028L is used to capture free surface.

The no-slip condition was applied on the hull surface. On inlet and side face, uniform velocity of U0 is imposed as boundary condition, while on outlet face, pressure outlet is applied. ie, the static pressure was extrapolated through the downstream boundary. The symmetry condition is applied on top boundaries.

Structured mesh was used in the whole region, and more grids are put near wall, fore and aft part, free surface. The total number of cells used for resistance purpose was about 6.5 million

4.3 Computational Mesh and Boundary Conditions for Self-Propulsion Test

For self-propulsion test, the full domain was used. Fig.2 shows the domain for self-propulsion test. Vertical room of 0.028L for free surface motion exists between the initial water surface and top boundary, as for resistance test. The number of cells for self-propulsion calculation was about 4.02 million.

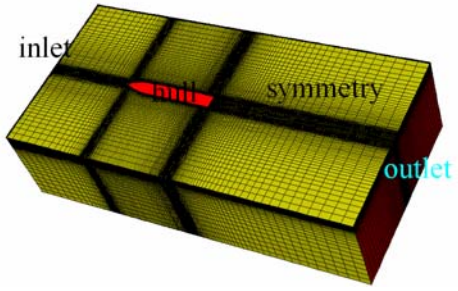

Fig.2 Computational domain for self-propulsion test

On the hull surface, no-slip condition applied, while the symmetric condition is applied on the top boundaries. On the inlet and side face, uniform velocity of U0 is used. To apply non-conformal interface between the propeller region and hull region, the sliding mesh technique was adopted around the propeller as shown in Fig.3.

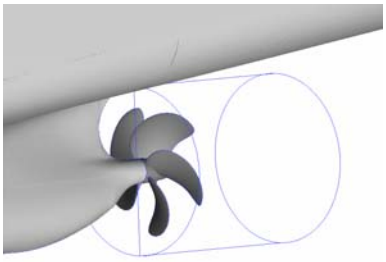

Fig.3 Configuration of sliding mesh

5. RESULTS AND DISCUSSION

5.1 Resistance test

The wave pattern from CFD is compared with the experimental data (Van et al 1998b, Kim et al 2001),see Fig.4. The lower part of the figure is from the experiment. The upper part is from CFD. From the figure we can see that CFD result agrees with the test well.

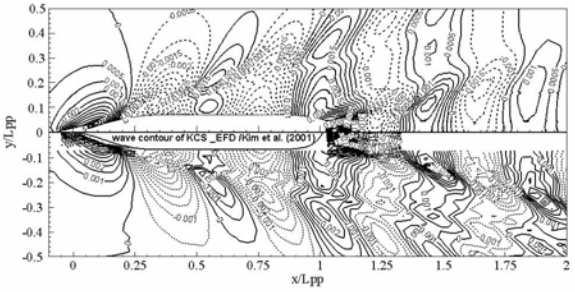

Fig.4 Comparison of Wave Patterns

From Fig.5 to 8, the comparison of wave profiles along the hull surface/center-plane and wave cut at Y/L_{pp}= -0.0741, -0.1509 and -0.4224 are presented. The free-surface wave solution shows good agreement with the experimental data. However, numerical diffusion causes under-prediction of free-surface wave solution in the aft part.

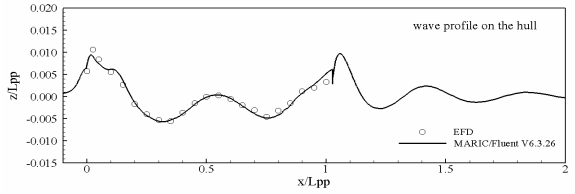

Fig.5 Comparison of Wave profile

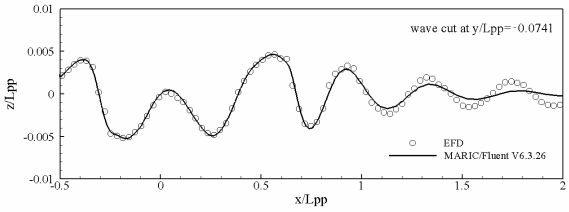

Fig.6 Comparison of Wave cut at Y/L_{pp}= - 0.0741

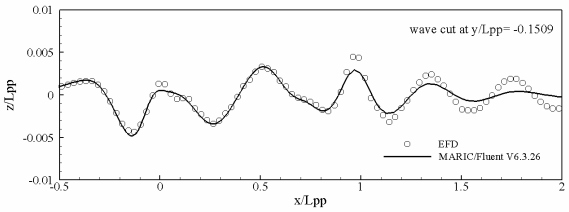

Fig.7 Comparison of Wave cut at Y/L_{pp}= - 0.1509

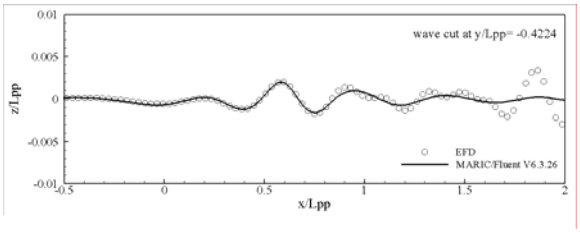

Fig.8 Comparison of Wave cut at Y/L_{pp}= - 0.4224

The wake distribution at X/L_{pp}=0.9825 was compared with the experimental data, as shown in Fig. 9. The upper one is the experimental data and lower one is the present study results. The right panel of each figure shows axial velocity contours and the left panel shows the cross flow vector and streamlines. The overall trend as well as distribution was very well reproduced.

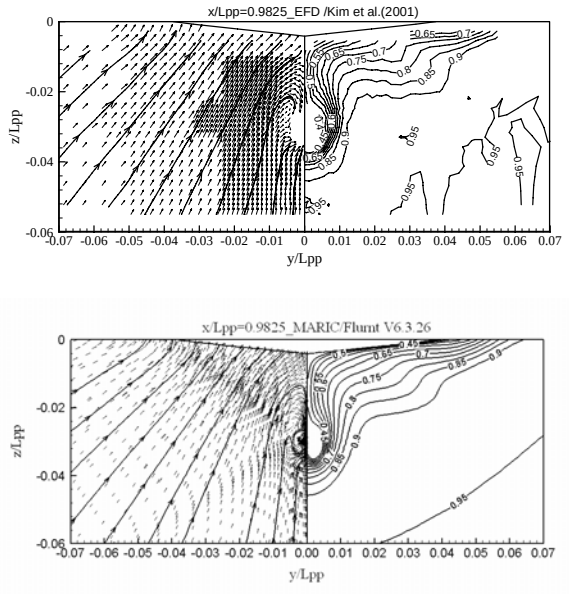

Fig.9 Comparison of wake plane at X/L_{pp}= 0.9825

5.2 Self-propulsion test

The sliding mesh technique approach was adopted for self-propulsion test with the rotating cylinder placed at the propeller location.

The computation was started with rotating propeller of n=9.5rps to get the steady flow field around the hull . Then unsteady calculation starts. For the full scale extension, as for the towing tank tests, the towing force (F_D) was considered to adjust the difference of the viscous force between the model and full scale ships.

Table 3 Unsteady result

rps	K_T	K_Q	error
9.5	0.163	0.0299	1.095e-04

The error value is defined as $(R_T - T - F_{D0})/0.5\rho U^2 S_M$.

The Axial velocity contours and cross flow vectors downstream of propeller plane at X/L_{PP}=0.9911 are compared with the experimental data (Hino 2005) as shown in Fig. 10. The trend of wake at propeller downstream is well predicted.

The comparison of velocity components downstream of propeller plane is shown in Fig. 11. Again, the overall trend shows good agreement. Still, the difference in the propeller hub area is a bit large.

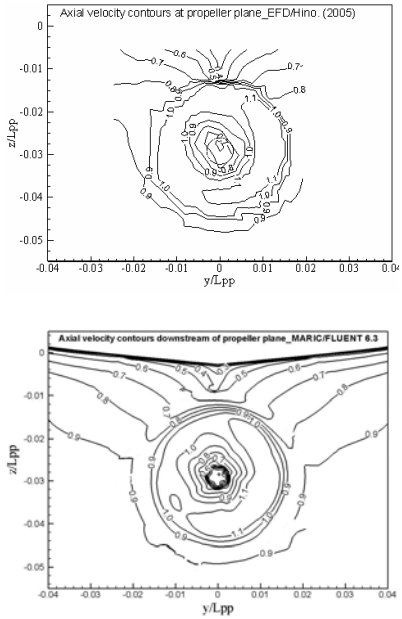

Fig.10 Comparison of axial velocity contours at X/L_{PP}=0.9911

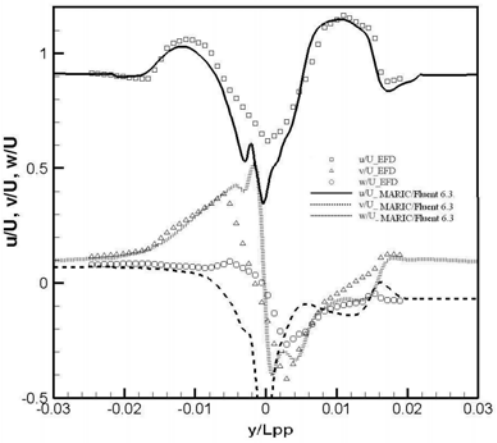

Fig.11 Velocity downstream of propeller plane (X/L_{PP}=0.9911) at Z/L_{PP}=-0.03

The pressure distribution on the hull surface is shown in Fig. 12. The pressure distribution around the bilge was well predicted both quantitatively and qualitatively. The effect of rotating propeller on the hull seems reasonable.

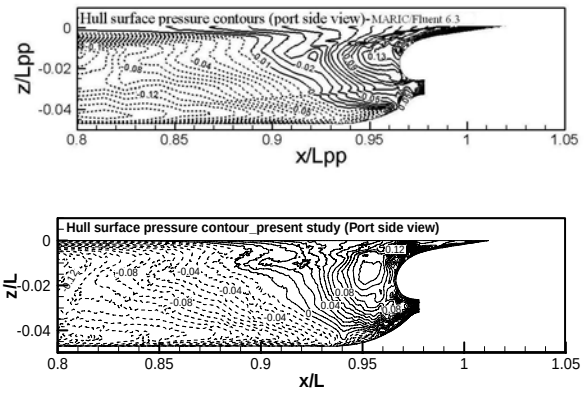

Fig.12 Hull surface pressure contours

6. CONCLUSION

In this article, structural grid is used to model ship body and propeller geometry for ship resistance and propulsion performance calculation. Sliding mesh technique is employed for rotating propeller in the propulsion . The computational results were compared with experimental data and agreed well generally. However, more work still needs to be done to put self-propulsion calculation into practice especially to reduce computing time.

REFERENCES

Larsson l, Stern F, Bertram V. Benchmarking of computational fluid dynamics for ship flows: the Gothenburg 2000 Workshop[J]. Journal of Ship Research, 2003, 47(1): 63-81

Chao, Y, and Karl, K (2005). "Numeric Propulsion Simulation for the KCS Container Ship," Proceedings of CFD workshop Tokyo 2005, Tokyo, Japan, pp.539-545.

Lübke, L (2005). "Numerical simulation of the Flow around the propelled KCS," Proceedings of CFD workshop Tokyo 2005, Tokyo, Japan, pp.587-592.

Hino, T., (2005 ed.), "Proceedings of CFD Workshop Tokyo 2005", NMRI report 2005.

Kim, J, Park, IR, and Van, SH (2005). "RANS Computations for KRISO Container Ship and VLCC Tanker using the WAVIS code," Proceedings of CFD workshop Tokyo 2005, Tokyo, Japan, pp. 598-603.

Tahara, Y, Wilson, R, and Carrica, P (2005). "Comparison of Free-Surface Capturing and Tracking Approaches in Application to Modern Container Ship and Prognosis for Extension to Self-Propulsion Simulator," Proceedings of CFD workshop Tokyo 2005, Tokyo, Japan, pp. 604-611.

Eca, L.&Hoekstra, M., "An evaluation of verification procedures for CFD application,' 24th Symposium on Naval Hydrodynamics, Fukuoka, Japan, 2002

Prediction of 5415 Resistance and Wave Pattern using Multi-Block Structural Grid

X-M. Feng H-M. Chen Q. Wu H. Yu J-B. Wang and R-Q. Cai
Marine Design and Research Institute of China, Shanghai, China.

X-L. Chen
Shanghai Supercomputer Center, Shanghai, China.

1. ABSTRACT

In this paper, numerical simulations of resistance and wave pattern on 5415 were performed using computational fluid dynamics (CFD) techniques, where a Reynolds-averaged Navier-Stokes equations solver was employed. Shear stress transport(SST) $\kappa-\omega$ model and Reynold stress model(RSM) were used for resistance prediction and wave pattern simulation. Multi-block structured meshes were used in the whole calculation domain for case 3.1a, 3.1b and 3.2. For case 3.2, sinkages and trims was calculated first before grid generation and viscous calculation. Free-surface effects were considered by adopting the volume of fluid(VOF) method for multi-phase flows. The computational results were validated by different grid sizes and comparing with the test data.

2. INTRODUCTION

With the rapid development of both software and hardware, it has become more and more common to carry out ship's resistance and wave pattern calculation using CFD technique, with consideration of sinkage and trim. However, during the process of actual application, mesh generation is still the most difficult issue which needs much effort. In this paper, multi-block structural grids are used for above three cases. To shorten time to stability, steady calculation with free surface is performed.

3. COMPUTATIONAL MODEL AND CONDITION

DTMB 5415 was selected as the object ship, The main particulars were described in Tables 1.

Table 1 Principal particulars of 5415

Main particulars		Full scale
Length between perpendiculars	Lpp (m)	142.0
Length of waterline	Lwl(m)	142.18
Maximum beam of waterline	Bwl (m)	19.06
Draft	T (m)	6.15
Displacement	(m3)	8424.4
Wetted area w/o rudder	Sw (m2)	2972.6
Wetted surface area of rudder	Sr (m2)	30.8
Block coefficient	(Cb)	0.507
Midship section coefficient	(Cm)	0.821
LCB (%Lpp), fwd+		-0.683
Service speed	U (knots)	18.0, 30.0
Fn		0.248, 0.413
Scale ratio	1:24.824 for Case 3.1a and Case 3.2	1:46.59 for Case 3.1b

4. COMPUTATIONAL METHOD

4.1 Mathematical modeling and Numerical Method

The governing equations were written as follows.

$$\frac{\partial \rho}{\partial t}+\nabla\cdot(\rho\vec{v})=0 \qquad (1)$$

$$\frac{\partial(\rho\vec{v})}{\partial t}+\nabla\cdot(\rho\vec{v}\vec{v})=-\nabla p+\nabla\cdot\bar{\bar{\tau}}+\rho g \qquad (2)$$

where $\vec{v}$ is the velocity vector in the Cartesian coordinate system, p the static pressure, and $\bar{\bar{\tau}}$ the stress tensor given by

$$\bar{\bar{\tau}} \equiv \mu[(\nabla\vec{v} + \nabla\vec{v}^T) - \frac{2}{3}\nabla\cdot\vec{v}I] \quad (3)$$

where μ is the molecular viscosity, I the unit tensor, and the second term on the right hand side the effect of volume dilation. The Reynolds averaged Navier-Stokes equations can be written in Cartesian tensor form as

$$\frac{\partial\rho}{\partial t} + \frac{\partial}{\partial x_i}(\rho\vec{v}_i) = 0 \quad (4)$$

$$\frac{\partial}{\partial t}(\rho u_i) + \frac{\partial}{\partial x_j}(\rho u_i u_j) = -\frac{\partial p}{\partial x_i} + \frac{\partial}{\partial x_j}[\mu(\frac{\partial u_i}{\partial x_j} + \frac{\partial u_j}{\partial x_i} - \frac{2}{3}\delta_{ij}\frac{\partial u_l}{\partial x_l})] + \frac{\partial}{\partial x_j}(-\rho\overline{u'_i u'_j}) \quad (5)$$

where δ_{ij} is the Kronecker delta, $-\rho\overline{u'_i u'_j}$ and the Reynolds stresses. These Reynolds stresses must be modeled to close equation (5), i.e., for turbulence closure. The VOF method is employed to handle the free-surface wave flow around the ship. Based on the local volume fraction of the q-th fluid, α_q, the appropriate variables and properties are assigned to each cell within the domain. The tracking of the interfaces between the phases is accomplished by the solution of a continuity equation for the volume fraction of phases. For the q-th phase, this equation has the following form.

$$\frac{\partial\alpha_q}{\partial t} + \vec{v}\cdot\nabla\alpha_q = 0 \quad (6)$$

$$\sum_{q=1}^{n}\alpha_q = 1 \quad (7)$$

$$\rho = \sum_{q=1}^{n}\alpha_q\rho_q \quad (8)$$

In the case of turbulence quantities, a single set of transport equations is solved, and the turbulence variables are shared by the phases throughout the field.

The computations were carried out using FLUENT v6.3. The governing equations were resolved using steady method. The second order accurate upwind scheme was selected for the convection terms, while the second order accurate central scheme was set for the diffusion terms and the volume fraction equation. The equations of the continuity and momentum were solved sequentially (Weiss and Smith, 1995). Residual was used to judge for convergence and all the residuals were set to 10^{-6}. Also, the constancy of the total force on the ship was chosen as another standard for convergence criterion.

4.2 Computational Mesh and Boundary Conditions for all cases

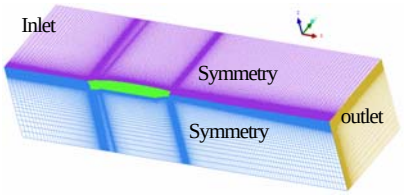

Fig.1 Computational domain for fixed condition

The computational domain is shown in Fig.1. Domain [X, Y, Z] was [-1.0-2.0L, 0.0-1.0L, -0.7L-0.024L], in which Z=0~0.024L is used to capture free surface.

The no-slip condition was applied on the hull surface. On inlet and side face, uniform velocity of U_0 was imposed as boundary condition, while on outlet face, pressure-outlet is applied. The symmetric condition is applied on the top boundary and at y=0.

Structured mesh was used in the whole region, and more grids were put near wall, fore and aft part, free surface. For case3.1a, three systematically refined grids fine (2.15M), medium (0.80M) and coarse (0.29M) were obtained using grid refinement ratio (r_G) of $\sqrt{2}$. Average $y+$ = 145. For case3.1b, hexahedral grid of 2.15M obtained an average $y+$ = 32. For case3.2, three hexahedral grids were set for different speeds: 3.75M for Fr=0.138, 2.65M for Fr=0.28 and 2.65M for Fr=0.41. Average $y+$ = 104.

5. RESULTS AND DISCUSSION

5.1 Case3.1a

The wave pattern from CFD agrees approximately with the corresponding experimental results as shown in Fig.2, but the under-prediction of the wave elevation of the numerical simulation is also observed, especially in the comparison of the wave elevation along three longitudinal cuts in Fig.3. The curves from the test seem sharper than those obtained from computation, and the differences become larger and larger as the distances between the cuts and the hull are farther and farther, which indicates that the under-prediction may be produced by the inadequate mesh and the numerical dissipation.

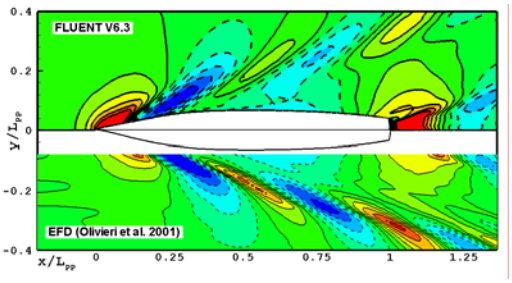

Fig.2 Comparison of Wave Patterns

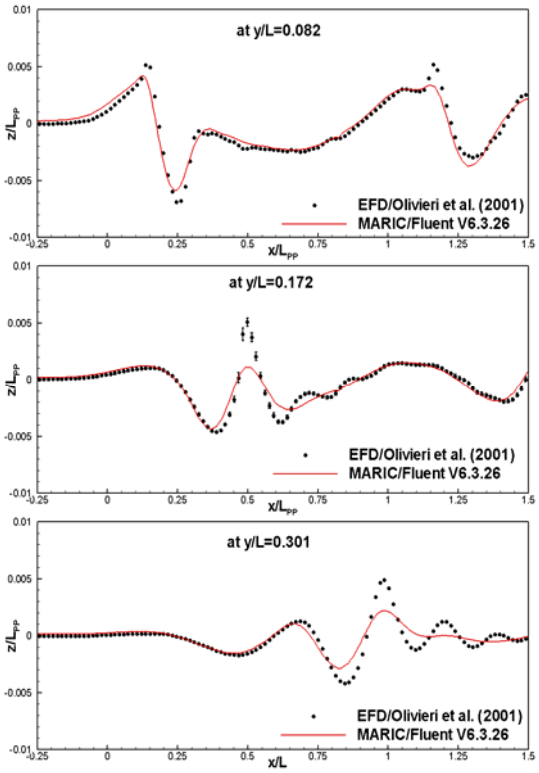

Fig.3 Wave elevation along three longitudinal cuts compared with EFD data

The axial velocity distribution at the propeller panel X/L_{PP}=0.935 is compared with the experimental data in Fig.4. The overall trend as well as distribution is very well reproduced.

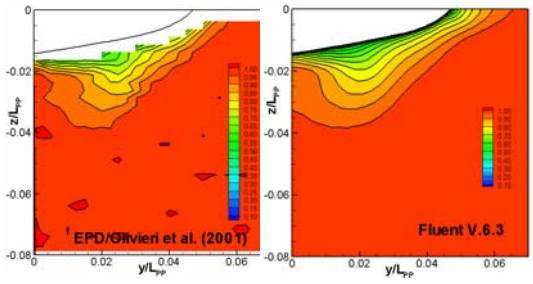

Fig.4 Comparison of the axial velocity at X/L_{PP}= 0.935

Verification study is performed to obtain grid convergence uncertainties (U_G) following the quantitative methodology and procedures proposed by Stern et al. (2006). U_I/ε_{12}=0.208,0.4 and 0.87 for c_T, c_F and c_P, respectively. Monotonic convergence is obtained for the resistance coefficients. $p_G/p_{G,th}$ is close to 1 for cT. U_G =2.98%D for c_T. E for c_T on fine grid = 2.96%D < U_V=3.1%D. Thus c_T prediction is validated.

Table 2 V&V study for FXτσ 5415 resistance prediction, Re = 1.19×107, Fr = 0.28, σ= -1.82x10-3, τ= -0.108°.

Parameters		EFD (D)	ITTC-57	V&V Study			r_G	ε_{21}%S_1	U_I/ε_{21}	$p_G/p_{G,th}$	U_G%S_1	U_P%D	U_V%
				Grid#3 (S_3)	Grid#2 (S_2)	Grid#1 (S_1)							
C_T×10³	Value	4.23		4.603	4.357	4.237	1.414	2.832	0.208	1.036	2.969	0.64	3.1
	E%D			-8.818	-3.002	-0.165							
C_P×10³	Value		2.91	3.074	3.004	3.004	1.414						
	E%ITTC			-5.636	-3.23	-3.23							
C_F×10³	Value	1.32		1.529	1.353	1.233	1.414						
	E%D			-15.833	-2.5	6.59							

5.2 Case3.1b

Similar to case 3.1a, the wave pattern and the wave elevations along three longitudinal cuts of case 3.1b also show that the numerical simulation under-predict the wave elevation compared with the experimental data, especially the wave crests, as seen in Fig. 5 and Fig. 6. The distribution of the axial velocity at propeller panel x/L=0.935 agrees well, but the TKE contour doesn't show the main features as the experiment does, partly brought by the inadequate grids and the numerical dissipation.

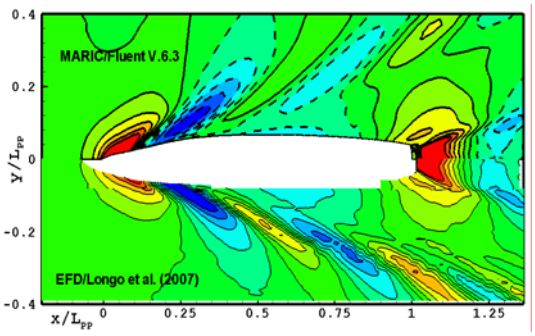

Fig.5 Comparison of Wave Patterns

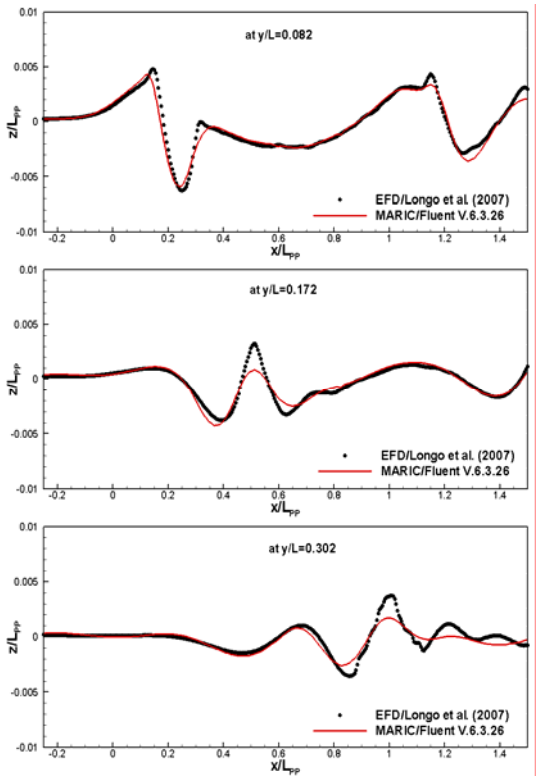

Fig.6 Wave elevation along three longitudinal cuts compared with EFD data

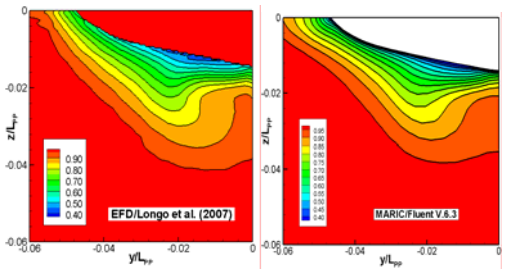

Fig.7 Comparison of the axial velocity at X/L_{PP}= 0.935

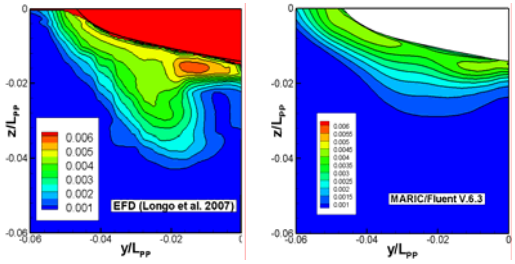

Fig.8 TKE distribution at x/L=0.935 compared with EFD data

5.3 Case3.2

The following tables list the resistance coefficients, sinkages and trims obtained from CFD and EFD at three velocities. It should be mentioned that the computations were firstly performed with another numerical code SHIPFLOW to obtain the sinkages and trims, which would be adopted in the following computations with FLUENT to solve the resistance coefficients. The comparison with the experimental data shows that although the errors of the sinkage and trim are relatively obvious, the resistance coefficients agree well with each other, especially in the cases of low *Fr* number. The process and results of the computation suggest that the combined calculations not only save simulating time but also predict more realistic resistance.

Table 3.2-1:FR$_{z\theta}$ 5415 resistance prediction, Re = 5.96×10^6, Fr = 0.138.

Parameters		EFD (D)	ITTC-57	V&V Study Grid#1 (S_1)
$C_T\times10^3$	Value	3.89		3.88
	E%D			0.257
$C_F\times10^3$	Value		3.29	3.217
	E%ITTC			2.219
$C_R\times10^3$	Value	0.605		0.663
	E%D			-9.587
$\sigma\times10^3$	Value	-0.504		-0.32
	E%D			-36.508
$\tau°$	Value	-0.028		-0.0225
	E%D			-19.643

Table 3.2-2: FR$_{z\theta}$ 5415 resistance prediction, Re = 1.19×10^7, Fr = 0.28.

Parameters		EFD (D)	ITTC-57	V&V Study Grid#1 (S_1)
$C_T\times10^3$	Value	4.23		4.21
	E%D			0.473
$C_F\times10^3$	Value		2.91	3.011
	E%ITTC			-3.471
$C_R\times10^3$	Value	1.32		1.199
	E%D			9.167
$\sigma\times10^3$	Value	-1.82		-1.49
	E%D			-18.132
$\tau°$	Value	-0.108		-0.094
	E%D			-12.963

Table 3.2-3: FR$_{z\theta}$ 5415 resistance prediction, Re = 1.75×10^7, Fr = 0.41.

Parameters		EFD (D)	ITTC-57	V&V Study Grid#1 (S_1)
$C_T\times10^3$	Value	6.67		6.41
	E%D			3.898
$C_F\times10^3$	Value		2.73	2.952
	E%ITTC			-8.132
$C_R\times10^3$	Value	3.94		3.458
	E%D			12.236
$\sigma\times10^3$	Value	-4.7		-3.6
	E%D			-23.404
$\tau°$	Value	0.421		0.5
	E%D			-18.765

6. CONCLUSION

In this article, multi-block structural grids are used for ship resistance prediction and wave pattern simulation. Sinkage and trim are considered. The computational results are compared with experimental data and agree well generally. However, more efforts still need to be paid to capture wave pattern precisely.

REFERENCES

Larsson L, Stern F, Bertram V. Benchmarking of computational fluid dynamics for ship flows: the Gothenburg 2000 Workshop[J]. Journal of Ship Research, 2003, 47(1): 63-81

Chao, Y, and Karl, K (2005). "Numeric Propulsion Simulation for the 5415 Container Ship," Proceedings of CFD workshop Tokyo 2005, Tokyo, Japan, pp.539-545.

Lübke, L (2005). "Numerical simulation of the Flow around the propelled 5415," Proceedings of CFD workshop Tokyo 2005, Tokyo, Japan, pp.587-592.

Hino, T., (2005 ed.), "Proceedings of CFD Workshop Tokyo 2005", NMRI report 2005.

Menter, F.R. 1994, "Two Equation Eddy Viscosity Turbulence Models for Engineering Applications," AIAA Journal, 32(8), 1598-1605.

ITTC - Quality Manual 7.5-03–01 – 01，CFD General “Uncertainty Analysis in CFD Verification and Validation Methodology and Procedures”.

Stern, F., Wilson, R. and Shao, J., 2006, “Quantitative approach to V&V of CFD simulations and certification of CFD codes,” International Journal of Numerical Methods in Fluids, 50, 1335-1355

Tahara, Y, Wilson, R, and Carrica, P (2005). "Comparison of Free-Surface Capturing and Tracking Approaches in Application to Modern Container Ship and Prognosis for Extension to Self-Propulsion Simulator," Proceedings of CFD workshop Tokyo 2005, Tokyo, Japan, pp. 604-611.

Eca, L.&Hoekstra, M., “An evaluation of verification procedures for CFD application,’ 24th Symposium on Naval Hydrodynamics, Fukuoka, Japan, 2002

Launder, B.E., Reece, G.J. and Rodi, W. 1975, “Progress in the Development of a Reynolds-Stress Turbulence Closure,” J. Fluid Mech., 68(3), 537-566.

Viscous free surface flow computations for self-propulsion conditions using PARNASSOS

Bram Starke, Auke van der Ploeg, Hoyte Raven

Maritime Research Institute Netherlands (MARIN), P.O.Box 28, 6700 AA Wageningen, Netherlands

INTRODUCTION

This paper presents results of computations for the 2010 CFD workshop in Gothenburg. It briefly describes the RANS method used, the particular treatment of the free surface boundary conditions, and the coupling between the RANS code and a boundary element method used for the propeller analysis. The computations for KCS (case 2.1 and 2.3a) and DTMB 5415 (case 3.1a and 3.2) are discussed in this paper, while the KVLCC2 computations (case 1.1a), including an extensive uncertainty analysis are described in (Eça, Hoekstra & Raven, 2010).

THE COMPUTATIONAL METHOD

RANS-solver

The method used in these computations is PARNASSOS, a code developed and used by MARIN and IST (Hoekstra, 1999; Van der Ploeg, Eça and Hoekstra, 2000). It solves the discretised Reynolds-averaged Navier-Stokes equations for a steady, 3D incompressible flow around a ship hull. Various eddy-viscosity turbulence models are available. For the computations for the DTMB 5415, the one-equation turbulence model of Menter (1997) was used. For the computation for the KCS we also used the two-equation k-ω SST model by Menter (1994). Both models were extended with a correction for the longitudinal vorticity according to Dacles-Mariani et al. (1995).

The discretisation is of finite-difference type. All terms in the momentum and continuity equations are discretised by second or third-order accurate difference schemes.

PARNASSOS can handle body-fitted, generally non-orthogonal HO- or CO-type grids, either single or multi-block structured.

For the cases studied, the inflow boundary was located $0.5L_{pp}$ in front of the bow, and the outflow boundary was located $1.5L_{pp}$ behind the transom. The lateral outer boundary was a quarter of a cylinder with axis $y=z=0$ and radius $1.0L_{pp}$. At this boundary tangential velocities and pressure found from a free-surface potential-flow computation were imposed. Since that computation gives good results already for much of the wave pattern, these boundary conditions (although of Dirichlet type) hardly cause any wave reflection.

The momentum and continuity equations are solved in fully coupled form. Therefore, the continuity equation need not be recast in a pressure correction or pressure Poisson equation, but can simply be solved as it is. After discretisation and linearisation, the three momentum equations and the continuity equation give rise to a matrix equation containing 4*4 blocks, which is solved using preconditioned GMRES. This fully coupled solution has been found to be robust and quite insensitive to the mesh aspect ratio. This allows solving the discretized equations on extremely contracted grids close to the wall. As a result, wall functions are not necessary, not even at full scale. More details about the solution strategy can be found in (van der Ploeg et al., 2000).

Free-Surface treatment

In our computations we have used the 'steady iterative formulation' (Raven & Van Brummelen, 1999; Raven & Starke, 2002; Raven, van der Ploeg, Starke, 2004) which, contrary to almost all other RANS/FS methods, involves no time-dependent terms; neither in the momentum equations, nor in the free-surface boundary conditions. The problem is solved by an iterative procedure, instead of by time integration. This iteration is based on the use of the "combined free-surface condition":

$$Fn^2 \; u\psi_x + v\psi_y + w\psi_z \; - w = 0 \quad \text{at} \quad z = \zeta \,, \qquad (1)$$

where ψ is the non-dimensional hydrodynamic pressure. This condition is obtained by substituting the wave elevation from the dynamic condition into the kinematic condition. Together with the dynamic condition it describes exactly the same problem as the original set of conditions; but it has the advantage of permitting a successful iterative procedure.

In the present applications, the 'balanced discretisation' derived in (Raven, van der Ploeg, Starke, 2004) has been used, which reduces the numerical damping of the waves to 5th order in the longitudinal step size Δx, and the numerical dispersion to 3rd order in the vertical spacing Δz. This contributes to a good accuracy of the wave pattern even at a distance from the hull.

Grids suited for both dry and wetted transom

Both test cases are transom-stern vessels. The transom of KCS is located above the still-water surface, and dry at the speed and draught concerned. That of DTMB 5415 is more deeply immersed and for Fn=0.28 it is wetted.

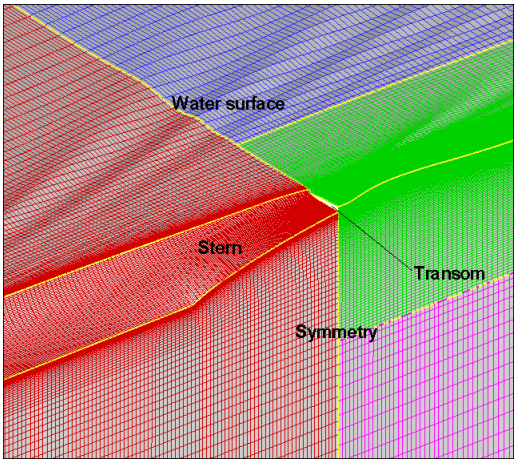

Fig. 1: Block topology and grid distribution near the transom. Shown is the coarsest grid used for DTMB 5415.

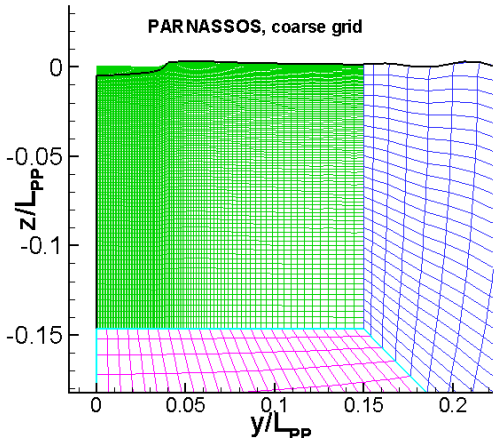

Fig. 2: Cross section of the coarsest grid for DTMB 5415 at the transom: the black line indicates the transom edge.

We use a block topology that allows an automatic prediction of the transom regime, thus suited to handle both wetted and dry transoms, and transoms that are dry at some lateral position and wetted at others. This topology, illustrated in Fig. 1, consists of four blocks. One block upstream of the transom contains an HO-type grid with a mild contraction towards the bow and the stern in longitudinal direction, and a strong contraction in wall-normal direction towards the hull in order to resolve the viscous sublayer. The upstream block has a non-conformal matching with the three blocks downstream of the transom, each containing HH-type grids. The grid nodes in the block immediately behind the transom are contracted both towards the symmetry plane and the free surface to get enough resolution near the transom, also in vertical direction at the wetted part of the transom.

The BEM for the propeller

For the analysis of the flow past a propeller, use is made of a boundary element method (BEM) that solves the incompressible potential flow equations for lifting surfaces. The method, designated PROCAL, is being developed within MARIN'S Cooperative Research Ships (CRS) for the unsteady analysis of cavitating propellers operating in a prescribed ship wake. It has been validated for open water characteristics, shaft forces, and sheet cavitation inception and extent. The code is a low order BEM that solves for the velocity disturbance potential. Initial validation studies and details on the mathematical and numerical model can be found in Vaz & Bosschers (2006) and Vaz (2005).

The coupling procedure between RANS and BEM

The steady RANS solver and the unsteady boundary element method are coupled in the following way:

- First a RANS computation is made for the case without propeller. This provides the resistance and the nominal wake field at the propeller plane.
- Then, a first propeller computation is made using PROCAL, for the propeller in this wake field at an estimated rotation rate. This provides a thrust and loading distribution. The unsteady loading distribution, in a ship-fixed coordinate system, is averaged in time (i.e. over all blade positions) to produce a steady, but circumferentially and radially non-uniform distribution. This is interpolated to the RANS grid.
- We restart the viscous-flow computation from the previous solution and impose this loading distribution as a force field acting on the flow, after scaling it such that the total thrust balances the resistance force acting on the hull. This yields a new total wake field, from which we then subtract the induced velocities coming from PROCAL to obtain the first estimate of the effective wake field.
- From the imbalance between the previous computed propeller thrust and the last resistance force on the hull, we deduce a correction of the rotation rate using the open-water diagram for the propeller. We then perform the next PROCAL computation, for the propeller in the effective wake at this new estimated rotation rate.
- We iterate between both methods until the *x*-forces balance and the rotation rate and loading distribution do not change any more. We then have obtained the matched solution for the self-propulsion point.

RESULTS

KRISO Container Ship (KCS)

The results for the KRISO container ship (KCS) are for model scale Reynolds number, Rn = 1.4×10^7, for Fn = 0.26, and at the design draught T = 10.8 m. First we present computations for the nominal flow field, i.e. ignoring propeller action, (case 2.1), to compare the predicted wave elevation, the velocity field in the propeller plane and pressure, friction and total resistance values with available experimental data. Then we present results of our approach to compute the ship self-propulsion point (case 2.3a), by coupling a steady RANS solver with an unsteady BEM for the propeller analysis.

At present we mainly have results for KCS on two different meshes: a base mesh (S_1) containing 3.1M cells and a coarsened mesh (S_3) derived from the initial mesh by removing every other cell in the *i*, *j* and *k*-direction, resulting in a mesh with 0.4M cells. Furthermore some results are presented on an intermediate mesh (S_2) where every other cell has been removed in the *j* and *k*-direction only, resulting in 0.8M cells. Since this mesh is not geometrically similar to the S_1 and S_3, it is omitted from all tables presented in this section. The numbers of cells mentioned here hold for case 2.1, where due to symmetry considerations only the starboard side of the ship was taken into account. For the computations in case 2.3a where the tangential forces exerted by the propeller on the flow break the symmetry, the mesh was mirrored to port side and thus the number of cells doubled (6.2M for S_1).

Mesh S_1 had 252 cells along the waterline. This corresponds to circa 100 cells per linear wave length ($\lambda_{lin}/L_{pp} = 2\pi Fn^2 = 0.425$). This obviously is an average value due to the streamwise clustering of cells towards the bow and the stern. The streamwise grid spacing at midship was approximately $0.01L_{pp}$. Near the bow the grid spacing was approximately $1/3^{rd}$ of that value, near the transom approximately $1/5^{th}$. In the wake the grid spacing smoothly increased to a streamwise cell size of $0.03L_{pp}$ near the outflow plane. In wall-normal direction the grid spacing increased from a maximum non-dimensional distance $Y^+_{max} = 0.3$ to approximately $0.06L_{pp}$ near the exterior boundary. In the final solutions the maximum changes in the pressure coefficient between two consecutive RANS sweeps was below $dC_P = 5 \times 10^{-6}$, and the maximum changes in the free-surface elevation below $dz/L_{pp} = 2.6 \times 10^{-4}$.

Case 2.1

Figure 3 shows that, due to the earlier mentioned 'balanced scheme' in the FSBC, numerical damping and dispersion in our method is very limited, even with the fairly modest mesh count in S_3. As a result very good agreement is found between the predicted wave elevations on all three grids and the experimental data. Even the short diverging wave visible in the z/L=0.1509 wave cut near $x/L_{pp} = 0.65$ is captured in meshes S_1 and S_2.

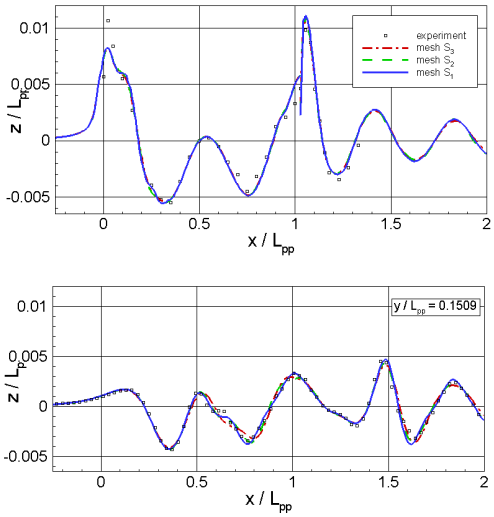

Fig. 3: Grid dependence of the wave elevation along the hull and the symmetry plane in the wake (top) and at the longitudinal position y/L_{pp}=0.1509 (bottom).

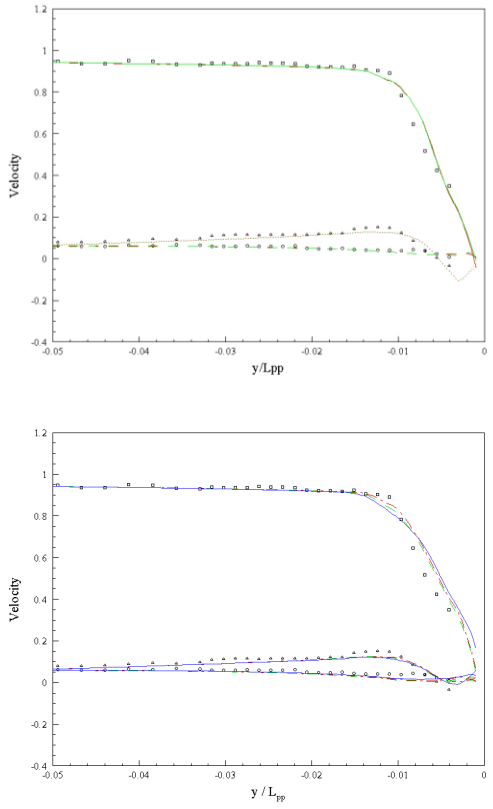

Fig. 4: Grid dependence of the velocity field in the propeller plane for two turbulence models (top: k-ω SST model, bottom: Menter's 1-eq. model).

Figure 4 shows the predicted velocity components in the propeller plane (x/L_{pp} = 0.9825) at z/L_{pp} = -0.0302 for the various meshes (S_1 red, S_2 green, S_3 blue lines). In this figure the *u*, *v* and *w*-component of the velocity vector are indicated by open squares, circles and triangles, respectively. Grid dependence is limited and the results obtained with the two-equation SST model are slightly better than those obtained with the one-equation model. Similar conclusions hold for the predicted resistance values listed in Table 1.

Table 1: Resistance values for KCS, case 2.1

	10^3 C_P	10^3 C_F	10^3 C_T
1-eq. model			
S_3	0.70	2.95	3.65
S_1	0.70	2.94	3.64
k-ω SST			
S_3	0.81	2.79	3.61

Case 2.3a

The objective of this case is to predict the ship self-propulsion point for KCS. This introduces another iteration loop (and convergence criterion) in the RANS/FS computations, since the rotation rate of the propeller has to be adjusted such that the thrust of the propeller balances the resistance force acting on the hull (minus the towing force, and with a roughness correction). The difference between the resistance force and the thrust was approximately 0.01N for the results presented in this section.

In order to minimize the computational effort we first only imposed the axial force field from the propeller analysis in the RANS/FS computation, after averaging between the port and starboard values; thus preserving symmetry and saving half the number of grid nodes. Upon convergence the solution was mirrored to port side and the computation was restarted with the full propeller force field including the radial and tangential components.

Table 2a: Resistance values for KCS, case 2.3a

	10^3 C_P	10^3 C_F	10^3 C_T
1-eq. model			
S_3	1.07	2.96	4.03
S_1	1.08	2.95	4.03
k-ω SST			
S_3	1.15	2.80	3.95

Table 2b: Propeller data for KCS, case 2.3a

	K_T	$10K_Q$	n [rps]
1-eq. model			
S_3	0.177	0.306	9.47
S_1	0.179	0.310	9.36
k-ω SST			
S_3	0.170	0.297	9.47

Table 2a and 2b present resistance values and propeller data for the symmetric case. Little grid dependence is found for the computations using Menter's one-equation turbulence model. The predicted total resistance value is approximately 2% lower than measured ($10^3C_{T,exp}$=3.966). For the k-ω model even better agreement is found, but this result is at present only available at the coarsest (S_3) mesh. Similar to the resistance force acting on the hull the predicted propeller thrust and torque are within a few per cent of the experimental values ($K_{T,exp}$=0.170, $10K_{Q,exp}$=0.288) and the predicted rotation rate is under-predicted by 1 per cent on the finest (S_1) mesh.

The asymmetric results including the radial and the tangential force field (that were submitted to the Gothenburg workshop) showed a reduction of the resistance force and required rotation rate, that can not be contributed to the asymmetric propeller loading only. This requires further research. Finally, Fig. 5 shows the location and the geometry of the propeller at an arbitrary blade position and the mean axial flow field at the y=0 plane for the present case.

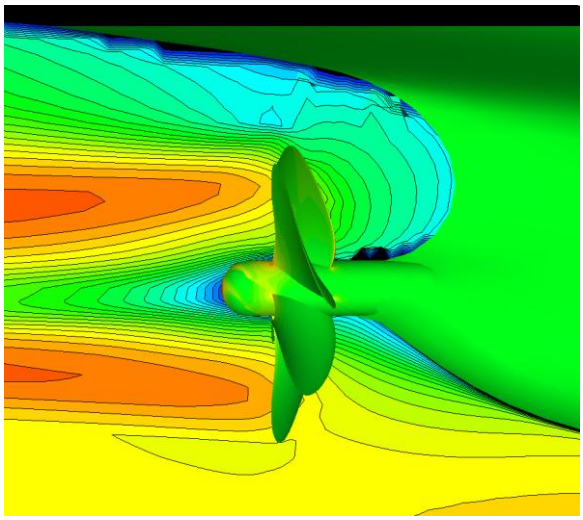

Fig. 5: Flow field at the y=0 plane for case 2.3a.

DTMB 5415

For DTMB 5415, all results are for model scale Reynolds number, Rn = $1.19x10^7$, for Froude number Fn = 0.28. Both the case with fixed trim and sinkage (case 3.1a) and with free trim and sinkage have been considered (case 3.2). The main aim of these computations is to enable comparisons with other CFD-codes and with measurements, and to study the grid dependence of the 4-block topology described above.

For case 3.1 and 3.2, the coarsest grid has 3.7 million cells for all 4 blocks together. The block along the hull ending at the transom (indicated in red in Fig. 1), consists of 290 x 120 x 52 = 1.8M cells. The block behind the transom (green in Fig. 1), consists of 144 x 99 x 99 = 1.4M cells.

In order to determine the sensitivity of the computed results with respect to the grid density, we performed computations on three refined grids, in which the

mesh size was halved in, respectively, the main stream (*x*-), the wall-normal (*y*-) and the direction normal to the water surface (*z*-). This refinement was performed in all blocks. Hence the total number of cells in each refined grid was 7.4 million.

The computed resistances and the computed dynamic trim and sinkage for DTMB 5415, case 3.2, obtained on the four grids, are shown in Table 3. The first column shows in which direction refinement of the mesh with a factor two was made. All resistances were non-dimensionalized with a wetted surface of $0.1476L_{pp}^2$.

Table 3. Resistance coefficients (x1000), dynamic trim (degrees) and sinkage (x1000 L_{pp}). Case 3.2

ref	C_{ph}	C_P	C_F	C_T	trim	sink
-	-0.47	1.66	3.11	4.29	0.089	1.75
x	-0.48	1.61	3.10	4.23	0.092	1.76
y	-0.48	1.67	3.12	4.31	0.085	1.76
z	-0.48	1.63	3.10	4.25	0.096	1.75

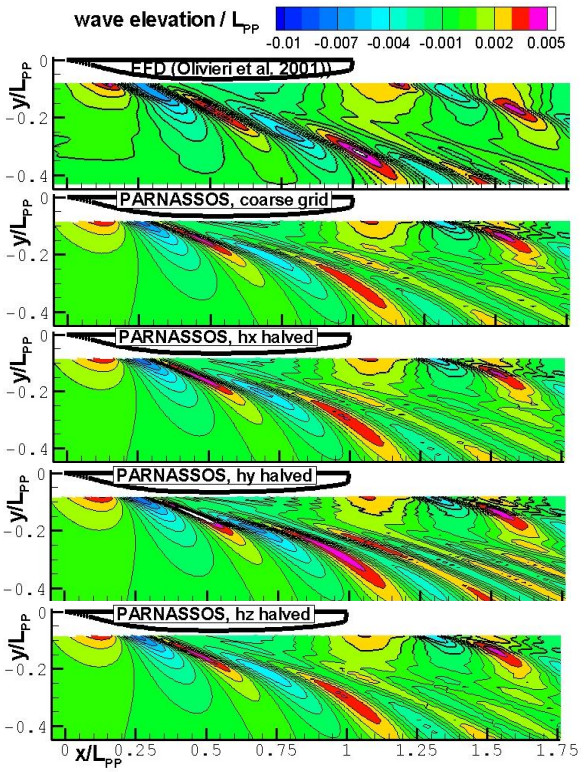

Fig. 6: Comparison of measured (top) and computed wave elevations for the DTMB 5415, case 3.1.

The wave elevations computed on each grid are compared with the measured wave elevation in Fig. 6. Note that the color scaling has been chosen in such a way that even a small difference in the predicted wave height in the crests results in a difference in the colors. Hence any numerical damping is immediately visible.

From these results it appears that in general the grid dependence in the computed results is small, although halving the mesh size in the wall-normal direction has the largest influence. In order to keep the total number of cells limited, we used a stretching of the cell size towards the outer boundary. This may lead to insufficient resolution further from the hull, and it may be better not to stretch the cells towards the outer boundary once a certain maximum mesh size has been reached.

Another aspect that has to be considered is that the free-surface fitting approach does not contain any model for wave-breaking. In this particular case this can explain some differences, especially in the bow-wave system. Nevertheless, the computed resistance coefficients are in general in good agreement with the measured value. When the mesh size in *x*-direction is halved, the predicted value for C_T is even on top of the measured value.

Figure 7 shows a comparison between measured wave elevation and the wave elevation computed on the coarsest grid. In general, the agreement is good.

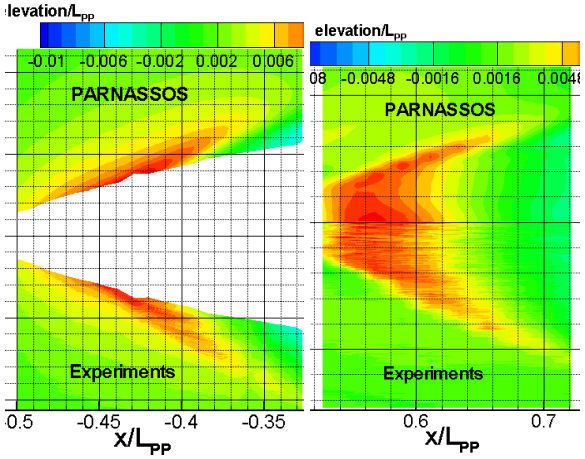

Fig. 7: Comparison of computed (top) and measured (bottom) wave elevation near the bow (left) and behind the stern (right).

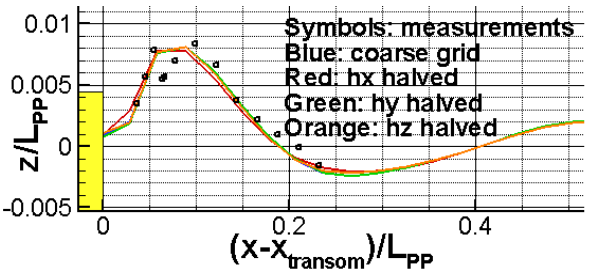

Fig. 8: Comparison of computed and measured wave heights at the center line behind the transom.

Figure 8 shows that the grid dependence in the computed wave heights behind the transom is very small. Halving the mesh size in *y*- or *z*-direction hardly affects the computed wave elevation. The height of the water column against the transom is almost the same on all grids. The coarse grid results (blue) are hardly visible, because they almost

coincide with the results in which *hy* is halved (green). Only mesh refinement in longitudinal direction (red) results in a slightly different wave height.

In the computations for the 2005 Tokyo workshop (Starke, van der Ploeg & Raven, 2005), we forced the transom to be dry. Therefore, the grid was set up to have the hull surface continuing aft into a grid boundary that followed the water surface. In the grid points at the transom edge the pressure was set to atmospheric, while in the free-surface points aft of it the combined FSBC was imposed. An interesting question is how strongly the wave pattern is influenced by the fact that the transom was forced to be dry? Therefore, Fig. 9 compares the result submitted to the Tokyo workshop (blue line) with the present result (red line). It is evident that the present result is significantly closer to the measurements than in the case where the transom was forced to be dry.

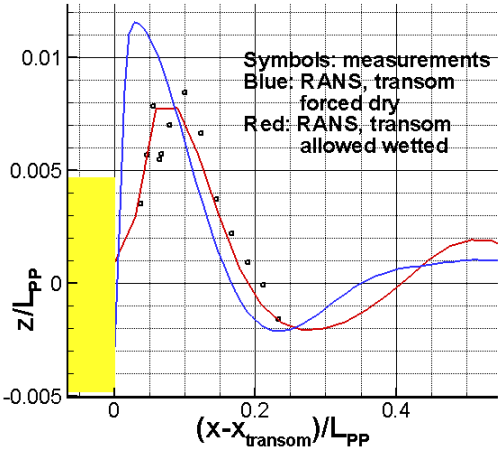

Fig. 9: Comparison of measured wave heights and wave heights computed by several methods.

CONCLUSIONS

The steady free-surface fitting method again provides efficient and accurate predictions of the wave patterns for KCS and DTMB 5415 test cases. Compared to the single-grid approach described in (Starke, van der Ploeg & Raven, 2005), much progress has been made. The 4-block topology allows for ample resolution along the wetted part of the transom, resulting in good agreement with the measured stern wave patterns. This is necessary for prediction of the transom flow regime and for a reliable computation of scale effects. In (van der Ploeg, Chao, Marzi & Wackers, 2010) it is shown that such scale effects can be quite significant.

The coupling of a steady RANS solver for the viscous around the hull, and an unsteady propeller panel code, is an efficient approach that permits accurate predictions of the propeller operation behind the ship.

REFERENCES

Dacles-Mariani, J., Zilliac, G.G., Chow, J.S., and Bradshaw, P., "Numerical/experimental study of a wingtip vortex in the near field", AIAA Jnl, Vol. 33-9, pp. 1561-1568, 1995.

Eça, L., Hoekstra, M., Raven H.C. "Calculation of the flow around the KVLCC2 tanker: case 1.1.a", CFD workshop Gothenburg, 2010.

Hoekstra, M., "Numerical simulation of ship stern flows with a space-marching Navier-Stokes method", PhD Thesis, Delft Univ. Techn., 1999.

Menter, F.R., "Two-equation eddy-viscosity turbulence models for engineering applications", AIAA Journal, Vol. 32, August 1994, pp. 1598-1605.

Menter, "Eddy viscosity transport equations and their relation to the k-ε model", Jnl Fluid Eng. Vol. 119, pp. 876-884, 1997.

Raven, H.C. and Van Brummelen, E.H., "A new approach to computing steady free-surface viscous flow problems", 1st MARNET-CFD workshop, Barcelona, Spain, 1999.

Raven, H.C. and Starke, A.R., "Efficient methods to compute ship viscous flow with free surface" 24th Symp. Naval Hydrodynamics, Fukuoka, Japan, 2002.

Raven, H.C., van der Ploeg, A. and Starke, A.R., "Computation of free-surface viscous flows at model and full scale by a steady iterative approach", 25th Symposium on Naval Hydrodynamics, St. John's, Newfoundland, CANADA, August 2004.

Van der Ploeg, A., Hoekstra, M., and Eça, L., "Combining accuracy and efficiency with robustness in ship stern flow computation", 23rd Symp. Naval Hydrodynamics, Val de Reuil, France, 2000.

Van der Ploeg, A., Chao, K., Marzi, J., Wackers, J., "Computation of Scale Effects in Free-Surface Flows near a Ship's Transom", 13th Num. Towing Tank Symposium, Duisburg, Germany, 2010.

Vaz, G., Bosschers, J., "Modelling of three dimensional sheet cavitation on marine propellers using a boundary element method", 6th Int. Symp. on Cavitation CAV2006, Wageningen, NL, Sept. 2006.

Vaz, G., "Modelling of sheet cavitation on hydrofoils and marine propellers using boundary element methods", PhD thesis, Instituto Superior Técnico, Lisbon, Portugal, 2005.

Windt, J., and Raven, H.C., "A composite procedure for ship viscous flow with free surface", 3rd Num. Towing Tank Symposium, Tjarno, Sweden, 2000.

FEASIBILITY STUDY ON NUMERICAL TOWING TANK APPLICATION TO PREDICTIONS OF RESISTANCE AND SELF-PROPULSION PERFORMANCES FOR A SHIP

Jin Kim, IL-Ryong Park, Kwang-Soo Kim and Suak-Ho Van
(Maritime and Ocean Engineering Research Institute/KORDI, KOREA)

1. SUMMARY

RANS(Reynolds−Averaged Navier-Stokes) equation based simulations are performed to predict the performances of resistance and self-propulsion characteristics for the KRISO VLCC Tanker (KVLCC2) and KRISO Container Ship (KCS) including sinkage and trim. All numerical grids are generated with own developed grid generator starting from 2D offset table of the hull forms. The numerical results are obtained using a RANS based general ship hydrodynamic code, WAVIS that uses a cell-centered finite volume method for the discretization of the governing equations. The free surface is captured using a two-phase level-set method and a realizable k-ε model is used for turbulence closure. The sinkage and trim are computed at one computational time step and applied in the succeeding time step through treatment in the non-inertial reference frame, which is performed with an interval of a fifth to tenth of the total number of iteration for simulation. The propeller effect is considered as body force obtained from unsteady lifting surface method for the simulation of self-propulsion condition. The verification and validation (V&V) analysis is applied to the total resistance coefficient as an integral variable for both fixed and free condition. For KVLCC2 and KCS model ships, computational errors are less than validation uncertainties such that the obtained numerical results are validated at the level of validation uncertainty 1.005~1.326%D. For KCS self-propulsion condition, since the data uncertainty was not given, only verification analysis is performed for the total resistance, thrust, torque, and rps. The simulation based self-propulsion factors are in good agreement with experimental results. The present study can lead to the following conclusion such that developed RANS based simulation for towing and self-propelled model ship is promising to be used as a tool for hull form designers.

2. INTRODUCTION

Computational ship hydrodynamic researchers have been making an endeavor to develop the reliable computational fluid dynamic (CFD) tool for the prediction of ship hydrodynamic performances. As a link to this effort, the experimental data for the flow around practical hull forms are obtained to validate the CFD code (Van et al., 1997, 1998a, and 1998b). These data are adopted as the benchmarking test cases for the Gothenburg 2000 Workshop (Larsson et al., 2000). These hull forms are much more modernized than those of the previous workshops (Larsson et al., 1991; Kodama, 1994). In the Gothenburg 2000 workshop, a modern container hull form such as KRISO container ship (KCS) gave a new challenge to simulate the transom wave field and also self-propelled condition. The linked CFD Workshop was held at Tokyo after 5 years. The topics of the CFD Workshop Tokyo 2005(Hino, 2005) were much broader compared to the earlier workshops, i.e., predictions of flows and the wave field in the towing condition in still water for fixed and free conditions of a model ship; double model flows for tanker KVLCC2M; self-propelled condition for the KCS; flows and hydrodynamic forces and moments in the obliquely towed condition for the KVLCC2M tanker; and flows and hydrodynamic forces in the diffraction condition for naval combatant DTMB 5415.

The present study is focused on the predictions of resistance in the fixed or free towing conditions and propulsion performances in self-propelled condition. The numerical methods have been developed through continuous studies such that RANS analysis for hull-propeller-rudder interactions (Kim et al., 2007) and treatment of large changes in hull attitude (Kim et al., 2010). In order to minimize the dependency of users like non-expert on CFD, grid generation methods are developed for application to all kinds of commercial ships, which have a single-screwed propeller. This method provides the computational grid within 30 minute from 2D offset table of the hull forms.

3. COMPUTATIONAL METHODS

3.1 Governing Equations and Free Surface formulations

The governing equations for turbulent free surface flow in the present study are the Reynolds-Averaged Navier-Stokes (RANS) equations for momentum transport and the continuity equation for mass conservation. The RANS and

the continuity equations are expressed in integral form for a control volume Ω with a surface boundary S.

$$\frac{d}{dt}\int_\Omega \rho u_i d\Omega + \int_S \rho u_i u_j dS = \int_S \tau_{ij} n_j dS + \int_\Omega \rho b_i d\Omega \quad (1)$$

$$\frac{d}{dt}\int_\Omega \rho d\Omega + \int_S \rho u_i n_i dS = 0 \quad (2)$$

where ρ is the fluid density, u_i=(u,v,w) are velocity components in the Cartesian coordinate system, n_i is the unit normal vector, τ_{ij} is the fluid stress tensor, and b_i is the body force vector. All the fluid variables are made dimensionless with respect to advancing speed of a ship U_o, the ship length L, and the fluid density ρ. The Reynolds number and the Froude number, are defined respectively as

$$\mathrm{Re} = \frac{\rho U_o L}{\mu}, \quad \mathrm{Fn} = \frac{U_o}{\sqrt{gL}} \quad (3)$$

Stress tensor τ_{ij} can be written using Boussinesq's isotropic eddy viscosity hypothesis as follows.

$$\tau_{ij} = \nu_e \left(\frac{\partial u_i}{\partial u_j} + \frac{\partial u_j}{\partial u_i}\right) - \frac{2}{3}\delta_{ij} k \quad (4)$$

Here, k is turbulent kinetic energy, δ_{ij} is the Kronecker delta function and ν_e is the effective viscosity, i.e., the sum of turbulent eddy viscosity (ν_t) and the fluid kinematic viscosity (ν). For the turbulence closure, the realizable k-ε model (Shih et al., 1995) is used with Launder and Spalding's wall function. The discretization of the governing equations is carried out by the finite volume methods. Convection terms are discretized using MUSCL scheme of the third order, and central difference scheme is utilized for diffusion terms. To ensure divergence-free velocity field, the SIMPLE method is employed. The details of the present numerical methods can be found in Kim et al. (2002)

The free surface is captured with the level-set method (Sussman et al., 1997). In order to obtain an accurate free surface solution and stable convergence, the computations are executed with a proper fine grid refinement around the free surface and with an adoption of implicit discretization scheme for the Level-Set formulation. Level-set function $\emptyset(x_i, t)$ is introduced to define the region of air, water, and free surface.

$$\begin{aligned} &\phi(x_i,t) > 0, \text{ if } x_i \in \text{water} \\ &\phi(x_i,t) < 0, \text{ if } x_i \in \text{air} \\ &\phi(x_i,t) = 0, \text{ if } x_i \in \text{free surface} \end{aligned} \quad (5)$$

The density and viscosity can be expressed with the function of $\phi(x_i,t)$ as follows:

$$\begin{aligned} \rho(\phi) &= \rho_a + (\rho_w - \rho_a) H(\phi) \\ \mu(\phi) &= \mu_a + (\mu_w - \mu_a) H(\phi) \end{aligned} \quad (6)$$

where, (ρ_w,μ_w) and (ρ_a,μ_a) represent the density and viscosity for water and air, respectively. $H(\phi)$, the Heaviside function is defined as $H(\phi>0)$=1, $H(\phi<0)$=0, and $H(\phi=0)$=0.5. The details can be found in Park et al. (2004).

3.2 Lifting Surface Method for Self-Propulsion simulation

Since the effective wake and the propeller loading depend on each other, the overall process must be iterative. The iterative processes consist of two components, the propeller solver (Lifting Surface Method) and the RANS solver. The iterative process can start with the propeller analysis using the nominal wake as inflow. Using the computed propeller loading, the body force representing the propeller in the RANS equations can be calculated. The RANS solver computes the total velocity using the body force in the previous step. The effective wake can be computed by subtracting the propeller induced velocity from the total velocity field. Finally, the propeller solver uses the effective wake as the inflow to compute the updated propeller loading. The iterative process continues until the change of the mean effective wake is less than 10^{-5}. The unsteady lifting surface method is utilized in the present study. The body force distribution is calculated from the instantaneous blade circulation distribution suggested by Choi (2000).

3.3 Grid generation

3.3.1 Surface grid

In the preliminary design stage, CFD is used as a one of useful tools to evaluate the performance of a new hull form reliably and quickly. However, it is cumbersome to describe a modern hull form by using only the offset table, since the complexity of bow and stern shapes require more information. In this study, in order to efficiently control the offset lines for surface grid generation, three-dimensional space curves described by non-uniform parametric spline with the slope controlled at any given points are employed. The important parameter chosen for interpolation is the accumulated chord length. In particular, the Ferguson basis, utilizing position vectors and tangent vectors at the end points, are selected since it is easy to handle the discontinuities of slope or curvature existing in hull surface profiles (Nowaki et al. 1995). If the curvature or slope at a point is not specified from the offset table, cubic spline curves are implemented.

The procedure of surface grid generation begins with an offset table provided by the designer that contains 10~30 offset points at 25~30 stations with bow and stern profiles. The first step is identifying the offset points having discontinuous slope or curvature. Then non-uniform parametric spline is utilized to generate sufficiently many interpolated points for the body plan and the side profile. These generated points on body plan and centerline profile are used for generating waterlines. It is necessary to make up additional station offsets in the bow and stern region to construct complicated bow and stern shape. After the waterlines are obtained, dense additional stations near bow and stern are generated using the waterline intersection points at constant longitudinal locations. The boundary of

surface grid topology constitutes of keel line, design waterline, bow and stern contours. The generated surface grids can be transformed into a rectangular domain, which provides the simplicity of application to flow solvers. To make the surface grid flexible, the longitudinal and transverse distribution can be arbitrarily adjusted with the girth length ratio. Once the transverse distribution is given, grid nodes at each station can be found, using the length ratio of dense station curves. The nodes at the same transverse ratio are connected to complete the longitudinal grid lines. The longitudinal distribution ratio will finally provide the hull surface grid. It is noteworthy that all the above procedures can be completed within one minute on PC when the original offset table is given.

3.3.2 Field grid

As described in the previous section, the surface grid contouring bow and stern profile constitutes one boundary surface of three-dimensional field grid system for viscous flow calculation. To implement the turbulence model and near-wall specifications for high Reynolds number flow, it is necessary to determine the distance and intersecting angles of the first grid points off the wall. The present field grid is consisted of a two block grid system: an inner block grid of H-O topology surrounding the hull surface and an adjacent background grid with the same grid topology. All six boundary surfaces of the background grid can be defined algebraically. Among the boundary surfaces of the inner grid, the hull surface grid is already given and the outer surface grid is defined algebraically. The two-dimensional grid systems on other planes are obtained by solving 2-D Poisson equation. After constituting all boundary surfaces, it is possible to use an algebraic method like trans-finite interpolation (TFI) to fill out the interior grid system. It is rather simple, but does not guarantee the normality of grid on the hull surface. In this study a three-dimensional Poisson equation is solved for the inner grid containing the hull surface to meet the requirement of grid orthogonality and controllability. Sorenson's method, known as GRAPE (Sorenson 1980), is extended into three-dimension to define the grid-controlling function of Poisson equation. More detailed descriptions on the field grid generation are found in Kim et al. (2002).

3.4 Hull attitude calculation

For a given hull form, the sinkage at the center of gravity (*CG*) is computed using the heave force coefficient in a non-dimensional form as

$$z_s = \frac{C_z \frac{1}{2}\rho_w U_o^2 S_w}{\rho_w g S_{wl} L_{pp}} = C_z F_r^2 \frac{S_w}{S_{wl}} \qquad (9)$$

where C_z is the heave force coefficient, S_w is the wetted surface area of the hull, S_{wl} is the waterline area, and F_r is the Froude number. In a similar way, trim is calculated using the pitch moment acting on the center of gravity of the hull. The trim angle θ is obtained introducing the second moment of inertia of the waterline area (I_{wl}) about the center of gravity as following:

$$\theta = \frac{C_{My} \frac{1}{2}\rho_w U_o^2 S_w L_{pp}}{\rho_w g I_{wl} L_{pp}^4} = C_{My} F_r^2 \frac{S_w}{I_{wl}} \qquad (10)$$

where C_{My} is the pitch moment coefficient. When the sinkage and trim are known, the sinkages at the bow (FP), the stern (AP), and the midship (*O*) of the hull form can be obtained in a straight way as

$$z_{sO} = z_s + \theta x_{CG}, \quad z_{sFP} = z_{sO} + \frac{\theta}{2}, \quad z_{sAP} = z_{sO} - \frac{\theta}{2} \qquad (11)$$

3.5 Verification & Validation (V&V) Study

Verification and validation (V&V) procedures for the estimation of simulation errors and uncertainties are followed by Stern et al. (2001). Total resistance is used for the integral variable in the V&V procedure. Grid studies were conducted using three grids, such as coarse, medium and fine grid systems. Non-integer grid refinement ratio $r_G = \sqrt{2}$ is selected in the current study. Table 1 shows the grid convergence of total resistance(C_T)coefficients for KVLCC2 and KCS with the rudders and the fixed towing condition, where the error E is defined as E(%) = (D-S)/D×100 and the solution changes between two simulations such as medium-fine and coarse-medium are defined as $\varepsilon_{21} = S_2 - S_1$ and $\varepsilon_{32} = S_3 - S_2$. These solutions are used to define the grid convergence ratio,

$$R_G = \varepsilon_{21}/\varepsilon_{32} \qquad (12)$$

Order of accuracy p_G, correction factor C_G, grid uncertainty U_G are defined at Stern et al. (2001).

Table 1 Grid convergence study for resistance coefficients(×10^{-3}) for KVLCC2 & KCS

KVLCC2	Coarse (S_3)	Medium (S_2)	Fine (S_1)	Exp.Data (MOERI)
C_T E%D ε	4.279 -4.114%	4.180 -1.706% 0.099	4.129 -0.457% 0.051	4.110
C_F	3.344	3.301	3.223	
C_P	0.935	0.879	0.906	
KCS	Coarse (S_3)	Medium (S_2)	Fine (S_1)	Exp.Data (MOERI)
C_T E%D ε	3.696 -3.908%	3.581 -0.675% 0.115	3.564 -0.197% 0.017	3.557
C_F	2.77	2.809	2.808	
C_P	0.926	0.772	0.756	

For KVLCC2 and KCS ship cases, the obtained grid convergence ratio R_G, order of accuracy p_G, grid

uncertainty U_G, error E, the experimental data uncertainty U_D, and validation uncertainty U_V are shown in Table 2. The validation uncertainty U_V can be calculated from the following equation.

$$U_V = \sqrt{U_{SN}^2 + U_D^2} \qquad (16)$$

Since $|E| < U_V$ for both cases, total resistances are validated at the level of 1.005%D and 1.326%D, respectively.

Table 2 Verification & validation of total resistance for KVLCC2 and KCS

Ship	R_G	p_G	U_G%S_I	E%D	U_D%D	U_V%
KVLCC2	0.52	1.88	0.096	0.457	1.0	1.005
KCS	0.15	5.52	0.871	0.197	1.0	1.326

4. COMPUTATIONAL RESULTS

4.1 KVLCC2 case

4.1.1 grid and test conditions

In this section, the numerical simulation of resistance tests for KVLCC2 is carried out using a model of 5.52 *m* of which the scale ratio to the ship is 58.0. For grid convergence test, three succeeding grids are designed with a refinement ratio of $\sqrt{2}$ as discussed in the previous section. In particular, in order to approach the short wave pattern generated around this type of low speed VLCC hull form, the number of grid points in the longitudinal direction is increased larger than that used for the KCS test cases. The total number of grid points for each grid resolution case is presented in Table 3.

Table 3 Grid information of KVLCC2

	Total cell number (Half body)
Coarse grid	0.65M
Medium grid	1.73M
Fine grid	4.93M

4.1.2 Wave field at the design speed in fixed towing condition

Fig. 1 and 2 shows the computed wave contours and cuts at different lateral positions in comparisons with measured data. Even though wave patterns of tanker shows short wave length and small amplitude, the present fine grid captured wave patterns very well. The computed results are in good agreement with experiment only except the regions far from the hull. This discrepancy is mostly caused from the numerical diffusion and coarseness of the grids in this region.

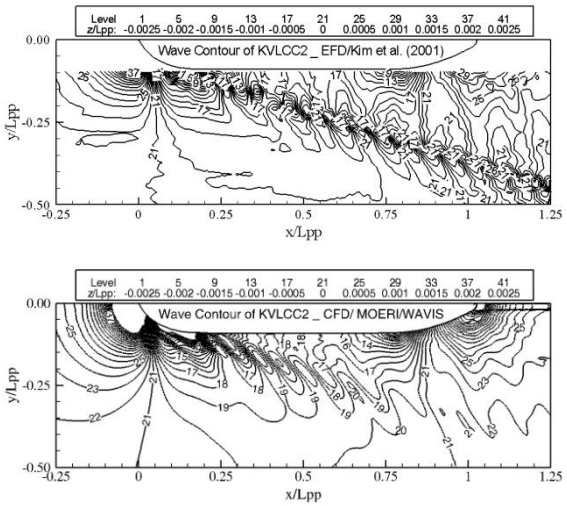

Fig.1 Comparisons of wave contours around KVLCC2

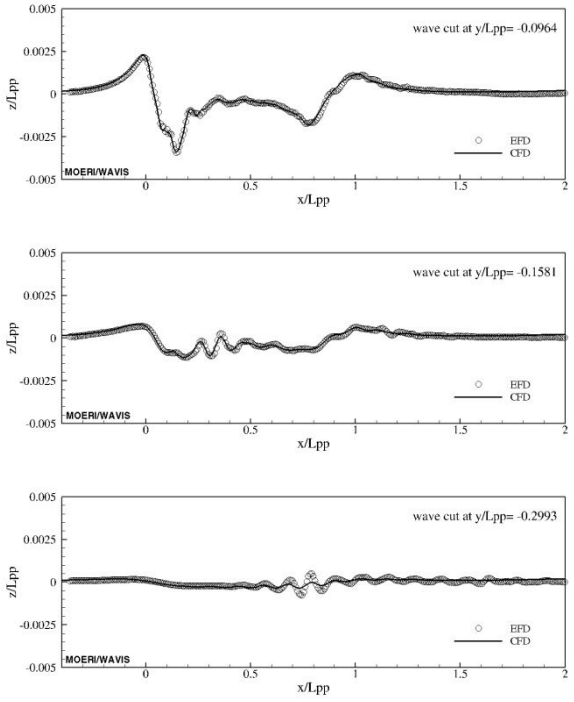

Fig.2 Wave cuts at different lateral positions

4.2 KCS case

4.2.1 grid and test conditions

The following three cases are simulated for KCS hull form.

- ✓ Resistance and flow characteristics at design speed in fixed towing condition without rudder.
- ✓ Resistance test at six speeds including trim and sinkage with rudder
- ✓ Self propulsion test at ship point in fixed towing condition with rudder

Table 4 shows total numbers of grid points for three different grid systems.

Table 4 Grid information of KCS

	Total cell number (Half body)	Total cell number (Full body)
Coarse grid	0.5M	1.0M
Medium grid	1.5M	3.0M
Fine grid	4.3M	8.6M

4.2.2 Flow and wave field at the design speed in fixed towing condition

The comparison of the wave patterns and wave profile along the hull surface between the experiment and present result computed from the Level-Set formulation is shown in the Fig. 3 and 4. The obtained wave contours and profile on the hull are in good agreement with the experiment.

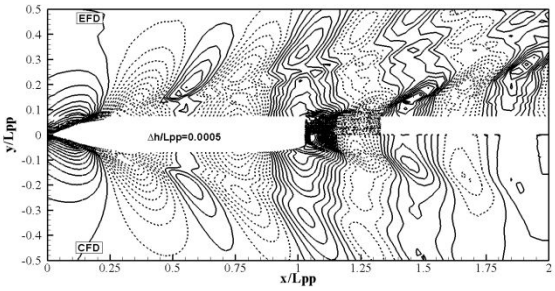

Fig.3 Comparisons of wave contours around KCS

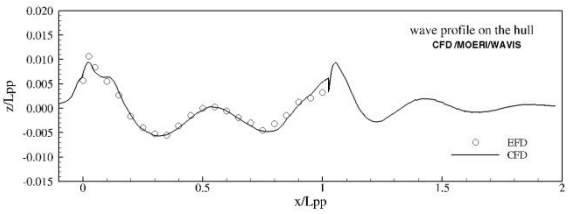

Fig.4 Comparisons of wave profile on the hull

4.2.3 Resistance tests at six speeds in free towing condition

Six different towing speeds are simulated with free condition in sinkage and trim. Fig. 5-7 shows the comparisons of total resistance coefficient, sinkage and trim respectively. Based on V&V analysis (Stern et al., 2001) numerical uncertainty are also expressed as horizontal long bar. The total resistance and trim are in good agreement with experiment, however computed sinkage are over estimated in small amount. Since the sinkage and trim are obtained from 2DOF motion equations and computed hull pressure, it is not easy to conclude the reason of these under estimations.

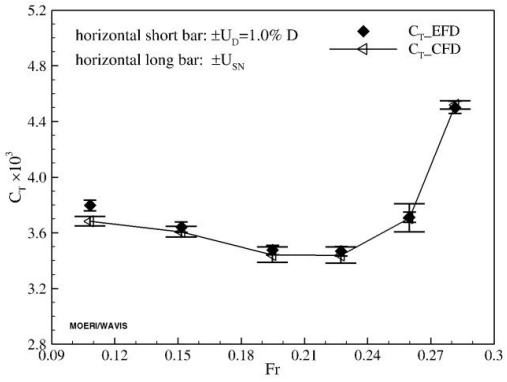

Fig.5 Total resistance coefficient vs Froude number

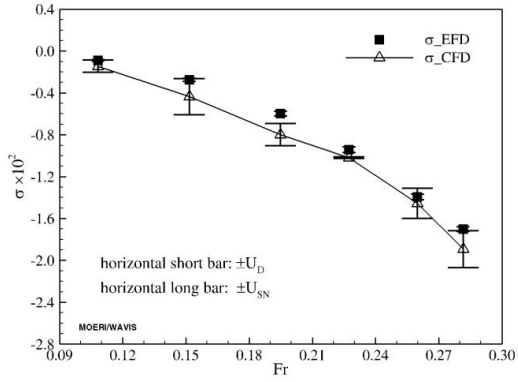

Fig.6 Sinkage vs Froude number

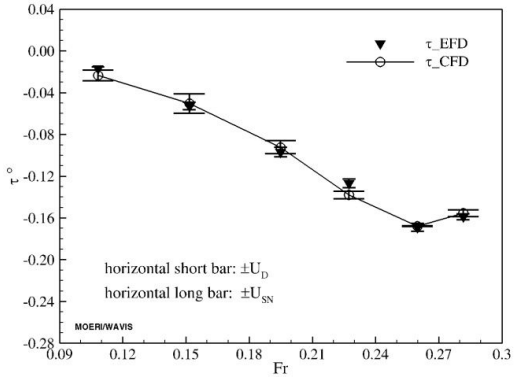

Fig.7 Trim vs Froude number

4.2.4 Self-propulsion test at ship point in fixed towing condition with rudder

The converged self-propulsion points for three different grids are shown in Table 5. The total resistance and rps show the monotonic convergence, but thrust and torque are converged in oscillatory behavior. The obtained fine grid results are well matched at the self-propulsion point of the experiment within errors of 0.025% for total resistance, 1.765% for thrust, 0.660% for torque, and 1.115% for rps. The flow behind a propeller is in good agreement with experiment in Fig. 8. The results of self-propulsion simulation is promising enough for hull form designers to use this tool for predictions of hull form performances.

Table 5 KCS self-propulsion

KCS	Coarse (S_3)	Medium (S_2)	Fine (S_1)	Exp.Data (NMRI)
C_T	4.184	4.007	3.965	3.966
E%D	-5.497%	-1.026%	0.025%	
C_F	2.831	2.834	3.223	
C_P	0.935	0.879	0.906	
K_T	0.174	0.166	0.167	0.170
E%D	-2.118%	2.366%	1.765%	
K_Q	0.0296	0.0276	0.0286	0.0288
E%D	-2.743%	4.035%	0.660%	
N(rps)	9.78	9.69	9.61	9.50
E%D	-2,954%	-1.958%	-1.115%	

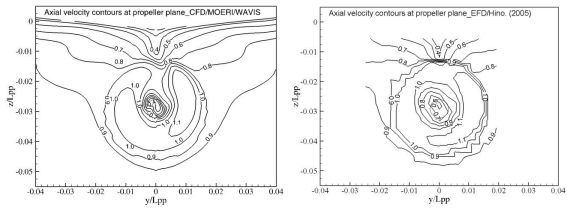

Fig.8 Axial velocity contour at x/Lpp=0.9911

5. CONCLUSION

The present methods are applied to the cases for typical resistance and propulsion tests in the towing tank. The present study can lead to the following conclusion such that developed RANS based simulation for towing and self-propelled model ship is very promising to be used as a tool to evaluate the performances of hull forms.

ACKNOWELDGEMENT

This research was supported by MOERI/KORDI basic research grant PES132A under the administration of Korea Research Council of Fundamental Science and Technology and also sponsored by research grant PNS131C under the administration of the ministry of knowledge economy, Korean government.

REFERENCES

Choi, J.K., (2000) "Vortical Inflow-Propeller Interaction using an Unsteady Three-Dimensional Euler solver," Ph.D. Thesis, Dept. of environmental and water resources engineering, Univ. of Texas, Austin, USA.

Hino, T. (ed) (2005) CFD Workshop Tokyo 2005, NMRI, Japan.

Kim, J., Kim. K.S., Park, I.R., and Van, S.H., (2010) "Numerical Simulations for High Speed Ships in Deep and Shallow Water with Sinkage and Trim," 2010 PRADS: Practical Design of Ships and Other Floating Structures, Vol. 1, pp. 16-24, Rio de Janeiro, Brasil.

Kim, K.S., Kim, J., Park, I.R., and Van, S.H., (2007) "RANS Analysis for Hull-Propeller-Rudder Interaction of a Comercial Ship by Using the Overset Grid Scheme," Proc. of the 9th International Conference in Numerical Ship Hydrodynamics, Vol. 3, pp. 251-264, Ann Arbor, MI, USA.

Kim, W.J., Kim, D.H., and Van, S.H., (2002) "Computational study on turbulent flows around modern tanker hull forms," International Journal for Numerical Methods in Fluids, Vol. 38, No. 4, pp. 377-406.

Kodama, Y. (ed) (1994) CFD Workshop Tokyo. Ship Research Institute, Ministry of Transport and Ship and Ocean Foundation, March 22–24, Tokyo, Japan.

Larsson L, Patel VC, Dyne G (eds) (1991) Flowtech research report, Flowtech International, Gothenburg, Sweden.

Larsson, L., Stern, F., Bertram, V. (2000) "Summary conclusions and recommendations of the Gothenburg 2000 workshop", Gothenburg 2000: A Workshop on Numerical Ship Hydrodynamics. Chalmers University of Technology, Gothenburg, Sweden

Nowaki, H., Bloor, M.I.G., Oleksiewicz, B., (1995) Computational Geometry for Ships, World Scientific Publishing Co.

Park, I.R., Kim, J., and Van, S.H., (2004) "Analysis of resistance performance of modern commercial ship hull form using a Level-Set method," Journal of the Society of Naval Architects of Korea, Vol.41, No.2, pp. 79-89 (in Korean).

Shih, T.-H., Liou, W.W., Shabir, A., and Zhu, J., (1995) "A new eddy viscosity model for high Reynolds number turbulent flows – model development and validation," Computers & Fluids, Vol. 24, pp.227-238.

Sorenson, R.L., (1980) "A computer program to generate two-dimensional grids about airfoils and other shapes by the use of Poisson equation," NASA TM 81198.

Stern, F., Wilson, R. V., Coleman, H., and Paterson, E., (2001) "Comprehensive approach to verification and validation of CFD simulations - Part 1: Methodology and Procedures," ASME J. Fluids Eng., Vol. 123, pp. 793-802.

Sussman, M., Fatemi, E., Smerera, P., and Osher, S., (1997) "An improved Level-Set method for incompressible two-phase flows," Computers and Fluids, Vol. 27, No. 5-6, pp. 663-680.

Van, S.H., Kim, W.J., Kim, D.H., et al (1997) "Measurement of Flows around a 3600TEU container ship model (in Korean)", Annual Autumn Meeting, SNAK, Seoul, Korea, pp. 815-820.

Van, S.H., Kim, W.J., Yim, D.H., Kim, G.T., Lee, C.J., and Eom, J.Y., (1998a) "Flow Measurement Around a 300K VLCC Model," Proceedings of the Annual Spring Meeting, SNAK, Ulsan, pp. 185-188.

Van, S.H., Kim, W.J., Yim, G.T., Kim, D.H., and Lee, C.J., (1998b) "Experimental Investigation of the Flow Characteristics Around Practical Hull Forms," Proceedings 3rd Osaka Colloquium on Advanced CFD Applications to Ship Flow and Hull Form Design, Osaka, Japan

A Scalable Multiphase RANSE Capability Based On Object-Oriented Programming and Its Applications to Ship Hydrodynamics

Sung-Eun Kim, Bong J. Rhee, Hua Shan, Joseph Gorski
(Naval Surface Warfare Center Carderock Division, West Bethesda, MD, U.S.A.)

Eric G. Paterson (ARL, Pennsylvania State University, PA, U.S.A.)
Kevin Maki (University of Michigan, Ann Arbor, MI, U.S.A.)

1. SUMMARY

We present a multiphase computational fluid dynamics capability (MPCFD) based on Reynolds-averaged Navier-Stokes equations (RANSE) aimed at predicting turbulent multiphase flows around ship hulls. The MPCFD capability employs finite-volume discretization that allows use of arbitrary polyhedral elements. Free surface is captured using a volume-fraction method capable of accurately resolving sharp interfaces. The coding is done using an open-source CFD software tool-kit (OpenFOAM) written in C++ that draws heavily upon object-oriented programming, the proven best practice in modern software engineering. The MPCFD capability is demonstrated for turbulent free surface flows around the DTMB 5415 model and the KVLCC2 double-model. It is shown that the RANSE-based approach can predict, with a remarkable accuracy, most of the salient features of the turbulent free-surface flows around the subject hulls including resistance, wave elevation, hull boundary layer and wake.

2. INTRODUCTION

As CFD technology matures, its realm in ship hydrodynamics has expanded, covering a much broader spectrum of applications than a decade ago when the last workshop was held, ranging from powering and propulsion to maneuvering to seakeeping. Geometrical, physical and operational complexity involved in ship hydrodynamics applications has kept adding features and functionalities in CFD codes on top of the basic flow solvers. Furthermore, CFD nowadays is frequently called upon to tackle multi-disciplinary applications such as fluid-structure interaction and hydroacoustics applications that require coupling of CFD codes with other computational mechanics software. Thus, general-purpose CFD codes, in attempts to cater to these diverse needs, have become increasingly larger and more complex. Software complexity is a serious issue which many legacy CFD codes face today, negatively impacting their overall efficacy in terms of quality assurance, packaging, maintenance and extensions.

This paper is concerned with a multiphase computational fluid dynamics (MPCFD) framework for ship hydrodynamics that has been developed using OpenFOAM (Weller et al., 1998), an open-source CFD software tool-kit written in C++ with software engineering in mind from its conception. It draws heavily upon object-oriented programming (OOP). We believe that modern software engineering practices realized by OOP in C++ will greatly facilitate collaborative development, quality assurance, deployment, maintenance, and extension of general-purpose CFD software. Efforts on the MPCFD framework had started out with propulsors as the target applications (Kim *et al*, 2010). Many capabilities developed to that end, such as the basic discretization schemes and the solution algorithms, also benefit ship hydrodynamics applications in general including free-surface flows around ship hulls. As of today, the MPCFD framework comprises a suite of modified and newly written application (top-level) solvers for single- and multi-phase flows, utilities and physics libraries built around the OpenFOAM CFD tool-kit. We loosely refer to the MPCFD capability as "NavyFOAM" in order to distinguish it from the standard OpenFOAM's offering.

We start with a brief description of NavyFOAM. This will be followed by the presentation of the computational results we obtained using NavyFOAM for the cases selected from the Gothenburg 2010 CFD Workshop problems. The computations were carried out for case 1.1a (KVLCC2 double-body model; $Re = 4 \times 10^6$), case 3.1a (DTMB 5415 – INSEAN model; fixed trim and sinkage; $Re = 1.19 \times 10^7$), case 3.1b (DTMB 5415 IOWA model; $Re = 5.13 \times 10^6$; fixed trim and sinkage), and case 3.2 (DTMB 5415; Re = 5.96×10^6, 1.19×10^7, 1.75×10^7, dynamic sinkage and trim). Due to the space limitation, we present here the results for Cases 1.1a, 3.1b, and 3.2.

3. NavyFOAM

3.1 Code architecture and top-level solvers

Object-oriented software design addresses the issue of software complexity by using "objects" abstracted out from applications at hand as low-level building blocks to assemble top-level applications. Classes – data and methods

- implemented with proper interfaces can be invoked from higher-level classes and top-level applications, facilitating data protection, encapsulation, layered development, code reuse, deployment, maintenance, and extension.

OpenFOAM makes heavy use of programming techniques offered by C++ language such as function and operator overloading, inheritance, and generic programming using templates, and dynamic binding using virtual base classes, all of which allow one to maximize code re-use, adopt layered development, easily assemble top-level applications using lower-level objects, and to make runtime-selection of numerical schemes, solution algorithms, physical models, and file I/O. Thus, top-level applications are surprisingly concise, unlike the ones written in procedural languages such as Fortran. The implementations encapsulate and hide all the details from the top-level applications.

NavyFOAM includes several top-level solvers aimed at ship hydrodynamics applications, including sRansFOAM (single-phase, steady RANSE solver), ransFSFOAM (RANSE-based free-surface solver), and ransFSDyMFOAM (RANSE-based free-surface solver with moving/deforming mesh), to name a few. That one has to deal with a number of top-level solvers for different applications often surprise those who are used to the idea of developing a monolithic CFD solver that can do everything. The philosophy adopted in OpenFOAM eschews the monolithic approach.

3.2 Governing equations

The governing equations employed in NavyFOAM vary depending on the top-level solver. sRansFOAM employs single-phase, incompressible Reynolds-averaged Navier-Stokes equations that comprise the continuity equation, the momentum equations, and the turbulence equations. The governing equations for two-phase flows adopt a homogeneous mixture formulation based on the concepts of phase indicator and weighted averaging or filtering of the original Navier-Stokes equations. In this formalism, compositions of individual phases are represented by their volume-fractions. Modeling of cavitation can be accommodated in the mixture formulation using mass-source terms in the volume-fraction equation representing phase change between liquid and vapor (Kim *et al*., 2010). Free-surface flows around ship hulls can be considered as a special case of mixture flow with a sharp interface between air and water. The top-level solver for this class of applications is ransFSFOAM**.** The governing equations for free-surface flows are a single set of Reynolds-averaged Navier-Stokes equations. The continuity equation is given by:

$$\nabla \cdot \mathbf{u} = 0 \tag{1}$$

The momentum equation can be written as:

$$\frac{\partial}{\partial t}(\rho \mathbf{u}) + \nabla \cdot \left\{ \rho (\mathbf{u} - \mathbf{u}_g) \mathbf{u} \right\} = \nabla \cdot \left\{ -p\mathbf{I} + \boldsymbol{\tau} \right\} + \rho \mathbf{g} + \Gamma \kappa \mathbf{n}_i \delta_i \tag{2}$$

where the viscous/turbulent stress is determined from:

$$\boldsymbol{\tau} = \mu_{eff} \left(\nabla \mathbf{u} + \nabla \mathbf{u}^T \right) - \frac{2}{3} \mathbf{I} \rho k$$

and $\mu_{eff} = \mu + \mu_t$, with k turbulent kinetic energy, $\mathbf{u}$ the fluid velocity, $\mathbf{u}_g$ the grid velocity, μ_{eff} the effective dynamic viscosity, $\mathbf{g}$ the gravitational acceleration, Γ the surface tension coefficient, κ the curvature of the interface, $\mathbf{n}_i$ the unit-normal to the interface, and δ_i the Dirac delta function defined on the interface.

The mixture properties like density and dynamic viscosity are computed as functions of γ from

$$\begin{aligned} \rho &= \gamma \rho_w + (1-\gamma)\rho_a \\ \mu &= \gamma \mu_w + (1-\gamma)\mu_a \end{aligned} \tag{3}$$

The volume-fraction is obtained solving an advection equation given by:

$$\frac{\partial \gamma}{\partial t} + \nabla \cdot \left\{ \gamma (\mathbf{u} - \mathbf{u}_g) \right\} = 0 \tag{4}$$

3.3 Numerical method

The NavyFOAM solvers employ cell-centered finite-volume spatial discretization which permits use of arbitrarily unstructured polyhedral meshes including hexahedron, tetrahedron, prism, wedge, to name a few. The linear reconstruction gradients for the flow-fields are evaluated for individual elements using least-square fitting of the neighboring cell data. A suite of convection discretization schemes are available. Among them, the second-order upwind scheme (linearUpwind) is both accurate and robust, being adequate for industrial applications. A space-conservation-law (SCL)-complying arbitrary Lagrangian-Eulerian (ALE) approach is used for moving/deforming meshes.

An implicit, segregated, iterative projection algorithm is employed for time-advancement of the solutions. The system of linear equations resulting from the discretized governing equations are solved using a choice from the iterative solvers such as Gauss-Seidel, diagonal incomplete Cholesky (DIC), preconditioned conjugate gradient (PCG), or generalized geometric multi-grid (GAMG) methods.

The runtime-selection feature in OpenFOAM allows one to change on-the-fly the discretization schemes, the solution algorithms, the solver parameters while the solver is running, greatly facilitating solution steering and parametric study.

3.4 Turbulence modeling

OpenFOAM offers a suite of RANSE turbulence models comprising one-equation and two-equation isotropic eddy-viscosity models such as k-ε and k-ω families. All the turbulence models in OpenFOAM are coded using a virtual base class and actual implementations, and packaged in modules (libraries). Like other physical models, a turbulence model can be selected via a runtime-selection table. Top-level RANSE solvers can be assembled without

knowing the details of turbulence models other than their interfaces. Since the virtual base class defines the interface, assembly of top-level client solvers is undeterred by turbulence model development

In NavyFOAM, we have added several more RANSE turbulence models including high-Re and low-Re (transitional flow) versions of Wilcox's 1998 k-ω model. Some changes were also made in the existing RANSE turbulence models to update the models and to improve

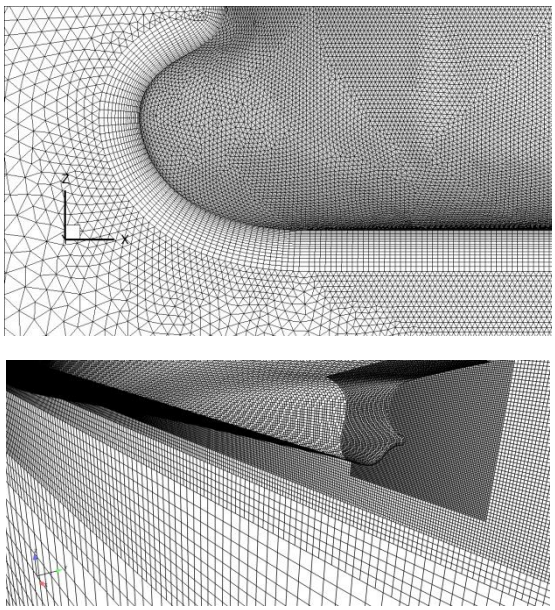

Figure 1. Computational meshes for KVLCC2. Top - unstructured hybrid mesh; bottom – unstructured hexahedral mesh (snappyHexMesh)

their robustness. Two-layer wall function approach (Kim *et al.*, 1998) was also implemented and made available for some selected models to handle both near-wall-resolving ($y^+ = 1$) and wall-function meshes.

3.5 Interface-capturing scheme

As mentioned earlier, NavyFOAM employs a volume-of-fluid (VOF) method for interface-capturing. To that end, Eq. (4), which is a pure convection equation, is numerically solved. Thus, the VOF approach conserves mass (or volumes of individual phases) all the time. OpenFOAM offers numerous advection schemes designed for general transport equations, including high-order upwind schemes. However, their performance in resolving sharp interfaces was largely poor. Several new advection schemes, which blend the pure downwind scheme and high-order upwind schemes were implemented and tested in NavyFOAM. These downwind-blended schemes clearly outperformed the existing advection schemes, resolving water-air interfaces within a single or two cells. The modified HRIC scheme (Muzaferija and Peric, 1998) was among the ones that worked better in terms of accuracy and robustness, and therefore was used in this study.

3.6 Moving mesh method for dynamic sinkage and trim

The solution of the dynamic sinkage and trim of surface ships requires that the body can move relative to the calm-water free-surface plane. Three popular techniques widely used are: (i) overset grid; (ii) deforming mesh; (iii) rigid mesh motion. In this study, we used a ALE-based rigid mesh motion approach, where the entire fluid domain moves in time with the hull in the two degrees-of-freedom. The rigid-mesh motion technique has several important advantages over the other two methods. First, the mesh motion is very easy to calculate. Secondly, this method is robust since the update of the mesh point positions is explicitly evaluated with the rigid-body translation and rotation. The method does not pose any difficulty to the scalability of the overall solution process when using parallel computing. Also, the method is conservative, and no interpolation between grids is needed.

The unsteady RANSE and the volume-fraction equations are solved together with the unsteady dynamical equations of ship motion. The rigid-body equations of ship motion are solved using a mixed explicit/implicit discretization scheme. The grid-flux due to the mesh motion is accounted for in such a way that it complies with the space-conservation-law (SCL).

4. RESULTS

4.1 KVLCC2 (Case 1.1a)

We ran sRansFOAM for this double-body flow case in which the free surface is replaced by a symmetry plane. We deliberately chose to use two unstructured meshes to

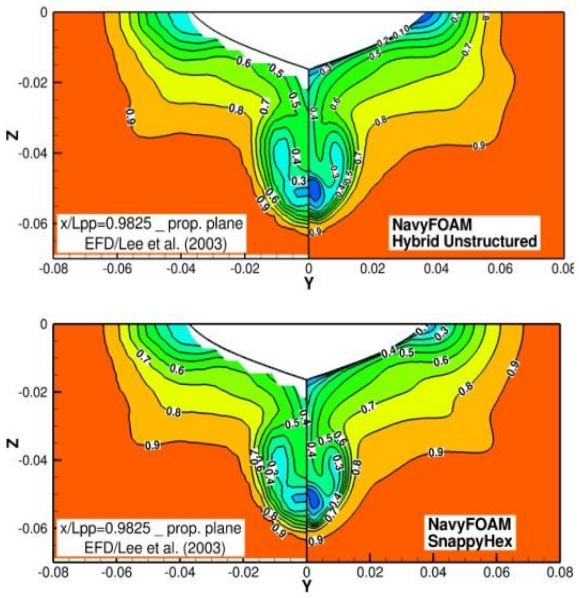

Figure 2. Contour of axial velocity at $x/L = 0.9825$ predicted on the two meshes. Top – hybrid (prism + tet) unstructured mesh; Bottom – snappyHexMesh.

evaluate spatial accuracy of the predictions. One of

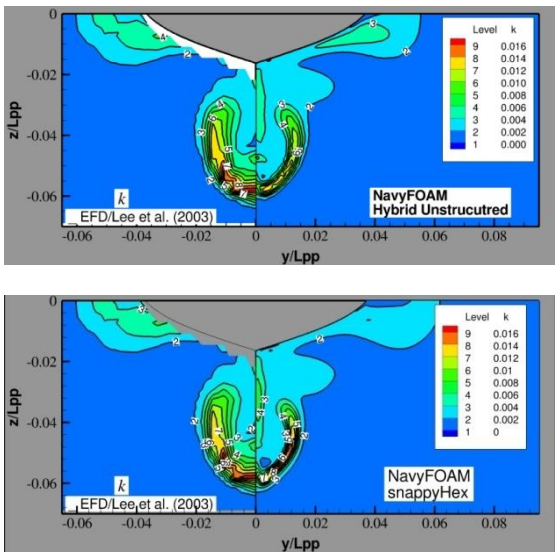

Figure 3. Contour of turbulent kinetic energy at x/L = 0.9825 predicted on t on the two meshes. Top – hybrid unstructured (prism + tet); Bottom - snappyHexMesh

them, shown at the top of Figure 1, is a hybrid unstructured mesh generated using SolidMesh developed at the SimCenter of the Mississippi State University. The

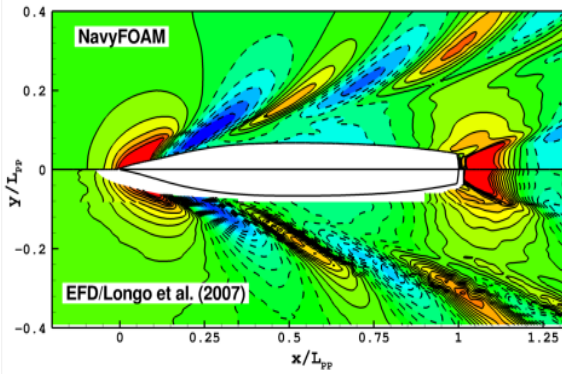

Figure 4. Contour of wave elevation for DTMB 5415 - Case 3.1b , SST k-ω model result on the 6 million cell mesh

mesh consists of prisms with triangular bases near the hull surface and tetrahedra in the rest of the domain. The total cell count is approximately 8 million. The other mesh, shown at the bottom of Figure 1, is a hexahedron-dominant unstructured mesh generated using the snappyHexMesh utility available in the standard OpenFOAM package. With the latter, we put in three-levels of embedded fine-mesh blocks to better resolve the near-body region. Its total number of elements is a little over 3 million. The near-wall mesh resolutions for both meshes are such that the distance from the wall is larger than 40 in wall units ($y^+ > 40$) over the large portion of the hull surface. So, the wall function approach was employed to provide the boundary conditions for the momentum equations and the turbulence equations. Wilcox's k-ω model (Wilcox, 1998) was used for turbulence closure for its good track record for this class of flows (Kim and Rhee, 2002).

The contours of mean axial velocity (U) at the propeller plane (x/L = 0.9823) are shown in Figure 2 for the two meshes. As can be seen, the characteristic shape of the U-contours ("hook"-shaped or "rabbit's ear-like) is closely captured by both meshes. The contours of turbulent kinetic energy at the same plane are depicted in Figure 3. The region of high turbulent kinetic energy, which originates from the upstream boundary layer and overlaps with the region of low axial velocity depicted in Figure 2 is reproduced reasonably well by the computations, although their peak values are somewhat underpredicted. The overall prediction accuracy shown here with the unstructured meshes used in this study is remarkably good and rarely seen in the literature.

4.2 DTMB 5415 – fixed trim and sinkage (Case 3.1b)

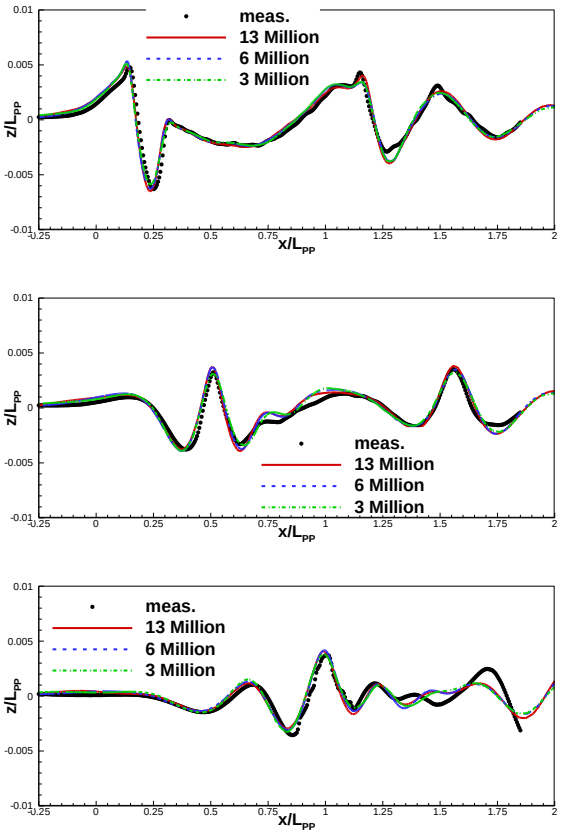

Figure 5. Wave elevations along three longitudinal cuts obtained using SST k-ω model on three different meshes: top - y/L = 0.082; middle - y/L = 0.172; bottom – y/L = 0.301.

The computations were carried out using ransFSFOAM for a single Froude number of 0.28 using

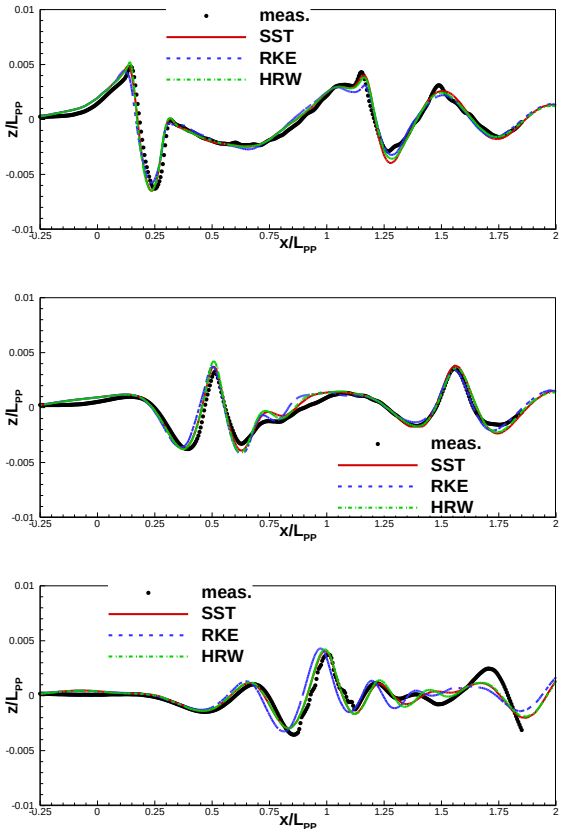

Figure 6. Wave elevations along three longitudinal cuts obtained using three different turbulence models on the 6 million cell mesh : top - y/L = 0.082; middle - y/L = 0.172; bottom – y/L = 0.301.

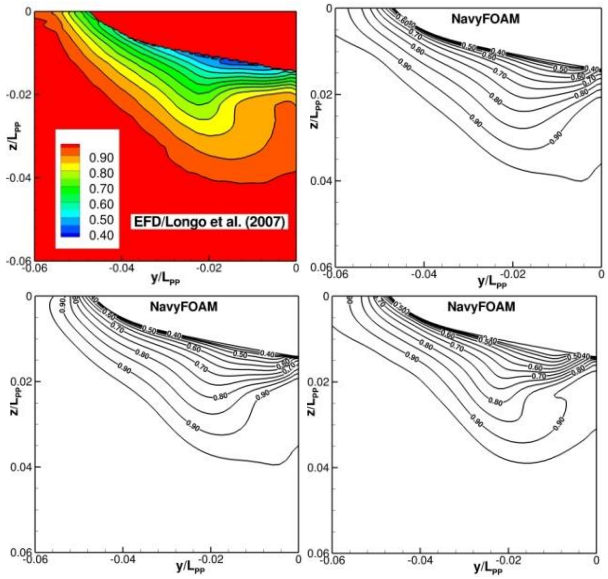

Figure 7. Contour of axial velocity (U) at $x/L = 0.935$ obtained on 6 million cells. Top left - measured; Top right-SST k-ω; Bottom left – realizable k-ε; Bottom right – Wilcox's k-ω

three different isotropic eddy-viscosity based turbulence models including the realizable k-ε (Shih *et al.*, 1995), SST k-ω (Menter 1994) and Wilcox's k-ω (Wilcox, 1998) models. The computational meshes were generated using GridPro (www.gridpro.com), a commercial meshing package well known for high-quality hexahedral meshes. Great care was taken to ensure that such salient features as the hull-generated waves, the boundary layer along the entire hull, and the wake – near-wake at least – be adequately resolved. To check grid-dependency of the solutions, three systematically refined hexahedral meshes were used with 13 million (fine), 6 million (medium), and 3 million (coarse) elements.

Although a time-marching, transient solution algorithm is employed in ransFSFOAM, our goal was to obtain steady-state solutions. An iterative implicit solution algorithm employed in ransFSFOAM greatly accelerated solution convergence by allowing us to use a fairly large time-step size ($\Delta t = 0.02\ L/U_0$). The transient computations were continued for sufficiently long periods of time until not only the global quantities such as the forces and moments acting on the hull but also other flow features like wave elevation, hull boundary layer and wake, all reach steady states.

Figure 4 illustrates the wave pattern predicted with the SST k-ω model result on the 6 million cell mesh, along with the measured one. Figure 5 shows the wave elevations along the three longitudinal cuts (y/L = 0.082, 0.172, 0.301) obtained using SST k-ω model on all three meshes. First of all, the results indicate grid-convergence of the predictions, all of which are in excellent agreement with the data. The results obtained using three different turbulence models on the medium (6 million cell) mesh are shown in Figure 6. The differences among the three results are measurable yet small. The realizable k-ε model results appreciably deviate from the other two k-ω model results.

Figure 7 shows the contours of axial velocity at x/L = 0.935 obtained using the three turbulence models on the 6 million cell mesh. All three turbulence models capture the gross feature of the boundary layer - the distorted velocity contours reflecting thickening of the stern boundary layer due to convergence of wall-limiting streamlines, and also the ensuing vortex sheet, the degree of which varies model to model. The prediction by Wilcox's k-ω model (the bottom-right figure) seems to be the closest to the measurement.

4.3 DTMB 5415 model – dynamic sinkage and trim (Case 3.2)

The dynamic sinkage and trim computations were carried out using ransFSDyMFOAM on a 1.5 million-cell hexahedral mesh for three different Reynolds numbers and the corresponding Froude numbers; $Re = 5.96 \times 10^6$, 1.19×10^7, 1.75×10^7, $Fn = 0.138, 0.28, 0.41$, respectively. As outlined earlier, unsteady RANSE was solved along with the equations of 2-DOF (heave and pitch) ship motion. The transient runs were continued until the resistance, the trim angle, and the sinkage reach statistically steady states. The time-averaged resistance, trim, and sinkage are shown in Figure 8 along with the experimental data. Despite the relatively coarse mesh

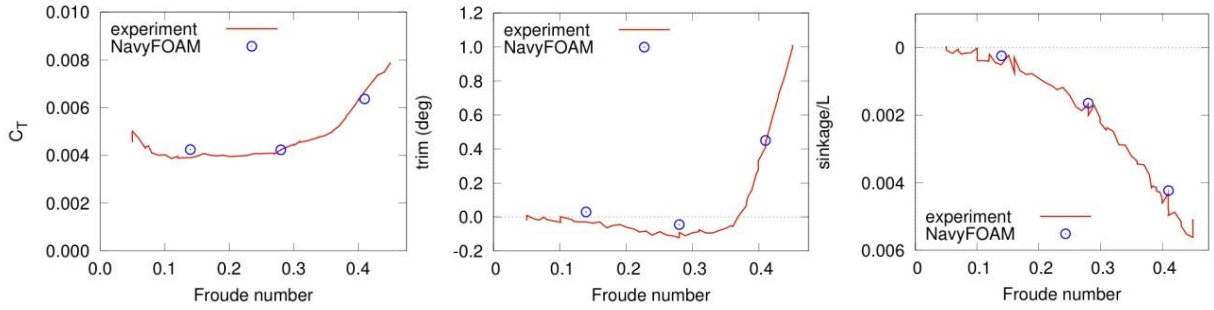

(a) sheet cavity at

Figure 8. Prediction of sinkage and trim for the DTMB 5415 model - total resistance (left), trim (center), and sinkage (right)

used in this study, the predictions are in fair agreement with the measurements.

5. CONCLUSION

A multiphase CFD capability aimed at ship hydrodynamics applications has been developed using a modern software engineering approach based on objected-oriented programming. The computations were carried out using the capability for a number of cases selected from the workshop problems, including the DTMB 5415 model and the KVLCC2 model. The following conclusions can be drawn from this study.

- The present multiphase RANSE approach based on the volume-of-fluid method, when used on meshes with adequate resolution and accurate 2nd-order numerics can predict most of the salient features of turbulent free-surface flows around surface ships with a remarkably good accuracy.
- Unstructured meshes, when used with appropriate 2nd-order numerics and turbulence models, can predict turbulent flows around ship hulls with accuracy largely comparable to that provided by structured meshes, holding a promise for naval applications involving complex geometry such as fully-appended ships.

6. ACKNOWLEDGEMENT

This effort has been mainly funded by the Department of Defense High Performance Computing Modernization Program (HPCMP) under the CREATE Ship's Hydrodynamics Program. The development of the software used in this study has greatly benefited from the waterjet project supported by Dr. Ki-Han Kim at the Office of Naval Research. Special thanks go to Dr. Peter Eiseman for providing the GridPro grids for the DTMB 5415 model, and to Delaney Keegan at NSWCCD for providing the KVLCC2 mesh.

REFERENCES

Kim, S.-E., Mathur, S. R., Murthy, J. Y., Choudhury, D., (1998) "A Reynolds-Averaged Navier-Stokes Solver Using Undstructured Mesh-Based Finite-Volume Scheme," AIAA Paper 98-0231.

Kim, S.-E. and Rhee, S. H., (2002) "Assessment of Eight Turbulence Models for a Three-Dimensional Boundary layer Involving Crossflow and Streamwise Vortices," AIAA Paper 2002-0852.

Kim, S.-E., Schroeder, S. and Jasak, H., (2010), "A Multiphase CFD Framework for Predicting Performance of Marine Propulsors," Thirteenth international Symposium on Transport Phenomena and Dynamics of Rotating Machinery, Honolulu, Hawaii, April 4 -9, 2010.

Lee, S.-J., Kim, H.-R., Kim, W.-J., and Van, S.-H., (2003), "Wind tunnel tests on flow characteristics of the KRISO 3,600 TEU containership and 300K VLCC double-deck ship models", J. Ship Res., Vol. 47, No 1, pp. 24-38

Longo, J., Shao, J., Irvine, M., and Stern, F. (2007), "Phase-Averaged PIV for the Nominal Wake of a Surface Ship in Regular Head Waves," ASME J. Fluids Eng, Vol. 129, pp. 524-540.

Menter, F. R., (1994), "Two-Euqation Eddy-Viscosity Turblence Models for Engineering Applications," AIAA J., Vol.32, No.8, 1994, pp.1598-1605.¥

Muzaferija S. and Peric M., (1998), "Computation of free surface flows using interfacetracking and interface-capturing methods," vol. 3, Computational Mechanics Publications, WIT Press, South Hampton, nonlinear water wave interaction edition 1998. pp. 59–100.

Shih, T.-H., Liou, W.W., Shabbir, A., and Zhu, J., "A New k-ε Eddy-Viscosity Model for High Reynolds Number Turbulent Flows - Model Development and Validation," *Computers & Fluids*, Vol. 24, No. 3, pp. 227-238, 1995.

Weller, H. G., Tabor, G., Jasak, H., and Fureby, C., "A Tensorial approach to computational continuum mechanics using object-oriented techniques," *Computers in Physics*, 12(6), pp. 620 – 631, 1998.

Wilcox, D. C., Turbulence Modeling for CFD, 2nd edition, DCW Industries, Inc., 1998.

FLOW SIMULATIONS USING NAVIER-STOKES SOLVER SURF

Takanori HINO (National Maritime Research Institute, Japan)
Kunihide OHASHI (National Maritime Research Institute, Japan)
Hiroshi KOBAYASHI (National Maritime Research Institute, Japan)

1. SUMMARY

The unstructured grid Navier-Stokes solver *SURF* is applied to various test cases, which include a double model flow around KVLCC2, towed and propelled free surface flows around KCS and a steady free surface flow and wave diffraction for DTMB 5415. For free surface modeling, a single-phase level-set method is adopted. Turbulence models used are the Explicit Algebraic Stress Model and Modified Spalart-Allmaras model. The propeller effect is taken into account by a body force model. It is shown that flow features of each case are well captured by the present solver with proper models.

2. FLOW SOLVER

The CFD method used is called *SURF* (Hino 1997, 1999), which is under development at National Maritime Research Institute. This solver employs unstructured grids and has capability of handling complex geometry. The governing equations of the present method are 3D Reynolds averaged Navier-Stokes equations for incompressible flows. Artificial compressibility approach is used to velocity-pressure coupling. Spatial discretization is based on a finite-volume method for an unstructured grid. A cell centered layout is adopted in which flow variables are defined at the centroid of each cell and a control volume is a cell itself.

The inviscid fluxes are evaluated by the second-order upwind scheme based on the flux-difference splitting of Roe. The evaluation of viscous fluxes is also second-order accurate. In case of unsteady flow simulations, a dual time stepping approach is used in order to recover incompressibility at each time step. It consists of the second order two-step backward scheme for the physical time stepping and the first order Euler implicit scheme for the pseudo time. In case of unsteady flow cases, the real time stepping is omitted. The linear equation system is solved by the symmetric Gauss-Seidel (SGS) method Multigrid method and local time stepping for the pseudo time are adopted for the fast convergence.

For free surface treatment, an interface capturing method using a single phase level set approach is employed.

Turbulence models implemented are the one equation model of Spalart-Allmaras and its modified version and two equation models based on k-ω and the Explicit Algebraic Stress Model (EASM). A body force model is employed to take into account a propeller effect. The body force distributions are calculated using a simplified propeller theory (Moriyama 1979).

3. TEST CASE 1.1a

The first test case is the comparison of a double model flow around KVLCC2 with the measurements in the wind tunnel. Flow details which include wake flows and Reynolds stress components are compared.

Computational grid is shown in Fig.1 and 2. The grid is generated by the commercial software *HEXPRESS*. Computational grid is consisted of 5.27 million hexahedra cells. Computational domain is set as $-1.0 \leq x/L_{pp} \leq 2.5, -1.0 \leq y/L_{pp} \leq 0.0, -1.0 \leq z/L_{pp} \leq 0.0$. The origin of the grid is set at a position where the fore perpendicular(FP) is crossed a water plane(z=0) at center plane(y=0). The minimum spacing on the wall is set as 3.7×10^{-6}. Explicit Algebraic Stress Model(EASM) (Deng et al. 2003, 2005) is used in this test case.

Fig.3 to 5 show the computed and measured normal-stress components $\overline{u_i'u_i'}$ and plotted their maximum values in the field. Computed results show similar distributions with measurements.

The relation of three components of the maximum Reynolds normal-stresses becomes $\overline{u'u'} : \overline{v'v'} : \overline{w'w'} = 0.017 : 0.009 : 0.010$ for the computed results, while in the measurement, the relation becomes $\overline{u'u'} : \overline{v'v'} : \overline{w'w'} = 0.018 : 0.011 : 0.010$.

Although the computed maximum values for each component are smaller than the measurement, the present computation with a non-linear turbulence model can simulate anisotropic relation in each components. The maximum value of the component $\overline{v'v'}$ of the measurement take place in y-symmetry plane,

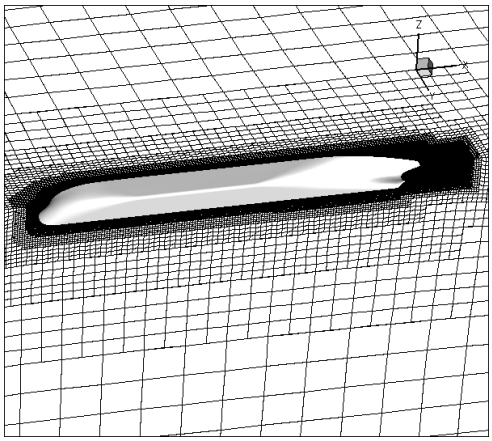

Fig. 1 Computational grid (over view)

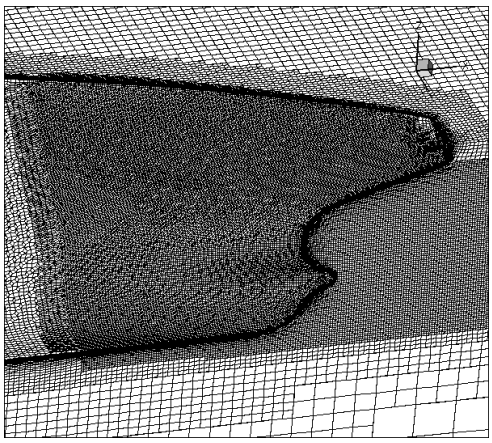

Fig. 2 Computational grid (near stern)

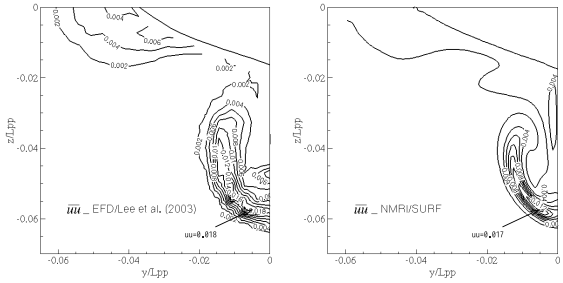

EFD CFD

Fig. 3 Normal-stress component $\overline{u'u'}$

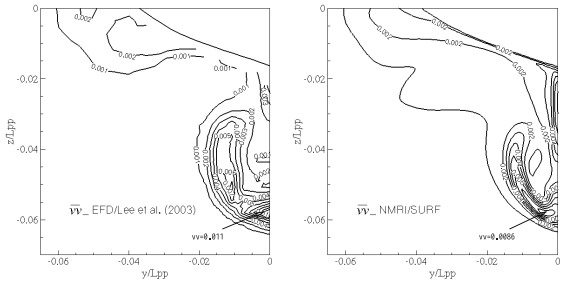

EFD CFD

Fig. 4 Normal-stress component $\overline{v'v'}$

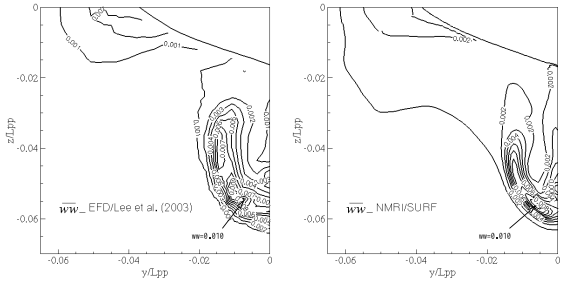

EFD CFD

Fig. 5 Normal-stress component $\overline{w'w'}$

which means the presence of the cross flows in the y-direction at $y = 0$. The present computation assumes the y-symmetry condition. Thus, no-cross flows are permitted in y-symmetry plane and which yields smaller $\overline{v'v'}$ component.

The flow velocity in the region near a y-symmetry plane and $r/R < 0.6$ is smaller than the measurement. This difference is caused by flow separations in the near stern end(Fig.6). The phenomena is dependent on the grid resolution and the turbulence model. The present computation with locally refined hexahedra cells is considered to have enough resolution in this region. Thus EASM produces large eddy viscosity in this region.

4. TEST CASE 2.1

Test Case 2.1 is for a free surface flow simulation around KRISO Container Ship (KCS) without a rudder in the fixed even keel condition with Froude number, $Fn = 0.26$ and Reynolds number, $Rn = 1.4 \times 10^7$. For a turbulence model, modified Spalart-Allmaras model is used. For the grid study, four grids with different density are generated using the commercial software *Gridgen*. Grid topology is O-O and the computational domain is $-1.5 \leq x/L_{pp} \leq 3.5$, $-2.0 \leq y/L_{pp} \leq 0.0$ and $-1.98 \leq z/L_{pp} \leq 0.0183$, where FP is located at $x = 0$ and the still water level is at $z = 0$. Table 1 shows the summary of grid parameters, where N, id, jd, kd are a total cell number and a cell number in i (longitudinal), j (girth) and k (outward) directions, respectively. Δ is the minimum grid spacing in k or i direction.

Fig.7 depicts the comparison of pressure distributions on hull surface and free surface for each grid. The pressure on free surface is defined as h/Fn^2, where h is wave height and Fn is Froude number. As expected, the more detailed features can be captured in the finer grids and numerical dissipation of wave amplitude away from the hull is apparent in the coarser grids.

Fig.8 is the comparison of wave profiles along a ship hull. As grids becomes finer, the bow wave crest becomes higher and the following shoulder wave is re-

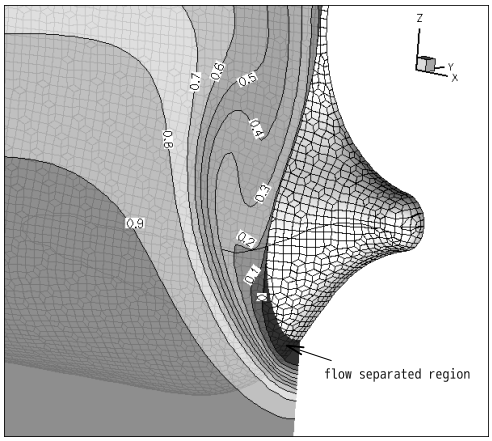

Fig. 6 Computational grid (near stern)

solved more clearly. However, the bow wave crest is under estimated and the stern wave is overestimated compared with the EFD data even in the finest grid (G1).

Computed resistance components are listed in Table 2. Although total resistance Ct and pressure resistance Cp show convergence with grid refinement, total resistance decreases and departs from the measured data as a grid becomes finer. One reason for this trend is the use of modified Spalart Allmaras turbulence model. In fact, other computations with this model generally show resistance values lower than measured data due to the excessive flow separations.

Table 1 Grid parameters

	N	id	jd	kd	$\Delta_{k=1}$	$\Delta_{i=1,id}$
G1	4,866,048	352	64	216	7.1e-7	1.4e-3
G2	1,867,776	256	48	152	1.0e-6	2.0e-3
G3	601,344	174	32	108	1.4e-6	2.8e-3
G4	311,296	128	24	76	2.0e-3	4.0e-3

Table 2 Computed resistance components

	Ct$\times 10^3$	Cp $\times 10^3$	Cf$\times 10^3$
EXP	3.56	—	2.830*
G1	3.366	0.6061	2.760
G2	3.378	0.6461	2.732
G3	3.454	0.7415	2.713
G4	3.584	0.9093	2.675

$C_* = R_*/0.5\rho U^2 S$ * Cf0:ITTC1957

5. TEST CASE 2.3a

Test Case 2.3a is for a free surface flow simulation around KRISO Container Ship (KCS) without a rudder in a self-propulsion condition. Reynolds number

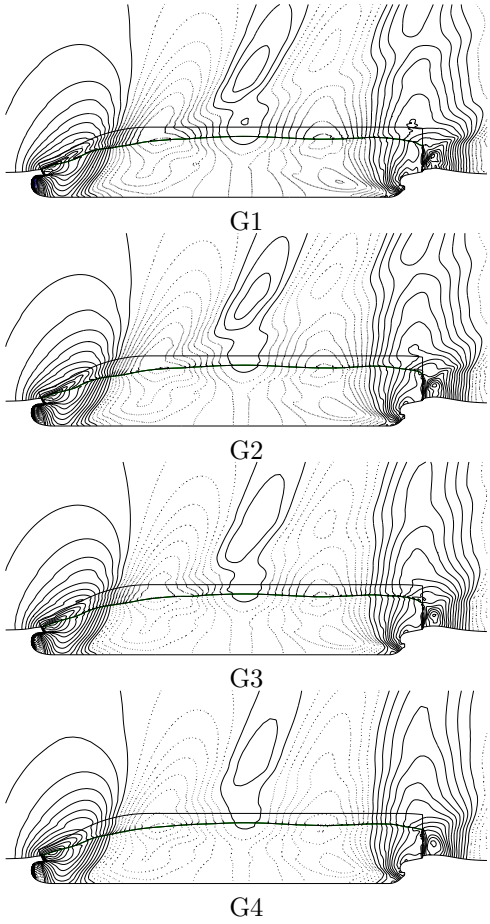

Fig. 7 Pressure distributions on hull surface and free surface

and Froude number are the same as the previous case. Grids used are mirrored in y from the G2, G3 and G4 grids in Table 1.

Computed self propulsion factors with the finest G2 grid are listed in Table 3 The thrust deduction factor t is overestimated by the present computation, while the wake fraction w_T shows good agreement with the measured data. The other factors associated with a propeller performance differ from the data. This is partly due to the propeller model adopted. Fig.9 depicts the comparison of propeller open water characteristics of the model propeller KP505. It is obvious that the computed curves of K_T and K_Q do not reproduce well the measured results.

Fig.10 shows the computed distributions of velocity u on the center plane both in towed and propelled conditions. Flow acceleration due to the propeller can be observed clearly.

The comparison of stern wave contours between towed and propelled conditions is shown in Fig.11. Flow acceleration due to a propeller amplifies the wave height behind a ship. Also seen is the asymmetric wave pattern in the propelled case, which indicates the effect of swirling flow in a propeller slipstream.

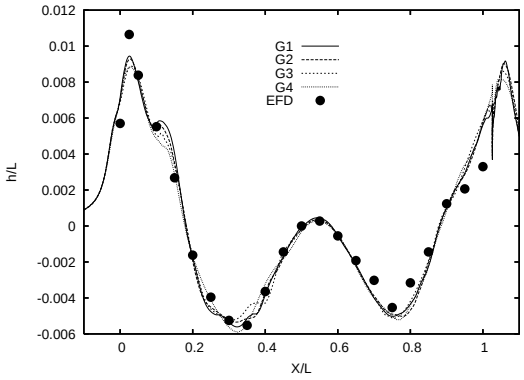

Fig. 8 Comparison of computed wave profiles

Table 3 Self propulsion factors of computation and measurement (at SRI).

Factors	Computed	Measured
$1-t$	0.829	0.85
$1-w_T$	0.787	0.79
K_T	0.181	0.17
K_Q	0.033	0.029
η_0	0.664	0.682
η_R	1.00	1.01

These plots show that the present method can capture flow features of propeller-hull interaction reasonably well.

6. TEST CASE 3.1b

This test case is for the steady free surface flow around DTMB 5415. Computational grid is shown in Fig.12 and 13. The grid is generated by *Gridgen*. Computational grid is consisted of 2.69 million hexahedra cells. Computational domain is set as $-1.5 \leq x/L_{pp} \leq 3.0, -2.0 \leq y/L_{pp} \leq 0.0, -1.96 \leq z/L_{pp} \leq 0.04$. The origin of the grid is set at a position where the fore perpendicular(FP) is crossed a water plane(z=0) at center plane(y=0). The averaged spacing on the wall is set as 5.82×10^{-6}. EASM(Deng et al. 2003, 2005) is used in this section as well.

Fig.14 to 16 show the computed and measured normal-stress components $\overline{u_i'u_i'}$ and plotted their maximum values in the field. Computed results are slightly larger than the measurement results.

The relation of three components of the maximum stresses becomes $\overline{u'u'} : \overline{v'v'} : \overline{w'w'} = 0.0053 : 0.0036 : 0.0033$ for the computed results, and in the measurement, the relation becomes $\overline{u'u'} : \overline{v'v'} : \overline{w'w'} = 0.0031 : 0.0015 : 0.0014$. Also, at the point near the measurement point, the relation of the computed results becomes $\overline{u'u'} : \overline{v'v'} : \overline{w'w'} = 0.0041 : 0.003 : 0.0026$.

Although the computed maximum values for each component are larger than the measurement, the present computation with the non-linear turbulence model can simulate the similar anisotropic relations in each components. From the point of view in the relation of three components, the maximum value of the component $\overline{u'u'}$ in the computation seems smaller than that in the measurement. Further improvement of the turbulence model is still required.

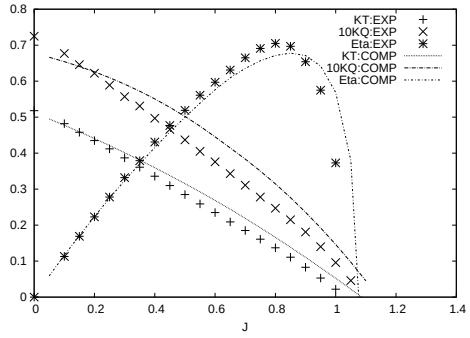

Fig. 9 Comparison of propeller open-water characteristics (KP505)

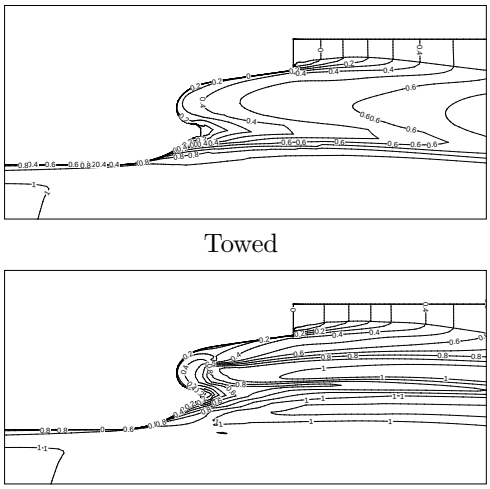

Towed

Propelled

Fig. 10 Comparison of u velocity at $y=0$ in towed and propelled conditions

7. TEST CASE 3.5

This is a dynamic case of wave diffraction for DTMB 5415. The computational grid is generated by *Gridgen* and consisted of 1.72 million hexahedra cells. Computational domain is set to $-1.5 \leq x/L_{pp} \leq 3.0, -2.0 \leq y/L_{pp} \leq 0.0, -1.96 \leq z/L_{pp} \leq 0.04$. The origin of the grid is set to a position where the fore perpendicular(FP) is crossed a water plane(z=0) at center plane(y=0). The averaged spacing on the wall is set as 3.38×10^{-6}. Again, EASM closure is used in this case.

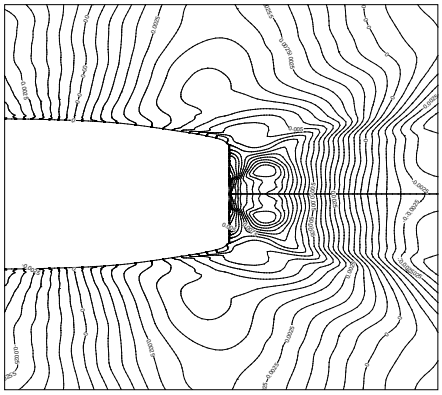

Towed

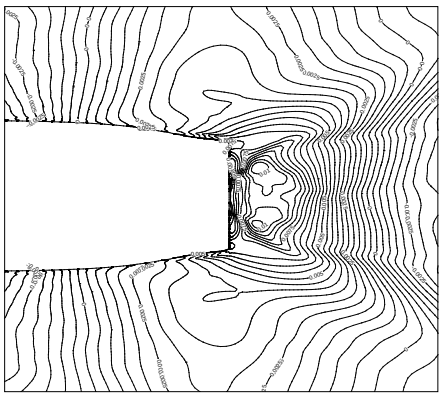

Propelled

Fig. 11 Comparison of stern waves in towed and propelled conditions

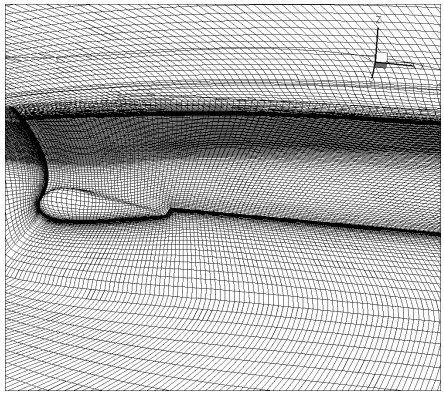

Fig. 12 Computational grid (fore part)

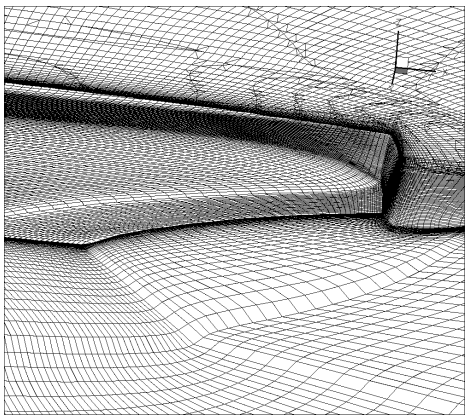

Fig. 13 Computational grid (aft part)

Since coupling between pressure and a velocity field is based on artificial compressibility approach in the present solver, dual time stepping method is used for a unsteady simulation. A maximum number of iteration in pseudo time to satisfy the continuity equation at each physical time step is set to be 15 in the present study. The non-dimensional physical time step size is set to $\Delta t = 0.005$. At first, a steady simulation without incident wave is carried out and a converged solution is obtained. Then the unsteady simulation with incident wave starts from the steady state results. The computation runs until the flow field becomes periodic in time.

Fig.17 shows the instantaneous wave height around the hull. It can be clearly seen that the incident wave and its diffraction due to the hull.

Fig.18 shows the comparison of the first phase of u-velocity at $x/L_{pp} = 0.935$. The difference between the computation and measurement is observed in the first phase of the velocity u as well as the other components v and w. In the analysis of EFD data, in case the first amplitudes is less than 10% of the maximum values, the first phase values of (u, v, w) are replaced by the values of $(0,\ \pi/3,\ -\pi/2)$, respectively. However, the maximum values of each component in EFD are not clear from the original paper (Long et al. 2007). On the other hand, the first phase values in the present CFD data are computed for all the field and this yields the difference between the computed and measured results.

8. CONCLUSION

The unstructured grid Navier Stokes Solver *SURF* is applied to viscous flows around three ship hulls, KVLCC2, KCS and DTMB 5415.

The first case is for a double model flow around KVLCC2. It is shown that Explicit Algebraic Stress Model (EASM) used for a turbulence closure can capture not only an averaged velocity field but also Reynolds stresses behind a blunt ship's stern.

The second and third cases are for free surface flows around KCS and the former is towed and the latter is propelled conditions. In the towed condition case, the use of a fine grid of 4.9 million cells makes it possible to predict the free surface shape well, although resistance is under-estimated possibly due to the turbulence model used, that is, Modified Spalart-Allmaras model. In the self-propulsion condition, the present body force model for propeller effect works reasonably well to capture flow features behind an operating propeller.

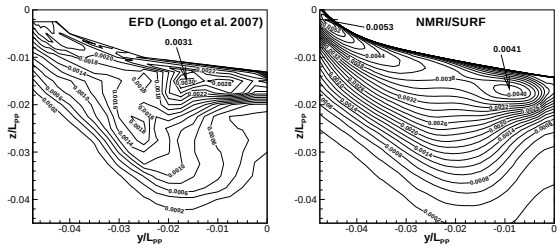

EFD CFD

Fig. 14 Normal-stress component $\overline{u'u'}$

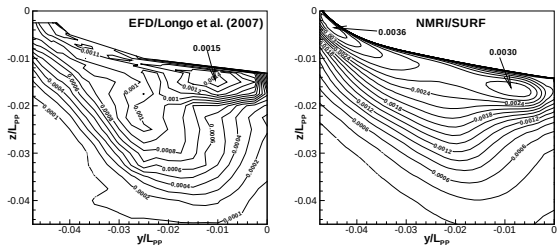

EFD CFD

Fig. 15 Normal-stress component $\overline{v'v'}$

The fourth case is for a free surface flow around DTMB 5415. The EASM closure is successfully applied to the flow field of a fine ship as well.

The last case is the wave diffraction problem around DTMB 5415. It is shown that the unsteady free surface flow can be computed by using the dual time stepping scheme.

Through these test cases, capability and applicability of the solver *SURF* have been demonstrated.

9. Acknowledgments

The authors gratefully acknowledge the valuable discussions with Dr.Michel Visonneau and the members of Laboratoire de Mécanique des Fluides of ECN regarding the development of EASM while the one of the authors (KO) was staying in ECN.

The part of this study is conducted with the support by Grant-in-Aid for Scientific Research (A) 21360439 from Japan Society for the Promotion of Science.

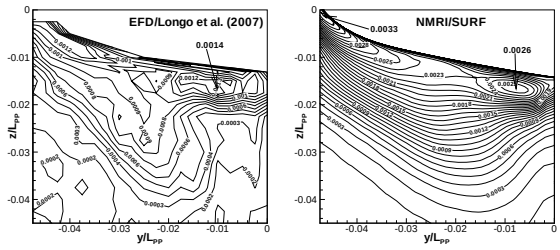

EFD CFD

Fig. 16 Normal-stress component $\overline{w'w'}$

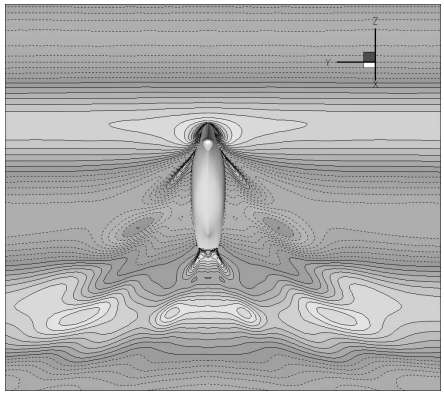

Fig. 17 Instantaneous wave elevation with wave motion

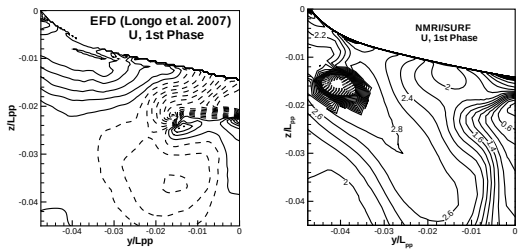

EFD CFD

Fig. 18 Comparison of first phase of velocity component u

REFERENCES

Hino, T., (1997)" A 3D Unstructured Grid Method for Incompressible Viscous Flows", J. of the Soc. Naval Archit. Japan, Vol.182

Hino, T., (1999), "An Interface Capturing Method for Free Surface Flow Computations on Unstructured Grids", J. of the Soc. Naval Archit. Japan , Vol.186

Moriyama, F., (1979), "On an Approximate Numerical Method for Estimating the Performance of Marine Propellers"(in Japanese), Papers of Ship Research Institute, Vol.16, No.6

Deng, G.B. and Visonneau, M., (2003), "On the prediction of swirling induced recirculation", 3rd Int. Sym. on Turbulence and Shear Flow Phenomena

Deng, G.B., Queutey, P. and Visonneau, M., (2005), "Three-dimensional flow computation with Reynolds stress and algebraic stress models", Proceedings of ERCOFTAC Int. Symp. on Eng. Turb. Modeling and Meas., pp.389-398.

Longo, J., Shao, J., Irvine, M., and Stern, F. (2007), "Phase-Averaged PIV for the Nominal Wake of a Surface Ship in Regular Head Waves", ASME J. Fluids Eng, Vol. 129, pp. 524-540.

COMPUTATION OF SINKAGE AND TRIM OF A BARE-HULL 5415 AT THREE FROUDE NUMBERS

Mark Hyman
Naval Surface Warfare Center – Panama City
United States

1. INTRODUCTION

The correct evaluation of ship sinkage and trim while underway is critical not just to obtain accurate information regarding powering requirements but also in determining flow details in the near field that may not have a large influence on resistance but are of interest for other reasons. Vortex shedding (frequency and strength) and bow and shoulder wave breaking are two examples though there are many others. As part of the Gothenburg 2010 workshop, sinkage and trim of the model 5415 hull form was computed at three Froude numbers (0.138, 0.28 and 0.41) using Version 4.5 of the CFDSHIP-Iowa Free-surface RaNS solver. Finding the equilibrium sinkage and trim position (as well as resistance components) at each Froude number was accomplished through the use of dynamic overset grids and relies on the SUGGAR software package to perform block-to-block communication. Influence of hull orientation at different Froude numbers on sonar dome and keel vorticity is also examined.

2. Solver

The solver used in the present work is Version 4.5 of the free-surface RaNS solver CFDSHIP-Iowa (Huang, et. al, 2008). This unsteady, semi-coupled, two-phase, level-set solver uses a structured, non-orthogonal, multi-block grid to solve the discretized RaNS equations in both the air and water phase, though in this application, the code was used as a single-phase solver. The air-water interface is "captured" with a level-set formulation coupled with interface sharpening.

In all the solutions presented, a fourth-order upwind scheme for the convection terms in the momentum equations and a second-order central scheme for diffusion terms was used. The level-set solution was obtained via second-order upwind differencing. The pressure poisson equation is solved with a projection method.

Ship sinkage and trim are obtained by applying moving overset grids. With this methodology, several sets of grid block are constructed, One grid set is fastened to the hull (which is resolved with a body-fitted grid) and moves within a second, background, set of grids. Grids are moved in a two step process. First hull surface forces and moments are computed and used to estimate a new hull orientation based on the flow field computed at the current time step. Then, the hull grid set is moved inside the background grid set and a new set of second order interpolation coefficients between the hull-fixed and background grids are computed using the SUGGAR (Nowak, 2005) library of routines. In the present case, the hull-fixed grids were allowed to move in heave and pitch as well as in surge (prescribed at the steady ship speed). The background grids moved at the prescribed surge speed only. Grids were moved using an explicit, first-order solver with an eight point filter. This is a reasonable and cost-effective choice for obtaining the steady-state hull orientation at a given speed. Another 6DOF methodology might be better suited for unsteady motion. Once the new set of block-to-block interpolation coefficients are available, the process of computing a flow field with the new hull orientation at the next time step can begin

3. Gridding methodology

Grid construction and assembly was undertaken with the desire to resolve waves near the ship hull (not the breaking region) and to capture the sonar dome vortex. This resulted in a four block system – shown in Figure 1 with sizes given in Table 1. Two blocks were hull-fixed; one is a hull boundary layer block, shown in blue, and the second is a refinement block, shown in green, placed just below the keel to resolve the dome/keel vortex. These blocks are straightforward to locate and construct since the fluid phenomena is known. In an effort to use the same grid for all cases, the axial resolution of both the hull grid and near-surface grid were tightened to capture the short wavelengths occurring at low Froude number.

Table 1 Grid sizes

Block 1	3736175
Block 2	1828575
Block 3	12109801
Block 4	5207085

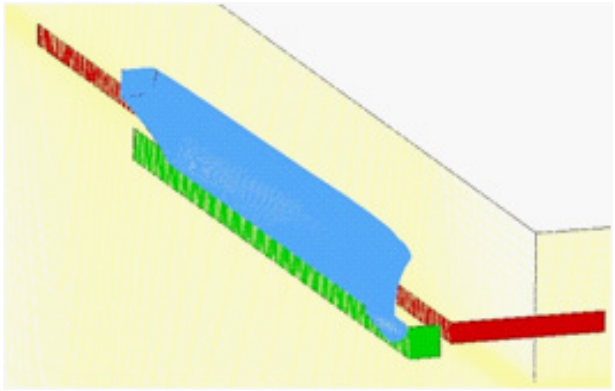

Figure 1 Grid layout for all runs

A second set of blocks was used as the background system, one to resolve the near-hull wave system, shown in red, and a second, shown in yellow, to satisfy the far-field boundary conditions. Less attention was given to resolving the transom flow and no refinement block was placed there. Resolution of near-hull waves is less straightforward without prior knowledge of the wave system and there is a trade-off between block complexity and size. Application of a surface-capturing method requires high grid density, particularly in the vertical direction, to locate the free surface. In the case of a highly deforming free surface, this means that a finely spaced grid must be used over the entire anticipated range of free-surface elevation. At higher Froude numbers, this vertical range can grow large. In addition, the longitudinal structure of the wave field must be considered. At different Froude numbers, wave peaks will be at different locations and there will be different numbers of peaks, so a grid intended for application over a range of Froude numbers, as this one was, must maintain acceptable longitudinal density along the entire hull length. Since there is no need, in the present work, to resolve the wave field away from the hull, the free-surface refinement block is finest in the lateral direction near the hull but resolution in that direction is reduced quickly beyond about y/L = 0.075.

4. Convergence

Convergence to a steady-state value was expected to be ensured by requiring that the change in all metrics (resistance and hull position) be reduced to a given low value. In practice some metrics, such as skin friction and trim angle, reached a low value fairly quickly while other metrics, such as wave drag and sinkage, required many more time steps. In addition, the shorter waves associated with the lower Froude number (0.138) led to a high frequency oscillation in hull position that was slow to damp. As a result, hull location and wave resistance at the lowest Froude number was assessed by averaging the last period of oscillation even though steady state had not been achieved.

5. Results

Results of the calculation are provided in this section. Here the focus is on both the sinkage and trim results and the ability of the code/grid system to capture and maintain the sonar dome and keel vortices. Overall results are given in table 2 which provide sinkage, trim and components of resistance together with percent error based on measured data. Generally, agreement was good with the exception of sinkage where errors on the order of 10% were observed at all Froude numbers.

Table 2 Tabulated computational results

Froude Number	Sinkage	Trim	Skin Friction	Wave Resistance	Total Resistance
0.138	-0.000435 13.6	-0.027 -3.8	0.00323 1.8	0.000560 7.4	0.00379 2.5
0.28	-0.00201 10.4	-0.116 7.7	0.00291 0.2	0.00147 11.3	0.00438 -3.5
0.41	-0.00538 14.4	0.448 6.4	0.00270 0.9	0.00366 6.9	0.00637 4.5

5.1 Results for Fr=0.138

Results of the calculations at the lowest Froude numbers are shown in figures 2a and 3a, in which plots of free surface elevations and keel vortical structure respectively are presented Figure 2a shows the expected short wavelength waves generated at low ship speed. Resolution of these short waves near the hull is important in obtaining the correct wave resistance. The relatively large error (7.4%) in this and higher Froude numbers, suggests that the free-surface refinement grid was not sufficiently fine. Hull sinkage error for this and higher Froude numbers was also large, typically on the order of 10% or more. On the other hand, both trim angle and the skin friction drag component were typically in better agreement with measured data.

The axial velocity contour and isosurface vorticity plot in Figure 3a show that this Froude number has the strongest vortical field associated with it. In all cases, the sonar dome vortex is quickly dissipated (whether this is due to an insufficient grid resolution or turbulent dissipation is unclear and will perhaps be answered by calculations with higher resolution). The keel vortex, begins just astern the sonar dome and becomes very pronounced in the propeller region near the transom.

5.2 Results for Fr=0.28

Results of the calculation at Fr=0.28 are shown in figures 2b and 3b with plots of surface elevation and deep vortical structure. In figure 2b, it can be seen that most of the wave field affecting wave drag is localized near the bow. This is true for all the Froude numbers for which computations were done. Astern the bow and shoulder wave, there is little near-hull free-surface deformation. This is likely to be the reason for poor agreement with measured results and bears further investigation. The sonar dome vortex is slightly stronger at this Froude number compared to the 0.138 calculation and the keel vortex is notably weaker though the velocity defect at the propeller plane is roughly equivalent to that seen at Fr=0.138.

5.3 Results for Fr=0.41

Figures 2c and 3c show the same quantities, free-surface elevation and keel-region vorticity The free surface at this speed is dominated by the "rooster tail" astern the transom and the large bow wave and subsequent deep trough in the mid-ship region. The grid is insufficiently dense to resolve the breaking at this and the lower Froude number. The sonar dome vortex is strongest at this speed and the keel vortex weakest indicating that, as trim angle and sinkage increase, deep vortical structures are very much influences. Of additional note is the intense vorticity generated at the transom at this Froude number as well as the completely dry transom (at Fr=0.28, the transom is still slightly wet).

6. Conclusions

Hull orientation (sinkage and trim) and resistance for the 5415 model hull was computed with the CFDSHIP-Iowa Version 4.5 solver coupled with a dynamic overset grid code. Compared to measured data, consistently lower errors were obtained for the trim angle (order 5 %) and skin friction drag (order 1 %) while larger errors were obtained for sinkage (order 10 %) and wave drag (order 8%). Further investigation is warranted for the poorer prediction of the last two metrics to determine if the errors are grid induced.

7. Acknowledgement

This work was performed under the sponsorship of Dr. Patrick Purtell at the Office of Naval Research, Code 333. This support is very gratefully acknowledged.

REFERENCES

Huang, J., Carrica, P. and Stern, F.,"Semi-coupled air/water immersed boundary approach for curvilinear dynamic grids with application to ship hydrodynamics", Intl. J. for Num. Meth. in Fluids, Feb. 2008, 58:591-624.

Nowack, R. "SUGGAR: a General Capability for Moving Body Overset Grid Assembly", AIAA Computational FluidDy

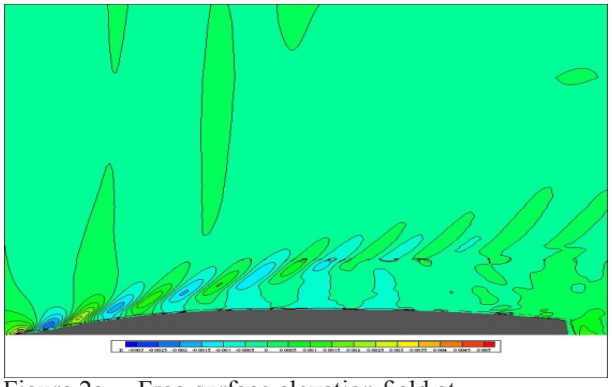

Figure 2a Free-surface elevation field at

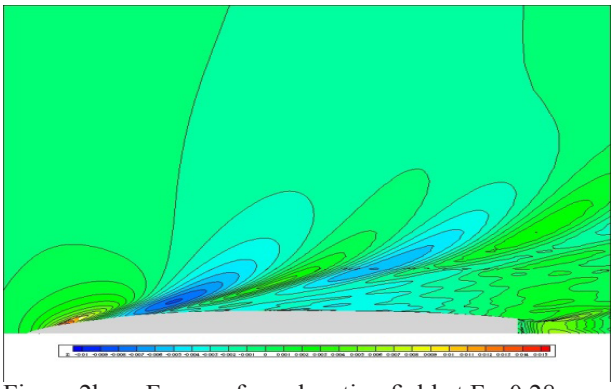

Figure 2b Free-surface elevation field at Fr=0.28

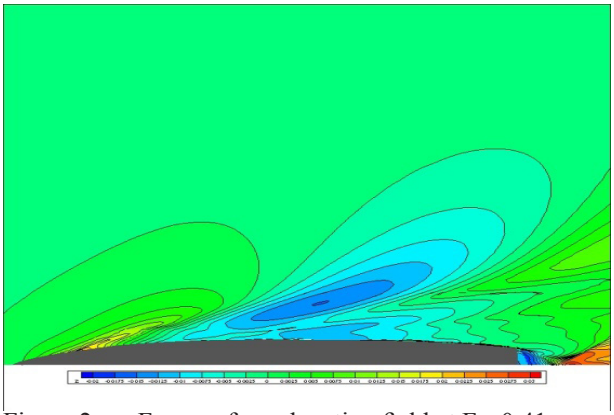

Figure 2c Free-surface elevation field at Fr=0.41

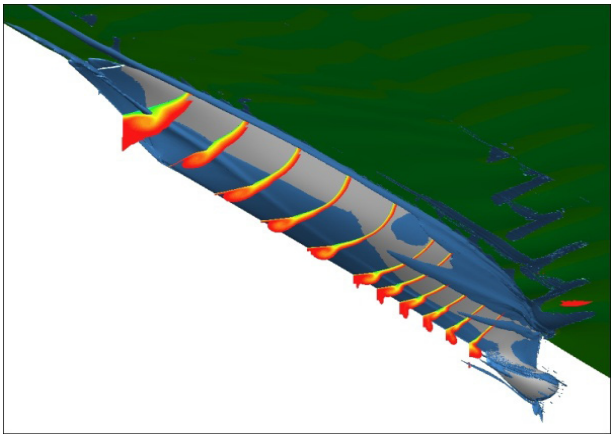

Figure 3a Keel/sonar dome vorticity field at Fr=0.138

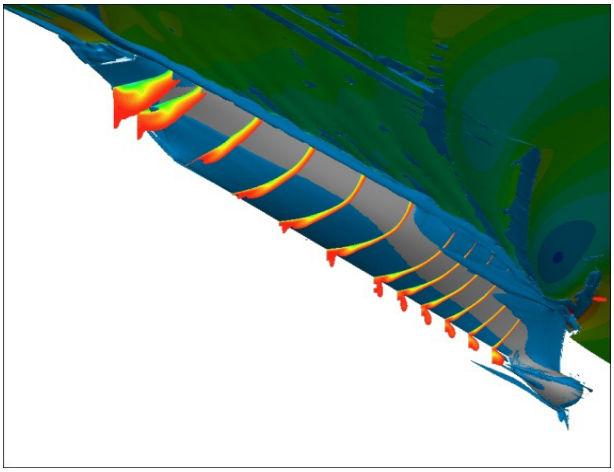

Figure 3b Keel/sonar dome vorticity field at Fr=0.28

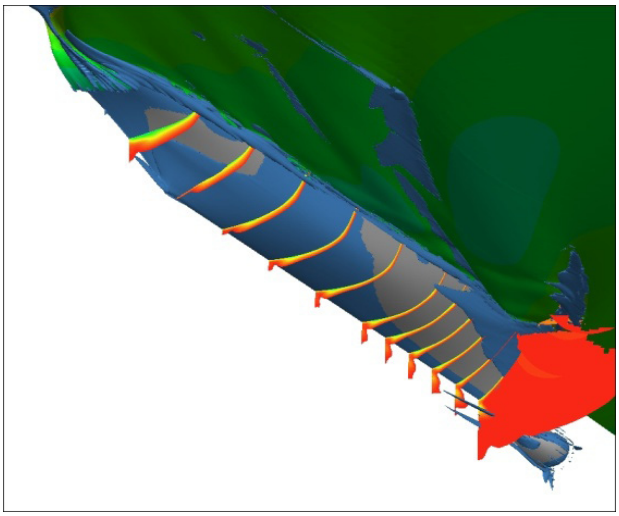

Figure 3c Keel/sonar dome vorticity field at Fr=0.41

COMPUTIONAL STUDY ON SHIP RESISTANCE AND FLOW FIELD OF KVLCC2

Bingjie Guo (Department of Marine Technology, NTNU, Norway)
Sverre Steen (Department of Marine Technology, NTNU, Norway)

ABSTRACT

The accuracy of a CFD calculation of ship resistance and flow field at the stern of the KVLCC2 tanker is studied. Three eddy viscosity models with free surface captured by volume of fluid method (VOF) are employed: the standard *k*-ω model, SST *k*-ω model and Reynolds Stress Model (RSM). The effect of trim caused by ship velocity on the ship resistance is also investigated. Numerical results are compared with the experimental results in terms of ship resistance and flow field. It is shown that the ship resistance and velocity distribution have good agreement with the experimental results, and wave profiles near the ship are also well predicted. The trim caused by ship velocity has relatively small effect on the ship resistance. The uncertainty analysis for the calculation of ship resistance shows that the numerical results are reliable.

1. INTRODUCTION

CFD calculation of the KVLCC2 tanker in model scale is studied here. The KVLCC2 tanker has a bulb at the bow and stern, and due to the strong bilge vortex, a distinctive hook pattern is formed in the axial velocity contours at the propeller plane (Gorski, 2002). For this model, extensive numerical and experimental studies had been performed. Experiments on this model in towing tank and wind tunnel were performed by Van S. H. et.al in 1998 and 1999. Then W.J. Kim (2001) measured the calm water resistance, wave pattern and local velocity at the design velocity in a towing tank and recommended to use them as the validation data for CFD calculations. Furthermore, to get spatial distribution of turbulence statistics, Sang-Joon Lee (2003) investigated the flow information in the stern and near-wake region of the model in a wind tunnel. Recently, to investigate the added resistance due to waves, the resistance, velocity and wave pattern characteristic are measured in calm water and in regular head sea waves (Guo & Steen, 2010).

Numerical simulations using Reynolds-averaged Navier-Stokes equations (RANS) for turbulent flows around ships are performed using different turbulence models. The selection of turbulence model is one of the key issues in predicting the nominal wake distribution at the propeller plane. RSM, *k*-ε models and *k*-ω models without free water surface are extensively tested to identify the stern flow characteristic of KVLCC2 by Svennberg (2000), which showed RSM model predicts the flow field in closest with the experiment and SST model gives result close to the RSM model. Some variations of *k*-ε models were further studied by Wu-Joan Kim et al (2002), where standard *k*-ε model, RNG-based *k*-ε model and realizable *k*-ε model were investigated. Their results showed that only the realizable *k*-ε model provided realistic wake distribution. For the resistance coefficient prediction in the Gothenburg 2000 Workshop, the *k*-ε models, *k*-ω models, RSM and algebraic stress models were utilized and it showed that the ship resistance estimation varies among different viscous models (Larsson, 2003). Eca L. et al (2009) further studied the resistance estimation with the effect from the grid density, iterative error, turbulent models, Reynolds number and computation domain size etc and it was shown that the effect of turbulence model selection is dominant in his case. Many of the mentioned calculation do not consider the effect of free surface but by adopting double body flow, while its effect is considered here. Meantime, light is also shed on the effect of the trim angle caused by the dynamic pressure field around the hull. The analysis of ship resistance and wave profile with/without trim angle is performed here to verify whether the trim angle can be neglected in the numerical calculation in calm water.

Firstly, the effect of turbulence model and grid refinement on free surface is explored. Three different turbulence models are further studied to predict nominal wake distribution at the propeller plane and the resistance coefficient. These are standard *k*-ω model, SST *k*-ω model and RSM. Finally, the analysis of ship resistance and wave profile with and without trim angle is performed.

2. NUMERICAL METHODS

The CFD results are obtained by solving RANS equations using the finite volume method. The governing equations are shown as follows:

$$\frac{\partial u_i}{\partial x_i} = 0 \qquad (1)$$

$$\frac{\partial u_i}{\partial t} + \frac{\partial (u_i u_j)}{\partial x_j} = -\frac{1}{\rho}\frac{\partial P}{\partial x_i} + \frac{\partial}{\partial x_j}(\gamma \frac{\partial u_i}{\partial x_j}) - \frac{\partial}{\partial x_j}\overline{u_i' u_j'} + g_i \qquad (2)$$

Where u_i u_j are average speed components respectively ($i, j = 1,2,3$), ρ is the density of fluid, P is the average press. γ is the coefficient of kinematic viscosity . g_i is the gravity acceleration, and $\frac{\partial}{\partial x_j}\overline{\rho u_i' u_j'}$ is the Reynolds stress. The problem caused by the unknown term of Reynolds stress must be solved by introduction of the additional equations. The standard k-ω two-equation turbulent model, SST k-ω model and RSM model are applied here with free water surface modeled by the VOF method. The calculation is performed with Fluent 6.3.26.

3. GRID SETTINGS

A grid convergence study with respect to ship resistance is performed with 1.18M, 2.13M, 4,24M and 5.89M cells. The results are given in Section 4. In each case, the mesh around the ship is improved with O-grid, and y^+ at the wall-adjacent cell is kept in the range of 30-60 except in a limited area close to the stern and in the air. A multi-block hexahedral mesh is used for calculation, which is produced with ICEM CFD.

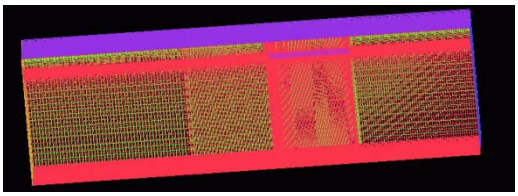

(a) The mesh in the calculation domain

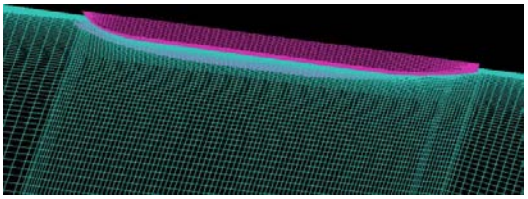

(b) The mesh on the free surface

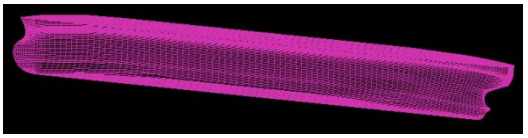

(c) The mesh around the ship

Fig.1 The mesh for KVLCC2

Calculation domain with the different boundary conditions is shown in Fig. 2. Only the port side of the hull is modeled, in order to exploit the symmetry of the flow. The domain has the following extent: $-3.0L_{pp}<x<2.5L_{pp}$, $0.0L_{pp}<y<1.5L_{pp}$ and $-1.6L_{pp}<z<025L_{pp}$, where L_{pp} is the length between perpendiculars. The symmetry condition is adopted at y=0 and the free surface lies at z=0. The ship stern (aft perpendicular) is located at x=0 and the bow is x= L_{pp}. The coordinate system here is different from the requirement of the G2010 workshop and it needs slight transformation for the comparison with the experimental results.

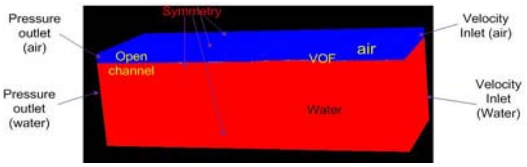

Fig.2 The boundary conditons

Open channel is used to consider the hydrostatic pressure distribution in the domain. 'Velocity inlet' is provided at the upstream boundary, 'Pressure outlet' is provided at the downstream boundary. The 'Symmetry' is given at bottom, top, middle and outside separately. Details are depicted in Fig.2. The simulation time step is $\Delta t = 0.002s$, and the simulation time for each case is more than 60 s.

4. DISCUSSION OF RESULTS

4.1 Free Surface Field

For modeling the free surface in viscous flow simulations, surface capturing methods, such as the VOF method or level-set, are more popular than surface-tracking methods to analyze complex interfacial topologies (Nobuaki, 2007). The VOF method is chosen here.

The wave elevation near the ship is given in this part. Moreover, the effects of grid and viscous model on the wave profile around the hull are also discussed.

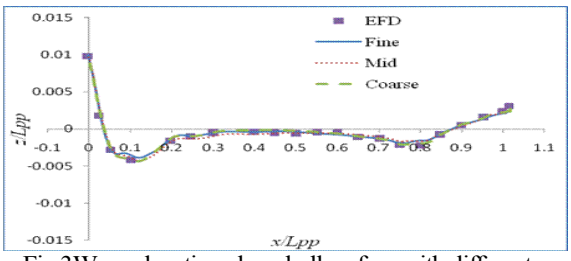

Fig.3Wave elevation along hull surface with different mesh sizes (SST k-ω model)

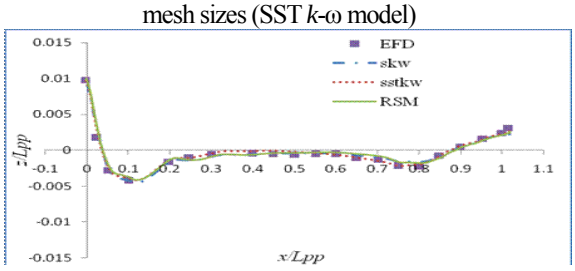

Fig.4 Wave elevation along hull surface with different viscous models (Medium mesh:2.13M cells)

The wave profile along the hull surface was measured by W.J.Kim, et al. (2001). Fig. 3 and Fig. 4 show the wave elevation with different mesh sizes and different viscous models. In Fig.3, the meshes 1.18M (coarse), 2.13M (medium), 4.24M (fine) are compared with the experimental results (EFD).

From Fig.3 – Fig.4, it is found that the difference between different models and meshes are negligibly small and it is concluded that there is quite small influence on the free surface around the model by the turbulence models and mesh sizes.

The wave cut at three different places is shown in Fig. 5 - Fig.6. From the figures, it can be seen that the wave profile is predicted well near the ship. Far from the ship, the mesh is coarse so here the wave profile is less well predicted. The wave elevation contours on the free surface near the ship is shown in Fig.7, and it can be seen that the free surface is well predicted by the SST *k*-ω model

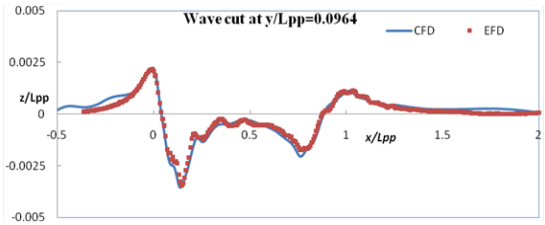

Fig.5 Wave profile at y/Lpp=0.0964 by SST *k*-ω model (Fine mesh:4.24 cells)

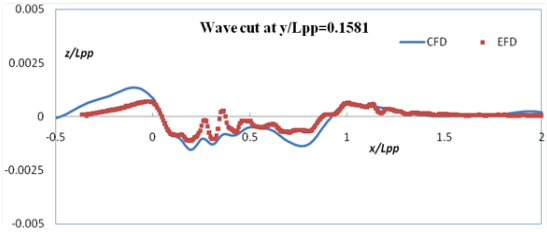

Fig.6 Wave profile at y/Lpp=0.01581 by SST *k*-ω model (Fine mesh:4.24 cells)

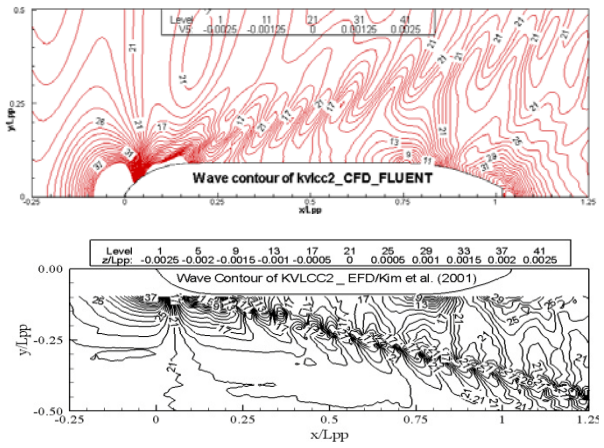

Fig. 7 Wave elevation contours by SST *k*-ω model (Fine meshes:4.24M cells)

4.2 Hull Surface Flow

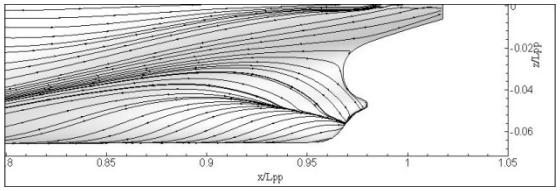

Fig. 8 Limiting streamline on the stern SST *k*-ω model (Fine meshes:4.24M cells)

Fig. 8 depicts the limiting streamline on the stern, which is of great interests as it is closely linked to the formation of stream-wise vortices, the hallmark of the flow past full ship. It is seen from Fig.8 that the upper lines move backwards all the way onto the upper part of the stern. Meanwhile, the topological structure of the limiting streamlines in Fig.8 shows the presence of a line along the bilge onto which the neighboring wall streamlines converges. It is seen that the lines, somewhat above mid-girth, start to bend downwards and the direction gets more and more vertical as the stern is approached. Near the bilge the lines moving downwards meet the lines from the bottom, and there a pronounced convergence line along the bilge is formed. This is the part where a vortex-type separation occurs, and the created vortex-sheet evolves into stream-wise vortices. This phenomenon can be caught by CFD calculation.

4.3 Flow Field at the Propeller Plane

One of the concerns in the turbulent flow around the ship is the velocity field at the propeller plane, due to its importance for the working conditions of the propeller. The grid refinement test on the flow field at the propeller plane is performed first. The results of three different meshes 1.18M (coarse), 2.13M (mid), 4.24M (fine) are compared in Fig. 9.

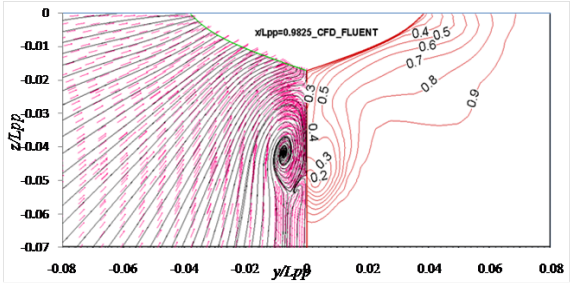

(a) Coarse meshes(1.18M) with SST *k*-ω model

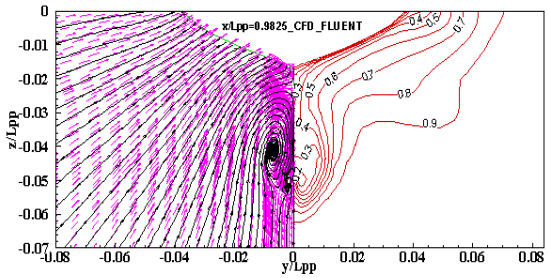

(b)Medium meshes(2.13M) with SST *k*-ω model

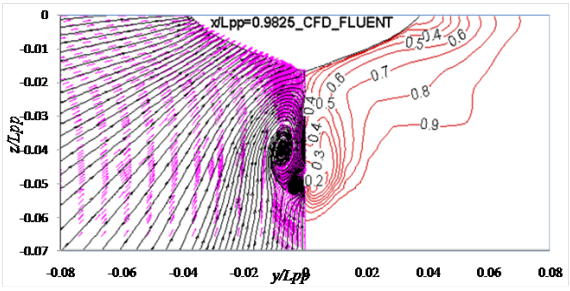

(b) Fine meshes(4.24M) with SST *k*-ω model

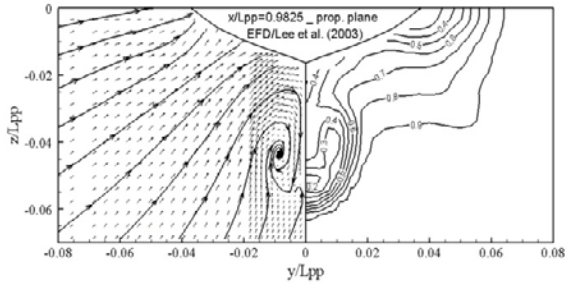

(c) Experimental results

Fig.9 Velocity field at y/L_{pp} =0.9825 from SST *k*-ω model with different meshes sizes, compared to EFD

It is found that the flow at the propeller plane changes slightly between different grids. The velocity contour and 'hook' flow in the propeller plane according to fine mesh have good agreement with experimental data, except near the propeller hub. The possible reason is that the propeller hub is cut off straight in the experiment (Svennberg, 2000), while it is round in the calculation.

The medium mesh could capture the main flow characteristics well. In order to save CPU time, this mesh is used to study the effect of viscous models on the flow at the propeller plane.

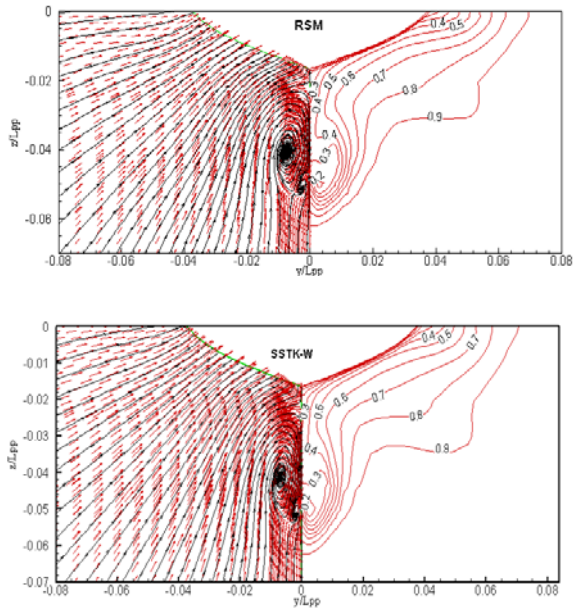

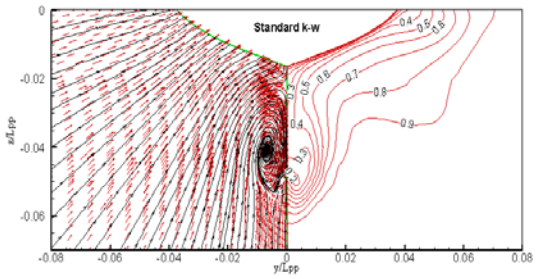

Fig. 10 Comparison of velocity field at the propeller plane (x/L_{pp}=0.9825), predicted by RSM (top), SST k-ω (middle), Standard k-ω (bottom). The mesh size in the three cases is 2.13M (medium meshes).

Fig.10 shows the axial velocity contours at the propeller plane with RSM, SST k-ω, and Standard k-ω models. The cross flow vector is consistent with the experimental results and the 'hook'-shaped flow pattern at the propeller plane is predicted with these three models. RSM and SST k-ω predict the second smaller vortex, while this is less visible in the result from Standard k-ω.

The flow near the propeller plane at x/L_{pp} =0.85, x/L_{pp} =1.1, and x/L_{pp} =0.9825 are given in Fig. 11, 12, and 13, showing numerical results compared to EFD. The numerical results are obtained with the medium size grid and SST *k*-ω model.

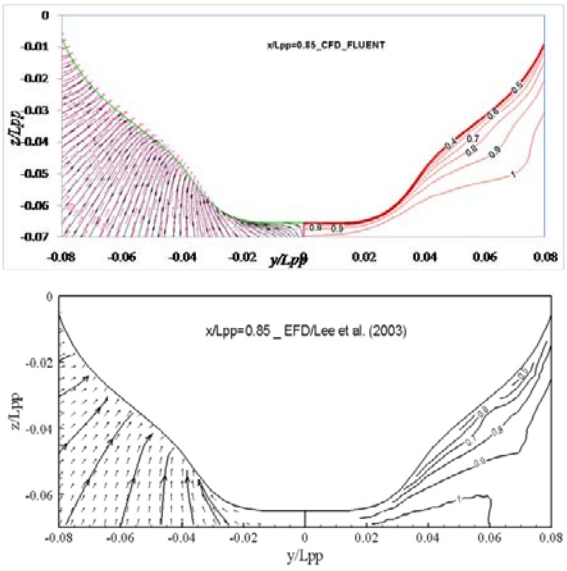

Fig. 11 Comparison of velocity field at x/L_{pp} =0.85 with SST *k*-ω model (Medium meshes: 2.13M cells)

From Fig.11, it can be seen that the cross flow with SST *k*-ω model is in good agreement with experimental result, except for velocity contour of *U*=1.

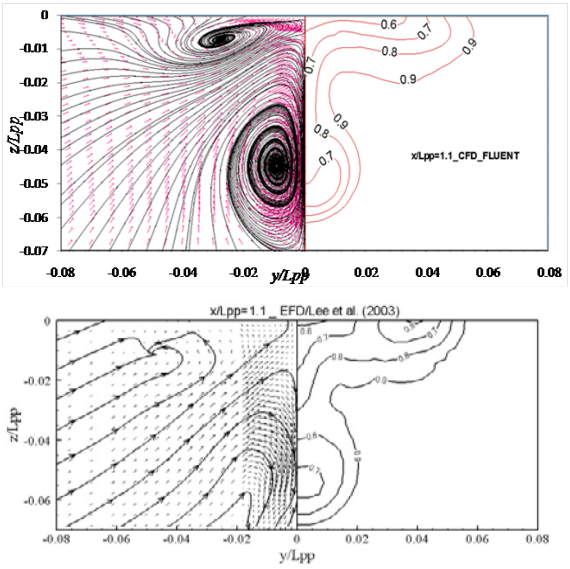

Fig. 12 Comparison of velocity field at x/L_{pp} =1.1 with SST k-ω model (Medium meshes: 2.13M cells)

From Fig.12, the velocity field with SST k-ω model doesn't agree well with the experimental result. There are two 'hooks' in the numerical calculation, which agree with the results given by SHIPFLOW 4.2(G2010) , while in the experiment these 'hooks' are not found.

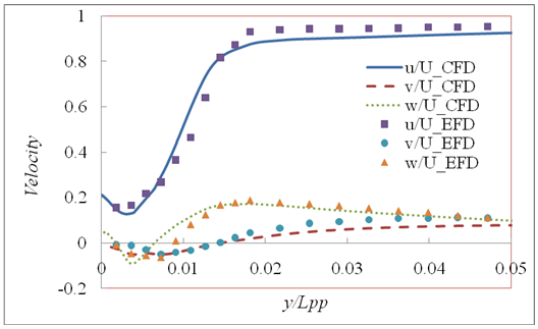

Fig. 13 Velocity profile at propeller plane (x/L_{pp} =0.9825) along z/L_{pp} = -0.05075 with SST k-ω model (Medium meshes: 2.13M cells).

Fig..13 shows the profiles of the mean velocity components (u, v, w) along z/L_{pp} = -0.05075 at the propeller plane. The velocity profiles from numerical calculation are consistent with those from experiment.

The prediction of u velocity is less satisfactory at y/L_{pp} >0.02. The possible reason is that the mesh in y direction is not fine enough. The velocity profile in y and z direction just have slight discrepancy with experimental data locally.

4.4 Turbulence Field at the Propeller Plane

The turbulence field at the propeller plane is also of interest. Due to the complexity of this calculation, the RSM model is used. Considering the CPU hours and memory capacity, the medium mesh (2.13M) is used. Turbulent kinetic energy k and five turbulent inertia tensors: $\overline{uu}$, $\overline{uv}$, $\overline{uw}$, $\overline{vv}$, $\overline{ww}$, are compared with the experimental results in Fig. 14-19.

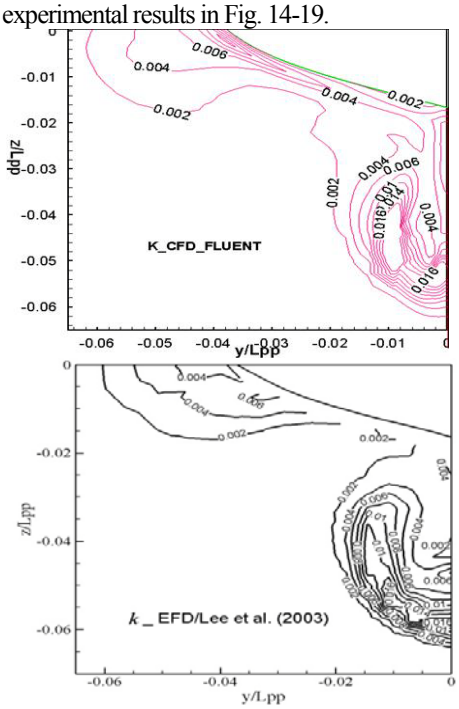

Fig.14 Turbulent kinetic energy contours at x/L_{pp} =0.9825, experiment (lower), predicted by RSM (upper)

Fig.14 shows the contours of both experimental and predicted turbulence energy at the propeller plane. The turbulent kinetic energy predicted by RSM agrees with the experimental results qualitatively. Both of these two figures show that the turbulence kinetic energy is comparatively higher in the boundary layer near the water-plane and the neighbor-hood of the free vortex-sheet.

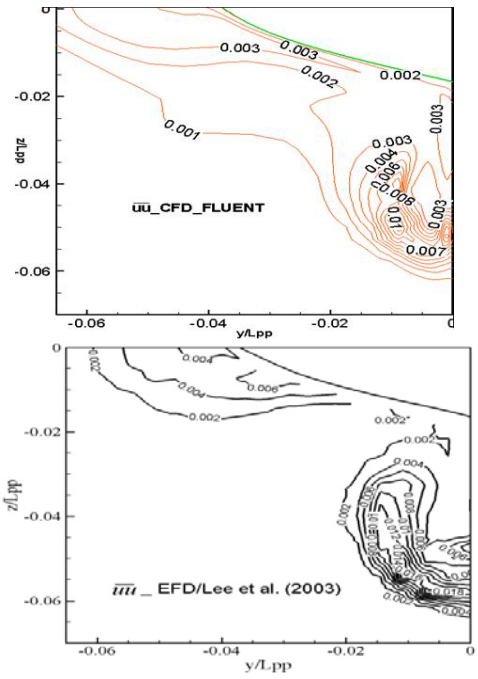

Fig.15 $\overline{uu}$ contours at x/L_{PP}=0. 9825, predicted by

RSM (upper), experiment (lower)

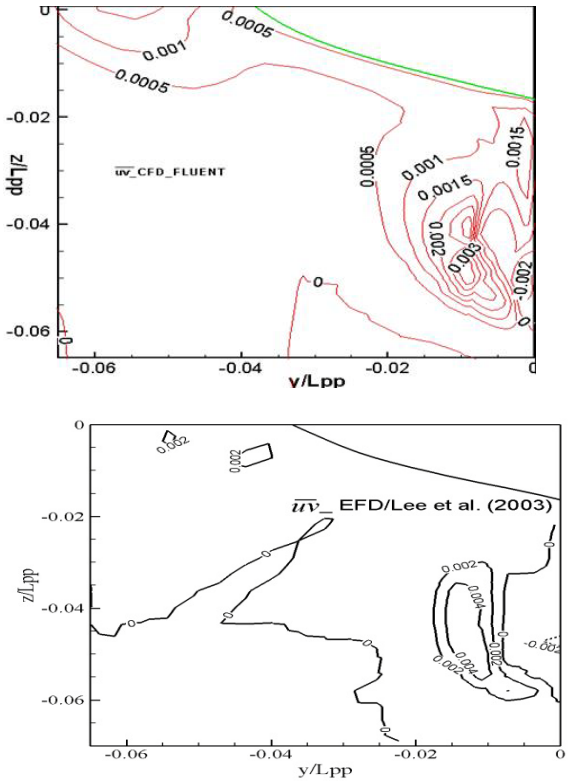

Fig .16 $\overline{uv}$ contours at x/L_{PP}=0. 9825, predicted by RSM (upper), experiment (lower)

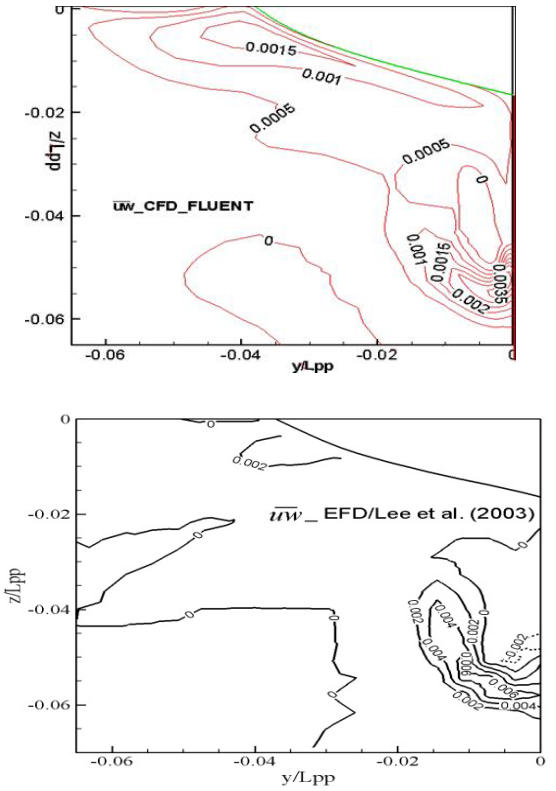

Fig.17 $\overline{uw}$ contours at x/L_{PP} =0. 9825, predicted by RSM (upper), experiment (lower)

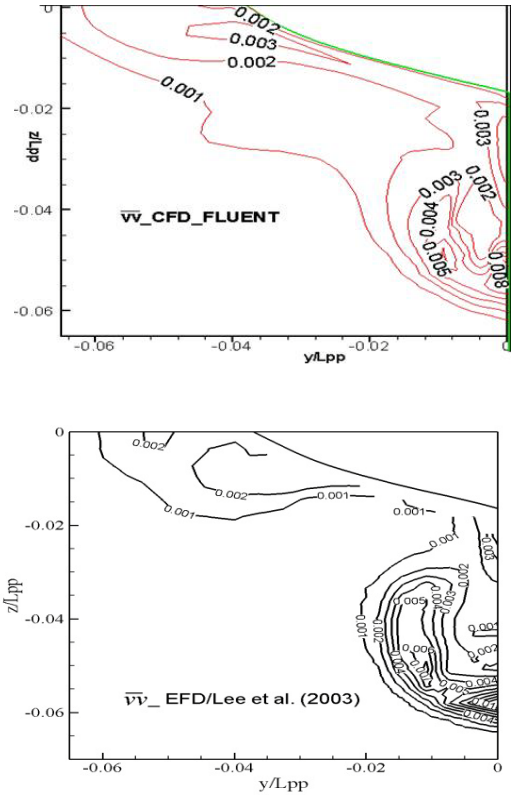

Fig .18 $\overline{vv}$ contours at x/L_{PP}=0. 9825, predicted by RSM (upper), experiment (lower)

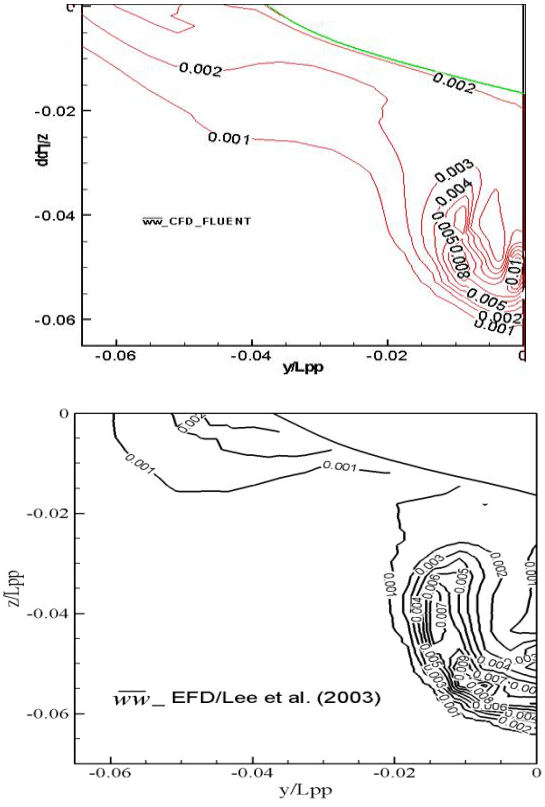

Fig .19 $\overline{ww}$ contours at x/L_{PP}=0. 9825, predicted by RSM (upper), experiment (lower)

The turbulent inertia tensors $\overline{u_i u_j}$ are related not only to fluid physical properties but also to local flow conditions such as: velocity, geometry, surface roughness and upstream history etc. Moreover, their values are also small. Thus, it is very difficult to measure and calculate them accurately. The experimental uncertainty is very large (Sang-Joon Lee, 2003) and thus it is expected that the numerical results are not in perfect agreement with the experimental results. However, there is a qualitative agreement between calculations and experiments. It is seen that the turbulent inertia tensors are also comparatively higher in the boundary layer near the water-plane and the neighborhood of the free vortex-sheet.

The value $\overline{uu}$ is much larger near the vortex-sheet than that of $\overline{uv}$, $\overline{uw}$, $\overline{vv}$, $\overline{ww}$, which is due to the influence of direct stress from stream-wise component in $\overline{uu}$ direction while transverse or intersected components receive the energy via pressure-strain interaction among the normal stress.

4.5 Ship resistance and uncertainty analysis

Total resistance around the ship hull consists mainly of wave making resistance and viscous resistance, with the latter further decomposed into frictional resistance and viscous pressure resistance. Many previous calculations for KVLCC2 neglected the effect of free surface. Considering the free water surface effect, the total drag force is calculated with different turbulence models and grids, the results of which are shown in Table 1 and Table 2.

Table 1 shows frictional, pressure and total ship resistance with three different viscous models: Standard *k*-ω, SST *k*-ω and RSM models. All these three models give satisfactory results (around 5% relative error for the worst case). RSM model gives better prediction of the ship resistance than the other two models, and the SST *k*-ω model is a bit better than the standard *k*-ω model. The resistance of SST *k*-ω is smaller than that of standard *k*-ω, which verifies that the SST *k*-*ω* has a limit on the turbulence viscosity close to the wall compared with standard *k*-*ω* model (Svennberg, 2000).

Table 1 Ship resistance calculated using different viscous models

	Standard *k*-ω	SST *k*-ω	RSM.	Exp
$C_T \times 10^3$	4.347	4.316	4.259	4.110
$C_f \times 10^3$	3.346	3.296	3.195	3.45
$C_p \times 10^3$	1.001	1.02	1.064	0.66

Table 2 shows the total ship resistance with different grids, calculated with SST *k*-ω. The ship resistance decreases with the increase of the mesh. From Case 3 to 2, as the increase of 2M cells, the decrease of estimated error is 2.6%. From Case 2 to 1, with almost same increase of around 2M grids, the decrease of estimated error is 1.1%. The estimation already comes to a very good accuracy.

Table 2 Ship resistance at Fn=0.142 with different grids

	Case4	Case3	Case2	Case1
G	Coarse	Medium	Fine	Finest
Mesh sizes	1186278	2131734	4241761	5892686
$C_T \times 10^3$	4.772	4.316	4.206	4.162
Error %	16.107	5.012	2.336	1.273

Since the ship geometry is very complicated and an O-grid is introduced around the hull, the mesh is sometimes refined around the hull and free surface locally. Thus, the mesh in the four cases is not refined at a uniform grid refinement rate. However, the variation is performed systematically in each direction.

(1)Grid Convergence Study

A grid convergence study is performed here, and the objective S is the ship resistance coefficient $C_T \times 10^3$ at the design speed (Fn=0.142). The verification method suggested by Stern et al. (2001) needs the samples to be monotonic converging, using only three grids.

Four cases are given here. Choose any three of them to check the convergence of the CFD results. The relevant convergence ratios are shown in Table 3.

Table 3 Convergence Ratio

	Case 1,2,4	Case 1,3,4	Case 2,3,4	Case 1,2,3
R_G	0.0777	0.3319	0.2411	0.4000

The total resistance coefficient $C_T \times 10^3$ shows monotonic convergence for any combinations of grids. Thus the Generalized Richardson Extrapolations could be used to estimate the Grid Uncertainty U_G. Since the grid refinement ratio between Case 1 and Case 2 is very small, and the mesh is only refined near the free surface in Case 1 compared with Case 2, they could not be chosen for the V&V analysis at the same time. Applying the methodology suggested by Stern et al. (2001,2004) and Celik et al.(2008) on the two groups of result, gives the results shown in Table 4.

The three finest grids(Case1,3,4) give $P_G = 6.590$,while the other grids(case 2,3,4) gives $P_G = 7.591$ .The order of convergence approaches the theoretical order, as the grids get fine enough, which shows our CFD results are convergent and reasonable.

Table 4 Verification of resistance coefficients (SST k-ω model)

Grid	R_G	r_{G21}	r_{G32}	P_G	$\delta_{RE,G1}$	F_s	U_G
Case 1,3,4	0.3319	1.4034	1.2158	6.590	0.0186	1.25	0.0233
Case 2,3,4	0.2411	1.2578	1.2158	7.591	0.0234	1.25	0.0290

Uncertainty is estimated using Generalized RE with safety factors (Stern, 2004). In Grid Convergence Index (GCI) approach, a standard three-grid error estimate from RE is multiplied by a factor of safety F_S to bound the simulation error. The exact value of the safety factor F_S is somewhat ambiguous and should be decided by experience. Roache recommends 1.25 for careful grid studies and 3 for case in which only two grids are used (Roache,1994).

(2) Iterative Convergence

Since the ship geometry is complex, the solution residual drop to a level of 10^{-4} for the case with finest grid. The method for estimation of iterative errors and uncertainties is based on examining iterative history of ship resistance. Solution residual drops from an initial value of about 10^{-3} to a final value of 10^{-4}(not shown). The iterative history of the total resistance (Finest mesh, 5.89M) is shown in Fig.20

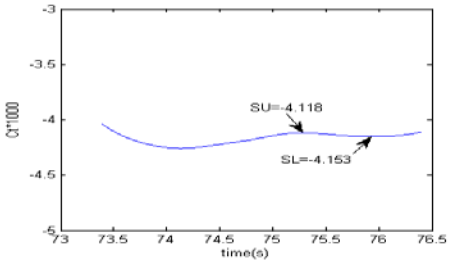

Fig.20 The iterative history of ship resistance from finest mesh (5.89M)

From the time history of the ship resistance, it can be seen that the amplitude of the solution envelope decrease as the iteration number increases. The solution is mixed convergent/oscillatory iterative convergent. The solution envelope is used to define the maximum $S_U = -4.118$ and minimum $S_L = -4.153$, and the iterative error U_I could be estimated as: $U_I = \left|\frac{1}{2}(S_U - S_L)\right| = 0.0175$.

(3) Validation Uncertainty

The Validation Uncertainty is analyzed on the finest meshes. The result is given in Table 5. It gives the correct value of $C_T \times 10^3$ between 4.112 and 4.212.

Table 5 The V&V of KVLCC2 Resistance

EFD(D)	U_G	U_I	U_D%D	U_V%D
4.11	0.0233	0.0175	1.0%	1.23%

4.6 Effect of trim and sinkage on resistance and flow

When the ship is running, its posture will be changed due to the dynamic pressure of the flow past the ship. It will sink down slightly, and mostly at the bow, resulting in a negative trim angle. The effect of the negative trim and sinkage on the ship resistance and flow calculation is studied. Calculations are performed on even keel without sinkage, and with sinkage and trim fixed to the values measured in the model test. The measured pitch angle is $-0.1238°$, and the sinkage is -11.674mm at the front perpendicular (FP) and 0.246mm at the aft perpendicular (AP).

The wave profiles around the ship hull at these two conditions are shown in Fig. 20, which shows that the trim has hardly any effect, except a minor difference near $x/L_{pp} = 0.1$.

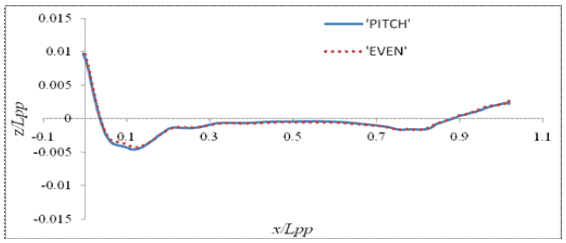

Fig.20 The wave profile around the ship hull

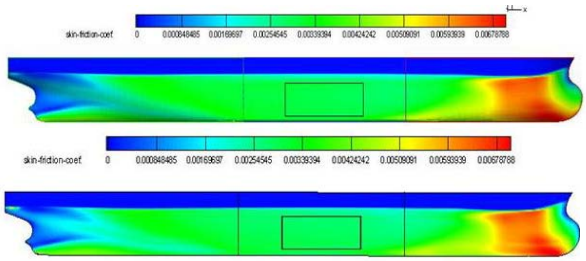

Fig. 21 Friction distribution

Fig.21 shows the frictional resistance distribution. It can be seen that there is a slight difference in frictional resistance near the ship stern.

The ship resistance corresponding to the even and trimmed conditions are shown in Table 6. It is seen that the difference is very small. It might be concluded from this study that for the current case, dynamic trim and sinkage are not important for the results.

Table 6 Ship resistance at even and trimmed conditions

	Even condition	trimmed condition
$C_T \times 10^3$	4.348	4.347

5. Conclusions

The numerical calculation of ship resistance and flow field at the stern for the KVLCC2 tanker is studied using three different turbulence models: standard k-ω model, SST k-ω model and RSM. The effect of trim for the resistance and flow is also investigated. The validation

and verification study shows that the results are reasonable and reliable. The following conclusions are made:

The resistance and flow field at the stern is well predicted by these three models. Comparatively RSM gives the best estimation, then SST k-ω model and standard k-ω model.

The free water surface elevation is independent of the turbulence models. The wave profile around hull is well captured in the simulation and the difference of the wave profile around hull amongst different meshes is negligible.

The turbulent kinetic energy k and five turbulent inertia tensors have been predicted and found to be in qualitative agreement with experimental results.

The trim and sinkage caused by forward speed have small effect on resistance and flow around the hull.

REFERENCES

Bingjie Guo, Sverre Steen, 2010, "*Added Resistance of A VLCC in short waves*", Proceedings of OMAE 2010, June 4th -11th, Shanghai, China

Fred Stern, Robert V. Wilson, Hugh W. Coleman and Eric G. Parson, 2001, "*Comprehensive Approach to Verification and Validation of CFD Simulations-Part 1: Methodology and Procedures*", Journal of Fluids Engineering, Vol. 123.pp.793-802

Fred Stern, Robert Wilson and Jun Shao, 2004, "*Quantitative V&V of CFD Simulations and Certification of CFD Codes with Examples*", Proceeding of CHT-04 ICHMT International Symposium on Advances in Computational Heat Transfer, Norway

Ismail B. Celik, Urmila Ghia, Patrick J. Roache, Christopher J. Freitas, Hugh Coleman, Peter E. Raad , 2008, "*Procedure for Estimation and Reporting of Uncertainty Due to Discretization in CFD Applications*", Journal of Fluids Engineering, Vol. 130

Joseph J.Gorski, 2002, "*Present State of Numerical Ship and Hydrodynamics and Validation Experiments*", Journal of Offshore Mechanics and Arctic Engineering, Vol.124 (79), pp.74-80

Larsson L., Stern F. and Bertram V., 2003, "*Benchmarking of Computational Fluid Dynamics for Ship Flows: the Gothenburg 2000 Workshop*", *Journal of Ship Research*, Volume 47, No 1, March

Nobuaki Sakamoto, Robert Vance Wilson and Frederick Stern, 2007, "*Reynolds Averaged Navier Stokes Simulations for High-Speed Wigley Hull in Deep and Shallow Water*", Journal of Ship Research. Vol. 51, No. 3, pp. 187–203

Roache P, 1994, "*Verification and Validation in Computational Science and Engineering*", Hermosa Publishers, Albuquerque

S.U. Svennberg, 2000, "*A test of turbulence models for steady flows around ships",* Gothenburg 2000: a workshop on numerical ship hydrodynamics, Gothenberg, Sweden.

Sang-Joon Lee, Hak-Rok Kim, Wu-Joan Kim and Suak-Ho Van, 2003, "*Wind Tunnel Tests on Flow Characteristics of the KRISO 3600 TEU Containership and 300K VLCC Double-Deck Ship Models* ", Journal of Ship Research, Vol.47, No.1,pp.24-3

Van S.H., Kim W.J., Yim G.T., Kim D.H., and Lee S.J., 1998, "*Experimental Investigation of the Flow Characteristics Around Practical Hull Forms*", Proceedings 3rd Osaka Colloquium on Advanced CFD Applications to Ship Flow and Hull Form Design, Osaka, Japan

Van S.H., Kim W.J. and Lee S.J., 1999, "*Wind Tunnel Test on Flow Characteristic of KRISO 300K VLCC double model*", Proceeding of Janpan-Korea Joint workshop on Maritime Hydrodynamics, Fukuoka, Japan

Wu-Joan Kim, Do-Hyun Kim and Suak-Ho Van, "*Computational study on turbulent flows around modern tanker hull forms*", International Journal for Numerical Methods in Fluids, Vol. 38, pp.377-406

W.J. Kim, S.H. Van, D.H. Kim, 2001, "*Measurement of flows around modern commercial ship models*", Experiments in Fluids, Vol.31, pp.567-578

Flexible CFD Meshing Strategy for Prediction of Ship Resistance and Propulsion Performance

Ju Hyun Lee and Shin Hyung Rhee
(Department of Naval Architecture and Ocean Engineering, Seoul National University, Seoul, Korea)

1. ABSTRACT

In the present study, we conducted resistance test and self-propulsion test for a ship's resistance and propulsion performance, using computational fluid dynamics techniques, where a Reynolds-averaged Navier-Stokes equations solver was employed. For convenience of mesh generation, unstructured meshes were used in the bow and stern region of a ship, where the hull shape is formed of delicate curved surfaces. On the other hand, structured meshes were generated for the middle part of the hull and the rest of the domain, i.e., the region of relatively simple geometry. To facilitate the rotating propeller for self-propulsion test, a sliding mesh technique was adopted. Free-surface effects were included by employing the volume of fluid method for multi-phase flows. The computational results were validated by comparing with the existing experimental data.

2. INTRODUCTION

Thanks to the great advancement of computer performance recently, computational analysis of ship resistance and propulsion using computational fluid dynamics (CFD) is being widely adopted, and the results are being applied to actual design of ships. In those applications, however, the difficulty in mesh generation is the most serious obstacle for non-expert users for utilizing CFD with maximum efficiency. In case of mesh generation around a ship hull, the bow and stern regions require special care and experience, because of the delicate and rapidly changing surfaces. This is true even for a bare hull and the complexity gets out of control, if propellers, rudders, and appendages are included. Therefore, a hybrid meshing approach using unstructured meshing near the complex geometry and structured meshing in the remaining simple geometry domain was suggested (Lee et al 2009).

In the present study, we extended the application further and executed resistance and self-propulsion tests using hybrid meshing, which employs unstructured meshing in the bow, stern, and propeller region and structured meshing in the remaining region. For self-propulsion tests, a sliding mesh technique, where the propeller is located in a disk volume and the volume itself rotates with non-conformal interfaces placed between the rotational and stationary sub-domains, was adopted.

3. COMPUTATIONAL MODEL AND CONDITION

KRISO container ship (KCS), a container carrier designed by MOERI, was selected as the object ship, and KP505, the propeller designed for KCS, was selected as the object propeller. The principal particulars are described in Tables 1 and 2.

Table 1 Principal particulars of KCS

Length between perpendiculars	7.2786 (m)
Beam	1.019 (m)
Draft	0.3418 (m)
Wetted surface area	9.4376 (m^2)
Speed	2.196 (m/s)
Reynolds number	1.4×10^7

Table 2 Principal particulars of KP505

Diameter	250.0 (mm)
A_e/A_0	0.800
Hub ratio	0.180
No. of blades	5
Blade section	NACA66 Thickness form + a=0.8 mean line Camber

4. COMPUTATIONAL METHOD

4.1 Mathematical modeling and Numerical Method

The governing equations are written for the mass and momentum conservation, such that

$$\frac{\partial \rho}{\partial t} + \nabla \cdot (\rho \vec{v}) = 0 \quad (1)$$

$$\frac{\partial (\rho \vec{v})}{\partial t} + \nabla \cdot (\rho \vec{v}\vec{v}) = -\nabla p + \nabla \cdot \bar{\bar{\tau}} + \rho g \quad (2)$$

where $\vec{v}$ is the velocity vector in the Cartesian coordinate system, p the static pressure, and $\bar{\bar{\tau}}$ the stress tensor given by

$$\bar{\bar{\tau}} \equiv \mu[(\nabla \vec{v} + \nabla \vec{v}^T) - \frac{2}{3} \nabla \cdot \vec{v} I] \quad (3)$$

where μ is the molecular viscosity, I the unit tensor, and the second term on the right hand side the effect of volume dilation. Once the Reynolds averaging approach for turbulence modeling is applied, the Navier-Stokes equations can be written in Cartesian tensor form as

$$\frac{\partial \rho}{\partial t} + \frac{\partial}{\partial x_i}(\rho \vec{v}_i) = 0 \quad (4)$$

$$\frac{\partial}{\partial t}(\rho u_i) + \frac{\partial}{\partial x_j}(\rho u_i u_j) = -\frac{\partial p}{\partial x_i} + \frac{\partial}{\partial x_j}[\mu(\frac{\partial u_i}{\partial x_j} + \frac{\partial u_j}{\partial x_i} - \frac{2}{3}\delta_{ij}\frac{\partial u_l}{\partial x_l})] + \frac{\partial}{\partial x_j}(-\rho \overline{u'_i u'_j}) \quad (5)$$

where δ_{ij} is the Kronecker delta, $-\rho \overline{u'_i u'_j}$ and the Reynolds stresses. These Reynolds stresses must be modeled to close equation (5), i.e., for turbulence closure. The VOF method is employed to handle the free-surface wave flow around the ship. Based on the local volume fraction of the q-th fluid, α_q, the appropriate variables and properties are assigned to each cell within the domain. The tracking of the interfaces between the phases is accomplished by the solution of a continuity equation for the volume fraction of phases. For the q-th phase, this equation has the following form.

$$\frac{\partial \alpha_q}{\partial t} + \vec{v} \cdot \nabla \alpha_q = 0 \quad (6)$$

Note that the volume fraction equation is not solved for the primary phase, but based on the following constraint

$$\sum_{q=1}^{n} \alpha_q = 1 \quad (7)$$

A single momentum equation is solved throughout the domain, and the resulting velocity field is shared among the phases. The momentum equation depends on the volume fractions of all phases through the fluid properties, which are determined by the presence of the component phases in each cell, e.g.,

$$\rho = \sum_{q=1}^{n} \alpha_q \rho_q \quad (7)$$

In the case of turbulence quantities, a single set of transport equations is solved, and the turbulence variables are shared by the phases throughout the field.

The computations were carried out using FLUENT v6.3, general purpose CFD software. The governing equations were discretized using implicit unsteady method. The second order accurate upwind scheme was selected for the convection terms, while the second order accurate central scheme was for the diffusion terms. The high resolution interface capturing scheme (HRIC) was used for the discretization of the volume fraction equation near the interface. The equations of the continuity and momentum were solved sequentially (Weiss and Smith, 1995). The k-ε turbulence model with a wall function was used for turbulence closure. To confirm the convergence, averaged residuals scaled by the initial imbalance of equations was checked. The criterion for the residual was 10^{-6}. In addition, the constancy of the total force on the ship or propeller was chosen as another standard for confirming the convergence.

4.2 Computational Mesh and Boundary Conditions for Resistance Test

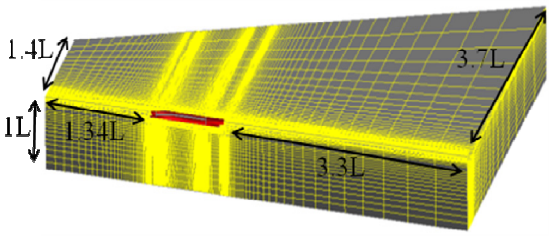

Fig.1 Computational domain for resistance test

The computational domain is shown in Fig.1 with its dimensions. In order to accommodate the free surface motion, there is vertical room of 0.047L between the top boundary and initial water surface.

The no-slip condition was applied on the hull surface. On the upstream and side boundaries, the total pressure including hydrostatic one was applied, while the static pressure was extrapolated through the downstream boundary. The top and bottom boundaries were considered as free slip wall.

Fig.2 shows the mesh on the hull surface. Unstructured meshing was used in the bow and stern region, while structured meshing was applied in the middle part of the hull. Between the unstructured and structured mesh sub-domains, non-conformal interfaces were placed. The total number of cells used for resistance test was about 1.79 million, of which 1,200,000 cells were tetrahedrons and 590,000 cells were hexahedrons.

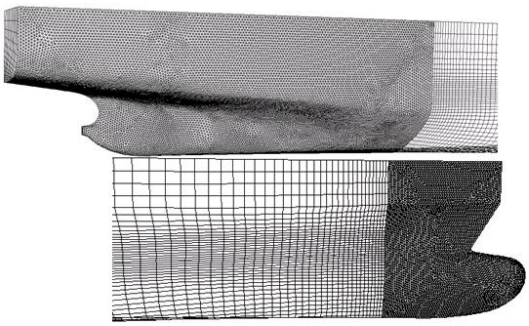

Fig.2 Hull surface mesh

4.3 Computational Mesh and Boundary Conditions for Self-Propulsion Test

For self-propulsion test, the full domain was used. Fig.3 shows the domain for self-propulsion test. Vertical room of 0.047L for free surface motion exists between the initial water surface and top boundary, as for resistance test. The number of cells for self-propulsion test was about 3.29 million tetrahedrons in the bow, stern and propeller regions, and 1.18 million hexahedrons in the remaining part. The total number of the cells for the computation was 4.47 million.

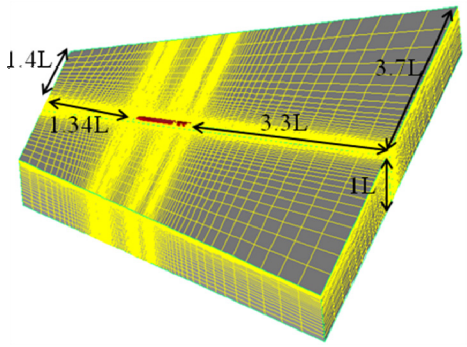

Fig.3 Computational domain for self-propulsion test

On the hull surface, no-slip condition applied, while the free slip condition is applied on the top and bottom boundaries. On the upstream and side boundaries, total pressure including hydrostatic one was applied. Through the downstream boundary, the static pressure was extrapolated, as for resistance test. To apply non-conformal interface between the propeller region and hull region, the sliding mesh technique was adopted around the propeller as shown in Fig.4.

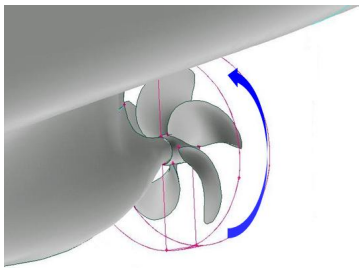

Fig.4 Configuration of sliding mesh

5. RESULTS AND DISCUSSION

5.1 Resistance test

The free-surface wave solutions were compared. Fig.5 shows the comparison of free-surface wave pattern with the experimental data (Van et al 1998b, Kim et al 2001). The lower part of figure, which means –y region, presents the wave pattern from the experiment. The opposite part, the +y region, means that from the present study. Although there are irregular contours lines caused by graphical reconstruction of interfaces in tetrahedral cells, the comparison looks quite good, especially near the hull. However, as for other CFD results, the diverging wave away from the hull are under-predicted due to numerical diffusion.

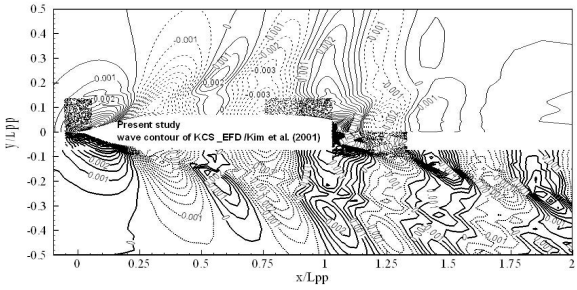

Fig.5 Comparison of Wave Patterns

From Fig.6 to 9, the comparison of wave profiles along the hull surface/center-plane and wave cut at Y/L_{PP}= -0.0741, -0.1509 and -0.4224 are presented. It is confirmed that, even across the non-conformal interfaces, the free-surface wave solution shows smooth transition and good agreement with the experimental data. As seen in the wave pattern comparison, numerical diffusion causes under-prediction of free-surface wave solution in present results.

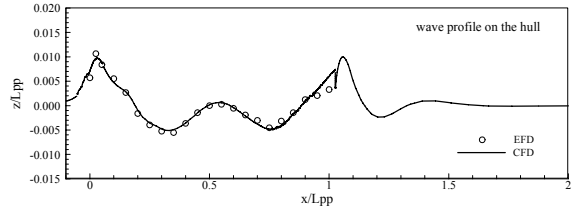

Fig.6 Comparison of Wave profile

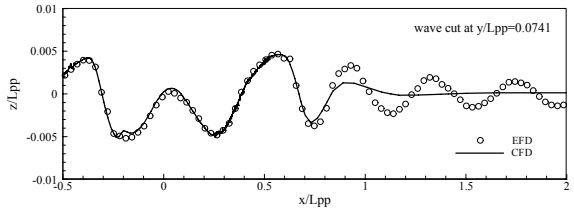

Fig.7 Comparison of Wave cut at Y/L_{PP}= - 0.0741

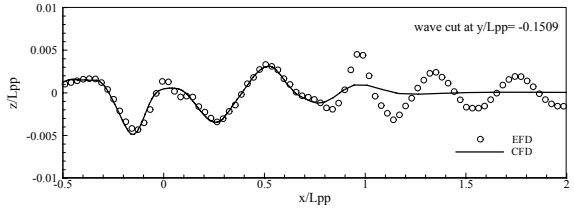

Fig.8 Comparison of Wave cut at Y/L_{PP}= - 0.1509

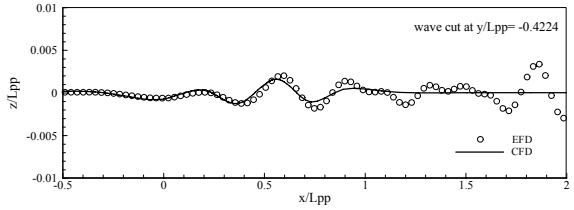

Fig.9 Comparison of Wave cut at Y/L_{PP}= - 0.4224

The wake distribution at X/L_{PP}=0.9825 was compared with the experimental data, as shown in Fig. 10. The upper one is the experimental data and lower one is the present study results. The right panel of each figure shows axial velocity contours and the left panel shows the cross flow vector and streamlines. The overall trend was reproduced well, but because of the tetrahedral cells in the region, the strong longitudinal vortices were slightly under-predicted.

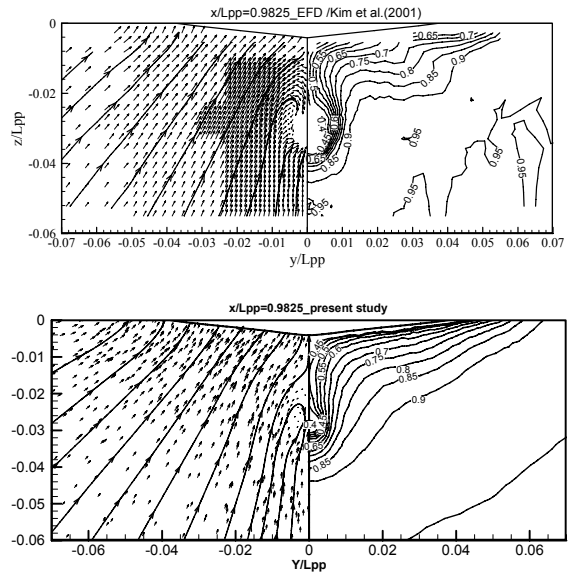

Fig.10 Comparison of wake plane at X/L_{PP}= 0.9825

5.2 Self-propulsion test

The sliding mesh technique approach was adopted for self-propulsion test with the rotating cylinder placed at the propeller location.

The computation was started with non-rotating propeller to first develop the steady flow field around the hull. Then the propeller was slowly rotated, and the revolution was gradually increased to the desired speed. The time step size was determined to make Courant number no smaller than 0.5. By rough estimate, the propeller revolution speeds of 9.5, 10.0, and 10.5 rps were considered, and the self-propulsion point was found by linear curve fitting using those three revolution speeds. For the full scale extension, as for the towing tank tests, the towing force (F_D) was considered to adjust the difference of the viscous force between the model and full scale ships.

Table 3 Calculation results of three rps cases

rps	J	K_T	K_Q	error
9.0	0.9761	0.1452	0.0281	5.88×10^{-4}
9.5	0.9247	0.1721	0.0307	-9.92×10^{-5}
10.0	0.8785	0.1903	0.0331	-3.95×10^{-4}

The computational results for the three revolution speeds are listed in Table 3, where the error value is defined as $(R_T - T - F_{D0})/0.5\rho U^2 S_M$. Based on these results, the self-propulsion point was searched using a linear interpolation, and the obtained revolution speed, K_T, and K_Q are presented in Table 4.

The Axial velocity contours and cross flow vectors downstream of propeller plane at X/L_{PP}=0.9911 are compared with the experimental data (Hino 2005) as shown in Fig. 11 and 12. The trend of wake at propeller downstream is well predicted.

The comparison of velocity components downstream of propeller plane is shown in Fig. 13. Again, the overall trend shows good agreement: however, in the computation, the propeller hub was not considered. Therefore, small errors were observed where the propeller hub is located.

Table 4 Result parameters of self propulsion test

Rps	K_T	K_Q
9.592	0.1700	0.03110

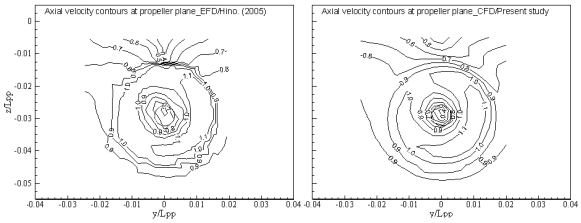

Fig.11 Comparison of axial velocity contours at X/L_{PP}=0.9911

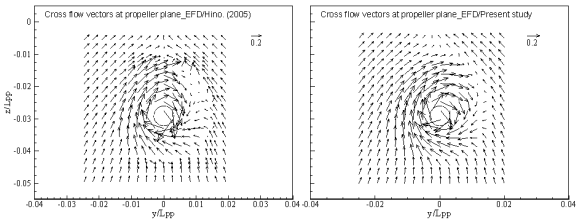

Fig.12 Comparison of cross flow vectors at X/LPP=0.9911

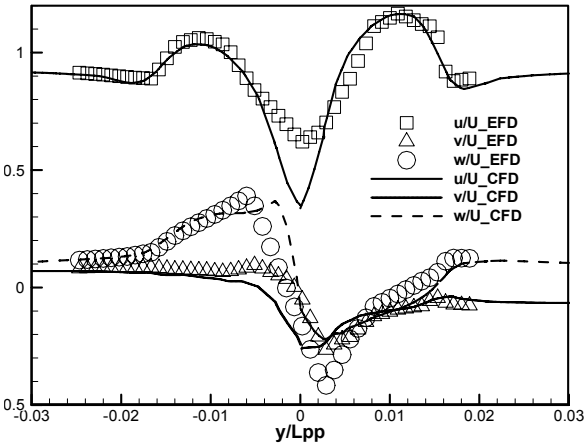

Fig.13 Velocity downstream of propeller plane (X/L_{PP}=0.9911) at Z/L_{PP}=-0.03

The pressure distribution on the hull surface is shown in Fig. 14. The pressure recovery around the bilge was well predicted both quantitatively and qualitatively. Also the effects of rotating propeller in the hull wake conform to those observed in the experiment.

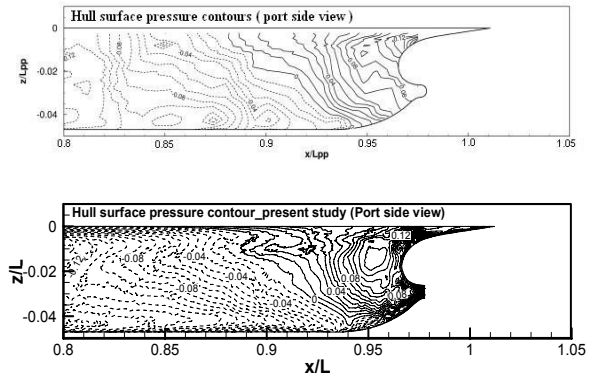

Fig.14 Hull surface pressure contours

6. CONCLUSION

In the present study, flexible meshing techniques, i.e., hybrid meshing for complex geometry regions and sliding mesh for rotating propeller, were employed to perform the three primary tests for ship resistance and propulsion performance. i.e., resistance, propeller open water, and self-propulsion tests. Unstructured meshing for the bow and stern regions, together with structured meshing for the remaining region, was used and non-conformal interfaces were placed between the sub-domains with different cell types. The sliding mesh technique, where the propeller was placed in a rotating cylindrical volume with non-conformal interfaces between the rotational and stationary sub-domains, was used to represent the rotating propeller in self-propulsion tests.

The computational results were compared with experimental data. The overall performance of the flexible meshing techniques was commendable. Development of the refinement of mesh generation procedure for the stern region is recommended for future work.

REFERENCES

Chao, Y, and Karl, K (2005). "Numeric Propulsion Simulation for the KCS Container Ship," Proceedings of CFD workshop Tokyo 2005, Tokyo, Japan, pp.539-545.

Kim, J, Park, IR, and Van, SH (2005). "RANS Computations for KRISO Container Ship and VLCC Tanker using the WAVIS code," Proceedings of CFD workshop Tokyo 2005, Tokyo, Japan, pp.598-603.

Lee, JH, Park, BJ, Seol, DM, Rhee, SH, Jun, DS, Chi, HR, and Ryu, MC (2009). "Hybrid Meshing Approach for Resistance Performance Prediction of a POD Propulsion Cruise Ship," Proceedings of ASCHT09, 2nd Asian Sympo. on Computational Heat Transfer and Fluid Flow, Jeju, Korea.

Lübke, L (2005). "Numerical simulation of the Flow around the propelled KCS," Proceedings of CFD workshop Tokyo 2005, Tokyo, Japan, pp.587-592.

Tahara, Y, Wilson, R, and Carrica, P (2005). "Comparison of Free-Surface Capturing and Tracking Approaches in Application to Modern Container Ship and Prognosis for Extension to Self-Propulsion Simulator," Proceedings of CFD workshop Tokyo 2005, Tokyo, Japan, pp.604-611

Van, S.H., Kim, W.J., Yim, G.T., Kim, D.H., and Lee, C.J., (1998b), "Experimental Investigation of the Flow Characteristics Around Practical Hull Forms," Proceedings 3rd Osaka Colloquium on Advanced CFD Applications to Ship Flow and Hull Form Design, Osaka, Japan

Kim, W.J., Van, D.H. and Kim, D.H., (2001), "Measurement of flows around modern commercial ship models", Exp. in Fluids, Vol. 31, pp 567-578

Hino, T., (2005 ed.), "Proceedings of CFD Workshop Tokyo 2005", NMRI report 2005.

RANS SIMULATIONS OF THE MULTIPHASE FLOW AROUND THE KCS HULLFORM

J B Banks (University of Southampton, UK)
A B Phillips (University of Southampton, UK)
P W Bull (QinetiQ Ltd, UK)
S R Turnock (University of Southampton, UK)

1. SUMMARY

A commercial RANS code is used to investigate the multiphase flow field surrounding the KCS hull form. Results are presented for the associated wave pattern (case 2.1), dynamic sinkage and trim (case 2.2b) and self propulsion parameters for the hull using a body force propeller model (case 2.3a). Simulated results showed good correlation with experimental wave pattern and sinkage and trim data. However greater accuracy in the simulated nominal wake is required to accurately match experimental self propulsion data.

2. INTRODUCTION

Traditionally the resistance of ships has been determined using towing tank experiments. Over the past two decades increased computational power has allowed numerical approaches to replicate and potentially start to replace towing tank experiments. This work investigates the quality of results that can be achieved using a commercial Reynolds Averaged Navier Stokes (RANS) flow solver, ANSYS CFX Version 12 (ANSYS, 2009). This work is a contribution to the Gothenburg 2010 workshop on CFD in ship hydrodynamics and compares the results from CFD based methods with model tests performed by participating towing tanks on the KRISO Container Ship (KCS).

3. THEORETICAL APPROACH

A finite volume method, using a Volume of Fluid (VOF) approach was used. This method is derived from the surface integration of the conservative form of Navier Stokes' equations over a control volume. Equations (1) and (2) are the incompressible Reynolds averaged Navier-Stokes (RANS) equations in tensor form and Equation (3) is the volume fraction transport equation (Peric and Ferziger, 2002).

$$\frac{\partial(\rho U_i)}{\partial t}+\frac{\partial(\rho U_i U_j)}{\partial x_j}=-\frac{\partial P}{\partial x_i}+\frac{\partial}{\partial x_j}\left[\mu\left(\frac{\partial U_i}{\partial x_j}+\frac{\partial U_j}{\partial x_j}\right)\right] -\frac{\partial}{\partial x_j}\left(\rho\overline{u'_i u'_j}\right)+f_i \quad (1)$$

$$\frac{\partial U_i}{\partial x_i}=0 \quad (2) \qquad \frac{\partial c}{\partial t}+\frac{\partial(cU_j)}{\partial x_j}=0 \quad (3)$$

The volume fraction c is defined as (V_{air}/V_{total}) and the fluid density, ρ, and viscosity, μ, are calculated as $\rho=\rho_{air}c+\rho_{water}(1-c)$ and $\mu=\mu_{air}c+\mu_{water}(1-c)$. External forces applied to the fluid are represented as f_i, which include buoyancy forces and momentum sources representing the influence of a propeller. The effect of turbulence is represented in (2) by the Reynolds stress tensor $\rho\overline{u'_i u'_j}$ and is modelled using a turbulence model.

3.1 Turbulence modelling

Both a Shear Stress Transport (SST) eddy viscosity model and a Baseline (BSL) Reynolds stress model (ANSYS, 2009) were used to evaluate the Reynolds stress tensor.

Case	Description	Turbulence model
2.1	Wave pattern	SST & BSL
2.2b	Sinkage and trim	SST
2.3a	Self propelled	SST

The SST model blends a variant of the k-ω model in the inner boundary layer and a transformed version of the k-ε model in the outer boundary layer and the free stream (Menter, 1994). This has been shown to be better at replicating the flow around the stern of a ship, than simpler models such as k-ε, single and zero equation models (Larsson *et al*, 2000, Hino, 2005). The BSL Reynolds stress model includes transport equations for each component of the Reynolds stress tensor. This allows anisotropic turbulence effects to be modelled helping to model complex flow features such as separation off curved surfaces (Peric and Ferziger, 2002). The BSL model is blend of a Reynolds stress-ω model for the inner boundary layer and ε based in the outer and free stream (Bull, 2005).

3.2 Sinkage and Trim

To capture the sinkage and trim experienced by a vessel travelling at a forward speed, the surface mesh representing the hull was displaced based on the total heave force and pitching moment acting on the vessel and the vessels water plane area and moment to change trim. This was achieved using CFXs in built "mesh morphing" model which is used to calculate the new node locations throughout the fluid domain at each time step, while maintaining mesh topology. The resulting vessel orientation has no net heave force or pitching moment.

3.3 Propeller models

To reduce the computational cost associated with self propulsion simulations a body force propeller model was used. This represents the impact of the propeller on the fluid as a series of axial and tangential momentum source terms, fb_x and fb_θ respectively. These are calculated using the Hough and Ordway Thrust and Torque distribution (Hough, 1965), as was implemented by (Stern *et* al, 1988). A detailed description of the methodology adopted here is presented in (Phillips et al, 2009, Phillips *et al*, 2010).

The momentum source terms were calculated based on the propeller rps (n), the open water propeller characteristics and the inflow velocity field providing the mean wake fraction $\bar{W}_t$, which is assumed to be equal to the Taylor wake fraction w_t.

Initially no momentum sources were applied, by setting n=0, providing the initial flow field entering the propeller domain. Once the convergence criteria were met the velocity components

entering the propeller disk are sampled providing the wake fraction. This is then used along with an initial estimate of n=9 to calculate the thrust and torque generated by the propeller, which are represented by axial and tangential momentum source terms. The rps is then iteratively varied using a Secant method (each time convergence is achieved) until;

$$|\text{Thrust} - \text{Drag} + \text{SFC}| < 1 \text{ N} .$$

4. NUMERICAL MODEL

Table 1 Numerical simulation properties.

Property	SOTON	QINETIQ
Half mesh No. of elements	~ 10M	~9M
y+ on the hull	~ 1 (max value 1.2)	< 10
Domain Physics	Homogeneous Water/Air multiphase, SST or BSL turbulence model, Automatic wall function, Buoyancy model –density difference, Standard free surface model	
Boundary physics:		
Inlet	Defined volume fraction and flow speed	
	Turb. Intensity= 0.05	Zero gradient
Outlet	Opening with entrainment with relative pressure = hydrostatic pressure	
Bottom/side wall	Wall with free slip condition	Outlets with hydrostatic pressure
Top	Opening with entrainment with relative pressure 0 Pa	
Hull	Wall with no slip condition	
Symmetry plane	Along centreline of the hull	
Solver settings:		
Advection scheme	High Resolution (ANSYS, 2009)	
Timescale control	Physical timescale function: 0.01[s] + 0.09[s]*step(atstep-20)+ 0.1[s]*step(atstep-200)	$0.03\left(\frac{L_{pp}}{Fn\sqrt{gL_{pp}}}\right)$
Convergence criteria	Residuary type: RMS	
	Target: 1e-5	Target: 1e-6
Multiphase control	Volume fraction coupling	
Processing Parameters:		
Computing System	Iridis 3 Linux Cluster (University of Southampton)	Linux cluster (QinetiQ Haslar)
Run type	Parallel (24 Partitions run on 3x8 core nodes each with 23 Gb RAM)	Parallel(up to 64 Partitions run on 8x8 core nodes each with 8 Gb RAM)

Simulations are performed using ANSYS CFX V12 (ANSYS, 2009). This is a commercial finite volume code, which uses collocated (nonstaggered) grids for all transport equations, coupling pressure and velocity using an interpolation scheme. The physical parameters and solver settings used to define the numerical solution are provided in Table 1, along with details of the computing resources used for the largest mesh.

5. MESHING TECHNIQUE

5.1 Wave Pattern (Case 2.1) - Southampton

A structured mesh was built using ANSYS ICEM around the full scale KCS hull geometry. The domain width and depth matched the dimensions of one half of the KRISO towing tank. The length was selected to allow one ship length in front of the hull and two behind. This was then converted to model scale dimensions each time a mesh was generated.

A blocking structure was developed that allowed a good quality surface mesh to be created over the hull (see Figure 1). It was found that collapsing the blocks under the stern down to a point provided the best overall mesh structure in this region. This approach allowed extra mesh density to be added in this localised area where large surface curvatures needed to be captured. Elements were also clustered within the region of the free surface to allow a sharp interface to be captured.

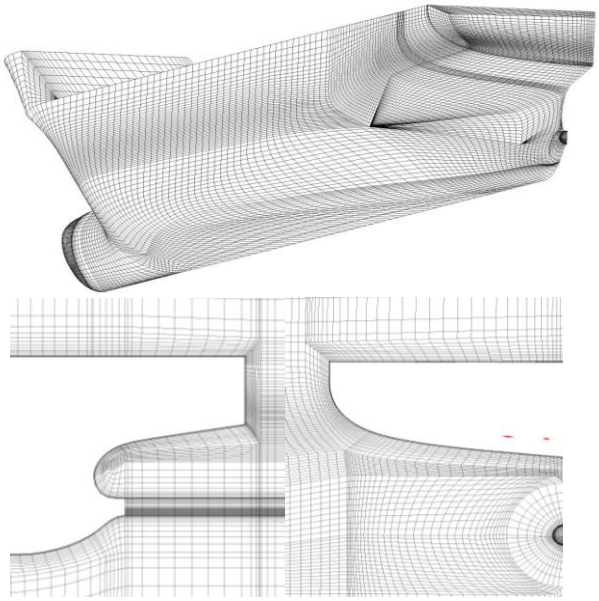

Fig.1 SOTON: Hull surface mesh structure (top), O-grid structure at stern from the side (left) and from the stern (right), for the initial mesh containing 0.8M elements.

Once satisfied with the surface mesh structure an O-grid blocking structure was grown out from the surface of the hull. The depth of the inner O-grid was matched to approximately that of the maximum expected boundary layer. Another outer O-grid was then created so as to provide a smooth transition between the near wall radial mesh and the far field Cartesian structure. Another key feature is the continuation of the O-grids about the propeller axis, towards the outlet of the domain. The outer O-grid was expanded to match the propeller diameter allowing a propeller model to be easily added later. Two splits were also placed within the outer domain blocking structure, one behind the hull and one offset from the hull centreline. This allowed the regions of high mesh density to be forced onto the free surface both on the hull surface and in the outer domain.

A half body mesh of 10M elements was produced with two $\sqrt{2}$ global mesh reductions, providing 4M and 1.5M element meshes, each with a y^+ of 1 over the hull. More details of this process can be found in (Banks et al, 2010).

5.2 Wave Pattern (Case 2.1) QinetiQ

In a similar manner, a structured mesh was built using ANSYS ICEM around the full scale KCS hull geometry. The domain length, width and depth were chosen based on the ship length with one ship length in front of the hull and two behind. The top and bottom of the domain were defined as one ship length below and a half ship length above the keel line, whilst the width was 1.3 ship lengths (see Fig.2).

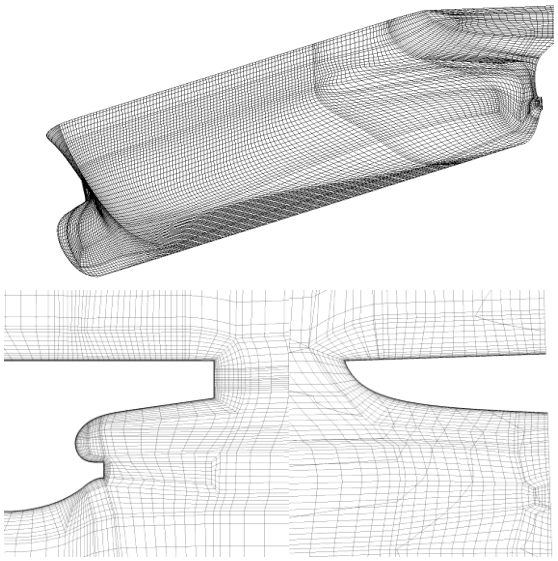

Fig.2 QINETIQ: Hull surface mesh structure (top), O-grid structure at stern from the side (left) and from the stern (right), for the coarsest mesh containing 1M elements.

The topological structure of the O-grids on the hull was defined to give a near uniform, quadrilateral surface grid on the hull surface for the baseline grids but with some control within the free-surface region. A small O-grid was also placed downstream of the propulsor hub which extended to just aft of the transom. The first cell height for the O-grid around the hull was chosen to give $y^+ < 10$ for the model scale flow Reynolds number.

Two sequences of grids were generated based on grid topologies with 4M and 5M cells. Finer and coarser grids were produced using global element refinement factors of 1.25 and 0.8 respectively to give a series of grids with 1M, 2M, 2.5M, 4M, 5M, 6.8M and 9M computation cells. Each of the grid spacings perpendicular to the outer boundaries of the domain were adjusted for the coarsest grids to provide smooth expansion rates.

5.3 Sinkage and Trim (Case 2.2b) – QinetiQ

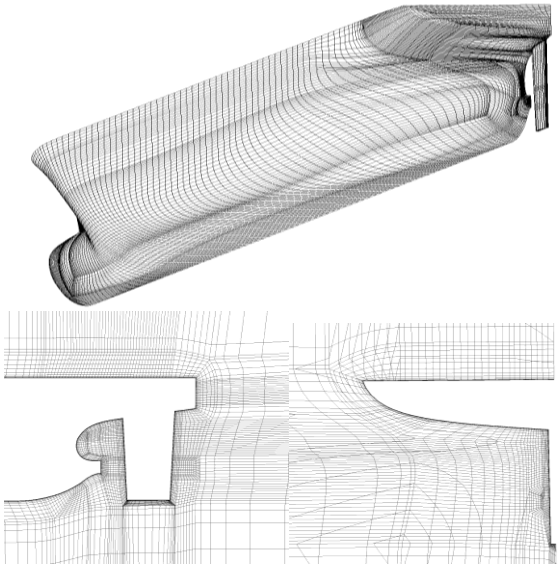

Fig.3 QINETIQ: Hull with rudder surface mesh structure (top), O-grid structure at stern from the side (left) and from the stern (right), for the coarse mesh containing 1M elements.

The rudder was included in the geometry definition for the ANSYS ICEM mesh generation process. Additional vertical splits were created in the overall topology for the 4M cell baseline grid which corresponded to the leading and trailing edge of the rudder and additional O-grid topologies were placed around the rudder. Additional grid points were required in the overall topology to resolve the rudder geometry, and its boundary layer, increasing the baseline grid from 4M cells to 5M cells.

Finer and coarser grids were produced using global element refinement factors of 1.25 and 0.8 respectively to give a series of grids with 680K, 1M, 1.7M, 3M, 5M and 9M computation cells.

5.4 Self propelled (Case 2.3a)

To incorporate a propeller model a separate cylindrical mesh was inserted into the Southampton mesh in the position of the propeller. The mesh density in the outer O-grid was increased to provide a higher mesh resolution entering and leaving the propeller domain. Due to the intrinsic asymmetry in self propelled simulations the entire domain had to be modelled by mirroring the half body mesh. As this doubles the total mesh density a further $\sqrt{2}$ mesh reduction was conducted to minimize computing requirements. This resulted in three half body meshes of 0.75M, 1.7M and 4.5M elements.

6. MESH SENSITIVITY STUDY

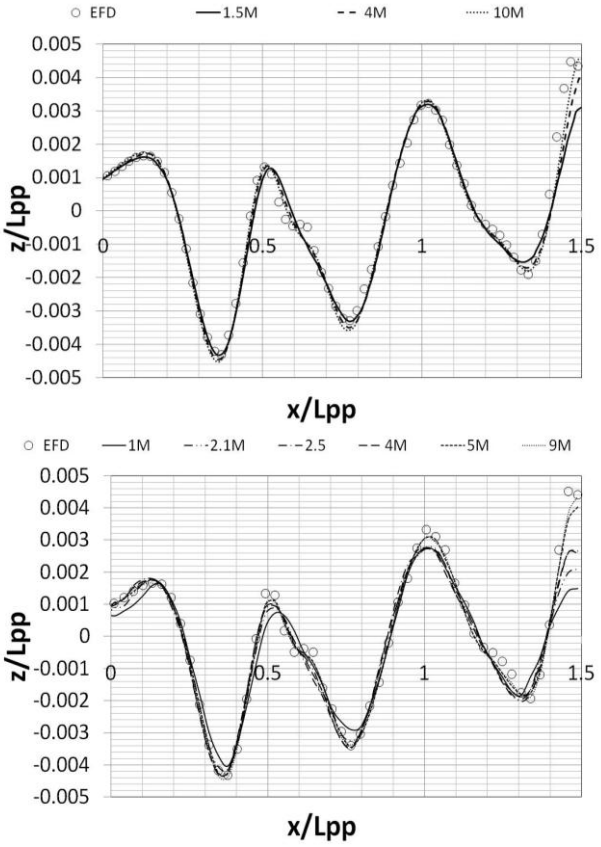

Fig.4 Comparison between experimental (EFD) and CFD wave elevation at a distance of y/Lpp=0.15 from the ship centreline at Fn=0.26. Southampton results (top), QinetiQ results (bottom). The Forward perpendicular is positioned at x/Lpp=0.

To observe the impact of mesh density on the different mesh structures (Southampton Vs QinetiQ) a wave cut profile, using the BSL turbulence model, was compared with EFD data for each of the different mesh densities (Fig.4). It can be seen that both of the mesh structures display significant sensitivity to mesh density astern of the hull, particularly at the next wave peak (x/Lpp = 1.5). However, over the rest of the observed wave cut we see good convergence between the highest mesh densities as well as with EFD data.

7. COMPARISON OF BSL WAVE PATTERN DATA (CASE 2.1)

To assess the influence of different meshes and numerical models a comparison of the wave pattern data obtained using the BSL Reynolds stress turbulence model from case 2.1 was made. In Fig.5 it can be seen that in both cases the global wave pattern shows good correlation to the EFD surface plot. Some variation is observed in the size of the stern wave leaving the transom and magnitude of the stern wave pattern further down stream of the hull. These can be directly compared in the wave cut profile.

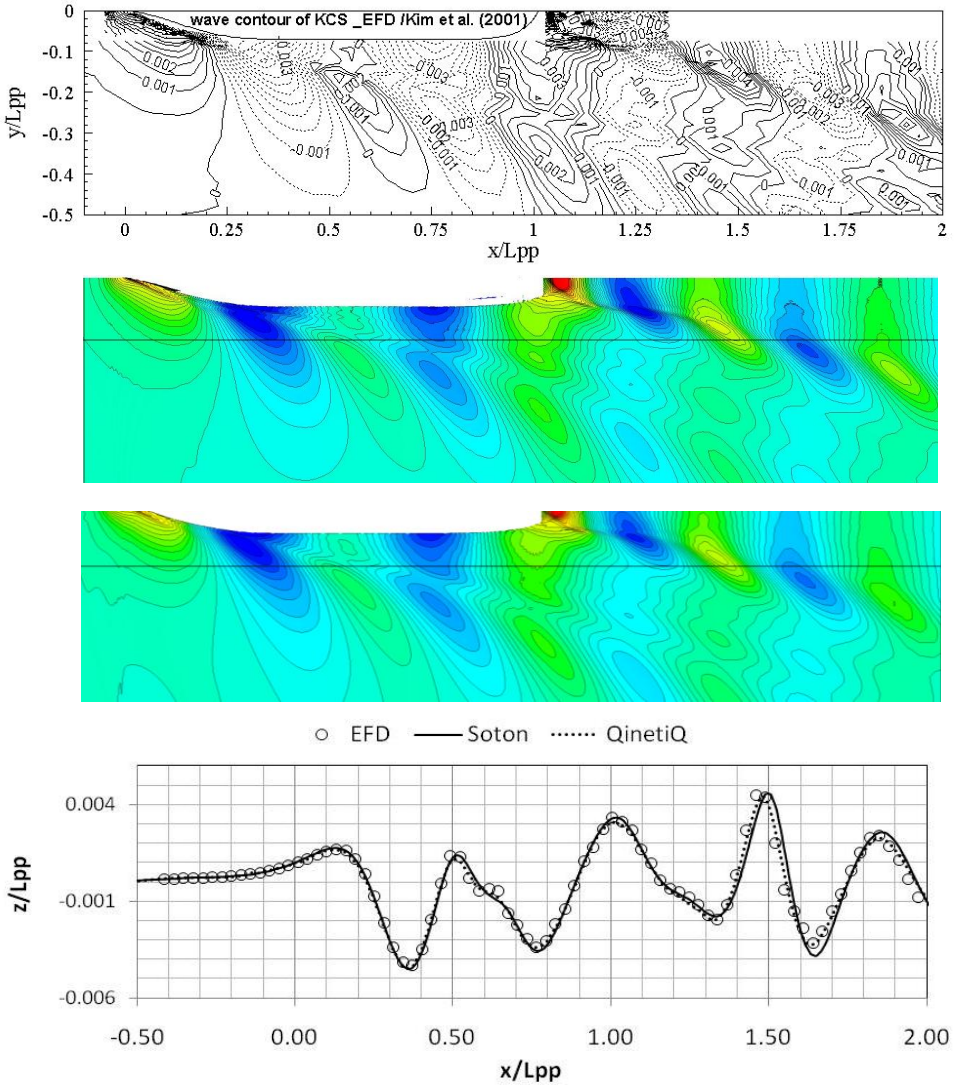

Fig.5 Free surface elevation, z/Lpp, of global wave pattern, at Fn=0.26, for (Top Down) Experimental data, SOTON CFD results and QinetiQ CFD results. Contours range from z/Lpp = -0.005 to 0.010 in steps of 0.0005. The straight lines represent the positions of the wave cut at y/Lpp= 0.15 which are plotted against EFD data for both meshes (Bottom).

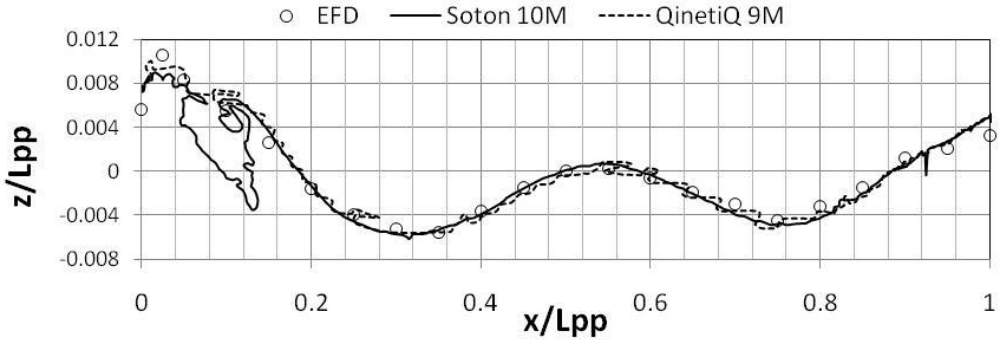

Fig.6 Comparison of free surface elevation along the surface of the hull plotted agaings EFD data at Fn=0.26.

In Fig.6 we can see that in both cases the free surface along the hull appears irregular with the Southampton results showing large gapes and drops in the free surface caused by air pockets on the hull surface near the bow and stern. This ventilation problem was also observed by QinetiQ whilst using a y^+ of 1 but was improved by increasing it to 5-10. It can be seen that this resulted in a more continuous free surface along the hull but with increased smaller undulations along its length.

The components of resistance obtained by both the Southampton and QinetiQ simulations for case 2.1 are also compared to the experimental data provided in (Kim *et al*, 2001) in Table 2. The static wetted surface area used in the calculation of force components was 9.5121 m^2. It can be seen that both turbulence models used by QinetiQ provided total resistances that agree closely with the experimental data, with the BSL model providing a slightly better match with the frictional and pressure components. The Southampton results, however, appear to over estimate all components of resistance, despite significant improvement being made to the pressure component using the BSL turbulence model. One of the factors contributing to this could be the increased air resistance due to the Southampton mesh containing the full topside geometry of the hull, see Fig.1 and Fig.2. Although air resistance is normally assumed small enough to neglect, it appears to be making up 2 – 5% of the total resistance and therefore potentially needs to be accurately modelled so as to match the experimental procedure. This topic is discussed in more detail in (Banks et al, 2010), where aerodynamic and hydrodynamic components of drag are presented. It should be noted that the ventilation problems seen in Fig.6 caused some of the hydrodynamic drag to be misrepresented as aerodynamic drag for the 10M element BSL case.

Table 2 Comparison of Resistance Components.

Mesh	Turbulence model	CT ($x10^3$)	CF ($x10^3$)	CP ($x10^3$)
Soton	SST	3.96	3.04	0.92
Soton	BSL	3.79	3.01	0.78
QinetiQ	SST	3.61	2.95	0.67
QinetiQ	BSL	3.60	2.87	0.73
Experimental		3.56		
Calculated from ITTC Procedure			2.83	0.73

8. SINKAGE AND TRIM - CASE 2.2B

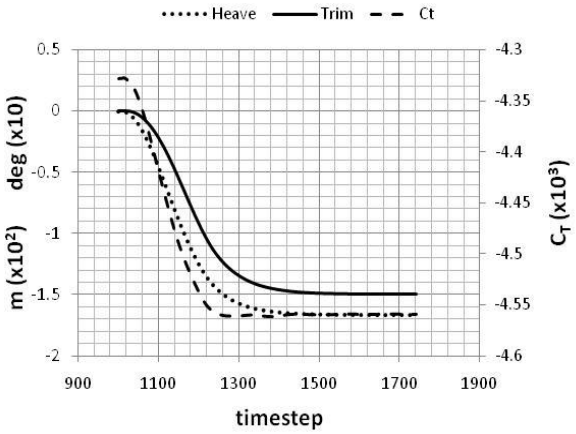

Fig.7 Example time history of a sinkage and trim simulation for Fn = 0.2816 using the finest mesh (9M).

In each simulation the hull geometry was fixed in position for the first 1000 timesteps to allow the fluid forces and moments to converge. From this point the hull is free to heave and trim for another 1000 timesteps or until convergence is reached. An example time history of this process is given in Fig.7, whereas the close correlation with the EFD data over the Froude number range can be seen in Fig.8.

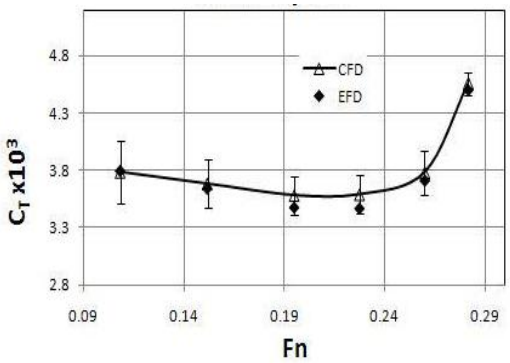

Fig.8 Comparison of EFD and CFD variation of total resistance with Froude number, with numerical uncertainty error bars.

8.1 Uncertainty analysis

The procedure adopted is presented in (Eca &Hoeksra, 2008). The experimental values for each mesh density were determined as the mean value over the last 200 iterations, with the standard deviation providing the iterative uncertainty U_I. The least squares fit to the data was conducted using the software environment Matlab, assuming a grid ratio of 1.2.

9. SELF PROPELED – CASE 2.3A

Table 3 Resistance propeller parameters for self propulsion at ship point.

Parameters	EFD	Coarse (1.5M)	Medium (3.4M)	Fine (9M)
$CT\times10^3$	4.162	4.344	4.321	4.287
$CF\times10^3$		2.903	2.959	2.988
$CP\times10^3$		1.441	1.362	1.300
K_T	0.170	0.200	0.199	0.202
K_Q	0.0288	0.034	0.033	0.034
w_T	0.208	0.281	0.279	0.296
n (rps) (for given SFC)	9.5	9.463	9.464	9.358

The results presented in Table 3 show noticeable discrepancies between the numerical and experimental results. The reason for this is two fold. The wake into the propeller plane has not been accurately captured, (see w_T values in Table 3) this has reduced the propeller advance coefficient value and thus increased the K_T and K_Q predicted from the open water curves. However, since the drag is also over predicted the required thrust is increased which causes the predicted rps to be nearly correct. However, while the results presented are less than ideal the methodology appears to work and provides a simple method of replicating the propeller forces and calculating the self propulsion parameters. However, further effort is required to ensure that the vessel drag and wake fraction are correctly predicted.

Fig.9 illustrates the velocity components downstream of the propeller. Variation in the axial component can be attributed to not replicating the hub geometry and the over prediction of thrust. The asymmetry is not captured due to the non-uniform inflow into the propeller plane not being included in the body force model.

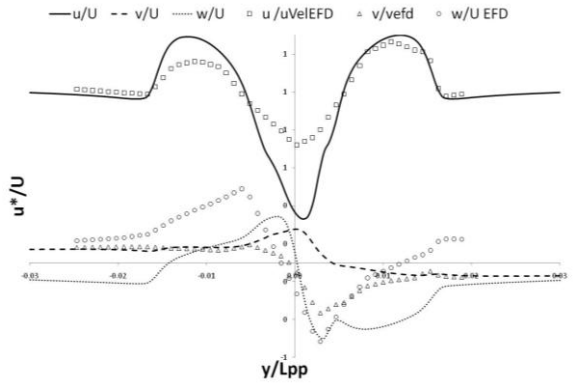

Fig.9 Velocity components down stream of propeller (x/Lpp=0.911, z/Lpp = -0.03)

10. DISSCUSION

10.1 Differences in Mesh structure

The main difference appears to be the surface mesh structure created on the hull. To accommodate the complex geometry of the KCS stern sections the QinetiQ mesh uses multiple O-grids to create a complex mesh structure localised to the hull surface. This leaves a relatively simple mesh structure in the outer domain. In contrast, the surface structure created in the SOTON mesh is maintained throughout the rest of the domain.

Apart from comparing the fundamental mesh structure it is important to assess how the elements are distributed in the two different meshes. Table 4 provides details of how the elements are distributed over different regions in the mesh. It should be noted that although both meshes leave 1xLpp ahead and 2xLpp astern of the hull the width and depth of the domains vary leading to different volumes.

An immediate observation is that the QinetiQ mesh places more cells ahead and along the waterline of the hull. Whereas the Southampton mesh, despite having a smaller free surface area, places more cells here, especially astern of the hull. Another important observation is the increase in hull surface and waterline nodes in case 2.2b due to the addition of the rudder.

Table 4 Comparison of mesh distribution.

Number of grid nodes in location:	Case 2.1		Case 2.2b
	Soton	QinetiQ	QinetiQ
Total in half hull domain	10312611	8791499	9251577
In hull O-grid	1694265	1354698	1354698
On static Free Surface	71504	66710	56056
Distribution ahead of hull	40	62	62
Distribution behind hull	101	67	67
Distribution to side of hull	80	76	76
Hull surface	64237	52827	77313
Along Static Waterline	366	396	434
Along hull midgirth (BWL)	97	74	118
Along hull midgirth (AWL)	40	26	27

10.2 Turbulence modelling

Both groups found that the BSL Reynolds stress model provided noticeably superior results for both the free surface deformation and components of resistance for case 2.1. Ideally this would also have been used in both cases 2.2b and 2.3a, however, reduced numerical stability made this impractical.

11. CONCLUSION

Numerical simulations of the KCS hull form are presented as part of the work jointly submitted by the University of Southampton and QinetiQ Ltd to the Gothenburg 2010 workshop. Despite the differences in meshing technique and numerical setup the wave pattern data obtained shows good correlation to each other and the experimental data. Simple and effective methods for modelling both the dynamic sinkage and trim, and the propeller behind a ship, have been implemented. However a greater level of detail is needed in the propeller inflow to achieve accurate self propelled results.

Both parties experienced problems with air ventilation on the wetted surface of the hull. It was found that this could be significantly reduced by increasing the y^+ from 1 to 5-10.

Another interesting finding was that when the entire topside hull geometry was modelled the air drag equated to 2-5% of the total hull drag, raising into question the common assumption that the air phase can be neglected in CFD simulations. Additional information about the experimental procedure regarding the air drag and the above water structure would enable validation of this component.

REFERENCES

ANSYS. (2009) ANSYS CFX, Release 12.0. ANSYS.

Banks, J., Phillips, A. B., Turnock, S. R., (2010) Free-surface CFD Prediction of Components of Ship Resistance for KCS, 13th Numerical Towing Tank Symposium, Duisburg, Germany.

Bull, P.W., (2005) Verification and Validation of KVLCC2M Tanker Flow, CFD Workshop Tokyo 2005.

Eca, L., Hoekstra, M., (2008) Testing Uncertainty Estimation and Validation Procedures in the Flow Around a Backward Facing Step, 3rd Workshop on CFD Uncertainty Analysis, Lisbon.

Hino T. (2005) CFD Workshop Tokyo 2005. In: The Proceedings of CFD Workshop Tokyo.

Hough, G.R., Ordway, D.E., The generalised actuator disc, Developments in Theoretical and Applied Mechanics, Vol 2, pp 317–336.

Kim, W.J., Van, D.H. and Kim, D.H., (2001) Measurement of flows around modern commercial ship models, Exp. in Fluids, Vol. 31, pp 567-578

Larsson L, Stern F, Bertram V. (2003) Benchmarking of Computational Fluid Dynamics for Ship Flows: The Gothenburg 2000 Workshop. Journal of Ship Research 2003, Vol47, pp 63–81.

Menter, F.R., (1994) Two-equation eddy-viscosity turbulence models for engineering applications. AIAA Journal, Vol 32, pp 1598 –605.

Peric, M., Ferziger, J.H., (2002) Computational Methods for Fluid Dynamics, Springer, 3rd edition.

Phillips, A.B., Turnock, S.R. and Furlong, M.E. (2009) Evaluation of manoeuvring coefficients of a self-propelled ship using a blade element momentum propeller model coupled to a Reynolds averaged Navier Stokes flow solver. Ocean Engineering, Vol 36, Issues 15-16, pp1217-1225.

Phillips, A.B., Turnock, S.R. and Furlong, M.E. (2010) Accurate capture of rudder-propeller interaction using a coupled blade element momentum-RANS approach. *Ship Technology Research (Schiffstechnik)*, Vol 57, pp 128-139.

Stern, F., Kim, H.T., Patel, N.M., Chen, H.C., (1988) A Viscous-Flow Approach to the Computation of Propeller-Hull Interaction. Journal of Ship Research , Vol 32, pp 246–262.

Estimation of Numerical Uncertainty of SHIPFLOW in Self-propulsion Simulation of KCS

Keunjae Kim (SSPA, Sweden)
Da-qing Li (SSPA, Sweden)

SUMMARY

This paper presents the results of the verification study performed for KCS, the case 2-3a and 2-3b proposed by the Gothenburg 2010 Workshop. Self-propulsion simulations have been made by SHIPFLOW with four geometrically similar grids. Verification study is performed to obtain grid convergence uncertainties (U_G) following the procedures proposed by Eca & Hoekstra. (2006). The computed resistance coefficient and propulsive factors are presented, and detail comparison of the computed flow fields at downstream behind the propeller plane is also made with available experiment data.

1. INTRODUCTION

This paper reports the results of the verification study performed in self-propulsion simulations for KCS. Two test cases are investigated; the case 2-3a: self-propulsion simulations at ship point in calm water and the case 2-3b: self-propulsion simulations at model point.

SHIPFLOW – CHAPMAN coupled with lifting line based propeller analysis module(LL) was used to test the applicability of LL module to self-propulsion simulation. Assuming that the effect of free surface on propeller-hull interaction is rather small in design draft condition, all computation made here are restricted to double-model flow in which the free surface is assumed to be flat and treated as a symmetry plane.

Verification study has been performed with four geometrically similar grids; the finest(10.0M grid points), fine(4.0M), medium(1.6M) and coarse(0.7M). The procedure used for uncertainty estimation is based on a least squares variant of the Grid Convergence Index method proposed by Eca and Hoekstra(2006).

2. NUMERICAL METHOD

2.1 SHIPFLOW – CHAPMAN

SHIPFLOW includes three flow analysis modules: A free surface wave elevation can be computed with the potential flow solver (XPAN), a thin boundary layer and transition can be evaluated with the boundary layer method (XBOUND) and a wake region resolved in the Reynolds Averaged Navier-Stokes (RANS) solver, the CHAPMAN code.

The CHAPMAN code is a new viscous solver included in SHIPFLOW under the name XCHAP and the Reynolds Averaged Navier - Stokes equations are solved for steady incompressible flow using a finite volume method. A first order Roe scheme is used for the convective terms and a flux correction is added to obtain a higher order of accuracy. In the code three turbulence models are implemented, the kω-SST, kω-BSL models and the explicit algebraic stress model, EASM. No wall functions are used in the code and the model equations are integrated to the wall. The momentum, pressure and turbulence equations are solved in a coupled manner with the alternating direction implicit (ADI) method.

2.2 Lifting Line Method

SHIPFLOW also includes a lifting line based propeller analysis module(LL). In this model, a finite-bladed propeller is first replaced with an infinite- bladed propeller. Then a series of vortex systems, such as bound vortices, hub vortices and free(trailing) vortices, are distributed to represent the propeller. The slipstream contraction is not considered in this model because the pitch and the radius of each vortex line are assumed to be constant. Only the steady part of induced velocity is taken into account, although this method is mainly proved for lightly loaded propellers by Hough and Ordway (1965). The method used in the calculations of the induced velocities of propeller can be found in Dyne (1967). The determination of the non-dimensional blade circulation is made by incorporating a method based on Goldstein's Kappa theory (see Goldstein 1929). The viscous drag of the blade is calculated in an approximate way by an empirical formula for blade section drag. The principle of this method is briefly described by Zhang(1990) and Li(1994).

2.3 Modelling propeller/hull interaction by body force approach

The effect of propeller is introduced in the RANS method as a body force for numerical modeling of propeller. By applying the body forces to numerical cells on the propeller disk, the flow is accelerated in the same way as suction of the flows by the propeller. The body force are calculated by propeller analysis code which is run iteratively with the

RANS solver. The velocity computed by RANS solver over the whole domain, subtracting the induced velocity estimated by propeller analysis code, leads to a effective wake. This effective wake will be the inflow to the propeller analysis code, which thus calculates axial and tangential body forces. These forces are then returned to the RANS solver in an iterative way.

In SHIPFLOW, a lifting line based propeller analysis code(LL) is coupled with RANS solver XCHAP. This coupling technique has been implemented in SHIPFLOW firstly by Zhang(1990) and further improved later by Li(1994). A validation of this method has been made by Han(2008) in her Ph D research work at Chalmers. The principle of the method is briefly described by Han.

3. TEST HULL

The test hull selected for case 2-3a and 2-3b is KCS(MOERI 3,600TEU Containership) representing the state of the art design today. The main dimensions are: length between perpendiculars(Lpp) 230m, beam(b) 32.2m. The propellers tested is KP505 which is fixed, right running, five blades propeller with a diameter of 7.9m. The hull and propeller geometry as well as other relevant condition are found in workshop web site(www.gothenburg2010.org). Flow measurements for model scale of the ship have been carried out by MOERI in 2001[Van et al, 1989 and Kim et al, 2001], NMRI in 2005[Hino et al] and FORCE in1992 [Simonsen et al, 2008], including velocity fields without and with rudder, thrust, torque, propulsive factors and sinkage and trim.

The Froude number chosen for these computations was 0.26, but the Reynolds number computed are 1.4x107 and 6.52x106 as model size tested are differ between MOERI/NMRI and FORCE(m). The propeller geometry was supplied by MOERI, but slight adjustment was introduced by SVA for small model tested at FORCE.

4. SELP-PROPULSION SIMULATION

4.1 Simulation Procedure

Computation were made at design speed Vs=24 Knots (Fr=0.26). Assuming that the effect of free surface on propeller-hull interaction is rather small in design draft condition, all computation made here are restricted to double-model flow in which the free surface is assumed to be flat and treated as a symmetry plane.

Before starting the self-propulsion simulation, the prediction of inflow to the propeller disc was made first. The propeller is modelled by cylindrical grid although the propeller is not working in the resistance computation. Thereafter self-propulsion simulation was started from the converged solution from resistance computation made with propeller and rudder grid. A sudden introduction of propeller effects by adding the body force terms in the momentum equations may cause instability during the iterative solution procedure. Therefore, the body force is added in gradual mode with relaxation factor of 0.15 until full body force is introduced.

In the self-propulsion simulation, the towing force SFC is applied and the propeller rpm adjusted until the self-propulsion point is reached; the propeller thrust force produced by propeller plus towing force may balance the resistance force (the increase of the resistance force acting on the hull due to the propeller suction in the self-propulsion situation). The towing force is based on model-ship correlation, roughness allowance and wave resistance correction. Wave resistance is computed from non-linear version of free surface potential flow module, SHIPFLOW-XPAN.

4.2 Computation Domain

The computational domain is both side - cylindrical and covers the whole hull as the flow is unsymmetrical due to rotation of propeller. The inlet, outlet position and the outer boundary of the domain are different from the approach used and different teams, but the minimum extent of the domain was used based on the study in earlier projects. The H-O grids used have singularity lines extending from the vicinity of the keel line from the aft bulb downstream. The centre plane is a folded surface and the implicit interpolation across the faces is used in the computations.

4.3 Boundary Condition

The computations are performed without a free surface and the slip condition (symmetry) is applied instead, where the normal velocity component is zero and for all other flow quantities the normal derivatives are zero. The no - slip condition, velocity equal to zero, is applied on the hull surface. On the outer boundary where the undisturbed flow enters the fluid domain the inflow condition is used and where it exits the domain the outflow condition is applied automatically. The inflow is characterized by the fixed velocity and turbulent quantities and the outflow by the fixed pressure.

5. UNCERTAINTY ESTIMATION

5.1 Uncertainty Estimation Procedure

An uncertainty estimation proposed by Eca, Hoekstra and Toxopeus (2005) is used. The following procedure were used:

- Determine the observed order of accuracy, p, from the available data
- For $0.95 \leq p < 2.05$, U_ϕ is estimated with the Grid Convergence Index proposed and the standard deviation U_S of the fit:

$$U_\phi = 1.25\,|\delta_{RE}| + U_S \qquad (1)$$

The extrapolated value is taken as

$\phi_0 = \phi_1 + \delta_{RE}$ where ϕ_1 is the value from the finest grid

- For $0 < p < 0.95$, the same error estimate is made but is then compared with the data range Δ_M multiplied by the safety factor 1.25, so that U_ϕ is obtained from:

$$U_\phi = min(1.25|\delta_{RE}| + U_S, \Delta_M) \quad (2)$$

If $\Delta_M > 1.25|\delta_{RE}| + U_S$ then $\phi_0 = \phi_1$

- For $p \geq 2.05$

$$U_\phi = max(1.25|\delta^*_{RE}| + U_S, \Delta_M) \quad (3)$$

where δ^*_{RE} is calculated from a function with fixed p=2 fitted to the data. The extrapolated value is $\phi_0 = \phi_1 + \delta^*_{RE}$

- If monotonic convergence is not observed

$$U_\phi = 3\,\Delta_M \text{ and } \phi_0 = \phi_1 \quad (4)$$

5.2 Case 1: Self-propelled condition at ship point in calm water

Self-propulsion simulations are made at Td=10.8m (fixed even keel condition) and design speed Fr=0.26(Re=$1.4x10^7$ in model scale). The self propulsion computation is to be carried out at the ship point following the experimental procedure. Thus, the rate of revolutions of the propeller n is to be adjusted to obtain force equilibrium in the longitudinal direction considering the applied towing force (Skin Friction Correction, SFC), i.e

$$T = R_T(SP) - SFC \quad (5)$$

where T is the computed thrust, RT(SP) is the total resistance at self propulsion and SFC = 30.272 N or towing force coefficient Ctow= $1.330x10^{-03}$(from the tests). Typically, with current version of SHIPFLOW, this type of simulation is made with double model flow and so wave resistance correction (Cw=$0.5380x10^{-03}$) were made. The applied towing force coefficient in the simulation is $0.7914x10^{-03}$.

5.2.1 Grid sets

Four geometrically similar single-block structured grids with H-O topology have been generated using grid refinement ratio $r_G of 2^{0.4}$ for the entire computational domain. The grids are prepared using the grid generator module XGRID of the SHIPFLOW software. The XGRID is restricted to have constant x-planes which makes that the grid nodes does not match the bow and stern contours. A stretching along the x-axis is used to refine the bow and stern regions where the surface curvature is large and the hull shape needs to be represented more accurately.

The propeller is modelled by cylindrical grid using 12x32x31cells in the axial, radial and tangential direction. The number of propeller grid cells has been kept constant in the grid refinement tests.

Table 1 presents the number of grid nodes of the four grids for self-propulsion simulation made. The number of grid cells varies from 9.2M cellss for the finest grid g1 to 0.8M cells for the coarse grid g4.

Table 1 Number of grid nodes of the four grids for self-propulsion simulation of KCS, Case 2-3a.

Grid	Nc	y+	r_G=hi/h1
1	9.2M(433x172x123)	0.4665	1
2	4.0M(328x130x93)	0.6156	1.3195
3	1.8M(249x98x71)	0.8122	1.7410
4	0.8M(188x74x54)	1.0718	2.2973

5.2.2 Resistance Coefficients

Results of resistance prediction are summarized in Table 2. In addition to resistance coefficients obtained for the four grids, the estimated iterative uncertainty in percentage of the converged solution is given.

Table 2 Resistance prediction for KCS, Case 2-3a.

Grid	C_F x10^3	Std %C_F	C_{PV} x 10^3	Std %C_{VP}	C_T x 10^3	Std %C_T
					3.550	
1	2.7594	0.03	0.2829	13.9	3.5803	1.11
2	2.7447	0.01	0.3037	6.05	3.5864	0.52
3	2.7128	0.00	0.3521	0.03	3.6029	0.00
4	2.6365	0.00	0.4627	0.01	3.6372	0.00
E%D					-0.85	
ε_{12}%S_1	0.53		7.36		0.17	
U_I/ε_{12}	0.049		1.88		6.53	
$p_G/p_{G,th}$	1.53		1.50		1.45	
Φ_0	2.7697		0.2667		3.5744	
$\Phi_{0,p=2}$	2.7937		0.2326		3.5643	
U_S	6.204e-04		1.308e-04		7.555e-04	
U_G%S_1	5.57		79.4		1.99	

Remarks:

1) Comparison Error, E%D=(D-S)/D100, where D is the EFD value, and S is the simulation value.
2) Relative change in solution: ε_{12}%S_1 = $|(S_1-S_2)/S_1|100$, "1" refers to the finest grid.
3) Iterative uncertainty U_I is based on fine grid solution.
4) p_G is the estimated order of accuracy and p_G,th is the theoretical order of accuracy.
5) U_G is the grid uncertainty

For the viscous pressure resistance coefficient, the estimated iterative uncertainty is rather high; 13.9% in the finest grid g1 and 6 % in the fine grid g2 while almost 0% for the two coarse grids. The iterative uncertainty is estimated in relative variation in percentage compared with a converged solution. In the present study, the convergence solution is obtained by taking an average value of the last 4,000

iterations. The iterative uncertainty is originated by the non-linearity of RANS equations and the turbulence model solved in CFD. A nonlinear EASM turbulence model is used in the present calculation and it suffers from a high level of uncertainty.

On the other hand, very small, all most 0%, variation is observed on the viscous frictional resistance for all grids tested. It seems that the iterative uncertainty estimation for frictional resistance component is quite reliable.

As expected from the well known fact that the variation of pressure resistance and frictional resistance is opposite as the grid density changes. As the number of grid increases, the pressure resistance decreases with a variation as high as 38%, while the frictional resistance increases with much smaller variation with 4.7%. Fortunately, however, the pressure resistance is a small part(around 10%) of total resistance and the impact of pressure resistance component on the uncertainty of total resistance can be limited.

The estimation of grid uncertainty is made according to the procedure proposed by Eca and Hoekstra(2006) at 2nd Workshop on CFD Uncertainty Analysis held in Lisbon. The error estimation is made using extrapolation formula with exponent; $U = U_0 + C\,h^p$. The three unknowns U_0, C and p are determined by a best root mean square fit using the solution obtained on the four grids. Fig. 1 presents the convergence of resistance components with the grid refinements. Monotonic convergence is obtained for the resistance coefficients; pG/pG,th are around 1.5. The estimated grid uncertainty $U_G\%S_1$ is 1.59.

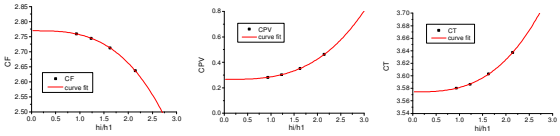

Fig.1 Convergence of resistance coefficients as function of grid refinement ratio, from the left; frictional resistance, viscous pressure resistance and total resistance.

5.2.3 Self-propulsion factors

The predicted self-propulsion factors(K_T. K_Q and rps) and force coefficients(C_F, C_P and C_T) for all four grids tested in Table 3. The force coefficients are from frictional and pressure components, but computed in the self-propulsion condition. The total force coefficient C_T is sum of total drag and towing force coefficient.

Table 3 Force coefficients, self-propulsion simulation for KCS.

Grid	K_T	K_Q	rps	C_F x10^3	C_{PV} x 10^3	C_T x 10^3
	0.170	0.0288	9.50			3.966
1	0.1791	0.0306	9.28	2.755	0.637	3.994
2	0.1797	0.0307	9.27	2.740	0.660	4.002
3	0.1837	0.0312	9.26	2.709	0.711	4.022
4	0.1848	0.0314	9.24	2.633	0.825	4.061
%stdev	0.68	0.55	0.26	0.02	5.17	0.84
E%D	-5.34	-6.26	2.33			-0.71
$\varepsilon_{12}\%S_1$	0.3652	0.3496	0.0793	0.5380	3.5172	0.1930
U_I/ε_{12}	0.0033	0.0005	0.0021	0.0009	0.0094	0.0063
$p_G/p_{G,th}$	0.131	0.06	0.0001	1.53	1.46	1.30
Φ_0	0.1556	0.0219	257.0	2.7652	0.6189	3.9858
$\Phi_{0,p=2}$	0.1779	0.0310	9.2757	2.7890	0.5851	3.9758
U_S	0.0014	0.0018	5.E-04	7.E-04	2.E-04	9.E-04
$U_G\%S_1$	15.02	12.4	0.1550	3.2663	21.467	1.1948

For the force coefficients, the estimated iterative uncertainty is much lower level as compared to the corresponding coefficients from resistance prediction. Due to action of propeller, the flow characteristics is more accelerating flows with much reduced vortical/separated flows near stern of the ship. Another interesting point to be noted is a large increase of pressure force component. This is due to suction of flows by propeller action, the pressure near stern area decreases resulting in the increase of pressure force component.

The observed order of grid convergence accuracy for all predicted self-propulsion factors and force components are shown in Fig. 2. Monotonic convergence is obtained; $p_G/p_{G,th}$ is arond 1.4 for all force coefficients, but between 0 and 1 for all propulsive factors. The estimated grid uncertainty $U_G\%S_1$ =15% and 12% for K_T and K_Q and <1% for rps.

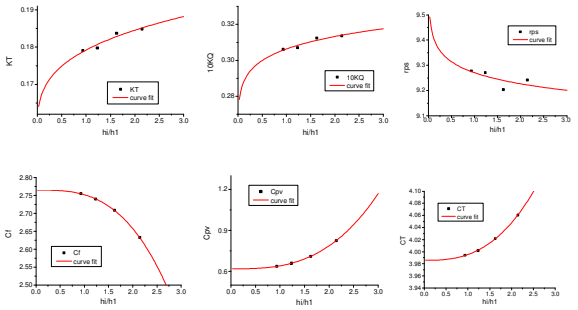

Fig. 2 Convergence of force coefficients and self-propulsion factors as function of grid refinement ratio, case 2-3a, from upper left; K_T. K_Q and rps, bottom left: C_F, C_P and C_T in self-propulsion condition.

5.2.4 Velocity Field at downstream of Propeller Plan

The velocity field computed at downstream of the propeller plane with the finest grid g1 and the coarsest grid g4 are compared with the measurement. Fig. 3 presents axial velocity contours at x/Lpp=0.9911. In general the calculation predicts the flow characteristics very well in several aspects. Both calculations and experiment indicated that the propeller gets more heavily loaded on the starboard side, resulting in a large acceleration and a higher velocity on the starboard side. The axial velocity is accelerated to a

maximum 1.2 times the ship speed. Very good agreement is achieved by g1 grid as compared to g4 grid. It confirms the improved prediction obtained with grid refinements.

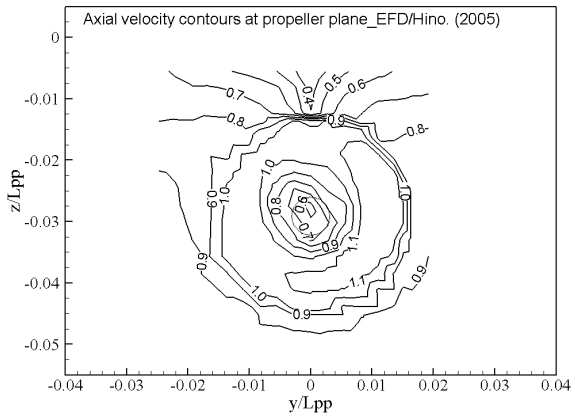

NMRI measurement

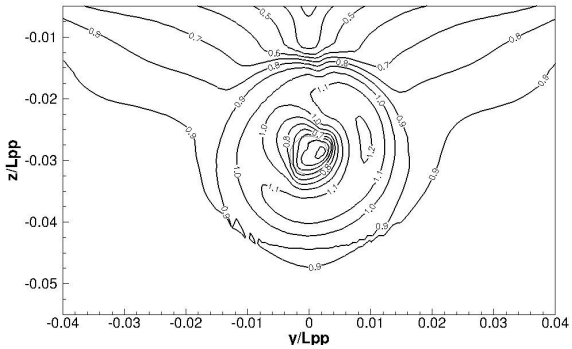

Computed velocity contours with g1 grid

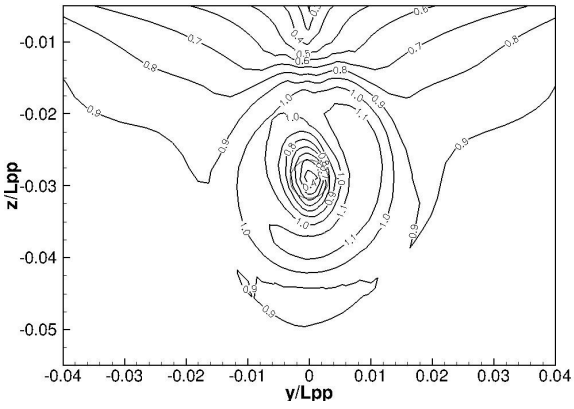

Computed velocity contours with g4 grid

Fig. 3 Axial velocity contours at x/Lpp=0.9911.

The Cross flow vector computed with all four grids is compared with measurements in Figs 4. Very good predictions were produced with all grids, but it confirms again the improved prediction obtained with grid refinements.

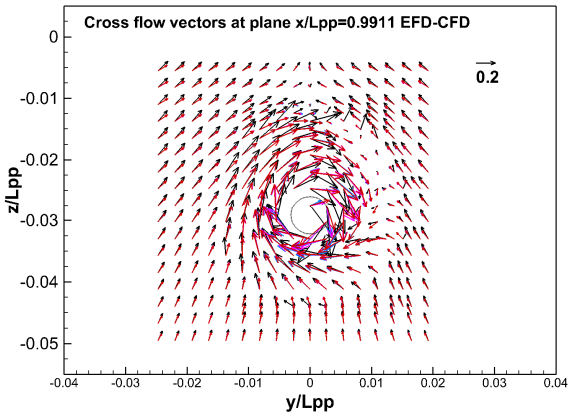

Fig.4 Cross flow vector plot at x/Lpp=0.9911, black: NMRI measurement, red: computation with g1 grid

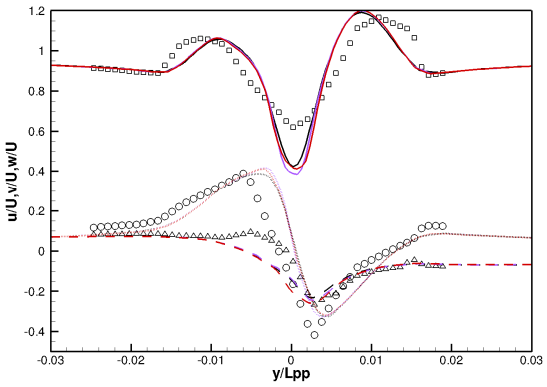

Fig.5 Mean velocity profiles at the position x/Lpp=0.9911 at z/Lpp=-0.03, black circle: NMRI measurement, red: computation with g1 grid, blue: computation with g4 grid

Fig. 5 display three components of mean velocity profiles at the position x/Lpp=0.9911 at z/Lpp=-0.03(downstream of propeller plane). The velocity contours predicted with four grids as well as measured contour are compared in the same figure. This comparison shows a good visual convergence behaviour with grid refinements.

5.2.5 Hull Surface Pressure

The hull surface pressure distribution is compared between computed and measured pressure distribution in Fig. 6. Some noticeable differences are found close to waterline. This is due to free surface, which is not considered in the computation. Another difference can be noted near bilge region; several minimum pressure points are shown in measured pressure distribution. No clear explanation can be made and further investigation may be required.

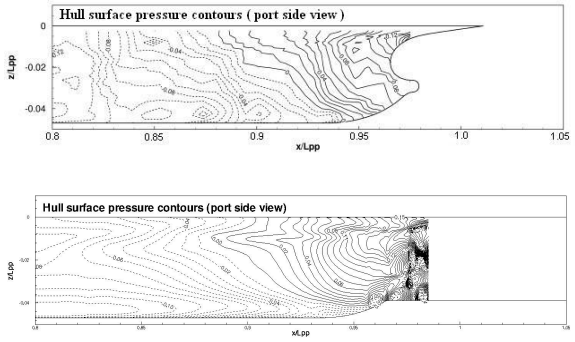

Fig.6 Pressure distribution on the hull surface, port side. top: NMRI measurement, bottom: computation with g1 grid

5.3 Case 2: Self-propelled condition at model point in calm water

In the second test case, numerical uncertainty estimation exercise is made for self-propulsion simulation of KCS at model point in calm water. The ship is free to trim and heave during the self-propulsion simulation without the towing force applied. Thus, the rate of revolutions of the propeller n is to be adjusted to obtain force equilibrium not only in longitudinal direction between ship resistance and propeller thrust but also in vertical direction between buoyancy force and sinking force. The self propulsion computation is carried out following the experimental procedure.

$$T = RT(SP) \qquad (6)$$

where T is the computed thrust, RT(SP) is the total resistance at self propulsion.

The towing tank tests were done by FORCE with 4.3671m scaled model in full load condition (sinkage σ=0.44m and trim angle τ=-0.143°) and design speed Vs=24 Knots. The simulation is made for initially fixed trimmed condition with double model flow approximation and so wave resistance correction(Cw= -0.580x10^{-03}) was made.

5.3.1 Grid Sets

The same four single-block structured H-O type grids are used as a background grid which covered the entire ship incl. propeller. In stern/wake flow computation, the overlapping grid technique with structured components was used to achieve high quality cells for the background hull and appendages.

The rudder blade was a rudder component based on NACA sections . Table 4 present the number of grid nodes of the four grids for self-propulsion simulation made.

Table 4 Number of grid nodes of the four grids for self-propulsion simulation of KCS, case 2-3b

Grid	Nc	y+	rG=hi/h1
1	9.6M(hull: 433x172x123, rudder: 133x58x58)	0.4665	1
2	4.2M(hull:328x130x93, Rudder: 101x44x44)	0.6156	1.3195
3	1.9M(hull:249x98x71, rudder: 76x33x33)	0.8122	1.7410
4	0.8M(hull:188x74x54, rudder: 58x25x25)	1.0718	2.2973

5.3.2 Resistance Coefficients

All predicted resistance coefficients are summarised in Table 5. Fig. 7 presents the convergence of resistance coefficients with the grid refinement tests. Similar observation can be seen to the case 2-3a; Monotonic convergence is obtained for the resistance coefficients; $p_G/p_{G,th}$ are around 1.5. The estimated grid uncertainty $U_G\%S_1$ is 1.1.

Table 5 Resistance prediction for KCS.

Grid	C_F x10^3	Std(%) C_F	C_{PV} x 10^3	Std(%) C_{VP}	C_T x 10^3	Std(%) C_T
1	3.059	0.028	0.3231	13.66	4.212	1.059
2	3.045	0.011	0.3455	6.128	4.221	0.507
3	3.015	0.006	0.4035	0.163	4.249	0.016
4	2.935	0.003	0.4936	0.006	4.259	0.002
$\varepsilon_{12}\%S_1$	0.45		6.91		0.20	
U_I/ε_{12}	0.06		1.98		5.2	
$p_G/p_{G,th}$	1.68		1.08		0.07	
Φ_0	3.0662		0.2868		3.7605	
$\Phi_{0,p=2}$	3.0944		0.2795		4.2040	
U_S	0.0012		0.0052		0.0084	
$U_G\%S_1$	5.06		65.9		1.11	

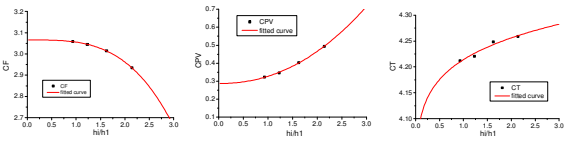

Fig.7 Convergence of resistance coefficients as function of grid refinement ratio, case 2-3b. from the left; frictional resistance, viscous pressure resistance and total resistance.

5.3.3 Self-propulsion factors

The predicted self-propulsion factors(KT. KQ and rps) and force coefficients(CF, CP and CT) for all four grids tested in Table 6.

Table 6 Force coefficients, self-propulsion simulation for KCS.

Grid	KT	KQ	rps	C_F x10^3	C_{PV} x 10^3	C_T x 10^3
	0.253	0.0408	14.15			5.222
1	0.2535	0.0398	13.45	3.101	0.792	4.663
2	0.2560	0.0400	13.39	3.088	0.811	4.668
3	0.2652	0.0412	13.22	3.060	0.884	4.715
4	0.2676	0.0415	13.17	2.983	0.970	4.723
%stdev	0.39	0.35	0.23	0.02	4.34	0.78

E%D	-0.18	2.45	4.98			10.70
ε_{12}%S_1	0.9966	0.7362	0.4314	0.4192	2.3990	0.1072
U_I/ ε_{12}	0.0009	0.0002	0.0707	0.0013	0.0143	0.3251
p_G/p_G,th	0.0018	0.0015	0.0018	1.713	0.939	0.088
Φ_0	-4.906	-6.994	116.40	3.108	0.7386	4.2258
$\Phi_{0,p=2}$	0.2511	0.3953	13.486	3.135	0.7456	4.6504
U_S	0.0030	0.0038	0.0527	0.0013	0.0123	0.0181
U_G%S_1	6.95	5.20	2.54	4.76	10.07	1.61

The observed order of grid convergence accuracy for all predicted self-propulsion factors and force components are shown in Fig. 8. Monotonic convergence is obtained; pG/pG,th is between 1.1 and 1.7 for C_F and C_{PV}, but close to 0 for all propulsive factors. The estimated grid uncertainty U_G%S1 =6.95% and 5.2% for K_T and K_Q and 2.5% for rps.

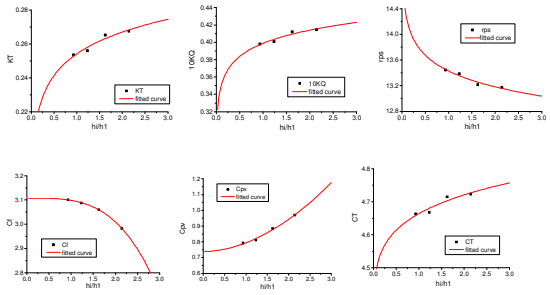

Fig. 8 Convergence of force coefficients and self-propulsion factors as function of grid refinement ratio, case 2-3b, from upper left; KT. KQ and rps, bottom left: CF, CP and CT in self-propulsion condition.

6. CONCLUSION

This paper presents the results of the verification study performed in self-propulsion simulations with SHIPFLOW for KCS, the case 2-3a and 2-3b proposed by Gothenburg 2010 Workshop. Four geometrically similar grids are used; the finest(10.0M grid points), fine(4.0M), medium(1.6M) and coarse(0.7M). The procedure used for uncertainty estimation is based on a least squares variant of the Grid Convergence Index method proposed by Eca and Hoekstra(2006). The present study indicates monotonic convergence for all integrated quantities; the estimated order of accuracy is higher than second order for force coefficients but more likely to be first order for self-propulsion factors.

REFERENCES

Eca Luis and Hoelstra Martin (2006): "Discretization Uncertainty Estimation based on Least Squares version of the Grid Convergence Index", 2nd Workshop on CFD Uncertainty Analysis, Lisbon, October 2006.

FLOWTECH International AB(2009): SHIPFLOW v4.3 Users Manual

Goldstein. S. (1929): "On the vortex theory of screw propellers". Proc. Roy. Soc.. London. Series A 123.

Zhang D H (1990) Numerical computation of ship stern/propeller flow. Ph D thesis. Department of Naval Architecture and Ocean Engineering. Chalmers University of Technology.

Li. D-Q and Dyne. G (1994) Investigation on propeller-rudder interaction by numerical methods. PhD thesis. Department of Naval Architecture and Ocean Engineering. Division of Hydrodynamics. Chalmers University of Technology. Gothenburg. Sweden.

Han. K J (2008) Numerical optimization of hull/propeller/rudder configurations. PhD thesis. Department of Naval Architecture and Ocean Engineering. Division of Hydrodynamics. Chalmers University of Technology. Gothenburg. Sweden.

Hough. G. R and Ordway. D. E.(1965) The generalized actuator disk. Development in Theoretical and Applied Mathematics. Vol II. 1965

Dyne (1967) A method for the design of ducted propellers in a uniform flow. Report No. 62. SSPA publications. Gothenburg. Sweden

Björn Regnström, Leif Broberg, Magnus Östberg, Nicolas Bethfield and Lars Larsson. (2005), "Drag prediction for the KVLCC2M hull" *CFD Workshop Tokyo 2005*

Keunjae Kim (2010), Self-propulsion Test Simulation Study with CHAPMAN + MPUF, SSPA Internal Project Report 40095164

Bjorn Regnstrom, Leif Broberg, Michal Orych and Magnus Ostberg, (2008), Verification and Validation of the Chapman Incompressible RANS Solver #rd Workshop on CFD Uncertainty Analysis, Lisbon

THE PREDICTION OF KCS RESISTANCE AND SELF-PROPULSION BY RANSE

W. Jin, Q. Gao, D. Vassalos
Ship Stability Research Center, University of Strathclyde, UK

1. SUMMARY

A RANS based CFD solver FLUENT was used to compute resistance and self-propulsion of a container model KCS (Gothenburg 2010 CFD workshop T2.1 and T2.3a). The computed hydrodynamics of resistance and self-propulsion, and flow fields were compared with experiment data provided by workshop organizer. General agreements are satisfactory.

2. NUMERICAL FORMULATIONS

2.1 Governing equations

The Reynolds averaged Navier-Stokes equations (RANSE) with K-ε turbulence model were solved. The VOF algorithm was applied to capture free surface. The governing equations can be written as follows.

2.1.1 Continuity equation

$$\nabla \bullet \mathbf{u} = 0 \tag{1}$$

2.1.2 RANSE equation

$$\frac{\partial \mathbf{u}}{\partial \mathrm{t}} + \mathbf{u} \bullet \nabla \mathbf{u} = -\frac{1}{\rho}\nabla \mathrm{p} - \mathbf{g} + \nu \nabla^2 \mathbf{u} \tag{2}$$

2.1.3 Turbulence model

$$\frac{\partial}{\partial t}(\rho K) + \nabla \cdot (\rho \mathbf{u} K) = \nabla \cdot (\Gamma_k \nabla K) + G_K - Y_K \tag{3}$$

$$\frac{\partial}{\partial t}(\rho \varepsilon) + \nabla \cdot (\rho \mathbf{u} \varepsilon) = \nabla \cdot (\Gamma_\varepsilon \nabla \varepsilon) + G_\varepsilon - Y_\varepsilon \tag{4}$$

2.1.4 VOF equation

$$\frac{\partial}{\partial t}(r_w) + \nabla \cdot (r_w \mathbf{u}) = 0. \tag{5}$$

2.2 Boundary conditions

The inlet is located at one ship length in front of bow where velocity components and volume fraction were imposed.

The outlet is at two ship length behind the stern where the hydrostatic pressure is specified.

Wall function was used on hull boundary. Yplus value is at the range of 50-100.

2.3 Numerics

Second order upwinding interpolation was used for convection flux. SIMPLE method was applied to obtain pressure. Geometric reconstruction of volume fraction was used to calculate wave elevation.

3. TEST CASE

The test cases T2.1 and 2.3a of the workshop was selected for benchmarking calculations. The main parameters are given as below.

Table 1 Main particulars of KCS

Main particulars		**Full scale**
Length between perpendiculars	L_{PP} (m)	230.0
Length of waterline	L_{WL} (m)	232.5
Maximum beam of waterline	B_{WL} (m)	32.2
Depth	D (m)	19.0
Draft	T (m)	10.8
Displacement	(m^3)	52030

Wetted area w/o rudder	S_W (m^2)	9424
Wetted surface area of rudder	S_R (m^2)	115.0
Block coefficient (CB)		0.6505
Midship section coefficient (CM)		0.9849
LCB (%L_{pp}), fwd+		-1.48
Vertical Center of Gravity	KG (m)	7.28
Metacentric height	GM (m)	0.60
Moment of Inertia	K_{xx}/B	0.40
Moment of Inertia	K_{yy}/L_{PP}, K_{zz}/L_{PP}	0.25
Propeller center from FP	x/L_{PP}	0.9825
Propeller center below WL	$-z/L_{PP}$	0.02913
Propeller model	KP505	
Propeller blades		5
Propeller section profile	NACA66	
Propeller Diameter	(m)	7.9
Hub ratio		0.18
Scale ratio		31.6

The sinkage and trim are: s= 0, t = 0°.
V=2.196 m/s
Re = 1.4×10^7
Fr = 0.26

3.1 Mesh

Two meshes with cells 2.5M and 7.9M were generated for the calculations of resistance and self-propulsion of KCS. In self-propulsion calculation, propeller was geometrically meshed separately with hull using interface technique. Roughly 3M cells are used in propeller block. No body force modeling is adopted. Grid uncertainty study was carried out in separate calculations. Special care was given to the number of cells within a wave length, in wave amplitude and boundary layer. The domain and hull surface mesh are shown in Figure 1.

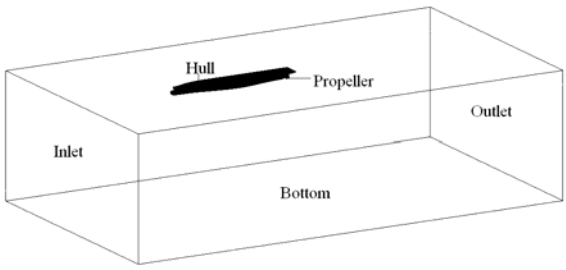

Figure 1 Domain and hull surface mesh

3.2 Parallel computing

The calculations were run on a High Performance Computer (HPC) with 8*130 (nodes) processors provided by Esteem Systems Ltd in partnership with SUN Microsystems (now Oracle).

The machine has a theoretical peak performance of 13 TeraFlops–thirteen thousand billion operations per second.

For a typical resistance calculation of 2M cells, it takes roughly 40 hours of clock time for computational time 30 seconds using 16 cores.

4. RESULTS AND ANALYSIS

The computational results are compared with experimental data from MOERI in the following section.

4.1 Resistance

The comparisons of wave cuts in test case T2.1 are given in Figure 2-4.

The computed wave cuts agree well with measured ones at up to 40% ship length. The crest, trough, wave steepness and phase are well predicted by calculation. However, further away from hull, the computed wave is suffering from numerical diffusion. The mesh resolution at far field is not good enough to capture wave oscillation.

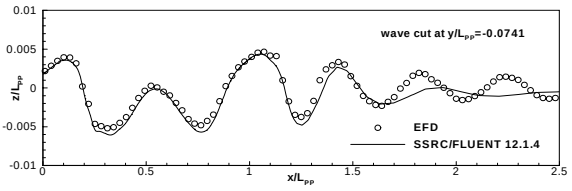

Figure 2 Wave cut, y/L_{PP} = -0.0741

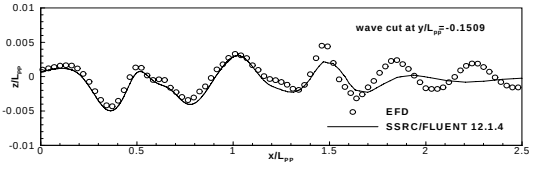

Figure 3 Wave cut, y/L_{PP} =–0.1509

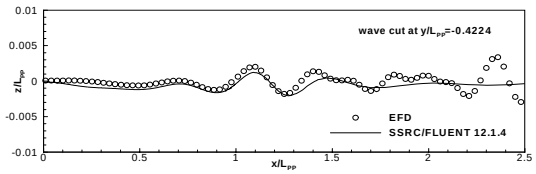

Figure 4 Wave cut, $y/L_{PP} = -0.4224$

The results of wave pattern are shown in Figure 5. The computed near field wave elevation coincides with measured one excellently. The bow wave, shoulder wave, stern wave and wave system are well predicted by calculation.

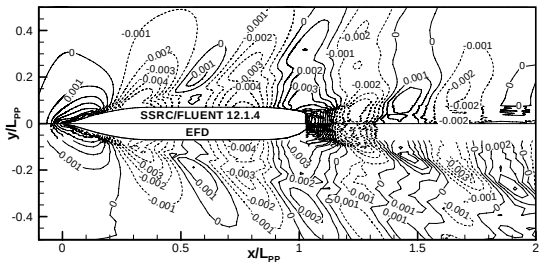

Figure 5 Comparison of wave elevations

The comparisons of velocity fields are shown in Figure 6-8. The computed velocity field at section x/L=0.9825 (propeller plane) in Figure 6 coincides well with measurement in Figure 7. The shape of axial velocity contour (cat ear or hook) and distribution of cross vector are well predicted by present calculation. Additionally, the comparison of 1D slice is made at z/L=-0.0302 in Figure 8. As we can see from the plot, axial velocity u is low near the center plane due to bossing effect, but recover very quick to 0.9 at y/L=0.008. Lateral velocity v is small (less than 10% of free stream) and zero at center plane due to symmetry condition. The vertical velocity w is positive in the outer boundary layer approaching stern due to geometric contraction of hull, but change sign near center plane. A minor cross vortex is formed. Overall, the agreements of computed and measured velocities are acceptable. The discrepancies near center plane are attributed to symmetric condition or turbulence model used.

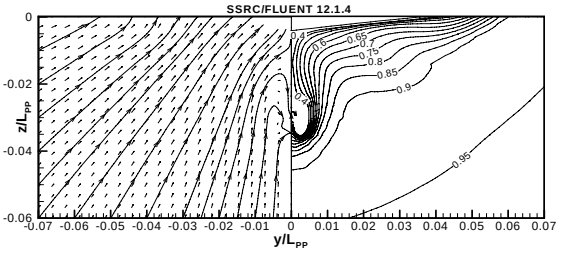

Figure 6 Computed velocity at x=0.9825

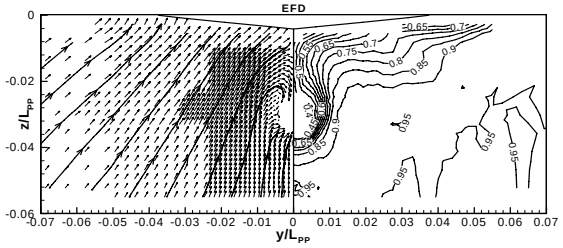

Figure 7 Measured velocity at x=0.9825

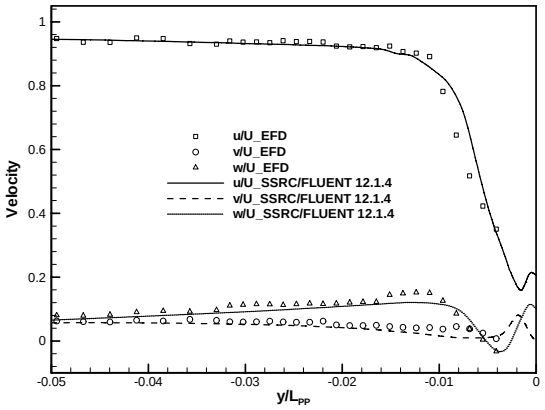

Figure 8 Comparison of velocity at x=0.9825, z=-0.0302

The computed total resistance coefficient is 3.51×10^{-3} which is 1.40% lower than model test data 3.56×10^{-3}.

In summary, good agreements between calculation and measurements are achieved for the calculation of resistance and flow field by RANS approach.

4.2 Self-propulsion

In the test case T2.3a of the workshop (computation of self-propulsion), a benchmarking study with prescribed propeller revolution (9.5rps) and a self-propulsion simulation at the ship point with adjusted propeller revolution were made.

The results at prescribed revolution are presented below.

The comparisons of axial velocity contours at section immediately behind propeller plane (x/L=0.9911) are shown in Figure 9-13. As we can see from the velocity plots with and without propeller, the operation of propeller changes flow field significantly. Flow is not symmetric about center plane anymore. The axial velocity increases remarkably in the propeller area due to acceleration effects. The maximum longitudinal velocity u/U is about 1.2 at starboard side due to clockwise rotation of propeller. The flow is mixed due to wake from hull and induction from propeller; and eventually, axial velocity is more or less evenly distributed circumferentially around propeller shaft.

Similarly, cross flow is accelerating in the propeller plane. Vortices are generated and spread downstream. The maximum magnitude of cross velocity is about 50% of

free stream.

Although qualitative similarity of computed and measured flow fields is seen, some discrepancies are observed as shown in Figure 13. The computed results underestimate the gain of axial velocity and overestimate the gain of cross flow.

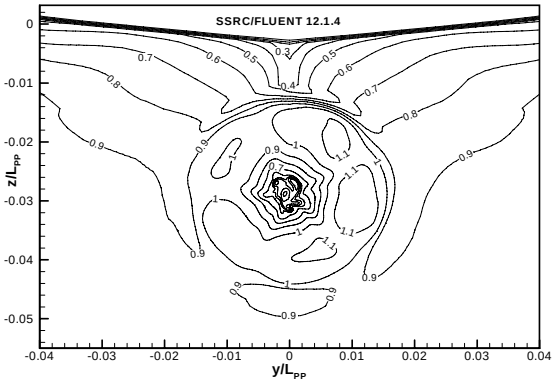

Figure 9 Computed u contour (x=0.9911)

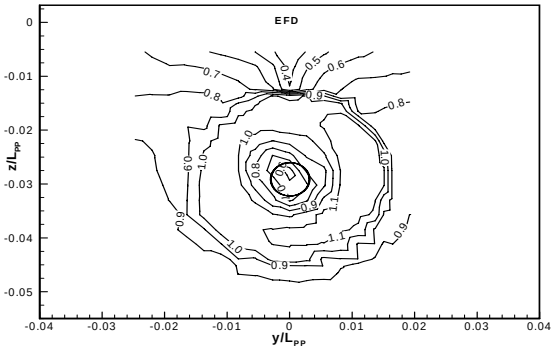

Figure 10 Measured u contour (x=0.9911)

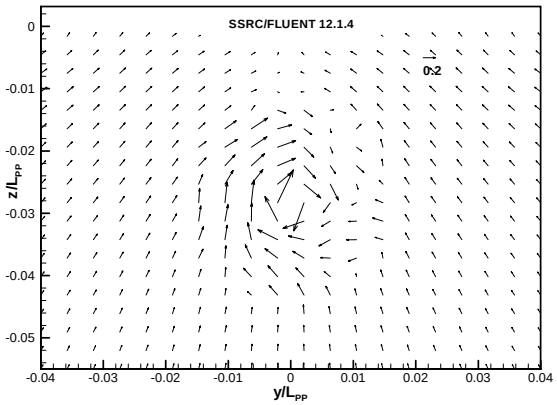

Figure 11 Computed cross stream

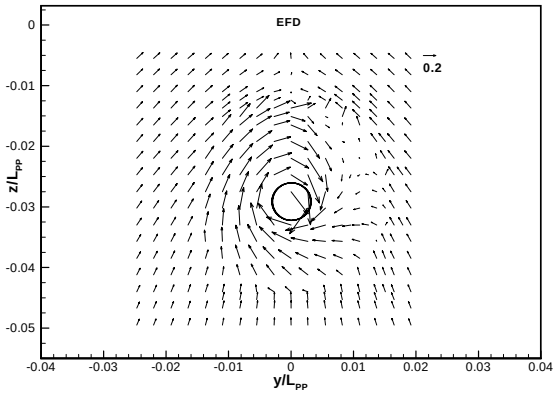

Figure 12 Measured cross stream

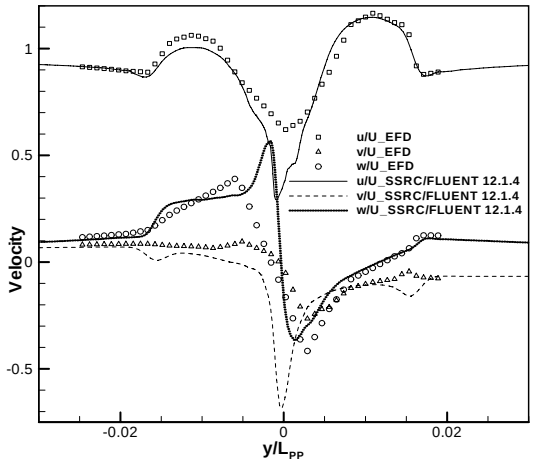

Figure 13 Comparison of velocity cut

The comparisons of pressure coefficients are given in Figure 14-17. The overall agreements between calculation and measurement are reasonably good. The pressure coefficients increase from parallel mid body to stern gradually; and keep same at mid ship but decreased at stern compared with those without propeller in Figure 16-17. Some discrepancies between calculation and measurement are witnessed. The computed Cp is lower than the measured at parallel mid body and higher than measurement near transom.

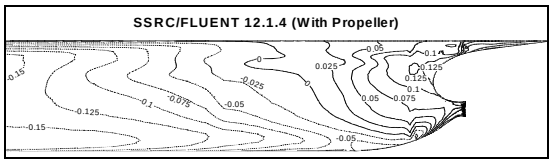

Figure 14 Computed Cp on port (with propeller)

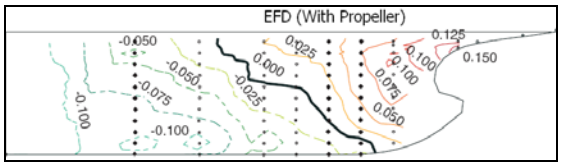

Figure 15 Measured Cp on port (with propeller)

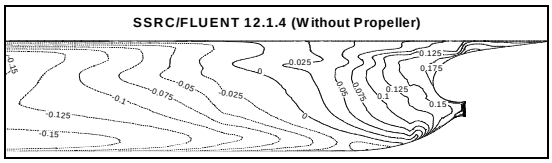

Figure 16 Computed Cp on port (without propeller)

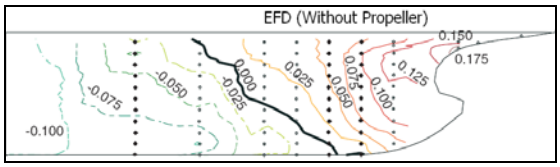

Figure 17 Measured Cp on port (without propeller)

The hydrodynamics is summarized in table 2.

Table 2 Hydrodynamics at rps=9.5

n(rps)	T(N)	Q(N· M)	$R_{T(SP)}$ (N)	(T+SFC-$R_{T(SP)}$)(N)
9.5	57.83	2.545	90.55	-2.47

As towing force SFC is 30.25N, the unbalanced force is -2.47N as shown in the table. Therefore, the revolution rate of propeller was adjusted (increased) for the purpose of self-propulsion.

The final results are given in table 3. In numerical self-propulsion test, the propeller revolution rate is 9.7rps, which is 2.11% larger than measurement. The main reason is higher computed ship resistance (3.9% larger than data). The error of predicted thrust is less than 2%.

Table 3 The results of self-propulsion computation

	$CT_{(SP)}(10^{-3})$	$CP_{(SP)}(10^{-3})$	$CF_{(SP)}(10^{-3})$	K_T	$10K_Q$	n(rps)
CFD	4.121	1.282	2.839	0.173	0.299	9.7
EFD	3.966	-	-	0.170	0.288	9.5
Err (%)	3.91	-	-	1.59	3.82	2.11

5. CONCLUSION

The detailed comparisons of computed and measured results on test cases of KCS (Gothenburg 2010 CFD workshop T2.1 and T2.3a) were carried out. Based on the validation study, the following conclusions can be drawn:

- The predicted total resistances agree better with measurement in resistance calculation than in self-propulsion simulation.
- The computed wave elevation agrees well with measurement at up to 40% ship length. However, further away, the computed wave is suffering from numerical diffusion.
- The computed velocity field coincides reasonably well with the data without propeller. However, notable difference is seen when propeller is in operation.
- The computed pressure coefficients show underestimation at parallel mid body and overestimation at stern.
- The predicted thrust and torque and rotational rate are close with the data. We can conclude that RANSE method can be used for prediction of self-propulsion with acceptable accuracy.

6. ACKNOWLEDGMENTS

This research has been financially supported by European Union FP7 program, ICT-231646, SHOAL: Search and monitoring of Harmful contaminants, Other pollutants And Leaks in vessels in port using a swarm of robotic fish.

REFERENCES

ANSYS FLUENT 12.0 Theory Guide, (2009)

http://www.gothenburg2010.org/

http://www.iihr.uiowa.edu/gothenburg2000/

ITTC Recommended Procedures and Guidelines, Testing and Extrapolation Methods, Resistance, Resistance Test, (2002), 705-02-02-01

Tahara Y., et al., (2006), "RANS simulation of a container ship using a single-phase level-set method with overset grids and the prognosis for extension to a self-propulsion simulator", *Journal of Marine Science and Technology*, Vol. 11, No. 4, p.209-228

Carrica, P.M., et al.,(2010), "Self-propulsion computations using a speed controller and a discretized propeller with dynamic overset grids", *Journal of Marine Science and Technology*

COMPUTATION OF WAVE DIFFRACTION BY RANS APPROACH

Q. Gao, W. Jin, D. Vassalos
Ship Stability Research Center, University of Strathclyde, UK

1. SUMMARY

A RANS based CFD solver FLUENT was used to study ship wave diffraction with speed (Gothenburg 2010 CFD workshop T3.5). Incoming wave was generated by user-defined inlet boundary condition. The computed forces and flow fields were compared with experiment data provided by workshop organizer. General agreements are satisfactory.

2. NUMERICAL FORMULATIONS

2.1 Governing equations

The Reynolds averaged Navier-Stokes equations (RANSE) with SST K-ω turbulence model were solved. The VOF algorithm was applied to capture free surface. The governing equations can be written as follows.

2.1.1 Continuity equation

$$\nabla \bullet \mathbf{u} = 0 \tag{1}$$

2.1.2 RANSE equation

$$\frac{\partial \mathbf{u}}{\partial t} + \mathbf{u} \bullet \nabla \mathbf{u} = -\frac{1}{\rho}\nabla p - \mathbf{g} + \nu \nabla^2 \mathbf{u} \tag{2}$$

2.1.3 Turbulence model

$$\frac{\partial}{\partial t}(\rho K) + \nabla \cdot (\rho \mathbf{u} K) = \nabla \cdot (\Gamma_k \nabla K) + G_K - Y_K \tag{3}$$

$$\frac{\partial}{\partial t}(\rho \omega) + \nabla \cdot (\rho \mathbf{u} \omega) = \nabla \cdot (\Gamma_\omega \nabla \omega) + G_\omega - Y_\omega \tag{4}$$

2.1.4 VOF equation

$$\frac{\partial}{\partial t}(r_w) + \nabla \cdot (r_w \mathbf{u}) = 0. \tag{5}$$

2.2 Boundary conditions

The inlet is located at one ship length in front of bow where velocity components and volume fraction were imposed.

The wave was generated at inlet using following inputs (the same as in model tests):

Wave length $\lambda/L=1.5$
Wave steepness: $Ak = 0.025$
Wave number $k=2\pi/\lambda$
Wave frequency for deep water $\omega=\sqrt{gk}$
Model speed V=1.89m/s
Wave encounter frequency $\omega_e = \omega + kV$
Period $T=2\pi/\omega_e$
Wave elevation at inlet $\zeta = \zeta_a \sin(kx - \omega_e t)$
X velocity $u = \zeta_a \omega e^{kz} \cos(kx - \omega_e t)$
Z velocity $w = \zeta_a \omega e^{kz} \sin(kx - \omega_e t)$

The incoming wave was generated at time 4L/U after mean inflow sweeps whole domain once and solution is converged.

The outlet is at two ship length behind the stern where the hydrostatic pressure is specified. No explicit wave damper is used. The coarse mesh at outlet damps wave numerically.

Wall function was used on hull boundary. Yplus value ranges from 30-50.

2.3 Numerics

Second order upwinding interpolation was used for convection flux. SIMPLE method was applied to obtain pressure. Geometric reconstruction of volume fraction was used to calculate wave elevation.

3. TEST CASE

The test case T3.5 of the workshop was selected as benchmarking calculation. The main dimension of the ship and computational parameters are given as below.

Table 1 Main parameters of the ship

Main particulars		**Full scale**
Length between perpendiculars	L_{PP} (m)	142.0
Length of waterline	L_{WL} (m)	142.18
Maximum beam of waterline	B_{WL} (m)	19.06
Draft	T (m)	6.15
Displacement	Delta (m^3)	8424.4
Wetted area w/o rudder	S_W (m^2)	2972.6
Wetted surface area of rudder	S_R (m^2)	30.8
Block coefficient (CB)	Delta/($L_{PP}B_{WL}$ T)	0.507
Midship section coefficient (CM)		0.821
LCB (%L_{PP}), fwd+		-0.683
Vertical Center of Gravity (from keel)	KG (m)	7.5473
Metacentric height	GM (m)	1.95
Moment of Inertia	K_{xx}/B	0.37
Moment of Inertia	K_{yy}/L_{PP}, K_{zz}/L_{PP}	0.25

Scale ratio: 46.59
The sinkage and trim are: s = -1.92×10^{-3}, t = -0.136°
Incident wave length λ = 1.5 LPP
Wave steepness: Ak = 0.025
Re= 4.86×10^{6}
Fr=0.28

3.1 Mesh

Fine mesh with cells 2M was generated for the simulation. Grid uncertainty study was carried out in separate calculations without wave. Special care was given to the number of cells within a wave length, in wave amplitude and the boundary layer. The domain and hull surface mesh are shown in Figure 1.

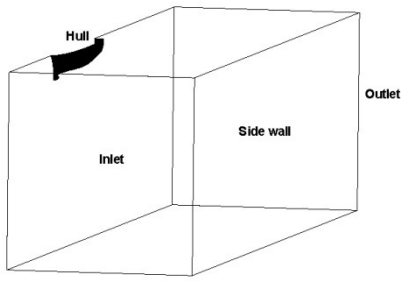

Figure 1 Domain and face mesh

3.2 Parallel computing

The calculations were run on a High Performance Computer (HPC) with 8*130 (nodes) processors provided by Esteem Systems Ltd in partnership with SUN Microsystems (now Oracle).

The machine has a theoretical peak performance of 13 TeraFlops–thirteen thousand billion operations per second.

For a typical resistance calculation of 2M cells, it takes roughly 30 hours of clock time for computational time 20 seconds using 16 cores.

4. RESULTS AND ANALYSIS

The computational results are compared with experimental data from IIHR. The comparisons of forces are given in Figure 2-4 and results of spectrum analysis are in table 2.

The comparison of surge forces is shown in Figure 2. It can be seen that computed surge force is larger in amplitude and mean values than measured one. Besides, there is a large phase difference. Both force time records show the same oscillation period and similar behavior of wave effects.

One thing should be noted that the data of resistances with and without wave (calm water) are the same in the published results. It seems that the measured resistance in head wave is undervalued. The reason is not clear yet.

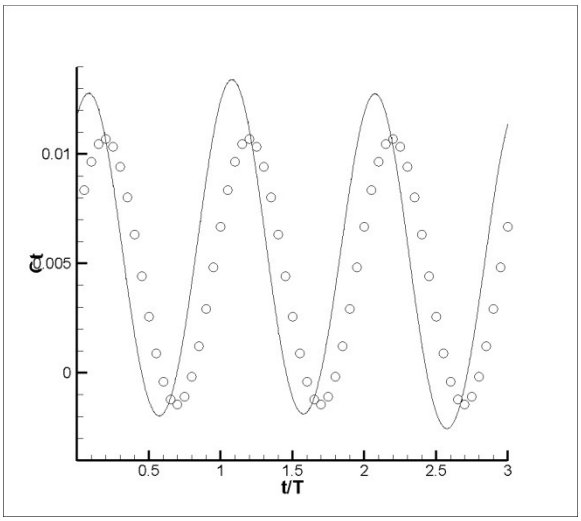

Figure 2 Surge force (Line: present, Symbol: Longo)

The comparison of heave forces is shown in Figure 3. It can be seen that computed heave force is larger in amplitude than measured one. The difference of mean values is maybe due to hydrostatic or steady motion effects. It seems that the amplitude of incoming wave in the calculation is larger than that in the measurement. Again, we notice the phase difference. This is maybe due to data sampling delay in the measurement. Both force time records show the same oscillation period and similar behavior of wave effects.

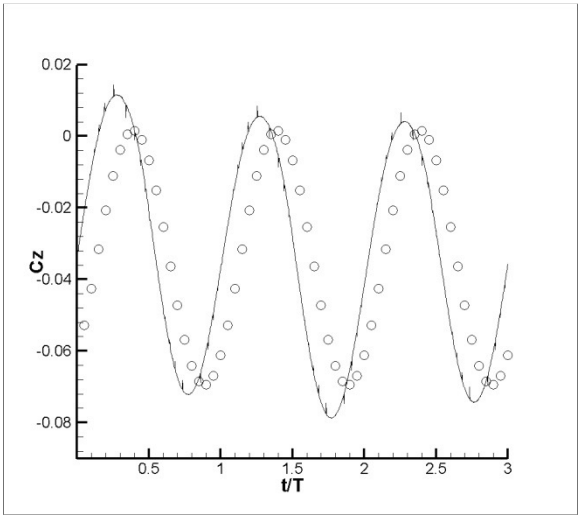

Figure 3 Heave force (Line: present, Symbol: Longo)

The comparison of pitch moments is shown in Figure 4. It can be seen that computed pitch moment is larger in amplitude than measured one. The difference of mean values is maybe due to hydrostatic or steady motion influences. Again, we notice the phase difference, which is similar as in the surge and heave forces.

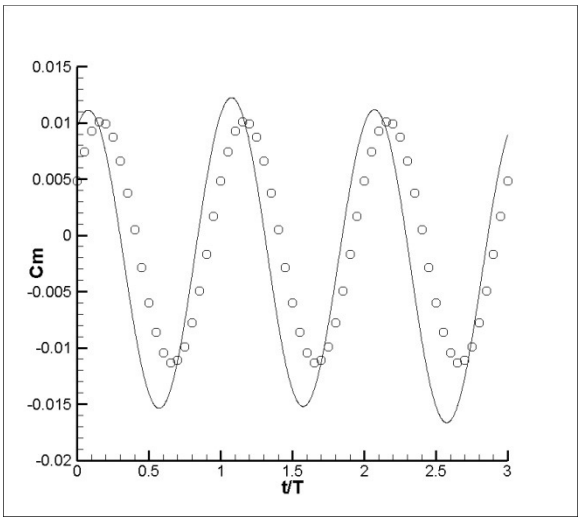

Figure 4 Pitch Moment (Line: present, Symbol: Longo)

From time series of forces, Fourier analysis is carried out and the results are summarized in table 2.

The results of 1st amplitudes show that computed forces are roughly 25% larger than measured ones, which are consistent with above analysis.

The results of 1st phases show that roughly 15 degrees phase difference between calculation and measurement, but not constant from force to force.

The difference of 0th amplitude of surge forces is up to 12.5%, which should be investigated further.

Table 2 Wave spectrum

Cases	CT		
	0th Amplitude	**1st Amplitude**	**1st Phase°**
Present	0.0052	0.00775	-50.4
Longo	0.00462	0.00608	-63.3
E%D	12.5	27.4	-20.4
Cases	CH		
	0th Amplitude	**1st Amplitude**	**1st Phase°**
Present	-0.0344	0.0431	-121
Longo	-0.0334	0.0357	-140
E%D	2.9	20.7	-13.5
Cases	CM		
	0th Amplitude	**1st Amplitude**	**1st Phase°**
Present	-0.00186	0.0136	-50.2
Longo	-6.08×10-4	0.0108	-58.8
E%D		25.9	-14.6

The comparisons of velocity contours are given in Figure 5-7.

The U contour in Figure 5 shows that the overall agreements are acceptable except near centerplane. It can be seen that measured U contour is not exactly satisfying

symmetric condition, while the symmetry is imposed in the calculation. As the calculation was run in batch mode, only one closest time instant is compared.

The boundary layer thickness and shape are consistent in the calculation and measurement.

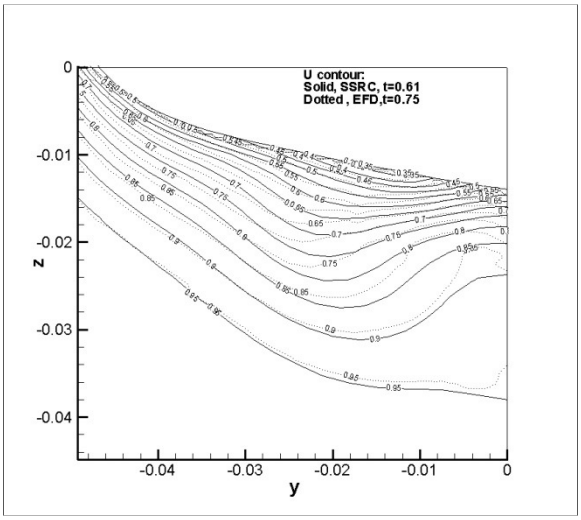

Figure 5 U contour (x/L=0.935)

The V contour in Figure 6 shows that the overall agreements are reasonably good except the location of bulge. It might be due to numerical diffusion or might be due to different time instant.

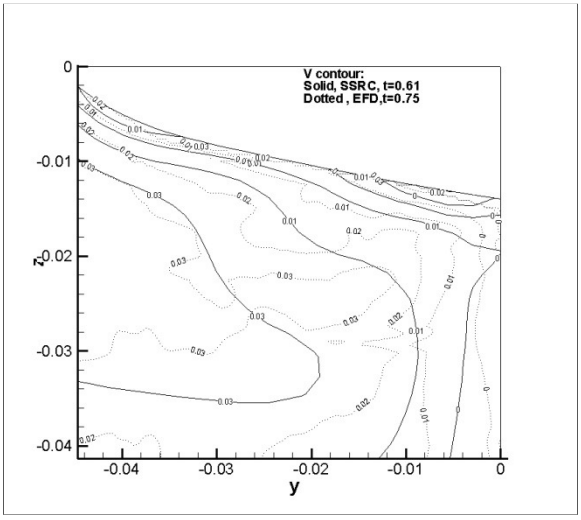

Figure 6 V contour (x/L=0.935)

The W contour in Figure 7 shows better agreements between calculation and measurement.

In summary, the agreements of computed and measured velocities are satisfactory.

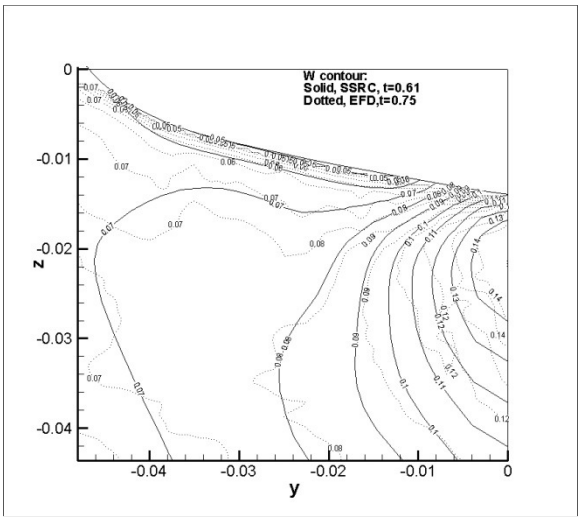

Figure 7 W contour (x/L=0.935)

The comparisons of wave elevations are shown in Figure 8-9. The measured bow wave, stern wave and wave system are nearly reproduced in the calculation. However, some discrepancies are noticed. In front of bow, computed wave pattern shows clear incoming wave and it is missing in the measurement. From midbody to transom, the computed wave system suffer from numerical diffusion. Maybe more mesh is needed in this area.

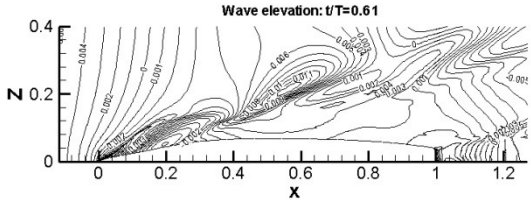

Figure 8 Computed wave elevation

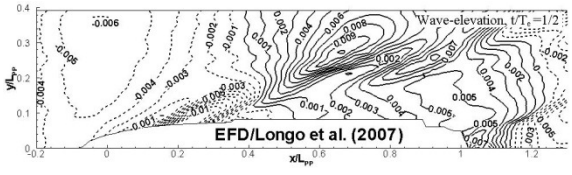

Figure 9 measured wave elevation

5. CONCLUSION

The comparison of computed and measured results on test case DTMB5415 (Gothenburg 2010 CFD workshop T3.5) were carried out. Based on the validation of simulation results, following conclusion can be drawn:

- The results of 1st amplitudes show that computed forces are roughly 25% larger than measured ones. It seems that wave amplitude in the calculation is larger than in the measurement.
- The results of 1st phases show that roughly 15

degrees phase difference between calculation and measurement, but not constant from force to force.

- The difference of 0th amplitude of surge forces is up to 12.5%. The measurement results seem to be undervalued.
- The comparisons of velocity contours and wave pattern show that overall agreements between calculation and measurement are acceptable. However, some discrepancies are seen. Whether it is due to mesh resolution or sampling time needs to be further investigated.
- In summary, RANS solver can predict wave diffraction with satisfactory accuracy.

6. ACKNOWLEDGMENTS

This research has been financially supported by European Union FP7 program, ICT-231646, SHOAL: Search and monitoring of Harmful contaminants, Other pollutants And Leaks in vessels in port using a swarm of robotic fish.

REFERENCES

Larsson, L., Stern, F. and Bertram, V., (2003), "Benchmarking of Computational Fluid Dynamics for Ship Flows: the Gothenburg 2000 Workshop", *Journal of Ship Research*, Volume 47, No 1, March

Ferziger, J.H. and Peric, M., (2002), "*Computational Methods for Fluid Dynamics*", 3rd Ed., Springer Verlag, Berlin, Heidelberg

Van, S.H., Kim, W.J., Yim, G.T., Kim, D.H., and Lee, C.J., (1998b), "Experimental Investigation of the Flow Characteristics Around Practical Hull Forms," Proceedings 3rd Osaka Colloquium on Advanced CFD Applications to Ship Flow and Hull Form Design, Osaka, Japan

Longo, J., Shao, J., Irvine, M., and Stern, F. (2007), "Phase-Averaged PIV for the Nominal Wake of a Surface Ship in Regular Head Waves," *ASME J. Fluids Eng*, Vol. 129, pp. 524-540

SIMULATION OF ROLL DECAY BY RANS APPROACH

Q. Gao, W. Jin, D. Vassalos
Ship Stability Research Center, University of Strathclyde, UK

1. SUMMARY

A RANS based CFD solver FLUENT was used to study ship roll decay with forward speed (Gothenburg 2010 CFD workshop T3.6). The DTMB5415 model is equipped with bilge keel and initial heel is set 10 degrees. The computed roll time record and flow fields were compared with experiment data provided by workshop organizer. General agreements are satisfactory.

2. NUMERICAL FORMULATIONS

2.1 Governing equations

The Reynolds averaged Navier-Stokes equations (RANSE) with SST K-ω turbulence model were solved. The VOF algorithm was applied to capture free surface. The governing equations can be written as follows.

2.1.1 Continuity equation

$$\nabla \bullet \mathbf{u} = 0 \tag{1}$$

2.1.2 RANSE equation

$$\frac{\partial \mathbf{u}}{\partial t} + \mathbf{u} \bullet \nabla \mathbf{u} = -\frac{1}{\rho}\nabla p - \mathbf{g} + \nu \nabla^2 \mathbf{u} \tag{2}$$

2.1.3 Turbulence model

$$\frac{\partial}{\partial t}(\rho K) + \nabla \cdot (\rho \mathbf{u} K) = \nabla \cdot (\Gamma_k \nabla K) + G_K - Y_K \tag{3}$$

$$\frac{\partial}{\partial t}(\rho \omega) + \nabla \cdot (\rho \mathbf{u} \omega) = \nabla \cdot (\Gamma_\omega \nabla \omega) + G_\omega - Y_\omega \tag{4}$$

2.1.4 VOF equation

$$\frac{\partial}{\partial t}(r_w) + \nabla \cdot (r_w \mathbf{u}) = 0. \tag{5}$$

2.2 Boundary conditions

The inlet is located at one ship length in front of bow where velocity components and volume fraction were imposed.

The outlet is at two ship length behind the stern where the hydrostatic pressure is specified.

Wall function was used on hull boundary. Yplus value ranges from 30-50.

2.3 Initial conditions

The calculation starts at 10 degrees heel without roll motion. The roll motion released at time 4L/U when mean inflow sweeps whole domain once and is converged.

2.3 Numerics

Second order upwinding interpolation was used for convection flux. SIMPLE method was applied to obtain pressure. Geometric reconstruction of volume fraction was used to calculate wave elevation.

3. TEST CASE

The test case T3.6 of the workshop was selected as benchmarking calculation. The main dimension of the ship and computational parameters are given as below.

Main particulars		**Full scale**
Length between perpendiculars	L_{PP} (m)	142.0
Length of waterline	L_{WL} (m)	142.18
Maximum beam of waterline	B_{WL} (m)	19.06

Draft	T (m)	6.15
Displacement	Delta (m^3)	8424.4
Wetted area w/o rudder	S_W (m^2)	2972.6
Wetted surface area of rudder	S_R (m^2)	30.8
Block coefficient (CB)	Delta /($L_{PP}B_{WL}T$)	0.507
Midship section coefficient (CM)		0.821
LCB (%L_{PP}), fwd+		-0.683
Vertical Center of Gravity (from keel)	KG (m)	7.5473
Metacentric height	GM (m)	1.95
Moment of Inertia	K_{xx}/B	0.37
Moment of Inertia	K_{yy}/L_{PP}, K_{zz}/L_{PP}	0.25

Scale ratio: 46.59
The sinkage and trim are: s = 2.93×10^{-4}, t = -3.47×10^{-2}°
Re= 2.56×10^{6}
Fr=0.138
Initial roll angle φ= 10°

3.1 Mesh

Fine mesh with cells 3M was generated for the simulation. Grid uncertainty study was carried out in separate calculations without roll. Special care was given to the number of cells within a wave length, the wave amplitude and the boundary layer. The half domain and hull surface mesh are shown in Figure 1.

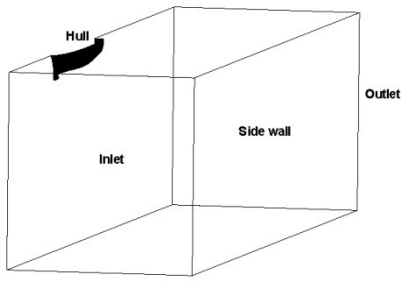

Figure 1 Domain and face mesh

3.2 Parallel computing

The calculations were run on a High Performance Computer (HPC) with 8*130 (nodes) processors provided by Esteem Systems Ltd in partnership with SUN Microsystems (now Oracle).

The machine has a theoretical peak performance of 13 TeraFlops–thirteen thousand billion operations per second.

For a typical resistance calculation of 3M cells, it takes roughly 40 hours of clock time for computational time 20 seconds using 16 cores.

4. RESULTS AND ANALYSIS

The computational results are compared with experimental data from IIHR. The comparison of roll decay time records is given in Figure 2.

It can be seen that the computed roll decay is generally consistent with the measured one. In the first 3 periods of roll decay, the agreements of phase angle are good; however, computed roll amplitudes are slightly higher than the measured results. After the 3rd period, the amplitudes are close but the phase difference gets larger.

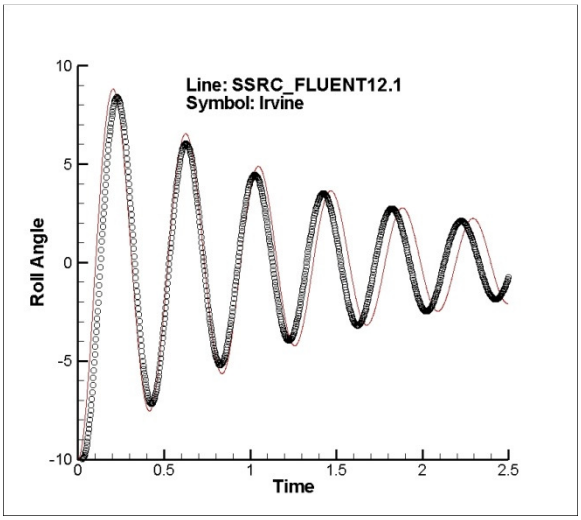

Figure 2 Roll decay record (Line: present, Symbol: Longo)

The comparison of velocity components at start of second period at x/Lpp=0.675 are given in Figure 3-8.

It can be seen from Figure 3-4 that the computed axial velocity contour agrees well with the measured data. The shape of contour is clearly deformed by the presence of bilge keel. The cross vortices are generated at the downwind of bilge keel and change longitudinal velocity significantly. The computed velocity contour is smooth; however, the measured result appears disturbance of noise.

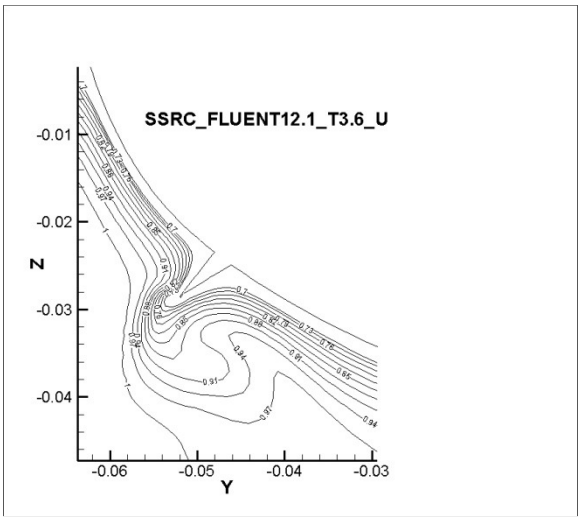

Figure 3 Computed U contour

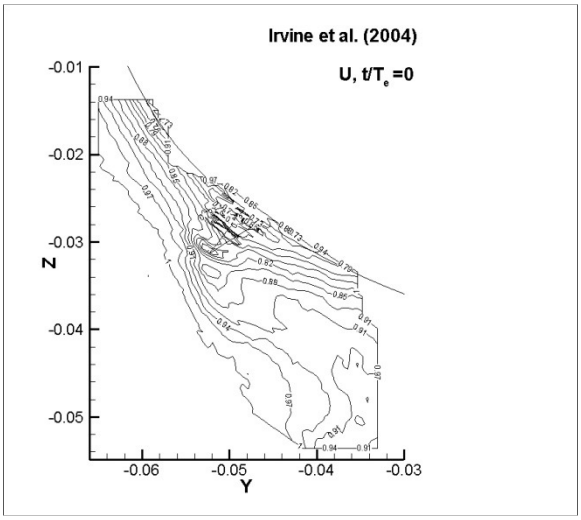

Figure 4 Measured U contour

The comparison of V contour in Figure 5-6 shows that the areas of negative and positive V velocity are close in calculation and measurement. However, the detail contour levels in the data are missing in the calculations. It is hard to conclude that if the difference is due to numerical diffusion in the calculation or noise of data sampling in the measurement.

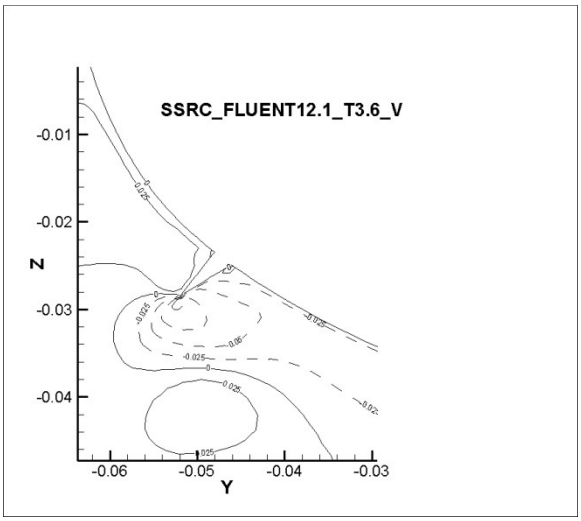

Figure 5 Computed V contour

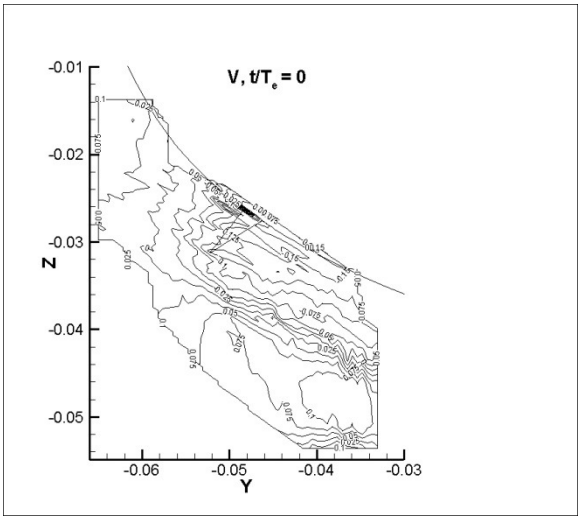

Figure 6 Measured V contour

The comparisons of W velocity contour are given in Figure 7-8. The overall agreements between calculation and measurements are good. Three separate patches of contour are close in the simulation and data. Again, the difference can be noticed at the smoothness of computed and measured contour.

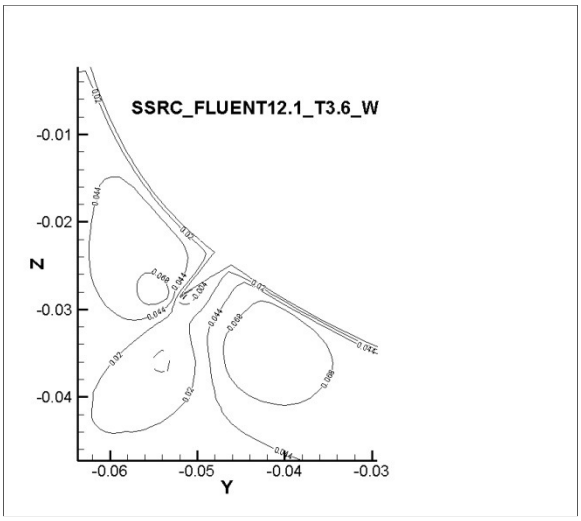

Figure 7 Computed W contour

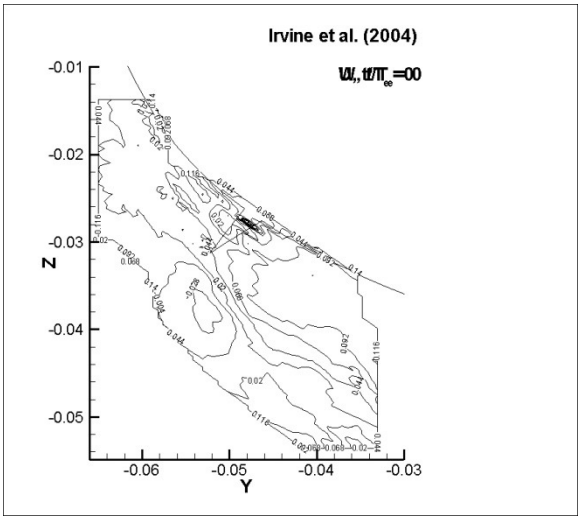

Figure 8 Measured W contour

The comparisons of wave pattern are given in Figure 9-10. Although computed bow and stern wave are close to the measured ones, the overall agreements are not satisfactory. The wave system in the data is not reproduced in the numerical simulation. The reason for the bias is low Froude number. At Froude number 0.138, the ratio of wave length and wave height to Lpp is about 1:8 and 1:200 respectively. Therefore, very fine mesh is required to capture the detailed wave pattern. Present mesh resolution is not good enough for the modeling short and low waves.

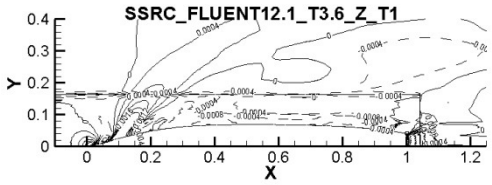

Figure 9 Computed wave elevation

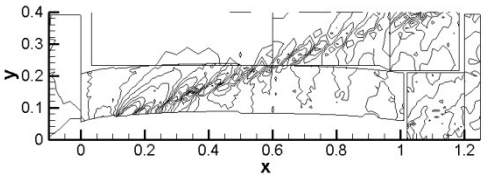

Figure 10 Measured wave elevation

The comparison of surge forces is shown in Figure 11. As we can see from the plot that measured surge force is oscillating around the computed one. The computed surge force is smooth and shows limited roll effects. The main part of surge force is from steady forward resistance. However, the data is highly scattering and the amplitude of oscillation is very high. We cannot conclude the roll effects on longitudinal force from measured data. Proper data filter is needed. The computed force is consistent with mean value from measurement data.

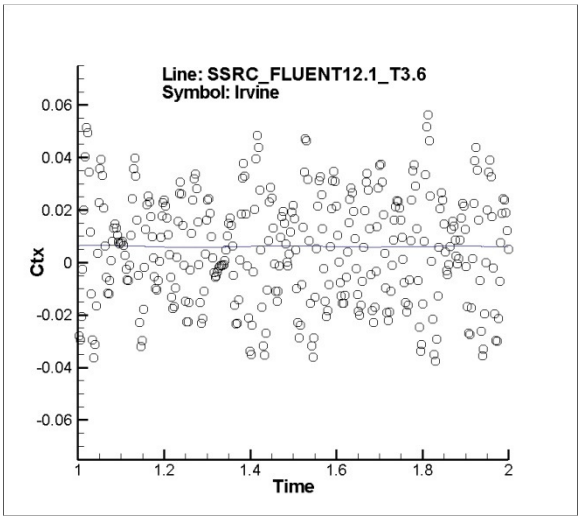

Figure 11 W contour (x/L=0.935)

5. CONCLUSION

The detailed comparison of computed and measured results on test case DTMB5415 (Gothenburg 2010 CFD workshop T3.6) were carried out. Based on the validation of simulation results, following conclusion can be drawn:

- Computed roll decay time record is consistent with measurement reasonably well.
- In overall, computed velocity distribution agrees with data. The computed results are over smooth. Oppositely, the measured results are over oscillating.
- Computed wave patterns fail to capture wave system of measurement. This is mainly due to mesh resolution. For better modeling of wave pattern, huge mesh is required in low Froude number.
- Measured surge force is oscillating near the computed results. The computed longitudinal force shows limited roll effects. The scatter of measurement data is mainly due to noise but not roll

effects.

- In summary, the roll decay is acceptably predicted by numerical simulations.

6. ACKNOWLEDGMENTS

This research has been financially supported by European Union FP7 program, ICT-231646, SHOAL: Search and monitoring of Harmful contaminants, Other pollutants And Leaks in vessels in port using a swarm of robotic fish.

REFERENCES

Larsson, L., Stern, F. and Bertram, V., (2003), "Benchmarking of Computational Fluid Dynamics for Ship Flows: the Gothenburg 2000 Workshop", *Journal of Ship Research*, Volume 47, No 1, March

Ferziger, J.H. and Peric, M., (2002), "*Computational Methods for Fluid Dynamics*", 3rd Ed., Springer Verlag, Berlin, Heidelberg

Van, S.H., Kim, W.J., Yim, G.T., Kim, D.H., and Lee, C.J., (1998b), "Experimental Investigation of the Flow Characteristics Around Practical Hull Forms," Proceedings 3rd Osaka Colloquium on Advanced CFD Applications to Ship Flow and Hull Form Design, Osaka, Japan

Irvine, M., Longo, J., Stern, F. (2004), "Towing Tank Tests for Surface Combatant for Free Roll Decay and Coupled Pitch and Heave Motions," Proc. 25th ONR Symposium on Naval Hydrodynamics, St Johns, Canada

INVESTIGATION OF THE KCS AT FROUDE NUMBER Fr = 0.26

Lars Ole Lübke (SVA Potsdam, Germany)

1. SUMMARY

The viscous flow around the KRISO Container ship (KCS) with free-surface has been investigated numerically. The ANSYS CFX software was used to solve the Reynolds-averaged Navier-Stokes equations (RANSE) on an unstructured mesh with tetrahedral and prismatic elements. A coarse, a medium and a fine mesh were generated, with the refinement being done inconsistently. In course of the investigation the wave contour and the integral results were compared with the corresponding measurements for the different meshes, a different near wall resolution and different blending functions for the convective fluxes. The comparison of the fine grid wave contour shows a good agreement with the measurements. For the integral results a large variation in accuracy is found for the different setups.

1. INTRODUCTION

The numerical simulation of the viscous flow around ships with and without free-surface has become a routine service at the Potsdam ship model basin (SVA). In all research and in many commercial projects conducted at the SVA are at some stage numerical simulations requested. The intention for the majority of numerical calculations is to visualize and understand the flow phenomena's or to carry out a qualitative comparison in order to rank different designs. However the expectations towards CFD rise and it is increasingly demanded to make quantitative declarations. For a reliable quantitative prediction of forces and moments in ship design however the methods have to be extensively tested and validated. This is the primarily intent of the Gothenburg Workshop and is therefore in accordance with the needs of the SVA.

In course of this paper the two-phase flow around the KCS model was investigated using the commercial software ANSYS CFX. Throughout the investigations the ship was fixed at zero sinkage and trim. In the solution domain an unstructured grid on basis of tetrahedral and prismatic elements was generated. For the calculations of the free-surface a capturing technique (VOF) was employed, which is solved in a coupled manner together with the mass and momentum conservation equations. All conducted calculations were steady state calculations. For the calculations three meshes of different fineness were generated. Furthermore for each mesh three different dimensionless wall distances were realized. In course of the investigations the blending function for the discretisation of the convective fluxes was varied and additionally the high resolution scheme of ANSYS CFX employed.

2. NUMERICAL MESH

The numerical meshes were generated with the commercial software package ANSYS ICEM CFD. The dimensions of the solution domain were multiples of the ships length, with the domain extending 1.5 L_{PP} upstream, 3.0 L_{PP} downstream, 1.5 L_{PP} sideward, 1.0 L_{PP} downwards and 7.0 T_{cwl} upwards, measured from the intersection point of the forward perpendicular with the construction waterline.

In the solution domain an unstructured numerical mesh was generated automatically, consisting out off prismatic and tetrahedral elements. Prismatic inflation layers were extruded around the hull and around the still water line independently from each other. For the latter the prism cells are arranged parallel to the still water line. The prismatic layers on the hull and around the still water line are non-intersecting. The gap between the two prismatic layers is filled with tetrahedral elements. The grid generation process can be subdivided into different steps, starting from the generation of the prismatic mesh around the still water line, the generation of the tetrahedral mesh in the rest of the solution domain, smoothing of the mesh, extruding the prismatic layer around the ship hull and the final mesh smoothing of the entire numerical grid at the end.

The spatial discretisation was investigated on three numerical meshes of different resolution. In Fig. 1 the numerical meshes in the still water plane are shown for the coarse (top), the medium (centre) and the fine (top) mesh. In the solution domain regions with mesh refinement were defined, in order to resolve the flow in regions of interest. The major changes between the meshes of different fineness occurred in the refined regions, which are basically the vertical resolution around the still water line, the wave

field behind and beside the ship (up to half a ship length behind the aft perpendicular) and around the ship hull itself. The grid resolution in the outer solution domain was left unchanged during refinement. The meshes were therefore not refined consistently. For the three meshes the grid resolution in the prismatic layer around the hull was also varied, giving dimensionless wall distances of $y^+ = 200$, 85 and 10. For smaller dimensionless wall distances the free surface elevation began to show defective regions close to the hull. Therefore the intention to resolve the boundary layer down to the wall was abandoned.

Table 1 Numerical mesh, node number in Millions

grid nodes [10^6]	$y^+ = 200$	$y^+ = 85$	$y^+ = 10$
coarse	0.833	0.855	0.993
medium	2.595	2.653	3.006
fine	4.889	4.950	5.320

The numerical meshes were generated for the ANSYS CFX solver, which is a vertex centered algorithm and generates the control volumes around the nodes internally. Therefore the node numbers for the different numerical meshes are given in Tab. 1. It has to be considered, that the number of nodes are considerably smaller than the number of cells for meshes primarily consisting out of tetrahedral cells.

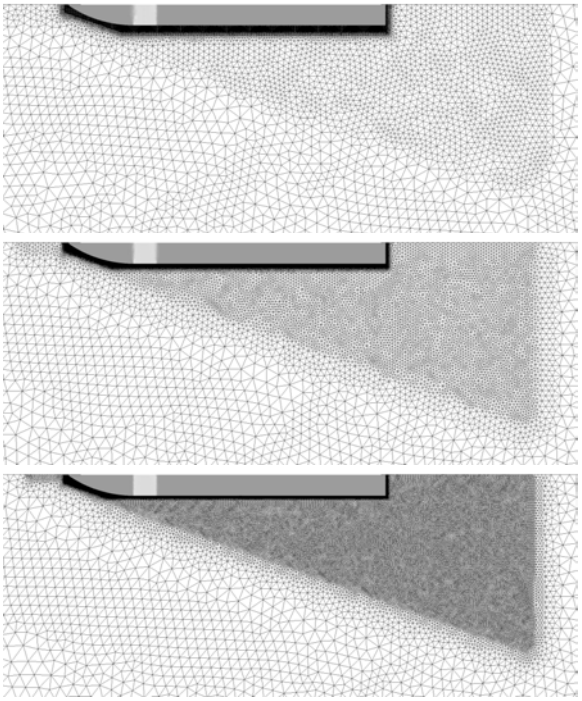

Fig.1 Coarse (top), medium (middle) and fine (bottom) mesh from the top

3. COMPUTATIONAL METHOD

The Reynolds-averaged Navier-Stokes equations (RANSE) are solved with the commercial software package ANSYS CFX12. In order to solve these partial differential equations a finite-volume approach on basis of unstructured meshes is used. ANSYS CFX is a vertex-centered method, which means that the control volumes are constructed around the vertices internally and are not identical to the control volume of the numerical mesh. The procedure employs an unstaggered and collocated variable arrangement. In order to avoid oscillation of the pressure field a correction to the continuity equation similar to the one by Rhie and Cow is used. The convective fluxes through the cell faces have to be determined in course of the discretisation. The convective fluxes are discretised as follows:

$$\phi_{ip} = \phi_{up} + \beta \cdot \nabla\phi \cdot \Delta\vec{r} \tag{1}$$

with ϕ_{up} being the value from the upstream node, $\nabla\phi$ the gradient and Δr as directional vector between the two neighboring nodes. The factor β enables different discretisation schemes. The local control of β within the High-Resolution scheme is based on the procedure of Bart and Jesperson.

For the calculation of the free surface a surface capturing method of the volume of fluid (VOF) type is employed. In order to keep the interface sharp an interface compression algorithm is used. The VOF equation is solved in a coupled manner, together with the velocity and mass conservation equations.

To solve the coupled equation system an algebraic multigrid method is used, employing as smoother an algorithm based on Incomplete-Lower-Upper factorisation (ILU). While the continuity, the momentum and VOF equations are solved in a coupled manner, the turbulence equations are solved segregated.

The k-ω SST (shear stress transport) turbulence model was used to model turbulence and combines the k-ε and the k-ω turbulence model, with the ε-formulation being expressed in term of ω. The different formulations are related by a blending function, using the k-ω-formulation close to no-slip walls and the k-ε-approach for the free stream turbulence. The model takes also the transport of the shear stress in the boundary layer into account, which is considered advantageous in case of flow separation. The SST model belongs to the family of two-equation turbulence models.

Further details of the numerical method can be found in the CFX user manual.

4. RESULTS

The calculations of the KCS without a rudder were carried out for a Froude number of Fr = 0.26 and a Reynolds number of Re = 1.4E+07. This configuration corresponds to the setup in test case 2.1, although the results were also used for case 2.2a (with rudder). Symmetry along the centre plane of the ship was utilized.

A steady state approach is used to solve the flow around the ship with free surface. In these calculations the time-step size serves as under-relaxation factor and has a great impact on the convergence rate. Therefore investigations were conducted in order to quantify this influence. All calculations were carried out with a variable time-step size. For the first 25 iterations the time-step is kept constant, starting with $t = 0.02$ s, while in the next 25 iterations the time-step is steadily increased until the maximum time-step is reached. The idea is to keep the disturbances at the beginning of the calculation, due to unphysical initial conditions (uniform distribution) as small as possible. The maximum time-step size was than varied, starting from $t = 0.2$ s and going up to 3.2 s, doubling the time-step size between every consecutive run. In the following the pressure resistance of the ship is used as a measure to investigate how fast a steady state solution is obtained, since it is more difficult to obtain a steady state solution for the pressure force in comparison to the frictional force. The calculations were carried out for 600 iterations. In Fig. 2 the history of the pressure forces on half of the ship (fine mesh) is plotted over the number of iterations for different runs. The investigations were conducted for the numerical mesh with a dimensionless wall-distance of approximately $y^+ = 200$. It shows that for a time-step size of $t = 0.2$ s the pressure force is still oscillating with a small amplitude after 600 iterations. However, with increasing the time-step size the fluctuations of the pressure force are reducing, until a steady state solution is obtained. For the fine mesh approximately 400 iterations are required for a steady state solution. For the coarse mesh a steady state solution is obtained within 300 iterations. This shows that a considerable speed up in calculation time can be achieved if the time-step size is chosen as large as possible. The magnitude of the forces is not affected by the time-step.

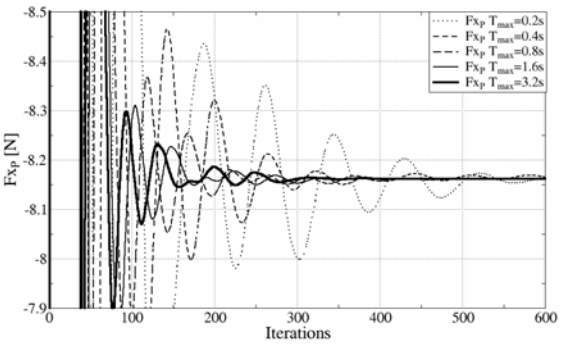

Fig.2 Investigation of the time step size on the pressure resistance of the ship, for the fine mesh

During all calculations the convergence criteria was set for the maximum residuals to be 10^{-4}. In general the maximum residuals could only be reduced below $5*10^{-4}$, with the highest residuals being encountered for the w-momentum equation. The maximum number of iterations was set to 600. In Fig. 3 the mean residuals (rout mean square- RMS) are plotted over the number of iterations for the fine grid calculation with a time-step size of $t = 1.6$ s and a dimensionless wall-distance of approximately $y^+ = 200$. The residual level was reduced by the order of three. Within 600 iterations a steady state solution was obtained for all meshes and settings.

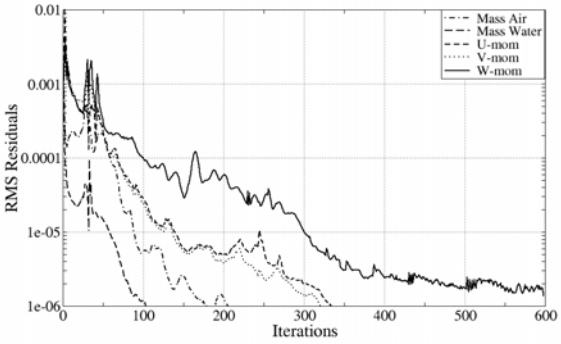

Fig.3 Convergence history, fine mesh, maximum time-step size t = 1.6 s, $y^+ = 200$

The free-surface flow was calculated on three different numerical meshes and compared to the corresponding measurements. In Fig. 4 the contour plots of the wave elevation are shown for the coarse (top), the medium (centre top), the fine mesh (centre bottom) and the experimental values (bottom). The calculations were carried out with the High-Resolution scheme of ANSYS CFX (convective fluxes).

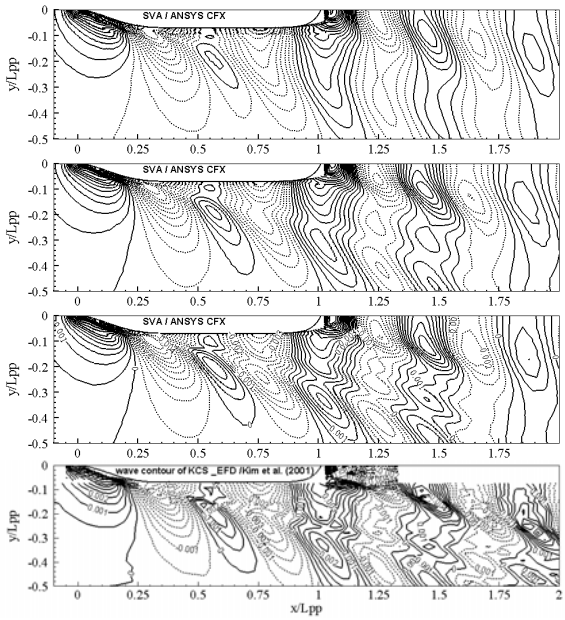

Fig.4 Contour plot of wave elevation for the coarse (top), the medium (centre top), the fine (centre bottom) mesh and the corresponding measurements (bottom)

The comparison of the calculated wave elevation at the fore ship shows for all three meshes a good agreement with the corresponding measurement. Going further aft the differences between the meshes get more significant. In case of the coarse grid, the longitudinal waves of the bow and the forward shoulder are diffusing away with increasing

run length, leaving the aft ship wave system with the transversal waves only. With the medium grid the longitudinal bow wave is captured, lacking however steepness. The longitudinal wave system of the forward shoulder is only tracked on the fine grid. The agreement between the calculated wave system on the fine mesh with the corresponding experimental data is good. Half a ship length downstream of the aft perpendicular the mesh gets considerably coarser, causing the wave system to be damped.

The treatment of the convective fluxes and the applied blending function have also a considerable influence on the wave system, since the pressure field around the ship and thus the dynamic boundary condition at the free surface is strongly influenced by these parameters. For this reason the investigation of the free surface elevation was also carried out for different blending functions, controlling the amount of upward- (UDS) and central-differencing-scheme (CDS) used for the discretisation of the convective fluxes at the cell faces. In Fig. 5 the wave contours for 20% CDS (top), 60% CDS (centre) and 100% CDS (bottom) are shown for the fine grid. With increasing fraction of CDS more details of the wave contour are resolved. For 20% CDS the wave field is basically composed out of the transversal waves and the wave contours resemble more the wave contours encountered on a coarse grid. The longitudinal waves of the bow start to get captured for a blending of 60% CDS. The wave contours for 100% CDS basically resemble the wave contours obtained with the high resolution scheme. With the High-Resolution scheme the blending function is locally varied with the aim to obtain values as high as possible. The figures show that in order to calculate a proper wave field the blending function must be chosen such that a high percentage of CDS is used.

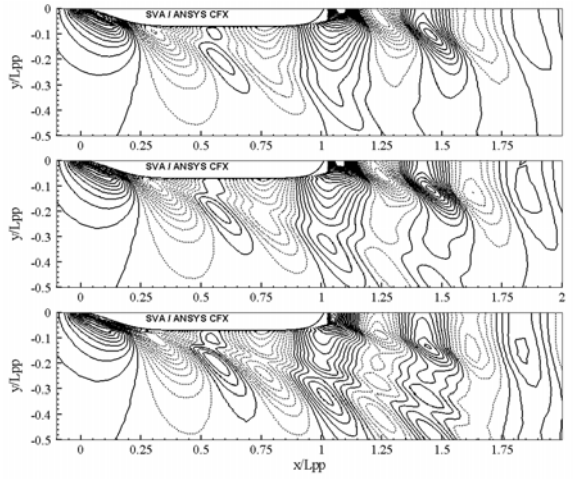

Fig.5 Contour plot of wave elevation on the fine mesh, 20% CDS (top), 60% CDS (centre) and 100% CDS (top)

The affect of the blending function between UDS and CDS on the ship resistance was also investigated. The calculations were conducted on the coarse, the medium and the fine grid. Additionally the calculations were carried out with the High-Resolution scheme. In Fig. 6 the results of the investigations are given for the frictional, the pressure and the total resistance. The horizontal lines in the figure are obtained with the High-Resolution scheme, while the tapered lines are obtained with the different blending functions. The coarse grid results are plotted with dotted, the medium grid results by a dashed and the fine grid results by a straight line. For the frictional resistance a circle and for the total resistance a square was chosen as symbol. On basis of this investigation the impact of the blending function and of the mesh density on the pressure, frictional and total resistance can be studied. The investigations were carried out on the numerical mesh with a dimensionless wall distance of $y^+ = 200$. The figure shows that with an increasing fraction of CDS the resistance is decreasing. The blending function has a larger impact on the pressure resistance than on the frictional resistance. The pressure resistance for 20% and 100% CDS differs by a factor of three, while for the frictional resistance the values differ by a factor of 1.5. The results show that the resistance is very sensitive with respect to the blending function. In the investigation a slight change in blending caused the resistance to alter by a few percent. For the calculations with the High-Resolution scheme the frictional resistance corresponds to the values obtained with approximately 80% CDS for all three meshes, while for the pressure resistance values in the range of 92 – 95% are obtained. For the total resistance the results for the High-Resolution scheme corresponds to blending factors of 85 – 90% CDS. The results show, that no grid independent solution was obtained. For the frictional resistance the results for the coarse, the medium and the fine mesh only begin to differ for higher fractions of CDS, while in case of the pressure resistance the differences between the meshes are decreasing with increasing amount of CDS.

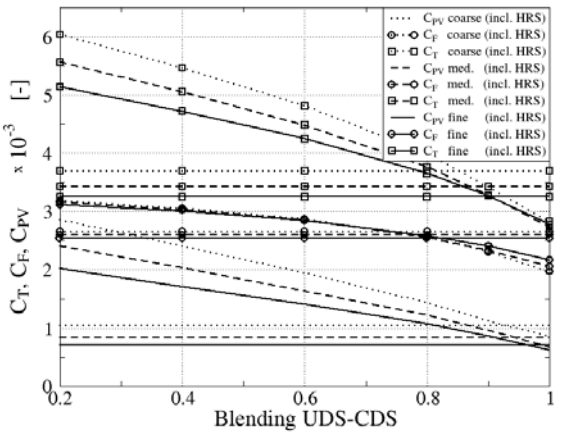

Fig.6 Resistance of KCS for the coarse, medium and fine grid for different blending function and the High-Resolution scheme HRS (straight lines)

Furthermore different spatial discretisations in the extruded prismatic inflation layer around the ship were tested, giving mean dimensionless wall distances on the ship hull of approximately $y^+ = 200$, 85 and 10. Wall functions can be applied down to values of approximately $y^+ = 11$. It was

intended to resolve the boundary layer down to the wall ($y^+ = 1$), however for smaller y^+-values the free-surface showed regions with disturbed free surface. Therefore a further refinement was abandoned. The calculations were conducted with the k-ω-SST turbulence model and scalable wall-functions, having the advantage that the method automatically blends between logarithmic wall functions and a Low-Reynolds-Number formulation (with respect to turbulent Reynolds number). In case of an adequate number of grid nodes in the numerical mesh the viscous sub-layer would be resolved. However the attempt to resolve the boundary layer down to the wall for tetrahedral/prismatic meshes is extremely expensive with respect to the number of required cells, due to the isotropic nature of prismatic elements. In Fig. 7 the frictional resistance C_F is plotted for the coarse, the medium and the fine grid over the dimensionless wall distance y^+. The coarse grid results are plotted as dotted, the medium grid results as dashed and the fine grid results as straight lines. The values are obtained with the High-Resolution scheme. The frictional resistance is increasing with decreasing y^+-values. For the investigated range of y^+-values, the frictional resistance changes by approximately 5% on all three meshes. Thus the near wall treatment for the used setup has a large influence on the resistance, since the frictional resistance accounts for roughly 75% of the total resistance.

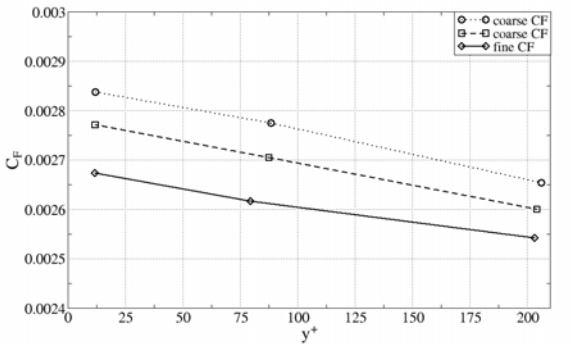

Fig.7 Frictional resistance for the coarse, the medium and the fine grid over for different y^+-values.

The investigations show the difficulty to predict the ship resistance accurately, since the resistance is dependent on a large number of parameters, from which a few have been investigated. Special attention was laid upon investigating the discretisation errors (blending and grid resolution).

In Tab. 2 the resistance for selected calculations of the KCS without rudder is given. Experimental values are only available for the KCS with rudder. The measured total resistance with rudder is $C_T = 3.56*10^{-3}$. In order to achieve a better agreement between measurement and calculation for the used numerical meshes and solver, the blending function must be altered between 80 – 90% CDS for y^+-values of about 200 (despite considering the rudder).

Investigation are currently conducted on block-structured meshes with a higher resolution.

Table 2 Resistance, fine mesh

discretisation	$C_{PV}[10^3]$	$C_F[10^3]$	$C_T[10^3]$
80% CDS, $y^+ = 200$	1.065	2.585	3.650
90% CDS, $y^+ = 200$	0.8545	2.412	3.267
100% CDS, $y^+ = 200$	0.6153	2.167	2.782
High-Res., $y^+ = 200$	0.7098	2.542	3.251
High-Res., $y^+ = 85$	0.7004	2.616	3.317
High-Res., $y^+ = 10$	0.7153	2.673	3.388

5. CONCLUSION

The KCS has been investigated numerically with the ANSYS CFX solver. The following issues shall be pointed out:

- It was shown that the time-step size in the steady-state calculations had a large influence on the rate of convergence. With an increasing time step size the required number of iterations could be significantly reduced.
- The comparison of the calculated wave field on the fine mesh with the corresponding measurements showed a good agreement.
- On the coarse mesh only the wave field around the fore ship was adequately resolved.
- The comparison of the wave field around the ship for different blending functions in the discretisation of the convective fluxes, shows that for a good resolution of the wave field not only the numerical mesh needs to be of adequate fineness but also the amount of CDS needs to be as high as possible.
- The investigation of the blending function for the convective fluxes between UDS and CDS showed also a large impact on the integral results, with a decreasing frictional and pressure resistance for a higher fraction of CDS.
- The influence of the blending function was higher on the pressure resistance.
- The results obtained with the High-Resolution scheme of ANSYS CFX correspond in case of the frictional resistance to about 80% CDS, for the pressure resistance to about 92 - 95% CDS and for the total resistance to about 85 -90% CDS, with the lower bounds obtained with the coarse and the higher bounds with the fine mesh.
- The calculations with different values for the dimensionless wall distance y^+ showed, that the near wall resolution influences the frictional resistance considerably. For the investigated range of y^+-values the frictional resistance varied by about 5%, with the

frictional resistance contributing by about 75% to the total resistance.

The calculations show a large variation in resistance for different setups. The ship resistance can be calculated correctly with a right combination of different significant parameters, such as (among others) the dimensionless wall distance, the discretisation of the convective fluxes and the fineness of the numerical grid. The correct combination of parameters has to be identified and used in a best-practice approach, which has to be regularly validated and adapted.

REFERENCES

Larsson, L., Stern, F. and Bertram, V., (2003), "Benchmarking of Computational Fluid Dynamics for Ship Flows: the Gothenburg 2000 Workshop", *Journal of Ship Research*, Volume 47, No 1, March

Ferziger, J.H. and Peric, M., (2002), "*Computational Methods for Fluid Dynamics*", 3rd Ed., Springer Verlag, Berlin, Heidelberg

Van, S.H., Kim, W.J., Yim, G.T., Kim, D.H., and Lee, C.J., (1998b), "Experimental Investigation of the Flow Characteristics Around Practical Hull Forms," Proceedings 3rd Osaka Colloquium on Advanced CFD Applications to Ship Flow and Hull Form Design, Osaka, Japan

Lübke, L., (2005), "Numerical Simulation of the Flow around the propelled KCS", Proceedings CFD Workshop Tokyo 2005

ANSYS CFX 12.1 user manual, 2009

RESISTANCE PREDICTION AND SEA KEEPING ANALYSIS WITH FreSCo+

M. Manzke, T. Rung (TUHH, Germany)

1. SUMMARY

The paper reports on approaches to analyse the wave-resistance for viscous, steady-state flows around ships. Attention is given to both, calm-water conditions and sea keeping employing narrow computational domains. Specific emphasis is devoted to means to enhance the computational efficiency for large-scale industrial applications. Accordingly, an appropriate initialisation and flexible approaches to advance the solution in time using different time-scales are addressed. The procedure is applied to the KVLCC2 tanker at Re=4.6 10^6 and Fn=0.142. Results obtained from the present approach reveal a reduction of wall-clock-time by more than one order of magnitude in conjunction with steady-state wave-resistance computations. For the sea keeping analysis a simple viscous/inviscid-coupling approach is suggested. Therein, the viscous RANS method is implicitly forced to comply with a prescribed inviscid solution towards the far-field boundaries. Employing consistent boundary conditions at all far-field boundaries, the method facilitates the use of small domains. This procedure is applied to the Kriso Container Ship (KCS) in head-waves. Results indicate that this approach allows to use very compact domains, whilst achieving accurate results.

2. INTRODUCTION

Viscous hydrodynamic flow simulations in the framework of unstructured, interface-capturing, finite-volume methods have matured to an industrial standard by now. Accordingly, the prediction of free-surface flows around floating bodies is a routine application for naval architects. With respect to resistance and propulsion aspects, the steady-state performance in calm-water conditions is usually of particular interest. Furthermore an enhanced interest into the performance and safety margins of vessels and structures exposed to hazardous operating conditions is seen recently.

Both topics are within predictive realms of most commercial and academic CFD procedures. However, there is still a pressing need to reduce the associated computational effort.

Although the final solution of a resistance prognosis refers to a steady-state situation, transient simulations have to be performed. Moreover, the numerical algorithms inhere an explicit time-step (Courant-number) dependency, which drastically enhances the computational effort. Accordingly, some 10.000 time-steps are often required to achieve a satisfactory level of force-convergence in conjunction with meshes that typically inhere a couple of million cells. The present paper outlines a technique to improve the computational efficiency based upon a sub-cycling strategy, that can be employed for the analysis of steady and unsteady flows, and an appropriate initialisation of the flow field.

The generation and propagation of waves for sea keeping analysis dominates the far-field and can accurately be simulated with efficient inviscid methods. In the vicinity of the floating body (e.g. a vessel), the diffraction of the travelling wave field becomes significant. Accordingly, the ability to mimic wave diffraction determines the accuracy of the computed forces and motions. Since viscous effects are force-crucial, inviscid approaches are deemed to be inappropriate. Viscous approaches, e.g. RANS methods, have proven capabilities to predict the response of floating bodies in turbulent flow. RANS methods are however afflicted with prohibitive efforts due to the associated grid requirements for an accurate propagation of incident waves towards the floating body and the Courant-number based time-step limitations. Therefore, small computational domains are desirable to reduce the number of cells and the computational effort. Coupled viscous/inviscid methods are the 2nd focus of the present contribution. Such approaches offer an attractive way to achieve small computational domains, provided that their merits are combined.

3. NUMERICAL METHOD

3.1 General

Results presented in this paper are obtained from the *FreSCo*$^+$ Navier-Stokes solver. The tool is a spin-off of *FreSCo* (Vaz et .al. 2009), a joint development of Hamburg University of Technology (TUHH), Hamburgische Schiffbau-Versuchsanstalt (HSVA) and Maritime Research

Institute Netherlands (MARIN), which was developed under the aegis of the FP6 EU-initiative *VIRTUE* (Marzi, 2008). The package is supplemented by an adjoint flow solver AD-*FreSCo*$^+$ dedicated to optimization (Stück et. al., 2010) and an overset-grid technique OVER-*FreSCo*$^+$ (Brunswig et. al. 2010).

The procedure solves the Navier-Stokes equations for a mixture of incompressible fluids

$$\rho \frac{DU_i}{Dt} = -\frac{\partial p}{\partial x_i} + \frac{\partial}{\partial x_j}\left(\mu + \mu_t\left(\frac{\partial U_i}{\partial x_j} + \frac{\partial U_j}{\partial x_i}\right)\right) + f_i\,, \quad (1)$$

$$\frac{\partial \rho}{\partial t} + \frac{\partial}{\partial x_i}\left(\rho U_i\right) = 0\,. \quad (2)$$

where U_i, x_i and f_i represent the cartesian coordinates of the velocity vector, the spatial coordinates and the body force and t, p, ρ, μ and μ_t denote to the time, pressure, local fluid mixture density, molecular mixture dynamic viscosity and turbulent viscosity.

The segregated algorithm is based on the strong conservation form of the momentum equations. It employs a cell-centered, co-located storage arrangement for all transport properties. Structured and unstructured grids, based on arbitrary polyhedral cells or hanging nodes, can be used. The implicit numerical approximation is second-order accurate in space and time. Integrals are approximated using the conventional mid-point rule. The solution is iterated to convergence using a pressure-correction scheme. Various turbulence-closure models are available with respect to statistical (*RANS*) or scale-resolving (*LES, DES*) approaches. Two-phase flows are addressed by interface-capturing methods based upon the Level-Set or Volume-of-Fluid (*VOF*) technique. Since the data structure is generally unstructured, suitable pre-conditioned iterative sparse-matrix solvers for symmetric and non-symmetric systems (e.g. *GMRES*, *BiCG*, or *BiCGStab*) from the PETSC library (Balay, 1997) can be employed. The algorithm is parallelized using a domain-decomposition technique based on a *Single Program Multiple Data* message-passing model, i.e. each process runs the same program on its own subset of data. Inter-processor communication employs the *MPI* communications protocol. Load balancing is achieved using the *ParMETIS* partitioning software.

The flow solver is supplemented by a 6 degrees of freedom floating-body motion solver, which is coupled to the flow solver in an explicit, semi-implicit or fully-implicit way and can handle multiple floating bodies.

3.2 Explicit Interface Sharpening

Although dedicated, downwind-biased interpolation schemes are used, the predicted free surface often tends to become blurred. Particularly when the cell-face is oblique to the free surface, the predictive accuracy might be disappointing on coarse meshes. The effect is more or less pronounced, depending on the choice of the interpolation scheme, the orientation of the grid and the application.

For flow field composed from immiscible fluids, an explicit sharpening approach (EIS) is applied as a supplement to traditional interpolation practices for the mixture fraction (e.g. Ubbink 1997). The technique is based on the identification of areas featuring a non-satisfying degree of sharpness and an explicit redistribution of mixture-fraction in these areas. The fully-conservative redistribution algorithm prioritizes the transfer in the direction of the body force. Accordingly, the number of partly filled control-volumes between air and water is reduced to a minimum and the interface is sharpened as illustrated in figure 1.

Fig.1 Breaking wave in front of the Blunt body and the interface compression maintained due to EIS.

3.3 Sub-Cycling

A careful inspection of the transient behaviour of the governing equation reveals, that the Courant-Number restriction experienced in implict interface-capturing schemes pertains only to the mixture-fraction transport. Other properties, e.g. momentum or turbulence parameters, can either be simulated in steady state or in conjunction with larger time steps. The present approach aims to reduce the computational effort using nested transient sub-cycles for the mixture-fraction equation, embedded in either a transient or steady-state advancement of the solution for all other flow properties. Accordingly, typical time-step ratios of 5-25 can be realized, which grossly corresponds to the achievable speed-up. Further details are available in Manzke et.al.(2010).

3.4 Advanced initialisation

Another difficulty of steady-state free-surface flow computations arises from inconsistencies of the initial fields. A frequent approach is to initialise the velocities with the ship velocity in combination with hydrostatic conditions for the free-surface elevation and pressure. This practice obviously refers to a sudden acceleration of the ship from rest to its design speed. It often generates spurious waves, which might reside inside the domain over a long period until they are convected out of the domain. In fact, a more thorough initialisation (Will, 2010) can speed up the computation to a large extent. The present initialisation

procedure is structured into two parts. Firstly, a preceding potential-flow simulation is used to determine the inviscid flow field. Accordingly, the induced velocities obtained from the potential-flow solution are evaluated at each control-volume center $x_{j_{(k)}}$ to determine a first initial velocity field, viz.

$$U_i(x_{j_{(k)}}) = U_{i_\infty} + \sum_n \frac{q_{(n)}}{\left\| x_{j_{(k)}} - x_{j_{(n)}} \right\|^3} (x_{j_{(k)}} - x_{j_{(n)}}) , \qquad (3)$$

where U_{i_∞} denotes the ship velocity and $q_{(n)}$ the source strengths. For each control volume center, the sum runs over the amount of sources n used within the potential flow solver. Subsequently, an approximation of the viscous boundary layer according to a log-law relation is imposed on the initial flow field. The (viscous) initialisation also pertains to an improved initialisation of the turbulence properties in the viscous boundary layer, e.g. in conjunction with a k-ω two-equation Boussinesq-viscosity model (Wilcox, 1998). Finally, the initial pressure is computed at each control-volume center from Bernoulli's equation. In this regard, pressure values below p_∞ are used to identify the air phase and are subsequently corrected to ambient air pressure.

3.5 Viscid/Inviscid Coupling

In order to efficiently capture seakeeping influences, a zonal viscous/inviscid-coupling approach seems to be a viable approach. The inviscid solution used for the present studies is obtained from the classical linear Airy theory (Faltinsen 1990) and ignores the presence of the floating body. Accordingly, the damping of the diffraction field has to be managed by an appropriate construction of a buffer-zone where the compliance between the composed flow and the inviscid flow is gradually enforced. The present suggestion aims to establish an implicit viscous/inciscid coupling which is supplemented by Dirichlet far-field conditions derived from the inviscid solution for momentum and mixture fraction. The implicit coupling is based on an appropriate manipulation of the coefficient matrix of the viscous solver. An important advantage of this coefficient-based implicit coupling over an explicit coupling strategy is the avoidance of stability and convergence problems. Further details on the coupling approach are given in Wöckner et. al. (2010).

3.6 Rigid Body Motions

A six degrees of freedom motion solver is coupled to the presented approach. It is based on an Euler angles, and uses the forces and moments acting on the floating body to determine its velocity and position in time. A local coordinate system originated in the center of gravity of the floating body is introduced to simplify the numerical integration of the motion equations. All degrees of freedom can be suppressed.

4. RESISTANCE PREDICTION

4.1 Numerical Grid and Setup

The first example refers to well known KVLCC2-tanker at Fn=0.142 and Re=4.6 10^6, where a vast amount of numerical and experimental data is available in Van et. al. (1998). Reported results are obtained on an unstructured mesh using local grid refinement in the vicinity of the hull. Figure 2 outlines the employed grid, which consist of 3.5 Mio. control-volumes.

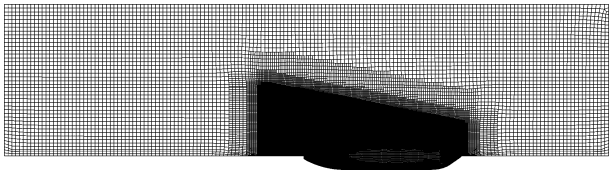

Fig.2 Grid used for RANS computation of KVLCC2.

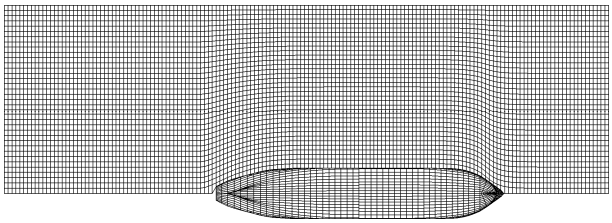

Fig.3 Grid used for potential flow computation of KVLCC2.

The corresponding potential flow grid is displayed in figure 3. The in-house potential flow solver ν–shallo has been used for the inviscid simulation.

A comparison of the inviscid and the initialised RANS solution is illustrated in figure 4. Small deviations in the surface elevation can be seen which are due to the different grid densities.

A transient simulation with 5 sub-cycles is performed and compared to a traditional simulation without sub-cycles and standard initialisation. The Wilcox k-ω turbulence model in conjunction with wall functions is used.

4.2 Results

An image of the final wave pattern – indicated by the iso-surface *c=0.5* - is depicted by figure 5 in comparison to measured EFD data reported by Kim et. al. (2001). The predicted wave pattern obtained from *FreSCo*$^+$ is generally in very good agreement with the experiments.

In conjunction with the present technique, force convergence is typically obtained after 2500 iterations.

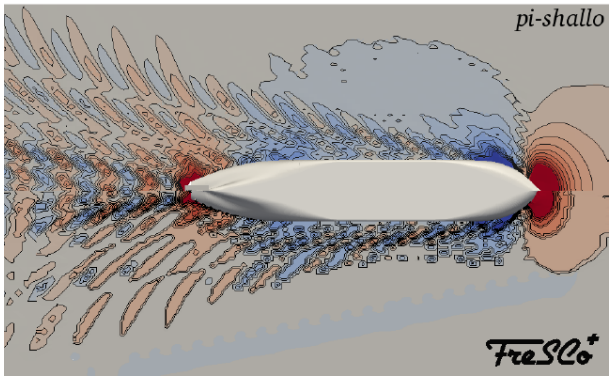

Fig.4 Comparison of wave elevation according to the potential flow (upper part) and initialisation of RANS calculation (lower part).

Figure 6 provides an overview of the evolution of the predicted force deviation from experiments for the conventional approach and the present approach. It is seen, that the application of the present approach exhibits improved convergence behaviour, and is converged within 3% of the wall clock time of the conventional approach.

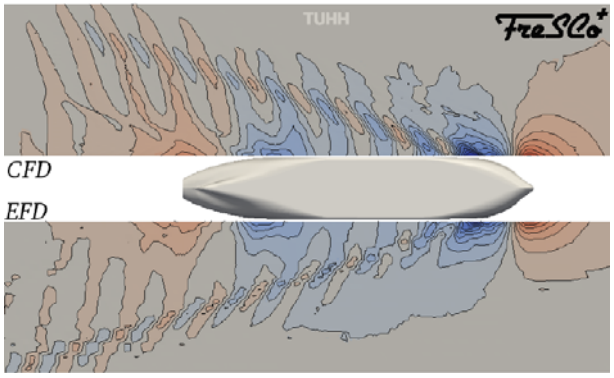

Fig.5 Comparison of final wave elevation of RANS calculation (upper part) with experimental results (lower part).

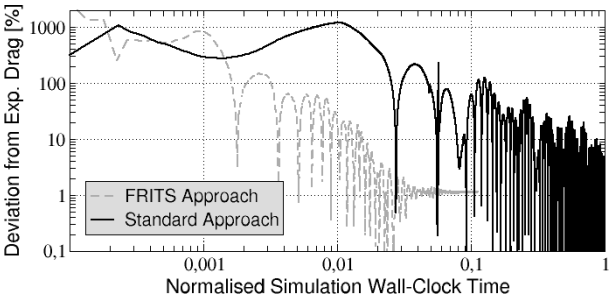

Fig.6 Deviation of predicted drag from experimental results for standard and improved approach

.

5. SEAKEEPING

5.1 Numerical Grid and Setup

See keeping simulations have been performed for three different conditions. The wave and ship parameters for these conditions are given in table 1.

Table 1 Summary of test case conditions

Condition No.	C2	C3	C4
Froude Number	0.26	0.26	0.33
Reynolds Number ($x10^6$)	6.52	6.52	8.27
Wave length λ/L_{pp}	1.15	2.00	1.33
Wave Height H_s (mm)	84	146	97

The numerical grid shown in figure 7 has been used to perform all sea keeping simulations. It captures a very small domain, with the inlet situated 1/3 L_{pp} in front of the ship, the outlet 2/3 L_{pp} behind the transom of the ship and the side 0.5 L_{pp} aside the ship. The grid consist of 800k hexahedral cells, where the majority of the cells is placed in the free surface region.

The incoming waves are prescribed using the inviscid/viscid coupling approach outlined in section 3.4.

The motion solver uses an implicit time integration procedure, therefore the rigid grid position is updated each outer iteration.

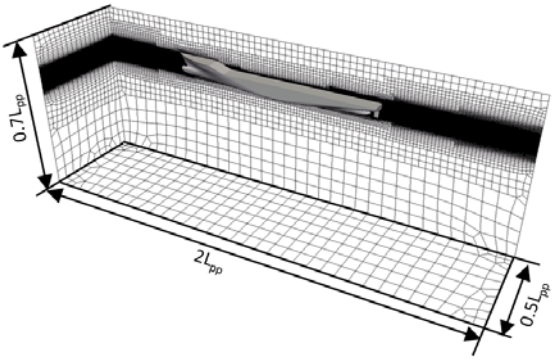

Fig.7 Numerical Grid for the KCS.

5.2 Results

Heave, pitch and total resistance time series for all cases are shown if figures 8-10.. It is seen that for all cases the heave and pitch motions are inline with the experimental results published by Simonsen et. al. (2008).

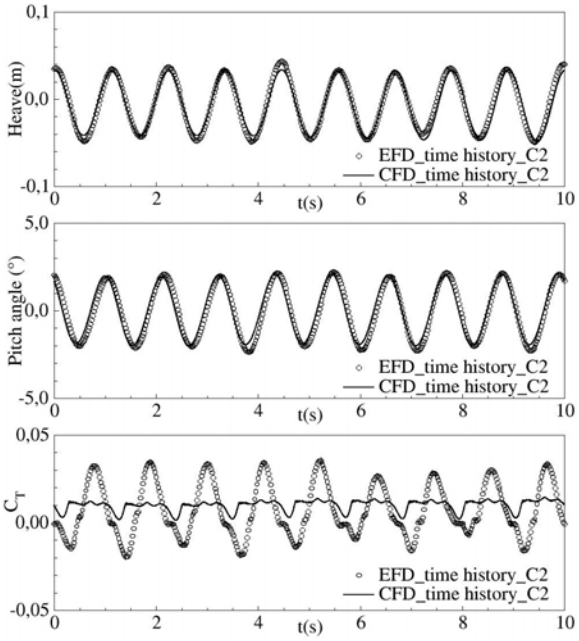

Fig.8 Time series of heave pitch and total resistance coefficient compared to experiment for case C2.

However, none of the time series for the total resistance coefficient shows a good agreement with experimental results. Looking at the average of the total resistance coefficient represented by the 0^{th} harmonic amplitude shown in table 2, an overestimation of the resistance in the order of 20% is seen.

Figure 11 shows four snapshots for case C2 of the ship moving in the waves. No reflections from the boundaries are observed.

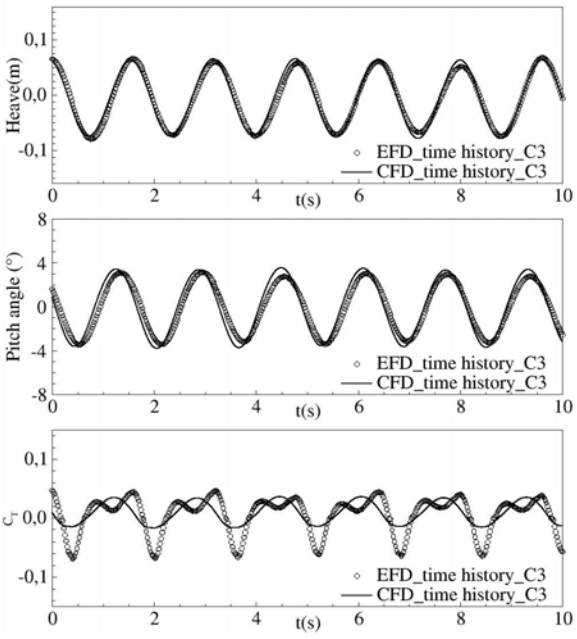

Fig.9 Time series of heave pitch and total resistance coefficient compared to experiment for case C3.

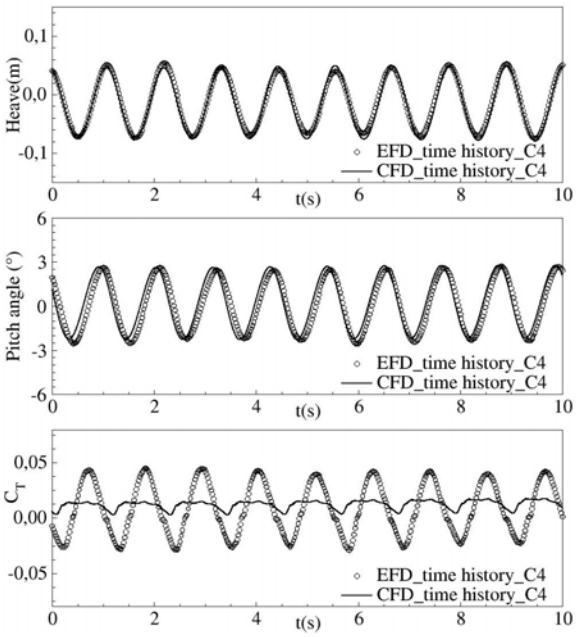

Fig.10 Time series of heave pitch and total resistance coefficient compared to experiment for case C4.

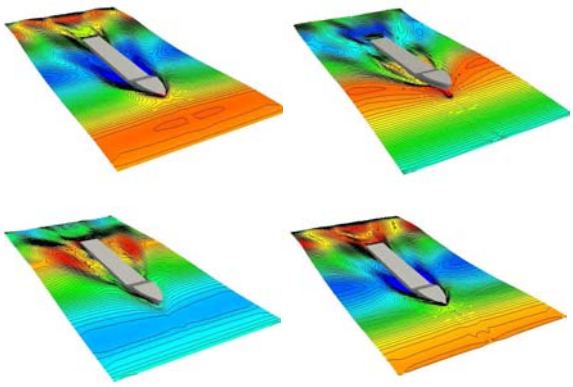

Fig.11 Example of free surface around the ship and motion of the ship

Table 2 0^{th} harmonic amplitude of total resistance coefficient for experiments and simulation.

Condition No.	C2	C3	C4
0^{th} EFD	$7.159x10^3$	$6.033x10^3$	$8.716x10^3$
0^{th} CFD	$8.628x10^3$	$7.841x10^3$	$10.533x10^3$

6. CONCLUSION

Performing a resistance prognosis sub-cycling and advanced initialisation techniques reduce time to solution by roughly two orders of magnitude, as it has been shown for the KVLCC2. This speedup in time to solution has no negative influence on the accuracy.

Sea keeping simulations can be carried out in very compact domains when a viscid/inviscid coupling procedure is used in the far field. Heave and pitch motions for the Kriso container ship are in very good agreement with experiments. However significant deviations are observed for the added resistance, in line with observations reported by other authors.

REFERENCES

Balay, S., Gropp, W.D., Curfman McInnes, L. and Smith, B.F. (1997) "Efficient Management of Parallelism in Object Oriented Numerical Software Libraries", Modern Software Tools in Scientific Computing, pp163-202.

Brunswig, J., Manzke, M. and Rung, T. (2010) "Explicit and Implicit Coupling Strategies for Overset Grids", 10th Symposium on Overset Composite Grids and Solution Strategies, NASA AMES Research Center, Moffett Field, California

Faltinsen, O. M., (1990) "*Sea Loads on Ships and Offshore Structures."* , Cambridge Univ. Press, Cambridge, UK.

Kim, W.J., Van, S.H. and Kim, D.H. (2001), "Measurement of flows around modern commercial ship models," , Exp. in Fluids, Vol. 31, pp 567-578.

Manzke, M., Will, J. and Rung, T. "Efficient Viscous Wave Resistance analysis", PRADS-Paper 2010-2253.

Marzi, J. (2008). "*VIRTUE* - Die Entwicklung des numerischen Schlepptanks" (in German). Jahrbuch der Schiffstechnischen Gesellschaft, Vol. 101, pp 364-373.

Simonsen, C., Otzen, J. and Stern, F. (2008)."EFD and CFD for KCS heaving and pitching in regular head waves." Proc. 27th Symp. Naval Hydrodynamics, Seoul, Korea

Stück, A., Kröger, J. and Rung, T. (2010) "Adjoint RANS for Aft-Ship Design", Eccomas Paper 2010-01384.

Ubbink, O. (1997) "Numerical prediction of two fluid systems with sharp interfaces". PhD thesis, Imperial College of Science, Technology and Medicine.

Van, S.H., Kim, W.J., Yim, D.H., Kim, G.T., Lee, C.J. and Eom, J.Y. (1998), "Flow Measurement Around a 300K VLCC Model," Proceedings of the Annual Spring Meeting, SNAK, Ulsan, pp. 185-188.

Vaz, G. and Jaouen, F. and Hoekstra, M. (2009), "Free Surface Viscous Flow Computations. Validation of URANS Code FreSCo.", OMAE2009-79398.

Wilcox, DC. (1998). "*Turbulence Modeling for CFD*", 2nd edition, DCW Industries.

Will, J. (2010) "Enhancement of the Computational Efficiency for Steady State Free Surface Flows around Ships", Diploma Thesis, Institute for Fluid Dynamics and Ship Theory, Hamburg University of Technology

Wöckner, K., Drazyk, W. and Rung, T. "An Efficient VOF-Based RANS Method to Capture Complex Sea States", OMAE Paper 2010-20674.

UNSTEADY VISCOUS FLOW CALCULATION AROUND THE KCS-MODEL WITH AND WITHOUT PROPELLER UNDER CONSIDERATION OF THE FREE SURFACE

M.Greve, M. Abdel-Maksoud (TUHH, Germany)
S. Eder, J. De Causmaecker (ANSYS, Germany)

1. INTRODUCTION

Different numerical investigations of the propulsion characteristics of the KCS Model were carried out without considering the free surface effect (see Abdel-Maksoud et al. (2000) and Lübcke (2005)). In the present paper the unsteady flow around the KCS in model scale in towed and self propelled condition under consideration of free surface effects was investigated. A Validation and Verification Study was carried out with three different meshes. For the grid generation the commercial software code ANSYS ICEM CFD (N.N. 2009a) and for calculation ANSYS CFX (N.N. 2009b) were used.

The main aims of the calculations are the determination of the ship resistance, the unsteady propeller induced pressure on the stern region and the propeller forces. Therefore the real propeller geometry was employed in the calculation.

2. NUMERICAL METHOD AND GRID GENERATION

The computatieons have been carried out with the commercial solver ANSYS CFX, a finite volume (U)RANS-method for structured hexaedral grids. A High-Resolution Advection Scheme is applied. The convection term is discretized using a 2nd-order upwind scheme and the diffusion term using 2nd-order trilinear approach. The velocity and pressure equations are fully coupled using an implicit algorithm. For solving the linear equation system an algebraic multigrid (AMG) accelerated incomplete lower-upper (ILU) factorization technique is used.

To evaluate the propulsive performance different computations were carried out: the ship in towed condition, the free-running propeller and the ship in self propelled condition. The simulated configurations are to be found in Table 1. All generated grids are multi-block structured using non-orthogonal hexaedral blocks. The grid is divided into two domains, the ship domain and the propeller domain. The latter lies within a small cylinder having a diameter of 1,17 times the propeller diameter (D) and a length of 0,25 D. The numerical grid for the propeller is generated within this domain and it can be easily integrated into the ship domain. The size of the ship domain is 2*Lpp in front of the ship, 4*Lpp aft of the ship and 2*Lpp to the side. Three different grids for the hull geometry are employed. The resolution of the grids generated are coarse (1.57 mio. elements), medium (4.96 mio. elements) and fine (16.43 mio. elements) having an refinement ratio of 1.5 between the meshes. The grid sizes (see Table 2) refer to half of the ship domain because the flow in the towed case is symmetric. The applied grid topology is shown in Fig.1 for the different configurations.

Configuration A
Configuration A contains the bare ship hull without appendages. For the calculation of the wave pattern and the ship resistance only half of the ship needs to be simulated and the midship plane is set up as a symmetry plane. The calculation is carried out in steady manner using a velocity inlet boundary condition. The outlet b.c. is set up as an opening with hydrostatic pressure applied according to the initial position of the free surface. The timestep is varied over the first 300 Iterations. It starts with 0.005 sec. and is raised up to 0.33 sec. successive. The turbulence model used is the SST-Model.

Configuration B
This configuration and the applied calculation setup is similar to configuration A but with a rudder employed in the simulation. The investigated grid resolutions for the validation and verification study are given in Table 2.

Configuration C
Configuration C contains only the propeller for simulating the open water performance. The grid for the propeller is created around one of the five blades and represents a 72° section of the above described cylindrical domain. The meshes can be copied and rotated around the propeller axis to represent the full propeller geometry. The grid around one blade consists of 325,272 elements and the full propeller has 1,626,360 elements. Periodic type b.c. is applied

which allows the consideration of the flow around one propeller blade only. The size of the domain is 10 D in front, 30 D aft of the propeller and 7 D to the side. Using multiple frames of reference the propeller-blade domain is set up as a rotating domain and the surrounding domain remains stationary. Frozen rotor b.c. is applied between rotating and non-rotating domain interfaces.

Configuration D
This configuration contains the full hull and propeller geometry using the medium grid for the hull. General grid interface b.c. is applied at the grid surface between the propeller blades. To consider the relative motion between the propeller and hull grid domain a sliding interface b.c. is applied. That allows the consideration of the transient effects (rotor/stator interaction). A steady calculation is first conducted with non-rotating propeller to establish the flow-field around the hull and the free surface elevation. After the flow around the ship and the free surface have developed an unsteady calculation is started with the steady flow-field as initial solution. Seven propeller revolutions are simulated using a time step corresponding to 3° of one propeller revolution.

3. RESULTS AND DISCUSSION

A Validation and Verification Study is carried out following the ITTC Guidelines (3) for the configuration B. Therefore first the medium grid is used for a convergence study to check iteration uncertainity. As shown in Table 3 the deviation between a residual target of 1E-04 and 1E-05 is about 10% whereas the deviation between 1E-05 and 5E-06 is negligible. For that reason the residual target 1E-05 is considered for further evaluation. Secondly a grid convergence study is carried out. The results are given in Table 7. Observed are the total resistance Coefficient C_T, the frictional resistance coefficient C_F and the pressure resistance coefficient C_{PV}. Calculations are made for the three grids S_1, S_2 and S_3 whereas S_1 refers to the finest grid. The validation uncertainity U_V is about 1%.

For configuration A the calculated result agrees well with the EFD data. Table 4 shows the deviation of the calculated C_T to the measured value. A comparison of the global wave field is given in Fig.2. Fig.3 and Fig.4 show that the surface pressure on the stern in front of the propeller is reduced and above it increased due to propulsion effects when compared to the towed case. The size of the separated flow area on the hull surface below the hub is increased due to the suction effect of the propeller.

The convergence of the forces in the unsteady calculation is shown in Fig.5 (left). The value of the tangential force is quite stationary because the wetted surface of the ship hull is nearly constant and the propeller suction has more influence on the pressure force. The residual force is the sum of ship resistance and propeller thrust. Because of the development of the stern wave field during the simulation the residual force needs several propeller revolutions for convergence. The thrust variation on the propeller blades over the last two revolutions is shown in Fig.5 (right). Table 5 shows the change of the ship resistance coefficients due to propulsion effects. The total resistance is increased by 15.5%. Due to the flow separation the frictional resistance of configuration D is lower than the related value of configuration A. Table 6 shows a comparison between measured and calculated integral values. The calculated k_T and k_Q are 1.9% and 5.6% lower than the measured results. The calculated wake fraction of Configuration D at 0.25 D in front of the propeller is 0.214. The thrust deduction factor equals to 0.126, which leads to a hull efficiency of 1.112.

Fig.6 and Fig.7 show the pressure distribution on the pressure (left) and suction sides (right) of the propeller blades for the blade angular positions 0° and 36°. Fig.8 shows the velocity contours at 0.25D in front of the propeller plane for the configuration A (left) and D (right). The velocities are much higher in the propelled case.

Fig.9 shows the crossflow velocity vectors at x=0.9911 aft of the propeller plane (left) and the velocities u/U, v/U and w/U in this plane at z=-0.03Lpp (right) for the above mentioned blade angles. Due to interactions between the flow around the propeller blades and the wake field the propeller flow is directed against the wake flow in the first quadrant (seen from behind) and above the propeller. The agreement of the computed velocities with the measured values shows some differences especially in the velocity component in z-direction (w) which may influence the characteristics of the u-velocities.

4. CONCLUSION

The computed results for the KCS model without propeller influence are satisfying. The investigation of the propulsion case under consideration of the free water surface shows fair results compared to the measured data. The numerical results allow the calculation of the interaction parameters between hull and propeller. For further investigations the grid density around the propeller especially at the grid interfaces could be increased.

REFERENCES

N.N., (2009a), ANSYS ICEM CFD User Documentation, Version 12.1

N.N., (2009b), ANSYS CFX User Documentation, Version 12.1
ITTC Guideline 7.5-03 01-01, (2002), "Uncertainity Analysis in CFD, Verification and Validation, Methodology and Procedures"
Abdel-Maksoud, M., Menter, F.R., Rieck, K. (2000), "Unsteady Numerical Investigation of the Turbulent Flow around the Container Ship Model (KCS) with and without Propeller", CFD Workshop Gothenburg 2000
Lübcke, L, (2005), "Numerical Simulation of the flow around the propelled KCS", CFD Workshop Tokyo 2005
Kim, W.J., Van, D.H., Kim, D.H., (2001), "Measurement of flows around modern commercial ship models", Exp. in Fluids, Vol. 31, pp 567-578

Table 1 Simulated cases

Configuration	Hull	Rudder	Propeller
A	Yes	No	No
B	Yes	Yes	No
C	No	No	Yes
D	Yes	No	Yes

Table 2 Number of elements for grids of hull domain used in Configuration B

	Coarsee	medium	Fine
Elements	1.571.946	4.955.063	16.427.453

Table 3 Convergence study for the total resistance coefficient C_T with rudder

residual	1E-03	1E-04	1E-05	5,00E-006
C_T*1E+03	11.603	3.284	3.632	3.634
Deviation to previous [%]	-	-71.69	10.60	0.03

Table 4 Convergence study for the total resistance coefficient C_T without rudder (Configuration A)

residual	1E-03	1E-04	1E-05	5E-06
C_T*1E+03	11.440	3.210	3.554	3.555
Deviation to previous [%]	-	-71.94	10.72	0.03
Deviation to EFD [%]	221.62	-9.75	-0.08	-0.05

Table 5 Model resistance with and without propeller

	Without propeller	With propeller	Change [%]
C_T	3.555	4.108	15.54
C_{PV}	0.564	1,252	122.03
C_F	2.991	2.856	-4.74
C_{F0}	2.83	2.83	

Table 6 Measured and calculated integral values

	Measured	Calculated
K_T	0.158	0.155
10*K_Q	0.303	0.286

Table 7 Results of V&V study for three different grids

Parameters		**EFD**	**S_3**	**S_2**	**S_1**	**ε_{12}**	**U_I**	**p_G/p_{th}**	**U_G**	**U_D**	**U_V**
C_T*10³	Value	3.557	3.410	3.590	3.602	0.34	5.92E-04	3.32	0.02	1.0	1.0003
	E	-	4.13	-0.92	-1.26	-	-	-	-	-	-
C_F*10³	Value	-	2.995	2.989	2.972	0.58	0.00E+00	-1.33	4.19	-	-
C_{PV}*10³	Value	-	0.416	0.601	0.630	4.64	4.31E-05	2.33	0.82	-	-

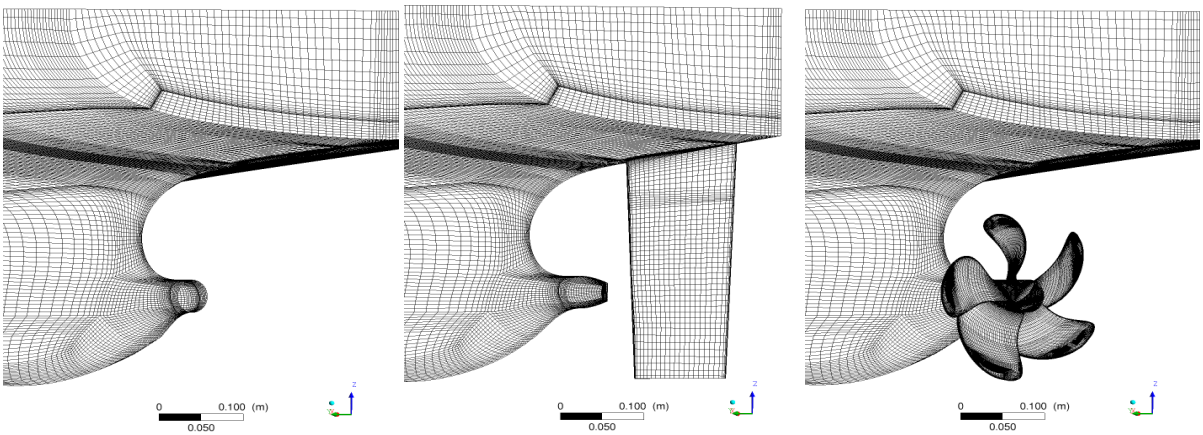

Fig.1 Surface grid of ship, rudder and propeller for configurations A (left), B (middle) and D (right).

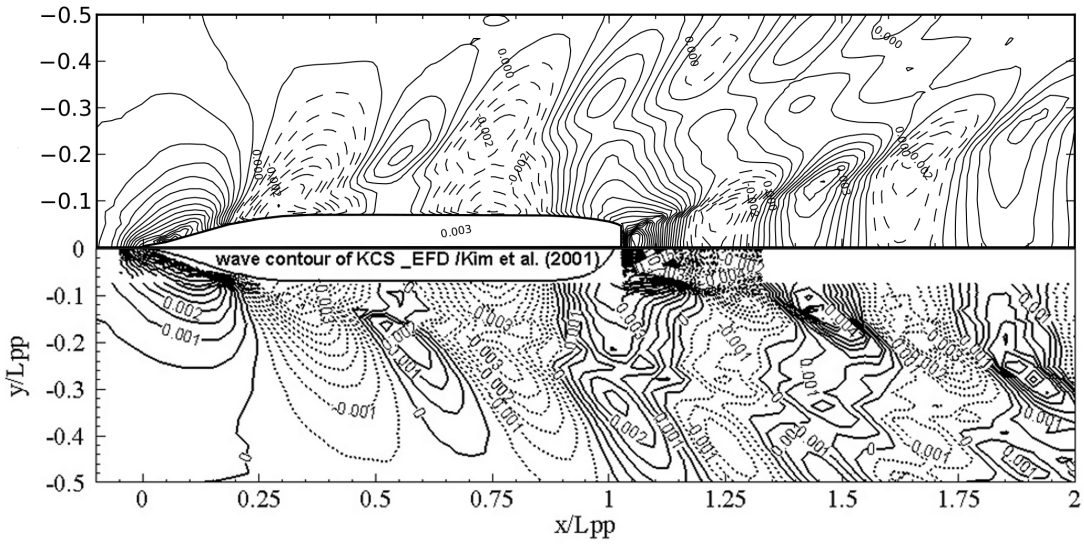

Fig.2 CFD wave elevation contour (upper part) compared with EFD data (lower part).

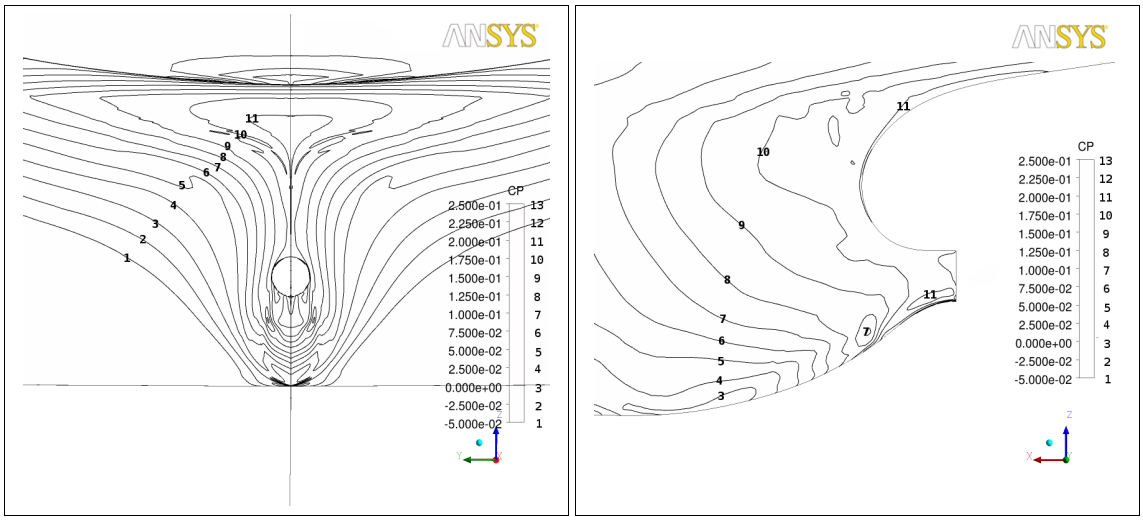

Fig.3 Surface pressure distribution, configuration A (without propeller), aft view (left) and side view (right)

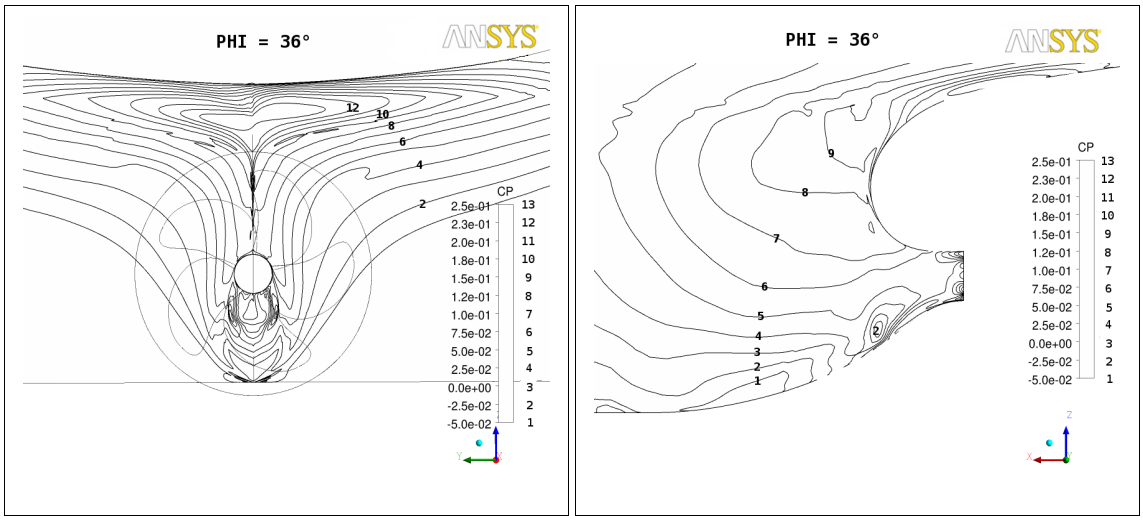

Fig.4 Surface pressure distribution, configuration D, $\phi = 36°$, aft view (left) and side view (right)

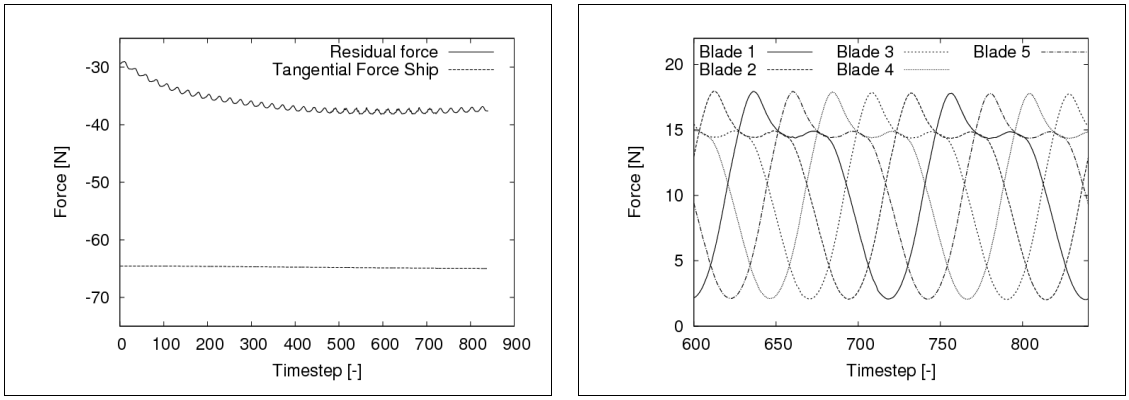

Fig.5 Left: Tangential force on ship and residual between ship-drag and propeller-thrust, Right: Unsteady forces acting on propeller blades of propeller rotations six (timestep 600-720) and seven (721-840).

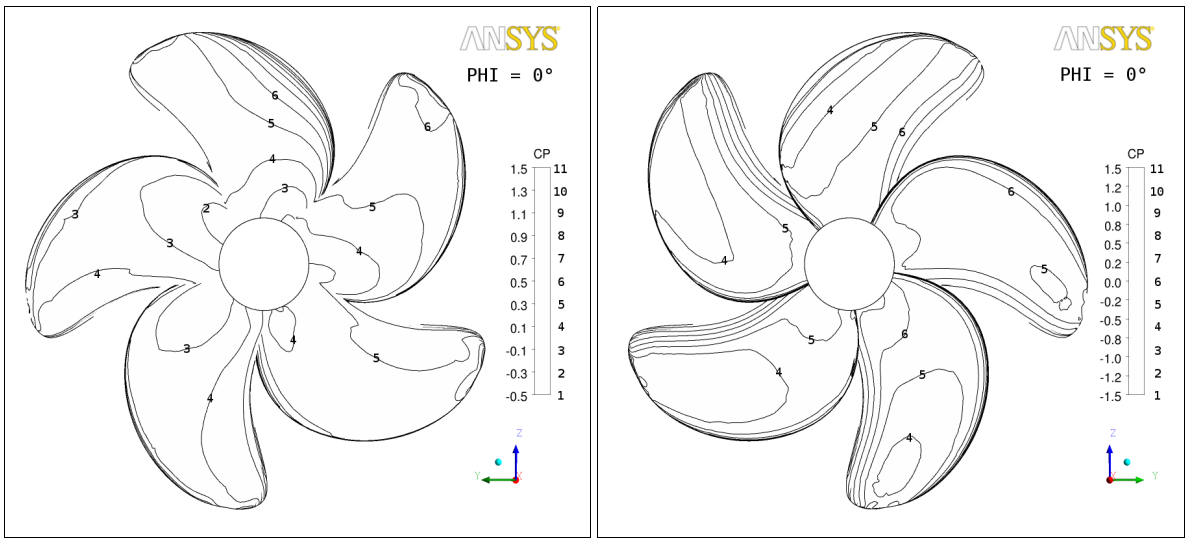

Fig.6 Pressure distribution, configuration D, $\phi = 0°$, pressure side (left) and suction side (right)

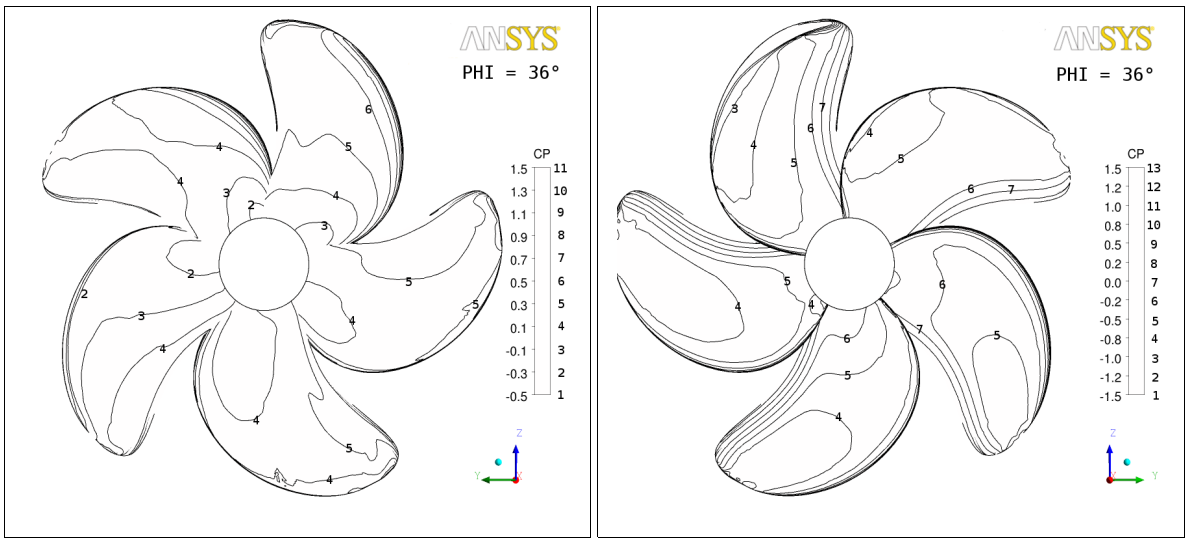

Fig.7 Pressure distribution, configuration D, $\phi = 36°$, pressure side (left) and suction side (right)

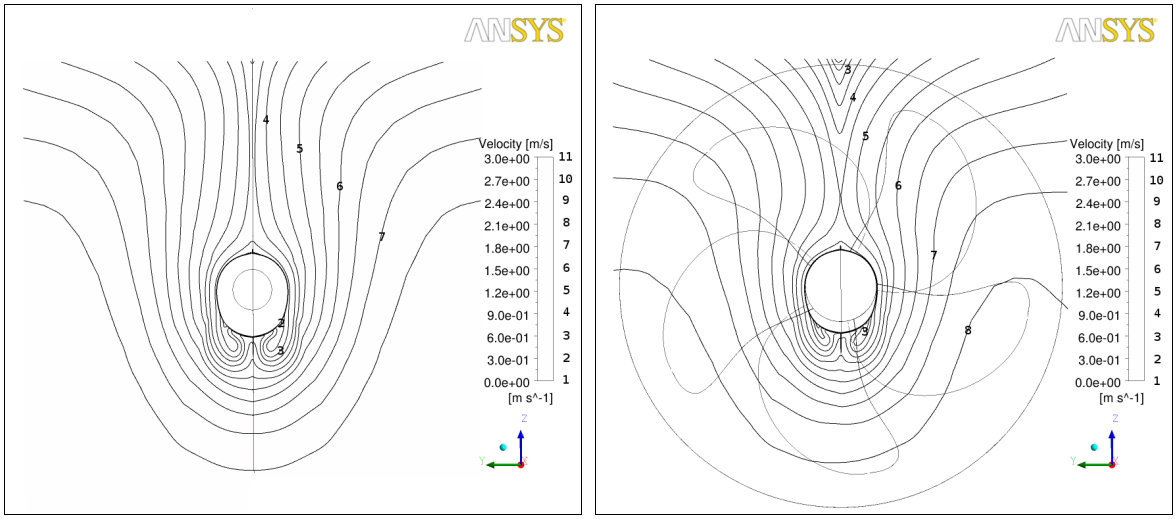

Fig.8 Calculated Velocities at x=0.9736Lpp, 0.25D in front of propeller, configuration A (left) and configuration D (right) for ϕ=36°

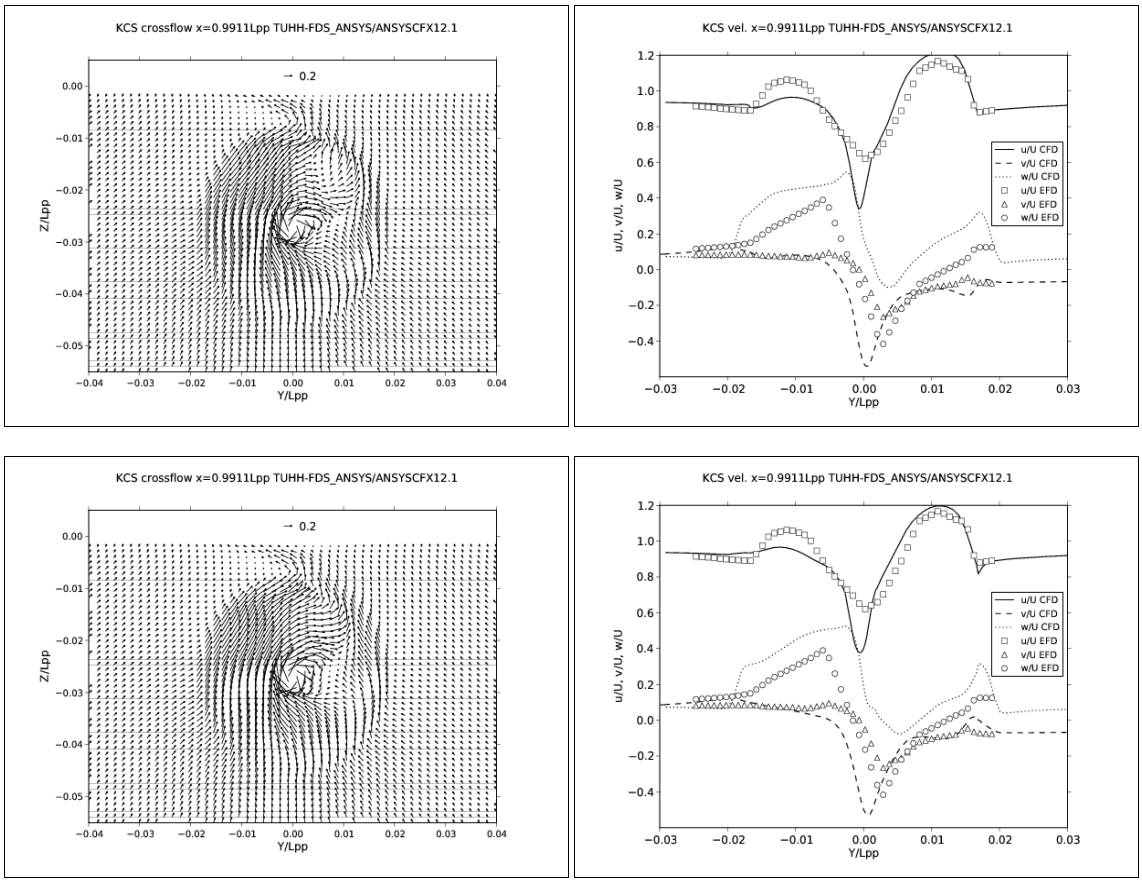

Fig.9 Velocities aft of propeller plane at x=0.9911Lpp for ϕ=0° (first row) and ϕ=36° (second row). Left pictures show crossflow vectors, right pictures show velocity components u/U, v/U and w/U at z/L=-0.03.

Multiphase URANS Simulations of Surface Combatant using Star-CCM+

Stefano Brizzolara & Diego Villa
Marine CFD Group, University of Genova – Italy
(stefano.brizzolara@unige.it , diego.villa@unige.it)

SUMMARY

The paper details the setup and results of a series of URANS simulations for the fast displacement hull, DTMB5415, test case 3.1 and 3.2 (fixed and free trim) of the Gothenburg 2010 CFD workshop. The commercial software Star-CCM+ v.4.04, in use since years by the Marine CFD Group of the University of Genova, has been selected. Details are given about the mesh generation, the configuration of numerical solver and the setup of the physical models. The comparison with the reference experimental results is generally good in terms of wave pattern and flow field, but still evidence some relevant quantitative error on global parameters, i.e. resistance and dynamic trim angle value of the experimental reference data. A possible source of error could be the unsteady fluctuating behavior evidenced by the numerical time histories of the numerically predicted pressure resistance component and pitching moment, perhaps correlated to the bow wave instability or regurgitating flow behind transom stern.

1. INTRODUCTION

Nowadays, a number of RANSE solvers exist; many of them specifically conceived for ship hydrodynamics, some others developed with the aim to be commercialized to a wider public and hence adapted to describe more general flow problems. The first benefit from more tuned numerical methods; the second from their versatility (possibility of generating complex meshes on complicated geometries) and integrability with other design software. Of course, there is an interest in validating also these commercial solvers. The total hull resistance in calm water including dynamic attitude is one of the items to be addressed. In fact, it continues to be proposed after Gothenburg 2000 and Tokyo 2005 workshops. But which level of accuracy can be expected by these general purpose methods and with which modeling techniques? The Marine CFD Group of the University of Genova is engaged in addressing this kind of questions for planing hull hydrodynamics (Brizzolara & Serra, 2007) (Brizzolara & Villa, 2009 and 2010) (Brizzolara & Federici, 2010), where perhaps less scientific efforts have been paid, as well as for fast conventional displacement hulls, as in the present test case, though normally with better accuracies with respect to experimental results (Brizzolara et al. 2009) than what obtained on this particular test case.

2. SOLVER CHARACTERISTICS

Star-CCM+ is a general purpose finite volume solver, with a powerful polyhedral unstructured mesher integrated into the working environment. The solver is able to simulate a multiphase immiscible flow using a Volume of Fluid approach solved in time, by a Eulerian implicit method. The transport equation for VOF is a solved with a second order scheme with a sharpening factor (Ferziger & Peric, 2002). All the equations are solved with the segregated flow technique, and the coupling between the continuity equation and the momentum equation (pressure-velocity link) is solved through the well know SIMPLE algorithm, in conjunction with an AMG linear solver to speed-up the convergence of the solution during iterations. Where appropriate, the unsteady simulations have used a 2-DOF (Degree Of Freedom) approach to find the dynamic equilibrium at high speed in terms of running trim and sinkage of the hull. The motion was applied by imposing a rigid body motion to all the mesh and writing the N-S equations in the moving reference frame.

Turbulence has been modeled with the Realizable k-ε two layer model, extrapolated at the solid boundaries of the domain (hull shell) with a 2 layer all y+ wall function. The gravity body force has been imposed, and the problem has been solved in terms of absolute pressure normalized to that at the free surface (reference value). Other specific details on the solver can be found in the User Manual (CD-Adapco, 2009).

3. MESH PREPARATION

The mesh has been prepared with the built-in mesher program. The mesher create unstructured polyhedral (trimmed in our case) cells using a Cartesian algorithm. The Cartesian mesh used in the far field can have progressive anisotropic (with different refinement factor in the three cardinal directions) cell refinements near the boundary surfaces of the domain. From the hull wall boundary, several layers of prismatic cells are generated with a geometric 3D offset technique from the quadrilateral panels discretizing the hull surface, to adequately capture the boundary layer development near non-slip wall. The transition (or connection) between this inner prisms layer and the far field Cartesian mesh is done through a layer of trimmed (irregular polyhedral) cells obtained simply cutting the Cartesian cells intersecting with the external surface of the prism layer.

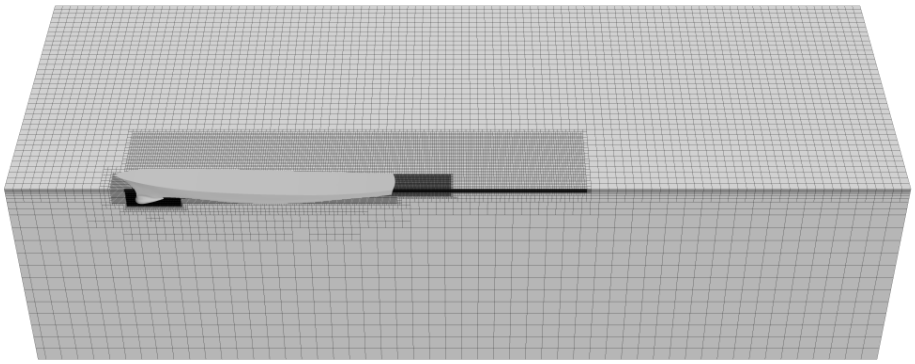

Figure 1: 3D view of Fine Mesh (Grid 1), with anisotropic progressive refinement

A grid-dependence study has been performed, repeating the calculations on four generated meshes of the same typology, with increasing refinement level depending on a single parameter which is the characteristic cells length, presented in Table 1 together with the resulting total number of cells.

Table 1: Characteristic lengths and total cell numbers for the four meshes refinement used in the convergence study

	grid -3-	grid -2-	grid -1-	grid -0-
Characteristic Length [m]	8.58	5.72	3.813	2.86
Number of cells	272k	710k	2049k	6045k

Depending on the zone of the domain, defined by some simple shaped control volumes, the mesher can use two type of refinements: an isotropic one, for which each cell is equally split along all the three Cartesian direction; an anisotropic refinement, in which the cell is cut along only one cardinal direction. Both refinements have been used in the in all the cases generated for the mesh sensitivity analysis. In particular, the isotropic one has been used near the bulb, the transom and the hull (with different refinement levels) to better capture the highly three dimensional flow; the anisotropic one, refined only on z-direction (same as gravity direction) has been used around the still free surface, in the near and far field to better define the wave pattern without increasing exponentially the number of cells.

Table 2 resumes the refinement factors assumed for the generated mesh typology in all the four.

Table 2: Cell refinement factors used for mesh sensitivity analysis. Values are in percentage of the characteristic length (Table 1)

	x-direction	y-direction	z-direction
Bulb	0.2	0.2	0.2
Transom	0.5	0.5	0.5
Hull	1	1	1
Near field (around FS)	2	2	0.2
Far field (around FS)	5	5	1

Figure 1 presents a sketch of the generated fine mesh, in its fine version (grid 1, about 2M elements), where the different refinement level clearly appear on the horizontal (still waterline) and longitudinal symmetry planes.
Figure 2 presents a close up view of the mesh in the forward bulb region, in case of the grid with the finest resolution (grid o, about 6M cells).

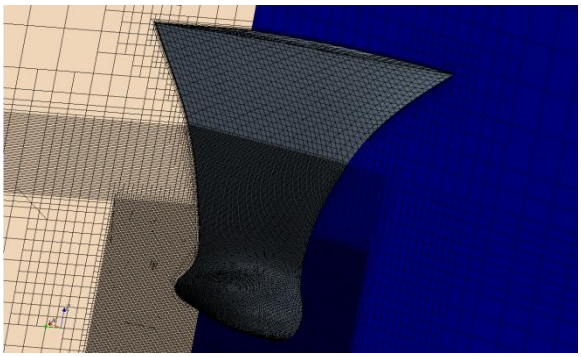

Figure 2: Mesh resolution around the sonar bulb in the Very-Finegrid (-0-).

4. RESULTS

The simulation have been performed for the workshop cases 3.1 and 3.2, using the model scale of the tests performed by Olivieri et al. at INSEAN. Another comprehensive database of model test results has been derived from Longo on a smaller model An accurate analysis of the two set of results highlight some discrepancy in the comparison of the measured near field wave patterns, as also arguable from the longitudinal wave profiles presented in Figure . Taking this experimental uncertainty into account, in general, the numerical results are rather well in agreement with the experimental measurements, in term of predicted flow field and wave pattern around the hull.

The following sub-sections present the main considerations originated during the analysis of the results for each type of simulation.
The first sub-section deals with simulation with imposed attitude, in which the hull sinkage and trim has been fixed according to the experimental values.
The second sub-section, instead, discuss the results obtained with the hull free to follow the rigid body dynamic with 2-DoF (pitch and heave) to reach at convergence the final dynamic equilibrium.

4.1 **Comments on results in the fixed trim condition**

The mesh sensitivity analysis study has been performed on this test cases with fixed dynamic attitude. The two graphs of Figure 3, show the variability of the total resistance coefficient C_T and the frictional (shear) resistance coefficient C_F with the four analyzed mesh densities, at the model speed corresponding to Fn=0.28. Also the relative percentage error on the towing model resistance (in case of C_T) and on the calculated CF with ITTC'57 friction line is represented in the graphs. As clear from figure 3, grid-1 with about 2M cells show already a good convergence, though showing a substantial error on the experimental value. The numerically predicted correctly value converges with increasing mesh density, but strangely setting on a higher deviation with respect to the experimental value.

The predicted wave pattern, in fact, correlates pretty well with the one obtained by Olivieri et al., as can visible from the comparison of figure 9. A closer look at the longitudinal wave cuts in Figure 8, substantially confirms the general good agreement, also taking into account the experimental data scatter between the two geosims tested in two different towing tanks, but also evidences the clear underestimation of the first wave peak at bow. This very steep divergent wave peak at bow, captured in the experiments, most probably refers to a very thin layer of water rising up on hull flare and then breaking and is still not enough captured in the simulations, even with the finest mesh.

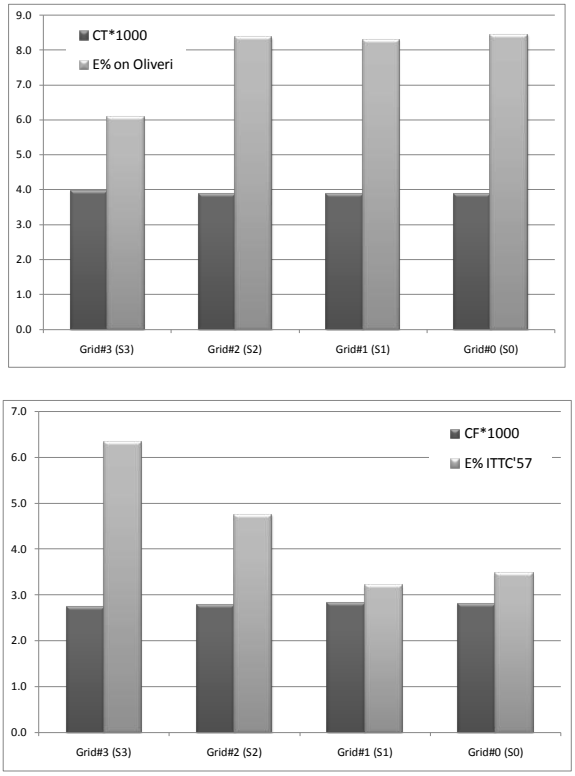

Figure 3: In order the rise and trim history during the simulation

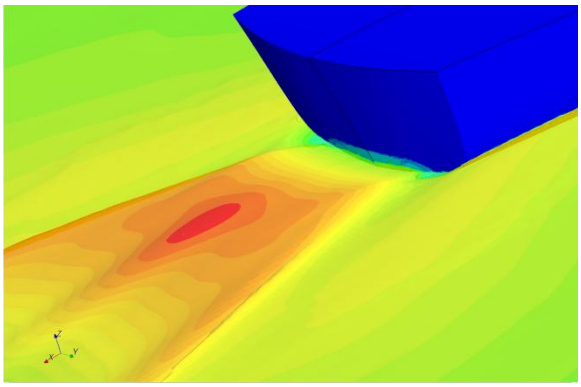

Figure 4: Details of the unsteady regurgitating (partly wetted) flow behind the transom, Fn=0.28, finest mesh (grid 0).

The example of time histories of the total, pressure and shear resistance given in figure 5, evidences an oscillating behavior of the pressure resistance signal that needs more than 40 seconds to dampen, for the finer mesh (grid-0), at Fn=0.28. decreasing the mesh density the oscillation become even more persistent. It is believed that this unsteady nature of the pressure forces on the hull can be due to the regurgitating flow behind the transom, that results partly wetted (see figure 4) and the breaking wave at bow.

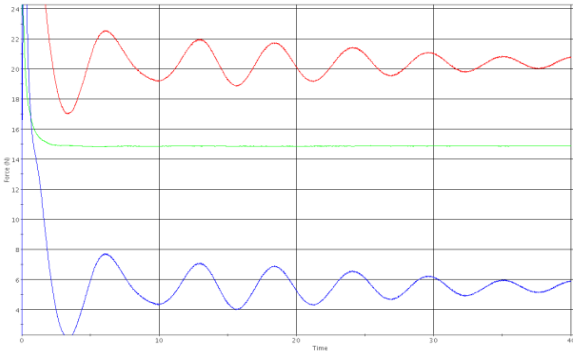

Figure 5: Typical time histories for drag components during unsteady simulation at Fn=0.28, on grid 0, with fixed exp. attitude. Total (red), shear (green) and pressure (bue) resistance.

4.2 **Comments on results in the free attitude condition**

Results presented at the workshop for this series of simulations have been obtained one grid-2 (700k cells). The unsteady simulation time required to dampen the oscillation of the sinkage and trim time histories, caused by the non equilibrium values initially guessed, would have required too long computing time with the other meshes. Indeed a total virtual transient simulation time of 50 seconds, with 6 inner iterations and a time-step of 10^{-3} seconds, for a total of 300k iterations was necessary to reach the final stabilized condition. Moreover it was demonstrated, on a single test case, that the final equilibrium condition does not depend significantly on the mesh resolution.

The numerical dynamic attitude results present large relative deviation with respect to the experimental data, except for the highest Froude number where the relative error on total resistance is around 5%, though that on dynamic trim remain still high (19%). Again that this problem should be attributed to the numerical instability

found in reaching the final dynamic equilibrium. As presented in figure 6 and 7 which resume the result found for all the three simulated speeds, for instance, the trim angle fluctuates around its mean value, with an amplitude of about 0.1 degrees. This fluctuation amplitude well comprises the absolute difference found with the experimental condition, demonstrating the uncertainty level of the numerical results.

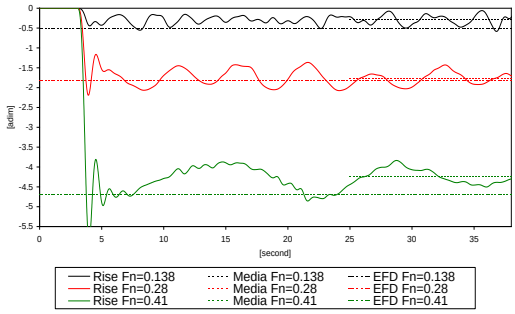

Figure 6: Time histories of rise, obtained on grid 2, at the three test speeds (Fn=0.128, 0.28 and 0.41).

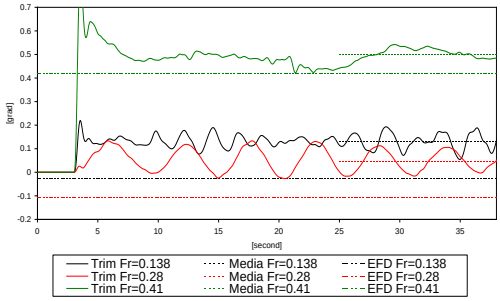

Figure 7: Time angle time histories (grid 2) obtained at the three test speeds (Fn=0.128, 0.28 and 0.41).

5. CONCLUSIONS

A set of unsteady RANSE calculation for the fast displacement hull DTMB5415 of a US Navy combatant (case 3.1 and 3.2 of the G2010 CFD workshop) has been performed with StarCCM+ code and compared against available EFD results. The solver possibility of dealing with unstructured grids and polyhedral cells makes it possible to generate a Cartesian mesh, optimal for reducing the cells number in the far field, while keeping a good definition around the free surface, and the hull surface, where a dense prism layer with hexahedral cells is used in combination with a transition region of trimmed (polyhedral) cells.

The convergence property of the solver with the created mesh typology has been demonstrated using four different grid resolutions from 270k to 6M cells. From this analysis it is possible to conclude that already a mesh with 1M cells reaches the convergence in terms of total resistance prediction.

The validation against available EFD data in fixed attitude, shows a general good agreement is found in terms of predicted wave pattern, with an important exception for the first divergent wave breaking on the bow flare. The oscillating behavior found for the pressure resistance component at the given speed of Fn=0.28 is attributed to the unstable partly wetted regurgitating flow behind the transom, as also confirmed by the scatter of the experimental wave height data found in that area. This together with the non adequate capturing of the first divergent bow wave, could be the reason of the error .

Simulation with free attitude have shown a considerable relative error against experimental data in terms of trim , sinkage and total resistance, but the absolute values of these errors are well inside the amplitude of the wavy time histories obtained as a result of the calculations, which do not damp with simulation time. Some additional investigations are planned to better understand this numerical problem.

6. AKNOWLEDGMENTS

Authors wish to thank the support of the supercomputing center of the Italian District for Marine Technology (formerly owned by SPEDIA). The calculations with finer meshes (grid 0 and 1) have been run on their parallel cluster with more than 100 available processors.

REFERENCES

Brizzolara S., Serra F. (2007) "Accuracy of CFD codes in the Prediction of Planing Surfaces Hydrodyamic Characteristics", Proceedings 2nd International Conference on Marine Research and Transportation. ICMRT'07. ISCHIA. 28-30 June (pp. A-1-A-12), ISBN: 88-901174-3-5.

Brizzolara S., Villa D. (2009), "A systematic CFD Analysis of Flaps / Interceptors Hydrodynamic Performance", Fast 2009 Int. Conference on High Speed Fast Ship Design, Athens. ISBN/ISSN: 9789602546864

Brizzolara S., Gaggero S, Grassi D, Villa D (2009) "CFD Modelling for Powering and Propulsion of Motor Yachts. Recent Developments and Applications of the Marine CFD Group", Proceedings of Design, Construction and Operation of Super and Mega Yachts. Genova Apr. 2009, vol. 1, p. 21-34, ISBN/ISSN: 978-1-905040-56-8

Brizzolara S., Villa D. (2010). "CFD simulations of Planing Hulls", Seventh International Conference on High-Performance Marine Vehicles, HIPER 2010. Melbourne, Florida, USA, 11-15 Oct.

Brizzolara S., Federici A. (2010) "CFD Modelling of Planing Hulls with Partially Ventilated Bottom". the William Froude Conference, Advances in Theoretical and Applied Hydrodynamics, 24-25 Nov. 2010, Portsmouth, UK (RINA), ISBN: 978-1-905040-77-3

Cd-Adapco (2009), "Star-CCM+ User and Theory Manual", version 4.04.011

Ferziger, J.H. and Peric, M., (2002), "*Computational Methods for Fluid Dynamics*", 3rd Ed., Springer Verlag, Berlin, Heidelberg.

Olivieri, A., Pistani. F., Avanaini, A., Stern, F., and Penna, R. (2001), "Towing Tank Experiments of Resistance, Sinkage and Trim, Boundary Layer, Wake, and Free Surface Flow Around a Naval Combatant INSEAN 2340 Model," Iowa Institute of Hydraulic Research, The Univ. of Iowa, IIHR Report No. 421, 56

Longo J., Stern F., (2005) "Uncertainty Assessment for Towing Tank Tests With Example for Surface Combatant DTMB Model 5415", Journal of Ship Research, Volume 49, Number 1, March 2005 , pp. 55-68(14)

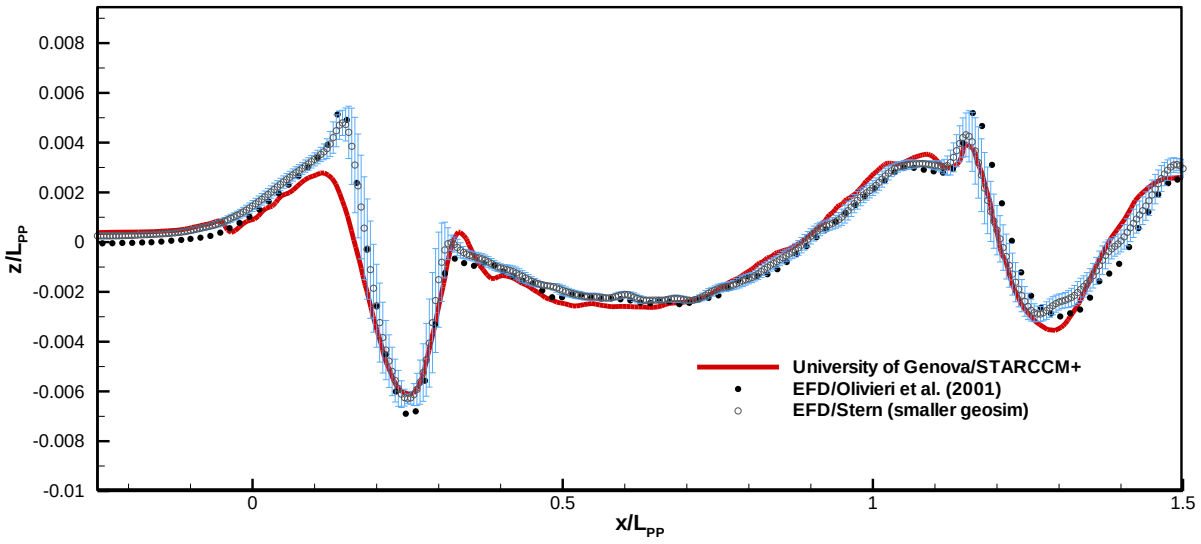

Figure 8: Longitudinal wave profile along the hull: experimental (on two geosims) vs. CFD result (grid 2), Fn=0.28.

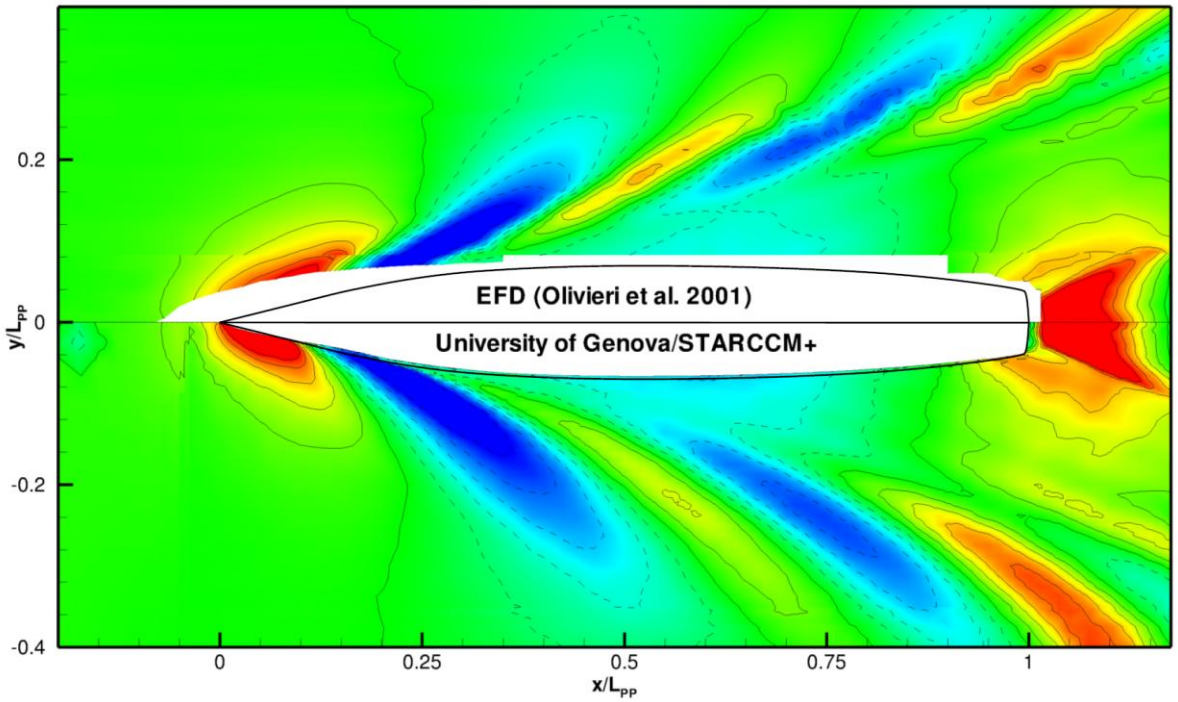

Figure 9: Near field wave pattern at Fn=0.28, fixed trim: experimental (top) vs. CFD (bottom) results.

SIMULATION OF FREE-SURFACE FLOW USING CODE FINFLO FOR KVLCC2 AND KCS CASES

J. Martio (VTT, Finland)
A. Sanchez Caja (VTT, Finland)
T. Sipilä (VTT, Finland)
I. Saisto (VTT, Finland)
T. Siikonen (FINFLO ltd., Finland)

1. SUMMARY

RANS solver FINFLO is used to simulate the turbulent free-surface flow around two ship hulls. FINFLO solves the three-dimensional RANS equations by the method of artificial compressibility. A non-linear free-surface boundary condition is implemented in the code for the treatment of hull flows. Calculations of the KRISO tanker (KVLCC2 model) and the KRISO container ship (KCS) are presented. The k-ω SST turbulence model has been utilized in the computations for both ships and submitted for the comparative study. Measurements from POSTECH and MOERI are available for validation purposes. They include free-surface waves, total resistance and velocities at different locations. Good correlation of resistance coefficients with measurements is obtained for both ships. The predictions of wave profiles are especially good for both cases near the hull.

1.1 Introduction

Since the last workshop held in Gothenburg Larsson, (2000), progress has been made in the use of CFD techniques for simulating the turbulent free-surface flow around modern ship forms. The computing capacity has considerably increased and the CFD methods have been extended to new users.

More than ten years ago the multi-purpose CFD code FINFLO Siikonen, (1996), was taken as the basis for the implementation of a non-linear free-surface boundary condition Sundell, (1997) within a moving grid concept Lehtimäki, (1998). In FINFLO the continuous derivatives in the governing RANS equations are replaced with equivalent finite volume expressions on a cell-centered mesh. A multigrid technique for the acceleration of convergence is included in the code.

The method has been successfully applied to the simulation of bulbous bows moderately piercing the water surface. A computational capability has been added in the code to calculate the trim and sinkage of the ship. Wave fields have been computed in model and full scale, and the effect of the propeller on the wave field has been illustrated Sánchez et al., (2007). An actuator disk model has been used for this purpose, which takes into account the axial and rotational acceleration induced by propeller in terms of body forces. Additionally the code has been extended to be able to handle overlapping grids with Chimera technique. Recently the code includes a multi-phase capability for modeling cavitation Sipilä et al., (2009).

In this paper, the results obtained with the FINFLO code for the proposed ship cases in the workshop are presented.

2. GOVERNING EQUATIONS

On a Cartesian co-ordinate *(x, y, z, t)* system, the RANS equations for an incompressible turbulent flow around a ship can be written in the following formulation:

$$\frac{\partial U}{\partial t} + \frac{\partial F}{\partial x} + \frac{\partial G}{\partial y} + \frac{\partial H}{\partial z} = 0 \qquad (1)$$

where

$$U = \begin{pmatrix} \rho \\ \rho u \\ \rho v \\ \rho w \end{pmatrix} \qquad \begin{aligned} F &= F_i - F_v \\ G &= G_i - G_v \\ H &= H_i - H_v \end{aligned} \qquad (2)$$

and

$$F_i = \begin{pmatrix} \rho u \\ \rho u^2 + \varphi \\ \rho vu \\ \rho wu \end{pmatrix} \quad G_i = \begin{pmatrix} \rho v \\ \rho uv \\ \rho v^2 + \varphi \\ \rho wv \end{pmatrix} \quad H_i = \begin{pmatrix} \rho w \\ \rho uw \\ \rho vw \\ \rho w^2 + \varphi \end{pmatrix}$$

$$F_v = \begin{pmatrix} 0 \\ \tau_{xx} \\ \tau_{xy} \\ \tau_{xz} \end{pmatrix} \qquad G_v = \begin{pmatrix} 0 \\ \tau_{xy} \\ \tau_{yy} \\ \tau_{yz} \end{pmatrix} \qquad H_v = \begin{pmatrix} 0 \\ \tau_{xz} \\ \tau_{yz} \\ \tau_{zz} \end{pmatrix} \qquad (3)$$

F_i, G_i and H_i are the inviscid fluxes; F_v, G_v and H_v are the viscous fluxes; u, v and w are the velocity components; ρ is the density.

The viscous stress tensors, τ_{ij} *(i, j=1, 2, 3)*, are defined as

$$\tau_{ij} = (\mu + \mu_t)\left(\frac{\partial u_i}{\partial x_i} + \frac{\partial u_j}{\partial x_i} - \frac{2}{3}(\nabla \cdot \vec{V})\delta_{ij} \right) \qquad (4)$$

where $\mu = \rho\nu$ and $\vec{V} = u\vec{i} + v\vec{j} + w\vec{k}$ is the kinematic viscosity and δ_{ij} is Kronecker's symbol. μ_t is the turbulent viscosity coefficient.

Based on the method of artificial compressibility, the equation of the state for a compressible fluid is given by

$$\varphi = c_0^2 \rho \qquad (5)$$

with

$$c_0 = \zeta_t \sqrt{u^2 + v^2 + w^2} \qquad (6)$$

where φ is the so-called piezometric pressure, c_0 is the artificial compressibility coefficient and ζ_t is constant.

Additionally the code has been extended to include the pressure-correction method.

2.1 Numerical solution

The treatment of the boundary layer near the free surface has been improved to correct the missing physics near the solid walls. The implicit time integration is used to solve the wave height. For the bulk flow, the inviscid fluxes and the viscous fluxes are evaluated by the use of the Roe's method, and a thin-layer approximation. The DDADI-factorization with a local time step is applied to update the solution vectors, and the convergence rate is improved by the V-cycle of the multigrid method. The wave height on the free surface is iteratively updated and the pressure is enforced to be constant. The grid points are redistributed at each iteration following a 3D background grid that extends to the air region. The solution is advanced until a steady state solution is reached.

3. INITIAL AND BOUNDARY CONDITIONS

Free stream pressure, uniform flow and flat free surface are set as initial conditions. The boundary conditions are as follows.

On the free surface, three components of the velocities *(u, v, w)* are extrapolated with zero-gradient normal velocity, i.e.

$$\frac{\partial u}{\partial n} = \frac{\partial v}{\partial n} = \frac{\partial w}{\partial n} = 0 \qquad (7)$$

A two-dimensional hyperbolic wave equation is evaluated for the wave height h on the actual location of the free surface,

$$\frac{\partial \rho h}{\partial t} + \nabla \cdot \rho \vec{V} h = \rho w \,. \qquad (8)$$

The boundary condition for the piezometric pressure is obtained as

$$\varphi = \rho g h \,. \qquad (9)$$

On the wetted part of the hull surface, no slip conditions are imposed, and a second order extrapolation is applied for the evaluation of the wall pressure. Uniform flow is specified at the external boundary. Mirror conditions for all variables are employed on the center-plane.

In the transom stern region, wetted- and dry-transom models are implemented for the KVLCC2 and the KCS model, respectively. For the latter, the flow is enforced to detach from transom edge as long as the wave height grows above the edge. Since the interpolation is restricted within a very small range off the transom, the approximation does not seriously affect the transom wake flow.

4. COMPUTATIONAL CONDITIONS

The computational conditions for the KVLCC2 and the KCS model correspond to the measurements from MOERI (see Table 1). For the present flow conditions, the transom is partially wetted for both ships. For the KVLCC2 hull a wetted transom model has been selected for the computations. However, for the KCS as the design waterline is located below the transom, it seemed more convenient to apply a dry-transom model. Some inaccuracies are, therefore, expected for the flow at the transom. The computations were performed with fixed sinkage and trim. For the resistance computations the rudder is modeled with the overlapping grid technique.

Different grids with a refinement ratio ranging from 0.39 to 2 are used for both the KVLCC2 and the KCS. Views of the fine grids are shown in Fig. 1, where an O-O topology is employed for both cases.

Table 1 Computational conditions and grids for the KVLCC2 and KCS models.

	KVLCC2	KCS
F_n	0.142	0.26
R_n	4.6×10^6	1.4×10^7
Fine mesh	5505024	4147200
y^+	about 1.0	about 1.0

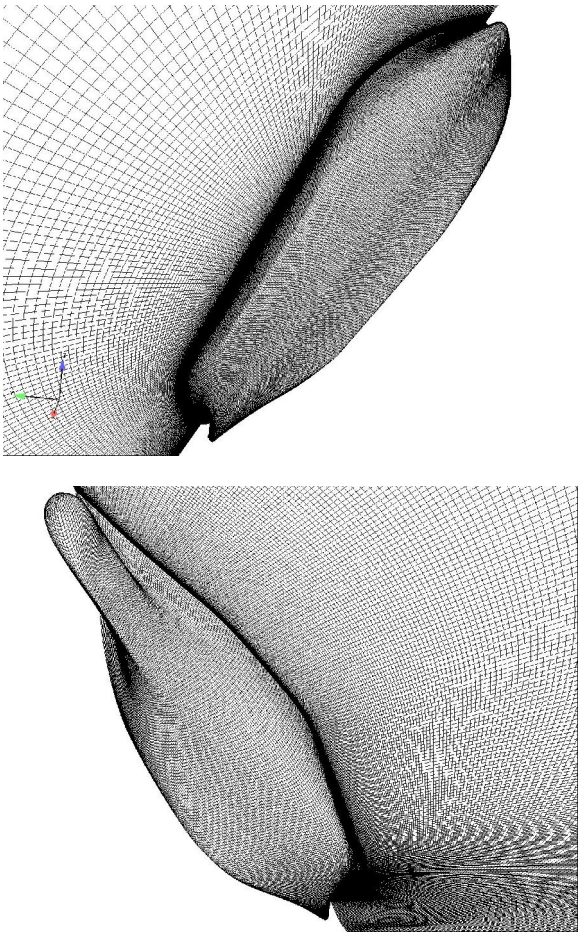

Fig.1 Views of the fine meshes. Upper: KVLCC2 model. Lower: KCS model

The Chimera grid used for the rudder is shown in Fig 2. The mesh consisted of seven blocks. Due the late delivery of the rudder geometry the calculations were conducted with geometry slightly different from the final one, keeping the same wetted area.

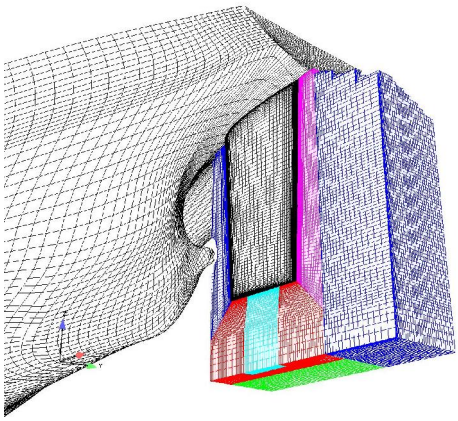

Fig.2 The rudder grid for the KVLCC2 modeled with Chimera technique

5. RESULTS

Figures 3-4 displays the two surface-wave cuts for both vessels. The wave profiles are close to measurements especially at locations close to the hull. However, the wave pattern is somewhat damped far from the hull. Some wave dispersion is seen downstream the hull for the KCS case.

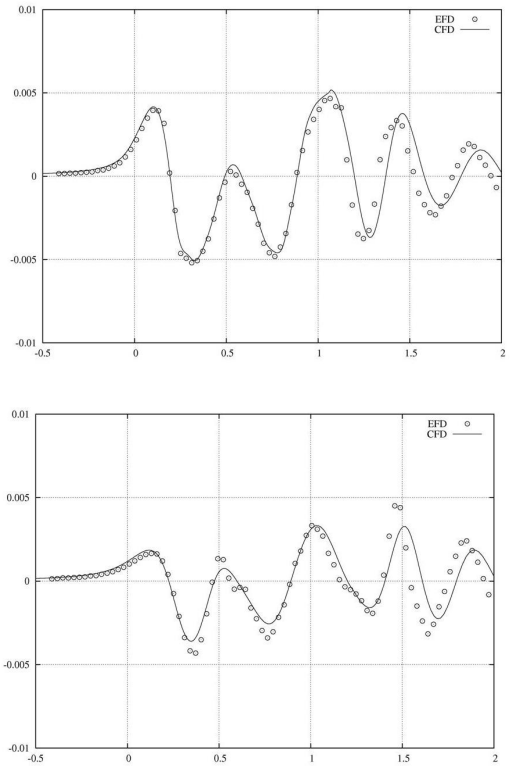

Fig.3 Calculated and experimental longitudinal wave cuts at y/Lpp=0.0741 (above) and y/Lpp=0.1509 (below) for the KCS hull.

Figure 4 shows the corresponding wave profiles for the tanker. For this case, the average wave system is captured reasonably well. Far away from the hull, details of wave patterns are not well detected.

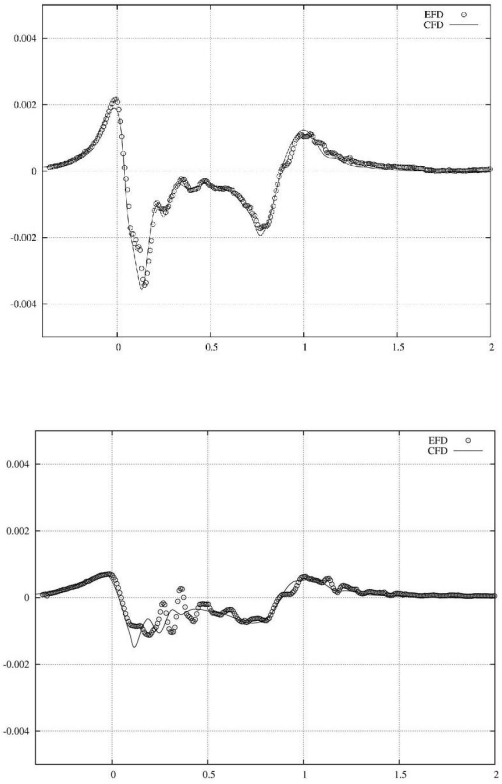

Fig.4 Calculated and experimental longitudinal wave cuts at y/Lpp=0.0964 (above) and y/Lpp=0.1581 (below) for the KVLCC2 hull.

The measured and computed velocity components on the propeller plane along a reference line are shown in Fig. 5 for the KCS case. The k-ω SST turbulence model was used. Trends are reasonably captured even though some differences are visible.

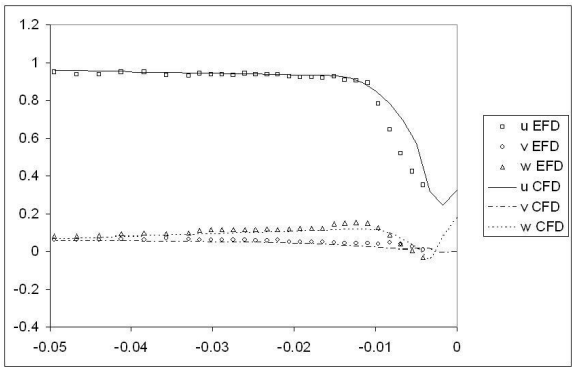

Fig.5 Velocity at the propeller plane (x/LPP= 0.9825) using the k-ω SST model. KCS

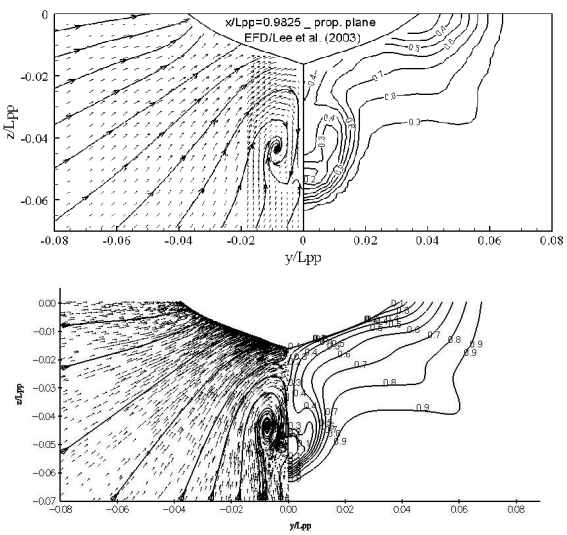

Fig.6 U contours (right panel), cross flow vectors and streamlines (left panel) at propeller plane (x/Lpp =0.9825) for KVLCC2. (Above measurements, below computations).

The velocity contours for the KVLCC2 at the propeller plane are shown Fig. 6. The measured hook-type wake pattern is partially captured even though more grid resolution could have improved the results. The calculations were made in air domain, i.e. using the compressible flow, in order to match the wind tunnel measurements. The utilized O-O-topology has not been fully optimized for wake evaluation. The k-ω SST turbulence model was applied also to the KVLCC2 case.

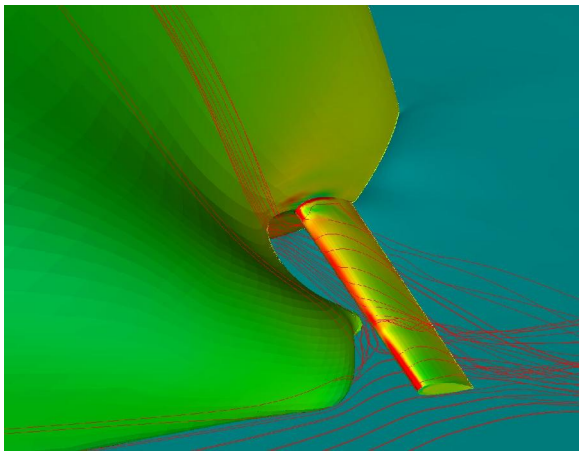

Fig.7 The computed pressure distribution and streamlines around the rudder (KVLCC2)

The calculated pressure distribution and streamlines are presented in Fig. 7 in perspective view. The rudder configuration was applied for the resistance computations. The calculated resistance coefficients with nine different grids are shown in Table 2 as well as an error comparison to measurements.

Table 2 The computed resistance coefficients and comparison error to experimental resistance coefficients

S (grid5~grid1)	4.416	4.464	4.398	4.191	4.216
$E\%D$	-7.45	-8.61	-7.01	-1.97	-2.58
S (grid9~grid6)		6.241	5.225	5.009	4.889
$E\%D$		-51.85	-27.14	-21.87	-18.96

6. CONCLUSION

The flow around two ship hulls has been simulated using the FINFLO RANS-code. The simulations were carried out with k-ω SST turbulence model. The wake patterns have been computed more accurately than in the year 2000 workshop held in Gothenburg due mainly to the use of finer grids. This has been possible thanks to the increase of computational power.

The wave systems were also well captured near the hull, which is especially important for the resistance predictions. At low Froude number it is difficult to obtain the wave system with accuracy far away from the hull.

REFERENCES

Larsson, L., Stern, F. and Bertram, V., (2003), "Benchmarking of Computational Fluid Dynamics for Ship Flows: the Gothenburg 2000 Workshop", *Journal of Ship Research*, Volume 47, No 1, March

Lehtimäki R., 1998, *Grid deformation tools for simulation of free surface flows*, In 6th International Conference on Numerical Field Simulation, London.

Sanchez-Caja, A. & Pylkkänen, J. V., Prediction of Effective Wake at Model and Full Scale Using a RANS Code with an Actuator Disk Model, *2nd International Conference on Maritime Research and Transportation* Ischia, Italy, June 2007

Siikonen T., 1996, *FINFLO user guide*, version 2.2, Laboratory of Applied Thermodynamics, Helsinki University of Technology, Finland.

Sipilä et al., *Cavitating Propeller Flows Predicted by RANS Solver with Structured and Small Reynolds Number Turbulence Model Appraoch*, Proceedings of the 7th International Symposium on Cavitation, Ann Arbor, Michigan, USA, 2009

Sundell, T. 1997. *Computations of the Free-Surface Flow Around a Ship Using NS Solver FINFLO*. VTT Technical Report M-206, VALB279, Finland.